ACCSCIENCE PUBLISHING

International Journal of BIOPRINTING

ACCSCIENCE PUBLISHING PTE. LTD.
Volume 9 Issue 6 (October 2023)
ISSN: 2424-8002 (online) ISSN: 2424-7723 (print)

ACCSCIENCE PUBLISHING

International Journal of Bioprinting

Print ISSN: 2424-7723

Online ISSN: 2424-8002

International Journal of Bioprinting is an international journal covering the technology, science and clinical application of the broadly defined field of Bioprinting. Bioprinting is defined as the use of 3D printing technology with materials that incorporate viable living cells or biological elements to produce tissue or biotechnological products. We are interested in the scientific topics spanning all stages of bioprinting process from concept creation to fabrication and beyond.

Scan to access website:

Scan to submit papers:

About the Publisher

AccScience Publishing is a publishing company based in Singapore. We publish a range of high-quality, open-access, peer-reviewed journals and books from a broad spectrum of disciplines.

Contact Us

Editorial Assistant
Puvanesswaray Ramakrishnan,
editor.ijb@accscience.com

AccScience Publishing
8 Burn Road, #15-03 Trivex, Singapore 369977.

Volume 9 • Issue 6 • October 2023
ISSN 2424-7723 (print) ISSN 2424-8002 (online)

INTERNATIONAL JOURNAL OF BIOPRINTING

Editor-in-Chief
Chee Kai Chua
Singapore University of Technology and Design, Singapore

ACCSCIENCE PUBLISHING

Full issue copyright © 2023 AccScience Publishing
All rights reserved. Without permission in writing from the publisher, this full issue publication in its entirety may not be reproduced or transmitted for commercial purposes in any form or by any means, electronic or mechanical, including photocopying, recording, or any information storage and retrieval system. Permissions may be sought from ijb.office@accscience.sg.

Article copyright © Respective Author(s)
See articles for copyright year. All articles in this full issue publication are open-access. There are no restrictions in the distribution and reproduction of individual articles, provided the original work is properly cited. However, permission to reuse copyrighted materials of an article for commercial purposes is applicable if the article is licensed under Creative Commons Attribution-NonCommercial License. Check the specific license before reusing.

INTERNATIONAL JOURNAL OF BIOPRINTING

ISSN: 2424-7723 (print)
ISSN: 2424-8002 (online)

Editorial and Production Credits

Publisher: AccScience Publishing
Managing Editor: Cathy Huang
Editorial Assistants: Puva Ramakrishnan, Flora Kang
Production Editors: Puva Ramakrishnan, Ian Wong
Special Issue Commissioning Editor: Cathy Huang
Article Layout and Typeset: BSMART Publishing (India)
Cover Design: BUTTON GRAPHIC DESIGN STUDIO (Malaysia)

For all advertising queries, contact ijb.office@accscience.sg.

Supplementary file

Supplementary files of articles can be obtained at https://accscience.com/journal/IJB/9/6.

About the Cover

Printing of a construct in action

Disclaimer

AccScience Publishing is not liable to the statements, perspectives, and opinions contained in the publications. The appearance of advertisements in the journal shall not be construed as a warranty, endorsement, or approval of the products or services advertised and/or the safety thereof. AccScience Publishing disclaims responsibility for any injury to persons or property resulting from any ideas or products referred to in the publications or advertisements. AccScience Publishing remains neutral with regard to jurisdictional claims in published maps and institutional affiliations.

International Journal of Bioprinting

Editorial Board

Editor-in-Chief

Chee Kai Chua
Singapore University of Technology and Design, Singapore

Associate Editors

Maling Gou
Sichuan University, China

Jiankang He
Xi'an Jiaotong University, China

Liliang Ouyang
Tsinghua University, China

Wai Yee Yeong
Nanyang Technological University, Singapore

Assistant Editor

Jia An
Singapore University of Technology and Design, Singapore

*Editorial Board Members**

Shweta Agarwala, *Denmark*
Paulo Jorge Da Silva Bartolo, *Singapore*
Charlotte Hauser, *Saudi Arabia*
Anthony Atala, *USA*
Eben Alsberg, *USA*
Andrea Barbetta, *Italy*
Mario Moisés Alvarez, *Mexico*
Aldo R. Boccaccini, *Germany*
Jason A. Burdick, *USA*
Richard James Bibb, *UK*
Martin Birchall, *UK*
Christian Celia, *Italy*
Boris Chichkov, *Germany*
Douglas B. Chrisey, *USA*
Jeremy Crook, *Australia*
Tal Dvir, *Israel*
Rui Domingues, *Portugal*
Eleonora Ferraris, *Belgium*
Elena Martínez Fraiz, *Spain*
Gunter Finkenzeller, *Germany*
Brunella Grigolo, *Italy*
Nikolaos Michailidis, *Greece*
Manuela Gomes, *Portugal*
Yongqiang Hao, *China*
Dong Nyoung Heo, *South Korea*
Mei He, *USA*
Ali Khademhosseini, *Japan*
Dimitrios A. Lamprou, *UK*
Khoon Lim, *Australia*
Laurence Meagher, *Australia*
Vladimir Mironov, *Russia*
Ali Nokhodchi, *UK*
Insup Noh, *South Korea*
Makoto Nakamura, *Japan*
Roger Narayan, *USA*
Joaquim Miguel Oliveira, *Portugal*
Aleksandr Ovsianikov, *Austria*
Alokesh Pramanik, *Australia*
Sang-Hyug Park, *South Korea*
Michael Raghunath, *Switzerland*
Jie Sun, *China*
Thomas Scheibel, *Germany*
Shinji Sakai, *Japan*
Kedong Song, *China*
Cijun Shuai, *China*
Ergün Süleyman, *Germany*
Savas Tasoglu, *Turkey*
Giovanni Vozzi, *Italy*
Sanjairaj Vijayavenkataraman, *UAE*
Seung-Schik Yoo, *USA*
Barbara Zavan, *Italy*
Yi Zhang, *China*
Yu Shrike Zhang, *USA*
Liqiang Wan, *China*
Sanjay Garg, *Australia*
Mikhael Bechelany, *France*
Fengyuan Liu, *UK*
Jingchao Jiang, *China*
Swee Leong Sing, *Singapore*
Amit Bandyopadhyay, *USA*
Gianluca Ciardelli, *Italy*
Maurice N Collins, *Ireland*
Dennis Douroumis, *UK*
Hyun-Do Jung, *South Korea*
Qing Jiang, *China*
Geun Hyung Kim, *South Korea*
David K. Mills, *USA*
Veronica MacChi, *Italy*
Ibrahim Tarik Ozbolat, *USA*

*Editorial Board Members as of October 18, 2023

ACCSCIENCE PUBLISHING

Volume 9 | Issue 6 | October 2023 | Page 1 – 565 |

International Journal of Bioprinting

https://accscience.com/journal/IJB

CONTENTS

1 **Electrospinning polyethylene terephthalate glycol** *RESEARCH ARTICLE*
Mohamed H. Hassan, Abdalla M. Omar, Evangelos Daskalakis, Bruce Grieve, Paulo J.D.S. Bartolo

11 **Computational fluid dynamics for the optimization of internal bioprinting parameters and mixing conditions** *RESEARCH ARTICLE*
Gokhan Ates, Paulo Bartolo

26 **Printed cisplatin on microneedle arrays for transdermal delivery enhances olaparibinduced synthetic lethality in a mouse model of homologous recombination deficiency** *RESEARCH ARTICLE*
Zoi Kanaki, Alexandra Smina, Chrysoula Chandrinou, Fotini E. Koukouzeli, Yiannis Ntounias, Nikolaos Paschalidis, Ilias Cheliotis, Marina Makrygianni, Jill Ziesmer, Georgios A. Sotiriou, Ioanna Zergioti, Constantin Tamvakopoulos, Apostolos Klinakis

40 **Sub-regional design of the bionic bone scaffolds using macrostructural topology** *RESEARCH ARTICLE*
Yangdong He, Long Chao, Chen Jiao, Hong Wang, Deqiao Xie, Guofeng Wu, Lin Wang, Changjiang Wang, Jianfeng Zhao, Lida Shen, Huixin Liang

57 **3D Aerosol Jet® printing for microstructuring: Advantages and Limitations** *RESEARCH ARTICLE*
Miriam Seiti, Olivier Degryse, Rosalba Monica Ferraro, Silvia Giliani, Veerle Bloemen, Eleonora Ferraris

75 **Organoid bioprinting strategy and application in biomedicine: A review** *REVIEW ARTICLE*
Chen He, Jiasheng Yan, Yusheng Fu, Jiuchuan Guo, Yuxing Shi, Jinhong Guo

96 **Development of an affordable extrusion 3D bioprinter equipped with a temperature controlled printhead** *RESEARCH ARTICLE*
Carlos Ezio Garciamendez-Mijares, Gilberto Emilio Guerra-Alvarez, Mónica Gabriela Sánchez-Salazar, Andrés García-Rubio, Germán García-Martínez, Anne-Sophie Mertgen, Carlos Fernando Ceballos-González, Edna Johana Bolivar-Monsalve, Yu Shrike Zhang, Grissel Trujillo-de Santiago, Mario Moisés Alvarez

110 **Exosome-based bioinks for 3D bioprinting applications in tissue engineering and regenerative medicine** *REVIEW ARTICLE*
Qian Wang, Yang Liu, Shuqing Zhang, Fan He, Tong Shi, Jizong Li, Zhimin Wang, Jia Jia

132 **3D-printed hydrogels dressings with bioactive borate glass for continuous hydration and treatment of second-degree burns** *RESEARCH ARTICLE*
Fateme Fayyazbakhsh, Michael J. Khayat, Candy Sadler, Delbert Day, Yue-Wern Huang, Ming C. Leu

151 **Advances of 3D printing in gastroenterology and where it might be going** *REVIEW ARTICLE*
Yuhang Zhang, Liuxiang Chen, Bing Hu

171 **Biomechanical evaluation of an anatomical bone plate assembly for thin patella fracture fixation fabricated by titanium alloy 3D printing** *RESEARCH ARTICLE*
Chi-Yang Liao, Shao-Fu Huang, Wei-Che Tsai, Yu-Hui Zeng, Chia-Hsuan Li, Chun-Li Lin

187 **The attractiveness of 4D printing in the medical field: Revealing scientific and technological advances in design factors and applications** *RESEARCH ARTICLE*
Angelica A. Martinez-De-Anda, Marisela Rodriguez-Salvador, Pedro F. Castillo-Valdez

200 **3D bioprinting and scaffold-free strategies for fabrication of multi-cellular tissues or organoids** *REVIEW ARTICLE*
Haoyu Li, Huixing Zhou, Chongwen Xu, Yen Wei, Xiuying Tang

222 **Bioprinting technology for the management of diabetic foot disease: Emerging applications, challenges, and prospects** *REVIEW ARTICLE*
Fan Xu, Shunli Rui, Cheng Yang, Xiaoyan Jiang, Wei Wu, Xianlun Tang, David G. Armstrong, Yu Ma, Wuquan Deng

239 **Recent progress on 3D-printed gelatin methacrylate-based biomaterials for articular cartilage repair** *REVIEW ARTICLE*
Liang Chen, Guowei Huang, Ming Yu, Yang Liu, Tao Cheng, Aiguo Li, Wen Wang, Shengnan Qin

257 **3D bioprinting for vascular grafts and microvasculature** *REVIEW ARTICLE*
Junpeng Zhu, Xinwang Wang, Lin Lin, Wen Zeng

273 **3D bioprinting for auricular reconstruction: A review and future perspectives** *REVIEW ARTICLE*
Anna Onderková, Deepak M. Kalaskar

308 **Rheology-informed hierarchical machine learning model for the prediction of printing resolution in extrusion-based bioprinting** *RESEARCH ARTICLE*
Dageon Oh, Masoud Shirzad, Min Chang Kim, Eun-Jae Chung, Seung Yun Nam

325 **3D printing and bioprinting in urology** *REVIEW ARTICLE*
Kun Liu, Nan Hu, Zhihai Yu, Xinzhou Zhang, Hualin Ma, Huawei Qu, Changshun Ruan

343 **Melt electrospinning writing PCL scaffolds after alkaline modification with outstanding cytocompatibility and osteoinduction** *RESEARCH ARTICLE*
Yubo Shi, Lei Wang, Liguo Sun, Zhennan Qiu, Xiaoli Qu, Jingyi Dang, Zhao Zhang, Jiankang He, Hongbin Fan

361 **3D bioprinting-based single liver tumor spheroid analysis for aflatoxin B1-induced drug-resistant cancer cell** *RESEARCH ARTICLE*
Viet Phuong Cao, Sera Hong, Joon Myong Song

373 **Biomimetic 3D bioprinting approaches to engineer the tumor microenvironment** *REVIEW ARTICLE*
Fabiano Bini, Salvatore D'Alessandro, Tarun Agarwal, Daniele Marciano, Serena Duchi, Enrico Lucarelli, Giancarlo Ruocco, Franco Marinozzi, Gianluca Cidonio

391 **Advancements in biomaterials and biofabrication for enhancing islet transplantation** *REVIEW ARTICLE*
Dayoon Kang, Jaewook Kim, Jinah Jang

413 **Lightweight load-bearing heat dissipation multifunctional pomelo peel-inspired structures fabricated by laser powder bed fusion** *RESEARCH ARTICLE*
Linxuan Li, Dongdong Gu, He Liu, Han Zhang, Junhao Shan, Yijuan Zhang

436 **Multiscale 3D bioprinting for the recapitulation of lung tissue** *REVIEW ARTICLE*
Pengbei Fan, *Fanli Jin*, *Yanqin Qin*, *Yuanyuan Wu*, *Qingzhen Yang*, *Han Liu*, *Jiansheng Li*

450 **Evaluation of a synthetic peptide-based bioink (PeptiInk Alpha 1) for in vitro 3D bioprinting of cartilage tissue models** *RESEARCH ARTICLE*
Patricia Santos-Beato, *Andrew A. Pitsillides*, *Alberto Saiani, Aline Miller*, *Ryo Torii, Deepak M. Kalaskar*

466 **Bioprinting of cell-laden protein-based hydrogels: From cartilage to bone tissue engineering** *REVIEW ARTICLE*
Mehran Khajehmohammadi, *Negar Bakhtiary*, *Niyousha Davari*, *Soulmaz Sarkari*, *Hamidreza Tolabi, Dejian Li*, *Behafarid Ghalandari*, *Baoqing Yu*, *Farnaz Ghorbani*

502 **Uncovering advances in final end-user applications, user acceptability, quality assurance, and digital technologies for 3D-printed oral drug delivery systems** *RESEARCH ARTICLE*
Veronica L. Rios-Mata, *Marisela Rodriguez-Salvador, Jia An*, *Chee Kai Chua*, *Pedro F. Castillo-Valdez*

524 **Strontium-doped calcium silicate scaffolds with enhanced mechanical properties and tunable biodegradability fabricated by vat photopolymerization** *RESEARCH ARTICLE*
Yinjin L, *Jin Su*, *Annan Chen*, *Yifei Li*, *Xi Yuan*, *Kezhuo Chen*, *Zhaoqing Li*, *Chunze Yan*, *Jian Lu*, *Yusheng Shi*

539 **3D printing of PCL-ceramic composite scaffolds for bone tissue engineering applications** *RESEARCH ARTICLE*
Santosh Kumar Parupelli, *Sheikh Saudi*, *Narayan Bhattarai*, *Salil Desai*

552 **Enhanced osteogenesis and bactericidal performance of additively manufactured MgOand Cu-added CpTi for load-bearing implants** *RESEARCH ARTICLE*
Sushant Ciliveri, *Amit Bandyopadhyay*

ACCSCIENCE PUBLISHING

International Journal of Bioprinting

RESEARCH ARTICLE

Electrospinning polyethylene terephthalate glycol

Mohamed H. Hassan[1]*, Abdalla M. Omar[1], Evangelos Daskalakis[1], Bruce Grieve[2], and Paulo J.D.S. Bartolo[1,3]

[1]Department of Mechanical, Aerospace and Civil Engineering, University of Manchester, Manchester, M13 9PL, United Kingdom

[2]Department of Electrical and Electronic Engineering, The University of Manchester, Manchester M13 9PL, United Kingdom

[3]Singapore Centre for 3D Printing, School of Mechanical and Aerospace Engineering, Nanyang Technological University, Singapore 639798, Singapore

Abstract

Polyethylene terephthalate glycol (PETG) is a difficult-to-spin material, and no previous papers have reported the correct conditions to create PETG meshes. To address this issue, a preliminary study on the solubility and electrospinnability of PETG using a range of solvent system was conducted and a Teas graph was established to select the ideal solvent system. Based on these preliminary results, electrospun PETG fibers were produced using a highly volatile binary solvent system consisting of dichloromethane (DCM) and trifluoroacetic acid (TFA). Produced meshes were extensively characterized, and the results demonstrated for the first time the ability of electrospun PETG meshes to support the inoculation and germination of yellow rust spores, thus confirming that PETG is an ideal material to be used for the fabrication of agriculture biosensors. The results also showed that the best solvent split was 85/15 (DCM/TFA).

Keywords: Electrospinning; Biomaterial; Yellow rust; Polyethylene terephthalate glycol; bioactive

***Corresponding author:**
Mohamed H. Hassan (mohamed.hassan@manchester.ac.uk)

Citation: Hassan MH, Omar AM, Daskalakis E, *et al*., 2023, Electrospinning polyethylene terephthalate glycol. *Int J Bioprint,* 9(6): 0024.
https://doi.org/10.36922/ijb.0024

Received: January 26, 2023
Accepted: March 05, 2023
Published Online: June 21, 2023

Copyright: © 2023 Author(s). This is an Open Access article distributed under the terms of the Creative Commons Attribution License, permitting distribution, and reproduction in any medium, provided the original work is properly cited.

Publisher's Note: AccScience Publishing remains neutral with regard to jurisdictional claims in published maps and institutional affiliations.

1. Introduction

Solution electrospinning is a simple electrostatic and versatile technique to produce micro- to nano-scale fiber meshes exhibiting large surface area to volume ratio[1-4]. In this process, a polymeric solution is ejected from a needle tip, positioned at a specific height over a grounded collector, by applying a high electrical field[5]. Typically, an electrospinning system consists of a high-voltage power supply, a capillary that includes the material container and a spinneret, and a grounded metal collector. The process starts by applying an electrical field between the needle tip and the metallic collector. A material droplet is formed at the end of the needle tip because of surface tension and viscoelastic stresses[6]. When the electrostatic forces overcome the surface tension of the material, the material droplet approaches a cone shape (Taylor cone), and a charged jet is ejected[7]. Then, the jet follows a path that is usually characterized by an initial stable region, where the fiber is parallel to the direction of the jet and its

diameter decreases monotonically by increasing the distance from the tip[5]. Afterward, the jet starts to coil and undergo bending instabilities that further reduces the fiber diameter. Fibers produced by electrospinning presents a large control over the fiber diameters, ranging from nano- to micro-meters[8,9]. These fibers compared to microfibers produced by other conventional spinning techniques, including melt spinning, dry spinning, and wet spinning, have significantly reduced diameters, thus increasing the specific surface area of the produced structures[10,11]. These distinctive features led to electrospinning being used for a range of applications such as support structures for cell attachment, proliferation, and differentiation[5,6,12,13], wound dressings[14,15], and sensing membranes[16,17]. Electrospinning was reported to be a viable technique for the encapsulation of cells, thus allowing the fabrication of cell-laden structures[18,19]. Modular systems, combining solution electrospinning and other additive manufacturing techniques such as extrusion, have been also proposed for the fabrication of hierarchical constructs[4,20,21]. In this work, electrospinning is investigated as a potential technology to produce the upper layer of the proposed biosensor for the early detection of yellow rust. The proposed biosensor consists of three layers, where the first layer imitates the morphology of wheat leaf, the second layer is the substrate layer where sucrose and agar are used as a feeding media for the germinate spore, and finally the third layer is made up of a nonenzymatic glucose sensor which is used to detect the glucose produced by the interaction between the invertase produced by the germinated spores and the substrate layer[22]. As electrospinning allows to produce meshes with high surface area, this will increase the capability to support pathogen inoculation and germination.

In previous work, it was also shown that polyethylene terephthalate glycol (PETG) is an ideal material for the fabrication of the upper layer due to its shape changing properties, biodegradability, and ability to support cell attachment and proliferation, suggesting a similar behavior regarding the yellow rust[23,24]. However, PETG has low solubility in most solvents, which are also usually highly volatile, making it difficult for electrospinning.

In this study, we investigated for the first-time the fabrication of electrospun PETG meshes. A preliminary study on the solubility and electrospinnability of PETG using a range of solvent systems was conducted, and a Teas graph was established to select the ideal solvent system. Based on these preliminary results, electrospun PETG fibers were produced and extensively characterized. The results also demonstrated for the first time the ability of electrospun PETG meshes to support the inoculation and germination of yellow rust spores, thus confirming that PETG is an ideal material to be used in the proposed biosensor. *Puccinia striiformis* f. sp. *tritici* is a causative fungal pathogen that causes wheat yellow rust, which is currently a global epidemic responsible for reduction in the wheat yield. Using sensing systems to detect such diseases can help in taking preventative actions to reduce its effect.

In this work, we also investigated for the first-time producing PETG meshes via electrospinning, investigated effects of different solvent splits on meshes quality, and optimized the electrospinning process parameters. Electrospinning is used as a proof of concept for future production of PETG meshes using more advanced techniques such as electrohydrodynamic printing (EHDP)[25]. Furthermore, the meshes bioactivity was assessed by growing yellow rust spores to prove the concept of usage in sensing systems.

2. Materials and methods

2.1. Materials

Polymeric electrospun meshes were produced using PETG with molecular weight of 300 g/mol purchased from RS components (Northants, UK). Solutions were prepared using acetic acid (AA; glacial, ACS reagent ≥99.7%), acetone (ACE; ACS reagent ≥99.5%), ethanol (ETH; 98%), dimethyl sulfoxide (DMSO; ACS reagent ≥99.9%), dimethylformamide (DMF; ACS reagent ≥99.8%), tetrahydrofuran (THF; ACS reagent ≥99.0%), dichloromethane (DCM; containing 40-150 ppm amylene as stabilizer, ACS reagent, ≥99.5%), and trifluoroacetic acid (TFA; 99%), which were all purchased from Sigma Aldrich (Dorset, UK).

2.2. Mapping spinnability–solubility of PETG on the Teas graph

The solubility of PETG in the different solvents was investigated using the Teas graph to identify the fractional cohesion parameters of solvents (hydrogen bonding, polar force, and dispersion force)[26-29]. Solubility was tested at 20% w/v polymer concentration, atmospheric pressure, and room temperature (20°C). Briefly, 2 g of PETG were added to 10 mL of single solvent systems (AA, ACE, ETH, DMSO, DMF, THF, DCM, or TFA) and binary solvent systems (DCM/DMF, DCM/AA, DCM/THF, or DCM/TFA). The mixture was stirred with a magnetic stirring bar at room temperature. The process was visually assessed after 1 h, 2 h, and 4 h. Then, solubilities were categorized as insoluble (no dissolution), partially soluble (dissolution achieved but at lower rate or lower capacity), and soluble (quick and complete dissolution), based on the time to form a homogeneous solution. The binary solvent systems were also identified and calculated using the lever rule assuming 1:1 ratio[30]. Finally, the solubility results of the binary solvent systems were compared to the single solvent

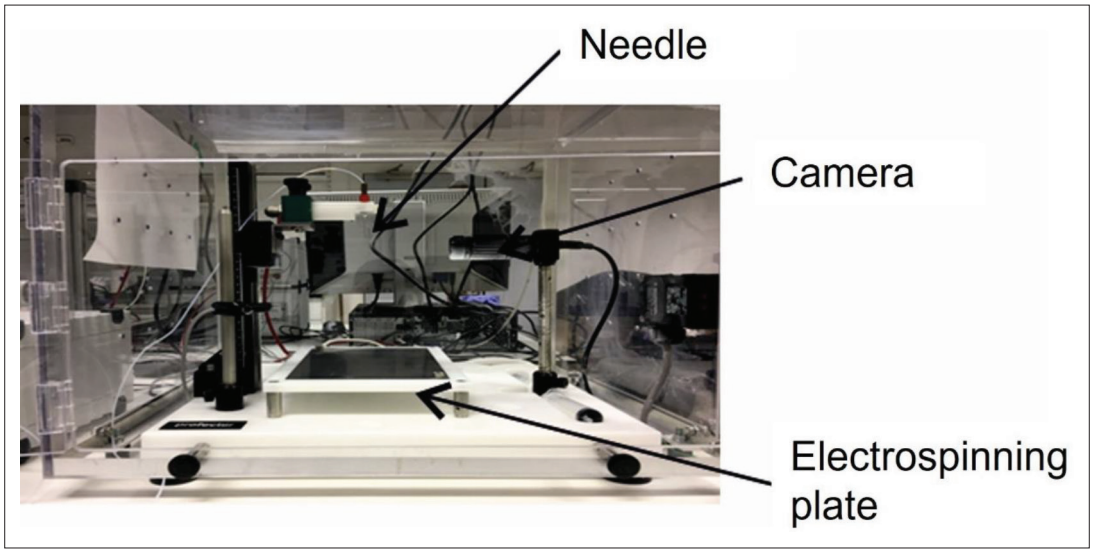

Figure 1. Electrospinning setup

systems on the Teas graph, and then the solubility region was constructed.

2.3. Mesh fabrication

Based on the solubility results, PETG (20% w/v) was dissolved in different splits of DCM/TFA (85/15, 70/30, 60/40, 50/50, 40/60, 30/70, 15/85 [% v/v]), and electrospun using solution electrospinning (Spraybase, Ireland) (Figure 1). Meshes were produced at room temperature with a voltage of 16 kV, a feed flow rate of 4 mL/h, a humidity of 45% (±5%), and a distance between the needle tip and the collector, which was covered with aluminum foil, of 150 mm. Finally, the obtained meshes were dried in vacuum for 48 hours to ensure the complete removal of solvents. These were considered the optimized parameters. Voltage values lower than 16 kV did not enable the formation of a stable jet but only caused a dropping effect, while values higher than 16 KV induced electrospraying. Moreover, flow rate values lower than 4 mL/h induced a fast evaporation of the solvent blocking the needle, while values above 4 mL/h caused a dropping effect.

2.4. Morphological analysis

The morphology of produced meshes was characterized using the scanning electron microscopy (SEM). For SEM, Quanta 650 (FEI company, Hillsboro, Oregon, USA) was used, all meshes were sputter coated with gold/palladium (Au/Pd (80/20)) using Quorum sputter coater (Quorum tech, east Sussex, UK). Imaging was carried out using an acceleration voltage of 15 kV. The obtained images were analyzed using the ImageJ software (Laboratory for Optical and Computational Instrumentation, University of Wisconsin, WI, USA), allowing to determine fiber diameter. For each mesh type, a total of 9 measurements were considered.

2.5. Chemical composition characterization

The chemical composition of produced meshes was analyzed using Fourier-transform infrared spectroscopy (FTIR) and Raman spectroscopy. FTIR was conducted using Varian 670-IR spectrometer (Agilent Technologies, CA, USA). Each sample was scanned 20 times at the resolution of 1 cm^{-1}, over a frequency scanning range from 800 to 3100 cm^{-1}. Raman spectroscopy was carried out using Renishaw inVia confocal Raman microscope (Renishaw Plc., Gloucestershire, UK) using laser (532 nm) with a grating of 1200 g/mm in a regular mode and use of 50× magnification on the microscope.

2.6. Inoculation

The ability of the electrospun meshes to sustain pathogen attachment and germination was assessed using the yellow rust spores' inoculation process. The meshes were placed in a tray in a stainless-steel pipe, simulating a wind tunnel. The spores were released in the pipe, landing on the meshes at the bottom of the pipe. The meshes were kept in the pipe for 15–30 min, ensuring that all spores have settled on the surfaces. Then, the inoculated surfaces were imaged under a light microscope to make sure that the spores were attached. Finally, the meshes were placed in the Innova 44 incubator (Eppendorf, Hamburg, Germany) set at 7°C for 24 h.

3. Results and discussion

3.1. Solubility and electrospinnability

Solubility, which describes how easy it is to dissolve the polymer in a solvent, and electrospinnability,

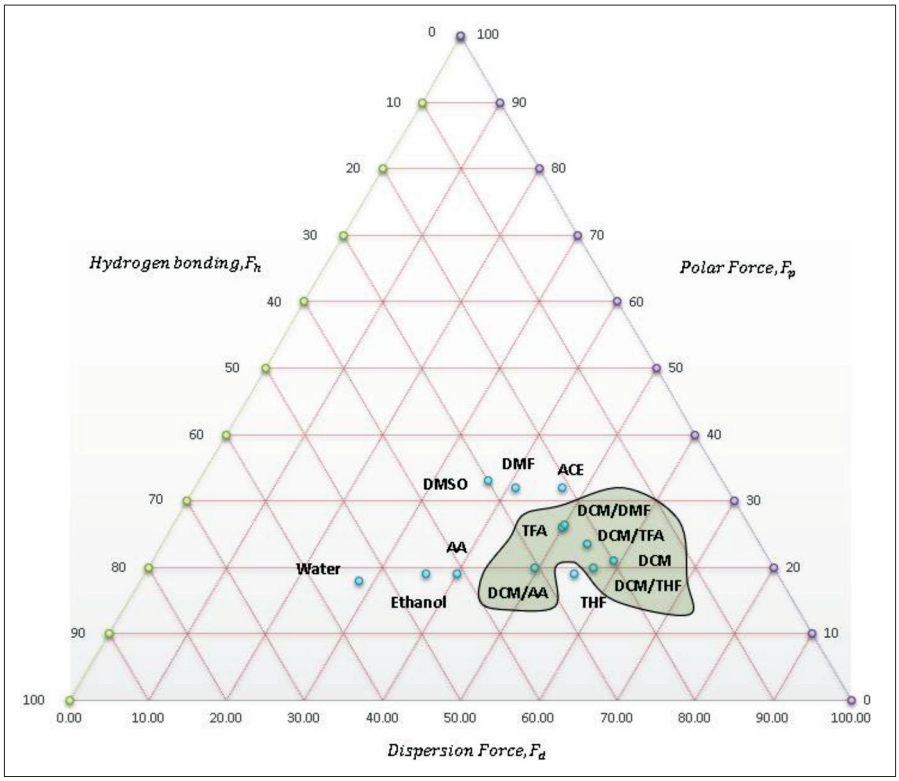

Figure 2. Solubility–spinnability map of PETG based on the Teas graph. The contoured region presents the solvents that can dissolve PETG into a homogenous solution.

which describes the ability of a polymeric solution to be stretched under a specific current, were investigated for different solvents, and the results are presented in Figure 2. The lower right quadrant in Figure 2 presents the best solutions for the dissolution of PETG in TFA or DCM. These solvents can produce nanofibers as single and binary solvent systems. As DCM showed the highest solubility, we decided to investigate its use combined with other solvents (binary solvent systems) such as DCM/DMF, DCM/AA, DCM/THF, and DCM/TFA. The results showed that the DCM/TFA binary solvent system allowed the best spinnability. Therefore, the effect of different splits of DCM/TFA on meshes production was investigated.

However, there were some challenges regarding the reproducibility of the meshes and stability of the Taylor cone due to the high evaporation rate of the solvents. Two parameters were investigated to address this issue. First, a high flow rate was used to stabilize the Taylor cone and counteract the rapid evaporation rate of the binary solvent system. Second, based on a preliminary investigation on the effect of the relative humidity on the spinnability, relative humidity was fixed at around 45% (±5%) allowing the best spinnability condition as the evaporation rate of the solvent would be limited.

3.2. Morphology

Figure 3 presents SEM images at 1000× magnification of the produced meshes. As seen from Figure 3A–G, the fiber thickness and porosity decreases by increasing the content of TFA (more viscous than DCM), while fiber roughness and bead content increases. Moreover, as DCM is a stronger solvent (higher polar force) but has a slower evaporation rate, it contributes to the formation of fibers with higher thickness. Therefore, by controlling the ratio between DCM and TFA, it is possible to control the thickness, roughness, and porosity of the fibers, thus allowing to create meshes with different fiber densities. In this study, the optimal mesh density, as shown in Figure 3D, is based on a 50/50 (% v/v) DCM/TFA system. This mesh exhibits optimal morphology by presenting thin fibers, lower porosities, and absence of beads.

Moreover, meshes produced from 85/15, 70/30, 60/40, 50/50 (% v/v) solutions were bead-free, while meshes produced from 40/60, 30/70, 15/85 (% v/v) solutions had beads.

Table 1 presents average fiber diameter per mesh. The average fiber diameter decreases proportionally with the decrease of DCM. This can be attributed to the volatility

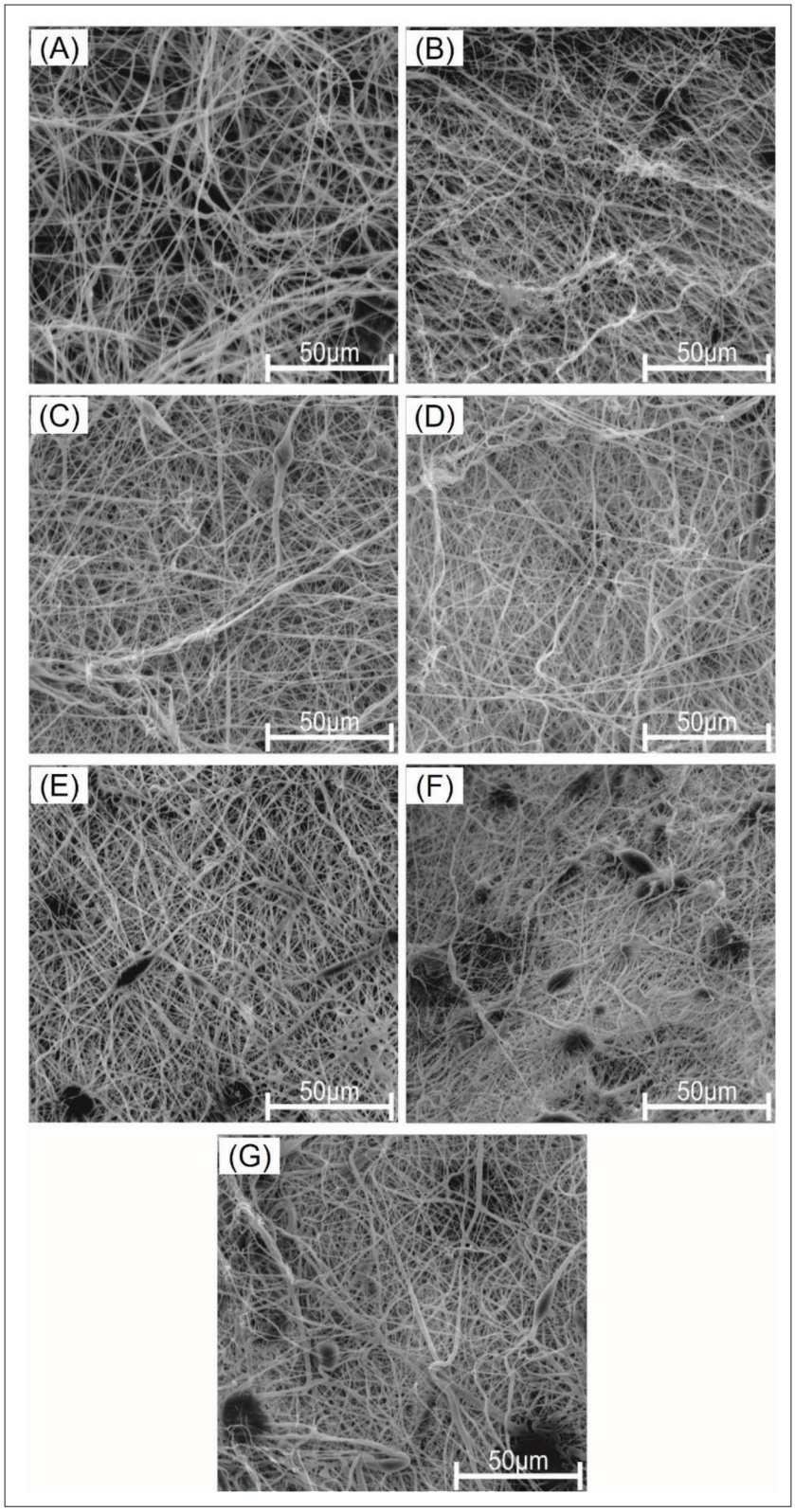

Figure 3. SEM image of the electrospun PETG using different solvent splits (DCM/TFA) with 1000× magnification. (A) 85/15, (B) 70/30, (C) 60/40, (D) 50/50, (E) 40/60, (F) 30/70, and (G) 15/85.

Table 1. Average fiber diameter based on the solvent split

Solution (DCM/TFA) (% v/v)	Fiber diameter (μm)
85/15	1.108 ± 0.181
70/30	0.800 ± 0.1307
60/40	0.677 ± 0.221
50/50	0.559 ± 0.162
40/60	0.428 ± 0.084
30/70	0.289 ± 0.079
15/85	0.243 ± 0.100

of the solvents, as TFA is more volatile than DCM, which causes rapid evaporation that leads to thinner fibers.

3.3. Mesh composition

The chemical composition of the electrospun PETG meshes was investigated using FTIR, a non-destructive analytical technique that allows to qualitatively assess the crystallinity of the electrospun meshes. Figure 4 shows the FTIR spectra for the different electrospun meshes. Common PETG characteristic peaks were recorded at 965 cm^{-1} (C–H stretching peak of cyclohexylene ring)[31], 1106 cm^{-1} (in-plane vibrations of the C–H bonds)[31], 1260 cm^{-1} (ester groups)[31], 1717 cm^{-1} (C=O ester group)[31], 2861 cm^{-1} and 2939 cm^{-1} (C–H symmetrical and asymmetrical stretching vibration in the aliphatic polymeric chains)[31].

As the C–H stretching of cyclohexene ring increases, it can be concluded that the cyclohexanedimethanol (CHDM; amorphous material) content also increases and crystallinity decreases[23]. Moreover, from the different solvent splits, it can be noted that the TFA dominant splits have a slightly higher crystallinity compared to DCM dominant splits.

Raman spectroscopy was used as a non-destructive, robust, and rapid analytical technique to qualitatively assess the chemical difference between different electrospun meshes. The results are presented in Figure 5. All obtained spectra were treated with baseline correction by subtracting a polynomial fit of the baseline from the raw spectra. This was done to remove the tilted baseline variation occurring due to different noises.

Common PETG characteristic peaks were obtained at 793 cm^{-1} (C–H ring out-of-plane bending + C = O bending)[32], 900 cm^{-1} (C–H ring out-of-plane-bending)[32], 1021 cm^{-1} (C–H ring in-plane bending)[32], 1116 cm^{-1} (C–O stretching)[32], 1273 cm^{-1} (C–O stretching of ester group)[32], 1377 cm^{-1} (gauche CH_2 wagging)[32], 1502 cm^{-1} (—CH_2 bending peak of the PETG macromolecular chain backbone)[32], 1613 cm^{-1} (symmetric stretching of the 1,4 para di-substituted benzene ring)[33], and 1727 cm^{-1} (C = O stretching of ester group)[32].

The crystallinity of PETG can be seen from the 1116 cm^{-1} (C–O stretching) as it is slightly shifted to the right and exhibits shoulder band at ~1190 cm^{-1}. In addition, the peak at 1727 cm^{-1} appears wider for lower crystalline materials. Both phenomena were observed in DCM dominant solvent splits, which were lower in crystallinity[34].

3.4. Inoculation

The bioactivity of produced meshes was assessed using spore inoculation. After inoculating the meshes with yellow rust spores, they were placed in the incubator for 24 h. The meshes were then removed from the incubator and inspected to assess its bioactivity. Figure 6A presents the SEM image at 0 h where the spores are shown to be dispersed on the meshes. Figure 6B shows the clusters growth of the fungal spores after 24 h. Figure 6C and D present magnified images of the germinated germ tubes, proving the bioactivity of the produced meshes that encourages the growth of fungal spores. This proves that the produced meshes are bioactive, enabling the growth of the fungal spores.

4. Conclusion

In this study, we investigated strategies to create PETG electrospinning meshes, a polymeric material that is difficult to spin. To the best of our knowledge, this was the first attempt to create PETG meshes using solution electrospinning. Multiple single and binary solvent systems were used to investigate the solubility of PETG, and it was found that DCM/TFA presented the best solubility–spinnability results among the different solvents. Optimal processing conditions were determined, and final meshes were produced at a flow rate of 4 mm/h, a voltage of 16 kV, and a humidity of 40%–50%. Meshes obtained under optimal processing conditions were chemically characterized using both FTIR and Raman spectroscopy, and the results showed that meshes produced using DCM dominant splits have lower crystallinity, where meshes produced using TFA dominant splits have higher crystallinity. This can be attributed to the difference in volatility and evaporation rate of DCM and TFA. Morphological characterization was performed using SEM and the results showed the presence of beads in TFA dominant splits, whereas DCM dominant splits were bead-free. Moreover, meshes produced using DCM/TFA (1:1) presents the best trade-off between fiber thickness and surface roughness. Inoculation on the optimal mesh was carried, to investigate the bioactivity, and the results demonstrated fungal germination and proliferation of the yellow rust spores on these meshes. Our results suggest that the produced electrospun PETG meshes have high potential to be used in sensing applications.

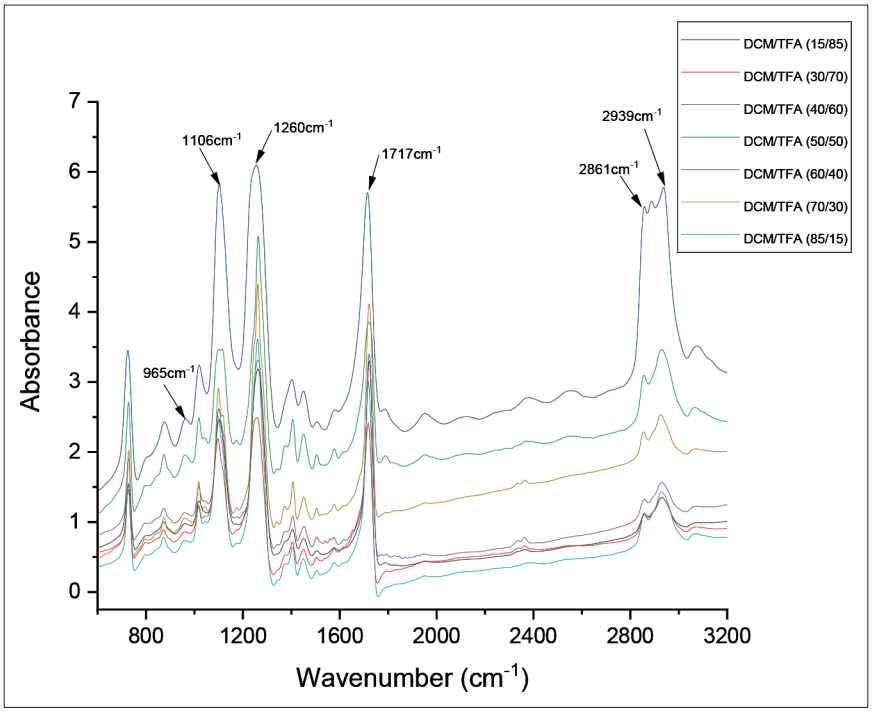

Figure 4. FTIR spectra of electrospun PETG using different solvent splits (DCM/TFA).

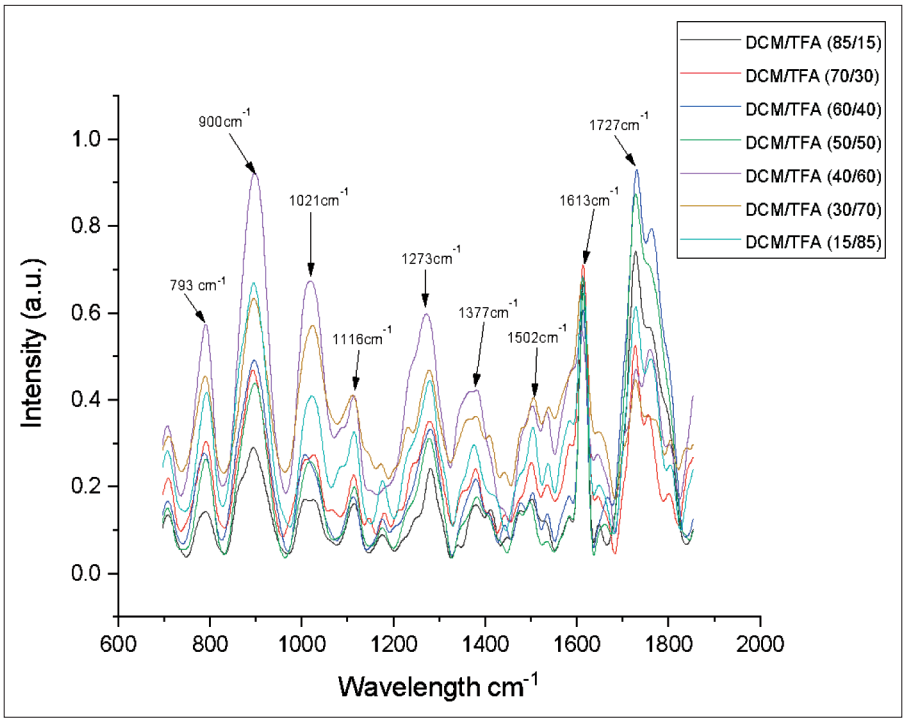

Figure 5. RAMAN spectra of electrospun PETG using different solvent splits (DCM/TFA).

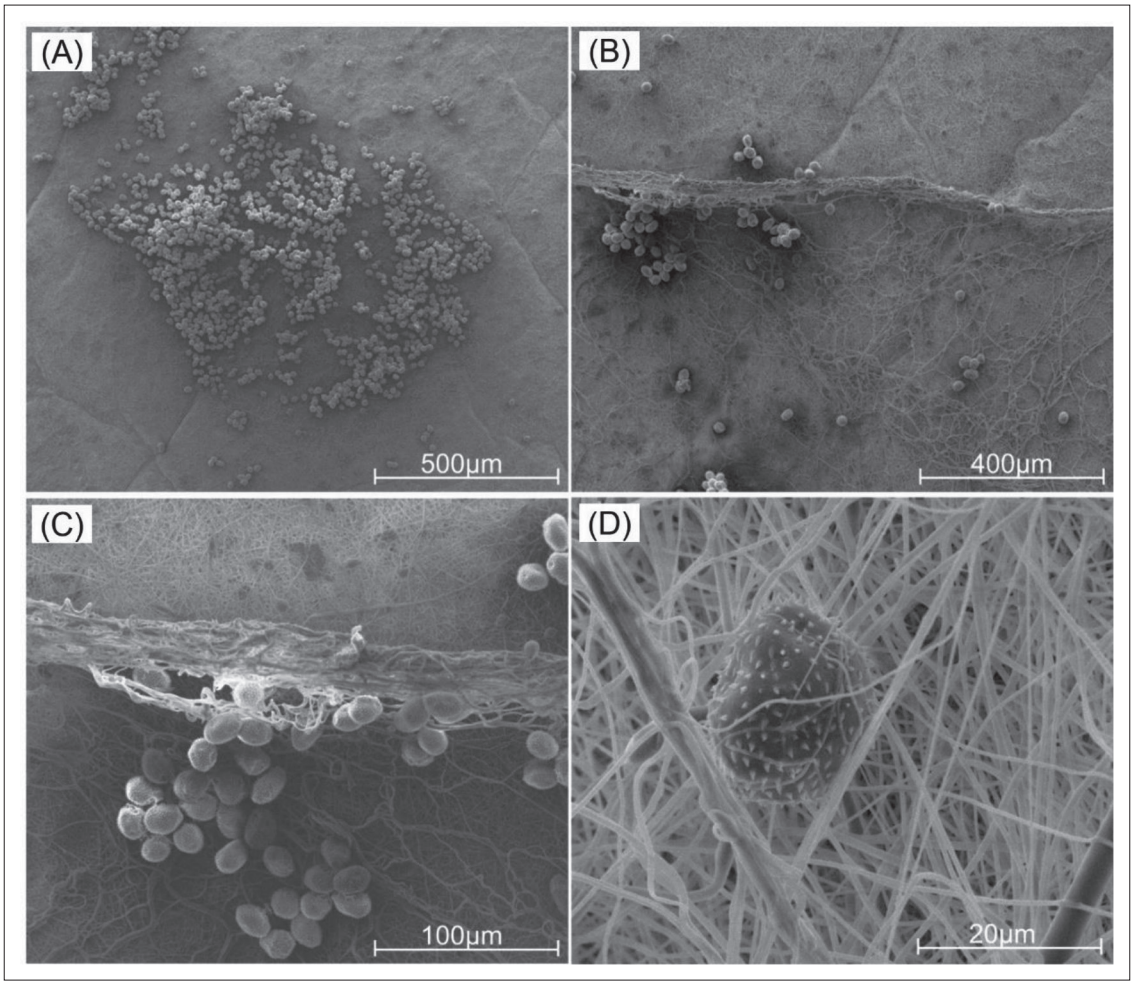

Figure 6. (A) SEM image of *P. striiformis* f. sp. *tritici* spores (100× magnification) at 0 h of inoculation. (B) SEM image of *P. striiformis* f. sp. *tritici* spores (200× magnification) after 24 h. (C) SEM image of the germinated *P. striiformis* f. sp. *tritici* spores (500× magnification). (D) SEM image of the germinated *P. striiformis* f. sp. *tritici* spores (2000× magnification).

Acknowledgments

None.

Funding

This project has been partially supported by the University of Manchester and UK Research and Innovation (UKRI) through the Engineering and Physical Sciences Research Council (EPSRC) of the UK (grant number: EP/V011766/1).

Conflict of interest

The authors declare no conflict of interest.

Author contributions

Conceptualization: Mohamed H. Hassan
Data curation: All authors
Formal analysis: Mohamed H. Hassan, Abdalla M. Omar, Evangelos Daskalakis
Funding acquisition: Paulo J.D.S. Bartolo
Investigation: Mohamed H. Hassan, Abdalla M. Omar, Evangelos Daskalakis
Methodology: Mohamed H. Hassan, Abdalla M. Omar, Evangelos Daskalakis
Project administration: Paulo J.D.S. Bartolo, Bruce Grieve
Resources: All authors
Software: Mohamed H. Hassan, Abdalla M. Omar, Evangelos Daskalakis
Supervision: Paulo J.D.S. Bartolo, Bruce Grieve
Validation: Mohamed H. Hassan, Abdalla M. Omar, Evangelos Daskalakis
Visualization: All authors
Writing – original draft: All authors
Writing – review and editing: All authors

All authors have read and agreed to the published version of the manuscript.

References

1. Mota C, Puppi D, Dinucci D, *et al.*, 2011, Dual-scale polymeric constructs as scaffolds for tissue engineering. *Materials*, 4(3): 527–542.
2. Dias JR, Sousa A, Augusto A, *et al.*, 2022, Electrospun polycaprolactone (PCL) degradation: An in vitro and in vivo study. *Polymers*, 14(16): 3397.
3. Aslan E, Vyas C, Yupanqui MJ, *et al.*, 2011, Preliminary characterization of a polycaprolactone-SurgihoneyRO electrospun mesh for skin tissue engineering. *Materials*, 15(1): 89.
4. Huang B, Aslan E, Jiang Z, *et al.*, 2020, Engineered dual-scale poly (ε-caprolactone) scaffolds using 3D printing and rotational electrospinning for bone tissue regeneration. *Addit Manuf*, 36: 101452.
5. Motamedi AS, Mirzadeh H, Hajiesmaeilbaigi F, *et al.*, 2017, Effect of electrospinning parameters on morphological properties of PVDF nanofibrous scaffolds. *Progr Biomater*, 6: 113–123.
6. Mei Q, Fu R, Ding Y, *et al.*, 2019, Electrospinning of highly dispersed Ni/CoO carbon nanofiber and its application in glucose electrochemical sensor. *J Electroanalyt Chem*, 847: 113075 %@ 1572–6657.
7. Yarin AL, Koombhongse S, Reneker DH, 2001, Taylor cone and jetting from liquid droplets in electrospinning of nanofibers. *J Appl Phys*, 90(9): 4836–4846.
8. Wu S, Liu J, Qi Y, *et al.*, 2021, Tendon-bioinspired wavy nanofibrous scaffolds provide tunable anisotropy and promote tenogenesis for tendon tissue engineering. *Mater Sci Eng C*, 126: 112181.
9. Li Y, Wang J, Qian D, *et al.*, 2021, Electrospun fibrous sponge via short fiber for mimicking 3D ECM. *J Nanobiotechnol*, 19(1): 131.
10. Li M, Qiu W, Wang Q, *et al.*, 2022, Nitric oxide-releasing tryptophan-based poly (ester urea) s electrospun composite nanofiber mats with antibacterial and antibiofilm activities for infected wound healing. *ACS Appl Mater Interfaces*, 14(14): 15911–15926.
11. Qi Y, Wang C, Wang Q, *et al.*, 2023, A simple, quick, and cost-effective strategy to fabricate polycaprolactone/silk fibroin nanofiber yarns for biotextile-based tissue scaffold application. *Eur Polym J*, 186: 111863.
12. Vyas C, Ates G, Aslan E, *et al.*, 2020, Three-dimensional printing and electrospinning dual-scale polycaprolactone scaffolds with low-density and oriented fibers to promote cell alignment. *3D Print Addit Manuf*, 7(3): 105–113.
13. Hunley MT, Long TE, 2008, Electrospinning functional nanoscale fibers: A perspective for the future. *Polym Int*, 57(3): 385–389.
14. Tang Y, Lan X, Liang C, *et al.*, 2019, Honey loaded alginate/PVA nanofibrous membrane as potential bioactive wound dressing. *Carbohydr Polym*, 219: 113–120.
15. Stojkovska J, Djurdjevic Z, Jancic I, *et al.*, 2018, Comparative in vivo evaluation of novel formulations based on alginate and silver nanoparticles for wound treatments. *J Biomater Appl*, 32(9): 1197–1211.
16. Yang X, Wang Y, Qing X, 2019, A flexible capacitive sensor based on the electrospun PVDF nanofiber membrane with carbon nanotubes. *Sens Actuators A Phys*, 299: 111579.
17. Hussain Z, Ullah S, Yan J, *et al.*, 2022, Electrospun tannin-rich nanofibrous solid-state membrane for wastewater environmental monitoring and remediation. *Chemosphere*, 307: 135810.
18. Townsend-Nicholson A, Jayasinghe SN, 2006, Cell electrospinning: A unique biotechnique for encapsulating living organisms for generating active biological microthreads/scaffolds. *Biomacromolecules*, 7(12): 3364–3369.
19. Hong J, Yeo M, Yang GH, *et al.*, 2019, Cell-electrospinning and its application for tissue engineering. *Int J Mol Sci*, 20(24): 6208.
20. Liu F, Vyas C, Poologasundarampillai G, *et al.*, 2018, Structural evolution of PCL during melt extrusion 3D printing. *Macromol Mater Eng*, 303(2): 1700494.
21. Bartolo P, Malshe A, Ferraris E, *et al.*, 2022, 3D bioprinting: Materials, processes, and applications. *CIRP Ann*, 71(2): 577–597.
22. Hassan MH, Omar AM, Daskalakis E, *et al.*, 2022, Multi-layer biosensor for pre-symptomatic detection of *Puccinia striformis*, the causal agent of yellow rust. *Biosensors*, 12(10): 829.
23. Hassan MH, Omar AM, Daskalakis E, *et al.*, 2020, Preliminary studies on the suitability of PETG for 4D printing applications, in *7th International Conference of Materials and Manufacturing Engineering (ICMMEN 2020)*, 6.
24. Hassan MH, Omar AM, E. Daskalakis, *et al.*, 2020, The potential of polyethylene terephthalate glycol as biomaterial for bone tissue engineering. *Polymers*, 12(12): 3045.
25. Paralı L, Koç M, Yıldız Z, 2022, 2D/3D direct writing of thermoplastics through electrohydrodynamic printing. *Polym Sci Series A*, 64(5): 559–572.
26. Luo C, Nangrejo M, Edirisinghe M, 2010, A novel method of selecting solvents for polymer electrospinning. *Polymer*, 51(7): 1654–1662.
27. Barton AF, 2017, *CRC Handbook of Solubility Parameters and Other Cohesion Parameters*, Routledge.
28. Heseltine PL, Ahmed J, Edirisinghe M, 2018, Developments in pressurized gyration for the mass production of polymeric fibers. *Macromol Mater Eng*, 303(9): 1800218.

29. Luo C, Stride E, Edirisinghe M, 2012, Mapping the influence of solubility and dielectric constant on electrospinning polycaprolactone solutions. *Macromolecules*, 45(11): 4669–4680.

30. Burke J, 1984, *Solubility Parameters: Theory and Application*. The AIC book and paper group annual, 3: 13–58.

31. Paszkiewicz S, Szymczyk A, Pawlikowska D, *et al.*, 2017, Synthesis and characterization of poly(ethylene terephthalate-co-1, 4-cyclohexanedimethylene terephtlatate)-block-poly (tetramethylene oxide) copolymers. *RSC Adv*, 7(66): 41745–41754.

32. Cole K, Guevremont J, Ajji A, *et al.*, 1994, Characterization of surface orientation in poly (ethylene terephthalate) by front-surface reflection infrared spectroscopy. *Appl Spectrosc*, 48(12): 1513–1521.

33. Alexiou VF, Mathioudakis GN, Andrikopoulos KS, *et al.*, 2020, Poly (ethylene terephthalate) carbon-based nanocomposites: A crystallization and molecular orientation study. *Polymers*, 12(11): 2626.

34. Ciera L, Beladjal L, Almeras X, *et al.*, 2014, Morphological and material properties of polyethyleneterephthalate (PET) fibres with spores incorporated. *Fibres Text East Eur,* 22(4): 29–36.

ACCSCIENCE PUBLISHING

International Journal of Bioprinting

RESEARCH ARTICLE

Computational fluid dynamics for the optimization of internal bioprinting parameters and mixing conditions

Gokhan Ates[1,3]*, Paulo Bartolo[1,2]*

[1]Department of Mechanical, Aerospace and Civil Engineering, The University of Manchester, Manchester, United Kingdom

[2]Singapore Centre for 3D Printing, School of Mechanical and Aerospace Engineering, Nanyang Technological University, Singapore

[3]Department of Mechanical Engineering, Abdullah Gul University, Kayseri, Turkey

Abstract

Tissue engineering requires the fabrication of three-dimensional (3D) multimaterial structures in complex geometries mimicking the hierarchical structure of biological tissues. To increase the mechanical and biological integrity of the tissue engineered structures, continuous printing of multiple materials through a printing head consisting of a single nozzle is crucial. In this work, numerical analysis was carried out to investigate the extrusion process of two different shear-thinning biomaterial solutions (alginate and gelatin) inside a novel single-nozzle dispensing system consisting of cartridges and a static mixer for varying input pressures, needle geometries, and outlet diameters. Systematic analysis of the dispensing process was conducted to describe the flow rate, velocity field, pressure drop, and shear stress distribution throughout the printing head. The spatial distribution of the biopolymer solutions along the mixing chamber was quantitatively analyzed and the simulation results were validated by comparing the pressure drop values with empirical correlations. The simulation results showed that the proposed dispensing system enables to fabricate homogenous material distribution across the nozzle outlet. The predicted shear stress along the proposed printing head model is lower than the critical shear values which correspond to negligible cell damage, suggesting that the proposed dispensing system can be used to print cell-laden tissue engineering constructs.

Keywords: 3D Printing; Bioprinting; Biomaterials; Computational fluid dynamics; Extrusion; Tissue engineering

***Corresponding authors:**
Gokhan Ates
(gokhan.ates@manchester.ac.uk)

Paulo Bartolo
(pbartolo@ntu.edu.sg)

Citation: Ates G, Bartolo P, 2023, Computational fluid dynamics for the optimization of internal bioprinting parameters and mixing conditions. *Int J Bioprint*, 9(6): 0219.
https://doi.org/10.36922/ijb.0219

Received: October 05, 2022
Accepted: December 21, 2022
Published Online: June 22, 2023

Copyright: © 2023 Author(s). This is an Open Access article distributed under the terms of the Creative Commons Attribution License, permitting distribution and reproduction in any medium, provided the original work is properly cited.

Publisher's Note: AccScience Publishing remains neutral with regard to jurisdictional claims in published maps and institutional affiliations.

1. Introduction

Three-dimensional (3D) bioprinting technology, within the rapidly evolving field of biomanufacturing, enables to engineer predesigned, volumetric tissue-like structures with a spatially controlled distribution of cells and biomolecules, making it a unique tool for a broad range of tissue engineering applications[1-3]. Bioinks are the bioprintable materials composed of hydrogels encapsulating cells or cell aggregates[4].

The most commonly used additive manufacturing (3D printing) techniques[5,6] to create cell-laden constructs are material jetting[7,8], extrusion-based[2,9], and light-based technologies[10,11]. Multimodal systems, integrating different printing principles into a single machine, have been also proposed[6]. Among these printing strategies, extrusion-based bioprinting is one of the most commonly used approach as it allows to print materials with a wide range of viscosities and to fabricate multimaterial/cellular volumetric biological constructs[12-14]. In extrusion bioprinting, biocompatible cell-laden hydrogels are loaded into the cartridges (reservoirs) and deposited on a bioprinting platform using one or several nozzles via pneumatic, mechanical, or solenoid actuation[5].

A key object of tissue engineering applications is the fabrication of multimaterial and multiscale heterogeneous constructs, mimicking the organized cellular architecture and functionality of natural tissues[15]. However, this is not achievable with single-material bioprinting approaches, as they often fail to replicate the complexity and variety of real tissues consisting of multiple layers of different cell types[16]. To overcome this shortcoming, multimaterial bioprinting emerged as a promising approach[6,15-17]. Multimaterial 3D bioprinting technique refers to the simultaneous or sequential deposition of two or more biomaterials in a predetermined manner to create region-specific characteristics and performances[16]. These type of heterogeneous bioconstructs have been fabricated using multireservoir and multinozzle printing systems[18]. However, the fundamental limitation of these multinozzle bioprinting systems is the considerably long printing time while switching between different bioinks, in addition to the need of accurate calibration of all printheads before the deposition process[3,19,20]. Moreover, multinozzle bioprinting systems result in a discontinuity in the printed filament morphology that adversely affect the mechanical integrity of the 3D-printed structures[19]. To overcome these limitations, several researchers focused on bioprinting of multiple hydrogels through a single nozzle[20-23].

Implementing multireservoir single-nozzle systems is simple, though this strategy is ineffective for systematically printing tissue engineering structures with continuous gradient features. A variety of mixers have been used to tackle this limitation by blending two or more biomaterials in various concentrations to facilitate multimaterial bioprinting tasks[23]. In this case, active and passive or static mixers have been extensively studied. Static mixers are usually easier to assemble and more biocompatible compared to active mixers, since they cause less shear stresses to the encapsulated cells[24]. Recently, Kenics static mixers (KSM) have been employed to enable chaotic bioprinting of multimaterial constructs[15] and this is a rapidly expanding field to overcome the restrictions of mixing highly viscous biomaterials[25].

Computational fluids dynamics (CFD), simulations of the biopolymer flow in extrusion-based bioprinting processes, are widely used to understand the relationship between printing parameters, nozzle size and geometry, viscous forces, and material properties during the bioprinting process. More specifically, it enables to determine inner parameters that are experimentally difficult to evaluate, such as pressure, velocity, flow rate, and also shear stresses on cells in the case of bioinks. It is known that the dispensing pressure, and particularly shear stresses, have a significant influence on cell survival[26-29]. However, only few simulation studies have investigated shear stresses and cell viability on extrusion-based bioprinting processes, considering different nozzle geometries and dispensing pressures[30-34]. Moreover, all these studies have only considered the simulation of a single-material bioprinting process.

In this work, we extensively investigated the extrusion process of non-Newtonian alginate and gelatin solutions, through an entire and novel dispensing system consisting of two cartridges, KSM integrated mixing chamber and a single nozzle. To the best of our knowledge, to date, no numerical study has yet investigated the inner parameters such as shear stress, pressure, and velocity field as well as mixing index within the KSM-embedded 3D model of printing head flow domain. The spatial distribution of the two different polymer solutions was quantitatively characterized by determining the mixing index. To understand the effect of the printing needle geometry on the inner parameters, cylindrical and conical nozzles with varying outlet diameters were investigated considering different printing pressures. The simulation results were validated by comparing predicted pressure drop results at different Reynolds numbers with existing empirical correlations. This model can be easily adapted to different biomaterials.

2. Materials and methods

2.1. Computational fluid dynamics analysis

A computational fluid dynamics (CFD) analysis was performed by using the simulation software package ANSYS® Academic Research Fluent 19.2 (ANSYS, Canonsburg, PA, USA) to numerically evaluate the mixing mechanism of two different biomaterials through a static mixer integrated printing head, and both the velocity and shear stress distribution profiles at the needle outlet during the extrusion process. Figure 1 shows the computer-aided design (CAD) model of the printing head equipped with cartridges, static mixer, and a cylindrical or a conical

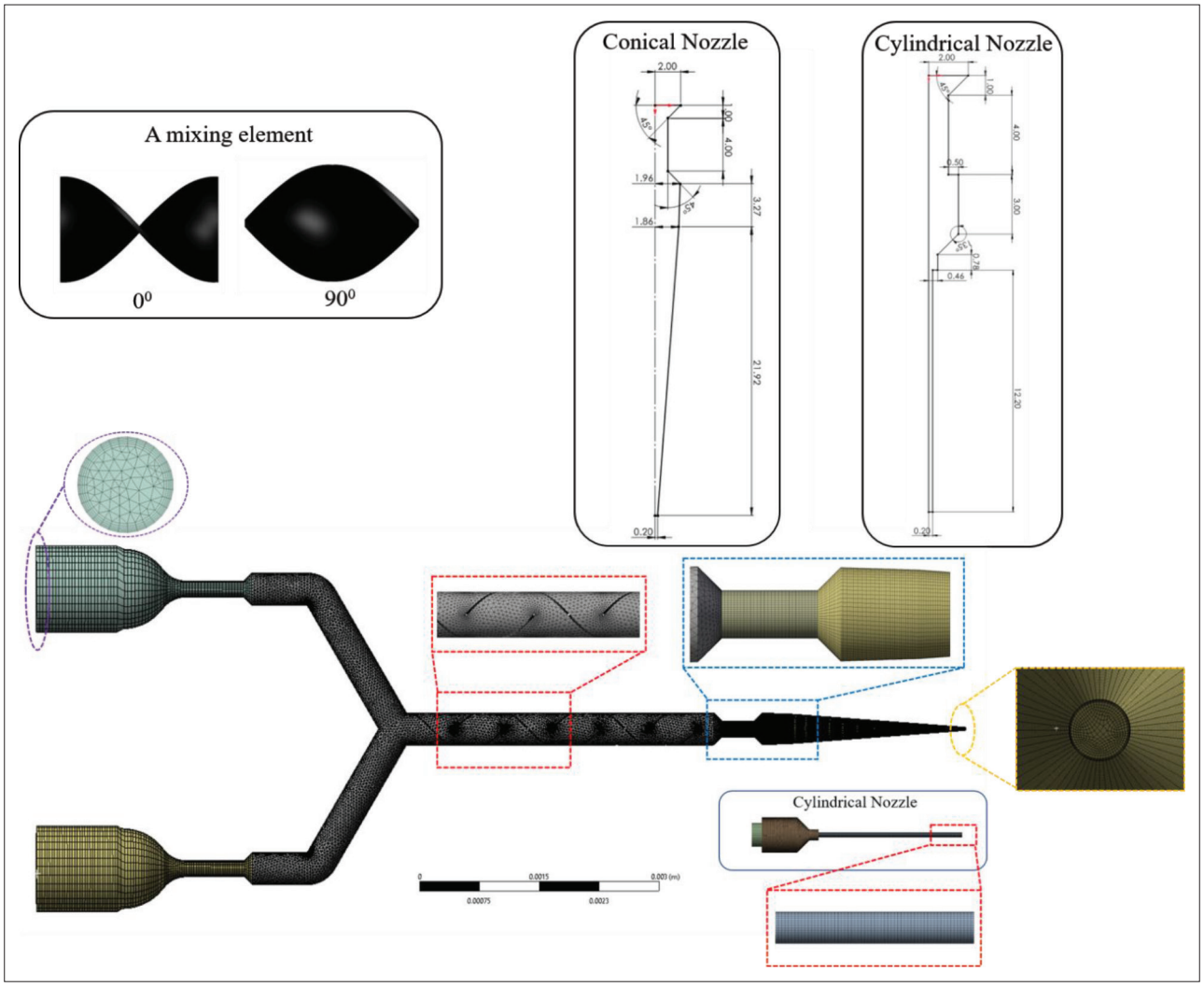

Figure 1. Representation of mesh generation on the printing head and corresponding dimensions in mm.

printing needle. In this study, a miniaturized Kenics-type static mixer[35-38], consisting of multiple helical mixing units alternating clockwise and counter-clockwise directions, was used in all simulations.

For the simulations, the material flow was assumed to be multicomponent, laminar, incompressible, isothermal, in steady state, and non-Newtonian, and have no chemical reactions occurring inside the printing head during the printing process. The volume continuity, momentum conservation, and transport equations for an incompressible flow are solved by finite volume method and given as follows[38]:

$$\nabla.(\rho u) = 0 \quad \text{(I)}$$

$$\nabla.(\rho uu) = -\nabla P + \nu\nabla^2 u \quad \text{(II)}$$

$$(u.\nabla)C = -\nabla^2 C \quad \text{(III)}$$

where u is velocity (m/s), α is the kinematic diffusivity coefficient (m^2s^{-1}), C represents one of the mixing fluid's concentration in the KSM channel, ρ is the fluid density (kg/m^3), and P denotes the pressure (Pa).

The relationship between shear stress and apparent shear rate for a non-Newtonian fluid can be described by the following power-law model[39].

$$\tau = k\dot{\gamma}^n \quad \text{(IV)}$$

where k is the fluid consistency index ($Pa.s^n$), and n is power-law index (dimensionless) that, depending on the material rheological behavior, assumes the following values[40]:

- n<1, the fluid exhibits a shear-thinning behavior
- n=1, the fluid exhibits a Newtonian behavior
- n>1, the fluid exhibits a shear-thickening behavior.

Table 1. Rheological parameters of alginate and gelatin solutions[34,42]

	Content	*n*	*k* [Pa s^n]
Alginate	0.5 w/v%	0.977	0.032
	1.0 w/v%	0.895	0.119
	1.5 w/v%	0.840	0.346
Gelatin	7.0 w/v%	0.795	0.240

Materials to be printed through pneumatic (compressed air), mechanical (piston or screw), or solenoid (electrical pulses) driven printheads must exhibit shear-thinning properties, as this behavior allows to reduce shear stresses during the printing process and to enhance cell viability. The shear rate $\dot{\gamma}(s^{-1})$ can be defined as follows:

$$\dot{\gamma} = \frac{du}{dr} = \frac{-\Delta P}{2\mu L} r \quad \text{(V)}$$

where r (m) is the radius of the pipe, L (m). According to Metzner *et al.*[41], the generalized Reynolds number for a shear-thinning fluid is given by:

$$Re = \frac{\rho u^{2-n} D^n}{\frac{k}{8}\left(\frac{6n+2}{n}\right)^n} \quad \text{(VI)}$$

where D is the pipe diameter (m).

In this study, non-crosslinked alginate and gelatin solutions were selected as the working fluids. The rheological data for both materials arepresented in Table 1.

In the simulations, all solid boundaries were considered as stationary walls, where the "nonslip" boundary condition was applied. Moreover, by adjusting the dispensing pressure at the inlet boundaries, different Reynolds numbers were obtained for the flow domain. The outlet boundary condition was set as atmospheric pressure in all simulations. The stationary solver was used to resolve the model, and calculations were carried out using pressure–velocity coupling (Coupled algorithm). To discretize the momentum and pressure formulation, a second-order upwind method was used, while the least-squares cell-based method was used for the gradients. The relaxation parameters for pressure and momentum were set as 0.5 and set to 1.0, for body forces and density, respectively. For all simulations, the relative residuals of the velocity and continuity components were less than 10^{-5}, after approximately 1000 iterations, corresponding to a reasonably short calculation time (≤30 min) on an Intel processor with four cores. Convergence analysis was also tested, by monitoring the area-weighted average values of the shear stress and the velocity at the outlet. A stationary solution was achieved when these parameters reached a state of convergence.

To further investigate the effect of nozzle geometries (cylindrical and conical) and process parameters on cell viability, the flow rate, velocity magnitude, and shear stresses at the outlet, as well the axial discharge of the dispensing pressure along the printing head, were evaluated for the converged solution. A variety of nozzle outlet diameters, ranging from 0.25 to 2.00 mm, were examined at different inlet pressures (0.1–3.0 bar) for both nozzle types.

2.2. Mesh independence test

The 3D flow domain of the KSM-integrated printing heads was discretized, using the selective meshing feature of ANSYS Workbench meshing tool to create as many structured (hexahedral) elements as possible, and fill the remaining parts with tetrahedron elements. In this case, as the printing head consists of multiple bodies, we used the patch conforming method for the Y-shaped main body including the KSM, and the sweep method for sweepable bodies, such as barrels, and the other cylindrical parts (Figure 1). The mesh quality was refined near the mixing elements, and inflation layers were created for the pipe walls, to capture the flow fields more precisely in those places. To obtain reliable numerical results, grid-independence tests were conducted for all needle geometries with varying outlet diameters. These preliminary test results enabled to establish the best node layout and cell density, for numerical accuracy and computational load. Thus, a mesh sensitivity study was performed to observe how the outlet velocity magnitude deviates as the number of grids increased. The discretization of the models used in CFD simulations for both nozzle types is shown in Figure 1.

As shown in Figure 2, the calculated maximum velocity magnitude was stabilized by increasing the number of elements. Grid independence was achieved for the cylindrical and conical nozzle models, with 6×10^5 elements and 8×10^5, respectively, beyond that no substantial changes were observed. Based on these preliminary convergence test results, a mesh of 7.3×10^5 and 9.8×10^5 elements were chosen as the optimal mesh density, as it provides high accuracy of results with a shorter computational time required for convergence. The maximum skewness for all model meshes were lower than 0.85, with a minimum value of 2.3×10^{-5} and a minimum element quality of 0.09, which according to the literature is a nice evidence of good mesh quality[43].

2.3. Mixing index

The distributive capacity of the Kenics mixer was also investigated for different flow velocities. Distributive mixing, also known as simple or extensive mixing, represents the spatial distribution of the components

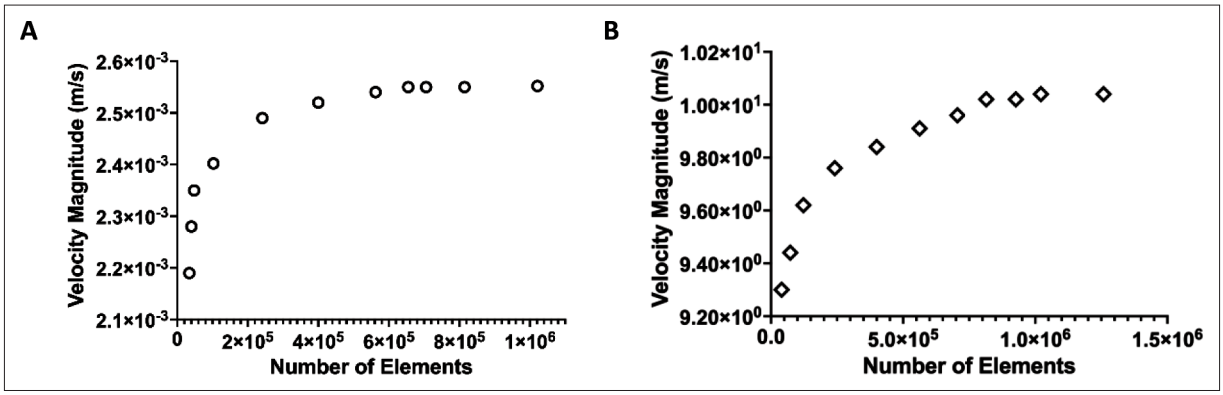

Figure 2. Mesh independence test results obtained for (A) the cylindrical and (B) the conical nozzle-integrated models.

across the fluid domain and, compared to dispersive mixing, it is easier to achieve. As the distributive mixing capacity of a mixer cannot be only judged based on the visual contour, it is essential to quantitatively evaluate the mixing performance. Therefore, the mixing efficiency of the static mixer was analyzed using a statistical measurement method based on the concept of intensity of segregation[44]. As previously reported by other studies on mixing processes[45-49], mixing can be quantified using the mixing index, denoted by M.I, at a cross-sectional plane perpendicular to the flow direction as follows:

$$M.I = 1 - \sqrt{\frac{\sigma^2}{\sigma^2_{\max}}} \quad \text{(VII)}$$

where σ^2_{max} denotes maximum possible variance at a cut-plane normal to the flow direction and σ^2 refers to the actual variance, which is defined as:

$$\sigma^2 = \frac{1}{n}\sum_{i=1}^{n}(c_i - \bar{c})^2 \quad \text{(VIII)}$$

where c^i is the mass fraction at i^{th} sampling point, $\bar{c}$ is the optimal mixing mass fraction and n is the number of sampling points on the associated plane. The optimal mass fraction ($\bar{c}$) at the cut plane is equal to 0.5 for symmetrical boundary conditions[49]. The maximum variance (σ^2_{max}) is determined by the following equation:

$$\sigma^2_{max} = \bar{c}(1 - \bar{c}) \quad \text{(IX)}$$

As the optimal maximum mass fraction, c, is equal to 0.5, in the case of equal flow of the two fluid streams, the value of σ^2_{max} is assumed to be 0.25. The mixing index varies from 0 (representing completely unmixed state) to 1 (completely mixed fluid). As the mixing index decreases from 1 to 0, a lesser amount of mixing is achieved. Equally, the higher mixing index represents higher mixing performance. However, it has been reported that numerical results might overestimate the mixing quality, owing to numerical diffusion[50].

2.4. Model validation

The validation of the CFD simulations was conducted by evaluating the pressure drop, as it is more sensitive to numerical oscillations in comparison to velocity[51]. Thus, the pressure drop values, obtained from the numerical simulations at different Reynolds numbers, were compared with the available empirical correlations[37,52-54]. In general, these correlations for static mixers are often stated in terms of a Z-factor[37]. The Z-factor is determined by the ratio of the pressure drop within the static mixer, ΔP, to the pressure drop in the empty pipe with the same length and diameter, ΔP_0[37], as follows[54]:

$$Z = \frac{\Delta P}{\Delta P_0} \quad \text{(X)}$$

For the laminar flow regime, the Z-factor for Kenics type mixers range between 5 and 8[44]. The pressure drop without a mixer is defined by the Hagen–Poiseuille equation[37]:

$$\Delta P_0 = \frac{32}{Re}\frac{\rho u^2 L}{D} \quad \text{(XI)}$$

Wilkinson and Cliff[37] presented a pressure drop correlation for Kenics mixers based on the Ergun equation, which is defined as:

$$Z = 7.19 + \frac{\Delta P}{32} \quad \text{(XII)}$$

Another commonly used equation, to estimate Z-factor in Kenics mixers, was developed by Grace[52] as follows:

$$Z = 3.24(1.5) + 0.21\sqrt{Re} \quad \text{(XIII)}$$

Shah and Kale[53] account for the volume drop caused by the presence of KSM elements by proposing the following equation:

$$Z = \frac{1}{16\varepsilon}\left(64.06 + 1.84\left(\frac{Re}{\varepsilon}\right)^{0.66}\right) \quad \text{(XIV)}$$

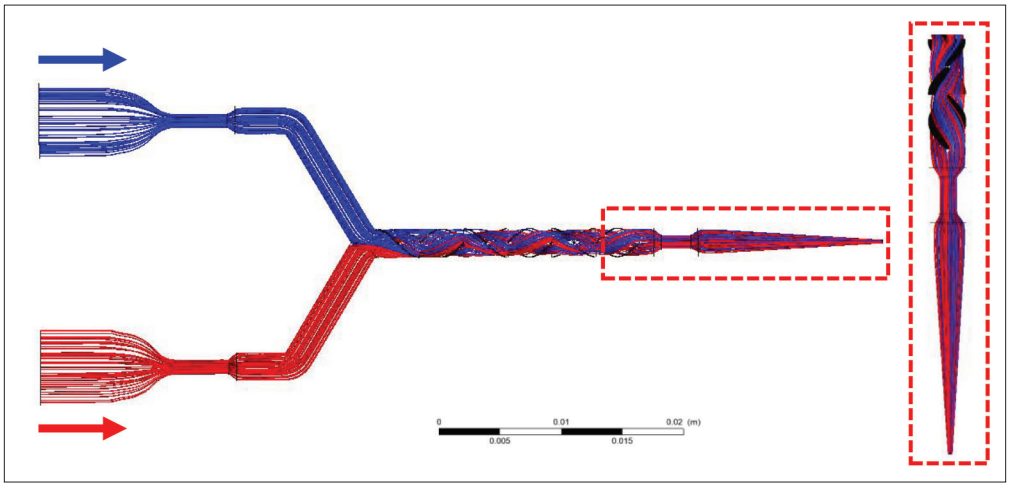

Figure 3. The working principle of the KSM-integrated printing head with conical nozzle. Alginate and gelatin solutions are represented by red- and blue-colored streams, respectively.

where εindicates the void fraction of the KSM and was set as 0.87.

Another important empirical correlation was proposed by Cybulski and Werdner[54] for Re<50:

$$Z = 5.4\left(1.5\right) + 0.028Re \quad \text{(XV)}$$

3. Results

3.1. Characterization of material distribution and mixing index

Chaotic advection, also named chaotic stirring, defined as stretching and folding of the fluid layers in a continuous manner, is widely employed in industrial mixing, particularly in the absence of turbulence flow[35,36]. In this case, chaotic advection was achieved by using the Kenics static mixer, which consists of helical mixing units assembled in a cylindrical pipe. CFD simulation was conducted to evaluate the working principle of the KSM system. In this model, each mixing unit of the KSM consecutively divides the incoming flow into two substreams. As the two different material solutions are injected through the printhead, the number of lamellae between them is exponentially increased by each successive mixing elements (Figure 3). The total number of lamellas produced, using n-element KSM, is equal to $s = 2^n$, where s represents the number of mixing units[15]. As the printing head includes six mixing elements, the total number of substreams at the outlet is equal to 32. Additionally, in the case of an uniform distribution of the streams, the thickness of each lamellae can be determined by $d_f/2^n$, where d_f corresponds to the diameter of each lamellae[28]. Then, it is possible to create an internal lamella with adjustable thickness and striation number by changing the number of mixing units in the KSM printing head.

The effect of the number of mixing units on the degree of mixing at different inlet velocities is presented in Figure 4 for the printing head model at different inlet pressures. Results show that the lowest mixing occurs at the cross-sectional plane, where no mixing element is present. As the fluids proceed to the outlet, uniform mass fraction distributions were progressively accomplished, and the mixing index significantly increased. Results also show that once the flow passes the fourth mixing element (near the exit), the mixing index remains almost the same for all considered cases. Similar results have been also reported, suggesting that high mixing quality can be achieved at the fourth or fifth element for nonreactive viscous fluids[55,56]. It is also important to note that the homogeneity of the mixture improves by increasing the extrusion pressure.

3.2. Outlet velocity

The volumetric flux was investigated for both cylindrical and conical nozzle printing heads. To understand the effect of printing pressure and various needle sizes on the flow rate, CFD simulations were conducted, and the results are presented in Figure 5. As observed, the volume flow rate increases by increasing the applied pressure. Moreover, at a constant extrusion pressure, the flow rate is directly proportional to the needle diameter for each nozzle type (Figure 5A and D). In the case of the cylindrical nozzle, the highest flow rate value was 47.75 µL, with a needle diameter of 1.00 mm and an inlet pressure of 3.0 bar, while the lowest flow rate was 0.01 µL with a needle diameter of 0.25 mm and a pressure of 0.5 bar. Additionally, as observed from Figure 5D, the volumetric flow rates are significantly higher in the case of a conical nozzle than in the case of a cylindrical nozzle. At 0.5 bar inlet pressure, for instance, the calculated area-weighted average flow rate in the conical nozzle is nearly 600-fold greater. Results seem

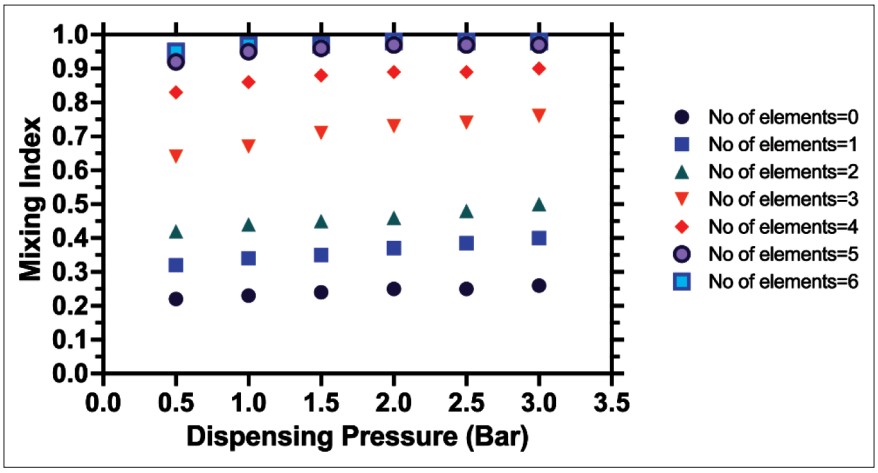

Figure 4. Mixing index results as a function of dispensing pressure for different number of mixing elements.

to indicate that the use of conical needles is the best option, if high volumetric flow rates are required. This is critical if the mixture of hydrogels being dispensed is highly viscous, and inconvenient to distribute with a cylindrical nozzle. It is also important to note that the equivalent flow rates of the printing heads with a cylindrical nozzle can be achieved with substantially lower dispensing pressures in conical nozzle systems. Numerically calculated area-weighted average outlet velocities under various extrusion pressures are presented in Figure 5B and E for cylindrical and conical nozzles.

As the mixture of both polymers moves from the mixing channel to the nozzle, which corresponds to an abrupt change in the cross-sectional area, a significant increase in the linear velocity occurs. Similar to the flow rate results, the velocity magnitude increases at the tip of the nozzles as the applied pressure increases. Results also show that the velocity magnitude reaches a peak value at a pressure of 3 bar and 1 bar for cylindrical and conical nozzles, respectively. It is also important to note that the velocity profile at the nozzle tip is one of the essential parameters, enabling to control the morphology and quality of printed fibers. In Figure 5C and F, the radial distribution of velocity at the nozzle outlet is plotted for different nozzle sizes (ranging from 0.25 to 1.20 mm) and a constant dispensing pressure of 1 bar. As can be observed in Figure 5C, the simulated velocity profiles exhibit a nearly parabolic, fully developed typical Newtonian-like fluid behavior, implying that the shear rates have a lower impact on the mixture viscosity. This can be explained by the low shear rate values, aroused during the deposition process for all considered cases.

The maximum shear rate of 521 s^{-1} was observed for the largest nozzle diameter. These results can be attributed to the power-law index of alginate and gelation solutions considered in the present study. Since the flow index (n) parameters of each hydrogel forming the mixture are close to 1, which represents a Newtonian fluid, the fluid exhibits a weak shear thinning behavior. However, similar to the results reported by Billiet *et al.* and Ortega *et al.*[34,57], conical nozzle-assembled printing head simulations exhibited higher shear rates. However, contrary to Newtonian fluid's parabolic flow profile, the velocity of the mixing fluid remains almost constant in the center of the nozzle, and rapidly decreases near the walls, where a layer of material mixture undergoes shear thinning (Figure 5F).

This shear-thinned fluid layer behaves as a lubricant, enabling the rest of the intact biomaterial (material at the center) to move through the nozzle in a flow configuration known as plug flow[58]. It is widely accepted that a plug-like flow characteristic might be the mechanism through which the bioinks protect cells from the harmful effects of the high shear stress values[58]. Due to the limited information in terms of flow rate, simulation setup, biomaterial rheology, and printing head geometries, comparison between previous studies is not meaningful. However, it is important to highlight that the flow rate, as a directly shear-determining quantity, is more trustworthy than dispensing pressure, in comparing shear conditions for different nozzle sizes and biomaterials. Figure 5G–L shows velocity distribution maps across the cylindrical and conical nozzles with different outlet diameters (0.25, 0.61, 1.00, and 1.20 mm) for the same applied pressure of 1 bar. As expected, the maximum velocity magnitudes were observed at the center of the nozzle tips. Since no-slip boundary conditions were applied between the biomaterial solution mixture and the walls, a radial velocity gradient was achieved from the walls to the center of the nozzle tip. According to the simulation results, minimum velocity

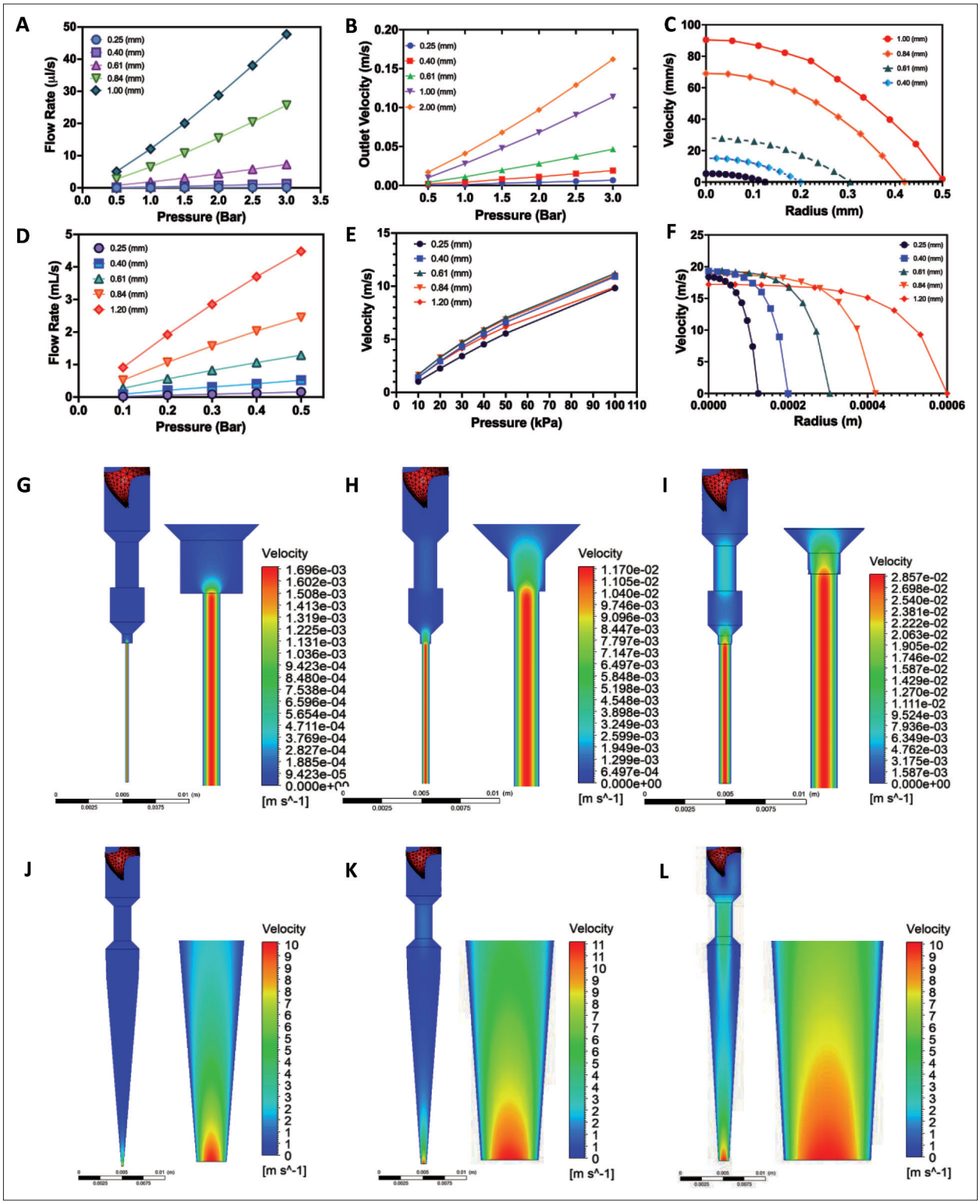

Figure 5. Simulation results for two types of printing needles. Cylindrical nozzle: (A) volumetric flow rate at the nozzle tip versus dispensing pressure, (B) area-weighted outlet average velocity, and (C) velocity profiles across the radius. Conical nozzle: (D) flow rate versus applied pressure, (E) area-weighted outlet average velocity under varying inlet pressures, and (F) the radial velocity distribution for various nozzle sizes. (G, H, I) Cylindrical and (J, K, L) conical nozzle velocity contour plots at 1 bar inlet pressure and different outlet diameters: (G, J) 0.25mm, (H, K) 0.61mm, (I) 1.00mm, and (L) 1.20mm for conical needle.

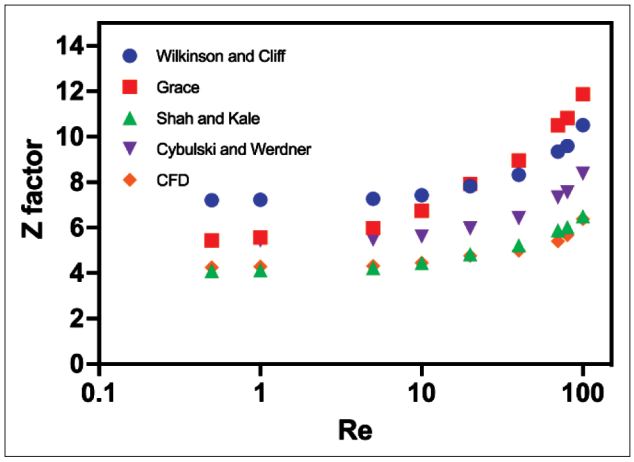

Figure 6. Comparisonbetween simulation results and results obtained from empirical correlations at various *Re* numbers.

values were obtained for the nozzles with smaller diameters, which are aligned with previous reported results[57,59].

3.3. Model validation and pressure drop

To validate the simulation results, the pressure drop values for different *Re* numbers ranging from 0.1 to 100 were compared with empirical correlations, as shown in Figure 6. As observed for the creeping flow ($Re < 10$), the *Z*-factor remains almost constant for the KSM. However, as the *Re* rises, an increment was observed in the *Z* values. Results from Figure 6 suggest that higher Reynolds numbers result in higher pressure drop. Moreover, our CFD results are well aligned with the results predicted by Equation XIV, for a given range of *Re* numbers. Based on the findings of Meng *et al.*[60], the Z-factor of a Kenics static mixer with an aspect ratio of 1.5 ranges from 5.64 to 8.63.

Previous studies investigating the deposition process only focused on the pressure drop inside the printing nozzle, without taking the barrels into account[30,54-55]. In this study, the pressure drop was comprehensively analyzed along the entire extrusion printing head, including barrels, KSM, and needles with different types and outlet diameters. As shown in Figure 7A and B, the pressure drop in the mixing chamber is negligible, as the inner diameter of the KSM is relatively larger than the nozzle diameters. For a dispensing pressure of 1 bar, the highest pressure drop occurred in the narrowing part of the printing head for all conical nozzle diameters (0.25, 0.40, 0.61, 0.84, and 1.00 mm) (Figure 7B and C). Moreover, as the mixture of the two polymeric solutions passes from the static mixer to the cylindrical needle, a significant pressure drop was observed regardless of the needle length (Figure 7D and E). hese results suggest that using finer nozzles will cause higher pressure drops, compared to nozzles with larger inner diameters. This can be attributed to the energy loss, caused by the wall-channel-related hydrodynamic resistance against the material flow, which requires higher dispensing pressures. Applying high pressures at the inlets can have a detrimental impact on the cell viability, also requiring the use of systems with more powerful pumps[28]. Nair *et al.*[61] also observed that the use of a nozzle tip, with a diameter of 0.15 mm and high extrusion pressure (40 psi≈ 2.75 bar), resulted in karyolysis as well as pyknosis.

3.4. Shear stress

The level of shear stress was carefully investigated in terms of key printing parameters, such as nozzle type, dispensing pressure, and needle diameter. Since the simulations were conducted for the entire printing head, the shear stress condition in the mixing chamber was first determined (Figure 8A). The simulation results showed that using the Kenics static mixer inside the printing head does not lead to a dramatic increase in the shear stress, as previously reported[28]. The shear stress distribution was further investigated for the cylindrical and conical nozzles at various dispensing pressures, and the results are presented in Figure 8B and C. As expected, results show that the nozzle is the most critical component of the entire printing system. This is mainly due to the abrupt narrowing of the cross-section in the nozzle domain, which results in a significant increase in the velocity field.

The shear stress inside the flow domain is generated by the velocity gradient[62-64]. Simulation results revealed that the maximum shear stress occurs at the needle walls, being minimum along the central axis for both needle types. Moreover, as observed from Figure 8B–E, for the same inlet pressure values, the highest shear stresses occur for the cone-shaped nozzle type (≈6 kPa). However, this is only visible at the very tip of the nozzle. On the other hand, the use of a cylindrical nozzle generates lower shear stresses along the nozzle length (≈1 kPa), but for a higher passage length (12 mm). Figure 8C depicts shear stress curves as a function of extrusion pressure for different conical nozzle diameters. The obtained results are similar to those obtained by Billiet *et al.*[34], who investigated the cell viability of HepG2 cells using different needle types. They carried out a finite element modeling simulation considering non-crosslinked cell-gelatin methacrylamide as the working fluid, and obtained higher peak shear stresses at 1 bar extrusion pressures for the conical nozzle in comparisonwith the cylindrical nozzle setup. Our results for conical shaped nozzle are also in a good agreement with reported studies by Emmermacher *et al.*[1] and Samandari *et al.*[28]. Figure 8D shows that, by reducing the needle outlet diameter or by increasing the dispensing pressure, the shear stress at the needle walls increases. However, these findings do not coincide with those from Liu *et al.*[65],

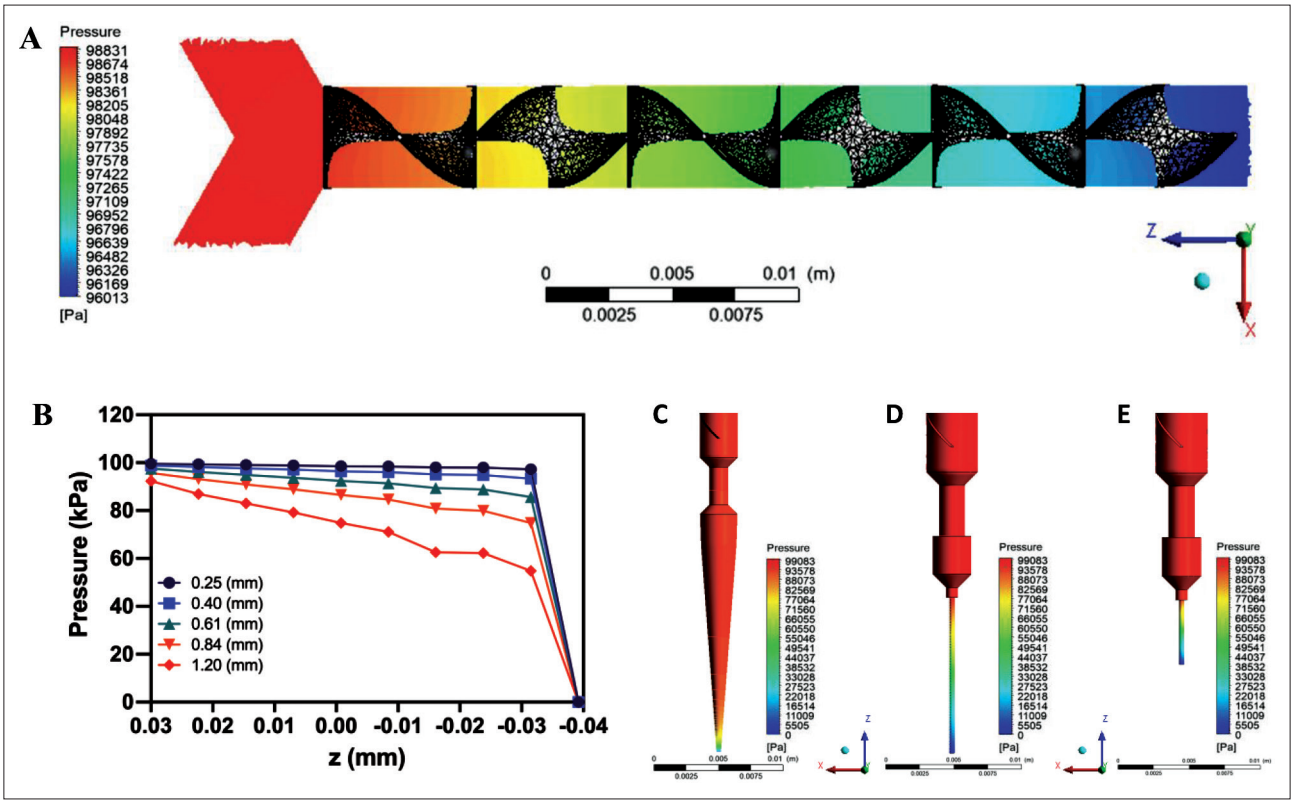

Figure 7. Pressure drop results for an inlet pressure of 1 bar. (A) The local pressure contour plot in the mixing chamber. (B) Variation of pressure along the axial direction of the printing head; contour plots of pressure drop for different nozzle types with outlet diameter of 0.4 mm. (C) Conical needle, (D) long cylindrical needle (12 mm), and (E) short cylindrical needle (5 mm).

as we obtained higher stress values for the conical nozzle type, which can be attributed to the different boundary conditions anddifferent bioink used in the simulations. Muller *et al.*[32] also investigated shear stresses for alginate/sulfate nanocellulose bioink through 2D axisymmetric finite element fluid flow simulations. They investigated the effect of shear stress using different nozzle types with varying outlet diameters. However, similar to Liu *et al.*[65], their findings cannot be directly compared with those from our study due to the different printing head geometry, applied biomaterials and boundary conditions.

In the case of cylindrical nozzles, shear stress distribution profiles at different inlet pressures (1, 2, and 3 bar) over the radius of nozzle outlet diameters ranging from 0.25 mm to 1.00 mm are illustrated in Figure 9. Results show that the shear stress distribution along the radial direction is linear, and it is nearly zero in the channel core. In addition, increasing the applied inlet pressure from 1 to 3 bar resulted in higher shear values, for all investigated nozzle diameters and shapes, which is aligned with other reported studies[32,33]. In all considered cases, the magnitude of the shear stress at the needle walls ranges between 0.5 and 4.8 kPa. The highest shear stress was obtained when a needle radius of 1.00 mm and 3 bar inlet pressure were employed, whereas the lowest stress occurred in the smallest cylindrical needle flow (0.25 mm) at 1 bar extrusion pressure.

These results seem to suggest that conically shaped needles are favored over straight needle types when the inlet pressure dependency is low, but this tends to disappear at greater dispensing pressures. We anticipate that at lower pressures, which correspond to longer passage time, the enhanced passage of high shear stress for the straight nozzle will have a greater impact on the cells. However, at higher extrusion pressures, the induced shear stress will be dramatically higher, and the lower passage time for the conical nozzle will no longer be able to compensate these high shear magnitudes. In their cell survival studies, Billiet *et al.*[34] showed that the conical nozzle exhibit high cell viability levels (>97% at low inlet pressures of <1 bar), but higher dispensing pressures resulted in substantial viability loss when compared to the straight nozzle type. Recently, Blaeser *et al.*[66] showed that for shear stress magnitudes below 5 kPa, the cell viability was almost not affected by the deposition process. The average cell viability was also examined for applied shear

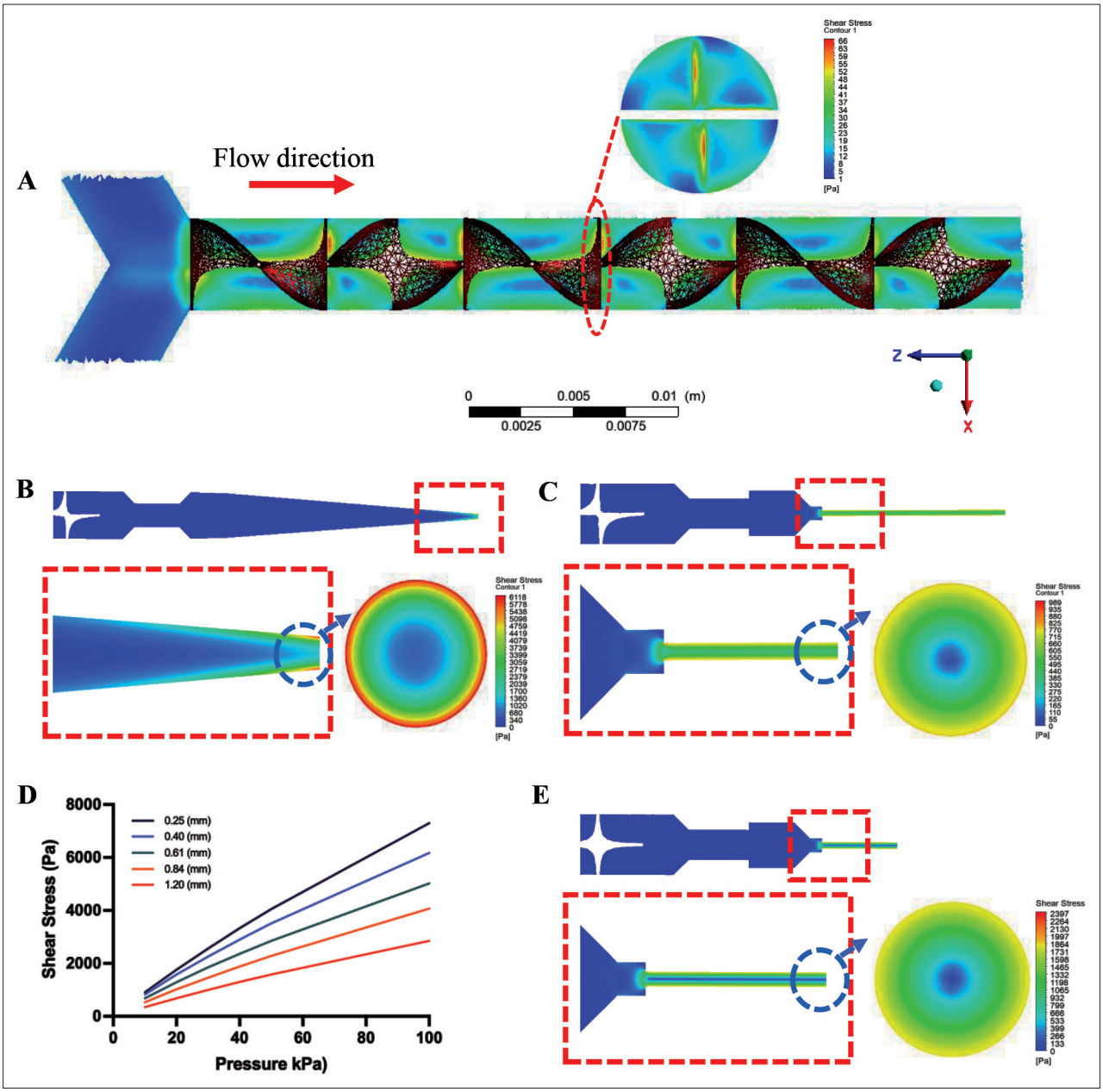

Figure 8. Shear stress distribution results for 1 bar of dispensing pressure. (A) Heat map of the shear stress along the KSM-inserted mixing channel. (B) Conical nozzle with a diameter of 0.4 mm.(C) Long cylindrical nozzle (12mm) with 0.4 mm outlet diameter.(D) Variation of shear stress as a function of applied pressure and nozzle diameter. (E)Contour plot of shear stress for short needle (5 mm).

stresses in the range of 5–10 kPa and >10kPa. Results revealed that the viability of cells decreased from 96% to 91% for moderate shear stresses (5–10 kPa), whereas a significant decrease was observed for the shear stresses over 10 kPa (76% of cell viability). Based on our simulation results, the maximum shear stress observed in the mixing channel was around 66 Pa. The highest shear stress for straight nozzles was below 5 kPa in all cases, whereas the peak stress values were obtained for conical needles with small outlet diameters (0.25 and 0.40 mm) at applied pressures of 1 bar. These results suggest that our printing heads will induce negligible cell damage. It should be noted that the rheological data, considered in our CFD simulations, was related to alginate and gelatin solutions without cells. However, several results demonstrated that, even in the case of high cell densities, no significant changes were observed on the bioink rheological characteristics[1,31,66,67].

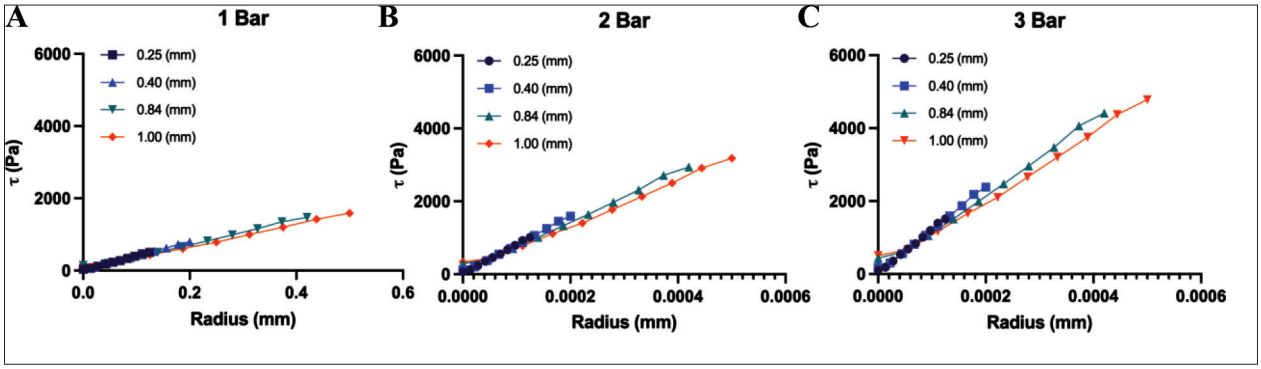

Figure 9. Shear stress profiles as a function of the cylindrical nozzle outlet radius at different inlet pressures. (A) 1 bar, (B) 2 bar, and (C) 3 bar.

4. Conclusion

The CFD model presented in this study enables to investigate the fluid flow of two different biopolymers in a KSM-integrated printing head during the extrusion process. The volumetric flow rate, pressure gradient, shear-thinning behavior of the alginate–gelatin mixture, and the shear stress that occurs in the fluid domain were successfully predicted using numerical results, allowing to optimize the bioprinting process and to reduce the laborious trial-and-error experimental approach. The spatial distribution of the biomaterials was analyzed at each successive cross-sectional planes along the mixing chamber. Due to the presence of chaotic advection, the proposed printhead exhibited high mixing performance, regardless of the applied pressure from the inlets. The volumetric flow rate and velocity field were deeply investigated for cylindrical and conical shaped nozzles, with different diameters under varying dispensing pressures. Results suggest that, if high bioprinting velocities are required, conical nozzles seem to be the most suitable option. It was also observed that the obtained maximum shear stress values were sufficiently low to sustain high cellular viability.

Future work will focus on the extrusion of multimaterials in the printing platform using a numerical model to further investigate operating parameters, such as the nozzle tip-build plate distance, relative velocity between nozzle and substrate, and morphological analysis of the fibers after the deposition process.

Acknowledgments

The first author acknowledges the support received from the Turkish Ministry of National Education.

Funding

This project has been partially supported by the University of Manchester and the Engineering and Physical Sciences Research Council (EPSRC) of the UK, the Global Challenges Research Fund (CRF), grant number EP/R01513/1.

Conflict of interest

The authors declare no conflict of interest. The funders had no role in the design of the study; in the collection, analyses, or interpretation of data; in the writing of the manuscript; or in the decision to publish the results.

Author contributions

Conceptualization: Paulo Bartolo
Investigation: Gokhan Ates
Methodology: Gokhan Ates
Writing – original draft: Gokhan Ates
Writing – review & editing: Paulo Bartolo

Ethics approval and consent to participate

Not applicable.

Consent for publication

Not applicable.

Availability of data

Data can be provided by request.

References

1. Emmermacher J, Spura D, Cziommer J, *et al.*, 2020, Engineering considerations on extrusion-based bioprinting: Interactions of material behavior, mechanical forces and cells in the printing needle. *Biofabrication*, 12(2):2–16.

   https://doi.org/10.1088/1758-5090/ab7553

2. Jiang T, Munguia-Lopez JG, Flores-Torres S, *et al.*, 2019, Extrusion bioprinting of soft materials: An emerging technique for biological model fabrication. *Appl Phys Rev*, 6(1).

   https://doi.org/10.1063/1.5059393

3. Trujillo-De Santiago G, Alvarez M, Samandari M, *et al.*, 2018, Chaotic printing: Using chaos to fabricate densely packed micro- and nanostructures at high resolution and speed. *Mater Horizons*, 5(5):813–822.

   https://doi.org/10.1039/c8mh00344k

4. Gungor-Ozkerim PS, Inci I, Zhang YS, *et al.*, 2018, Bioinks for 3D bioprinting: An overview. *Biomater Sci*, 6(6):915–946.

   https://doi.org/10.1039/c7bm00765e

5. Bartolo P, Malshe A, Ferraris E, *et al.*, 2022, 3D bioprinting: Materials, processes, and applications. *CIRP Ann*, 71(2): 577–597.

   https://doi.org/10.1016/j.cirp.2022.06.001

6. Liu F, Vyas C, Yang J, *et al.,* 2021, A review of hybrid biomanufacturing systems applied in tissue regeneration, in *Virtual Prototyping & Bio Manufacturing in Medical Applications*, 187–213.

   https://doi.org/10.1007/978-3-030-35880-8_8

7. Li X, Liu B, Pei B, *et al.,* 2020, Inkjet bioprinting of biomaterials. *Chem Rev*, 120(19):10793–10833.

   https://doi.org/10.1021/acs.chemrev.0c00008

8. Ng WL, Xi H, Shkolnikov V, *et al.*, 2021, Controlling droplet impact velocity and droplet volume: Key factors to achieving high cell viability in sub-nonoliter droplet-based bioprinting. *Int J Bioprint*, 8(1):424.

   https://doi.org/10.18063/IJB.V8I1.424

9. Zhuang P, Ng WL, An J, *et al.*, 2019, Layer-by-layer ultraviolet assisted extrusion-based (UAE) bioprinting of hydrogel constructs with high aspect ratio for soft tissue engineering applications. *PLoS One*, 14(6):e0216776.

   https://doi.org/10.1371/journal.pone.0216776

10. Ng WL, Lee JM, Zhou M, *et al.*, 2020, Vat polymerization-based bioprinting-process, materials, applications and regulatory challenges. *Biofabrication*, 12(2):022001.

    https://doi.org/10.1088/1758-5090/ab6034

11. Li W, Mille LS, Robledo JA, *et al.*, 2020, Recent advances in formulating and processing biomaterial inks for vat polymerization-based 3D printing. *Adv Healthc Mater*, 9(15):e2000156.

    https://doi.org/10.1002/adhm.202000156

12. Ning L, Chen X, 2017, A brief review of extrusion-based tissue scaffold bio-printing. *Biotechnol J*, 12(8).

    https://doi.org/10.1002/biot.201600671

13. Ozbolat IT, Hospodiuk M, 2016, Current advances and future perspectives in extrusion-based bioprinting. *Biomaterials*, 76:321–343.

    https://doi.org/10.1016/j.biomaterials.2015.10.076

14. Kang D, Hong G, An S, *et al.*, 2020, Bioprinting of multiscaled hepatic lobules within a highly vascularized construct. *Small*, 16(13):1–9.

    https://doi.org/10.1002/smll.201905505

15. Chávez-Madero C, Derby MD, Samandari M, *et al.*, 2020, Using chaotic advection for facile high-throughput fabrication of ordered multilayer micro-and nanostructures: Continuous chaotic printing. *Biofabrication*, 12(3).

    https://doi.org/10.1088/1758-5090/ab84cc

16. Ravanbakhsh H, Karamzadeh V, Bao G, *et al.,* 2021, Emerging technologies in multi-material bioprinting. *Adv Mater*, 33(49).

    https://doi.org/10.1002/adma.202104730

17. Costantini M, Testa S, Mozetic P, *et al.*, 2017, Microfluidic-enhanced 3D bioprinting of aligned myoblast-laden hydrogels leads to functionally organized myofibers in vitro and in vivo. *Biomaterials*, 131:98–110.

    https://doi.org/10.1016/j.biomaterials.2017.03.026

18. Prendergast ME, Burdick JA, 2020, Recent advances in enabling technologies in 3D printing for precision medicine. *Adv Mater*, 32(13).

    https://doi.org/10.1002/adma.201902516

19. Sodupe-Ortega E, Sanz-Garcia A, Pernia-Espinoza A, *et al.*, 2018, Accurate calibration in multi-material 3D bioprinting for tissue engineering. *Materials (Basel)*, 11(8):1–19.

    https://doi.org/10.3390/ma11081402

20. Kolesky DB, Truby RL, Gladman AS, *et al.*,2014, 3D bioprinting of vascularized, heterogeneous cell-laden tissue constructs. *Adv Mater*, 26(19):3124–3130.

    https://doi.org/10.1002/adma.201305506

21. Nadernezhad A, Khani N, Skvortsov G, *et al.*, 2016, Multifunctional 3D printing of heterogeneous hydrogel structures. *Sci Rep*, 6.

    https://doi.org/10.1038/srep33178

22. Liu W, Zhang YS, Heinrich MA, *et al.*, 2017, Rapid continuous multimaterial extrusion bioprinting. *Adv Mater*, 29(3):1–8.

    https://doi.org/10.1002/adma.201604630

23. Colosi C, Shin SR, Manoharan V, *et al.*, 2016, Microfluidic bioprinting of heterogeneous 3D tissue constructs using low-viscosity bioink. *Adv Mater*, 28(4):677–684a.

    https://doi.org/10.3390/MI11050459

24. Wang J, Zhang N, Chen J, *et al.,* 2019, Finding the optimal design of a passive microfluidic mixer. *Lab Chip*, 19(21):3618–3627.

    https://doi.org/10.1039/c9lc00546c

25. Ceballos-González CF, Bolívar-Monsalve EJ, Quevedo-Moreno DA, *et al.*, 2021, High-throughput and continuous chaotic bioprinting of spatially controlled bacterial microcosms. *ACS Biomater Sci Eng*, 7(6):2408–2419.

    https://doi.org/10.1021/acsbiomaterials.0c01646

26. Li M, Tian X, Schreyer DJ, *et al.,* 2011, Effect of needle geometry on flow rate and cell damage in the dispensing-based biofabrication process. *Biotechnol Prog*, 27(6):1777–1784.

    https://doi.org/10.1002/btpr.679

27. Andrew CD, Susan EC, Emily MR., *et al*., 2016, A comparison of different bioinks for 3D bioprinting of fibrocartilage and hyaline cartilage. *Biofabrication*, 8(4):45002.

    https://doi.org/10.1088/1758-5090/8/4/045002

28. Samandari M, Alipanah F, Majidzadeh AK, *et al.,* 2021, Controlling cellular organization in bioprinting thrountalizationgh designed 3D microcompartme. *Appl Phys Rev*, 8(2).

    https://doi.org/10.1063/5.0040732

29. Yu Y, Zhang Y, Martin JA, *et al.,* 2013, Evaluation of cell viability and functionality in vessel-like bioprintable cell-laden tubular channels. *J Biomech Eng*, 135(9):1–9.

    https://doi.org/10.1115/1.4024575

30. Li M, Tian X, Zhu N, 2010, Modeling process-induced cell damagein the biodispensing process. *Tissue Eng Part C: Methods*, 16(3):533–542.

    https://doi.org/10.1089=ten.tec.2009.0178533

31. Chiesa I, Ligorio C, Bonatti AF, *et al.*, 2020, Modeling the three-dimensional bioprinting process of β-sheet self-assembling peptide hydrogel scaffolds. *Front Med Technol*, 2:1–16.

    https://doi.org/10.3389/fmedt.2020.571626

32. Müller M, Öztürk E, Arlov Ø, *et al.,* 2017, Alginate sulfate–nanocellulose bioinks for cartilage bioprinting applications. *Ann Biomed Eng*, 45(1):210–223.

    https://doi.org/10.1007/s10439-016-1704-5

33. Serna JA, Florez SL, Talero VA, *et al.,* 2019, Formulation and characterization of a SIS-based photocrosslinkable bioink. *Polymers (Basel)*, 11(3):1–10.

    https://doi.org/10.3390/polym11030569

34. Billiet T, Gevaert E, De Schryver T, *et al.,* 2014, The 3D printing of gelatin methacrylamide cell-laden tissue-engineered constructs with high cell viability. *Biomaterials*, 35(1):49–62.

    https://doi.org/10.1016/j.biomaterials.2013.09.078

35. Mahammedi A, Ameur H, Ariss A, *et al.,* 2017, Numerical investigation of the performance of Kenics static mixers for the agitation of shear thinning fluids. *J Appl Fluid Mech*, 10(3):989–999.

    https://doi.org/10.18869/acadpub.jafm.73.240.27314

36. Hobbs DM, Swanson PD, Muzzio FJ, 1998, Numerical characterization of low Reynolds number flow in the Kenics static mixer. *Chem Eng Sci*, 53(8):1565–1584.

    https://doi.org/10.1016/S0009-2509(97)00132-2

37. Nyande BW, Mathew Thomas K, Lakerveld R, 2021, CFD analysis of a Kenics static mixer with a low pressure drop under laminar flow conditions. *Ind Eng Chem Res*, 60(14):5264–5277.

    https://doi.org/10.1021/acs.iecr.1c00135

38. Bird RB, 2007, Transport Phenomena Rev, 2nd ed, New York, Wiley.

39. Chhabra RP, Richardson JF, 2011, Chapter 1. Non-Newtonian fluid behaviour, in *Non-Newtonian Flow and Applied Rheology: Engineering Applications*, 536.

    https://doi.org/10.1016/b978-075063770-1/50002-6

40. Neofytou P, 2005, A 3rd order upwind finite volume method for generalised Newtonian fluid flows. *Adv Eng Softw*, 36(10):664–680.

    https://doi.org/10.1016/j.advengsoft.2005.03.011

41. Metzner AB, 1957, Non-Newtonian fluid flow relationships between recent pressure-drop correlations. *Ind Eng Chem*, 49(9):1429–1432.

    https://doi.org/10.1021/ie50573a049

42. Blaeser A, Million N, Campos DFD, *et al.*, 2016, Laser-based in situ embedding of metal nanoparticles into bioextruded alginate hydrogel tubes enhances human endothelial cell adhesion. *Nano Res*, 9(11):3407–3427.

    https://doi.org/10.1007/s12274-016-1218-3

43. Thompson JF, Soni BK, Weatherill NP, 1999, *Handbook of Grid Generation*, Boca Raton, FL, CRC Press.

    https://doi.org/10.1201/9781420050349

44. Thakur RK, Vial C, Nigam KDP, *et al.,* 2003, Static mixers in the process industries—A review, 81.

    https://doi.org/10.1205/026387603322302968

45. Rafeie M, Welleweerd M, Hassanzadeh-Barforoushi A, *et al.,* 2017, An easily fabricated three-dimensional threaded lemniscate-shaped micromixer for a wide range of flow rates. *Biomicrofluidics*, 11(1).

    https://doi.org/10.1063/1.4974904

46. Santana HS, Silva JL, Taranto OP, 2015, Numerical simulation of mixing and reaction of Jatropha curcas oil and ethanol for synthesis of biodiesel in micromixers. *Chem Eng Sci*, 132:59–168.

    https://doi.org/10.1016/j.ces.2015.04.014

47. Zhang J, Luo X, 2018, Mixing performance of a 3D micro T-mixer with swirl-inducing inlets and rectangular constriction. *Micromachines*, 9(5).

https://doi.org/10.3390/mi9050199

48. Shah I, Kim SW, Kim K, *et al.,* 2019, Experimental and numerical analysis of Y-shaped split and recombination micro-mixer with different mixing units. *Chem Eng J*, 358:691–706.

https://doi.org/10.1016/j.cej.2018.09.045

49. Raza W, Hossain S, Kim KY, 2017, Effective mixing in a short serpentine split-and-recombination micromixer. *Sensors Actuators B Chem*, 258:381–392.

https://dx.doi.org/10.1016/j.snb.2017.11.135

50. Mouheb NA, Malsch D, Montillet A, *et al.,* 2012, Numerical and experimental investigations of mixing in T-shaped and cross-shaped micromixers. *Chem Eng Sci*, 68(1):278–289.

https://doi.org/10.1016/j.ces.2011.09.036

51. Rauline D, Tanguy PA, Le Blévec JM, *et al.*, 1998, Numerical investigation of the performance of several static mixers. *The Canadian J Chem Eng*, 76(3):527–535.

https://doi.org/10.1002/cjce.5450760325

52. Grace HP, 1982, Dispersion phenomena in high viscosity immiscible fluid systems and application of static mixers as dispersion devices in such systems. *Chem Eng Commun*, 14(3–6):225–277.

https://doi.org/10.1080/00986448208911047

53. Shah NF, Kale DD, 1991, Pressure drop for laminar flow of non-Newtonian fluids in static mixers. *Chem Eng Sci*, 46(8):2159–2161.

https://doi.org/10.1016/0009-2509(91)80175-X

54. Haddadi MM, Hosseini SH, Rashtchian D, *et al.,* 2020, Comparative analysis of different static mixers performance by CFD technique: An innovative mixer. *Chin J Chem Eng*, 28(3):672–684.

https://doi.org/10.1016/j.cjche.2019.09.004

55. Ates G, Bartolo P, 2021, Numerical simulation of multimaterial polymer mixing for bioprinting applications. *J Addit Manuf Technol*, 1(3):606.

https://10.18416/JAMTECH.2111606

56. Hozumi T, Ohta S, Ito T, 2015, Analysis of the calcium alginate gelation process using a Kenics static mixer. *Ind Eng Chem Res*, 54(7):2099–2107.

https://doi.org/10.1021/ie5044693

57. Ortega ES, Sanz-Garcia A, Pernia-Espinoza A, *et al.,* 2019, Efficient fabrication of polycaprolactone scaffolds for printing hybrid tissue-engineered constructs. *Materials (Basel)*, 12(4):1–18.

https://doi.org/10.3390/ma12040613

58. Aguado BA, Mulyasasmita W, Su J, *et al.,* 2012, Improving viability of stem cells during syringe needle flow through the design of hydrogel cell carriers. *Tissue Eng Part A*, 18(7-8): 806–815.

https://doi.org/10.1089/ten.tea.2011.0391

59. Gómez-Blanco JC, Mancha-Sánchez E, Marcos AC, *et al.,* 2020, Bioink temperature influence on shear stress, pressure and velocity using computational simulation. *Processes*, 8(7):1–18.

https://doi.org/10.3390/PR8070865

60. Meng HB, Song MY, Yu YF, *et al.,* 2017, Enhancement of laminar flow and mixing performance in a lightnin static mixer. *Int J Chem React Eng*, 15(3):1–21.

https://doi.org/10.1515/ijcre-2016-0112

61. Nair K, Gandhi M, Khalil S, *et al.*, 2009, Characterization of cell viability during bioprinting processes. *Biotechnol J*, 4(8):1168–1177.

https://doi.org/10.1002/biot.200900004

62. Sarker M, Chen XB, 2017, Modeling the flow behavior and flow rate of medium viscosity alginate for scaffold fabrication with a three-dimensional bioplotter. *J Manuf Sci Eng Trans ASME*, 139(8):1–14.

https://doi.org/10.1115/1.4036226

63. Paxton N, Smolan W, Böck T, *et al.,* 2017, Proposal to assess printability of bioinks for extrusion-based bioprinting and evaluation of rheological properties governing bioprintability. *Biofabrication*, 9(4).

https://doi.org/10.1088/1758-5090/aa8dd8

64. Snyder J, Son AR, Hamid Q, et al., 2015, Mesenchymal stem cell printing and process regulated cell properties. *Biofabrication*, 7(4).

https://doi.org/10.1088/1758-5090/7/4/044106

65. Liu W, Heinrich MA, Zhou Y, *et al.*, 2017, Extrusion bioprinting of shear-thinning gelatin methacryloyl bioinks. *Adv Healthc Mater*, 6(12):1–11.

https://doi.org/10.1002/adhm.201601451

66. Blaeser A, Campos DFD, Puster U, *et al.*, 2016, Controlling shear stress in 3D bioprinting is a key factor to balance printing resolution and stem cell integrity. *Adv Healthc Mater*, 5(3):326–333.

https://doi.org/10.1002/adhm.201500677

67. Manojlovic V, Djonlagic J, Obradovic B, *et al.,* 2006, Investigations of cell immobilization in alginate: Rheological and electrostatic extrusion studies. *J Chem Technol Biotechnol*, 81(4):505–510.

https://doi.org/10.1002/jctb.1465

ACCSCIENCE PUBLISHING

International Journal of Bioprinting

RESEARCH ARTICLE

Printed cisplatin on microneedle arrays for transdermal delivery enhances olaparib-induced synthetic lethality in a mouse model of homologous recombination deficiency

Zoi Kanaki[1], Alexandra Smina[1], Chrysoula Chandrinou[2], Fotini E. Koukouzeli[1], Yiannis Ntounias[1], Nikolaos Paschalidis[1], Ilias Cheliotis[2], Marina Makrygianni[2], Jill Ziesmer[3], Georgios A. Sotiriou[3], Ioanna Zergioti[2], Constantin Tamvakopoulos[1], and Apostolos Klinakis[1]*

[1]Biomedical Research Foundation Academy of Athens, 4 Soranou Efessiou Street, 11527 Athens, Greece

[2]Department of Physics, School of Mathematical and Physical Sciences, National Technical University of Athens, Heroon Polytehneiou 9, 15780 Athens, Greece

[3]Department of Microbiology, Tumor and Cell Biology, Karolinska Institutet, SE-171 77 Stockholm, Sweden

(This article belongs to the *Special Issue: Laser bioprinting technologies*)

Abstract

Small molecule inhibitors targeting specific proteins are claiming a continuously growing share in cancer therapy, more commonly in combination with traditional chemotherapeutic drugs. While these inhibitors are taken orally, the majority of chemotherapies are administered through intravenous injection in the hospital premises. Alternative routes for chemotherapy administration would allow more frequent administration at lower dosing by the patient oneself, allowing combination treatment with reduced side effects. Here, we employed laser printing to prepare microneedles for transdermal delivery of cisplatin. Combination treatment with cisplatin transdermally and the poly (ADP-ribose) polymerase (PARP) inhibitor olaparib orally leads to effective treatment in a cancer xenograft mouse model *in vivo*, while reducing the risk for systemic side effects. This work opens new avenues in anti-cancer therapy by allowing the administration of chemotherapy without the need for intravenous injection alone or in combination with other therapies.

Keywords: Laser-induced forward transfer; Microneedles; Metronomic chemotherapy; Transdermal dosing; Synthetic lethality; Homologous recombination deficiency

***Corresponding author:**
Apostolos Klinakis
(aklinakis@bioacademy.gr)

Citation: Kanaki Z, Smina A, Chandrinou C, *et al*., 2023, Printed cisplatin on microneedle arrays for transdermal delivery enhances olaparib-induced synthetic lethality in a mouse model of homologous recombination deficiency. *Int J Bioprint*, 9(6): 0048. https://doi.org/10.36922/ijb.0048

Received: February 10, 2023
Accepted: March 23, 2023
Published Online: June 23, 2023

Copyright: © 2023 Author(s). This is an Open Access article distributed under the terms of the Creative Commons Attribution License, permitting distribution, and reproduction in any medium, provided the original work is properly cited.

Publisher's Note: AccScience Publishing remains neutral with regard to jurisdictional claims in published maps and institutional affiliations.

1. Introduction

Chemotherapy has been the cornerstone of anti-cancer therapy for several decades now. More recently, advances in next-generation sequencing allowed the identification of several actionable mutations which can be exploited therapeutically toward personalized approaches in cancer treatment[1]. Novel targeted therapies such as small molecules and antibodies that emerged after the 2000s showed great promise and were approved for

clinical use[2]. Among those, small molecules targeting poly (ADP-ribose) polymerase (PARP1/2) became the first drug designed to exploit synthetic lethality, a genetic concept described in model organism almost a century ago[3]. PARP1/2 proteins play an important role in the repair of single-strand breaks of the DNA[4].

An initial observation that cells carrying inactivating mutations in the *BRCA1* or *BRCA2* genes cannot survive PARP inhibition[5,6] catalyzed efforts to therapeutically target PARP proteins in cancer. Because women with germline mutations in these genes are at risk of developing breast and ovarian cancer, the first of a series of approvals by the U.S. Food and Drug Administration (FDA) for PARP1/2 inhibitors (PARPi) came in 2014 for the small molecule olaparib[7] against ovarian cancer in patients carrying *BRCA1* and *BRCA2* mutations. These mutations disrupt a DNA repair pathway known as homologous recombination (HR) repair, which is used to repair double-strand breaks[8]. PARP inhibition leads to unrepaired single-strand breaks, which in turn produce double-strand breaks, which cannot be repaired by HR-deficient cells, such as those carrying inactivating mutations in *BRCA1* and *BRCA2*. Eventually, these cells accumulate intolerable levels of DNA damage and are driven to cell death.

Besides the development of multiple PARPi which are approved for several indications as monotherapy[9], multiple studies have focused on the combination of PARPi with chemotherapy or other targeted therapies[10,11]. As serious dose-limiting toxicities were observed, a new trial (clinicaltrials.gov identifier: NCT00782574) aimed to establish the maximum tolerable dose and to evaluate the pharmacokinetics and preliminary efficacy of olaparib in combination with cisplatin in patients with advanced solid tumors. This study indicated that systematic administration of olaparib orally (100 mg or 200 mg twice a day) in combination with a standard single dose of cisplatin (75 mg/m^2) in the beginning of each 21-day cycle was not tolerable[12]. Some of the observed toxicities have been previously described in olaparib clinical trials, while others are clearly associated with cisplatin. Intermittent administration of olaparib at a lower dose (50 mg twice a day), which is close to the minimum dose of 60 mg twice daily that achieves 90% PARP inhibition[13], together with a reduced dose of cisplatin (60 mg/m^2), improved tolerability[12] and showed improved objective response rate, in comparison to olaparib monotherapy in previous phase II clinical trials[14-16]. These findings imply that there is obviously room for dose optimization. One solution could be the administration of lower doses of cisplatin in more frequent intervals. However, metronomic dosing of this platinum-based drug would be practically limited, since cisplatin is administered intravenously while PARPi is taken orally. Thus, alternative administration routes for cisplatin would be beneficial.

Microneedles (MNs) have emerged as an alternative approach for transdermal drug delivery because they allow transdermal administration, reduced pain, and delivery of molecules of high molecular weight. Drug-coated MNs, which are suitable for both hydrophilic and hydrophobic drugs[17-19], are ideal for low-dose administration of chemotherapeutic drugs, such as cisplatin[20-22]. This approach would eliminate the need to visit the hospital for intravenous administration of the drug. However, limited drug quantity and drug material waste, as well as uniformity of coating, are major limitations of this approach.

Recently, three-dimensional (3D) printing technologies have emerged as a valuable tool in the biomedical field. These technologies allow for the layer-by-layer construction of 3D structures using a variety of materials. The 3D printing approaches can be utilized to coat MNs by transporting little microdroplets of the active pharmaceutical ingredient (API) solution onto the MNs, hence creating uniform layers. Inkjet printing has been successfully used for MN coating for transdermal delivery of anti-cancer drugs[23-25]; however, limitations with the deposition of highly viscous inks onto a given substrate are encountered, and nozzle clogging is observed[26,27]. Laser-induced forward transfer (LIFT)[28], on the other hand, offers superior resolution, nozzle-free, and viscosity-independent laser printing of organic and inorganic material. We have previously used the LIFT technology to coat MNs with the chemotherapeutic drug gemcitabine. Transdermal application of the MNs in animal models leads to drug release, achieving substantial plasma levels[29].

Here, we exploited LIFT to coat MNs for transdermal delivery of cisplatin in mice. Pharmacokinetic studies indicated that transdermal application of the MNs produced cisplatin plasma levels that were low but detectable particularly at the later time points of the study (24 h). We generated mouse xenograft models using HR-deficient non-small cell lung cancer cells, and, by exploiting synthetic lethality, we showed that transdermal delivery of cisplatin in combination with oral olaparib leads to effective treatment *in vivo*.

2. Materials and methods

2.1. Materials

Olaparib and cisplatin (powder, 99.70%) were purchased from MedChemExpress (Monmouth Junction, NJ, USA). Ketamine was purchased from Richter Pharma AG (Wels, Austria). Xylazine was purchased from Neocell Pharmaceuticals (Athens, Greece). The LC-MS grade solvents ammonium acetate, formic acid (FA),

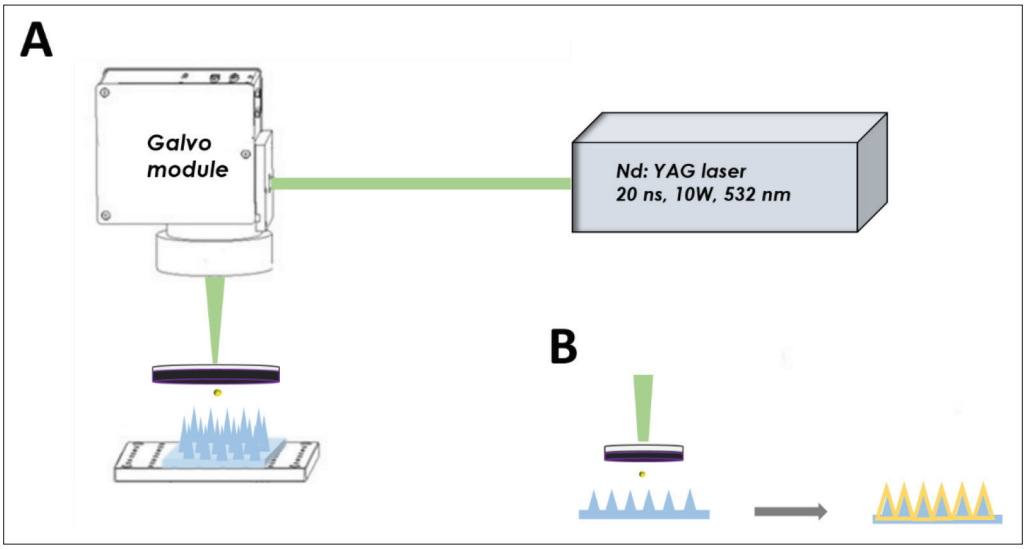

Figure 1. Schematic representation of the LIFT printing process for coating the MNs with cisplatin solution. (A) LIFT setup. (B) Coating process.

water (H_20), and methanol (≥99.8%) were procured from Fisher Scientific (Loughborough, UK). Acetonitrile (ACN; LC-MS grade) was bought from Carlo Erba (Milan, Italy). Sodium diethyldithiocarbamate trihydrate (DDTC) was obtained from Sigma Aldrich (Sigma-Aldrich Chemie GmbH, Munich, Germany). Blank (control) plasma was prepared via centrifugation of whole blood in a Heraeus Biofuge Pico. Midazolam was kindly provided by Onassis Cardiac Surgery Center (Athens, Greece) in the context of a research program in the form of a solution of Dormixal 15 mg/3 mL.

2.2. Cisplatin solubility

Due to the poor solubility properties of cisplatin in both H_20 and ethanol (EtOH)[30], solubility experiments were performed in distinct solvent mixtures to determine the optimal solvent system and highest concentration of the compound that would be compatible with the LIFT technology. We initially tested a range of cisplatin concentrations in H_20, achieving a soluble concentration of the compound (1 mg/mL). Following that, we checked cisplatin solubility in a solvent system of 10% glycerol in H_20, considering glycerol as a compatible reagent with the LIFT printing process. The solubility of cisplatin in the 10% glycerol in H_20 solvent system was low (<1 mg/mL). Since water mediates displacement of the chloride atoms in cisplatin (aquation) with unknown effects in the compound's pharmacological action, we further tested cisplatin solubility in saline and a 10% glycerol in saline solvent system, respectively. Since cisplatin was insoluble in the glycerol–saline mixture even at 1 mg/mL, saline was opted as the most ideal vehicle for the laser printing conditions and the *in vivo* administration.

2.3. MN array fabrication

Polymethylmethacrylate (PMMA; MW 120k, Sigma-Aldrich) was used to create MN arrays as previously reported[31] by dissolving it at 30 w/v% in ethyl lactate (≥98 %, Sigma-Aldrich) for 1.5 h at 150°C. The 100 pyramidal chambers in the MN molds (Micropoint Technologies) have a base length and height of 200 μm and 600 μm, respectively. The MN mold was cast with 50 mg of 30 w/v% PMMA, which was then centrifuged for 30 min at 3500 rpm and allowed to dry overnight in the fume hood.

2.4. LIFT process

The setup used for the LIFT printing of cisplatin solutions on MNs is designed for high-speed printing and is presented in Figure 1. The laser source is a DPSS Nd:YAG laser (Sol 10W 532 nm, BrightSolutions, Prado PV, Italy) emitting a wavelength of 532 nm with a maximum output power of 10 W. It delivers pulse duration of around 20 ns, with a repetition rate of 1–100 kHz, respectively, and a Gaussian beam profile. The laser beam is scanned with speeds up to 3 m/sec by utilizing a 2D galvanometric mirror scanning system (intelliSCAN III 10, SCANLAB, Puchheim, Germany) and an f-theta lens implementing a focal length of 100 mm. A beam expander configuration consisting of a two-lens setup transformed the output laser's beam into the desired 10-mm input size for the galvanometric scanning head. After leaving the laser source, the laser beam travels through the optical setup to determine its size and shape before irradiating a donor substrate that contains the substance to be deposited. The imaging system monitored the whole process in real time via a customized microscope system equipped with a camera enabling the accurate alignment of the target and substrate materials.

The donor substrate consisted of a transparent glass coated with a Ti film laser absorbing interlayer, onto which 5 μL of the cisplatin solution (1 mg/mL in saline) were drop cast. The receiver substrate was the MN patch onto which the cisplatin solution was transferred.

The printing process has been described previously[29]. Briefly, by focusing the laser beam onto the donor substrate, a high-pressure vapor pocket is produced at the interface of the deposited API solution and the Ti layer as a result of the donor's Ti layer absorbing the laser pulse. For each laser beam pulse, an nL droplet of cisplatin solution is printed onto the MN substrates as a result of this high-pressure vapor pocket expanding and propelling the supernatant fluid into a dynamic jet that drives the API solution to the receiver substrate at a high-impact velocity. The donor–receiver substrate distance was kept at 700 μm. On the MNs substrate, the laser transfer produced a continuous cisplatin film (5 × 5 mm) of 5 μL of the API solution. The LIFT process was repeated two more times on the same MN patch to achieve a total nominal amount of 15 μL of cisplatin solution. The coated MN patches' morphology was determined by scanning electron microscopy (SEM; FESEM Nova NanoSEM 230, by FEI Europe, Eindhoven, Netherlands).

2.5. Preparation of cisplatin stock and standard solutions

Stock solutions of cisplatin were prepared by dissolving approximately 3 mg of the compound in saline at a final concentration of 1 mg/mL. For preparation of cisplatin working solutions, serial dilutions in ACN:H_20 (1:1, v/v) were prepared in the concentration ranges of 50 ng/mL to 25 μg/mL. The internal standard midazolam was prepared by serially diluting Dormixal 15 mg/3 mL in ACN:H_20 (1:1, v/v) to 100 ng/mL. All stock and working solutions were stored at 4°C until the day of sample preparation in mouse plasma.

2.6. Pharmacokinetic studies

Cisplatin was administered in mice transdermally or intraperitoneally for evaluation of its pharmacokinetic properties per dosing route. For transdermal administration of cisplatin in mice, MN patches with 15 μg of LIFT-printed cisplatin were prepared. Furthermore, for intraperitoneal dosing of the platinum-based compound, a solution of 600 μg/mL in saline was prepared. Four mice were used for administration per dosing route, and all mice were equally dosed with 60 μg of cisplatin in MN or administered with cisplatin intraperitoneally. A serial cheek bleeding protocol was performed in mice at 2, 4, 24, and 72 h after MN application or intraperitoneal injection. The collected blood samples were placed in heparinized Eppendorf tubes, containing 10 μL heparin (5000 IU/mL), which were then placed immediately on ice and centrifuged for 10 min at 3000 rpm. Plasma was then stored in a -80°C freezer until the time of analysis. Mice were then euthanized.

For sample preparation, mouse plasma (50 μL) was placed in low-retention Eppendorf tubes and was spiked with 5 μL of cisplatin working solutions for the preparation of standards. A DDTC solution (1% DDTC in 0.1N NaOH) was then added (15 μL), and samples were vortexed and incubated in a water bath (40°C) for 30 min for the formation of the Pt-DDTC complex. Following the incubation step, 500 μL of cold ACN with internal standard (IS, midazolam, 1 ng/mL) was added to the precipitate of proteins. Subsequently, samples were vortexed for 2 min and centrifuged at 13,000 rpm for 10 min. The supernatant containing the Pt-DDTC complex and IS was transferred into glass tubes, and evaporation to dryness followed (50°C) for approximately 60 min. Samples were then reconstituted in 150 μL of H_20:ACN:FA (80:20:0.1%), centrifuged for 1 min, and then transferred into 96-well plates for liquid chromatography tandem mass spectrometry (LC-MS/MS) analysis[32].

2.7. Detection and quantification of cisplatin via LC-MS/MS

The amount of cisplatin in standard and unknown samples was determined via a LC-MS/MS methodology, previously reported by Agilent[32] with slight modifications, that quantifies cisplatin after derivatization with a DDTC reagent and formation of a Pt-DDTC complex. For the setup of the bioanalytical assay and sample analyses, a Triple Quad 5500+ LC-MS/MS System – QTRAP (AB SCIEX LLC, CA, USA) was used. Chromatographic separation of the analyte of interest was accomplished via a dC18 column (Waters, Atlantis, 2.1 × 50 mm, 3 μM) at a flow rate of 0.3 mL/min. Mobile phases included solution A (100% H_20, 0.1% formic acid [FA]), solution B (100% ACN), and needle wash (ACN:MeOH:H_20, 1:1:1), and injection volume for each sample was 10 μL. Elution of the analyte was achieved by applying a gradient system described as follows: T = 0–0.5 min for 95% A and 5% B, T = 1.0 min for 25% A and 75% B, T = 1.5 min for 10% A and 90% B, T = 2.5–4.0 min for 5% A and 95% B, T = 5.0 min for 95% A and 5% B. The transitions monitored via multiple reaction monitoring were m/z 492.5/422.1 for cisplatin at 2.67 min and m/z 326.1/291.1 at 2.44 min for midazolam, respectively. Additionally, transitions m/z 640.4/116.1 and 640.4/492.0 for cisplatin and 326.1/209.1 for midazolam, respectively, were used for confirmation of the bioanalytical result. The mass spectrometry (MS) system was operated using positive electrospray ionization mode (ESI). The applied bioanalytical methodology

and linearity of cisplatin was tested in a concentration range of 10–1000 ng/mL in mouse plasma with a limit of quantification (LOQ; at 10 ng/mL).

2.8. Cell expansion

H1437 cells were originally purchased from the American Type Culture Collection (ATCC). Cells were grown in Dulbecco's Modified Eagle's Medium (DMEM) supplemented with 10% fetal bovine serum and penicillin/streptomycin in a humidified chamber with 5% CO_2.

2.9. Efficacy study

NOD.Cg-Prkdc scid Il2rg tm1Wjl/SzJ mice (NSG mice; Stock No.: 005557)[33,34] were purchased from the Jax repository (Bar Harbor, ME, USA) and bred in individually ventilated cages under specific pathogen-free conditions, under veterinarian supervision, in full compliance with Federation of Laboratory Animal Science Associations recommendations in the Animal House Facility of the Biomedical Research Foundation of the Academy of Athens (BRFAA, Greece). All procedures for care and treatment of animals were approved by the Institutional Committee on Ethics of Animal Experiments and the Greek Ministry of Agriculture (Protocol #1392861, 28/12/22).

H1437 and H1437 KMT2C/KD cells were grown in DMEM supplemented with 10% fetal bovine serum and penicillin/streptomycin. Two million of cells were injected subcutaneously in the right flank of approximately 6-week-old male NSG mice. Tumor dimensions were measured with a caliper. When tumors grew to a diameter of approximately 0.3 cm, the mice were randomly assigned to groups. No exclusion criterion was applied. Four groups of at least 8 mice for either H1437 or the KMT2C/KD derivative were used for *in vivo* administration of olaparib, olaparib/cisplatin (Olap/C-IP), olaparib/cisplatin-MNs (Olap/C-MN), and vehicle. Cisplatin was administered to mice either transdermally or intraperitoneally. The efficacy of the vehicle cohort, Olap/C-IP cohort, and Olap/C-MN cohort was compared with one another. Cisplatin dosing was 3 mg/kg of cisplatin either intraperitoneally or transdermally, i.e., 60 μg/dose. Furthermore, 50 mg/kg olaparib in saline solution containing 12.5% dimethylsulfoxide (DMSO) and 12.5% Kolliphor® EL (Sigma-Aldrich) was administered orally on a daily basis. This is the typical amount of olaparib administered in mice for therapeutic purposes by most groups.

For transdermal application of cisplatin, mice were anesthetized with a ketamine:xylazine mix (90 mg/kg ketamine and 10 mg/kg xylazine) as previously described[29,35]. MN application onto the skin of mice was previously described[29]. Briefly, the opposite (left) non-tumor-bearing flank of the mouse was shaved, and four MN patches, with each containing 15 μg of cisplatin, were pressed with the thumb for approximately 2 min and then taped with 3M™ Steri-Strip™ Reinforced Adhesive Skin Closures (Digas, Athens, Greece) for 60 min. The vehicle cohort was treated daily with saline solution containing 12.5% DMSO and 12.5% Kolliphor® EL orally, and every 5 days with saline intraperitoneally. After 15 days, the mice were sacrificed with cervical dislocation, and the tumors were dissected, weighed, and photographed.

2.10. Cisplatin uptake measurement with mass cytometry-CyTOF

Frozen murine lung tumor tissue specimens were thawed in ice-cold dissociation solution (PBS supplemented with 2 mM EDTA). Tissues were further dissected into small pieces with an average size of approximately 27–30 mm^3 (3 × 3 × 3 mm). Then, using a culture dish filled with dissociation solution, tissue was pressed through a 100-μm nylon mesh with the plunger of a 5-mL syringe to prepare a cell suspension. During this step, the nylon mesh was in contact with the surface of the liquid in the culture dish. The mesh was then rinsed two or three times with ice-cold dissociation solution. Resulting suspension was then filtered through a 40-μm nylon mesh and adjusted on top of a 50-mL polypropylene Falcon tube, and dissociation solution was added to a final volume of 15 mL followed by centrifugation at 300 × *g* for 7 min. Cells were then washed twice with 5 mL of Maxpar Cell Staining Buffer (CSB) from Standard BioTools Inc. (SB; South San Francisco, CA, USA; formerly known as Fluidigm) and centrifuged at 300 × *g* for 5 min. Following washing, cells were fixed with freshly prepared 2%, filtered, methanol-free formaldehyde solution (prepared from 16% stock solution; Sigma-Aldrich) for 10 min at room temperature. Fixed cells were then centrifuged at 800 × *g* for 5 min and stained with DNA intercalator solution (1:1000 dilution of 125 μM Cell-ID™ Intercalator-Ir) in Maxpar Fix and Perm buffer (all from SB, USA) and incubated at 4°C overnight. The following day, cells were washed twice with CSB buffer and cell acquisition solution (SB, USA). Immediately before the acquisition, cells were re-suspended in cell acquisition solution supplemented with EQ Four Element Calibration Beads (EQ4 beads from SB), diluted 1:10, at a final cell concentration 1×10^6 cells/mL. Acquisition was performed on a Helios™ mass cytometry system (SB). To maximize data quality, the acquisition rate on the Helios was maintained at a rate of <400 events/s. Acquired data were normalized using EQ4 beads (SB method) with CyTOF software (version 10.7.1014). Normalized fcs files were analyzed with bivariate dot plots and histograms in FlowJo™ v10.8 Software (BD Life Sciences, Franklin Lakes, NJ, USA). Graphs and statistical analysis were performed using GraphPad Prism 9 (version 9.2.0 for Windows, GraphPad

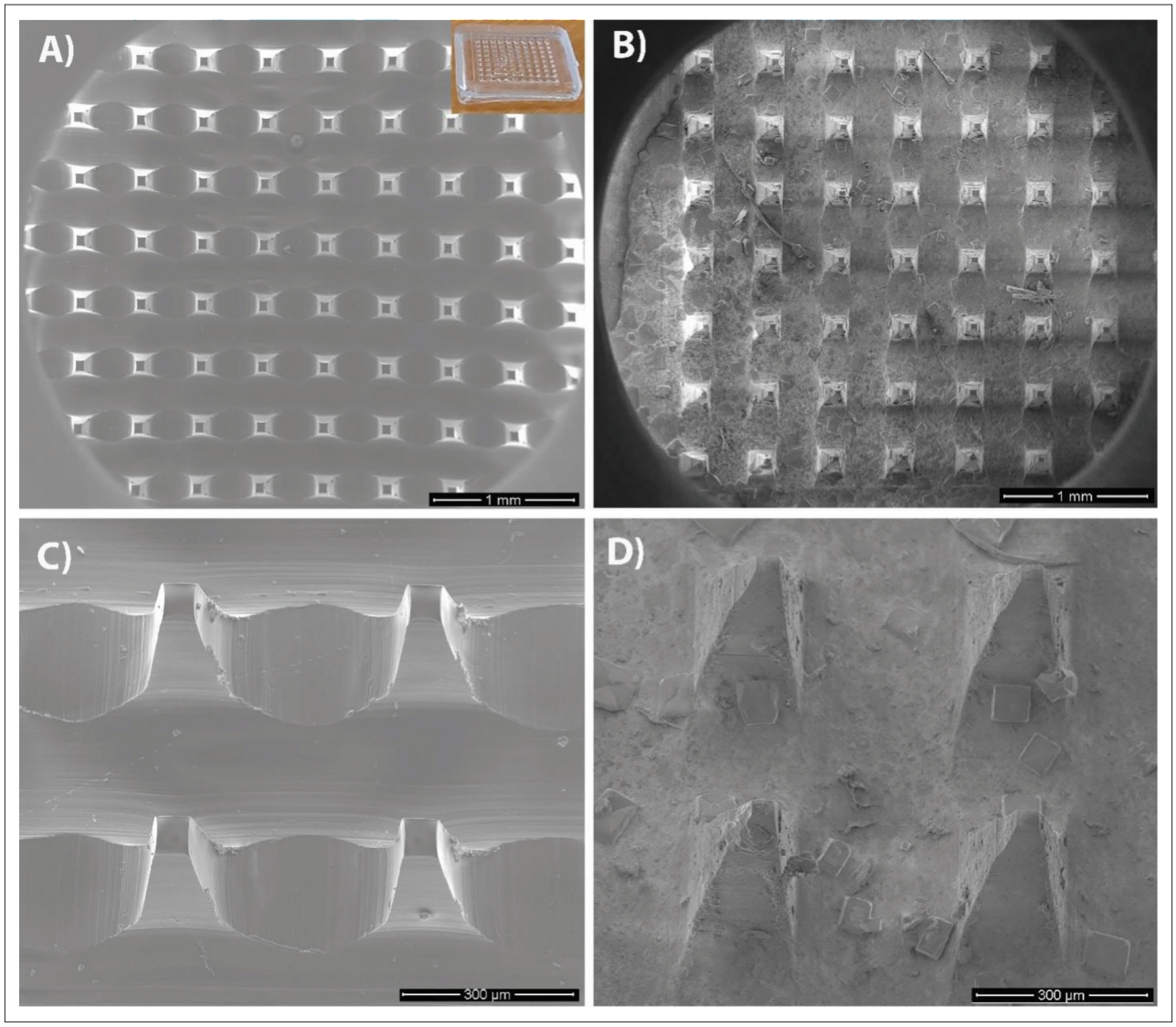

Figure 2. Representative SEM images before (A, C) and after (B, D) coating the MNs with cisplatin solution via the LIFT process. (A, B) Top view; (C, D) tilted at 20°. Insert in (A) shows the MN patch.

Software, San Diego, CA, USA). For comparisons, one-way analysis of variance (ANOVA) with Bonferroni correction was performed. Results were statistically significant at *adjusted $p < 0.05$ and ****adjusted $p < 0.0001$.

3. Results

3.1. Morphological characterization of LIFT-printed cisplatin solutions on MNs

The cisplatin solution was physically adsorbed onto the substrate as a result of the successful direct transfer of the API solution using LIFT printing, which depends on the high velocity and pressure that the liquid droplets have upon impact with the MNs substrate. The optimum printing fluence was 1 J/cm^2, while the laser spot size was 150 µm. Figure 2 shows SEM images from before and after coating the MNs with cisplatin via the LIFT process. It can be seen from the images that the cisplatin solution uniformly coated the MNs from the tip to the base and around the MN structures. The cubic structures present in the images are the salt crystals from the saline solution that was used for the API preparation[36].

3.2. Quantification of cisplatin in mouse plasma after intraperitoneal administration and administration with MNs

For the determination of cisplatin levels in mouse plasma after transdermal administration of the compound in MN, a LC-MS/MS method was developed and applied (depicted in Figure 3). Intraperitoneal injection of cisplatin was also

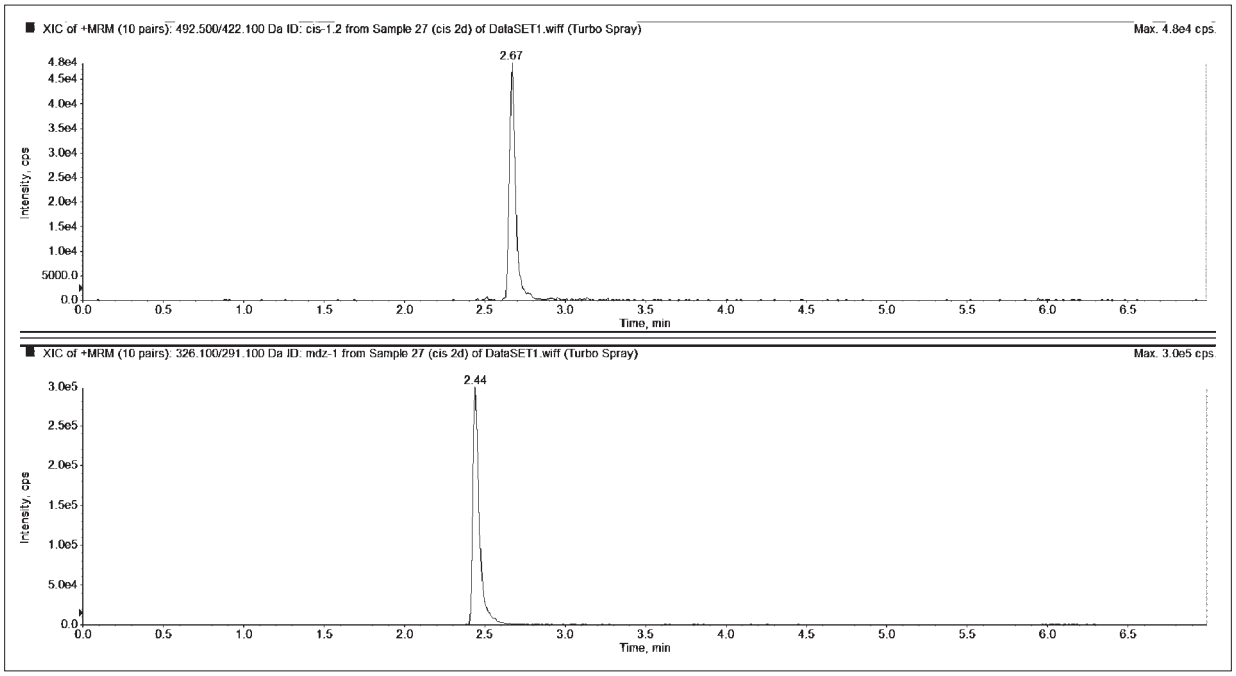

Figure 3. Representative LC-MS/MS chromatogram for cisplatin in mouse plasma at 4 h following intraperitoneal dosing of 60 µg in mice. For detection and quantification of cisplatin in plasma, the transition 492.5/422.1 with RT 2.67 min was used. Midazolam was used as internal standard (IS) with transition 326.1/291.1 and RT 2.44 min.

performed with the same dosing (60 µg for 20-g mice), in order to compare the levels of the compound in circulation between the distinct routes of administration. The 60 µg cisplatin corresponding to a 3 mg/Kgr dose is 50% of the standard dose that our group and others routinely use in mouse models of cancer for *in vivo* treatment.

Following intraperitoneal dosing of 60 µg of cisplatin in mice, plasma concentrations peaked at 2 and 4 h with average concentrations at 263 ± 63 ng/mL and 359 ± 28 ng/mL, respectively. At 3 days post dosing, average plasma concentrations decreased to approximately 10 ± 2 ng/mL. Previous findings from Johnsson *et al.*[37] reported concentrations of approximately 500 ng/mL in mouse whole blood and serum after a 3.75 mg/kg of cisplatin intraperitoneal dose in mice at 1 h post dosing. Administration of the same amount of cisplatin (60 µg) in mice via transdermal MN application yielded low concentrations of the compound at 2 and 4 h in plasma with concentrations of Below Limit of Quantification (BLQ; detected values were 5 and 6 ng/mL respectively). It is noteworthy, however, that although cisplatin levels declined 24 h post intraperitoneal administration, detectable amounts of the compound in plasma were found at 24 and 72 h after MN dosing, with concentrations of 21 ± 2.5 ng/mL and 9 ± 2 ng/mL, respectively. The results are depicted in Figure 4. The data provide some evidence for sustained release of cisplatin in bloodstream when loaded onto MN substrates. However, further experiments are required to confirm this observation.

3.3. Efficacy studies in mouse models of cancer

It has been previously shown that loss of the lysine (K)-specific methyltransferase 2C (KMT2C, also known as MLL3), which belongs to the mixed-lineage leukemia (MLL) family of histone methyltransferases, leads to HR deficiency in various cell types[38-40]. We have also shown that human cancer cell lines in which KMT2C levels have been knocked down with shRNAs present an exceptional response to the PARPi ilaparib[38]. *KMT2C* is mutated in 15% of human non-small cell lung cancer (TCGA PanCancer Atlas). On the other hand, HR deficiency and the potential use of PARPi in lung cancer are becoming fields of intense research in the field of cancer therapeutics. Mutation in genes encoding proteins involved in the HR repair or DNA damage response in general is identified in human lung cancer cases, while mutations signatures implying HR deficiency are also identified[41-43].

To assess whether the HR deficiency can be exploited therapeutically through combination therapy with olaparib orally and cisplatin through transdermal delivery of MNs printed with cisplatin, we used the non-small cell lung cancer cell line H1437, in which *KMT2C* has been knocked down with lentiviral expression of shRNAs[38]. When tumors grew to a diameter of approximately 0.3 cm, mice

A

Samples	Average Calculated Concentration of Cisplatin in Mouse Plasma ± SEM (ng/mL)
2h IP	263 ± 63
4h IP	359 ± 28
24h IP	157 ± 41
72h IP	10 ± 2
2h MN	BLQ (5)
4h MN	BLQ (6)
24h MN	21 ± 3
72h MN	9 ± 2

B

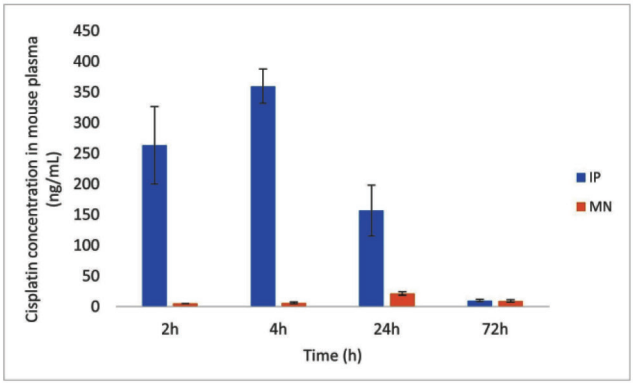

Figure 4. Determination of cisplatin levels in mouse plasma following intraperitoneal dosing and administration in MN. (A) Table presents the average of the quantified concentrations of cisplatin in mouse plasma at 2, 4, 24, and 72 h after administration in MN and intraperitoneal injection (n = 4). (B) Comparison of cisplatin concentrations in plasma after dosing with MN and intraperitoneal administration at 4 timepoints. Each timepoint was evaluated in quadruplicates for both dosing routes, and results are presented as average concentration ± standard error of the mean (SEM). Abbreviations: IP, intraperitoneal; MN, microneedle.

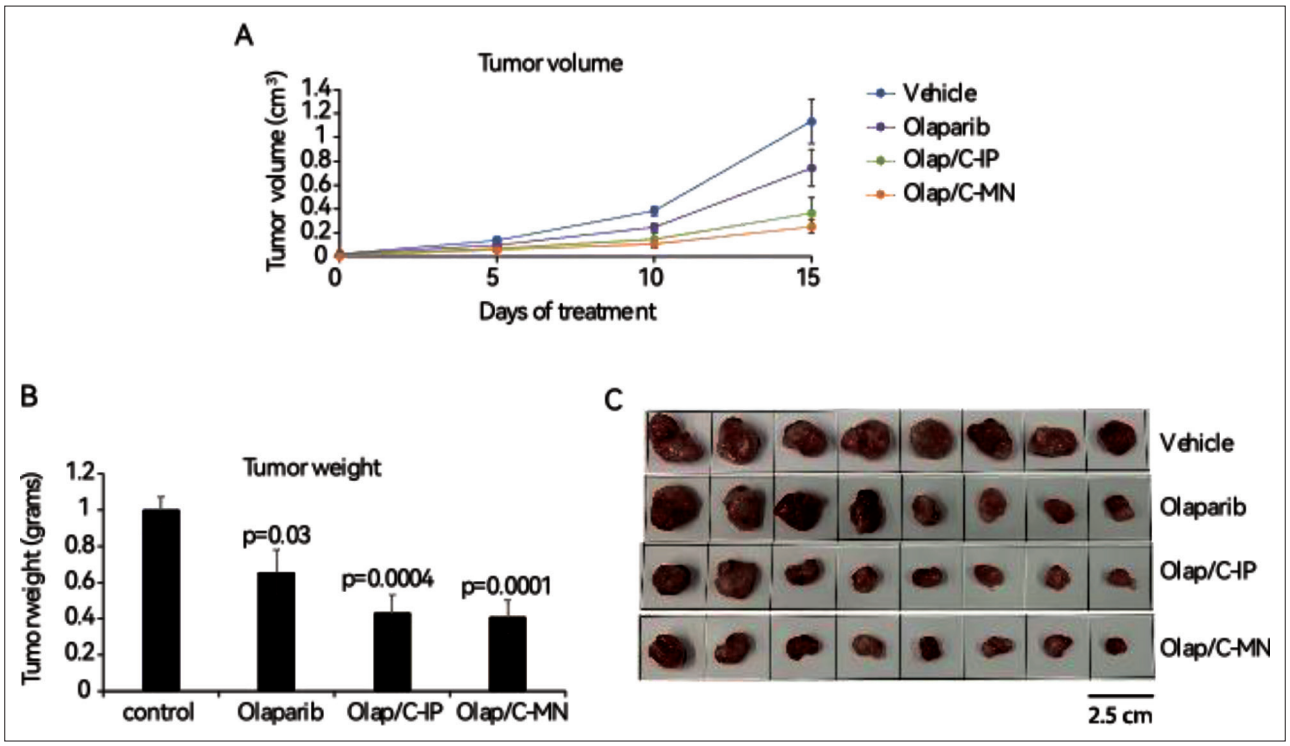

Figure 5. *In vivo* treatment of HR-deficient cells. (A) Plot indicating tumor volume during treatment. (B) Tumor weight at the end of the treatment. For (A) and (B), average of all tumors (n = 8) within indicated cohorts is shown. (C) Photograph of dissected tumors on the last day of treatment.

were allocated into four groups. While oral olaparib alone was effective in slowing down tumor growth, application of the transdermal MNs on days 0, 5, and 10 practically blocked tumor growth *in vivo*, as indicated by tumor volume (Figure 5A) and tumor weight (Figure 5B and C). These results showed that synthetic lethality is much higher when the combinatorial olaparib and cisplatin treatment is used.

This phenomenon is specific for the HR-deficient H1437 KMT2C/KD cells, as indicated by experiments with the parental cell line. As indicated in Figure 6, olaparib alone had a negligible effect, while combination with transdermal cisplatin, though more effective, had an effect that was less pronounced than that in the KMT2C/KD cells, further supporting the superior efficacy of PARPi in HR-deficient cells.

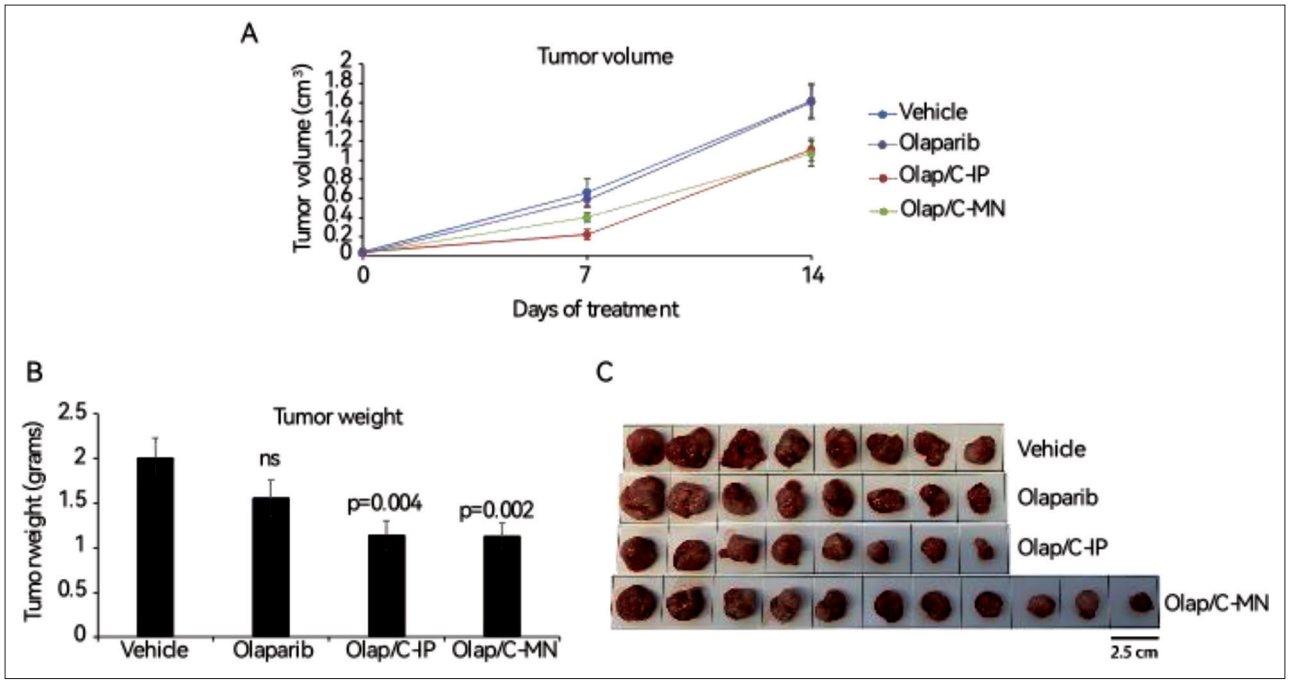

Figure 6. *In vivo* treatment of HR-proficient cells. (A) Plot indicating tumor volume during treatment. (B) Tumor weight at the end of the treatment. For (A) and (B), average of all tumors within indicated cohorts is shown. (C) Photograph of dissected tumors on the last day of treatment.

3.4. Cisplatin uptake

To measure cisplatin uptake at the single cell level, we employed mass cytometry-CyTOF (cytometry by time-of-flight) technology. In this technique, single cells are vaporized, atomized, and ionized allowing the atomic composition of each cell to be measured by a time-of-flight mass spectrometry system (ICP TOF MS)[44]. The presence of Pt, rather than intact cisplatin, in the cells is detected using this mass cytometry-CyTOF technology. As expected, intraperitoneal administration achieves higher Pt, derived from cisplatin amount in the tumors, both in terms of percentage of cells with detectable levels (99.2% vs. 64.7%), and mean intensity of positive cells (10 vs. 500) (Figure 7). The results are consistent with the findings from the pharmacokinetic study, in which cisplatin was monitored in plasma.

Our results indicate that olaparib treatment in HR-deficient tumors can be combined with the application of transdermal MNs for the administration of cisplatin at lower doses, avoiding the need for hospital trips, while ameliorating or even eliminating toxic side effects associated with the high intravenous dosing of cisplatin.

4. Discussion

Since the 2000s, an explosion in the development of new targeted therapies has revolutionized the field of cancer treatment. Targeted therapies are rarely administered alone. Instead, in the majority of schemes, these therapies are combined with chemotherapeutic drugs. Besides the opportunity for personalized treatment as a result of molecular indications and the generally less severe side effects, many targeted therapies offer the advantage of oral administration daily or even twice daily without the need for hospital visit. Chemotherapies, on the other hand, are mostly administered intravenously, requiring long stays at the hospital, often for a whole day. Moreover, patients receive a very high dose of the chemotherapeutic drug, leading to a high systemic concentration, which declines quickly until the new treatment. Thus, alternative methods for anti-cancer drug administration need to be developed. An interesting solution is oral metronomic dosing, which facilitates frequent drug administration by the patient[45]. We recently proposed transdermal MNs for metronomic dosing with gemcitabine[29].

API-coated MNs can be used for delivery of both hydrophilic and hydrophobic drugs[18,19]. Their ideal use is for low-dose administration of potent drugs, which are efficacious at low circulating amounts. There have been many methods employed in the past, such as dip coating[46], gas jet drying[47], and spray coating[48] with noted limitations[49,50], such as the difficult coating procedure because of the limited amount of drug coating, uniform coating, material waste, and precise drug dosing. In the last decade, 3D printing technologies such as inkjet printing, thermal, piezoelectric, and electrostatic printing, extrusion bioprinting, and LIFT have been used. As mentioned above, inkjet printing has been used before[25];

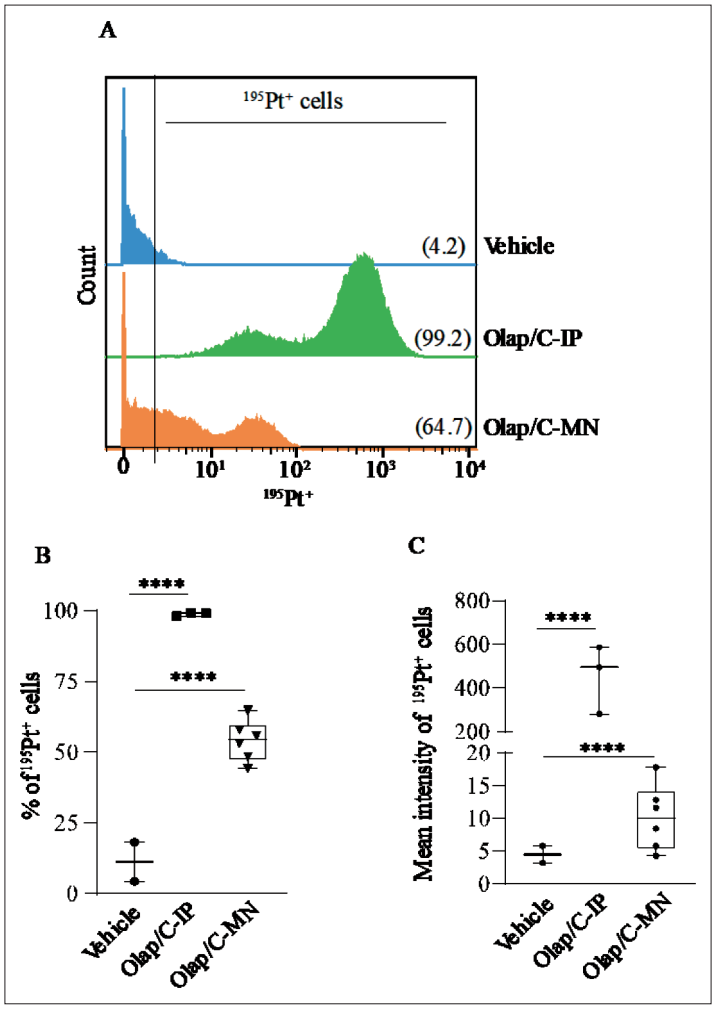

Figure 7. Analysis of cisplatin uptake in single cells from murine lung tumor tissue with mass cytometry-CyTOF. (A) shows the representative histogram displaying distribution of cisplatin (195Pt)-positive cells (% number in brackets) in lung tumor tissue of mice treated with vehicle, Olap/C-IP, or Olap/C-MN. Box and whiskers plots of % of 195Pt cells and mean intensity of 195Pt in all samples analyzed are shown in (B) and (C), respectively.

however, it has limitations with high-viscosity materials, due to the excessive force required to eject highly viscous drops. Moreover, inkjet printing is also associated with nozzle clogging[26,27]. It should also be noted that with most conventional drug coating approaches on MNs, the amount of API used on the MNs prior to coating is not controlled, but rather the eventual drug loading is only calculated using loading efficiency equations, after the coating is applied[51,52]. LIFT is highly efficient as it only utilizes the amount that is needed for each printing, thus reducing API and solvent waste. PARPi have emerged as promising therapy for tumors with HR deficiency leading to prolonged and sustained clinical response[53]. Though initially approved for ovarian and breast cancer patients carrying germline mutations in *BRCA1* and *BRCA2*, PARPi are now approved for pancreatic ductal adenocarcinoma[54] and prostate adenocarcinoma[55] with mutations in *BRCA1/2* and HR-related genes, respectively. In addition, additional PARPi were approved as maintenance, first-line, or second-line therapy in ovarian carcinoma, based on somatic *BRCA1/2* mutations, HR deficiency score (independently or in consideration of *BRCA1/2* mutations), or even without any HR deficiency-related indication if tumors responded favorably to cisplatin treatment. The rapidity of new approvals, revisions, and withdrawals of existing PARPi approvals indicates how dynamic this field is, with second-generation PARPi already under development. The general consensus in the field is that *BRCA1* and *BRCA2* mutations alone are not sufficient to stratify patients with solid malignancies who can benefit from PARPi. Mutations in other DNA repair genes, next-generation sequencing panels, and functional assays assessing HR repair are being employed in ongoing clinical studies[56]. Due to its frequency and dire prognosis, lung

cancer is attracting great interest in these studies. In this regard, tumors with mutations in *KMT2C*, which encodes a histone modifier with a rather indirect role in HR repair, emerge as a promising stratification marker for identifying patients who could benefit from PARPi. Together with identifying tumors with somatic mutations in HR-related genes and/or proven HR deficiency through molecular analysis or functional assays, this collection of diagnostic techniques can very likely identify patients who comprise a significant portion of the total lung cancer cases.

Since PARPi interfere with DNA damage repair, combination with other DNA-damaging agents such as cisplatin could be advantageous. Clinical practice, however, has indicated that combination of PARPi and cisplatin at the respective standard monotherapy dose is intolerable due to toxicity. Their combination, however, at lower dose seems to lead to clinical benefit in HR-deficient tumors[12]. Cisplatin intercalates into DNA generating intrastrand and interstrand adducts that, if not resolved, physically obstruct DNA polymerases during DNA replication, leading to the generation of double-strand breaks[57]. Cisplatin could remain in the human body, and traces of it can be found in the urine of patients even after 8 years from the treatment[58]. We thus hypothesize that because of its high potency and long excretion kinetics, even low levels of cisplatin could lead to increased DNA damage. Because PARPi is efficacious already as monotherapy in HR-deficient tumors, we hypothesize that even low levels of cisplatin are sufficient to sensitize cells to PARPi and maximize synthetic lethality.

To eliminate the need for hospital visit for intravenous administration of cisplatin, we have developed transdermal MNs which have been coated with cisplatin through LIFT technology. Cisplatin can be readily detectable in the blood stream and also in the tumors in mouse models of non-small cell lung cancer. Although these levels are lower than those achieved through intraperitoneal administration, the two approaches have comparable efficacy when combined with oral olaparib. The obvious advantage of transdermal administration of cisplatin without the need for hospital visits, as well as the ability to precisely adjust the dose with the use of LIFT technology, offers an attractive approach for combination therapies with cisplatin.

5. Conclusion

This work demonstrates for the first time that cisplatin printed onto MNs can be used for transdermal administration in mouse models of cancer. Transdermally-administered cisplatin reaches the bloodstream as well as the tumor itself, and although drug levels are lower than those obtained with intraperitoneal injection, they are sufficient to achieve strong response in HR-deficient lung tumors when the treatment is combined with oral administration of the olaparib. The proposed approach alleviates the cytotoxic side effects of the combination therapy while eliminating the need for intravenous administration of cisplatin in the hospital.

Acknowledgments

None.

Funding

This work has been co-financed by the European Union and Greek national funds through the Operational Program Competitiveness, Entrepreneurship, and Innovation, under the call RESEARCH–CREATE–INNOVATE (project code: T1EDK-00976). G.A.S. acknowledges funding from the European Research Council (ERC) under the European Union's Horizon 2020 research and innovation program (ERC Grant agreement no. 758705).

Conflict of interest

The authors declare no conflict of interest.

Author contributions

Conceptualization: Zoi Kanaki, Constantin Tamvakopoulos, Ioanna Zergioti, Apostolos Klinakis

Formal analysis: Zoi Kanaki, Alexandra Smina, Chrysoula Chandrinou, Ilias Cheliotis, Georgios A. Sotiriou, Apostolos Klinakis

Investigation: Zoi Kanaki, Chrysoula Chandrinou, Fotini E. Koukouzeli, Yiannis Ntounias, Nikolaos Paschalidis, Marina Makrygianni, Jill Ziesmer, Constantin Tamvakopoulos, Apostolos Klinakis

Methodology: Zoi Kanaki, Alexandra Smina, Chrysoula Chandrinou, Fotini E. Koukouzeli, Yiannis Ntounias, Nikolaos Paschalidis, Ilias Cheliotis, Jill Ziesmer, Georgios A. Sotiriou, Ioanna Zergioti, Constantin Tamvakopoulos, Apostolos Klinakis

Writing – original draft: Zoi Kanaki, Alexandra Smina, Chrysoula Chandrinou, Nikolaos Paschalidis, Jill Ziesmer, Georgios A. Sotiriou, Constantin Tamvakopoulos, Ioanna Zergioti, Apostolos Klinakis

Writing – review & editing: Zoi Kanaki, Alexandra Smina, Chrysoula Chandrinou, Nikolaos Paschalidis, Jill Ziesmer, Georgios A. Sotiriou, Constantin Tamvakopoulos, Ioanna Zergioti, Apostolos Klinakis

Ethics approval and consent to participate

All procedures for care and treatment of animals were approved by the Institutional Committee on Ethics of

Animal Experiments and the Greek Ministry of Agriculture (Protocol #1392861, 28/12/22).

Consent for publication

Not applicable.

Availability of data

Data available on request.

References

1. Tsimberidou AM, Fountzilas E, Nikanjam M, *et al.*, 2020, Review of precision cancer medicine: Evolution of the treatment paradigm. *Cancer Treat Rev*, 86(June): 102019.

   https://doi.org/10.1016/j.ctrv.2020.102019

2. Zhong L, Li Y, Xiong L, *et al.*, 2021, Small molecules in targeted cancer therapy: Advances, challenges, and future perspectives. *Signal Transduct Target Ther*, 6(1): 201.

   https://doi.org/10.1038/s41392-021-00572-w

3. Lord CJ, Ashworth A, 2017, PARP inhibitors: Synthetic lethality in the clinic. *Science*, 355(6330): 1152–1158.

   https://doi.org/10.1126/science.aam7344

4. Ray Chaudhuri A, Nussenzweig A, 2017, The multifaceted roles of PARP1 in DNA repair and chromatin remodelling. *Nat Rev Mol Cell Biol*, 18(10): 610–621.

   https://doi.org/10.1038/nrm.2017.53

5. Farmer H, McCabe N, Lord CJ, *et al.*, 2005, Targeting the DNA repair defect in BRCA mutant cells as a therapeutic strategy. *Nature*, 434(7035): 917–921.

   https://doi.org/10.1038/nature03445

6. Bryant HE, Schultz N, Thomas HD, *et al.*, 2005, Specific killing of BRCA2-deficient tumours with inhibitors of poly(ADP-ribose) polymerase. *Nature*, 434(7035): 913–917.

   https://doi.org/10.1038/nature03443

7. Menear KA, Adcock C, Boulter R, *et al.*, 2008, 4-[3-(4-cyclopropanecarbonylpiperazine-1-carbonyl)-4-fluorobenzyl]-2H-phthalazin-1-one: a novel bioavailable inhibitor of poly(ADP-ribose) polymerase-1. *J Med Chem*, 51(20): 6581–6591.

   https://doi.org/10.1021/jm8001263

8. Moynahan ME, Jasin M, 2010, Mitotic homologous recombination maintains genomic stability and suppresses tumorigenesis. *Nat Rev Mol Cell Biol*, 11(3): 196–207.

   https://doi.org/10.1038/nrm2851

9. Kim D, Nam HJ, 2022, PARP inhibitors: Clinical limitations and recent attempts to overcome them. *Int J Mol Sci*, 23(15).

   https://doi.org/10.3390/ijms23158412

10. Vikas P, Borcherding N, Chennamadhavuni A, *et al.*, 2020, Therapeutic potential of combining PARP inhibitor and immunotherapy in solid tumors. *Front Oncol*, 10(April): 570.

    https://doi.org/10.3389/fonc.2020.00570

11. Klinakis A, Karagiannis D, Rampias T, 2020, Targeting DNA repair in cancer: Current state and novel approaches. *Cell Mol Life Sci*, 77(4): 677–703.

    https://doi.org/10.1007/s00018-019-03299-8

12. Balmana J, Tung NM, Isakoff SJ, *et al.*, 2014, Phase I trial of olaparib in combination with cisplatin for the treatment of patients with advanced breast, ovarian and other solid tumors. *Ann Oncol*, 25(8): 1656–1663.

    https://doi.org/10.1093/annonc/mdu187

13. Fong PC, Boss DS, Yap TA, *et al.*, 2009, Inhibition of poly(ADP-ribose) polymerase in tumors from BRCA mutation carriers. *N Engl J Med*, 361(2): 123–134.

    https://doi.org/10.1056/NEJMoa0900212

14. Audeh MW, Carmichael J, Penson RT, *et al.*, 2010, Oral poly(ADP-ribose) polymerase inhibitor olaparib in patients with BRCA1 or BRCA2 mutations and recurrent ovarian cancer: A proof-of-concept trial. *Lancet*, 376(9737): 245–251.

    https://doi.org/10.1016/S0140-6736(10)60893-8

15. Tutt A, Robson M, Garber JE, *et al.*, 2010, Oral poly(ADP-ribose) polymerase inhibitor olaparib in patients with BRCA1 or BRCA2 mutations and advanced breast cancer: A proof-of-concept trial. *Lancet*, 376(9737): 235–244.

    https://doi.org/10.1016/S0140-6736(10)60892-6

16. Gelmon KA, Tischkowitz M, Mackay H, *et al.*, 2011, Olaparib in patients with recurrent high-grade serous or poorly differentiated ovarian carcinoma or triple-negative breast cancer: A phase 2, multicentre, open-label, non-randomised study. *Lancet Oncol*, 12(9): 852–861.

    https://doi.org/10.1016/S1470-2045(11)70214-5

17. Larraneta E, Lutton REM, Woolfson AD, *et al.*, 2016, Microneedle arrays as transdermal and intradermal drug delivery systems: Materials science, manufacture and commercial development. *Mat Sci Eng R*, 104(June): 1–32.

    https://doi.org/10.1016/j.mser.2016.03.001

18. Pearton M, Saller V, Coulman SA, *et al.*, 2012, Microneedle delivery of plasmid DNA to living human skin: Formulation coating, skin insertion and gene expression. *J Control Release*, 160(3): 561–569.

    https://doi.org/10.1016/j.jconrel.2012.04.005

19. Zhao X, Coulman SA, Hanna SJ, *et al.*, 2017, Formulation of hydrophobic peptides for skin delivery via coated microneedles. *J Control Release*, 265(November): 2–13.

    https://doi.org/10.1016/j.jconrel.2017.03.015

20. Lan X, Zhu W, Huang X, *et al.*, 2020, Microneedles loaded with anti-PD-1-cisplatin nanoparticles for synergistic cancer immuno-chemotherapy. *Nanoscale*, 12(36): 18885–18898.

    https://doi.org/10.1039/d0nr04213g

21. Lan X, She J, Lin DA, *et al.,* 2018, Microneedle-mediated delivery of lipid-coated cisplatin nanoparticles for efficient and safe cancer therapy. *ACS Appl Mater Interfaces*, 10(39): 33060–33069.

    https://doi.org/10.1021/acsami.8b12926

22. Fu JJ, Li CW, Liu Y, *et al.*, 2020, The microneedles carrying cisplatin and IR820 to perform synergistic chemo-photodynamic therapy against breast cancer. *J Nanobiotechnol,* 18(1): 146.

    https://doi.org/10.1186/s12951-020-00697-0

23. Uddin MJ, Scoutaris N, Klepetsanis P, *et al.*, 2015, Inkjet printing of transdermal microneedles for the delivery of anticancer agents. *Int J Pharm*, 494(2): 593–602.

    https://doi.org/10.1016/j.ijpharm.2015.01.038

24. Ross S, Scoutaris N, Lamprou D, *et al.*, 2015, Inkjet printing of insulin microneedles for transdermal delivery. *Drug Deliv Transl Res*, 5(4): 451–461.

    https://doi.org/10.1007/s13346-015-0251-1

25. Uddin MJ, Scoutaris N, Economidou SN, *et al.*, 2020, 3D printed microneedles for anticancer therapy of skin tumours. *Mater Sci Eng C Mater Biol Appl*, 107(February): 110248.

    https://doi.org/10.1016/j.msec.2019.110248

26. Tarbox TN, Watts AB, Cui Z, *et al.*, 2018, An update on coating/manufacturing techniques of microneedles. *Drug Deliv Transl Res*, 8(6): 1828–1843.

    https://doi.org/10.1007/s13346-017-0466-4

27. Haj-Ahmad R, Khan H, Arshad MS, *et al.*, 2015, Microneedle coating techniques for transdermal drug delivery. *Pharmaceutics*, 7(4): 486–502.

    https://doi.org/10.3390/pharmaceutics7040486

28. Papazoglou S, Zergioti I, 2017, Laser induced forward transfer (LIFT) of nano-micro patterns for sensor applications. *Microelectron Eng*, 182(October): 25–34.

    https://doi.org/10.1016/j.mee.2017.08.003

29. Kanaki Z, Chandrinou C, Orfanou IM, *et al.*, 2022, Laser-induced forward transfer printing on microneedles for transdermal delivery of gemcitabine. *Int J Bioprint*, 8(2): 554.

    https://doi.org/10.18063/ijb.v8i2.554

30. Hall MD, Telma KA, Chang KE, *et al.*, 2014, Say no to DMSO: dimethylsulfoxide inactivates cisplatin, carboplatin, and other platinum complexes. *Cancer Res*, 74(14): 3913–3922.

    https://doi.org/10.1158/0008-5472.CAN-14-0247

31. Ziesmer J, Tajpara P, Hempel NJ, *et al.*, 2021, Vancomycin-loaded microneedle arrays against methicillin-resistant Staphylococcus aureus skin infections. *Adv Mater Technol*, 6(7): 2001307.

    https://doi.org/10.1002/admt.202001307

32. Shaik AN, Altomare DA, Lesko LJ, *et al.*, 2017, Development and validation of a LC-MS/MS assay for quantification of cisplatin in rat plasma and urine. *J Chromatogr B Analyt Technol Biomed Life Sci*, 1046(March): 243–249.

    https://doi.org/10.1016/j.jchromb.2016.11.027

33. Coughlan AM, Harmon C, Whelan S, *et al.*, 2016, Myeloid engraftment in humanized mice: Impact of granulocyte-colony stimulating factor treatment and transgenic mouse strain. *Stem Cells Dev*, 25(7): 530–541.

    https://doi.org/10.1089/scd.2015.0289

34. Shultz LD, Lyons BL, Burzenski LM, *et al.*, 2005, Human lymphoid and myeloid cell development in NOD/LtSz-scid IL2R gamma null mice engrafted with mobilized human hemopoietic stem cells. *J Immunol*, 174(10): 6477–6489.

    https://doi.org/10.4049/jimmunol.174.10.6477

35. Kanaki Z, Voutsina A, Markou A, *et al.*, 2021, Generation of non-small cell lung cancer patient-derived xenografts to study intratumor heterogeneity. *Cancers (Basel)*, 13(10).

    https://doi.org/10.3390/cancers13102446

36. Falcon-Suarez IH, Livo K, Callow B, *et al.*, 2020, Geophysical early warning of salt precipitation during geological carbon sequestration. *Sci Rep,* 10(1): 16472.

    https://doi.org/10.1038/s41598-020-73091-3

37. Johnsson A, Olsson C, Nygren O, *et al.*, 1995, Pharmacokinetics and tissue distribution of cisplatin in nude mice: Platinum levels and cisplatin-DNA adducts. *Cancer Chemother Pharmacol*, 37(1–2): 23–31.

    https://doi.org/10.1007/BF00685625

38. Rampias T, Karagiannis D, Avgeris M, *et al.*, 2019, The lysine-specific methyltransferase KMT2C/MLL3 regulates DNA repair components in cancer. *EMBO Rep,* 20(3).

    https://doi.org/10.15252/embr.201846821

39. Ray Chaudhuri A, Callen E, Ding X, *et al.*, 2016, Replication fork stability confers chemoresistance in BRCA-deficient cells. *Nature*, 535(7612): 382–387.

    https://doi.org/10.1038/nature18325

40. Chang A, Liu L, Ashby JM, *et al.,* 2021, Recruitment of KMT2C/MLL3 to DNA damage sites mediates DNA damage responses and regulates PARP inhibitor sensitivity in cancer. *Cancer Res*, 81(12): 3358–3373.

    https://doi.org/10.1158/0008-5472.CAN-21-0688

41. Diossy M, Sztupinszki Z, Borcsok J, *et al.*, 2021, A subset of lung cancer cases shows robust signs of homologous recombination deficiency associated genomic mutational signatures. *NPJ Precis Oncol*, 5(1): 55.

https://doi.org/10.1038/s41698-021-00199-8

42. Zhou Z, Ding Z, Yuan J, *et al.*, 2022, Homologous recombination deficiency (HRD) can predict the therapeutic outcomes of immuno-neoadjuvant therapy in NSCLC patients. *J Hematol Oncol*, 15(1): 62.

https://doi.org/10.1186/s13045-022-01283-7

43. Wu S, Zhang Y, Zhang Y, *et al.*, 2022, Mutational landscape of homologous recombination-related genes in small-cell lung cancer. *Cancer Med*, 12(4): 4486–4495.

https://doi.org/10.1002/cam4.5148

44. Chang Q, Ornatsky OI, Koch CJ, *et al.*, 2015, Single-cell measurement of the uptake, intratumoral distribution and cell cycle effects of cisplatin using mass cytometry. *Int J Cancer*, 136(5): 1202–1209.

https://doi.org/10.1002/ijc.29074

45. Skavatsou E, Semitekolou M, Morianos I, *et al.*, 2021, Immunotherapy combined with metronomic dosing: An effective approach for the treatment of NSCLC. *Cancers (Basel)*, 13(8).

https://doi.org/10.3390/cancers13081901

46. Ameri M, Kadkhodayan M, Nguyen J, *et al.*, 2014, Human growth hormone delivery with a microneedle transdermal system: Preclinical formulation, stability, delivery and PK of therapeutically relevant doses. *Pharmaceutics*, 6(2): 220–234.

https://doi.org/10.3390/pharmaceutics6020220

47. Chen X, Prow TW, Crichton ML, *et al.*, 2009, Dry-coated microprojection array patches for targeted delivery of immunotherapeutics to the skin. *J Control Release*, 139(3): 212–220.

https://doi.org/10.1016/j.jconrel.2009.06.029

48. Vrdoljak A, McGrath MG, Carey JB, *et al.*, 2012, Coated microneedle arrays for transcutaneous delivery of live virus vaccines. *J Control Release*, 159(1): 34–42.

https://doi.org/10.1016/j.jconrel.2011.12.026

49. Gill HS, Prausnitz MR, 2007, Coating formulations for microneedles. *Pharm Res*, 24(7): 1369–1380.

https://doi.org/10.1007/s11095-007-9286-4

50. Ingrole RSJ, Gill HS, 2019, Microneedle coating methods: A review with a perspective. *J Pharmacol Exp Ther*, 370(3): 555–569.

https://doi.org/10.1124/jpet.119.258707

51. Bhatnagar S, Kumari P, Pattarabhiran SP, *et al.*, 2018, Zein microneedles for localized delivery of chemotherapeutic agents to treat breast cancer: Drug loading, release behavior, and skin permeation studies. *AAPS PharmSciTech*, 19(4): 1818–1826.

https://doi.org/10.1208/s12249-018-1004-5

52. Infante JR, Benhadji KA, Dy GK, *et al.*, 2015, Phase 1b study of the oral gemcitabine 'Pro-drug' LY2334737 in combination with capecitabine in patients with advanced solid tumors. *Invest New Drugs*, 33(2): 432–439.

https://doi.org/10.1007/s10637-015-0207-9

53. Rose M, Burgess JT, O'Byrne K, *et al.*, 2020, PARP inhibitors: Clinical relevance, mechanisms of action and tumor resistance. *Front Cell Dev Biol*, 8(September): 564601.

https://doi.org/10.3389/fcell.2020.564601

54. Brown TJ, Reiss KA, 2021, PARP inhibitors in pancreatic cancer. *Cancer J*, 27(6): 465–475.

https://doi.org/10.1097/PPO.0000000000000554

55. Beatson EL, Chau CH, Price DK, *et al.*, 2022, PARP inhibitors on the move in prostate cancer: Spotlight on Niraparib & update on PARP inhibitor combination trials. *Am J Clin Exp Urol*, 10(4): 252–257.

56. van der Wiel AMA, Schuitmaker L, Cong Y, *et al.*, 2022, Homologous recombination deficiency scar: Mutations and beyond-implications for precision oncology. *Cancers (Basel)*, 14(17).

https://doi.org/10.3390/cancers14174157

57. Frankenberg-Schwager M, Kirchermeier D, Greif G, *et al.*, 2005, Cisplatin-mediated DNA double-strand breaks in replicating but not in quiescent cells of the yeast Saccharomyces cerevisiae. *Toxicology*, 212(2–3): 175–184.

https://doi.org/10.1016/j.tox.2005.04.015

58. Schierl R, Rohrer B, Hohnloser J, 1995, Long-term platinum excretion in patients treated with cisplatin. *Cancer Chemother Pharmacol*, 36(1): 75–78.

https://doi.org/10.1007/BF00685736

ACCSCIENCE PUBLISHING

International Journal of Bioprinting

RESEARCH ARTICLE

Sub-regional design of the bionic bone scaffolds using macrostructural topology

Yangdong He[1,2†], Long Chao[1,2†], Chen Jiao[1,2], Hong Wang[1], Deqiao Xie[1], Guofeng Wu[3], Lin Wang[4], Changjiang Wang[5], Jianfeng Zhao[1,2*], Lida Shen[1,2*], and Huixin Liang[6,7*]

[1]Institute of Additive Manufacturing (3D Printing), Nanjing University of Aeronautics and Astronautics, Nanjing, 210016, China

[2]Jiangsu Key Laboratory of Digital Medical Equipment Technology, Nanjing University of Aeronautics and Astronautics, Nanjing, 210016, China

[3]Stomatological Digital Engineering Center, Nanjing Stomatological Hospital, Nanjing, 210008, China

[4]Nanjing Chamlion Laser Technology Co., Ltd, Nanjing, 210012, China

[5]Department of Engineering and Design, University of Sussex, Brighton, BN1 9RH, United Kingdom

[6]State Key Laboratory of Pharmaceutical Biotechnology, Division of Sports Medicine and Adult Reconstructive Surgery, Department of Orthopedic Surgery, Nanjing Drum Tower Hospital, The Affiliated Hospital of Nanjing University Medical School, Nanjing, 210008, China

[7]Jiangsu Engineering Research Center for 3D Bioprinting, Nanjing, 210008, China

[†]These authors contributed equally to this work.

***Corresponding authors:**
Jianfeng Zhao
(zhaojf@nuaa.edu.cn)

Lida Shen
(ldshen@nuaa.edu.cn)

Huixin Liang
(hxliang@nuaa.edu.cn)

Citation: He Y, Chao L, Jiao C, *et al*., 2023, Sub-regional design of the bionic bone scaffolds using macrostructural topology. *Int J Bioprint*, 9(6): 0222.
https://doi.org/10.36922/ijb.0222

Received: October 07, 2022
Accepted: November 11, 2022
Published Online: June 27, 2023

Copyright: © 2023 Author(s). This is an Open Access article distributed under the terms of the Creative Commons Attribution License, permitting distribution, and reproduction in any medium, provided the original work is properly cited.

Publisher's Note: AccScience Publishing remains neutral with regard to jurisdictional claims in published maps and institutional affiliations.

Abstract

With the increasing demand for bone repair, the bionic bone scaffolds have become a research hotspot. A sub-regional design method of the bionic bone scaffolds, using macrostructural topology, is proposed in this paper, aiming to provide a functionally enhanced region division method for the gradient design. The macrostructural topology was carried out by the bi-directional evolutionary structural optimization (BESO), dividing the predefined design domain into sub-region A and sub-region B. Subsequently, a combined probability sphere model and a distance-to-scale coefficient mapping model are established to implement the graded porosification based on the Voronoi tessellation. This approach takes geometric and mechanical continuity into fully account and assures a reasonable distribution of characteristic parameters, yielding to improve the mechanical strength under specific stress conditions. Finally, the scaffolds were fabricated by the laser powder bed fusion (LPBF) process using the Ti-6Al-4V powder. The results of compression tests are satisfactory, showing that the as-built specimens implement sub-regional functionality. The apparent elastic modulus and the ultimate strength range, respectively, between 1.50 GPa and 7.12 GPa (for the first module) and between 38.55 MPa and 268.03 MPa (for the second module), which conform to the required level of natural bone, providing a possibility for clinical application.

Keywords: Functionally graded porous materials; Bionic scaffolds; Bi-directional evolutionary structural optimization; Voronoi tessellation; Laser powder bed fusion

1. Introduction

With the acceleration of population aging and the frequent occurrence of traffic accidents, bone defect has become a hot issue in the field of bone tissue engineering. Since the self-healing cycle of natural bone takes a long time and its reconstruction ability is limited, appropriate artificial implants have become the primary choice[1]. Porous scaffold is the most common form of artificial implants. The introduction of porous features can reduce the apparent elastic modulus of artificial implants to a level close to that of a natural bone, yielding to reduces the phenomenon of stress shielding[2,3]. With the development of additive manufacturing technology, it is quite mature to realize the direct manufacturing of ultra-high precision porous scaffolds[4,5]. In order to unify the mechanical and biological properties of implants, Ti-6Al-4V scaffolds, fabricated by the laser powder bed fusion (LPBF) process, are one of the common artificial prostheses[6-9].

Human bone has a natural graded-pore distribution, allowing it to realize special functions at different gradient positions[10,11]. In the clinical environment, the porous scaffolds from previous studies cannot simulate the graded distribution of natural bone, leading to a mismatch in elastic modulus with the surrounding bone after implantation[12,13]; therefore, it will be losing the mechanical stability and the positive stress stimulation to primary bone tissue[14]. These losses will lead to osteoporosis and even atrophy, ending up with a failure to implant because of the looseness at the interface[15]. In order to simulate the graded distribution of a natural bone, an increasing number of researchers turn their attention to functionally graded porous materials (FGPMs)[16,17]. In bone tissue engineering, FGPMs mimic the gradient of the bone by controlling the nucleating points distribution of the porous scaffolds, or by setting the graded porosity[18]. Therefore, FGPMs have a more complex internal structure, which also puts forward higher requirements for researchers. In previous studies, Wang *et al.* designed a Voronoi porous scaffold with graded distribution in the *z*-axis direction, which lacked clear graded distribution standard[12]. Deering *et al.* generated an anisotropic Voronoi porous implant by dividing the plane unevenly along the *z*-axis direction, which was too subjective to reflect the graded distribution of natural bone[19]. In addition, Liu *et al.* established an elasticity-to-density mapping model, and generated FGPMs based on the Voronoi tessellation, which relied on the intensive division of a finite element mesh, resulting in a huge amount of data[20]. From the above studies, it is clear that there are still many limitations in the current research and the designs of FGPMs. In addition, there are few studies on controllable and graded design of the bionic bone scaffolds, and many pivotal problems still remain unsolved.

Topology optimization is the most classic method of mechanical optimization. According to the mechanical conditions and the optimization objectives, researchers can obtain the optimal configuration of the internal structure of the model through iterative calculation of finite element analysis, and they can achieve the optimal distribution of materials with respect to the targeted performance[21,22]. Many studies believe that FGPMs and topology optimization methods are highly unified in nature[23,24], and that the latter can be used as the basis for FGPMs design[25,26]. For example, Alzahrani *et al.* proposed a relative density mapping (RDM) method, which introduced the topology optimization method into the lattice structure design[27]. In addition, Zhao *et al.* used the local relative density mapping method to generate the corresponding two-dimensional cellular porous structure according to the optimized solid isotropic material with penalization (SIMP) continuum topology optimization results with variable density[28]. Wang *et al.* carried out concurrent design of hierarchical structures for regular porous structures according to the results of continuum topology optimization[29]. Radman *et al.* optimized the topology of the porous structure with regular basic structure units, which showed the characteristic of graded distribution of density[26]. It was found that the FGPMs design, using topology optimization information, targets mainly the two-dimensional regular porous structures or the three-dimensional (3D) structures with repeated simple basic structural units. Introducing the topology optimization into the bionic bone scaffolds design field has broad prospects. In engineering applications, the bi-directional evolutionary structural optimization (BESO) is widely used as a common topology optimization method. The simultaneous deletion and growth of materials reflects the bidirectional nature of the BESO method, which greatly ensures the geometric and mechanical continuity of the topology optimization continuum. BESO reduces the maximum stress inside the structure to the greatest extent, providing a highly accurate solution for optimizing the stress distribution inside the structure[30-32]. In addition, the results of BESO can show the main load-bearing area and the force transfer path inside the macroscopic model[33,34]. It is a pioneering and a reasonable attempt to take the BESO information as the design basis of the bionic bone scaffolds, and to show how to establish the relationship between the topology optimization design and the porous structure design. This will present the main challenge in this work.

In our previous studies, a parametric design method of the porous scaffolds based on the Voronoi tessellation was proposed, and the mechanical and biological properties were fully discussed[12,13,35,36]. Regrettably, however, our

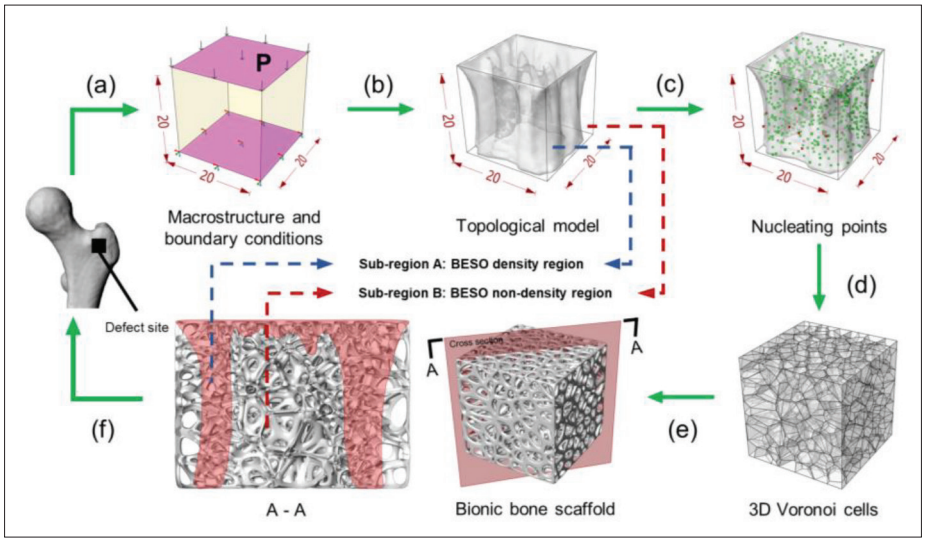

Figure 1. Design procedures for the bionic bone scaffold.

previous design method did not implement the graded distribution of the characteristic parameters, which is the most critical design of the bionic bone scaffolds. Referring to previous studies, we propose in this work a sub-regional design methodology of the bionic bone scaffolds, based on the macrostructural topology and the **Voronoi tessellation**. It is worth pointing out that the definition of macrostructure in this paper is the original model for BESO while the corresponding microstructure represents the FGPMs populated in the design domain. The design domain is divided into sub-region A (representing the BESO density region) and sub-region B (representing the BESO non-density region) as the guideline for pores' graded design. It is worth noting that, with a mechanical continuity concern, the porosity and the aperture values in sub-region B follows the distance-to-scale coefficient mapping model, presenting a gradient change. Additionally, the as-designed models were analyzed in this work through mechanical simulation and were validated after being fabricated by the LPBF process, using the Ti-6Al-4V powder, to study the quasi-static compressive behavior. Notably, this approach considers the overall problem of shape and the property control under the synergistic constraints of mechanics, biology, geometry, and LPBF process, and it delivers a full discussion regarding the influence of irregularity and scale coefficient on mechanical properties of the as-built specimens.

This paper is divided as follows: section 2 presents the design and the methodology approaches; section 3 shows the obtained results, from a simulation and implementation points of view, and the comparison; and the last section concludes this work and proposes some ideas, which will be implemented in future.

2. Design and methods

The BESO methodology was introduced to realize the macrostructural topology in this paper. The bionic bone scaffolds were designed using the novel CAD software Rhinoceros3D© (Robert McNeel & Associates, v.7.0 SR4) with the plugin Grasshopper™ v.1.0.0007. The flow chart in Figure 1 illustrates the procedures for modeling this bionic bone scaffold, including (a) bone defect site analysis, (b) macrostructural topology, (c) Boolean operation according to the combined probability sphere model, (d) 3D Voronoi tessellation based on the graded nucleating points, (e) porosification based on the distance-to-scale coefficient mapping model, and finally (f) fabrication and implantation.

2.1. Design and parametric characterization of the bionic bone scaffolds

To realize the most reasonable graded distribution, the topological information of the macroscopic model is needed. Based on the axiom of the uniform strain energy density, the maximization structural strength requires minimizing the strain energy[37]. In this paper, the design variable is the unit density, and the optimization objective is to minimize the strain energy of the macrostructure. The mathematical model of strength optimization under the constraint of equilibrium equation is expressed as follows:

$$\begin{aligned} & U(\rho_i) = \frac{1}{2} P^T \delta \\ & s.t.\ K^T \delta = P \\ & \sum_{i=1}^{n} V_i \rho_i - f_v V^* = 0 \\ & E_i = \rho_i^p E_i^* \\ & \rho_i = \rho_{min} \ or \ 1 \end{aligned} \tag{I}$$

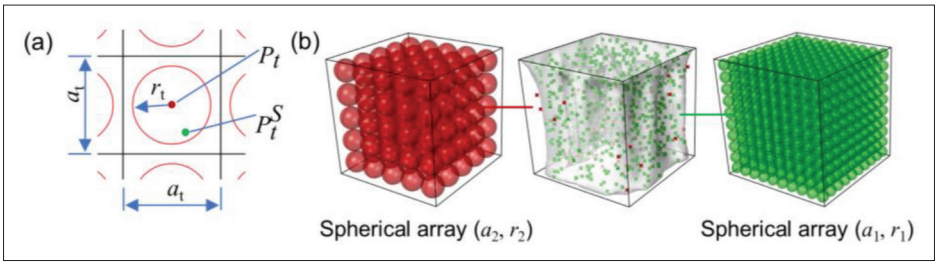

Figure 2. Generation of the graded Voronoi nucleating points where one can see (a) design parameters of the combined probability sphere model, (b) combined probability sphere model and Voronoi nucleating points, where $\{P_{1i}^S\}_{i=1}^N$ is marked red while $\{P_{2j}^S\}_{j=1}^M$ is marked green.

where i = 1, 2, …, n represents the volume mesh number of the macroscopic model and ρ_i is a binary design variable representing the cell density of the *i-th* volume mesh. A mesh cell is considered deleted when $\rho_i = \rho_{min}$, and it is considered reserved when ρ_i = 1. The variables U, K, δ, and P represent, respectively, the strain energy, the total stiffness matrix, the displacement vector, and the external load vector acting on the structure. V_i is the volume of the *i-th* volume mesh cell while V^* is the initial volume of the macroscopic model. f_v is the volume fraction coefficient, representing the ratio of the target volume to the initial volume. In addition, E_i^* and E_i represent, respectively, the elastic modulus of the *i-th* volume mesh cell before and after the topological optimization. Finally, the penalty coefficient p has a fixed value (equal to 3) in this work referring to previous studies[38].

It is obvious that the 20 × 20 × 20 mm³ design domain was divided into two sub-regions by the topological model. After extensive tests, it was found that arranging nucleating points only in sub-region A leads to extremely poor geometric continuity. Meanwhile, open meshes were even observed, leading to forming failure. Therefore, this study improved the methodology of generating controllable nucleating points that was adopted in previous studies[12], proposing a combined probability sphere model where a_1 and a_2 are the dot pitch of sphere centers ($a_1 > a_2$). It is worth noting that the following constraints were added:

(i) $r_1 / a_1 = r_2 / a_2$ for the purpose of ensuring geometric continuity and design controllability, where r_1 and r_2 represent the radius of spheres generated from regular dot matrices P_{1i} and P_{2j}, respectively;

(ii) $0 < r_t < a_t / 2$ where $t \in \{1,2\}$ is a binary design variable, representing two different types of the regular dot matrix.

The same r / a value provided an extremely high controllability and consistency to the design procedure, effectively alleviating the possible stress concentration and geometric mutation phenomenon. The Boolean operation process based on the combined probability sphere model is shown in Figure 2. It is worth pointing out that the values

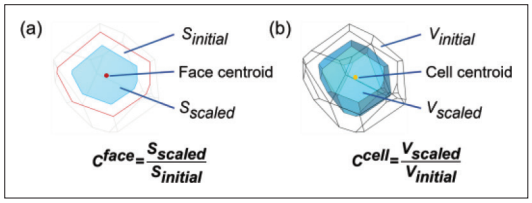

Figure 3. Definition of the scale coefficient where one can see (a) C^{face} and (b) C^{cell}.

of a_t and r_t are indeterminate, and the specific values will be discussed in section 3. For random points P_1^S, generated from the probability sphere model with dot pitch of a_1, the Boolean operation was used to get a point set $\{P_{1i}^S\}_{i=1}^N$ in sub-region B. In contrast, only the interior and the surface points in sub-region A were retained as a point set $\{P_{2j}^S\}_{j=1}^M$ for P_2^S. By combining these two sets of points $\{P_{1i}^S\}_{i=1}^N$ and $\{P_{2j}^S\}_{j=1}^M$, a set of irregular points $\{S_k\}_{k=1}^{N+M}$ was defined as the nucleating points of the bionic bone scaffolds. The irregularity ε of this scaffold is defined by the distance from a random point P_t^S to its corresponding probability sphere center P_t:

$$\varepsilon = \frac{1}{N+M}\left(\sum_{i=1}^{N}\frac{dist(P_{1i},P_{1i}^S)}{a_1} + \sum_{j=1}^{M}\frac{dist(P_{2j},P_{2j}^S)}{a_2}\right) \quad \text{(II)}$$

where N and M represent, respectively, the quantities of P_1^S and P_2^S after the Boolean operations. The number of nucleating points (NNP) is equal to the sum value of N and M ($NNP = N + M$). The variables $dist(P_{1i}, P_{1i}^S)$ and $dist(P_{2j}, P_{2j}^S)$ denote the distance from the random point P_t^S to the center of its corresponding probability sphere P_t in 3D Euclidean space. Since the radius of the probability sphere was restricted, ε can be easily deduced ($0 < \varepsilon < 0.5$).

The point set $\{S_k\}_{k=1}^{N+M}$ was processed using the Voronoi 3D Grasshopper™ plugin to obtain the 3D Voronoi cell structure. The scale coefficient C was introduced to realize the deflation of Voronoi faces and the Voronoi cells. As shown in Figure 3, C can be further divided into two variables, C^{face} and C^{cell}, where they represent, respectively,

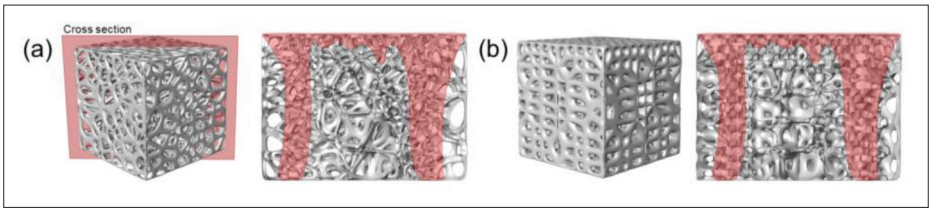

Figure 4. The as-designed models where a_1 = 4000 μm and a_2 = 2000 μm are held constant and the set of values of C_1, C_2, and ε are respectively (a) 50%, 90%, and 0.47 and (b) 20%, 80%, and 0.06.

the scaling of Voronoi face (Figure 3a) and of Voronoi cell (Figure 3b) with respect to their corresponding centers.

In addition, the bionic bone scaffolds should have specific regional functionality; this will require that the graded distribution of pore locations should be considered, and more importantly, the graded porosity should also be taken into account. A distance-to-scale coefficient mapping model, based on the shortest distance from $\{P_{1i}^S\}_{i=1}^N$ to sub-region A, was computed, where its core is calculating the shortest distance d_i (i = 1, 2, …, N) from each point in the point set $\{P_{1i}^S\}_{i=1}^N$ to the topological model that is determined. The values were ordered from smallest to largest and the maximum value d_{max} in d_i was determined. Thus, C^{cell}, corresponding to the *i-th* nucleating point, can be described as follows:

$$C_i^{cell} = C_1 + \frac{d_i}{d_{max}}(C_2 - C_1) \quad \text{(III)}$$

where C_1 represents the lower limit of the predefined value of the scale coefficient while C_2 corresponds to its upper limit. The value $C^{cell} = C_1$ was set for the Voronoi cells in sub-region A while in sub-region B, the value of C^{cell} was set to a graded value ranging between C_1 and C_2, depending on the mapping model. The gradient setting of C^{cell} in sub-region B was aimed to maximize the mechanical continuity and enhance the regional functionality of cell adhesion, especially alleviating the mutation phenomenon at the junction of the two sub-regions.

Almost all studies did not distinguish between C^{cell} and C^{face}, which exhibited a lack of adaptability to this bionic bone scaffold. Previous work has shown that the dot pitch is the most important factor influencing the aperture at a certain scale coefficient[12,13]. Due to the introduction of the combined probability sphere model, the nucleating points were mainly concentrated in sub-region A, which already resulted in a graded distribution of aperture. When the same scale coefficient used for C^{cell} is applied to C^{face}, it will lead to a large increase in aperture less than 60 μm and greater than 1200 μm, significantly reducing the functionality of the scaffolds to induce osteoblasts in order to proliferate and differentiate in sub-region B. To solve the problem, this study proposed a solution through the following relational formula:

$$C_i^{face} = C_1 + C_2 - C_i^{cell} = C_2 - \frac{d_i}{d_{max}}(C_2 - C_1) \quad \text{(IV)}$$

Then, the final 3D porous interconnection structure was obtained by the Boolean operation between the initial 3D Voronoi cell structure and the scaling results. Finally, Weaverbird v.0.9.0.1 was used to soften the trabecular-like mesh model. Figure 4 shows the as-designed models with different design variables. It is clear that each characteristic parameter has achieved the predetermined design goal.

It is important to mention that the porosity of the bionic bone scaffolds can be parametrically modified by changing C_1 and C_2. Similarly, the specific surface area can be adjusted, when needed, at constant porosity by controlling the dot pitch and the scale coefficient. Equation IV brings an extremely great improvement to the specific surface area in sub-region B, which positively induces the adhesion and proliferation of osteoblasts. The effect of specific surface area on permeability will be investigated in a future work. The aperture D (defined by the equivalent diameter method) of the bionic bone scaffolds is affected by the synergy of C^{face} and the design variables of the combined probability sphere model. The target aperture range can be obtained by adjusting C^{face} when the probability sphere model is determined. Furthermore, it is worth pointing out that our approach is applicable to any type of 3D printers.

2.2 Finite element analysis of the bionic bone scaffolds

As mentioned in section 2.1, the graded Voronoi nucleating points have a random distribution, and the randomness arises from the combined probability sphere model. In order to evaluate the effect of randomness on the mechanical properties and the porosity, four as-designed models, denoted as randomness series, were generated using four different random seeds. Other design parameters were kept the same where a_1 = 4000 μm, a_2 = 2000 μm, C_1 = 50%, C_2 = 90%, and ε = 0.47. Moreover, the dot pitch a_t was supposed to be another possible factor that affect the mechanical properties of the bionic bone scaffolds. Two series of the as-designed models with different a_1

Table 1. LPBF process parameters

	Laser power (W)	Scanning speed (mm/s)	Hatch spacing (mm)	Layer thickness (mm)	Laser focus (mm)	Atmosphere
Value	160	1250	0.08	0.03	0.08	Ar

values (denoted as a_1 series) and a_2 values (denoted as a_2 series) were set up to evaluate the effect of dot pitch on the mechanical properties and the porosity, where a_2 = 2000 μm (for a_1 series) and a_1 = 4000 μm (for a_2 series) were held constant. Other design variables were kept the same as those in randomness series.

To assess the expected mechanical behavior of the as-designed models, the finite element analysis (FEA) on ideal as-designed models was performed using the commercial software Workbench (ANSYS, Inc., v.18.0). The FEA models were assumed to be linear, elastic, and homogeneous. The material properties were set to Ti-6Al-4V, where Young's modulus was equal to 113.8 GPa, Poisson's ratio equal to 0.342, and the yield stress equal to 895 MPa. The loading conditions and the boundary constraints were as follows: the top of the as-designed model was loaded with a pressure of 80 MPa while the bottom boundary was fixed. The stress distribution under pressure was investigated through parameter settings and model meshing and solving. The mechanical properties of the as-designed models were evaluated by the maximum Von-Mises stress value under the same loading condition.

2.3 Fabrication and compressive testing of the bionic bone scaffolds

The as-built specimens were fabricated using the LPBF machine (NCLM2120, China). The process parameters, optimized by orthogonal tests, are shown in Table 1. The commercial Ti-6Al-4V extra low interstitial (ELI) powder supplied by EOS GmbH was used in the experiment, meeting ISO 5832-3 and ASTM F1472 norms.

The characteristic parameters that affect the mechanical properties of the porous biomaterials mainly include porosity and aperture. Generally, the effect of porosity is dominant[39,40]. Irregularity is also one of the possible influences due to the introduction of the probability sphere model. In this study, two sets of uniaxial compression tests were set up to investigate the effects of irregularity and of graded porosity on the compressive performance. As shown in Table 2, the as-built specimens with different ε values were denoted as irregularity series and those with different combinations of C_1 and C_2 values were denoted as scale coefficient series. The other design variables were as follows: a_1 = 3333 μm and a_2 = 1333 μm. Besides, a solid part of 20 × 20 × 0.5 mm³ was fixed at the top and at the bottom acting as the compensation area for the wire-electrode cutting process and the boundary area for the compression test. Note that three identical specimens were prepared for each model and the test results represent the average values of these specimens.

Table 2. Design parameters of as-built specimens

Series	No.	C_1 (%)	C_2 (%)	ε
Irregularity series	01	50	90	0.06
	02			0.12
	03			0.18
	04			0.25
	05			0.30
	06			0.39
	07			0.47
	08			0.50
Scale coefficient series	09	50	90	0.47
	10	50	80	
	11	50	70	
	12	50	60	
	13	60	90	
	14	70	90	
	15	80	90	

According to the national standard GB/T 31930-2015, the static compression tests were performed using a universal testing machine (UTM5305H) at a constant speed equal to 0.5 mm/min. The loading and displacement were recorded until the struts broke. Known as apparent elastic modulus of cellular metals, the elastic modulus represents the slope of the elastic straight lines, determined by the elastic loading between 70% and 20% of plateau stress. The ultimate strength was defined by the first maximum compressive strength, which determined the load-bearing capacity of the as-built specimens.

3. Results and discussion

3.1. Relationship between design variables and characteristic parameters

Different combinations of dot pitch should be discussed first, as this paper presented a combined probability sphere model. It is obvious from section 2.1 that adjusting the dot pitch essentially controls the upper limit of the aperture. The first step was to determine the range of a_1 in order to meet the optimal aperture (60–1200 μm) for bone implants[11,41]. The values of a_1 for the as-designed models

Table 3. Values of a1 for different scale coefficients

C (%)	a_1 (μm)	r_1 (μm)	Davg (μm)
50	3333	833	1127
60	2857	714	1131
70	2500	625	1139
80	2222	555	1139
90	2000	500	1138

with different scale coefficients are shown in Table 3, where D_{avg} refers to the average aperture. Figure 5a–c depict the aperture frequency distribution when the value of a_1 changes. Note that the aperture frequency refers to the ratio of the number of occurrences of a certain aperture value to the total number of pores. It is clear that a_2 is the dominant factor influencing the aperture distribution. In addition, the influence of a_1 on the aperture distribution becomes smaller as a_2 decreases, which is shown by the increasing similarity of the aperture frequency curves. Therefore, a large a_1, within a reasonable range, can be set to improve the computational efficiency. However, it will lead to a significant increase in the proportion of apertures smaller than 60 μm when a_2 takes a too small value, affecting the permeability of the scaffolds. Therefore, based on extensive simulations, the values of a_1 and a_2 equal to 3333 μm and 1333 μm, respectively, in this study were chosen. These values are suitable for this macrostructure, taking the target aperture range and computational efficiency into account. Besides, randomness was supposed to be one of the possible influencing factors of the aperture distribution as the generation of Voronoi nucleating points relied on the random seeds. Therefore, five samples were generated with different random seeds and the aperture distribution is shown in Figure 5d. It is obvious that although there were perturbations in aperture frequency curves, the overall distribution remained the same and the perturbations occurred mainly ranging from 100 μm to 1000 μm, with little effect on the actual bone implantation performance. To conclude, the combined probability sphere model design was effective, and the tests were highly reproducible.

Figure 6a shows that there is a strong linear relationship between ε and r / a. Irregularity of the bionic bone scaffolds is linked to the ratio of r / a in this study to simplify the calculation process. Variations of characteristic parameters with different values of ε are shown in Table 4, where Φ refers to the porosity. It is clear that D_{avg} and Φ are proportional to ε when $\varepsilon < 0.3$, and tend to stabilize when $0.3 \leq \varepsilon < 0.5$. *NNP* decreases gradually as ε increases, which is attributed to the increase in probability of random points appearing in sub-region B as the range of perturbations increases. In general, the influence of ε on *NNP* can be ignored when $\varepsilon < 0.5$. Notably, it is found that Φ and *NNP* decrease significantly when $\varepsilon = 0.58$, further validating the rationality of its value range. As for Figure 6b, it

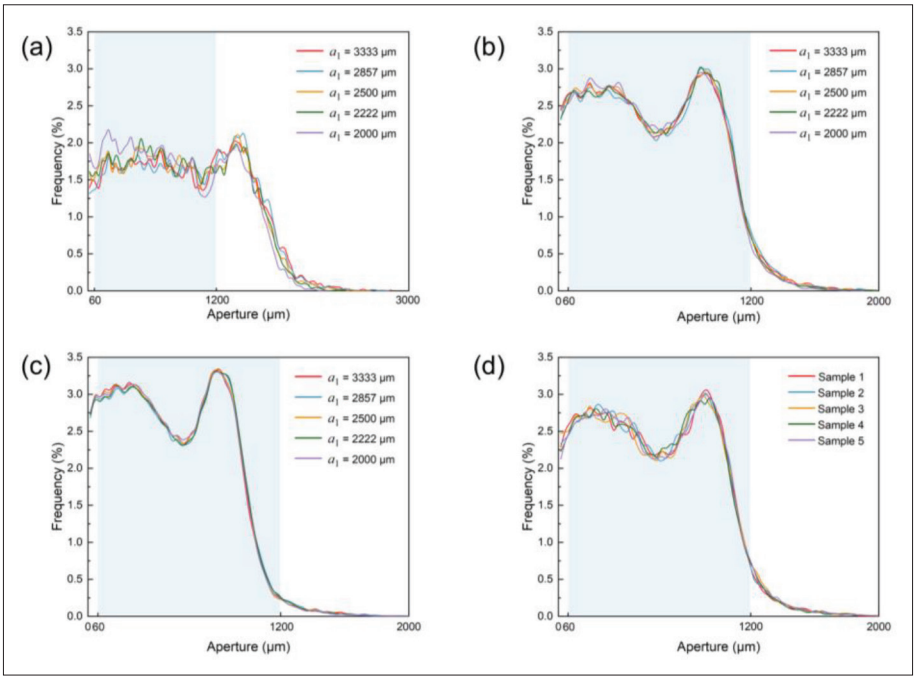

Figure 5. Aperture frequency distribution of the as-designed models with design parameters of C_1 = 50%, C_2 = 90%, and ε = 0.25 where (a) a_2 = 2000 μm, (b) a_2 = 1333 μm, (c) a_2 = 1000 μm, and (d) influence of randomness.

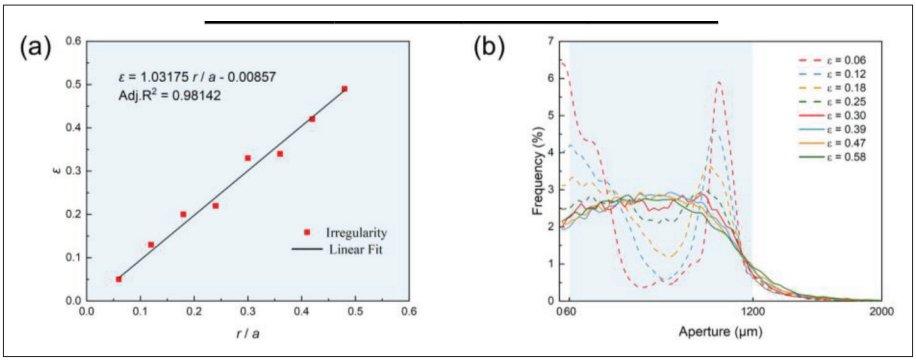

Figure 6. The as-designed models with different values of ε where (a) represents the relationship between *r* / *a* and ε, and (b) shows the influence of ε on the aperture frequency distribution.

Table 4. Relationship between ε and the characteristic parameters

E	NNP	Φ (%)	Davg (μm)
0.06	2498	67.90	641.70
0.12	2487	69.88	673.78
0.18	2484	69.24	696.02
0.25	2482	70.26	716.32
0.30	2480	72.28	729.88
0.39	2483	72.63	730.57
0.47	2479	72.43	730.18
0.58	2435	69.05	730.16

shows the aperture frequency curves for different values of *ε*. Specifically, the quantity of the apertures at 15 μm and 1000 μm levels is significantly larger when $\varepsilon \leq 0.25$, leading to excessive span of the apertures and causing discontinuities in the mechanical properties. At the same time, the proportion of apertures smaller than 60 μm is too high and the positive stimulus to induce osteoblast adhesion and proliferation is lost, affecting the actual performance of the bone implants. The aperture values are mainly in the range between 60 μm and 1200 μm when $\varepsilon > 0.25$, and there will be no sudden changes in mechanical properties at vulnerable parts when the aperture values fall within the range.

Figure 7a and b present the influence of the scale coefficient on the porous biomaterials in sub-region A. Figure 7a, where C^{cell} is maintained constant, demonstrates the effect of a single factor C^{face}. It is obvious that different values of dot pitch have little effect on *Φ*, which is consistent with our previous works[12,13]. Apart from that, D_{avg} and *Φ* are proportional and linearly related to C^{face}. Figure 7b, where C^{face} is maintained constant, demonstrates the effect of C^{cell}. Similarly, the different dot pitch values have little effect on *Φ*, which is proportional and linearly related to C^{cell}. However, D_{avg} remains unchanged as C^{cell} increases when the value of dot pitch is determined, which indicated that the aperture is only controlled by C^{face}.

Figure 7c shows the gradient change of the characteristic parameters. It can be observed that D_{avg} decreases when the ratio C^{cell} / C^{face} increases, which is diametrically opposed to the results of previous studies setting $C^{cell} = C^{face}$ as shown in Figure 7d. This peculiar phenomenon illustrates the effectiveness of the design, ensuring the mechanical continuity of sub-region B and increasing the specific surface area, leading to an improvement in the bio-functionality. An upward trend of *Φ* is shown, indicating that the graded porosity distribution is realized. With the simplification according to Equation IV, the relationship between C^{cell} / C^{face} and *Φ* can be fitted and a unary expression is shown as follows:

$$\Phi = (91.94915 - 20.31354e^{-\frac{(\frac{C^{cell}}{140-C^{cell}}-0.60613)^2}{1.61989}}) \times 100\% \quad (V)$$

The local porosity can be calculated as shown in Figure 7e. Figure 7f shows the change of the overall porosity. It is clear that the scale coefficient exhibits a strong linear relationship with the porosity. The overall target porosity of the bionic bone scaffolds can be controlled by the scale coefficient.

The above results demonstrate that the as-designed bionic bone scaffolds are highly controllable. Design variables can be flexibly adjusted to accommodate the changes of the target characteristic parameters. In addition, the results of the aperture frequency diagrams demonstrate the superiority and the effectiveness of this methodology to achieve an optimal aperture distribution for porous biomaterials. Since the aperture is a complex function of the C^{face}, a_t, r_t, and d_t, this task will be developed in a future study. The discussion on the scale coefficient proves that the as-designed models achieve a graded distribution of porosity, which could be accurately calculated based on Equation V.

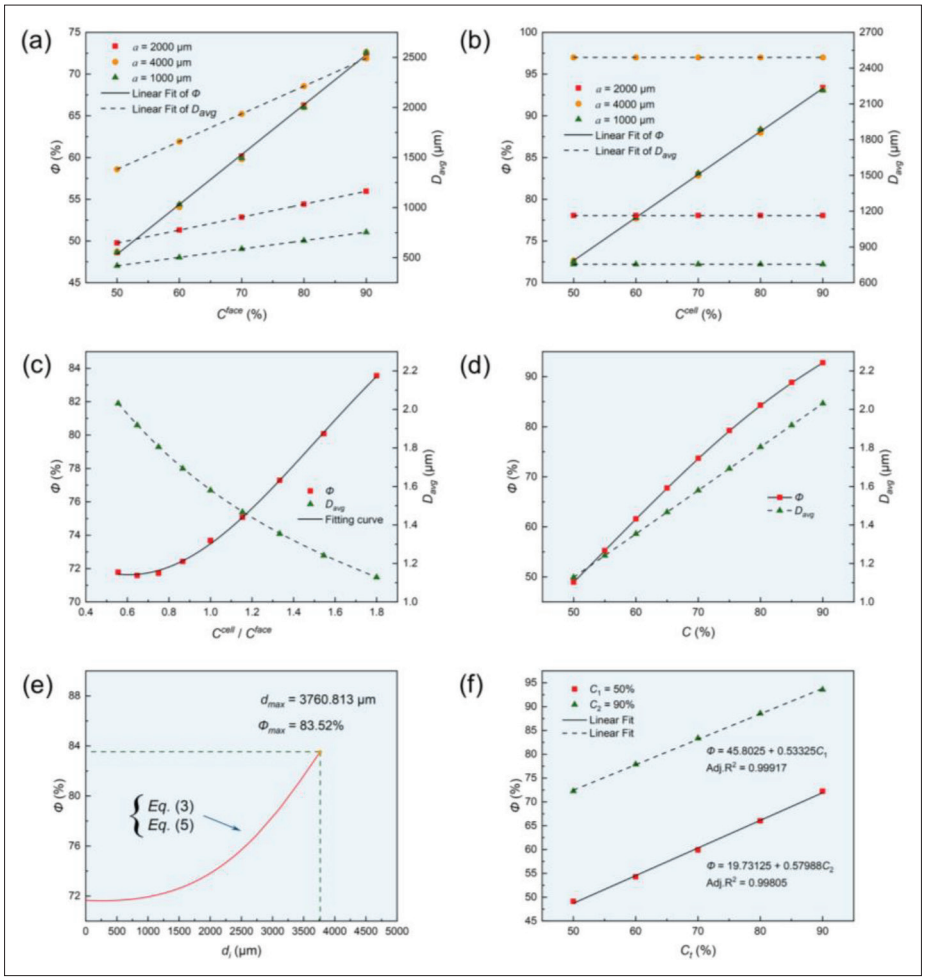

Figure 7. Characteristic parameters of the as-designed models with ε = 0.47 where one can see (a) influence of C^{face} where C^{cell} = 50%, (b) influence of C^{cell} where C^{face} = 90%, (c) variation trend with C^{cell} / C^{face}, (d) variation trend with C (C^{cell} = C^{face}), (e) influence of d_i, and (f) influence of C_i.

3.2. Finite element analysis of as-designed models

Randomness arose from the combined probability sphere model in this study. Figure 8 shows the FEA result of the four as-designed models in randomness series. The four models share roughly the same stress nephogram. The range of maximum von Mises stress values varies between 1403.27 MPa and 1468.75 MPa. Meanwhile, the range of porosity values varies between 72.33% and 73.08%. The results demonstrate that randomness has a negligible effect on stress distribution and porosity, further verifying the feasibility of the combined probability sphere model.

Similarly, it can be concluded from Figure 9a that a_1 has little effect on the compressive property of the as-designed models. The maximum von Mises stress and porosity reach value ranges of 1423.95–1497.63 MPa and 72.83%–74.55%, respectively. With the increase of a_1, stress nephograms are basically unchanged, which means that *NNP* in sub-region B has a negligible effect on the mechanical property and the porosity. As depicted in Figure 9b, the FEA models in a_2 series have maximum von Mises stress values of 1427.63 MPa, 1718.27 MPa, 2106.50 MPa, and 2842.75 MPa, respectively. In addition, the corresponding values of porosity are 72.62%, 72.13%, 71.61%, and 73.92%, respectively. More struts exceed the yield strength as the value of a_2 increases, which means *NNP* in sub-region A has a greater influence on the mechanical property.

Randomness and a_1 bring a small change to *NNP* while a_2 is the opposite, as it has a great influence on the structural strength, which shows a great consistency with the discussions in section 3.1. The reason for variation of *NNP* in randomness series was the random perturbation of points, which resulted in a perturbation in the number of points retained and deleted by the Boolean operation.

3.3. Mechanical characterization of the as-built specimens

The as-built specimens fabricated by LPBF are shown in Figure 10. For ease of labeling in the figure, the as-built

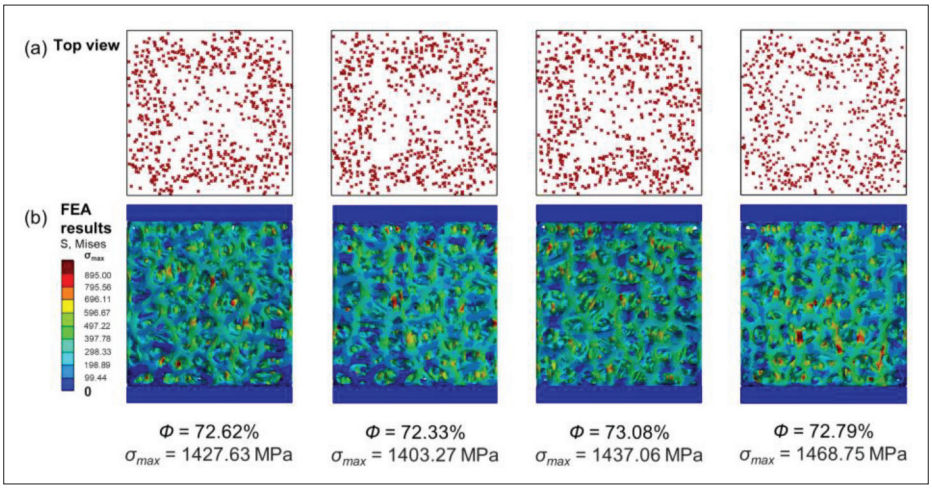

Figure 8. FEA results of randomness series where one can see (a) the top view of the Voronoi nucleating points and (b) the stress nephograms.

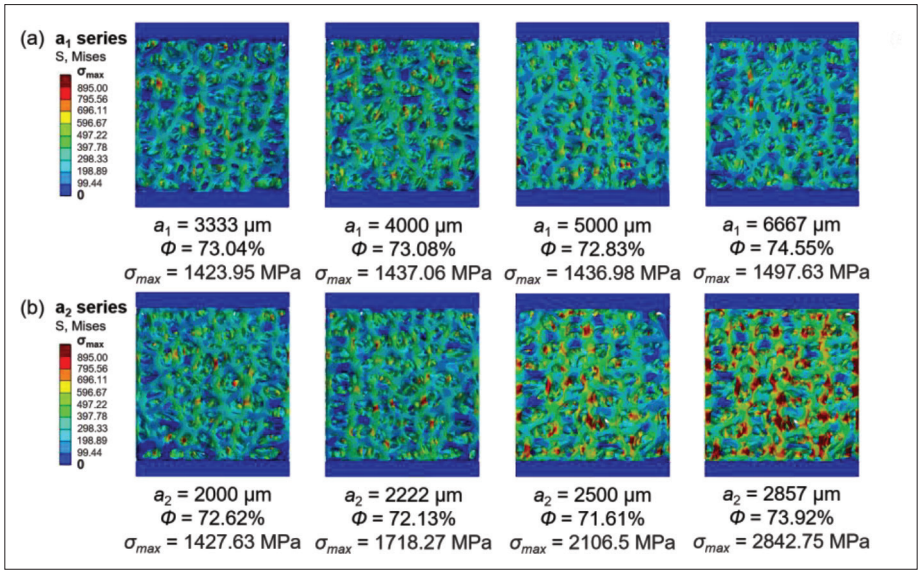

Figure 9. FEA results where one can see the stress nephograms of (a) a_1 series and (b) a_2 series.

specimens were numbered (refer to Table 2). Table 5 lists the porosity of the as-designed models and the as-built specimens. The deviation of porosity between models and specimens is less than 4%, demonstrating that all struts were precisely manufactured to a predetermined size and shape.

The results of the static compression tests of the as-built specimens are summarized in Figure 11. The stress–strain curves are typical for the as-built specimens, including the linear increase in stress and a plateau region with fluctuating stresses. Meanwhile, an initial approximate parabola is observed in each stress–strain curve, going upwards at the beginning of loading. This might be attributed to the lack of fusion powder from manufacturing defects, which may lead to an uneven contact interface between pressure head and specimens[36,42,43].

Apparent elastic modulus (E) and ultimate strength (S) are the pivotal characteristic parameters for evaluating the mechanical properties of porous biomaterials. As depicted in Figure 12a and d, specimens with constant design parameters of C_1 = 50% and ε = 0.47 (No. 09, 10, 11, and 12) have an ultimate strength range of 190.19–268.03 MPa. Meanwhile, the corresponding elastic modulus reaches a value range of 4.52–7.12 GPa. Given a certain C_1 and ε, the as-built specimens with a larger C_2 have a higher porosity value (refer to Table 5), which results in a smaller apparent elastic modulus and an ultimate strength. This result is consistent with the classic foam metal model[44,45]. With the

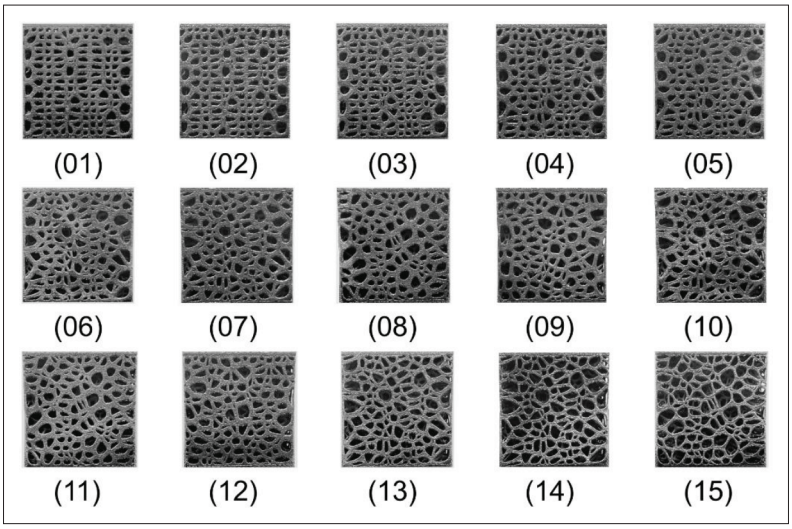

Figure 10. Bionic bone scaffolds fabricated by LPBF process.

Table 5. Porosity of the as-designed models and the as-built specimens

Part number	Porosity (%)		Deviation (%)
	3D model	LPBF specimen	
(01)	67.90	65.33	2.57
(02)	69.88	68.75	1.13
(03)	69.24	66.93	2.31
(04)	70.26	68.45	1.81
(05)	72.28	69.66	2.62
(06)	72.63	70.59	2.04
(07)	72.43	71.36	1.07
(08)	71.05	69.84	1.21
(09)	72.25	70.06	2.19
(10)	66.03	64.97	1.06
(11)	59.93	57.27	2.66
(12)	54.29	53.18	1.11
(13)	77.89	75.94	1.95
(14)	83.36	79.83	3.53
(15)	88.59	85.08	3.51

application of Gibson–Ashby model[46,47], the expressions can be fitted as follows:

$$S = 375.64(1-\frac{\Phi}{100})^{0.52} \quad \text{(VI)}$$

$$E = 16.27(1-\frac{\Phi}{100})^{1.06} \quad \text{(VII)}$$

Similarly, the ultimate strength of specimens with constant design parameters of C_2 = 90% and ε = 0.47 (No. 09, 13, 14, and 15) ranges from 38.55 to 190.19 MPa (refer to Figure 12b). Meanwhile, Figure 12e depicts that the corresponding elastic modulus reaches a value range of 1.5–4.52 GPa. Thus, the Gibson–Ashby formula can be rewritten as follows:

$$S = 1551.18(1-\frac{\Phi}{100})^{1.63} \quad \text{(VIII)}$$

$$E = 20.83(1-\frac{\Phi}{100})^{1.17} \quad \text{(IX)}$$

The increasement of C_1 and C_2 leads to a greater porosity. The diameter of struts decreases accordingly, resulting in the decay of stiffness and an easier deformation. Figure 13 shows the growth rate diagrams of E and S as porosity decreases. In this study, the growth rate is defined as the ratio of ΔS (ΔE) to S_0 (E_0), where the corresponding value of S (E) is determined as S_0 (E_0) when design variable C_1 or C_2 takes the value of its upper limit. When the porosity is determined only through the variable C_2 ranging from 60% to 90% with a constant C_1 = 50% (No. 09, 10, 11, and 12), the ultimate strength increases by 10% as C_2 decreases by about 10% (Figure 13a). The growth rate of E is slightly higher than that of S. Similarly, when the porosity is determined only through the variable C_1 ranging from 50% to 80% with a constant C_2 = 90% (No. 09, 13, 14, and 15), S and E increase significantly with the decrease of C_1. As depicted in Figure 13b, the growth rate of S is almost 10 times greater than that in Figure 13a as C_1 decreases by 10%. Given a certain C_1 = 50%, porous biomaterials in sub-region A have a constant C^{cell} value equal to 50% and a variable C^{face} value ranging between 60% and 90%. S increases as C^{face} decreases, but the amplitude of the change is not significant. Similarly, given a certain C_2 = 90%, porous biomaterials in sub-region A have a constant C^{face} value equal to 90% and a variable C^{cell} value ranging between 60%

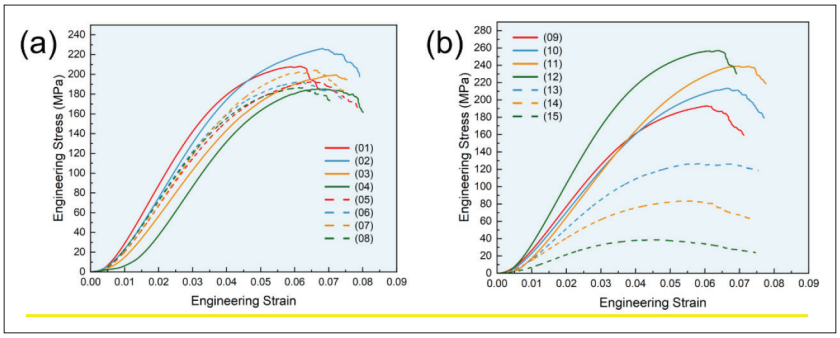

Figure 11. Static compression tests for (a) irregularity series and (b) scale coefficient series.

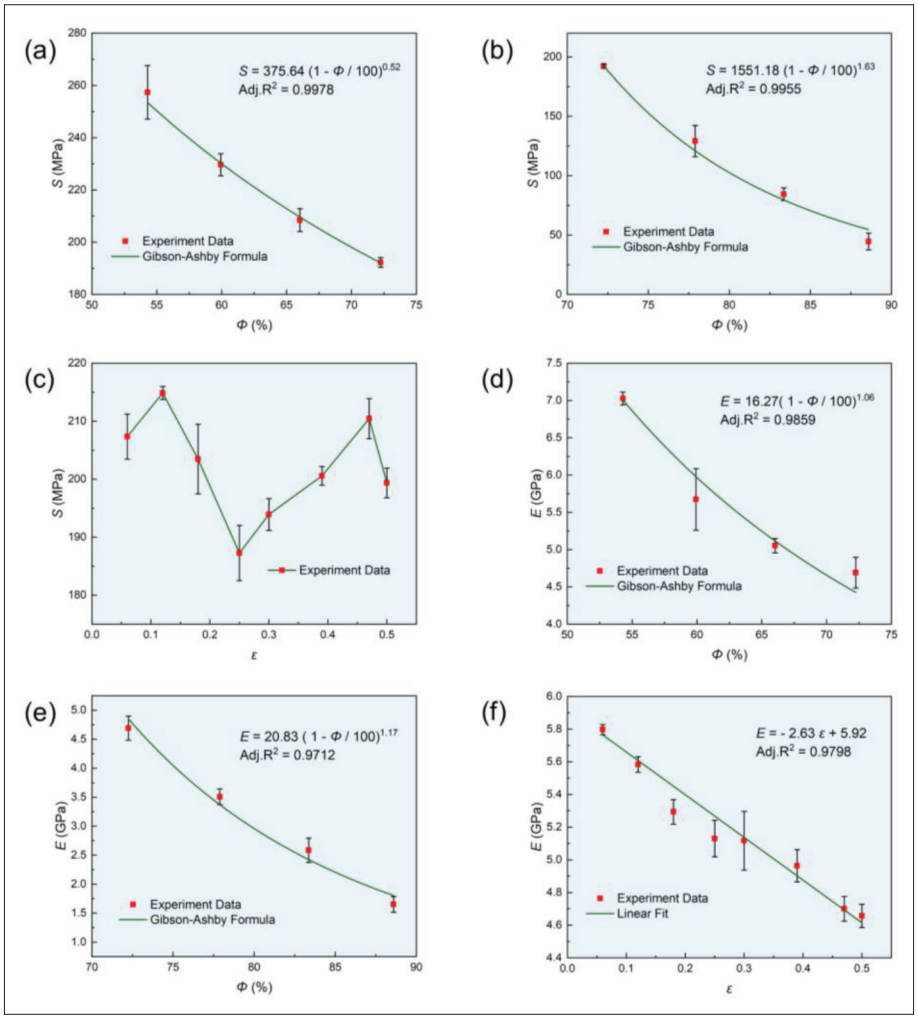

Figure 12. Mechanical properties calculated from raw data for (a) *S* of specimens with variable C_2, (b) S of specimens with variable C_1, (c) *S* of specimens with variable ε, (d) *E* of specimens with variable C_2, (e) *E* of specimens with variable C_1, and (f) *E* of specimens with variable ε.

and 90%. *S* increases as C^{cell} decreases, and the magnitude of the change is much larger than the former case. It can be concluded, by comparison, that the compressive properties of the as-built specimens are closely related with C^{cell} and C^{face}, where C^{cell} is considered dominant. The effectiveness of this design method is proven according to the growth rate results. The strength of porous biomaterials is mainly controlled by the porosity in sub-region A. Meanwhile, the results are consistent with findings in section 3.1 and section 3.2.

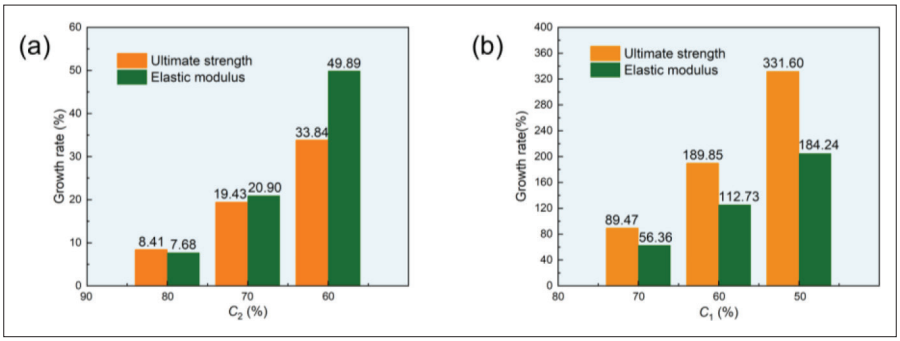

Figure 13. Growth rate of *S* and *E* for (a) C_1 = 50% and (b) C_2 = 90%.

As shown in Figure 12c and f, specimens in irregularity series have an apparent elastic modulus range between 4.67 GPa and 5.83 GPa. *E* decreases almost linearly as irregularity increases. Meanwhile, *S* reaches a value range of 182.51–216.14 MPa, showing an irregular change trend, different from *E*. For instance:

(i) *S* of the as-built specimen, with ε = 0.12, is equal to 216.14 MPa, which is the maximum value in ε series whereas the corresponding value of *E* is 5.62 GPa;

(ii) *S* of the as-built specimen, with ε = 0.25, is equal to 182.51 MPa, which is the minimum value whereas the corresponding value of *E* is 5.23 GPa;

(iii) *S* of the as-built specimen, with ε = 0.47, is equal to 213.55 MPa whereas the corresponding value of *E* is 4.77 GPa.

A previous study demonstrated that irregularity at low levels leads to a reduction in strength, which is caused by the initial instability of the unit cell[48]. The increase of irregularity makes more struts change from vertical or horizontal position to inclined position, which is the possible reason for the reduction of the structural stiffness. Thus, a new stress balance will be established and the compressive strength will tend to be stable as the irregularity exceeds a certain value. Furthermore, pores and cracks will inevitably appear in the as-built specimens during the LPBF process. Cracks, related to the direction of struts, have a significant impact on the compressive strength, which also lead to the fluctuation of the experiment data[49-51].

As mentioned in previous studies[52,53], the natural cancellous bone has a Young's modulus range between 0.1 GPa and 4.5 GPa and an ultimate strength range between 1.5 MPa and 38 MPa. Meanwhile, the cortical bone has a Young's modulus range of 5–23 GPa and an ultimate strength range of 35–283 MPa. In this study, the quasi-static compressive behavior of the as-built specimens is researched. The as-built specimens present a satisfying

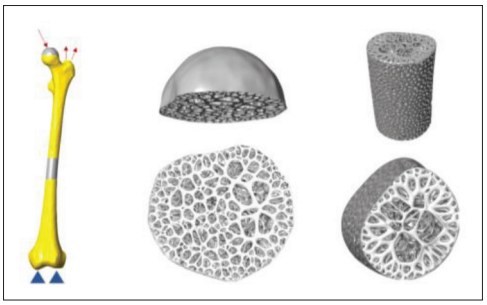

Figure 14. Bionic bone scaffolds for femoral defect site.

mechanical performance. The apparent elastic modulus ranges from 1.50 GPa to 7.12 GPa, which is in conformance to the required level of natural bone. Besides, the ultimate strength ranges between 38.55 MPa and 268.03 MPa, showing a more excellent stress resistance ability similar to cortical bone level. Compared to the previous studies, the bionic bone scaffolds proposed in this work present a better mechanical continuity with a more reasonable gradient match in elastic modulus and structural strength. Therefore, it can be foreseen that this bionic bone scaffold will help to form a maximum degree of continuous mechanical conduction with the surrounding host bone, further reducing the possibility of the stress shielding. In addition, as shown in Figure 14, this approach is adaptable to models with complex macrostructure, providing more possibilities for engineering application of graded porous biomaterials.

4. Conclusion and future work

In this paper, a sub-regional design methodology of the bionic bone scaffolds, based on the macrostructural topology, was innovatively proposed. The relationship between design parameters and characteristic parameters was fully discussed, indicating that this bionic bone scaffold is highly controllable. The as-designed models were fabricated by the LPBF process using the Ti-6Al-4V powder. The results of FEA and the quasi-static compression tests proved the effectiveness in

practical application. The main results are summarized as follows:

(i) This approach enabled us to carry out accurate and controllable gradient design according to the macrostructural topology, and to implement the graded distribution of the characteristic parameters.

(ii) The combined probability sphere model, proposed in this paper, realized a graded and random distribution of the Voronoi nucleating points, and provided greater freedom in the morphology of the bionic bone scaffolds within a controllable range, further improving the geometric and mechanical continuity at the junction of the two sub-regions.

(iii) The distance-to-scale coefficient mapping model, proposed in this paper, provided the guideline for the graded design of the porous biomaterials in sub-region B, where the specific surface area and the mechanical properties were greatly improved with the differentiated design of C^{face} and C^{cell}, reducing the possibility that fragile struts, far from sub-region A, will fracture first.

(iv) The FEA results showed that randomness and a_1 value have negligible effect on the compressive property and the porosity of as-designed models, proving a high repeatability of tests. Meanwhile, the value of a_2 is considered to have a great influence on the compressive property, proving that the relative density of porous biomaterials in sub-region A is closely related to the structural strength.

(v) The results of quasi-static compression tests demonstrate that ε, C_1, and C_2 affect the compressive behavior of the as-built specimens, proving that C^{cell} of the porous biomaterials in sub-region A has a dominant influence on the compressive property. Meanwhile, the bionic bone scaffolds, proposed in this work, present a satisfying mechanical performance where the apparent elastic modulus and ultimate strength ranges are 1.50–7.12 GPa and 38.55–268.03 MPa, respectively. It can be concluded that the as-built specimens have the same stiffness level of the cancellous bone but with a better stress resistance ability, similar to that of the cortical bone. Significantly, the apparent elastic modulus can be tailored conveniently by adjusting the scale coefficient.

As for the future works, the properties of the bionic bone scaffolds will be further investigated. In addition, research on the bionic bone scaffolds with complex macroscopic models and loading conditions has become the principal work for the next stage. Besides, we also plan to set different topological objectives for the macrostructure to realize multifunctionality of the scaffolds. It is expected that this research can provide some insights into the FGPMs design.

Acknowledgments

The authors extend their sincere gratitude to those who contributed in instructions and experiments.

Funding

This work was supported by Jiangsu Provincial Key Research and Development Program (grant number BE2019002) and Postdoctoral Science Foundation of China (grant numbers 2020M671475, 2020M671455, 2020TQ0141). The authors also extend their sincere thanks to those who guided us in the experiments.

Conflict of interest

The authors declare that they have no known competing financial interests or personal relationships that could have appeared to influence the work reported in this paper.

Author contributions

Conceptualization: Yangdong He, Lida Shen
Investigation: Changjiang Wang, Lin Wang, Deqiao Xie, Chen Jiao, Hong Wang
Methodology: Yangdong He, Long Chao, Huixin Liang
Resources: Jianfeng Zhao, Lida Shen, Huixin Liang, Guofeng Wu
Writing – original draft: Yangdong He
Writing – review & editing: Yangdong He, Long Chao, Huixin Liang, Lida Shen

Ethics approval and consent to participate

Not applicable.

Consent for publication

Not applicable.

Availability of data

The datasets used and analyzed during the present study can be obtained from the corresponding author on request.

References

1. Pina S, Oliveira JM, Reis RL, 2015, Natural-based nanocomposites for bone tissue engineering and regenerative medicine: A review. *Adv Mater*, 27:1143–1169.

https://doi.org/10.1002/adma.201403354

2. Geetha M, Singh AK, Asokamani R, *et al.*, 2009, Ti based biomaterials, the ultimate choice for orthopaedic implants—A review. *Prog Mater Sci*, 54:397–425.

   https://doi.org/10.1016/j.pmatsci.2008.06.004

3. Choi K, Kuhn JL, Ciarelli MJ, *et al.*, 1990, The elastic-moduli of human subchondral, trabecular, and cortical bone tissue and the size-dependency of cortical bone modulus. *J Biomech*, 23:1103–1113.

   https://doi.org/10.1016/0021-9290(90)90003-l

4. Melancon D, Bagheri ZS, Johnston RB, *et al.*, 2017, Mechanical characterization of structurally porous biomaterials built via additive manufacturing: experiments, predictive models, and design maps for load-bearing bone replacement implants. *Acta Biomater*, 63:350–368.

   https://doi.org/10.1016/j.actbio.2017.09.013

5. Kantaros A, Chatzidai N, Karalekas D, 2016, 3D printing-assisted design of scaffold structures. *Int J Adv Manuf Technol*, 82:559–571.

   https://doi.org/10.1007/s00170-015-7386-6

6. Tshephe TS, Akinwamide SO, Olevsky E, *et al.*, 2022, Additive manufacturing of titanium-based alloys—A review of methods, properties, challenges, and prospects. *Heliyon*, 8:20.

   https://doi.org/10.1016/j.heliyon.2022.e09041

7. Zhao D, Huang Y, Ao Y, *et al.*, 2018, Effect of pore geometry on the fatigue properties and cell affinity of porous titanium scaffolds fabricated by selective laser melting. *J Mech Behav Biomed Mater*, 88:478–487.

   https://doi.org/10.1016/j.jmbbm.2018.08.048

8. Yan X, Li Q, Yin S, *et al.*, 2019, Mechanical and in vitro study of an isotropic Ti6Al4V lattice structure fabricated using selective laser melting, *J Alloy Compd*, 782:209–223.

   https://doi.org/10.1016/j.jallcom.2018.12.220

9. Gomez S, Vlad MD, Lopez J, *et al.*, 2016, Design and properties of 3D scaffolds for bone tissue engineering, *Acta Biomater*, 42:341–350.

   https://doi.org/10.1016/j.actbio.2016.06.032

10. Rumpler M, Woesz A, Dunlop JWC, *et al.*, 2008, The effect of geometry on three-dimensional tissue growth, *J R Soc Interface*, 5:1173–1180.

    https://doi.org/10.1098/rsif.2008.0064

11. Biemond JE, Aquarius R, Verdonschot N, *et al.*, 2011, Frictional and bone ingrowth properties of engineered surface topographies produced by electron beam technology. *Arch Orthop Trauma Surg*, 131:711–718.

    https://doi.org/10.1007/s00402-010-1218-9

12. Wang G, Shen L, Zhao J, *et al.*, 2018, Design and compressive behavior of controllable irregular porous scaffolds: Based on Voronoi-tessellation and for additive manufacturing. *ACS Biomater Sci Eng*, 4:719–727.

    https://doi.org/10.1021/acsbiomaterials.7b00916

13. Du Y, Liang H, Xie D, *et al.*, 2020, Design and statistical analysis of irregular porous scaffolds for orthopedic reconstruction based on Voronoi tessellation and fabricated via selective laser melting (SLM). *Mater Chem Phys*, 239:121968.

    https://doi.org/10.1016/j.matchemphys.2019.121968

14. Van Bael S, Chai YC, Truscello S, *et al.*, 2012, The effect of pore geometry on the in vitro biological behavior of human periosteum-derived cells seeded on selective laser-melted Ti6Al4V bone scaffolds. *Acta Biomater*, 8:2824–2834.

    https://doi.org/10.1016/j.actbio.2012.04.001

15. Gongyi H, 2007, Characteristics of osteoporosis-related fracture and clinical study. *Basic Clin Med*, 27:1088–1092.

16. Barbaros I, Yang YM, Safaei B, *et al.*, 2022, State-of-the-art review of fabrication, application, and mechanical properties of functionally graded porous nanocomposite materials. *Nanotechnol Rev*, 11:321–371.

    https://doi.org/10.1515/ntrev-2022-0017

17. Liu B, Chen H, Cao W, 2019, A novel method for tailoring elasticity distributions of functionally graded porous materials. *Int J Mech Sci*, 157–158:457–470.

    https://doi.org/10.1016/j.ijmecsci.2019.05.002

18. George SM, Nayak C, Singh I, *et al.*, 2022, Multifunctional hydroxyapatite composites for orthopedic applications: A review. *ACS Biomater Sci Eng*, 8:3162–3186.

    https://doi.org/10.1021/acsbiomaterials.2c00140

19. Deering J, Dowling KI, DiCecco LA, *et al.*, 2021, Selective Voronoi tessellation as a method to design anisotropic and biomimetic implants. *J Mech Behav Biomed Mater*, 116:104361.

    https://doi.org/10.1016/j.jmbbm.2021.104361

20. Liu B, Cao W, Zhang L, *et al.*, 2021, A design method of Voronoi porous structures with graded relative elasticity distribution for functionally gradient porous materials. *Int J Mech Mater Des*, 17:863–883.

    https://doi.org/10.1007/s10999-021-09558-6

21. Davoodi E, Montazerian H, Mirhakimi AS, *et al.*, 2022, Additively manufactured metallic biomaterials, *Bioact Mater*, 15:214–249.

    https://doi.org/10.1016/j.bioactmat.2021.12.027

22. Zhou J, Xia L, Huang K, 2022, Design-oriented topology optimization of structures. *J Ship Mech*, 26:538–546.

23. Xu FX, Zhang X, Zhang H, 2018, A review on functionally graded structures and materials for energy absorption. *Eng Struct*, 171:309–325.

https://doi.org/10.1016/j.engstruct.2018.05.094

24. Li H, Luo Z, Gao L, *et al.*, 2018, Topology optimization for concurrent design of structures with multi-patch microstructures by level sets. *Comput Meth Appl Mech Eng*, 331:536–561.

https://doi.org/10.1016/j.cma.2017.11.033

25. Terriault P, Brailovski V, 2018, Modeling and simulation of large, conformal, porosity-graded and lightweight lattice structures made by additive manufacturing. *Finite Elem Anal Des*, 138:1–11.

https://doi.org/10.1016/j.finel.2017.09.005

26. Radman A, Huang X, Xie YM, 2012, Topology optimization of functionally graded cellular materials. *J Mater Sci*, 48:1503–1510.

https://doi.org/10.1007/s10853-012-6905-1

27. Alzahrani M, Choi SK, Rosen DW, 2015, Design of truss-like cellular structures using relative density mapping method. *Mater Des*, 85:349–360.

https://doi.org/10.1016/j.matdes.2015.06.180

28. Zhao F, 2018, Variable density cellular structure design method base on local relative density mapping. *J Mech Eng*, 54:121–8.

https://doi.org/10.3901/jme.2018.19.121

29. Wang C, Gu X, Zhu J, *et al.*, 2020, Concurrent design of hierarchical structures with three-dimensional parameterized lattice microstructures for additive manufacturing. *Struct Multidiscip O*, 61:869–894.

https://doi.org/10.1007/s00158-019-02408-2

30. Xia L, Xia Q, Huang XD, *et al.*, 2018, Bi-directional evolutionary structural optimization on advanced structures and materials: A comprehensive review. *Arch Comput Method Eng*, 25:437–478.

https://doi.org/10.1007/s11831-016-9203-2

31. Lee TU, Xie YM, 2022, Optimizing load locations and directions in structural design. *Finite Elem Anal Des*, 209:8.

https://doi.org/10.1016/j.finel.2022.103811

32 Bi MH, Tran P, Xia LW, *et al.*, 2022, Topology optimization for 3D concrete printing with various manufacturing constraints. *Addit Manuf*, 57:15.

https://doi.org/10.1016/j.addma.2022.102982

33. Han YS, Xu B, Duan ZY, *et al.*, 2022, Stress-based topology optimization of continuum structures for the elastic contact problems with friction. *Struct Multidiscip O*, 65:22.

https://doi.org/10.1007/s00158-022-03169-1

34. Han YS, Xu B, Duan ZY, *et al.*, 2022, Stress-based multi-material structural topology optimization considering graded interfaces. *Comput Meth Appl Mech Eng*, 391:31.

https://doi.org/10.1016/j.cma.2022.114602

35. Zhu L, Liang H, Lv F, *et al.*, 2021, Design and compressive fatigue properties of irregular porous scaffolds for orthopedics fabricated using selective laser melting, *ACS Biomater Sci Eng*, 7:1663–1672.

https://doi.org/10.1021/acsbiomaterials.0c01392

36. Liang H, Yang Y, Xie D, *et al.*, 2019, Trabecular-like Ti-6Al-4V scaffolds for orthopedic: fabrication by selective laser melting and in vitro biocompatibility. *J Mater Sci Technol*, 35:1284–1297.

https://doi.org/10.1016/j.jmst.2019.01.012

37. Li Y, 2014, *Deformable Geometry Design with Controlled Mechanical Property Based on 3D Printing*, University of Southern California, 162.

38. Radman A, 2021, Combination of BESO and harmony search for topology optimization of microstructures for materials. *Appl Math Model*, 90:650–661.

https://doi.org/10.1016/j.apm.2020.09.024

39. Hutmacher DW, 2000, Scaffolds in tissue engineering bone and cartilage. *Biomaterials*, 21:2529–2543.

https://doi.org/10.1016/s0142-9612(00)00121-6

40. Yan QY, Cheng Y, Wang RR, *et al.*, 2022, Recent advances in 3D porous MXenes: Structures, properties and applications. *J Phys D-Appl Phys*, 55:15.

https://doi.org/10.1088/1361-6463/ac2db2

41. Prananingrum W, Naito Y, Galli S, *et al.*, 2016, Bone ingrowth of various porous titanium scaffolds produced by a moldless and space holder technique: an in vivo study in rabbits. *Biomed Mater*, 11:8.

https://doi.org/10.1088/1748-6041/11/1/015012

42. Babaie E, Bhaduri SB, 2018, Fabrication aspects of porous biomaterials in orthopedic applications: A review, *ACS Biomater Sci Eng*, 4:1–39.

https://doi.org/10.1021/acsbiomaterials.7b00615

43. Zheng YH, Han Q, Wang JC, *et al.*, 2020, Promotion of osseointegration between implant and bone interface by titanium alloy porous scaffolds prepared by 3D printing. *ACS Biomater Sci Eng*, 6:5181–5190.

https://doi.org/10.1021/acsbiomaterials.0c00662

44. Zhang S, 2016, Foam metal research and application progress. *Powder Metall Technol*, 34:222–227.

45. Qiu SW, Zhang XN, Hao QX, *et al.*, 2015, Research progress on simulation modeling of metal foams. *Rare Metal Mat Eng*, 44:2670–2676.

46. Gibson LJ, 2003, Cellular solids. *MRS Bull*, 28:270–271.

https://doi.org/10.1557/mrs2003.79

47. Gibson LJ, Ashby MF, 1997, *Cellular Solids: Structure and Properties*, Cambridge University Press, Cambridge, 387–428.

48. Mullen L, Stamp RC, Brooks WK, *et al.*, 2009, Selective laser melting: A regular unit cell approach for the manufacture of porous, titanium, bone in-growth constructs, suitable for orthopedic applications. *J Biomed Mater Res Part B*, 89B:325–334.

https://doi.org/10.1002/jbm.b.31219

49. Craeghs T, Clijsters S, Yasa E, *et al.*, 2011, Determination of geometrical factors in Layerwise laser melting using optical process monitoring. *Opt Lasers Eng*, 49:1440–1446.

https://doi.org/10.1016/j.optlaseng.2011.06.016

50. Wauthle R, Vrancken B, Beynaerts B, *et al.*, 2015, Effects of build orientation and heat treatment on the microstructure and mechanical properties of selective laser melted Ti6Al4V lattice structures. *Addit Manuf*, 5:77–84.

https://doi.org/10.1016/j.addma.2014.12.008

51. Popovich A, Sufiiarov V, Borisov E, *et al.*, 2015, Microstructure and mechanical properties of Ti-6Al-4V manufactured by SLM. *Key Eng Mater (Switzerland)*, 651–653: 677–682.

https://doi.org/10.4028/www.scientific.net/KEM.651-653.677

52. Sevilla P, Aparicio C, Planell JA, *et al.*, 2007, Comparison of the mechanical properties between tantalum and nickel-titanium foams implant materials for bone ingrowth applications. *J Alloy Compd*, 439:67–73.

https://doi.org/10.1016/j.jallcom.2006.08.069

53. Morgan EF, Bayraktar HH, Keaveny TM, 2003, Trabecular bone modulus-density relationships depend on anatomic site. *J Biomech*, 36:897–904.

https://doi.org/10.1016/s0021-9290(03)00071-x

ACCSCIENCE PUBLISHING

International Journal of Bioprinting

RESEARCH ARTICLE

3D Aerosol Jet® printing for microstructuring: Advantages and Limitations

Miriam Seiti[1], Olivier Degryse[1], Rosalba Monica Ferraro[2], Silvia Giliani[2], Veerle Bloemen[3], and Eleonora Ferraris[1]*

[1]Manufacturing Processes and Systems (MaPS), Mechanical Engineering, KU Leuven, Sint Katelijne Waver, 2860, Belgium

[2]Department of Molecular and Translational Medicine, "Angelo Nocivelli" Institute for Molecular Medicine, University of Brescia, ASST Spedali Civili, Brescia, Italy

[3]Prometheus, Division of Skeletal Tissue Engineering, KU Leuven, Leuven, Belgium

(This article belongs to the *Special Issue: Related to 3D printing technology and materials*)

Abstract

Aerosol Jet® printing (AJ®P) is a direct writing printing technology that deposits functional aerosolized solutions on free-form substrates. Its potential has been widely adopted for two-dimensional (2D) microscale constructs in printed electronics (PE), and it is rapidly growing toward surface structuring and biological interfaces. However, limited research has been devoted to its exploitation as a three-dimensional (3D) printing technique. In this study, we investigated AJ®P capabilities for 3D microstructuring of three inks, as well as their advantages and limitations by employing three proposed 3D AJ®P strategies (continuous jet deposition, layer-by-layer, and point-wise). In particular, 3D microstructures of increasing complexity based on silver nanoparticle (AgNPs)-, poly(3,4-ethylenedioxythiophene)polystyrene sulfonate (PEDOT:PSS)-, and collagen-based inks were investigated at various aspect ratios and resolutions. Biocompatibility assays were also performed to evaluate inks cytotoxicity effects on selected cellular lineages, including neuronal and osteoblast cell lines. Results show the possibility to print not only arrays of micropillars of different aspect ratios (AgNPs-ARs ~ 20, PEDOT:PSS-ARs ~ 4.5, collagen-ARs ~ 2.5), but also dense and complex (yet low reproducible) leaf- or flake-like structures (especially with the AgNPs-based ink), and lattice units (collagen-based ink). Specifically, this study demonstrates that the fabrication of 3D AJ®-printed microstructures is possible only with a specific set of printing parameters, and firmly depends on the ink (co-)solvents fast-drying phenomena during the printing process. Furthermore, the data concerning inks biocompatibility revealed high cytotoxicity levels for the AgNPs-based ink, while low ones for the PEDOT:PSS and the collagen-based inks. In conclusion, the paper provides general guidelines with respect to ink development and print strategies for 3D AJ®P microstructuring, opening its adoption in a vast range of applications in life science (tissue engineering, bioelectronic interfaces), electronics, and micromanufacturing.

Keywords: Aerosol Jet® printing; 3D microstructures; Micropillars; Microlattices; Ink biocompatibility

***Corresponding author:**
Eleonora Ferraris
(eleonora.ferraris@kuleuven.be)

Citation: Seiti M, Degryse O, Ferraro RM, *et al*., 2023, 3D Aerosol Jet® printing for microstructuring: Advantages and limitations. *Int J Bioprint*, 9(6): 0257.
https://doi.org/10.36922/ijb.0257

Received: December 02, 2022
Accepted: January 10, 2023
Published Online: June 28, 2023

Copyright: © 2023 Author(s). This is an Open Access article distributed under the terms of the Creative Commons Attribution License, permitting distribution, and reproduction in any medium, provided the original work is properly cited.

Publisher's Note: AccScience Publishing remains neutral with regard to jurisdictional claims in published maps and institutional affiliations.

1. Introduction

Microfabrication processes for high aspect ratio (AR) three-dimensional (3D) structures have been widely investigated since the beginning of the 21st century. In particular, the microforming process aims to produce semi-planar or 3D structures from nanometers to sub-millimeters scales[1]. As reported by Vaezi *et al.*[2], many traditional and state-of-the-art processes are currently accessible from subtractive lithography-based, additive manufacturing (AM)-based, and hybrid-based approaches. The range of applications is in continuous expansion, ranging from electronics and life science to aerospace and automotive. In particular, 3D periodic microstructures, such as arrays of pillars or lattice units, with well-defined geometrical characteristics (aspect ratio [AR], diameter, height, and interspacing), have been efficiently used for microelectromechanical systems (MEMS)[3], energy harvesting 3D microbatteries[4,5], bioinspired architectures[6], microsensors (electrochemical sensing[7], microactuators[8]), micro-optical devices[9], circuit packaging[10], among others[11]. In life science, 3D periodic microstructures have also been embedded in bacterial sensors[12], scaffold-based cell culture systems for guiding and cell growth[13-17], electrophysiological recording sensors[18], and microbial electrolytic cell[19].

In the case of AM, 3D structures are produced by direct printing through a functional (multi)-material deposition process. AM methods to fabricate 3D nano/microstructures have been extensively reported in the literature, including two-photon polymerization, (superfine) inkjet printing (IJP), stereolithography, syringe extrusion printing, etc.[20,21]. Among AM techniques, Aerosol Jet® printing (AJ®P) was introduced in the early 1990s by Optomec© Inc. (USA), mainly for printed electronics (PE) applications on free-form (e.g., flat/curved, rigid/flexible) substrates. AJ®P is a noncontact, maskless, direct writing (DW) material jet-based technology which, differently from the others previously mentioned, enables the deposition of (multi-) functional materials in the form of an aerosol through a nozzle at a variable stand-off distance, z [1–5] mm, from the substrate. The result is a well-defined printed pattern, with a minimum feature size starting from 15 μm up to a few cm in width and 0.1 μm in thickness. A high variety of ink viscosities in the range of 1–1000 mPas can be AJ®-printed, from low (ultrasonic configuration) to high (pneumatic configuration) viscous solutions, without the use of photo-sensitive materials. Although limited AJ®P ink formulations are available in the market, most of the IJP inks can be AJ®-printed if aerosolized, showing less clogging occurrences. Moreover, compared to laser-based AM techniques, AJ®P offers a relatively high process speed up to 12 m/min, flexible solutions with start-up costs from 70,000 to a half million of euros, and the printing on objects with 3 or 5 axes over an usual area of 20 × 30 × 20 mm[20]. Side backs of this technology are intrinsic in the complex aerosol dynamics, which occur across the printing process, often resulting in a poor process control and repeatability. However, process optimizations have been investigated both from an industrial and academic perception, especially encouraging its use in the last decade. Two-dimensional (2D) applications have been extensively reviewed mainly for PE, such as conformal printing, antennas, batteries, smart packaging, wearable devices, and (stretchable) sensors[22-25]. Despite an increasing interest in research and several emerging applications in bioelectronics[26], surface structuring, and biological interfaces[27], the exploitation of this technology as a 3D printing technique is still very limited, and only a couple of examples have been reported in the literature. This is mainly related to the fact that this technology was developed for planar-printed electronics and only a few studies have investigated the actual possibility to use it for 3D printing as well.

Saleh *et al.*[28] were the first to AJ®-print silver nanoparticles (AgNPs)-based fully dense truss elements, like lattices and micropillars arrays at high ARs ~ 20. Zips *et al.*[29] also AJ®-printed a composite of poly(3,4-ethylenedioxythiophene) polystyrene sulfonate (PEDOT:PSS) and multiwalled carbon nanotube ink with an AR ~ 3.3. Finally, Hohnholz *et al.*, Di Novo *et al.*, and Vlnieska *et al.* explored the use of photo-reactive polymers, such as polydimethylsiloxane (PDMS) and ultraviolet (UV)-curable adhesives or epoxies to obtain 3D-printed structure with AJP[30-32]. In each case, the ink formulation and print parameters were controlled and adapted for the specific application. However, these works are dictated by trial-and-error explorations and they lack a thorough investigation on 3D AJ®P capabilities and limitations, associated with different inks formulations.

This paper aims at fulfilling this research gap with the purpose of identifying guidelines for AJ®P of 3D microstructures of increasing complexity, with respect to materials and print strategies. Three inks, among which Newtonian and non-Newtonian fluids, that drastically differentiate in ink composition and application functionality (electronics, bioelectronics, and biological interfaces) and three print strategies were selected and combined in this study to realize 3D-printed structures of different complexity and aspect ratios.

This work is the first to provide a systematic discussion on 3D AJ®P capabilities for different ink compositions and print strategies, and it highlights the ability of AJ®P as a 3D microfabrication technology, emphasizing its future use for 3D micromanufacturing, electronics, and life science.

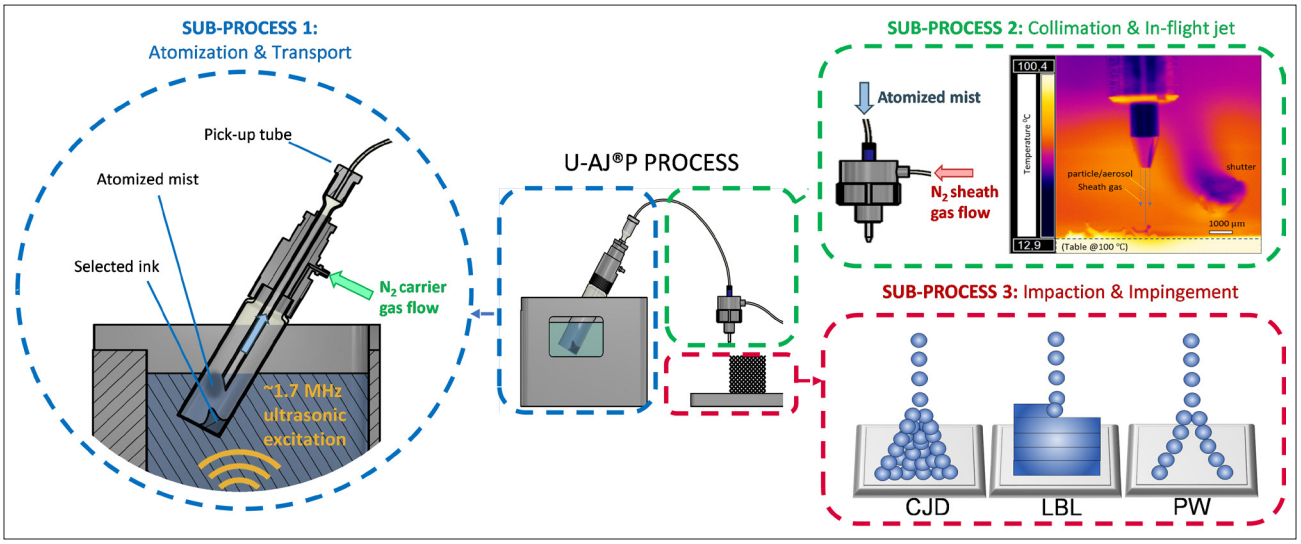

Figure 1. The AJ®P process in ultrasonic configuration (U-AJ®P), divided into the three physical sub-processes: (i) atomization and transport, (ii) collimation and in-flight jet, and (iii) impaction and impingement according to a specific printing strategy, such as continuous jet deposition (CJD), layer-by-layer (LBL), or point-wise (PW) approach. Reproduced with permission[56], Copyright 2022, Elsevier.

2. Material and methods

2.1. Fundamentals of AJ®P and ink formulation

AJ®P is a direct writing, nozzle-based technique which allows the atomization and deposition of a (multi)-functional ink on a free-form substrate, at high microscale resolutions and accuracy. In an ultrasonic configuration (U-AJ®P), a functional ink is atomized into a mist, which is then accelerated through a carrier gas flow (CGF, 0–50 sccm) (generally an inert gas, such as N_2) into a transport tube till the deposition head. Here, the aerosol beam was collimated and aerodynamically focused in the nozzle by an annular gas flow, known as sheath gas flow (SGF, 0–200 sccm), typically N_2. Afterward, the jet exited from the nozzle (i.e., in-flight jet) and then impacted on the desired substrate. Eventually, a postprocess step was applied to cure or crosslink the printed structure. Figure 1 depicts the AJ®P technique, divided into its three physical sub-processes: (i) atomization and transport, (ii) collimation and in-flight jet, and (iii) impaction and impingement[33], according to a selected print strategy (continuous jet deposition, layer-by-layer, and point-wise), as explained in section 2.3. Typical AJ®P functional inks are defined as stable solutions or nano-dispersions (colloids) with a viscosity, η, in the range of 1–1000 mPas (10–20 mPas for U-AJ®P), and surface tension, σ, around 20–75 mN/m. Three elements are typically distinguished: (i) a loading content, (ii) a (co-)solvent system, and (iii) additives. Standard loading contents are conductive metal (Ag, Cu, Au, Pt) nanoparticles (NPs), with a maximum loading content of 40–60 wt.% and an average particle size of 50 nm (U-AJ®P)[34]. Polymeric particles (e.g., PEDOT:PSS) at variable concentration and size are also widely used. Novel inks currently under research can include ceramics, such as hydroxyapatite (HAp), or biomolecules. The ink co-solvent system comprises a main solvent and co-solvents. The former is a liquid medium (usually water at 20–60 v/v% for U-AJ®P), which suspends the particle loading and evaporates during the in-flight jet, impaction, and (thermal) postprocess. The latter is instead a combination of co-solvents chosen to control ink atomization, wetting, evaporation rate during printing, and/or to target specific needs. Their concentrations (usually 5–20 v/v%) mostly depend on volatility (boiling point and vapor pressure), and viscosity. Particularly, highly volatile co-solvents (e.g., alcohols) support the mist transport by the CGF from the vial to the tube[35], while less volatile ones act as humectants during the transport, in-flight and impaction to avoid fast drying of the printed ink, which typically results in impaired print-quality[33]. Eventually, additives (e.g., surfactants, stabilizers, binders, crosslinkers, initiators, and/or functional compounds) can be incorporated based on the target application.

2.2. Inks and substrates preparation

Three aqueous inks were selected as U-AJ®P materials, among which a non-Newtonian commercial AgNPs-based ink (Novacentrix, USA), an own-formulated PEDOT:PSS-based pseudo-elastic dispersion (Sigma Aldrich, Belgium), and a Newtonian own-developed collagen-based solution. Table 1 reports the main features for each of the fluid. The AgNPs-based ink was investigated in its standard formulation and in a diluted form with distilled (DI) water, in a ratio of 1:4. The PEDOT:PSS-based ink was

Table 1. AJ®P inks selected for the print investigation of 3D microstructures and related features[a]

	AJ®P inks and features		
Ink	Metal-based	Polymer-based (synthetic)	Polymer-based (natural)
Supplier	Novacentrix Metalon® JS-A221AE (USA)	Sigma Aldrich (BE) and own-developed formulation	Enzyme extracted Bovine Collagen Type I [3 mg mL^{-1}] supplemented with hydroxyapatite nanoparticles
Abbreviation	AgNP-based ink	PEDOT:PSS-based ink	Collagen-based ink
Type	Nano-dispersion		Solution
Density, ρ [g/cm^3]	-	~1	~1
Viscosity, η [mPas]	5.9	≤ 10	100–150
Surface tension, σ[mN/m]	35.2	75	76
Main solvent	DI water	DI water	0.01 M HCl
Co-solvents	Diethylene glycol (≥ 3 – ≤ 10 v/v%), isopropyl alcohol (≥ 2 – ≤ 10 v/v%)	Own-formulation: polyethylene glycol and ethylene glycol	Glycerol (1 M)
Loading particle	35nm $Ø_{avg}$ (50 wt.%)	PEDOT:PSS (1.3 wt.%)	200 nm $Ø_{avg}$ Hap (3–6 mg/mL)
Additives	-	Carboxymethyl cellulose	1 M glycerol
Notes (resistivity, ρ [Ω·cm])	Conductive, $\rho = 4.2 \times 10^{-4}$ to 9.1×10^{-6} Ω·cm	Conductive, $\rho = 1.66 \times 10^{-3}$ Ω·cm	Bioactive and osteoconductive ink

[a] (i) an AgNPs-based ink for electronics, (ii) a PEDOT:PSS-based ink for bioelectronics, and (iii) a collagen-based ink for biological interfaces.

analyzed in its standard commercial solution and as an own-formulated composition. In addition, a collagen and collagen composite ink were formulated by dissolving freeze-dried collagen type I in 0.01 M hydrochloric acid (HCl) at a concentration of 3 mg mL^{-1}. The collagen was extracted according to a previously published protocol[36]. The composite ink was prepared for use in bone tissue applications. Hence, HAp was added to the collagen solution as particle loading by adding 6 v/v% of a 10 wt.% aqueous HAp suspension (< 200 nm; Sigma Aldrich, BE), as this 1:2 collagen to HAp ratio mimics the composition of human bone tissue. Glass slides (Superfrost or Micro cover glasses, VWR, BE) were selected as reference substrate and ultrasonically cleaned at T = 25°C (EMMI - 20 HC, Emag) for 10 min prior to use, with a mixture of DI water and 2-propanol (IPA, Sigma Aldrich, BE). Before printing, the conductive inks were ultrasonically sonicated for 10 min at 25°C. On the other hand, for the collagen inks, glass cover slips (Ø12 mm, VWR, Belgium) were used as the reference substrate and cleaned in an ultrasonic bath using MilliQ water and ethanol, before being stored in a 1× phosphate-buffered saline (PBS; Lonza, BE) in order to remove any surface charges. The collagen inks could not be ultrasonically homogenized as this would result in degradation of the collagen molecule, as shown by Gibney *et al.*[36].

2.3. AJ®P tools and experimental methodology

An Optomec AJ®P 300s system equipped with an ultrasonic atomizer (U-AJ®P) was used to print samples. Three 3D AJ®P printing strategies, i.e., a continuous jet deposition (CJD), a traditional layer-by-layer (LBL), and a point-wise (PW) approach, were exploited. CJD is a continuous deposition of the aerosol jet on a given spot, while LBL is the traditional layer-by-layer printing in a pattern. Finally, PW is a spot-by-spot of the aerosol jet in a pattern. Unlikely, LBL and PW, CJD does not require the use of a shutter and a print speed, s [mm/sec]. For each strategy, the nozzle was settled at a stand-off distance, z (mm), of 3 mm (increase of + 0.5 mm every + 0.5 mm height of the printed microstructures). For CJD, a continuous deposition of aerosolized material on a single spot was performed with the aim to realize 3D high ARs pillars. In the LBL approach, the targeted samples were arrays of 6 × 4 pillars, each one detected as a circle of 50 μm in diameter. The geometry was designed using AutoCAD software (Autodesk, USA) and then converted in a .prg toolpath code compatible with the printer using VM Tools (VMware, USA). The PW approach was instead used to realize lattice units of pyramidic shape. A MatLab script was created, which controlled the shutter opening time (in milliseconds, ms) as well as the position of the print table. Accordingly, the print head moves in a square-shaped sequence and stops at the corners where the shutter opens for a short period (50–100 ms) before moving to the next point. By decreasing the square dimensions by each layer, the corner-points ultimately coincide in the center, generating a pyramid. By using a slow printing speed (s = 0.01 mm/s), the deposited material is allowed to dry, providing a supporting surface for the consecutive printed layer.

Table 2. AJ®P print parameters and postprocess used for the print investigation for 3D microstructures, divided by ink type and print strategy

	Print parameters (23°C, 50% rh)			
Printer and offset, *z* [mm]	Optomec AJ300s (USA), 3 mm			
Ink	AgNPs-based or water-diluted (1:4) ink, 1 mL		PEDOT:PSS-based (standard and own-formulated) ink, 850 µL	Collagen-based ink
Substrate	VWR Superfrost Glass Slides			VWR Cover Glasses
Printing strategy	CJD	LBL	CJD or LBL	CJD, LBL or PW
Nozzle, Ø [µm]	300	100	150	150
Focusing Ratio, R_f = SGF/CGF	40:10	30:18	35:18	40:19
Platen temperature, *T* [°C]	40	100	80	37
Printing speed, *s* (mm/s)	0	0.4	0.4	0 (CJD) 0.4 (LBL) 0.01 (PW)
Printed patterns	CJD-not required / LBL: 6×4 array, Ø = 50 µm			Pillars (Ø = 50 µm) and pyramids
Number of layers, *n* (#)	1	50	50	50 (LBL)
Postprocessing	Thermal sintering (200°C, 1h)		Thermal annealing (140°C, 1h)	Chemical crosslinking (EDC-NHS)

Table 2 discloses the print parameters and print strategy used for each ink (ambient conditions 22°C, 55%rh). Every parameter was selected after a trial-and-error screening for 3D printing, with as output of interest: (i) the plate temperature, *T* (°C), which facilitates drying out and presintering, and (ii) the focusing ratio, R_f (#), that is the ratio between *SGF* and *CGF*, which regulates the jet focusing during in-flight and evaporation rate upon deposition. R_f also avoids a common phenomenon in AJ®P: the overspray (OS), that is undesired material deposited in the form of porous drops or streams along the printed pattern. For each ink, a homogenous aerosol mist was obtained in at least 15 min after starting the U-AJ®P atomization. After all, 10 min were used to reach the deposition of a stable ink before starting printing. In case of using a heated platen, the substrates were allowed to reach thermal equilibrium by placing them on the platform for 10 min. After printing, a postprocess was executed based on the selected ink. In detail, a thermal sintering (200°C, 1 h) and a thermal annealing (140°C, 1 h) process were pursued on AgNPs- and PEDOT:PSS-based inks (Heraeus, DE), respectively, to ensure full evaporation of the co-solvents and particle aggregation. The collagen samples normally also undergo crosslinking postprinting using a chemical crosslinking approach reported by Gibney *et al.*[36]. However, the crosslinking of collagen was out of the scope of this work.

Each experiment was repeated at least three times. Visual inspection and geometrical analyses were performed using an optical microscope (Hirox KH8700) or a scanning electron microscope (SEM) (Tescan Vega 3, Czech Republic). Particularly, the final shapes were inspected in terms of height (*h*, µm), width base-tip (*w*, µm), AR, internal structure (bulk, hollow), process reproducibility (low, medium, high), and printing time (*t*, s). Geometrical dimensions were detected via the software ImageJ.

2.4 *In vitro* biocompatibility assessment

The exploitation of 3D AJ®P can be foreseen in several application domains for customized multimaterial and multifunctional 3D microstructuring, among which life sciences, particularly the fields of tissue engineering and bioelectronics, is impendent. In this context, in vitro biocompatibility is a crucial requirement for the use of such 3D AJ®-printed microstructures. Therefore, potential cytotoxicity effects were evaluated for all three inks. Specifically, cell viability assays were performed with respect to specific applications for each ink.

2.4.1. AgNPs-based inks

Commercial AgNPs-based inks have already been proven by the same authors to have serious cytotoxicity effects (dose- and time-dependent) on different cellular lineages[37]. To confirm the results obtained from previous data, a direct rATP assay (CellTiter-Glo® 3D Cell Viability, Promega cat. no. G9681) was here performed on human-induced pluripotent stem cells (h-iPSCs)-derived neural stem cells (NSCs) after 48 h of culture on a commercial AgNPs-based ink (SI-AJ 20X, Agfa NV, BE). This PE dispersion has a silver content of 19 wt%, a $Ø_{avg,particle\ size}$ ~ 100 nm, and a viscosity of 12–18 mPas. Compared to the AgNPs-based ink proposed for the printing of 3D microstructure, this ink also contains glycol-type solvents, but a lower Ag content (~ 60% lower) and a larger $Ø_{avg,particle\ size}$ (100 nm vs 35 nm). Since the cytotoxicity effects increase

in the presence of higher AgNPs concentrations and smaller AgNPs sizes (at an equal mass)[38], we can deduce that the cytotoxicity level of the AgNPs-based ink used for the printing 3D microstructure printing will be even greater than the ink analyzed. The samples used were three replicas of 10 printed lines (line width ~ 400 µm, line length 1 cm, n = 40 layers), thermally sintered at 200°C for 1 h on a biocompatible electrospun porous polyacrylonitrile (PAN) substrate used as a neural scaffold[37]. Samples were first washed for 3 h in 1× PBS (Sigma Aldrich, IT), which was sterilized by autoclaving process, and disposed in a 24-well with a sterile tweezers. Cell culture on plastic dish was used as experimental positive control. A control h-iPSC line derived from commercial human fibroblast (HFs) cell line (BJ cell line ATCC® CRL-2522™) previously reprogrammed[39] to differentiate into NSCs[40]. Before cell seeding, Matrigel was coated on the substrates at 37°C for 1 h. Afterward, NSCs were enzymatically detached with accutase (Thermo Fisher Scientific) and passed through a 100-µm strainer in order to obtain a single-cell suspension that was collected and centrifuged at 1300 rpm for 4 min. The supernatant was removed and h-iPSCs-derived NSCs were seeded at a cellular density of 6×10^4 cells/cm^2 on the samples. A concentrated cell suspension was deposited onto each support and incubated for 20 min before filling each well with a proper volume of neural expansion medium. Cells were maintained at 37°C in a saturated humidity atmosphere containing 95% air and 5% CO_2. After 48 h, a direct rATP assay was performed to measure the quantity of viable cells by quantifying the adenosine triphosphate (ATP), typical marker for metabolic cellular activity. Cells were lysed on the samples using the CellTiter-Glo 3D Reagent and incubated at room temperature for 25 min in order to stabilize the luminescent signal. The total volume was transferred into a 96-well opaque-walled multiwell plate and the luminescence was recorded using a Tecan Infinite® M200 microplate reader (Tecan, Männedorf, Switzerland). Parallelly, an ATP standard curve (range of 10 µM–10 nM) was created using rATP disodium salt (Promega cat. P1132) to compare the samples luminescence to the standard ones in order to determine the correct ATP concentration. Hence, the ATP concentration recorded from each sample was calculated and plotted.

Immunofluorescence assays were also conducted on the AgNPs-based SI-AJ20X ink in order to detect cellular morphology (cellular cytoskeleton and nuclei). After being drop-casted on glass coverslips, the ink was thermally sintered, washed, and sterilized as previously described. HFs (BJ cell line) were cultured in a Dulbecco's Modified Eagle Medium (DMEM), supplemented with 10% fetal bovine serum (FBS), 1% penicillin/streptomycin, and 1% L-glutamine (all Euroclone), and maintained in an incubator. Later, HFs were seeded at a concentration of 2×10^4 cells/cm^2 onto the samples, incubated for 20 min and before filling the well with DMEM. Cells were then fixed at day 5 using the Fix&Perm Sample Kit® (SIC) for 30 min (fixation and permeabilization), and later incubated for 45 min with a blocking solution (iBind™ 5× Buffer, Invitrogen). Finally, samples were stained with phalloidin (Sigma Aldrich) and counterstained with Hoechst 33342 to mark cell cytoskeletal and nuclei, respectively. Samples mounted on a glass slide were then detected under a fluorescence inverted microscope (Olympus IX70) and analyzed with the Image-Pro Plus software v7.0 (Media Cybernetics).

2.4.2. PEDOT:PSS-based ink

Similarly to the AgNPs-based ink, cell biocompatibility assays were also carried out on the own-formulated PEDOT:PSS ink, being the one with the best results obtained in each print strategy. A direct rATP assay was performed on h-iPSCs-derived NSCs at 72 h as the protocol previously described for the AgNPs-based ink. Differently, the samples (three replicas) were printed squares (6 × 6 mm, n = 20 layers), thermally sintered at 150°C for 1 h on a biocompatible Au/Ti substrate, as a potential bioelectronic interface for cell monitoring. A concentrated suspension of 6×10^4 cells/cm^2 was cultured on the samples, and plastic was again used as positive control. In addition, immunofluorescence assays on the same printed squares were performed on HFs with the same procedure of the AgNPs-based ink.

2.4.3. Collagen-based ink

Cell viability assays on collagen-based inks were performed to evaluate their biocompatibility in the vision of their use for bone tissue engineering applications according to the protocol reported in Degryse *et al.*[41] A mouse calvaria preosteoblast cell line (MC3T3-E1) was expanded in T175 culture flasks in MEM alpha medium (Bioconcept), with the addition of 10% FBS (Gibco), 100 U mL^{-1} penicillin, and 100 µg mL^{-1} streptomycin at 37°C, 90% rH and 5% CO_2. Every 2 days, the medium was refreshed until a confluency of 80% was reached, then cells were trypsinized (TrypLE; Gibco) and subcultured. Collagen films for each ink composition (collagen, collagen-HAp) were prepared in triplicate by casting 250 µL in a 24-well plate, and drying the inks for 24 h under a chemical hood. A UV-light exposition (254 nm) for 1 h was used to sterilize the thin films, later washed in ethanol and 1× PBS solution. Eventually, MC3T3-E1 cells were seeded on the top of collagen films at a concentration of 1×10^4 cells per cm^2 (24-well plate). MC3T3-E1 were also seeded on 24-well plates at the same concentration (positive control). A Live-Dead staining (ThermoFisher Scientific) was performed at two time points (1 and 7 days) following the manufacturer's

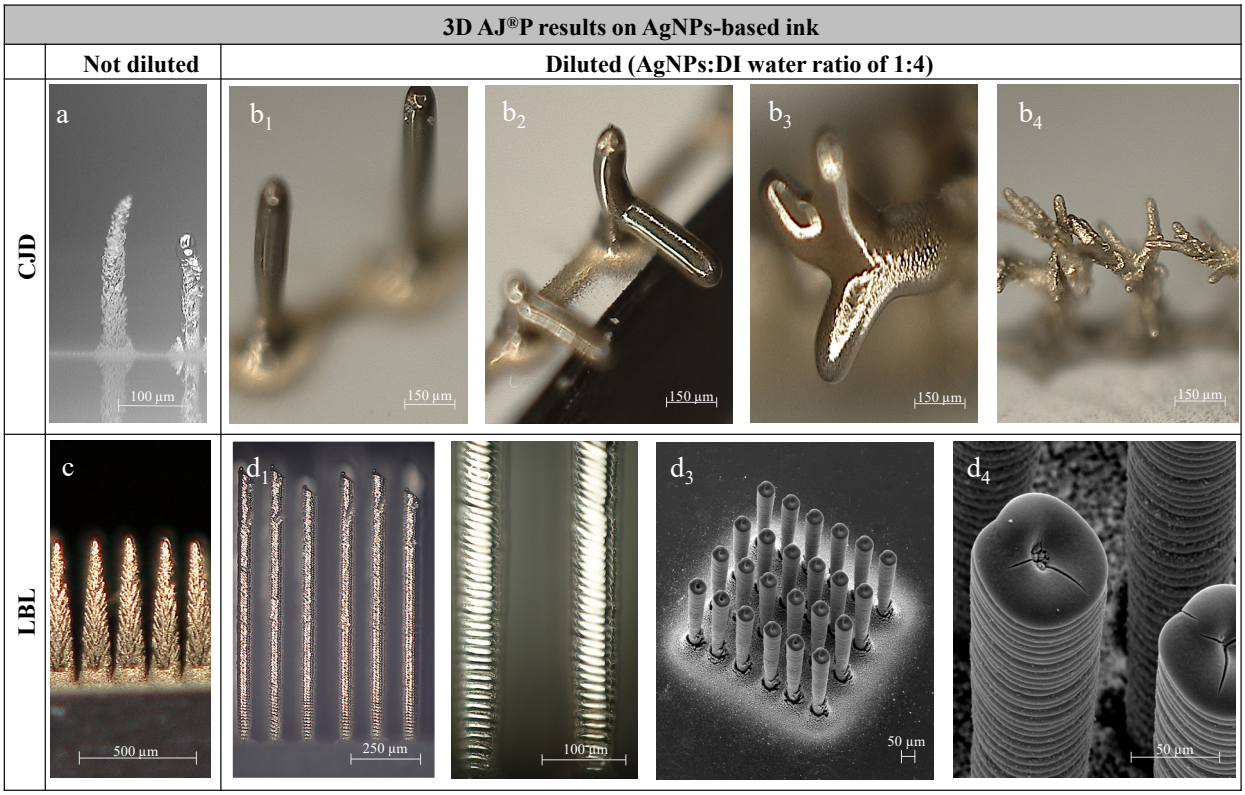

Figure 2. Results for the 3D AJ®P of microstructures for AgNPs-based ink, along with print strategy and ink dilution. (a) Nondiluted and (b_{1-4}) diluted 3D-CJD AgNPs-based ink; (c) nondiluted and (d_{1-4}) diluted 3D-LBL AgNPs-based ink.

protocol. Particularly, after medium removal, samples were washed twice with PBS and a staining solution (0.5 µL mL^{-1} calcein-AM and 2.0 µL mL^{-1} ethidium homodimer-1 [EthD-1] in PBS) was added to each well at a volume of 200 µL/well. After 30 min of incubation, fresh medium was used to replace the staining solution and cellular images were taken with a fluorescence microscope (Olympus). Live cells were distinguished by the presence of ubiquitous intracellular esterase activity, determined by the enzymatic conversion of the virtually nonfluorescent cell-permeant calcein-AM to the intensely fluorescent calcein. The polyanionic dye calcein was well retained within live cells, producing an intense, uniform green fluorescence in live cells. EthD-1 entered cells with damaged membranes and underwent a 40-fold enhancement of fluorescence upon binding to nucleic acids, thereby producing a bright red fluorescence in dead cells. EthD-1 was excluded by the intact plasma membrane of live cells.

3. Results

3.1. AgNPs-based ink

Figure 2 illustrates the results of AJ®P AgNPs-based inks. Nondiluted and diluted solutions were both investigated for 3D-CJD and 3D-LBL printing of microstructures according to the print parameters of Table 2. It is observed that nondiluted AgNPs-based ink generated dendritic-like structures with a rough surface. Instead, the diluted version gave rise to denser and smoother 3D printed structures. A certain degree of complexity is also achievable. Moreover, the 3D-LBL strategy is preferred over than 3D-CJD due to the higher degree of repeatability and control over printing.

With respect to the 3D-CJD strategy, Figure 2a shows a 3D-CJD dendritic-like pillar achieved with the nondiluted solution, which can also have a significant amount of overspray due to a dry printing. For this reason, printing was barely repeatable.

Figure 2b instead depicts 3D-CJD pillars or branches obtained using a diluted ink (AgNPs:DI water ratio of 1:4). In this case, vertically aligned pillars are approximately 590 ± 42 µm in height, with a base diameter of 92.95 ± 11.98 µm, a tip diameter of 54.64 ± 5.04 µm, and a 1<AR<12 based on the applied focusing ratio (R_f) . For instance, in Figure $2b_1$, pillars with an AR = 1.7 are obtained at R_f = 4, with a medium process reproducibility. With an increasing complexity printing approach, poly-branches (duo-, tri-, multibranch, Figures $2b_{2-4}$) were created from a mono-

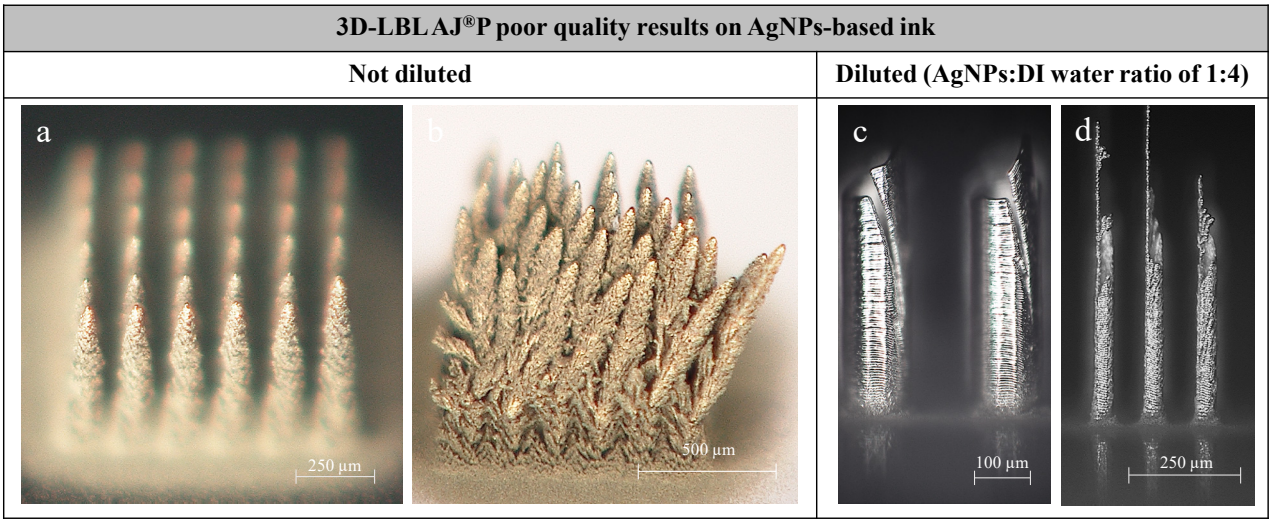

Figure 3. Results for poor-quality 3D AJ®P microstructures (6 × 4 array) for AgNPs-based ink using the 3D-LBL strategy. (a) Nondiluted and (c, d) diluted 3D-LBL AgNPs-based ink.

branch, which subsequently divided in multibranches (i.e., leaf-like structure) during the CJD printing (printing time < 3 s). However, the more branches it is, the more complex it is to reproduce them in the meaning that no control can be imposed on the direction of branch generation, resulting in similar, but not repeatable, structures.

Alternatively, Figure 2c and d show 3D microstructures achieved with a 3D-LBL strategy. All 3D-LBL micropillars were obtained when the platen temperature was increased from $T_{CJD, AgNPs}$ = 40°C to $T_{LBL, AgNPs}$ = 100°C, initiating an in-loco presintering process. Compared to 3D-CJD, a smaller nozzle $Ø_{LBL, AgNPs}$ = 100 µm, a higher $CGF_{LBL, AgNPs}$ = 18 sccm, a lower $R_{f,\ LBL, AgNPs}$ = 1.67 and a lower print speed, $s_{LBL, AgNPs}$ = 0.4 mm/sec, are selected to obtain the most controllable LBL jet deposition. Particularly, using the nondiluted AgNPs-based ink, frost/tree-like pillars (row of five pillars) with a diameter base of 110.39 ± 9.82 µm, a tip diameter of 18.99 ± 2.18 µm, and a height of 955.79 ± 15.17 µm, were obtained (Figure 2c, see **Videoclip S1**). These structures are easier to be reproduced compared to 3D-CJD multibranches; however, better defined and repeatable structures can be obtained when the ink is diluted (Figure 2d). In such condition, 3D-LBL rows (such as six pillars, Figures $2d_{1-2}$) or arrays (such as 6 × 4, Figures $2d_{3-4}$) of vertically aligned micropillars can be easily disposed. The average height is 960.42 ± 37.69 µm (equal to 50 printed layers), the diameter is 47.74 ± 5.62 µm (uniform along the *z*-axis), the AR is ca. 20 (Figure $2d_3$), and the printing time is ~ 5 min. In this case, optical and SEM images show that the printed pattern is clearly visible, with a growth rate of ~ 8 ± 1 µm/layer. Particular attention should be given to the tip of the pillars: if in general the tip is depicted as in Figure $2d_4$, that is plane and compact, it is possible that sometimes the tip can present a hollowed structure (inner diameter < 20 µm, Figure $2d_3$) or a mark-up on a left side (Figure $2d_1$). This discrepancy is caused by an unstable aerosol jet deposition rate along the printed layers, which may vary over time due to an intrinsic process variability caused by thermodynamic equilibrium changes of the aerosol along the printing subprocesses, especially in subprocess 1. AJ®P has indeed well-known variability/consistency issues and a quantitative analysis of the deposition rate change will be part of further studies. Eventually, a substantial overspray is also visible at the bottom of the printed pillars. Accordingly, it is recommended to maintain a minimum interpillars distance of 200 µm to avoid material overlap caused by the overspray.

Figure 3 instead illustrates poor quality results in the use of 3D-LBL AJ®P for AgNPs-based ink. This sequence of figures aims to demonstrate the importance to properly select the right combination of (non)-diluted ink, print parameter window, and CAD file. Figure 3a and b show frost-like structures obtained with the nondiluted ink. These highly porous structures (high overspray present onto the substrate) were obtained by dry printing a doubled CAD circle (Ø = 100 µm), a print nozzle three times higher than the previous one ($Ø_{LBL, AgNPs}$ = 300 µm), and a speed almost 17 times faster ($s_{LBL, AgNPs}$ = 7 mm/s). Moreover, by changing the $R_{f,\ LBL, AgNPs}$ from 2 to 4, that is $CGF_{LBL, AgNPs}$ = 20 sccm and $SGF_{LBL, AgNPs}$ from 40 (Figure 3a) to 80 sccm (Figure 3b), a drastic pillar overlapping is visible. This is due to the effect of the SGF, which deviates the aerosol jet impingement on the substrate, producing waved and overlapped frost-like

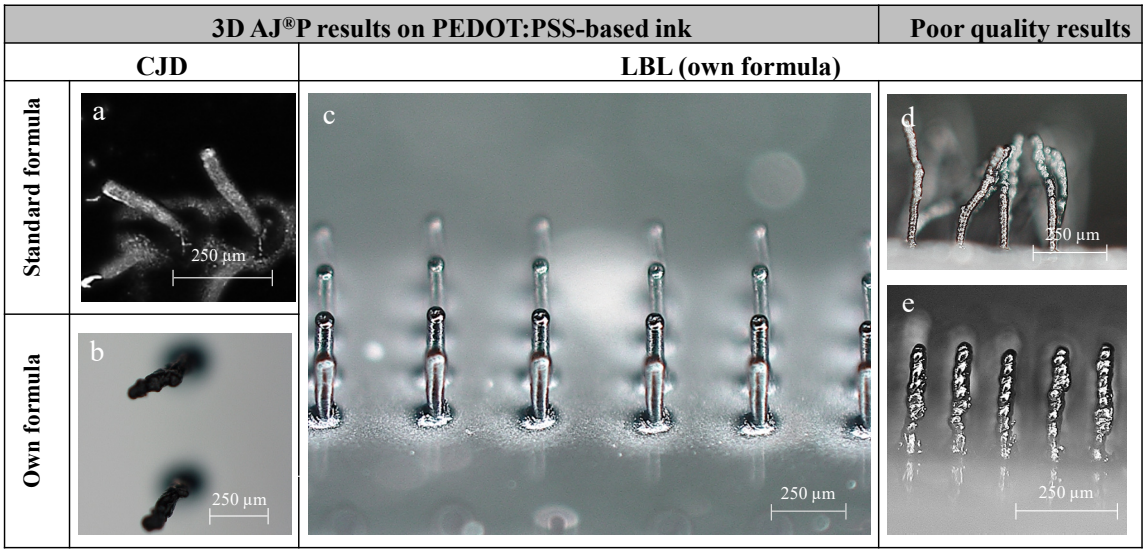

Figure 4. Results for the 3D AJ®P of microstructures for PEDOT:PSS-based ink, along with print strategy and characterization. (a) Standard formula and (b) own formula of 3D-CJD PEDOT:PSS-based ink; (c) own formula of 3D-LBL PEDOT:PSS-based ink. (d, e) Poor-quality results for 3D-LBL PEDOT:PSS-based ink own formula.

structures. Instead, Figure 3c and d highlight defected pillars printed with the diluted ink, which have fractures that increase in intensity and dimension as print layers increase. This result is caused by the use of a $s_{LBL,\ AgNPs}$ = 1 mm/s, that is 2.5 faster than the previous one, and it is visible both in the configuration with a doubled CAD circle (Ø = 100 µm, Figure 3c), and the previous one (Ø = 50 µm, Figure 3d).

3.2. PEDOT:PSS-based ink

The second type of ink explored is PEDOT:PSS-based. Table 2 summarizes the print parameters. As reported in Figure 4, only the own-formula combined with the adoption of the 3D-LBL technique was successfully printed in 3D structures. Figure 4a and b show the 3D-CJD AJ®P of micropillars bent more than 130 ° printed with both inks and at a low process reproducibility. Instead, Figure 3c shows an array of 3D-LBL AJ®-printed micropillars with a compact internal structure, with an average height of 256.25 ± 5.26 µm (50 layers), a diameter of 56.79 ± 4.79 µm, for a maximum AR = 4.5 (printing time ~ 5 min, see **Videoclip S2**). These structures were 3D-printed at the same print speed of the AgNPs-based diluted ink, but the achievable accuracy was lower. The possibility to obtain poly-branches was also rare, most likely due to a higher ink viscosity. Furthermore, the platen temperature was set at $T_{PEDOT:PSS}$ = 80°C, which is 20°C lower than the one used for the AgNPs-based ink, $T_{LBL,\ AgNPs}$ = 100°C, since lower ones did not allow the building up of 3D structures (as 3D-CJD), and higher ones produced thin pillars with a rough surface (Figure 4e), which was caused by a fast water evaporation, with the water content in the ink higher than in the AgNPs-based ink.

Figure 4d and e depict poor-quality results obtained by 3D-LBL of PEDOT:PSS-based ink. In particular, Figure 4d shows the printing of a set of five micropillars with a higher $R_{f,\ LBL,\ PEDOT:PSS}$ = 5 (instead of 2), by using a higher $SGF_{LBL,\ PEDOT:PSS}$ = 50 sccm (instead of 35 sccm) and a lower $CGF_{LBL,\ PEDOT:PSS}$ = 10 sccm (instead of 18 sccm). All the other parameters were kept the same. Similar to what was observed with the AgNPs-based ink, the effect of the SGF, which forces the bending of pillars and diverses the aerosol jet direction (especially at higher print layers), was significant. Moreover, since the CGF was almost half of the previous one, the diameter of pillars was reduced by ~ 47%, with an average diameter of 26.64 ± 4.92 µm. Furthermore, as previously anticipated, the change in the platen temperature can also have a significant effect: Figure 4e indeed illustrates the printing of 5 micropillars at $T_{LBL,\ PEDOT:PSS}$ = 100°C (instead of 80°C), with n = 25. From the image, it is clearly visible a rougher and more deformed surface than the set of pillars reported in Figure 4c, with an average pillars diameter equal to 39.13 ± 4.03 µm, that is ~ 30% thinner than the one printed at $T_{LBL,\ PEDOT:PSS}$ = 80°C. As previously observed with the AgNPs-based ink, also in the case of this PEDOT:PSS-based ink, only specific parameter conditions allow a repeatable and uniform 3D AJ®P. Further studies will analytically and systematically investigate this statement.

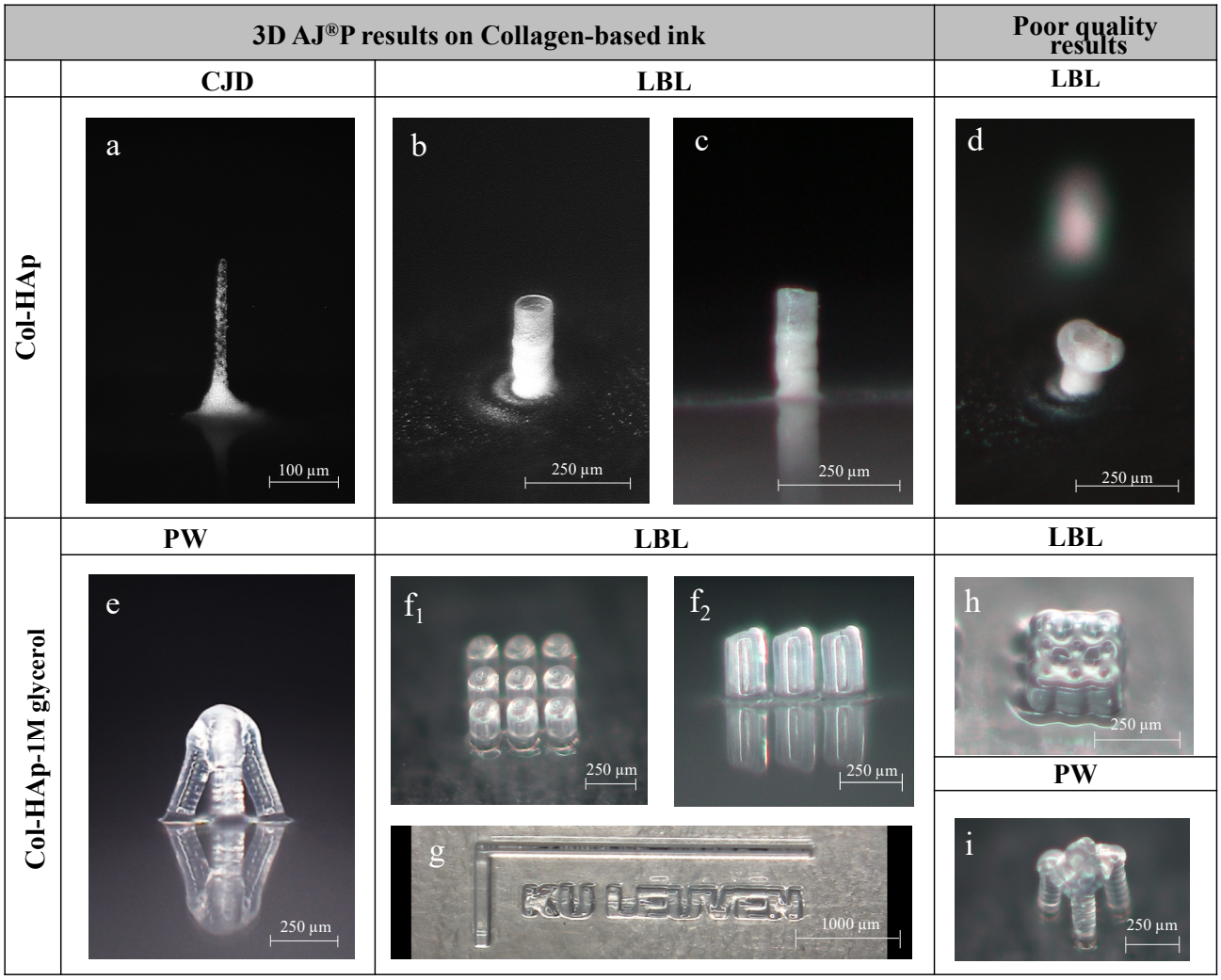

Figure 5. Results for the 3D AJ®P of microstructures for collagen-based inks, along with printing strategy and ink formulation; particularly, 3D AJ®P of Col-Hap ink for 3D-CJD (a) and 3D-LBL (b, c). (d) Poor-quality results for 3D-LBL Col-Hap ink. (e) 3D AJ®P of Col-Hap-1M glycerol ink for 3D-PW (Reproduced with permission[56], Copyright 2022, Elsevier), and ($f_{1,2}$, g)3D-LBL. Poor quality results for Col-Hap-1M glycerol ink, with 3D-LBL (h) and 3D-PW (i).

3.3. Collagen-based ink

The third type of ink assessed for their potential in 3D AJ® printing is collagen-based, and more specifically a Col-HAp ink with and without the addition of 1 M glycerol. Glycerol is often used to improve the thermal stability of proteins such as collagen. This has been observed in multiple studies, which implemented an increase in the denaturation temperature[42-48]. Nevertheless, as studied by Na *et al*., glycerol has the ability to prevent fibrillogenesis of collagen, which could prevent the collagen from gelating[48]. Table 2 reports the print parameters used. The bed temperature was kept at $T_{Collagen}$ = 30°C (<37°C) to prevent collagen denaturation during printing. As shown in Figure 5, both inks are nicely printable in 3D structures, but the addition of 1 M glycerol to the solvent mixture results in more complex prints. Again, the 3D-LBL strategy gives better results and higher reproducibility than the 3D-CJD one. Col-Hap ink can be 3D-CJD printed in the shape of dense and elongated microcones (AR ~ 3–19) (Figure 5a), with a height of ~ 220 µm, a width base of ~ 76 µm, a width tip of ~ 11 µm, and an average width of 16.52 ± 1.45 µm. Col-Hap can be also 3D-LBL-printed in shapes such as hollowed pillars with an AR = 2.4, a height of 213.43 ± 7.38 µm, and a width of 90.46 ± 8.59 µm (Figure 5b and c).

Figure 5d outlines poor-quality results using the 3D-LBL with the Col-Hap ink, which was caused by pooling of the ink (same set of print parameters). This can best be described as the accumulation of ink and the formation of

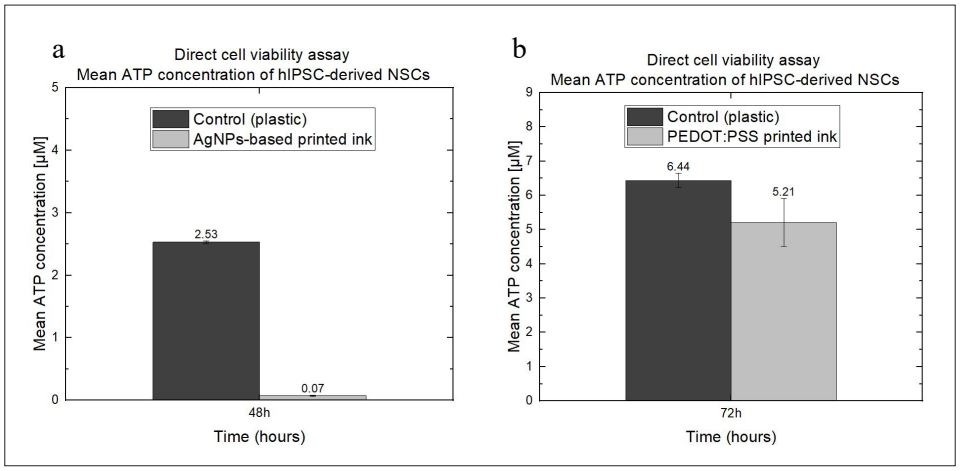

Figure 6. Biocompatibility assays. rATP relative concentration of h-iPSC-derived NSCs cultured on AJ® printed (a) AgNPs-based ink (time point 48 h) and (b) PEDOT:PSS-based ink (own formula, time point 72 h), with plastic as positive control.

large droplets, which results in unstable printing. This is a side effect that occurs after the condensation of the aerosol in the transportation tube[33]. A way to avoid it is to clean the tube after 2–3 h of continuous printing.

The printing of Col-Hap-1 M glycerol ink was performed using, firstly, the 3D-PW approach in the form of a pyramid-like structure to resemble a unit cell of a lattice structure (Figure 5e). The pyramid has a height of ± 400 µm (22.0 ± 0.5 µm layer height) and a width-based tip of 97.3 ± 3.9 µm (see **Videoclip S3**). Second, the ink was also 3D-LBL-printed as an array of 3 × 3 pillars and as the KU LEUVEN university logo. Figure 5f$_1$ and f$_2$ show the array of pillars, as top and side view, respectively (height of 223.28 ± 46.51 µm, diameter of 159.37 ± 2.98 µm, printing time ~ 5 min). Poor-quality results are reported in Figure 5h and i. The pillars in the array shown in Figure 5h are connected through capillary effects, whereby ink flows in between the pillars. Again, the accumulation of deposited ink into large droplets leads to instabilities in the deposition step. This can be clearly seen in Figure 5i where the tip of the pyramid is deformed by pooling of the ink.

3.4. *In vitro* biocompatibility assessment

3.4.1. AgNPs-based ink

Figure 6a reports the results of the direct rATP assay conducted on h-iPSC-derived NSCs at time point 48 h on a printed AgNPs-based ink. As expected, the AgNPs-based ink results in drastic high levels of cytotoxicity already at 48 h, showing no cellular survival (rATP values equal to zero). Therefore, no direct contact between NSCs cells and AgNPs-based ink is recommended. Similarly, fluorescence microscopy image of HFs on drop-casted AgNPs-based ink (Figure 7a and c) confirms that the ink is not biocompatible. In fact, HFs cultured on plastic dish as positive control tend to grow adherent on the surface, spreading their cytoskeletal with well-defined and linear edges, while HFs on AgNPs-based ink are less and with sharp-cornered shape, and are more related to an unhealthy state.

3.4.2. PEDOT:PSS-based ink

Figure 6b presents the direct rATP concentration (µM) of h-iPSC-derived NSCs when seeded on the printed PEDOT:PSS-based ink (own formula) and on plastic (positive control) at 72 h. Different from the AgNPs-based ink, the results revealed that the PEDOT:PSS chosen exhibits low cytotoxicity levels, with the rATP recorded only ~ 20% lower than that of the plastic. This discrepancy can be caused by a hydrophobic behavior of the ink, which induces low cellular adhesion. Immunofluorescent assays of HFs on printed samples (Figure 7b) indeed show a good and healthy cellular proliferation at day 5. Even if the confluence has not been reached yet as for the plastic control (Figure 7b), and the fibroblasts' shape is not in the typical elongated and spread morphology, these results are drastically better than the ones with the AgNPs-based ink. Further studies (indirect rATP assays) will be carried out to confirm the biocompatibility of the ink.

3.4.3. Collagen-based ink

Finally, Figure 8 shows the results of the Live-Dead™ staining performed of MC3T3-E1 (osteoblast precursor cell line) cultured on Col- and Col-Hap-based printed films. The immunofluorescence images show the majority of cells positive for the green staining, and the increase of their number till day 7. No appreciable percentage of red fluorescence and sign of dead cells was detected. These data demonstrate a good cell proliferation and viability. As expected, since collagen is the most abundant protein and HAp is the main component of the natural bone[49], MC3T3-E1 cells manifest the higher proliferation on the

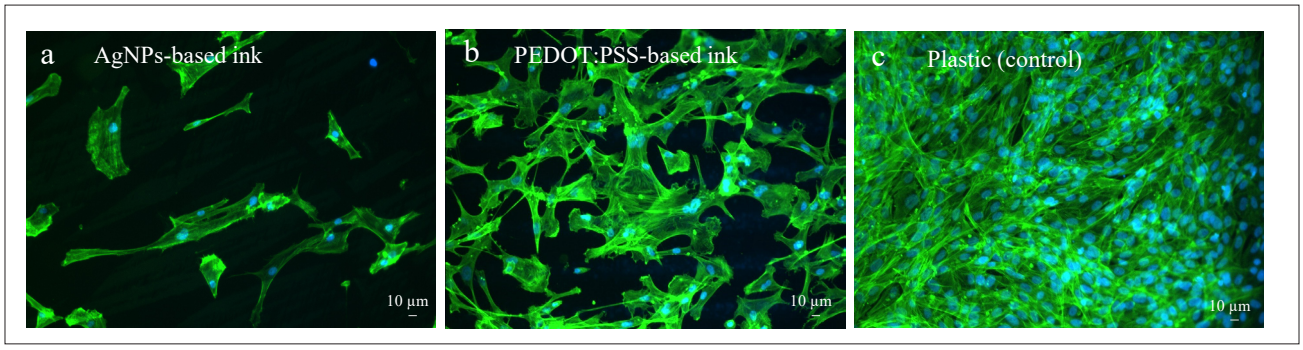

Figure 7. Fluorescence microscopy images of HFs at day 5 on (a) drop-casted AgNPs-based ink, (b) AJ® printed PEDOT:PSS-based ink, and (c) plastic as positive control (phalloidin in green, nuclei in blue).

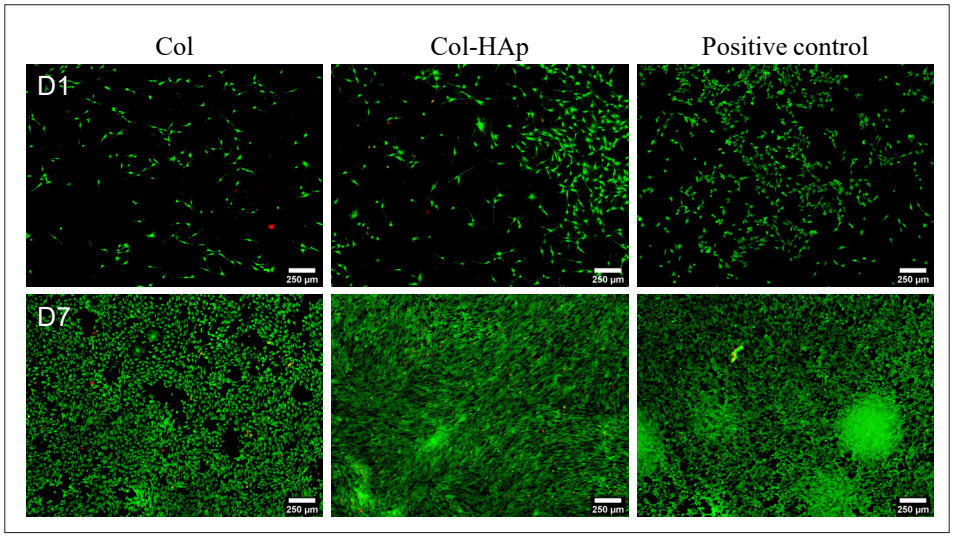

Figure 8. Live-dead assay of MC3T3 cells seeded onto AJ®-printed collagen-based thin films and positive control at days 1 and 7.

Col-HAp, reaching over confluent cellular layers already after 7 days.

4. Discussion

This paper covers the fabrication of 3D microstructures by means of the AJ®P technology, with focus on the effects of inks composition and print strategies. Table 3 gives a general overview of the results obtained in each scenario. Three functional inks among AgNPs-, PEDOT:PSS-, and collagen-based solutions were investigated according to different print strategies, that is, 3D CJD, LBL, and PW printing of structures with at least an AR = 1 and in a fast printing time (≤ 10 min). For all cases, the typical conditions for a satisfactory AJ®P deposition are defined as: (i) stable aerosol generation, (ii) optimal evaporation rate of the in-flight jet, and (iii) adequate ink-substrate interaction. Thus, the selection of the (co-)solvents system plays a fundamental role, which must balance high and low volatile solvents in order not to exceed a certain concentration margin (different from case to case), beyond which the printed ink becomes too wet (2D printing). Moreover, this selection must consider a trade-off between printability and potential biocompatibility needs, avoiding the use of toxic compounds.

Among the three inks, the 3D-LBL AgNPs-based ink demonstrated the best ability to print reproducible 3D microstructures (pillars) at the highest ARs and resolutions. This is caused by its high loading particle, which can be fine-tuned (through dilution) for 2D and 3D printing. In the case of 3D printing with the nondiluted solution, the solid particle content (~ 50 wt.%) is too high compared to the cosolvent concentration (≤ 20 v/v%), leading to a faster evaporation rate in the transport and in-flight jet, eventually causing the deposition of rough, dendritic-like structures. Instead, the dilution allowed the printing of a wetter aerosol, reducing the ink drying effect. AgNPs-based 3D microstructures can be applied in the PE fabrication of highly conductive, cost-effective, and customizable 3D passive and active elements for energy harvesting devices, batteries, (optoelectronic) sensors, and so on. However,

Table 3. Results for the 3D AJ®P of microstructures for each ink and print strategy investigated, along with the geometrical characterization, the process reproducibility, and the printing time

3D AJ®P Results							
Ink	**Print strategy**	**Height, *h* (μm)**	**Width base-tip, *w* (μm)**	**Aspect ratio, *AR* (#)**	**Internal structure**	**Process reproducibility**	**Printing time, *t* (s)**
Nondiluted AgNPs-based	CJD	~ 230	~ 30	7.6	Dendritic-like	Low	60
	LBL	955.8 ± 15.2	110.4 ± 9.8 18.9 ± 2.2	8 < AR < 50		High	60 < t < 300
Diluted AgNPs-based	CJD	590 ± 42 (pillar)	92.9 ± 11.9 54.6 ± 5.1	1< AR <12	Dense	Low	3
	LBL	960.4 ± 37.7	47.7 ± 5.6	20	Hollow	High	300 (for array 6 × 4)
PEDOT: PSS-std	CJD	~ 240	~ 35	6.8 (bended)	Dense	Low	30
PEDOT: PSS-own formula	CJD	~ 300	~ 70	4.3 (bended)		Low	15
	LBL	256.3 ± 5.3	56.8 ± 4.8	4.5		Medium	70
Col-HAp	CJD	~ 220	~ 76, ~ 11	~2.5	Dense	High	30
	LBL	213.4 ± 7.4	90.5 ± 8.6	~2.4	Hollow	High	60
Col-HAp-1 M glycerol	PW	±400 μm (22.0 ± 0.5 layer height)	97.3 ± 3.9	~4	Dense	Low	300
	LBL	223.3 ± 46.5	159.4 ± 2.9	~1.4	Hollow	High	300 (for array 6 × 4)

their use in life science applications must be wisely considered. AgNPs are known to induce cytotoxicity, mainly in a dose-, size-, shape-, and time-dependent way, due to the surface oxidation of AgNPs, which activates the release of Ag^+ ions in the medium culture, eventually leading to oxidative stress and cellular death[50-52]. As denoted by the rATP and immunofluorescence assays in the present study, the release of such Ag^+ ions from exposed AgNPs printed patterns indeed induced high levels of cytotoxicity on h-iPSC-derived NSCs and HFs. Hence, the use of 2D/3D AgNPs-based printed constructs is recommended only if they are properly coated at an adequate thickness with biocompatible, saline water-resistant, dielectric encapsulator. For example, the authors demonstrated the biocompatibility of electrical patches composed of AJ®-printed AgNPs-based circuits encapsulated in polydimethylsiloxane (PDMS) on both HFs and B-Lymphoblastoid cell lines till day 21[53].

In order to avoid this issue, in the context of life science, the use of biocompatible inks is preferable, such as PEDOT:PSS- and collagen-based inks. PEDOT:PSS shows good potential as bioconductive 3D AJ®P ink for multifunctional applications in the field of bioelectronics. Particularly, the addition of polyethylene glycol (PEG) and carboxymethyl cellulose (CMC) to the standard PEDOT:PSS formulation supported the build-up of well-defined 3D micropillars, due to their action as binders and loading contents. The own-formulated PEDOT:PSS-based ink also shows good levels of biocompatibility at 72 h when in contact with h-iPSC-derived NSCs, as reported by the rATP cytotoxicity assays. Therefore, this type of ink has potential to be used for 3D AJ®P microstructures for bioelectronic sensing or lab-on-a-chip devices.

Alternatively, collagen exhibits excellent biocompatibility with MC3T3 cells (Live-Dead™ assay till day 7), being the most abundant protein in mammals, especially in the bone tissue. Due to the presence of specific cellular recognition amino acid sequences, collagen indeed plays a crucial role in cellular processes, such as cell attachment and proliferation. For instance, collagen type I and II inks have recently been AJ®-printed to produce dense collagen films for applications in corneal tissue engineering[36]. However, printing of 3D structures is new to this respect. In order to mimic the composition of human bone tissue, HAp nanoparticles (<200 nm) were incorporated into the ink in a biomimetic ratio (1:2 Col:HAp ratio). As mentioned previously, the solid loading of the inks plays a crucial role in 3D printing using AJ®P. Hence, it was hypothesized that the addition of HAp nanoparticles could improve the 3D printing behavior of the collagen composite inks. The collagen-HAp ink allowed for the printing of hollowed pillars, but more complex structures could not be fabricated using this ink composition. Hence, the effect of adding glycerol was assessed, as it is believed that adding a solvent with low volatility could aid in the build-up of 3D structures. Indeed, the addition of glycerol allowed for the fabrication of more complex structures, such as the pyramid shown in Figure 5e. These pyramids could be used as unit-cells for more complex lattice structures. It should be noted, however,

that the addition of glycerol resulted in thicker walls for the hollow pillars, closing the central channel. Hence, adding glycerol improved the 3D printing capabilities, but reduced the printing resolution and accuracy. It is suggested that adding a solvent with low volatility, such as glycerol, aids in the build-up of material by keeping the ink hydrated. Moreover, as glycerol has a higher viscosity compared to the aqueous collagen solution, it ensures cohesion of the structure upon deposition, as the viscosity of the deposited droplets increases while drying out in the in-flight jet, resulting in a gel-like liquid being deposited. This combined effect of wetting the ink and increasing the viscosity while drying eventually leads to the printing of 3D structures.

Preliminary insights on the process window 3D AJ® printability have been also investigated for each ink, comparing good- and poor-quality results. For all cases, it is clear that a strict control over specific print parameters combinations is crucial to obtain the desired output, in terms of 3D AJ®P (no 2D deposition), reproducibility, and desired quality. Based on the authors' observations, the print nozzle is recommended to have a $Ø \leq 150$ µm in order to obtain high-resolution 3D microstructures. Larger nozzle diameters indeed favor a 2D AJ®P (increased mass flow rate) or less control over the in-flight jet and overspray. If necessary, it is suggested to use $R_f \geq 4$ and low *CGFs*. Moreover, any type of *in situ* presintering, -annealing, or -crosslinking while printing is suggested to initiate and have control over the building up of the structure. In this study, AgNPs- and PEDOT:PSS-based inks were thermally presintered and preannealed, respectively, with the thermal treatment chosen as postprinting process due to the possibility to change the platen T from room temperature to 200°C. Other postprocessing methods include plasma, laser, photonic, or microwave sintering[54]. Their selection and relative parameters are believed to affect the quality, dimension, and shape of the 3D microstructures. In this case, specifically in the 3D-LBL approach, AgNPs-based ink requires an ideal T = 100°C, while the PEDOT:PSS-based ink a T = 80°C. Since the two inks have water as main solvent, the *in situ* presintering process applied mainly affected the overall dimension and shape deformation of the printed structures. Hence, no further significant difference was detected after the postprinting thermal process. The specific value of temperature depends on the properties of the ink, especially particle mass loading and (co-)solvents boiling points. Trial tests are recommended to detect the most suitable T for the designated ink. Instead, in the case of Col-based inks (or similar), since the temperature must be kept at $T \leq 37$°C to avoid any degradation, it may be interesting to explore other methods, such as UV-crosslinking, to improve the printing quality and time. The two main gas flows, that is *CGF* and *SGF*, have the most significant impact on the output quality. For 3D AJ®P, the authors detected narrowed gas flow working windows, that is, $10 \leq CGF \leq 19$ and $30 \leq SGF \leq 40$ sccm, with a R_f in the range of 1.66–4. Specifically, at an equal *CGF* = (18–19) sccm, a relative higher *SGF* was necessary in Col-based inks (*SGF* = 40 sccm) and in the PEDOT:PSS-based ink (*SGF* = 35 sccm) than in the AgNPs-based ink (*SGF* = 30 sccm). The cause may the detected in the volatility of the ink co-solvent systems, which require higher *SGFs* in the presence of low volatile co-solvents, such as glycerol (normal boiling point, *NBP* = 290°C) or PEG (*NBP* = 250°C), while lower SGFs for high volatile ones or mixtures, such as DEG (*NBP* = 244°C) and IPA (*NBP* = 82.4°C) in the AgNPs-based ink. This hypothesis is based on the assumption that the aerosolized microdroplets are in the same size range of 1–5 µm and that the higher is the microdroplets weight and loading content, the lower is the *SGF* value. Further analyses to validate this statement are ongoing by means of phase Doppler anemometry (PDA) systems. With respect to the building-up of the microstructures. It is suggested to avoid values of *SGF* > 40 sccm for a stand-off distance z = 3 mm, in order to reduce any bending and diversion of the in-flight aerosol jet, which may result in a remarkable overspray. The maximum *ARs* ~ 20 were obtained with the AgNPs-based ink, which are 8 and 4.5 times higher than Col- and PEDOT:PSS-based inks, respectively. The AgNPs-based ink indeed contains a high particle loading content and volatile co-solvents, hence it is able to resist the SGF effect even at high *ARs* (no bending). This statement is strictly correlated to the R_f, CAD, and print speed used. CAD patterns and gas flows indeed directly influenced the s (mm/s). After screening investigations, the speed was chosen at s = 0.4 mm/s for 3D-LBL and at s = 0.1 mm/s for 3D-PW. Higher speeds induced the printing of porous structures with wide depositions of overspray, while lower ones provoked excessive deposition of materials over each step, with restraints on the building-up of uniform layers.

5. Conclusion and future perspectives

This paper focuses on the feasibility and validation of 3D printability with the AJP process. To summarize, the AJ®P technique is considered an enabling 3D printing technology to realize high AR 3D bio(electrical) microstructures. Three inks categories, that is, metal NPs-based (AgNPs), conductive polymers (PEDOT:PSS), and natural polymers (collagen), were printed and investigated with at least two of the three main print AJ®P strategies, i.e., CJD, LBL, and PW. The results indicate that an ideal 3D U-AJ®P ink should have: (i) standard U-AJ®P ink requirements, (ii) a solid (metal, polymeric, ceramic) loading content in the range of 10–25 wt.% and additional binders, (iii) a co-solvent

system comprising humectants for a balanced evaporation rate, and (iv) controlled print parameters, such as T, R_f, and s. Indeed, all inks investigated required a low $s \leq 0.4$ mm/s (at equal CAD patterns), a R_f in the range of 1.66–4, and a $T \geq 40$°C (except for Col-based inks due to degradation). the particle loaded ones a $T \geq 40$°C. From a print strategy perspective, 3D-CJD is recommended for stand-alone free-form complex structures, which do not require strict repeatability; a 3D-LBL strategy is preferred for vertically aligned, multilayered arrays ($AR_{AgNPs} \sim 20$, $AR_{PEDOT:PSS} \sim 4.5$, $AR_{Collagen} \sim 2.5$); and the 3D-PW approach is preferred for complex repeatable geometries, such as lattice units. The commercial diluted AgNPs-based ink showed the best results in terms of geometrical accuracy, repeatability, and ARs, mostly due to the nature of its particle loading content and co-solvents chosen. Still, the own formulated PEDOT:PSS- and the Col-based inks demonstrated good abilities at lower ARs, especially with the 3D-LBL and 3D-PW approach, respectively. Limitations of such inks are restricted to very complex CAD patterns, which probably require the choice of an instant (*in situ*) postprinting process (e.g., UV-curing). These conclusions are applicable for ink compositions similar to the ones proposed. For instance, other metallic NPs rather than Ag, such as Cu, Au, Pt[55], are AJ®-printable for 3D-printed electronics via an ultrasonic configuration, if a similar loading content, particle size and shape (spherical, Ø ~ 50 nm), and co-solvent system is used.

In general, the main 3D-AJ®P advantages compared to other AM techniques are: (i) inks versatility for various applications, (ii) noncontact, maskless printing with flexible working distance, (iii) 3D microstructuring down to 50 µm, (iv) fast 3D printing time (< 5 min for an array of 6 × 4 micropillars), (v) high reproducibility and ARs with the 3D-LBL approach, and (vi) complex structures with the PW approach. Instead, the disadvantages include: (i) limited portfolio of commercial optimized AJ®P inks, (ii) low reproducibility for CJD approach, (iii) necessity of an *in situ* and postprinting process on the green parts, and (iv) few commercial solutions. Due to a currently limited amount of AJ®P inks in the market (only addressed to PE), this study gives the basis to develop custom-made 3D AJ®P inks, and also prompts toward sustainability, biodegradability, and recyclability. Based on the ink chosen, 3D-printed microstructures can be potentially exploited for a vast range of prototypes in life science (tissue engineering, bioelectronic interfaces), electronics, and MEMS. Particularly, they may be used in the assembly step of the manufacturing process of (flexible) 3D-printed electronics, thermo-electrics devices, batteries, or microelectrode arrays, with special attention on the surface wettability. More considerations must be taken in life science applications, in which biocompatibility of the chosen ink (including particle loading content, cosolvents, additives) is a crucial factor to be considered with respect to the selected cellular lineage.

The performance of the microstructures, such as electro-chemical functionalities and mechanical characterizations, will be investigated in future application-driven works. Moreover, future studies will also be focused on a quantitative characterization of the process and materials, such as the significance of boiling temperature and vapor pressure over the resulting structure. For the collagen inks, a crosslinking approach will be studied, so as to improve the mechanical properties of the printed structures. Furthermore, the use of methacrylated collagen (ColMA) combined with UV-irradiation and other noble metal NPs-based inks will be assessed for 3D AJ®P.

Acknowledgments

The authors gratefully acknowledge the Research Foundation Flanders (FWO) for the doctoral fellowship granted to Miriam Seiti (1SB1120N) and Olivier Degryse (1S86620N). The authors also acknowledge the Angelo Nocivelli Foundation.

Funding

This work was supported by Research Foundation Flanders (FWO) for the doctoral fellowship granted to Miriam Seiti (1SB1120N) and Olivier Degryse (1S86620N).

Conflict of interest

The authors declare no conflict of interests.

Author contributions

Conceptualization: Eleonora Ferraris, Seiti Miriam, Olivier Degryse

Investigation: Seiti Miriam, Olivier Degryse (for the printing investigation); Rosalba Monica Ferraro, Olivier Degryse, Seiti Miriam (for the biocompatibility assays)

Methodology: Eleonora Ferraris, Seiti Miriam, Olivier Degryse

Formal analysis: Seiti Miriam, Olivier Degryse

Writing – original draft: Seiti Miriam

Writing – review & editing: All authors

Ethics approval and consent to participate

Not applicable.

Consent for publication

Not applicable.

Availability of data

Data are available by request to the authors.

Further disclosure

Parts of the findings have been presented in the international conference Additive Manufacturing for a Better World (SUTD, Singapore, August 23–25, 2022).

References

1. Xu J, Wang X, Wang C, et al., 2021, A review on micro/nanoforming to fabricate 3D metallic structures. *Adv Mater*, 33(6):2000893.

   https//doi.org/10.1002/adma.202000893

2. Vaezi M, Seitz H, Yang S, 2013, A review on 3D micro-additive manufacturing technologies. *Int J Adv Manuf Technol*, 67:1721–1754.

3. Yunas J, Mulyanti B, Hamidah I, et al., 2020, Polymer-based MEMS electromagnetic actuator for biomedical application: A review. *Polymer*, 12:1184.

   https://doi.org/10.1007/s00170-012-4605-2

4. Moitzheim S, Put B, Vereecken PM, 2019, Advances in 3D thin-film Li-ion batteries. *Adv Mater Interfaces*, 6(15):1900805.

   https//doi.org/10.1002/admi.201900805

5. Moitzheim S, Balder JE, Ritasalo R, et al., 2019, Toward 3D thin-film batteries: Optimal current-collector design and scalable fabrication of TiO2 thin-film electrodes. *ACS Appl Energy Mater*, 2(3):1774–1783.

   https//doi.org/10.1021/acsaem.8b01905

6. Kong T, Luo G, Zhao Y, et al., 2019, Bioinspired superwettability micro/nanoarchitectures: Fabrications and applications. *Adv Funct Mater*, 29(11):1808012.

   https//doi.org/10.1002/adfm.201808012

7. Penmatsa V, Kim T, Beidaghi M, et al., 2012, Three-dimensional graphene nanosheet encrusted carbon micropillar arrays for electrochemical sensing. *Nanoscale*, 4(12):3673–3678.

   https//doi.org/10.1039/c2nr30161j

8. Lao Z, Xia N, Wang S, et al., 2021, Tethered and untethered 3D microactuators fabricated by two-photon polymerization: A review. *Micromachines*, 12(4):465.

   https//doi.org/10.3390/mi12040465

9. Qian Y, Magginetti DJ, Jeon S, et al., 2020, Heterogeneous optoelectronic characteristics of Si micropillar arrays fabricated by metal-assisted chemical etching. *Sci Rep*, 10(1):1–10.

   https//doi.org/10.1038/s41598-020-73445-x

10. Park YG, Min H, Kim H, et al., 2019, Three-dimensional, high-resolution printing of carbon nanotube/liquid metal composites with mechanical and electrical reinforcement. *Nano Lett*, 19(8):4866–4872.

    https//doi.org/10.1021/acs.nanolett.9b00150

11. Lejeune M, Chartier T, Dossou-Yovo C, et al., 2009, Ink-jet printing of ceramic micro-pillar arrays. *J Eur Ceram Soc*, 29(5):905–911.

    https//doi.org/10.1016/j.jeurceramsoc.2008.07.040

12. Jannah F, Kim JH, Lee JW, et al., 2018, Immobilized polydiacetylene lipid vesicles on polydimethylsiloxane micropillars as a surfactin-based label-free bacterial sensor platform. *Front Mater*, 5:57.

    https//doi.org/10.3389/fmats.2018.00057

13. Cutarelli A, Ghio S, Zasso J, et al., 2020, Vertically-aligned functionalized silicon micropillars for 3D culture of human pluripotent stem cell-derived cortical progenitors. *Cells*, 9(1):88.

    https//doi.org/10.3390/cells9010088

14. Wang X, Yu H, Yang T, et al., 2021, Density regulation and localization of cell clusters by self-assembled femtosecond-laser-fabricated micropillar arrays. *ACS Appl Mater Interfaces*, 13(49):58261–58269.

    https//doi.org/10.1021/acsami.1c13818

15. Fan S, Qi L, Li J, et al., 2021, Guiding the patterned growth of neuronal axons and dendrites using anisotropic micropillar scaffolds. *Adv Healthc Mater*, 10(12):2100094.

    https//doi.org/10.1002/adhm.202100094

16. Palankar R, Glaubitz M, Martens U, et al., 2016, 3D micropillars guide the mechanobiology of human induced pluripotent stem cell-derived cardiomyocytes. *Adv Healthc Mater*, 5(3):335–341.

    https//doi.org/10.1002/adhm.201500740

17. Klein F, Richter B, Striebel T, et al., 2011, Two-component polymer scaffolds for controlled three-dimensional cell culture. *Adv Mater*, 23(11):1341–1345.

    https//doi.org/10.1002/adma.201004060

18. Liu Y, McGuire AF, Lou HY, et al., 2018, Soft conductive micropillar electrode arrays for biologically relevant electrophysiological recording. *Proc Natl Acad Sci U S A*, 115(46):11718–11723.

    https//doi.org/10.1073/pnas.1810827115

19. Yadav A, Verma N, 2019, Efficient hydrogen production using Ni-graphene oxide-dispersed laser-engraved 3D carbon micropillars as electrodes for microbial electrolytic cell. *Renew Energy*, 138:628–638.

    https//doi.org/10.1016/j.renene.2019.01.100

20. Goh GL, Zhang H, Chong TH, et al., 2021, 3D printing of multilayered and multimaterial electronics: A review. *Adv Electron Mater*, 7(10):2100445.

https//doi.org/10.1002/aelm.202100445

21. Tan HW, Choong YYC, Kuo CN, et al., 2022, 3D printed electronics: Processes, materials and future trends. *Prog Mater Sci*, 127:100945.

https//doi.org/10.1016/j.pmatsci.2022.100945

22. Cooper C, Hughes B, 2020, Aerosol jet printing of electronics: An enabling technology for wearable devices. *Pan Pac Microelectron Symp*, 1–11.

https//doi.org/10.23919/PanPacific48324.2020.9059444

23. Machiels J, Verma A, Appeltans R, et al., 2021, Printed electronics (PE) as an enabling technology to realize flexible mass customized smart applications. *Proc CIRP*, 96:115–120.

https//doi.org/10.1016/j.procir.2021.01.062

24. Goh GL, Dikshit V, Koneru R, et al., 2022, Fabrication of design-optimized multifunctional safety cage with conformal circuits for drone using hybrid 3D printing technology. *Int J Adv Manuf Technol*, 120(3–4):2573–2586.

https//doi.org/10.1007/s00170-022-08831-y

25. Paulsen JA, Renn M, Christenson K, et al., 2012, Printing conformal electronics on 3D structures with aerosol jet technology, in *Future of Instrumentation International Workshop (FIIW) Proceedings,* IEEE, 1–4.

https//doi.org/10.1109/FIIW.2012.6378343

26. Seiti M, Ginestra PS, Ferraro RM, et al., 2022, Aerosol Jet® printing of poly(3,4-ethylenedioxythiophene): Poly(styrenesulfonate) onto micropatterned substrates for neural cells in vitro stimulation. *Int J Bioprint*, 8(1):504.

https//doi.org/10.18063/ijb.v8i1.504

27. Williams NX, Watson N, Joh DY, et al., 2020, Aerosol jet printing of biological inks by ultrasonic delivery. *Biofabrication*, 12(2):025004.

https//doi.org/10.1088/1758-5090/ab5cf5

28. Saleh MS, Hu C, Panat R, 2017, Three-dimensional microarchitected materials and devices using nanoparticle assembly by pointwise spatial printing. *Sci Adv*, 3(3):e1601986.

https//doi.org/10.1126/sciadv.1601986

29. Zips S, Grob L, Rinklin P, et al., 2019, Fully printed µ-needle electrode array from conductive polymer ink for bioelectronic applications. *ACS Appl Mater Interfaces*, 11(36):32778–32786.

https//doi.org/10.1021/acsami.9b11774

30. Hohnholz A, Obata K, Nakajima Y, et al., 2019, Hybrid UV laser direct writing of UV-curable PDMS thin film using aerosol jet printing. *Appl Phys A Mater Sci Process*, 125(2):1–6.

https//doi.org/10.1007/s00339-018-1902-0

31. Di Novo NG, Cantù E, Tonello S, et al., 2019, Support-material-free microfluidics on an electrochemical sensors platform by aerosol jet printing. *Sensors*, 19(8).

https//doi.org/10.3390/s19081842

32. Vlnieska V, Gilshtein E, Kunka D, et al., 2022, Aerosol jet printing of 3D pillar arrays from photopolymer ink. *Polymers*, 14(16):3411.

https//doi.org/10.3390/polym14163411

33. Secor EB, 2018, Principles of aerosol jet printing. *Flex Print Electron*, 3(3).

https//doi.org/10.1088/2058-8585/aace28

34. Wilkinson NJ, Smith MAA, Kay RW, et al., 2019, A review of aerosol jet printing—A non-traditional hybrid process for micro-manufacturing. *Int J Adv Manuf Technol*, 1–21.

https//doi.org/10.1007/s00170-019-03438-2

35. Williams BA, Trejo ND, Wu A, et al., 2017, Copper–zinc–tin–sulfide thin films via annealing of ultrasonic spray deposited nanocrystal coatings. *ACS Appl Mater Interfaces*, 9(22):18865–18871.

https//doi.org/10.1021/acsami.7b04414

36. Gibney R, Ferraris E, 2021, Bioprinting of collagen type I and II via aerosol jet printing for the replication of dense collagenous tissues. *Front Bioeng Biotechnol*, 9:1–12.

https//doi.org/10.3389/fbioe.2021.786945

37. Seiti M, Ginestra P, Ferraro RM, et al., 2020, Nebulized jet-based printing of bio-electrical scaffolds for neural tissue engineering: A feasibility study. *Biofabrication*, 12(2):025024.

https//doi.org/10.1088/1758-5090/ab71e0

38. Johnston HJ, Hutchison G, Christensen FM, et al., 2010, A review of the in vivo and in vitro toxicity of silver and gold particulates: Particle attributes and biological mechanisms responsible for the observed toxicity. *Crit Rev Toxicol*, 40(4):328–346.

https//doi.org/10.3109/10408440903453074

39. Ali E, Ferraro RM, Lanzi G, et al., 2020, Generation of induced pluripotent stem cell (iPSC) lines from a Joubert syndrome patient with compound heterozygous mutations in C5orf42 gene. *Stem Cell Res*, 49:102007.

https//doi.org/10.1016/j.scr.2020.102007

40. Ferraro RM, Ginestra PS, Giliani S, et al., 2020, Carbonization of polymer precursors substrates to direct human iPSC-derived neurons differentiation and maturation. *Proc CIRP*, 39–44.

https//doi.org/10.1016/j.procir.2020.05.116

41. Degryse O, Bloemen V, Ferraris E, 2022, Collagen composite inks for Aerosol Jet® printing in bone tissue engineering applications. *Proc CIRP*, 110(C):180–185.

https//doi.org/10.1016/j.procir.2022.06.033

42. Hart GJ, Russell AE, Cooper DR, 1971, The effects of certain glycols, substituted glycols and related organic solvents on the thermal stability of soluble collagen. *Biochem J*, 125(2):599–604.

https//doi.org/10.1042/bj1250599

43. Penkova R, Goshev I, Gorinstein S, et al., 1999, Stabilizing effect of glycerol on collagen type I isolated from different species. *Food Chem*, 66(4):483–487.

https//doi.org/10.1016/S0308-8146(99)00097-7

44. Usha R, Ramasami T, 2008, Role of solvents in stability of collagen. *J Therm Anal Calorim*, 93(2):541–545.

https//doi.org/10.1007/s10973-006-7887-5

45. Li J, Li G, 2011, The thermal behavior of collagen in solution: Effect of glycerol and 2-propanol. *Int J Biol Macromol*, 48(2):364–368.

https//doi.org/10.1016/j.ijbiomac.2010.12.013

46. Ronsin O, Caroli C, Baumberger T, 2017, Preferential hydration fully controls the renaturation dynamics of collagen in water-glycerol solvents. *Eur Phys J E*, 40(5):1–5.

https//doi.org/10.1140/epje/i2017-11545-1

47. Vagenende V, Yap MGS, Trout BL, 2009, Mechanisms of protein stabilization and prevention of protein aggregation by glycerol. *Biochemistry*, 48(46):11084–11096.

https//doi.org/10.1021/bi900649t

48. Na GC, Butz LJ, Bailey DG, et al., 1986, In vitro collagen fibril assembly in glycerol solution: Evidence for a helical cooperative mechanism involving microfibrils. *Biochemistry*, 25(5):958–966.

https//doi.org/ 10.1021/bi00353a003

49. Yu L, Rowe DW, Perera IP, et al., 2020, Intrafibrillar mineralized collagen-hydroxyapatite-based scaffolds for bone regeneration. *ACS Appl Mater Interfaces*, 12(16):18235–18249.

https//doi.org/10.1021/acsami.0c00275

50. Pongrac IM, Ahmed LB, Mlinarić H, et al., 2018, Surface coating affects uptake of silver nanoparticles in neural stem cells. *J Trace Elem Med Biol*, 50:684–692.

https//doi.org/10.1016/j.jtemb.2017.12.003

51. Zhang XF, Liu ZG, Shen W, et al., 2016, Silver nanoparticles: Synthesis, characterization, properties, applications, and therapeutic approaches. *Int J Mol Sci*, 17(9):1534.

https//doi.org/10.3390/ijms17091534

52. McShan D, Ray PC, Yu H, 2014, Molecular toxicity mechanism of nanosilver. *J Food Drug Anal*, 22(1):116–127.

https//doi.org/10.1016/j.jfda.2014.01.010

53. Ferraro RM, Seiti M, Ginestra PS, et al., 2022, Biocompatibility evaluation of encapsulated silver-based printed circuits for in-vitro long-term sensing devices. *Proc CIRP*, 110(C):99–104.

https//doi.org/10.1016/j.procir.2022.06.020.

54. Renn MJ, Schrandt M, Renn J, et al., 2017, Localized laser sintering of metal nanoparticle inks printed with Aerosol Jet® technology for flexible electronics. *J Microelectron Electron Packag*, 14:132–139.

https//doi.org/10.4071/imaps.521797

55. Wei Tan H, An J, Kai Chua C, et al., 2019, Metallic nanoparticle inks for 3D printing of electronics. *Adv Electron Mater*, 5(5):1800831.

https//doi.org/10.1002/aelm.201800831

56. Seiti M, Degryse O, Ferraris E, 2022, Aerosol Jet® printing 3D capabilities for metal and polymeric inks. *Mater Today Proc*, 70:38–44.

https//doi.org/10.1016/j.matpr.2022.08.488

ACCSCIENCE PUBLISHING

International Journal of Bioprinting

REVIEW ARTICLE

Organoid bioprinting strategy and application in biomedicine: A review

Chen He[1], Jiasheng Yan[2], Yusheng Fu[1], Jiuchuan Guo[1], Yuxing Shi[1], and Jinhong Guo[1,2]*

[1]School of Information and Communication Engineering, University of Electronic Science and Technology of China, Chengdu, China

[2]School of Sensing Science and Engineering, Shanghai Jiao Tong University, Shanghai, China

(This article belongs to the *Special Issue: Bioprinting Tissues for Disease Modeling, Drug Development and Drug Testing*)

Abstract

Organoids are three-dimensional cell structures cultured *in vitro*. They are self-organizing and can mimic real organs in structure and function. Bioprinting technology breaks through some limitations of organoid manufacturing, making it more widely used in drug screening, regenerative medicine, and other fields. In this review, we first introduce bioinks and bioprinting methods for stem cell and organoid bioprinting, then summarize several vascularization strategies for bioprinting organoids, and present applications in biomedicine. In the future, the development of microfluidic technology and four-dimensional bioprinting technology may be conducive to forming better bioprinted organoids.

Keywords: Bioprinting; Organoid; Tissue engineering

***Corresponding author:**
Jinhong Guo
(guojinhong@sjtu.edu.cn)

Citation: He C, Yan J, Fu Y, *et al*., 2023, Organoid bioprinting strategy and application in biomedicine: A review. *Int J Bioprint*, 9(6): 0112. https://doi.org/10.36922/ijb.0112

Received: April 3, 2023
Accepted: May 16, 2023
Published Online: June 30, 2023

Copyright: © 2023 Author(s). This is an Open Access article distributed under the terms of the Creative Commons Attribution License, permitting distribution, and reproduction in any medium, provided the original work is properly cited.

Publisher's Note: AccScience Publishing remains neutral with regard to jurisdictional claims in published maps and institutional affiliations.

1. Introduction

Organoids are defined as collections of organ-specific cells. These cells are cultured through *in vitro* three-dimensional (3D) culture systems, self-organized through cell sorting and spatially constrained cell lineage differentiation, and exhibit a high degree of structural and functional similarity to *in vivo* tissues or organs[1]. According to different cell sources, organoids can be divided into tissue-derived organoids and pluripotent stem cell (PSC)-derived organoids. Tissue-derived organoids are composed of tissue-derived cells (TDCs), which include normal stem/progenitor cells, differentiated cells, and cancer cells. These TDCs are typically obtained from biopsy samples of tissue and organs from humans or animals. On the other hand, PSC-derived organoids are generated from PSCs, such as embryonic stem cells (ESCs) or induced pluripotent stem cells (iPSCs)[2,3].

In 2009, Sato *et al.* successfully cultivated the first 3D organoid using mouse intestinal stem cells (ISCs). They cultured intestinal organoids with crypt-villus by planting mouse intestinal adult stem cells into matrix glue *in vitro*, using a serum-free medium supplemented with three growth factors: R-spondin1, EGF, and Noggin[4]. Since then, the field of organoids has developed rapidly. At present, many types of organoids have been successfully constructed, including heart[5,6], kidney[7], liver[8], brain[9], and tumor[10] organoids.

Organoids are widely used in disease modeling, drug development, and personalized treatment because their self-organizing characteristics are similar to biological intrinsic processes, enabling the simulation of the formation process and physiological and pathological state of organ tissues. Since 2020, significant research progress has been made in applying organoids to COVID-19 disease modeling[11,12]. To research how colon and alveolar cells react to SARS-CoV-2 infection, Han *et al.* created human pluripotent stem cell (HPSC)-derived lung organoids (hPSC-LOs) and colon organoids (hPSC-COs). By high-throughput screening of pharmaceuticals that have received FDA approval, they also discovered three medications with antiviral effectiveness against SARS-CoV-2[12].

In order to give full play to the potential of organoid technology, the problems in organoid manufacturing must be solved. The culture method of organoids mainly relies on the traditional 3D culture technology, which utilizes the self-organizing properties of stem cells. However, it has many limitations, such as lack of repeatability, limited size, lack of vascular system, and communication between immune cells and organs[13]. Due to the above-mentioned limitations, 3D bioprinting technology is currently applied to organoid cultivation, replacing manual organoid construction for growing more complex large organoids.

3D bioprinting is derived from 3D printing (also known as additive manufacturing [AM]). Unlike 3D printing, which uses adhesive materials such as powdered metal or plastic, 3D bioprinting uses bioinks as printing materials that are deposited layer by layer spatially to create a tissue-like growth structure. The application of bioprinting technology in organoid manufacturing can control the composition and distribution of bioinks more accurately compared with manual construction; hence, it is expected to realize the stable construction of organoids with high precision, high throughput, and batch automation. In 2021, Lawlor *et al.* used extrusion bioprinting to successfully generate self-organizing kidney organoids with high cell number and viability reproducibility. The produced organs were comparable to manually engineered kidney organoids in terms of morphology, component cell types, and gene expression levels, demonstrating the feasibility of replacing manual organoid engineering with bioprinting methods. In addition, 3D bioprinting can also change the biophysical characteristics of organoids, including volume size, number of cells, and conformational configuration, which has excellent advantages[14].

At present, 3D bioprinting technology is mainly used for bioprinting stem cells for the construction of organoids and then promoting the differentiation of stem cells through growth factors and small molecules, as well as mechanical signaling pathways of extracellular matrix (ECM) materials. Bioprinting of organoids with complex structures remains a challenge[15].

This paper reviews the recent progress and application of bioprinting organoids. Firstly, the bioink and bioprinting methods used in bioprinted organoids are introduced. Secondly, the vascularization strategies of bioprinted organoids are summarized and analyzed in view of the insufficient vascularization of traditional organoids. Then, the applications of bioprinted organoids in drug screening, regenerative medicine, and tumor research are introduced. At the same time, the application of microfluidic technology and more advanced bioprinting methods to solve the defects of existing bioprinting organoids is discussed. Finally, the article concludes with a summary and a look into the possible future directions of developing bioprinting organoid technology (Figure 1).

2. Organoid bioprinting

The selection of bioink and printing methods is critical to realizing organoid bioprinting. Bioink is the necessary condition for the success of organoid bioprinting. A suitable printing method can better play the characteristics of bioink and get a better printing effect. Here, we introduce currently used bioinks and printing methods.

2.1. Bioink for organoid bioprinting

The printing materials used in 3D bioprinting are known as bioinks, and their properties are typically determined by three metrics: printability, biocompatibility, and mechanical properties. Printability refers to the forming characteristics of bioink, which is related to many factors, such as the viscosity of the material and printing parameters. The bioink with good formability shows good flow during printing and can be cured quickly after printing. Biocompatibility requires that the bioinks have an environment similar to the ECM *in vivo*, facilitating the development and communication of cells after printing. Mechanical properties require the bioink to have sufficient strength to support the subsequent culture process[16]. In addition, bioinks for stem cell and organoid bioprinting need to be biodegradable and cell nontoxic. The selection of the most appropriate bioink in bioprinting is usually considered in combination with the specific target tissue, cell type, and bioprinting method[17].

The main components of bioink are cells and biological materials. Hydrogels are 3D network structure gels composed of hydrophilic polymers through crosslinking, which can highly simulate a natural ECM environment *in vitro*. They are the most widely used bioink materials. Hydrogel bioinks usually comprise natural polymers, synthetic polymers, and decellularized extracellular

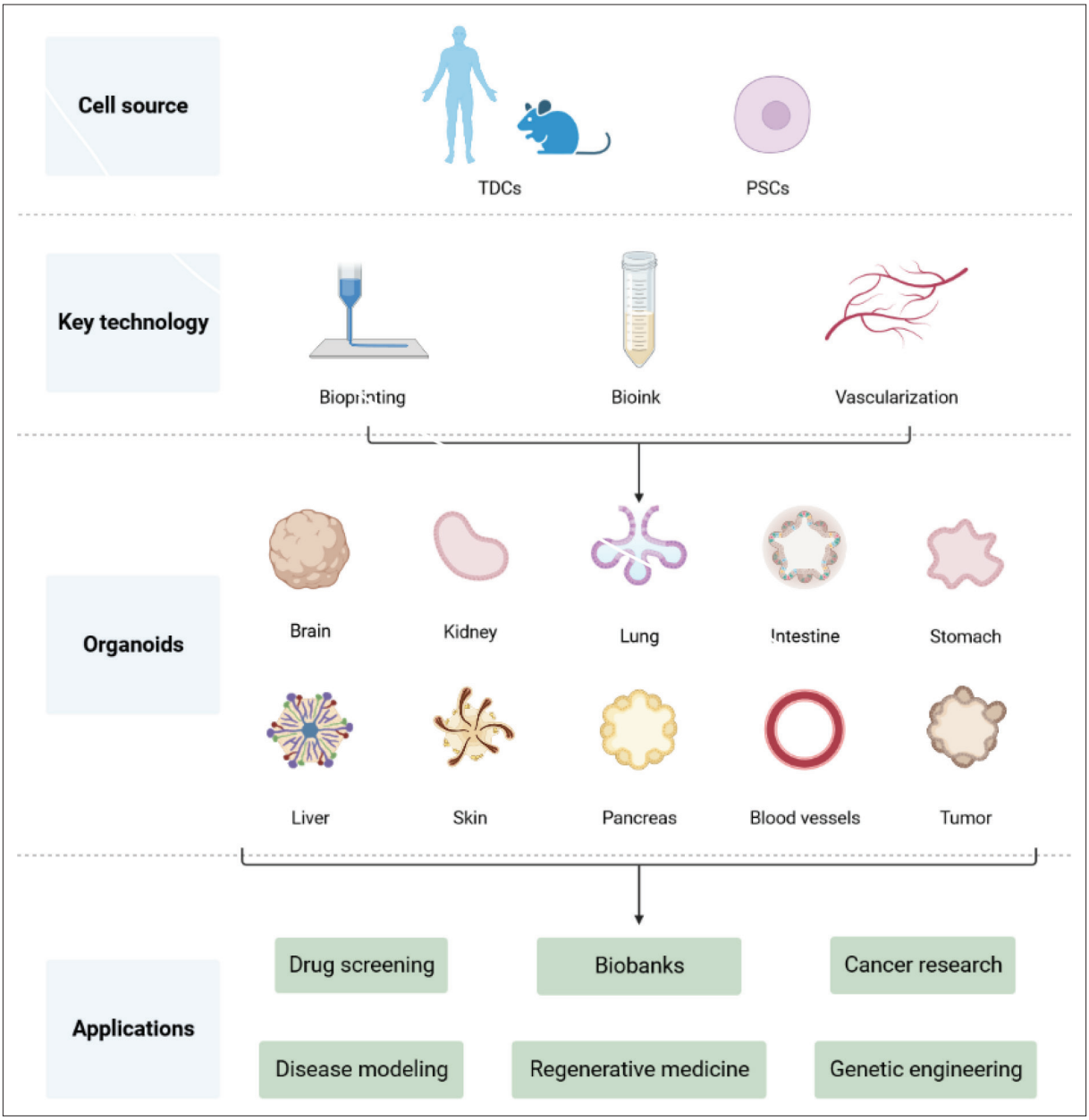

Figure 1. Key technologies and typical applications of bioprinted organoids. Organoids can be realized through bioink, bioprinting methods, and vascularization strategies. Applications of bioprinted organoids include but are not limited to drug screening, biobank, cancer research, disease modeling, regenerative medicine, genetic engineering, etc. Created using BioRender.com.

matrix (dECM)[17]. Natural bioinks include alginate, gelatin, fibrin, collagen, and hyaluronic acid (HA). Synthetic bioinks include polyethylene glycol (PEG), Pluronic, and other types (Table 1).

Natural bioinks have good biocompatibility but generally have problems such as poor printability, which could be less conducive to printing complex tissue structures. Synthetic bioinks provide good printability but poor biocompatibility and may produce toxic degradations[15]. By improving bioink characteristics, using compound bioink, or developing new bioink materials, bioink performance can be effectively improved.

Oxidative reactions have demonstrated controlled degradation of alginate. Jia *et al.* explored the application of oxide-alginate in bioprinting[36]. They used hADSCs/oxide-alginate as bioinks for bioprinting through a piston-driven deposition system. The results show that oxidized alginate bioinks with a specific density and viscosity can maintain

Table 1. Comparison of properties of bioinks for stem cell bioprinting

Type	Bioink	Benefits	Drawbacks	Bioprinting cell types	Reference
Polysaccharides	Alginate	Fast gelation, low cost, good stability	Limited biodegradation	Human iPSCs, human neural stem cells	[18,19]
Polysaccharides	HA	Good rheology, high viscosity	Poor stability, poor mechanical properties	Adipose-derived stem cells, iPSCs	[20,21]
Protein-based	Gelatin	Good biodegradability, low antigenicity, easy to process	Inherent low viscosity, poor mechanical properties	Human adipose tissue-derived stem cells (hASCs), umbilical cord-derived mesenchymal stem cells, and endothelial cells	[22,23]
Protein-based	Silk fibroin	Good mechanical properties, high elasticity	Poor printability	Human inferior turbinate tissue-derived mesenchymal stem cells (hTMSCs), bone marrow mesenchymal stem cells	[24,25]
Protein-based	Fibrin	Promotes angiogenesis and induces cell attachment and proliferation	Poor mechanical properties	Human dental pulp stem cells (hDPSCs), human amniotic fluid stem cells	[26-28]
Protein-based	Collagen	Rich in RGD sequences, promoting cell attachment	Slow gel rate, poor mechanical properties	hASCs, rat bone marrow-derived stem cells	[29-31]
dECM-based	dECM	Provides a natural extracellular matrix environment for cells rich in cell growth and differentiation factors	Low viscosity, poor mechanical properties, fast degradation rate	hASCs, hTMSCs	[32]
Synthetic polymer-based	PEG	Customizable and strong mechanical properties, no cytotoxicity or immunogenicity	Bioinert, not conducive to cell attachment	Bone marrow-derived human mesenchymal stem cells	[33,34]
Synthetic polymer-based	Pluronic	Good printability, temperature-sensitive gel	Poor biocompatibility, poor mechanical properties	Human mesenchymal stem cells	[35]

uniform cell suspension during printing, providing higher printing resolution and better cell viability. It also proves that oxidized alginate bioinks can effectively regulate stem cells' proliferation and diffusion behavior without affecting printability and structural integrity. Wu *et al.* proposed that sodium citrate is also an effective method to improve the insufficient degradation of alginate[37]. They used human corneal epithelial cells (HCECs)/collagen/gelatin/alginate hydrogel as bioinks and bioprinted using extrusion bioprinting technology. The controlled degradation of alginate was also achieved by using a culture medium containing sodium citrate, which resulted in the better proliferation and expression ability of specific marker proteins in the printed HCECs. To eliminate the inherent low viscosity of gelatin, He *et al.* used reversible quadruple-hydrogen-bonded ureido-pyrimidinone (UPy) and enzyme-responsive tyramine moieties (Tyr) sequence to chemically modified gelatin and developed a new type of gelatin bioink Gel-UPy-Tyr[38]. They used human bone marrow mesenchymal stem cells (hBMSC)/Gel-UPy-Tyr as bioinks for bioprinting by extrusion bioprinting, demonstrating that Gel-UPy-Tyr has temperature-programmable viscosity and enzyme-curing properties, providing better printability while maintaining higher cell viability and promoting the proliferation of hBMSC.

Due to excellent biocompatibility and good printability, composite bioinks have been widely used in stem cells and organoid bioprinting. Li *et al.* created a novel type of bioink called GelMA/alginate/PEGDMA/xanthan gum hydrogel bioink which can be printed at room temperature, by incorporating PEGDMA and xanthan gum into gelatin methacrylate (GelMA)/alginate-based hydrogels. Among them, the GelMA provides good biocompatibility and is helpful for cell adhesion and growth; the fast alginate gelation ensures structural integrity after printing; PEGDMA improves mechanical properties; and xanthan gum is a viscosity enhancer to improve printability[39]. They used hMSCs/GelMA/alginate/PEGDMA/xanthan gum as bioinks, combined with extrusion bioprinting technology to print, and the cells still had strong vitality and proliferation ability after printing. Yu *et al.* synthesized KEGC bioink from keratin methacrylate (KEMA) and glycol chitosan methacrylate (GCMA), wherein keratin provides biological

function. Glycol chitosan improves mechanical strength and biocompatibility[40]. Using hASCs/KEGC as bioinks, they were bioprinted by extrusion bioprinting technology, and the printed cells remained highly viable and could be continuously cultured. In addition, nanoparticles are widely used in bioinks because of their excellent properties. It can interact with polymers to adjust their properties and can also be used to transmit cellular signals. Alcala-Orozco *et al.* developed Sr-GelMA nanocomposite bioink consisting of strontium carbonate (Sr) nanoparticles and GelMA, where GelMA provides good biocompatibility, and Sr improves printability[41]. They bioprinted hMSC/Sr-GelMA with extrusion bioprinting technology, and the printed cells maintained high viability (>95%). In addition, Sr also promoted osteogenic differentiation of hMSCs. In addition, studies have shown that introducing solid micro scaffolds into composite bioinks can also improve the cell viability of organoid bioprinting[42].

Self-assembling peptides are highly similar to the ECM, both structurally and mechanically, and have been applied in bioprinting as a novel bioink material[43]. Cofiño *et al.* developed a bioink blend of self-assembling peptide RAD16-I with methylcellulose (MC). RAD16-I is not immunogenic and cytotoxic, and can support the attachment, growth, maintenance, and differentiation of various cells. MC is added to enhance the viscosity of the bioink[43]. They used hMSCs/RAD16-I/MC as bioinks, and the printed structure has high shape fidelity and stability while maintaining high cell viability. Alhattab *et al.* developed two kinds of ultrashort peptide bioinks using Ac-Ile-Ile-Cha-Lys-NH2 (IIZK) and Ac-Ile-Cha-Cha-Lys-NH2 (IZZK) peptide sequences, respectively, and combined with human bone marrow mesenchymal stem cells (hBM-MSCs) for bioprinting. The cells showed high activity after printing, and the two ultrashort peptide bioinks promoted the chondrogenic differentiation of hBM-MSCs[44].

dECM refers to the remaining ECM after the removal of cellular components from tissues through decellularized technology[45]. Although dECM bioinks have limitations such as low viscosity, poor mechanical properties, and fast degradation rate, they also have many outstanding advantages compared with natural and synthetic bioinks. DECM has excellent tissue-specific functions, provides cells with a natural ECM environment, and is rich in cell growth and differentiation factors and various proteins. Due to these properties, dECM bioinks are gradually being widely used in bioprinting[46]. The limitations of dECM can be improved by mixing dECM with other bioink materials. Xu *et al.* developed a novel bioink in which porcine intestinal dECM provided an ECM environment, and photosensitive GelMA provided rapid gelation and good photocuring properties. Other components of the bioinks serve different functions; for instance, the photoinitiator lithium phenyl (2,4,6-trimethylbenzoyl) phosphinate (LAP) triggers chemical crosslinking between polymers, and HA improves biocompatibility and viscosity[47]. By printing the dECM-HA bioink of mixed mouse crypts and GelMA/LAP pregel, and seeded with submucosal cells, they successfully established a co-culture system of submucosal cells and intestinal organoids and found that it enhanced the function and proliferation of ISCs. Zhang *et al.* combined dECM with silk fibroin protein to develop SF-dECM bioink, in which dECM was derived from natural cartilage tissue and provided a matching ECM environment for bone marrow mesenchymal stem cells (BMSCs). Silk fibroin improves mechanical strength[48]. The structure printed by this bioink mixed with BMSCs can support the proliferation of BMSCs and promote cartilage differentiation (Figure 2).

2.2. 3D bioprinting technology for organoid bioprinting

With the integration of organoids and 3D bioprinting technology, more and more printing methods have been applied to the bioprinting of stem cells or organoids. According to different principles, the commonly used printing methods are divided into three categories: extrusion-based bioprinting, droplet-based bioprinting, and photocuring-based bioprinting[49]. In addition, more new bioprinting technologies have been gradually developed, such as coaxial bioprinting[50], acoustic bioprinting[51], and magnetic bioprinting[52] (Table 2, Figure 3).

2.2.1. Extrusion-based bioprinting

The extrusion-based bioprinting (EBB) technology consists of two main parts: a fluid distribution system for extruding and an automatic robotic system for printing. The fluid distribution system is driven by pressure-assisted pneumatic, piston, or screw systems, and the bioink is extruded from the nozzle and deposited in the form of cylindrical silk[53]. EBB technology can be used to print biomaterials with viscosity ranging from 30 to 6×10^7 mPa/s, suitable for bioinks with high viscosity. Its characteristics of continuous deposition of filaments can provide better structural integrity for bioprinting, so EBB technology has been widely applied in organoid bioprinting. However, EBB technology also has many limitations. Firstly, EBB technology's resolution can only reach about 100 μm, which reduces printing accuracy and limits the function of printing tissue. Secondly, high shear stress caused by extrusion of high-viscosity bioink reduces cell vitality, and the survival rate of cells after EBB technology printing is usually between 40% and 86%. It is significantly lower than

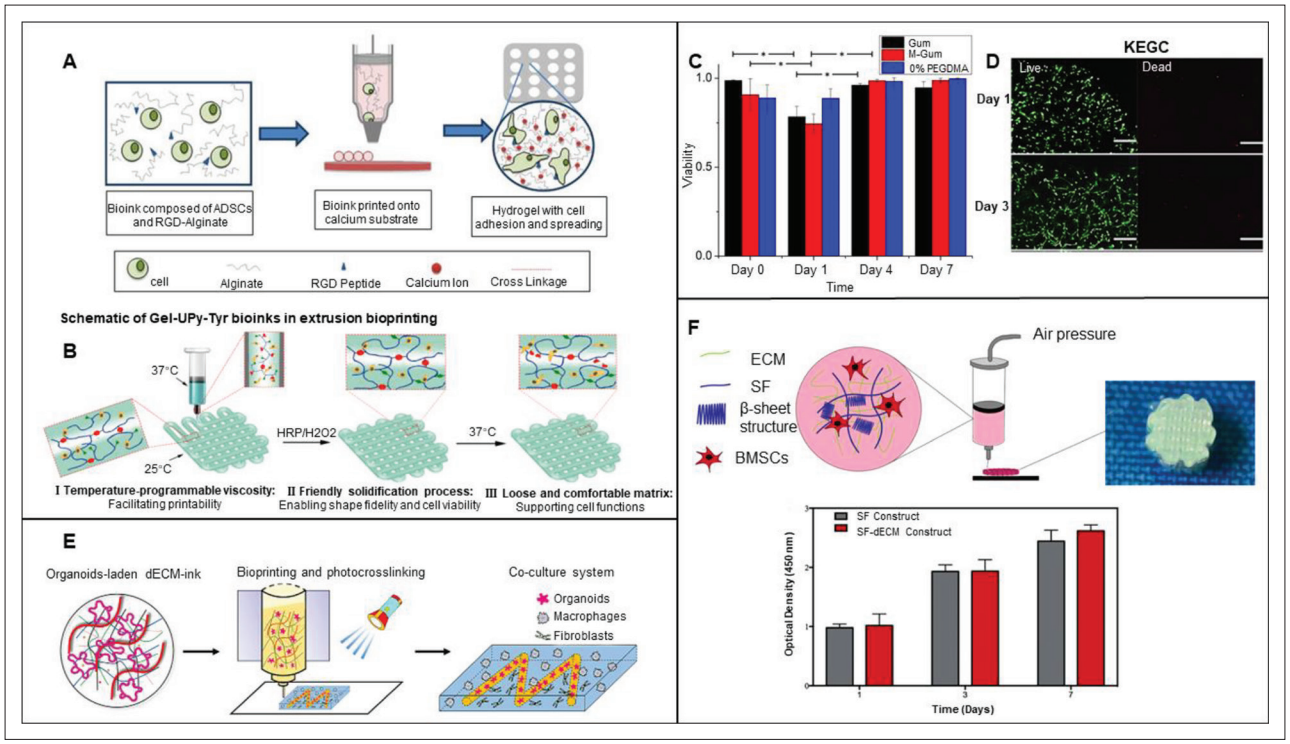

Figure 2. Bioinks for stem cell and organoid bioprinting. (A) Oxidized alginate and ADSCs for bioprinting as bioinks. Reprinted with permission from ref.[36]. Copyright 2014 Elsevier. (B) Gel-UPy-Tyr bioink for extrusion bioprinting. Reprinted with permission from ref.[38]. Copyright IOP Publishing. (C) hMSCs activity in printed bioinks, 0% PEGDMA (10% GelMA + 1.25% alginate + 0% PEGDMA + 3% gum), Gum (10% GelMA + 1.25% alginate + 2% PEGDMA + 3% gum), M-Gum (10% GelMA + 1.25% alginate + 2% PEGDMA + 3% crosslinked gum). Reprinted with permission from [39]. Copyright 2022 Elsevier. (D) hASCs live and dead staining in KEGC mixed bioink printed showed that living cells were stained green, with a high cell survival rate and good migration ability. Reprinted with permission from [40]. Copyright 2023 ACS Publications. (E) Preparation of intestinal organoids and submucosal cell co-culture system using bioprinting and dECM bioink (from ref.[47] licensed under Creative Commons Attribution 4.0 license). (F) Bioprinting using SF-dECM bioinks and BMSCs activity in print structures measured by CCK-8. Reprinted with permission from ref.[48]. Copyright 2023 Elsevier.

other bioprinting technologies[16]. Reducing the size of the nozzle is an effective method to improve the resolution. However, the decrease in the size of the nozzle is prone to blockage and increases the extrusion pressure, which leads to a decrease in cell survival rate. Therefore, when using extrusion-based bioprinting technology, appropriate parameters should be set in combination with multiple factors such as viscosity, printability, and cell survival rate of bioink[54]. In light of this, developing new EBB technologies can effectively improve the areas where the limitations of traditional EBB technologies are found.

The shear stress generated by the extrusion of bioinks with low viscosity is minor and will not significantly impact cell activity, but the complex organizational structure cannot be firmly maintained after printing[55]. Suspension bioprinting (also known as embedded bioprinting) enables the printing of low-viscosity bioinks that effectively improve cell survival. Unlike the traditional extrusion printing method, which deposits bioink in cylindrical silk on a flat surface, suspension printing introduces a suspension medium, which deposits bioink in a support bath containing the suspension medium. A suspension medium is a yield stress material, showing solid and liquid properties according to the critical stress. When no external force is applied, the suspended medium behaves like a solid under critical stress. When the printing nozzle moves in the suspended medium, the generated force exceeds the critical stress, above which the suspended medium flows like a liquid. When the nozzle passes through, the suspended medium quickly returns to the solid form in a self-healing manner[56,57]. The characteristics of the suspended medium support the printing of low-viscosity bioink, maintain the stability of the printing structure, and realize all-around printing, free from the constraints of construction direction, complex geometric shape, and other factors[57]. Lee *et al.* developed a freeform reversible embedded suspended hydrogel (FRESH) technology, which uses gelatin particles as the suspension medium to support the printing process. When heated to 37°C, the suspension medium will melt and release the printed structure[58]. Using collagen as bioink and human embryonic stem cell-

Table 2. More 3D bioprinting for stem cell or organoid bioprinting

3D bioprinting technology	Basic principle	Benefits	Drawbacks	Bioprinted stem cells or organoids	References
Coaxial bioprinting	One of EBB technologies, concentric nozzles are stacked to form coaxial nozzles for printing a variety of bioinks.	Enables the construction of layered tubular structures with adjustable biological/mechanical properties, with cell viability dependent on extrusion speed and nozzle diameter	Low resolution, 7 mm–210 μm	Mesenchymal stem cells (MSC)	[49,50,74]
Acoustic bioprinting	One of the DBB technologies, bioinks are ejected in droplet form by force generated by sound waves.	High resolution (~37 μm) and cell viability (>90%), high printing speed	The movement of the print head interferes with the droplet ejection and is not suitable for high-viscosity bioinks.	Bladder tumor organoids	[51,61,75]
Electrohydrodynamic jetting (EHDJ) bioprinting	One of the DBB technologies that use a high-voltage-driven electric field to pull the bioink out of the nozzle hole in the form of a droplet	With a better resolution of 2–5 μm, cell viability >90%, suitable for printing high-viscosity bioinks	Difficult to print complex structures and cell viability may be affected in the long term after printing, making it unsuitable for precise bioprinting applications	Human adipose stem cells	[49,60,61,63,64]
Microvalve bioprinting	A DBB technology in which a microvalve controls the opening of the nozzle hole and the bioink is sprayed out of the open nozzle hole in the form of a droplet when the air pressure is high enough	Accurate cell localization, high cell survival rate >86%, fast printing speed	The size of the nozzle hole limits the printing of bioinks within a specific viscosity range (1 to 200 mPa/s).	Human embryonic stem cells	[61,76,77]
Magnetic bioprinting	By magnetizing cells with magnetic nanoparticles, the magnetic force is used to control the spatial pattern of the desired morphology of the cell aggregates.	Cell vitality >90%, reasonable spatial control, synthesis of endogenous ECM, can quickly print a variety of tissue structures	The cytotoxicity of magnetic nanoparticles may cause adverse effects on cells.	Salivary glands organoids	[52,78] [79,80]

https://doi.org/10.36922/ijb.0112

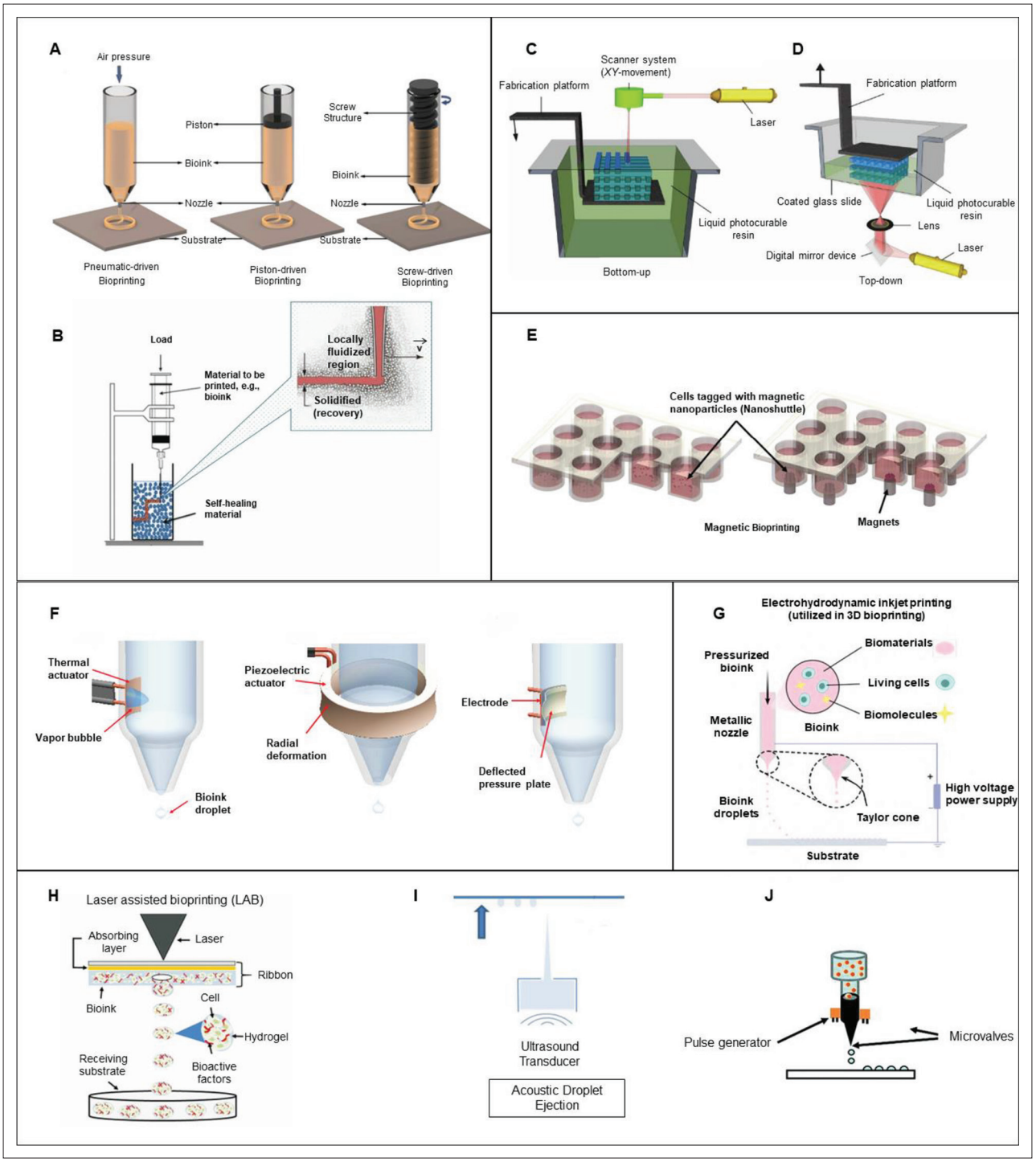

Figure 3. Bioprinting technology. (A)–(B) Extrusion-based bioprinting: (A) Extrusion bioprinting (pneumatically driven, piston-driven, screw-driven) (from ref.[16] licensed under CC BY-NC-ND 4.0). (B) Suspension bioprinting (from ref.[59] licensed under Creative Commons Attribution 4.0 license). (C)–(D) Photocuring-based bioprinting: (C) Stereolithographic bioprinting (from ref.[69] licensed under Creative Commons Attribution 4.0 license). (D) Digital light processing bioprinting (from ref.[69] licensed under Creative Commons Attribution 4.0 license). (E) Magnetic bioprinting. Reprinted with permission from ref.[78]. Copyright 2020 Elsevier. (F)–(J): Droplet-based bioprinting: (F) Inkjet bioprinting (thermal inkjet, piezoelectric inkjet, electrostatic inkjet). Reprinted with permission from ref.[61]. Copyright 2016 Elsevier. (G) Electrohydrodynamic jetting bioprinting. Reprinted with permission from ref.[64]. Copyright 2023 Springer Nature. (H) Laser-assisted bioprinting (from ref.[65] licensed under CC BY-NC 4.0). (I) Acoustic bioprinting (from ref.[79] licensed under CC BY-NC 4.0). (J) Microvalve bioprinting (from ref.[76] licensed under Creative Commons Attribution 3.0 license).

derived cardiomyocytes (hESC-CMs), they achieved high-resolution bioprinting of cardiac organoids with systolic function using FRESH technology. Suspension bioprinting also has some limitations[59]. The first limitation is that the integrity of the printing structure may be compromised when the structure is extracted from the suspended medium. The second limitation is that the suspended medium restricts the printing process. For example, the bioink cannot be bioprinted at the temperature that the suspended medium cannot accommodate.

In addition, the research proves that mixed printing with other bioprinting technologies was also an effective measure to improve the limitations of traditional EBB technology. Yeo *et al.* developed a hybrid bioprinting technology combining traditional EBB technology and electrohydrodynamic jetting. Human adipose stem cells in the cell load structure printed by this technology could still maintain high cell vitality. It has been confirmed that the hybrid bioprinting technique can achieve rapid and stable bioprinting of cell-loaded structures without loss of cell viability[60].

2.2.2. Droplet-based bioprinting

Droplet-based bioprinting (DBB) technology is printed by stacking independently separated droplets with higher resolution than EBB's technology. According to the different principles of droplet formation, bioprinting technology can be divided into inkjet bioprinting, laser-assisted bioprinting (LAB), electrohydraulic dynamic jet (EHDJ) bioprinting, acoustic bioprinting, and microvalve bioprinting. Among these, inkjet bioprinting and LAB are currently more widely used.

Inkjet bioprinting, in which bioink is ejected as a droplet from a nozzle when a pressure pulse is generated, may contain multiple print heads, each equipped with a fluid chamber containing bioink and one or more nozzles with a minimum diameter of 18 μm. According to the driving mechanism of the pressure pulse, inkjet bioprinting can also be subdivided into thermal inkjet, piezoelectric inkjet, and electrostatic inkjet[61]. Inkjet bioprinting has good performance, based on: Firstly, it can generate droplets at a high-speed rate (up to 30 kHz), and the size of the droplets generated is tiny, resulting in a very high resolution (about 50 μm). Secondly, inkjet bioprinting has good cell activity, and the cell survival rate is generally 80% to 95%[62]. As inkjet bioprinting is a non-contact printing technique, the droplets are not subjected to any harm by the print head moving after injection. Additionally, inkjet bioprinting has a print head with multiple nozzles that can print multiple bioinks simultaneously, enabling the creation of multicellular tissues or organs[63]. Nevertheless, inkjet bioprinting has significant limitations. First, droplet spatter is inevitable in the injection process, leading to the decline of resolution[64]. In addition, due to the limitation of nozzle size, inkjet bioprinting is only suitable for bioinks with low viscosity and cell density. Otherwise, the nozzle blockage is likely to happen during the printing process, resulting in poor durability of the print head[63].

LAB techniques, including laser-guided direct writing (LGDW) and laser-induced forward transfer (LIFT), are more commonly used due to their excellent performance. The LIFT device for bioprinting consists of three parts: A laser source (mainly nanosecond laser), a target plate, and a receiving substrate. The target plate consists of clear glass, an absorbing layer (made of metal), and a bioink layer. The laser energy vaporizes the absorbing layer of metal to produce high-pressure bubbles that squeeze the bioink out as droplets. The absorbent layer can also avoid direct contact between the bioink and the laser, protecting it from the laser[65]. LIFT has significant advantages over inkjet bioprinting, as it is a nozzle-free printing method hence no nozzle clogging problem, making it suitable for printing bioinks with high viscosity and cell density, with a resolution of up to micron, 95% cell viability after printing, and normal cell proliferation[66]. Sorkio *et al.* used LIFT technology to print limbal epithelial stem cells (hESC-LESC) and hASCs derived from human embryonic stem cells to simulate natural corneal tissue structure, and the cells maintained good vitality after printing[30]. However, LAB still has limitations despite its advantages over others. The vaporization of the metal absorption layer may lead to metal residue in the structure of bioprinting, causing pollution. In addition, it is necessary to manufacture multiple target plates when printing multiple bioinks, necessitating longer manufacturing time and higher cost[67].

2.2.3. Photocuring-based bioprinting

Photocuring-based bioprinting uses light to solidify bioinks. The technique can be subdivided into stereolithography (SLA) and digital light processing (DLP) according to different ways of curing.

SLA uses a UV point light source and point-to-point irradiation of bioinks to cure layer by layer selectively and eventually form complex structures[68]. SLA has no nozzle limitation compared to extrusion-based bioprinting technology, so it has higher resolution (generally less than 100 μm) and cell viability (up to 85%). It should be noted that UV light sources may cause damage to cells during the printing process, resulting in reduced cell viability[69]. Grix *et al.* used SLA technology combined with HepaRG and human stellate cells and successfully achieved accurate bioprinting of liver organoids. The printed liver tissue equivalent was found to maintain cell viability for at least

14 days, confirming the potential application of SLA technology in organoid bioprinting[70].

Unlike SLA technology, DLP uses an ultraviolet surface light source. The light projected from a digital micromirror device illuminates an entire layer of bioink, curing an entire layer at a time. Hence, DLP has a much faster printing speed than SLA[71]. In addition, DLP has a high resolution (less than 20 μm) and cell viability (more than 90%). DLP technology is widely used in bioprinted organoids due to its excellent performance. Xie *et al.* bioprinted hydrogel microspheres (MSs) containing BMSC using DLP technology, which maintained good cell viability after printing and successfully constructed callus organoids after cartilage induction[72]. However, DLP technology still has room for improvement. Currently, DLP printing technology with different light sources is being investigated to further reduce the impact on cells and improve cell viability. Additionally, DLP technology has a high demand for bioinks. While meeting traditional requirements, bioinks also need to ensure the photo-polymerization speed and the fidelity of the printing structure[73].

3. Tissue vascularization strategies

The lack of vascularization is a significant drawback of large-scale tissue construction, as the natural diffusion of oxygen and nutrients can only support tissue growth up to a size of 150 μm. This is also true for organoids, which face similar challenges. As traditionally-constructed organoids grow beyond a certain size, the exchange of oxygen, nutrients, and metabolites can no longer be achieved through natural diffusion, thereby resulting in the loss of cell vitality and the development of necrotic cores[81]. Przepiorski *et al.* used a rotating bioreactor to generate hiPSCs-differentiated kidney organoids. They found that the core cells of kidney organoids with a diameter greater than 700 mm were significantly reduced. The cell viability was not as good as kidney organoids with a smaller diameter[82]. Therefore, it is essential to realize the vascularization of organoids. Bioprinting technology has been widely used in vascularization due to its excellent performance. Various techniques are now available to achieve the vascularization of bioprinted organoids, including growing the organoids directly onto 3D-printed vascular structures, using growth factors to encourage angiogenesis, and combining endothelial cells with stem cells or organoids to create organoids with blood vessels[15] (Figure 4).

The printing of blood vessel structures can be divided into direct and indirect printing. Direct bioprinting mainly uses mixed bioinks, while indirect printing uses sacrificial bioinks.

3.1. Direct bioprinting vascularization

Direct printing involves using bioink and bioprinting technology to print out tubular structures. Coaxial bioprinting technology is often used in the direct printing of blood vessels. However, without a supporting material, the printed blood vessel structure is prone to deformation or collapse during the printing process[83]. As a result, the direct printing of blood vessels demands high-quality bioink with better printability, mechanical properties, and angiogenic potential[84]. Jia *et al.* developed a hybrid bioink consisting of GelMA, sodium alginate, and PEGTA, with excellent printability, biocompatibility, and mechanical properties that support the survival and proliferation of vascular cells. By using this cell-loaded hybrid bioink and coaxial bioprinting technology, they have successfully achieved direct bioprinting of perfused vascular structures[85]. Hong *et al.* also applied gelatin to the printing of blood vessel structures. They synthesized gelatin-PEG-tyramine (GPT) mixed bioinks, in which tyramine has rapid crosslinking properties, and PEG acts as the spacer material between gelatin and tyramine to promote rapid gelation. They demonstrated one-step bioprinting of perfumable vascular structures using GPT bioinks and coaxial bioprinting[86]. In addition to mixed bioinks, chemically modified natural bioinks can also be used for vascularization direct bioprinting. Barrs *et al.* developed a novel peptide-functionalized alginate hydrogel bioink using RGD (integrin-binding state for cell adhesion) and a vascular endothelial growth factor (VEGF)-mimetic peptide with matrix metalloproteinase cleavable linker (MMPQK) for modification of oxidized alginate. Direct bioprinting of vascularized tissue units (VTUs), consisting of the blood vessel and tissue-specific components, was successfully achieved using RGD/MMPQK bioink for vascular components and tissue-specific bioink for tissue-specific components[87].

3.2. Indirect bioprinting vascularization

Indirect printing involves the use of sacrificial bioinks to print vascular structures. These bioinks can be removed physically or chemically after printing, leaving a perfusive and endothelialized hollow lumen. It should be noted that sacrificial bioinks are usually bioprinted with extrusion-based bioprinting technology. However, the lack of resolution in this technology limits the application of sacrificial bioinks in the bioprinting of small-diameter blood vessels[84]. Additionally, the complexity of indirect printing technology may affect the size and function of the resulting vascular structures. Kolesky *et al.* adopted Pluronic F127 as the sacrificial bioink and GelMA as the bioink. Pluronic F127 appears in a solid state, GelMA ink in a liquid state when the temperature is higher than 22°C, and Pluronic F127 in a liquid state and GelMA ink appear in a solid state when the temperature is lower than 4°C.

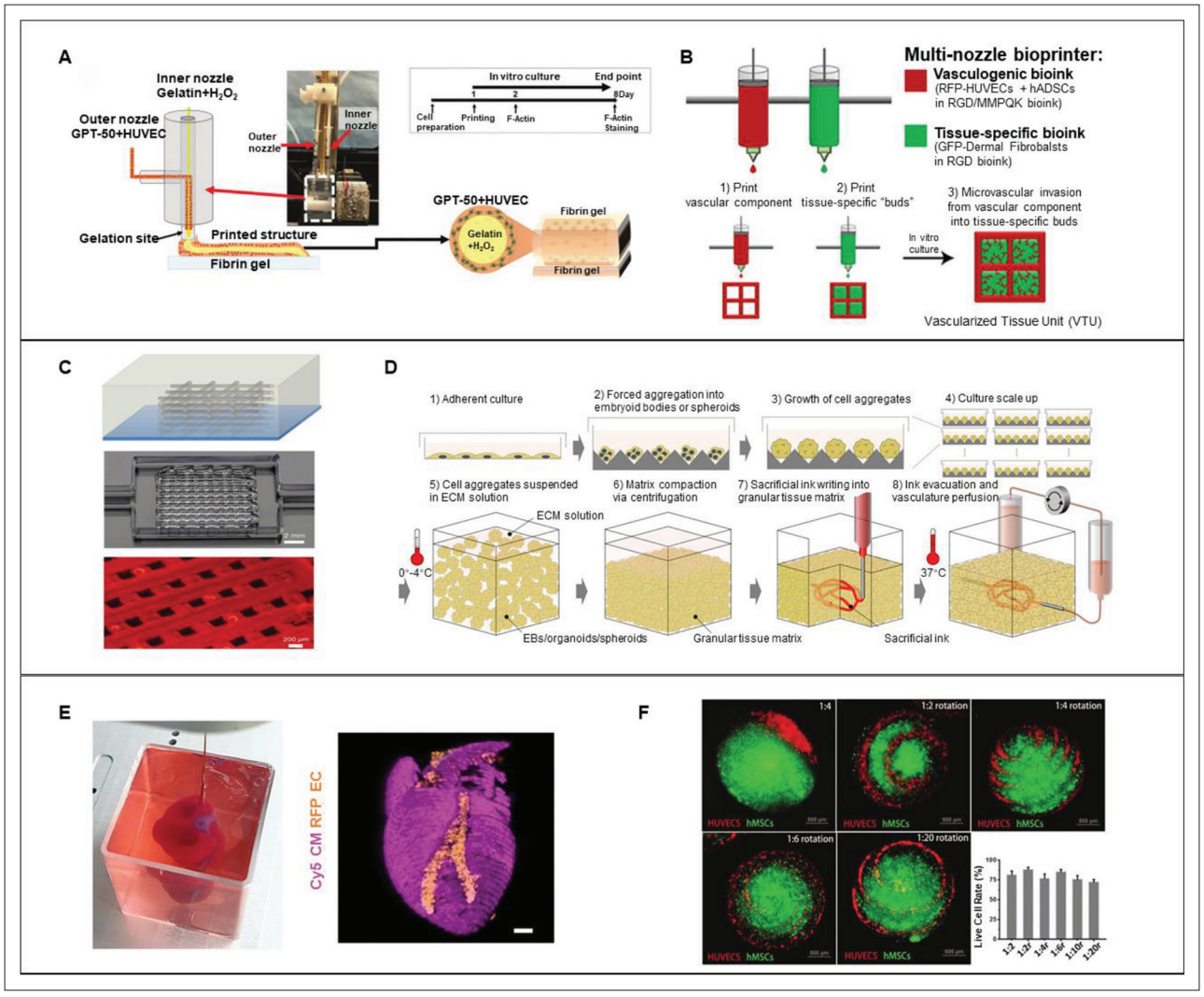

Figure 4. Vascularization of bioprinted organoids. (A)–(B) Direct bioprinting vascularization: (A) Coaxial bioprinting of GPT bioinks containing HUVEC. Reprinted with permission from ref.[86]. Copyright 2013 Royal Society of Chemistry. (B) Direct bioprinted vascularization tissue units. Reprinted with permission from ref.[87]. Copyright 2021 American Chemical Society. (C)–(D) Indirect bioprinting vascularization: (C) Pluronic F127 as a sacrifice bioink to print 3D microvascular network. Reprinted with permission from ref.[88]. Copyright 2014 John Wiley & Sons. (D) Schematic diagram of SWIFT technical process (from ref.[89] licensed under the CC BY-NC 4.0). (E) DECM personalized hydrogel bioink-printed heart containing blood vessels and its 3D confocal image (CMs, induced pluripotent stem cell (iPSCs) derived cardiomyocytes, ECs, endothelial cells) (from ref.[93] licensed under Creative Commons Attribution 4.0 license). (F) Airflow-assisted bioprinted helical vascularization structure. Reprinted with permission from ref.[94]. Copyright 2018 John Wiley & Sons.

As a result, the sacrificial bioinks can be easily removed at low temperatures, and Pluronic F127's bioenergy allows it to be printed and removed without damage to cells. After removing the sacrificial bioinks, they successfully obtained perfusive channels and realized vascular structure after endothelialization culture[88]. Using patient-specific induced iPSC-derived organoids as organ building blocks (OBB) and the sacrificial write functional tissue (SWIFT) methodology, Skylar *et al.* created a unique method for producing vascularized organ-specific tissues with high cell density and maturation. They used heart organs as OBBs and gelatin as sacrificial bioinks. At 37°C, the gelatin sacrificial bioinks were removed upon melting, and a perfusable vascular channel was successfully achieved in the heart tissue[89]. Bioprinted kidney organoids have been proven to have better maturity. The combination of bioprinted organoids as OBBs and SWIFT technology may realize the construction of centimeter-level kidney organoids with blood vessels[90].

3.3. Vascular growth factor

Vascular growth factors, such as vascular endothelial growth factor (VEGF), primary fibroblast growth

factor (bFGF), and others, can promote angiogenesis and development. Compared with other bioinks, dECM has been identified as a promising bioink material for vascular bioprinting due to its rich composition of proteins and growth factors. In fact, bioinks based on dECM have been successfully used in vascular bioprinting. Wang *et al.* combined pancreatic extracellular matrix (pECM) with hyaluronic acid methacrylate (HAMA) to develop a new bioink. The study confirmed the ability of dECM to promote the formation of new blood vessels[91]. However, the preparation of dECM requires a decellularization process, during which many growth factors may be lost. Therefore, Wang *et al.* modified the above bioinks by combining GelMA, pECM, and platelet-rich plasma (PRP) to prepare a new bioink that is readily available and rich in various growth factors. At the same time, it also has good printability. The improved bioink also showed better angiogenic ability[92]. Islet organoids printed by the above two bioinks and DLP technology may have potential application value in islet transplantation. Noor *et al.* prepared personalized hydrogel bioink using dECM derived from the omental tissue of patients and successfully printed the vascularized heart structure in the supporting material. The printed structure was extracted from the supporting material through enzymatic hydrolysis or chemical degradation, and this extraction method did not significantly compromise the cell vitality[93].

In addition, studies have shown that combining endothelial cells with stem cells or organoids is also an effective method of organoid vascularization. Zhao *et al.* have developed a new airflow-assisted bioprinting technique to print multifunctional helical microstructures inside microspheres. Using this technique, they successfully created osteoblast-like organs with vascularized spiral structures, which involved printing endothelial cell spiral structures into bone marrow MSC microspheres. *In vitro*, bone marrow MSCs were induced to differentiate into osteoblasts, and endothelial cells produced vascularized cells[94].

4. Biomedical applications of bioprinted organoids

With appropriate bioink, bioprinting, and tissue vascularization strategies, complex organoids that are highly similar to tissues and organs in the body can be constructed. To date, bioprinting has been utilized extensively in drug screening, regenerative medicine, tumor research, and many other areas. Several organoids, including hearts, livers, and kidneys, have been created using this technique (Figure 5).

4.1. Drug screening

The development of new drugs usually requires a large amount of cost. Before clinical trials, drugs must be screened for various aspects, such as activity, toxicity, metabolism, efficacy, side effects, and dose response[95]. Two-dimensional (2D) cell culture models and experimental animal models are often used in traditional drug screening models, but there are many problems with traditional drug screening models. The 2D cell culture model supports the observation of cell morphology at the cellular level, but it lacks the interaction between cells and does not simulate the complex *in vivo* environment. Animal models improve complexity, but differences between animal and human genomes make animal models inaccurate predictors of drug response, and there are ethical and moral controversies associated with animal models[95,96]. Taken together, evaluating a new drug usually takes 12–15 years, and 50% of new drug development will fail due to unpredictable toxic reactions[97]. Therefore, the research of an accurate drug screening model is essential.

Bioprinted organoids, highly similar to tissue organs *in vivo*, are widely used in drug screening as an alternative to traditional drug screening models. As many drugs can cause varying degrees of damage to the liver and kidney, these organs, which are crucial for human drug metabolism and detoxification, are also important for toxicity tests. In addition, bioprinting can also support the application of high-throughput screening technology and improve drug screening efficiency[97].

Lawlor *et al.* successfully constructed kidney organoids using extrusion bioprinting technology and tested them for the toxicity of aminoglycosides. This all-purpose antibiotic can heal infections brought on by Gram-negative germs, but it frequently causes acute tubular necrosis, which damages the kidneys[14]. Lawlor *et al.* treated printed kidney-like organs using aminoglycosides, and cell viability was estimated by ATP (adenosine triphosphate, a direct source of energy for vital activities) content after 72 h. The results showed that the activity of the treated cells decreased, and the decrease showed concentration-dependent characteristics, which confirmed that bioprinted organoids are practical tools used in toxicity test. Bouwmeester *et al.* created liver structures using intrahepatic bile duct cell organoids (ICOs) and extrusion-based bioprinting techniques. After printing, the organoids in the structure maintained relatively stable cell viability for 10 days. They exposed organoids in the bioprinted structures to acetaminophen (APAP, a hepatotoxic compound) on the 7th day after printing. After 72 h of exposure, organoid cell activity decreased to 21%–45%, and the organoid shape was damaged, indicating cellular stress. It demonstrated that liver structures obtained by combining organoids

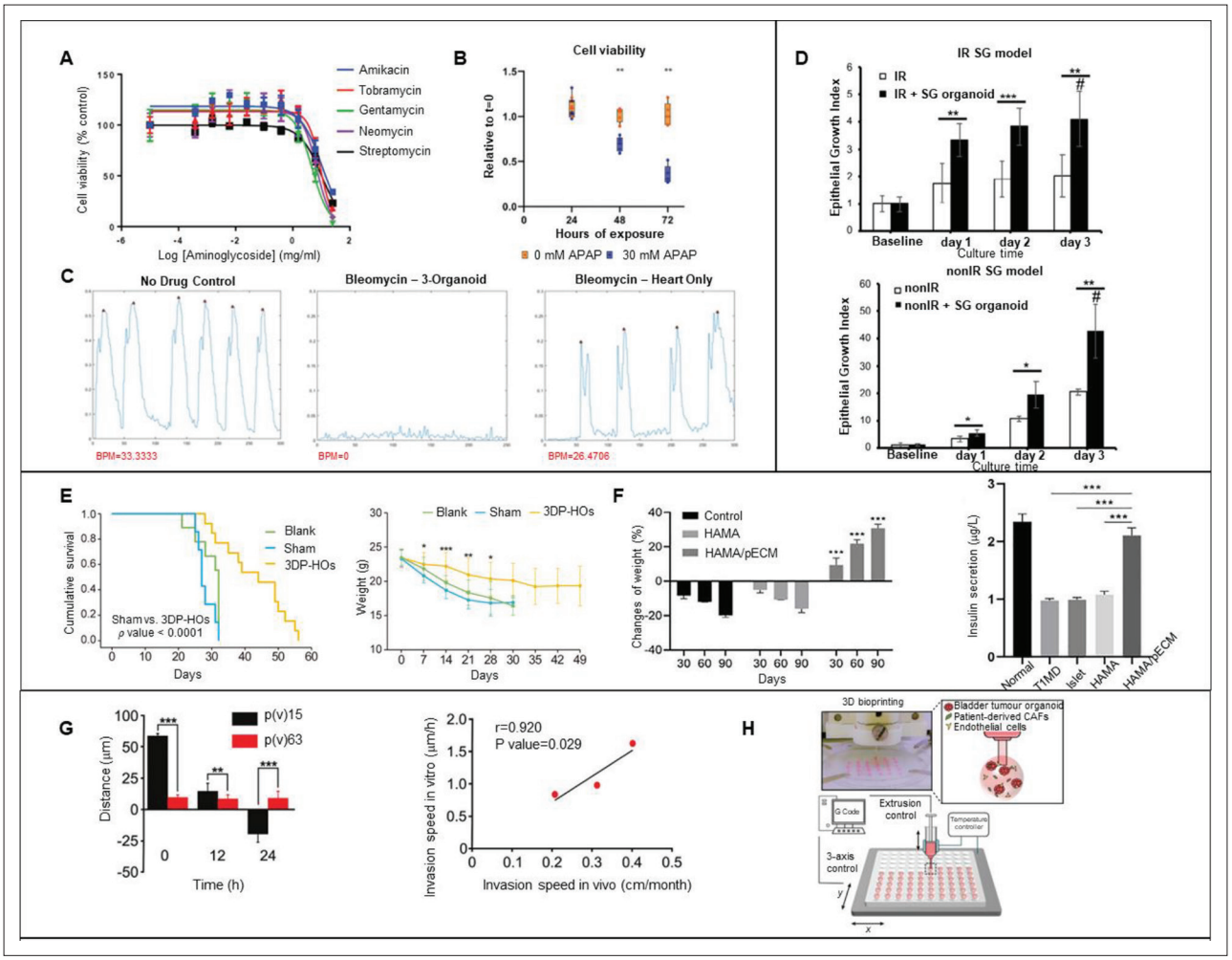

Figure 5. Biomedical applications of bioprinted organoids. (A)–(C) Drug screening: (A) Cell viability of bioprinted kidney organoids after 72 h treatment with aminoglycosides. Reprinted with permission from ref.[14]. Copyright 2020 Springer Nature. (B) Cell viability of organoids in bioprinted liver structures exposed to acetaminophen (APAP) from day 7 post-printing (from ref.[98] licensed under Creative Commons Attribution 4.0 license). (C) The beating of cardiac organoids after adding bleomycin to three types of bioprinted organ systems (from ref.[99] licensed under Creative Commons Attribution 4.0 license). (D)–(F) Regenerative medicine: (D) Epithelial growth index of SG after bioprinted SG organoids were transplanted into radiation injury and health SG models. Reprinted with permission from ref.[52]. Copyright 2018 Elsevier. (E) Survival curves and body weight changes of mice after bioprinted liver organoids were transplanted into F/R mice. Blank (control group), Sham (sham operation group), 3DP-Hos (organoid transplantation group) (from ref.[101] licensed under the CC BY-NC 4.0). (F) Changes in mice's body weight and serum insulin levels after bioprinted islet organoids were transplanted into mice. From left to right were normal mice, diabetic mice, simple islet transplantation group, HAMA ink islet transplantation group, and HAMA/pECM ink islet transplantation group. Reprinted with permission from ref.[91]. Copyright 2022 Elsevier. (G)–(H) Tumor studies: (G) Acoustic bioprinting PDMs simulated tumor invasion, changes in invasion distance, and correlation between tumor invasion rate and primary tumor spread rate (p(v)13 and p(v)15 represented patient source numbers 13 and 15). Reprinted with permission from ref.[103]. Copyright 2022 John Wiley & Sons. (H) Construction of bladder tumor assembly by bioprinting. Reprinted with permission from ref.[105]. Copyright 2020 Springer Nature.

and bioprinting techniques could be used to predict drug-induced liver injury[98].

The environment inside the human body is complicated, and tissues and organs are highly interconnected, so the evaluation of drugs by a single organoid model is not comprehensive enough. In order to better simulate the complex reactions and interactions between tissues in the drug screening process, the study of a multi-organoid system is of great significance. Skardal *et al.* developed a lung–liver–heart three-organ platform using bioprinting technology and validated bleomycin, a drug known to treat some cancers that cause severe pulmonary fibrosis and inflammation[99]. Cardiac organoids remained unaffected when treated with bleomycin alone. However, when the three-organ platform was treated with bleomycin, cardiac organoids stopped beating, suggesting bleomycin might induce other tissues in the system to produce factors that

affect the functionality of cardiac organoids. It is confirmed that the single organoid model may miss unanticipated toxicity and side effects in drug screening.

4.2. Regenerative medicine

Donor shortage and immune rejection have been major medical challenges, with only 10% of the global demand for organs currently reported to be met[100]. At the same time, the uncertain outcomes of organ transplantation increase the risk of infection. Therefore, how to construct biological tissues and organs *in vitro* to improve portability and limit the risk of immune response is an urgent challenge to be addressed[100]. Bioprinted organoids, which can replicate the structure and function of native tissues, have broad application prospects in regenerative medicine and can be used as organ transplant donors.

Xie *et al.* induced callus organoids generated by bioprinting *in vitro* and transplanted the callus organoids into a 5 mm × 4 mm cylindrical defect at the distal end of the rabbit femur. Four weeks after implantation, they observed that the callus organoids promoted the formation of new bone, and the newly generated bone tissue almost filled the defect site. Compared to the 2–3-month recovery time required in traditional tissue engineering, bioprinting offers a faster solution for bone repair, achieving rapid bone healing[72]. Adine *et al.* used magnetic bioprinting technology to print salivate glands (SG) organoids and transplanted SG organoids into an *in vitro* model. After transplantation, SG organoids were found to significantly stimulate the epithelial and neuronal growth of damaged SG, which is of great significance for treating dry mouth syndrome[52].

Yang *et al.* bioprinted liver organoids using HepaRG cells, and the printed organoids obtained liver functions such as albumin secretion, drug metabolism, and glycogen storage 7 days after differentiation. They transplanted liver organoids into F/R mice (a modulated model of liver damage that inhibits immune rejection, where deletion of the Fah gene leads to the accumulation of toxic tyrosine metabolites in liver cells that cause liver damage). They found that the liver organoids matured further and formed functional blood vessels. After transplantation, the survival period of mice was significantly prolonged, and the degree of weight loss was reduced, confirming that the transplantation of liver organoids could alleviate the liver failure of animals and has the potential to be used as organ transplant donors[101]. It is worth mentioning that the bioprinted liver organoids contain functions such as protein secretion, which may have potential applications in the production of biological agents. Wang *et al.* implanted islet organoids based on HAMA/pECM bioink bioprinting into diabetic mice. After 12 weeks of implantation, the islet organoids were still alive, and the mice could recover regular blood sugar within 60 min after meals, and their weight also showed a rising trend[91].

4.3. Cancer research

Cancer is a severe disease that poses a threat to life, and its morbidity and mortality are increasing. However, the mechanisms by which cancer occurs and its treatment are still poorly understood. Patient-derived 2D tumor culture and xenotransplantation have been widely used to simulate tumor invasion and therapeutic response. However, 2D models cannot fully summarize biochemical and biophysical signals of the tumor environment, and xenotransplantation also has problems such as genetic variability[102,103]. An ideal model for studying tumors is an organoid that mimics the histology, immunohistochemistry, and genetic heterogeneity of tumors but does not contain the mesenchymal cellular elements and intercellular connections found in the actual tumor tissue. In this regard, bioprinting technology can precisely control the distribution of cells and biomaterials, mimicking the spatial and chemical distribution of natural tissues, and therefore has great potential for applications in building complex tumor models and reconstructing tumor microenvironments[104].

Gong *et al.* generated bladder tumor organoids with acoustic bioprinting and murine-derived bladder tumor cells. The printed organs had a survival rate of more than 85% and maintained an immune milieu comparable to the original tissue for 2 weeks. In addition, after 2 days of co-culture of printed organoids and autologous lymphocytes, they observed the generation of tumor-specific T cells that can kill tumor organoids, suggesting that bioprinted organoids can be used for individualized immunotherapy[51]. Chen *et al.* used the same printing technique to print patient-derived microtissues (PDMs, consisting of colorectal tumors and healthy organoids derived from colorectal cancer (CRC) patients), simulated tumor invasion in CRC patients, and demonstrated the application of PDMs in drug screening[103]. In drug screening, two drugs (5-FU and Erbitux, the drugs for the treatment of colon cancer disease) were selected, and organoids were tested under different drug concentrations. Then, the distance between the tumor and healthy organs served as a measure of tumor invasion potential. The results showed that organoids were more sensitive to Erbitux. As long-term cultured bladder organoids lack vital components of a normal bladder (such as tissue matrix and muscle layer), Kim *et al.* proposed the assembly concept to tackle the problem. They successfully constructed bladder tumor assembly through bioprinting technology, combined with patient-derived bladder tumor organoids, endothelial cells (HULECs), and patient-derived cancer-related fibroblasts

(CAFs), which could accurately simulate the pathological characteristics of tumors *in vivo*. The study proved that bioprinted tumor assemblies have the same drug response as manually constructed tumor assemblies, and at the same time can be used for high-throughput drug screening[105].

5. Future outlook and summary

Organoid growth factors are mainly produced from patient-derived induced pluripotent stem cells and human stem cell differentiation. Due to their excellent ability to simulate human development and diseases, organoids have great application potential in drug testing and future organ replacement. However, organoids cultivated by traditional methods have size, complexity, and maturity limitations. Its more comprehensive application has been severely limited[106]. Bioprinting is regarded as a promising biomanufacturing technology because it can accurately deposit bioink materials and cells in space.

Bioprinting has been shown to improve the size limitations of traditional organoid culture techniques. Bioprinting-Assisted Tissue Emergence (BATE) technique prints stem cells or organoids into an ECM that encourages spontaneous self-organization using extrusion-based bioprinting technology and microscopy. This enables the construction of centimeter-scale intestinal organoids by controlling geometry and cell density[107]. Bioprinting also enables repeatable, consistent construction of organoids. A new immersion bioprinting technology prints organoids in a support bath with HA as the suspension medium, avoiding the influence of orifice wall on printing during the manufacture of high-throughput organoids, and the printed organoids have a high degree of consistency in volume and geometry[108].

However, there are still many shortcomings in bioprinting organoids. Firstly, in terms of bioinks, organoid bioprinting has high requirements for bioinks. An ideal bioink material should possess the characteristics of biocompatibility, mechanical and structural integrity, biodegradability, non-cytotoxicity, and immunogenicity, as well as the ability to provide a highly biomimetic environment for cells. Besides that, it should be commercially available[109]. These requirements have greatly limited the development of bioinks, so it is urgent to create new formulations of bioinks. Recently, a new glycerohydrogel bioink has been proposed that demonstrates outstanding bacteriostatic properties and long-term shape fidelity of printed tissues, as well as cytoprotection ability during printing, cryopreservation, and transportation[110]. The new bioinks could have great applications in organoid bioprinting. Secondly, in terms of bioprinting technology, high-cell-density bioinks allow the cells in the printed tissue to be close enough for cell-to-cell communication. However, most current bioprinting methods are unsuitable for high-cell density bioinks, and resolution and printing speed are limited. Finally, insufficient vascularization of organoids is also a problem that needs to be addressed. Microfluidic technology and four-dimensional (4D) bioprinting technology may be the effective ways to solve the above problems.

The application of microfluidic technology to the real-time distribution of cell concentration can successfully assist bioprinting to realize the construction of tissues and organoids with high cell density[111]. Microfluidics can also be applied to the vascularization of organoids by printing microfiber scaffolds to construct vascularized tissues[112]. Since the microenvironment of 3D bioprinting structure may not elicit appropriate biological responses, which will limit the application of 3D bioprinting, recently, 4D bioprinting technology has been investigated to solve the abovementioned problems. 4D bioprinting is a technology that combines 3D bioprinting with stimulus-response materials, also known as innovative materials, which can change their properties according to stimuli. Therefore, the structure of 4D bioprinting can more accurately simulate native tissues[113]. Photocured silk fibroin (Sil-MA) hydrogels can deform in a typical cell culture medium, and the tracheal structures obtained by combining with DLP bioprinting technology have great application potential in regenerative medicine[114]. However, 4D bioprinting is still at an early stage of development, and more research is needed in the future. More recently, a strategy to apply artificial intelligence (AI) to organoid bioprinting has also been proposed, with the potential to build more standardized organoids with an improved resolution by leveraging AI's monitoring and verification capabilities[115].

Since single organoid bioprinting cannot fully predict the crosstalk between organs, organoid bioprinting may develop into multi-tissue organoid bioprinting in the future with the development of bioinks and bioprinting techniques.

In summary, this paper introduces bioprinted organoids, reviews the progress of bioinks, bioprinting techniques, and tissue vascularization strategies, and demonstrates the application of bioprinted organoids in biomedicine. Although there are still many shortcomings in bioprinting organoid technology, it is believed that with the development of research, this technology will be more mature.

Acknowledgments

None.

Funding

This work is funded by the financial support from National Natural Science Foundation of China (62122017).

Conflict of interest

The authors declare no conflict of interest.

Author contributions

Conceptualization: Chen He, Jiasheng Yan
Funding acquisition: Jinhong Guo
Project administration: Jinhong Guo
Supervision: Yusheng Fu, Jiuchuan Guo, Yuxing Shi
Writing - original draft: Chen He, Jiasheng Yan
Writing - review & editing: Chen He, Jiasheng Yan

Ethics approval and consent to participate

Not applicable.

Consent for publication

Not applicable.

Availability of data

Not applicable.

References

1. Lancaster MA, Knoblich JA, 2014, Organogenesis in a dish: Modeling development and disease using organoid technologies. *Science*, 345(6194): 1247125.

   https://doi.org/10.1126/science.1247125

2. Hofer M, Lutolf MP, 2021, Engineering organoids. *Nat Rev Mater*, 6(5): 402–420.

   https://doi.org/10.1038/s41578-021-00279-y

3. Zhao Z, Chen X, Dowbaj AM, *et al.*, 2022, Organoids. *Nat Rev Methods Primers*, 2(1): 94.

   https://doi.org/10.1038/s43586-022-00174-y

4. Sato T, Vries RG, Snippert HJ, *et al.*, 2009, Single Lgr5 stem cells build crypt-villus structures in vitro without a mesenchymal niche. *Nature*, 459(7244): 262–265.

   https://doi.org/10.1038/nature07935

5. Lewis-Israeli YR, Wasserman AH, Gabalski MA, *et al.*, 2021, Self-assembling human heart organoids for the modeling of cardiac development and congenital heart disease. *Nat Commun*, 12(1): 5142.

   https://doi.org/10.1038/s41467-021-25329-5

6. Hofbauer P, Jahnel SM, Papai N, *et al.*, 2021, Cardioids reveal self-organizing principles of human cardiogenesis. *Cell*, 184(12): 3299–3317.e22.

   https://doi.org/10.1016/j.cell.2021.04.034

7. Takasato M, Er PX, Chiu HS, *et al.*, 2015, Kidney organoids from human iPS cells contain multiple lineages and model human nephrogenesis. *Nature*, 526(7574): 564–568.

   https://doi.org/10.1038/nature15695

8. Hu H, Gehart H, Artegiani B, *et al.*, 2018, Long-term expansion of functional mouse and human hepatocytes as 3D organoids. *Cell*, 175(6): 1591–1606.e19.

   https://doi.org/10.1016/j.cell.2018.11.013

9. Lancaster MA, Renner M, Martin C-A, *et al.*, 2013, Cerebral organoids model human brain development and microcephaly. *Nature*, 501(7467): 373–379.

   https://doi.org/10.1038/nature12517

10. Neal JT, Li X, Zhu J, *et al.*, 2018, Organoid modeling of the tumor immune microenvironment. *Cell*, 175(7): 1972–1988.e16.

    https://doi.org/10.1016/j.cell.2018.11.021

11. Monteil V, Kwon H, Prado P, *et al.*, 2020, Inhibition of SARS-CoV-2 infections in engineered human tissues using clinical-grade soluble human ACE2. *Cell*, 181(4): 905–913.e7.

    https://doi.org/10.1016/j.cell.2020.04.004

12. Han Y, Duan X, Yang L, *et al.*, 2021, Identification of SARS-CoV-2 inhibitors using lung and colonic organoids. *Nature*, 589(7841): 270–275.

    https://doi.org/10.1038/s41586-020-2901-9

13. Garreta E, Kamm RD, Chuva de Sousa Lopes SM, *et al.*, 2021, Rethinking organoid technology through bioengineering. *Nat Mater*, 20(2): 145–155.

    https://doi.org/10.1038/s41563-020-00804-4

14. Lawlor KT, Vanslambrouck JM, Higgins JW, *et al.*, 2021, Cellular extrusion bioprinting improves kidney organoid reproducibility and conformation. *Nat Mater*, 20(2): 260–271.

    https://doi.org/10.1038/s41563-020-00853-9

15. Rawal P, Tripathi DM, Ramakrishna S, *et al.*, 2021, Prospects for 3D bioprinting of organoids. *Bio-Des Manuf*, 4(3): 627–640.

    https://doi.org/10.1007/s42242-020-00124-1

16. Gu Z, Fu J, Lin H, *et al.*, 2020, Development of 3D bioprinting: From printing methods to biomedical applications. *Asian J Pharm Sci*, 15(5): 529–557.

    https://doi.org/10.1016/j.ajps.2019.11.003

17. Gungor-Ozkerim PS, Inci I, Zhang YS, *et al.*, 2018, Bioinks for 3D bioprinting: An overview. *Biomater Sci*, 6(5): 915–946.

    https://doi.org/10.1039/C7BM00765E

18. Gu Q, Tomaskovic-Crook E, Lozano R, *et al.*, 2016, Functional 3D neural mini-tissues from printed gel-based

bioink and human neural stem cells. *Adv Healthc Mater*, 5(12): 1429–1438.

https://doi.org/10.1002/adhm.201600095

19. Faulkner-Jones A, Fyfe C, Cornelissen D-J, *et al.*, 2015, Bioprinting of human pluripotent stem cells and their directed differentiation into hepatocyte-like cells for the generation of mini-livers in 3D. *Biofabrication*, 7(4): 044102.

https://doi.org/10.1088/1758-5090/7/4/044102

20. Nguyen D, Hägg DA, Forsman A, *et al.*, 2017, Cartilage tissue engineering by the 3D bioprinting of iPS cells in a nanocellulose/alginate bioink. *Sci Rep*, 7(1): 658.

https://doi.org/10.1038/s41598-017-00690-y

21. Sakai S, Ohi H, Hotta T, *et al.,* 2018, Differentiation potential of human adipose stem cells bioprinted with hyaluronic acid/gelatin-based bioink through microextrusion and visible light-initiated crosslinking. *Biopolymers*, 109(2): e23080.

https://doi.org/10.1002/bip.23080

22. Eswaramoorthy SD, Dhiman N, Joshi A, *et al.,* 2021, 3D bioprinting of mesenchymal stem cells and endothelial cells in an alginate-gelatin-based bioink. *J 3D Print Med*, 5(1): 23–36.

https://doi.org/10.2217/3dp-2020-0026

23. Kolan KCR, Semon JA, Bromet B, *et al.*, 2019, Bioprinting with human stem cells-laden alginate-gelatin bioink and bioactive glass for tissue engineering. *Int J Bioprint*, 5(2.2): 3–15.

https://doi.org/10.18063/ijb.v5i2.2.204

24. Ni T, Liu M, Zhang Y, *et al.*, 2020, 3D bioprinting of bone marrow mesenchymal stem cell-laden silk fibroin double network scaffolds for cartilage tissue repair. *Bioconjugate Chem*, 31: 1938–1947.

https://doi.org/10.1021/acs.bioconjchem.0c00298

25. Das S, Pati F, Choi Y-J, *et al.*, 2015, Bioprintable, cell-laden silk fibroin–gelatin hydrogel supporting multilineage differentiation of stem cells for fabrication of three-dimensional tissue constructs. *Acta Biomater,* 11: 233–246.

https://doi.org/10.1016/j.actbio.2014.09.023

26. Skardal A, Mack D, Kapetanovic E, *et al.,* 2012, Bioprinted amniotic fluid-derived stem cells accelerate healing of large skin wounds. *Stem Cells Translat Med*, 1(11): 792–802.

https://doi.org/10.5966/sctm.2012-0088

27. Han J, Kim DS, Jang H, *et al.,* 2019, Bioprinting of three-dimensional dentin–pulp complex with local differentiation of human dental pulp stem cells. *J Tissue Eng,* 10: 2041731419845849.

https://doi.org/10.1177/2041731419845849

28. Ren Y, Yang X, Ma Z, *et al.,* 2021, Developments and opportunities for 3D bioprinted organoids. *Int J Bioprint*, 7(3): 18–36.

https://doi.org/10.18063/ijb.v7i3.364

29. Koo Y, Kim GH, 2022, Bioprinted hASC-laden collagen/HA constructs with meringue-like macro/micropores. *Bioeng Transl Med,* 7(3): e10330.

https://doi.org/10.1002/btm2.10330

30. Sorkio A, Koch L, Koivusalo L, *et al.*, 2018, Human stem cell based corneal tissue mimicking structures using laser-assisted 3D bioprinting and functional bioinks. *Biomaterials*, 171: 57–71.

https://doi.org/10.1016/j.biomaterials.2018.04.034

31. Moncal KK, Ozbolat V, Datta P, *et al.*, 2019, Thermally-controlled extrusion-based bioprinting of collagen. *J Mater Sci*, 30(5): 55.

https://doi.org/10.1007/s10856-019-6258-2

32. Pati F, Jang J, Ha D-H, *et al.*, 2014, Printing three-dimensional tissue analogues with decellularized extracellular matrix bioink. *Nat Commun,* 5(1): 3935.

https://doi.org/10.1038/ncomms4935

33. Gao G, Yonezawa T, Hubbell K, *et al.,* 2015, Inkjet-bioprinted acrylated peptides and PEG hydrogel with human mesenchymal stem cells promote robust bone and cartilage formation with minimal printhead clogging. *Biotechnol J,* 10(10): 1568–1577.

https://doi.org/10.1002/biot.201400635

34. Gao G, Schilling AF, Hubbell K, *et al.*, 2015, Improved properties of bone and cartilage tissue from 3D inkjet-bioprinted human mesenchymal stem cells by simultaneous deposition and photocrosslinking in PEG-GelMA. *Biotechnol Lett*, 37(11): 2349–2355.

https://doi.org/10.1007/s10529-015-1921-2

35. Armstrong JPK, Burke M, Carter BM, *et al.*, 2016, 3D bioprinting using a templated porous bioink. *Adv Healthc Mater,* 5(14): 1724–1730.

https://doi.org/10.1002/adhm.201600022

36. Jia J, Richards DJ, Pollard S, *et al.*, 2014, Engineering alginate as bioink for bioprinting. *Acta Biomater,* 10(10): 4323–4331.

https://doi.org/10.1016/j.actbio.2014.06.034

37. Wu Z, Su X, Xu Y, *et al.,* 2016, Bioprinting three-dimensional cell-laden tissue constructs with controllable degradation. *Sci Rep*, 6(1): 1–10.

https://doi.org/10.1038/srep24474

38. He H, Li D, Lin Z, *et al.*, 2020, Temperature-programmable and enzymatically solidifiable gelatin-based bioinks enable facile extrusion bioprinting. *Biofabrication,* 12(4): 045003.

https://doi.org/10.1088/1758-5090/ab9906

39. Li J, Moeinzadeh S, Kim C, *et al.*, 2023, Development and systematic characterization of GelMA/alginate/PEGDMA/xanthan gum hydrogel bioink system for extrusion bioprinting. *Biomaterials*, 293: 121969.

https://doi.org/10.1016/j.biomaterials.2022.121969

40. Yu K-F, Lu T-Y, Li Y-CE, *et al.,* 2022, Design and synthesis of stem cell-laden keratin/glycol chitosan methacrylate bioinks for 3D bioprinting. *Biomacromolecules*, 23(7): 2814–2826.

    https://doi.org/10.1021/acs.biomac.2c00191

41. Alcala-Orozco CR, Mutreja I, Cui X, *et al.,* 2020, Design and characterisation of multi-functional strontium-gelatin nanocomposite bioinks with improved print fidelity and osteogenic capacity. *Bioprinting*, 18: e00073.

    https://doi.org/10.1016/j.bprint.2019.e00073

42. Rousselle A, Ferrandon A, Mathieu E, *et al.,* 2022, Enhancing cell survival in 3D printing of organoids using innovative bioinks loaded with pre-cellularized porous microscaffolds. *Bioprinting,* 28: e00247.

    https://doi.org/10.1016/j.bprint.2022.e00247

43. Cofiño C, Perez-Amodio S, Semino CE, *et al.*, 2019, Development of a self-assembled peptide/methylcellulose-based bioink for 3D bioprinting. *Macromol Mater Eng*, 304(11): 1900353.

    https://doi.org/10.1002/mame.201900353

44. Alhattab D, Khan Z, Alshehri S, *et al.*, 2023, 3D bioprinting of ultrashort self-assembling peptides to engineer scaffolds with different matrix stiffness for chondrogenesis. *Int J Bioprint*, 9(4): 719.

    https://doi.org/10.18063/ijb.719

45. Jeong W, Kim MK, Kang H-W, 2021, Effect of detergent type on the performance of liver decellularized extracellular matrix-based bio-inks. *J Tissue Eng*, 12: 20417314219970 91.

    https://doi.org/10.1177/20417314219970 91

46. Panwar A, Tan L, 2016, Current status of bioinks for micro-extrusion-based 3D bioprinting. *Molecules*, 21(6): 685.

    https://doi.org/10.3390/molecules21060685

47. Xu Z, Huang J, Liu Y, *et al.*, 2023, Extracellular matrix bioink boosts stemness and facilitates transplantation of intestinal organoids as a biosafe Matrigel alternative. *Bioeng Transl Med,* 8(1): e10327.

    https://doi.org/10.1002/btm2.10327

48. Zhang X, Liu Y, Luo C, *et al.,* 2021, Crosslinker-free silk/decellularized extracellular matrix porous bioink for 3D bioprinting-based cartilage tissue engineering. *Mater Sci Eng C*, 118: 111388.

    https://doi.org/10.1016/j.msec.2020.111388

49. He Y, Gu Z, Xie M, *et al.,* 2020, Why choose 3D bioprinting? Part II: Methods and bioprinters. *Bio-Des Manuf*, 3(1): 1–4.

    https://doi.org/10.1007/s42242-020-00064-w

50. Chen J, Zhou D, Nie Z, *et al.,* 2022, A scalable coaxial bioprinting technology for mesenchymal stem cell microfiber fabrication and high extracellular vesicle yield. *Biofabrication*, 14(1): 015012.

    https://doi.org/10.1088/1758-5090/ac3b90

51. Gong Z, Huang L, Tang X, *et al.*, 2021, Acoustic droplet printing tumor organoids for modeling bladder tumor immune microenvironment within a week. *Adv Healthc Mater,* 10(22): 2101312.

    https://doi.org/10.1002/adhm.202101312

52. Adine C, Ng KK, Rungarunlert S, *et al.,* 2018, Engineering innervated secretory epithelial organoids by magnetic three-dimensional bioprinting for stimulating epithelial growth in salivary glands. *Biomaterials*, 180: 52–66.

    https://doi.org/10.1016/j.biomaterials.2018.06.011

53. Pati F, Jang J, Lee JW, *et al.,* 2015, Extrusion bioprinting, in *Essentials of 3D Biofabrication and Translation*, Academic Press, Boston, 123–152.

    https://doi.org/10.1016/B978-0-12-800972-7.00007-4

54. Shinkar K, Rhode K, 2022, Could 3D extrusion bioprinting serve to be a real alternative to organ transplantation in the future? *Ann 3D Print Med*, 7: 100066.

    https://doi.org/10.1016/j.stlm.2022.100066

55. Lim W, Kim GJ, Kim HW, *et al.,* 2020, Kappa-Carrageenan-based dual crosslinkable bioink for extrusion type bioprinting. *Polymers*, 12(10): 2377.

    https://doi.org/10.3390/polym12102377

56. Moxon SR, Cooke ME, Cox SC, *et al.*, 2017, Suspended manufacture of biological structures. *Adv Mater*, 29(13): 1605594.

    https://doi.org/10.1002/adma.201605594

57. Cooke ME, Rosenzweig DH, 2021, The rheology of direct and suspended extrusion bioprinting. *APL Bioeng,* 5(1): 011502.

    https://doi.org/10.1063/5.0031475

58. Lee A, Hudson AR, Shiwarski DJ, *et al.*, 2019, 3D bioprinting of collagen to rebuild components of the human heart. *Science*, 365(6452): 482–487.

    https://doi.org/10.1126/science.aav9051

59. McCormack A, Highley CB, Leslie NR, *et al.,* 2020, 3D printing in suspension baths: Keeping the promises of bioprinting afloat. *Trends Biotechnol,* 38(6): 584–593.

    https://doi.org/10.1016/j.tibtech.2019.12.020

60. Yeo M, Ha J, Lee H, *et al.*, 2016, Fabrication of hASCs-laden structures using extrusion-based cell printing supplemented with an electric field. *Acta Biomater,* 38: 33–43.

    https://doi.org/10.1016/j.actbio.2016.04.017

61. Gudapati H, Dey M, Ozbolat I, 2016, A comprehensive review on droplet-based bioprinting: Past, present and future. *Biomaterials*, 102: 20–42.

    https://doi.org/10.1016/j.biomaterials.2016.06.012

62. Saunders RE, Derby B, 2014, Inkjet printing biomaterials for tissue engineering: Bioprinting. *Int Mater Rev,* 59(8): 430–448.

https://doi.org/10.1179/1743280414Y.0000000040

63. Li X, Liu B, Pei B, *et al.*, 2020, Inkjet bioprinting of biomaterials. *Chem Rev*, 120(19): 10793–10833.

https://doi.org/10.1021/acs.chemrev.0c00008

64. Zhao D, Xu H, Yin J, *et al.*, 2022, Inkjet 3D bioprinting for tissue engineering and pharmaceutics. *J Zhejiang Univ Sci A*, 23(12): 955–973.

https://doi.org/10.1631/2023.A2200569

65. Ventura RD, 2021, An overview of laser-assisted bioprinting (LAB) in tissue engineering applications. *Med Lasers,* 10(2): 76–81.

https://doi.org/10.25289/ML.2021.10.2.76

66. Dou C, Perez V, Qu J, *et al.*, 2021, A state-of-the-art review of laser-assisted bioprinting and its future research trends. *CBEN*, 8(5): 517–534.

https://doi.org/10.1002/cben.202000037

67. Murphy SV, Atala A, 2014, 3D bioprinting of tissues and organs. *Nat Biotechnol*, 32(8): 773–785.

https://doi.org/10.1038/nbt.2958

68. Huang Y, Zhang X-F, Gao G, *et al.*, 2017, 3D bioprinting and the current applications in tissue engineering. *Biotechnol J*, 12(8): 1600734.

https://doi.org/10.1002/biot.201600734

69. Zheng Z, Eglin D, Alini M, *et al.*, 2021, Visible light-induced 3D bioprinting technologies and corresponding bioink materials for tissue engineering: A review. *Engineering*, 7(7): 966–978.

https://doi.org/10.1016/j.eng.2020.05.021

70. Grix T, Ruppelt A, Thomas A, *et al.*, 2018, Bioprinting perfusion-enabled liver equivalents for advanced organ-on-a-chip applications. *Genes*, 9(4): 176.

https://doi.org/10.3390/genes9040176

71. Goodarzi Hosseinabadi H, Dogan E, Miri AK, *et al.*, 2022, Digital light processing bioprinting advances for microtissue models. *ACS Biomater Sci Eng*, 8(4): 1381–1395.

https://doi.org/10.1021/acsbiomaterials.1c01509

72. Xie C, Liang R, Ye J, *et al.,* 2022, High-efficient engineering of osteo-callus organoids for rapid bone regeneration within one month. *Biomaterials*, 288: 121741.

https://doi.org/10.1016/j.biomaterials.2022.121741

73. Li H, Dai J, Wang Z, *et al.*, 2022, Digital light processing (DLP)-based (bio)printing strategies for tissue modeling and regeneration. *Aggregate,* 4(2): e270.

https://doi.org/10.1002/agt2.270

74. Xu H, Su Y, Liao Z, *et al.*, 2022, Coaxial bioprinting vascular constructs: A review. *Eur Polym J,* 179: 111549.

https://doi.org/10.1016/j.eurpolymj.2022.111549

75. Vijayavenkataraman S, Yan W-C, Lu WF, *et al.*, 2018, 3D bioprinting of tissues and organs for regenerative medicine. *Adv Drug Deliv Rev,* 132: 296–332.

https://doi.org/10.1016/j.addr.2018.07.004

76. Ng WL, Lee JM, Yeong WY, *et al.*, 2017, Microvalve-based bioprinting – process, bio-inks and applications. *Biomater Sci*, 5(4): 632–647.

https://doi.org/10.1039/C6BM00861E

77. Faulkner-Jones A, Greenhough S, King J, *et al.*, 2013, Development of a valve-based cell printer for the formation of human embryonic stem cell spheroid aggregates. *Biofabrication*, 5(1): 015013.

https://doi.org/10.1088/1758-5082/5/1/015013

78. Matai I, Kaur G, Seyedsalehi A, *et al.,* 2020, Progress in 3D bioprinting technology for tissue/organ regenerative engineering. *Biomaterials*, 226: 119536.

https://doi.org/10.1016/j.biomaterials.2019.119536

79. Lee JM, Sing SL, Zhou M, *et al.,* 2018, 3D bioprinting processes: A perspective on classification and terminology. *Int J Bioprint*, 4(2): 151.

https://doi.org/10.18063/ijb.v4i2.151

80. Adine C, Ferreira J, 2020, Bioprinting strategies to engineer functional salivary gland organoids, in *Organ Tissue Engineering*, Springer International Publishing, Cham, 1–22.

https://doi.org/10.1007/978-3-030-18512-1_5-1

81. Grebenyuk S, Ranga A, 2019, Engineering organoid vascularization. *Front Bioeng Biotechnol*, 7: 39.

https://doi.org/10.3389/fbioe.2019.00039

82. Przepiorski A, Sander V, Tran T, *et al.,* 2018, A simple bioreactor-based method to generate kidney organoids from pluripotent stem cells. *Stem Cell Rep,* 11(2): 470–484.

https://doi.org/10.1016/j.stemcr.2018.06.018

83. Zhang Y, Kumar P, Lv S, *et al.*, 2021, Recent advances in 3D bioprinting of vascularized tissues. *Mater Design,* 199: 109398.

https://doi.org/10.1016/j.matdes.2020.109398

84. Barrs RW, Jia J, Silver SE, *et al.,* 2020, Biomaterials for bioprinting microvasculature. *Chem Rev*, 120(19): 10887–10949.

https://doi.org/10.1021/acs.chemrev.0c00027

85. Jia W, Gungor-Ozkerim PS, Zhang YS, *et al.*, 2016, Direct 3D bioprinting of perfusable vascular constructs using a blend bioink. *Biomaterials*, 106: 58–68.

https://doi.org/10.1016/j.biomaterials.2016.07.038

86. Hong S, Kim JS, Jung B, *et al.*, 2019, Coaxial bioprinting of cell-laden vascular constructs using a gelatin–tyramine bioink. *Biomater Sci*, 7(11): 4578–4587.

https://doi.org/10.1039/C8BM00618K

87. Barrs RW, Jia J, Ward M, *et al.,* 2021, Engineering a chemically defined hydrogel bioink for direct bioprinting of microvasculature. *Biomacromolecules*, 22(2): 275–288.

https://doi.org/10.1021/acs.biomac.0c00947

88. Kolesky DB, Truby RL, Gladman AS, *et al.*, 2014, 3D Bioprinting of vascularized, heterogeneous cell-laden tissue constructs. *Adv Mater*, 26(19): 3124–3130.

https://doi.org/10.1002/adma.201305506

89. Skylar-Scott MA, Uzel SGM, Nam LL, *et al.,* 2019, Biomanufacturing of organ-specific tissues with high cellular density and embedded vascular channels. *Sci Adv*, 5(9): eaaw2459.

https://doi.org/10.1126/sciadv.aaw2459

90. Humphreys BD, 2021, Bioprinting better kidney organoids. *Nat Mater*, 20(2): 128–130.

https://doi.org/10.1038/s41563-020-00881-5

91. Wang D, Guo Y, Zhu J, *et al.*, 2022, Hyaluronic acid methacrylate/pancreatic extracellular matrix as a potential 3D printing bioink for constructing islet organoids. *Acta Biomater,* S1742706122003750.

https://doi.org/10.1016/j.actbio.2022.06.036

92. Zhu B, Wang D, Pan H, *et al.,* 2023, Three-in-one customized bioink for islet organoid: GelMA/ECM/PRP orchestrate pro-angiogenic and immunoregulatory function. *Colloid Surf B: Biointerfaces,* 221: 113017.

https://doi.org/10.1016/j.colsurfb.2022.113017

93. Noor N, Shapira A, Edri R, *et al.*, 2019, 3D Printing of personalized thick and perfusable cardiac patches and hearts. *Adv Sci*, 6(11): 1900344.

https://doi.org/10.1002/advs.201900344

94. Zhao H, Chen Y, Shao L, *et al.*, 2018, Airflow-assisted 3D bioprinting of human heterogeneous microspheroidal organoids with microfluidic nozzle. *Small*, 14(39): 1802630.

https://doi.org/10.1002/smll.201802630

95. He Y, Nie J, Xie M, *et al.*, 2020, Why choose 3D bioprinting? Part III: Printing in vitro 3D models for drug screening. *Bio-Des Manuf*, 3(3): 160–163.

https://doi.org/10.1007/s42242-020-00067-7

96. Yan J, Li Z, Guo J, *et al.*, 2022, Organ-on-a-chip: A new tool for in vitro research. *Biosens Bioelectron*, 216: 114626.

https://doi.org/10.1016/j.bios.2022.114626

97. Gao G, Ahn M, Cho W-W, *et al.*, 2021, 3D printing of pharmaceutical application: Drug screening and drug delivery. *Pharmaceutics*, 13(9): 1373.

https://doi.org/10.3390/pharmaceutics13091373

98. Bouwmeester MC, Bernal PN, Oosterhoff LA, *et al.*, 2021, Bioprinting of human liver-derived epithelial organoids for toxicity studies. *Macromol Biosci*, 21(12): 2100327.

https://doi.org/10.1002/mabi.202100327

99. Skardal A, Murphy SV, Devarasetty M, *et al.,* 2017, Multi-tissue interactions in an integrated three-tissue organ-on-a-chip platform. *Sci Rep*, 7(1): 8837.

https://doi.org/10.1038/s41598-017-08879-x

100. Jain P, Kathuria H, Dubey N, 2022, Advances in 3D bioprinting of tissues/organs for regenerative medicine and in-vitro models. *Biomaterials*, 287: 121639.

https://doi.org/10.1016/j.biomaterials.2022.121639

101. Yang H, Sun L, Pang Y, *et al.*, 2021, Three-dimensional bioprinted hepatorganoids prolong survival of mice with liver failure. *Gut*, 70(3): 567–574.

https://doi.org/10.1136/gutjnl-2019-319960

102. Kang Y, Datta P, Shanmughapriya S, *et al.*, 2020, 3D bioprinting of tumor models for cancer research. *ACS Appl Bio Mater*, 3(9): 5552–5573.

https://doi.org/10.1021/acsabm.0c00791

103. Chen H, Wu Z, Gong Z, *et al.*, 2022, Acoustic bioprinting of patient-derived organoids for predicting cancer therapy responses. *Adv Healthc Mater,* 11(13): 2102784.

https://doi.org/10.1002/adhm.202102784

104. Mao S, Pang Y, Liu T, *et al.*, 2020, Bioprinting of *in vitro* tumor models for personalized cancer treatment: A review. *Biofabrication*, 12(4): 042001.

https://doi.org/10.1088/1758-5090/ab97c0

105. Kim E, Choi S, Kang B, *et al.,* 2020, Creation of bladder assembloids mimicking tissue regeneration and cancer. *Nature*, 588: 664–669.

https://doi.org/10.1038/s41586-020-3034-x

106. Schneeberger K, Spee B, Costa P, *et al.*, 2017, Converging biofabrication and organoid technologies: The next frontier in hepatic and intestinal tissue engineering? *Biofabrication*, 9(1): 013001.

https://doi.org/10.1088/1758-5090/aa6121

107. Brassard JA, Nikolaev M, Hübscher T, *et al.*, 2021, Recapitulating macro-scale tissue self-organization through organoid bioprinting. *Nat Mater*, 20(1): 22–29.

https://doi.org/10.1038/s41563-020-00803-5

108. Clark CC, Yoo KM, Sivakumar H, *et al.*, 2023, Immersion bioprinting of hyaluronan and collagen bioink-supported 3D patient-derived brain tumor organoids. *Biomed Mater*, 18(1): 015014.

https://doi.org/10.1088/1748-605X/aca05d

109. Hospodiuk M, Dey M, Sosnoski D, *et al.*, 2017, The bioink: A comprehensive review on bioprintable materials. *Biotechnol Adv,* 35(2): 217–239.

https://doi.org/10.1016/j.biotechadv.2016.12.006

110. Liu M, Jiang S, Witman N, *et al.*, 2023, Intrinsically cryopreservable, bacteriostatic, durable glycerohydrogel inks for 3D bioprinting. *Matter*, 6(3): 983–999.

https://doi.org/10.1016/j.matt.2022.12.013

111. Serex L, Sharma K, Rizov V, *et al.,* 2021, Microfluidic-assisted bioprinting of tissues and organoids at high cell concentrations. *Biofabrication*, 13(2): 025006.

https://doi.org/10.1088/1758-5090/abca80

112. Zhang YS, Pi Q, van Genderen AM, 2017, Microfluidic bioprinting for engineering vascularized tissues and organoids. *JoVE*, (126): 55957.

https://doi.org/10.3791/55957

113. Amukarimi S, Mozafari M, 2021, 4D bioprinting of tissues and organs. *Bioprinting*, 23: e00161.

https://doi.org/10.1016/j.bprint.2021.e00161

114. Kim SH, Seo YB, Yeon YK, *et al.*, 2020, 4D-bioprinted silk hydrogels for tissue engineering. *Biomaterials*, 260: 120281.

https://doi.org/10.1016/j.biomaterials.2020.120281

115. Lee H, 2023, Engineering in vitro models: Bioprinting of organoids with artificial intelligence. *Cyborg Bionic Syst,* 4: 0018.

https://doi.org/10.34133/cbsystems.0018

ACCSCIENCE PUBLISHING

International Journal of Bioprinting

RESEARCH ARTICLE

Development of an affordable extrusion 3D bioprinter equipped with a temperature-controlled printhead

Carlos Ezio Garciamendez-Mijares[1,2,3†], Gilberto Emilio Guerra-Alvarez[1,2†], Mónica Gabriela Sánchez-Salazar[1,4], Andrés García-Rubio[1,2,3], Germán García-Martínez[1,2,3], Anne-Sophie Mertgen[1,4], Carlos Fernando Ceballos-González[1,4], Edna Johana Bolivar-Monsalve[1,4], Yu Shrike Zhang[3], Grissel Trujillo-de Santiago[1,2,5*], and Mario Moisés Alvarez[1,2,5*]

[1]Centro de Biotecnología-FEMSA, Tecnológico de Monterrey, Monterrey, Nuevo León, México

[2]Departamento de Ingeniería Mecatrónica y Eléctrica, Tecnológico de Monterrey, Monterrey, Nuevo León, México

[3]Division of Engineering in Medicine, Department of Medicine, Brigham and Women's Hospital, Harvard Medical School, Harvard, Cambridge, Massachusetts, USA

[4]Departamento de Bioingeniería, Tecnológico de Monterrey, Monterrey, Nuevo León, México

[5]Research and Development Unit, Forma Foods, Monterrey, Nuevo León, México

[†]These authors contributed equally to this work.

***Corresponding authors:**
Mario Moisés Alvarez (mario.alvarez@tec.mx)

Grissel Trujillo-de Santiago (grissel@tec.mx)

Citation: Garciamendez-Mijares CE, Guerra-Alvarez GE, Sánchez-Salazar MG, *et al*., 2023, Development of an affordable extrusion 3D bioprinter equipped with a temperature-controlled printhead. *Int J Bioprint*, 9(6): 0244. https://doi.org/10.36922/ijb.0244

Received: October 31, 2022
Accepted: December 22, 2022
Published Online: July 5, 2023

Copyright: © 2023 Author(s). This is an Open Access article distributed under the terms of the Creative Commons Attribution License, permitting distribution and reproduction in any medium, provided the original work is properly cited.

Publisher's Note: AccScience Publishing remains neutral with regard to jurisdictional claims in published maps and institutional affiliations.

Abstract

Bioprinters show great promise as enablers of regenerative medicine and other biomedical engineering applications. In this work, we present a flexible and cost-effective design for a do-it-yourself bioprinter capable of printing/bioprinting gelatin methacryloyl (GelMA) and Pluronic constructs at flow rates of 0.05–0.1 mL/min and effective resolutions of 500–700 µm. The most distinctive feature of this bioprinter is its ability to control the rheology of bioinks simply by adjusting the extrusion temperature during printing. This is achieved by circulating temperature-controlled water within the printhead, which is engineered as a single 3D-printed component consisting of a water-recirculation jacket surrounding the ink/bioink cartridge. The flexibility to circulate either warm or cold water allows the system to be adapted according to the needs dictated by the bioink composition. Herein, we demonstrate the ability to control the printability of GelMA or Pluronic fibers by decreasing or increasing the temperature, respectively, thereby regulating its viscosity. In addition, any commercial needle with a Luer lock can be incorporated into the printhead, allowing the easy fabrication of fibers of different diameters with a single printhead. We showed that our bioprinter is capable of printing simple 2D constructs with high fidelity (i.e., lines of GelMA with a thickness of ~522 ± 36.83 µm can be printed at linear speeds of 100 mm min^{-1}) and 3D constructs composed of as many as five layers of cell-laden 5% GelMA. We also demonstrated that C2C12 cells bioprinted through needle tips (300 µm in diameter) exhibit adequate post-printing viability (~90%), as well as spreading after 7 days of culture. The presentation of this bioprinter may contribute appreciably to the expansion of bioprinter use due to its low overall cost of manufacture, flexibility and open-source character, amenability to modification and adaptation for use with different 3D-printed printheads, and ability to bioprint using GelMA.

Keywords: Do-it-yourself bioprinter; GelMA; Open-source; Bioprinting; Temperature-controlled printhead; Temperature-dependent rheology.

1. Introduction

Bioprinters show great promise in tissue engineering and regenerative medicine[1-5]. At present, a wide spectrum of bioprinters is available from several companies[2,6,7]. Commercial bioprinters currently support relevant research and developmental efforts[7-10]. Nevertheless, bioprinting is still far from being a mature or widespread technology in bioengineering laboratories[9,11,12].

Indisputably, one of the most prominent limitations for the development of bioprinting in these fields is the present cost of commercial bioprinters, particularly for researchers in academic[2,13] and educational settings[10,14]. State-of-the-art commercial bioprinters have a market value between 20,000 and 1,000,000 USD[15,16]. An additional problem, frequently mentioned by users, is the lack of flexibility and ease of customization of the available devices[17]. A significant fraction of the bioprinting community still perceives commercial bioprinters as equipment that is difficult to modify or adapt for use in new or specific applications. The relatively high cost of the commercial equipment and the perception of insufficient flexibility have therefore motivated the development of a good number of low-cost do-it-yourself (DiY) or open-source bioprinters[13,18-22].

The bioinks available for bioprinting add other technical limitations that further restrict the more extensive use of currently available bioprinters[1,17,23,24]. One of the more serious of these limitations is the restricted resolution imposed by the rheology of the bioinks[17,25-27]. For instance, gelatin methacryloyl (GelMA), one of the most widely used inks in bioprinting[17] and tissue engineering[28] applications, has rheological properties that depend strongly on temperature[29,30]. Specifically, GelMA must be kept cool during extrusion to ensure sufficient viscosity for bioprinting, as its effective viscosity significantly increases at a temperature range of 15°C to 5°C compared to room temperature conditions[25,29,31]. A consistent viscosity is crucial for GelMA printability; therefore, manipulation of the rheology, and thus the resolution, of GelMA-based inks/bioinks by controlling the extrusion temperature is a promising approach. Unfortunately, only a limited number of bioprinters can control the bioink temperature in the range of 5°C–15°C, and these devices again tend to be cost prohibitive[2].

In the present study, we describe the transformation of a commercially available 3D printer ($200–300 USD) into a fully functional 3D bioprinter capable of bioink temperature control in the range of 5°C–35°C. This extrusion-based bioprinter is equipped with a cooling/heating jacket integrated into the printhead and is ideally suited for use with printing inks whose viscosities strongly rely on temperature. By precisely controlling the temperature during extrusion, we demonstrate considerable control of the rheological properties of the inks/bioinks and therefore their printability. We also provide a protocol that will allow the reader to reproduce this open-source device, and we include detailed information on both the hardware development and the bioprinting process. Lastly, we demonstrate that our bioprinter is capable of printing GelMA-based and Pluronic-based inks with high fidelity and resolution, as well as cell-laden bioinks that show adequate cell viability after extrusion.

2. Materials and methods

2.1. 3D printer

The modification process and method explained in this work are based on the Anet A8 3D (Anet 3D Printer, France) printer, but they will also work on other similar 3D printers (e.g., Prusa i3 clones), with minor changes.

2.2. 3D printer modifications

After successful assembly of the 3D printer, which can be accomplished in less than 8 h, several modifications were made to convert it to a bioprinter. Each modification was implemented to increase the resolution and quality of subsequent (bio)prints. Most of the modifications were taken directly from open-source designs found on Thingiverse*[32] and are described in the following sections. As a note to the reader, the open-source standard tessellation language STL files are also available in the **Supplementary File**.

We improved the mechanical robustness of the 3D printer to increase its resolution. We did this by 3D-printing several parts using polylactic acid (PLA), or a similar 3D printer filament, and then incorporating them onto the printer frame. The first modification consisted of adding T-corner supports to minimize vibrations from wobbling of the upper frames of the printer (**Figure S1A** and **B**). We then added belt-tensioner mechanisms to the *X*- and *Y*-axes (**Figure S1C** and **D**) to increase the resolution; these belt-tensioners could be adjusted as needed, thereby minimizing vibrations. Finally, large braces were added to the front and rear frames on the underside of the (bio)printer to eliminate small vibrations that could lead to (bio)printing offsets (**Figure S1E** and **F**). **Figure S1** also shows a visual representation of the location of the 3D-printed modifications/additions in relation to the original printer frame.

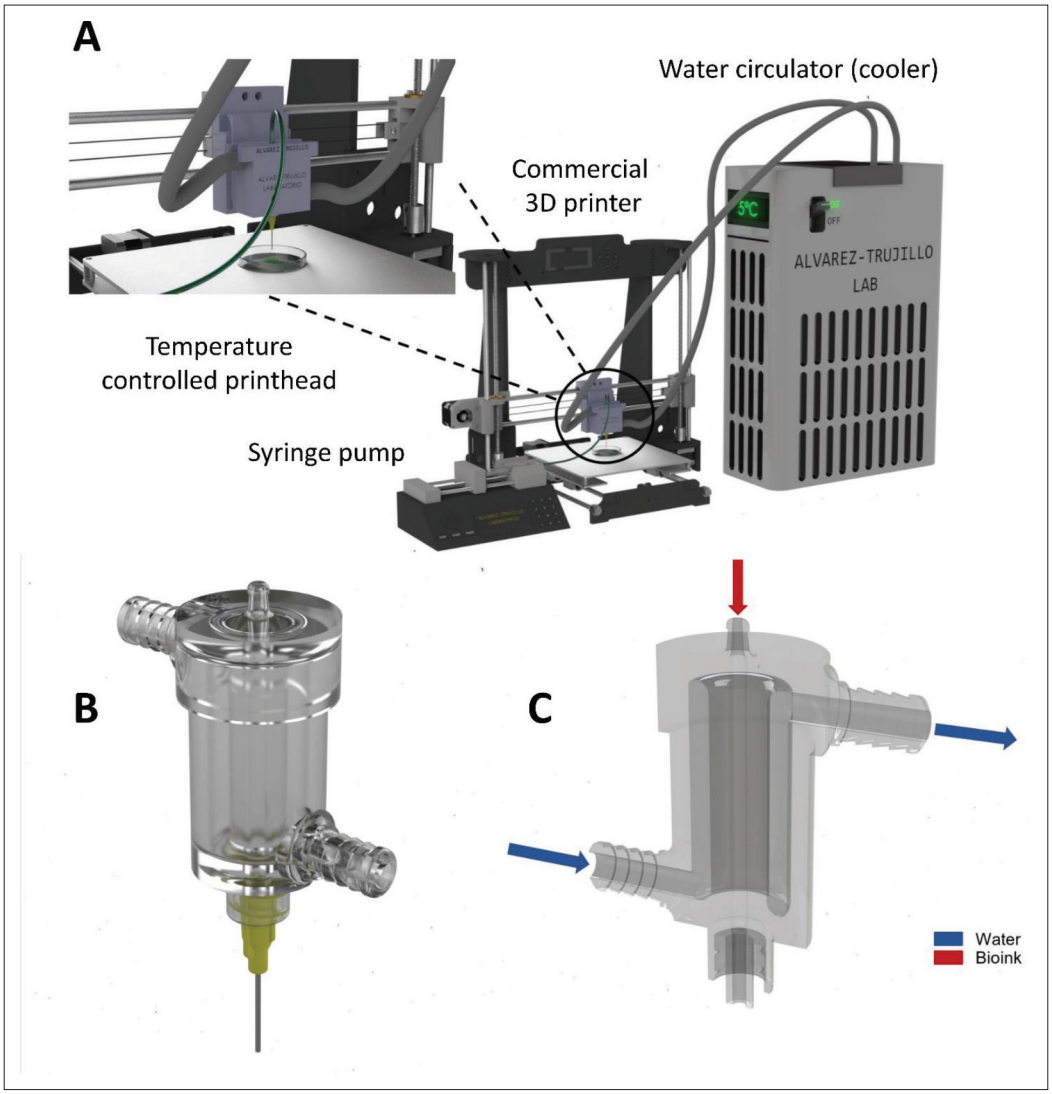

Figure 1. Schematic of the bioprinter system. (A) Full system showing the integrated printhead, modified 3D printer, syringe pump, water cooler, and tubing. Close-up image shows the extruder mount with the bioink and water tubing connected to the printhead. (B) Cooling printhead with a water jacket to cool the extruded bioink and Luer lock connector allowing interchanges of needles of any size. (C) Schematic of the counterflow of the bioink inside the bioink chamber and the encapsulating circulating water compartment in the printhead jacket.

The electronics of the printer were also modified as follows. The stock electronic components of the printer, including the motherboard and an LCD 2004 screen, were replaced with an Arduino Mega 2560 board, a RepRap Arduino Mega Pololu Shield (RAMPS) 1.4 controller, three Pololu A4988 stepper motor drivers, and a RAMPS 20 × 4 LCD display board. The extruder motor, cooling fans, extruder heater, and thermistor were also disconnected and removed. The original power supply of the printer was retained, as were the *X*-, *Y*-, and *Z*-axis motors. A diagram of the final electrical wiring is provided in **Figure S2**. In addition, two attachments for the new electronics were 3D-printed: a case for the LCD display board and an adapter to support the Arduino Mega on the left side panel of the frame (**Figure S3A** and **B**).

2.3. Bioprinter setup

The bioprinter setup consisted of the modified Anet A8 3D printer, the cooling/heating printhead, a Yamato CF301 water circulator (Yamato Scientific, Japan), a Chemyx Fusion 200 syringe pump (Chemyx Inc., USA) (Figure 1A), a 21G blunt-tip needle, and a 10-mL syringe (containing the desired bioink) connected to plastic tubing (0.25 cm in internal diameter) approximately 13 cm in length. The water circulator system was used with maximum flow at approximately 7.2 L min^{-1}, and the default control system.

A mixture of 40% ethanol and 60% tap water (v/v) was used in the water circulator reservoir to prevent freezing. For cooling applications, prior to printing, the Yamato CF301 circulator was set to a temperature of −5°C to −10°C and was left for 30 min to ensure the stabilization of the circulating water temperature. The room temperature was set to 20°C and left to stabilize for 30 min as well. The ink/bioink-loaded syringe was purged to remove air bubbles and then placed for 20 min in a refrigerator set at a temperature of 4°C. The circulator hose was connected to the side fittings of the cooling nozzle (Figure 1B) to enable a counter-flow between the water and the ink/bioink (i.e., the ink traveled in the downward direction while the water circulated in the upward direction) to maintain the water jacket full and maximize heat transfer (Figure 1C).

2.4. Cooling/heating nozzle and mount fabrication

The temperature-controlled printhead (i.e., the cooling/heating printhead) is a distinctive feature of the bioprinter described here (Figure 1B and C). This printhead was 3D-printed at a resolution/layer height of 80 µm from white Peopoly professional ultraviolet (UV) resin (Moai Peopoly, USA) using a stereolithography apparatus (SLA) printer obtained from the same supplier. The cooling/heating nozzle had internal volumes of 0.197 cm^3 and 4.35 cm^3 for the ink reservoir and the external circulating water, respectively. The bottom tip of the cooling/heating nozzle had a male Luer lock fitting that enabled the use of different commercial needles with varying diameters. The sides of the printhead had two fittings for connection to a cooling/heating water circulator. The top had a small fitting for insertion of the plastic tubing that serves as the inlet for the inks/bioinks.

The original extruder of the 3D printer was replaced with a custom-made *X*-axis extruder carriage and mounted to hold the cooling nozzle (**Figure S3C** and **D**). These accessories were also 3D-printed using PLA (Hatchbox, USA) at a layer height of 0.28 mm. The corresponding designs are provided in the **Supplementary File**. The custom carriage used the same screws that held the stock carriage, whereas the new mount required four M3 screws with their respective hex nuts to secure the cooling/heating nozzle. We reduced the number of screws needed by employing a coupling design inspired by traditional Japanese joinery[33] to attach the custom carriage mount.

2.5. Inks preparation and rheological characterization

GelMA with 10% methacryloyl substitution was prepared in-house according to previously published protocols[28]. The GelMA ink was prepared by dissolving GelMA in Dulbecco's phosphate-buffered saline (DPBS, Sigma-Aldrich, USA) at 5% (w/v) at 70°C for 20 min. This GelMA solution was combined with 0.056% (w/v) lithium phenyl-2,4,6-trimethylbenzoylphosphinate (LAP) (Cellink, Sweden) used as a photoinitiator. The GelMA ink was fed into a syringe, allowed to cool down to room temperature, and then stored in a refrigerator at 4°C until used for bioprinting. An aqueous solution of 25% Pluronic F-127 (w/v) for additional printing experiments was prepared by stirring in a water bath precooled with ice. The powder was added and agitated for 40 min until complete dissolution.

The rheology of the GelMA and Pluronic hydrogels was evaluated using an MCR 500 rheometer (Anton-Paar Rheoplus, Austria) equipped with a Peltier cooler for temperature control. Parallel plate geometry (50 mm) was used with a gap of 0.5 mm to determine rheological properties. The GelMA and Pluronic inks were tempered at 37°C before rheology testing; their viscosity was measured with a temperature ramping from 40°C to 10°C at a cooling rate of 1°C min^{-1} and a constant shear rate of 1 s^{-1}. Shear stress was evaluated by varying the shear rate range between 0.01 and 1000 s^{-1} in a rotational test at 14°C. The storage (G′) and loss (G″) moduli were measured as a function of temperature at a constant frequency of 1 Hz and a constant strain of 0.1% in a temperature range of 4°C–40°C at a cooling rate of 1°C min^{-1}.

2.6. Printing/bioprinting protocols

Our printing/bioprinting workflow consisted of preparing a 3D model of a desired structure using computer-aided design (CAD) software (SolidWorks, Dassault Systèmes, France, in our case), exporting the model as a STL file, and then slicing the file to obtain the G-code of the print. Repetier-Host (Repetier, Germany) was used as the host software[2] for manual control of the bioprinter, for slicing STL files into G-code, and for running printing routines. Standard petri dishes were used as printing platforms, and a laser-cut piece of polymethyl methacrylate (PMMA) and binder clips were used to anchor the petri dish to the printer bed to maximize stability (**Figure S3E**). We attained the correct height of the first layer for a particular construct by dampening a piece of paper with ethanol and placing it on the surface of the petri dish (**Figure S3E**). The printhead was then manually moved over the petri dish and lowered progressively until slight friction was observed between the paper and the needle. After removal of the syringe containing the ink/bioink from the refrigerator, the syringe outlet was carefully connected to the inlet of the printhead using plastic tubing, and the syringe was placed on the syringe pump, which was located beside the bioprinter. Approximately 30 cm of space was cleared around the bioprinter, and all surfaces were cleaned with 70% ethanol to minimize

the possibility of sample contamination and any potential damage to the system. A scheme of the complete bioprinter setup is shown in Figure 1A.

A syringe pump flow rate of 0.1 mL/min was used to extrude the ink/bioink down to the tip of the cooling nozzle. The flow rate was then changed and maintained at 0.05 mL/min to avoid freezing the bioink and clogging the cooling/heating nozzle. We ascertained that a stream of filament of constant thickness was observed for at least 20 s to ensure good bioprinting quality. In cases of clogging due to unexpected freezing of the bioink, the tubing on the top was disconnected and hot water at 70°C was injected into the printhead through the top fitting. Subsequently, the bioprinting protocol was restarted.

2.7. Printability assays

A series of experiments was conducted to study the effect of the nozzle feed rate on the thickness of the printed GelMA or Pluronic lines and to determine the optimal printing parameters. We analyzed three different feed rates at a fixed flow rate in a single test to generate a custom G-code. This G-code enabled the sequential printing of three different squares (5 × 5 mm^2), in which the linear velocity decreased from the first to the third. The printability was quantitatively analyzed by measuring the dimensions (i.e., line thickness and square area) of the printed squares by image analysis with ImageJ[34,35]. Different 2D structures were also printed utilizing our printhead, with and without temperature control.

2.8. Cell culture, cell-laden bioink preparation, and cell viability assessment

C2C12 myoblasts (CRL 1772, ATCC, USA) were cultured to about 80% confluency in Dulbecco's modified Eagle's medium (DMEM, Sigma-Aldrich, USA) supplemented with 10% fetal bovine serum (Thermo Fisher, USA) and 1% penicillin-streptomycin (Sigma-Aldrich, USA) at 37°C, 5% CO_2, and 100% humidity. For bioink preparation, the cultured C2C12 cells were trypsinized, collected, and resuspended in the GelMA pregel solution at a concentration of 1 × 10^6 cells/mL. This bioink was charged into a 10-mL syringe (BD Plastics, USA) and refrigerated at 4°C for 20 min before loading into the syringe pump for bioprinting.

The GelMA-based bioink was bioprinted in a grid pattern and in the shape of the logo of Tecnologico de Monterrey using a flow rate of 0.05 mL/min, a feed rate (i.e., nozzle linear speed) of 300 mm/min, and a water circulation temperature of −5°C. The bioprinted patterns were subsequently UV-crosslinked using an Omnicure 2000 (Excelitas Technologies, USA) apparatus for 60 s at 800 mJ/s. DMEM was added to the bioprinted structures until further assessment.

For evaluation of the postprinting cell viability, the cells were stained using a Live/Dead kit (Thermo Fisher, USA). The staining solution was directly pipetted over the bioprinted structures, and the samples were incubated for 30 min at 37°C at 5% CO_2 and 100% humidity. After two washes with DPBS, the samples were imaged using an Axio M2 Observer fluorescence microscope (ZEISS, Germany). The images were processed and the dimensions of the structures with cells were analyzed using open-source Fiji software (Image J). For dimension analyses, at least 12 measurements per dimension were taken to calculate the means and standard deviations.

In a different set of experiments, a C2C12-laden bioink was bioprinted into three multilayered 1 × 1-cm^2 squares and cultured for 7 days under the same conditions (37°C, 5% CO_2, and 100% humidity) to observe long-term survival and elongation. After the culture period, the cells were stained with phalloidin/4′,6-diamidino-2-phenylindole (DAPI) to observe the cellular structures. Micrographs were obtained with a Zeiss Axio M2 Observer fluorescence microscope.

2.9. Statistical analysis

Data are presented as the mean ± standard deviation from at least three repetitions (n = 3). Significant differences ($p < 0.05$) were found by analysis of variance (ANOVA).

3. Results and discussion

3.1. Bioprinter development

We developed a cost-effective bioprinter capable of bioprinting simple cell-laden GelMA constructs. We used the Anet A8 3D printer, a commercially available fused-deposition model, as our mechanical backbone. This 3D printer has been used before as a frame to develop cost-effective bioprinters[18,36], due to its relatively low cost (currently between 200 and 300 USD), easy assembly, and off-the-shelf availability. In addition, the use of this 3D printer is supported by a vast community of users globally, making it widely useful for customizing—a quality that is tremendously lacking in commercial bioprinters. The (bio)printer was assembled by closely following the manufacturer's directions and subsequently subjected to in-house modifications using common maker tools. As an additional resource, many tutorials are available on the internet describing the procedures for assembly of the Anet A8 3D printer. Figure 1A shows the overall architecture of our Anet A8-derived bioprinter.

In this project, we used the concept of "a printer that prints itself." Before conducting any modifications, we used the as-supplied 3D printer to print the modifications needed to increase the stability and robustness of our bioprinting machine. The *X*-axis carriage and printhead

mount were also printed utilizing the same 3D printer (**Figure S3C** and **D**) using PLA as the printing filament. We have provided all the STL files (**Supplementary File**) required to 3D-print the pieces needed for successful conversion of the Anet A8 into a high-performance 3D bioprinter.

While the Anet A8 has been used by others as a frame to develop low-cost bioprinters[18,36], we embedded additional features that greatly enhance the capabilities and versatility of our bioprinter. For instance, the mechanical driving system of the Anet A8 printer was adapted for control by a RAMPS controller based on the Arduino Mega and Marlin firmware. This enabled full access to user modifications, thereby greatly enhancing the flexibility of this bioprinting system. For the purposes of this project, we used original Marlin firmware and the Anet A8 configuration files. Once the motherboard had a firmware installed, and all of the electrical connections are established, we connected the printer to a host software to allow for manual control as well as G-code uploads. Several guides describing the installation of an open-source 3D printer firmware, such as Marlin, on an Arduino Mega board have been developed and are widely available.

This printer/bioprinter is also extremely flexible in terms of the needles that can be used, the range of temperatures controlled by the printhead jacket, the flow rate of the ink/bioink used, and the feed rate of the printhead. In this work, we used a standard 21G needle as the printhead tip, a range of feed rates (i.e., linear speeds) between 100 and 300 mm/min, and a spectrum of flow rates between 0.05 and 0.1 mL/min produced by the syringe pump.

3.2. Performance of the cooling/heating system

As previously mentioned, the most differentiating attribute of our DiY bioprinter with respect to existing DiY models is its ability to control temperature during extrusion. To achieve this control, we substituted the original printing nozzle with a 3D-printed printhead engineered for temperature control by water recirculation during extrusion (Figure 1B; see illustrative videos [**Movie S1**; **Movie S2**] with link given in **Supplementary File**). The CAD model and corresponding STL file are included in the **Supplementary File** to enable its reproduction and use. This printhead consisted of a straight cylindrical ink chamber housing an inlet that accepts conventional plastic tubing (0.25 cm in I.D.). The cylindrical ink reservoir was enclosed in a chamber (or jacket) that allows recirculation of water for temperature control. The sides of the recirculating printhead chamber are designed with an inlet and outlet to accept conventional rubber hoses coming from and returning to the water-recirculating system. In the experiments reported here, we used a Yamato water circulator with a water reservoir capacity of 4 L. However, any conventional laboratory water circulator would be suitable. The printhead design that we present here has not been engineered for optimal mass transfer; however, its performance was satisfactory, as we will show, to assure the printability of our hydrogel-based bioinks under conventional laboratory settings and experimental conditions (i.e., room temperature between 20°C and 25°C, 10% in-house-made or commercial GelMA bioinks, etc.)

In our described setup, we continuously measured and controlled the temperature in the water bath and circulating water, which is significantly different than the actual temperature of the extruded bioink. This temperature difference (i.e., 7°C ± 2.2°C) is due to the low thermal conductivity of the resin and water and to the internal wall thickness between the water jacket and the bioink chamber (~2 mm in thickness) (Figure 1C).

3.3. Printability assays

In principle, this bioprinter and printhead can be used to ensure printability of any bioink matrix that requires specific temperature control during extrusion to attain a desired viscosity. For demonstration purposes, we first chose GelMA, one of the most widely used hydrogels in tissue engineering and bioprinting research, as our bioink matrix. GelMA is known to have a printability that highly depends on its rheology[25,29,31], and several recent papers have described the rheological behavior of GelMA hydrogels in the range of temperatures of interest here[29,31]. We also ran rheological determinations ourselves for the GelMA formulations utilized in the present study (Figure 2A). The GelMA viscosity increased in the temperature range between 15°C and 5°C and showed viscosity variations of more than one order of magnitude in this range (Figure 2Ai). In general, similar trends can be observed in alternative GelMA-based formulations commonly used in bioprinting applications (i.e., GelMA-alginate blends; Figure 2A). The intersection between the storage and loss moduli, which determines the gel–liquid transition, occurred in the range of 20°C–25°C, for typical GelMA-based inks (Figure 2Aii). Therefore, temperature control is clearly crucial to ensure printability and reproducible bioprinting results.

We conducted printing experiments using a 5% (w/v) GelMA formulation to assess the printability at different feed rates[34], ink extrusion rates (i.e., flow rates), and temperatures of the recirculating water. For that, we printed a series of squares with an intended dimension of 5 × 5 mm^2 and connected by lines using a 5% (w/v) GelMA bioink with fluorescent microparticles (Figure 2B). During a single printing trace, the bioprinter was challenged to extrude at three different and increasing feed rates while

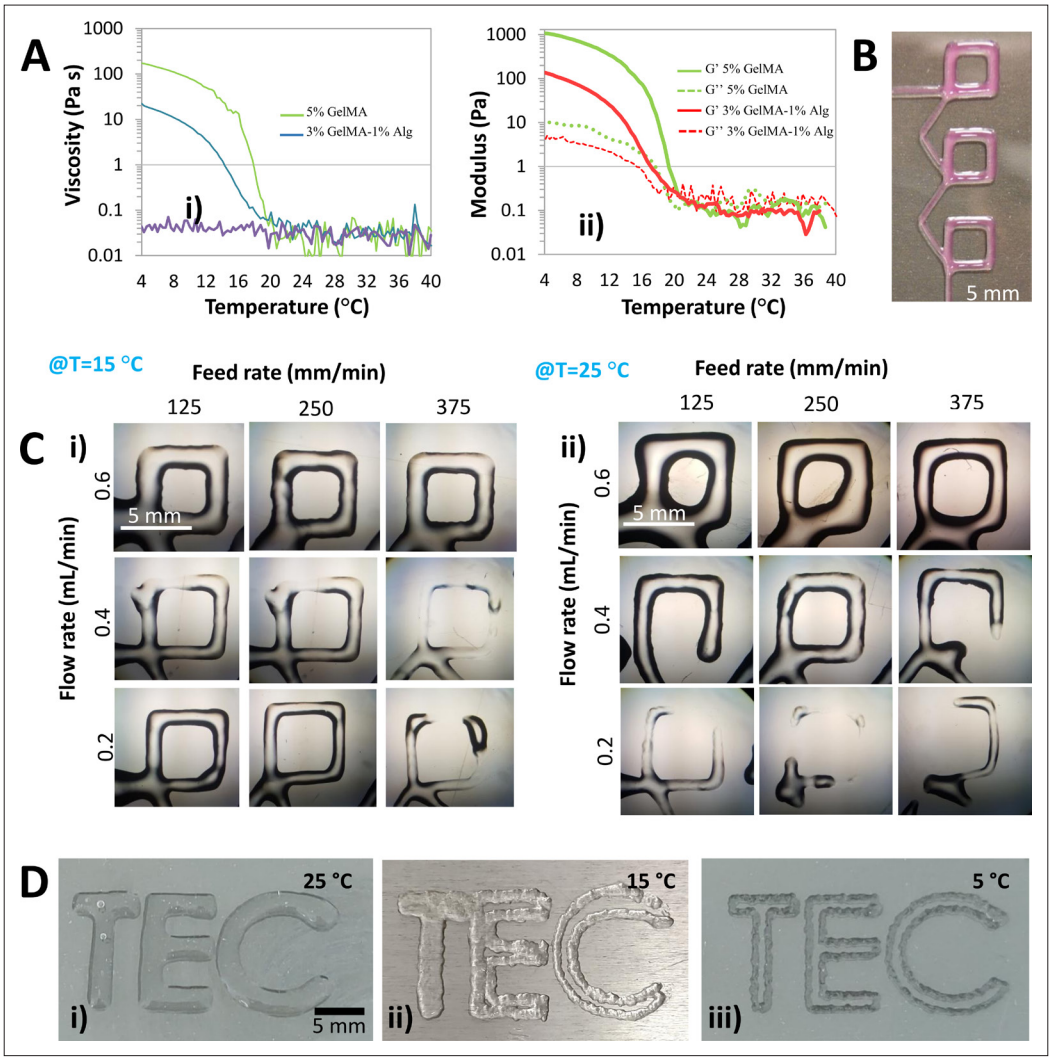

Figure 2. Printing with GelMA at different temperatures, flow rates, and feed rates. (A) The rheology of GelMA-based hydrogels depends strongly on the printing temperature: (i) Viscosity, and (ii) storage and loss moduli of 5% (w/v) GelMA and 3% GelMA+1% alginate at different temperatures. (B) A triad of squares (programmed in G-code) was used to analyze the resolution of GelMA printings at different feed rates (linear printhead speeds) and flow rates. (C) Printing of GelMA 5 × 5 mm^2 at different feed rates and flow rates and temperatures: (i) water cooling set at 15°C and (ii) 25°C. (D) Side-by-side comparison of a 5% GelMA ink extruded (i) without temperature control (i.e., ~25°C), and with temperature control at (ii) 15°C and 5°C.

holding the GelMA flow rate and water temperature constant. In the design used here, the cylindrical ink/bioink chamber ended in a male Luer lock connector that accepts standard needles as extruder tips. Figure 2C shows the sets of squares printed through a 21G needle at the temperature settings of 15°C and 20°C for the water circulator at three different GelMA feed rates. These settings induce temperatures of ~20°C and 25°C at the tip of the printing nozzle, respectively; temperature values that are in the neighborhood of the gel–liquid transition. The resolution and fidelity of the printed squares improves qualitatively as the temperature setting decreases, and completely closed squares can be obtained in most of the feed and flow rate combinations tested. The printability of the 5% GelMA ink improved remarkably when the temperature setting of the water cooler was further decreased to ~0°C. Figure 2D shows the comparison between three letters printed without any temperature control (i.e., ~25°C; Figure 2Di) and with temperature control (i.e., water circulator set at 0°C; Figure 2Dii). The definition of each letter improves dramatically and their shape is retained through UV crosslinking (i.e., ~60 s).

Next, we further assessed the printability of series of squares printed at low-temperature settings. Figure 3A shows the sets of squares printed through a 21G needle at the low temperature setting of 0°C for the water circulator at three different GelMA feed rates. Note that

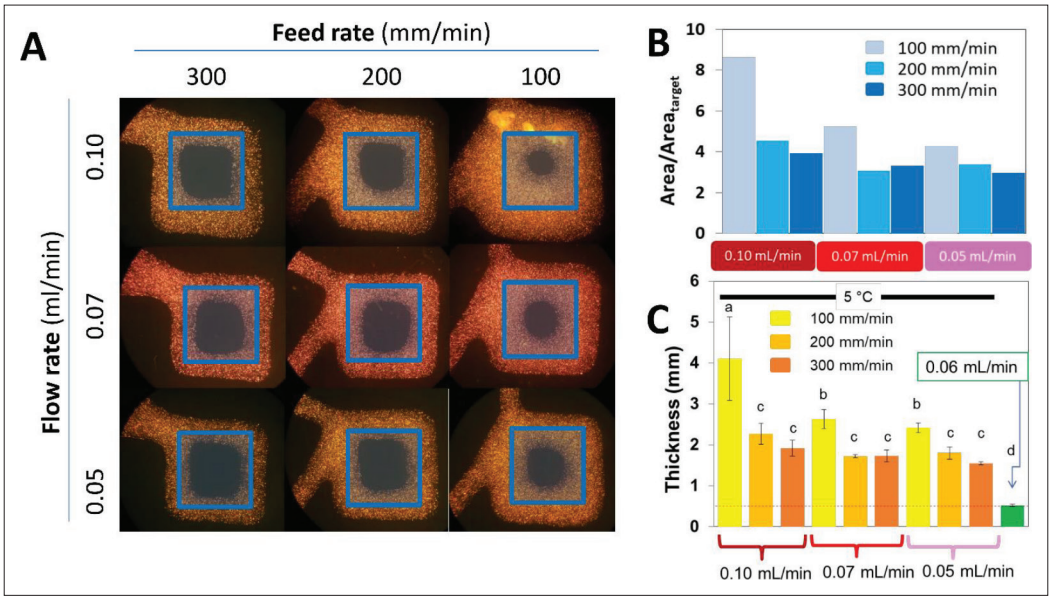

Figure 3. Printing experiments with temperature control. (A) Parameter matrix (i.e., feed rate vs. flow rate) to investigate suitable printing parameters. Quantification of the (B) the surface area of the internal space defined by each of the squares, and (C) the line thickness for different feed rates and flow rate within the parameter matrix.

the average diameter for all sides in every individual square was statistically similar, suggesting adequate and equal reproducibility of traces in the *X*- and *Y*-axes. For each GelMA feed rate, the average diameter of the printed filament was strongly correlated with the flow rate. As the printhead speed increased, the amount of ink deposited per mm decreased and the fidelity of the lines improved (Figure 3B). Increasing the feed rate too much led to discontinuities in the printed construct, as shown in Figure 2D. A more visual representation of the relationship between feed rate, flow rate, and quality of the printed fiber is shown in illustrative videos (Grid; Tecnologico de Monterrey logo with link given in **Supplementary File**).

Printability was attainable over a relatively wide range of conditions. As shown in **Figure** 3, the characteristic features of the GelMA squares (i.e., height, diagonal distance, average thickness of lines, and surface area) were a function of the feed rates and the flow rates. For example, we calculated the surface area of the internal space defined by each of the squares (Figure 3B). This quantity is a strong and integral indicator of fidelity that incorporates the effects of line thickness in *X* and *Y* (each with three repeats) and fidelity around angles. The average thickness of lines printed at different feed rates and flow rates is shown in Figure 3C. This indicator revealed a significant improvement in fidelity with increasing feed rate. This observation was valid for each of the printing sets (Figures 2C and 3A) conducted at different ink flow rates and temperatures. The fidelity also increased as the flow rate was decreased at a fixed feed rate.

These observations were expected and consistent. As the flow rate decreases at a constant feed rate, or the feed rate increases at a fixed flow rate, the mass of ink deposited per linear unit of length decreases. This results in higher fidelity, since a smaller amount of material is deposited on a larger surface area (**Movie S2**). For comparison, we present a complex pattern of our university logo and GelMA squares, produced using the same set of feed rates and flow rates but without temperature control. Under these conditions, the bioprinting quality suffered due to the lower viscosity of the ink formulation induced by the higher temperature. Without temperature control, the ink lost its consistency, and the printing quality decreased (Figure 2C and D).

In principle, the strategy of controlling the temperature of the ink/bioink to fine tune its viscosity and improve its printability can be applied to a variety of inks that show temperature-dependent rheology. For illustration purposes, we present a printing experiment using a 25% Pluronic F-127 ink at different feed rates, flow rates, and temperatures. Pluronic-based inks have been widely used in printing and bioprinting applications, mainly as sacrificial (i.e., fugitive) materials[37,38]. Counterintuitively, Pluronic-based inks are low-viscosity liquids at low temperatures and become gels at room and higher temperatures[39,40] (Figure 4A and B). For instance, the 25% Pluronic F-127 solution that we used in our experiments behaves as low-viscosity liquid at temperatures below 20°C and exhibits an abrupt increase in viscosity at temperatures ranging from

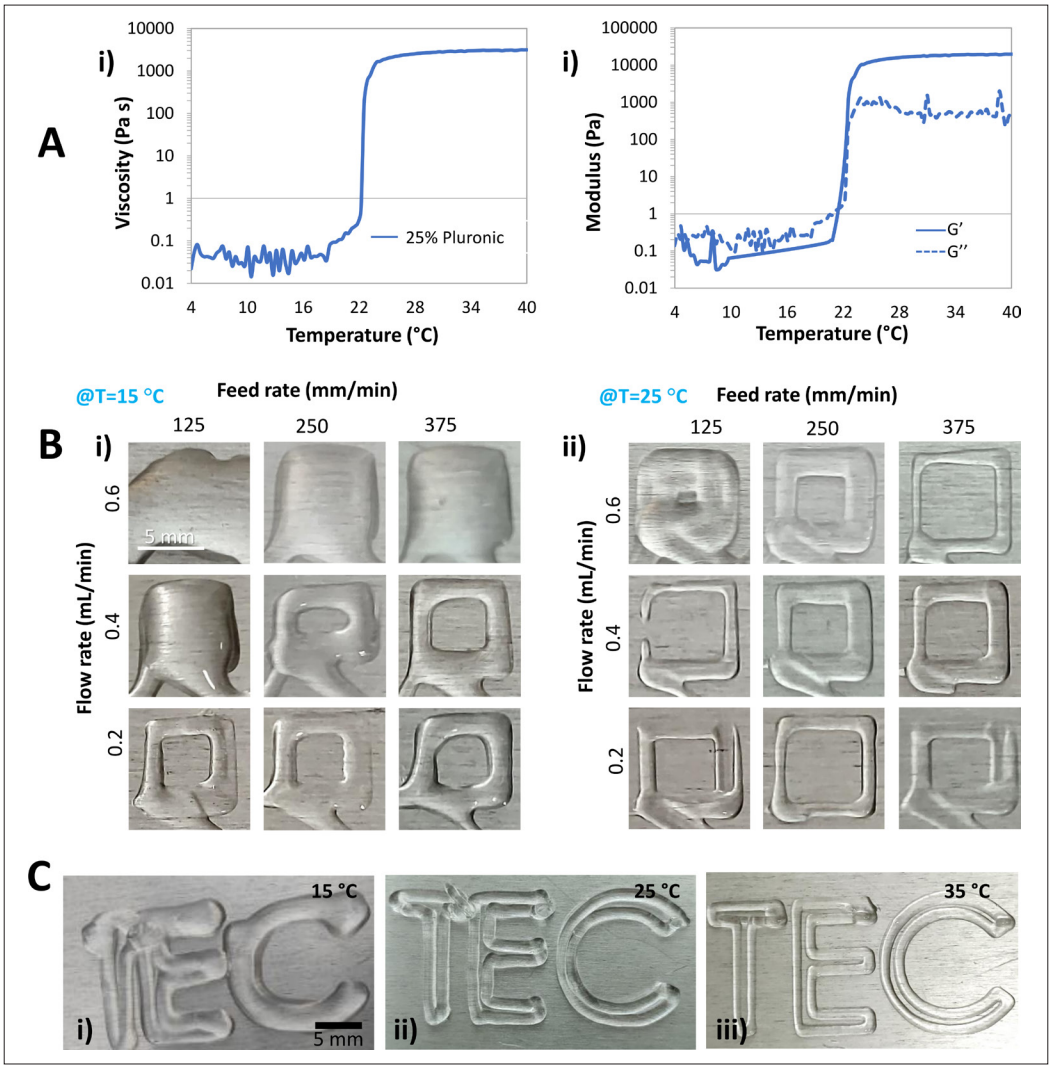

Figure 4. Printing with 25% Pluronic F-217 at different temperatures, flow rates, and feed rates. (A) The rheology of Pluronic-based hydrogels depends strongly on the printing temperature: (i) viscosity and (ii) storage and loss moduli of 25% (w/v) Pluronic F127 at different temperatures. (B) A triad of squares (programmed in G-code) was used to analyze the resolution of Pluronic printings at different feed rates (linear printhead speeds) and flow rates. (C) Side-by-side comparison of a 25% Pluronic F-127 ink printed with a temperature control set at (i) 15°C, (ii) 25°C, and (iii) 35°C.

20°C to 25°C (Figure 4Ai). Our Pluronic ink transitions to gel at approximately 22.5°C (Figure 4Aii). Consistently, controlling the printing temperature above this value (in this case, by heating) greatly improves their printability (Figure 4B and C).

3.4. Multilayer and multimaterial printing

Ideally, a bioprinter should be able to print several layers of hydrogel-based inks. Therefore, we tested the "stackability" of GelMA with this bioprinter. We designed models using CAD software (SolidWorks) and then sliced the STL files to generate different G-codes (i.e., a single-layer multi-hexagon array (Figure 5Ai), a multilayer hexagon array (Figure 5Aii, iii), our own Lab name (Figure 5B), and the Tecnologico de Monterrey logo (Figure 5C). All of these experiments resulted in self-standing structures with good fidelity. We were able to print a high-resolution and self-standing hexagonal grid of up to 5 layers of 5% (w/v) GelMA (Figure 5Aii). Furthermore, the prints of the Alvarez-Trujillo Lab name and Tecnologico de Monterrey logos were successful; this printing exercise clearly confirmed the capability of our DiY bioprinter to follow curved trajectories (Figure 5B and C) with GelMA (Figure 5Cii) and Pluronic-based inks (Figure 5Ciii). The printing of the Alvarez-Trujillo Lab logo and the Tecnologico de Monterrey sports logo, a bicolor ram, verified the ability of our bioprinter to perform sequential multi-material printing (Figure 5D and E). In this case, we first printed the blue ink, then deposited the black and yellow ink, and finally deposited the blue ink. Note that the

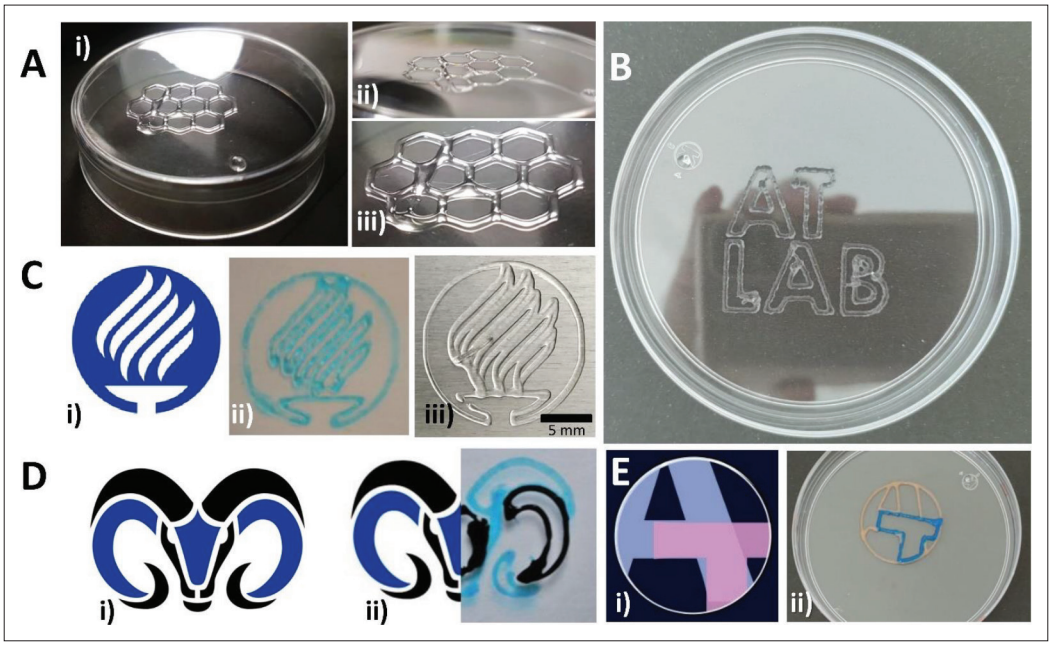

Figure 5. 3D bioprinting capabilities of the printing system using GelMA inks. (A) Complex 3D honeycomb structure: (i, ii) one layer and (iii) five layers. (B) Alvarez-Trujillo Lab name. (C) The Tecnologico de Monterrey school emblem: (i) actual logo, (ii) GelMA, and (iii) Pluronic constructs printed with temperature control (i.e., at 5°C and 35°C, respectively). (D) Multimaterial printing of the Tecnologico de Monterrey mascot, and (E) the Alvarez-Trujillo Lab logo: (i) actual logo and (ii) GelMA construct printed with temperature control. All figures were printed with 5% GelMA; and using printhead water cooling set at 0°C.

positioning of the nozzle after changing inks was correct, and we saw good fidelity at the blue-black and yellow-blue interfaces.

One point worth noting is that having a basic understanding of G-code would be very beneficial to the user for several reasons. First, the distance between the petri dish surface and the tip of the cooling nozzle is not always constant due to different thicknesses of the bottom surfaces of petri dishes or different needle lengths. Therefore, manual editing of the first-layer height of the print in G-code is required. The feed rate (i.e., the linear speed of the printhead) can also be easily modified in the G-code. Redundant G-code commands can also be removed (i.e., extruder and platform heating temperature, cooling fan, and overlapping trajectories of the printhead).

Currently, the syringe pump and the printer do not obey the same controller. This is not ideal but has not been a relevant problem in our printing experiments using a single ink. However, for multimaterial printing, a master control capable of coordinating the action of the pumps and the positioning system must be considered.

3.5. Bioprinting experiments

The printability of cell-laden bioinks may differ significantly from that exhibited by pristine bioinks. Several reports have suggested that the rheology and printability of bioinks may depend on the cell concentration[41,42]. Therefore, we ran a second set of bioprinting experiments using cell-laden GelMA. For these experiments, we prepared a 5% (w/v) GelMA formulation loaded with 1×10^6 C2C12 cells/mL. We bioprinted a grid and the Tecnologico de Monterrey logo using this bioink formulation. After bioprinting, the patterns were crosslinked using UV light for 60 s. The corresponding cell-laden patterns are presented in Figure 6A. The cell viability after printing and crosslinking was confirmed by the presence of mostly live (green- or blue-stained cells in Figure 6A, respectively) and relatively few dead (red-stained cells in Figure 6B) cells.

The dimensions of the cell-laden patterns were also measured (Figure 6A–C). Single-line definition, shown as (X), (Y), and (A), exhibited values of 612 ± 63 μm, 466 ± 51 μm, and 485 ± 51 μm, respectively. Nodes (Z) in the grid and edges (B) in the logo showed approximately double the thickness at 1128 ± 76 μm and 1176 ± 308 μm, respectively (Figure 6C). To the best of our knowledge, this value of thickness is similar to or even lower than those previously reported for similar bioprinting experiments using GelMA with open-source bioprinters[2] or custom-built bioprinters[34]. Our bioprinter and engineered printhead enables a wide range of control of bioprinting conditions and geometries, while also providing high postbioprinting cell viabilities. These viability values will most probably vary depending on the chosen cell lines and types used.

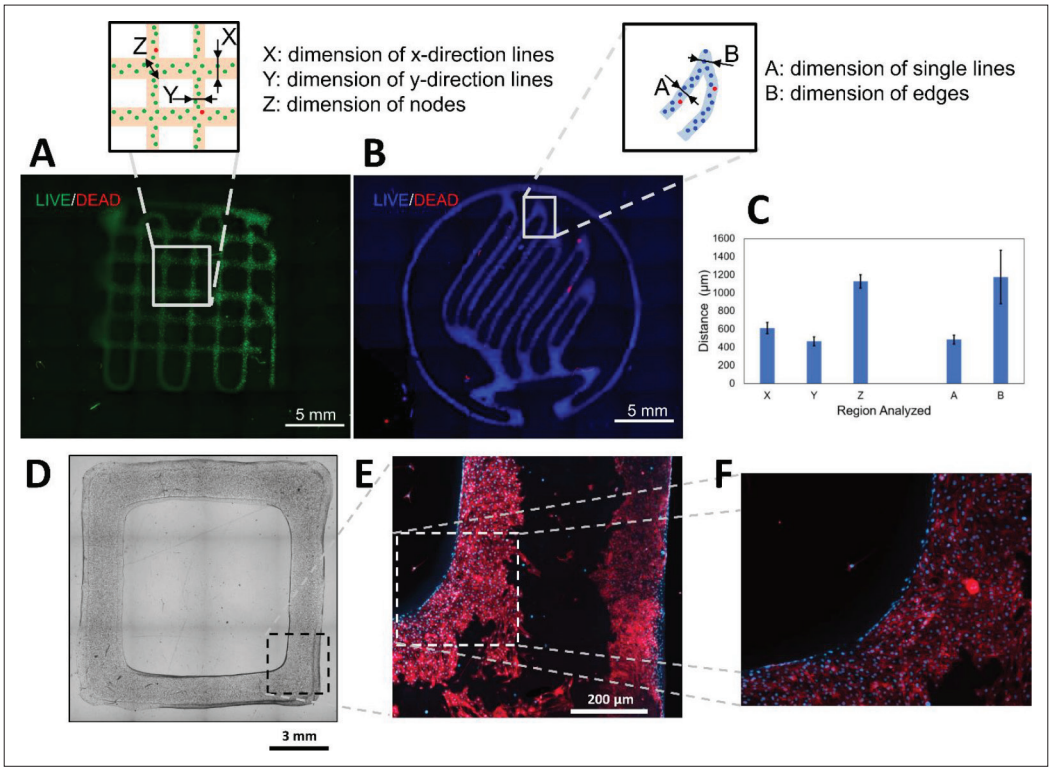

Figure 6. Cell viability assays. (A) Printed grid of a C2C12-laden GelMA bioink visualized with live (green)/dead (red) staining (left). The zoomed-in illustration indicates the dimensions measured to obtain the definition of the printing. (B) Printed logo of Tecnologico de Monterrey using a C2C12-laden GelMA bioink and visualized with live (blue)/dead (red) staining; blue was chosen because it is the color of the logo (right). The zoomed-in illustration indicates the dimensions measured to obtain definition of the printing. (C) Dimensions of the printed pattern were analyzed by image analysis and displayed as means with standard deviations (n > 11 measurements per group). (D) Printed square of C2C12-laden GelMA bioink visualized in bright field. (E, F) Zoomed-in images of the right lower corner of the square in panel (D) after staining with phalloidin/DAPI show the distribution of C2C12 cells proliferating across the structure after 7 days of culture.

However, our results demonstrate the feasibility of using this extrusion system in the context of frequently used cell lines, and support the relatively benign nature of this bioprinting cooling extrusion system.

Taken together, our results suggest that this bioprinting setup could effectively bioprint viable cellular constructs using GelMA-based bioinks. Note that these bioprinting experiments were not conducted under sterile conditions, and yet they were sufficiently adequate for demonstrating cell viability immediately after bioprinting. The final bioprinting experiments demonstrated that sterility could be assured by adding penicillin-streptomycin to the bioink and washing the constructs with PBS supplemented with antibiotics before added with the culture medium. These precautions allowed the survival of the bioprinted C2C12 cells in the constructs for longer periods (7 days tested) without evidence of contamination (Figure 6D–F). In the future, however, the bioprinter will need enhancements that can provide a sterile environment for bioprinting purposes. GelMA is one of the most widely used biomaterials in tissue engineering research, but one that has proven challenging to print consistently without temperature control. This challenge can be overcome by using our DiY cooling printhead.

4. Conclusion

The work presented in this paper showcases the development of a low-cost open-source bioprinter that has the ability to provide precise control of the printability of inks/bioinks by the inclusion of an extruder with integrated temperature control. This is done by converting a commercial 3D printer into a bioprinter by employing the strategy of "printing your own printer." To do this, several modifications were printed and installed on a commercial printer, and a new electronics system was incorporated. The extruder was designed and printed to enable the circulation of temperature-controlled water (cold water, in this specific case) around the ink chamber through a 3D-printed jacket system. We also show the effects of different printing parameters, such as the feed rate, flow rate, and temperature, on the resolution of printed constructs. Complex 3D structures are printed at resolutions comparable to or even better than similar open-source

projects. The ability to bioprint cell-laden constructs with retained cell viability is also positively illustrated.

This work demonstrates a method to more accurately control the rheology of 3D printer inks, such as GelMA or Pluronic acid, whose viscosity is improved with temperature control. Moreover, the printing system described here may be used as a simple platform to analyze the effect of different temperatures, flow rates, and feed rates on fidelity and printability.

Future work should address the limitations and opportunities provided by the current setup. The first concern involves the optimization of the thermal conductivity of the printhead, and thermal analysis and simulations can be conducted to determine the most efficient cooling/heating design.

The integration of the syringe pump with the bioprinter (i.e., combining the motor and DiY printhead into one component) should also be investigated, but for the purposes of this work, we focused on the development of a temperature controlling printhead. A sterile enclosure should also be designed and fixed to the bioprinter to ensure sterile conditions for all bioprinting sessions, especially when cells are used. These additions will be very interesting contributions to the present system. Nevertheless, our current findings show promising results and should be readily reproducible by other laboratories seeking affordable methods to make further progress in the tissue engineering field.

Acknowledgments

We gratefully acknowledge the experimental contributions of Alberto Emanuel Aceves Colin. The authors also acknowledge the primary antibodies provided by Santa Cruz Biotechnology Inc. in form of free samples. MGSS, CFCG, and EJBM gratefully acknowledge financial support granted by CONACyT (Consejo Nacional de Ciencia y Tecnología, México) in the form of Graduate Program Scholarships. GTdS and MMA acknowledge funding from the UC-MEXUS program. GTdS acknowledges funding received from CONACyT and L'Oréal-UNESCO-CONACyT-AMC (National Fellowship for Women in Science, México). MMA and GTdS acknowledge funding provided by CONACyT in the form of Scholarships as members of the National System of Researchers (grant SNI 26048 and SNI 256730) and funding provided by Saya Bio.

Funding

MGSS, CFCG, and EJBM gratefully acknowledge financial support granted by CONACyT (Consejo Nacional de Ciencia y Tecnología, México) in the form of Graduate Program Scholarships. GTdS and MMA acknowledge funding from the UC-MEXUS program. GTdS acknowledges funding received from CONACyT and L'Oréal-UNESCO-CONACyT-AMC (National Fellowship for Women in Science, México). MMA and GTdS acknowledge funding provided by CONACyT in the form of Scholarships as members of the National System of Researchers (grant SNI 26048 and SNI 256730) and funding provided by Saya Bio. The authors also acknowledge the primary antibodies provided by Santa Cruz Biotechnology Inc. in form of free sample.

Conflict of interest

The authors have no conflicts of interest.

Author contributions

Conceptualization: Mario Moisés Alvarez, Grissel Trujillo-de Santiago, Andrés García-Rubio

Formal analysis: Mario Moisés Alvarez

Investigation: Carlos Ezio Garciamendez-Mijares, Gilberto Emilio Guerra-Alvarez, Andrés García-Rubio, Mónica Gabriela Sánchez-Salazar, Anne-Sophie Mertgen, Carlos Fernando Ceballos-González, Edna Johana Bolivar-Monsalve, German Garcia-Martinez

Methodology: Mario Moisés Alvarez, Grissel Trujillo-de Santiago, Andrés García Rubio, Carlos Ezio Garciamendez-Mijares, Gilberto Emilio Guerra-Alvarez, Mónica Gabriela Sánchez-Salazar, German Garcia-Martinez

Writing—original draft: Mario Moisés Alvarez, Carlos Ezio Garciamendez-Mijares

Writing—review & editing: Mario Moisés Alvarez, Yu Shrike Zhang, Grissel Trujillo-de Santiago

Ethics approval and consent to participate

Not applicable.

Consent for publication

Not applicable.

Availability of data

All date needed to reproduce the experiments described in this contribution have been made available in the main body of the paper or in the **Supplementary File**.

Further disclosure

Part of the entire set of findings has been presented in AIChE Meeting, 2020.

References

1. Atala A, Forgacs G, 2019, Three-dimensional bioprinting in regenerative medicine: Reality, hype, and future. *Stem Cells Transl Med*, 8(8):744–745.

   https//doi.org/10.1002/sctm.19-0089

2. Garciamendez-Mijares CE, Agrawal P, García Martínez G, *et al.*, 2021, State-of-art affordable bioprinters: A guide for the DiY community. *Appl Phys Rev*, 8(3):031312.

   https//doi.org/10.1063/5.0047818

3. Thakur PC, Cabrera DD, DeCarolis N, *et al.*, 2018, Innovation and commercialization strategies for three-dimensional-bioprinting technology: A lean business model perspective. *J Commer Biotechnol*, 24(1):78–87.

   https//doi.org/10.5912/jcb856

4. Zou Q, Grottkau BE, He Z, *et al.*, 2020, Biofabrication of valentine-shaped heart with a composite hydrogel and sacrificial material. *Mater Sci Eng C*, 108:110205.

   https//doi.org/10.1016/j.msec.2019.110205

5. Osouli-Bostanabad K, Masalehdan T, Kapsa RM, *et al.*, 2022, Traction of 3D and 4D printing in the healthcare industry: From drug delivery and analysis to regenerative medicine. *ACS Biomater Sci Eng*, 8(7):2764–2797.

   https//doi.org/10.1021/ACSBIOMATERIALS.2C00094

6. Choudhury D, Anand S, Naing MW, 2018, The arrival of commercial bioprinters—Towards 3D bioprinting revolution! *Int J Bioprinting*, 4(2):139.

   https//doi.org/10.18063/IJB.v4i2.139

7. Ke D, Niu C, Yang X, 2022, Evolution of 3D bioprinting-from the perspectives of bioprinting companies. *Bioprinting*, 25:e00193.

   https//doi.org/10.1016/J.BPRINT.2022.E00193

8. Xu K, Han Y, Huang Y, *et al.*, 2022, The application of 3D bioprinting in urological diseases. *Mater Today Bio*, 16:100388.

   https//doi.org/10.1016/J.MTBIO.2022.100388

9. Shinkar K, Rhode K, 2022, Could 3D extrusion bioprinting serve to be a real alternative to organ transplantation in the future? *Ann 3D Print Med*, 7:100066.

   https//doi.org/10.1016/J.STLM.2022.100066

10. Panda S, Hajra S, Mistewicz K, *et al.*, 2022, A focused review on three-dimensional bioprinting technology for artificial organ fabrication. *Biomater Sci*, 10(18):5054–5080.

    https//doi.org/10.1039/D2BM00797E

11. Zhang B, Luo Y, Ma L, *et al.*, 2018, 3D bioprinting: An emerging technology full of opportunities and challenges. *Bio-Design Manuf*, 1(1):2–13.

    https//doi.org/10.1007/S42242-018-0004-3

12. De Maria C, Díaz Lantada A, Jämsä T, *et al.*, 2022, Biomedical engineering in low- and middle-income settings: Analysis of current state, challenges and best practices. *Health Technol (Berl)*, 12(3):643–653.

    https//doi.org/10.1007/S12553-022-00657-8/FIGURES/7

13. McElheny C, Hayes D, Devireddy R, 2017, Design and fabrication of a low-cost three-dimensional bioprinter. *J Med Devices Trans ASME*, 11(4):1–9.

    https//doi.org/10.1115/1.4037259

14. Bisram RY, Bender LM, Niemi SR, *et al.*, Toward Economical 3D Bioprinters for High School Science Laboratories.

15. Allevi, Allevi 1.

    https://www.allevi3d.com/allevi-1/.

16. CellInk, Holograph X.

    https://www.cellink.com/bioprinting/holograph-x/

17. Ozbolat IT, Hospodiuk M, 2016, Current advances and future perspectives in extrusion-based bioprinting. *Biomaterials*, 76:321–343.

    https//doi.org/10.1016/j.biomaterials.2015.10.076

18. Kahl M, Gertig M, Hoyer P, *et al.*, 2019, Ultra-low-cost 3D bioprinting: Modification and application of an off-the-shelf desktop 3D-printer for biofabrication. *Front Bioeng Biotechnol*, 7(July):1–12.

    https//doi.org/10.3389/fbioe.2019.00184

19. Yenilmez B, Temirel M, Knowlton S, *et al.*, 2019, Development and characterization of a low-cost 3D bioprinter. *Bioprinting*, 13(March):e00044.

    https//doi.org/10.1016/j.bprint.2019.e00044

20. Krige A, Haluška J, Rova U, *et al.*, 2021, Design and implementation of a low cost bio-printer modification, allowing for switching between plastic and gel extrusion. *HardwareX*, 9:e00186.

    https//doi.org/10.1016/J.OHX.2021.E00186

21. Pérez Cortez JE, Sánchez VH, Vázquez-Lepe E, *et al.*, 2022, Retrofitting of an affordable 3D printer: Towards a material efficient and low-cost bioprinting system. *Procedia CIRP*, 110:150–155.

    https//doi.org/10.1016/J.PROCIR.2022.06.028

22. Wagner M, Karner A, Gattringer P, *et al.*, 2021, A super low-cost bioprinter based on DVD-drive components and a raspberry pi as controller. *Bioprinting*, 23:e00142.

    https//doi.org/10.1016/J.BPRINT.2021.E00142

23. McCormack A, Highley CB, Leslie NR, *et al.*, 2020, 3D printing in suspension baths: Keeping the promises of bioprinting afloat. *Trends Biotechnol*, 38(6):584–593.

    https//doi.org/10.1016/j.tibtech.2019.12.020

24. Liu F, Liu C, Chen Q, *et al.*, 2018, Progress in organ 3D bioprinting. *Int J Bioprint*, 4(1):1–15.

    https//doi.org/10.18063/IJB.v4i1.128

25. Liu W, Heinrich MA, Zhou Y, *et al.*, 2017, Extrusion bioprinting of shear-thinning gelatin methacryloyl bioinks. *Adv Healthc Mater*, 6(12):1601451.

    https//doi.org/10.1002/adhm.201601451

26. Maciel BR, Baki K, Oelschlaeger C, *et al.*, 2022, The influence of rheological and wetting properties of hydrogel-based bio-inks on extrusion-based bioprinting. *Chem Ing Tech*, 94(3):393–401.

    https//doi.org/10.1002/CITE.202100139

27. Talluri DJS, Nguyen HT, Avazmohammadi R, *et al.*, 2022, Ink rheology regulates stability of bioprinted strands. *J Biomech Eng*, 144(7):074503.

    https//doi.org/10.1115/1.4053404/1131087

28. Yue K, Trujillo-de Santiago G, Alvarez MM, *et al.*, 2015, Synthesis, properties, and biomedical applications of gelatin methacryloyl (GelMA) hydrogels. *Biomaterials*, 73:254–271.

    https//doi.org/10.1016/j.biomaterials.2015.08.045

29. Bolívar-Monsalve EJ, Ceballos-González CF, Borrayo-Montaño KI, *et al.*, 2021, Continuous chaotic bioprinting of skeletal muscle-like constructs. *Bioprinting*, 21:e00125.

    https//doi.org/10.1016/J.BPRINT.2020.E00125

30. Celikkin N, Mastrogiacomo S, Dou W, *et al.*, 2022, In vitro and in vivo assessment of a 3D printable gelatin methacrylate hydrogel for bone regeneration applications. *J Biomed Mater Res Part B Appl Biomater*, 110(9):2133–2145.

    https//doi.org/10.1002/JBM.B.35067

31. Ying G, Jiang N, Yu C, *et al.*, 2018, Three-dimensional bioprinting of gelatin methacryloyl (GelMA). *Bio-Design Manuf*, 1(4):215–224.

    https//doi.org/10.1007/s42242-018-0028-8

32. West J, Kuk G, 2016, The complementarity of openness: How MakerBot leveraged Thingiverse in 3D printing. *Technol Forecast Soc Change*, 102:169–181.

    https//doi.org/10.1016/J.TECHFORE.2015.07.025

33. Magrisso S, Zoran A, 2019, Digital joinery for hybrid carpentry. *Lect Notes Civ Eng*, 24:441–461.

    https//doi.org/10.1007/978-3-030-03676-8_16

34. Gillispie GJ, Han A, Uzun-Per M, *et al.*, 2020, The influence of printing parameters and cell density on bioink printing outcomes. *Tissue Eng Part A*, 26(23–24):1349–1358.

    https//doi.org/10.1089/TEN.TEA.2020.0210

35. Tavares-Negrete JA, Aceves-Colin AE, Rivera-Flores DC, *et al.*, 2021, Three-dimensional printing using a maize protein: Zein-based inks in biomedical applications. *ACS Biomater Sci Eng*, 7(8):3964–3979.

    https//doi.org/10.1021/ACSBIOMATERIALS.1C00544/SUPPL_FILE/AB1C00544_SI_004.MOV

36. Ioannidis K, Danalatos RI, Champeris Tsaniras S, *et al.*, 2020, A custom ultra-low-cost 3D bioprinter supports cell growth and differentiation. *Front Bioeng Biotechnol*, 8:1279.

    https//doi.org/10.3389/FBIOE.2020.580889/BIBTEX

37. Bolívar-Monsalve EJ, Ceballos-González CF, Chávez-Madero C, *et al.*, 2022, One-step bioprinting of multi-channel hydrogel filaments using chaotic advection: Fabrication of pre-vascularized muscle-like tissues. *Adv Healthc Mater*, 11(24):2200448.

    https//doi.org/10.1002/ADHM.202200448

38. Kolesky DB, Truby RL, Gladman AS, *et al.*, 2014, 3D bioprinting of vascularized, heterogeneous cell-laden tissue constructs. *Adv Mater*, 26(19):3124–3130.

    https//doi.org/10.1002/ADMA.201305506

39. Jalaal M, Cottrell G, Balmforth N, *et al.*, 2016, On the rheology of Pluronic F127 aqueous solutions. *J Rheol (NY)*, 61(1):139.

    https//doi.org/10.1122/1.4971992

40. Lenaerts V, Triqueneaux C, Quartern M, *et al.*, 1987, Temperature-dependent rheological behavior of Pluronic F-127 aqueous solutions. *Int J Pharm*, 39(1–2):121–127.

    https//doi.org/10.1016/0378-5173(87)90206-7

41. Xu C, Zhang M, Huang Y, *et al.*, 2014, Study of droplet formation process during drop-on-demand inkjetting of living cell-laden bioink. *Langmuir*, 30(30):9130–9138.

    https//doi.org/10.1021/la501430x

42. Schwartz R, Malpica M, Thompson GL, *et al.*, 2020, Cell encapsulation in gelatin bioink impairs 3D bioprinting resolution. *J Mech Behav Biomed Mater*, 103:103524.

    https//doi.org/10.1016/J.JMBBM.2019.103524

ACCSCIENCE PUBLISHING

International Journal of Bioprinting

REVIEW ARTICLE

Exosome-based bioinks for 3D bioprinting applications in tissue engineering and regenerative medicine

Qian Wang[1†], Yang Liu[1†], Shuqing Zhang[1], Fan He[2], Tong Shi[3], Jizong Li[3*], Zhimin Wang[4*], and Jia Jia[1,2*]

[1]School of Life Sciences, Shanghai University, Shanghai, China

[2]Sino-Swiss Institute of Advanced Technology, School of Micro-electronics, Shanghai University, Shanghai, China

[3]Shanghai Center of Biomedicine Development, Shanghai, China

[4]Shanghai-MOST Key Laboratory of Health and Disease Genomics, Shanghai Institute for Biomedical and Pharmaceutical Technologies (SIBPT), Shanghai, China

(This article belongs to the *Special Issue: 3D Printing for Tissue Engineering and Regenerative Medicine*)

Abstract

Bioprinting is an emerging technology for tissue engineering and regenerative medicine. Despite its fast, accurate manufacture for tissues and organs *in vitro*, bioprinting has been seriously limited for biofabrication because of the restricted approaches to reproducing the extracellular matrix (ECM) with sufficient bioactivities for bioprinted cells. Exosomes are natural biological particles with proteins, lipids, or genetic materials. They have distinct properties and unique biological functions to manipulate cellular behaviors and cell fates, showing great potential to support cells for bioprinting. Here, we reviewed the recent progresses of exosome-advanced bioprinting for tissue engineering and regenerative medicine. Firstly, we offer an overview of the basics of exosomes and the current representative applications of exosomes in bone tissue engineering, immunological regulations, angiogenesis, and neural regenerations. Then, a brief introduction about the bioinks and the currently developed bioprinting methods is provided. We further give an in-depth review of the biomedical applications of bioprinting with exosomes, majorly in bone engineering, vascular engineering, therapy of neuron injury, and skin regeneration. We also conclude with an outlook on the challenges of the unmet needs of bioprinting cells with correspondent ECM environments through bioprinting with exosomes.

Keywords: Exosomes; Bioprinting; Bioinks; Regenerative medicine; Tissue engineering

†These authors contributed equally to this work.

***Corresponding authors:**
Jizong Li (jizongli@stcsm.sh.gov.cn)

Zhimin Wang (wangzhm@chgc.sh.cn)

Jia Jia (jiajia748@126.com)

Citation: Wang Q, Liu Y, Zhang S, *et al*., 2023, Exosome-based bioinks for 3D bioprinting applications in tissue engineering and regenerative medicine. *Int J Bioprint*, 9(6): 0114. https://doi.org/10.36922/ijb.0114

Received: April 4, 2023
Accepted: May 12, 2023
Published Online: July 7, 2023

Copyright: © 2023 Author(s). This is an Open Access article distributed under the terms of the Creative Commons Attribution License, permitting distribution, and reproduction in any medium, provided the original work is properly cited.

Publisher's Note: AccScience Publishing remains neutral with regard to jurisdictional claims in published maps and institutional affiliations.

1. Introduction

Bioprinting is derived from three-dimensional (3D) printing technology. It can apply cells, proteins, DNA, and other biological materials into personalized 3D models or 3D biological functional structures through printing technology *in vitro*. Bioprinting operated with computer-assisted designs (CADs) has exhibited the potential to reproduce the complexity of native tissues in terms of the mechanical properties, the

specific structures, and the interactions between cells and their extracellular matrices (ECMs)[1-3].

Bioprinting has unique advantages for tissue engineering and regenerative medicine. Although tissue engineering and regenerative medicine are two different research topics, they share the common goal of generating tissues or organs, either *in vitro* (tissue engineering) or *in vivo* (regenerative medicine). Tissue engineering and regenerative medicine usually require the wise combination and organization of biomaterials, cells, and biological factors to fabricate structures to simulate (in tissue engineering) or to replace (in regenerative medicine) the targeted tissues or organs, thereby enabling drug testing, disease modeling, trauma repair, and reconstruction of tissue functions. The difficulty of these technologies lies in the spatial positioning of multiple types of cells and the deposition of different amounts of cells with ECMs or ECM mimics. In contrast, 3D bioprinting can precisely regulate the proportions, the positions, and even the densities of specific types of cells along with biomaterials for tissue reconstruction, fully demonstrating the advantages of bioprinting in terms of directed spatial manipulation and layer-by-layer material controls[4]. Therefore, bioprinting has been widely used, including muscle repair[5], vascular regeneration[6], bone injury treatment[7], and skin wound healing[8].

However, current bioprinting strategies still suffer from high costs, inconvenient *in vitro* cell culture and storage, as well as problems from multiple perspectives, such as nutritional acquisition, immune rejection, and maladaptation after *in vivo* implantation[2,9]. To address these problems, diverse strategies to fabricate engineered ECMs have been developed. One of the practical solutions comes from the usage of exosomes in bioink.

Exosomes are natural biological particles that transport proteins, lipids, or genetic materials to the recipient cells. They come from various sources and have certain biological functions of the parent cells, demonstrating potential immune privileges. Exosomes from different sources have distinct functions, which exhibit good potential for adaptation to various situations. At the same time, exosomes are easier to store than cells and can be easily applied to multiple systems[10,11]. Compared to employing living cells, bioprinting with exosomes can reduce *in vivo* rejection, achieve targeted exosome delivery, and overcome the regulatory and cost-effectiveness issues, thus addressing multiple challenges in tissue engineering. Therefore, bioprinting with exosomes is expected to advance the field of tissue engineering and regenerative medicine significantly.

In this review, we will discuss the current research progresses of the combination between bioprinting and exosomes in tissue engineering, highlighting the representative applications in bone engineering, vascular regeneration, nerve repair, and skin regeneration (Figure 1). At the same time, we will provide an outlook on the future research directions of bioprinting with exosomes.

2. Exosomes

2.1. The basics of exosomes

Exosomes were first discovered in sheep reticulocytes in 1983 but were once thought to be a cellular metabolic waste[12-14]. In 2007, Valadi *et al.* discovered that cells could exchange genetic materials via RNAs in exosomes[15], which ignited public interest in these new genetic information carriers. The 2013 Nobel Prize in Physiology or Medicine was awarded to the discoverers of the intracellular vesicular transport and control mechanism, highlighting the importance of the studies of exosomes. Since then, researchers have identified a variety of exosomes with different functions, and a growing number of scholars have begun to focus on the enormous potential and values of exosomes for tissue development, disease diagnosis, and therapeutics.

Exosomes are membrane vesicles released into the ECM by the fusion of intracellular multi-vesicular bodies with the cell membrane. They contain various proteins, lipids, and RNAs and are widely found in biological fluids. Exosomes have important roles in the transmission of materials and information between parent cells and offspring cells while retaining some of the biological functions of the parent cells[16]. In addition, exosomes also have reduced immunogenicity, enhanced permeability, and good retention effects, enabling them to modulate several complex biological activities (Figure 2)[17].

2.2. Current applications for exosomes

Exosomes have various biological functions (Figure 3)[18]. It can stimulate anti-tumor immune responses, aid angiogenesis in tumor metastasis[17], and play important roles in the propagation of misfolded proteins to influence the development of neuroinflammation in neurodegenerative diseases[19]. Exosomes are also rapidly evolving in the fields of immunomodulation, cancer therapy, and regenerative medicine.

2.2.1. Bone tissue engineering

In bone-related disease injuries, exosomes from mesenchymal stem cells (MSCs) can mediate cartilage repair by enhancing cell proliferation and infiltration, reducing apoptosis, and modulating immune responses[20]. A series of *in vivo* studies showed that the administration of exosomes from MSCs effectively reduced the production of pro-inflammatory cytokines in chondrocytes, increased the

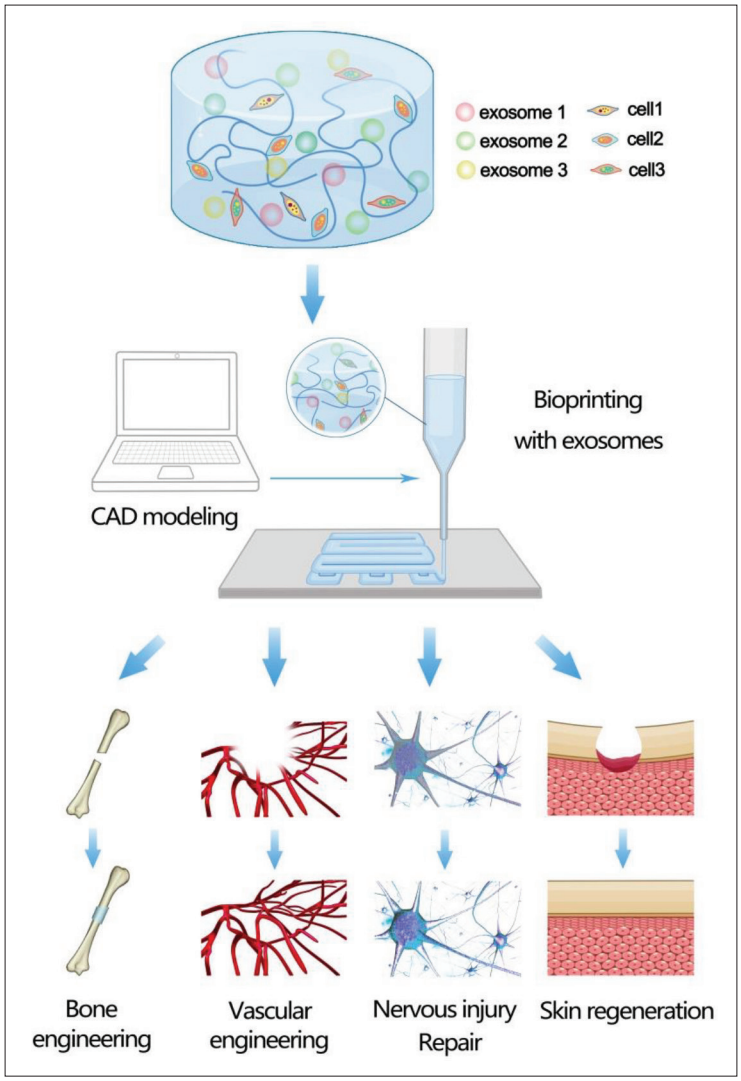

Figure 1. The general scheme of exosomes-advanced bioprinting and its applications. Through CAD modeling to recapitulate the structures of the damaged regions, exosomes can improve the bioprinted constructs for the applications of bone engineering, vascular engineering, nervous injury repair, and skin regeneration.

expression of ECM components in cartilage, and ultimately enhanced the regeneration of cartilage tissues[21-24].

2.2.2. Immunological regulation

The two main mechanisms of exosomes acting in immune regulation are their direct actions on the targeted cells to initiate downstream signals and the miRNA-mediated (indirect) regulations[18]. Cancer cell-derived exosomes can block the maturation and migration of dendritic cells through PD-L1 (programmed death ligand-1)[25]. Meanwhile, exosomes from tumors can inhibit RFXAP (regulatory factor X-associated protein), an essential transcription factor for MHC-II (major compatibility complex II) in dendritic cells, via miR-212-3p, thereby reducing MHC-II expression and inducing immune tolerance in dendritic cells[26].

2.2.3. Angiogenesis

Exosomes can also be involved in the differentiation of vascular cells, the promotion of blood flow restoration, and the formation of the capillary network during angiogenesis. For instance, MSC-exosomes can increase endothelial cell lumen formation and promote angiogenesis[27]. Subcutaneous injection of the exosomes from human umbilical MSCs in a nude mouse model significantly increased neovascularization around the infarct areas *in vivo*[28]. In addition, the exosomes from stem cells also have the ability to induce angiogenesis in the resting state[29].

2.2.4. Neural degeneration

Certain neuronal exosomes are involved in the accumulation of misfolded proteins in the brain and accelerate the progression of neurodegenerative disease,

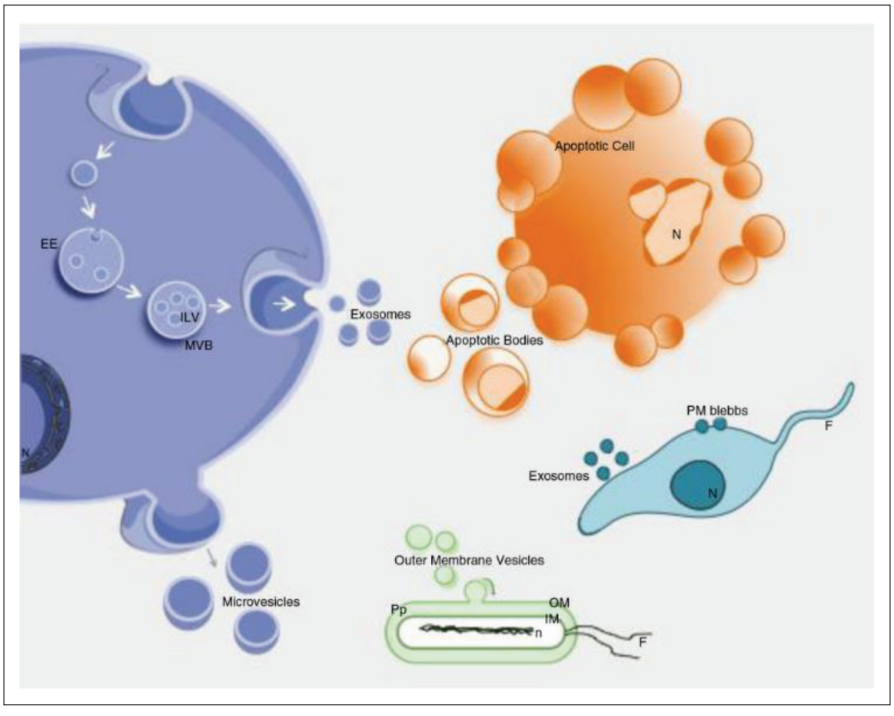

Figure 2. Biogenesis and release of extracellular vesicles. Extracellular vesicles can be broadly classified into three main classes: (a) Microvesicles are produced by outward budding and fission of the plasma membrane; (b) exosomes are formed within the endosomal network and released upon fusion of multi-vesicular bodies with the plasma membrane; (c) apoptotic bodies are released as blebs of cells undergoing apoptosis. EE: early endosome; F: flagella; ILV: intraluminal vesicles; IM: inner membrane; MVB: multi-vesicular body; N: Nucleus; n: nucleoid; OM: outer membrane; PM: plasma membrane ; Pp: periplasm. Reprinted with permission from ref.[17]. Copyright 2015 John Wiley and Sons, Inc.

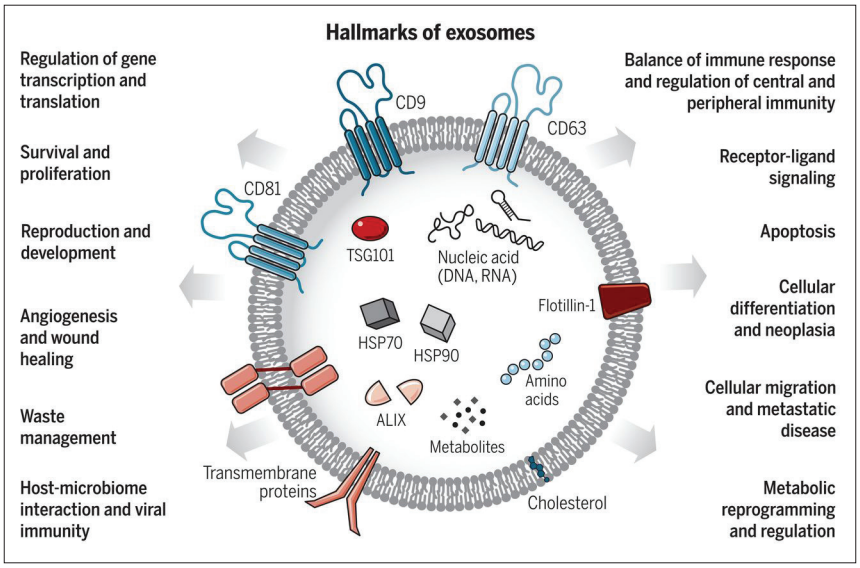

Figure 3. Exosomes: A cell-to-cell transit system in the human body with pleiotropic functions. Reprinted with permission from ref.[18]. Copyright 2020 American Association for the Advancement of Science.

while others can help remove these misfolded proteins and perform detoxification, showing the neuroprotective functions. Haney *et al.* developed an exosomal drug delivery system based on oxidase, which was tested both *in vivo* and *in vitro* with Parkinson's models and demonstrated the significant neuroprotective effects of this system, offering further possibilities for the treatment of neurodegenerative diseases[30].

2.3. Exosomes and decellularized extracellular matrix (dECM)

Recently, there has been another biologically derived material widely used in bioprinting called decellularized ECM (dECM). It is a combination of 3D scaffolds, proteins, and bioactive small molecules that remain after removing all or part of the cellular and nucleic acid components. It is typically derived from animal, human, or plant tissues[31]. While dECM can be used as a bioink in bioprinting, it differs significantly from exosomes due to the variations in their sources, collection methods, bioink preparation processes, and ink properties. Common methods for preparing dECM involve either vascular system perfusion or immersion/stirring[32]. During printing, collagen cross-linking serves as the primary mechanism of solidification. Therefore, it is mainly compatible with digital light processing or extrusion-based approaches[33].

Unlike dECM, exosomes can be collected using centrifugation techniques and subjected to surface processing[34]. By adding specific scaffolding proteins, cytokines, hydrogels, or other materials, exosomes can be turned into bioinks that primarily deliver signaling molecules, proteins, and nucleic acids. Exosomes contain signaling molecules that play a significant role in tissue repair, giving them potential for applications in bioprinting[35]. Compared to dECM, exosome therapy has fewer ethical limitations, lower immunogenicity, and reduced risks of ectopic transplantation[36]. Therefore, it has been applied to the bioprinting of different tissues or organs, such as blood vessels [37-39], bones[36,40], skin[41], nerves[42-44], corneas[45], etc. For instance, Zhang *et al.* developed a 3D PLA scaffold based on MSC exosomes[40]. It reduced pro-inflammatory markers and ROS (reactive oxygen species), showing immune regulation potential, and enhanced osteogenic differentiation, contributing to bone formation. Shafei *et al.* used an alginate hydrogel with Adipose-derived Stem Cells (ASC) exosomes as a bioactive scaffold[46]. It had beneficial effects on wound closure and promoted re-epithelialization. The applications of exosomes in different tissues will be discussed in detail later in the text. However, it should be noted that exosomes are highly sensitive to environmental factors such as temperature and pressure since they exist as extracellular vesicles, causing their storage and transport more challenging. Further explorations are also needed to understand the functional mechanisms of exosomes.

Similar to exosomes, dECM may also contain signaling molecules that can regulate cell behaviors and promote cell adhesion, migration, and differentiation[47,48]. In addition, research has demonstrated that dECM materials have potential applications in tissue remodeling and organ regeneration by enhancing cellular functions and promoting a variety of tissue remodeling processes[49]. The dECMs from different sources of the tissues have shown higher tissue-specific heterogeneities for their potential applications compared to the applications of exosomes. Currently, many dECM inks are derived from porcine tissues[50,51], raising questions about their biocompatibilities for later clinical applications. Additionally, their overall biocompatibilities also require further investigation since dECM materials are extracted from real biological tissues that are influenced by age, health status, and environmental factors. Batch variations and instabilities are also issues that need addressing.

In summary, both dECM and exosomes have the potential for applications in tissue engineering. However, further research is needed to explore their applications and overcome their respective limitations.

3. Bioprinting

3D printing technology, as an emerging field in regenerative medicine, is showing great potential compared to traditional technologies. It has offered a huge possibility for digital designs with low manufacturing costs. Derived from 3D printing technology, bioprinting, especially organ printing, has developed rapidly in recent years. With technological advances, plenty of great demonstrations have been fulfilled in various fields, such as bone engineering, artificial vascular, nerve injury treatment, skin regeneration, and so on. In order to meet the distinct functions required in these different applications, the appropriate bioinks and printing methods need to be designed and engineered.

3.1. Bioink

Bioink is an important factor that directly affects cell survival and biomaterial constituent in tissue engineering and regenerative medicine. Hydrogel is a commonly used bioink which can mimic the physical characteristics of ECMs in the body. Generally, two types of hydrogels are used for bioink: natural-derived hydrogels and synthetic hydrogels. The materials of natural-derived hydrogels are mainly generated from the body of the organisms, such as collagen, alginate, agarose, hyaluronic acid, etc. On the other hand, a synthetic hydrogel is usually synthesized by chemical methods. Its physical and chemical properties are usually controllable to meet specific requirements for bioprinting, such as good biocompatibility for a high cell survival rate and optimal viscosity for high printing resolution. Commonly used synthetic bioink includes polyethylene glycol (PEG) and Pluronics F127. For the specific introductions of bioinks, please refer to the review by Barrs *et al.*[52] In addition, according to the preparation methods of hydrogels, they can be divided into physically

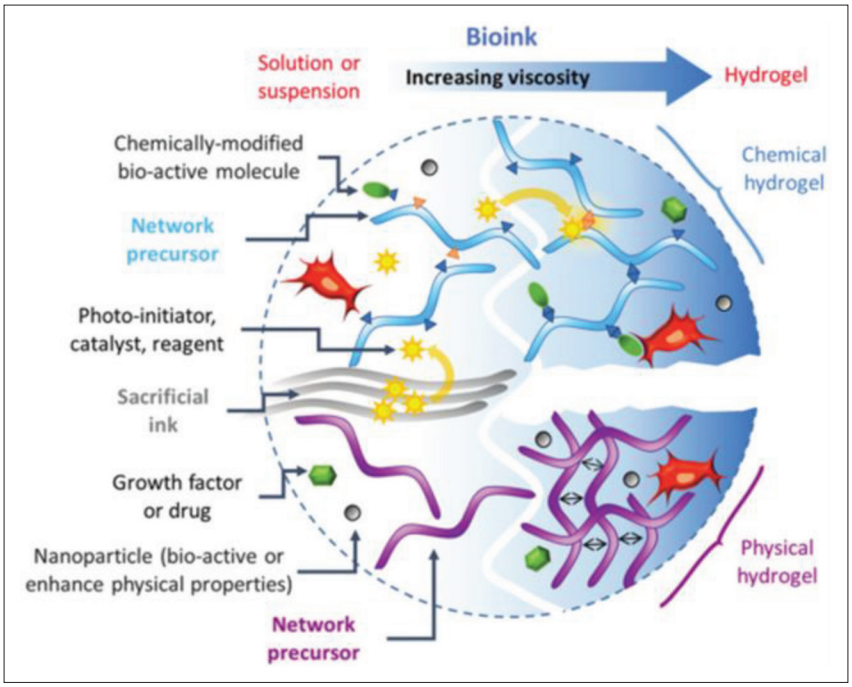

Figure 4. Bioink systems for printing. Reprinted with permission from ref.[53]. Copyright 2019 Royal Society of Chemistry.

cross-linked hydrogels and chemically cross-linked hydrogels (Figure 4). The specific principles and examples for hydrogel preparations can refer to the review by Valot *et al.*[53].

3.2. Printing methods

There are several distinct available printing methods. Here, we briefly introduce three printing methods categorized according to ASTM standards, which are extrusion-based, jetting-based, and vat photopolymerization (VP)-based bioprinting.

3.2.1. Extrusion-based bioprinting

One of the most common bioprinting methods is extrusion-based bioprinting (Figure 5A). It combines a fluid distribution system and an automated robotic system. The fluid-dispensing system can be driven by a pneumatic-, mechanical-(piston or screw-driven), or solenoid-based system[54]. The working procedure of extrusion-based bioprinting includes three steps: (i) the hot-melt material (as the bioink) is liquidized through the heater; (ii) the bioink is pumped into filaments and sent to the hot-melt nozzle; (iii) the nozzle head squeezes out of the bioink. Through printing, CAD layered data can control the path during the squeezing out of bioink and place it in the specified positions to solidify. The printed materials can bond with the surrounding materials, stacking layer by layer[55]. Therefore, a stable bioink is needed for this approach. However, this technology has shortcomings, such as a limited cell survival rate and relatively low resolutions[56].

3.2.2. Jetting-based bioprinting

Inkjet bioprinting is derived from commercial two-dimensional (2D) inkjet printing technologies (Figure 5B). The main difference between this technology and extrusion-based bioprinting is that the bioink is produced at a point where the nozzle head hits. Therefore, jetting-based bioprinting has the advantage of high resolution. For jetting-based bioprinting, its bioink must be liquid-like in case of blocking the nozzle. Besides, the viscosity of biological ink is also difficult to control[57]. Meanwhile, the side effect brought by high resolution is slow printing speed. In addition, the discontinuous droplets can also lead to a weak mechanical strength of the bioprinted structure[58]. Therefore, it is recommended to adjust the mechanical properties of bioink to guarantee the printing quality. For instance, Suntornnond *et al.* modified GelMA through saponification and heat treatment, effectively improving its printability and biocompatibility in thermal injection printing[59].

3.2.3. Vat photopolymerization (VP)-based bioprinting

The working principle of VP-based bioprinting (laser-assisted bioprinting [LAB]) is that the laser focuses on the glass plate absorption layer to produce a high-pressure liquid foam and to push the cells to the acceptable

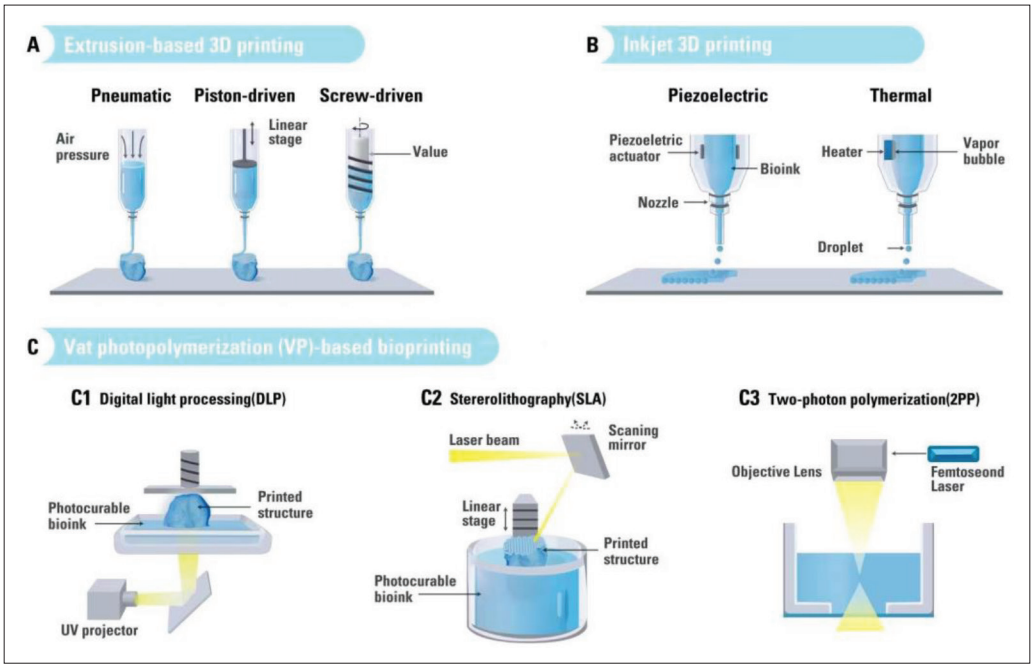

Figure 5. Representative demonstrations of 3D bioprinting methods. (A) Extrusion-based 3D printing; (B) Inkjet 3D printing; (C) Vat photopolymerization (VP)-based bioprinting: C1, digital light processing (DLP); C2, stereolithography (SLA); C3, two-photon polymerization (2PP)[61].

substrate[60]. The VP-based bioprinting is divided into stereolithography (SLA), digital light processing (DLP), and two-photon polymerization (2PP)[61].

In the SLA system (Figure 5C1), two different methods can be used for optical solidification: (i) top-down printing approach, that is, the scanning laser solidification above the vat cures a layer of resin on the build platform, and it is lowered into the vat to repeat the curing process; (ii) bottom-up printing approach, that is, the scanning laser is located at the bottom of the vat, and the build platform is raised above the bioresin vat via a "peeling" step between each printed layer. DLP (Figure 5C2) is another method for optically curing biological resin. Using digital micromirror devices (DMD) in DLP helps to obtain a layer of optical solid resin instead of single-point solidification in SLA. 2PP (Figure 5C3) process is caused by three-order non-linear absorption within the focal region; the beam of the flying laser is closely focused on the photoresist (liquid biological resin) on the glass coverslip with an oil-immersion objective lens to fabricate high-resolution 3D structures beyond the optical diffraction limit by moving the focused beam within the photoresist.

The advantage of VP-based bioprinting is that the nozzle is open; thus, there is no nozzle blockage issue. At the same time, the cell damage is limited, leading to a 95% cell survival rate[62]. However, the effect of laser on cells is not well-defined yet, which may have considerable cytotoxicity[63].

4. Biomedical applications of bioprinting with exosomes

4.1. Bone engineering

Traditional bone transplantation is still one of the common ways to treat bone damage or loss. However, due to the body's rejection, allografts are likely to cause a series of complications[64], so their application is limited. Applying tissue engineering approaches (e.g., bioprinting or organ printing) to repair bone damage and loss is a relatively novel way and also a hot research topic at present.

However, the bioactivities of several traditional bioink for bone repair are limited[65]. Meanwhile, exosomes with the size of 50–120 nm have relatively high biocompatibility and a strong ability to promote bone formation, providing a new idea for the strategies of bone regeneration. Great bone specificity and strong bone regeneration properties make exosomes significantly valuable for therapeutics, which can enhance bone growth to treat clinical bone diseases[66]. Therefore, loading exosomes into bioink for bone tissue bioprinting has become one of the practical options to build highly bioactive structures for bone repair.

Sun *et al.* applied 3D printing technology to construct porous scaffolds with β-tricalcium phosphate (β-TCP) bioceramic-induced macrophage exosomes[36]. The system exhibited a predefined structure and a persistent release of exosomes, displaying improved effects in immunomodulatory and osteogenesis/angiogenesis

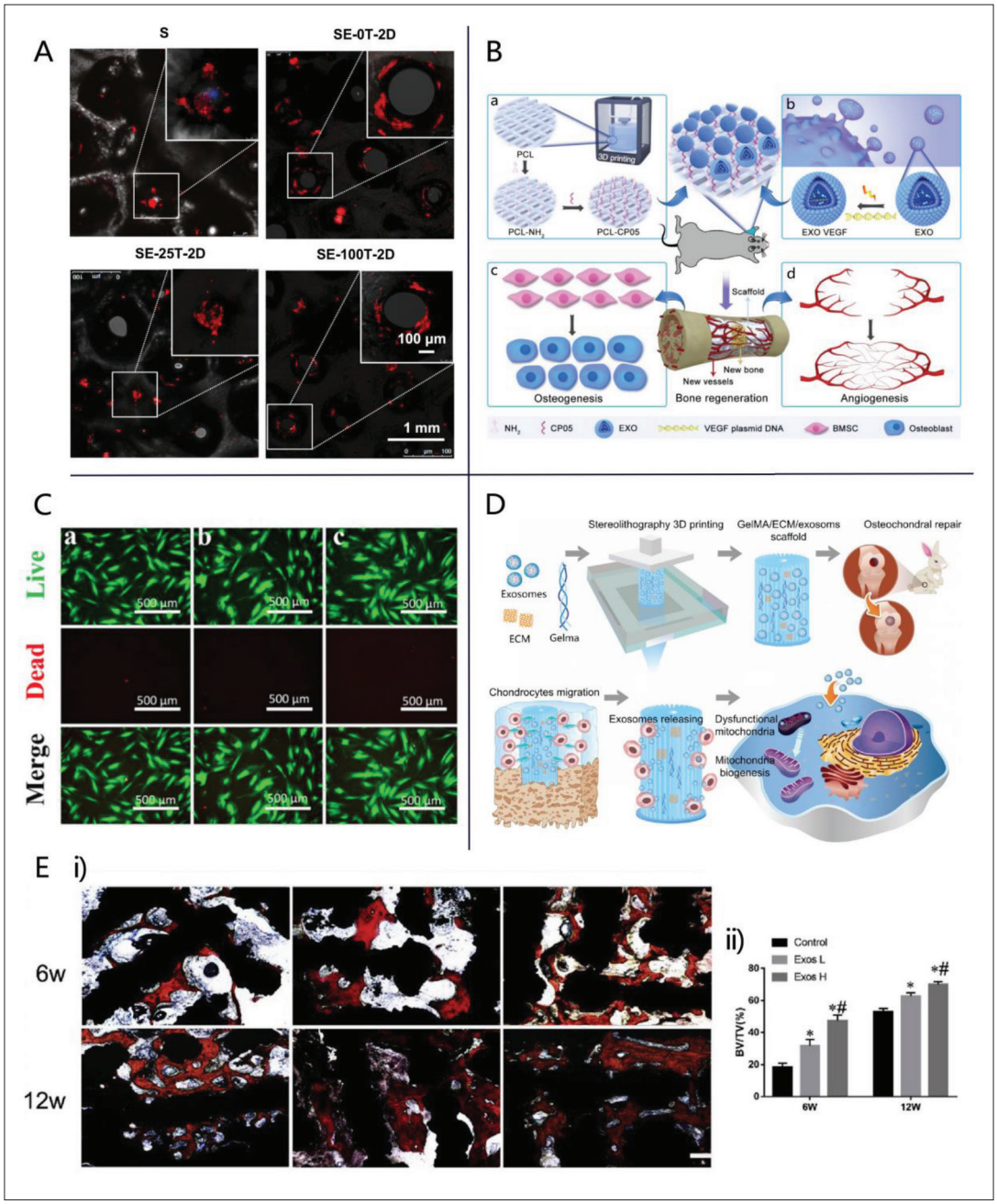

Figure 6. Bioprinting with exosomes for biomedical applications in bone engineering. (A) Representative fluorescence images of Human umbilical Vein Endothelial Cells (HUVECs) on scaffolds on day 1. Cells were stained with TRITC–phalloidin (red). Adapted with permission from ref.[36]. Copyright 2021 Springer Nature Limited. (B) General scheme of engineered exosome-enhanced therapies on osteogenesis and angiogenesis. (a) 3D-printed porous PCL scaffolds were modified with 1,6-hexanediamine to generate the amino group on PCL scaffolds that were subsequently modified with the exosomal anchor peptide CP05. (b) Engineered exosomes were fabricated by encapsulating the VEGF plasmid DNA into ATDC5-derived exosomes. The well-designed bone scaffolds were constructed by combining the engineered exosomes with the CP05-modified 3D-printed scaffolds, and eventually implanted into a rat radial defect model to promote osteogenesis (c) and angiogenesis (d). Adapted with permission from ref.[67]. Copyright 2021 Ivyspring International Publisher. (C) Live/dead assay of human bone marrow stem cells (hBMSCs) co-cultured with different scaffolds for 3 days. The cells were stained with fluorescein diacetate (FDA, green) and propidium iodide (PI, red) and were examined by confocal microscopy. Green indicated living cells, and dead cells were labeled as red fluorescence. Group a = control, group b = PLA scaffold, group c = PLA-Exo scaffold. Adapted with permission from ref.[40]. Copyright 2022 BioMed Central Ltd., part of Springer Nature. (D) Schematic illustration of the one-step operation system for facilitating osteochondral defect regeneration. Adapted with permission from ref.[68]. Copyright 2019 Ivyspring International Publisher. (E) Effect of different scaffolds on bone regeneration. (i) Van Gieson staining results in the different groups at 6 and 12 weeks. (ii) Quantitative analysis of BV/TV in the different groups[36-40]. Adapted with permission from ref[69]. Copyright 2020 Elsevier LTD.

(Figure 6A). It provided a novel inspiration for bone regeneration and the design of therapeutic biomaterials with improved immune regulations.

Of the essential elements of tissue engineering, cell seeding is important for inducing effective tissue regeneration. However, cell-based tissue engineering approaches also have many drawbacks, such as limited sources and restricted expansion capacities of donor cells, immune rejection, and many others. Thus, cell-free tissue engineering has been extensively explored in regenerative medicine as a safe, effective, and off-the-shelf strategy. Zha *et al.* developed a cell-free tissue engineering system using functional exosomes instead of seeding cells[67]. Gene-activated engineered exosomes were constructed by using ATDC5-derived exosomes to encapsulate the VEGF gene. The specific exosomal-anchored peptide CP05 acted as a flexible linker, effectively linking the engineered exosome nanoparticles with 3D-printed porous bone scaffolds (Figure 6B). The scaffolds were tested to effectively induce the bulk of vascularized bone regeneration, illuminating the potential of functional exosomes in acellular tissue engineering.

MSCs have strong proliferative ability and multi-directional differentiation potential. It can secrete cytokines through paracrine effects to repair tissues. Zhang *et al.* developed a bioactive 3D PLA scaffold using an exosome-based strategy[40]. PLA-Exo scaffold can reduce the expression of the pro-inflammatory markers and limit the production of the ROS, indicating its immunoregulatory potential. Meanwhile, the authors confirmed that it could enhance osteogenic differentiation in the osteogenic tests, showing potential applications in bone tissue regeneration (Figure 6C).

Similarly, Chen *et al.* also designed a bioscaffold for delivering MSC exosomes. They fabricated a 3D-printed cartilage ECM/gelatin methacrylate/exosome scaffold with radially oriented channels using desktop-stereolithography technology (Figure 6D), which significantly facilitated cartilage regeneration in the animal model[68]. At the same time, the 3D-printed radial exosome scaffolds also can be a promising strategy for early osteoarthritis treatment.

In addition to the direct combination of bone bioprinting and osteogenic exosomes for bone tissue repair, the following system also offered new opportunities for the applications of exosomes in bone bioprinting. Wu *et al.* added the Schwann cell-derived exosomes to bone marrow stromal cell culture environments and found they could effectively promote the migration, proliferation, and differentiation of bone marrow stromal cells[69] (Figure 6E). In addition, the combination of exosomes and porous Ti6Al4V implants provided both mechanical support and open pores, exhibiting good biological activity. It was also a therapeutic strategy with a high potential for treating bone defects.

Exosomes are considered a powerful supplement for cell therapy in regenerative medicine for their excellent biocompatibility, efficient cell internalization, and strong load capacities. However, exosomes still have some shortcomings, such as low yield, unstable efficiency, and lacking drug delivery routes, which can affect the further applications of biomolecular carriers. Zha *et al.* developed a novel exosome-mimetics, which had a similar structure and biomarkers in comparison with the routine exosomes[70]. It can be generated with a high yield and has been applied to construct an engineered gene-activated matrix for local therapy, opening up a new idea for using exosomes.

Furthermore, some researchers have also provided new ideas to improve the therapeutic efficacy of exosomes. Li *et al.* developed a stem cell-mediated gene therapy in which mediator MSCs were genetically engineered by the bone morphogenetic protein-2 gene to produce exosomes with enhanced bone regeneration potency[71]. The accelerating effect in bone healing and good biocompatibility suggested the potential clinical application of this strategy if applied with bioprinting.

In summary, though exosomes have been widely studied, the research of 3D bioprinting with exosomes has been initiated in bone tissue engineering and holds great potential in tissue regeneration.

4.2. Vascular engineering

Exosome bioprinting technology has also been applied to vascular engineering. The application of exosomes in 3D printing can promote the sustained release of exosomes and improve their biological activity. Sun *et al.* used 3D printing technology to construct porous scaffolds for macrophage exosomes (BC-Exos) induced by β-tricalcium phosphate (phosphate bioceramics), and realized 3D-printed BC-Exo scaffolds. The system had a predefined structure and enabled the continuous release of exosomes (Figure 7A)[36]. It also showed significant immunomodulatory effects and improved osteogenesis/angiogenesis properties. This design of a cell-free 3D-printed scaffold using biomaterials to activate macrophage exosomes has increased the application of immune cell-derived exosomes in tissue regeneration and provided a new direction for the design of bioprinted systems. This study suggested that the 3D printing of bioceramics-induced macrophage exosomes can be a useful strategy for tissue engineering and regenerative medicine.

In terms of the clinical application of exosomes derived from bone marrow MSCs, Zhang *et al.* developed a system

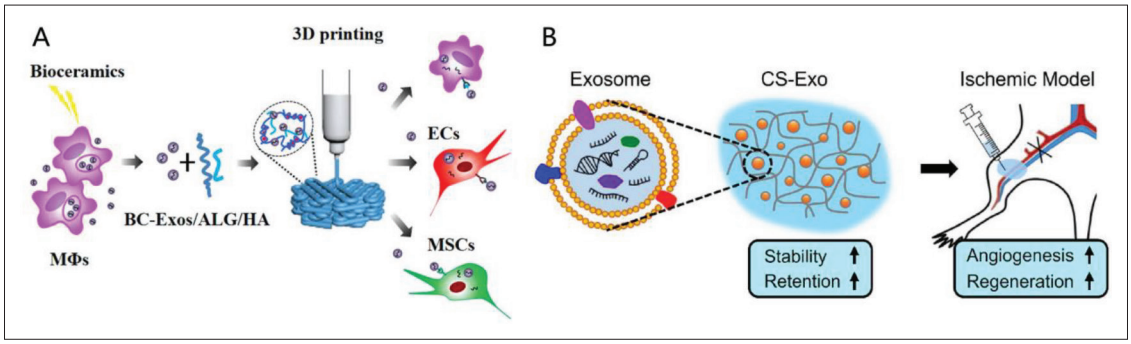

Figure 7. Exosomes promote bioprinting for vascular engineering. (A) Schematic illustration showing the preparation of bioceramic-induced macrophage exosomes (BC-Exos) and 3D printing of BC-Exos for immunomodulation, osteogenesis, and angiogenesis of macrophages, mesenchymal stem cells (MSCs), and endothelial cells. Adapted with permission from ref.[36]. Copyright 2021 Springer Nature Limited. (B) Schematic illustration of hP-MSCs-derived exosomes incorporated with CS hydrogel for muscle regeneration. Adapted with permission from ref.[72]. Copyright 2018 American Chemical Society.

combining exosomes with chitosan hydrogels to enhance the therapeutic effect of human placenta-derived MSCs (hP-MSCs) derived exosomes[72] (Figure 7B). The chitosan hydrogels had the characteristics that can enhance the retention and stability of exosomes. In addition, the hydrogels also further improved the therapeutic effect of angiogenesis in hindlimb ischemia, as shown by firefly luciferase imaging. This strategy may be of great practical value for cell-free therapy.

4.3. Nerve injury repair

Nervous injury includes central nervous injury and peripheral nerve injury. It has the characteristics of high incidence and inaccurate pathogenesis; furthermore, it still lacks a clear treatment strategy yet[73]. In recent years, many researchers have focused on bioprinting scaffolds with exosomes. These systems have the following advantages: (A) They can effectively maintain the exosomes of the damaged part and retain its performance and structural characteristics. (B) The exosomes are released into ECM to adjust the phenotype of neighboring cells. (C) It can be combined with the injured tissues to support the migration of neighboring cells. Once the neighboring cells migrate to the biological scaffold, the exosomes can be absorbed to promote tissue regeneration[74].

Liu *et al.* prepared 3D-printed collagen/silk fibroin/hypoxia-pretreated human umbilical cord MSCs (HUCMSCs)-derived exosomes scaffolds (3D-CS-HMExos) and implanted it into the injured brain of the small hunting dog to treat traumatic brain injury (TBI)[75]. The experimental results showed that the method could effectively promote nerve regeneration after TBI and, at the same time, inhibit neuritis and the apoptosis of neurotic cells, providing a new strategy for treating TBI (Figure 8A). Additionally, Hsu *et al.* developed alginate and HUCMSCs exosomes[78]. The scaffold had anti-inoculation, anti-inflammatory, and neurotrophic effects. It also has been shown that the pain caused by L5/6 spinal nerve ligation (SNL) can be treated by this scaffold.

Rao *et al.* combined biodegradable chitin with exosomes derived from the gums to treat the sciatic defects of rats[79]. The study results showed that exosomes were effective for treating nerve injuries, and it was a method of nerve regeneration with excellent performance. Han *et al.* proposed a controllable 3D external hydrogel mixed microneedle array patch to achieve the method of repairing spinal cord injury (Figure 8B)[76]. They cultivated the exogenous body of 3D mesenchymal stem cells (MSC-EXO). Different from other studies of the single-layer (2D) exterior body of hydraulic gel, 3D-EXO can maintain the stem nature and improve the effects of MSCs. In addition, the study also compared the effects of 2D and 3D exosomes on the treatment of nerve repair, and the results showed that the 3D exosomes have higher therapeutic efficiency. This result also revealed that biological 3D printing could effectively improve the efficiency of the repair.

At present, the demonstrations of biological 3D printing technology with exosomes are still limited, but many studies have been put into treatment with exosomes and hydrogels. Liu *et al.* tested the rigidity of hydrogels in loaded exosomes in nerve repair[80]. The study showed that soft hydrogel can better repair peripheral nerve damage. This result also revealed the selection criteria of hydrogels in nerve repair. Li *et al.* used exosomes derived from the human MSC in an EXOO-PGEL (EXOO-PGEL) for peptides[77]. The tissue nerve-derived injury has developed an innovative strategy for exogenous physical delivery for spinal cord injury treatment (Figure 8C). Wang *et al.* used retinal ganglion cells of rats (RGC) exosomes as nano-sized vesicles, loading PACAP38 through exosomes anchoring peptide CP05 (Exopacap38) to treat external injuries

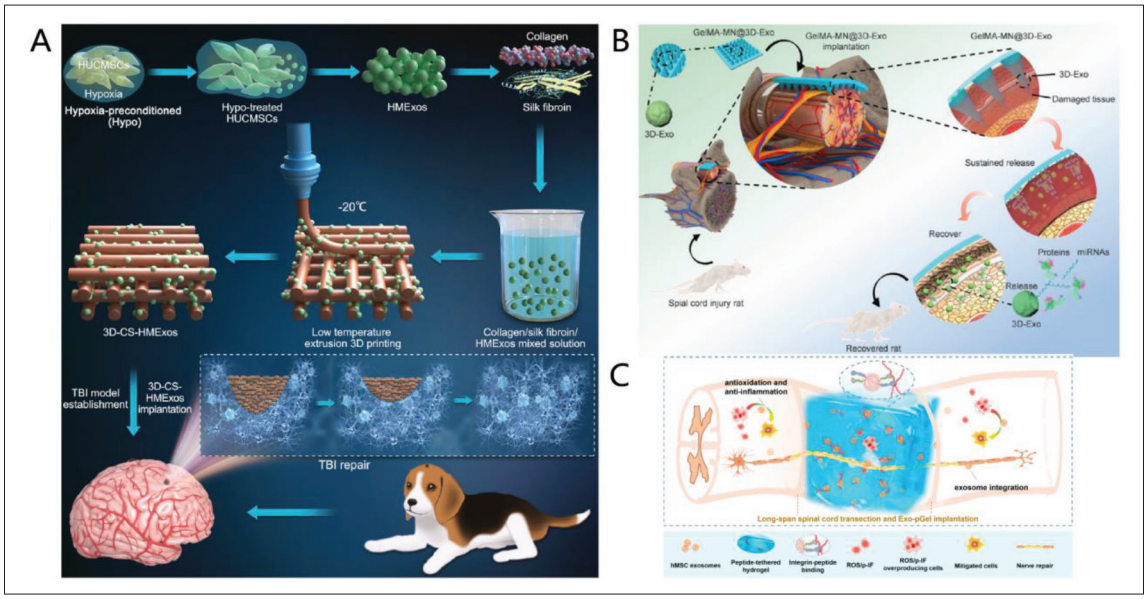

Figure 8. The applications of biomedical engineering for nerve injury repair. (A) 3D-printed collagen/silk fibroin/hypoxia-pretreated human umbilical cord mesenchymal stem cells (HUCMSCs)-derived exosomes scaffolds (3D-CS-HMExos) and implanted in the injured brain of the small hunting dog, which used to treat traumatic brain injury (TBI). Adapted with permission from ref.[75]. Copyright 2022 Frontiers Media S. A. (B) The controllable three-dimensional exterior hydrogel mixed microneedle array patch to achieve the repair of spinal cord injury. Adapted with permission from ref.[76]. Copyright 2022 American Chemical Society. (C) The exogenous body derived from human MSC was fixed in an exo-PGEL (Exo-PGEL) that promoted spinal cord regeneration and recovery of hind limbs. Adapted with permission from ref.[77]. Copyright 2020 American Chemical Society.

(traumatic optic neuropathy[TON])[81]. It overcame the shortcomings of low tissue penetration and a short half-life period and improved the transfer efficiency of neurogenic peptides.

Bioprinting technology with exosomes is an innovative strategy for treating nerve damage. Compared with other bioink, exosomes can effectively improve bioactivity. The potential of exosomes in treating neural diseases, including those related to neurotransmitters, is evident from their nature discussed in the first chapter and this section.

4.4. Skin regeneration

Conventional means of skin repair include topical application of relevant drugs, exposure to lasers, and skin grafting[82,83]. In recent years, researchers have discovered the linkage between exosomes and skin diseases[84,85]. They found that exosomes can participate in the physiological and pathological processes of the skin, such as regulating the secretion of pro-inflammatory cytokines in the microenvironment of skin, promoting vascularization and collagen deposition in some skin defect diseases, as well as regulating the proliferation and differentiation of skin fibroblasts[86-88]. Most importantly, people have discovered that exosomes positively affect skin regeneration and repair.

Shafei *et al.* used an alginate hydrogel loaded with adipose stem cell-derived exosomes as a bioactive scaffold and found that it not only had good effects on wound closure, but also promoted a high degree of re-epithelialization [46]. They characterized the physical and biochemical properties of the hydrogel and found that the prepared exosome-hydrogel had excellent biodegradability and biocompatibility. The exosome-hydrogel significantly improved wound closure, collagen synthesis, and angiogenesis in the wound area. The results of this study also provided a cell-free therapeutic strategy for wound healing treatments using composite structures of exosomes-encapsulated alginate hydrogels, showing its great potential for application in bioprinting.

One of the common complications of diabetes is impaired wound healing, characterized by inadequate angiogenesis and susceptibility to infections, which can lead to non-healing chronic diabetic ulcers[89]. Wang *et al.* prepared a polysaccharide-based dressing (FEP) exosome-contained scaffold dressing with heat-sensitive, injectable, adhesive, self-healing, antibacterial, hemostatic, and UV shielding properties to stimulate early angiogenesis in diabetic wounds[90]. It has been demonstrated that the system thus promoted skin healing and reconstruction. The scaffold can chronically release exosomes from adipose stem cells, enhancing the proliferation, migration, and tubular formation of stimulated HUVECs, and promoting diabetic wound healing. The synergistic effects of these stimulatory responses promoted granulation tissue

formation and collagen deposition, driving wound re-epithelization and significantly increasing the regeneration of skin appendages. In addition, it also reduces the formation of scar tissue. Exosome-loaded FEP hydrogels have shown great potential in promoting diabetic wound healing, providing strong evidence for their clinical potential in skin regeneration.

Exosomes combined with bioprinting for skin tissue engineering may mainly refer to the exosome-contained, bioprinted scaffolds to aid wound closure and promote the stable release of therapeutic exosomes in predesigned areas. The combination improves therapeutic efficacy and further takes advantage of the high bioactivity of exosomes[91]. Although it is still at an early stage of development and more focus on the research is needed, based on the current demonstrated examples about the combination of exosomes and hydrogels, it may be possible to modify the designs of exosome-loaded hydrogels and apply them to the preparation of bioinks, thus building high-activity exosome-bioprinting systems, which will be one of the promising research directions in the field of regenerative medicine in the near future.

4.5. Other applications

4.5.1. Corneal repair

Currently, bioprinting with exosomes has not yet been systematically studied in the field of corneal repair. However, there has been relatively in-depth research on using exosomes for the treatment of corneal injury. For instance, Samaeekia *et al.* isolated corneal mesenchymal stem cell (cMSCs) exosomes from humans and found a significant healing effect of the exosomes on corneal epithelial cell damage[92]. Shojaati *et al.* demonstrated that exosomes produced by corneal stromal stem cells (CSSC) inhibited the formation of fibrotic scarring after corneal injury and stimulated the regeneration of transparent stromal tissue[93].

Several different 3D bioprinting strategies have been developed for the fabrication of corneal donor graft materials. Sorkio *et al.* used stem cells and laser-assisted bioprinting to produce a 3D corneal tissue that mimicked the structure of natural corneal tissue. The cells in the structure maintained good viability[94]. Isaacson *et al.* used a low-viscosity bioink made from sodium alginate and methacrylated type I collagen to produce an artificial corneal substitute by 3D bioprinting, which also had good biocompatibilities and bioactivities[95].

4.5.2. Oral repair

The oral cavity contains various tissues, such as teeth, jaw, gums, oral mucosa, gland, and cartilage. Stem cells in these tissues can secrete different functional exosomes, and these exosomes have different biological effects. For example, studies have found that exosomes secreted from dental pulp stem cells (DPSCs-E) inhibited the differentiation of $CD4^+$T cells into T helper 17 cells (Th17) and reduced the secretions of pro-inflammatory factors IL-17 and TNF-α, while promoted the polarization of $CD4^+$T cells into Treg and increased the release of anti-inflammatory factors IL-10 and TGF-β[96]. Wei *et al.* used stem cells from human exfoliated deciduous teeth (SHED)-derived exosomes (SHED-Exo) in the bone loss area caused by periodontitis in a mouse model[97]. SHED-Exo specifically promoted BMSCs osteogenesis and inhibited adipogenesis. In addition, SHED-Exo can further promote osteogenic differentiation and bone formation in BMSCs.

Meanwhile, in dental medicine, biological 3D printing technology has been widely used to cure diseases such as tooth osteo-deficiency. Tian *et al.* mixed sodium alginate (SA), gelatin (Gel), and nano-hydroxyapatite (na-HA) to prepare a hydrogel composite[98]. Human periodontal ligament stem cells (HPDLSCs) were mixed with SA/Gel/na-HA printing slurry to create a "bioink" to prepare SA/Gel/na-HA/hPDLSCs cell bioscaffolds. The results showed that the SA/GEL/N-HA composite hydrogel had good streaming performance and was suitable for printing. Cell biological stent had good biocompatibility and was conducive to the osteoma of HPDLSCs.

In all, there have been great potential for the use of exogenous biological printing for corneal repair and oral repair, while the current research applications still have great challenges from the perspective of real clinical applications.

5. Summary

3D bioprinting technology is a new field that has emerged in recent years. However, their translational application in the clinic is still lagging due to their limited ability to produce bioprinted constructs with the necessary biological activities to integrate with host tissues. Exosomes have high biological activity as an important medium of information transmission in organisms. They have become one of the potential materials for application in bioprinting systems. Combining exosomes as bioink with bioprinting technology can compensate for the lack of biological activity of traditional 3D bioprinting. Traditional 3D bioprinting bioinks for scaffold manufacturing include alginate, gelatin, and collagen. Gelatin is a soluble protein compound obtained by partial hydrolysis of collagen, which is the main fibrin component in bone, cartilage, and skin[99], while natural alginate is a bioinert material (i.e., it lacks cell adhesion part) with limited biodegradation[100-102]. Compared with the above biological materials, exosomes have shown higher biological activity and targeting in cell signaling and drug release[103]. Therefore, exosomes can

effectively affect the activity of cells and the development of tissues through multiple signaling pathways without causing immune responses. In addition, some stem cell-derived exosomes also have exhibited immunomodulatory and tissue regeneration abilities[104]. From the perspective of enhancing the biological activity of biological ink by exosomes, this paper briefly introduced exosomes and 3D bioprinting technology and summarized the application and progress of exosomes and 3D bioprinting technology in bone, blood vessel, nerve, and skin in recent years. At present, there have been many studies on the use of exosome hydrogels for the treatment of diseases. This paper briefly combed them and outlined their advantages and disadvantages, as detailed in Table 1.

However, despite the exciting progress to date, several challenges remain. Firstly, good-quality exosomes should be obtained before printing. However, the current challenge lies not only in the isolation of exosomes before preparing exosome-rich bioinks. At present, the methods for extracting exosomes mainly include differential centrifugation[105], volume exclusion chromatography[106], and immunoaffinity capture[107]. Each method has advantages and disadvantages, but the extraction method to be used is determined by the sample source and the intended use of exosomes. A few studies have been conducted on the rapid and accurate preparation of bioactive exosomes with a low loss rate[108]. Secondly, during the printing process, it is necessary to ensure that the exosomes are put into the bioprinting system while maintaining sufficient biological activity. For instance, integrating exosomes with bone tissue engineering materials gives rise to a favorable environment for exosomes to exert their functions[24]. However, it has also been found that exosomes cannot exert sustained function due to their short half-life. Although the combination of exosomes and liposomes can complement each other, sustained release of exosomes has not been demonstrated to accumulate in the bone marrow[109]. In the area of angiogenesis, there have been cases in which chitosan hydrogels have been used to improve the stability of proteins and microRNAs in exosomes significantly. However, the release of exosomes depended on the permeation and biodegradation of chitosan hydrogel, which made this process difficult to control[72]. A class of peptide-modified adhesive hydrogels (Exo-pGel) therapies provided a promising strategy for the effective treatment of central nervous system diseases based on exosome implantation. In another study, the combination of size exclusion chromatography and ultracentrifugation was used, and before ultracentrifugation, the qEV column was used to exclude microvesicles from the total extracellular vesicles (EVs), and the highly bioactive exosomes were successfully isolated and purified[77]. The exosomes, after being added to biomaterials, can enhance the osteogenic ability of the body and treat neurological diseases. However, maintaining the biological activity of exosomes is still a great challenge. Thirdly, 3D printing can print a variety of tissues and organs, but the current applications of exosomes are limited, and the studies on their functions and clinical applications are inadequate. This paper mainly focuses on the fields of bone engineering, vascular engineering, nerve injury treatment, and skin regeneration. In conclusion, the applications of exosomes to promote bioprinting in tissue engineering and regenerative medicine in other fields such as liver tissue regeneration, kidney tissue regeneration, and lung tissue regeneration have great potential and need to be developed.

Table 1. Summaries of recent studies in the four fields of bone, skin, nerve, and vascular using exosomal hydrogels to treat diseases

Field	Source of exosomes	Components of hydrogel	Diseases treated	Results-pros	Results-cons	Reference
Bone	BMSC-exosomes	SIS hydrogels doped with 3-(3,4-dihydroxyphenyl) propionic acid	Fracture	Enhanced bioactivity and promoted the active role of exosomes in osteogenic differentiation of BMSCs.	Need to enhance the mechanical properties.	[110]
	BMSC-exosomes	Alginate-dopamine, chondroitin sulfate, and regenerating filament protein	Cartilage defects	Induced differentiation of BMSCs into chondrocytes to repair the chondral defects in the patellar groove of rats.	Need to evaluate further safety and efficacy.	[111]
	M2D-Exos	HA@SDF-1α/M2D-Exos hydrogel	Fracture	Had local antibacterial activity; promoted the proliferation of hMSCs and HUVECs; stimulates ECM mineralization; promoted osteogenesis and angiogenesis; ultimately promoted fracture healing.	Need to evaluate the influence of different types of injuries or the severity of fractures on the repair results.	[112]
	PDLSCs-Exos	Alginate-gelatin cross-linked hydrogel	Alveolar bone defect	Repaired alveolar bone defects in rats.	The detection of exosomes in hydrogels was not ideal.	[113]
	hMSC-exosomes	Coral hydroxyapatite/ filamentous protein/glycolic chitosan/bi-functionalized polyethylene glycol hydrogel	Fracture	Promoted bone healing, bone morphogenetic protein 2 (BMP2) deposition, bone collagen deposition and maturation, and angiogenesis in SD rat model.	Need a negative control group to prove the effects of the hydrogel.	[114]
Skin	hMSC- exosomes	Poloxam 407, carboxymethyl chitosan, natural non-toxic cross-linker Genipin	Full thickness skin wounds	Had good wound protection effect and moisture retention function without stimulating or pro-inflammatory effects on wound; biodegradable and dual-sensitive (thermo and pH-sensitive); improved wound healing and tissue regeneration of skin appendages.	Need to test the sensitivity of the hydrogel to UV light and to evaluate the penetration of the UV light through skin.	[41]
Nerve	hMSC-exosomes	Peptide-modified adhesive hydrogel	Spinal cord regeneration	Induced efficient, comprehensive cell mitigation to the injured microenvironment	The loss of stem cells restricted the treatment effect	[77]
	BMSC-exosomes	GMPE (GelMA-polypyrrole) hydrogels	Spinal cord injury	Inhibited inflammation; enhanced the recruitment of NSCs; promoted the regeneration of neurons and myelin-associated axons	Did not verify the recovery of the hydrogel in the later stage of the mouse model	[42]
	ADSC-Exo	Thermosensitive hydroxyethyl chitosan/sodium β-glycerophosphate hydrogel	Post-operative erectile dysfunction induced by cavernous nerve injury (CNI-ED)	Enhanced retention of ADSC-Exo at the site of injury; significant improved the erectile function in CNI-ED rats.	No test of the degree of degradation of the hydrogel.	[43]
	MSC-Exos	Photocrosslinked hyaluronic acid methacrylate hydrogel	Peripheral nerve injury (PNI)	Soft hydrogel-regulated exosome rapid release; better repaired PNI and motor dysfunction *in vivo* compared to rigid hydrogel.	Need to analyze the mechanism of the exosome-loaded hydrogels inhibiting inflammation.	[80]

https://doi.org/10.36922/ijb.0114

	SHED-Exo	Bioactive antioxidant poly(citric acid-gallic acid)-based hybrid hydrogel	Traumatic brain injury (TBI)	Thermosensitive, injectable, self-healing, antioxidant, low cytotoxicity, and ultralong sustained release of SHED-Exo; enhanced the therapeutic potential of SHED-Exo.	Did not achieve the effective influence on the prognosis of traumatic brain injury (TBI).	[44]
	Hypoxia-stimulated MSCs-derived exosomes (sub-exo)	Binding peptide PPFLMLLKGSTR-modified hyaluronic acid hydrogel	Traumatic Spinal Cord Injury (SCI)	Improved angiogenesis, nerve regeneration, and functional motor restoration; Enhanced the therapeutic regenerative outcomes of MSC-derived exosomes, promoting the regeneration of the injured spinal cord.	No statistical differences were displayed between hypo-Exo and Exo.	[115]
Blood vessel	Gingival mesenchymal stem cells(GMSCs)-Exos	Chitosan/Silk Hydrogel Sponge	Diabetes	Promoted the healing of Streptozotocin (STZ)-induced diabetic rat skin wounds, promoted the re-epithelialization, deposition, and remodeling of ECM, and promoted angiogenesis and neurite growth.	Clinical trial data are lacking.	[116]
	Umbilical cord mesenchymal stem cell-derived exosomes (UMSC-Exo)	PGN hydrogel (PA-GHRPS peptide+peptide NapFF)	Myocardial infarction	Improved myocardial function by reducing inflammation, fibrosis, and apoptosis and promoting angiogenesis.	The mechanical properties and stability need to be further improved.	[117]
	ADSC-exo	Four-arm SH-PEG cross-linked with Ag^+ hydrogel	Thin endometrium	Promoted angiogenesis and endometrial regeneration, facilitating the recovery of fertility.	The purity and quality of exosomes need to be further studied and evaluated to ensure their safety and efficacy.	[38]
	AMSCs-exo	Anti-microbial peptide-based FHE hydrogel	Diabetic wound	Promoted neovascularization and cell proliferation; accelerated granulation, re-epithelialization, and collagen remodeling at the trauma site; accelerated the healing process of diabetic wounds.	Need to address the cost and safety of the method.	[118]
	Macrophage-exo	Alginate+hyaluronic acid	*In vitro* model	Improved the angiogenic activity of HUVECs.	Need to study the relationship between the biological activity and therapeutic effect with the morphology and structure of bioceramic-induced macrophage exosomes (BC-Exos).	[36]

https://doi.org/10.36922/ijb.0114

Table 2. Summaries of the studies discussed in the four fields of bone, skin, nerve, and vascular using exosomal bioprinting to treat diseases

Field	Source of exosomes	Components of hydrogel	Diseases treated	Results-Pros	Results-Cons	Reference
Bone	Macrophage-exo	Sodium alginate and hyaluronic acid.	Regular immuno-modulation, osteogenesis, and angiogenesis	Distinct immunomodulatory effects and osteogenesis/angiogenesis	Systemic immunogenicity or off-target effects is not clear.	[36]
	ATDC5 (a chondrogenic progenitor cell line)-exo	PCL (polycaprolactone)	Large segmental bone defects	Excellent biocompatibility; enhanced therapy	Need to improve the production and purification techniques of exosomes	[67]
	HBMSCs-exo	PLA (Polylactic acid)	Osteogenic and immunoregulatory	Reduced the pro-inflammatory markers and ROS production in inflammatory macrophages and enhanced osteogenic differentiation	Need to improve its biofunctionality	[40]
	BMSCs-exo	Decellularized cartilage ECM, and gelatin methacrylate (GelMA) hydrogel	Osteoarthritis	Efficient for cells and tissues ingrowth, nutrients and waste exchange, ECM deposition and cell interaction	Need to determine the mechanisms of the immune response towards allografts	[68]
	Schwann cells-exo	Titanium (Ti) alloys	Bone defects	Provided both mechanical support and open pores; exhibited good biological activity	Need to check the mechanism underlying the effects of SC-derived exosomes	[69]
	ATDC5(a chondrogenic progenitor cell line)-exo	Soft chitosan (CS) and hard poly lactic acid(PLA)	vascularized osteogenesis	Equivalent functions but higher yields in comparison with the routine exosomes	Need to verify its reliability and effectiveness	[70]
Blood vessel	Macrophage-exo	Alginate + hyaluronic acid	In vitro model	Improved angiogenic activity	Need to optimize and study the morphology and structure of BC-exosomes	[36]
	MSC-derived exo	Chitosan hydrogel +hP-MSCs	Hindlimb ischemia	Enhanced the retention and stability of exosomes; enhanced the therapeutic effect	Difficult to control the release of exosomes	[72]
Nerve	HUCMSCs-derived exo	Collagen/silk fibroin scaffolds	Traumatic brain injury (TBI)	Promote the nerve regeneration after TBI; Inhibited neuritis and the apoptosis of neurotic cells	Insufficient vessel growth associated with injury	[75]
	HUCMSCs-derived exo	Sponge-like alginate scaffold	Nerve injury-induced pain	Slowly releases HUCMSCs exosomes	The loss of stem cells restricts the treatment effect	[78]
	Gingival mesenchymal stem cells-exo	Chitin conduits	Peripheral nerve injury	Increased the number and diameter of nerve fibers and promoted myelin formation	Cannot act in the body for a long time	[79]
	MSCs-exo	GelMA hydrogel	Spinal cord injury (SCI)	Reduced SCI-induced inflammation and glial scarring	Cannot be effectively released in the body for a long time	[76]
	MSC-exos	Photocrosslinked hyaluronic acid methacrylate hydrogel	Peripheral nerve injury (PNI)	Regulated exosome rapid release to repair PNI and motor dysfunction in vivo	Need to analyze the mechanism of exosome-loaded hydrogels inhibiting inflammation	[80]
	hMSC- exo	Peptide-modified adhesive hydrogel	Spinal cord regeneration	Provided an exosome-encapsulated ECM to the injured nerve tissue; induced efficient cell mitigation to the injured sites	The loss of stem cells restricts the treatment effect	[77]
Skin	ASCs-exo	Alginate	Full-thickness skin wounds	Excellent biodegradability and biocompatibility; no side effect or infection; improved vascularization; enhanced wound closure, re-epithelialization, collagen deposition and angiogenesis	Rapid clearance rate and relatively short half-life *in vivo*; Function is relatively too single	[46]
	ADSCs-exo	FEP hydrogel (F127 + polyethylenimine + aldehyde pullulan)	Diabetic wounds	Promoted the granulation tissue formation and collagen formation; generated the skin appendages, and accelerated the healing process in diabetic wounds	The effectiveness of therapy in both types of diabetes is not clear	[90]
Oral	Human periodontal ligament stem cells-exo	Sodium alginate (SA), gelatin (Gel), and nano-hydroxyapatite (na-HA)	Bone defects	Had good rheological properties to be suitable for printing; Had good biocompatibility for osteogenic differentiation of hPDLSCs.	No test of the degree of degradation of the hydrogel and the continuously release of exosomes	[98]

https://doi.org/10.36922/ijb.0114

Acknowledgments

None.

Funding

Zhimin Wang reports financial support was provided by National Natural Science Foundation of China (No. 51833006) and Innovation Promotion Program of NHC and Shanghai Key Labs, SIBPT (No. CX2023-03). Jia Jia reports financial support was provided by Shanghai University (No. N-58-D305-22-204). Jizong Li reports financial support was provided by Science and Technology Commission of Shanghai Municipality (No. 17DZ2260600 & No. 22692116403).

Conflict of interest

The authors declare no conflict of interest.

Author contributions

Conceptualization: Qian Wang, Yang Liu, Jizong Li, Zhimin Wang, Jia Jia

Formal analysis: Qian Wang, Yang Liu, Shuqing Zhang, Fan He, Tong Shi

Methodology: Qian Wang, Yang Liu, Jizong Li, Zhimin Wang, Jia Jia

Supervision: Jia Jia

Writing – original draft: Qian Wang, Yang Liu, Shuqing Zhang, Fan He, Jizong Li, Zhimin Wang, Jia Jia

Writing – review & editing: Jizong Li, Zhimin Wang, Jia Jia

Ethics approval and consent to participate

Not applicable.

Consent for publication

Not applicable.

Availability of data

Not applicable.

Reference

1. Matai I, Kaur G, Seyedsalehi A, *et al.*, 2020, Progress in 3D bioprinting technology for tissue/organ regenerative engineering. *Biomaterials,* 226: 119536.

   https://doi.org/10.1016/j.biomaterials.2019.119536

2. Heinrich MA, *et al.,* 2019, 3D bioprinting: From benches to translational applications. *Small,* 15: e1805510.

   https://doi.org/10.1002/smll.201805510

3. Tavafoghi M, Darabi MA, Mahmoodi M, *et al.,* 2021, Multimaterial bioprinting and combination of processing techniques towards the fabrication of biomimetic tissues and organs. *Biofabrication,* 13(4): 042002.

   https://doi.org/10.1088/1758-5090/ac0b9a

4. Murphy SV, Atala A, 2014, 3D bioprinting of tissues and organs. *Nat Biotechnol,* 32: 773–785.

   https://doi.org/10.1038/nbt.2958

5. Samandari M, Quint J, Rodríguez-delaRosa A, *et al.,* 2022, Bioinks and bioprinting strategies for skeletal muscle tissue engineering. *Adv Mater,* 34: e2105883.

   https://doi.org/10.1002/adma.202105883

6. Dobos A, Gantner F, Markovic M, *et al.,* 2021, On-chip high-definition bioprinting of microvascular structures. *Biofabrication,* 13: 015016.

   https://doi.org/10.1088/1758-5090/abb063

7. Freeman FE, Burdis R, Kelly DJ, 2021, Printing new bones: From print-and-implant devices to bioprinted bone organ precursors. *Trends Mol Med,* 27: 700–711.

   https://doi.org/10.1016/j.molmed.2021.05.001

8. Zhou F, Hong Y, Liang R, *et al.,* 2020, Rapid printing of bio-inspired 3D tissue constructs for skin regeneration. *Biomaterials,* 258: 120287.

   https://doi.org/10.1016/j.biomaterials.2020.120287

9. Moghaddam AS, Khonakdar, HA, Arjmand M, *et al.,* 2021, Review of bioprinting in regenerative medicine: Naturally derived bioinks and stem cells. *ACS Appl Biomater,* 4: 4049–4070.

   https://doi.org/10.1021/acsabm.1c00219

10. Herrmann IK, Wood MJA, Fuhrmann G, 2021, Extracellular vesicles as a next-generation drug delivery platform. *Nat Nanotechnol,* 16: 748–759.

    https://doi.org/10.1038/s41565-021-00931-2

11. van Niel G, D'Angelo G, Raposo G, 2018, Shedding light on the cell biology of extracellular vesicles. *Nat Rev,* 19: 213–228.

    https://doi.org/10.1038/nrm.2017.125

12. Pan BT, Johnstone RM, 1983, Fate of the transferrin receptor during maturation of sheep reticulocytes in vitro: Selective externalization of the receptor. *Cell,* 33: 967–978.

    https://doi.org/10.1016/0092-8674(83)90040-5

13. Harding C, Heuser J, Stahl P, 1983, Receptor-mediated endocytosis of transferrin and recycling of the transferrin receptor in rat reticulocytes. *J Cell Biol,* 97: 329–339.

    https://doi.org/10.1083/jcb.97.2.329

14. Pan BT, Blostein R, Johnstone RM, 1983, Loss of the transferrin receptor during the maturation of sheep reticulocytes in vitro. An immunological approach. *Biochem J,* 210: 37–47.

    https://doi.org/10.1042/bj2100037

15. Valadi H, Ekström K, Bossios, *et al.,* 2007, Exosome-mediated transfer of mRNAs and microRNAs is a novel mechanism of genetic exchange between cells. *Nat Cell Biol,* 9: 654–659.

https://doi.org/10.1038/ncb1596

16. Katsuda T, Kosaka N, Takeshita F, *et al.*, 2013, The therapeutic potential of mesenchymal stem cell-derived extracellular vesicles. *Proteomics,* 13: 1637–1653.

https://doi.org/10.1002/pmic.201200373

17. Yáñez-Mó M, Siljander PRM, Andreu Z, *et al.*, 2015, Biological properties of extracellular vesicles and their physiological functions. *J Extracell Vesicles*, 4(1): 27066.

https://doi.org/10.3402/jev.v4.27066

18. Kalluri R, LeBleu VS, 2020, The biology, function, and biomedical applications of exosomes. *Science,* 367: eaau6977

19. Budnik V, Ruiz-Cañada C, Wendler F, 2016, Extracellular vesicles round off communication in the nervous system. *Nat Rev,* 17: 160–172.

https://doi.org/10.1038/nrn.2015.29

20. Zhang S, Chuah SJ, Lai RC, *et al.,* 2018, MSC exosomes mediate cartilage repair by enhancing proliferation, attenuating apoptosis and modulating immune reactivity. *Biomaterials,* 156: 16–27.

https://doi.org/10.1016/j.biomaterials.2017.11.028

21. Kim YG, Choi J, Kim K, 2020, Mesenchymal stem cell-derived exosomes for effective cartilage tissue repair and treatment of osteoarthritis. *Biotechnol J,* 15: e2000082.

https://doi.org/10.1002/biot.202000082

22. Jiang S, Tian G, Yang Z, *et al.,* 2021, Enhancement of acellular cartilage matrix scaffold by Wharton's jelly mesenchymal stem cell-derived exosomes to promote osteochondral regeneration. *Bioact Mater,* 6: 2711–2728.

https://doi.org/10.1016/j.bioactmat.2021.01.031

23. Hongxing Hu, Lanlan Dong, Ziheng Bu, *et al.,* 2020, miR-23a-3p-abundant small extracellular vesicles released from Gelma/nanoclay hydrogel for cartilage regeneration. *J Extracell Vesicles,* 9: 1778883.

https://doi.org/10.1080/20013078.2020.1778883

24. Wang, W, Liang X, Zheng K, *et al.,* 2022, Horizon of exosome-mediated bone tissue regeneration: The all-rounder role in biomaterial engineering. *Mater Today Bio,* 16: 100355.

https://doi.org/10.1016/j.mtbio.2022.100355

25. Wang G, Xie L, Li B, *et al.,* 2021, A nanounit strategy reverses immune suppression of exosomal PD-L1 and is associated with enhanced ferroptosis. *Nat Commun,* 12: 5733.

https://doi.org/10.1038/s41467-021-25990-w

26. Ding G, Zhou L, Qian Y, *et al.,* 2015, Pancreatic cancer-derived exosomes transfer miRNAs to dendritic cells and inhibit RFXAP expression via miR-212-3p. *Oncotarget,* 6: 29877–29888.

https://doi.org/10.18632/oncotarget.4924

27. Huang P, Wang L, Li Q, *et al.,* 2020, Atorvastatin enhances the therapeutic efficacy of mesenchymal stem cells-derived exosomes in acute myocardial infarction via up-regulating long non-coding RNA H19. *Cardiovasc Res,* 116: 353–367.

https://doi.org/10.1093/cvr/cvz139

28. Ma T, Chen Y, Chen Y, *et al.,* 2018, MicroRNA-132, Delivered by mesenchymal stem cell-derived exosomes, promote angiogenesis in myocardial infarction. *Stem Cell Int,* 2018: 3290372.

https://doi.org/10.1155/2018/3290372

29. Andaloussi SEL, Mäger I, Breakefield XO, *et al.*, 2013, Extracellular vesicles: Biology and emerging therapeutic opportunities. *Nat Rev,* 12: 347–357.

https://doi.org/10.1038/nrd3978

30. Haney MJ, Klyachko NL, Zhao Y, *et al.,* 2015, Exosomes as drug delivery vehicles for Parkinson's disease therapy. *J Control Release,* 207: 18–30.

https://doi.org/10.1016/j.jconrel.2015.03.033

31. Lykke-Andersen S, Brodersen DE, Jensen TH, 2009, Origins and activities of the eukaryotic exosome. *J Cell Sci,* 122: 1487–1494.

https://doi.org/10.1242/jcs.047399

32. Garreta E, Oria R, Tarantino C, *et al.,* 2017, Tissue engineering by decellularization and 3D bioprinting. *Mater Today,* 20: 166–178.

https://doi.org/10.1016/j.mattod.2016.12.005

33. Santschi M, Vernengo A, Eglin D, *et al.*, 2019, Decellularized matrix as a building block in bioprinting and electrospinning. *Curr Opin BiomedEng,* 10: 116–122.

https://doi.org/10.1016/j.cobme.2019.05.003

34. Yang D, Zhang W, Zhang H, *et al.,* 2020, Progress, opportunity, and perspective on exosome isolation - efforts for efficient exosome-based theranostics. *Theranostics,* 10: 3684–3707.

https://doi.org/10.7150/thno.41580

35. Gu C, Feng J, Waqas A, *et al.,* 2021, Technological advances of 3D scaffold-based stem cell/exosome therapy in tissues and organs. *Front Cell Dev Biol,* 9: 709204.

https://doi.org/10.3389/fcell.2021.709204

36. Sun YH, Zhang BJ, Zhai D, *et al.*, 2021, Three-dimensional printing of bioceramic-induced macrophage exosomes: Immunomodulation and osteogenesis/angiogenesis. *Npg Asia Mater,* 13(1): 72.

https://doi.org/10.1038/s41427-021-00340-w

37. Tang Q, Lu B, He J, *et al.,* 2022, Exosomes-loaded thermosensitive hydrogels for corneal epithelium and stroma regeneration. *Biomaterials,* 280: 121320.

https://doi.org/10.1016/j.biomaterials.2021.121320

38. Lin J, Wang Z, Huang J, *et al.,* 2021, Microenvironment-protected exosome-hydrogel for facilitating endometrial regeneration, fertility restoration, and live birth of offspring. *Small,* 17(11): 2007235.

https://doi.org/10.1002/smll.202007235

39. Rolland TJ, Peterson TE, Singh RD, *et al.,* 2022, Exosome biopotentiated hydrogel restores damaged skeletal muscle in a porcine model of stress urinary incontinence (vol 29, 58, 2022). *NPJ Regen Medi*, 7(1): 1–17.

https://doi.org/10.1038/s41536-022-00260-5

40. Zhang Y, Huo M, Wang Y, *et al.,* 2022, A tailored bioactive 3D porous poly(lactic-acid)-exosome scaffold with osteo-immunomodulatory and osteogenic differentiation properties. *J BiolEng,* 16(1):1–14.

https://doi.org/10.1186/s13036-022-00301-z

41. Li Q, Gong S, Yao W, *et al.,* 2021, Exosome loaded genipin crosslinked hydrogel facilitates full thickness cutaneous wound healing in rat animal model. *Drug Deliv,* 28: 884–893,

https://doi.org/10.1080/10717544.2021.1912210

42. Fan L, Liu C, Chen X, *et al.,* 2022, Exosomes-loaded electroconductive hydrogel synergistically promotes tissue repair after spinal cord injury via immunoregulation and enhancement of myelinated axon growth. *Adv Sci,* 9(13): 2105586.

https://doi.org/10.1002/advs.202105586

43. Liu S, Li R, Dou K, *et al.,* 2023, Injectable thermo-sensitive hydrogel containing ADSC-derived exosomes for the treatment of cavernous nerve injury. *Carbohydr Polym,* 300: 120226.

https://doi.org/10.1016/j.carbpol.2022.120226

44. Li Y, Wang Min, Sun Meng, *et al.,* 2022, Engineering antioxidant poly (citrate-gallic acid)-exosome hybrid hydrogel with microglia immunoregulation for traumatic brain injury-post neuro-restoration. *Compos Part B-Eng,* 242: 110034.

https://doi.org/10.1016/j.compositesb.2022.110034

45. Yu Z, Hao R, Du J, *et al.,* 2022, A human cornea-on-a-chip for the study of epithelial wound healing by extracellular vesicles. *iScience,* 25: 104200.

https://doi.org/10.1016/j.isci.2022.104200

46. Shafei S, Khanmohammadi M, Heidari R, *et al.,* 2020, Exosome loaded alginate hydrogel promotes tissue regeneration in full-thickness skin wounds: An in vivo study. *J Biomed Mater Res Part A,* 108: 545–556.

https://doi.org/10.1002/jbm.a.36835

47. Badylak SF, Taylor D, Uygun K, 2011, *Annual Review of Biomedical Engineering,* Annual Reviews Inc, 27–53.

48. Song JJ, Ott HC, 2011, Organ engineering based on decellularized matrix scaffolds. *Trends Mol Med,* 17: 424–432.

https://doi.org/10.1016/j.molmed.2011.03.005

49. Londono R, Badylak SF, 2015, Biologic scaffolds for regenerative medicine: Mechanisms of in vivo remodeling. *Ann Biomed Eng,* 43: 577–592.

https://doi.org/10.1007/s10439-014-1103-8

50. Yi HG, Jeong YH, Kim Y, *et al.,* 2019, A bioprinted human-glioblastoma-on-a-chip for the identification of patient-specific responses to chemoradiotherapy. *Nat Biomedi Eng,* 3: 509–519.

https://doi.org/10.1038/s41551-019-0363-x

51. Wu Y, Wang J, Shi Y, *et al.,* 2017, Implantation of brain-derived extracellular matrix enhances neurological recovery after traumatic brain injury. *Cell Transplant,* 26: 1224–1234.

https://doi.org/10.1177/0963689717714090

52. Barrs RW, Jia J, Silver SE, *et al.*, 2020, Biomaterials for bioprinting microvasculature. *Chem Rev,* 120: 10887–10949.

https://doi.org/10.1021/acs.chemrev.0c00027

53. Valot L, Martinez J, Mehdi A, *et al.*, 2019, Chemical insights into bioinks for 3D printing. *Chem Soc Rev,* 48: 4049–4086.

https://doi.org/10.1039/c7cs00718c

54. Ozbolat IT, Hospodiuk M, 2016, Current advances and future perspectives in extrusion-based bioprinting. *Biomaterials,* 76: 321–343.

https://doi.org/10.1016/j.biomaterials.2015.10.076

55. Xia Z, Jin S, Ye K, 2018, Tissue and organ 3D bioprinting. *SLAS Technol,* 23: 301–314.

https://doi.org/10.1177/2472630318760515

56. Leucht A, Volz AC, Rogal J, *et al.*, 2020, Advanced gelatin-based vascularization bioinks for extrusion-based bioprinting of vascularized bone equivalents. *Sci Rep,* 10: 5330.

https://doi.org/10.1038/s41598-020-62166-w

57. Li X, Liu B, Pei B, *et al.,* 2020, Inkjet bioprinting of biomaterials. *Chem Rev,* 120: 10793–10833.

https://doi.org/10.1021/acs.chemrev.0c00008

58. Miri AK, Khalilpour A, Cecen B, *et al.,* 2019, Multiscale bioprinting of vascularized models. *Biomaterials,* 198: 204–216.

https://doi.org/10.1016/j.biomaterials.2018.08.006

59. Suntornnond R, Ng WL, Huang X, *et al.*, 2022, Improving printability of hydrogel-based bio-inks for thermal inkjet bioprinting applications via saponification and heat treatment processes. *J Mater Chem B,* 10: 5989–6000.

https://doi.org/10.1039/d2tb00442a

60. Malda J, Visser J, Melchels FP, *et al.,* 2013, 25th anniversary article: Engineering hydrogels for biofabrication. *Adv Mater,* 25: 5011–5028.

https://doi.org/10.1002/adma.201302042

61. Ng WL, Lee JM, Zhou M, *et al.,* 2020, Vat polymerization-based bioprinting-process, materials, applications and regulatory challenges. *Biofabrication,* 12: 022001.

https://doi.org/10.1088/1758-5090/ab6034

62. Zhang B, Gao L, Ma L, *et al.,* 2019, 3D bioprinting: A novel avenue for manufacturing tissues and organs. *Engineering,* 5: 777–794.

https://doi.org/10.1016/j.eng.2019.03.009

63. Kingsley DM, Roberge CL, Rudkouskaya A, *et al.,* 2019, Laser-based 3D bioprinting for spatial and size control of tumor spheroids and embryoid bodies. *Acta Biomater,* 95: 357–370.

https://doi.org/10.1016/j.actbio.2019.02.014

64. Sohn H-S, Oh J-K, 2019, Review of bone graft and bone substitutes with an emphasis on fracture surgeries. *Biomater Res,* 23(1): 1–7.

https://doi.org/10.1186/s40824-019-0157-y

65. Liang Q, Ma Y, Yao X, *et al.*, 2022, Advanced 3D-printing bioinks for articular cartilage. *Int J Bioprint,* 8: 15–30.

https://doi.org/10.18063/ijb.v8i3.511

66. Fan J, Lee CS, Kim S, *et al.,* 2020, Generation of small RNA-modulated exosome mimetics for bone regeneration. *ACS Nano,* 14: 11973–11984.

https://doi.org/10.1021/acsnano.0c05122

67. Zha Y, Li Y, Lin T, *et al.,* 2021, Progenitor cell-derived exosomes endowed with VEGF plasmids enhance osteogenic induction and vascular remodeling in large segmental bone defects. *Theranostics,* 11: 397–409.

https://doi.org/10.7150/thno.50741

68. Chen P, Zheng L, Wang Y, *et al.,* 2019, Desktop-stereolithography 3D printing of a radially oriented extracellular matrix/mesenchymal stem cell exosome bioink for osteochondral defect regeneration. *Theranostics,* 9: 2439–2459.

https://doi.org/10.7150/thno.31017

69. Wu Z, Pu P, Su Z, *et al.,* 2020, Schwann cell-derived exosomes promote bone regeneration and repair by enhancing the biological activity of porous Ti6Al4V scaffolds. *Biochem BiophysRes Commun,* 531: 559–565.

https://doi.org/10.1016/j.bbrc.2020.07.094

70. Zha Y, Lin T, Li Y, *et al.,* 2020, Exosome-mimetics as an engineered gene-activated matrix induces in-situ vascularized osteogenesis. *Biomaterials,* 247: 119985.

https://doi.org/10.1016/j.biomaterials.2020.119985

71. Li F, Wu J, Li D, *et al.,* 2022, Engineering stem cells to produce exosomes with enhanced bone regeneration effects: An alternative strategy for gene therapy. *J Nanobiotechnol,* 20(1): 1–23.

https://doi.org/10.1186/s12951-022-01347-3

72. Zhang K, Zhao X, Chen X, *et al.,* 2018, Enhanced therapeutic effects of mesenchymal stem cell-derived exosomes with an injectable hydrogel for hindlimb ischemia treatment. *ACS Appl Mater Interfaces,* 10: 30081–30091.

https://doi.org/10.1021/acsami.8b08449

73. Nagappan PG, Chen H, Wang DY, 2020, Neuroregeneration and plasticity: A review of the physiological mechanisms for achieving functional recovery postinjury. *Mil Med Res,* 7: 30.

https://doi.org/10.1186/s40779-020-00259-3

74. Poongodi R, Chen Y-L, Yang T-H, *et al.,* 2021, Bio-scaffolds as cell or exosome carriers for nerve injury repair. *Int J Mol Sci,* 22:

https://doi.org/10.3390/ijms222413347

75. Liu X, Wang J, Wang P, *et al.,* 2022, Hypoxia-pretreated mesenchymal stem cell-derived exosomes-loaded low-temperature extrusion 3D-printed implants for neural regeneration after traumatic brain injury in canines. *Front Bioeng Biotechnol,* 10: 1025138.

https://doi.org/10.3389/fbioe.2022.1025138

76. Han M, Yang H, Lu X, *et al.,* 2022, Three-dimensional-cultured MSC-derived exosome-hydrogel hybrid microneedle array patch for spinal cord repair. *Nano Lett,* 22: 6391–6401.

https://doi.org/10.1021/acs.nanolett.2c02259

77. Li L, Zhang Y, Mu J, *et al.,* 2020, Transplantation of human mesenchymal stem-cell-derived exosomes immobilized in an adhesive hydrogel for effective treatment of spinal cord injury. *Nano Lett,* 20: 4298–4305.

https://doi.org/10.1021/acs.nanolett.0c00929

78. Hsu JM, Shiue SJ, Yang KD, *et al.,* Locally applied stem cell exosome-scaffold attenuates nerve injury-induced pain in rats. *J Pain Res,* 13: 3257–3268.

https://doi.org/10.2147/JPR.S286771

79. Rao F, Zhang D, Fang T, *et al.,* 2019, Exosomes from human gingiva-derived mesenchymal stem cells combined with biodegradable chitin conduits promote rat sciatic nerve regeneration. *Stem Cells Int,* 2019: 2546367.

https://doi.org/10.1155/2019/2546367

80. Liu Z, Tong H, Li J, *et al.,* 2022, Low-stiffness hydrogels promote peripheral nerve regeneration through the rapid release of exosomes. *Front Bioeng Biotechnol,* 10: 922570.

https://doi.org/10.3389/fbioe.2022.922570

81. Wang T, Li Y, Guo M, *et al.,* 2021, Exosome-mediated delivery of the neuroprotective peptide PACAP38 promotes retinal ganglion cell survival and axon regeneration in rats with traumatic optic neuropathy. *Front Cell Develop Biol,* 9: 659783.

https://doi.org/10.3389/fcell.2021.659783

82. Sun BK, Siprashvili Z, Khavari PA, 2014, Advances in skin grafting and treatment of cutaneous wounds. *Science,* 346: 941–945.

https://doi.org/10.1126/science.1253836

83. Avci P, Gupta A, Sadasivam M, *et al.,* 2013, Low-level laser (light) therapy (LLLT) in skin: Stimulating, healing, restoring. *Semin Cutan Med Surg,* 32: 41–52

84. Xiong M, Zhang Q, Hu W, *et al.,* 2021, The novel mechanisms and applications of exosomes in dermatology and cutaneous medical aesthetics. *Pharmacol Res,* 166: 105490.

https://doi.org/10.1016/j.phrs.2021.105490

85. Wang WM, Wu C, Jin HZ, 2019, Exosomes in chronic inflammatory skin diseases and skin tumors. *Exp Dermatol,* 28: 213–218.

https://doi.org/10.1111/exd.13857

86. Griffiths CEM, Cumberbatch M, Tucker SC, *et al.,* 2001, Exogenous topical lactoferrin inhibits allergen-induced Langerhans cell migration and cutaneous inflammation in humans. *Br J Dermatol,* 144: 715–725.

https://doi.org/10.1046/j.1365-2133.2001.04125.x

87. An Y, Lin S, Tan X, *et al.,* 2021, Exosomes from adipose-derived stem cells and application to skin wound healing. *Cell Prolif,* 54: e12993.

https://doi.org/10.1111/cpr.12993

88. Shi A, Li J, Qiu X, *et al.,* 2021, TGF-β loaded exosome enhances ischemic wound healing in vitro and in vivo. *Theranostics,* 11: 6616–6631.

https://doi.org/10.7150/thno.57701

89. Holl J, Kowalewski C, Zimek Z, *et al.,* 2021, Chronic diabetic wounds and their treatment with skin substitutes. *Cells,* 10(3): 655.

https://doi.org/10.3390/cells10030655

90. Wang M, Wang C, Chen M, *et al.,* 2019, Efficient angiogenesis-based diabetic wound healing/skin reconstruction through bioactive antibacterial adhesive ultraviolet shielding nanodressing with exosome release. *ACS Nano,* 13: 10279–10293.

https://doi.org/10.1021/acsnano.9b03656

91. Huang J, Xiong J, Yang L, *et al.,* 2021, Cell-free exosome-laden scaffolds for tissue repair. *Nanoscale,* 13: 8740–8750.

https://doi.org/10.1039/d1nr01314a

92. Samaeekia R, Rabiee B, Putra I, *et al.,* 2018, Effect of human corneal mesenchymal stromal cell-derived exosomes on corneal epithelial wound healing. *Invest Ophthalmol Vis Sci,* 59: 5194–5200.

https://doi.org/10.1167/iovs.18-24803

93. Shojaati G, Khandaker I, Funderburgh ML, *et al.,* 2019, Mesenchymal stem cells reduce corneal fibrosis and inflammation via extracellular vesicle-mediated delivery of miRNA. *Stem Cells Transl Med,* 8: 1192–1201.

https://doi.org/10.1002/sctm.18-0297

94. Sorkio A, Koch L, Koivusalo L, *et al.,* 2018, Human stem cell based corneal tissue mimicking structures using laser-assisted 3D bioprinting and functional bioinks. *Biomaterials,* 171: 57–71.

https://doi.org/10.1016/j.biomaterials.2018.04.034

95. Isaacson A, Swioklo S, Connon CJ, 2018, 3D bioprinting of a corneal stroma equivalent. *Exp Eye Res,* 173: 188–193.

https://doi.org/10.1016/j.exer.2018.05.010

96. Ji L, Bao L, Gu Z, *et al.,* 2019, Comparison of immunomodulatory properties of exosomes derived from bone marrow mesenchymal stem cells and dental pulp stem cells. *Immunol Res,* 67: 432–442.

https://doi.org/10.1007/s12026-019-09088-6

97. Wei J, Song Y, Du Z, *et al.,* 2020, Exosomes derived from human exfoliated deciduous teeth ameliorate adult bone loss in mice through promoting osteogenesis. *J Mol Histol,* 51: 455–466.

https://doi.org/10.1007/s10735-020-09896-3

98. Tian Y, Liu M, Liu Y, *et al.,* 2021, The performance of 3D bioscaffolding based on a human periodontal ligament stem cell printing technique. *J Biomed Mater Res Part A,* 109: 1209–1219.

https://doi.org/10.1002/jbm.a.37114

99. Gómez-Guillén MC, Giménez B, López-Caballero ME, *et al.*, Functional and bioactive properties of collagen and gelatin from alternative sources: A review. *Food Hydrocoll,* 25: 1813–1827.

https://doi.org/10.1016/j.foodhyd.2011.02.007

100. Rowley JA, Madlambayan G, Mooney DJ, 1999, Alginate hydrogels as synthetic extracellular matrix materials. *Biomaterials,* 20: 45–53.

https://doi.org/10.1016/S0142-9612(98)00107-0

101. Norotte C, Marga FS, Niklason LE, *et al.*, 2009, Scaffold-free vascular tissue engineering using bioprinting. *Biomaterials,* 30: 5910–5917.

https://doi.org/10.1016/j.biomaterials.2009.06.034

102. Billiet T, Vandenhaute M, Schelfhout J, *et al.*, 2012, A review of trends and limitations in hydrogel-rapid prototyping for tissue engineering. *Biomaterials,* 33: 6020–6041.

https://doi.org/10.1016/j.biomaterials.2012.04.050

103. Samanta S, Rajasingh S, Drosos N, *et al.,* 2018, Exosomes: New molecular targets of diseases. *Acta Pharmacologica Sinica,* 39: 501–513.

https://doi.org/10.1038/aps.2017.162

104. Kishore R, Khan M, 2017, Cardiac cell-derived exosomes: Changing face of regenerative biology. *Eur Heart J,* 38: 212–215.

https://doi.org/10.1093/eurheartj/ehw324

105. Faught E, Henrickson L, Vijayan MM, 2017, Plasma exosomes are enriched in Hsp70 and modulated by stress and cortisol in rainbow trout. *J Endocrinol,* 232: 237–246.

https://doi.org/10.1530/JOE-16-0427

106. Hong CS, Funk S, Muller L, *et al.*, 2016, Isolation of biologically active and morphologically intact exosomes from plasma of patients with cancer. *J Extracell Vesicles,* 5: 29289.

https://doi.org/10.3402/jev.v5.29289

107. Zarovni N, Corrado A, Guazzi P, *et al.,* 2015, Integrated isolation and quantitative analysis of exosome shuttled proteins and nucleic acids using immunocapture approaches. *Methods,* 87: 46–58.

https://doi.org/10.1016/j.ymeth.2015.05.028

108. Zhang Y, Liu Y, Liu H, *et al.*, 2019, Exosomes: Biogenesis, biologic function and clinical potential. *Cell Biosci,* 9: 19.

https://doi.org/10.1186/s13578-019-0282-2

109. Hu Y, Li X, Zhang Q, *et al.,* 2021, Exosome-guided bone targeted delivery of Antagomir-188 as an anabolic therapy for bone loss. *Bioact Mater,* 6: 2905–2913.

https://doi.org/10.1016/j.bioactmat.2021.02.014

110. Ma S, Wu J, Hu H, *et al.,* 2022, Novel fusion peptides deliver exosomes to modify injectable thermo-sensitive hydrogels for bone regeneration. *Mater Today Bio,* 13: 100195.

https://doi.org/10.1016/j.mtbio.2021.100195

111. Zhang FX, Liu P, Ding W, *et al.,* 2021, Injectable mussel-inspired highly adhesive hydrogel with exosomes for endogenous cell recruitment and cartilage defect regeneration. *Biomaterials,* 278: 121169.

https://doi.org/10.1016/j.biomaterials.2021.121169

112. Chen L, Yu C, Xiong Y, *et al.,* 2022, Multifunctional hydrogel enhances bone regeneration through sustained release of stromal cell-derived factor-1α and exosomes. *Bioact Mater*, 25: 460–471.

https://doi.org/10.1016/j.bioactmat.2022.07.030

113. Zhao Y, Gong Y, Liu X, *et al.,* 2022, The experimental study of periodontal ligament stem cells derived exosomes with hydrogel accelerating bone regeneration on alveolar bone defect. *Pharmaceutics,* 14(10): 2189.

https://doi.org/10.3390/pharmaceutics14102189

114. Wang L, Wang J, Zhou X, *et al.,* 2020, A new self-healing hydrogel containing hucMSC-derived exosomes promotes bone regeneration. *Front Bioeng Biotechnol,* 8: 564731.

https://doi.org/10.3389/fbioe.2020.564731

115. Mu J, Li L, Wu J, *et al.,* 2022, Hypoxia-stimulated mesenchymal stem cell-derived exosomes loaded by adhesive hydrogel for effective angiogenic treatment of spinal cord injury. *Biomater Sci,* 10: 1803–1811.

https://doi.org/10.1039/d1bm01722e

116. Shi Q, Qian Z, Liu D, *et al.,* 2017, GMSC-derived exosomes combined with a chitosan/silk hydrogel sponge accelerates wound healing in a diabetic rat skin defect model. *Front Physiol,* 8: 904.

https://doi.org/10.3389/fphys.2017.00904

117. Han C, Zhou J, Liang C, *et al.*, 2019, Human umbilical cord mesenchymal stem cell derived exosomes encapsulated in functional peptide hydrogels promote cardiac repair. *Biomater Sci,* 7(7): 2920–2933.

118. Wang C, Wang M, Xu T, *et al.,* 2019, Engineering bioactive self-healing antibacterial exosomes hydrogel for promoting chronic diabetic wound healing and complete skin regeneration. *Theranostics,* 9: 65–76.

https://doi.org/10.7150/thno.29766

ACCSCIENCE PUBLISHING

International Journal of Bioprinting

RESEARCH ARTICLE

3D-printed hydrogels dressings with bioactive borate glass for continuous hydration and treatment of second-degree burns

Fateme Fayyazbakhsh[1,2,3]*, Michael J. Khayat[4], Candy Sadler[5], Delbert Day[6], Yue-Wern Huang[3,7], and Ming C. Leu[1,2,3]

[1]Department of Mechanical and Aerospace Engineering, Missouri University of Science and Technology, Rolla, Missouri, USA

[2]Intelligent System Center, Missouri University of Science and Technology, Rolla, Missouri, USA

[3]Center for Biomedical Research, Missouri University of Science and Technology, Rolla, Missouri, USA

[4]Department of Materials Engineering, McGill University, Montréal, Quebec, Canada

[5]Wound Clinic, Phelps Health Hospital, Rolla, Missouri, USA

[6]Department of Material Science and Engineering, Missouri University of Science and Technology, Rolla, Missouri, USA

[7]Department of Biological Sciences, Missouri University of Science and Technology, Rolla, Missouri, USA

Abstract

Recent advances in additive manufacturing have led to the development of innovative solutions for tissue regeneration. Hydrogel materials have gained significant attention for burn wound treatment in clinical practice among various advanced dressings due to their soothing and moisturizing activity. However, prolonged healing, pain, and traumatic removal due to the lack of long-term wound hydration are some of the challenges in the treatment of second-degree burn wounds. In this study, 3D-printed dressings were fabricated using gelatin, alginate, and bioactive borate glass (BBG) using an extrusion-based bioprinter. After ionic crosslinking, the 3D-printed dressings were characterized for mechanical properties, degradation rate, hydration activity, and *in vitro* cell viability using human fibroblasts. The results demonstrated that in 3D-printed dressings with 20 wt% BBG, Young's modulus increased by 105%, and 10-day degradation rate decreased by 62%. Addition of BBG prevented the burst release of water from hydrogel dressings and enabled the continuous water release for up to 10 days, which is crucial in treating second-degree burn wounds. 3D-printed hydrogel dressings with BBG showed long-term cell viability that can be a result of the accumulative release of therapeutic ions from BBG particulate. The *in vivo* wound healing functionality of the dressings was investigated using a rat model with a second-degree burn wound. Our animal study showed that the 3D-printed dressings with BBG exhibited faster wound closure, non-adhesive contact, non-invasive debridement, and non-traumatic dressing removal. Histological analysis suggested that 3D-printed dressings contributed to more uniform re-epithelialization and tissue remodeling compared to the non-printed hydrogels of the same compositions. Critically, 3D-printed dressings with BBG led to significant regeneration of hair follicles compared to the 3D-printed hydrogel, non-printed hydrogel, and the control groups. The superior outcome of the 3D-printed hydrogel–BBG20 dressings can be attributed to the bioactive formulation, which

***Corresponding authors:**
Fateme Fayyazbakhsh
(f.fba@mst.edu)

Citation: Fayyazbakhsh F, Khayat MJ, Sadler C, *et al.*, 2023, 3D-printed hydrogels dressings with bioactive borate glass for continuous hydration and treatment of second-degree burns. *Int J Bioprint*, 9(6): 0118.
https://doi.org/10.36922/ijb.0118

Received: April 06, 2023
Accepted: June 02, 2023
Published Online: July 14, 2023

Copyright: © 2023 Author(s). This is an Open Access article distributed under the terms of the Creative Commons Attribution License, permitting distribution, and reproduction in any medium, provided the original work is properly cited.

Publisher's Note: AccScience Publishing remains neutral with regard to jurisdictional claims in published maps and institutional affiliations.

promotes moist wound healing for longer time periods, and the non-adhesive porous texture of the 3D-printed dressings with increased wound-dressing interactions. Our findings provided proof of concept for the synergistic effect of bioactive formulation and the porous texture of the 3D-printed hydrogel dressings incorporated with BBG on continuous water release and, consequently, on second-degree burn wound healing.

Keywords: Hydrogel wound dressing; Burn wound healing; 3D printing; Bioactive borate glass; Continuous water release

1. Introduction

Burn wound healing is a complex and delicate molecular-cellular process to restore skin functions and repair tissue damage[1]. Burn injuries represent a major public health issue and are among the most severe injuries[2], with approximately 10,000 annual deaths in the United States[3]. Each year approximately 1.1 million patients suffering from burn wounds are admitted to hospitals in the United States, and approximately 660,000 among them are diagnosed with second-degree burn wounds[4-6].

Second-degree burn is characterized by damage to the integrity of the entire epidermis and varied depths of the dermis that typically require immediate medical care[7]. The current standard of care in clinical practice for second-degree burn wound treatment includes topical antimicrobial agents and advanced dressings such as contact dressing and hydrogel dressings. The primary goal of the advanced dressings is to promote optimal wound healing while providing pain relief and protection from infection[8,9]. Although the existing advanced wound dressings cover a broad range of moderate to high exuding wounds, a small number of wound care products are specifically designed for low exuding wounds, *e.g.*, second-degree burns. Despite good clinical outcomes for wet wounds, the majority of these products end up with inadequate healing and poor hydration in second-degree burn wounds[10,11]. Topical agents, such as silver sulfadiazine, are typically associated with pain and prolonged healing due to wound dehydration, poor re-epithelialization, traumatic removal, and non-transparent appearance[10-22]. Hydrogel dressings provide a moist environment for the second-degree wound and help with pain relief. However, frequent changes of hydrogel dressings in second-degree burn wounds can be time-consuming, potentially traumatic to the healing tissue, and may lead to complications such as dehydration or maceration if poorly managed. Hence, there is an immense need to develop advanced wound dressings for second-degree burn wound treatment with desired features, such as bioactive formulation, soothing effect, tunable water absorption/release, non-adhesive contact, and skin-like mechanical properties[6,16,23,24].

Bioactive glass materials are a class of bioceramics that have the ability to bond with living tissues and promote specific biological responses when exposed to body fluids. These materials have been studied extensively for their potential use in hard tissue engineering and implant coating[25,26]. Bioactive glass materials comprise a mixture of oxides from biologically active elements, such as Si, B, Ca, Mg, Ag, Ce, Cu, and Zn, among others. The multiple therapeutic ions released from bioactive glass can react with proteins and enzymes to stimulate the proliferation and differentiation of cells involved in wound healing, such as mesenchymal stem cells, fibroblasts, and endothelial cells[26,27]. There are three major types of bioactive glass which are classified based on the dominant network forming oxide in the glass formulation: silicate glass, phosphate glass, and borate glass, among which the latter has the fastest degradation rate[28]. Recently, the US Food and Drug Administration (FDA) has cleared a bioactive borate glass (BBG) product (Mirragen, ETS Wound Care, Missouri, USA) for treatment of chronic wound healing[29]. In addition to its ability to promote cellular activity, BBG can enhance wound healing by (i) regulating the secretion of essential growth factors and matrix metalloproteinase (MMPs) to promote angiogenesis and extracellular matrix (ECM) remodeling[30-37], (ii) preventing bacterial growth[32,38,39], and (iii) alleviating the adverse inflammatory response by scavenging the reactive oxygen species[40,41]. Several studies showed that boron in BBG positively affects different stages of wound healing. It has been shown that boron can promote angiogenesis by stimulating tissues to secrete specific growth factors and modulate keratinocytes and endothelial cellular responses[26,31,36,42,43]. One of the key advantages of using BBG over other additives is its potential for incorporating a wide variety of dopants, including copper and zinc to promote the release kinetics of bioactive ions, regulate degradation rate, and potentially impart additional therapeutic properties to the glass[44]. Copper has been shown to stimulate the proliferation of endothelial cells by inducing local hypoxia to stimulate the expression of vascular endothelial growth factor (VEGF)[33,45]. Several studies have reported the positive effect of zinc dopant on the antimicrobial activity and inflammatory response[46-48].

Despite the good clinical outcome for wet wounds, however, BBG alone is ineffective in treating dry wounds, *e.g.*, burn wounds, due to the wound dehydration and lack of reacting medium. Besides, the fast degradation

rate and ion release from BBG make it highly reactive, which can damage the fragile wound bed in the case of burn wounds[49]. On the other hand, the burst release of therapeutic ions from BBG can increase the local pH to alkaline range, which can cause local toxicity and tissue damage. An effective approach to address this challenge is to incorporate BBG particulates in natural hydrogel matrices. The BBG–hydrogel complex can take advantage of the synergistic activity of therapeutic ions from BBG and the soothing effect of the hydrogels, making it effective for burn wounds. While the hydrogels provide water for wound hydration, BBG particulates prevent the burst release of water molecules from the hydrogel network, making it stable on the wound surface for longer time periods.

Hydrogels are large 3D molecules composed of hydrophilic polymer chains that absorb and retain large amounts of water[50]. Hydrogels are an essential class of advanced wound dressings that can donate or absorb water in accordance with the wound condition[7,51,52]. Since 1977 when hydrogels were introduced as wound dressings for the first time[53], their biological performance has been enhanced by adding glass materials, peptides, and growth factors[54-56]. In 2019, Zhu *et al.* incorporated ZnO/silicate glass and epidermal growth factor (EGF) into alginate/chitosan hydrogel compound. Their results showed that the ZnO/silicate glass promoted the formation of granulation tissue, deposition of collagen and myofibril, release of anti-inflammatory factors, angiogenesis, and wound closure[57]. In 2020, Zhu *et al.* showed that silicate glass/alginate compound can modulate the inflammatory response and angiogenesis[52]. Chen *et al.* incorporated GelMa with cerium-doped silicate glass to develop an injectable compound for treatment of diabetic ulcers. Their results showed that cerium-doped glass improved the angiogenesis and antibacterial activity of the hydrogel by regulating the anti-inflammatory response[28]. In another research published in 2022, Mehrabi *et al.* developed *in situ* forming hydrogel dressing by incorporation of borate glass into chitosan/carboxymethyl cellulose hydrogel compound. Their results showed consistent angiogenesis, remodeling, and accelerated wound healing in diabetic rats[58]. Although the use of novel hydrogels incorporated with bioactive glass has paved the road for effective wound treatment, the majority of these hydrogel dressings are amorphous gels with poor mechanical stability on the wound and short-term wound coverage. These shortcomings may result in frequent change of wound dressing that cause pain and infection.

3D printing, as a rapidly developing manufacturing technology, enables the programmable and customizable high-throughput fabrication of wound dressings with multiple materials and geometries[59]. Our previous research showed that 3D-printed dressings with an adequate gelatin/alginate ratio promote burn wound healing[51]. We highlighted that the 3D-printed porous surface supports non-adhesive contact and increases the available surface for wound-dressing interactions compared to non-printed dressings of the same composition. However, wound dehydration remains a major clinical challenge in burn wound treatment. In the research, we incorporated 3D-printed hydrogel dressings with BBG, which allows for controlling the release of water and therapeutic ions as well as enhancing the dressing fixity on the wound for longer time. To the best of our knowledge, the current research investigates the use of 3D-printed glass-hydrogel wound dressings for the first time.

In this study, 3D-printed dressings with gelatin, alginate, and various amounts of BBG were fabricated and characterized to enhance the functionality of burn wound care products. After measuring the mechanical properties, degradation rate, hydration activity, water release rate, and *in vitro* biocompatibility, an *in vivo* wound healing study was conducted to investigate the effect of BBG and 3D-printed porous contact on treatment of second-degree burn wounds using a rat model. BBG powder, non-printed hydrogels of the same formulation, and a commercial product were included in the experiment.

2. Materials and methods

2.1. Materials

Gelatin type B (from bovine skin, gel strength: 225 g Bloom), sodium alginate (alginic acid sodium salt from brown algae, medium viscosity), calcium chloride anhydrous, Dulbecco's Modified Eagles Medium (DMEM), phosphate-buffered saline (PBS), fetal bovine serum (FBS), 1% penicillin/streptomycin (pen/strep), MTT, and trypsin/EDTA were purchased from Sigma-Aldrich (St. Louis, Missouri, USA). BBG (particle size <20 μm) was provided by ETS Wound Care (Missouri, USA). All materials were used as received without further modification.

2.2. Bioink preparation

In this study, the gelatin:alginate ratio of 5:3 was selected as the primary hydrogel matrix based on our previous findings, which demonstrated the optimal balance in terms of mechanical properties, printability, and biocompatibility in this hydrogel compound[16]. To prepare the hydrogel–BBG bioinks, different concentrations of BBG (0, 10, and 20 wt% of dry material) were mixed with 7 mL of deionized (DI) water and vigorously stirred for 24 h at room temperature. After centrifuging and filtering, the resulting supernatants were mixed with 500 mg of gelatin powder and stirred for 10 min at 40°C to obtain 5% (w/v)

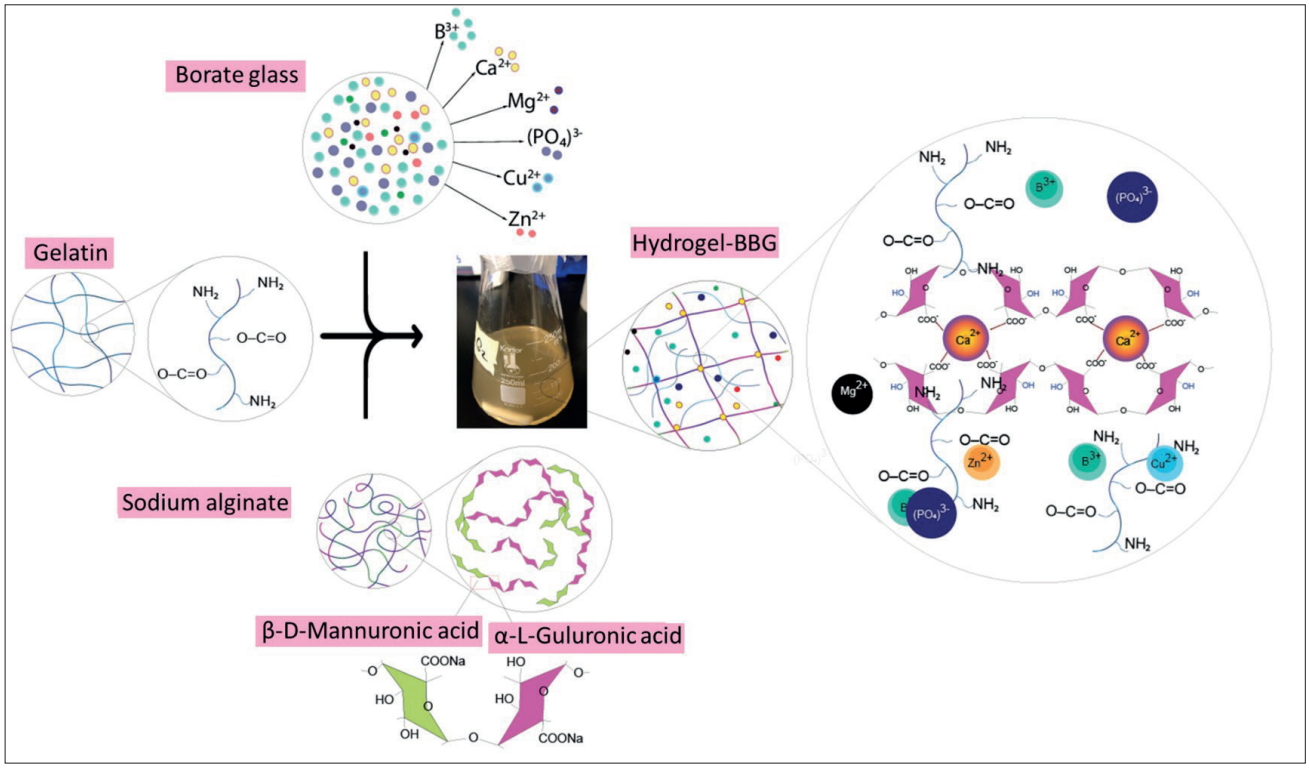

Figure 1. Schematic of the structure of gelatin, BBG, sodium alginate, and hydrogel–BBG blend. Gelatin and alginate are semi-interpenetrating networks (semi-IPN), whereby the free volume decreases due to (i) the electrostatic interactions between BBG particulates and gelatin–alginate chains and (ii) the formation of crosslinks between alginate chains.

gelatin, gelatin-BBG10, and gelatin-BBG20 solutions. A 10 w/v% stock solution of sodium alginate was prepared by dissolving 1000 mg of sodium alginate powder in 10 mL of DI water. To achieve a gelatin:alginate ratio of 5:3, 3 mL of the sodium alginate stock solution was added dropwise to the gelatin–BBG solutions and stirred at 800 rpm for 40 min at 40°C to obtain clear homogeneous compounds of hydrogel, hydrogel–BBG10, and hydrogel–BBG20 bioinks. The schematic microstructure of gelatin, alginate, BBG, and their mixture is shown in Figure 1.

2.3. 3D printing

In this research, extrusion-based 3D printing technology was utilized using the Inkredible® bioprinter (CELLINK Corporation, Sweden). The dressings were printed directly onto sterile Petri dishes with the print head temperature adjusted at 25°C and 35°C for hydrogel and hydrogel–BBG bioinks, respectively. The dressings were printed at 2.5 mm/s speed and 100 kPa pressure with a geometry of square (30 × 30 × 3 mm^3) and dog bone (30 × 10 × 5 mm^3) for different tests. The 3D-printed dressings were immersed in 0.2 M calcium nitride ($CaNO_3$) solution for 10 min to form crosslinks between alginate chains. After crosslinking, 3D-printed dressings were rinsed with DI water three times and stored at 4°C.

2.4. Mechanical testing

The dog-bone-shaped dressings were tested for mechanical properties using the Universal Instron 5969 Dual Column Testing System (Instron, Massachusetts, USA) and the BlueHill Universal Software (n = 5). The scaffolds were assessed using a uniaxial tensile load frame at 5 mm/min, typical for polymer specimens to measure the modulus of elasticity, yield strength, and yield strain of the scaffolds in accordance with the ASTM F2150-8 standard.

2.5. Evaluation of chemical structure

The chemical structures of the bioinks were identified using a Nicolet iS50 Fourier-transform infrared spectroscopy (FTIR) spectrophotometer (Thermo Scientific, Massachusetts, USA) equipped with a diamond crystal cell of attenuated total reflection (ATR) accessory. All the spectra were recorded at a resolution of 4 cm^{-1} with 32 scans with a data spacing of 0.482 cm^{-1} in the mid-infrared region (4000–400 cm^{-1}). The obtained spectra were analyzed with OMNIC 9.2.41 software (Thermo Scientific, Massachusetts, USA). The infrared (IR) spectrum data from Sigma Aldrich were used to identify characteristic chemical bonds in gelatin, alginate, and water.

2.6. Swelling capacity and biodegradation rate measurement

The swelling capacity and degradation rate of the 3D-printed dressings were measured by measuring the gravimetric changes of the samples after immersing in PBS. The samples were weighed, immersed in PBS, and kept at 32°C to reach equilibrium swelling and subsequent degradation. The weight changes in determined time intervals were recorded for up to 7 days as the dressings are intended to stay on burn wounds for up to 7 days (n = 5). The dressing's swelling capacity and degradation rate were calculated using the following equations:

$$\text{Swelling capacity } (\%) = \frac{W_{max} - W_{Dry}}{W_{Dry}} \times 100 \quad \text{(I)}$$

$$\text{Degradation rate (mg/min)} = \frac{W_0 - W_{day10}}{10 \times 24 \times 60} \quad \text{(II)}$$

where W_{Dry} is the initial dry weight, W_{max} is the maximum weight of the scaffolds after immersion, and W_{day10} is the weight after 10 days of immersion in PBS.

2.7. Hydration activity and water release kinetics measurement

To measure the effect of BBG on the water release rate, the hydration activity was measured, as described in our previous work[16]. Briefly, the total amount of water in each sample was measured using thermogravimetric analysis (TGA) on 250°C for 10 min (SDT Q600 V20.9 Build 20, Universal V4.5A TA Instruments, Minnesota, USA). The weight change was considered the total water content (n = 5)[60].

To predict the hydration activity of the samples on burn wounds, the water release rate from each sample was measured using an ethylcellulose super absorbent foam (Shield Line LLC, New Jersey, USA), as a model of the dehydrated burn wound. After placing the 3D-printed dressings on the foam surface, the gravimetric changes were measured after 24 h at 32°C, as the temperature of the burned area is often lower than the normal body temperature[61]. The 24-h hydration is a key factor in burn wound treatment outcome, as the systemic capillary leak, intravascular fluid loss, and significant fluid shifts mostly occur within the first 24 h, peaking at around 6–8 h after injury[62,63]. The total water content and water release rate were calculated using the following equations:

$$\text{Total water content } (\%) = \frac{W_0 - W_H}{W_0} \times 100 \quad \text{(III)}$$

$$\text{Water release rate } (\%) = \frac{W_0 - W_{24}}{W_0 - W_H} \times 100 \quad \text{(IV)}$$

where W_0 is the initial weight, W_H is the weight after heating at 250°C, and W_{24} is the weight after 24 h placing on dry surfaces.

The water release profile was calculated and plotted against time (up to 10 days). To determine the water release kinetics, the release profile was analyzed using different kinetic models, including zero-order, first-order, Higuchi, Korsmeyer–Peppas, and Hixon–Crowell for each dressing formulation[64].

2.8. MTT assay

The MTT assay was used to study the effect of BBG on the viability and proliferation of human dermal primary fibroblast cells (ATCC, Virginia, USA) at passages 3 and 4. 3D-printed dressings were weighed and exposed to ultraviolet light (345 nm) for 15 min per side, then immersed in DMEM with no further treatment. The sample extracts were collected and filtered after 1, 3, and 7 days of immersion (five replications). The sample extracts were used to indirectly evaluate the cell viability in accordance with the ISO-10993 standard. The DMEM culture media with no further treatment was considered the control sample. Cells were cultured in DMEM containing 10% FBS and 1% pen/strep until they reached 80%–90% confluence. Cells were seeded in 96-well plates at a density of 10^4 cells/well with 100 µL of DMEM containing 10% FBS and 1% pen/strep. The plates were incubated at 37°C with 5% CO_2. After 24 h, the initial culture media were discarded and replaced by 90 µL sample extracts with 10% FBS and 1% pen/strep. Following 24 h of treatment, 100 µL of 0.5 M MTT solution was added to each well and incubated for 4 h. Formazan crystals were solubilized using isopropanol, and after 30 min, the absorbance was measured at 545 nm using an ELISA reader (Stat Fax 2100, Awareness Technology Inc., Florida, USA).

2.9. Animal test

2.9.1. In vivo burn wound model

All *in vivo* experiments were approved by the Missouri S&T Institutional Animal Care and Use Committee (IACUC) (Reference No. 177-20). The ability of the 3D-printed wound dressings for the treatment of second-degree burn wound was evaluated by creating a circular burn wound in the dorsal area of Sprague Dawley rats using a hot aluminum bar. Thirty-six Sprague Dawley rats (Charles River, Missouri, USA) were divided into six groups with six animals per group:

(i) Control: Wounds covered with petrolatum gauze as the current standard of care

(ii) BBG powder: Wounds covered with BBG powder

(iii) Non-printed hydrogel: Wounds covered with non-printed hydrogel

(iv) 3D-printed hydrogel: Wounds covered with 3D-printed hydrogel dressings

(v) Non-printed hydrogel–BBG: Wounds covered with non-printed hydrogel–BBG

(vi) 3D-printed hydrogel–BBG: Wounds covered with 3D-printed hydrogel–BBG dressings

The animals were anesthetized using isoflurane. After shaving the dorsal area, the skin was cleaned with iodine and then sterilized with alcohol swabs three times. The second-degree burn was made by placing a 100°C aluminum bar with a diameter of 20 mm on the dorsal area for 10 s. After implementation, the wounds were disinfected by Dermoplast antiseptic spray (Advantice Health LLC, New Jersey, USA). After applying the dressings, the wounds were covered with Petrolatum Gauze and Elastikon bandages (3M, Minnesota, USA). Figure 2 shows the application of dressing on the wounds in the three groups. All animals were monitored for post-operative care on a daily basis. The wounds were assessed and photographed under isoflurane every 7 days. Prior to rebandaging, any necrotic tissue present on the wound surface was removed using sharp debridement if needed. Sharp debridement was performed by a trained medical professional using sterile surgical instrument, following established protocols. Necrotic tissue was defined as non-viable tissue that appeared black, brown, or gray in color and had a dry, leathery texture. The extent of necrotic tissue removal was documented for each sample. The animals were euthanized after 4 weeks using a lethal dose of CO_2. Wound tissue explants were collected and fixed in formalin solution overnight for further histology investigation.

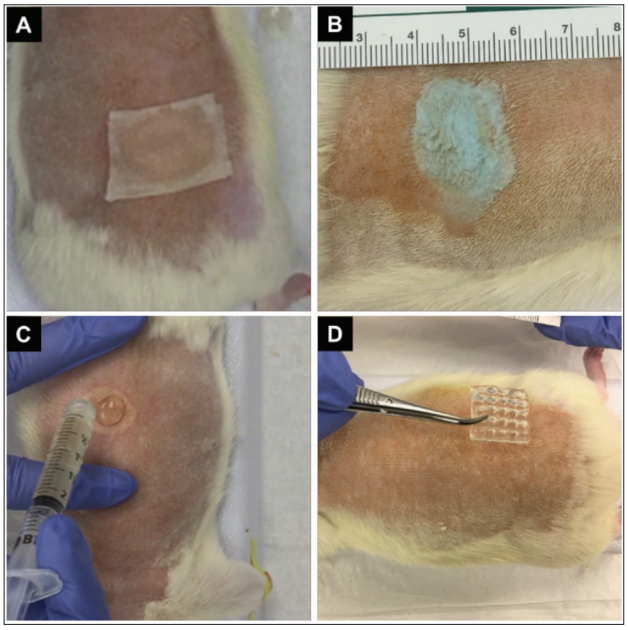

Figure 2. Animal test to evaluate second-degree burn wound healing using a rat model in six groups. Burn wounds covered with (A) petrolatum gauze, (B) BBG powder, (C) non-printed hydrogel and hydrogel–BBG, and (D) 3D-printed hydrogel and hydrogel–BBG dressings.

2.9.2. Wound closure

Wounds were rebandaged and photographed every 7 days to track the wound size, color, edge, re-epithelialization, necrotic tissue formation, and secondary trauma caused by dressing removal. A sterile disposable ruler was placed in close proximity to the wound, serving as a scale for measurement purposes. The wound size was quantified by tracing the wound border in each photograph using ImageJ software. The wound closure was calculated as follows:

$$\text{Wound closure (\%)} = \frac{A_0 - A_w}{A_0} \times 100 \quad \text{(V)}$$

where A_0 is the wound area after wound creation, and A_w is the wound area at time t (*i.e.*, 1, 2, 3, and 4 weeks). Traumatic removal was evaluated by assessing the presence of traumatic laceration, bleeding, and redness in wound margins and surrounding tissues after the dressing removal.

2.9.3. Histology analysis

Full-thickness wound tissue explants (25 × 25 mm^2) were resected and fixed overnight in 10% neutral buffered formalin, then cut into tissue blocks (25 × 1 mm^2) that include wound bed, margins, and surrounding skin. Tissue blocks were processed and paraffinized using a fully automated tissue processor (TissueTek 2000, Sakura Finetek, California, USA). Tissue blocks were sectioned at 5 μm thickness and stained with hematoxylin and eosin (H&E). The slides were imaged using a transmitted light bright field microscope (Olympus BX53 microscope fitted with an Olympus DP70 digital camera) with a 10× objective lens. The entire tissue sections were scanned, digitally photographed, and "stitched" together to form a single composite image using Adobe Photoshop (Adobe Inc., California, USA). Quantitative histomorphometry was performed to measure the epidermal layer, dermal layer, and granulation tissue thickness. H&E images were blindly graded by two trained graders with sections scored on a scale of 0–4 regarding re-epithelialization, dermal regeneration, and granulation tissue formation[65], as described in Table 1.

2.10. Statistical analysis

In this research, all experiments were conducted with a minimum of five replications for each sample per test. All data were reported as the mean ± standard deviation (SD). One-way analysis of variance (ANOVA) was employed to determine statistical difference among different groups.

Table 1. Qualitative histological grading criteria adopted from Altavilla *et al.*[65]

Score	Re-epithelialization	Dermal regeneration	Granulation tissue formation
0	No epidermal organization	No dermal organization	Very thin or no granular layer
1	Very little epidermal organization	Very little dermal organization	Thin granulation layer
2	Little epidermal organization	Little dermal organization	Moderate granulation layer
3	Moderate epidermal organization	Moderate dermal organization	Thick granular layer
4	Complete remodeling of the epidermis	Complete remodeling of dermis	Very thick granular layer

This statistical test enables the evaluation of overall group differences and determines if there are significant differences between the means of these groups. Following the ANOVA, the Student's *t*-test is performed for pairwise comparisons between specific groups. This test allows for the determination of statistically significant differences between the means of two groups. Significance was set at the P-value <0.05. Statistical analyses were performed using GraphPad Prism 9.

3. Results and discussion

3.1. Mechanical properties

The 3D-printed hydrogel–BBG dressings were fabricated using extrusion-based 3D printing technology with different percentages of BBG content. Figure 3 shows the appearance and Young's modulus of the 3D-printed dressings after crosslinking with calcium ions. Traditionally, mechanical properties, such as bone scaffolds, are considered key characteristics for load-bearing tissue engineering scaffolds. However, the mechanical behavior of skin substitutes and wound dressings has become an increasingly important focus of preclinical studies. Mechanical properties can significantly impact the performance and clinical outcomes of these products, including level of pain and trauma experienced during application, coverage, and removal. In order to promote moist wound healing, the dressings are required to exhibit adequate mechanical properties to integrate with the wound bed and surrounding tissue, while simultaneously providing effective coverage against external pathogens and traumas. Also, dressings should exhibit elasticity in the range of surrounding skin to support the body movement and normal activities without pain and falling apart[66]. The Young's modulus (E) of normal skin fluctuates between 0.42 MPa and 0.85 MPa[67] and has the highest value of approximately 1 MPa[68]. The tensile testing results from this work strongly support the positive effect of BBG on the elasticity of the 3D-printed dressings: (i) stronger chemical bonds between BBG particles and alginate chains and (ii) reinforcement of hydrogel network with BBG particles. It is generally accepted that the stronger chemical bonds in the hydrogel network result in higher mechanical strength and lower permeability. By increasing the amount of BBG from 0 to 10 and 20 w/v%, Young's modulus increased by 39% and 105%, respectively.

3.2. Chemical structure

Typically, the hydrogel-based bioinks provide favorable permeability to oxygen and nutrients. In order to evaluate the interactions between the gelatin, alginate, and BBG particulates, the chemical structure of the samples was studied by FTIR spectroscopy, and the resulting spectra are presented in Figure 4. Alginate and gelatin have overlapping carboxylate groups and hydroxyl groups with 3200–3500 cm^{-1} characteristic peaks, which is also overlapping with O-H stretching bonds in water. The amide I, II, and III bonds in gelatin and C=O bond as the characteristic bond of alginate were observed in all samples at a narrow peak at 1659–1243 cm^{-1} bands[16]. By increasing the BBG content, the intensity of hydrogen bonds decreases due to the formation of crosslinks that show the hydroxyl groups in alginate are involved in crosslinks with divalent metals instead of hydrogen bonds. It can be a result of the interactions between bivalent metals (*e.g.*, Ca^{2+}, Mg^{2+}, Cu^{2+}, Zn^{2+}) released from BBG and alginate and the formation of crosslinks[69]. Bands associated with alginate showed significant changes by adding BBG. The bands associated with guluronic acid groups appeared between 500–450 cm^{-1} and 821 cm^{-1} were increased by BBG content, which shows the formation of =C-H groups. By increasing the BBG content, peaks associated with B-O and B-O_3 appeared at 1402 cm^{-1} band[70,71], which increased in hydrogel–BBG20 compared to hydrogel–BBG10. The peaks associated with metallic oxides within BBG, such as Ca-O, Mn-O, Cu-O, and Zn-O, appeared at 1000–600 cm^{-1} bands[72-76]. The C-O-C stretching bonds at 1080–1030 cm^{-1} and C=O bonds at 1621 cm^{-1} in guluronic acid increased by BBG, which confirms the formation of crosslinks in alginate in the presence of ions released from BBG[69]. The C-H stretching bands at 2600 cm^{-1} slightly appeared in hydrogel–BBG10 and increased in hydrogel–BBG20, confirming the interactions between ions released from BBG and gelatin chains, and the formation of crosslinks

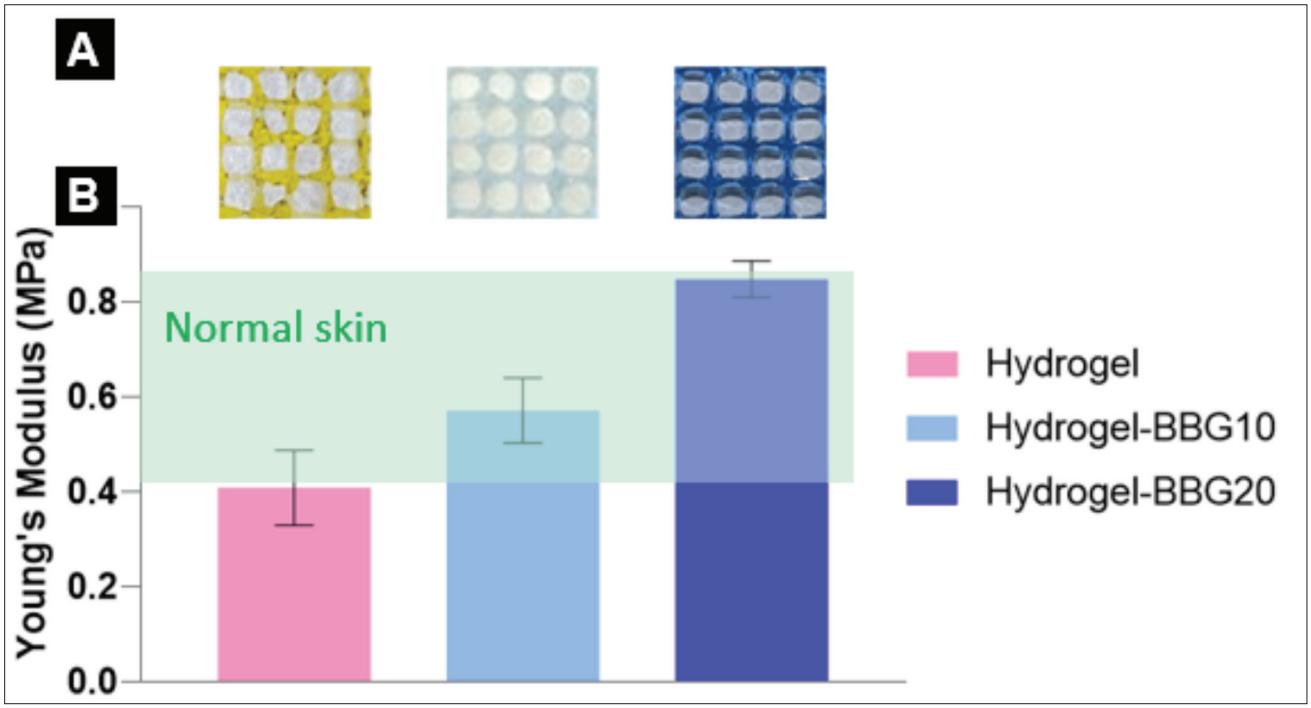

Figure 3. BBG improved the printing outcome, consistency, and Young's modulus of 3D-printed dressings. (A) Photographs of the 3D-printed dressings. Hydrogel–BBG20 dressings showed the finest mesh structure and best shape fidelity. (B) The Young's modulus of the 3D-printed dressings, compared to the normal unwounded skin. Both samples with BBG exhibited Young's modulus in the range of normal skin (n = 5). The Young's modulus of the normal skin is adopted from[67,68].

within alginate chains. The slight increase in O-H bonds at 2901 and 1021 cm^{-1} shows the increase in hydrogen bonds and interactions between water molecules and ions released from BBG. The appearance of peaks at 1630 cm^{-1} can be attributed to the reactions between proton donator groups in gelatin amide groups and the cations released from BBG. The formation of intermolecular hydrogen bonds between water molecules, ions, and different overlapping functional groups in gelatin and alginate makes a favorable entanglement for enhanced mechanical behavior at certain ratios of hydrogel:BBG. In the same line with mechanical testing results, forming covalent crosslinks between bivalent ions and guluronic acid blocks in alginate results in lower permeability and higher mechanical stiffness in samples with higher BBG content. Lower permeability reduces the transport of water molecules and maintains the structural integrity and stability of the hydrogel over time. The higher degree of crosslinking between alginate and BBG content can slow down the release of water which is desired for treatment of burn wounds.

3.3. Degradation rate and stability

The swelling/weight change and degradation rate of the 3D-printed dressing are shown in Figure 5. The addition of BBG has negligible influences on the hydrogels and swelling capacity, while the 10-day degradation rate decreased by 29% and 62% after adding 10 and 20 w/v% BBG, respectively. BBG improved the stability of the hydrogel by increasing the degradation time from 10 to 14 days. It can result from (i) stronger electrostatic interactions, including hydrogen bonds and van der Waals bonds between BBG and hydrogel chains and (ii) covalent crosslinks between alginate chains in the presence of ions released from BBG. As illustrated in Figure 1, adding BBG decreased the free volume within the hydrogel network, increasing the density and decreasing the samples' permeability. The crosslinking process of sodium–alginate results from Na–Ca replacement and formation of the egg-box structure. Since each Ca^{2+} ion can bond to two carboxylate groups, the ions can crosslink the polymer chains, which results in the formation of an insoluble, gel-like substance. This is associated with the presence of guluronic acid blocks, as shown in Figure 4.

3.4. Hydration activity and water release kinetics

We studied the water content and water donation ability of the 3D-printed dressings to predict their functionality for clinical burn wound treatment. The initial water content slightly decreased by adding BBG content, as 3D-printed hydrogel, hydrogel–BBG10, and hydrogel–BBG20 dressings showed 94.36 ± 0.29, 94.01 ± 0.09, and 93.71 ± 0.24% water content, respectively. Figure 6 depicts the 10-day water release from the dressings on ethylcellulose

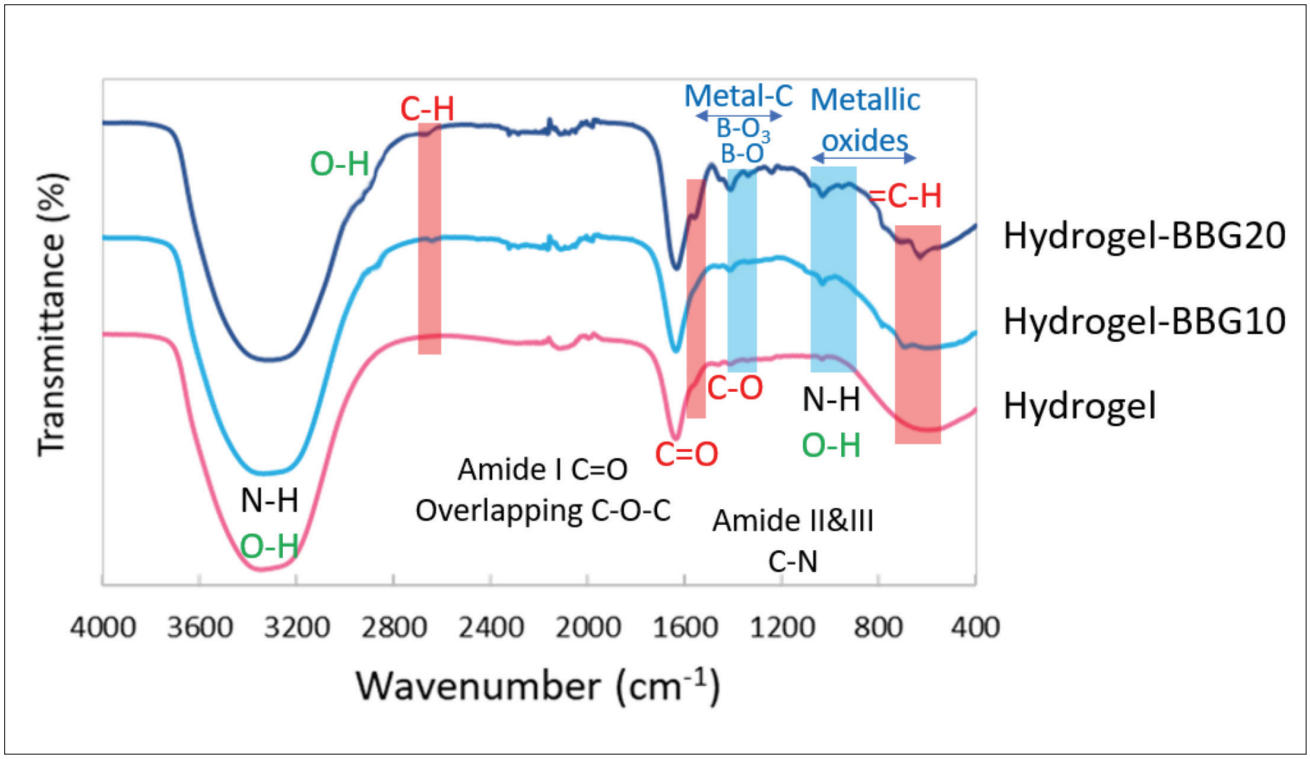

Figure 4. Fourier-transform infrared spectroscopy spectra of the hydrogel–BBG blends. The characteristic IR bands associated with BBG, gelatin, alginate, and water are shown by blue, black, red, and green text/boxes, respectively. BBG increased the intramolecular hydrogen bonds and formation of crosslinks between alginate chains.

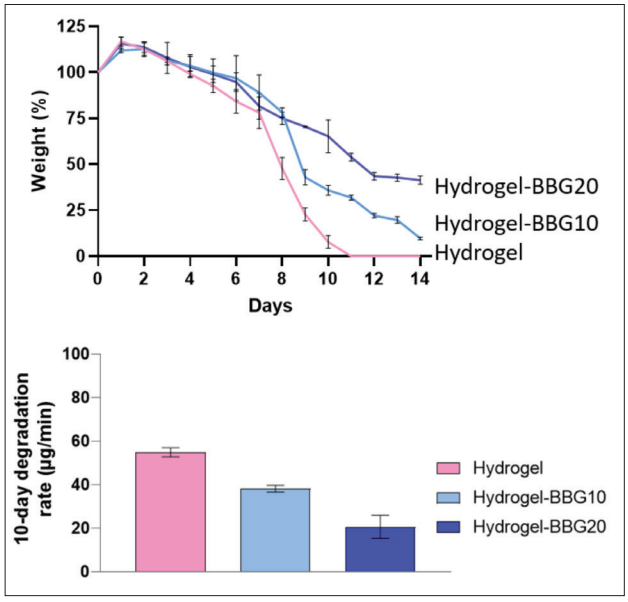

Figure 5. The swelling capacity, degradation profile, and 10-day degradation rate of the 3D-printed dressings in PBS (n = 5). BBG did not significantly affect swelling capacity (P >0.05), but it decreased the degradation rate. Samples with higher gelatin content showed a faster degradation rate and higher swelling capacity. BBG also increased the stability of the hydrogel: the 3D-printed hydrogel dressings without BBG degraded at day 10, whereas the BBG–hydrogel dressing lasted for 14 days. BBG particulates decreased the permeability of the hydrogel.

substrate as a super-absorbent surface representing the dehydrated surface of burn wounds. It results from lower free volume in samples with higher BBG content and stronger chemical bonds. On the other hand, the crosslinking reaction between alginate chains and bivalent ions is a condensation reaction that releases water to build larger molecules[77]. Hence, increasing the degree of crosslinking decreases the amount of water entrapped within the hydrogel network. Adding BBG decreased the water release rate and prevented the burst release of water content in the first day. The overnight water release decreased by 25% and 42% in samples with 10 and 20 w% BBG compared to the plain hydrogel. The slower water release is a key factor for continuous water release and burn wound treatment outcomes, as the dressing can stay effective on the wound for a longer time, which decreases pain and infection risk associated with rebandaging, as well as the treatment costs. BBG particulates can act as physical barriers to water molecules' movement; hence, the water molecules require higher energy and longer time to escape the hydrogel network.

To evaluate the efficiency of the hydrogel–BBG complex as a carrier for the controlled release of water, the release kinetics was analyzed using the *in vitro* cumulative water release data (Figure 6) at 32°C for 10 days. The graph

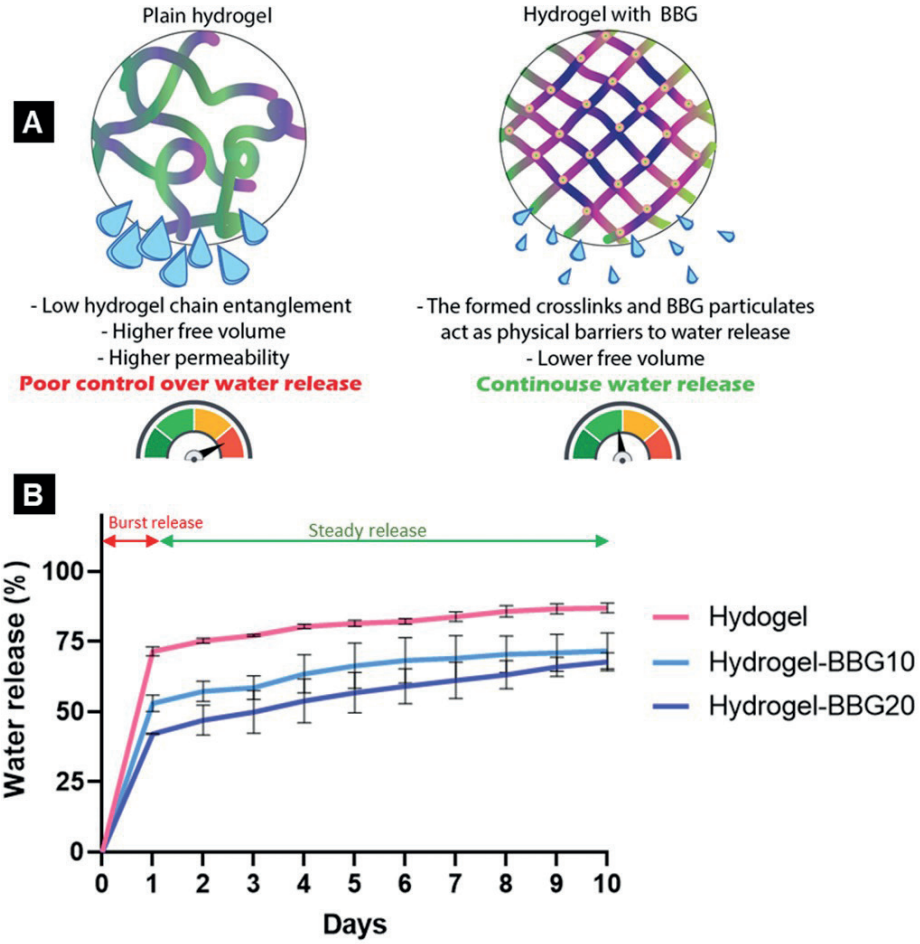

Figure 6. (A) Schematic of the effect of BBG on water release. (B) Ten-day hydration activity of the 3D-printed dressing on a super-absorbent surface to simulate dry burn wound surface (n = 5). BBG improved the water release by decreasing burst release and increasing the long-lasting water release. BBG decreased the permeability in the hydrogel, which justifies its slower degradation rate and sustained water release.

was fitted with different kinetic models in accordance with square root values, as shown in Table 2. The Higuchi model was selected as the best-fitted release kinetic model for all samples, which implies that the kinetic of water release from 3D-printed hydrogel, hydrogel–BBG10, hydrogel–BBG20 dressings, and SA/Pec/TA-Ag nanocomposite follows the Higuchi square root model. This model allows for quantifying drug release from thin ointment films, hydrogel scaffolds, transdermal patches, and matrix devices over the skin[78,79], which perfectly matches our 3D-printed dressings as porous hydrogel scaffold indicated for dermal contact and wound healing.

As shown in Figure 6, the release profile for all samples started with an initial burst release and was followed by sustained release, *i.e.*, steady release. As shown in Table 2, BBG improved the 10-day water release by (i) decreasing the initial burst release and (ii) increasing the sustained water release rate. It means the 3D-printed dressings with 20 wt% BBG can gradually release more water per day. In contrast, the plain hydrogel dressing releases the majority of the entrapped water at the first day, instead of gradual release.

3.5. Cell viability

The *in vitro* biocompatibility of 3D-printed dressings was evaluated by the MTT assay using primary human dermal fibroblasts (HDF) (Figure 7). 3D-printed hydrogel dressings showed significantly higher cell viability on days 1 and 3, and a decline on day 7 compared to the samples with BBG. The 7-day extracts from 3D-printed hydrogel–BBG20 showed the highest cell viability compared to the 3D-printed plain hydrogel and hydrogel–BBG10 (P < 0.05, n = 6), with no significant difference with the control group (P > 0.05). The decline in 7-day cell viability of the

Table 2. Release kinetic models and parameters for water release from 3D-printed dressings

Release kinetics model	Hydrogel	Hydrogel–BBG10	Hydrogel–BBG20
Zero-order	$R^2 = 0.9494$	$R^2 = 0.9183$	$R^2 = 0.9815$
First-order	$R^2 = 0.9826$	$R^2 = 0.9446$	$R^2 = 0.9960$
Korsmeyer–Peppas	$R^2 = 0.7389$	$R^2 = 0.7112$	$R^2 = 0.6782$
Higuchi[a]	$R^2 = 0.9891$	$R^2 = 0.9696$	$R^2 = 0.9983$
Hixon Crowell	$R^2 = 0.5432$	$R^2 = 0.5831$	$R^2 = 0.7138$
Drug release parameters			
Burst release (%)	71.51 ± 1.59	53.07 ± 2.87	42.14 ± 0.2
Total release (%)	87.09 ± 1.73	71.77 ± 6.44	67.86 ± 3.2
Sustained release (%)	15.58 ± 3.27	18.69 ± 3.82	25.79 ± 3.07
Sustained release/burst release	0.21	0.38	0.55
Release rate (mg/day)	1.73	2.07	2.85

[a]The water release kinetics in all samples demonstrate the highest coefficient of determination (R2 value) when fitted to the Higuchi model compared to other models..

hydrogel dressings (without BBG) can be associated with the time-dependent denaturation of amino acid sequences in gelatin and acidic degradation of alginate. These results show that the biocompatibility of the samples is time-dependent and promoted by increasing the cumulative therapeutic ions released from BBG while negatively affected by the timely decomposition of the gelatin–alginate compound. The ion released from BBG shifts the pH to alkaline ranges, while the hydrogel degradation shifts the pH to acidic ranges. The improved cell viability in hydrogel–BBG20 samples indicates that the BBG content dominantly affects cell viability. In the same line, the reduced cell viability in hydrogel–BBG10 samples compared to hydrogel–BBG20 samples shows that in this sample, the cell viability is mainly affected by the adverse interactions between alkaline ions and acidic residues resulting from the decomposition of alginate. Hence, the hydrogel–BBG20 samples provide a favorable balance between the alkaline pH caused by ion released from BBG and the acidic degradation of alginate. On the other hand, the neutralized pH can preserve the arginine-glycine-aspartic acid (RGD) sequences for a longer time and enhance cell proliferation and growth[80].

3.6. Animal test

To assess the effect of BBG on the wound-healing activity of the 3D-printed dressings, we conducted an *in vivo* study using a rat model with a second-degree burn wound. We compared the wound closure time, re-epithelialization, and granulation tissue formation in the 3D-printed hydrogel and hydrogel–BBG20 dressings with the non-printed hydrogels of the same formulation. The as-received BBG powder and commercial petrolatum gauze served as control groups. Wound images on days 0, 7, 14, 21, and 28 were analyzed to estimate the wound contraction/closure ranging from the initial deep partial-thickness burn of 20 mm diameter on day 0 to the total wound closure on day 28. Figures 8 and 9 present the changes in wound appearance and area, *i.e.*, wound closure, as a key factor in wound assessment. All samples showed faster wound closure compared to the control and BBG powder groups. Despite the excellent outcomes for chronic wounds, BBG has no therapeutic effect on burn wounds, which is due to the absence of aqueous media for therapeutic ion release and transfer to the wound. These results also re-affirm the positive effect of water release and hydrogel coverage on burn wound healing. Among the hydrogel samples, 3D-printed hydrogel–BBG20 showed the fastest wound closure and earliest re-epithelialization ($P < 0.05$, $n = 6$). Both 3D-printed and non-printed dressings with BBG showed smooth wound margins compared to the plain hydrogel samples with uneven wound margins. In contrast, the BBG powder group showed the formation of thick scab layer, *i.e.*, dry and rough wound crust. The 3D-printed samples with and without BBG showed significantly faster wound closure than the non-printed dressings of the same composition.

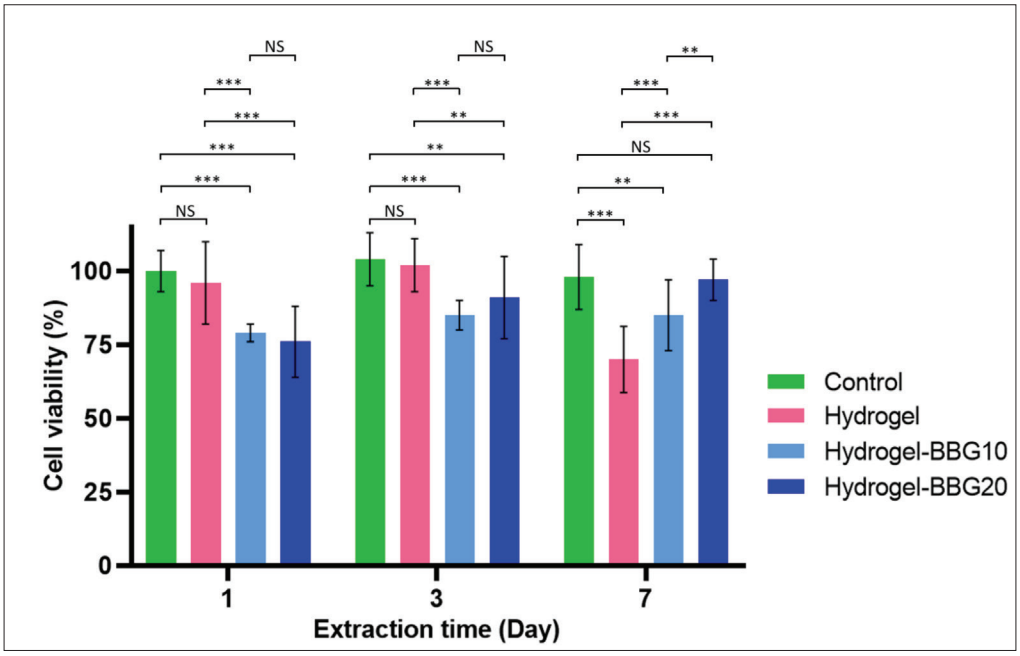

Figure 7. *In vitro* cell viability of the 3D-printed dressings using primary human dermal fibroblast after 1, 3, and 7 days of exposure. Hydrogel samples showed higher cell viability on days 1 and 3, and a decline on day 7 compared to samples with BBG showing lower cell viability. While BBG increased the cell viability after 7 days, which indicates the long-term effect of therapeutic ions released from BBG. In hydrogel samples, the short-term higher cell viability can be a result of RGD sequences present in gelatin[80]. $n = 6$; $^{*}P < 0.05$, $^{**}P < 0.01$, $^{***}P < 0.001$, and NS denotes non-significant difference.

Faster wound healing reduces the burden of second-degree burn wound by allowing the patients to resume their daily activities with shorter recovery time. The presence of an open wound is associated with pain, discomfort, and secondary trauma. Additionally, impaired or prolonged wound closure in second-degree burn wounds increases the risk of bacterial colonization and subsequent infection. Thus, faster wound healing contributes to patients' quality of life by reducing pain, discomfort, and complications such as infection[81,82].

Table 3 compares different parameters of wound healing recorded during weekly wound assessment. None of the samples developed an infection or adverse inflammatory response. The thickest and largest necrotic tissue was seen in the BBG group, followed by the control group. Both samples required sharp debridement for the removal of necrotic tissue. The sharp debridement as an invasive procedure slows the healing time and results in significant pain with further analgesia administration. In contrast, the 3D-printed hydrogel and hydrogel–BBG20 dressings and non-printed hydrogels of the same formulations developed smaller necrotic tissue and enabled autolytic debridement, *i.e.*, the non-invasive spontaneous removal of necrotic tissue. The dressing removal in the BBG powder and control groups required intensive force and sharp instruments that caused severe damage to the fragile wound bed and surrounding tissues due to the adherence of the wound to the dressing surface. In the non-printed hydrogel and hydrogel–BBG20 groups, the wounds were thoroughly rinsed prior to rebandaging to detach the dressing residues from the wound surface non-invasively. The porous contact in 3D-printed hydrogel and hydrogel–BBG20 dressings allowed for the easy and atraumatic removal of these dressings from the wound surfaces with no pain or damage to the granulation tissue or re-epithelialization layer. Unlike the non-printed hydrogel, BBG powder, and control groups, the 3D-printed hydrogel and hydrogel–BBG20 dressings and non-printed hydrogel–BBG dressings showed smooth wound margins and optimal wound closure, which can be attributed to (i) the bioactive formulation and continuous hydration in the 3D-printed and non-printed hydrogel–BBG20 groups, which promote the moist wound healing for longer time periods and (ii) the non-adhesive contact and porous texture of the 3D-printed dressings, which increase the available surface for wound-dressing interactions. The poor wound healing activity in the non-printed hydrogel dressings (without BBG) may result from the fast and excessive water release, which causes early wound maceration (*i.e.*, excessive water absorption in the wound and surrounding tissues) with long-term wound dehydration[82,83]. As shown in Figures 6 and 8, the poor control over water release in the non-printed samples results in inadequate wound hydration

Figure 8. Gross examination of wound healing over 28 days ($n = 6$). Wound images from the control and treatment groups. 3D-printed and non-printed hydrogels with BBG showed earlier re-epithelization, less necrotic tissue, and smoother wound margins. In contrast, the 3D-printed dressings with porous contact surface support the non-adhesive removal of wound dressings.

during the 7-day wound coverage. The dry surface of the BBG powder and petrolatum gauze in the control group can only protect the wound from infection and water loss due to evaporation, which results in wound dehydration and prolonged healing.

Figure 10 shows representative H&E-stained slides obtained from different groups to investigate epidermal regeneration (ER), dermal regeneration (DR), and granulation tissue formation (GT), which are key factors in wound healing analysis. The control and non-printed hydrogel groups showed the thickest ER layer, *i.e.*, hyperkeratosis, which is associated with poor skin regeneration. The non-printed hydrogel–BBG20, 3D-printed hydrogel, and 3D-printed hydrogel–BBG20 dressings developed thicker epidermal layer. In contrast, both 3D-printed dressings showed even ER, which indicates the positive effect of the porous texture of the 3D-printed contact on tissue regeneration. Despite the poor wound healing, the BBG powder group showed slight regeneration of hair follicles. The non-printed hydrogel–BBG20 and 3D-printed hydrogel–BBG20 showed the highest regeneration of hair follicles, which shows the significant effect of BBG on post-burn regeneration of hair follicles. The distinctive regeneration of hair follicles in these samples can be due to the continuous hydration and non-adhesive surface with aligned pores. The 3D-printed

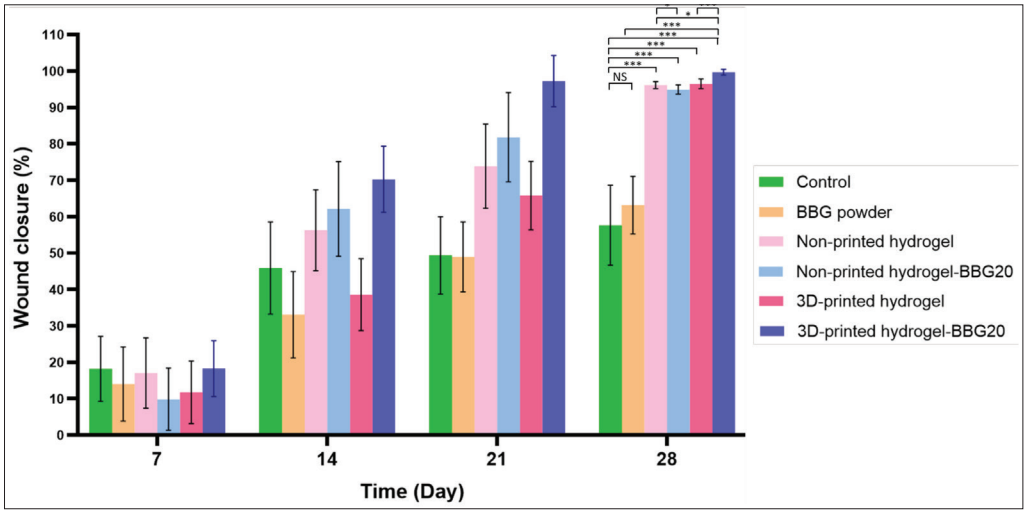

Figure 9. *In vivo* burn wound closure of the dressings in the control and test groups. 3D-printed dressings with BBG showed the fastest wound closure (*i.e.*, smaller wound size) after 28 days, followed by 3D-printed hydrogel and non-printed hydrogel–BBG dressings. $n = 6$; $^{*}P < 0.05$, $^{**}P < 0.01$, $^{***}P < 0.001$, and NS denotes non-significant difference.

Table 3. Wound assessment for different study groups

Dressing	Moist wound healing	Granulation tissue (days 14 and 21)	Re-epithelialization (days 21 and 28)	Wound margins
Control	Not seen	3-2	2-2	Red—Thick crust
BBG powder	Not seen	4-3	1-3	Brown—Thick crust
Non-printed hydrogel	Partially seen	3-2	2-4	Pink—Sloping
Non-printed hydrogel–BBG20	Seen	2-0	4-4	Light pink—Smooth, flat
3D-printed hydrogel	Seen	3-1	3-4	Pink—Smooth, flat
3D-printed hydrogel–BBG20	Seen	2-0	4-4	Light pink—Smooth, flat

samples, regardless of the formulation, increased the regeneration of skin appendages by providing a favorable interface for cell–material interaction within the pores. The non-printed hydrogel–BBG samples, 3D-printed hydrogel, and hydrogel–BBG dressings showed higher numbers and faster regeneration of hair follicles compared to the other samples. The non-printed and 3D-printed hydrogel–BBG20 dressings developed thicker and more hair follicles toward the epidermal layer, while in the BBG powder, non-printed hydrogel, and 3D-printed hydrogel groups, the hair follicles were shorter, and still in the dermal layer, indicating slower growth and development of hair follicles. Therefore, the synergistic effect of BBG and 3D-printed porous surface enhanced the regeneration of follicles in terms of population and growth rate. The presence of GT after 21 days is a major indication of immature wound healing and prolonged tissue regeneration. Further, more sweat glands and skin appendages (yellow arrowheads) appeared in all groups, with slightly higher regeneration in the 3D-printed hydrogel–BBG20 group. The control group showed the highest GT on day 28, confirming poor wound closure in this sample (Figure 8). More specifically, GT refers to the chronically vascularized tissue that represents persistent inflammation, mainly composed of pink and granular tissue with macrophages and proliferating fibroblasts[84]. The persistence of GT at week 4 represents the immature wound healing and failed treatment. All samples showed slight GT formation compared to the control groups, showing that both 3D-printed porous texture and BBG content positively affected tissue regeneration. Recent research showed that a reduction in the formation of GT is associated with improved scar outcomes[85]. The 3D-printed samples with and without BBG showed uniform dermal regeneration that can be associated with the 3D-printed porous pattern in these samples. Our findings confirmed that the favorable degradation rate, controlled water release, skin-like mechanical properties, and porous non-adhesive contact surface in 3D-printed hydrogel–BBG20 dressings could promote the outcomes of burn wound healing.

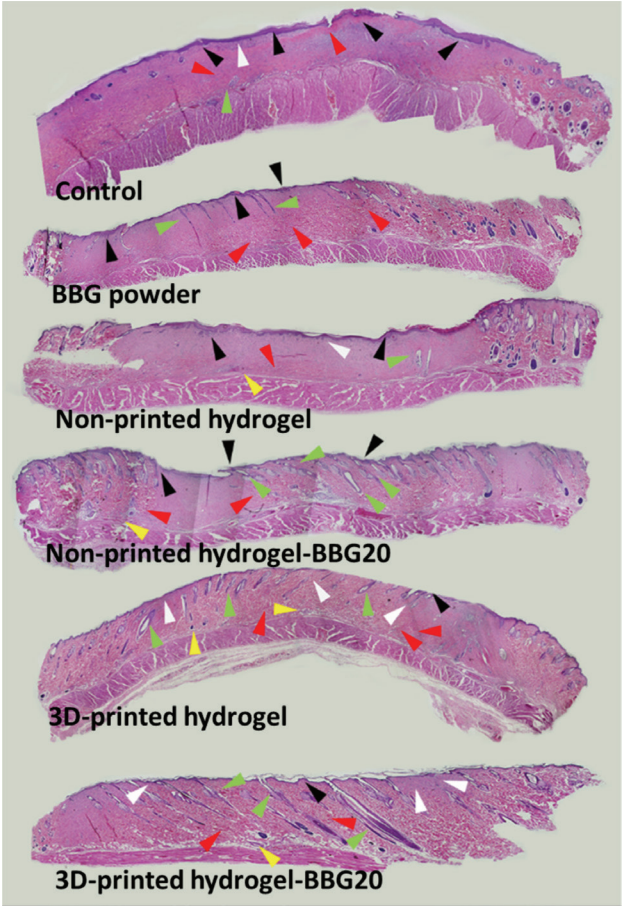

Figure 10. Representative the wound tissues stained with H&E at 10× magnification. 3D-printed dressing composed of hydrogel–BBG20 accelerated wound healing and guided the regeneration of hair follicles in second-degree thermal burns in a rat model. BBG guided wound healing to normal wound closure rather than wound contracture by promoting formation of a uniform epidermal layer, regeneration of hair follicles, and mature granulation tissue formation. Compared to the non-printed samples with the same formulation, the 3D-printed dressings with and without BBG improved the uniform regeneration of the dermal layer. Guides labeled in the figure: hyperkeratosis (black arrowhead), epidermal regeneration (outmost layer in dark purple), dermal layer (white arrowhead), granulation tissue (red arrowhead), hair follicle (green arrowhead), and sweat glands (yellow arrowhead).

Our results provide substantial evidence on the effects of BBG on mechanical properties, degradation rate, and hydration activity in 3D-printed gelatin–alginate dressings. The therapeutic ions released from BBG decreased the early cell viability of the samples. At the same time, the favorable interactions between the acidic degradation of alginate and the presence of RGD sequences from gelatin improved the 7-day cell viability of the samples. Electrostatic interactions between BBG particulates and hydrogel chains increase the stiffness and decrease the permeability of the dressings. The lower permeability in 3D-printed hydrogel–BBG20 slows down the degradation rate, increases the stability of the dressings, and regulates the water release rate from the hydrogel. Our findings showed that adding BBG to the gelatin–alginate compound enables controlled water release for up to 10 days, which is a key feature for burn wound healing. The kinetics of water release from 3D-printed dressings was fitted with the Higuchi model that refers to transdermal patches and hydrogel films. Accordingly, BBG content positively affected the *in vivo* wound healing outcomes in terms of dermal/epidermal regeneration and restoration of hair follicles in second-degree burn wound treatment. Overall, the addition of 20 wt% BBG promotes the functionality of 3D-printed hydrogel dressing by synergistic effect of continuous water release from 3D-printed dressings, favorable interactions between RGD sequences in gelatin, acidic degradation of alginate, and cumulative release of therapeutic ions from BBG.

4. Conclusion

In this study, we developed 3D-printed bioactive wound dressings using gelatin, alginate, and borate glass (BBG). The incorporation of BBG improved the tensile stiffness and cell viability of the 3D-printed dressings and regulated water release for maintaining optimal wound moisture. The safety and efficacy of the 3D-printed hydrogel–BBG dressings on second-degree burn wounds was assessed in a rat model. The 3D-printed hydrogel dressings incorporated with 20 wt% BBG showed faster wound closure and lower wound contracture compared to the non-printed hydrogel of the same composition, FDA-approved bioactive glass, and the standard of care. BBG content positively contributes to superb healing outcomes in the context of dermal/epidermal regeneration and hair follicle restoration. The clinical significance of incorporating BBG into 3D-printed hydrogel dressings lies in bioactive formulation, non-adhesive contact, and ability to maintain optimal wound moisture for up to 7 days. These features can potentially enhance the patient outcome by reducing the need for frequent dressing changes, minimizing the pain and the risk of infection, and promote faster wound closure.

The outcome of this study provides promising insights into using bioactive formulations for 3D printing as a versatile technology in tissue engineering and regenerative medicine. Our study has the potential to further research on more complicated bioinks incorporated with nanoparticles, signaling factors, and bioactive reagents to enhance the efficacy of bioactive hydrogel dressings. Advancements in fabrication methods and 3D printing of BBG, hydrogel, and other bioactive materials will contribute to the development of patient-specific dressings and skin substitutes, enabling customizable wound healing approaches. Therefore, the scalability and cost-effectiveness, as well as addressing the specific regulatory requirements of 3D-printed biomedical

products, should be further advanced to ensure safe and effective deployment of these technologies in clinical settings. Another promising avenue in wound healing research is the advancement of stimuli-responsive dressings, *i.e.*, smart dressings, capable of responding to specific physiological cues. For example, the pH-sensitive ion release and tunable water release from BBG–hydrogel dressings can be further investigated and combined with biosensors and 4D printing technologies to develop smart wound dressings that can rapidly detect infection and release therapeutic agents based on wound condition or environmental parameters (pH, temperature, oxygen level, moisture level, bacterial load, *etc.*). Another promising future direction in wound healing research is the integration of bioinformatics and artificial intelligence in wound monitoring, assessment, and documentation. The transparent appearance and programmable functionality of the hydrogel–BBG dressings can be combined with bioinformatics and artificial intelligence technologies to potentially enhance wound care by providing objective wound assessments, automating wound documentation, and facilitating data-driven decision-making. Finally, we envision that hydrogel–BBG bioinks can be extended by incorporating stem cells and other signaling factors to facilitate scarless wound healing and complex chronic ulcers and radiation burn injuries. Overall, our findings presented in this paper hold significant potential for improving patient outcomes and advancing the future research in the field of wound healing.

Acknowledgments

The authors wish to express sincere thanks to Drs. Anthony Convertine, Douglass Bristow, Nathan Leigh, Richard Watters, and Baojun Bai for their consultation advice and infrastructure support.

Funding

This work was funded by Midwest Biomedical Accelerator Consortium (MBArC), an NIH Research Evaluation and Commercialization Hub (REACH), and by Ozark Biomaterial Initiative (OBI).

Conflict of interest

The authors declare they have no competing interests.

Author contributions

Conceptualization: Fateme Fayyazbakhsh, Yue-Wern Huang, Ming C. Leu, Delbert Day
Data curation: Fateme Fayyazbakhsh, Michael J. Khayat, Yue-Wern Huang
Formal analysis: Fateme Fayyazbakhsh, Michael J. Khayat
Funding acquisition: Fateme Fayyazbakhsh, Ming C. Leu
Investigation: Fateme Fayyazbakhsh, Yue-Wern Huang, Ming C. Leu
Methodology: Fateme Fayyazbakhsh, Candy Sadler, Yue-Wern Huang, Delbert Day
Project administration: Ming C. Leu
Writing – original draft: Fateme Fayyazbakhsh
Writing – review & editing: Candy Sadler, Yue-Wern Huang, Ming C. Leu

Ethics approval and consent to participate

All *in vivo* experiments were approved by the Missouri S&T Institutional Animal Care and Use Committee (IACUC) (Reference No. 177-20).

Consent for publication

Not applicable.

Availability of data

To make the raw data used in this work available to readers, we can provide it upon request via email. Interested readers can contact us directly at f.fba@mst.edu to inquire about accessing the raw data..

References

1. Greenhalgh DG, 2019, Management of burns. *N Engl J Med,* 380(24): 2349–2359.
2. Stoica AE, Chircov C, Grumezescu AM, 2020, Hydrogel dressings for the treatment of burn wounds: An up-to-date overview. *Materials*, 13(12): 2853.
3. Centers for Disease Control and Prevention. U.S. Department of Health and Human Services, Burns: Fact Sheet. 2004.

   https://www.cdc.gov/masstrauma/factsheets/public/burns.pdf.
4. Zavlin D, Chegireddy V, Boukovalas S, *et al.*, 2018, Multi-institutional analysis of independent predictors for burn mortality in the United States. *Burns Trauma*, 6: 24–34.
5. Yu T-C, Zhang X, Smiell J, *et al.*, 2020, Healthcare resource utilization, treatment patterns, and cost of care among patients with thermal burns and inpatient autografting in two large privately insured populations in the United States. *Burns*, 46(4): 825–835.
6. Sen CK, 2019, *Human Wounds and Its Burden: An Updated Compendium of Estimates*. Mary Ann Liebert, Inc., New York, United States 39–48.
7. Kordestani SS, 2019, *Atlas of Wound Healing-E-Book: A Tissue Regeneration Approach*, Elsevier, Missouri, United States.
8. Middelkoop E, Sheridan RL, 2018, 15—Skin substitutes and 'the next level'. In: Herndon DN, editor. *Total Burn*

Care (Fifth Edition), Elsevier, 167–173.e162, Amsterdam, Netherlands.

9. Hayes TR, Su B, 2011, 15—Wound dressings. In: Bosworth LA, Downes S, editors. *Electrospinning for Tissue Regeneration*, Woodhead Publishing, 317–339, Sawston, United Kingdom.
10. Rogers AD, Jeschke MG, 2016, Managing severe burn injuries: Challenges and solutions in complex and chronic wound care. *Chronic Wound Care Manage Res*, 3: 59–71.
11. Kowal S, Kruger E, Bilir P, *et al.*, 2019, Cost-effectiveness of the use of autologous cell harvesting device compared to standard of care for treatment of severe burns in the United States. *Adv Ther*, 36(7): 1715–1729.
12. Zheng W, Zhao D-L, Zhao Y-Q, *et al.*, 2022, Effectiveness of platelet rich plasma in burn wound healing: A systematic review and meta-analysis. *J Dermatol Treatment*, 33(1): 131–137.
13. Dhaliwal K, Lopez N, 2018, Hydrogel dressings and their application in burn wound care. *Br J Commun Nurs*, 23(Suppl 9): S24–S27.
14. Bazaliński D, Karnas M, Wołkowicz M, *et al.*, 2018, ZASTOSOWANIE LARW LUCILIA SERICATA W OCZYSZCZANIU RAN PRZEWLEKŁYCH-OPIS TRZECH PRZYPADKÓW. *Leczenie Ran*, 15(3): 153–159.
15. Wang Y, Beekman J, Hew J, *et al.*, 2018, Burn injury: Challenges and advances in burn wound healing, infection, pain and scarring. *Adv Drug Deliv Rev*, 123: 3–17.
16. Fayyazbakhsh F, Khayat MJ, Leu MC, 2022, 3D-printed gelatin-alginate hydrogel dressings for burn wound healing: A comprehensive study. *Int J Bioprint,* 8(4): 274–291.
17. Kordestani SS, 2019, *Atlas of Wound Healing: A Tissue Engineering Approach*, Elsevier Health Sciences, Missouri, United States.
18. Rowan MP, Cancio LC, Elster EA, *et al.*, 2015, Burn wound healing and treatment: Review and advancements. *Crit Care*, 19(1): 243.
19. Shpichka A, Butnaru D, Bezrukov EA, *et al.*, 2019, Skin tissue regeneration for burn injury. *Stem Cell Res Ther,* 10(1): 94.
20. Sood A, Granick MS, Tomaselli NL, 2014, Wound dressings and comparative effectiveness data. *Adv Wound Care*, 3(8): 511–529.

    https://doi.org/10.1089/wound.2012.0401
21. Huangfu Y, Li S, Deng L, *et al.*, 2021, Skin-adaptable, long-lasting moisture, and temperature-tolerant hydrogel dressings for accelerating burn wound healing without secondary damage. *ACS Appl Mater Interfaces*, 13(50): 59695–59707.
22. Szymański K, Waś J, 2014, POTENCJALNE MOŻLIWOŚCI LECZENIA I REGENERACJI SKÓRY W ROZLEGŁYCH RANACH OPARZENIOWYCH PRZY ZASTOSOWANIU SUBSTYTUTÓW REGENERUJĄCYCH SKÓRĘ. *Leczenie Ran*, 11(1): 1338–1363.
23. Selig HF, Lumenta DB, Giretzlehner M, *et al.*, 2012, The properties of an "ideal" burn wound dressing: What do we need in daily clinical practice? Results of a worldwide online survey among burn care specialists. *Burns*, 38(7): 960–966.
24. Markiewicz-Gospodarek A, Kozioł M, Tobiasz M, *et al.*, 2022, Burn wound healing: Clinical complications, medical care, treatment, and dressing types: The current state of knowledge for clinical practice. *Int J Environ Res Public Health*, 19(3): 1338.
25. Zheng K, Kapp M, Boccaccini AR, 2019, Protein interactions with bioactive glass surfaces: A review. *Appl Mater Today*, 15: 350–371.
26. Mehrabi T, Mesgar AS, Mohammadi Z, 2020, Bioactive glasses: A promising therapeutic ion release strategy for enhancing wound healing. *ACS Biomater Sci Eng,* 6(10): 5399–5430.
27. Solanki AK, Lali FV, Autefage H, *et al.*, 2021, Bioactive glasses and electrospun composites that release cobalt to stimulate the HIF pathway for wound healing applications. *Biomater Res,* 25(1): 1.

    https://doi.org/10.1186/s40824-020-00202-6.
28. Chen Y-H, Rao Z-F, Liu Y-J, *et al.*, 2021, Multifunctional injectable hydrogel loaded with cerium-containing bioactive glass nanoparticles for diabetic wound healing. *Biomolecules*, 11(5): 702.
29. U.S. Food and Drug Administration. U.S. Department of Health and Human Services, Establishment Registration & Device Listing, Mirragen Advanced Wound Matrix, 510(k) Premarket Notification.

    https://www.accessdata.fda.gov/cdrh_docs/pdf16/K161067.pdf.
30. Ege D, Zheng K, Boccaccini AR, 2022, Borate bioactive glasses (BBG): Bone regeneration, wound healing applications, and future directions. *ACS Appl Bio Mater*, 5(8): 3608–3622.

    https://doi.org/10.1021/acsabm.2c00384
31. Bi L, Rahaman MN, Day DE, *et al.*, 2013, Effect of bioactive borate glass microstructure on bone regeneration, angiogenesis, and hydroxyapatite conversion in a rat calvarial defect model. *Acta Biomater*, 9(8): 8015–8026.
32. Lin Y, Brown RF, Jung SB, *et al.*, 2014, Angiogenic effects of borate glass microfibers in a rodent model. *J Biomed Mater Res Part A*, 102(12): 4491–4499.
33. Zhao S, Li L, Wang H, *et al.*, 2015, Wound dressings composed of copper-doped borate bioactive glass microfibers stimulate angiogenesis and heal full-thickness skin defects in a rodent model. *Biomaterials*, 53: 379–391.
34. Jung SB, 2010, Borate based bioactive glass scaffolds for hard and soft tissue engineering. Doctoral Dissertation, Missouri University of Science and Technology.

    https://scholarsmine.mst.edu/doctoral_dissertations/2075

35. Jung S, 2013, *Treatment of Chronic Wounds With Bioactive Borate Glass Fibers. An Introduction to Bioceramics*, World Scientific, Tuck Link, Singapore, 487–493.

36. Hu H, Tang Y, Pang L, *et al.*, 2018, Angiogenesis and full-thickness wound healing efficiency of a copper-doped borate bioactive glass/poly (lactic-co-glycolic acid) dressing loaded with vitamin E in vivo and in vitro. *ACS Appl Mater Interfaces*, 10(27): 22939–22950.

37. Zhou J, Wang H, Zhao S, *et al.*, 2016, In vivo and in vitro studies of borate based glass micro-fibers for dermal repairing. *Mater Sci Eng, C*, 60: 437–445.

38. Ottomeyer M, Mohammadkah A, Day D, *et al.*, 2016, Broad-spectrum antibacterial characteristics of four novel borate-based bioactive glasses. *Adv Microbiol,* 6(10): 776–787.

39. Thyparambil NJ, Gutgesell LC, Bromet BA, *et al.*, 2020, Bioactive borate glass triggers phenotypic changes in adipose stem cells. *J Mater Sci Mater Med,* 31(4): 1–15.

40. Mouriño V, Vidotto R, Cattalini J, *et al.*, 2019, Enhancing biological activity of bioactive glass scaffolds by inorganic ion delivery for bone tissue engineering. *Curr Opin Biomed Eng,* 10: 23–34.

41. Ramos Rivera C, 2020, *Development of HIF-Mimicking Materials for Chronic Wound Healing*, University College London, London, United Kingdom.

42. Schuhladen K, Stich L, Schmidt J, *et al.*, 2020, Cu, Zn doped borate bioactive glasses: Antibacterial efficacy and dose-dependent in vitro modulation of murine dendritic cells. *Biomater Sci,* 8(8): 2143–2155.

43. Chebassier N, Ouijja EH, Viegas I, *et al.*, 2004, Stimulatory effect of boron and manganese salts on keratinocyte migration. *Acta Dermatovenereol,* 84(3): 191–194.

44. Ege D, Zheng K, Boccaccini AR, 2022, Borate bioactive glasses (BBG): Bone regeneration, wound healing applications, and future directions. *ACS Appl Biol Mater,* 5(8): 3608–3622.

    https://doi.org/10.1021/acsabm.2c00384

45. Salvo J, Sandoval C, 2022, Role of copper nanoparticles in wound healing for chronic wounds: Literature review. *Burns Trauma*, 10: tkab047 (1–9).

46. Mutlu N, Kurtuldu F, Unalan I, *et al.*, 2022, Effect of Zn and Ga doping on bioactivity, degradation, and antibacterial properties of borate 1393-B3 bioactive glass. *Ceram Int,* 48(11): 16404–16417.

47. Kermani F, Nazarnezhad S, Mollaei Z, *et al.*, 2023, Zinc- and copper-doped mesoporous borate bioactive glasses: Promising additives for potential use in skin wound healing applications. *Int J Mol Sci,* 24(2): 1304.

48. Lin P-H, Sermersheim M, Li H, *et al.*, 2017, Zinc in wound healing modulation. *Nutrients*, 10(1): 16.

49. Balasubramanian P, Grünewald A, Detsch R, *et al.*, 2016, Ion release, hydroxyapatite conversion, and cytotoxicity of boron-containing bioactive glass scaffolds. *Int J Appl Glass Sci,* 7(2): 206–215.

50. Chai Q, Jiao Y, Yu X, 2017, Hydrogels for biomedical applications: Their characteristics and the mechanisms behind them. *Gels*, 3(1): 6.

51. Fayyazbakhsh F, Amato M, Khayat MJ, *et al.*, editors, 2022, In-vivo evaluation of 3D printed hydrogel wound dressings for burn wound healing. *Tissue Eng Part A,* 28(S1):S527–S538.

52. Zhu Y, Ma Z, Kong L, *et al.*, 2020, Modulation of macrophages by bioactive glass/sodium alginate hydrogel is crucial in skin regeneration enhancement. *Biomaterials*, 256: 120216.

53. Manning JH, Stark JH, 1977, Diester crosslinked polyglucan hydrogels and reticulated sponges thereof. Google Patents.

54. Kamoun EA, Kenawy E-RS, Chen X, 2017, A review on polymeric hydrogel membranes for wound dressing applications: PVA-based hydrogel dressings. *J Adv Res,* 8(3): 217–233.

55. Li J, Mooney DJ, 2016, Designing hydrogels for controlled drug delivery. *Nat Rev Mater,* 1(12): 1–17.

56. Bruggeman KF, Williams RJ, Nisbet DR, 2018, Dynamic and responsive growth factor delivery from electrospun and hydrogel tissue engineering materials. *Adv Healthc Mater,* 7(1): 1700836.

57. Zhu J, Jiang G, Song G, *et al.*, 2019, Incorporation of ZnO/bioactive glass nanoparticles into alginate/chitosan composite hydrogels for wound closure. *ACS Appl Biol Mater,* 2(11): 5042–5052.

58. Mehrabi A, Karimi A, Mashayekhan S, *et al.*, 2022, In-situ forming hydrogel based on thiolated chitosan/carboxymethyl cellulose (CMC) containing borate bioactive glass for wound healing. *Int J Biol Macromol,* 222: 620–635.

59. Yang Z, Ren X, Liu Y, 2021, Multifunctional 3D printed porous GelMA/xanthan gum based dressing with biofilm control and wound healing activity. *Mater Sci Eng C*, 131: 112493.

60. Pirayavaraporn C, Rades T, Tucker IG, 2012, Determination of moisture content in relation to thermal behaviour and plasticization of Eudragit RLPO. *Int J Pharmaceut,* 422(1-2): 68–74.

61. Martineau L, Shek PN, 2006, Evaluation of a bi-layer wound dressing for burn care: I. Cooling and wound healing properties. *Burns*, 32(1): 70–76.

    https://doi.org/10.1016/j.burns.2005.08.009.

62. Rice P, Orgill DP, 2008, Emergency care of moderate and severe thermal burns in adults. UpToDate, Wolters Kluwer Marx JA, Grayzel J, eds.

    https://www.uptodate.com/contents/emergency-care-of-moderate-and-severe-thermal-burns-in-adults

63. Schaefer TJ, Lopez ON, 2020, Burn resuscitation and management. StatPearls [Internet].

64. Singhvi G, Singh M, 2011, In-vitro drug release characterization models. *Int J Pharm Stud Res*, 2(1): 77–84.

65. Altavilla D, Saitta A, Cucinotta D, *et al.*, 2001, Inhibition of lipid peroxidation restores impaired vascular endothelial growth factor expression and stimulates wound healing and angiogenesis in the genetically diabetic mouse. *Diabetes*, 50(3): 667–674.

66. Koehler J, Brandl FP, Goepferich AM, 2018, Hydrogel wound dressings for bioactive treatment of acute and chronic wounds. *Eur Polym J,* 100: 1–11.

67. Pawlaczyk M, Lelonkiewicz M, Wieczorowski M, 2013, Age-dependent biomechanical properties of the skin. *Postepy Dermatol Alergol*, 30(5): 302–306.

https://doi.org/10.5114/pdia.2013.38359

68. Li C, Guan G, Reif R, *et al.*, 2012, Determining elastic properties of skin by measuring surface waves from an impulse mechanical stimulus using phase-sensitive optical coherence tomography. *J R Soc Interface*, 9(70): 831–841.

69. Peretiatko CDS, Hupalo EA, Da Rocha Campos JR, *et al.*, 2018, Efficiency of zinc and calcium ion crosslinking in alginate-coated nitrogen fertilizer. *Orbital Electron J Chem*, 10: 218–225.

70. Swamy BJRS, Vijay R, Babu PR, *et al.*, 2016, Influence of γ-ray-induced effects on dielectric dispersion of CuO-doped calcium fluoroborophosphate glass system. *Ionics*, 22: 1625–1634.

71. Zhang P, Pu Y, Wu Y, *et al.*, 2016, Influence of replacement of B_2O_3 by SiO_2 on the structure and magnetic properties of BaO-Fe_2O_3-SiO_2-B_2O_3-CeO_2 glass-ceramics. *J Superconduct Novel Magn,* 29: 1557–1560.

72. Fayyazbakhsh F, Solati-Hashjin M, Keshtkar A, *et al.*, 2017, Novel layered double hydroxides-hydroxyapatite/gelatin bone tissue engineering scaffolds: Fabrication, characterization, and in vivo study. *Mater Sci Eng C*, 76: 701–714.

73. Fayyazbakhsh F, Solati-Hashjin M, Keshtkar A, *et al.*, 2017, Release behavior and signaling effect of vitamin D3 in layered double hydroxides-hydroxyapatite/gelatin bone tissue engineering scaffold: An in vitro evaluation. *Colloids Surfaces B Biointerfaces*, 158: 697–708.

74. Köse D, Necefoğlu H, 2008, Synthesis and characterization of bis (nicotinamide) m-hydroxybenzoate complexes of Co (II), Ni (II), Cu (II) and Zn (II). *J Therm Anal Calorim,* 93: 509–514.

75. Visser H, Dubé CE, Armstrong WH, *et al.*, 2002, FTIR spectra and normal-mode analysis of a tetranuclear manganese adamantane-like complex in two electrochemically prepared oxidation states: Relevance to the oxygen-evolving complex of photosystem II. *J Am Chem Soc,* 124(37): 11008–11017.

76. Zahir MH, Rahman MM, Irshad K, *et al.*, 2019, Shape-stabilized phase change materials for solar energy storage: MgO and $Mg(OH)_2$ mixed with polyethylene glycol. *Nanomaterials*, 9(12): 1773.

77. Łabowska MB, Skrodzka M, Sicińska H, *et al.*, 2023, Influence of cross-linking conditions on drying kinetics of alginate hydrogel. *Gels*, 9(1): 63.

78. Paul D, 2011, Elaborations on the Higuchi model for drug delivery. *Int J Pharmaceut,* 418(1): 13–17.

79. Siepmann J, Peppas NA, 2011, Higuchi equation: Derivation, applications, use and misuse. *Int J Pharm*, 418(1): 6–12.

https://doi.org/10.1016/j.ijpharm.2011.03.051

80. Klimek K, Ginalska G, 2020, Proteins and peptides as important modifiers of the polymer scaffolds for tissue engineering applications: A review. *Polymers (Basel)*, 12(4): 1–38.

https://doi.org/10.3390/polym12040844

81. Frew Q, Rennekampff H-O, Dziewulski P, *et al.*, 2019, Betulin wound gel accelerated healing of superficial partial thickness burns: Results of a randomized, intra-individually controlled, phase III trial with 12-months follow-up. *Burns*, 45(4): 876–890.

https://doi.org/10.1016/j.burns.2018.10.019

82. Singer AJ, Boyce ST, 2017, Burn wound healing and tissue engineering. *J Burn Care Res*, 38(3): e605–e613.

https://doi.org/10.1097/bcr.0000000000000538

83. Benson A, Dickson WA, Boyce DE, 2006, ABC of wound healing: Burns. *BMJ*, 333(Suppl S3): 283–339.

84. Jones K, 2015, *Fibrotic Response to Biomaterials and All Associated Sequence of Fibrosis. Host Response to Biomaterials*. Elsevier, Amsterdam, Netherlands, 189–237.

85. Kolimi P, Narala S, Nyavanandi D, *et al.*, 2022, Innovative treatment strategies to accelerate wound healing: Trajectory and recent advancements. *Cells*; 11(15): 1–46.

https://doi.org/10.3390/cells11152439

ACCSCIENCE PUBLISHING

International Journal of Bioprinting

REVIEW ARTICLE

Advances of 3D printing in gastroenterology and where it might be going

Yuhang Zhang†, Liuxiang Chen†, and Bing Hu*

Department of Gastroenterology and Hepatology, West China Hospital, Sichuan University, Chengdu, Sichuan, China

(This article belongs to the *Special Issue: Advances in 3D bioprinting based on lab-on-a-chip platforms for precision oncology*)

Abstract

Gastrointestinal (GI) system comprises a great number of organs and tissues of various functions, both hollow and solid. However, it is still a less well-developed area for three-dimensional (3D) printing (3DP) applications compared to orthopedics. Clinical applications of 3DP in the GI system are presently restricted to preoperative planning, surgical guidance, and education for students, residents, and patients, either for laparoscopy or endoscopy. Several surgery-related accessories have been designed to facilitate surgical procedures. The results are promising but not adequately proven due to a lack of reasonable study design and proper comparisons. Other important requirements for GI systems in clinical scenarios are structural reconstruction, replacement, defect repair, drug screening, and delivery. Many 3D-printed decellularized, cell-seeded, or even bioprinted scaffolds have been studied; however, most studies were conducted on small animal or *in vitro* models. Although encouraging results have been obtained, there is still a long way to go before products compatible with humans in size, histology, and functions can be printed. The key points to achieving this goal are the printing material, cell type and source, and printing technology. The ultimate goal is to print tissue and organ substitutes with physiological functions for clinical purposes in both time- and cost-effective ways.

Keywords: 3D printing; Bioprinting; Gastroenterology; Surgery; Endoscopy

1. Introduction

Three-dimensional (3D) printing (3DP) has evolved since Bill Master introduced the concept in 1984[1], and it has been popular in various fields, such as industry, architecture, education, and medicine. In medical areas, 3DP is predominantly used in orthopedics, maxillofacial surgery, stomatology, and cranial and spinal surgery, where tissues and organs are solid and non-deformable on radiological images. Most articles recognized the positive role of 3DP in reducing operational time, decreasing radiation, and improving outcomes[2]. 3DP is also particularly useful in producing patient-specific implantable objects[3], and it is particularly true in bone grafts[4]. In comparison, the gastrointestinal system is less well-explored, perhaps due to there being multiple organs and tissues involved and their complex anatomical relationships. They are different from solid organs as they are soft and deformable, with peristaltic ability and complex interactions with host microbiomes.

†These authors contributed equally to this work.

***Corresponding author:**
Bing Hu (hubingnj@163.com)

Citation: Zhang Y, Chen L, Hu B, 2023, Advances of 3D printing in gastroenterology and where it might be going. *Int J Bioprint*, 9(6): 0149. https://doi.org/10.36922/ijb.0149

Received: April 29, 2023
Accepted: June 1, 2023
Published Online: July 17, 2023

Copyright: © 2023 Author(s). This is an Open Access article distributed under the terms of the Creative Commons Attribution License, permitting distribution, and reproduction in any medium, provided the original work is properly cited.

Publisher's Note: AccScience Publishing remains neutral with regard to jurisdictional claims in published maps and institutional affiliations.

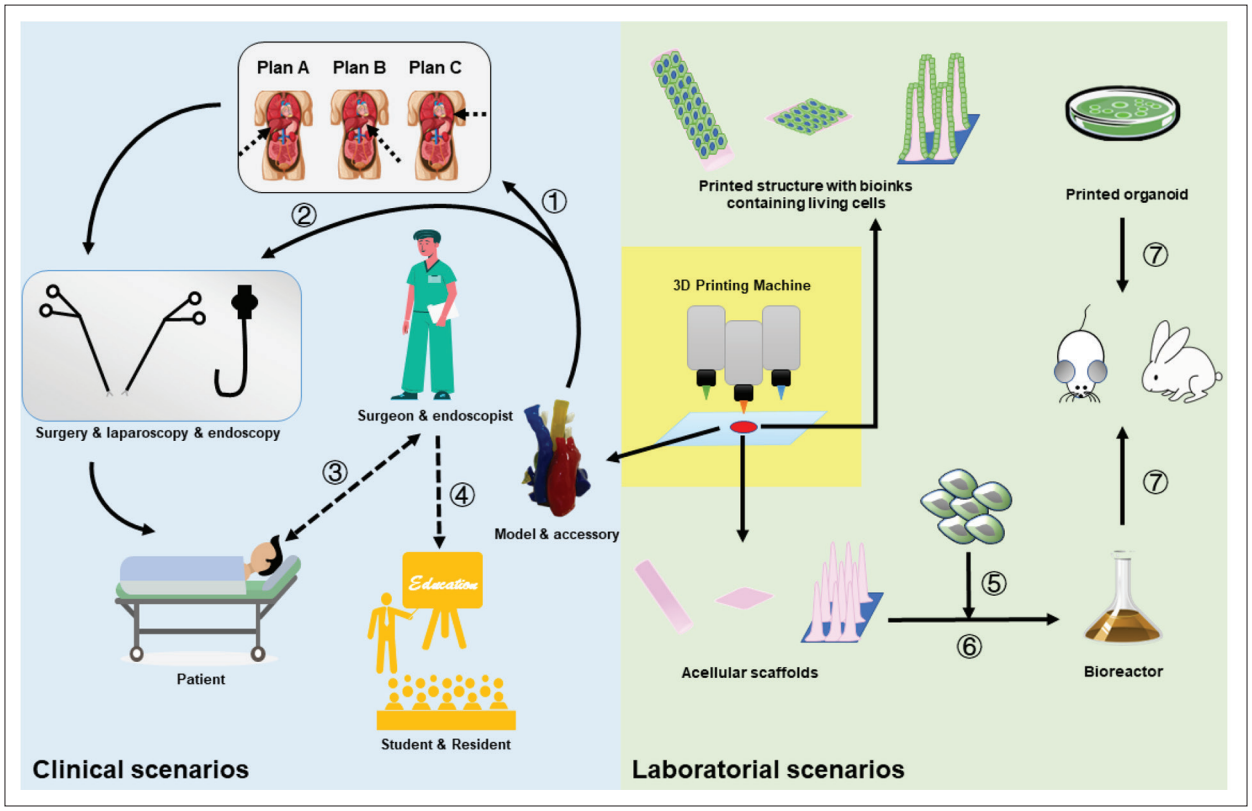

Figure 1. A schematic diagram of the applications of 3D printing and bioprinting in gastroenterology, both clinical and laboratorial. (1) Preoperative planning; (2) Accessory production for laparoscopy or endoscopy; (3) Communication and education for the patients; (4) Clinical education and skill training; (5) Cell seeding; (6) Maturation (cell expansion and differentiation); (7) Transplantation.

As gastrointestinal (GI) system is embodied in thoracic and abdominal cavities, different types of surgeries, such as laparotomy, laparoscopy, and gastrointestinal endoscopy, are performed. One unique characteristic of the alimentary tract is its abundant blood supply and variations of blood vessels[5]. It often requires the precise anatomy knowledge and spatial imagination of doctors to imaginatively reconstruct the 3D structures from two-dimensional (2D) images produced by computed tomography (CT) or magnetic resonance imaging (MRI) scans, which is not "real" enough. 3D printing can be seen as an extension of those medical images[6].

Patient-specific prototyping of anatomical structures accords with the growing popularity of precision medicine. 3DP models help clinicians, especially those with less experience, perceive a better understanding of anatomical structures before applying surgical or laparoscopic procedures[7,8]. Many researchers have tried 3DP gastrointestinal organs and tissues for various purposes, including preoperative planning, education, and implantable object production. However, their printing technologies vary greatly. There are approximately seven kinds of 3D printers, including vat photopolymerization, material jetting, binder jetting, material extrusion, powder bed fusion, sheet lamination, and direct energy deposition, which have been extensively summarized previously[9].

Unlike orthopedics, where 3DP and its productions are extensively studied both in laboratories and in patients, studies concerning gastroenterology are sparsely documented, and most of the state-of-the-art experiments are on rodents. In this review, we summarize what is going on with 3DP in gastrointestinal surgery, laparoscopy, and endoscopy from the perspectives of preoperative planning, education, and object production. Then, we discuss some progress of 3D bioprinting in this area and leave a short outlook at the end (Figure 1). 3D printing technologies and inks, which have been extensively discussed elsewhere[10-13], are not illustrated here.

2. 3D printing in gastrointestinal surgery

Gastrointestinal surgery is one of the most complex operations because it involves a wide range of organs and adjacent anatomic structures, such as the heart, lung, blood, and lymphatic vessels. At present, surgeons view and evaluate the operational area mainly through

tomographic images acquired by enhanced CT or MRI; or, better, through virtual 3D reconstruction by software. Compared to these imaging modalities, printed 3D models provide more detailed visual and tactile information and experience. Furthermore, surgeons could rehearse surgical procedures on the real model to select surgical devices, choose an optimized operative approach, and define other intraoperative matters that need attention.

2.1. Operative planning and guidance

Preoperative planning and intraoperative guidance are some of the most researched topics regarding the esophageal aspect. Most studies conclude that 3D models, especially of blood vessels, help identify anatomical variants, reduce operative time and blood loss, and optimize the operative approach. This is especially true when encountering complicated cases. In 2015, Dickinson *et al.* of Mayo Clinic reported two complex cases of aortoesophageal fistula complicated by previous cervical esophagostomy and thoracoplasty and multiple esophageal diverticula secondary to esophageal dysmotility[14]. The printed life-size models helped doctors examine anatomical structures closely and directly, providing valuable chances for operational rehearsal and multidisciplinary consultation. Hamada *et al.* also reported a case where a surgery for cT3N4M0 stage III esophageal cancer was complicated by major vascular malformation (double aortic arch)[15]. The authors firmly acknowledged the efficacy of the 3DP model for preoperative simulation. Much of the difficulties they faced during surgery were what they had expected when simulating on the model. A similar function was reported in a robotic surgery for guiding anti-reflux surgery complicated by tortuous thoracic aorta compression[16].

Regarding the colic aspect, Garcia-Granero *et al.* reported using 3DP models to facilitate the planning of laparoscopic right hemicolectomy and D3 lymphadenectomy[17]. The model contained only blood vessels because the lymph nodes are usually located around the gastrocolic trunk of Henle (GCTH), where its origin from the mesentery is often variable. No obvious intraoperative bleeding was recorded, and all D3 nodes were found negative. Hojo *et al.* also printed a 3D model to rehearse laparoscopic surgery of descending colon cancer complicated by a 69 mm abdominal aortic aneurysm[18]. The authors acknowledged the benefit of planning port sites and avoiding vascular injury and postoperative adhesion. For rectal surgery, Hamabe *et al.* printed 3D pelvic models for rectal cancer that could be sagittally cleaved for clearer inspection. However, the printing material was hard and not elastic, leading to less operational simulation value[19].

The 3DP model is particularly helpful for simulating solid organs, such as the liver, spleen, and pancreas, in addition to hollow organs, because of their non-deformable nature. Igami *et al.* reported that the 3DP liver model helped to plan a resection strategy for a small metastatic tumor that could be neither touched nor seen during laparoscopic surgery and increased the success rate of R0 resection[20]. The model could distinctly locate and describe tumors, bile ducts, and blood vessels to predict the functional status of the liver postresection. However, the printed model was whitish, so the vessels had to be dyed manually. Later, in 2017, Witowski *et al.* also reported a similar but much more cost-effective 3DP colorectal liver metastatic model[21]. The researchers used desktop-fused deposition modeling (FDM) printing technology, which is cheaper than jetting. However, this FDM printer could only print a small part of the whole model at a time, and assembling multiple parts was needed. Therefore, this printing strategy is semiautomated, time-consuming, and usually requires several printers, despite costing less than others. Similar successful outcomes were reported for retroperitoneal tumors[22] and for avoiding large-for-size syndrome in pediatric liver transplantation[23]. Interestingly, Villarreal *et al.* reported two cases in which 3DP models were used in the planning and practice of complex hepatic separation of conjoined twins[24]. In this case, the authors referred to similar 3DP models documented in previously published literature.

Fistulas are not uncommon in general surgery and abdominal diseases. They are sometimes complicated because the fistula may involve multiple organs or tissues, and the fistula canals may vary. Therefore, researchers used 3D printing as an isolation technique to illustrate the fistula's complete picture. Huang *et al.* employed 3D printing to construct a stent that could match well with the angled intestinal tract (105°) that connected the enterocutaneous fistula[25]. The stent significantly reduced enteric effluent loss, allowing enteric nutrition and future fistula resection; however, a small amount of effluent leakage still occurred after the postural shift, indicating a need for further improvement in printing precision or material. One of the most common non-traumatic causes for enteric fistula might be attributed to Crohn's disease. Guz *et al.* reported a case in which an MRI image-based 3DP model provided a direct rotatable view and tactility of the location and degree of Crohn's disease-related perianal fistula[26]. The authors argued that this technique could do more than merely surgical planning by possibly lowering interobserver bias in interpreting radiological information.

2.2. Education and research

Another major function of the 3DP model is facilitating activities in education for medical students, residents,

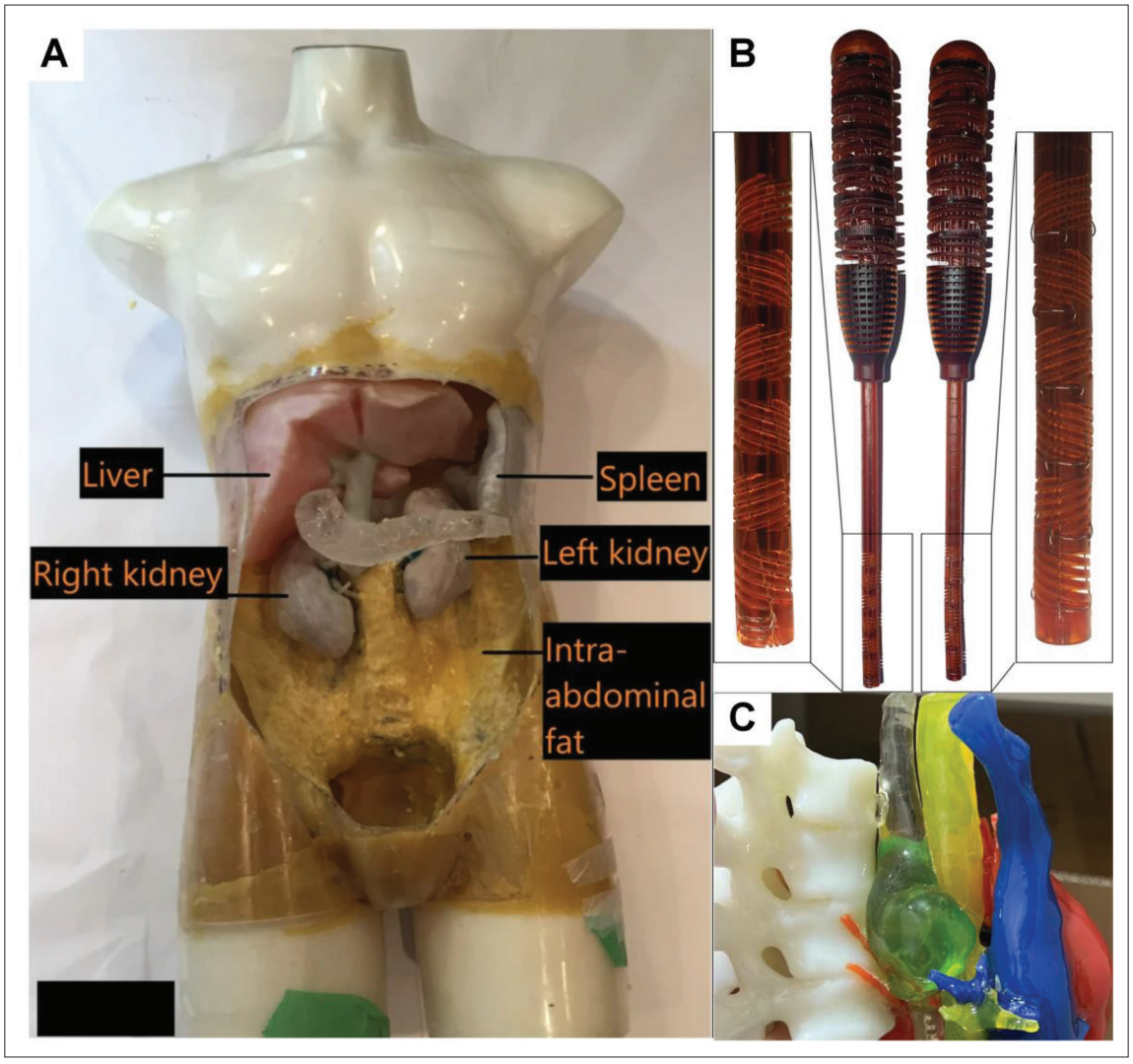

Figure 2. Illustrations of several applications of 3D-printed objects. (A) An abdominal cavity filled with 3D-printed organs that match the radiological density in real CT scan[35]; (B) 3D-printed steerable instruments that improve flexibility in laparoscopy[60]; (C) A 3D-printed model of esophageal submucosal tumor (green) to be resected using endoscopic submucosal dissection and its adjacent anatomy. Figure 2A–B are reprints of original images with permission (The images are licensed under Creative Commons Attribution 4.0 International License).

and patients, such as teaching, training, and counseling. For example, an anorectal fistula is intractable to assess because of its anatomical winding routes and complex connections. Most importantly, they are difficult to illustrate. Sahnan *et al.* used MRI images to construct a 3DP model of fistula canals and adjacent structures[27]. The authors believed that real 3D models improved surgeons' understanding of the complex anatomical relationship between the fistula and sphincter and provided better clinician–patient relationships and medical education. Hojo *et al.* of Tokyo University retrospectively created 3DP models of the superior mesenteric artery and superior mesenteric vein based on the surgeries carried out for laparoscopic right hemicolectomy with D3 lymphadenectomy in five patients[28]. Young surgeons could refer to the spatial relationships when reviewing operative videos of laparoscopic right hemicolectomy, which the author believed could shorten learning curves. Similar recognition of its usefulness in education and simulation has also been achieved among both experts and residents in bowel anastomosis[29], tracheoesophageal prosthesis placement[30], laparoscopic pyloromyotomy for neonates[31], laparoscopic preperitoneal inguinal hernia repair[32], laparoscopic bariatric surgery[33], and cystic duct variations in laparoscopic cholecystectomy[34].

For a purer educative and research purpose, Anwari *et al.* developed a 3DP anthropomorphic phantom based on CT images (Figure 2A)[35]. The phantom was created

organ-specifically and modularly. The highlight of the model is that different organs were printed and filled with different materials that mimicked radiological density in real CT scans, like water, liquid urethane rubber, agar-based solution, etc. The model could be scanned using CT, and the image was comparable to that of real human bodies. This model is particularly useful in anatomical and radiological courses for medical students for better correlation between anatomy and radiology. Similar demonstrations using 3D models for situs ambiguus of gastrointestinal organs[36], superior mesenteric artery plexus[37], and liver segments[38] were also documented.

The 3DP model is patient-friendly tool for communicating the medical-related information as well as facilitating the consent acquisition process. Almost all the cases reported above acknowledged that the printed model had positive effect on doctor–patient communication, patient's understanding of the operation's necessity, procedure, and expected difficulties or complications, and helped family members have realistic expectations. For postoperative care education, the model shows some benefits. For example, patient-specific postcolectomy stoma care training using a life-size printed model is helpful for patients to understand and reduce skin problems after self-practicing on the model[39].

The above studies are mainly presented as case reports, the conclusions of which were not validated[40]. A pilot study focusing on laparoscopic splenectomy enrolled 12 patients and 10 surgical residents, and both patients and residents highly confirmed the better illustrative and educative effects of 3DP models[41]. Luzon *et al.* included 23 patients and confirmed that the patient-specific 3DP model was useful in right colectomy and D3 mesenterectomy[42]. The accuracy of interanatomical structural distance measurement was validated by comparison with virtual 3D and intraoperative measurements. However, no clinical outcomes pertaining to surgery, e.g., time, blood loss, complications, hospital stay, cost, and prognosis, were included in these studies. In a prospective study, researchers from China found that 3DP models could help reduce the operation time (average 39.2 min), bleeding volume (average 45.1 ml), and medical expense (6.74%) while increasing rates of lymph node dissection (average 3.3) and patient satisfaction in right hemicolon cancer surgery[43]. Hojo *et al.* also reported a greater number of pelvic lymph nodes dissected for rectal cancer in the 3DP group, using a retrospective propensity score matching method[44].

In addition to education, there is also research concerning preoperative skill evaluation. Nishihara *et al.* previously constructed a 3DP model for the simulation of transabdominal preperitoneal (TAPP) inguinal hernia repair (IHR)[32]. Four years later, they used this TAPP model to evaluate surgeons' skills preoperatively and found that the model could distinguish surgeons with different levels of laparoscopic IHR experience[45]. A similar outcome of the laparoscopic choledochojejunostomy model was reported by Xia *et al.* based on the Objective Structured Assessment of Technical Skills (OSATS) scoring system[46]. Therefore, patient-specific 3DP models might be added to medical curricula for both education and evaluation. The 3DP model is more beneficial to less experienced residents and students rather than experts. The educative effect is particularly good among medical interns in understanding complex GI structures like Henle's trunk[47], practicing suturing[48], and perceiving oncopathological anatomy in different scenarios[49]. Quantitative analysis revealed that both surgeons and patients recognized 3DP models as useful, authentic, and favorable and scored median to high in preoperative planning, promoting learning, helping patients, and making effective and less conflicting decisions[7,50]. Surgical plans made upon 3DP models usually have a higher consistency with intraoperative findings[51].

The 3DP model is most useful in low-volume medical centers where rare and complex cases are hardly seen. While we have seen its many benefits, there remain problems to be solved: (i) Printing cost is high and time is long, and sometimes reprint is needed because of low quality[42]; (ii) Few comparisons are designed (traditional surgery vs. 3DP, 3DP vs. virtual reality); (iii) Evaluation criteria are mostly subjective; (iv) Sample size is too small to yield convincing result. A summary of the above-mentioned applications is listed in Table 1.

2.3. Accessory production

Apart from printing models for planning and education, printing-customized 3D tools might also be promising. Steinemann *et al.* tried to produce a space holder using 3DP to facilitate an intra-esophageal mucosal purse-string suture in Barrett's esophagus[52]. They found that the space holder helped resect more mucosa on sacrificed pigs but increased operational time and stitching variance. Another animal experiment of minipigs conducted by Yang *et al.* tested the usefulness of a 3DP biopolymer device in duct-to-mucosa pancreaticojejunostomy[53]. After 24 weeks of observation, they concluded that the device was promising for pancreatoenteric reconstruction with feasible procedural time and no adverse events. However, further controlled studies are warranted for validation. One special design might be the PLAFOKON operating platform, a flexible 3DP single-port overtube that was intervention-specific for individuals[54]. Other 3DP objects include spiral polymer stent for malignant esophageal stenosis[55], enteroatmospheric fistula tent[56,57], gastric

Table 1. 3D printing for surgical operation, education, and simulation

Author	Year	Image source	Data format	Image processing software	Output format	3D printing software	Printing machine
Igami *et al.*[20]	2014	CT/MRI	N/A	PLUTO	STL	PLUTO	AGILISTA3100
Dickinson *et al.*[14]	2015	CT	DICOM	Proprietary software	STL	Mimics software	Objet350 Connex
Pietrabissa *et al.* [41]	2016	CT	DICOM	ITK-SNAP	STL	—	Object 30 Pro 3D
Tominaga *et al.*[39]	2016	Artec 3D scanner	N/A	Geomagic FreeForm	STL	—	Objet260 Connex
Hamabe *et al.*[19]	2017	CT	DICOM	Zedview	N/A	Geomagic Freeform	Objet500 Connex3
Witowski *et al.*[21]	2017	CT	DICOM	Horos	STL	Meshmixer & Blender	Desktop Ultimaker 2+
Huang *et al.*[25]	2017	CT	N/A	N/A	STL	N/A	N/A
Nishihara *et al.*[32]	2017	CT	DICOM	N/A	N/A	N/A	Objet500 Connex3
Barber *et al.*[30]	2018	—	—	Fusion 360	N/A	—	Ultimaker 2+
Garcia-Granero *et al.*[17]	2018	CT	DICOM	Cella-supplied	STL	N/A	N/A
Sahnan *et al.*[27]	2018	MRI	DICOM	Open-source software	STL	Cura 3.0.4 & Ultimaker B.V.	Ultimaker 3 Extended
Luzon *et al.*[42]	2019	CT	DICOM	Osirix MD v. 8.5.2, Mimics Medical, 3-matic Medical	STL, MXP	PreForm	The Form1+
Hamada *et al.*[15]	2019	CT	N/A	N/A	N/A	N/A	Rais 3D N2 Plus
Marano *et al.*[16]	2019	CT	N/A	N/A	STL	N/A	N/A
Anwari *et al.*[35]	2020	CT	DICOM	Vitrea, v.6.9 & Slicer v4.7.0	STL	Blender v.2.78 & Cura v.15.04.5	Rostock Max V2
Chen *et al.*[47]	2020	CT	DICOM	—	N/A	Geomagic Studio 2014	N/A
Etherton *et al.*[36]	2020	CT/MRI	N/A	Analyze 12.0	STL	Autodesk Mesh mixer v.3.5.474	Raise3D N2 Plus & Ultimaker 2 Extended+
Sun *et al.*[22]	2020	CT	N/A	Mimics 16.0	N/A	Mimics 16.0	Stratasys C 350
Casas-Murillo *et al.*[34]	2021	MRI	DICOM	3D Slicer v.4.8.0	STL	Meshmixer v. 3.5.474	3D Zortrax
Guler *et al.*[49]	2021	CT/MRI	DICOM	3D Slicer v.4.10.1	STL	—	Mass Portal Pharaoh xd 20 & Form Labs2
Guz *et al.*[26]	2021	MRI	DICOM	3D Slicer v.4.8.0	STL	Blender 2.77a	3D ProJet 460Plus
Hojo *et al.*[28]	2021	CT	N/A	OsiriX MD	STL	Meshmixer v.3.5	Axiom Dual Extruder
Oxford *et al.*[29]	2021	—	—	Fusion 360	N/A	Cura	Ultimaker S3/S5
Luzon *et al.*[37]	2022	Nano-CT	DICOM	ITK-snap	STL	Ultimaker Cura v. 4.9.1	Ultimaker S3
Park *et al.*[23]	2022	CT	N/A	Mimics 21.0	N/A	Cinema 4D	Cubicreator & Cubicon Single Plus
Xia *et al.*[46]	2023	CT	DICOM	Mimics 23.0	STL	Magic24	N/A

Abbreviations: ABS, acrylonitrile butadiene styrene; CT, computed tomography; DICOM, digital imaging and communications in medicine; FDM, fused deposition modeling; GCTH, gastrocolic trunk of Henle; IHR, inguinal hernia repair; MRI, magnetic resonance imaging, PLA, polylactic acid; PU, polyurethane; PVA, polyvinyl alcohol; SLA, stereo lithography appearance; SMA, superior mesenteric artery; SMV, superior mesenteric vessel; STL, stereolithography; TAPP, transabdominal peritoneal; TEPP, tracheoesophageal puncture and prosthesis; TPU, thermoplastic polyurethane; —, not required; * refers to the percentage of lifesize organs.

Printing material	Printing technique	Model name	Model size*	Printing time	Printing cost
Rigid acrylic resin	N/A	Liver	70%	18 h–36 h	50,000–110,000 yen
Liquid photopolymer	Polyjet	Thorax	100%	N/A	N/A
Rigid photopolymer	Polyjet	Spleen	N/A	20 h	N/A
N/A	N/A	Stoma	N/A	Several days	100 USD
Ultraviolet-cured resin	N/A	Pelvic structure	N/A	34 h 20 min–37 h 30 min	250,000 Yen
PLA	FDM	Liver	N/A	72 h	150 USD
TPU	FDM	Fistula patch	100%	N/A	N/A
N/A	N/A	Laparoscopy simulator in TAPP IHR	N/A	N/A	N/A
PLA	N/A	TEPP placement simulator	N/A	N/A	N/A
ABS, PU rubber	N/A	GCTH	N/A	N/A	N/A
N/A	N/A	Perianal fistula	N/A	1 h	N/A
Resin-based polymers	SLA	SMV	100%	4 h–6 h	21–34 USD
N/A	N/A	Esophageal cancer, Double aortic arch	N/A	N/A	N/A
Photopolymer resin	SLA	Esophagus, proximal stomach, thoracic aorta, diaphragmatic crus	100%	48 h	23,000 euros
ABS, flexible urethane rubber, beeswax	FDM	Abdominal structure mannequin	100%	N/A	900 CAD
TPU, resin, silica gel	N/A	Gastrocolic trunk	N/A	N/A	N/A
PLA, TPU	FDM	Situs ambiguus	N/A	497 h	130 USD
N/A	N/A	Retroperitoneal tumor	N/A	18 h	N/A
ABS, P53 silicone rubber, and Elmer's slime	FDM	Laparoscopic simulator for cystic duct and its variants	N/A	N/A	0.9–11.7 USD
N/A	N/A	Cancer model	100%	15 h	N/A
VisiJet PXL Core	N/A	Fistula of Crohn's disease	N/A	6 h	N/A
PLA, TPU	FDM	SMV	100%	8 h–20 h	10 USD
N/A	N/A	Intestinal anastomosis simulator	N/A	N/A	2.67–131 USD
PLA, PVA	N/A	SMA plexus	50%	24 h–32 h	N/A
N/A	FDM	Abdominal cavity	N/A	9 h 36 min	1.6 USD
Silica gel	FDM	Choledochojejunostomy model	N/A	N/A	N/A

Table 2. 3D printing for endoscopic operation, education, and simulation

Author	Year	Application	Image source	Data format	Image processing software	Output format	3D printing software	Printing machine
Lee *et al.*[65]	2018	Endoscopic biopsy	CT	DICOM	3D Slicer v.4.5.0	STL	Netfabb professional v.5	Clone S270 & Clone K300
Yang *et al.*[61]	2018	ERCP	CT/MRI	DICOM	Mimics Innovation Suite v17.0	STL	N/A	ProJet 4500
Lee *et al.*[64]	2019	Endoscopic hemostasis	CT	DICOM	3D Slicer v.4.5.0	STL	Netfabb professional v.5	Form 2
Kwon *et al.*[67]	2020	ERCP	CT	N/A	In-house software	STL	MeshLab and MeshMixer	3DM Tough-3.6
Dhir *et al.*[109]	2015	EUS-guided biliary drainage	MRI	N/A	N/A	N/A	N/A	Viper SI2
Holt *et al.*[68]	2018	Endoscopic ampullectomy	N/A	N/A	N/A	N/A	Solid Works 2014	Connex 260v

Abbreviations: CT, computed tomography; DICOM, digital imaging and communications in medicine; ERCP, endoscopic retrograde cholangiopancreatography; FDM, fused deposition modeling; MRI, magnetic resonance imaging; PLC, polycarbonate; SLA, stereo lithography appearance; STL, stereolithography; *refers to the percentage of lifesize organs.

phantoms of different phases[58], device for sutureless end enterostomy[59], and multisteerable configurations for laparoscopy (Figure 2B)[60]. These are listed in Table 3.

3. 3D printing in gastrointestinal endoscopy

Similar to open surgery or laparoscopic surgery, 3D printing also facilitates GI endoscopy in preoperative planning and guidance (Table 2), education (Table 2), and accessory production (Table 3).

3.1. Preoperative planning and guidance

Yang *et al.* reported that the 3DP model could accurately display hilar cholangiocarcinoma (HCC) and its relationship with the surrounding bile duct, which could be used to guide endoscopic retrograde cholangiopancreatography (ERCP) in HCC patients and improve the success rate[61]. Recently, our team updated the concept of endoscopic submucosal dissection (ESD) based on 3DP (Figure 2C). A large esophageal submucosal tumor was successfully removed by endoscopy under the guidance of the 3DP model, which can distinctly display the tumor anatomy and details of important adjacent organs such as the bronchus, aorta, and spine[62].

3.2. Education

Endoscopy is an important tool for the diagnosis and treatment of digestive diseases, but it is a challenging technique that requires extensive training. Traditionally, novices learn basic endoscopic skills under the guidance of experienced endoscopists. Although this provides direct supervision and real-time evaluation by instructors, it may inadvertently lead to patient discomfort, prolonged operation time, and increased training costs. Experienced endoscopists usually have higher overall resection rates, shorter operative times, and fewer adverse events[63]. Adequate training models of different GI disease scenarios, which are often difficult in real clinical settings, are needed to train less-experienced learners. Therefore, simulator-based endoscopy training has been widely used and validated over the past few decades.

Lee *et al.* created a new 3DP stomach hemostatic simulator with two hemostasis modules for hemoclipping and injection, which can effectively train beginners in GI hemostatic skills[64]. They also created a 3DP gastric biopsy simulator that could improve biopsy skills[65]. For advanced endoscopic techniques such as endoscopic retrograde cholangiopancreatography (ERCP), anatomical differences, realistic sense, and durability are major concerns for simulation[66]. Kwon *et al.* optimized the ERCP model using the 3DP technique, which helped learners successfully and repeatedly complete basic biliary intubation, difficult intubation, stone extraction, mechanical lithotomy, stent implantation, and balloon dilation[67]. Should ERCP fail, a printed biliary duct prototype could also be used for training and practicing endoscopic ultrasound (EUS)-guided biliary drainage. Endoscopic ampullectomy is another technically challenging procedure. The effect of a 3DP endoscopic ampullectomy training model has been preliminarily confirmed, which may solve the problem of limited training opportunities[68].

3.3. 3D-printed endoscopic accessories

Similar to surgical applications, 3DP is equally useful in producing endoscopic accessories. Zizer *et al.* developed a 3DP overtube system and confirmed its efficacy in

Printing material	Printing technique	Model name	Model size*	Printing time	Printing cost
Platinum silicone rubber	FDM	Stomach	N/A	N/A	N/A
Visijet C4 Spectrum Core	N/A	Hilar cholangiocarcinoma and bile duct	N/A	N/A	N/A
Silicone	SLA	Stomach	N/A	N/A	N/A
Silicone	N/A	Stomach and duodenum	N/A	N/A	N/A
PLC	SLA	Bile duct	N/A	N/A	N/A
Silicone rubber, polymer resin	Polyjet	Stomach, duodenal ampulla	N/A	N/A	1482 USD

accelerating endoscopic submucosal dissection (ESD) progress in a porcine model[69]. To improve diagnostic and therapeutic effects, Ko *et al.* fabricated four types of tailored endoscopic caps for ESD, endoscopic mucosal resection (EMR), peroral endoscopic myotomy (POEM), and Trucut biopsy, and applied them in 39 patients[70]. To improve the adenoma detection rate, a sideoptic-enhanced cap was printed[71]. There are also 3DP versatile pedal fixators to improve ergonomics during endoscopic procedures[72] and devices to ease endoscopic cell sheet transplantation[73].

4. Scaffold production

A few attempts have been made on animals for GI tract reconstruction. In 2015, researchers covered artificial esophageal defects in rabbits with poly-ε-caprolactone (PCL) mesh[74]. Although the growth of smooth muscle and epithelial cells was observed, a relatively high proportion (9/15) of rabbits developed diverticula due to the fast degradation of the material. Later in 2016, Park *et al.* from South Korea refined the technique by coating printed PCL scaffolds with fibrin, thrombin, and rabbit mesenchymal stem/stromal cells (rMSCs). They found that the scaffold endured mechanical strength after implantation into rabbit esophageal defects without leakage and that the MSC-seeded scaffold had a complete covering with epithelial cells, while the nude scaffold did not[75]. For better structural simulation, a circumferentially printed acellular PCL model with improved strength was cultured in rat omentum and transplanted to repair this rat's esophageal transection after cellularization and vascularization[76]. However, the planted graft lacked peristalsis and was easily obstructed due to its small diameter. Kim *et al.* later compared this omentum bioreactor with a mesenchymal stem cell-based bioreactor, where a two-layered printed artificial esophageal scaffold was incubated[77]. They found that both bioreactors enabled over 80% mucosal regeneration in rat esophageal defects. It also seemed that different printing materials have different cellular activities. Park *et al.* revealed that in a rat esophageal defect model, both adipose-derived mesenchymal stem cell (ADSC)-seeded 3DP PCL and ADSC-seeded 3DP polyurethane-nanofiber (PU-Nf) had greater tissue regeneration than nude scaffold groups[78]. Interestingly, smooth muscle regeneration was greater in the PCL scaffold, while epithelium regeneration was greater in the PU-Nf scaffold. Perhaps cocktail formulations of inks might be considered for the expansion of different cells.

3DP scaffolds can also be used as loading systems for extracellular matrices and drugs. Ha *et al.* used 3DP to load esophagus-derived decellularized extracellular matrix (EdECM) hydrogel onto printed rod-shaped PCL stent[79]. They tested the stent in a radiation esophagitis rat model and observed fast remission of inflammation. Later in 2021, Kim *et al.* loaded tetracycline onto a 3DP PCL patch and implanted the patch into an artificial esophageal fistula in rats[80]. The patch could continuously release drugs for over 30 days and had good sealing, antibacterial, antimacrophage, and proregenerative effects. A similar printed stent loaded with 5-fluorouracil was applied in malignant esophageal stenosis[81]. In spite of these applications, 3DP scaffolds of intestinal microvilli and crypts with either hydrogels or silk fibroin protein can serve as models that better mimic physiological and barrier functions, which might be exploited to explore

Table 3. 3D printing of accessories

Author	Year	Application	Object name	Purpose	3D printing software	Printing machine	Printing technique	Printing material	Printing time	Printing cost
Maeda *et al.*[73]	2015	Endoscopy	Cell sheet carrier	Endoscopic cell sheet transplantation	N/A	Objet350 Connex	N/A	MED610	N/A	N/A
Ko *et al.*[70]	2016	Endoscopy	Tailored endoscopic caps	Facilitating EMRC, ESD, POEM, and TCB	N/A	Objet260 Connex	FDM & Polyjet	Silicon	N/A	N/A
Walter *et al.*[71]	2017	Endoscopy	Sideoptic caps	Colonoscopic examination	N/A	N/A	N/A	PLA	N/A	1 euro
Steinemann *et al.*[52]	2018	Laparoscopy	Space holder	Intraesophageal suturing	Autodesk Inventor 2016 & Autodesk Meshmixer v.10.10.170	Ultimaker B.V.	FFF	PLA	5 h	5 euros
Lin *et al.*[55]	2019	Endoscopy	Spiral polymer stent	Inoperative esophageal malignancy	CAD software	Ultimaker 2	N/A	TPU/PLA	N/A	N/A
Xu *et al.*[56]	2019	Surgery	Fistula stent	Plugging enteroatmospheric fistula	Solid work software	N/A	FDM	TPU	N/A	N/A
Yang *et al.*[53]	2019	Surgery	Biopolymer device	Simplify pancreaticojejunostomy	N/A	Fused Deposition Modeling	FDM	PLA	N/A	N/A
Durán Muñoz-Cruzado *et al.*[57]	2020	Surgery	Custom device	NPWT	Regemat 3D designer	Regemat 3D	N/A	PCL	4 h	N/A
Kwon *et al.*[58]	2020	Research	Anthropomorphic gastric phantom	Facilitate intragastric balloon investigation	3-matic 9.0	Objet500 Connex3	N/A	Agilus Transparent	N/A	N/A
Sejor *et al.*[59]	2020	Surgery	Custom device	Simplify enterostomy	Rhinoceros 6	Factory 2.0 & Raise 3D N2 Dual Plus	N/A	N/A	N/A	N/A
Culmone *et al.*[60]	2022	Laparoscopy	Multisteerable instruments	Reduce rigidity of surgical instruments	N/A	Perfactory Mini XL	Vat photopolymerization	Epoxy photopolymer resin	N/A	N/A
Bernhard *et al.*[54]	2022	Surgery	PLAFOKON	Specific robotic surgical platform	PLAFOKON planning tool	N/A	SLS	Polyamide 12	A few hours	N/A

Abbreviations: CAD, computer-aided; EMRC, endoscopic mucosal resection; ESD, endoscopic submucosal dissection; FDM, fused deposition modeling; FFF, fused filament fabrication; NPWT, negative pressure wound therapy; PCL, polycaprolactone; PLA, polylactic acid; POEM, peroral endoscopic myotomy; SLS, selective laser sintering; TCB, Trucut biopsy; TPU, thermoplastic polyurethane.

https://doi.org/10.36922/ijb.0149

disease pathogenesis, drug screening, and microbiome interaction[82,83]. The related literature is summarized in Table 4.

While the advantages of printed scaffolds are unanimously recognized (e.g., highly customized and controllable, compatible with many types of materials, and producing delicate micro structures)[84], there are still disadvantages (e.g., expensive equipment, time-consuming, low printing resolution, and requirement of bioreactor). The ideal printed scaffolds should have tubular structures with contiguous epithelial linings of different functions (e.g., acid and mucus secretion, absorption) and properties of nutrient provision, peristaltic pumping, and the microbiome. PCL is one of the most commonly used printing materials. However, it is not very friendly to cell adhesion, although it is reported to have fair biocompatibility, durability, processability, and relatively slow degradability[79,85]. Further refinement of both inks and experimental steps is required to meet experimental and clinical requirements.

5. What can 3D bioprinting do?

The above-mentioned printed scaffolds are primarily biomimetic structures without cells. Thus, bioprinting, where bioinks containing living cells, is later introduced (Table 5). There are generally three kinds of bioprinting technologies at the micrometric scale[10]: extrusion-based[86], jetting-based (inkjet and laser-assisted)[87], and vat photopolymerization (stereolithography and digital light processing)[88]. It is faster and more efficient than traditional methods as it excludes cell seeding and repopulation processes. Most importantly, 3D bioprinting is able to create grafts with spatial relocations of bioinks with living cells and with microenvironments for cell expansion. Therefore, 3D bioprinting is most suitable for stratified organs with different layers of cells like GI tract. The treatment of GI diseases requiring surgical interventions usually involves organ reconstruction, defect repair, and stenosis treatment. The success rate of intestinal allografts is still relatively low due to their immunogenicity. Therefore, implantable organs and materials that do not lead to immunological rejection, coagulopathy, pathogen transmission, and hazardous decomposition byproduct are needed. Functional tubular organs need a special design to mimic histological layers and physiological functions. 3D bioprinting has been attempted in creating hollow organs such as the esophagus, small intestine, and bile duct, but not yet in the stomach.

In 2019, Takeoka *et al.* bioprinted scaffold-free 3D tubular structures to repair rat esophageal defects. They found that a greater proportion of mesenchymal stem cells tended to induce greater strength and cellular activity[89]. Madden *et al.* used bioinks of human intestinal myofibroblasts (hIMFs) and human intestinal epithelial cells (hIECs) to print layer by layer onto the transwell membrane to form a bilayer structure. Differentiation into polarized and tightly joined epithelial subpopulations such as chromaffin cells and goblet cells was observed[90]. However, the researchers used this model to test drugs only rather than mechanical properties, peristaltic characteristics, and biocompatibilities. Further efforts can be made to develop implantable sheets and even hollow intestinal sections. Maina *et al.* 3D bioprinted a biopatch consisting of hydrogel, rat venous smooth muscle cells, and aortic fibroblast cells[91]. They implanted this patch into a rat enterostomy and found that the sealed intestine maintained integrity with the intraluminal pulsatile flow and exhibited robust histological formation of villi and crypts. To better mimic the histological architecture of villi, Kim *et al.* fabricated a collagen bioink-based intestinal model in which a single villus was 183 μm wide and 770 μm tall[92]. The model also contained vascular structure, making it perform better in cell growth, mucus secretion, barrier formation, and even absorption function than the 2D model and 3D model without vasculature. Kim further improved the bioink by adding decellularized small intestinal submucosa[93]. They demonstrated that the updated version had a better performance in cell activities than the previously reported version[92,93]. Very few studies have explored its application in the biliary system. Yan *et al.* printed models with ink containing cholangiocytes and laminin-like amphiphiles that comprise the base membrane. They found that the cells could organize and develop tubular structures with branches[94]. Boyer *et al.* also invented a 3D bioprinted biliary stent infused with collagen, human placental MSCs, and cholangiocytes, aiming to improve biliary stent patency and patient care[95].

Instead of tubular structures, 3D bioprinting of liver organoids has also been attempted in recent years. Yang *et al.* introduced a printed hepatorganoid that consisted of HepaRG cells and bioinks of sodium alginate and gelatin[96]. The organoid obtained functions of drug metabolism, synthesis of protein, and glycogen storage after proper culture both *in vitro* and *in vivo*. The planted organoid significantly prolonged the survival of liver failure mice.

The challenges for 3D bioprinting are finding the optimal formulation of biomaterials with cell components that meet the requirements of bioprinting, especially for hollow organs. Caution should be taken regarding questions about personalized ink formulation (i.e., biological composition, viscosity, mechanical properties, postprocessing gelatin, and clinical grade), nozzle clotting, cell damage, and prototype sterilization[97]. Hydrogels, whether natural or

Table 4. 3D printing of decellularized scaffolds

Author	Year	Animal model	Printed object	Application	Printing machine	Printing material
Park *et al.*[75]	2016	Rabbit	Artificial esophageal patch	Repairment of partial esophageal defect	3D Bioplotter	PCL
Chung *et al.*[76]	2018	Rat	Tubular scaffold	Repairment of transectional esophageal defect	BT-3000	PCL
Kim *et al.*[77]	2019	Rat	Esophageal graft	Repairment of transectional esophageal defect	3D Bioplotter	PCL/PU
Boyer *et al.*[95]	2019	*In vitro*	Biliary stent	Biliary procedures	MakerBot Replicator	PVA
Fouladian *et al.*[81]	2020	*In vitro*	Esophageal stent	Malignant esophageal stenosis	Ultimaker S5	PU+5-FU
Ha *et al.*[79]	2021	Rat	Esophageal stent	Treating radiation esophagitis	2RPS	PCL
Kim *et al.*[80]	2021	Rat	Artificial esophageal patch	Repairment of partial esophageal defect	Simplify 3D v. 4.0	PCL+TCN
Park *et al.*[78]	2021	Rat	Artificial esophageal patch	Repairment of partial esophageal defect	3D Bioplotter	PCL/PU

Abbreviations: ADSC, adipose-derived mesenchymal stem cell; EdECM, esophagus-derived decellularized extracellular matrix; FDM, fused deposition modeling; 5-FU, 5-fluorouracil; MSCs, mesenchymal stem cells; PMSCs, placental mesenchymal stem cells; PCL, polycaprolactone; PU, polyurethane; PVA, polyvinyl alcohol; TCN, tetracycline.

synthetic, are promising materials due to their biochemical ability to promote cellular activity. Therefore, hydrogels are often the first option in 3D bioprinting. However, it is weak in terms of mechanical properties, so it is still not the ideal option[10]. An ideal bioink should be one that has slow degradation and could be replaced by regenerative tissues. Yeleswarapu *et al.* solved this problem by innovatively using a stereolithography-based 3D printer[98]. They used esophageal muscle dECM to fabricate tubular structures, which sustained good biocompatibility and mechanical strength. From reported cases, we can see that bioinks derived from decellularized ECM seem to have better cellular activity. Furthermore, light-activated bioprinting materials might be a good choice to avoid thermal or cryogenic injury to cells in bioinks[99]. To refine printing techniques, Nam *et al.* developed an extrusion-based printing technique named "dragging technique" to fabricate a multilayered tubular scaffold with delicate pore characteristics, which previous techniques could not[100]. Pi *et al.* presented, in another way, a microfluidic bioprinting technology called a multichannel coaxial extrusion system (MCCES)[101]. The system could print circumferentially multilayered tubular structures, which were perfusable, with adequate cellular functionality in a single step.

The previously mentioned models were printed *in vitro*. Zhao *et al.* innovatively proposed a concept of *in situ* bioprinting *in vivo*, and brought this into reality by installing a micro bioprinter to the endoscope[102]. A printed circuit microelectromechanical system (PC-MEMS) technique was used to build the printing platform. They tested it by bioprinting a gelatin–alginate scaffold with human gastric epithelial and smooth muscle cells to repair a wound on a stomach model. Recently, Thai *et al.* also reported an *in situ* 3DP technique compatible with robotic surgery and tested it on colon phantoms and fresh porcine tissues[103]. However, it should be emphasized that these are not truly *in vivo*. In the future, live animal models are needed to simulate a real endoscopic procedure.

6. Outlook for 3D printing in gastroenterology

While we have seen encouraging reports of 3DP applications in gastroenterology, much is left unclarified and unsolved. Using traditional 3D printing, creating a 1:1 duplicate of anatomical structures in surgical areas instead of virtual ones that cannot be touched does lead to a seemingly better clinical outcome. However, most of the studies are presented as cases or case series of small samples. Few comparative studies have provided low-grade evidence about the effect of the 3DP model in preoperative planning and education. Many of the endpoints cannot be objectively evaluated, leaving suspicion about their credibility, even though comparisons have been made. Therefore, in future clinical studies assessing the applicability of 3DP models in helping surgery and education, several factors need to be addressed: (i) the studies need to be designed in a prospective manner with proper controls, either as randomized controlled trials (RCTs) or as cohort studies; (ii) validated endpoint events

Printing technique	Seeded cells	Extracellular matrix	Bioreactor	Results
Extrusion	Rabbit MSCs	Fibrin, thrombin	None	Better cell regeneration in MSC group
3D printing & electrospinning	None	None	Omentum	Better cell regeneration in MSC group
3D printing & electrospinning	Human MSCs	None	Custom-made & omentum	Satisfactory tissue regeneration with both bioreactors
N/A	Human PMSCs, human primary cholangiocytes	Collagen	Growth medium	Satisfactory cholangiocytes coating
FDM	None	None	None	Sustained release of 5-FU over 110 days
Extrusion	None	EdECM-based hydrogel	None	Rapid resolution of inflammatory response
Extrusion	None	None	None	Better tissue regeneration and antibacterial activity
3D printing & electrospinning	ADSC	Matrigel & fibronectin	Growth medium	Better cell regeneration in ADSC group

that make a subjective evaluation of improvement of skills and patient satisfaction more credible (e.g., structured scoring systems); and (iii) an adequate sample size that meets statistical principles.

When it comes to 3D printing, several limitations, such as high expenses, long printing time, change in size, and low printing resolution, hinder its widespread patient-specific application. Printing technology and materials need further refinement to achieve time-effective and cost-effective results while producing high-resolution[104], durable, and biocompatible models and objects. Implantable objects also have to endure sterile procedures and challenging physical or chemical environments *in vivo*. Researchers may also consider printing GI models with lifelike textures and histological layers (e.g., mucosa and submucosa) to provide better simulative effects. Another question for models concerning surgery and patient education is that who should cover the printing cost.

To better meet the clinical demands of organ replacement, reconstruction, and repair, either cell-seeded scaffolds or bioprinted scaffolds have to acquire physiological properties such as secretion, absorption, and peristalsis that resemble native tissues. While researchers have realized some of those properties, such as in the regenerations of multilayer epithelium and smooth muscle, they were mostly performed on mice, rats, or rabbits. Such experiments have not been conducted in larger mammals. Whether the scaffolds can be immediately transplanted or they should be left in a bioreactor after bioprinting remains to be explored. We expect the cells to self-assemble to form a native histological structure. Should 3D bioprinted grafts be applied to the human gastroenterological system, several questions must be answered first: (i) What kind of cells are needed and where do we get them? (ii) What kind of bioink best stimulates cell growth and differentiation? (iii) Is the bioink formulation a panacea or tissue-specific? (iv) Does the printing technology and material support a 1:1 duplicate of native human organ or tissue with mechanical, microbiological, immunological, and neurological functions as well as microenvironments of blood and lymphatic vessels, and how fast can it be? (v) Is 3D-printed organoid transplantation an alternative to organ or tissue transplantation, and for what kind of scenarios might it be suitable?

In the end, machine learning (ML) has been popular in the last decades, and several attempts have been made in process optimization, defect detection, dimensional accuracy analysis, bioink design, and cellular viability prediction[105-108]. While many challenges remain, how artificial intelligence might be integrated into tissue design, bioink formulation, cell sorting and culture, printing, and monitoring in gastroenterology is still an interesting task in the future.

7. Conclusion

Although much seems to have been tried, gastroenterology is still a less developed area for 3D printing and bioprinting. However, it is promising for vast clinical requirements. Preoperative planning, realistic simulation, evaluation

Table 5. 3D bioprinting of gastrointestinal grafts

Author	Year	Animal model	Printed object	Application	Printing machine	Bioink formulation	Printing technique	Bioreactor	Results
Kim *et al.*[92]	2018	*In vitro*	Small intestinal villi model with vessels	Mimicking human intestine	DTR3-2210 T-SG	HUVECs, Caco-2 cells + collagen	Extrusion	Growth medium	Successful mimicking of 3D geometry and physiology of human intestine
Madden *et al.*[90]	2018	*In vitro*	Human intestinal tissue model	Drug development	Novogen Bioprinter	IMF, Caco-2 cells + Novogel	N/A	Custom-made	Mimic injury response to drug-induced toxicity and inflammation
Yan *et al.*[94]	2018	*In vitro*	Nanostructural scaffold	Promoting bile duct formation	Envision TEC (GMBH) 3D Bioplotter	Cholangiocytes + thiolated gelatin, PA	Extrusion	Growth medium	Formation of functional tubular structure
Takeoka *et al.*[89]	2019	Rat	Tubular structure	Regeneration of esophagus	Regenova bio-3D printer	Cellular spheroids of NHDFs, HUVECs, human bone marrow-derived MSCs, HESMCs	Kenzan method	Custom-made	Greater proportion of MSCs with greater mechanical strength and tissue regeneration
Kim *et al.*[93]	2020	*In vitro*	Small intestinal villi model	Mimicking human intestine	DTR3-2210 T-SG	Caco-2 cells + SIS, collagen	Extrusion	Growth medium	Better epithelial mimicking than pure collagen
Maina *et al.*[91]	2021	Rat	Biopatch	Repairment of small intestinal injury	Novogen mmx-07	Venous SMC, aortic FC + hydrogel	Inkjet	Growth medium	Villi and crypt formation, and complete restoration of epithelium
Yang *et al.*[96]	2019	Mice	Hepatorganoid	Treating liver failure	Spp1603	HepaRG cells + alginate, gelatin	Extrusion	Growth medium	Display synthetic functions and prolong liver injury mice survival

Abbreviations: FC, fibroblast; HESMCs, human esophagus smooth muscle cells; HUVECs, human umbilical vein endothelial cells; MSCs, mesenchymal stem cells; NHDFs, normal human dermal fibroblasts; PA, peptides amphiphile; SIS, small intestinal mucosa; SMC, smooth muscle cell.

https://doi.org/10.36922/ijb.0149

of therapy response, and organ/tissue replacement for precision medicine are what we are now endeavoring to explore. More importantly, we need to discover areas that we have not tried with 3D printing, where it might boost medical progress and bring real benefits to patients.

Acknowledgments

None.

Funding

None.

Conflict of interest

The authors declare no conflict of interest.

Author contributions

Conceptualization: Yuhang Zhang, Bing Hu
Writing – original draft: Yuhang Zhang, Liuxiang Chen
Writing – review & editing: Yuhang Zhang

Ethics approval and consent to participate

Not applicable.

Consent for publication

Not applicable.

Availability of data

Not applicable.

Reference

1. Williams EM, 1984, Computer automated manufacturing process and system. US4665492A, July 2, 1984.
2. Tack P, Victor J, Gemmel P, *et al.*, 2016, 3D-printing techniques in a medical setting: A systematic literature review. *Biomed Eng Online*, 15(1): 115.

   http://doi.org/10.1186/s12938-016-0236-4
3. Aimar A, Palermo A, Innocenti B, 2019, The role of 3D printing in medical applications: A state of the art. *J Healthc Eng*, 2019: 5340616.

   http://doi.org/10.1155/2019/5340616
4. Brachet A, Bełżek A, Furtak D, *et al.*, 2023, Application of 3D printing in bone grafts. *Cells*, 12(6).

   http://doi.org/10.3390/cells12060859
5. Sharbidre KG, Aziz MU, Mohd Z, 2022, Review of abdominal vascular variations: Imaging and clinical implications. *Radiographics*, 42(1): E27–E28.

   http://doi.org/10.1148/rg.210093
6. Ballard DH, Wake N, Witowski J, *et al.*, 2020, Radiological Society of North America (RSNA) 3D Printing Special Interest Group (SIG) clinical situations for which 3D printing is considered an appropriate representation or extension of data contained in a medical imaging examination: Abdominal, hepatobiliary, and gastrointestinal conditions. *3D Print Med*, 6(1): 13.

   http://doi.org/10.1186/s41205-020-00065-6
7. Marconi S, Pugliese L, Botti M, *et al.*, 2017, Value of 3D printing for the comprehension of surgical anatomy. *Surg Endosc*, 31(10): 4102–4110.

   http://doi.org/10.1007/s00464-017-5457-5
8. Li C, Zheng B, Yu Q, *et al.*, 2021, Augmented reality and 3-dimensional printing technologies for guiding complex thoracoscopic surgery. *Ann Thorac Surg*, 112(5): 1624–1631.

   http://doi.org/10.1016/j.athoracsur.2020.10.037
9. Pietrabissa A, Marconi S, Negrello E, *et al.*, 2020, An overview on 3D printing for abdominal surgery. *Surg Endosc*, 34(1): 1–13.

   http://doi.org/10.1007/s00464-019-07155-5
10. Farhat W, Chatelain F, Marret A, *et al.*, 2021, Trends in 3D bioprinting for esophageal tissue repair and reconstruction. *Biomaterials*, 267: 120465.

    http://doi.org/10.1016/j.biomaterials.2020.120465
11. Vrana NE, Gupta S, Mitra K, *et al.*, 2000, From 3D printing to 3D bioprinting: The material properties of polymeric material and its derived bioink for achieving tissue specific architectures. *Cell Tissue Bank*, 23(3): 417–440.

    http://doi.org/10.1007/s10561-021-09975-z
12. Willson K, Atala A, 2022, Medical 3D printing: tools and techniques, today and tomorrow. *Annu Rev Chem Biomol Eng*, 13: 481–499.

    http://doi.org/10.1146/annurev-chembioeng-092220-015404
13. Zhang J, Wehrle E, Rubert M, *et al.*, 2021, 3D bioprinting of human tissues: Biofabrication, bioinks, and bioreactors. *Int J Mol Sci*, 22(8).

    http://doi.org/10.3390/ijms22083971
14. Dickinson KJ, Matsumoto J, Cassivi SD, *et al.*, 2015, Individualizing management of complex esophageal pathology using three-dimensional printed models. *Ann Thorac Surg*, 100(2): 692–697.

    http://doi.org/10.1016/j.athoracsur.2015.03.115
15. Hamada K, Taniyama Y, Yashima Y, *et al.*, 2022, Determination of the best surgical strategy for thoracic esophageal resection concurrent with double aortic arch using a three-dimensional model: A case report. *Transl Cancer Res*, 11(9): 3322–3328.

    http://doi.org/10.21037/tcr-22-468

16. Marano L, Ricci A, Savelli V, *et al.*, 2019, From digital world to real life: A robotic approach to the esophagogastric junction with a 3D printed model. *BMC Surg*, 19(1): 153.

http://doi.org/10.1186/s12893-019-0621-6

17. Garcia-Granero A, Sánchez-Guillén L, Fletcher-Sanfeliu D, *et al.*, 2018, Application of three-dimensional printing in laparoscopic dissection to facilitate D3-lymphadenectomy for right colon cancer. *Tech Coloproctol*, 22(2): 129–133.

http://doi.org/10.1007/s10151-018-1746-9

18. Hojo D, Nishikawa T, Takayama T, *et al.*, 2019, 3D printed model-based simulation of laparoscopic surgery for descending colon cancer with a concomitant abdominal aortic aneurysm. *Tech Coloproctol*, 23(8): 793–797.

http://doi.org/10.1007/s10151-019-02060-4

19. Hamabe A, Ito M, 2017, A three-dimensional pelvic model made with a three-dimensional printer: Applications for laparoscopic surgery to treat rectal cancer. *Tech Coloproctol*, 21(5): 383–387.

http://doi.org/10.1007/s10151-017-1622-z

20. Igami T, Nakamura Y, Hirose T, *et al.*, 2014, Application of a three-dimensional print of a liver in hepatectomy for small tumors invisible by intraoperative ultrasonography: Preliminary experience. *World J Surg*, 38(12): 3163–3166.

http://doi.org/10.1007/s00268-014-2740-7

21. Witowski JS, Pędziwiatr M, Major P, *et al.*, 2017, Cost-effective, personalized, 3D-printed liver model for preoperative planning before laparoscopic liver hemihepatectomy for colorectal cancer metastases. *Int J Comput Assist Radiol Surg*, 12(12): 2047–2054.

http://doi.org/10.1007/s11548-017-1527-3

22. Sun G, Ding B, Yu G, *et al.*, 2020, Three-dimensional printing - Assisted planning for complete and safe resection of retroperitoneal tumor. *J X-ray Sci Technol*, 28(3): 471–480.

http://doi.org/10.3233/xst-190636

23. Park S, Choi GS, Kim JM, *et al.*, 2022, 3D printing model of abdominal cavity of liver transplantation recipient to prevent large-for-size syndrome. *Int J Bioprint*, 8(4): 609.

http://doi.org/10.18063/ijb.v8i4.609

24. Villarreal JA, Yoeli D, Masand PM, *et al.*, 2020, Hepatic separation of conjoined twins: Operative technique and review of three-dimensional model utilization. *J Pediatr Surg*, 55(12): 2828–2835.

http://doi.org/10.1016/j.jpedsurg.2020.06.047

25. Huang JJ, Ren JA, Wang GF, *et al.*, 2017, 3D-printed "fistula stent" designed for management of enterocutaneous fistula: An advanced strategy. *World J Gastroenterol*, 23(41): 7489–7494.

http://doi.org/10.3748/wjg.v23.i41.7489

26. Guz W, Ożóg Ł, Aebisher D, *et al.*, 2021, The use of magnetic resonance imaging technique and 3D printing in order to develop a three-dimensional fistula model for patients with Crohn's disease: Personalised medicine. *Prz Gastroenterol*, 16(1): 83–88.

http://doi.org/10.5114/pg.2020.101629

27. Sahnan K, Adegbola SO, Tozer PJ, *et al.*, 2018, Innovation in the imaging perianal fistula: A step towards personalised medicine. *Therap Adv Gastroenterol*, 11: 1756284818775060.

http://doi.org/10.1177/1756284818775060

28. Hojo D, Kawai K, Murono K, *et al.*, 2021, Establishment of deformable three-dimensional printed models for laparoscopic right hemicolectomy in transverse colon cancer. *ANZ J Surg*, 91(7–8): E493–E499.

http://doi.org/10.1111/ans.16659

29. Oxford K, Walsh G, Bungay J, *et al.*, 2021, Development, manufacture and initial assessment of validity of a 3-dimensional-printed bowel anastomosis simulation training model. *Can J Surg*, 64(5): E484–E490.

http://doi.org/10.1503/cjs.018719

30. Barber SR, Kozin ED, Naunheim MR, *et al.*, 2018, 3D-printed tracheoesophageal puncture and prosthesis placement simulator. *Am J Otolaryngol*, 39(1): 37–40.

http://doi.org/10.1016/j.amjoto.2017.08.001

31. Williams A, McWilliam M, Ahlin J, *et al.*, 2018, A simulated training model for laparoscopic pyloromyotomy: Is 3D printing the way of the future? *J Pediatr Surg*, 53(5): 937–941.

http://doi.org/10.1016/j.jpedsurg.2018.02.016

32. Nishihara Y, Isobe Y, Kitagawa Y, 2017, Validation of newly developed physical laparoscopy simulator in transabdominal preperitoneal (TAPP) inguinal hernia repair. *Surg Endosc*, 31(12): 5429–5435.

http://doi.org/10.1007/s00464-017-5614-x

33. Jeffries S, Watt A, Harutyunyan R, *et al.*, 2022, The development of a novel bariatric laparoscopic simulator. *Ann Int Conf IEEE Eng Med Biol Soc*, 2022: 633–636.

http://doi.org/10.1109/embc48229.2022.9871246

34. Casas-Murillo C, Zuñiga-Ruiz A, Lopez-Barron RE, *et al.*, 2021, 3D-printed anatomical models of the cystic duct and its variants, a low-cost solution for an in-house built simulator for laparoscopic surgery training. *Surg Radiol Anat*, 43(4): 537–544.

http://doi.org/10.1007/s00276-020-02631-3

35. Anwari V, Lai A, Ursani A, *et al.*, 2020, 3D printed CT-based abdominal structure mannequin for enabling research. *3D Print Med*, 6(1): 3.

http://doi.org/10.1186/s41205-020-0056-9

36. Etherton D, Tee L, Tillett C, *et al.*, 2020, 3D visualization and 3D printing in abnormal gastrointestinal system manifestations of situs ambiguus. *Quant Imaging Med Surg*, 10(9): 1877–1883.

http://doi.org/10.21037/qims-20-661

37. Luzon JA, Thorsen Y, Nogueira LP, *et al.*, 2022, Reconstructing topography and extent of injury to the superior mesenteric artery plexus in right colectomy with extended D3 mesenterectomy: A composite multimodal 3-dimensional analysis. *Surg Endosc*, 36(10): 7607–7618.

http://doi.org/10.1007/s00464-022-09200-2

38. Chedid VG, Kamath AA, Knudsen JM, *et al.*, 2020, Three-dimensional-printed liver model helps learners identify hepatic subsegments: A randomized-controlled cross-over trial. *Am J Gastroenterol*, 115(11): 1906–1910.

http://doi.org/10.14309/ajg.0000000000000958

39. Tominaga T, Takagi K, Takeshita H, *et al.*, 2016, Usefulness of three-dimensional printing models for patients with stoma construction. *Case Rep Gastroenterol*, 10(1): 57–62.

http://doi.org/10.1159/000442663

40. Papazarkadas X, Spartalis E, Patsouras D, *et al.*, 2019, The role of 3D printing in colorectal surgery: Current evidence and future perspectives. *In Vivo*, 33(2): 297–302.

http://doi.org/10.21873/invivo.11475

41. Pietrabissa A, Marconi S, Peri A, *et al.*, 2016, From CT scanning to 3-D printing technology for the preoperative planning in laparoscopic splenectomy. *Surg Endosc*, 30(1): 366–371.

http://doi.org/10.1007/s00464-015-4185-y

42. Luzon JA, Andersen BT, Stimec BV, *et al.*, 2019, Implementation of 3D printed superior mesenteric vascular models for surgical planning and/or navigation in right colectomy with extended D3 mesenterectomy: comparison of virtual and physical models to the anatomy found at surgery. *Surg Endosc*, 33(2): 567–575.

http://doi.org/10.1007/s00464-018-6332-8

43. Chen Y, Bian L, Zhou H, *et al.*, 2020, Usefulness of three-dimensional printing of superior mesenteric vessels in right hemicolon cancer surgery. *Sci Rep*, 10(1): 11660.

http://doi.org/10.1038/s41598-020-68578-y

44. Hojo D, Murono K, Nozawa H, *et al.*, 2022, Improvement in surgical outcomes using 3-dimensional printed models for lateral pelvic lymph node dissection in rectal cancer. *Dis Colon Rectum*, 65(4): 566–573.

http://doi.org/10.1097/dcr.0000000000002327

45. Nishihara Y, Isobe Y, 2021, Preoperative skill evaluation in transabdominal preperitoneal (TAPP) inguinal hernia repair using a three-dimensional printed TAPP repair simulator. *Surg Endosc*, 35(1): 270–274.

http://doi.org/10.1007/s00464-020-07389-8

46. Xia J, Mao J, Chen H, *et al.*, 2023, Development and evaluation of a portable and soft 3D-printed cast for laparoscopic choledochojejunostomy model in surgical training. *BMC Med Edu*, 23(1): 77.

http://doi.org/10.1186/s12909-023-04055-0

47. Chen Y, Qian C, Shen R, *et al.*, 2020, 3D printing technology improves medical interns' understanding of anatomy of gastrocolic trunk. *J Surg Edu*, 77(5): 1279–1284.

http://doi.org/10.1016/j.jsurg.2020.02.031

48. Boyajian MK, Lubner RJ, Roussel LO, *et al.*, 2020, A 3D printed suturing trainer for medical students. *Clin Teach*, 17(6): 650–654.

http://doi.org/10.1111/tct.13176

49. Guler E, Ozer MA, Bati AH, *et al.*, 2021, Patient-centered oncosurgical planning with cancer models in subspecialty education. *Surg Oncol*, 37: 101537.

http://doi.org/10.1016/j.suronc.2021.101537

50. Povey M, Powell S, Howes N, *et al.*, 2021, Evaluating the potential utility of three-dimensional printed models in preoperative planning and patient consent in gastrointestinal cancer surgery. *Ann R Coll Surg Engl*, 103(8): 615–620.

http://doi.org/10.1308/rcsann.2020.7102

51. Witowski J, Budzyński A, Grochowska A, *et al.*, 2020, Decision-making based on 3D printed models in laparoscopic liver resections with intraoperative ultrasound: A prospective observational study. *Eur Radiol*, 30(3): 1306–1312.

http://doi.org/10.1007/s00330-019-06511-2

52. Steinemann DC, Müller PC, Apitz M, *et al.*, 2018, An ad hoc three dimensionally printed tool facilitates intraesophageal suturing in experimental surgery. *J Surg Res*, 223: 87–93.

http://doi.org/10.1016/j.jss.2017.10.026

53. Yang YY, Zhao CQ, Wang LS, *et al.*, 2019, A novel biopolymer device fabricated by 3D printing for simplifying procedures of pancreaticojejunostomy. *Mater Sci Eng C*, 103: 109786.

http://doi.org/10.1016/j.msec.2019.109786

54. Bernhard L, Krumpholz R, Krieger Y, *et al.*, 2022, PLAFOKON: A new concept for a patient-individual and intervention-specific flexible surgical platform. *Surg Endosc*, 36(7): 5303–5312.

http://doi.org/10.1007/s00464-021-08908-x

55. Lin M, Firoozi N, Tsai CT, *et al.*, 2019, 3D-printed flexible polymer stents for potential applications in inoperable esophageal malignancies. *Acta Biomater*, 83: 119–129.

http://doi.org/10.1016/j.actbio.2018.10.035

56. Xu ZY, Ren HJ, Huang JJ, *et al.*, 2019, Application of a 3D-printed "fistula stent" in plugging enteroatmospheric fistula with open abdomen: A case report. *World J Gastroenterol*, 25(14): 1775–1782.

http://doi.org/10.3748/wjg.v25.i14.1775

57. Durán Muñoz-Cruzado V, Calero Castro FJ, Padillo Eguía A, *et al.*, 2020, Using a bio-scanner and 3D printing to create an innovative custom made approach for the management of complex entero-atmospheric fistulas. *Sci Rep*, 10(1): 19862.

http://doi.org/10.1038/s41598-020-74213-7

58. Kwon J, Choi J, Lee S, *et al.*, 2020, Modelling and manufacturing of 3D-printed, patient-specific, and anthropomorphic gastric phantoms: A pilot study. *Sci Rep*, 10(1): 18976.

http://doi.org/10.1038/s41598-020-74110-z

59. Sejor E, Debs T, Petrucciani N, *et al.*, 2020, Feasibility and efficiency of sutureless end enterostomy by means of a 3D-printed device in a porcine model. *Surg Innov*, 27(2): 203–210.

http://doi.org/10.1177/1553350619895631

60. Culmone C, van Starkenburg R, Smit G, *et al.*, 2022, Comparison of two cable configurations in 3D printed steerable instruments for minimally invasive surgery. *PloSone*, 17(10): e0275535.

http://doi.org/10.1371/journal.pone.0275535

61. Yang Y, Zhou Z, Liu R, *et al.*, Application of 3D visualization and 3D printing technology on ERCP for patients with hilar cholangiocarcinoma. *Exp Ther Med*, 15(4): 3259–3264.

http://doi.org/10.3892/etm.2018.5831

62. Ye L, Yang D, Huang Y, *et al.*, 2020, 3D-printed model in the guidance of tumor resection: A novel concept for resecting a large submucosal tumor in the mid-esophagus. *Endoscopy*, 52(8): E273–E274.

http://doi.org/10.1055/a-1090-6940

63. Oyama T, Yahagi N, Ponchon T, *et al.*, 2015, How to establish endoscopic submucosal dissection in Western countries. *World J Gastroenterol*, 21(40): 11209-11220.

http://doi.org/10.3748/wjg.v21.i40.11209

64. Lee DS, Ahn JY, Lee GH, 2019, A newly designed 3-dimensional printer-based gastric hemostasis simulator with two modules for endoscopic trainees (with Video). *Gut Liver*, 13(4): 415–420.

http://doi.org/10.5009/gnl18389

65. Lee S, Ahn JY, Han M, *et al.*, 2018, Efficacy of a three-dimensional-printed training simulator for endoscopic biopsy in the stomach. *Gut Liver*, 12(2): 149–157.

http://doi.org/10.5009/gnl17126

66. Gallo C, Boškoski I, Matteo MV, *et al.*, 2021, Training in endoscopic retrograde cholangio-pancreatography: A critical assessment of the broad scenario of training programs and models. *Expert Rev Gastroenterol Hepatol*, 15(6): 675–688.

http://doi.org/10.1080/17474124.2021.1886078

67. Kwon CI, Shin Y, Hong J, *et al.*, 2020, Production of ERCP training model using a 3D printing technique (with video). *BMC Gastroenterol*, 20(1): 145.

http://doi.org/10.1186/s12876-020-01295-y

68. Holt BA, Hearn G, Hawes R, *et al.*, 2015, Development and evaluation of a 3D printed endoscopic ampullectomy training model (with video). *Gastrointest Endosc*, 81(6): 1470–1475.

http://doi.org/10.1016/j.gie.2015.03.1916

69. Zizer E, Roppenecker D, Helmes F, *et al.*, 2016, A new 3D-printed overtube system for endoscopic submucosal dissection: first results of a randomized study in a porcine model. *Endoscopy*, 48(8): 762–765.

http://doi.org/10.1055/s-0042-104345

70. Ko WJ, Song GW, Hong SP, *et al.*, 2016, Novel 3D-printing technique for caps to enable tailored therapeutic endoscopy. *Dig Endosc*, 28(2): 131–138.

http://doi.org/10.1111/den.12546

71. Walter BM, Hann A, Frank R, *et al.*, 2017, A 3D-printed cap with sideoptics for colonoscopy: A randomized ex vivo study. *Endoscopy*, 49(8): 808–812.

http://doi.org/10.1055/s-0043-105071

72. Yzet C, Rivory J, Mochet M, *et al.*, 2022, A 3D-printed innovative pedal fixator for connecting different pedal-operated tools to improve work ergonomics during advanced diagnostic and therapeutic endoscopic procedures. *Endoscopy*, 54(11): E650–E651.

http://doi.org/10.1055/a-1732-7477

73. Maeda M, Kanai N, Kobayashi S, *et al.*, 2015, Endoscopic cell sheet transplantation device developed by using a 3-dimensional printer and its feasibility evaluation in a porcine model. *Gastrointest Endosc*, 82(1): 147–152.

http://doi.org/10.1016/j.gie.2015.01.062

74. Diemer P, Markoew S, Le DQ, *et al.*, 2015, Poly-ε-caprolactone mesh as a scaffold for in vivo tissue engineering in rabbit esophagus. *Dis Esophagus*, 28(3): 240–245.

http://doi.org/10.1111/dote.12172

75. Park SY, Choi JW, Park JK, *et al.*, 2016, Tissue-engineered artificial oesophagus patch using three-dimensionally printed polycaprolactone with mesenchymal stem cells: A preliminary report. *Interact Cardiovasc Thorac Surg*, 22(6): 712–717.

http://doi.org/10.1093/icvts/ivw048

76. Chung EJ, Ju HW, Yeon YK, *et al.*, 2018, Development of an omentum-cultured oesophageal scaffold reinforced by a 3D-printed ring: Feasibility of an in vivo bioreactor. *Artif Cells Nanomed Biotechnol*, 46(sup1): 885–895.

http://doi.org/10.1080/21691401.2018.1439039

77. Kim IG, Wu Y, Park SA, *et al.*, 2019, Tissue-engineered esophagus via bioreactor cultivation for circumferential esophageal reconstruction. *Tissue Eng Part A*, 25(21–22): 1478–1492.

http://doi.org/10.1089/ten.TEA.2018.0277

78. Park H, Kim IG, Wu Y, *et al.*, 2021, Experimental investigation of esophageal reconstruction with electrospun polyurethane nanofiber and 3D printing polycaprolactone scaffolds using a rat model. *Head Neck*, 43(3): 833–848.

http://doi.org/10.1002/hed.26540

79. Ha DH, Chae S, Lee JY, *et al.*, 2021, Therapeutic effect of decellularized extracellular matrix-based hydrogel for radiation esophagitis by 3D printed esophageal stent. *Biomaterials*, 266: 120477.

http://doi.org/10.1016/j.biomaterials.2020.120477

80. Kim SD, Kim IG, Tran HN, *et al.*, 2021, Three-dimensional printed design of antibiotic-releasing esophageal patches for antimicrobial activity prevention. *Tissue Eng Part A*, 27(23–24): 1490–1502.

http://doi.org/10.1089/ten.TEA.2020.0268

81. Fouladian P, Kohlhagen J, Arafat M, *et al.*, 2020, Three-dimensional printed 5-fluorouracil eluting polyurethane stents for the treatment of oesophageal cancers. *Biomater Sci*, 8(23): 6625–6636.

http://doi.org/10.1039/d0bm01355b

82. Rudolph SE, Longo BN, Tse MW, *et al.*, 2022, Crypt-Villus scaffold architecture for bioengineering functional human intestinal epithelium. *ACS Biomater Sci Eng*, 8(11): 4942–4955.

http://doi.org/10.1021/acsbiomaterials.2c00851

83. Taebnia N, Zhang R, Kromann EB, *et al.*, 2021, Dual-material 3D-printed intestinal model devices with integrated Villi-like scaffolds. *ACS Appl Mater Interfaces*, 13(49): 58434–58446.

http://doi.org/10.1021/acsami.1c22185

84. Boys AJ, Barron SL, Tilev D, *et al.*, 2020, Building scaffolds for tubular tissue engineering. *Front Bioeng Biotechnol*, 8: 589960.

http://doi.org/10.3389/fbioe.2020.589960

85. Tan YJ, Yeong WY, Tan X, *et al.*, 2016, Characterization, mechanical behavior and in vitro evaluation of a melt-drawn scaffold for esophageal tissue engineering. *J Mech Behav Biomed Mater*, 57: 246–259.

http://doi.org/10.1016/j.jmbbm.2015.12.015

86. Lee SC, Gillispie G, Prim P, *et al.*, 2020, Physical and chemical factors influencing the printability of hydrogel-based extrusion bioinks. *Chem Rev*, 120(19): 10834–10886.

http://doi.org/10.1021/acs.chemrev.0c00015

87. Suntornnond R, Ng WL, Huang X, *et al.*, 2022, Improving printability of hydrogel-based bio-inks for thermal inkjet bioprinting applications via saponification and heat treatment processes. *J Mater Chem B*, 10(31): 5989–6000.

http://doi.org/10.1039/d2tb00442a

88. Ng WL, Lee JM, Zhou M, *et al.*, 2020, Vat polymerization-based bioprinting-process, materials, applications and regulatory challenges. *Biofabrication*, 12(2): 022001.

http://doi.org/10.1088/1758-5090/ab6034

89. Takeoka Y, Matsumoto K, Taniguchi D, *et al.*, 2019, Regeneration of esophagus using a scaffold-free biomimetic structure created with bio-three-dimensional printing. *PloS one*, 14(3): e0211339.

http://doi.org/10.1371/journal.pone.0211339

90. Madden LR, Nguyen TV, Garcia-Mojica S, *et al.*, 2018, Bioprinted 3D primary human intestinal tissues model aspects of native physiology and ADME/Tox functions. *iScience*, 2: 156–167.

http://doi.org/10.1016/j.isci.2018.03.015

91. Maina RM, Barahona MJ, Geibel P, *et al.*, 2021, Hydrogel-based 3D bioprints repair rat small intestine injuries and integrate into native intestinal tissue. *J Tissue Eng Regen Med*, 15(2): 129–138.

http://doi.org/10.1002/term.3157

92. Kim W, Kim G, 2018, Intestinal villi model with blood capillaries fabricated using collagen-based bioink and dual-cell-printing process. *ACS Appl Mater Interfaces*, 10(48): 41185–41196.

http://doi.org/10.1021/acsami.8b17410

93. Kim W, Kim GH, 2020, An intestinal model with a finger-like villus structure fabricated using a bioprinting process and collagen/SIS-based cell-laden bioink. *Theranostics*, 10(6): 2495–2508.

http://doi.org/10.7150/thno.41225

94. Yan M, Lewis PL, Shah RN, 2018, Tailoring nanostructure and bioactivity of 3D-printable hydrogels with self-assemble peptides amphiphile (PA) for promoting bile duct formation. *Biofabrication*, 10(3): 035010.

http://doi.org/10.1088/1758-5090/aac902

95. Boyer CJ, Boktor M, Samant H, *et al.*, 2019, 3D printing for bio-synthetic biliary stents. *Bioengineering (Basel, Switzerland)*, 6(1).

http://doi.org/10.3390/bioengineering6010016

96. Yang H, Sun L, Pang Y, *et al.*, 2021, Three-dimensional bioprinted hepatorganoids prolong survival of mice with liver failure. *Gut*, 70(3): 567–574.

http://doi.org/10.1136/gutjnl-2019-319960

97. Pien N, Palladino S, Copes F, *et al.*, 2022, Tubular bioartificial organs: From physiological requirements to fabrication processes and resulting properties. A critical review. *Cells Tissues Organs*, 211(4): 420–446.

http://doi.org/10.1159/000519207

98. Yeleswarapu S, Chameettachal S, Pati F, 2021, Integrated 3D printing-based framework-A strategy to fabricate tubular structures with mechanocompromised hydrogels. *ACS Appl Biomater*, 4(9): 6982–6992.

http://doi.org/10.1021/acsabm.1c00644

99. Han H, Park Y, Choi YM, *et al.*, 2022, A bioprinted tubular intestine model using a colon-specific extracellular matrix bioink. *Adv Healthc Mater*, 11(2): e2101768.

http://doi.org/10.1002/adhm.202101768

100. Nam H, Jeong HJ, Jo Y, *et al.*, 2020, Multi-layered free-form 3D cell-printed tubular construct with decellularized inner and outer esophageal tissue-derived bioinks. *Sci Rep*, 10(1): 7255.

http://doi.org/10.1038/s41598-020-64049-6

101. Pi Q, Maharjan S, Yan X, *et al.*, 2018, Digitally tunable microfluidic bioprinting of multilayered cannular tissues. *Adv Mater*, 30(43): e1706913.

http://doi.org/10.1002/adma.201706913

102. Zhao W, Xu T, 2020, Preliminary engineering for in situ in vivo bioprinting: A novel micro bioprinting platform for in situ in vivo bioprinting at a gastric wound site. *Biofabrication*, 12(4): 045020.

http://doi.org/10.1088/1758-5090/aba4ff

103. Thai MT, Phan PT, Tran HA, *et al.*, 2023, Advanced soft robotic system for in situ 3D bioprinting and endoscopic surgery. *Adv Sci*, 10(12): e2205656.

http://doi.org/10.1002/advs.202205656

104. Wijnen N, Brouwers L, Jebbink EG, *et al.*, 2021, Comparison of segmentation software packages for in-hospital 3D print workflow. *J Med Imaging*, 8(3): 034004.

http://doi.org/10.1117/1.Jmi.8.3.034004

105. Yu C, Jiang J, 2020, A perspective on using machine learning in 3D bioprinting. *Int J Bioprint*, 6(1): 253.

http://doi.org/10.18063/ijb.v6i1.253

106. Tian S, Stevens R, McInnes BT, *et al.*, 2021, Machine assisted experimentation of extrusion-based bioprinting systems. *Micromachines*, 12(7).

http://doi.org/10.3390/mi12070780

107. Shin J, Lee Y, Li Z, *et al.*, 2022, Optimized 3D bioprinting technology based on machine learning: A review of recent trends and advances. *Micromachines*, 13(3).

http://doi.org/10.3390/mi13030363

108. Lee J, Oh SJ, An SH, *et al.*, 2020, Machine learning-based design strategy for 3D printable bioink: Elastic modulus and yield stress determine printability. *Biofabrication*, 12(3): 035018.

http://doi.org/10.1088/1758-5090/ab8707

109. Dhir V, Itoi T, Fockens P, *et al.*, 2015, Novel ex vivo model for hands-on teaching of and training in EUS-guided biliary drainage: creation of "Mumbai EUS" stereolithography/3D printing bile duct prototype (with videos). *Gastrointest Endosc*, 81(2): 440–446.

http://doi.org/10.1016/j.gie.2014.09.011

ACCSCIENCE PUBLISHING

International Journal of Bioprinting

RESEARCH ARTICLE

Biomechanical evaluation of an anatomical bone plate assembly for thin patella fracture fixation fabricated by titanium alloy 3D printing

Chi-Yang Liao[1,2,3], Shao-Fu Huang[1,4], Wei-Che Tsai[1], Yu-Hui Zeng[1], Chia-Hsuan Li[1,4], and Chun-Li Lin[1,4]*

[1]Department of Biomedical Engineering, National Yang Ming Chiao Tung University, Taipei, Taiwan

[2]Department of Orthopedics, Tri-Service General Hospital Songshan Branch, National Defense Medical Center, Taipei, Taiwan

[3]Department of Surgery, Tri-Service General Hospital Songshan Branch, National Defense Medical Center, Taipei, Taiwan

[4]Medical Device Innovation and Translation Center, National Yang Ming Chiao Tung University, Taipei 112, Taiwan

Abstract

This study established and evaluated the feasibility of a three-dimensional (3D)-printed titanium anatomical surface with adjustable thin bone plate assembly (AATBP) for patella fracture fixation. The AATBP was 1.6 mm in thickness and divided into a proximal plate (PP) with locking screw holes and a distal plate (DP) (0.4 mm in thickness) with compressive screw holes for assembly using a ratchet mechanism to adjust the total fixation height according to the patella size. Two pairs of hooks were designed on the proximal/distal edges to allow passage through the tendon to grip the fractured fragments. 3D printing combined with Computer Numerical Control (CNC) drilling was performed to manufacture the AATBP. Four-point bending and surface roughness tests were performed to evaluate the AATBP mechanical behavior. A cyclic (300 times) load test with 15-kg weights was adopted to compare the biomechanical stability between the AATBP and conventional tension band wiring (TBW) fixations. A parallel finite element (FE) analysis was achieved to understand the fracture gap and bone stress in the two different fixations on a transverse patella fracture. The result showed that the maximum AATBP manufacturing error was 3.75%. The average fracture gaps on the medial/lateral sides after cyclic loads were 2.38 ± 0.57 mm/2.30 ± 0.30 mm for TBW and 0.03 ± 0.01 mm/0.06 ± 0.03 mm for AATBP fixations. The same trend occurred in the FE simulation. This study confirmed that a complicated thin bone plate, including the anatomical surface, hooks, and ratchet with size-adjustable characteristics, can be fabricated using metal 3D printing with acceptable manufacturing error and reasonable anatomical surface/thin bone plate assembly fitness. Biomechanical cyclic tests and FE simulation showed that the AATBP fixation is superior to the conventional TBW for patella transverse fractures.

Keywords: Metal 3D printing; Anatomical surface; Assembly; Patella fracture; Bone plate

***Corresponding author:**
Chun-Li Lin
(cllin2@nycu.edu.tw)

Citation: Huang S-F, Tsai W-C, Zeng Y-H, *et al*., 2023, Biomechanical evaluation of an anatomical bone plate assembly for thin patella fracture fixation fabricated by titanium alloy 3D printing. *Int J Bioprint*, 9(6): 0117. https://doi.org/10.36922/ijb.0117

Received: April 5, 2023
Accepted: June 17, 2023
Published Online: July 18, 2023

Copyright: © 2023 Author(s). This is an Open Access article distributed under the terms of the Creative Commons Attribution License, permitting distribution, and reproduction in any medium, provided the original work is properly cited.

Publisher's Note: AccScience Publishing remains neutral with regard to jurisdictional claims in published maps and institutional affiliations.

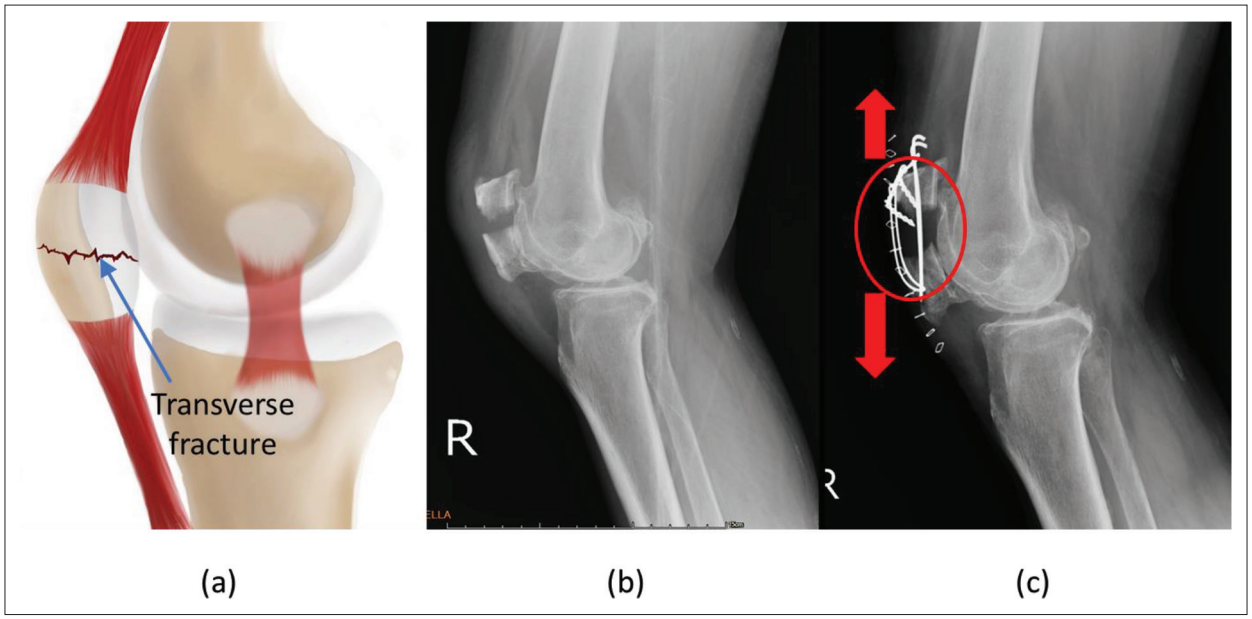

Figure 1. (a) Illustration of transverse fracture of the patella. (b) X-ray image of transverse fracture of the patella before surgery. (c) Fractured fragments cannot be fixed stably, and a gap was generated 2 weeks after surgery using a conventional band wire.

1. Introduction

Transverse fractures are the most common type of patella fractures in those aged between 30 and 60 years old[1-5]. Surgical intervention with anterior tension band wiring (TBW) (using K-wires directly or cannulated lag screws) is necessary to reposition the articulating surface, achieve early mobilization, and reconstruct extensor function. However, clinical complications including fixation failure, migration, and skin irritation arise, requiring revision surgery with implant removal in up to 65% of cases[4,6-8]. Although a bilateral fixed-angle plate was introduced to provide greater stiffness and lower fracture gap dehiscence for transverse patella fractures[3], problems emerged with inaccurate pre-bending and alignment, bone screw interference, and lack of holding power for bone fragments[4].

As the patella functions as a transmitter of tensile forces generated by the quadriceps muscles and as an effective lever arm for the knee extensor mechanism, patella integrity is crucial for proper knee function and physiological locomotion[9]. The enormous tensile force on the patella generated by the quadriceps and patellar tendons cannot restore the fracture fragments effectively, representing the key failure in surgical treatment using traditional band wire fixation (Figure 1)[3,4,10].

In a suitable patella fracture fixation plate design, there is a need to ensure enough holding power to effectively restore and fix the proximal and distal fractured fragments. It has been suggested that a hook mechanism should be used while providing a compressive effect on the fractured bone fragments to maintain structural stability[11,12]. Moreover, the anatomical shape and adjustable size need to be considered for patella anterior surface fitness and variation in size. It is essential that the fixation bone plate be designed as thin as possible to avoid clinical irritation because the patella is very close to the skin. Whether these complicated mechanical structures can be processed using three-dimensional (3D) printing is an important issue to be resolved.

This study developed a titanium 3D-printed anatomical contour bone plate with hook mechanisms and size adjustable assembly thin bone plates (AATBP) for patella fracture fixation. The anatomical surface/thin bone plate assembly fitness, manufacturing error, and bending/surface roughness tests for the AATBP were evaluated to understand the capability of metal 3D printing and bone plate mechanical behavior. Cyclic load tests and finite element (FE) analysis were performed to compare the biomechanical stability between this specifically designed osteosynthesis system and the conventional anterior TBW for use on transverse patella fractures.

2. Materials and methods

2.1. AATBP design

We designed a fractured patella fixation bone plate and noted an AATBP with a fixed medial–lateral width and adjustable height in the proximal–distal direction with an anatomically curved surface. The AATBP anatomical

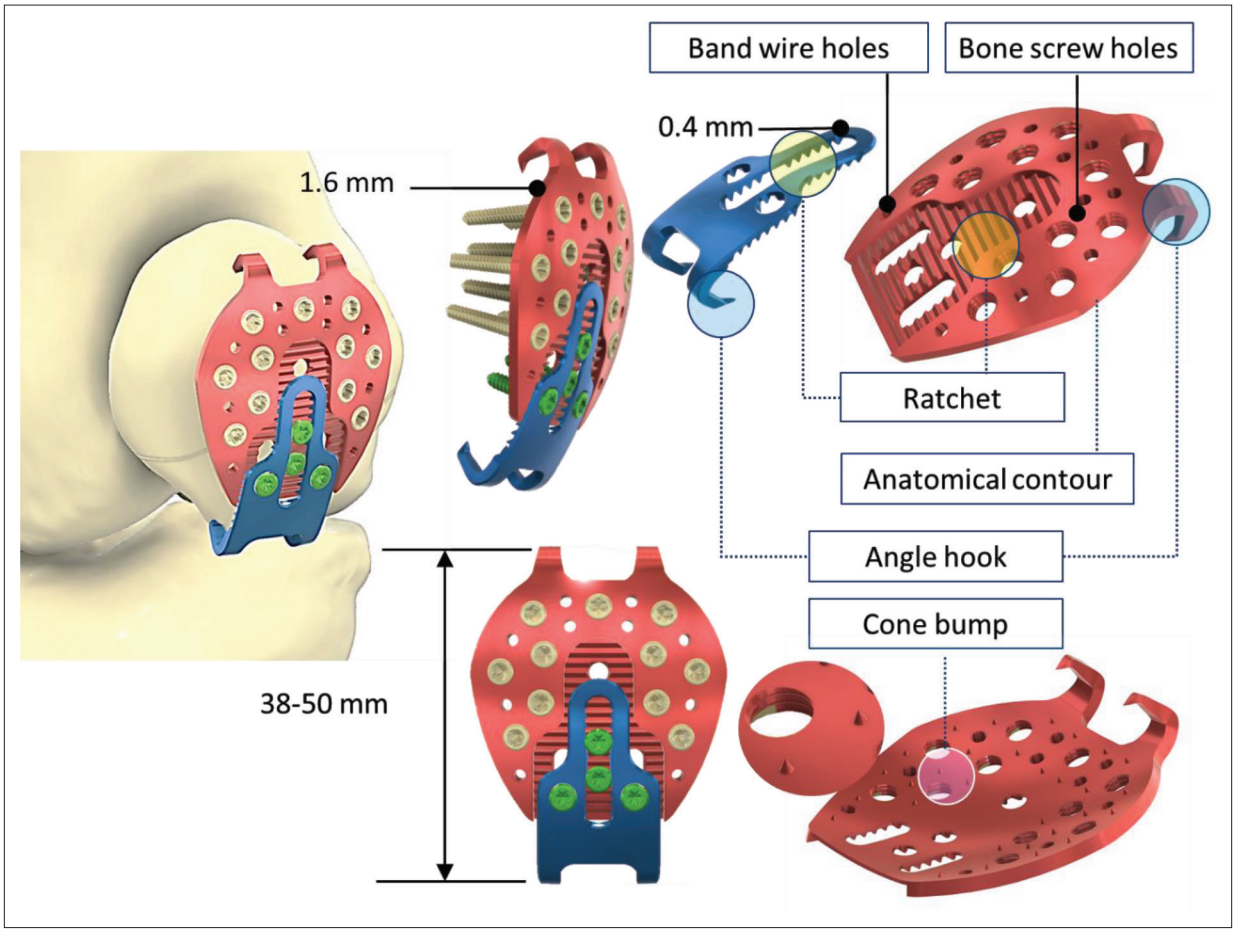

Figure 2. AATBP design concept with an anatomical curved surface of 1.6-mm thickness, including a DP with 0.4-mm thickness to ratchet onto the proximal plate (PP) for height adjustment.

curved surface was intended to adaptively fit to the patella surface curvature. The curved surface was obtained using a standard artificial patella made of polyurethane foam (Sawbones; Pacific Research Laboratories Inc., Vashon, WA, USA). This was used to capture the patella surface via a computed tomography (CT) scan, followed by reconstruction in image processing software (Mimics 22.0; Materialize NV, Leuven, Belgium). The AATBP thickness was designed to be 1.6 mm, which was divided into two thin pieces at the proximal and distal parts. The distal plate (DP; 0.4 mm in thickness) can be ratcheted and assembled onto the center of the proximal plate (PP). These two plates can be adjusted to extend the fixation total height from 38 to 50 mm to fit the relative positions according to the patella size (Figure 2).

Two pairs of hooks were designed onto the DP and PP edges that can pass through the tendon to grip the fractured patella fragments. Eleven locking and two compressive screw holes (2.4 mm in diameter) with medial–lateral symmetry in the PP and DP, respectively, were also created to allow selective bone screw insertion to fix the AATBP to the fractured patella. A straight slot in the DP was also designed to allow the screw insertion accompanied by the adjustment of AATBP height. Ten 1.5-mm wire holes were created in the PP to allow the band wire to pass through, thereby enhancing the fixation capability when necessary. Cone bumps with a height of 0.6 mm were designed and randomly distributed onto the back of the PP, i.e., the surface contacting the bone surface, to increase bone plate and patella retention (Figure 2).

To verify the AATBP anatomical surface design feasibility, we randomly selected two males (48 and 71 years old) and one female (74 years old) from the CT database and reconstructed their complete and normal patella image models. The AATBP and three normal patella models were imported into CAD software (PTC Creo V6.0; PTC Inc., Needham, MA, USA) to evaluate the fitness (gap distances) between AATBP and three normal patellae on the inferior surface. The AATBP midline and each patella were aligned first. The total height (proximal–

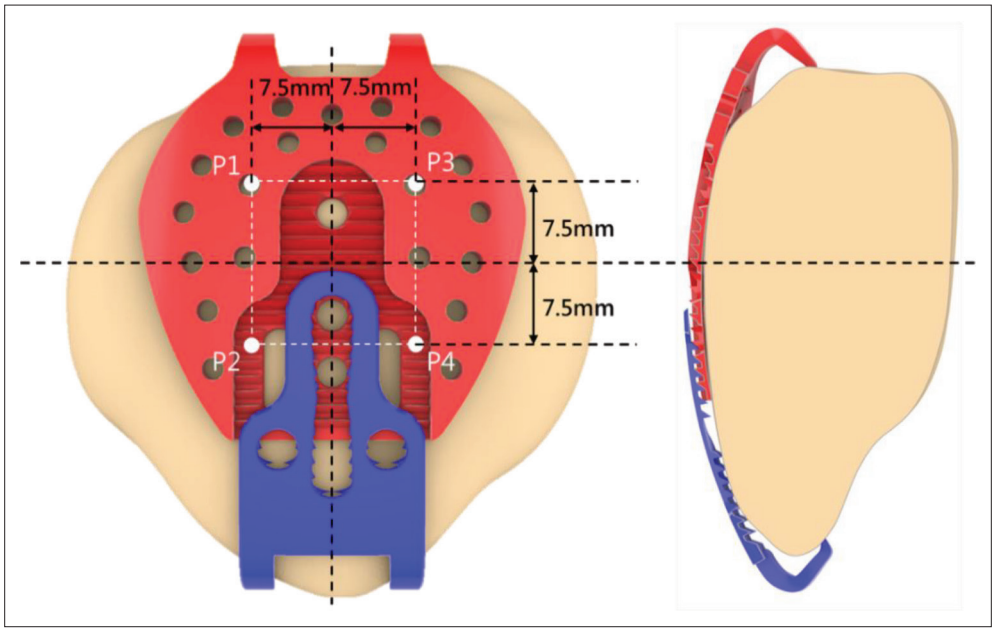

Figure 3. Illustration of the gap distance measurement between the AATBP and the patella at the positions of the four vertices of a 15 mm × 15 mm square in the AATBP center.

distal direction) of the AATBP was adjusted using its attached ratchet to allow two pairs of hooks to grip at relative positions on the proximal and distal ends of the three patellae. The gap distances between the AATBP and each patella at four vertices of a 15 mm × 15 mm square defined the AATBP center (Figure 3).

2.2. AATBP 3D printing

The AATBP without screw holes was manufactured using selective laser melting of a metal powder bed fusion machine (AM250; Renishaw, Wotton-under-Edge, UK), noted as a 3D printing system with commercial titanium alloy powder (diameter of Ti6Al4V powder ranges between 15 μm and 45 μm). The 3D printing system was operated at a laser power of 400 W, a scanning rate of 0.6 m/s, and an exposure time of 125 s[13]. The metal powder was selectively scanned and melted by a laser during the process. The component was complete after the powder was crystallized. In the present study, the manufacturing accuracy, hatching space, and layer thickness were 30, 90, and 30 μm, respectively. The 3D-printed AATBP surface burring without screw holes was removed and polished using a magnetic polisher with stainless steel pins (Ø =1 mm, L = 3 mm) at a speed of 2,700 rpm. The device was then cleaned using ultrasonic oscillations (Figure 4)[13].

There were high demands for screw holes with thread accuracy down to 0.02 mm and screw hole surface without cracks. All PP and DP screw holes were generated using traditional XXX (CNC) positioning drilling to control the manufacturing accuracy within a small error margin and enable the commercial screw to fit the hole within an acceptable error range.

Our 3D printer and CNC machining laboratories were certified under the Good Manufacturing Practice (GMP) quality management system (Certificate Number: QMS0940; A Plus Biotechnology Co. Ltd, Taipei, Taiwan). This ensured that the bone plate manufactured using 3D printing and CNC drilling can provide a practical foundation for approaches that meet GMP regulations, such as printing biocompatible materials in a biologically safe manner to meet the ISO10993 standard, as well as demonstrating a commitment to safety and quality.

The AATBP in this study was designed using computer-aided design (CAD) software. The detailed dimensions of all AATBP features in the CAD software were defined as the actual dimensions. The height, width, and thickness dimensions of the PP and DP as well as the ratchet and cone height pitch (shown in Figure 5 and defined in Table 1) were measured using a precision measuring system (ARCS Precision Technology Co., Ltd., Taiwan) on three randomly selected AATBP samples and compared with the corresponding actual values. We defined that the error for each dimension to be within 5%, namely the printed accuracy of our assembly bone plate should meet the requirements for implant manufacture.

2.3. AATBP bending strength and surface roughness tests

To provide a comprehensive mechanical strength reference for the AATBP used in the patella fracture cases, four-point

Figure 4. (a) 3D-printed AATBP prototypes without screw/wire holes and (b) 3D-printed AATBP with back cone bump after screw/wire holes generation by CNC machining.

bending tests were carried out according to the American Society for Testing and Materials (ASTM) protocols (ASTM F382-17), which are the main reference methods for FDA-approved bone plate functional testing[14].

Static testing was performed using the Instron E10000 testing machine (INSTRON, Canton, MA, USA) to obtain the sample proof load and bending strength (Figure 6). The rigid extension segments used to effectively lengthen the bone plate due to the AATBP do not have a symmetrical section and require a sufficiently long symmetrical section. The geometric profile at the proximal and distal sides of the rigid extension segments for the AATBP were designed according to geometric features of their corresponding contact bone plate and fabricated using a metal 3D printer.

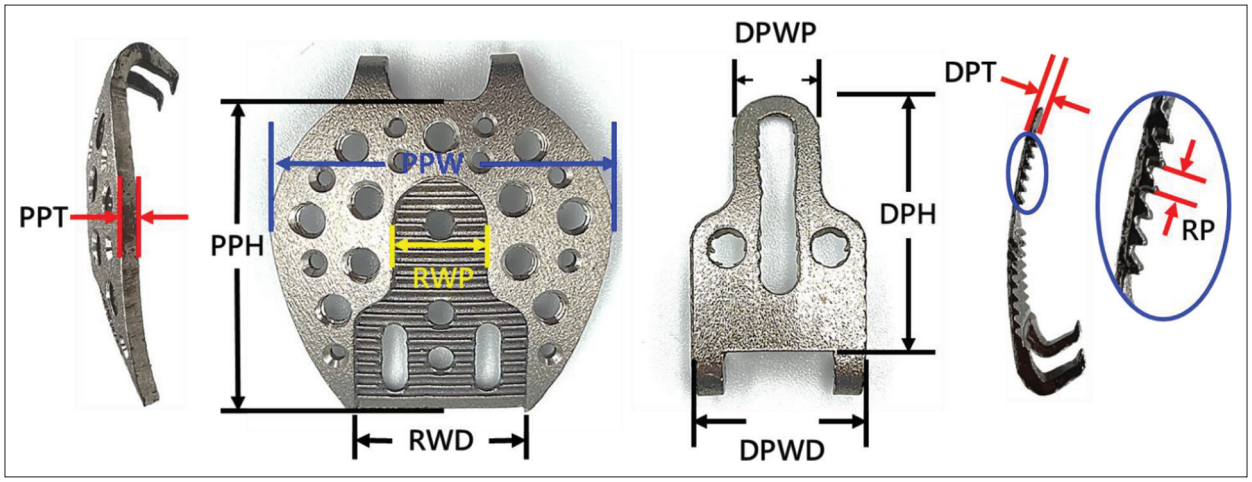

Figure 5. Illustration of all detailed dimensions.
Abbreviations: PPT: proximal plate thickness; PPW: proximal plate width; PPH: proximal plate height; RWP: ratchet width in the proximal side; RWD: ratchet width in the distal side; DPH: distal plate height; DPWP: distal plate width in the proximal side; DPWD: distal plate width in the distal side; DPT: distal plate thickness; RP: ratchet pitch.

Table 1. Detailed dimension verification between 3D printed manufacturing and CAD (true) for AATBP

Item	PPT	PPW	PPH	RWP	RWD	DPH	DPWP	DPWD	DPT	RP
CAD	1.60	34.3	32.3	9.40	17.6	25.6	8.30	16.5	0.43	1.30
3DP (Avg.)	1.66	34.4	32.1	9.50	17.5	25.5	8.50	16.6	0.44	1.32
Abs error (%)	3.75	0.29	0.62	1.06	0.57	0.39	2.41	0.61	2.33	1.54

Unit: mm
Abbreviations: 3DP: 3D printing; CAD: computer-aided design; PPT: proximal plate thickness; PPW: proximal plate width; PPH: proximal plate height; RWP: ratchet width in the proximal side; RWD: ratchet width in the distal side; DPH: distal plate height ; DPWP: distal plate width in the proximal side; DPWD: distal plate width in the distal side; DPT: distal plate thickness; RP: ratchet pitch.

The bone plate was fixed onto the corresponding rigid extension segments, and the loading rollers contacted the rigid extension segments of the test setup during the test (Figure 6). Center span (a) is the distance between the loading rollers, and the loading span distance (h) is the distance between the loading roller and nearest support roller. The corresponding distances for a and h for the AATBP were both 40 mm (Figure 6). Three samples were placed on the four-point bending test clamp to load at a cross-head rate of 0.05 mm/s until failure occurred. The proof load (P) (the intersection line of a 0.2% offset from the linear portion of the load–displacement curve) and the bending strength were obtained from multiplying the proof load by the loading span distance (h) and dividing by 2 ($P \times h/2$), according to the ASTM F382 standard test method. The failure pattern for each sample was examined visually to assess the failure mechanism (Figure 6).

Surface roughness (Ra) on the three AATBPs randomly selected from all plates were measured on the L1, L2 (interior surface), and L3 (posterior surface) segments of PP and L4 (interior surface) segment on the DP using a portable measuring instrument with 6×10^{-3} μm resolution (SJ-210, Mitutoyo Co, Ltd., Tokyo, Japan) to understand the surface roughness of 3D-printed components (Table 2).

2.4. Biomechanical static/dynamic testing

3D CAD models of the patella and corresponding femoral condyle reconstructed from Sawbone CT images were fabricated using a 3D printer (Dimension 1200es SST; Stratasys, Ltd., Eden Prairie, MN, USA) with acrylonitrile butadiene styrene (ABS) material (ABS-P430; Stratasys, Ltd.). Fifteen ABS patellae were identically osteotomized horizontally in the center to mimic a transverse fracture and passed through a polyester tension belt (25 mm in width) loop, which plays the role of quadriceps and patellar tendons. The fractured patellae were divided randomly into three groups (5 per group) to perform the static/dynamic biomechanical tests for conventional TBW and the dynamic AATBP fixations, as described below according to the groups.

For the TBW fixation sample, two K-wires (Syntec Scientific Co., Taiwan) of 2.0 mm in diameter were inserted orthogonally into the patella osteotomy plane and parallel to each other on its medial 1/3 and lateral 1/3. The roll

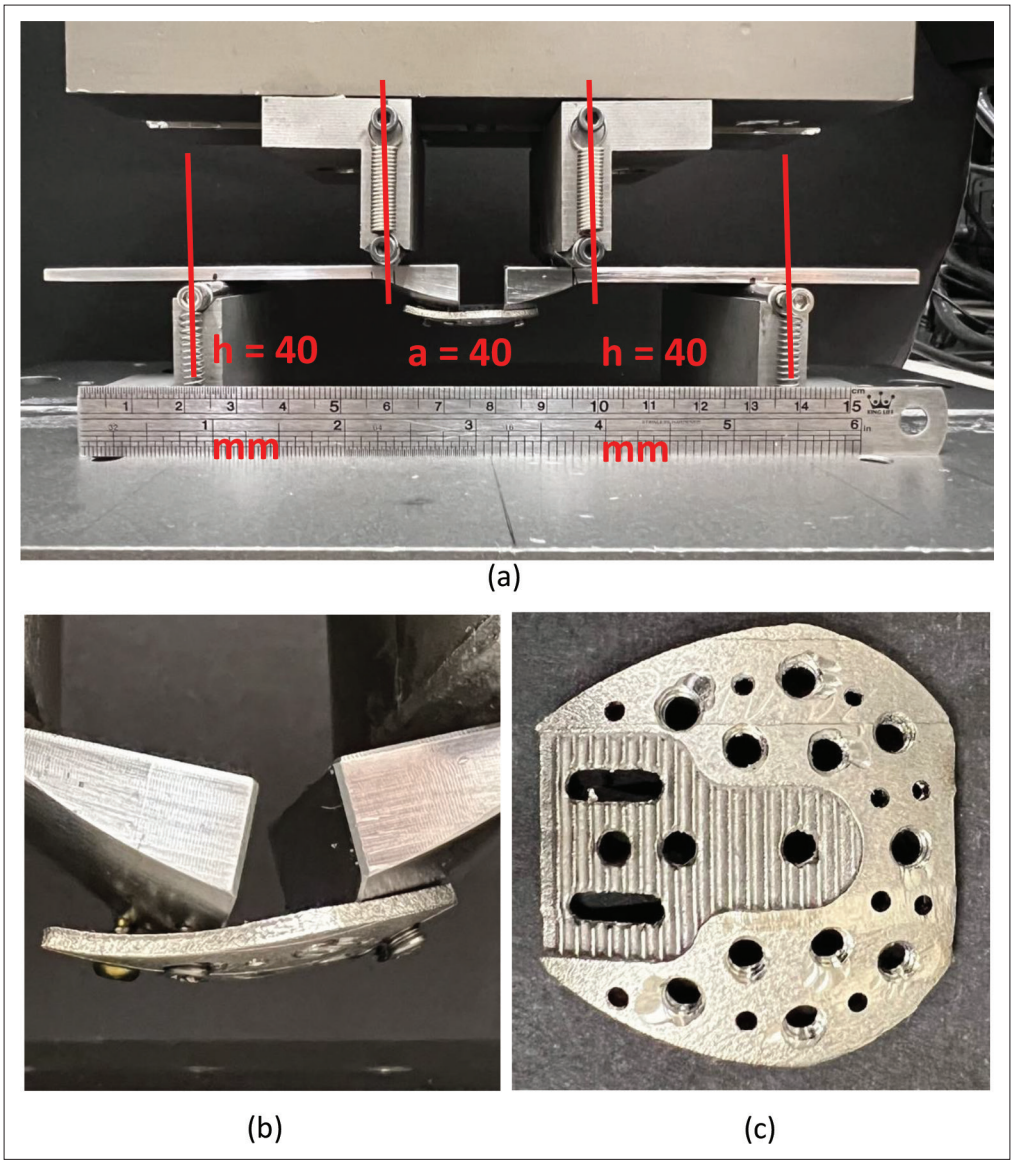

Figure 6. (a) Illustration of the four-point bending test according to ASTM F382; the AATBP was fixed onto the corresponding rigid extension segments; the loading rollers contacted the rigid extension segments of the test setup during the test; (b) locking screw loosening after test; and (c) the position of the AATBP damage.

wire loop (Syntec Scientific Co., Taiwan) with a diameter of 1.25 mm was laid around the protruding K-wire ends, forming a figure-of-eight on the patella anterior surface. Two knots were twisted into the distal part of the K-wire and tightened. The proximal part of the K-wire was bent, cut, and impacted to ensure its complete contact with the ABS bone surface (Figure 7a)[15].

For AATBP fixation, PP and DP were adjusted to the assembly using a ratchet mechanism for fitting the patella height (about 46.8 mm) and holding the fractured fragments by the corresponding hook pairs passing through the belt. The AATBP curved surface can be adjusted as much as possible to coincide with the anterior curved surface of the patella before being secured. Five locking and three compressive screws of 2.4 mm in diameter (A Plus Biotechnology Co. Ltd, Taipei, Taiwan) distributed with medial–lateral symmetry were inserted into PP and DP, respectively, to fix the fractured patella. These screws spanned the fracture gap (Figure 7a).

To evaluate the PP and distal DP assembly flatness through the ratchet teeth, three AATBPs were randomly selected and erected to allow the anterior surface to be positioned parallel to the ARCS light source. This allowed assembly tightness error measurement between the two

Table 2. Surface roughness measured positions for the AATBP and corresponding obtained results

	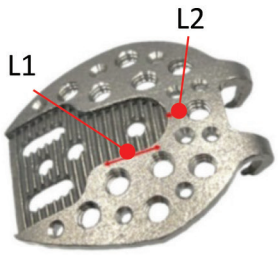	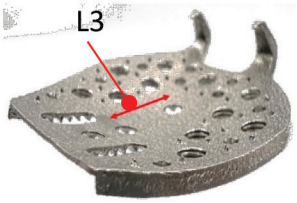	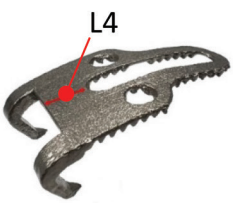	
Sample 1	4.135	5.960	5.454	3.323
Sample 2	4.427	5.495	4.438	3.545
Sample 3	4.698	5.325	6.264	3.824
Mean ± Std (μm)	4.42 ± 0.28	5.59 ± 0.33	5.39 ± 0.91	3.56 ± 0.25

Unit: μm

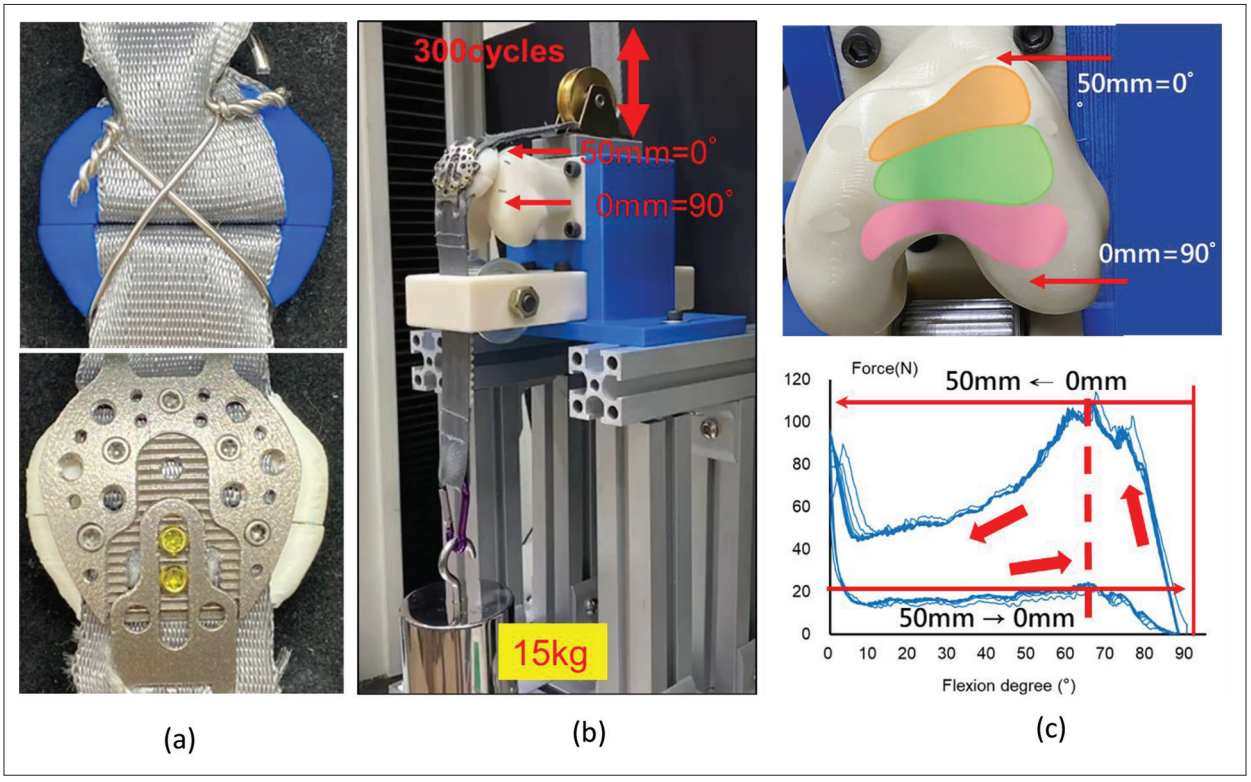

Figure 7. (a) Samples using TBW (top) and AATBP (down) fixation for fractured patella. (b) Dynamic biomechanical testing device. (c) Position-controlled stroke of corresponding femur contact positions (top) from 0° to 90° (50 mm to 0 mm) knee flexion and back to 0° (0 mm to 50 mm) (down) extension in each cycle at a constant velocity.

thin bone plates at the proximal and distal positions (Figure 8).

Five TBW and one AATBP fixation samples were clamped vertically on the Instron machine. A 20 N preload was necessary to reflect the fact that the tension belt loop needed to be extended to a point at which a linear increase in the force–displacement diagrams could be observed. Static tensile failure tests on each sample were performed with 5 mm/min speed until the fracture gap exceeded 2 mm, and the force–displacement diagram was recorded. Note that the force corresponding to the region in the diagram has volatility.

For the dynamic tests, all patellae were evaluated in simulated 90° knee flexion to 0° full extension using a

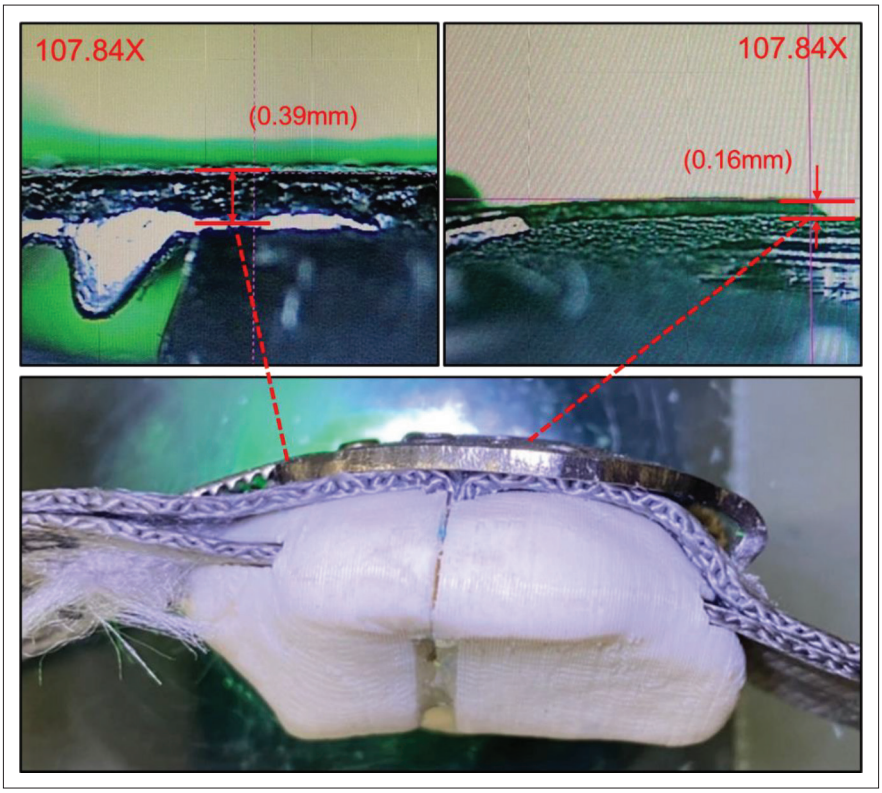

Figure 8. Assembly tightness error measurement between the PP and DP at the proximal (top-right) and distal positions (top-left).

printed ABS femur condyle as a pivot point following the biomechanical model from the literature (Figure 7b and c)[2,3,4,16]. Tension was applied via the previously attached polyester belt loop, and corresponding proximal (quadriceps tendon) and distal (patella tendon) belts were connected to the Instron load cell and the 15-kg (about 150 N) vertical downward weight, respectively. Each cycle load test simulated the patella–femur contact positions from 90° knee flexion (set travel distant was 0 mm) and back to 0° full extension (travel distant was 50 mm) with a constant velocity of 5 mm/s. Another five TBW and AATBP fixation samples were tested subsequently for 300 cycles by carrying out a position-controlled (50 mm) stroke. The quadriceps tendon force obtained from the load cell relative to flexion–extension stroke displacement in each load cycle was recorded and plotted (Figure 7c). In addition, the fracture gap was measured at the medial and lateral border of each patella before and after the last testing cycle using a digital caliper.

2.5. Finite element analysis

The 3D CAD models of the transverse fracture patella matched the conventional TBW (included K-wire and figure-of-eight roll wire loop), and the AATBP fixations were generated and imported into the ANSYS Workbench (V18, Swanson Analysis, Houston, Pennsylvania, USA). Two FE models of the transverse fracture patella fixed with TBW and AATBP were generated with quadratic 10-node tetrahedral structural solid elements and a total of 44099/181769 elements and 72721/314783 nodes for TBW/AATBP models, respectively (Figure 9). Frictional contact elements with different coefficients of friction were adopted from the literature to simulate the contact behaviors on bone–bone (at the fracture site), AATBP–bone, and wire–bone surfaces[17-20]. The corresponding values were 0.45, 0.3, and 0.3, respectively. Cortical, cancellous bones, AATBP, fixation screws, and K-wire were defined with linear elastic and isotropic properties adopted from the relevant literature. The wire loop material property was considered as a bi-linear hardening plastic behavior to mimic the permanent deformation of stainless wire, and the yield stress and tangent modulus were also adopted from the literature[17-20].

Nodes on the patella proximal side (base) were constrained in all directions as the boundary conditions. A tension force of 150 N similar to the load condition in the biomechanical test was applied to the patellar apex parallel to the long axis to mimic patella tendon force (Figure 9)[17-20]. The articulating part of the distal femur was not taken into account in this FE analysis, and thus, relevant data was obtained from the literature[17-20]. The inferior patella

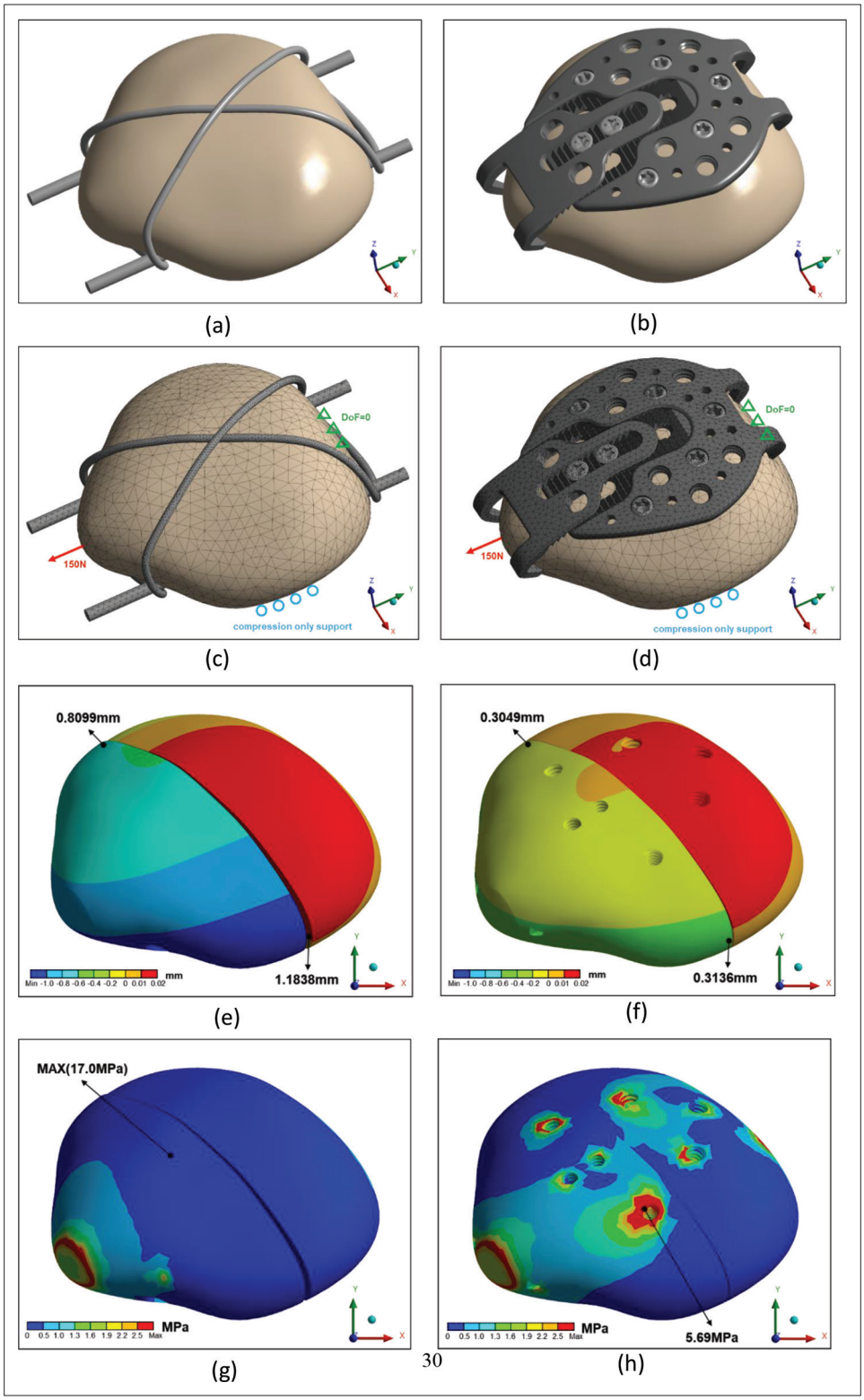

Figure 9. (a) The solid mode for TBW fixation; (b) the solid model for AATBO fixation; (c) the mesh model for TBW TWB fixation; (d) the mesh model for AATBP fixation; (e) simulated displacement result for TBW fixation; (f) simulated displacement result for AATBP fixation; (g) simulated von Mises bone stress result for TBW fixation; and (h) simulated von Mises bone stress result for AATBP fixation.

Table 3. Results of the mean (standard deviation) gap distances between AATBP and each of the patella surfaces at the positions of the four vertices (P1, P2, P3, and P4)

	P1	P2	P3	P4
Sample 1	0.50	0.41	0.09	1.01
Sample 2	0.30	0.73	0.11	1.14
Sample 3	1.36	0.16	0.49	0.57
Mean ± Std (mm)	0.72 ± 0.46	0.43 ± 0.23	0.23 ± 0.18	0.91 ± 0.24

Unit: mm

surface was defined as a compression-only support in analysis that enables the surfaces to only bear compression and not tension forces to mimic support from distal femur condyles (Figure 9). The fractured gap distances at the medial and lateral sides for two fixation models and maximum von Mises strain of bone around the screw hole were recorded.

3. Results

3.1. Design and 3D printing feasibility analysis

The mean (standard deviation) gap distance results between the AATBP and each of the patella surfaces at the positions of the four vertices (P1, P2, P3, and P4) of the 15 mm × 15 mm square for the three patellae were 0.72 ± 0.46 mm, 0.43 ± 0.23 mm, 0.23 ± 0.18 mm, and 0.91 ± 0.24 mm (Table 3). The AATBP manufacturing errors were both within 5% (maximum error of 3.75%), which showed that the metal 3D printing equipment used in this study has good precision and was suitable for medical applications (Table 1). The assembly tightness errors between the PP and DP at the proximal and distal positions were only 0.34 and 0.17 mm, respectively (Table 4).

3.2. AATBP bending strength and surface roughness

In the static four-point bending test, the values of the average proof load and bending strength for AATBP were 58.38 ± 4.51 N and 1167 ± 90.39 N·mm, respectively. The failure mode of the AATBP after static tensile test showed that the plate was damaged around the screw holes because screws were pulled out from the rigid extension segment (Figure 6b and c). The surface roughness test results showed that the mean (standard deviation) surface roughness for L1, L2, L3, and L4 segments were 4.42 ± 0.28 μm, 5.59 ± 0.33 μm, 5.39 ± 0.91 μm, and 3.56 ± 0.25 μm, respectively (Table 2).

3.3. Biomechanical static/dynamic testing

The static test for TBW fixation found that the average fractured gap distance before and after the cyclic loads was 3.06 ± 1.97 mm (>2 mm), and the corresponding force was 351.98 N. The average force of the region with a volatility in the force–displacement curve was recorded as 143.58 N (Figure 10). In contrast, the AATBP fixation force–displacement curve was found to be smooth until tensile testing stopped. The dynamic test results showed that the average fractured gap distances at the medial/lateral sides before and after cyclic load testing were 2.38 ± 0.57 mm/2.30 ± 0.30 mm for TBW and 0.03 ± 0.01 mm/0.06 ± 0.03 mm for AATBP fixations (Table 5). This showed that the variations in the fractured gap distances were significantly different between TBW and AATBP, irrespective of whether the medial or lateral side was analyzed, with all $p < 0.05$ using the Kruskal–Wallis test because sample sizes were relatively small, and it could not be determined whether the data were normally distributed. Figure 11 shows all samples fixed with TBW/AATBP after dynamic testing to show the fracture gaps, and we found no sustained damage on the AATBPs.

Table 4. Results of the assembly tightness error between the PP and DP

Assembly tightness error between PP and DP		
Sample	**Proximal side (mm)**	**Distal side (mm)**
1	0.39	0.16
2	0.31	0.15
3	0.33	0.20
Mean ± Std (mm)	0.34 ± 0.04	0.17 ± 0.03

Unit: mm

3.4. Finite element analysis

The FE analysis result showed that the fractured gap distances at the medial/lateral sides for TBW and AATBP fixation models were 0.8099 mm/1.1838 mm and 0.3049 mm/0.3136 mm, respectively. The AATBP fixation fracture gap was found obviously smaller than those of TBW fixation under receiving tensile loads regardless of medial or lateral sides. The maximum von Mises stress of the bones were found around the medial wire hole and lateral bottom locking screw hole for TBW and AATBP fixations, respectively (Figure 9). The corresponding value for TBW fixation was 17 MPa and much higher than that of 5.69 MPa for AATBP fixation. Nevertheless, both bony stress values were a lot smaller than the bone fracture strength.

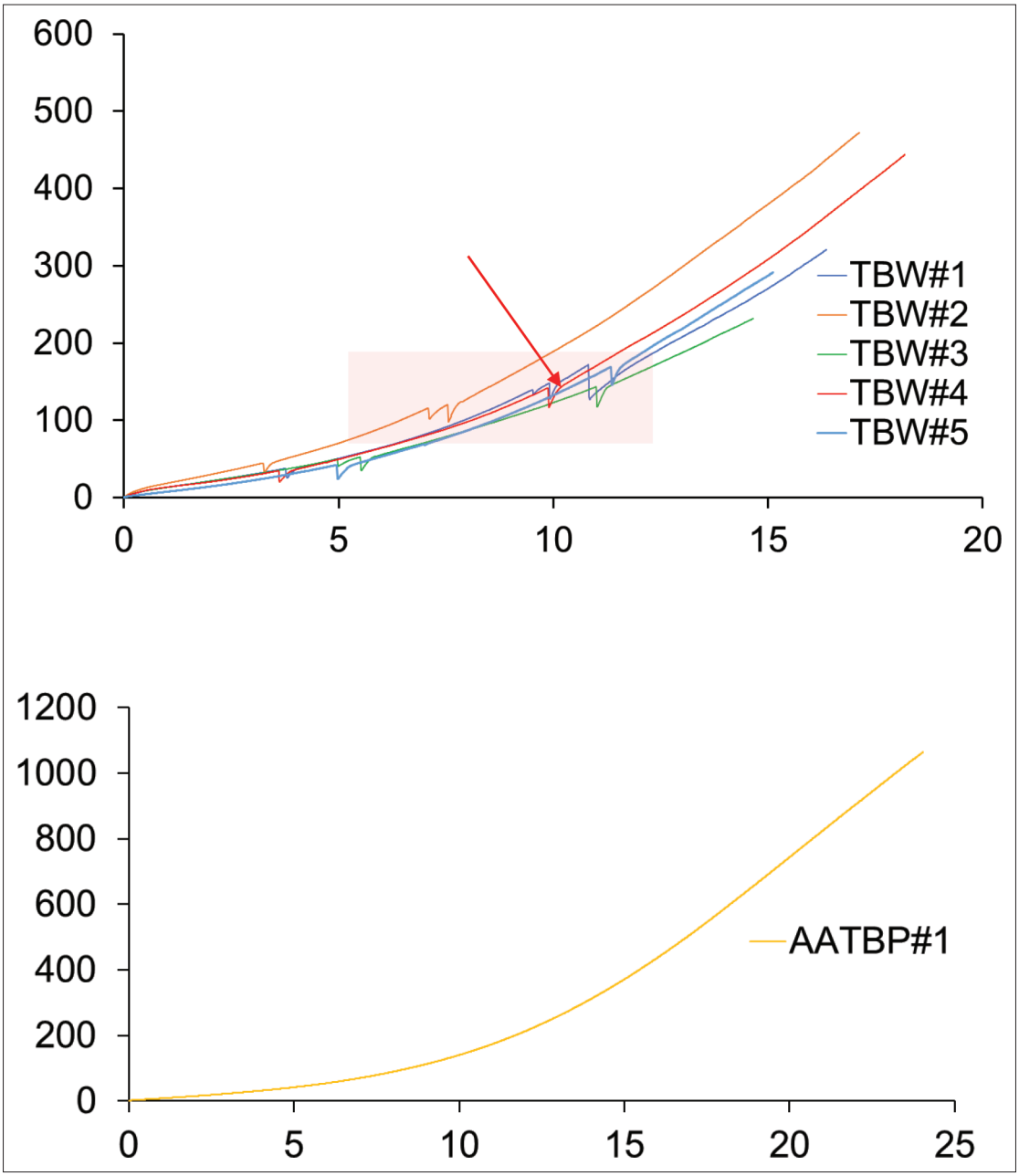

Figure 10. Static test force–displacement curves for TBW (top) and AATBP (down) fixations.

4. Discussion

It has been clearly shown that a fixation bone plate for transverse patella fractures was more stable than those using only band wires and screws combined with band wires from the literature[3,4]. However, a suitable design for the fixation bone plate needs to be relatively complicated in order to achieve the various functions necessary for fulfilling unmet clinical needs. This cannot be achieved using traditional manufacturing processing. The AATBP proposed in this study included two anatomical thin plates with a hook mechanism to hold fractured fragments, a ratchet mechanism to adjust plate height, and cone bumps at the plate base to enhance retention. Therefore, traditional processing methods, even those using five-axis CNC machines, may not be able to meet such complex manufacturing requirements. Precise 3D printing is needed to manufacture the AATBP.

The fixation bone plate should be designed to fit the patella anterior surface as much as possible to restore the fractured bone correctly since it has a curved contour.

Table 5. Results of variation in the fractured gap distances at the medial/lateral sides before and after dynamic tests and corresponding maximum forces

Fixation	Sample	Medial side (mm)	Lateral side (mm)	Maximum force (N)
TBW	#1	2.05	2.26	320
	#2	3.4	2.81	427.25
	#3	2.16	2.24	292.5
	#4	2.13	2.06	330
	#5	2.17	2.11	318.15
	Mean ± Std	2.38 ± 0.57	2.30 ± 0.30	337.58 ± 52.00
AATBP	#1	0.03	0.1	262.25
	#2	0.02	0.02	271.25
	#3	0.03	0.08	238.13
	#4	0.03	0.04	242.13
	#5	0.04	0.05	260.52
	Mean ± Std	0.03 ± 0.01	0.06 ± 0.03	254.86 ± 14.12

The titanium alloy bone plate with ductile material properties can be bent during the surgical process when the plate is manufactured using a traditional cutting method. However, the bone plate is no longer bendable and exhibits brittleness when the manufactured process is changed to 3D printing. The design accuracy for the curved surface becomes more important. The AATBP anatomical anterior surface was obtained by capturing the Sawbone patella surface, and it was confirmed that this bone plate surface shape design is feasible since the largest gap distance between the AATBP and the normal patella surface is only 0.91 mm.

Since there is no comparable fixation bone plate mechanical strength for patella fractures, the proof load and bending strength of the commercial dorsal fixation bone plate for distal radius fracture obtained using the same testing method according to ASTM F382 were selected as the comparable index to identify the mechanical capability of our AATBP. The proof load and bending strength were 47.36 ± 5.36 N and 1183 ± 134 N·mm obtained from the literature[21]. Since the center span (a) and the loading span distance (h) of these two bone plate tests were different, bending strength was only compared, and we found that there was no significant difference between the radius dorsal fixation plate and the AATBP. This implied that the mechanical strength of the AATBP developed in this study met the clinical needs. For the surface roughness compression, the average surface roughness of an oblique lumbar interbody fusion cage used in this study was 9.143 μm, which is from literature[22]. This value was about 1.92 times (9.143 μm/4.74 μm) the AATBP average roughness measured [(4.42 + 5.59 + 5.39 + 3.56)/4 = 4.74 μm] in this study. This phenomenon also showed that the surface roughness of the components manufactured by 3D printing fell within a reasonable range.

The most important issue in AATBP 3D printing is that the assembly tightness error of the two thin bone plates at the proximal and distal ends must be minimized. The ratchet manufacturing must be sufficiently accurate to allow assembly surface flatness control within the unsuitable skin touch feeling range. The maximum value for the average tightness error for two thin bone plate assemblies was only 0.34 mm when produced by our metal 3D printing machine, with values of 30 μm for both the manufacturing accuracy and the layer thickness. This value cannot be perceived through the touch with hand and is also less than the total thickness of 1.6 mm for the AATBP. This implies that a similar assembly bone plate design can be fabricated when the manufacturing accuracy requirement for the metal 3D printing machine is less than 30 μm.

Commercial locking and compressive bone screws were selected to match our AATBP because bone screws did not need to be manufactured by 3D printing. This is beneficial for reducing manufacturing cost, time, and accuracy requirements. In the traditional manufacturing process, the required accuracy for bone screws can be 0.02 mm, with relatively good ductility and suitability for a large allowable rotation angle for bone insertion. However, the 3D printing manufacturing process usually confers a tendency for the material to be brittle and not suitable for bone screw manufacturing when no special post-processing is performed. We therefore only tapped threads or drilled holes into our AATBP using five-axis machining for the corresponding bone screw insertion.

Fifteen-kilogram downward weights were applied on the dynamic cyclic loads because a volatility in force was found at the critical value in the force–displacement curve during the static test for TBW fixation. This implied that

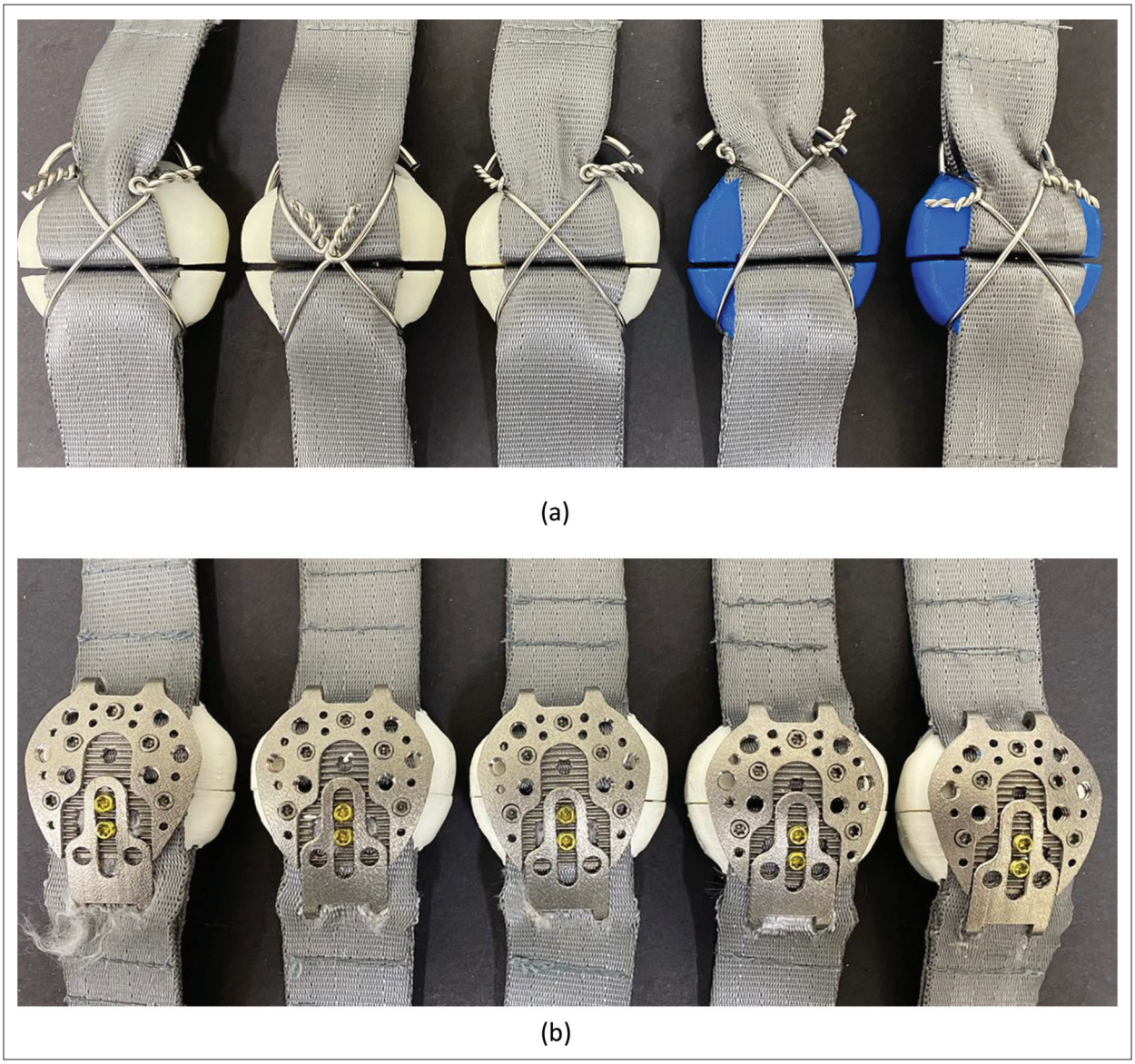

Figure 11. The fractured gap distances at the medial/lateral sides and situations for all fixation patella samples after cyclic tests for (a) TWB and (b) AATBP fixations.

the fractured patella was starting to become unstable. A biomechanical test platform as described in the literature was set up to evaluate the dynamic biomechanical behavior of the fractured patella after TBW and AATBP fixations[2-5]. The force test results showed that the maximum force can be obtained at an extension angle of 60° (Figure 7c), which is consistent with the literature reporting the motion pattern of the knee joint. This also means that this platform can be used in similar tests in the future[23]. The results showed that the corresponding force at 60° was 254.86 ± 14.12 N for AATBP and 337.58 ± 52.00 N for TBW fixation. This clearly indicated that the conventional TBW fixation cannot hold on to the fractured patella fragments and that the quadriceps tendon needs to bear greater force to maintain the fixation system balance.

The fracture gap distance results at the medial/lateral sides before and after the dynamic test showed that the fractured patella stability after fixation was greater and the gap distances were approximately zero when 3D-printed AATBP fixation was used. This was almost 75 (2.24 mm/0.03 mm) times less for the medial direction and 40 (2.30 mm/0.06 mm) times less for the lateral direction than when using TBW fixation. This is reasonable because the fractured patella proximal and distal fragments were effectively grasped by the hooks and forced into the fractured gap.

The patella fragments were also fixed by bone screws and AATBP. This was clearly different from the fixation using TBW without holding power and suggested that AATBP can be further applied to *in vivo* tests.

The FE simulation and biomechanical test results showed the same trend, i.e., fractured gap distances at the medial/lateral sides for TBW were both higher than that of AATBP fixation models. The TBW fixation cannot hold the fracture segments of the patella efficiency, and the maximum bone stress found around the medical wire inserted into the patella might cause the fracture segments to slide. The bone stress concentration for the AATMP fixation was found around the screw. The corresponding maximum stress value was 5.69 MPa and at the lateral bottom screw hole. Although the maximum stress value was much lower than the tensile ultimate strength (135 MPa), it should be noted that it may cause locking screw loosening[24].

The patella fracture types are not limited to transverse fractures but also include other forms of comminuted fractures or proximal/distal fractures. The main objective of surgical treatment is to restore these comminuted bones to their original anatomical positions while maintaining their stability. A fixation bone plate designed to have good encircling energy (holding power) for the fractured patella is recommended. Our AATBP and the experimental/simulation results presented herein manifest this property and can be applied to the main patella fracture of the transverse type, as well as other fracture forms in the future.

Although the AATBP was designed with an anatomical contour and has been confirmed to be adaptable for use, this bone plate may not enable clinicians to do much manual bending during surgery due to the limitations of 3D-printed materials and post-manufacturing processing. More rigorous *in vivo* experiments may be required to further confirm the clinical utility of the AATBP, although the biomechanical stability was confirmed in this study.

5. Conclusion

This study confirmed that the thin structural bone plate for patella fixation, comprising anatomical surface, hook, small cone, and size-adjustable ratchet mechanism, can be fabricated using 3D metal printing with acceptable manufacturing error and reasonable anatomical surface/thin bone plate assembly fitness, mechanical bending strength, and surface roughness. The biomechanical cyclic test results showed that the fracture gap between two AATBP fixation fracture segments after cyclic loads was smaller and superior to conventional TBW for patella transverse fractures. The FE simulation result addressed the stress concentration around the screw holes and noted the high risk for screw loosening.

Acknowledgments

None.

Funding

This study is supported in part by MOST project 108-2622-E-010-001-CC2 and 110-2222-E-032-003-MY2, Taiwan.

Conflict of interest

The authors declare no conflicts of interest.

Author contributions

Conceptualization: C.Y. Liao, Chun-Li Lin
Investigation: Shao-Fu Huang, Wei-Che Tsai, Yu-Hui Zeng, Chia-Hsuan Li
Methodology: Chun-Li Lin
Writing – original draft: C.Y. Liao, Chun-Li Lin
Writing – review & editing: C.Y. Liao, Chun-Li Lin

Ethics approval and consent to participate

Not applicable.

Consent for publication

Not applicable.

Availability of data

Not applicable.

References

1. Lee KH, Lee Y, Lee YH, *et al.*, 2019, Biomechanical comparison of three tension band wiring techniques for transverse fracture of patella: Kirschner wires, cannulated screws, and ring pins, *J Orthop Surg*, 27(3): 2309499019882140.

2. Gibert S, Kowaleski MP, Matthys R, *et al.*, 2016, Biomechanical comparison of pin and tension-band wire fixation with a prototype locking plate fixation in a transverse canine patellar fracture model. *Vet Comp Orthop Traumatol*, 29(1): 20–28.

3. Wild M, Eichler C, Thelen S, *et al.*, 2010, Fixed-angle plate osteosynthesis of the patella - an alternative to tension wiring? *Clin Biomech*, 25(4): 341–347.

4. Thelen S, Schneppendahl J, Jopen E, *et al.*, 2012, Biomechanical cadaver testing of a fixed-angle plate in comparison to tension wiring and screw fixation in transverse patella fractures. *Injury*, 43(8): 1290–1295.

5. Thelen S, Schneppendahl J, Baumgärtner R, *et al.*, 2013, Cyclic long-term loading of a bilateral fixed-angle plate in comparison with tension band wiring with K-wires or

cannulated screws in transverse patella fractures. *Knee Surg Sports Traumatol Arthrosc*, 21(2): 311–317.

6. D'Ambrosio M, Tang A, Menken L, *et al.*, 2022, Adjunct neutralization plating in patella fracture fixation: A technical trick, *OTA Int*, 5(4): e217.
7. Stoffel K, Zderic I, Pastor T, *et al.*, 2023, Anterior variable-angle locked plating versus tension band wiring of simple and complex patella fractures - a biomechanical investigation. *BMC Musculoskelet Disord*, 24(1): 279.
8. Kumar G, Mereddy PK, Hakkalamani S, *et al.*, 2010, Implant removal following surgical stabilization of patella fracture. *Orthopedics*, 33(5): 301–304.
9. Dargel J, Gick S, Mader K, *et al.*, 2010, Biomechanical comparison of tension band- and interfragmentary screw fixation with a new implant in transverse patella fractures. *Injury*, 41(2): 156–160.
10. Wagner FC, Neumann MV, Wolf S, *et al.*, 2020, Biomechanical comparison of a 3.5 mm anterior locking plate to cannulated screws with anterior tension band wiring in comminuted patellar fractures. *Injury*, 51(6): 1281–1287.
11. Meda PVK, Machani B, Sinopidis C, *et al.*, 2006, Clavicular hook plate for lateral end fractures: A prospective study. *Injury*, 37(3): 277–283.
12. Hung LK, Su KC, Lu WH, *et al.*, 2017, Biomechanical analysis of clavicle hook plate implantation with different hook angles in the acromioclavicular joint, *Int Orthop*, 41(8): 1663–1669.
13. Chen CH, Chang WJ, Chen YS, *et al.*, 2022, Development of a novel hybrid suture anchor for osteoporosis by integrating titanium 3D printing and traditional machining. *Int J Bioprint*, 8(4): 608.
14. Standard Specification and Test Method for Metallic Bone Plates, ASME F382-17
15. Lee KH, Lee Y, Lee YH, *et al.*, 2019, Biomechanical comparison of three tension band wiring techniques for transverse fracture of patella: Kirschner wires, cannulated screws, and ring pins. *J Orthop Surg*, 27(3): 2309499019882140.
16. Sharkey NA, Donahue SW, Smith TS, *et al.*, 1997, Patellar strain and patellofemoral contact after bone–patellar tendon–bone harvest for anterior cruciate ligament reconstruction. *Arch Phys Med Rehabil*, 78(3): 256–263.
17. Chang CW, Chen CH, Li CT, *et al.*, 2020, Role of an additional third screw in the fixation of transverse patellar fracture with two parallel cannulated screw and anterior wire. *BMC Musculoskelet Disord*, 21(1): 752.
18. Chang CW, Chen YN, Li CT, *et al.*, 2018, Role of screw proximity in the fixation of transverse patellar fractures with screws and a wire. *J Orthop Surg*, 26(3): 2309499018789705.
19. Chen CH, Chen YN, Li CT, *et al.*, 2019, Roles of the screw types, proximity and anterior band wiring in the surgical fixation of transverse patellar fractures: A finite element investigation. *BMC Musculoskelet Disord*, 20(1): 99.
20. Ling M, Zhan S, Jiang D, *et al.*, 2019, Where should Kirschner wires be placed when fixing patella fracture with modified tension-band wiring? A finite element analysis. *J Orthop Surg Res*, 14: 14.
21. Liu HC, Zeng YH, Lin CL, 2021, Mechanical comparison of a novel hybrid and commercial dorsal double plating for distal radius fracture: In vitro fatigue four-point bending and biomechanical testing. *Materials (Basel)*, 14(20): 6189.
22. Lai PL, Huang SF, Wang HW, *et al.*, 2023, Design an anatomical contour titanium 3D printed oblique lumbar interbody fusion cage with porous structure and embedded fixation screws for patients with osteoporosis. *Int J Bioprint* 9(5): 445–458.
23. Bini RR, 2017, Patellofemoral and tibiofemoral forces during knee extension: simulations to strength training and rehabilitation exercises. *Fisioter Mov*, 30(Suppl 1): S267–5.
24. Morgan EF, Unnikrisnan GU, Hussein AI, 2018, Bone mechanical properties in healthy and diseased states. *Annu Rev Biomed Eng*, 20: 119–143.

ACCSCIENCE PUBLISHING

International Journal of Bioprinting

RESEARCH ARTICLE

The attractiveness of 4D printing in the medical field: Revealing scientific and technological advances in design factors and applications

Angelica A. Martinez-De-Anda, Marisela Rodriguez-Salvador*, and Pedro F. Castillo-Valdez

Tecnologico de Monterrey, Escuela de Ingeniería y Ciencias, Monterrey, Nuevo León, México

Abstract

Currently, there is an increasing demand in the medical field for low-cost, high-quality products as well as personalized solutions, and different manufacturing methods are being investigated to provide innovative solutions. Four-dimensional (4D) printing is a promising technology that could overcome the challenges associated with the applications of three-dimensional printing in regenerative medicine and biomedical devices. A revolution is expected in this regard, and it is essential to keep abreast of the latest developments. Under this context, the purpose of this paper is to reveal scientific and technological advances of 4D printing in the medical field using a competitive technology intelligence (CTI) methodology. To this end, publications were analyzed from the Scopus database between January 1, 2017, and May 9, 2023. The main trends were identified for both design factors and applications. In the first case, the following were considered: 4D printing methods, external stimuli, materials, mathematical models, and interaction mechanisms. In contrast, in the second case, the applications of 4D printing involved were considered: drug delivery systems, stents, and scaffolds. The obtained design factors results included improvements in mechanical properties of hydrogels by adding magnetic nanoparticles, biopolyurethane, and other materials, the development of cell-friendly bioprinting methods to print cellular structures, and the use of theoretical-experimental approaches to predict shape deformation of structures. While for applications, results included advances in the development of expandable drug delivery systems, fabrication of stents for the treatment of vascular and tracheal stenosis, and the design of scaffolds to treat cartilage defects and bone regeneration. This study provides insights to researchers, academics, and companies involved in research and development as well as innovation that are looking for new solutions to improve health by incorporating breakthrough technologies such as 4D printing.

Keywords: 4D printing; Competitive technology intelligence; Medical field; Design factors; 4D applications

***Corresponding author:**
Marisela Rodriguez-Salvador
(marisrod@tec.mx)

Citation: Martinez-De-Anda AA, Rodriguez-Salvador M, Castillo-Valdez PF, 2023, The attractiveness of 4D printing in the medical field: Revealing scientific and technological advances in design factors and applications. *Int J Bioprint*, 9(6): 1112.
https://doi.org/10.36922/ijb.1112

Received: June 21, 2023
Accepted: July 7, 2023
Published Online: July 21, 2023

Copyright: © 2023 Author(s). This is an Open Access article distributed under the terms of the Creative Commons Attribution License, permitting distribution, and reproduction in any medium, provided the original work is properly cited.

Publisher's Note: AccScience Publishing remains neutral with regard to jurisdictional claims in published maps and institutional affiliations.

1. Introduction

The technological advances in three-dimensional (3D) printing have revolutionized the global manufacturing industry, pushing the boundaries of traditional manufacturing

methods and providing novel research and development (R&D) areas[1]. Through 3D printing, also called additive manufacturing, it is also possible to fabricate complex geometries by printing materials through a layer-by-layer method using computer-aided controls, facilitating a faster development of novel ideas. This technology has gained huge attention in the medical field because of its capacity to offer cost-effective, customized, and personalized solutions such as medical devices, medicine, and equipment[2]. However, 3D printing faces challenges in certain applications such as regenerative medicine and tissue engineering because of its static structures. Due to these limitations, four-dimensional (4D) printing technology has emerged and rapidly gained the attention of researchers because of its capability to fabricate dynamic structures and novel applications in the medical field. 4D printing is a revolutionary technology that uses 3D printing methods and smart materials to produce dynamic structures capable of self-transforming in response to a given stimulus, improving their performance and functions[3]. 4D printing involves time as an additional dimension, representing the change of shape over time due to a variation in its environment[4]. According to the literature, the design of 4D-printed structures considers mainly the correlation of five factors: (i) printing methods, (ii) external stimuli, (iii) materials, (iv) mathematical models, and (v) interaction mechanisms[5,6].

The medical field has benefited from technological advances in these design factors; however, no research has studied the existent technological tendencies of the design factors and applications in this field. For this aim, competitive technology intelligence (CTI) helps to identify technological trends. CTI is a process utilized to ethically gather and analyze information from legal sources to ultimately produce intelligence and support a decision-making process regarding R&D[7]. Several CTI methodologies have been developed, among which the eight-step methodology proposed by Rodriguez-Salvador and Castillo-Valdez is used[8]. In this context, the purpose of this study is to reveal technological advances in design factors and applications of 4D printing in the medical field using a CTI methodology, with the aim of supporting the decision-making process of researchers, academics, and companies regarding the direction of their efforts in R&D and innovation.

2. 4D printing design factors

As mentioned above, the five main design factors of 4D printing are: (i) printing methods, (ii) materials, (iii) external stimuli, (iv) mathematical models, and (v) interaction mechanisms[5].

(i) Printing methods: This considers the manufacturing process established within additive manufacturing technology, which fabricates products layer by layer using a wide variety of materials[9]. Use of smart materials in 3D printing processes allows printed structures to be responsive to stimuli, and with time added as a new dimension for 3D-printed models, 4D printing is conceptualized[10]. Techniques such as material extrusion, vat photopolymerization, powder bed fusion, and material jetting are the most used to print 4D objects[11]. Material extrusion is subdivided into fused deposition modeling (FDM) and direct ink writing (DIW). Vat photopolymerization is subdivided into stereolithography (SLA) and digital light processing (DLP)[12]. While powder bed fusion process comprises selective laser sintering (SLS) and selective laser melting (SLM), material jetting method includes inkjet printing (IJP)[13]. The chosen technique depends on both the material to be used as well as the desired properties or functions of the final structure. The printing method can also be chosen to facilitate and/or enhance the shape-memory functionality of the construct[14].

(ii) Materials: The benefits of 4D printing come from the materials that make this technique possible; the quality of the final 4D-printed product depends strongly on them. In the literature, these materials are called stimuli-responsive materials (SRMs)[15], and they play an important role in receiving, transmitting, and processing the applied stimulus[14]. A desirable characteristic of these materials is their ability to deform into a temporary state and return to their original form by changing the stimulus. The main subcategories of SRMs identified are temperature-responsive materials, pH-responsive materials, moisture-responsive materials, electric and field-responsive materials, light-responsive materials, acoustic-responsive materials, and multiple responsive materials. Some of these, such as alginate-based pH-sensitive materials, hybrid hydrogel-polyaniline materials, graphene-based nanomaterials, magnetically responsive materials, etc., have great potential to be used in bioinks for 4D bioprinting[16].

There are other types of materials such as shape change material (SCM), shape memory materials (SMMs), liquid crystal elastomers (LCE), and hydrogels. SMMs are driven by shape memory effect (SME), which means they are capable of returning to their initial shape after a temporary deformation when the appropriate stimulus is applied again[17] (Figure 1a); most of the time the stimulus is heat. Several SMMs

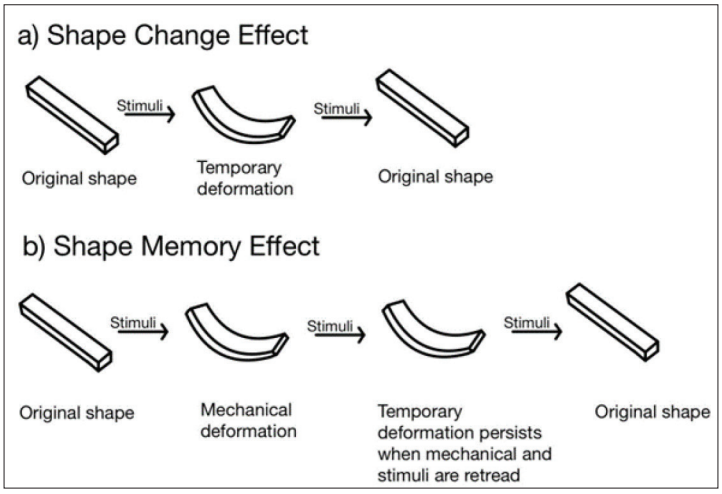

Figure 1. (a) Shape change effect. (b) Shape memory effect. (Adapted from Subeshan *et al.* (2021)[18])

have been produced, such as shape memory gels (SMG), shape memory hybrids (SMH), shape memory alloys (SMA), shape memory metals (SMMet), shape memory polymers (SMP), and shape memory ceramics (SMC). Among these, SMP and SMA are the most investigated in the literature[19]. The main advantages of SMP include high strain recovery, low density, low cost of raw material, fabrication and processing, biocompatibility, and biodegradability[20], and they can respond to temperature, light, and chemical stimuli[12]. On the other hand, the main characteristics of SMA are elasticity, high strength and low elastic modulus, high corrosion resistance, biocompatibility, and non-ferromagnetic properties[21], and they can respond to load and temperature stimuli and are typically used in biomedical and engineering fields[6]. Regarding SCM, the most common materials are semi-crystalline networks (SCNs), interpenetrating network (IPN)[22], electro-active polymers, and piezoelectrical materials[20]. The difference between SMM and SCM is the ability of SCM to return instantaneously to their original form after the applied stimulus is removed (Figure 1b); this is the shape change effect (SCE) mechanism. LCE are attractive to researchers because of their ability to have large, reversible, and fast dimension deformations[23]. They are used in applications such as soft robots, artificial muscles, and sensors[24]. Hydrogels are widely used in the literature due to their ability to drastically increase their volume and are frequently printed along other polymers to increase their strength. These materials are particularly useful in biomedical and engineering applications[25].

(iii) External stimuli: As mentioned, SRMs can respond to external stimuli such as physical, chemical, and biological stimuli. Physical stimuli are classified into temperature, liquid/moisture, light, magnetic field, and electrical field. Temperature, light, and moisture stimuli are the most frequently used in literature[26]. Chemical stimuli are identified as variations in physiological conditions, for instance, pH levels or ionic concentrations. The pH stimulus is frequently used in drug delivery systems, especially for diseases like cancer, infections, and degenerative and cardiovascular diseases where there is an imbalance of pH levels[6]. Finally, biological stimuli refer to variations in molecules, such as glucose, enzymes, proteins, nucleic acids, and peptides. The SRMs develop shape-shifting behaviors, such as folding, curling, twisting, expansion, and contraction[27].

(iv) Mathematical models: These are divided into two categories. The first is backward prediction, which focuses on the printing profile (printing paths and nozzle size) given the required final form and its properties. The second category is forward prediction, which aims to determine the transformation process of the structure to achieve the final shape[28]. The mathematical models connect four fundamental elements: material structure (filament size, orientation, interfilament spacing, etc.), desired final shape (bending and twisting angle, length, volume, etc.), material properties (shear modulus, elastic modulus), and stimulus properties.

(v) Interaction mechanisms: This refers to the order of the steps required to obtain the desired final shape[29]. An example of this is the SME for SMA and SMMet, which includes mechanisms such as one-way shape memory effect (OWSME), two-way memory effect

(TWSME; also known as reversible shape memory), and pseudo elasticity[30]. Other mechanisms of action are: (i) asymmetrical swelling for moisture stimuli; (ii) temperature-induced changes in material crystallinity, swelling, and hydrophobicity for temperature stimuli; (iii) pH-dependent variation in electrostatic interaction for pH stimuli; and (iv) magneto-thermal effect for electrical/magnetic stimuli[10].

These five design factors have a determinant effect on 4D printing particularly for providing new solutions to health. Therefore, this study explores the technological advances of 4D printing in the medical field as well as its applications.

3. Methodology

This research is based on the eight-step CTI iterative methodology proposed by Rodriguez-Salvador and Castillo-Valdez (2021)[8]: (i) Process planning; (ii) identification of data sources; (iii) search strategy design; (iv) data collection; (v) information analysis; (vi) feedback from experts; (vii) validation and delivery of results; and (viii) decision making.

The process planning step involves setting the research topic, objective, participants, due dates, and key assignments to complete the research. In this respect, the objective is the identification of technology advances of 4D printing in medical field in terms of its applications and design factors, such as materials, printing methods, mathematical models, and interaction mechanisms.

In the data source identification step, primary and secondary sources were defined. For the primary sources, experts in 4D printing technology with a focus on the medical field were selected according to their number of publications and citations. Also, experts in the field of CTI were contacted. For the secondary sources, the Scopus database was selected to gather scientific publications. It is a highly reliable database, which covers more than 240 disciplines, over 1.8 billion cited references, and 17.5 million open-access items[31].

The search strategy design step concerns the establishment of a method to collect the required data for the analysis. For this, a query was created to gather scientific papers from the Scopus database. To improve the data collection and narrow down the search to the defined scope, relevant terms related to 4D printing were detected after a state-of-the-art review. These were organized and classified as follows: (i) terms related to 4D printing, (ii) materials, and (iii) those referring to the medical field.

The query was built to gather documents of type "article" published between January 1, 2017, and May 9, 2023, as follows:

(TITLE-ABS-KEY ((((“4D” OR “four-dimensional” OR “4-dimensional”) W/0 (print* OR bioprint* OR biofabricat* OR fabricat* OR tech* OR product*) OR (“additive” W/0 manufact*)) OR ((“smart” OR “intelligent” OR “shape-memory” OR “shape-change” OR “responsive” OR “elastomer” OR “hydrogel” OR “multi” OR *composite) W/0 (material* OR biomaterial* OR bioink*) AND 4D)) AND (*medic* OR health* OR pharma* OR “drug” OR “organ” OR “bone” OR “tissue” OR “implant” OR “scaffold” OR cardi* OR “vascular” OR “stent” OR biocompat*))) AND (LIMIT-TO (DOCTYPE,”ar”)) AND (LIMIT-TO (PUBYEAR, 2023) OR LIMIT-TO (PUBYEAR, 2022) OR LIMIT-TO (PUBYEAR, 2021) OR LIMIT-TO (PUBYEAR, 2020) OR LIMIT-TO (PUBYEAR, 2019) OR LIMIT-TO (PUBYEAR, 2018) OR LIMIT-TO (PUBYEAR, 2017)).

In the data collection step, the query was introduced into the Scopus database, obtaining a total of 358 papers, which were manually examined to refine the results according to the following criteria: (i) review articles were not considered in this research, (ii) articles must be in the English language, and (iii) topic must be related to printing methods, materials, mathematical models, interaction mechanisms, or application of 4D printing in the medical field. After an extensive examination, 178 papers were found suitable for the analysis, which were manually classified according to the five design factors described above: (i) printing methods, (ii) external stimuli, (iii) materials, (iv) mathematical models, and (v) interaction mechanisms. After a preliminary review of the documents obtained, the factor "external stimuli" was discarded as a category since this element was already included in the materials and applications categories.

In the information analysis step, raw data were converted into valuable and actionable intelligence for the user[32]. To accomplish this, it is important to combine the use of the automated analytical tools of databases used, in this case Scopus, with a manual examination based on own expertise as intelligence analysts and supported with the expert's view in the field of study. The analysis usually begins with a meticulous review of the collected data. One method used to conduct the analysis is the 5W+H technique to identify "what?" (to compare, develop, create, incorporate), "how?" (resource management), "when?", "where?" (university or country), "why?", and "with whom?" (collaborations) of the documents gathered[8]. An analysis was performed to obtain the publication trends of design factors and applications.

Experts with an extensive background in 3D and 4D printing were contacted during the CTI cycle to request an assessment of the results, especially in the steps of information collection strategy, data collection, and information analysis. Their advice was used to eliminate unsuitable data and unrelated information. Furthermore, experts validated the reliability of the data obtained.

4. Results and discussion

4.1. Publication trends

As mentioned before, 358 publications on 4D printing in the medical field were gathered from Scopus between January 1, 2017, and May 9, 2023. An analysis of the 178 relevant publications was performed to obtain the publication trends in design factors and applications of 4D printing in the medical field. In Figure 2, it was found that the number of published documents increased over the years, implying that this field of study has gained attention of researchers especially in the last 3 years (2020–2022).

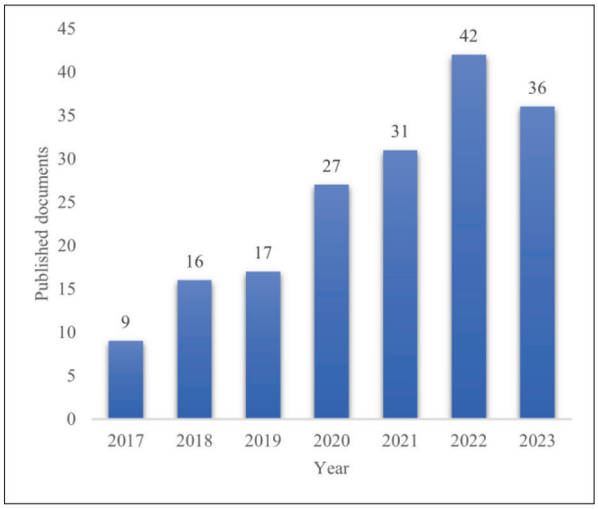

Figure 2. Published documents in 4D printing from 2017 to May 2023.

4.2. Global trends in 4D printing in the medical field

4.2.1. Design factors

In the analysis, four global trends in the materials category were identified. The first trend is the addition of materials such as magnetic nanoparticles, poly(acrylic acid), and carboxymethyl chitosan among others to improve hydrogel mechanical properties. Abdullah and Okay (2023) proposed 4D-printed hydrogels based on poly(acrylic acid) with shape memory and self-healing properties that can actuate around body temperature. Printed hydrogel exhibited a high elastic modulus (215 MPa) and high toughness showing great potential for biomedical applications[33]. Song *et al.* (2023) presented a biodegradable hydrogel ink prepared with biopolyurethane, carboxymethyl chitosan (CMCS), and carbomer (CBM)[34]. The ink exhibited high tensile strength (maximum stress of 0.66 MPa, elongation at break of 643%), great water retention (85.87%), ionic conductivity (8.59 S m^{-1}), and excellent sensing performance (S = 0.051 kPa^{-1} and GF = 2.9). It can be applied in tissue engineering and other fields. The second trend identified was the combination of SMMs to improve operation cycles, recovery rate, toughness, etc.[34]. Pyo *et al.* (2018) integrate an SMA with an SMP to obtain a shape memory composite (SMC). The volume fraction of SMA:SMP of 1:5 was found to be the optimum ratio for good operation cycles, giving the largest length change (8 mm) and the fastest response (4 s). The results were favorable for the applications of stents and valve controllers[35]. According to Bodkhe and Ermanni[36], it should be as poly-lactic acid (PLA) and polyesteramide (PEA) and piezoelectric barium titanate nanoparticles. This SMC has a recovery rate of approximately 98% and a linear response in the force range of 0.1–1 N. This material can be used in electroactive scaffolds and artificial organs for surgical training[36]. Lin *et al.* (2022) prepared a 4D-printed shape memory polybutylene succinate/polylactic acid (PBS/PLA) composite filament, which showed great photothermal properties and dynamic, remote, and accurately controlled 4D transformation using near-infrared (NIR) irradiation as a stimulus. It can be utilized for porous scaffolds and tissue engineering. The third trend found was the fabrication of tunable metamaterials capable of undergoing large deformations[37]. Bodaghi and Lio (2019) developed a tunable metamaterial with reversible thermo-mechanical memory operations that exhibited elastic-plastic and hyper-elastic behaviors at different temperatures with a wide deformation range[38]. It can be cold- and hot-programmed to facilitate its application in self-deployable biomedical stents[38]. In 2020, Xin *et al.* (2020) developed a chiral metamaterial with tunable, programmable, and reconfigurable properties that had bending and stretching behaviors, making it great for tissue engineering applications[39]. Wan *et al.* (2022) investigated three types of programmable metamaterials: triangular, square, and honeycomb lattice metamaterials[40]. Results found that the metamaterials with triangular and square lattices underwent large deformations and auxetic behavior, and their Poisson's ratios and elastic modulus can be programmed by adjusting the topical parameters and temperature. This material can be used in biomedical scaffolds[40]. The fourth trend concerns the fabrication of innovative inks. As previously mentioned, SRMs for 4D applications are categorized into temperature-responsive materials, pH-responsive materials, moisture-responsive materials, electric and magnetic field-responsive materials, light-responsive materials, acoustic-responsive materials, and multiple stimuli-responsive materials. Ashammakhi *et al.* (2018) studied potential bioinks for

each of these kinds of materials, for example, in terms of the first three categories; according to the authors, the most predominantly researched temperature-responsive materials are poly(N-isopropylacrylamide) (PNIPAM)-based polymers since they have a relatively low critical solution temperature (LCST) of ≈32°C; while for pH-responsive materials, alginate has an important role in 3D bioprinting and consequently exhibits an attractive potential to be used in 4D bioinks; and for moisture-responsive materials, cellulose fibrils embedded in a soft acrylamide matrix to print composite hydrogels with high swelling capacity have been studied[16].

Regarding specific contributions, by combining biocompatible hydrogels and magneto-reactive materials, Simińska-Stanny *et al.* (2022) have recently produced soft actuators printed by multimaterial direct ink printing (4D printing)[41]. Non-cytotoxic and biocompatible bionanocomposites were studied for biomedical applications. Hydrogel structures were printed using a BioX 3D printer (CELLINK, Sweden). The author's proposal involves the combination of magnetically responsive hydrogel materials with programmable patterning to meet biocompatibility and functionality requirements of future soft robotics for medicine and biomedical engineering applications[41]. On the other hand, a cellulose–hydrogel composite ink for 4D printing applications was developed by Mulakkal *et al.* (2018)[42]. They created an ink formulation through a 3D extrusion process using a commercially available Prusa Mk2, and a petal architecture was chosen to analyze the 3D printing capabilities and subsequent 4D morphing of the designed cellulose formulations. They claimed that a sustainable and cost-effective ink was produced, aiming to make 4D printing more accessible and encourage the adoption of this technology[42]. Mathews *et al.* (2017) fabricated a 4D bionanoink composition containing monomers, crosslinker, photoinitiator, bacteriorhodopsin, carbon nanotubes, and silver nanoparticles[43]. The acrylic-based composition was developed considering the same proportions of 2-hydroxyethyl methacrylate (2-HEMA) and di(ethylene glycol) dimethacrylate (dEGdMA) and 15% of crosslinker di(trimethylolpropane) tetraacrylate (dTMP4A). A biophoton-electrochemical cell was printed by SLA using an Ember 3D printer with a 405-nm LED source. The result is a bionanoink with improved bioactivity and durability[43].

Regarding the printing methods category, two trends were identified. The first trend involves the investigation of the effect of printing parameters on printed parts. Eryildiz (2023) studied the effect of 4D printing parameters, such as sample thickness, nozzle temperature, deformation temperature, and holding time, on the percentage of shape recovery. The results showed that by increasing the deformation, holding time, and nozzle temperature, the maximum percentage of recovery for PLA was increased. Conversely, increasing the thickness of the sample showed a negative effect on shape recovery[44]. On the other hand, Pieri *et al.* (2023) studied the degree to which the printing process parameters (of an extrusion-based process), such as temperature, extrusion rate multiplier, and fiber orientation, affect the shape-memory properties of an SMP, and their effect on shape memory fixing and recovery ratios was evaluated. The results demonstrated that fiber orientation has a significant impact on the fixing ratio and the recovery ratio, whereas temperature and extrusion rate multiplier have almost no effect on these properties. Also, a cell viability assay was realized on 3D-printed samples with varying temperatures and extrusion rate multiplier; the results showed that a reduction in extrusion rate multiplier increased cell viability and that fiber orientation impacted shape memory functionality. This study can provide insights on optimizing biomedical applications[45]. Solis and Czekanski (2022) investigated the effect of the printing temperature on PNIPAM hydrogel properties manufactured using DLP[46]. When the printing temperature varied between 5, 10, and 15°C, the results showed that increasing the temperature by 10°C caused a reduction in 50% in the maximum swelling capacity, almost a 10% increase in water retention, and a 6.5°C variation in the low critical solution temperature. The second trend concerns the development of cell-friendly bioprinting methods[46]. Stroganov *et al.* (2018) proposed an innovative approach for 4D biofabrication of 3D cellular structures using thermosensitive shape-changing polymer films with a photolithographically patterned surface that is able to selectively absorb cells in specific regions. This method holds the potential in bioscaffolds fabrication and finds use in tissue engineering[47]. Ding *et al.* (2022) presented a 4D bioprinting process that allowed the formation of a shape-morphing cell condensate-laden bilayer system that had tunable deformability and microgel degradation, enabling controllable morphological transformations and on-demand liberation of deformed cell condensates[48]. Díaz-Payno *et al.* (2023) reported a 4D bioprinting method to fabricate curved structures from hyaluronan and alginate with potential use in cartilage engineering[49]. In 2020, Kim *et al.* proposed a cell-friendly and biocompatible 4D bioprinting system based on DLP, which is applicable in tissue engineering[50].

Concerning the mathematical models category, two trends were identified. The first trend considers the use of theoretical-experimental approaches to predict shape deformation. Zhao *et al.* (2022) applied an effective method to predict the folding angle of a 3D-printed thermo-responsive hydrogel/elastomer bilayer structure and analyzed the effect of variations in manufacturing and material properties on the folding angle[51]. This method

used thermal expansion to model the temperature-responsive hydrogel, and the percentage error between the theoretical and experimentally measured folding angle was about 5%. Also, it improved the design, control, and prediction of 3D-printed stimuli-responsive shape-morphing structures that have applications in biomedical devices[51]. Inverardi *et al.* (2021) proposed an experimental/computational method to design shape memory devices fabricated by hot processing[52]. First, a thermal, mechanical, and shape memory characterization under different testing conditions with different samples was realized. Then, a prototype was fabricated, temporally deformed, and tested to compare the simulation with the obtained results[52]. Wagner *et al.* (2017) designed a 3D-printed auxetic metamaterial that can be programmed into flexible shapes and recover its initial shape[53]. This material was utilized to construct a beam model to predict forces and deformations of a complex structure. A great correlation was established between the finite element simulation and experimental data from a bending test. A second complex shape was built and programmed into a random shape, and its shape was recovered as predicted. The second trend focuses on the utilization of algorithms and statistical models for batch optimization and deformation[53]. Suryavanshi *et al.* (2023) used experimental data of a new thermo-responsive self-folding feedstock to train machine learning algorithms for batch optimization, which was later used for drug delivery applications[54]. Ren *et al.* (2023) created theoretical deformation models using machine learning methods to acquire information on the stiffness deformation and pressure of the material at different temperatures[55]. This model was applied in a cardiac-mimicking actuator showing the promising applicability in medical assistive devices, artificial muscles, and soft robotics, among others[55].

With respect to the interaction mechanisms category, two trends were identified. The first one is about the use of the SME for folding and bending behaviors. Großmann *et al.* (2022) investigated the use of shape memory behavior to fold and contain objects fabricated from thermoplastic polyurethane filaments in water-soluble hard gelatin capsules; later, the unfolding time and dimensional recovery were examined as functions of material properties and shape[56]. Diverse flexible dosage forms were designed to make the unfolded size suitable for gastric retention, showing different behaviors depending on the shape and material[56]. On the other hand, Pandey *et al.* (2022) examined the SME of PLA and polycaprolactone (PCL) polymers, using PLA like an unchangeable phase of the polymers to memorize the original shape and PCL as a reversible phase to promote the transformation and fixation to a non-permanent shape when thermal stimulus was applied[57]. A tracheal scaffold was printed to analyze the shape memory behavior[57]. Bodaghi *et al.* (2018) produced adaptive structures with a dual and triple SME by creating hot–cold programming of SMPs, whose self-bending behavior was experimentally demonstrated[58].

The second trend concerns research on innovative materials and processes to fabricate reversible structures. As Lee *et al.* (2020) explain, while one-way shape deformation is one-directional, two-way memory provides reversibility through two persistent states (original and deformed) according to the stimulation conditions applied and with no physical contact[59]. They created a contactless shape mechanism to enhance reversible 4D printing using a combination of stimuli to overcome challenges associated with low response, shape morphing, and other limitations of SMP-based materials. Their research showed the potential of reversible 4D printing for soft robotics[59]. Additionally, Lee *et al.* (2017) exhibited an important research opportunity involving the effect of TWSME in metals and metal alloys, which are mainly stimulated by methods such as thermomechanical (heating and cooling to contract or expand their shape) and electrochemical hydrogenation; however, they still have limitations, but improving their performance can be useful for applications in robotics, aerospace, and biomedical industries[60]. Moreover, they also indicated combining two or more stimuli to achieve reversibility is one of the future research directions[60]. Recently, Parimita *et al.* (2023) studied a chitosan hydrogel ink that showed a displacement field caused by a concentration gradient after the edge of the structure was dipped inside a solvent[61]. The concentration gradient between the hydrophilic chitosan and hydrophobic silane layers of the material caused a bending behavior in the printed structure that can only be reversed by soaking the structure in ethanol in order to lower the concentration gradient[61]. On the other hand, Wu *et al.* (2018) proposed a 4D printing method that used a grayscale pattern to administer the light power distribution of a UV projector in digital light processing[62]. This method generated reversible self-folding structures with different curing angles and crosslinking densities at different locations. The bending behavior of these structures can be induced due to volume shrinkage after uncured oligomers are removed from the crosslinked network. This behavior can be reversed, and the structure can swell by the absorption of acetone. According to the authors, this method has huge potential in the fabrication of smart structures and endovascular stents[62].

4.2.2. Applications

Regarding the applications category, three trends were identified. The first trend involves the development of drug delivery devices designed in a compact shape, which can expand subsequently after the stimuli is applied.

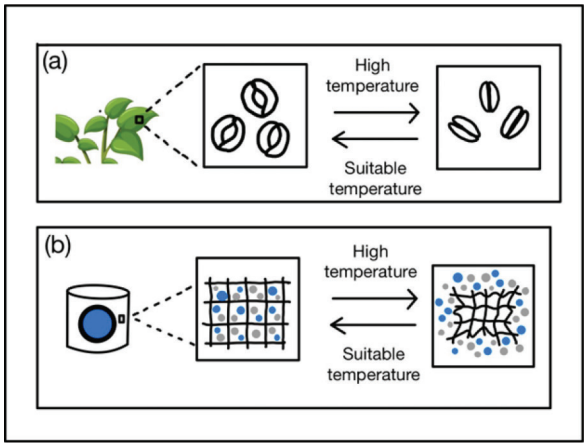

Figure 3. (a) Diagram of stomatal response to temperature and (b) PNIPAM hydrogel network. (Adapted from Zu *et al.* (2022)[64])

In 2019, Melocchi *et al.* (2019) presented an expandable device for gastric retention fabricated from pharmaceutical-grade poly(vinyl alcohol) that was designed to be ingested in a temporary compact shape, which then returns its original shape within 3 min after exposure to aqueous fluids at 37°C[63]. Finally, when the device is expanded, the drug is released. Models containing allopurinol were fabricated by FDM or hot melt extrusion, and drug release was slowed down using Eudragit® RS/RL-based coatings[63]. Zu *et al.* (2022) elaborated a PNIPAM hydrogel capsule inspired by plant stomata using an extrusion-based printing method[64]. The PNIPAM hydrogel responds to temperature in the same way as stomata; when the temperature rises, the internal pore size decreases, and when the temperature is suitable, in this case 34.9°C, the pore size increases, allowing the drug to be released (Figure 3). This capsule has a unique self-regulated drug delivery showing excellent potential for biomedical applications. The second trend concerns the use of 4D printing technology to fabricate stents used as a treatment for vascular and tracheal stenosis[64]. In 2020, Lin *et al.* fabricated two vascular stents from shape memory PLA with negative Poisson's ratio structures[65]. These thermo-responsive stents are designed to be introduced into the vertebral artery in a compact form, which then expand at the narrow vessel when temperature increases, showing potential for the treatment of vascular stenosis (Figure 4)[65]. In 2021, Zhang *et al.* printed different designs of tracheal stents from shape memory PLA with added particles of Fe_3O_4[66]. The stents exhibited a magnetic driving effect that allowed structure recovery process within 40 s and had a recovery rate of more than 99% when exposed to a magnetic field. This research contributes to advances in customized implantable medical devices and minimally invasive surgery[66]. Also in 2021, Zhou *et al.* created a shape memory peripheral stent, which sustains long-term drug release, and this stent exhibited

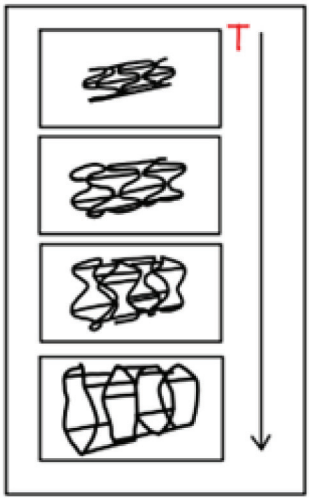

Figure 4. Behavior of stent when exposed to temperature. (Adapted from Lin *et al.* (2020)[65])

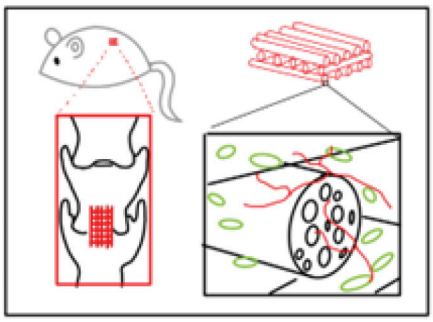

Figure 5. Posterolateral lumbar spinal scaffold. (Adapted from Hwangbo *et al.* (2021)[70])

improved wettability and a good biocompatibility with human umbilical vein endothelial cells[67]. In 2019, Kim *et al.* fabricated a bifurcated stent for branch vessels with a small diameter[68]. The third trend is the fabrication of scaffolds for the treatment of cartilage defects and bone regeneration. For instance, Zhao *et al.* (2019) fabricated a biodesigned tracheal scaffold from SMP[69]. This scaffold showed high strength, stability, and capability to adjust to the complex surrounding conditions in the soft tissue of the patient, and changed sizes depending on the size of the trachea. This design demonstrated great performance and has the potential to replace the traditional design[69]. On the other hand, Hwangbo *et al.* (2021) produced a biomimetic collagen/hydroxyapatite scaffold with several microchannels around the structure that promoted osteogenesis, new bone generation, and ingrowth of blood vessels. This scaffold was used in a mouse model for posterolateral lumbar spinal fusion, showing the potential in bone graft replacement to improve the rates of successful fusion (Figure 5)[70]. In 2023, Deng *et al.* fabricated a bionic cartilage scaffold from an SMC that responded to close-to-

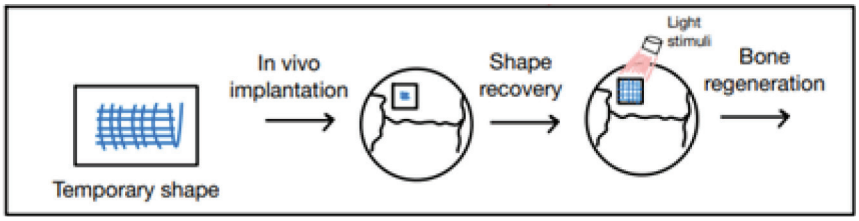

Figure 6. Schematic implementation of the scaffold. (Adapted from Wang *et al.* (2020)[72])

body temperature and could expand from a compact shape to an unfolded shape to match the cartilage defect[71]. This research provided new alternatives for minimally invasive treatments of cartilage defects[71]. On the other hand, Wang *et al.* (2020) presented bone tissue-engineered scaffolds with shape recovery behavior, great mechanical strength, and bone-forming capabilities[72]. For implantation, the scaffold was preheated to obtain a temporary compact shape, and then it was cooled down for shape fixation, allowing it to return to its original shape prior to implantation into irregular bone cracks (Figure 6)[72].

5. Conclusion

In this study, technological advances of 4D printing in the medical field were defined through the detection of relevant trends using a scientometric analysis performed as a part of a CTI methodology. The trends identified were grouped into five categories as follows: materials, printing methods, mathematical models, interaction mechanisms, and applications. Regarding the "materials" category, magnetic nanoparticles, biopolyurethane, and chitosan are used to improve mechanical properties of hydrogels, such as strength (0.66–22.9 MPa), elastic modulus (215 MPa), and ionic conductivity (8.59–9.64 Sm^{-1}), among others. Additionally, we detected an important progress in SMCs, that is, combinations of SMPs, SMAs, nanoparticles, and other materials are favored to improve operation cycles, recovery rate (98%), toughness, etc. Advances in tunable and programmable metamaterials have demonstrated the capability of these materials to undergo large deformations, which make them applicable in biomedical stents and scaffolds. Finally, hydrogels, magneto-reactive materials, and compositions containing monomers were utilized in the fabrication of biocompatible, sustainable, and cost-effective innovative bioinks and bionanoinks in order to improve their bioactivity and durability. In the "printing methods" category, the effects of the process parameters, including nozzle temperature, extrusion rate, and fiber orientation, have significant impact on the deformation, fiber orientation, fixing ratio, and shape recovery process of the structure. Cell-friendly bioprinting methods have potential uses in the fabrication of 3D cellular structures, cell condensate-laden bilayers, tissue, and bioscaffolds. In the "mathematical models" category, the theoretical-experimental and machine learning methods successfully predicted shape deformation with a high percentage of accuracy. Concerning the "interaction mechanisms" category, the SME is principally used as a folding and unfolding mechanism. Also, contributions regarding the reversibility of materials structures were identified. Finally, in the "applications" category, SMMs are oriented to the development of drug delivery devices that are designed in a compact shape and then expand in response to a specific temperature (as the stimuli) to release the drug. In addition, the use of 4D printing technology in stents is remarkable since it can be used as treatment for vascular and tracheal stenosis, and they are designed to adjust to the diameter of the vertebral artery and trachea. Research on scaffolds for the treatment of cartilage defects and bone regeneration are currently ongoing.

The technological advances revealed in this study support researchers, academics, and companies in their decision-making processes regarding the direction of their efforts in R&D and innovation in the medical field, providing opportunities to boost areas of interest and to find unexplored lines of development.

Acknowledgments

The authors acknowledge the institutional funding received from Tecnologico de Monterrey and the National Council of Humanities, Science and Technology of Mexico (CONAHCYT) through Graduate Studies Scholarships and Academic Scholarships provided by CONAHCYT as members of the National System of Researchers (Sistema Nacional de Investigadores).

Conflict of interest

The authors declare no conflict of interest.

Author contributions

Conceptualization: Angelica A. Martinez-De-Anda, Marisela Rodriguez-Salvador, Pedro F. Castillo-Valdez
Formal analysis: Angelica A. Martinez-De-Anda

Investigation: Angelica A. Martinez-De-Anda, Pedro F. Castillo-Valdez
Methodology: Angelica A. Martinez-De-Anda, Marisela Rodriguez-Salvador, Pedro F. Castillo-Valdez
Writing – original draft: Angelica A. Martinez-De-Anda
Writing – review & editing: Marisela Rodriguez-Salvador, Pedro F. Castillo-Valdez

Ethics approval and consent to participate

Not applicable.

Consent for publication

Not applicable.

Availability of data

Data available on request from the authors

Declaration Statement

The current paper is a portion of a Master dissertation from Tecnologico de Monterrey presented in June 2022.

References

1. Javaid M, Haleem A, Singh RP, *et al*., 2022, 3D printing applications for healthcare research and development. *Glob Health J*, 6(4): 217–226.

   https://doi.org/10.1016/j.glohj.2022.11.001

2. Dodziuk H, 2016, Applications of 3D printing in healthcare. *Polish J Thorac Cardiovasc Surg*, 13(3): 283–293.

   https://doi.org/10.5114/kitp.2016.62625

3. Gazzaniga A, Foppoli A, Cerea M, *et al*., 2023, Towards 4D printing in pharmaceutics. *Int J Pharmaceut X,* 5: 2590–1567.

   https://doi.org/10.1016/j.ijpx.2023.100171

4. Pingale P, Dawre S, Dhapte-Pawar V, *et al*., 2023, Advances in 4D printing: From stimulation to simulation. *Drug Deliv Transl Res,* 13(1): 164–188.

   https://doi.org/10.1007/s13346-022-01200-y

5. Momeni F, Liu X, Ni J, 2017, A review of 4D printing. *Mater Des*, 122: 42–79.

   https://doi.org/10.1016/j.matdes.2017.02.068

6. Ghosh S, Chaudhuri S, Roy P, *et al*., 2022, 4D printing in biomedical engineering: A state-of-the-art review of technologies, biomaterials, and application. *Regen Eng Transl Med*, 1–27.

   https://doi.org/10.1007/s40883-022-00288-5

7. Rodriguez-Salvador M, Perez-Benitez BE, Padilla-Aguirre KM, 2021, Discovering the latest scientific pathways on tissue spheroids: Opportunities to innovate. *Int J Bioprint*, 7(1): 331.

   https://doi.org/10.18063/ijb.v7i1.331

8. Rodriguez-Salvador M, Castillo-Valdez P, 2021, Integrating science and technology metrics into a competitive technology intelligence methodology. *J Intell Stud Bus*, 11(1): 69–77.

   https://doi.org/10.37380/jisib.v1i1.696

9. Sahafnejad-Mohammadi I, Karamimoghadam M, Zolfagharian A, *et al*., 2022, 4D printing technology in medical engineering: a narrative review. *J Brazilian Soc Mech Sci Eng,* 44(6): 233.

   https://doi.org/10.1007/s40430-022-03514-x

10. Agarwal T, Hann SY, Chiesa I, *et al*., 2021, 4D printing in biomedical applications: Emerging trends and technologies. *J Mater Chem B*, 9(37): 7608–7632.

    https://doi.org/10.1039/D1TB01335A

11. Joharji L, Mishra R, Alam F, *et al*., 2022, 4D printing: A detailed review of materials, techniques, and applications. *Microelectron Eng*, 265: 111874.

    https://doi.org/10.1016/j.mee.2022.111874

12. Chu H, Yang W, Sun L, *et al*., 2020, 4D printing: A review on recent progresses. *Micromachines,* 11(9): 796.

    https://doi.org/10.3390/mi11090796

13. Alshahrani HA, 2021, Review of 4D printing materials and reinforced composites: Behaviors, applications, and challenges. *J Sci: Adv Mater Devices*, 6(2): 167–185.

    https://doi.org/10.1016/j.jsamd.2021.03.006

14. Bajpai A, Baigent A, Raghav S, *et al.,* 2020, 4D printing: Materials, technologies, and future applications in the biomedical field. *Sustainability*, 12(24): 10628.

    https://doi.org/10.3390/su122410628

15. Maiti T, Hann SY, Chiesa I, *et al.,* 2021, 4D printing in biomedical applications: Emerging trends and technologies. *J Mater Chem B,* 9(37): 7608–7632.

    https://doi.org/10.1039/D1TB01335A

16. Ashammakhi N, Ahadian S, Zengjie F, *et al.,* 2018, Advances and future perspectives in 4D bioprinting. *Biotechnol J*, 13(12): 1800148.

    https://doi.org/10.1002/biot.201800148

17. Zhang X, Yang Y, Yang Z, *et al.,* 2023, Four-dimensional printing and shape memory materials in bone tissue engineering. *Int J Mol Sci*, 24(1): 814.

    https://doi.org/10.3390/ijms24010814

18. Subeshan B, Baddam Y, Asmatulu E, 2021, Current progress of 4D-printing technology. *Prog Addit Manuf*, 6: 495–516.

    https://doi.org/10.1007/s40964-021-00182-6

19. Rastogi P, Kandasubramanian B, 2019, Breakthrough in the printing tactics for stimuli-responsive materials: 4D printing. *Chem Eng J*, 366: 264–304.

https://doi.org/10.1016/j.cej.2019.02.085

20. Sun L, Huang WM, Ding Z, *et al.*, 2012, Stimulus-responsive shape memory materials: A review. *Mater Des*, 33: 577–640.

https://doi.org/10.1016/j.matdes.2011.04.065

21. Melocchi A, Uboldi M, Inverardi N, *et al.*, 2019, Expandable drug delivery system for gastric retention based on shape memory polymers: Development via 4D printing and extrusion. *Int J Pharm*, 571: 118700.

https://doi.org/10.1016/j.ijpharm.2019.118700

22. McLellan K, Sun YC, Naguib HE, 2022, A review of 4D printing: Materials, structures, and designs towards the printing of biomedical wearable devices. *Bioprinting*, 27: e00217.

https://doi.org/10.1016/j.bprint.2022.e00217

23. Ren L, He Y, Ren L, *et al.*, 2023, Multi-parameter-encoded 4D printing of liquid crystal elastomers for programmable shape morphing behaviors. *Addit Manuf*, 61: 103376.

https://doi.org/10.1016/j.addma.2022.103376

24. Zhang C, Lu X, Fei G, *et al.*, 2019, 4D printing of a liquid crystal elastomer with a controllable orientation gradient. *ACS Appl Mater Interfaces*, 11(47): 44774–44782.

https://doi.org/10.1021/acsami.9b18037

25. Patil AN, Sarje SH, 2021, Additive manufacturing with shape changing/memory materials: A review on 4D printing technology. *Mater Today: Proc*, 44: 1744–1749.

https://doi.org/10.1016/j.matpr.2020.11.907

26. Aldawood F, 2023, A comprehensive review of 4D printing: State of the arts, opportunities, and challenges. *Actuators*, 12(3): 101.

https://doi.org/10.3390/act12030101

27. Pei E, Loh GH, 2018, Technological considerations for 4D printing: An overview. *Prog Addit Manuf*, 3(1-2): 95–107.

https://doi.org/10.1007/s40964-018-0047-1

28. Zhang Z, Demir KG, Gu GX, 2019, Developments in 4D-printing: A review on current smart materials, technologies, and applications. *Int J Smart and Nano Mater*, 24(1): 205–224.

https://doi.org/10.3390/ijms24010814

29. Raina A, Haq MI, Javaid M, *et al.*, 2021, 4D printing for automotive industry applications. *J Inst Eng*, 102: 1–9.

https://doi.org/10.1007/s40033-021-00284-z

30. Jani JM, Leary M, Subic A, *et al.*, 2014, A review of shape memory alloy research, applications, and opportunities. *Mater Des*, 56: 1078–1113.

https://doi.org/10.1016/j.matdes.2013.11.084

31. *Scopus*, 2023, Retrieved from ELSEVIER.

https://www.elsevier.com

32. Herring JP, 1999, Key intelligence topics: A process to identify and define intelligence needs. *Compet Intell Rev*, 10(2): 4–14.

https://doi.org/10.1002/(SICI)1520-6386(199932)10:2<4::AID-CIR3>3.0.CO;2-C

33. Abdullah T, Okay O, 2023, 4D printing of body temperature-responsive hydrogels based on poly(acrylic acid) with shape-memory and self-healing abilities. *ACS Appl BioMater*, 6(2): 703–711.

https://doi.org/10.1021/acsabm.2c00939

34. Song M, Zhu G, Guo J, 2023, 4D printing of biodegradable shape memory double-network hydrogel for highly bionic devices. *J Mater Res Technol*, 24: 2935–2945.

https://doi.org/10.1016/j.jmrt.2023.03.180

35. Pyo Y, Kang M, Jang J, *et al.*, 2018, Design of a shape memory composite(SMC) using 4D printing technology. *Sens Actuator A Phys*, 283: 187–195.

https://doi.org/10.1016/j.sna.2018.08.049

36. Bodkhe S, Ermanni P, 2020, 3D printing of multifunctional materials for sensing and actuation: Merging piezoelectricity with shape memory. *Eur Polym J*, 132: 109738.

https://doi.org/10.1016/j.eurpolymj.2020.109738

37. Lin C, Liu L, Liu Y, *et al.*, 2022, 4D printing of shape memory polybutylene succinate/polylactic acid (PBS/PLA) and its potential applications. *Compos Struct*, 279: 114729.

https://doi.org/10.1016/j.compstruct.2021.114729

38. Bodaghi M, Liao W, 2019, 4D printed tunable mechanical metamaterials with shape memory operations. *Smart Mater Struct*, 28(4): 045019.

https://doi.org/10.1088/1361-665X/ab0b6b

39. Xin X, Liu L, Liu Y, *et al.*, 2020, 4D printing auxetic metamaterials with tunable, programmable, and reconfigurable mechanical properties. *Adv Funct Mater*, 30(43): 2004226.

https://doi.org/10.1002/adfm.202004226

40. Wan M, Yu K, Sun H, 2022, 4D printed programmable auxetic metamaterials with shape memory effects. *Compos Struct*, 279: 114791.

https://doi.org/10.1016/j.compstruct.2021.114791

41. Simińska-Stanny J, Nizioł M, Szymczyk-Ziółkowska P, *et al.*, 2022, 4D printing of patterned multimaterial magnetic hydrogel actuators. *Addit Manuf*, 49: 102506.

https://doi.org/10.1016/j.addma.2021.102506

42. Mulakkal, MC, Trask RS, Ting VP, *et al*, 2018, Responsive cellulose-hydrogel composite ink for 4D printing. *Mater Des*, 160: 108–118.

https://0-doi-org.biblioteca-ils.tec.mx/10.1016/j.matdes.2018.09.009

43. Mathews AS, Abraham S, Kumaran SK, *et al,* 2017, Bio nano ink for 4D printing membrane proteins. *RSC Adv*, 7(66): 41429–41434.

https://doi.org/10.1039/c7ra07650a

44. Eryildiz M, 2023, Influence of process parameters on the shape recovery properties of 4D-printed polylactic acid parts produced by fused deposition modeling. *J Mater Eng Perform*, 32: 1–12.

https://doi.org/10.1007/s11665-023-07946-x

45. Pieri K, Felix B, Zhang T, *et al*., 2023, Printing parameters of fused filament fabrication affect key properties of four-dimensional printed shape-memory polymers. *3D Print Addit Manuf*, 10(2): 279–288.

https://doi.org/10.1089/3dp.2021.0072

46. Solis D, Czekanski A, 2022, The effect of the printing temperature on 4D DLP printed pNIPAM hydrogels. *Soft Matter*, 18(17): 3422–3429.

https://doi.org/10.1039/D2SM00201A

47. Stroganov V, Pant J, Stoychev G, *et al*., 2018, 4D biofabrication: 3D cell patterning using shape-changing films. *Adv Funct Mater*, 28(11): 1706248.

https://doi.org/10.1002/adfm.201706248

48. Ding A, Lee S, Tang R, *et al*., 2022, 4D cell-condensate bioprinting. *Small*. 18(36): 2202196.

https://doi.org/10.1002/smll.202202196

49. Díaz-Payno P, Kalogeropoulou M, Muntz I, *et al*., 2023, Swelling-dependent shape-based transformation of a human mesenchymal stromal cells-laden 4D bioprinted construct for cartilage tissue engineering. *Adv Healthc Mater*, 12(2): 2201891.

https://doi.org/10.1002/adhm.202201891

50. Kim S, Seo Y, Yeon Y, *et al*., 2020, 4D-bioprinted silk hydrogels for tissue engineering. *Biomaterials*, 260: 120281.

https://doi.org/10.1016/j.biomaterials.2020.120281

51. Zhao J, Kazemi H, Kim H, *et al*., 2022, Effect of variations in manufacturing and material properties on the self-folding behaviors of hydrogel and elastomer bilayer structures. *Soft Matter*, 18(46): 8771–8778.

https://doi.org/10.1039/D2SM01104B

52. Inverardi N, Scalet G, Melocchi A, *et al*., 2021, Experimental and computational analysis of a pharmaceutical-grade shape memory polymer applied to the development of gastroretentive drug delivery systems. *J Mech Behav Biomed Mater*, 124: 104814.

https://doi.org/10.1016/j.jmbbm.2021.104814

53. Wagner M, Chen T, Shea K, 2017, Large shape transforming 4D auxetic structures. *3D Print Addit Manuf*, 4(3): 133–142.

https://doi.org/10.1089/3dp.2017.0027

54. Suryavanshi P, Wang J, Duggal I, *et al*., 2023, Four-dimensional printed construct from temperature-responsive self-folding feedstock for pharmaceutical applications with machine learning modeling. *Pharmaceutics*, 15(4): 1266.

https://doi.org/10.3390/pharmaceutics15041266

55. Ren L, He Y, Ren L, *et al*., 2023, Multi-parameter-encoded 4D printing of liquid crystal elastomers for programmable shape morphing behaviors. *Addit Manuf*, 61: 103376.

https://doi.org/10.1016/j.addma.2022.103376

56. Großmann L, Kieckhöfer M, Weitschies W, *et al*., 2022, 4D prints of flexible dosage forms using thermoplastic polyurethane with hybrid shape memory effect. *Eur J Pharm Biopharm*, 181: 227–238.

https://doi.org/10.1016/j.ejpb.2022.11.009

57. Pandey H, Mohol S, Kandi R, 2022, 4D printing of tracheal scaffold using shape-memory polymer composite. *Mater Lett*, 329: 133238.

https://doi.org/10.1016/j.matlet.2022.133238

58. Bodaghi M, Damanpack A, Liao W, 2018, Triple shape memory polymers by 4D printing. *Smart Mater Struct*, 27(6): 065010.

https://doi.org/10.1088/1361-665X/aabc2a

59. Lee AY, Zhou A, An J, *et al.,* 2020, Contactless reversible 4D-printing for 3D-to-3D shape morphing. *Virtual Phys Prototyp*, 15(4): 481–495.

https://doi.org/10.1080/17452759.2020.1822189

60. Lee AY, An J, Chua CK, 2017, Two-way 4D printing: a review on the reversibility of 3D-printed shape memory materials. *Engineering*, 3(5): 663–674.

61. Parimita S, Kumar A, Krishnaswamy H, *et al*., 2023, Solvent triggered shape morphism of 4D printed hydrogels. *J Manuf Process*, 85: 875–884.

https://doi.org/10.1016/j.jmapro.2022.11.065

62. Wu J, Zhao Z, Kuang X, *et al*., 2018, Reversible shape change structures by grayscale pattern 4D printing. *Multifunct Mater*, 1(1): 015002.

https://doi.org/10.1088/2399-7532/aac322

63. Melocchi A, Uboldi M, Inverardi N, *et al*., 2019, Expandable drug delivery system for gastric retention based on shape memory polymers: Development via 4D printing and extrusion. *Int J Pharm*, 571: 118700.

https://doi.org/10.1016/j.ijpharm.2019.118700

64. Zu S, Wang Z, Zhang S, *et al*., 2022, A bioinspired 4D printed hydrogel capsule for smart controlled drug release. *Mater Today Chem*, 24: 100789.

https://doi.org/10.1016/j.mtchem.2022.100789

65. Lin C, Zhang L, Liu Y, *et al*., 2020, 4D printing of personalized shape memory polymer vascular stents with

negative Poisson's ratio structure: A preliminary study. *Sci China Technol Sci*, 63(4): 578–588.

https://doi.org/10.1007/s11431-019-1468-2

66. Zhang F, Wen N, Wang L, *et al*., 2021, Design of 4D printed shape-changing tracheal stent and remote controlling actuation. *Int Journal Smart Nano Mater*, 12(4): 375–389.

https://doi.org/10.1080/19475411.2021.1974972

67. Zhou Y, Zhou D, Cao P, *et al*., 2021, 4D printing of shape memory vascular stent based on βCD-g-polycaprolactone. *Macromol Rapid Commun*, 42(14): 2100176.

https://doi.org/10.1002/marc.202100176

68. Kim D, Kim T, Lee YG, 2019, 4D printed bifurcated stents with kirigami-inspired structures. *J Vis Exp*, (149): e59746 DOI: 10.3791/59746.

https://doi.org/10.3791/59746

69. Zhao W, Zhang F, Leng J, *et al*., 2019, Personalized 4D printing of bioinspired tracheal scaffold concept based on magnetic stimulated shape memory composites. *Compos Sci Technol*, 184: 107866.

https://doi.org/10.1016/j.compscitech.2019.107866

70. Hwangbo H, Lee H, Roh E, *et al*., 2021, Bone tissue engineering via application of a collagen/hydroxyapatite 4D-printed biomimetic scaffold for spinal fusion. *Appl Phys Rev*, 8(2): 021403.

https://doi.org/10.1063/5.0035601

71. Deng Y, Zhang F, Liu Y, *et al*., 2023, 4D printed shape memory polyurethane-based composite for bionic cartilage scaffolds. *ACS Appl Polym Mater*, 5(2): 1283–1292

https://doi.org/10.1021/acsapm.2c01833

72. Wang C, Yue H, Liu J, *et al*., 2020, Advanced reconfigurable scaffolds fabricated by 4D printing for treating critical-size bone defects of irregular shapes. *Biofabrication*, 12(4): 045025.

https://doi.org/10.1088/1758-5090/abab5b

ACCSCIENCE PUBLISHING

International Journal of Bioprinting

REVIEW ARTICLE

3D bioprinting and scaffold-free strategies for fabrication of multi-cellular tissues or organoids

Haoyu Li[1], Huixing Zhou[1]*, Chongwen Xu[1], Yen Wei[2]*, and Xiuying Tang[3]*

[1]School of Mechanical-Electronic and Vehicle Engineering, Beijing University of Civil Engineering and Architecture, Beijing 100044, China

[2]The Key Laboratory of Bioorganic Phosphorus Chemistry & Chemical Biology (Ministry of Education), Department of Chemistry and the Tsinghua Center for Frontier Polymer Research, Tsinghua University, Beijing 100084, China

[3]College of Engineering, China Agricultural University, Beijing 100083, China

Abstract

The biofabrication of multi-cellular tissues or organoids (MTOs) has been challenging in regenerative medicine for decades. Currently, two primary technological approaches are being explored: scaffold-based strategies utilizing three-dimensional (3D) bioprinting techniques and scaffold-free strategies employing bioassembly techniques. 3D bioprinting techniques include jetting-based, extrusion-based, and vat photopolymerization-based methods, and bioassembly techniques include Kenzan, fluid-based manipulation and microfluid, bioprinting-assisted tissue emergence, and aspiration-assisted technology methods. Scaffold-based strategies primarily concentrate on the construction of scaffold structures to provide an extracellular environment, while scaffold-free strategies primarily emphasize the assembly methods of building blocks. Different biofabrication technologies have their advantages and limitations. This review provides an overview of the mechanisms, advantages, and limitations of scaffold-based and scaffold-free strategies in tissue engineering. It also compares the strengths and weaknesses of these two strategies, along with their respective suitability under different conditions. Moreover, the significant challenges in the future development of convergence strategies, specifically the integration of scaffold-based and scaffold-free approaches, are examined in an objective manner. This review concludes that integrating scaffold-based and scaffold-free strategies could overcome the problems in the biofabrication of MTOs. A novel fabrication method, the BioMicroMesh method, is proposed based on the convergence strategy. Concurrently, the development of a desktop-scale integrated intelligent biofabrication device, the BioMicroMesh system, is underway. This system is tailored to the BioMicroMesh method and incorporates cell aggregate spheroids preparation, 3D bioprinting, bioassembly, and multi-organoid co-culture functions, providing an objective perspective on its capabilities.

Keywords: Multi-cellular tissues or organoids (MTOs); Biofabrication strategies; Scaffold-based and scaffold-free strategies; 3D bioprinting; Bioassembly; BioMicroMesh

***Corresponding authors:**
Huixing Zhou
(perc_zhx@126.com)

Yen Wei
(weiyen@tsinghua.edu.cn)

Xiuying Tang
(txying@cau.edu.cn)

Citation: Li H, Zhou H, Xu C, *et al*., 2023, 3D bioprinting and scaffold-free strategies for fabrication of multi-cellular tissues or organoids. *Int J Bioprint*, 9(6): 0135. https://doi.org/10.36922/ijb.0135

Received: April 14, 2023
Accepted: June 3, 2023
Published Online: July 25, 2023

Copyright: © 2023 Author(s). This is an Open Access article distributed under the terms of the Creative Commons Attribution License, permitting distribution, and reproduction in any medium, provided the original work is properly cited.

Publisher's Note: AccScience Publishing remains neutral with regard to jurisdictional claims in published maps and institutional affiliations.

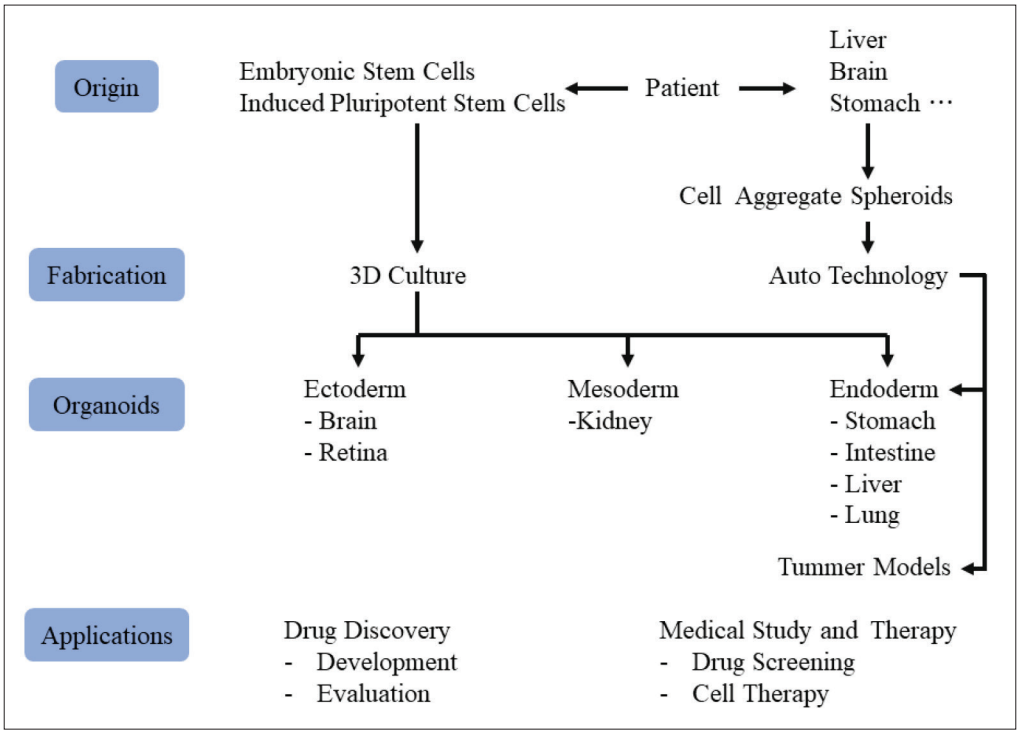

Figure 1. The schematic diagram of origin, fabrication path, organoids type, and applications of multi-cellular tissues or organoids.

1. Introduction

Previously, the term "organoid" was used to describe diverse types of three-dimensional (3D) culture systems which resemble the organ model to varying extents[1]. In the past decade, Lancaster and KNoblich[2] and Clevers[3] have proposed a tighter definition of "3D organoid": (i) contains one or more organ-specific cell types; (ii) is derived from embryonic stem cells (ESCs), induced pluripotent stem cells (iPSCs), or tissue-specific adult stem cells (ASCs); (iii) exhibits functions of the original organ to some extent. Bioengineering using patient-derived organoids is a hot topic right now[4]. Given that tissues or organoids typically consist of various types of stem cells, as shown in Figure 1, they can be called multi-cellular tissue or organoids (MTOs). The significance of MTOs is to fill the gap in cell behavior between animal model experiments and increase the accuracy of research[4]. Due to species discrepancies, animal models cannot fully replicate the physiological characteristics of the human body, and this is where patient-derived organoids come into play, as organoids technology can be used in disease mechanism studies, drug discovery research and screening, and regenerative medicine in human.

Cell heterogeneity is the prerequisite for constructing complex tissues or organoids[5]. However, each organ has its uniqueness. Thus, the MTOs biofabrication process differs for different organoid types. Conventional organoid culture protocols use a homogenous culture medium without gradients of nutrients or gases[6]. The protocols require the cells to be suspended or encapsulated in a 3D environment to guide spatial cell patterning. However, there are still numerous shortcomings and challenges in the traditional organoids culture[7]: (i) lack of maturity and impaired function compared with human tissues; (ii) poor operability, such as the transport of nutrients and metabolites, depends on diffusion, and the manipulation of the polarity of organoids is challenging; (iii) uncontrollable randomness (heterogeneity), where there are also significant random differences in formation efficiency, morphology, and function. The MTOs fabrication technology is still in the infancy step. Nevertheless, there are two paths for organoid fabrication: based on conventional natural differentiation and modern automated biofabrication technology.

Biofabrication mainly describes natural and technological processes in tissue engineering and regenerative medicine[8]. In this review, biofabrication refers to the process based on modern automation technology, as shown in Figure 2. Biofabrication technology has brought about a paradigm improvement in MTOs fabrication. Before the rise of biofabrication techniques, the fusion of developmental biology and cellular self-organization was the dominant paradigm of tissue engineering and regenerative medicine. Automation

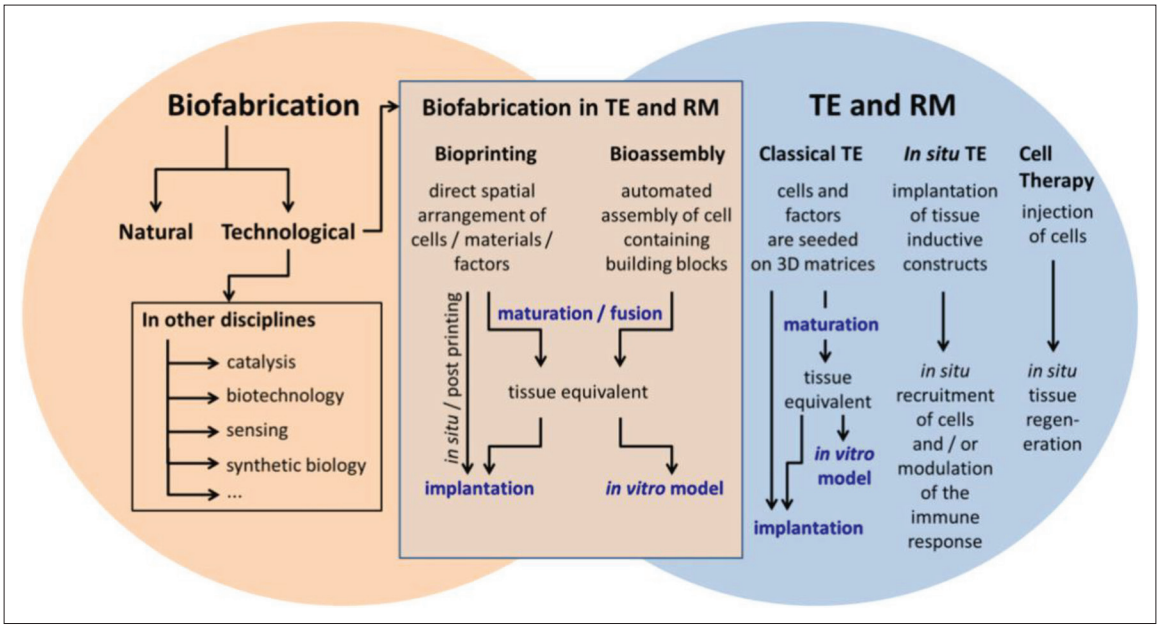

Figure 2. The schematic diagram of the term "Biofabrication" and its location. Reprinted with permission from Ref. [8]. Copyright © 2016 IOP Publishing Ltd.

of biofabrication technology has overcome the challenges in traditional tissue or organoid engineering in that cell position cannot be controlled precisely[9,10]. Therefore, the coordinated development and collaborative work of bioprinting and bioassembly technology expand the means of manipulating organoid growth. It also helps to improve the standardization of organoid fabrication and realize the reproducibility and functionalization of organoids.

Biofabrication can be achieved via two strategies[8]: bioprinting scaffold-based and bioassembly-based scaffold-free strategies. Martin *et al.*[11] have proposed the concept of "organogenesis by design." The concept leverages bioprinting to impose geometric designs and sizes to direct a pool of printed stem cells toward a developing organoid. Compared to traditional symmetrical, spherical self-assembly, the self-patterning of the bioprinted cells can be guided through user-defined micropatterning. Alternately, bioprinting can be utilized in a bottom-up approach whereby numerous small tissues or organoid units are deposited spatiotemporally to drive subsequent development. The patterning imposed during biofabrication intends to instruct the formation of more complex, large-scale organogenesis from the smaller intermediate organ progenitor building blocks[12].

MTOs fabrication based on modern automation technologies such as organ-on-a-chip, assemblies, and 3D bioprinting is preferred[6]. However, MTOs fabrication strategies rely on their developmental and self-organizing processes. There are several technological challenges to fabricating functionally acceptable MTOs[13]. One of the limitations of organoid fabrication is that organoids stop developing and die after growing to a specific size due to limitations in nutrient and oxygen diffusion, as well as nuclear-cytoplasmic ratio and other factors[14]. For example, cerebral organoids can grow to the size of 3 mm when cultured in a spinning bioreactor[2,3]. 3D bioprinting was employed to create scaffold-free cellular patches for diaphragm reconstruction using tabular cell constructs consisting of human dermal fibroblasts (hDFs) and human umbilical vein endothelial cells (hUVECs)[15], which were xenotransplanted into immunodeficient rats with a 12 × 10 mm rectangular defect in the diaphragm. In organoid generation, it is difficult to determine the optimal time node for establishing vascularization, so the technology for fabricating vascularized organoids has aroused the interest of many researchers[16]. The other limitation is low fabrication efficiency. For example, the directed differentiation of pluripotent stem cells (hPSC) into specific organoids holds promise for drug screening, disease modeling, and kidney organ transplantation, but these applications are hampered by organoid variability, immaturity of nephrons, low yield, and limited size[17]. Other challenges include the inability to mimic the immune microenvironment fully, the lack of precise spatial order, structure, and size randomization, the inability to form cell-to-cell support rapidly, and the establishment of coexistence systems[18].

The mechanisms, advantages, and limitations of various technics based on scaffold-based and scaffold-free strategies are examined in this review. In the discussion

section, we compared the advantages, disadvantages, and applicability of scaffold-based and scaffold-free strategies. We believe that a balanced consideration of both approaches is necessary to achieve the common goal of manufacturing functional tissue-like structures (MTOs). Subsequently, we delved into the discussion of convergence strategies and hybrid biofabrication technologies. The vision for future prospective hybrid technology involves emerging convergence strategies for fabricating complex MTOs. Subsequently, a novel MTOs biofabrication method based on the convergence strategy, the BioMicroMesh method (BMMm), is introduced for the first time. Concurrently, the development of new MTOs biofabrication equipment, the BioMicroMesh system (BMMs), is underway, aiming to provide precise experimental variable control and ensure the fabrication of commercial MTOs models for biological research. It is hoped that this review will encourage further research and development in MTOs manufacturing and related specialized equipment.

2. Scaffold-based strategy with 3D bioprinting techniques

Scaffold-based strategy is a pivotal approach in the fabrication of MTOs constructs, as scaffolds form the fundamental architecture of such constructs, and 3D bioprinting technology serves as the mainstream methodology for scaffold manufacturing[19,20]. Scaffolds play a crucial role in providing structural support for cellular adhesion and subsequent MTOs maturation[21,22]. 3D bioprinting technology is an additive fabrication method that prints scaffolds layer-by-layer automatically. The technology has become a promising strategy in cell-laden tissue engineering or MTOs restoration[12,23]. In a general sense, 3D bioprinting can be divided into four development stages[24]. Stage I involves the printing of non-biocompatible structures that can be used as models for surgery planning. Stage II encompasses the printing of biocompatible but non-biodegradable products, such as implanted prostheses. Stage III focuses on the printing of biocompatible and biodegradable products that can serve as scaffolds to enhance tissue damage repair or regeneration. Finally, Stage IV involves cellular printing to create biomimetic 3D structures using cells[24]. In this article, we provide a comprehensive definition of bioprinting that encompasses the stages of development from Stage III to Stage IV. Based on the different printing mechanisms, 3D bioprinting technology can be categorized into three main types: jetting-based[20], extrusion-based[25], and vat photopolymerization-based[26]. Table 1 summarizes the characteristics of three techniques in terms of printhead, printing speed, resolution, cell viability, cell density, crosslinking method, features, advantages, and disadvantages.

Table 1. Comparison of major types of scaffold-based 3D bioprinting techniques

	Jetting-based	Extrusion-based	Vat photopolymerization-based
Nozzle	Exist	Exist	No
Printing speed	Fast (1–10^4 drop/s)	Slow (10–50 μm/s)	Medium (200–1600 mm/s)
Resolution	50–100 μm	100–500 μm	10–100 μm
Cell viability	>85%	80%	>95%
Cell density	10^6–10^7 cells/ml	10^8–10^9 cells/ml	>10^8 cells/ml
Crosslinking method	Chemical, photocrosslinking	Chemical, photocrosslinking, shear dilution, temperature	Chemical, photocrosslinking
Features	• Can be equipped with multiple nozzles • Requires the printed biomaterial to be in liquid form • Complex nozzle structure • Easy accessibility	• Printable high-viscosity biomaterials • Wide range of printable biocompatible materials • Most commonly used • Highly controlled printing structure	• High resolution (lateral around 20–50 μm, vertical around 25–100 μm) • Ability to print a wide range of viscosities of bioresin (up to 5 Pa·s) • Potential to fabricate highly complex structures, support structure fabrication possible • Faster printing speed and the ability to print large-scale structures with micron-level resolution
Limitations	• The thermal actuator is potentially prone to reduced equipment structural stability and compromised cell viability. • Printhead is prone to wear and clogging. • Cannot print high-viscosity materials or high concentrations of cells • Low drive pressure	• Limited resolution range • High mechanical pressure and shear stress leading to reduced cell viability	• Harmful effects of UV rays, resulting in more DNA damage • Cytotoxic effects from increased light intensity and photoinitiator concentration • Material degradation and bubble damage in two-photon polymerization (2PP) technology
Reference	[118–120]	[121,122]	[121,123]

2.1. Jetting-based bioprinting

The mechanism of jetting-based bioprinting is the drop-on-demand (DOD) patterning of bioink droplets onto a substrate to create two-dimensional (2D) and 3D models, as shown in Figure 3A. This method relies on various mechanisms for generating and ejecting the bioink droplets[27], such as the vaporization of bubbles by a heater in a thermal style[28], deformation under electrode pressure in an electrostatic style[29], vibration of a piezoelectric actuator in a piezoelectric style[30,31], or the application of high voltage field energy from nozzle electrodes in an electrohydrodynamic style[32,33]. As stated in Table 1, one of the advantages of jetting-based bioprinting is that it selectively ejects droplets when the signal reaches the required levels, allowing for the precise formation of predetermined patterns. Moreover, due to the comparable size of the inkjet nozzle (50 μm) to that of a cell, it is also suitable for single-cell printing. The high-resolution printing capability facilitates the fabrication of smaller tissues and organs, while the distinctive printing patterns promote enhanced interactions between cells and the extracellular matrix[34]. However, shear stress or pressure during printing or collision with the substrate after ejection in jetting-based bioprinting may damage the cell. Nonetheless, the proportion of cells affected by such damage is relatively low, and the efficiency and high-throughput capabilities of inkjet printing outweigh its drawbacks. A novel method for creating multiple cell types and extracellular matrix tissue structures uses inkjet printing technology[35,36]. However, the studies highlight the potential of inkjet technology for fabricating complex hybrid tissue structures requiring multiple cell types. Further investigation is needed to optimize the printing parameters and analyze the stability and functionality of the printed tissues.

2.2. Extrusion-based bioprinting

Extrusion-based bioprinting is a commonly employed technique that allows for precise deposition of bioinks by extruding material from a nozzle[37]. In general, the biomaterial can be extruded from cartridges using either pneumatic pressure or mechanical forces, such as piston-driven or screw-driven mechanisms, as shown in Figure 3B. Extrusion-based bioprinting allows for printing bioinks with high cell densities (10^8–10^9 cells per ml) and the simultaneous deposition of multiple cell types to create heterogeneous structures, as shown in Table 1. However, this technique presents challenges related to cell viability due to shear stress-induced damage and nozzle clogging. To enhance the performance of extrusion-based bioprinting, optimization of bioink composition, selection of appropriate nozzle size, and careful material choice are necessary. Prior to printing, adjusting printing parameters such as pressure, speed, and layer thickness is essential to achieve improved outcomes. A couple of studies using extrusion-based bioprinting demonstrated the essential requirement of a multi-cellular composition of the 3D liver model consisting of hepatic parenchymal HepaRG cells, stellate cells (LX-2), and human umbilical vein endothelial cells (HUVECs), in order to construct a liver fibrogenesis model[38,39]. However, due to the complex cellular composition and multi-scale spatial arrangement between cells and extracellular matrix in MTOs, the formulation of bioinks remains a challenge[40]. The multi-cellular 3D bioprinting and bioink material design strategies proposed in the literature[40,41] show great potential in the development of MTOs that mimic the native microenvironment of organs. However, this conceptual framework still relies on different types of scaffolds, making it difficult to construct multi-tissue organoids that truly reflect their physiological relevance.

2.3. Vat photopolymerization-based bioprinting

Vat photopolymerization-based (VP-based) bioprinting involves the creation of scaffold structures using photopolymerization reactions in which a photocurable liquid bioresin is exposed to the light of a specific wavelength[26]. The mechanism of VP-based bioprinting is shown in Figure 3C. This technique encompasses various methods such as stereolithography (SLA), digital light processing (DLP), and two-photon polymerization (2PP).

SLA utilizes laser refraction and scanning in a vat to cure bioresin, with options for top-down or bottom-up printing[26]. It offers high resolution and the ability to print complex structures but has limitations due to harmful UV rays. As stated in Table 1, SLA techniques offer advantages such as high lateral and vertical printable resolution (around 20–50 μm and 25–100 μm, respectively), the ability to print a wide range of viscosities (up to 5 Pa·s), high printable cell density (up to 10^8 cells per ml), and the potential to fabricate highly complex structures with support structures. On the other hand, DLP uses a digital micromirror device to crosslink bioresin, allowing for faster printing and large-scale structures with micron-level resolutions[42]. Lastly, the 2PP system employs a near-infrared femtosecond laser light source (around 740 nm wavelength) to fabricate microstructures with nanoscale resolution (up to sub-100 nm)[43]. The femtosecond laser is tightly focused on the bioresin using an oil-immersed objective lens. Polymerization in 2PP is initiated by exciting molecules through two-photon absorption. This process occurs rapidly (mm/seconds of scanning speed) and enables the fabrication of highly complex structures at any spatial position. However, the application of 2PP in bioprinting is limited by drawbacks such as material degradation caused by high laser power and bubble damage[43]. A manufacturing method for MTOs called

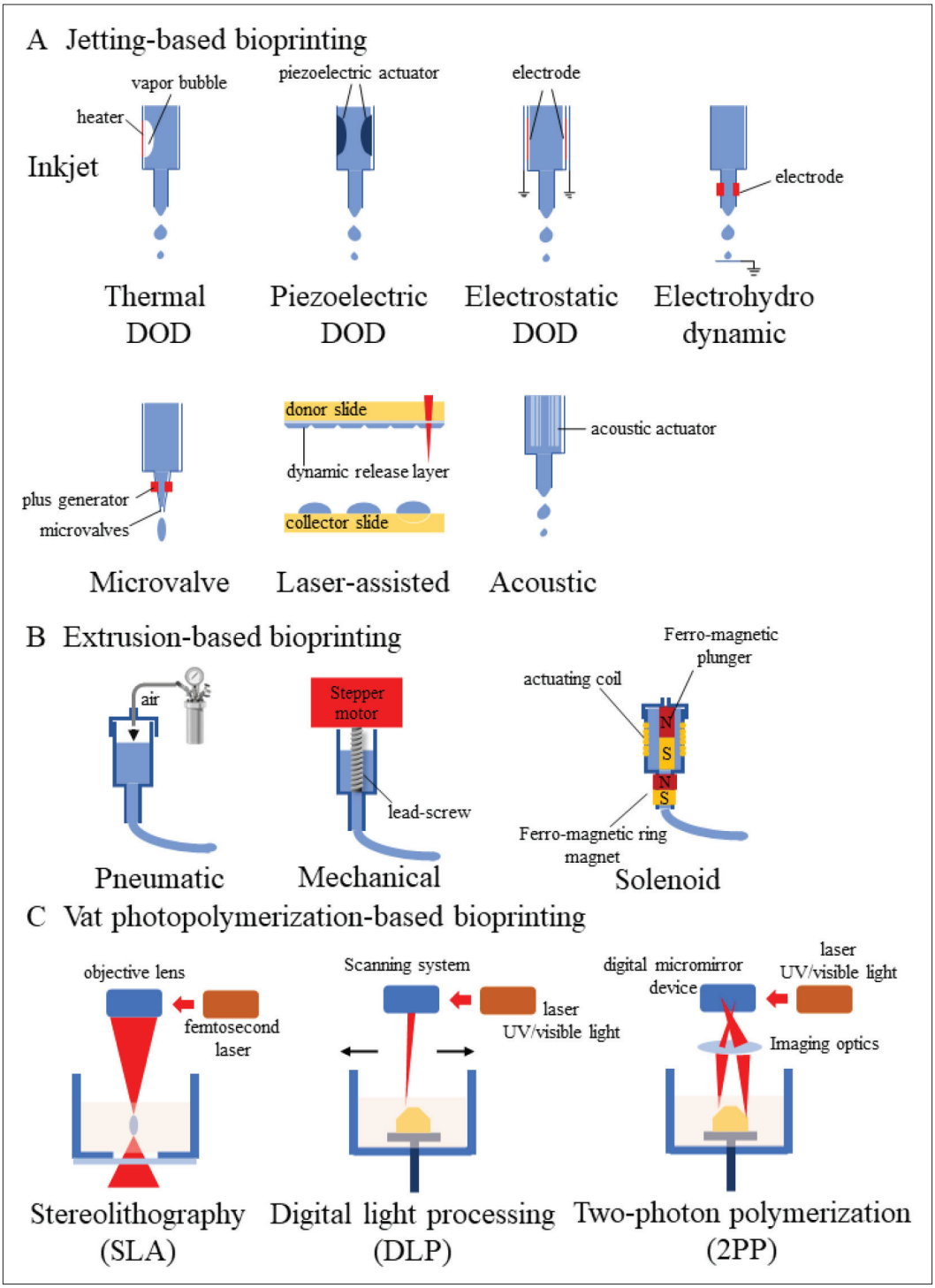

Figure 3. The mechanism diagram of the scaffold-based strategy with 3D bioprinting techniques. (A) Different mechanisms for droplet generation include thermal style, electrostatic style, piezoelectric style, electrohydrodynamic style, microvalve, laser-assisted style, and acoustic style. Reprinted with permission from Ref. [56]. Copyright © Y. Wang *et al*. (B) Different mechanisms for extrusion include pneumatic, mechanical, and solenoid. Reprinted from Ref. [112], Creative Commons Attribution 4.0 International (CC BY 4.0). (C) Different mechanisms for vat photopolymerization include stereolithography (SLA), digital light processing (DLP), and two-photon polymerization (2PP). Reprinted with permission from Ref. [26] Copyright © 2020 IOP Publishing Ltd. Reused images in Fig. 3A and B are released under Creative Commons Attribution 4.0 International (CC BY 4.0).

photopolymerization of orderly extruded multi-materials (POEM) has been proposed, developed, and fully characterized[44], and a novel workflow utilizing machine learning to achieve precise control over the stiffness of elastomeric scaffolds enables the fabrication of multi-scale structures with MTOs applications[45]. However, their applications in bioprinting are limited due to the harmful effects of UV rays (resulting in more DNA damage with shorter wavelengths) and cytotoxic effects from increased light intensity and photoinitiator concentration. To mitigate DNA damage, the use of visible light sources and biocompatible photoinitiators is necessary. The drawbacks of VP-based bioprinting exceed its benefits. The inherent characteristics of this technique render it inappropriate for generating complete tissue constructs that meet the requirements of regenerative medicine[46]. Nevertheless, this approach can be employed to achieve precise patterning of multi-cellular microenvironments, such as the tumor microenvironment, for the purpose of disease modeling or drug testing[47].

The scaffold is used to provide material support and a conducive cell growth environment for MTOs. An ideal scaffold should possess sufficient mechanical stability and biocompatibility for cell viability. Excessive cell aggregation leading to hypoxic necrosis is a major reason for the failure of MTOs fabrication. Therefore, the use of porous structures should be maximized to increase the cell attachment surface area and maintain the good breathability of MTOs. Additionally, non-toxic and safe biocompatible materials should be employed for the scaffold. Thin film and fiber structures can complement the mechanical-support stability and serve as plastic-support structures on the outer surface once MTOs are initially formed. Therefore, the optimal scaffold structure should involve a combination of these four types of structures, with a particular emphasis on the rational use of porous structures. According to the classification based on structural forms, the scaffolds produced through 3D bioprinting can be categorized into the following types: porous, hydrogel, fiber, and film scaffolds[48], as shown in Figure 4. Porous structures provide a suitable environment for ECM secretion and nutrient delivery, while hydrogel structures are highly biocompatible with controlled degradation. Fiber structures promote cell behavior but require surface functionalization, and film structures maintain natural ECM but necessitate partial decellularization.

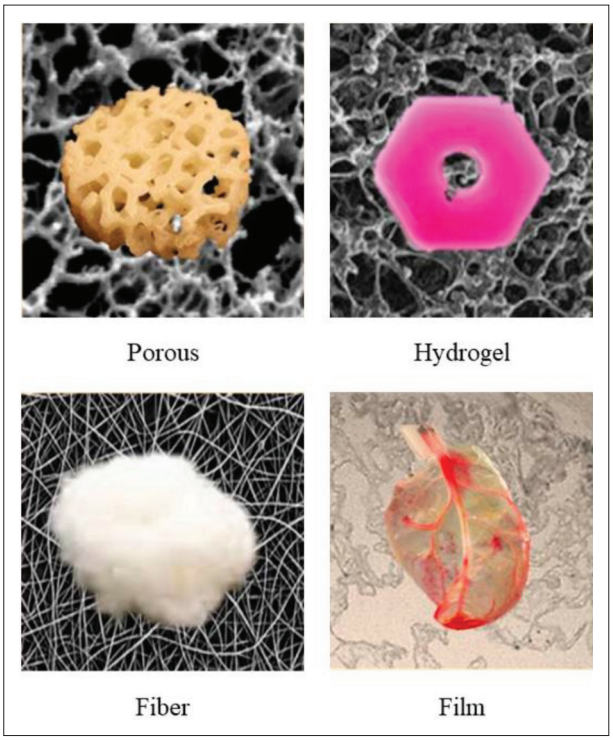

Figure 4. Different forms and morphological structures of scaffolds for biomedical applications. Reprinted from Ref. [48], Creative Commons Attribution 4.0 International (CC BY 4.0).

3. Scaffold-free strategy with bioassembly techniques

The scaffold-free strategy represents an alternative approach for MTOs fabrication, where cell-aggregated spheroids and microtissue building blocks are assembled in specific bioassembly techniques, akin to constructing Lego bricks while incorporating a culture medium to support cell survival and fusion during the biofabrication process[10,49]. The foundation of this strategy lies in cell–cell adhesion, a critical regulatory factor governing the morphology and functionality of MTOs both *in vivo* and *in vitro*[50]. Numerous studies have concluded that cell-aggregated spheroids exhibit excellent scalability and controllability. In the scaffold-free strategy, aggregate spheroids serve as the smallest fabrication unit, mimicking the cell–cell and cell–extracellular matrix communication and interactions observed during embryonic development and MTOs construction[51].

The distinguishing feature of the scaffold-free strategy is that the manufacturing of MTOs does not rely on scaffolds or only requires temporary scaffolds. Instead, it relies on the precise assembly of building units and subsequent cultivation of MTOs. Replicating complex 3D organ structures and tissue microenvironments using conventional scaffold-based 3D bioprinting technologies is challenging due to the inability to precisely define the spatial distribution of cells[52]. Moreover, as scaffold-based approaches advance, issues and limitations such as immune responses, infection risks, and potential disease transmission associated with bioinks and biomaterials have

emerged[53]. The advantages of the scaffold-free strategy compensate for the limitations of scaffold-based strategies. The scaffold-free strategy is particularly suitable for fabricating complex heterogeneous structures containing multiple cell types[54,55]. This bottom-up assembly approach holds promise as a module for constructing intricate MTOs[56]. The key bioassembly technologies based on the scaffold-free strategy include the Kenzan and aspiration-assisted technology, fluid-based manipulation, suspended bioprinting, and bioprinting-assisted tissue emergence. A comparison of four techniques is presented in Table 2, considering aspects such as resolution, printing speed, building scale, features, advantages, and disadvantages. It should be noted that the implementation process of the scaffold-free strategy involves the preparation of aggregate spheroids or building blocks, followed by bioassembly based on different techniques, and, finally, the cultivation of MTOs. The preparation of aggregate spheroids or building blocks also involves various complex microscale techniques, which will not be discussed in this review. This review focuses solely on the technology related to bioassembly processes based on cell aggregates.

3.1. Kenzan and aspiration-assisted technology

Kenzan techniques, or microneedle array techniques, offer a pathway to assemblies of aggregate spheroids in which the spatial organization, cell–cell communication, and extracellular matrix production of natural tissue morphogenesis are recapitulated[43,57]. As shown in Figure 5A, the adsorption end effector of the robot, such as Cyfuse Regenova[58], picks up the prefabricated aggregate spheroids, and the robotic arm pierces the spheroids on a microneedle array in the bioreactor according to a predetermined path, where the microneedle array is only temporary support[35]. When the tissue matures, the microneedles are removed, as shown in Figure 5A. It is worth noting that the end effector of the device developed based on the Kenzan method is precisely the aspiration-assisted bioprinting technique, which allows for the precise positioning of cell aggregates in the 3D space[59]. In this method, minimal aspiration force (critical lifting pressure) is utilized to position the cell aggregates, overcoming gravity, buoyancy force, hydraulic drag, and the thermodynamic barrier at the interface while maintaining cell viability above 80%. This technique has been applied in the engineering of osteochondral tissues[59].

The microneedle array is made of stainless steel, with needles around 150 microneedles in diameter and 500 microneedles spacing between adjacent needles to allow contact with adjacent aggregate spheroids[60]. The diameter of the cell-aggregated spheroids is about 140–500 microneedles[57,61]. The diameter and geometric

Table 2. Comparison of major types of scaffold-free strategy with bioassembly techniques

	Kenzan and aspiration-assisted technology	Fluid-based manipulation	Suspended-based techniques	Bioprinting-assisted tissue emergence
Resolution	10–200 μm	1 nm–300 μm	100–180 μm	100–500 μm
Printing speed	400 μm/s	-	5.6 mm/s	10–50 μm/s
Construct size (longest dimension)	12 mm	10 mm	40 mm	12 mm
Feature and advantage	• Recapitulation of natural tissue morphogenesis • Precise positioning of cell aggregates • Large-scale structure generation • Potential for organ pre-vascularization	• High biocompatibility • Essential for structural fabrication • Microscale accuracy	• High-resolution printing capability • Long-term culture support for bone and cartilage • Generation of complex architectures • Perfusion of living matrix with oxygenated media • Compatibility with various organoids	• Enables spontaneous formation of larger MTOs • Precise control over initial spatial organization and density of building units • Does not require overly complex bioprinting modalities
Disadvantage	• Lower resolution for unknown cell combinations and culture conditions • Physiological alterations due to spheroid size and compaction • Manual positioning inefficiency at the single-cell scale	• Limitations with large cell numbers and thicker tissues • Biocompatibility concerns • Size constraints in optically induced dielectrophoresis (ODEP) devices • Technical challenges for each technique	• Limited biomimicry due to dense nature of the bioinks • Challenges in achieving full endothelialization	• Placement of spheres in the scaffold is done manually • Requires suitable conditions and post-printing remodeling for geometric complexity
Reference	[43,105,124]	[125]	[126–128]	[129]

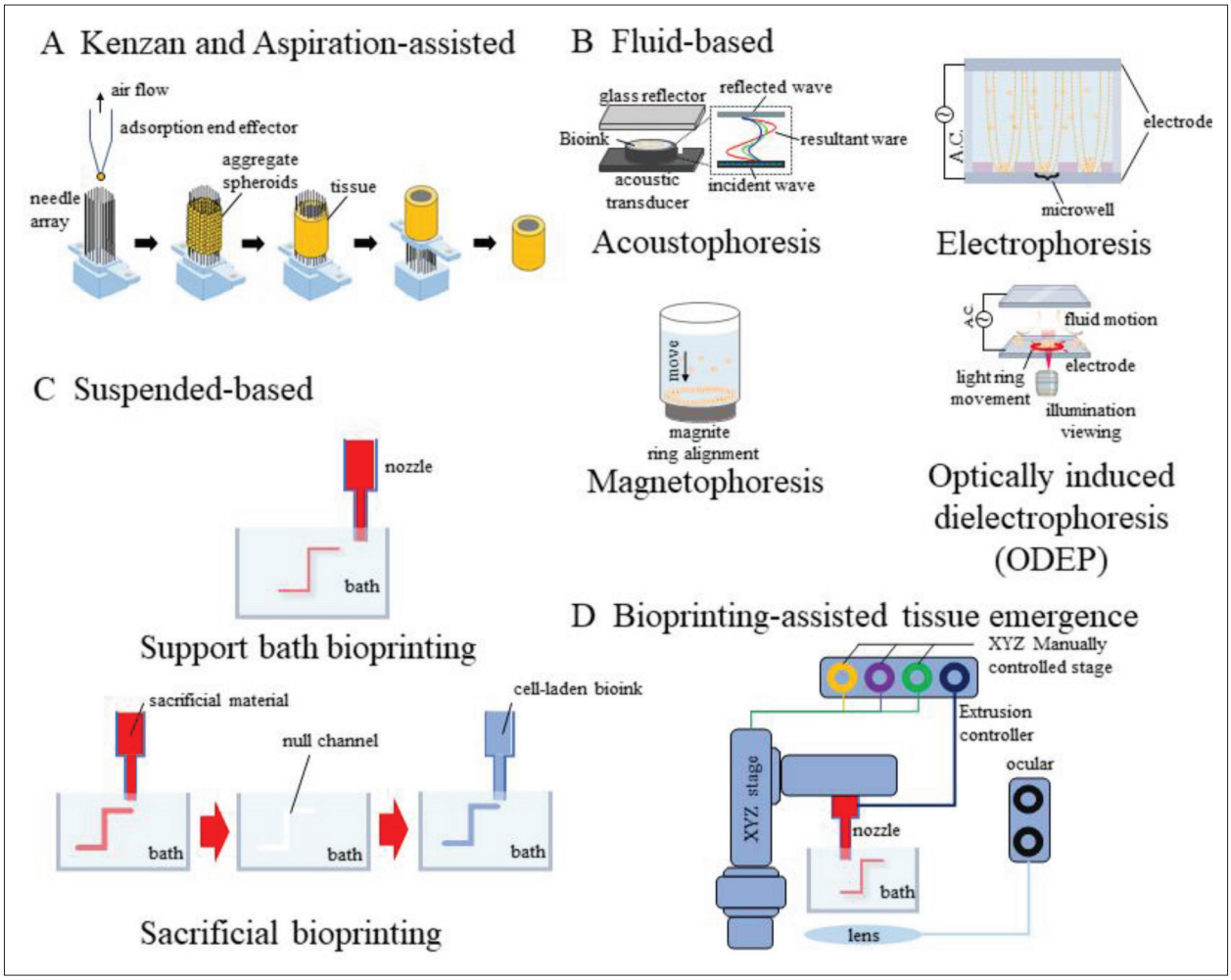

Figure 5. The mechanism diagram of the scaffold-free strategy with bioassembly techniques. (A) Cell construct fabrication using the Kenzan method. Reprinted from Ref. [113], Creative Commons Attribution 4.0 International (CC BY 4.0). (B) Fluid-based manipulation. The acoustophoresis method is a transducer that generates incident waves, interfering with waves reflected from a glass reflector on top of an assembly media chamber. Reprinted with permission from Ref. [77]. Copyright © 2016 John Wiley & Sons Inc. Electrically induced reversible assembly of living multiple cell aggregate spheroids. Magnetic force-based 2D and 3D cell culture techniques. Reprinted from Ref. [114]. Creative Commons Attribution 4.0 International (CC BY 4.0). ODEP force-based manipulation via light-induced localized electrical fields. Light can be directed to generate arbitrarily shaped cell-encapsulated microstructures, such as a circle shape. Reprinted with permission from Ref. [115]. Copyright © 2018 AIP Publishing Ltd. (C) Suspended-based bioprinting. Support bath bioprinting uses a liquid-like solid medium to physically support bioprinted structures while enabling nutrient diffusion. Sacrificial bioprinting creates temporary support structures that are later removed to enable complex internal architectures in bioprinted constructs. Reprinted from Ref. [116], Creative Commons Attribution 4.0 International (CC BY 4.0). (D) Bioprinting-assisted tissue emergence uses biobuilding blocks that can be spatially arranged to form interconnected and evolving cellular constructs by 3-axial manually controller plate. Reprinted from Ref. [117], Creative Commons Attribution 4.0 International (CC BY 4.0).

relationships of the needle space need to match the diameter of the spheroids. Ideally, the diameter of the needle should not exceed the radius of the cell-aggregated spheroids. Otherwise, it will cause more damage to the cells, and the needle spacing needs to be equal to the diameter of the cell sphere. The number of cell-aggregated spheroids that the microneedle can carry depends on the cell type and the degree of spheroid compaction. The aggregate spheroids used in the Kenzan technique need to strike a balance between cell adhesion and matrix richness. If the adhesion is too large, it will lead to the insertion and arrangement of the spheroids, and if the matrix richness is increased, the performance of the spheroids will be changed[43,57,62-64]. The use of iPSC-derived vascular cell-aggregated spheroids as building blocks for scaffold-free biofabrication was reported, demonstrating the potential of Kenzan technology in promoting organ pre-vascularization[29]. The significant advantage of Kenzan technology is that it allows the generation of large-scale structures with enhanced cells.

However, Kenzan method has some challenges. The first is the low-resolution problem. Since the needle spacing defines a relatively narrow spheroid diameter range, the resolution depends on the size of the spheroids. Therefore, this may prove challenging for an optimal spheroid generation when considering unknown cell combinations and culture conditions[60]. However, Murata *et al.*[43] believed that the Kenzan method could quickly expand and fuse external cells. Compared with the scaffold-based strategy, its resolution can be further reduced by the migration and fusion of cells inside the spheroid so that the mechanism can be further reduced, thereby improving the resolution[65,66]. The second challenge is that spheroid size, uniformity, and compaction issues can alter the physiological conditions for oxygen and metabolite diffusion[67]. Ozbolat *et al.*[68] proposed that cells can be cultured by secondary attachment to the surface of spheroids or hydrogel beads to improve spatial heterogeneity. Consider developing aggregate spheroids that continuously release oxygen and nutrients and integrate them into the tissues they build[69]. The third challenge is that the Kenzan method is similar to the aspiration biosystem method, which also faces the inefficiency of manual positioning in the configuration of heterogeneous structure spheroids at the single-cell scale.

3.2. Fluid-based manipulation

Assembling spheroids or tissue building blocks into MTOs is challenging, as MTOs typically involve complex biological interfaces, such as cardiac organoids and osteochondral constructs. In this regard, fluid-based manipulation has emerged as effective means for spatially organizing spheroids[70]. Fluid-based manipulation is commonly used with microfluidic devices to sort, capture, pattern, and encapsulate cells with high biocompatibility[71,72]. This technology is characterized by a contactless and label-free cell manipulation method, which is increasingly used in organ-on-a-chip devices and is an essential technique for aligning and patterning cells in structural fabrication. According to different mechanisms, there are acoustophoresis, magnetophoresis, and optically induced dielectrophoresis techniques. These techniques utilize fluid flow, acoustic waves, magnetic fields, or light-induced electric fields to manipulate and position particles or cells in a fluidic environment.

Acoustophoresis, as shown in Figure 5B, involves the use of surface acoustic wave (SAW) actuators to create precise and localized sound fields, enabling the manipulation and alignment of cells in 3D space[73]. However, limitations arise when dealing with large numbers of cells or thicker target tissues, and the high natural frequency of SAW devices can lead to temperature increases and unnecessary fluid movement[74–77]. On the other hand, bulk acoustic wave transducers operating at lower frequencies have been explored to overcome these challenges[78,79]. Acoustic holography technology holds promise for larger length scales, as it allows for modulating the phase and shaping the acoustic intensity distribution.

Electrophoresis- and magnetofluid-based manipulations rely on electrophoresis and magnetophoresis, respectively, to move and levitate cells, as shown in Figure 5B. Paramagnetic chelates like gadolinium are commonly used in these techniques[80], but concerns regarding biocompatibility have been raised. Mitigating cytotoxic effects can be achieved using low-toxicity salts, increasing magnetic field strengths, or conducting magnetic bioassembly in microgravity environments[81]. Notably, microgravity experiments conducted on the International Space Station have shown the successful construction of 3D tissue using implant-grade human chondrocytes.

Optically induced dielectrophoresis (ODEP) technology employs focused light to generate a dielectrophoresis field[82]. ODEP devices consist of a fluid medium sandwiched between a photoconductive material and separate electrodes[83], as shown in Figure 5B. By altering the illumination position, various electrode patterns can be formed, enabling precise manipulation tasks such as cell aggregation, isolation, pairing, and fusion. However, ODEP devices have a relatively small vertical size due to the requirement of electrodes on both sides of the fluid domain.

Fluid-based manipulation techniques offer unique advantages for cell manipulation and assembly. Acoustophoresis provides microscale accuracy, magnetophoresis enables controlled cell movement through magnetic fields, and optically induced dielectrophoresis allows precise cell manipulation using focused light. However, limitations such as challenges with large cell numbers, biocompatibility issues, and size constraints exist within each technique.

3.3. Suspended-based techniques

Suspension-based techniques encompass two main approaches: support bath bioprinting and sacrificial bioprinting. In the support bath technique, as shown in Figure 5C, a suspension medium containing tightly packed granular hydrogel microgels is used as a liquid-like solid support for the printed structure. This medium allows for the deposition of individual cells or cell aggregates while enabling the diffusion of nutrients and waste through the interstitial spaces between the microgels[84]. This approach has demonstrated high-resolution printing, capable of reproducing personalized tissues and organs[85]. It has also been applied to support the bioprinting of bone and cartilage, where cellular condensations are maintained within a mechanically stable support medium for long-term culture[86].

On the other hand, as shown in Figure 5C, the sacrificial bioprinting technique reverses the support bath paradigm. Here, a sacrificial ink is printed into a slurry-like support bath composed mainly of cellular spheroids[87]. By combining a suitable extracellular matrix and organ building blocks, the support bath exhibits shear-thinning behavior, yielding ahead of the printing nozzle and self-healing behind it, similar to traditional embedded printing techniques that use microgels. Notably, the extracellular matrix solution alone lacks the necessary rheological properties to support embedded 3D printing. However, the extracellular matrix stiffens at physiological temperatures, preserving the geometry formed within the organ building blocks by the sacrificial ink during its removal.

The sacrificial bioprinting technique enables the generation of networks of perfusable tubular features within the printed constructs, which can serve as templates for vascular channels exceeding 40 mm in length and 4 mm in thickness. Cell viability is maintained within the densely populated living matrix by perfusing hyper-oxygenated culture media through printed channels. Attempts have also been made to endothelialize the lumen of these channels with HUVECs, although achieving a confluent layer of endothelial cells throughout the entire lumen has not been fully realized. Nonetheless, the results suggest that HUVECs can adhere to the fusing embryonic bodies and remain in place during perfusion. Patent channels have been successfully printed into various organ blocks, including compacted embryonic bodies, cerebral organoids, and cardiac spheroids, without disrupting the complex architectures present within these developing organoids[63].

Suspension-based 3D bioprinting techniques offer unique advantages and challenges. The support bath approach utilizing microgel support baths allows for high-resolution printing and unrestricted diffusion but may be limited in biomimicry due to the dense nature of the bioinks. On the other hand, the sacrificial bioprinting technique, with sacrificial printing into cellular spheroid-based support baths, enables the generation of complex architectures and perfusable vascular networks, but achieving full endothelialization remains a challenge. Both techniques contribute to the advancement of 3D bioprinting in terms of tissue engineering and organ fabrication.

3.4. Bioprinting-assisted tissue emergence

Bioprinting-assisted tissue emergence aims to enable the spontaneous formation of larger centimeter-scale multi-cellular organotypic tissues by utilizing bioprinting to precisely control the initial spatial organization, texture, and density of the building blocks[88]. As shown in Figure 5D, the bioprinting-assisted tissue emergence system integrates an extrusion-based printing system, a support bath printing system, and a manual control console system. This system provides an effective method of spatial 3D positioning: the extrusion-based printing system creates precise spatial templates, the manual control system regulates the spatial position of the syringe pump's tip, and the bioprinted bioink is extruded into a suspension bath and crosslinked at 37°C to maintain stability in the spatial environment.

The sphere-based modular assembly method has limited applicability, and biofabrication technologies based on cells or spheroids assembly must consider size control, production efficiency, heterotypic cell co-culture, vascularization, as well as *in vitro* pretreatment and maturation[51]. This method is unsuitable for tissues or organoids with high mechanical properties, such as muscles and bones, as these tissues or organoids typically thrive under high physiological conditions[70]. The scaffold-free approach results in tissues with poor mechanical properties and may rely on temporary scaffolding until the tissue is fully mature[12]. Bioprinting-assisted tissue emergence allows for spatial and temporal control over the introduction of support cells, which play a crucial regulatory role in the development of organoids, thus enhancing growth and development[88]. Although bioprinting equipment requires considerable precision, this method does not necessitate overly complex bioprinting modalities. Instead, the bioprinter is used to accurately and precisely control experimental variables, such as cell density, initial tissue geometry, and the proximity and positioning of co-deposited heterogeneous cell populations. However, a drawback is that the placement of spheres in the scaffold is done manually[89]. Interestingly, the development of the bioprinting-assisted tissue emergence technique demonstrates that highly complex printing methodologies are not necessary to strictly define spatial control over organoid/spheroid deposition. Instead, by finding and adjusting suitable conditions between developing organoids and the surrounding environment, the geometric complexity of the final tissue can be achieved through post-printing remodeling and self-organization. Therefore, bioprinting appears to be best suited as a tool within a design strategy to define initial conditions and create a favorable environment for the naturally programmed organoid building blocks and their relevant support cells to self-organize into specific tissues or organs[70].

4. Discussion and perspective

4.1. Which is better: scaffold-based or scaffold-free?

Both scaffold-based and scaffold-free strategies should be combined. Scaffold-based strategies are preferable for

manufacturing structurally complex and mechanically robust MTOs, while scaffold-free strategies are more suitable for creating biologically scalable constructs that better mimic native tissue environments. The integration of both approaches enables the utilization of their respective strengths and the mitigation of their limitations, thereby advancing the development of functional multi-cellular tissues and organoids.

Scaffold-based and scaffold-free strategies are employed for manufacturing MTOs. Scaffold-based strategies involve using scaffold structures as physical support for guiding cell growth and organization, providing structural integrity, and facilitating the formation of MTOs architectures. Biocompatible materials are crucial for scaffold manufacturing to support cell viability[90]. While 3D bioprinting offers precise fabrication of complex scaffold structures and allows for co-printing multiple cell types and biomaterials, it also has limitations[91]. The limited availability and performance of biocompatible materials and bioinks pose challenges related to ink contamination and toxicity[92]. Furthermore, 3D bioprinting is relatively slow and can encounter issues like nozzle clogging and large equipment size due to the complexity of the printing apparatus[93].

On the other hand, scaffold-free strategies aim to create MTOs without using exogenous scaffolds. These strategies rely on the inherent self-assembly and organization abilities of cells to form functional tissues. Cells are cultured and allowed to aggregate or undergo spheroid formation, promoting cell–cell interactions and extracellular matrix deposition[94]. Scaffold-free approaches offer advantages such as simplified fabrication processes, enhanced cell–cell communication, and the potential to recapitulate native tissue organization[95]. The advantages of scaffold-free strategies directly address the drawbacks of scaffold-based strategies. However, they often face challenges in achieving precise control over MTOs architecture and may have limited scalability[96].

The choice between scaffold-based and scaffold-free strategies depends on the specific requirements of the desired MTOs. Scaffold-based approaches are advantageous for fabricating complex and anatomically accurate structures, providing mechanical support, and enabling the incorporation of multiple cell types. In contrast, scaffold-free strategies offer simplicity, better mimicry of native tissue microenvironments, and potential scalability for high-throughput applications. Ultimately, a combination of both strategies may be employed to harness their respective strengths and overcome limitations, advancing the development of functional multi-cellular tissues and organoids. Table 3 summarizes

Table 3. Comparison of scaffold-based, scaffold-free, and convergence strategy

	Scaffold-based	Scaffold-free	Convergence
Initial cell density	Good	Bad	Good
Mechanical properties	Bad	Good	Good
Possibility of tissue self-assembly	Good	Bad	Good
Functionalization with biomolecules	Bad	Good	Good
Advantages	• Provides mechanical support • Controls cell distribution • Promotes vascularization	• Closer to natural environment • Simplifies manufacturing process • Reduces risk of immune response	• Integrated biomanufacturing technologies, including 3D bioprinting, bioprocessing, and automation, achieve a balance between scale, biosafety, and resolution. • Automated biomanufacturing technologies improve and accelerate the printing or self-assembly of tissues and organ samples with high accuracy and throughput. • The integration of melt electrospinning writing technology and extrusion bioprinting technology creates stable, high-strength, and large-scale layered structures with spatial distribution of different cell types.
Disadvantages	• Requires additional steps and materials • Potential immune response • May affect cell functionality	• Tissue morphology instability • Difficulty in controlling cell distribution • Lack of mechanical support	• The printing speed of current devices limits the practical application of fusion strategies, and slow printing speed is an obstacle that needs to be addressed. • The process of achieving complex bioprocessing and large-scale organ sample models is complex, involving precise positioning and assembly of multiple cell types.
Reference	[130]	[113]	[89]

the characteristics of scaffold-based, scaffold-free, and hybrid strategies and provides a qualitative comparison in terms of initial cell density, mechanical properties, the possibility of tissue self-assembly, functionalization with biomolecules, advantages, and disadvantages.

4.2. Convergence strategy and hybrid biofabrication techniques

The convergence strategy integrates scaffold-based and scaffold-free strategies to achieve a balanced biofabrication scale, biosecurity, and resolution. This is accomplished through the utilization of hybrid biofabrication technologies, including 3D bioprinting, bioassembly, and automation. 3D bioprinting is employed for manufacturing extracellular matrix or basic assembly modules, while assembly techniques are employed to position the modules and complete the target object. Automation technology is implemented to replace manual operations, reduce errors, and enhance production efficiency.

Automated biofabrication techniques enable convergence strategy, allowing to print the specific scaffold structures required for organoids with high accuracy and throughput. Better and faster printing or self-organization of tissue or organoids can be achieved with automated biofabrication techniques. In addition, stem cell suspensions can self-organize into millimeter-scale structures and be further printed into more extensive and complex MTOs, using the resulting geometry scaffold structure to guide organoid formation[18,97]. Integrating melt near-field direct writing technology and extrusion bioprinting technologies creates stable, high-strength, large-size hierarchies utilizing the spatial distribution of different cell types[98]. Fibers with 500 nm–100 μm diameters and complex pattern deposition were prepared using melt input direct writing and melt near-field direct writing technology[99].

The emerging convergence strategy represents a convergent research direction with the potential to enable disruptive solutions and advance the field of tissue function and regenerative medicine[89]. Fabrication of modules for bioassembly, such as aggregate spheroids, tissue blocks, and scaffolds, is carried out separately and independently to avoid damage to cells[89]. It is thought that by changing the nature of the temporary scaffold or module used for assembly, the system can be optimized for different cell and tissue types, resulting in the construction of more complex and functional MTOs. 3D bioprinting should be used to create complex microenvironments, not just to build cell structures[100]. A scaffold-free strategy has been reported to successfully construct structures with curved surfaces and vascular-like structures[101,102]. Scaffolds and microstructural devices can provide a valuable platform to help guide the development of microtissues and self-organizing structures[103]. It can provide a careful balance between engineering guidance and dynamic remodeling within a developing organization if designed and implemented. Successful tissue-guided implementation can have significant implications for the engineering of spatially complex tissues such as articular cartilage, where controlling the structure of collagen networks remains a crucial challenge in the field.

For the first time, *in vitro* research was carried out on the combination of melt near-field direct writing technology and multi-cellular spheroids, which can produce high-precision fiber structure scaffolds up to 2 μm, and biological scaffolds constructed by melt near-field direct writing technology have the advantages of easy operation and visualization[104]. Moreover, it is reported that when the size of the spheroid and the scaffold pore match, the survival rate can reach 90%. Integrating the advantages of vacuum adsorption and suspension-bath printing, a high-resolution method was developed to transfer spheroids into self-healing support hydrogels, thus patterning them and fusing them into high-cell density microtissues at pre-set spatial locations[105], successfully printed an iPSC-derived cardiac microtissue model with spatially controlled and proportional cardiomyocytes and fibroblasts to mimic the structural and functional properties of scarring cardiac tissue triggered after myocardial infarction, including decreased contractility and irregular electrical activity.

Slow printing is an obstacle that can be overcome. The performance of the current equipment used for printing stands is bottlenecked in terms of speed. Even with the advanced two-photon polymerization (2PP) printer developed by Faraji Rad *et al.*[106], it is about 100 times faster than any commercially available device. The required small bracket will also take more than 37 h to fill a 5-mm deep cylinder with a diameter of 5 mm[89]. Slow printing can be solved by storing materials, scaffolds, and aggregate spheroids in advance, or scaffold fabrication and bioassembly can be carried out simultaneously through fusion strategies.

A method is being developed, known as BMMm, which aims to achieve a patterned arrangement of heterogeneous aggregate spheroids in 3D space. This method has the potential to construct large-scale (centimeter) tissues or organoids with intricate structures, as demonstrated in Figure 6. This method includes micromesh patterns, different types of aggregate spheroids, and other auxiliary devices, such as temperature monitoring sensors and oxygen delivery pipelines. Preparing complex bioink is unnecessary in BMMm, and aggregate spheroids are the primary assembly unit, maintaining the advantage of a

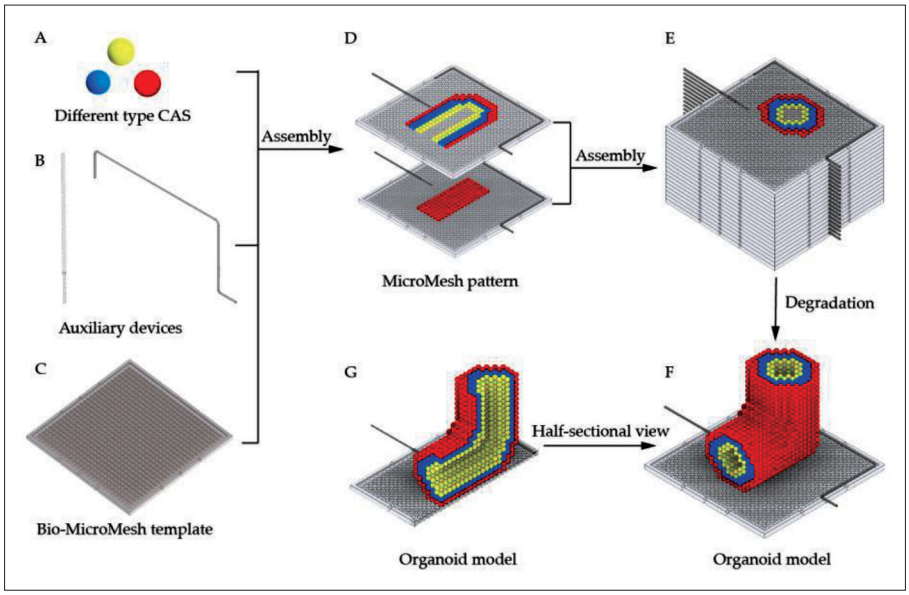

Figure 6. The schematic of BioMicroMesh method (BMMm). (A) Different types of cell-aggregate spheroids (CAS). (B) Auxiliary devices, such as temperature monitoring sensors and oxygen delivery pipelines. (C) BioMicroMesh template. (D) Use heterogeneous cells to form micromesh patterns of different shapes. (E) Organoid models are composed of heterogeneous cells. (F) The micromesh template is degraded to obtain a complete organoid model. (G) Observe the organoid model from the perspective of a half-sectional view.

scaffold-free strategy. In addition, this method overcomes the disadvantages of biosystem technology: aggregate spheroids cannot be accurately located in 3D space, heterogeneous aggregate spheroids assembly is complex, and the process of making large-scale organoid models is complicated. 3D bioprinting technology is used to make the template required for BMMm, which has holes for placing the spheroids, protruding structures for fixing the position of the spheroids, channels for placing auxiliary equipment, and outer borders for assembling each other. Specific template shapes, sizes, holes, and passage positions can all be individually designed. Different types of cells are placed in different positions, and complex heterogeneous cell organoid models can be manufactured through the automation of the manipulator.

4.3. Automation equipment development perspective

The slow development of biofabrication equipment has hindered the translation of cutting-edge research results into market and clinical applications. A comprehensive analysis of existing achievements and technological development trends can help bridge the gap between laboratory research outcomes and large-scale utilization[107]. Such an approach takes into account both cutting-edge research results and the actual market and clinical application needs.

Bioprinters are essential for precise control of experimental variables, including cell density, initial tissue geometry, and cell population proximity and localization, allowing for the robust study of the influence of these and other factors on spontaneous cell self-organization into organoids. The development of bioprinting-assisted tissue emergence technology has shown that sophisticated printing methods are not necessary to define spatial control over cell aggregate spheroid deposition. Instead, identifying and designing appropriate conditions between developing organoids and the surrounding environment allows for post-print remodeling and self-organization of printed cells to create geometrically complex final tissue structures. Bioprinting is best suited as a tool in a design strategy to define initial conditions and create an enabling environment for naturally programmed organoid building blocks and their supporting cells to self-organize into a particular tissue or organ[12].

Equipment is essential for the physical embodiment of biofabrication technology. While biofabrication strategy guides multi-cellular tissue or organoid manufacturing, the equipment provides the necessary physical carriers for the realization of technical processes. The development of equipment is crucial for promoting technology and large-scale production of physical entities necessary for organoid manufacturing. Many tissue engineering construction strategies have been invested in clinical translation and have even begun to be marketed. Tissue or organ models built using biofabrication strategies for tissue engineering can be used in drug testing and poison testing in the future, which will involve high reproducibility, high efficiency, low error, and low cost of biological tissue or organoid manufacturing,

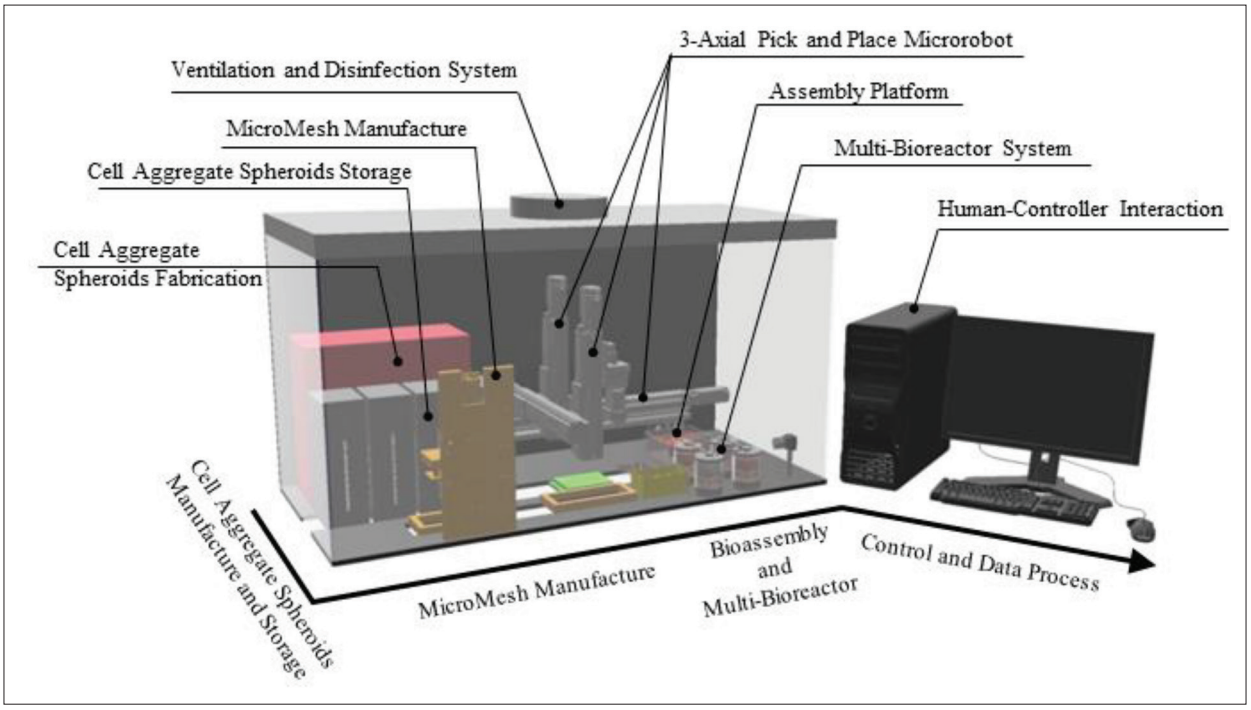

Figure 7. The components of the BioMicroMesh system: spheroid maintenance module, BioMicroMesh template fabrication platform, bioassembly platform, multi-organ culture, and collaboration platform.

so it is essential to develop devices that meet these needs[16]. At the same time, the research and development of intelligent biofabrication equipment that meets the needs can break through the boundary between scaffold-based and scaffold-free strategies and assist the development of fusion strategy. This point of view has been passed on[108].

The placement method of the aggregate spheroids, if 3D-printed and bioassembled robots fused, will allow the creation of more complex, metabotropic, higher-fidelity biological tissue structures and the precise placement of different cell types in 3D, resulting in the construction of multi-cellular organoids. Because the fusion strategy combines the advantages of the scaffold-based and the scaffold-free strategies, manual placement of the spheroids into the scaffold limits the throughput of such procedures. Fortunately, this problem can be solved with currently available technology, as several recent reports have used various robotic systems capable of autonomously maneuvering and placing spheres[6,52,109]. However, the development of technology and equipment is the means to promote this balance. The above equipment can only be used for the placement of aggregate spheroids and cannot be combined with 3D-printed scaffolds. Therefore, developing unmanned and intelligent assembly line biofabrication equipment that integrates scaffold-based and scaffold-free strategies is an essential direction for future equipment research, especially developing low-cost small desktop equipment, which will help promote the promotion and use of instruments and equipment experimental efficiency.

Our research group developed a rotary-forming device with a multi-nozzle multi-channel temperature deposition system (MTDS) in 2017 to construct vessel-like structures[110,111]. We are currently developing the BioMicroMesh system (BMMs), as shown in Figure 7, a biofabrication device that combines 3D bioprinting and bioassembly technology for fully automated tissue and organoid model manufacturing. The BMMs comprises six parts: cell aggregate spheroids manufacture and storage, micromesh manufacture, ventilation and disinfection, pick and place microbot, multi-bioreactor, and master controller. BMMs uses 3D bioprinting techniques to manufacture micromesh templates and bioassembly techniques to pick and place heterogeneous cell aggregate spheroids for assembling into complete tissue structures or organoid models.

5. Conclusion

The scaffold-based and scaffold-free strategies for the biofabrication of multi-cellular tissues or organoids are discussed in this review. The scaffold-based strategy is effective in constructing the microenvironment necessary for tissue or organoid survival, but it is becoming more complex and requires cumbersome preparation of bioinks.

The scaffold-free strategy, on the other hand, is better at assembling complex structures and MTOs but requires accurate space positioning of cell aggregate spheroids. Integrating both strategies could address the challenges in organoid biofabrication. This review also introduces the BMMm, which aims to achieve a patterned arrangement of heterogeneous cell aggregate spheroids in space to build larger-scale tissue or organoids with complex structures. The BMMs is being developed as an intelligent biofabrication device tailored to the BMMm. It combines 3D bioprinting and bioassembly technology to allow for fully automated fabrication of tissue or organoid models. The BMMs are expected to enable a compact desktop design and facilitate the manufacturing process of tissue or organoid models with automation, intelligence, process orientation, and high precision. The BMMm and BMMs aim to improve the high reproducibility of research results, facilitate the mass production of organoid models, and improve medical efficiency.

Acknowledgments

None.

Funding

None.

Conflict of interest

The authors declare no conflict of interest.

Author contributions

Conceptualization: Haoyu Li, Huixing Zhou
Investigation: Haoyu Li, Huixing Zhou
Writing – original draft: Haoyu Li, Huixing Zhou
Writing – review & editing: Huixing Zhou, Chongwen Xu, Yen Wei, Xiuying Tang

Ethics approval and consent to participate

Not applicable.

Consent for publication

Not applicable.

Availability of data

Not applicable.

References

1. Prior N, Inacio P, Huch M, 2019, Liver organoids: From basic research to therapeutic applications. *Gut*, 68(12): 2228–2237.

https://doi.org/10.1136/gutjnl-2019-319256

2. Lancaster MA, Knoblich JA, 2014, Organogenesis in a dish: Modeling development and disease using organoid technologies. *Science*, 345(6194): 1247125.

https://doi.org/10.1126/science.1247125

3. Clevers H, 2016, Modeling development and disease with organoids. *Cell*, 165(7): 1586–1597.

https://doi.org/10.1016/j.cell.2016.05.082

4. Meran L, Tullie L, Eaton S, *et al.*, 2022, Bioengineering human intestinal mucosal grafts using patient-derived organoids, fibroblasts and scaffolds. *Nat Protoc*, 18(1): 108–135.

https://doi.org/10.1038/s41596-022-00751-1

5. Carosio S, Barberi L, Rizzuto E, *et al.*, 2013, Generation of ex vivo-vascularized muscle engineered tissue (X-MET). *Sci Rep,* 3(1): 1–9.

https://doi.org/10.1038/srep01420

6. Kratochvil MJ, Seymour AJ, Li TL, *et al.*, 2019, Engineered materials for organoid systems. *Nat Rev Mater*, 4(9): 606–622.

https://doi.org/10.1038/s41578-019-0129-9

7. Hofer M, Lutolf MP, 2021, Engineering organoids. *Nat Rev Mater*, 6(5): 402–420.

https://doi.org/10.1038/s41578-021-00279-y

8. Groll J, Boland T, Blunk T, *et al.*, 2016, Biofabrication: Reappraising the definition of an evolving field. *Biofabrication*, 8(1): 013001.

https://doi.org/10.1088/1758-5090/8/1/013001

9. Heinrich MA, Liu W, Jimenez A, *et al.*, 2019, 3D-Bioprinting: From benches to translational applications. *Small*, 15(23): 1805510.

https://doi.org/10.1002/smll.201970126

10. Moroni L, Burdick JA, Highley C, *et al.*, 2018, Biofabrication strategies for 3D in vitro models and regenerative medicine. *Nat Rev Mater,* 36(4): 21–37.

11. Martin I, Malda J, Rivron NC, 2019, Organs by design: Can bioprinting meet self-organization? *Curr Opin Organ Transplant,* 24(5): 562–567.

https://doi.org/10.1097/MOT.0000000000000679

12. Kačarević Ž, Rider P, Alkildani S, *et al.*, 2018, An introduction to 3D-bioprinting: Possibilities, challenges and future aspects. *Materials*, 11(11): 2199.

https://doi.org/10.3390/ma11112199

13. Ahn CB, Lee J-H, Kim JH, *et al.*, 2022, Development of a 3D subcutaneous construct containing insulin-producing beta cells using bioprinting. *Bio-Des Manuf*, 5(2): 265–276.

https://doi.org/10.1007/s42242-021-00178-9

14. Chen EP, Toksoy Z, Davis BA, *et al.*, 2021, 3D-bioprinting of vascularized tissues for in vitro and in vivo applications. *Front Bioeng Biotechnol*, 9: 664188.

https://doi.org/10.3389/fbioe.2021.664188

15. Zhang X-Y, Yanagi Y, Sheng Z, *et al.*, 2018, Regeneration of diaphragm with bio-3D cellular patch. *Biomaterials*, 167: 1–14.

https://doi.org/10.1016/j.biomaterials.2018.03.012

16. Burdis R, Kelly DJ, 2021, Biofabrication and bioprinting using cellular aggregates, microtissues and organoids for the engineering of musculoskeletal tissues. *Acta Biomater*, 126: 1–14.

https://doi.org/10.1016/j.actbio.2021.03.016

17. Lawlor KT, Vanslambrouck JM, Higgins JW, *et al.*, 2021, Cellular extrusion bioprinting improves kidney organoid reproducibility and conformation. *Nat Mater,* 20(2): 260–271.

https://doi.org/10.1038/s41563-020-00853-9

18. Ren Y, Yang X, Ma Z, *et al.*, 2021, Developments and opportunities for 3D bioprinted organoids. *Int J Bioprint*, 7(3): 364.

https://doi.org/10.18063/ijb.v7i3.364

19. Chan BP, Leong KW, 2008, Scaffolding in tissue engineering: general approaches and tissue-specific considerations. *Eur Spine J*, 17(S4): 467–479.

https://doi.org/10.1007/s00586-008-0745-3

20. Ng WL, Huang X, Shkolnikov V, *et al.*, 2021, Controlling droplet impact velocity and droplet volume: Key factors to achieving high cell viability in sub-nanoliter droplet-based bioprinting. *Int J Bioprint*, 8(1): 424.

https://doi.org/10.18063/ijb.v8i1.424

21. Willerth SM, Sakiyama-Elbert SE, 2019, Combining stem cells and biomaterial scaffolds for constructing tissues and cell delivery. *StemJournal*, 1(1): 1–25.

https://doi.org/10.3233/STJ-180001

22. Ji S, Guvendiren M, 2019, 3D printed wavy scaffolds enhance mesenchymal stem cell osteogenesis. *Micromachines (Basel)*, 11(1): 31.

https://doi.org/10.3390/mi11010031

23. Di Marzio N, Eglin D, Serra T, *et al.*, 2020, Bio-fabrication: Convergence of 3D-Bioprinting and nano-biomaterials in tissue engineering and regenerative medicine. *Front Bioeng Biotechnol,* 8: 326.

https://doi.org/10.3389/fbioe.2020.00326

24. Mei Q, Rao J, Bei HP, *et al.*, 2021, 3D-Bioprinting photo-crosslinkable hydrogels for bone and cartilage repair. *Int J Bioprint,* 7(3): 367.

https://doi.org/10.18063/ijb.v7i3.367

25. Ozbolat IT, Hospodiuk M, 2016, Current advances and future perspectives in extrusion-based bioprinting. *Biomaterials*, 76: 321–343.

https://doi.org/10.1016/j.biomaterials.2015.10.076

26. Ng WL, Lee JM, Zhou M, *et al.*, 2020, Vat polymerization-based bioprinting—process, materials, applications and regulatory challenges. *Biofabrication*, 12(2): 022001.

https://doi.org/10.1088/1758-5090/ab6034

27. Seol Y-J, Kang H-W, Lee SJ, *et al.*, 2014, Bioprinting technology and its applications. *Eur J Cardiothorac Surg*, 46(3): 342–348.

https://doi.org/10.1093/ejcts/ezu148

28. Cui X, Boland T, D'Lima DD, *et al.*, 2012, Thermal inkjet printing in tissue engineering and regenerative medicine. *Recent Pat Drug Deliv Formul*, 6(2): 149–155.

https://doi.org/10.2174/187221112800672949

29. Nakamura M, Iwanaga S, Henmi C, *et al.*, 2010, Biomatrices and biomaterials for future developments of bioprinting and biofabrication. *Biofabrication*, 2(1): 014110.

https://doi.org/10.1088/1758-5082/2/1/014110

30. Wijshoff H, 2010, The dynamics of the piezo inkjet printhead operation. *Phys Rep,* 491(4–5): 77–177.

https://doi.org/10.1016/j.physrep.2010.03.003

31. Christensen K, Xu C, Chai W, *et al.*, 2015, Freeform inkjet printing of cellular structures with bifurcations. *Biotechnol Bioeng*, 112(5): 1047–1055.

https://doi.org/10.1002/bit.25501

32. Park J-U, Hardy M, Kang S, *et al.*, 2007, High-resolution electrohydrodynamic jet printing. *Nat Mater,* 6(10): 782–789.

https://doi.org/10.1038/nmat1974

33. Poellmann MJ, Barton KL, Mishra S, *et al.*, 2011, Patterned hydrogel substrates for cell culture with electrohydrodynamic jet printing. *Macromol Biosci,* 11(9): 1164–1168.

https://doi.org/10.1002/mabi.201100004

34. Li X, Liu B, Pei B, *et al.*, 2020, Inkjet bioprinting of biomaterials. *Chem Rev,* 120(19): 10793–10833.

https://doi.org/10.1021/acs.chemrev.0c00008

35. Xu T, Zhao W, Zhu J-M, *et al.*, 2007, Bio-printing of living organized tissues using an inkjet technology. *FASEB J*, 21(5): A636–A636.

https://doi.org/10.1096/fasebj.21.5.A636-b

36. Zhou Y, Zhao Q, Wang M, 2023, Biomanufacturing of biomimetic three-dimensional nanofibrous multicellular constructs for tissue regeneration. *Colloids Surf B*, 223: 113189.

https://doi.org/10.1016/j.colsurfb.2023.113189

37. Jiang T, Munguia-Lopez JG, Flores-Torres S, *et al.*, 2019, Extrusion bioprinting of soft materials: An emerging technique for biological model fabrication. *Appl Phys Rev,* 6(1): 011310.

https://doi.org/10.1063/1.5059393

38. Cuvellier M, Ezan F, Oliveira H, *et al.*, 2021, 3D culture of HepaRG cells in GelMa and its application to bioprinting of a multicellular hepatic model. *Biomaterials*, 269: 120611.

https://doi.org/10.1016/j.biomaterials.2020.120611

39. Janani G, Priya S, Dey S, *et al.*, 2022, Mimicking native liver lobule microarchitecture in vitro with parenchymal and non-parenchymal cells using 3D-bioprinting for drug toxicity and drug screening applications. *ACS Appl Mater Interfaces*, 14(8): 10167–10186.

https://doi.org/10.1021/acsami.2c00312

40. Jian H, Li X, Dong Q, *et al.*, 2023, In vitro construction of liver organoids with biomimetic lobule structure by a multicellular 3D-Bioprinting strategy. *Cell Prolif,* 56(5): e13465.

https://doi.org/10.1111/cpr.13465

41. Du L, Qin C, Zhang H, *et al.*, 2023, Multicellular bioprinting of biomimetic inks for Tendon-to-Bone regeneration. *Adv Sci*, 2301309.

http://doi.org/10.1002/advs.202301309

42. Zhu W, Ma X, Gou M, *et al.*, 2016, 3D printing of functional biomaterials for tissue engineering. *Curr Opin Biotechnol*, 40: 103–112.

https://doi.org/10.1016/j.copbio.2016.03.014

43. Murata D, Arai K, Nakayama K, 2020, Scaffold-free bio-3D printing using spheroids as "bio-inks" for tissue (re-) construction and drug response tests. *Adv Healthc Mater*, 9(15): e1901831.

https://doi.org/10.1002/adhm.201901831

44. Tavares-Negrete JA, Babayigit C, Najafikoshnoo S, *et al.*, n.d., A novel 3D-bioprinting technology of orderly extruded multi-materials via photopolymerization. *Adv Mater Technol,* 8(12): 2201926.

https://doi.org/10.1002/admt.202201926

45. Kiratitanaporn W, Guan J, Berry DB, *et al.*, 2023, Multi-modal vat photopolymerization for microscale modulation of scaffold stiffness assisted via machine learning. *SSRN*

https://doi.org/10.2139/ssrn.4450557

46. Vijayavenkataraman S, Yan W-C, Lu WF, *et al.*, 2018, 3D-Bioprinting of tissues and organs for regenerative medicine. *Adv Drug Deliv Rev,* 132: 296–332.

https://doi.org/10.1016/j.addr.2018.07.004

47. Burks HE, Phamduy TB, Azimi MS, *et al.*, 2016, Laser direct-write onto live tissues: A novel model for studying cancer cell migration. *J Cel Physiol,* 231(11): 2333–2338.

https://doi.org/10.1002/jcp.25363

48. Jahangirian H, Azizi S, Rafiee-Moghaddam R, *et al.*, 2019, Status of plant protein-based green scaffolds for regenerative medicine applications. *Biomolecules*, 9(10): 619.

https://doi.org/10.3390/biom9100619

49. Mekhileri NV, Lim KS, Brown GCJ, *et al.*, 2018, Automated 3D bioassembly of micro-tissues for biofabrication of hybrid tissue engineered constructs. *Biofabrication*, 10(2): 024103.

https://doi.org/10.1088/1758-5090/aa9ef1

50. Halbleib JM, Nelson WJ, 2006, Cadherins in development: Cell adhesion, sorting, and tissue morphogenesis. *Genes Dev,* 20(23): 3199–3214.

https://doi.org/10.1101/gad.1486806

51. Turksen K, ed., 2018, Cell biology and translational medicine, Volume 3: Stem cells, bio-materials and tissue engineering, Springer International Publishing, Cham, 1107.

https://doi.org/10.1007/978-3-030-04185-4

52. Zhang Q, Ma L, Ji X, *et al.*, 2022, High-strength hydroxyapatite scaffolds with minimal surface macrostructures for load-bearing bone regeneration. *Adv Funct Mater*, 32(33): 2204182.

https://doi.org/10/gqpwqm

53. Forgacs G, 2018, In 3D Bioprinting in regenerative engineering: Applications of extrusion bioprinting, CRC Press, Boca Raton: Taylor & Francis, 51–75.

https://doi.org/10.1201/b21916-3

54. dos Santos BC, Noritomi PY, da Silva JVL, *et al.*, 2022, Biological multiscale computational modeling: A promising tool for 3D-Bioprinting and tissue engineering. *Bioprinting*, 28: e00234.

https://doi.org/10.1016/j.bprint.2022.e00234

55. Sung K, Patel NR, Ashammakhi N, *et al.*, 2021, 3-Dimensional bioprinting of cardiovascular tissues. *JACC*, 6(5): 467–482.

https://doi.org/10.1016/j.jacbts.2020.12.006

56. Wang Y, Wang J, Ji Z, *et al.*, 2022, Application of bioprinting in ophthalmology. *Int J Bioprint*, 8(2): 552.

https://doi.org/10.18063/ijb.v8i2.552

57. Murata D, Fujimoto R, Nakayama K, 2020, Osteochondral regeneration using adipose tissue-derived mesenchymal stem cells. *IJMS*, 21(10): 3589.

https://doi.org/10.3390/ijms21103589

58. Aguilar IN, Smith LJ, Olivos DJ, *et al.*, 2019, Scaffold-free bioprinting of mesenchymal stem cells with the regenova printer: Optimization of printing parameters. *Bioprinting*, 15: e00048.

https://doi.org/10.1016/j.bprint.2019.e00048

59. Ayan B, Heo DN, Zhang Z, *et al.*, 2020, Aspiration-assisted bioprinting for precise positioning of biologics. *Sci Adv,* 10(1): 13148.

https://doi.org/10.1126/sciadv.aaw5111

60. Moldovan NI, Hibino N, Nakayama K, 2017, Principles of the Kenzan method for robotic cell spheroid-based three-dimensional bioprinting, *Tissue Eng Part B Rev,* 23(3): 237.

https://doi.org/10.1089/ten.teb.2016.0322

61. Smith LJ, Li P, Holland MR, *et al.*, 2018, FABRICA: A bioreactor platform for printing, perfusing, observing, & stimulating 3D tissues. *Sci Rep,* 8(1): 7561.

https://doi.org/10.1038/s41598-018-25663-7

62. Holland I, Logan J, Shi J, *et al.*, 2018, 3D biofabrication for tubular tissue engineering. *Bio-Design Manuf,* 1(2): 89–100.

https://doi.org/10.1007/s42242-018-0013-2

63. Manning KL, Thomson AH, Morgan JR, 2018, Funnel-guided positioning of multicellular microtissues to build macrotissues. *Tissue Eng Part C Methods*, 24(10): 557–565.

https://doi.org/10.1089/ten.tec.2018.0137

64. van Pel DM, Harada K, Song D, *et al.*, 2018, Modelling glioma invasion using 3D-Bioprinting and scaffold-free 3D culture. *J Cell Commun Signal,* 12(4): 723–730.

https://doi.org/10.1007/s12079-018-0469-z

65. Nakanishi Y, Okada T, Takeuchi N, *et al.*, 2019, Histological evaluation of tendon formation using a scaffold-free three-dimensional-bioprinted construct of human dermal fibroblasts under in vitro static tensile culture. *Regen Ther*, 11: 47–55.

https://doi.org/10.1016/j.reth.2019.02.002

66. Taniguchi D, Matsumoto K, Tsuchiya T, *et al.*, 2018, Scaffold-free trachea regeneration by tissue engineering with bio-3D printing. *Interact CardioVasc Thorac Surg*, 26(5): 745–752.

67. Yurie H, Ikeguchi R, Aoyama T, *et al.*, 2017, The efficacy of a scaffold-free Bio 3D conduit developed from human fibroblasts on peripheral nerve regeneration in a rat sciatic nerve model. *PloS One*, 12(2): e0171448.

https://doi.org/10.1371/journal.pone.0171448

68. Ozbolat IT, 2015, Scaffold-based or scaffold-free bioprinting: Competing or complementing approaches? *J Nanotechnol Eng Med,* 6(2): 024701.

https://doi.org/10.1115/1.4030414

69. Guan Y, Niu H, Liu Z, *et al.*, 2021, Sustained oxygenation accelerates diabetic wound healing by promoting epithelialization and angiogenesis and decreasing inflammation. *Sci Adv,* 7(35): eabj0153.

https://doi.org/10.1126/sciadv.abj0153

70. Banerjee D, Singh YP, Datta P, *et al.*, 2022, Strategies for 3D bioprinting of spheroids: A comprehensive review. *Biomaterials*, 291: 121881.

http://doi.org/10.1016/j.biomaterials.2022.121881

71. Huang TJ, 2019, Acoustofluidics: Merging acoustics and microfluidics for biomedical applications. *J Acoust Soc Am,* 145(3): 1786–1786.

https://doi.org/10.1121/1.5101531

72. Devendran C, Carthew J, Frith JE, *et al.*, 2019, Cell adhesion, morphology, and metabolism variation via acoustic exposure within microfluidic cell handling systems. *Adv Sci,* 6(24): 1902326.

https://doi.org/10.1002/advs.201902326

73. Karthick S, Pradeep PN, Kanchana P, *et al.*, 2018, Acoustic impedance-based size-independent isolation of circulating tumour cells from blood using acoustophoresis. *Lab Chip*, 18(24): 3802–3813.

https://doi.org/10.1039/C8LC00921J

74. Ozcelik A, Rufo J, Guo F, *et al.*, 2018, Acoustic tweezers for the life sciences. *Nat Methods*, 15(12): 1021–1028.

https://doi.org/10.1038/s41592-018-0222-9

75. Jonnalagadda US, Hill M, Messaoudi W, *et al.*, 2018, Acoustically modulated biomechanical stimulation for human cartilage tissue engineering. *Lab Chip*, 18(3): 473–485.

https://doi.org/10.1039/C7LC01195D

76. Bouyer C, Chen P, Demirci U, *et al.*, 2016, Bio-acoustic levitational assembly of heterocellular multilayer constructs for tissue engineering. *J Acoust Soc Am,* 140(4): 3370–3370.

https://doi.org/10.1121/1.4970762

77. Bouyer C, Chen P, Güven S, *et al.*, 2016, A bio-acoustic levitational (BAL) assembly method for engineering of multilayered, 3D brain-like constructs, using human embryonic stem cell derived neuro-progenitors. *Adv Mater*, 28(1): 161–167.

https://doi.org/10.1002/adma.201503916

78. Tian Z, Wang Z, Zhang P, *et al.*, 2020, Generating multifunctional acoustic tweezers in Petri dishes for contactless, precise manipulation of bioparticles. *Sci Adv,* 6(37): eabb0494.

https://doi.org/10.1126/sciadv.abb0494

79. Melde K, Mark AG, Qiu T, *et al.*, 2016, Holograms for acoustics. *Nature*, 537(7621): 518–522.

https://doi.org/10.1038/nature19755

80. Afsaneh H, Mohammadi R, 2022, Microfluidic platforms for the manipulation of cells and particles. *Talanta Open*, 5: 100092.

https://doi.org/10.1016/j.talo.2022.100092

81. Guimarães CF, Soto F, Wang J, *et al.*, 2022, Engineered living bioassemblies for biomedical and functional material applications. *Curr Opin Biotechnol,* 77: 102756.

https://doi.org/10.1016/j.copbio.2022.102756

82. Shi L, Zhong X, Ding H, *et al.*, 2022, Continuous separation of microparticles based on optically induced dielectrophoresis. *Microfluid Nanofluid*, 26(1): 6.

https://doi.org/10.1007/s10404-021-02512-0

83. Yang C-M, Yu J-C, Chu P-Y, *et al.*, 2022, The utilization of tunable transducer elements formed by the manipulation

of magnetic beads with different sizes via optically induced dielectrophoresis (ODEP) for high signal-to-noise ratios (SNRs) and multiplex fluorescence-based biosensing applications. *Biosensors*, 12(9): 755.

https://doi.org/10.3390/bios12090755

84. Bhattacharjee T, Gil CJ, Marshall SL, *et al.*, 2016, Liquid-like solids support cells in 3D. *ACS Biomater Sci Eng*, 2(10): 1787–1795.

https://doi.org/10.1021/acsbiomaterials.6b00218

85. Noor N, Shapira A, Edri R, *et al.*, 2019, 3D printing of personalized thick and perfusable cardiac patches and hearts. *Adv Sci,* 6(11): 1900344.

https://doi.org/10.1002/advs.201900344

86. Jeon O, Lee YB, Jeong H, *et al.*, 2019, Individual cell-only bioink and photocurable supporting medium for 3D printing and generation of engineered tissues with complex geometries. *Mater Horiz*, 6(8): 1625–1631.

https://doi.org/10.1039/C9MH00375D

87. Skylar-Scott MA, Uzel SGM, Nam LL, *et al.*, 2019, Biomanufacturing of organ-specific tissues with high cellular density and embedded vascular channels. *Sci Adv,* 5(9): eaaw2459.

https://doi.org/10.1126/sciadv.aaw2459

88. Brassard JA, Nikolaev M, Hübscher T, *et al.*, 2021, Recapitulating macro-scale tissue self-organization through organoid bioprinting. *Nat Mater,* 20(1): 22–29.

https://doi.org/10.1038/s41563-020-00803-5

89. Ovsianikov A, Khademhosseini A, Mironov V, 2018, The synergy of scaffold-based and scaffold-free tissue engineering strategies. *Trends Biotechnol,* 36(4): 348–357.

https://doi.org/10.1016/j.tibtech.2018.01.005

90. Poh PS, Lingner T, Kalkhof S, *et al.*, 2022, Enabling technologies towards personalization of scaffolds for large bone defect regeneration. *Curr Opin Biotechnol,* 74: 263–270.

https://doi.org/10.1016/j.copbio.2021.12.002

91. Ponnada S, Babu Gorle D, Chandra Bose RS, *et al.*, 2022, Current insight into 3D printing in solid-state lithium-ion batteries: A perspective. *Batter Supercaps*, 5(8): e202200223.

https://doi.org/10.1002/batt.202200223

92. Badhe RV, Chatterjee A, Bijukumar D, *et al.*, 2023, Current advancements in bio-ink technology for cartilage and bone tissue engineering. *Bone*, 171: 116746.

https://doi.org/10.1016/j.bone.2023.116746

93. Jafari A, Ajji Z, Mousavi A, *et al.*, 2022, Latest advances in 3D-bioprinting of cardiac tissues. *Adv Mater Technol,* 7(11): 2101636.

https://doi.org/10.1002/admt.202101636

94. Caprio ND, Burdick JA, 2022, Engineered biomaterials to guide spheroid formation, function, and fabrication into 3D tissue constructs. *Acta Biomater,* 165: 4–18..

https://doi.org/10.1016/j.actbio.2022.09.052

95. Cooper SM, Rainbow RS, 2022, The developing field of scaffold-free tissue engineering for articular cartilage repair. *Tissue Eng Part B Rev,* 28(5): 995–1006.

https://doi.org/10.1089/ten.teb.2021.0130

96. Pignatelli C, Campo F, Neroni A, *et al.*, 2022, Bioengineering the vascularized endocrine pancreas: A fine-tuned interplay between vascularization, extracellular-matrix-based scaffold architecture, and insulin-producing cells. *Transpl Int*, 35: 10555.

https://doi.org/10.3389/ti.2022.10555

97. Levato R, Jungst T, Scheuring RG, et al., 2020, From shape to function: The next step in bioprinting. *Adv Mater,* 32(12): 1906423.

https://doi.org/10.1002/adma.201906423

98. de Ruijter M, Ribeiro A, Dokter I, *et al.*, 2019, Simultaneous micropatterning of fibrous meshes and bioinks for the fabrication of living tissue constructs. *Adv Healthc Mater,* 8(7): 1800418.

99. Lv S, Nie J, Gao Q, *et al.*, 2020, Micro/nanofabrication of brittle hydrogels using 3D printed soft ultrafine fiber molds for damage-free demolding. *Biofabrication*, 12(2): 025015.

https://doi.org/10.1088/1758-5090/ab57d8

100. Chakraborty J, Ghosh S, 2020, Cellular proliferation, self-assembly, and modulation of signaling pathways in silk fibroin gelatin-based 3D bioprinted constructs. *ACS Appl Bio Mater*, 3(12): 8309–8320.

https://doi.org/10.1021/acsabm.0c01252

101. Yu Y, Moncal KK, Li J, *et al.*, 2016, Three-dimensional bioprinting using self-assembling scalable scaffold-free "tissue strands" as a new bioink. *Sci Rep*, 6(1): 28714.

https://doi.org/10.1038/srep28714

102. Dissanayaka WL, Zhu L, Hargreaves KM, *et al.*, 2014, Scaffold-free prevascularized microtissue spheroids for pulp regeneration. *J Dent Res*, 93(12): 1296–1303.

https://doi.org/10.1177/0022034514550040

103. Laurent J, Blin G, Chatelain F, *et al.*, 2017, Convergence of microengineering and cellular self-organization towards functional tissue manufacturing. *Nat Biomed Eng*, 1(12): 939–956.

https://doi.org/10.1038/s41551-017-0166-x

104. McMaster R, Hoefner C, Hrynevich A, *et al.*, 2019, Tailored melt electrowritten scaffolds for the generation of sheet-like tissue constructs from multicellular spheroids. *Adv Healthc Mater,* 8(7): 1801326.

https://doi.org/10.1002/adhm.201801326

105. Daly AC, Davidson MD, Burdick JA, 2021, 3D-Bioprinting of high cell-density heterogeneous tissue models through spheroid fusion within self-healing hydrogels. *Nat Commun,* 12(1): 1–13.

https://doi.org/10.1038/s41467-021-21029-2

106. Faraji Rad Z, Prewett PD, Davies GJ, 2021, High-resolution two-photon polymerization: the most versatile technique for the fabrication of microneedle arrays. *Microsyst Nanoeng*, 7(1): 1–17.

https://doi.org/10.1038/s41378-021-00298-3

107. Santoni S, Gugliandolo SG, Sponchioni M, *et al.*, 2022, 3D-Bioprinting: Current status and trends—a guide to the literature and industrial practice. *Bio-Des Manuf*, 5(1, SI): 14–42.

https://doi.org/10.1007/s42242-021-00165-0

108. Struzyna LA, Watt ML, 2021, The emerging role of neuronal organoid models in drug discovery: Potential applications and hurdles to implementation. *Mol Pharmacol*, 99(4): 256–265.

https://doi.org/10.1124/molpharm.120.000142

109. Zhang Y, Li W, Pan P, *et al.*, 2022, Programmable construction of vasculature by printing in cementitious materials for self-healing application. *Compos Part B Eng,* 242: 110056.

https://doi.org/10.1016/j.compositesb.2022.110056

110. Liu H, Zhou H, Lan H, *et al.*, 2018, Multinozzle multichannel temperature deposition system for construction of a blood vessel. *SLAS Technol,* 23(1): 64–69.

https://doi.org/10.1177/2472630317712221

111. Liu H, Zhou H, Lan H, *et al.*, 2017, 3D printing of artificial blood vessel: Study on multi-parameter optimization design for vascular molding effect in alginate and gelatin. *Micromachines*, 8(8): 237.

https://doi.org/10.3390/mi8080237

112. Wang S, Chen X, Han X, *et al.*, 2023, A review of 3D printing technology in pharmaceutics: Technology and applications, now and future. *Pharmaceutics*, 15(2): 416.

https://doi.org/10.3390/pharmaceutics15020416

113. Murata D, Arai K, Nakayama K, 2020, Scaffold-free bio-3D printing using spheroids as "bio-inks" for tissue (re-) construction and drug response tests. *Adv Healthc Mater*, 267(1): 1901831.

https://doi.org/10.1002/adhm.201901831

114. Yaman S, Anil-Inevi M, Ozcivici E, *et al.*, 2018, Magnetic force-based microfluidic techniques for cellular and tissue bioengineering. *Front Bioeng Biotechnol,* 6: 192.

https://doi.org/10.3389/fbioe.2018.00192

115. Hsiao Y-C, Wang C-H, Lee W-B, *et al.*, 2018, Automatic cell fusion via optically-induced dielectrophoresis and optically-induced locally-enhanced electric field on a microfluidic chip. *Biomicrofluidics*, 12(3): 034108.

https://doi.org/10.1063/1.5028158

116. Hinton TJ, Jallerat Q, Palchesko RN, *et al.*, 2015, Three-dimensional printing of complex biological structures by freeform reversible embedding of suspended hydrogels. *Sci Adv,* 1(9): e1500758.

https://doi.org/10.1126/sciadv.1500758

117. Augustine R, Nuthana Kalva S, Ahmed R, *et al.*, 2021, 3D bioprinted cancer models: Revolutionizing personalized cancer therapy. *Transl Oncol,* 14(4): 101015.

https://doi.org/10.1016/j.tranon.2021.101015

118. Xu F, Celli J, Rizvi I, *et al.*, 2011, A three-dimensional in vitro ovarian cancer coculture model using a high-throughput cell patterning platform. *Biotechnol J,* 6(2): 204–212.

https://doi.org/10.1002/biot.201000340

119. Chang R, Nam J, Sun W, 2008, Direct cell writing of 3D microorgan for in vitro pharmacokinetic model. *Tissue Eng Part C Methods*, 14(2): 157–166.

https://doi.org/10.1089/ten.tec.2007.0392

120. Norotte C, Marga FS, Niklason LE, *et al.*, 2009, Scaffold-free vascular tissue engineering using bioprinting. *Biomaterials*, 30(30): 5910–5917.

https://doi.org/10.1016/j.biomaterials.2009.06.034

121. Ren Y, Yang X, Ma Z, *et al.*, 2021, Developments and opportunities for 3D bioprinted organoids. *Int J Bioprint*, 7(3): 364.

https://doi.org/10.18063/ijb.v7i3.364

122. Leberfinger AN, Ravnic DJ, Dhawan A, *et al.*, 2017, Concise review: Bioprinting of stem cells for transplantable tissue fabrication. *Stem Cell Transl Med,* 6(10): 1940–1948.

https://doi.org/10.1002/sctm.17-0148

123. Lam EHY, Yu F, Zhu S, *et al.*, 2023, 3D-bioprinting for next-generation personalized medicine. *Int J Mol Sci,* 24(7): 6357.

https://doi.org/10.3390/ijms24076357

124. Chansoria P, Schuchard K, Shirwaiker RA, 2021, Process hybridization schemes for multiscale engineered tissue biofabrication. *WIREs Nanomed Nanobiotechnol,* 13(2): e1673.

https://doi.org/10.1002/wnan.1673

125. Kang B, Shin J, Park H-J, *et al.*, 2018, High-resolution acoustophoretic 3D cell patterning to construct functional collateral cylindroids for ischemia therapy. *Nat Commun*, 9(1): 1–13.

https://doi.org/10.1038/s41467-018-07823-5

126. Morita T, Watanabe S, Sasaki S, 2023, Multiaxis printing method for bent tubular structured gels in support bath for achieving high dimension and shape accuracy. *Precis Eng,* 79: 109–118.

https://doi.org/10.1016/j.precisioneng.2022.09.004

127. Wang X, 2013, Overview on biocompatibilities of implantable biomaterials, in *Advances in Biomaterials Science and Biomedical Applications*, IntechOpen, Vienna, Austria.

https://doi.org/10.5772/53461

128. Shao L, Gao Q, Xie C, *et al.*, 2020, Sacrificial microgel-laden bioink-enabled 3D-Bioprinting of mesoscale pore networks. *Bio-Des Manuf*, 3(1): 30–39.

https://doi.org/10.1007/s42242-020-00062-y

129. Brunel LG, Hull SM, Heilshorn SC, 2022, Engineered assistive materials for 3D-Bioprinting: Support baths and sacrificial inks. *Biofabrication*, 14(3): 032001.

https://doi.org/10.1088/1758-5090/ac6bbe

130. Lee JM, Sing SL, Zhou M, *et al.*, 2018, 3D-Bioprinting processes: A perspective on classification and terminology. *Int J Bioprint*, 4(2).

https://doi.org/10.18063/ijb.v4i2.151

ACCSCIENCE PUBLISHING

International Journal of Bioprinting

REVIEW ARTICLE

Bioprinting technology for the management of diabetic foot disease: Emerging applications, challenges, and prospects

Fan Xu[1], Shunli Rui[1], Cheng Yang[1], Xiaoyan Jiang[1], Wei Wu[2], Xianlun Tang[3], David G. Armstrong[4], Yu Ma[1]*, and Wuquan Deng[1]*

[1]Department of Endocrinology, School of Medicine, Chongqing Emergency Medical Center, Chongqing University Central Hospital, Chongqing 400014, China

[2]Key Laboratory for Biorheological Science and Technology of Ministry of Education, State and Local Joint Engineering Laboratory for Vascular Implants, Bioengineering College of Chongqing University, Chongqing 400030, China

[3]Chongqing Key Laboratory of Complex Systems and Bionic Control, College of Automation, Chongqing University of Posts and Telecommunications, Nan'an district, Chongqing 400065, China

[4]Department of Surgery, Keck School of Medicine of University of Southern California, Los Angeles, CA 90033, USA

(This article belongs to the *Special Issue: Bioprinting strategies for managing skin diseases and injuries*)

Abstract

Most conventional therapies have limitations in the repair of complex wounds caused by chronic inflammation in patients with diabetic foot ulcers (DFUs). In response to the demand for more biotechnology strategies, bioprinting has been explored in the regeneration field in recent years. However, challenges remain regarding the structure of complex models and the selection of proper biomaterials. The purpose of this review is to introduce the current applications of bioprinting technology in chronic diabetic foot wound healing. First, the most common application of bioprinting in producing skin equivalents to promote wound healing is introduced; second, functional improvements in the treatment of chronic and difficult-to-heal DFU wounds facilitated by bioprinting applications are discussed; and last but not least, bioprinting applications in addressing unique diabetic foot disease characteristics are summarized. Furthermore, the present work summarizes material selection and correlations between three-dimensional (3D) bioprinting and a variety of biomimetic strategies for accelerating wound healing. Novel, biotechnological tools such as organoids for developing new biomaterials for bioprinting in the future are also discussed.

Keywords: Bioprinting; Wound; Skin; Diabetic foot disease; Biomaterial

***Corresponding authors:**
Yu Ma (81846846@qq.com)

Wuquan Deng
(wuquandeng@cqu.edu.cn)

Citation: Xu F, Rui S, Yang C, *et al.*, 2023, Bioprinting technology for the management of diabetic foot disease: Emerging applications, challenges, and prospects. *Int J Bioprint*, 9(6): 0142.
https://doi.org/10.36922/ijb.0142

Received: April 17, 2023
Accepted: June 12, 2023
Published Online: July 31, 2023

Copyright: © 2023 Author(s). This is an Open Access article distributed under the terms of the Creative Commons Attribution License, permitting distribution, and reproduction in any medium, provided the original work is properly cited.

Publisher's Note: AccScience Publishing remains neutral with regard to jurisdictional claims in published maps and institutional affiliations.

1. Introduction

Bioprinting is an emerging technology with widespread applications in regenerative medicine[1]. In recent years, various types of scaffold materials and biomaterial inks have been developed for biomedical applications[2]. Currently, bioprinting is used not only for implants and treatment *in vivo* but also for model construction and

mechanistic research *in vitro*[1]. Although most studies are still in the preclinical research stage, their application prospects are beyond doubt[3]. The emergence of new technologies and concepts, such as hydrogels and stem cells, provides new material choices for bioprinting[4-5]. The combination of these biotechnologies and bioprinting will accelerate the development of regenerative medicine[6].

Bioprinting has attracted much attention with regard to skin regeneration and repair of refractory chronic wounds because it has the potential to produce three-dimensional (3D) skin equivalents[7]. Chronic wound healing has been a difficult problem for decades[8]. Especially, with an increase of diabetes incidence rate, a growing number of patients become troubled by one of the complications of diabetes, i.e., diabetic foot ulcers (DFUs)[9]. Wounds in patients with diabetes usually heal poorly due to inflammation, infection, immune dysfunction, and impaired angiogenesis[8-10]. Usually, amputation is required in DFU patients because of chronic, severe, and intractable skin ulcers[9-10]. The pain inflicted by chronic and difficult-to-heal DFU wounds, as well as the corresponding medical burden on society, is difficult to be neglected[10-11].

Some studies have shown that bioprinting has unique advantages in improving wound healing in DFU patients by means of producing antibacterial and anti-inflammatory materials and promoting angiogenesis[12-14]. However, bioprinting for diabetic wound treatment is still far from clinical application[13]. The use of bioprinting in diabetic wound management should be more targeted[14]. In this review, we introduce the current applications of bioprinting technology, including the bioprinting of skin equivalents for wound repair, functional improvements in the treatment of chronic wounds facilitated by bioprinting applications, and bioprinting applications in addressing unique diabetic foot disease characteristics, so that guidance can be provided for future research and translational applications of bioprinting in the field of diabetic foot wound treatment.

2. Bioprinting of skin equivalents for promoting wound healing

DFUs are usually accompanied by wounds that are difficult to heal. There are various clinical management methods for promoting wound healing[10,15]. Skin transplantation is an option, but the insufficient supply of autologous split skin transplantation materials is a global challenge[13,16]. Skin equivalents can also be used to promote wound healing[16-17]. Hence, good skin equivalents become a major demand in wound repair, and producing them via bioprinting seems to be feasible.

Traditional skin engineering typically involves the creation of a simplified model consisting of two compartments based on the two major structures of the skin (epidermis and dermis)[18]. The polymer or protein scaffold is combined with fibroblasts to form a construct that is immersed in a culture medium to simulate the dermis, and then keratinocytes are added to the upper layer of the construct and exposed to the gas–liquid interface to form a fully keratinized epidermis[18-19]. This construction method can endow the product with morphology and biological functions that have a certain degree of similarity to those of human skin[19].

However, to act as a barrier to damages from external factors, such as pathogenic toxins and ultraviolet rays, the skin, as the largest human organ, is equipped with a complex structure that includes the hypodermis, namely, the subcutaneous tissue, in addition to the epidermis and dermis[19,20]. Not only are keratinocytes and fibroblasts formed in the epidermis and dermis, but immune cell populations, nerve endings, and glands are also formed[20,21]. Due to the lack of natural skin features, such as hair follicles, innervation, and vascularization, existing skin tissue equivalents are considered functionally inadequate[21].

Bioprinting allows the accurate arrangement of cells and biomaterials, which can facilitate the construction of complex multilayer structures[22]. The primary goal of skin bioprinting is to improve the tissue authenticity of traditional skin equivalents, allowing the accurate placement of multiple cell types and skin accessories[23]. 3D printing technology has, at the very least, been proven *in vivo* to be capable of producing skin substitutes for diabetic wounds[12,14,24].

2.1. Skin bioprinting process

The current skin bioprinting process mainly includes the following four steps[18]: preprocessing, printing, postprocessing, and evaluation (Figure 1). In the preprocessing stage, cell and ink bioprinting materials should be selected properly, and the whole design of the printing process, including the printing method, imaging technology, blueprinting, and organization of the toolpath, needs to be preset[23]. In the following step, a 3D conduct is created by layering cell-laden bioinks[2,23]. The common bioprinting methods include laser-assisted bioprinting, droplet-based bioprinting, and extrusion bioprinting[23,25]. These methods can be integrated into a bioprinting system[26]. After that, dermal fibroblast proliferation and epidermal keratinocyte differentiation are induced in the postprocessing step to attain the mechanical properties and structure of the printed conduct[25]. This 3D conduct is usually cultured in Petri dishes at an air–liquid interface[23].

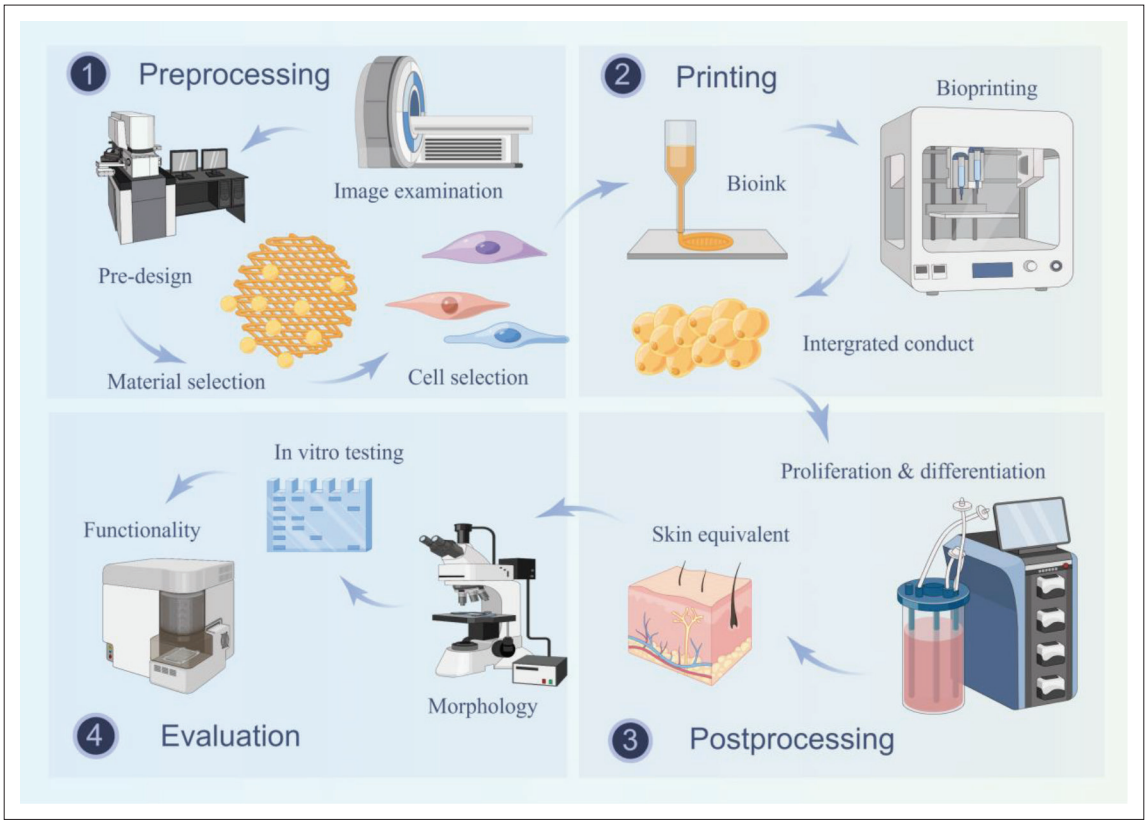

Figure 1. The current skin bioprinting process

Table 1. Comparison of three common skin bioprinting strategies

Bioprinting strategy	Advantages	Disadvantages	Challenges
Laser-assisted bioprinting	High-viscosity biomaterials with minimal risk of clogging, and high printing precision and cell viability	Less economical and largely time-consuming	Optimization of the printing parameters
Inkjet bioprinting	Low cost, widespread use, efficient printing speed, and high cell viability and resolution	Nozzle clogging and low concentration	Shear stress
Extrusion bioprinting	Most commonly used, high cell densities, and good compatibility with biomaterials	High shear stress, lower printing speed and resolution, and lower cell viability	Gelation and shear thinning properties of materials

Additionally, it can be cultured in a variety of bioreactors, including stirred flasks, perfusion systems, rotating wall vessels, and many others[23,26]. In addition, before applying the bioprinting product, one final check is conducted. Several key indicators must be considered, such as sustained dermal cell viability, extracellular matrix (ECM) production, and biomechanical testing[23].

2.2. Skin bioprinting strategies

The nomenclature of bioprinting technologies is often related to the mechanisms involved in these technologies[25]. Pressure-assisted system is the most commonly used bioprinting technology due to low cost[25]. In addition, there are other systems, such as piezoelectric-, thermal-, laser-, acoustic-, and microfluidic-driven bioprinting, which are typically more expensive[26].

In skin bioprinting, novel technologies, including laser-assisted bioprinting, inkjet bioprinting, and extrusion bioprinting, have been widely used[26]. Table 1 summarizes these three technologies in detail[25-29].

Recent studies have combined cell spheroids with 3D bioprinting technology to explore the regeneration of skin appendages[29]. Zhang *et al.*[30] demonstrated a method for the symbiosis of hair follicles and sweat glands *in vitro* by attaching hair follicle spheres to a novel sweat gland scaffold prepared based on extrusion-based bioprinting.

Table 2. Natural polymers for scaffolds

Polymer		Advantages	Disadvantages
Natural polymer	Gelatin	Low-cost, good injectability, and possessing ability to promote cell adhesion and proliferation	Lack of thermal stability, quick degradation rate, and poor mechanical properties
	Collagen	No high temperatures required for pH neutralization and highly permeable	Poor mechanical properties, low viscosity, and time-consuming gelation
	Fibrin	Good cell adhesion and possessing ability to promote wound healing	Time-consuming gelation, poor mechanical properties, and poor extrusion and shape fidelity
	Alginate	Easily modified and maintains moist wound environment	Poor mechanical properties and shear thinning behavior
Synthetic polymer	Poly(lactic-co-glycolic acid)	Low-cost, widespread use, good mechanical properties, and modifiable degradation rate	Higher temperatures and pressures needed
	Polycaprolactone	Easy to process, good mechanical properties, and low degradation rate	High printing temperatures and pressures, time-consuming, and low cell adhesion
	Polyurethane	Low printing temperature, good mechanical properties and elasticity, and possessing ability to promote cell adhesion and proliferation	Additional crosslinking stage required
	Polyethylene glycol	Promotes M2 macrophage polarization and wound healing, good mechanical properties, and easily modifiable	Time-consuming, additional processing step required, and other supporting biomaterials required

In addition, the development of automated-assisted technology has increased the potential of *in situ* bioprinting technology[30-32]. *In situ* technology can be used to directly print at specific anatomical locations on living organisms and design living cells, growth factors, and biomaterials with precise positioning[31]. Robots and handheld devices are commonly used to fabricate complex shapes and curved surfaces *in situ*[32]. With the help of robotics, bioprinting tasks can be facilitated with high accuracy and automation levels without exhausting the operator[32]. Typical robotic-assisted bioprinting includes Cartesian coordinate robots, articulated robots, and parallel robots[32]. Cubo *et al.*[33] confirmed that a Cartesian printer can produce engineered skin that is very similar to human skin. This group used biological ink containing human plasma and primary human fibroblasts and keratinocytes obtained from skin biopsies to print human bilayered skin and tested the function of this bilayered skin in an immunocompromised mouse model[33].

2.3. Bioinks

Bioinks include biomaterials that form temporary scaffolds, seed cells, and microenvironmental factors that regulate cells[34]. This bioprinting component determines the printability of scaffolds and can be endowed with specific functions by adding factors[14,34].

2.3.1. Biomaterials

The primary features of biomaterials are nontoxicity and good biocompatibility[34]. Gelatin, collagen, fibrin, alginate, and other natural compounds similar to the outer matrix have been widely used as biomaterials in bioprinting[34-37]. Some synthetic polymers, including polyurethane, polycaprolactone (PCL), poly(lactic-co-glycolic acids), and polyethylene glycol, have also been used to complement natural materials to endow them with stable structures and controllable mechanical properties by mixing synthetic and natural materials together[34-39]. Table 2 summarizes these polymers in detail[34-41].

2.3.2. Seed cells

The keratinocytes and fibroblasts comprised in the structure of the epidermis and dermis are the preferred seed cells for skin bioprinting[42]. Other types of seed cells, such as melanocytes, have also been explored[43]. For *in vivo* experiments, stem cells, especially mesenchymal stem cells, adipose-derived stem cells, and induced pluripotent stem cells are favored by researchers due to their valuable differentiation ability and low immunogenicity[44-45]. However, there are still ethical concerns regarding the application of stem cell, as well as difficulties in controlling the direction of differentiation, which could cause tumorigenesis if not properly controlled[46].

2.3.3. Regulation factors

Cytokines and chemokines are often added to biological inks[47], but it is difficult to simulate complex microenvironments and intercellular interactions with the addition of only one or several regulatory factors[48]. In recent years, decellularized extracellular matrix (dECM) has become a new choice of bioink[49]. It performs well in skin bioprinting due to its retained partial ECM

structure and functionality, excellent biocompatibility, and printability[49]. However, how to eliminate the immunogenicity of heterologous dECM while preserving the microstructure and biological activity of dECM as much as possible remains a challenge[50]. More natural mixtures of microenvironmental factors, such as platelet-rich plasma and exosomes, have also gradually attracted attention with regard to bioprinting[51-52].

2.4. Current applications and challenges

The most anticipated clinical application of skin bioprinting is the quick replacement of damaged skin in partial- and full-thickness wounds, such as burn wounds and diabetic wounds[25,52]. With the development of vascularized bioprinted skin and hair follicle models[30,53], the structure of bioprinted skin has become increasingly similar to the structure of real skin. A recently developed full-thickness skin equivalent was applied to construct skin equivalents with real skin structural features, such as the subcutaneous layer and accessories[54-55]. Jorgensen *et al.*[55] used a composite hydrogel bioink containing gel, glycerin, and hyaluronic acid (HA) to construct a skin equivalent and suspended a variety of cells in the fibrinogen bioink to print a three-layer patch structure. After 21 days, layered epidermis, mature dermis, and angiogenesis were observed[55]. Their results confirmed that the full-thickness skin equivalent was more similar to normal skin than the hydrogel of the control group[55].

While skin bioprinting is used in wound healing and production of skin equivalent grafts based on a clear medical need, it also has great application value in skin modeling for the study of some diseases and drug transdermal effects *in vitro*[56]. Compared to conventional skin models, 3D-printed skin models exhibit a higher level of biological complexity to increase the level of information that can be obtained on drug–skin interactions[57].

However, optimal materials for scaffolds and bioinks, especially intelligent materials for four dimensional (4D) printing, are still being developed, and achieving skin heterogeneity remains a challenge in the design of bioprinted skin[58]. Product deformation after printing with respect to the printed design is difficult to prevent due to the softness of skin[59]. Currently, there are still structural and functional differences between bioprinted skin and natural skin[60]. Achieving a balance between the proliferation and differentiation of various types of cells can help solve the cocultural challenges posed by the introduction of multiple cell types[61]. Further development of new design methods related to bioprinting processes or a hybrid system of two or more bioprinting methods may be a solution for overcoming the design challenges of skin bioprinting[62].

3. Functional improvements in chronic wound treatment facilitated by bioprinting applications

Wound healing is a complex dynamic process. Generally, wounds that encompass the superficial layer of the epidermis or dermis quickly reach an ideal healing state[63]. However, scar repair often occurs in wounds that reach into the deep dermis and subcutaneous tissue[64]. When wounds are subject to repeated infection, excessive inflammatory reactions, circulatory dysfunction, and immune imbalance, the formation of a skin barrier with a complete structure and a set of functions during the repair process becomes difficult[63]. Thus, acute wounds become chronic wounds, and it is difficult to achieve ideal healing[65].

DFU wounds are usually chronic and persistent[66], and other common chronic wounds include venous leg ulcers (VLUs) and pressure ulcers (PU)[63,67]. These wounds share the common pathophysiological characteristics of chronic wounds[68]. Conventional therapy cannot effectively restore chronic wounds due to their complex pathophysiological mechanisms[68]. However, the ability of bioprinting to accurately arrange cells and the functional diversity of bioprinting ink have shown good application prospects in the treatment of diabetic chronic wounds[69-70]. Here, the pathological and physiological characteristics of chronic wounds and the functional improvements in chronic wound treatment facilitated by bioprinting are introduced.

3.1. Molecular mechanisms of difficult-to-heal chronic wounds

The development of multiomics and the subsequent in-depth research on its mechanisms have revealed the pathophysiological characteristics of chronic wounds and their environments as well as aided in the exploration of therapeutic targets[70-71]. The main skin structures involved include the epidermis, dermis, and extracellular matrix, as well as resident cells, such as keratinocytes, fibroblasts, immune cells, and endothelial cells[65]. Understanding the pathophysiological changes and therapeutic targets of these structures at the cellular level can facilitate the development of novel bioprinted scaffolds and ink materials tailored to the characteristics of chronic wounds[70].

3.1.1. Keratinocytes

As the main cells that constitute the epidermal structure, keratinocytes are activated on wound surfaces and restore the epidermal barrier through migration, proliferation, and differentiation[63,65]. In addition, a large number of growth factors and cytokines secreted by keratinocytes recruit other cells, promoting matrix formation and angiogenesis[65]. In chronic wounds, keratinocytes become ineffective in the process of re-epithelialization

due to excessive proliferation, impaired migration, and imbalanced differentiation, resulting in impaired barrier function along with the excessive keratinization of the epidermis[71]. In addition, there are also functional impairments in the communication between keratinocytes and immune cells, such as T cells, in chronic wounds[72]. Histological studies have found that the disorder of keratinocytes in chronic wounds is related to the abnormal expression of cell cycle-related proteins such as myc proto-oncogene protein (c-myc)[73]. Upregulation of those cell cycle-related oncogenes, such as c-myc, and the Wnt pathway downregulated by myc gene family (including c-myc) may increase the risk of wound healing[73-74]. The cell cycle-related oncogenes dysregulated in DFU wound could be potential therapeutic targets in wound healing. For example, Su *et al.*[75] found that using programmed death ligand 1 (PD-L1) embedded in hydrogel, which can promote cell cycle progression and suppress T-cell activation, to treat wounds in mice can reduce inflammation and improve re-epithelialization. However, there is currently a lack of further research on the use of bioinks with this type of potential therapeutic targets in bioprinting for DFU treatment.

3.1.2. Fibroblasts

As the main secretor of extracellular matrix, fibroblast activation plays a crucial role in wound healing through immune cell recruitment, angiogenesis, and wound contraction[65]. Fibroblasts in the dermis have strong heterogeneity in both acute and chronic wounds[63,76]. Phenotypic dysfunction and cellular aging are common characteristics of their inability to promote normal healing processes in chronic wounds[63]. Persistent hypoxia in the lower limbs of DFU patients is one of the causes of fibroblast aging and is accompanied by impaired maturation of collagen and production of hypoxia-inducible factor (HIF), transforming growth factor (TGF), and epidermal growth factor (EGF) receptor[77-78]. Another cause is the decreased level of growth factors secreted by fibroblasts, such as platelet-derived growth factor BB (PDGF-BB), fibroblast growth factor (FGF), and EGF[78]. Single-cell sequencing experiments have also facilitated the discovery of unique subsets of fibroblasts in DFU chronic wounds due to persistent inflammatory conditions, which are also responsible for the inability of fibroblasts to heal properly[71,79]. The healing-enriched fibroblasts (HE-Fibro), a unique population of fibroblasts identified by single-cell sequencing in patients whose DFU has healed, may promote wound repair by overexpressing proteins related to ECM remodeling (matrix metalloproteinase [MMP]-1, MMP-3), as well as immune and inflammatory regulator genes including tumor necrosis factor alpha induced protein 6 (TNFαIP6) and chitinase 3-like 1 (CHI3L1)[79]. Further research is needed to investigate the main functional proteins of HE-Fibro, which is a seed cell, in order to embed those proteins into bioinks.

3.1.3. ECM components

Chronic wounds exhibit ECM damage and dysfunction, especially the disordered expression of MMPs, MMP protease inhibitors, and tissue inhibitors of matrix metalloproteinases (TIMPs), which can lead to the degradation of the collagen matrix in ECM and play a key role in normal wound healing[80-81]. Single-cell sequencing showed that the fibroblasts with high expression of CHI3L1 on the DFU wound surface express a large amount of MMPs to promote ECM remodeling[79]. In addition to MMP protease inhibitors, other protease inhibitors, such as serine proteases, also degrade important components of ECM, such as fibronectin (FN) and important growth factors and their receptors[80]. The development of drugs for targeting the dynamic transformation of the external matrix, protease inhibition, and activation pathways, such as that of MMPs, can facilitate effective methods for DFU chronic wound treatment[82].

3.1.4. Inflammation and angiogenesis

It was found recently that the inflammatory response of chronic wounds is characterized by a persistently low degree of inflammation, which impairs endothelial function in the long term and causes disorders, such as macrophage polarization disorders and neovascularization disorders, but is weaker than the inflammatory response of acute wounds[65,83]. Therefore, in chronic wounds, it is difficult to achieve high intense of short-term inflammation that is beneficial for acute wound healing[83]. Usually, the persistent abnormal inflammatory state of DFU aggravates the infiltration of fibroblasts on the wound surface, leading to endothelial dysfunction[83]. Abnormal infiltration of fibroblasts alters the normal ECM environment by secreting proteins (mainly MMPs), thereby hindering the generation of new blood vessels, and causing hypoxia in the wound[80-81]. The inflammatory state of DFU also abnormally activates M1 type macrophages that promote inflammation, but the M1 type macrophages of DFU are unable to transform into anti-inflammatory M2 type macrophages normally, resulting in persistent inflammation state that cannot subside[65,72]. The mechanisms of DFU causing the dysfunction of fibroblasts and macrophages remain to be fully delineated. A further understanding of the changes in the cellular inflammatory environment and their impact on wound healing can help improve clinical outcomes and wound treatment[84]. *In vivo* and *in vitro* experiments have confirmed that regulating inflammation can promote DFU healing[84-85]. Current research focuses on targeted supplementation of cytokines that are lacking

in dysfunctional fibroblasts to alleviate inflammation-induced damage, including direct supplementation of cytokines or administration of probiotics that can regulate secretion of cytokine[83-85].

Neovascularization provides immune cells, oxygen, and nutrients for highly metabolic wound repair and transport of metabolic waste, which are critical for the healing of chronic wounds in the elderly and those with microcirculation disorders, such as patients with severe DFUs[85]. In addition to chronic hypoxia and nutritional disorders, another serious consequence of angiogenesis dysfunction is the inability to recruit sufficient endothelial progenitor cells (EPCs) to the wound surface[86]. Hyperbaric oxygen therapy can help improve angiogenesis and EPC dysfunction and promote DFU wound healing[86-87].

3.2. Bioprinting applications for wound chronicity

Although skin transplantation is still the gold standard for the treatment of chronic wounds[13], bioprinted scaffolds still have unique advantages compared to other skin engineering materials in the treatment of chronic wound healing[88]. In particular, they can promote healing by addressing the angiogenic disorders and inflammation that occur after the healing of chronic wounds, such as DFUs[88]. Here, we introduce studies that employed bioprinting using different functional materials in the treatment of chronic wounds.

3.2.1. Different scaffold materials and bioinks for promoting chronic wound healing

There are physical and biochemical factors involved in skin engineering that cannot be accurately controlled by traditional techniques and cannot be fulfilled by a single biomaterial[89]. Therefore, bioprinting methods rely on programmable microscales to control material and cell deposition, as well as combining a variety of complex materials, including natural ECM components, to simulate a repair environment with certain biological functions and skin structures, making these methods incomparable to traditional skin engineering methods[89]. Especially in inflammatory and infected wounds, some scaffolds eliminate inflammation and infection, thereby promoting wound healing[90-93]. For example, Prasad *et al.*[91] encapsulated curcumin in an oil gel 3D fiber network to treat bacterial biofilm-related infections, such as *Staphylococcus aureus*, and promote DFU wound healing. Xia *et al.*[92] loaded curcumin into gelatin methacryloyl (GelMA)-containing adipose-derived stem cells to evaluate its therapeutic effect on DFU wounds through *in vitro* experiments. They found that the gel could reduce apoptosis and reactive oxygen species production, which could promote DFU wound healing[92]. Ullah *et al.*[93] demonstrated through *in vivo* experiments that a scaffold developed by combining nicotinamide with human dermal fibroblasts had a promoting effect on the healing of infected wounds.

Due to the characteristics of chronic wounds such as insufficient blood oxygen supply and difficult healing, recent studies have proposed a variety of materials and methods for improving angiogenesis and local oxygen supply[94-95]. Ma *et al.*[94] added a uniform strontium silicate (SS) microcylinder to a bioink as a stable inducer of angiogenesis in skin substitutes composed of a bioprinted multicellular system. Inspired by symbiotic relationships, Wang *et al.*[95] proposed using *in situ* microfluidic-assisted 3D printing to incorporate unicellular microalgae (*Chlorella pyrenoidosa*) into a scaffold to form a live photosynthetic scaffold, which could alleviate local hypoxia on the wound surface through the photosynthesis of microalgae, promote extracellular matrix synthesis, and accelerate wound healing. In addition, 3D-printed patches containing angiogenic factors could also improve ischemia and hypoxia on the wound surface and promote wound healing[96-97]. Guan *et al.*[96] developed a bioprintable peptide patch and promoted the angiogenic properties of the patch by covalently coupling the peptide QHREDGS with GelMA and hyaluronic acid methacryloyl (HAMA) biological patches. Liao *et al.*[97] covalently crosslinked intravascular growth factor (VEGF) onto a biological patch composed of alginate polysaccharide and chondroitin sulfate methacrylic acid groups through calcium ions and ultraviolet light, simplifying the single chemical coupling step and extending the VEGF release time.

3.2.2. Personalized printing and novel printing strategies for complex wounds

The shape of DFU wounds is irregular, the depth varies, and the structure is complex[98]. Bioprinting fulfills the needs of personalized and accurate treatment by producing models in varying designs using different printing strategies[99].

Embedded bioprinting is a novel type of bioprinting that outperforms traditional bioprinting strategies, such as extrusion bioprinting, in terms of the fineness and complexity of 3D-printed pendants or hollow structures[100]. It has great potential in solving the vascularization problem in 3D-printed scaffold[101]. Embedded printing can better preserve the shape of hydrogels by printing in a prefilled matrix[102]. In addition, a new printing strategy has been developed that involves printing cell aggregates, without using hydrogel as a biological ink, into 3D tissue constructs with a certain spatial structure and then assembling these constructs into integrated tissues[102-103]. Skylar-Scott *et al.*[103] used this method to construct organ building blocks (OBBs) derived from patient-specific pluripotent stem cells and then assembled perfusion-capable vascular

channels in a high-cell-density matrix through embedded printing. This study indicated that embedded bioprinting can be used to create functional tissue or organ structures, especially vascular structures, and has broad application prospects in the field of regenerative medicine, especially in the treatment of DFU chronic wounds in patients with angiogenic disorders[102-103].

To produce customized tissue-engineered skin for chronic and irregular wound treatment, Wu *et al.*[104] developed a planar/curved bioprintable hydrogel. The hydrogel was composed of polyurethane and gelatin and contained three kinds of cells: fibroblasts, keratinocytes, and endothelial progenitor cells[104]. Moreover, this curved bioprintable hydrogel with three cell types could promote complete repair of chronic irregular wound in a rat model after 28 days, which proved the enormous application potential of this hydrogel that allows customization according to wound shape in chronic wound healing[104]. The integrated development of *in situ* printing technology and bioprinting systems mentioned above also meets the requirements of on-site on-demand production and rapid treatment in the future[104-105].

Usually, DFU patients have significant differences in wound depth[15]. Therefore, DFU may involve repairing different types of tissue interfaces[106]. The organizational interface is a key structure in coordinating the interaction between two different organizations, and the possible damage to the organizational interface that may occur in DFU patients including skin, neurovascular/muscular interfaces, and even cartilage–bone interfaces[10,106]. The self-healing ability of these organizational interfaces is usually limited[106]. Transplantation of autologous, allogeneic, or synthetic grafts is currently being used to treat tissue interfaces with limited effectiveness[13,15], mainly due to the inability to form multilayer structures similar to tissue interfaces in a short period of time[106]. Computer-assisted bioprinting technology makes it possible for various biomaterials to be accurately arranged layer by layer in space[102-103]. The use of biomaterials such as cells and cytokines for personalized modeling and printing of patient wounds has great application prospects in DFU wound interface tissue repair[106]. However, the current physical and chemical properties of biomaterials and the accuracy of bioprinting methods cannot meet the requirements for repairing complex tissue interface structures[106]. Although bioprinting can build nanoscale constructs, it cannot simultaneously maintain the activity of seed cells and the microenvironment [106]. Therefore, further studies to explore suitable biomaterials and bioprinting strategies for repairing tissue interfaces through bioprinting are warranted in the future.

4. Bioprinting applications for unique diabetic foot disease characteristics

In 2019, the International Working Group on the Diabetic Foot (IWGDF) proposed eight key factors of the diabetic foot classification score based on a literature review and expert opinions to provide guidance for the management of DFU infection and the blood circulation reconstruction, although they believe that there is still no classification that can predict the outcome of a single ulcer (Figure 2)[107]. The main eight factors are end-stage renal disease, peripheral arterial disease, loss of protective sensation, infection , depth, location (forefoot/hindfoot), size of ulcers, and number (single/multiple) of ulcers[107]. In addition, the chronic wounds of patients with diabetic foot disease also have a unique high-glucose environment that affects wound healing[108]. To treat DFU wounds using bioprinting, new treatment options tailored to the characteristics of DFU wounds should be developed.

Here, we introduce recent bioprinting applications for unique diabetic foot disease characteristics in detail.

4.1. Imaging and algorithm technology-assisted bioprinting for DFU treatment

Traditional imaging methods, such as 3D magnetic resonance imaging (MRI), are used to evaluate the blood circulation of DFU wounds[10,107]. To further enhance the ability of bioprinting to accurately evaluate DFU wounds and reconstruct biomimetic tissues, more auxiliary imaging and modeling methods have been developed[109-112]. Tian *et al.*[109] proposed to quantitatively describe the 3D structure of skin collagen tissue using fractal dimension analysis after analyzing skin under different pathological conditions. Xu *et al.*[110] subsequently used small angle X-ray scattering (SAXS) combined with the potential fractal characteristics of collagen to design a analysis tool for quantitating collagen to evaluate dermis and grafts and verified the analysis effect in a diabetic mouse model. In addition, Pena *et al.*[111] used two infrared cameras and an infrared projector to form a WoundVue camera for initial DFU wound measurement and periodic detection and evaluated the reliability of the camera by comparing the wound area, depth, and other indicators measured by the camera and an established Visitrak system. Parsa *et al.*[112] proposed that optical coherence tomography (OCT) can be used to evaluate DFU wound characteristics and blood flow through a single-center nonrandomized observational study to improve guidance for treatment option selection.

Algorithm-assisted bioprinting is also a new strategy for improving the therapeutic effect of bioprinting on DFU wounds[113-117]. Li *et al.*[114] developed a step-by-step algorithm that combined adaptive mesh generation

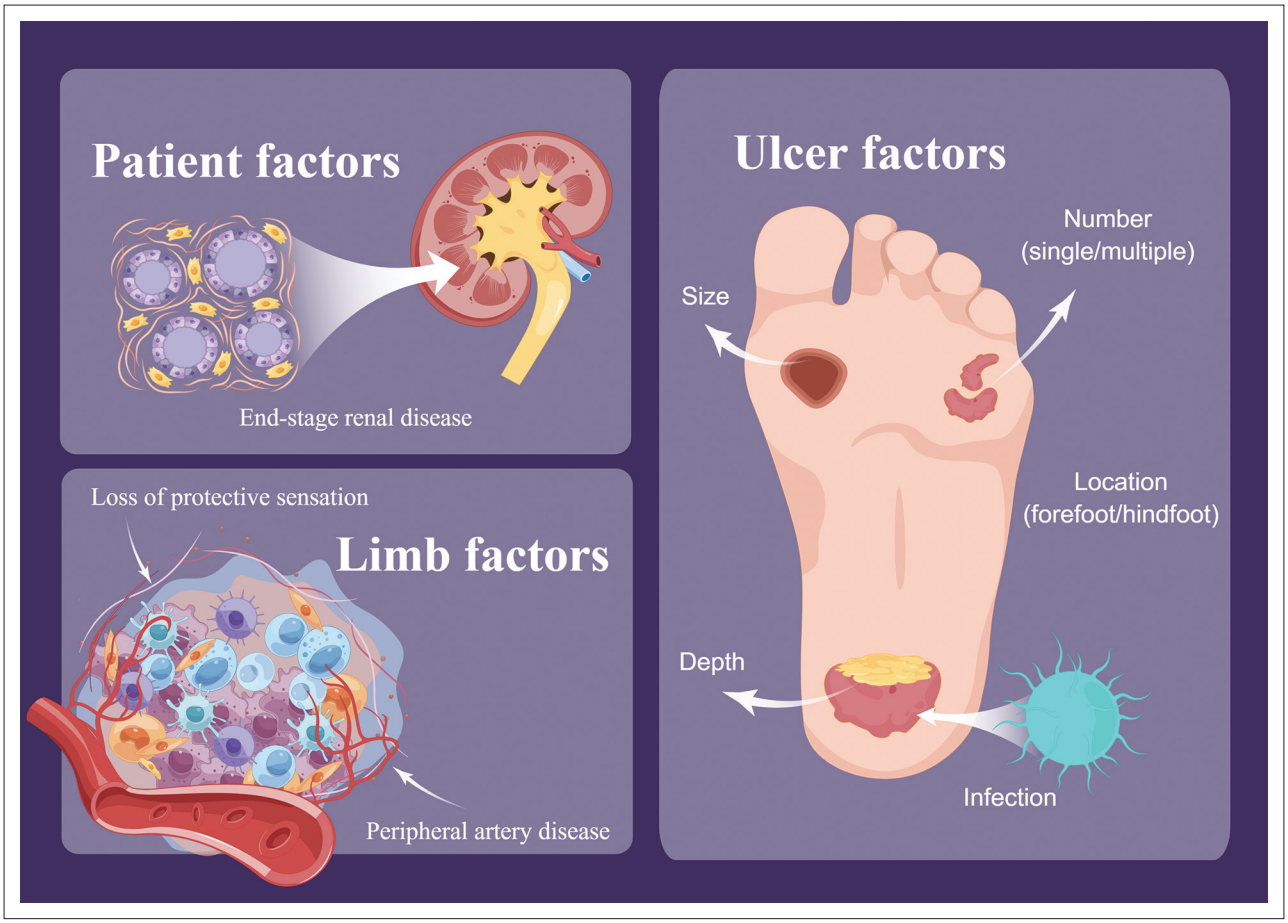

Figure 2. Eight key factors of the diabetic foot classification score

algorithms with greedy search algorithms to assist in the customization of biomimetic tissues with heterogeneous microstructures using extrusion bioprinting technology in geometric code-driven mode. Gholami *et al.*[115] designed a conceptual tool based on the semiautomatic segmentation of wound images to assist in the bioprinting of skin patches so that they can better match the shape of wounds. Zahia *et al.*[116] proposed an end-to-end system based on deep learning that could produce a single two-dimensional (2D) image and 3D mesh of pressure injuries through sensors, perform fine external segmentation of wound images, and accurately measure depth, area, and volume, thereby assisting in the evaluation of pressure injury and wound healing. Zhao *et al.*[117] developed an adaptive interface detection algorithm that utilized OCT technology to evaluate the structural parameters and quality of artificial skin products.

Portable biointegrated bioprinting systems, such as customized handheld bioprinters, can also be applied to treat complex and irregular wounds while eliminating the need for complex imaging systems and algorithms[118-120]. Nuutila *et al.*[119] reported a growth factor-containing scaffold that was printed *in situ* on pigs. *In vivo* and *in vitro* experiments have shown that this handheld printer can easily print customized curved surfaces on tissues, promoting full-thickness wound healing[119]. In addition, a multifunctional hemostatic platform developed based on 3D printing combined with electrospinning and photolithography technology could help solve the problem of chronic wound bleeding as well as promote ECM formation and wound healing[120].

4.2. Applications of bioprinting in hyperglycemic environments

Because diabetes induces a unique pathophysiological high-glucose environment, bioprinting is first used to establish a disease model for DFU skin[121]. Kim *et al.*[122] used three kinds of cells, including human diabetes dermal fibroblasts (dHDFs), diseased human subcutaneous preadipocytes (dHPAs), and human epidermal keratinocytes (nHEKs), which were isolated from donors with type 2 diabetes, to construct diabetic skin models through bioprinting in a high-glucose environment, and

used human umbilical vein endothelial cells (HUVECs) to introduce a vascular structure into the model. By detecting the molecular expression, collagen precipitation, angiogenesis, and other indicators, it was determined that the model had characteristics that were very similar to the skin characteristics of the DFU patients[122]. This patient-derived skin model has good application prospects in the research on cellular crosstalk mechanisms and the screening of therapeutic drugs[122].

The use of bioprinting technology to control hyperglycemic environments is also an application of bioprinting in the treatment of DFUs[123-128]. A high-glucose microenvironment not only limits the availability of growth factors and promotes the expression of inflammatory factors, but also hinders immune cell recruitment, causes microvascular dysfunction, and affects wound healing[123]. Several clinical studies have proven that hypoglycemic treatment can improve the healing of DFUs and reduce the risk of amputation[124-125,128]. The use of bioprinted microneedle technology can improve the delivery efficiency of hypoglycemic drugs to help DFU patients control blood sugar, thus improving the healing of DFU wounds[125-126]. In addition, loading hypoglycemic drugs into a 3D scaffold for the local hypoglycemic treatment of wounds can be a therapeutic strategy for improving DFU healing[127]. Kamel *et al.*[127] confirmed that treatment with 3D chitosan composite scaffolds loaded with pioglitazone hydrochloride (PG) in a rat model significantly improved healing compared to the treatment without PG loading. Adding immunomodulators to bioinks may also improve the external matrix environment and promote DFU healing[66,128].

4.3. 3D-printed products for DFU prevention and limb prostheses

The use of foot-assisted devices for gait adjustment can help prevent DFUs from occurring[129-131]. Compared to traditional customized brackets and insoles made of gypsum and other materials, customized auxiliary devices produced by 3D printing have an adjustable hardness and their shape is more suitable for application[132]. In addition, bioprinting can also be used to customize exquisite castings to compensate for limb defects caused by DFU amputation[133]. Compared to the Paris plaster used in clinical practice, customized plaster made using 3D printing technology can alleviate skin necrosis caused by inaccurate model fitting and improve patient satisfaction[133].

4.4. Potential applications of bioprinting combined with novel technologies

Hydrogels and stem cells are commonly combined with bioprinting[134-135]. Hydrogels are often used as a kind of bioink in bioprinting[134]. Stem cells are attached to biological scaffolds as seed cells[135]. Manso *et al.*[136] applied bioprinted biocuratives containing mesenchymal stem cells (MSCs) to the back wounds of diabetic mice. These biocuratives containing MSCs and alginate saline gel as the matrix could promote the deposition of mouse skin collagen and the wound healing more than the biocuratives without MSCs could[136]. Adipose stem cells are also commonly used as seed cells for bioprinting to promote DFU healing[92,137].

Recently, novel strategies have also been developed that involve the direct use of stem cells without loading other scaffold materials, such as *in situ* printing and embedded printing methods mentioned above. Yastı *et al.*[138] used adipose-derived stem cells (ADSCs) to obtain autologous adipose tissue and then achieved autologous minimally manipulated homologous adipose tissue (AMHAT) transplantation in DFU wounds with customized shapes through 3D printing in a small sample of patients. This study demonstrated that transplantation using 3D printing can reduce the total time needed for wound healing and scar formation, although the cost may be higher than that of ordinary autologous tissue transplantation[138]. Furthermore, embedded printing technology can be combined with organoid technology to accurately combine organoid units into complex biomimetic structures, compensating for the limitations of existing bioprinting methods with regard to biomimetic skin size and facilitating the treatment of DFU wounds with greater degrees of damage[139]. Table 3 shows the recent studies on AMHAT combined with 3D printing technology in DFU treatment[138-141].

Organoid technology can assist embedded *in situ* bioprinting in building finer and larger biomimetic skin structures[142], and exosomes and other novel immune modulators, such as platelet-rich plasma (PRP), can also be used as alternative bioprinting materials to produce functional bioprinted skin substitutes to promote DFU wound healing[143]. Crosslinking these exosomes with scaffolds can also help prolong the release of new types of regulatory factors, such as exosomes and PRP, and solve the problems of rapid metabolism and short action time[143]. Huang *et al.*[144] used coaxial microfluidic 3D bioprinting technology and the calcium ion chemical dual crosslinking method to load PRP on a multilayer bioactive shell core fibrous hydrogel, which reduced drug delivery frequency by 33% compared with that of ordinary hydrogel and ensured slow but continuous release of growth factors in PRP. This hydrogel also showed outstanding therapeutic effects on DFUs by reducing inflammation[144].

5. Perspectives

The development of bioprinting methods for the production of skin equivalents and the adjuvant treatment

Table 3. Studies on AMHAT combined with 3D-printing technology in DFU treatment

Biomaterials	Design	Result	Year
Extracellular matrix (MA-ECM) prepared from AMHAT by 3D bioprinting	40 subjects with DFUs randomly divided into test group (MA-ECM treatment) and control group (standard wound care)	The test group showed complete wound closure within 4 weeks, while the majority of patients in the control group showed delayed wound healing compared to the test group.	2021 [140]
AMHAT dispensed by a 3D-bioprinting device (Dr. INVIVO)	A single-arm pilot study of 10 consecutive patients with a history of chronic DFUs	Sixty percent of the patients showed complete wound closure, and the mean time for closure was 49.1 days (95% CI: 29.9–68.3). There were no adverse events.	2022 [141]
3D-AMHAT with fibrin gel	A total of 10 patients with DFUs	Seventy percent of the patients showed complete healing and no adverse events.	2023 [139]
AMHAT in the customized shape of DFU wounds	A clinical prospective interventional pilot study of 20 patients with DFUs	The total time for wound healing and scar formation was reduced compared to grafting.	2023 [138]

of chronic wound healing is a continued endeavor. Through continuously innovating bioink and scaffold materials, as well as developing new bioprinting strategies, such as *in situ* printing, embedded printing, and machine-assisted printing, bioprinted skin structures are becoming more similar to natural skin structures and possess certain skin functions. There are already some bioprinted materials with vascular structures, although vascularization remains a challenge. These results suggest that bioprinting has broad application prospects in the treatment of chronic DFU wounds.

Nevertheless, the repair of tissue interfaces in deep DFU wounds poses a huge problem because the healing of existing grafts at these tissue interfaces is not ideal. The existing bioprinting technology cannot meet the structural and functional requirements of the skin tissue interface. With the development of algorithms and artificial intelligence, as well as the emergence of multisystem integration and portable printing platforms, we believe that this issue will be resolved in the future.

Acknowledgments

The diagrams were painted on the Figdraw website (codes: UOORUe2842; UAIYUbb908).

Funding

This study was supported by the Joint Medical Key Research Programs of Chongqing Science and Technology Bureau and Health Commission Foundation (No. 2023ZDXM009), the Natural Science Foundation of Chongqing Municipal Science and Technology Bureau (No. CSTB2022NSCQ-MSX0489) awarded to Dr. Wuquan Deng and Dr. Shunli Rui, and the Chongqing medical scientific research project (Joint project of Chongqing Health Commission and Science and Technology Bureau, No. 2020FYYX241) awarded to Dr. Xiaoyan Jiang. This study is also partially supported by National Institutes of Health, National Institute of Diabetes and Digestive and Kidney Diseases (award number 1R01124789-01A1), and National Science Foundation (NSF) Center to Stream Healthcare in Place (#C2SHiP; CNS Award Number 2052578 awarded to Prof. David G. Armstrong).

Conflict of interest

The authors declare no conflict of interest.

Author contributions

Conceptualization: Wuquan Deng and Fan Xu
Writing – original draft: Fan Xu, Shunli Rui, Cheng Yang, Xiaoyan Jiang, Wei Wu, Xianlun Tang, David G. Armstrong
Writing – review & editing: Yu Ma, Wuquan Deng

Ethics approval and consent to participate

Not applicable.

Consent for publication

Not applicable.

Availability of data

Not applicable.

References

1. Mota C, Camarero-Espinosa S, Baker MB, *et al.*, 2020, Bioprinting: From tissue and organ development to in vitro models. *Chem Rev*, 120(19): 10547–10607.

2. Valot L, Martinez J, Mehdi A, *et al.*, 2019, Chemical insights into bioinks for 3D printing. *Chem Soc Rev,* 48(15): 4049–4086.

3. Xu HQ, Liu JC, Zhang ZY, *et al.*, 2022, A review on cell damage, viability, and functionality during 3D bioprinting. *Mil Med Res*, 9(1): 70.
4. GhavamiNejad A, Ashammakhi N, Wu XY, *et al.*, 2020, Crosslinking strategies for 3D bioprinting of polymeric hydrogels. *Small,* 16(35): e2002931.
5. Skeldon G, Lucendo-Villarin B, Shu W, 2018, Three-dimensional bioprinting of stem-cell derived tissues for human regenerative medicine. *Philos Trans R Soc Lond B Biol Sci*, 373(1750): 20170224.
6. Ravanbakhsh H, Karamzadeh V, Bao G, *et al.*, 2021, Emerging technologies in multi-material bioprinting. *Adv Mater,* 33(49): e2104730.
7. Yan WC, Davoodi P, Vijayavenkataraman S, *et al.*, 2018, 3D bioprinting of skin tissue: From pre-processing to final product evaluation. *Adv Drug Deliv Rev*, 132 (2018): 270–295.
8. Las Heras K, Igartua M, Santos-Vizcaino E, *et al.*, 2020, Chronic wounds: Current status, available strategies and emerging therapeutic solutions. *J Control Release*, 328 (2020): 532–550.
9. Grennan D, 2019, Diabetic foot ulcers. *JAMA*, 321(1): 114.
10. Schaper NC, van Netten JJ, Apelqvist J, *et al,* 2020, IWGDF Editorial Board. Practical Guidelines on the prevention and management of diabetic foot disease (IWGDF 2019 update). *Diabetes Metab Res Rev,* 36(Suppl 1): e3266.
11. Abbas ZG, Boulton AJM, 2022, Diabetic foot ulcer disease in African continent: 'From clinical care to implementation' - Review of diabetic foot in last 60 years - 1960 to 2020. *Diabetes Res Clin Pract*, 183 (2022): 109155.
12. Tan CT, Liang K, Ngo ZH, *et al.*, 2020, Application of 3D bioprinting technologies to the management and treatment of diabetic foot ulcers. *Biomedicines*, 8(10): 441.
13. Masri S, Zawani M, Zulkiflee I, *et al.*, 2022, Cellular interaction of human skin cells towards natural bioink via 3D-bioprinting technologies for chronic wound: A comprehensive review. *Int J Mol Sci,* 23(1): 476.
14. Glover K, Stratakos AC, Varadi A, *et al.*, 2021, 3D scaffolds in the treatment of diabetic foot ulcers: New trends vs conventional approaches. *Int J Pharm,* 599(2021): 120423.
15. Sun Y, Gao Y, Chen J, *et al.*, 2019, Evidence mapping of recommendations on diagnosis and therapeutic strategies for diabetes foot: An international review of 22 guidelines. *Metabolism*, 100 (2019): 153956.
16. Manita PG, Garcia-Orue I, Santos-Vizcaino E, *et al.*, 2021, 3D bioprinting of functional skin substitutes: From current achievements to future goals. *Pharmaceuticals (Basel)*, 14(4): 362.
17. He P, Zhao J, Zhang J, *et al.*, 2018, Bioprinting of skin constructs for wound healing. *Burns Trauma*, 6(2018): 5.
18. Yan WC, Davoodi P, Vijayavenkataraman S, *et al.*, 2018, 3D bioprinting of skin tissue: From pre-processing to final product evaluation. *Adv Drug Deliv Rev*, 132(2018): 270–295.
19. Kim HS, Sun X, Lee JH, *et al.*, 2019, Advanced drug delivery systems and artificial skin grafts for skin wound healing. *Adv Drug Deliv Rev,* 146(2019): 209–239.
20. Chouhan D, Dey N, Bhardwaj N, *et al.*, 2019, Emerging and innovative approaches for wound healing and skin regeneration: Current status and advances. *Biomaterials*, 216(2019): 119267.
21. Jeong HJ, Nam H, Jang J, *et al.*, 2020, 3D bioprinting strategies for the regeneration of functional tubular tissues and organs. *Bioengineering (Basel)*, 7(2): 32.
22. Yanez M, Rincon J, Dones A, *et al.*, 2015, In vivo assessment of printed microvasculature in a bilayer skin graft to treat full-thickness wounds. *Tissue Eng Part A*, 21(1–2): 224–233.
23. Datta P, Barui A, Wu Y, *et al.*, 2018, Essential steps in bioprinting: From pre- to post-bioprinting. *Biotechnol Adv*, 36(5): 1481–1504.
24. Assad H, Assad A, Kumar A, 2023, Recent developments in 3D bio-printing and its biomedical applications. *Pharmaceutics*, 15(1): 255.
25. Huang C, Yuan W, Chen J, *et al.*, 2023, Construction of smart biomaterials for promoting diabetic wound healing. *Molecules*, 28(3): 1110.
26. Bittner SM, Guo JL, Melchiorri A, *et al.*, 2018, Three-dimensional printing of multilayered tissue engineering scaffolds. *Mater Today (Kidlington)*, 21(8): 861–874.
27. Ng WL, Qi JTZ, Yeong WY, *et al.*, 2018, Proof-of-concept: 3D bioprinting of pigmented human skin constructs. *Biofabrication*, 10(2): 025005.
28. Lawlor KT, Vanslambrouck JM, Higgins JW, *et al.*, 2021, Cellular extrusion bioprinting improves kidney organoid reproducibility and conformation. *Nat Mater,* 20(2): 260–271.
29. LaBarge W, Morales A, Pretorius D, *et al.*, 2019, Scaffold-free bioprinter utilizing layer-by-layer printing of cellular spheroids. *Micromachines (Basel)*, 10(9): 570.
30. Zhang Y, Enhejirigala, Yao B, *et al.*, 2021, Using bioprinting and spheroid culture to create a skin model with sweat glands and hair follicles. *Burns Trauma*, 9(2021): tkab013.
31. Samandari M, Mostafavi A, Quint J, *et al.*, 2022, In situ bioprinting: Intraoperative implementation of regenerative medicine. *Trends Biotechnol,* 40(10): 1229–1247.
32. Dong H, Hu B, Zhang W, *et al.*, 2022, Robotic-assisted automated in situ bioprinting. *Int J Bioprint*, 9(1): 629.
33. Cubo N, Garcia M, Del Cañizo JF, *et al.*, 2016, 3D bioprinting of functional human skin: Production and in vivo analysis. *Biofabrication*, 9(1): 015006.
34. Tan SH, Ngo ZH, Sci DB, *et al.*, 2022, Recent advances in the design of three-dimensional and bioprinted scaffolds for

full-thickness wound healing. *Tissue Eng Part B Rev*, 28(1): 160–181.

35. Gungor-Ozkerim PS, Inci I, Zhang YS, *et al.*, 2018, Bioinks for 3D bioprinting: An overview. *Biomater Sci,* 6(5): 915–946.
36. Wang H, Yu H, Zhou X, *et al.*, 2022, An overview of extracellular matrix-based bioinks for 3D bioprinting. *Front Bioeng Biotechnol*, 10(2022): 905438.
37. Tao G, Wang Y, Cai R, *et al.*, 2019, Design and performance of sericin/poly(vinyl alcohol) hydrogel as a drug delivery carrier for potential wound dressing application. *Mater Sci Eng C Mater Biol Appl*, 101(2019): 341–351.
38. Chen CS, Zeng F, Xiao X, *et al.*, 2018, Three-dimensionally printed silk-sericin-based hydrogel scaffold: A promising visualized dressing material for real-time monitoring of wounds. *ACS Appl Mater Interfaces*, 10(40): 33879–33890.
39. Gonzalez-Fernandez T, Tenorio AJ, Campbell KT, *et al.*, 2021, Alginate-based bioinks for 3D bioprinting and fabrication of anatomically accurate bone grafts. *Tissue Eng Part A,* 27(17–18): 1168–1181.
40. Lee SC, Gillispie G, Prim P, *et al.*, 2020, Physical and chemical factors influencing the printability of hydrogel-based extrusion bioinks. *Chem Rev,* 120(19): 10834–10886.
41. Jin SG, 2022, Production and application of biomaterials based on polyvinyl alcohol (PVA) as wound dressing. *Chem Asian J,* 17(21): e202200595.
42. Baltazar T, Merola J, Catarino C, *et al.*, 2020, Three dimensional bioprinting of a vascularized and perfusable skin graft using human keratinocytes, fibroblasts, pericytes, and endothelial cells. *Tissue Eng Part A*, 26(5–6): 227–238.
43. Pontiggia L, Van Hengel IA, Klar A, *et al.*, 2022, Bioprinting and plastic compression of large pigmented and vascularized human dermo-epidermal skin substitutes by means of a new robotic platform. *J Tissue Eng*, 13(2022): 20417314221088513.
44. Skylar-Scott MA, Huang JY, Lu A, *et al.*, 2022, Orthogonally induced differentiation of stem cells for the programmatic patterning of vascularized organoids and bioprinted tissues. *Nat Biomed Eng*, 6(4): 449–462.

    https://doi.org/10.1038/s41551-022-00856-8. Epub 2022 Mar 24. PMID: 35332307; PMCID: PMC9506705.
45. Abaci HE, Guo Z, Coffman A, *et al.*, 2016, Human skin constructs with spatially controlled vasculature using primary and iPSC-derived endothelial cells. *Adv Healthc Mater*, 5(14): 1800–1807.
46. Tasoglu S, Demirci U, 2013, Bioprinting for stem cell research. *Trends Biotechnol*, 31(1): 10–19.
47. Ker ED, Nain AS, Weiss LE, *et al.*, 2011, Bioprinting of growth factors onto aligned sub-micron fibrous scaffolds for simultaneous control of cell differentiation and alignment. *Biomaterials*, 32(32): 8097–8107.
48. Elkhoury K, Chen M, Koçak P, *et al.*, 2022, Hybrid extracellular vesicles-liposome incorporated advanced bioink to deliver microRNA. *Biofabrication*, 14(4).

    https://doi.org/10.1088/1758-5090/ac8621.
49. Abaci A, Guvendiren M, 2020, Designing decellularized extracellular matrix-based bioinks for 3D bioprinting. *Adv Healthc Mater*, 9(24): e2000734.
50. Choudhury D, Tun HW, Wang T, *et al.*, 2018, Organ-derived decellularized extracellular matrix: A game changer for bioink manufacturing? *Trends Biotechnol*, 36(8): 787–805.
51. Chen J, Zhou D, Nie Z, *et al.*, 2021, A scalable coaxial bioprinting technology for mesenchymal stem cell microfiber fabrication and high extracellular vesicle yield. *Biofabrication*, 14(1).
52. Wu J, Piao Y, Liu Q, *et al.*, 2021, Platelet-rich plasma-derived extracellular vesicles: A superior alternative in regenerative medicine? *Cell Prolif*, 54(12): e13123.

    https://doi.org/10.1111/cpr.13123. Epub 2021 Oct 5. PMID: 34609779; PMCID: PMC8666280.
53. Cui H, Zhu W, Holmes B, *et al.*, 2016, Biologically inspired smart release system based on 3D bioprinted perfused scaffold for vascularized tissue regeneration. *Adv Sci (Weinh)*, 3(8): 1600058.

    https://doi.org/10.1002/advs.201600058. PMID: 27818910; PMCID: PMC5074245.
54. Zhao W, Chen H, Zhang Y, *et al.*, 2022, Adaptive multi-degree-of-freedom in situ bioprinting robot for hair-follicle-inclusive skin repair: A preliminary study conducted in mice. *Bioeng Transl Med*, 7(3): e10303.
55. Jorgensen AM, Varkey M, Gorkun A, *et al.*, 2020, Bioprinted skin recapitulates normal collagen remodeling in full-thickness wounds. *Tissue Eng Part A,* 26(9–10): 512–526.

    https://doi.org/10.1089/ten.TEA.2019.0319. Epub 2020 Jan 28. PMID: 31861970; PMCID: PMC7249461.
56. Maver T, Mohan T, Gradišnik L, *et al.*, 2019, Polysaccharide thin solid films for analgesic drug delivery and growth of human skin cells. *Front Chem*, 7: 217.
57. Jahanshahi M, Hamdi D, Godau B, *et al.*, 2020, An engineered infected epidermis model for in vitro study of the skin's pro-inflammatory response. *Micromachines (Basel)*, 11(2): 227.
58. Cui C, Kim DO, Pack MY, *et al.*, 2020, 4D printing of self-folding and cell-encapsulating 3D microstructures as scaffolds for tissue-engineering applications. *Biofabrication*, 12(4): 045018.
59. Spoerk M, Arbeiter F, Raguž I, *et al.*, 2019, Mechanical recyclability of polypropylene composites produced by material extrusion-based additive manufacturing. *Polymers (Basel)*, 11(8): 1318.
60. Xu HQ, Liu JC, Zhang ZY, *et al.*, 2022, A review on cell damage, viability, and functionality during 3D bioprinting. *Mil Med Res*, 9(1): 70.

61. Guillemot F, Mironov V, Nakamura M, 2010, Bioprinting is coming of age: Report from the International Conference on Bioprinting and Biofabrication in Bordeaux (3B'09). *Biofabrication*, 2(1): 010201.

62. Mu R, Campos de Souza S, Liao Z, *et al.*, 2022, Reprograming the immune niche for skin tissue regeneration - From cellular mechanisms to biomaterials applications. *Adv Drug Deliv Rev*, 185(2022): 114298.

63. Las Heras K, Igartua M, Santos-Vizcaino E, *et al.*, 2020, Chronic wounds: Current status, available strategies and emerging therapeutic solutions. *J Control Release*, 328(2020): 532–550.

64. Kolimi P, Narala S, Nyavanandi D, *et al.*, 2022, Innovative treatment strategies to accelerate wound healing: Trajectory and recent advancements. *Cells*, 11(15): 2439.

65. Martin P, Nunan R, 2015, Cellular and molecular mechanisms of repair in acute and chronic wound healing. *Br J Dermatol*, 173(2): 370–378.

66. Felgueiras HP, 2023, Emerging antimicrobial and immunomodulatory fiber-based scaffolding systems for treating diabetic foot ulcers. *Pharmaceutics*, 15(1): 258.

67. Eming SA, Martin P, Tomic-Canic M, 2014, Wound repair and regeneration: mechanisms, signaling, and translation. *Sci Transl Med*, 6(265): 265sr6.

68. Gravel SP, Ben Khalifa Y, McGuirk S, *et al.*, 2023, PGC-1s shape epidermal physiology by modulating keratinocyte proliferation and terminal differentiation. *iScience*, 26(4): 106314.

69. Chouhan D, Dey N, Bhardwaj N, *et al.*, 2019, Emerging and innovative approaches for wound healing and skin regeneration: Current status and advances. *Biomaterials,* 216(2019): 119267.

70. Huang F, Lu X, Yang Y, *et al.*, 2023, Microenvironment-based diabetic foot ulcer nanomedicine. *Adv Sci (Weinh)*, 10(2): e2203308.

71. Theocharidis G, Baltzis D, Roustit M, *et al.*, 2020, Integrated skin transcriptomics and serum multiplex assays reveal novel mechanisms of wound healing in diabetic foot ulcers. *Diabetes*, 69(10): 2157–2169.

72. Aitcheson SM, Frentiu FD, Hurn SE, *et al.*, 2021, Skin wound healing: Normal macrophage function and macrophage dysfunction in diabetic wounds. *Molecules*, 26(16): 4917.

73. Zhang J, Yang P, Liu D, *et al.*, 2021, Inhibiting hyper-O-GlcNAcylation of c-Myc accelerate diabetic wound healing by alleviating keratinocyte dysfunction. *Burns Trauma*, 9(2021): tkab031.

74. Qi W, Yang C, Dai Z, *et al.*, 2015, High levels of pigment epithelium-derived factor in diabetes impair wound healing through suppression of Wnt signaling. *Diabetes*, 64(4): 1407–1419.

75. Su D, Tsai HI, Xu Z, *et al.*, 2019, Exosomal PD-L1 functions as an immunosuppressant to promote wound healing. *J Extracell Vesicles*, 9(1): 1709262.

76. Sinha S, Sparks HD, Labit E, *et al.*, 2022, Fibroblast inflammatory priming determines regenerative versus fibrotic skin repair in reindeer. *Cell*, 185(25): 4717–4736.e25.

77. Pichu S, Vimalraj S, Sathiyamoorthy J, *et al.*, 2018, Association of hypoxia inducible factor-1 alpha exon 12 mutation in diabetic patients with and without diabetic foot ulcer. *Int J Biol Macromol*, 119(2018): 833–837.

78. Dhamodharan U, Karan A, Sireesh D, *et al.*, 2019, Tissue-specific role of Nrf2 in the treatment of diabetic foot ulcers during hyperbaric oxygen therapy. *Free Radic Biol Med*, 138(2019): 53–62.

79. Theocharidis G, Thomas BE, Sarkar D, *et al.*, 2022, Single cell transcriptomic landscape of diabetic foot ulcers. *Nat Commun*, 13(1): 181.

80. Chen J, Qin S, Liu S, *et al.*, 2023, Targeting matrix metalloproteases in diabetic wound healing. *Front Immunol*, 14(2023): 1089001.

81. Lobmann R, Ambrosch A, Schultz G, *et al.*, 2002, Expression of matrix-metalloproteinases and their inhibitors in the wounds of diabetic and non-diabetic patients. *Diabetologia*, 45(7): 1011–1016.

82. Li N, Zhan A, Jiang Y, *et al.*, 2022, A novel matrix metalloproteinases-cleavable hydrogel loading deferoxamine accelerates diabetic wound healing. *Int J Biol Macromol*, 222(Pt A): 1551–1559.

83. Yu FX, Lee PSY, Yang L, *et al.*, 2022, The impact of sensory neuropathy and inflammation on epithelial wound healing in diabetic corneas. *Prog Retin Eye Res*, 89(2022): 101039.

84. Srivastava P, Sondak T, Sivashanmugam K, *et al.*, 2022, A review of immunomodulatory reprogramming by probiotics in combating chronic and acute diabetic foot ulcers (DFUs). *Pharmaceutics*, 14(11): 2436.

85. Xiao Y, Zhao H, Ma X, *et al.*, 2022, Hydrogel dressing containing basic fibroblast growth factor accelerating chronic wound healing in aged mouse model. *Molecules*, 27(19): 6361.

86. Huang X, Liang P, Jiang B, *et al.*, 2020, Hyperbaric oxygen potentiates diabetic wound healing by promoting fibroblast cell proliferation and endothelial cell angiogenesis. *Life Sci*, 259(2020): 118246.

87. Sharma R, Sharma SK, Mudgal SK, *et al.*, 2021, Efficacy of hyperbaric oxygen therapy for diabetic foot ulcer, a systematic review and meta-analysis of controlled clinical trials. *Sci Rep*, 11(1): 2189.

88. Guo JL, Longaker MT, 2022, Bioprinted hydrogels for fibrosis and wound healing: Treatment and modeling. *Gels*, 9(1): 19.

89. Nessbach P, Schwarz S, Becke TD, *et al.*, 2022, Angiogenic potential of co-cultured human umbilical vein endothelial cells and adipose stromal cells in customizable 3D engineered collagen sheets. *J Funct Biomater*, 13(3): 107.

90. Li Y, Xu T, Tu Z, *et al.*, 2020, Bioactive antibacterial silica-based nanocomposites hydrogel scaffolds with high angiogenesis for promoting diabetic wound healing and skin repair. *Theranostics*, 10(11): 4929–4943.

91. Prasad YS, Miryala S, Lalitha K, *et al.*, 2020, An injectable self-healing anesthetic glycolipid-based oleogel with antibiofilm and diabetic wound skin repair properties. *Sci Rep,* 10(1): 18017.

92. Xia S, Weng T, Jin R, *et al.*, 2022, Curcumin-incorporated 3D bioprinting gelatin methacryloyl hydrogel reduces reactive oxygen species-induced adipose-derived stem cell apoptosis and improves implanting survival in diabetic wounds. *Burns Trauma*, 10(2022): tkac001.

93. Ullah F, Javed F, Mushtaq I, *et al.*, 2023, Development of highly-reproducible hydrogel based bioink for regeneration of skin-tissues via 3-D bioprinting technology. *Int J Biol Macromol*, 230: 123131.

94. Ma J, Qin C, Wu J, *et al.*, 2021, 3D printing of strontium silicate microcylinder-containing multicellular biomaterial inks for vascularized skin regeneration. *Adv Healthc Mater*, 10(16): e2100523.

95. Wang X, Yang C, Yu Y, *et al.*, 2022, In situ 3D bioprinting living photosynthetic scaffolds for autotrophic wound healing. *Research (Wash D C)*, 2022(2022): 9794745.

96. Guan G, Qizhuang Lv, Liu S, *et al.*, 2021, 3D-bioprinted peptide coupling patches for wound healing. *Mater Today Bio,* 13(2021): 100188.

97. Liao W, Duan X, Xie F, *et al.*, 2023, 3D-bioprinted double-crosslinked angiogenic alginate/chondroitin sulfate patch for diabetic wound healing. *Int J Biol Macromol*, 236(2023): 123952.

98. Jo Y, Hwang DG, Kim M, *et al.*, 2023, Bioprinting-assisted tissue assembly to generate organ substitutes at scale. *Trends Biotechnol*, 41(1): 93–105.

99. Albanna M, Binder KW, Murphy SV, *et al.*, In situ bioprinting of autologous skin cells accelerates wound healing of extensive excisional full-thickness wounds. *Sci Rep*, 9(1): 1856.

100. Wu Y, Fortunato GM, Okesola BO, *et al.*, 2021, An interfacial self-assembling bioink for the manufacturing of capillary-like structures with tuneable and anisotropic permeability. *Biofabrication*, 13(3).

101. Jia W, Gungor-Ozkerim PS, Zhang YS, *et al.*, 2016, Direct 3D bioprinting of perfusable vascular constructs using a blend bioink. *Biomaterials*, 106(2016): 58–68.

102. Fang Y, Guo Y, Wu B, *et al.*, 2023, Expanding embedded 3D bioprinting capability for engineering complex organs with freeform vascular networks. *Adv Mater*, 35(22): e2205082.

103. Skylar-Scott MA, Uzel SGM, Nam LL, *et al.*, 2019, Biomanufacturing of organ-specific tissues with high cellular density and embedded vascular channels. *Sci Adv*, 5(9): eaaw2459.

104. Wu SD, Dai NT, Liao CY, *et al.*, 2022, Planar-/curvilinear-bioprinted tri-cell-laden hydrogel for healing irregular chronic wounds. *Adv Healthc Mater*, 11(16): e2201021.

105. Pagan E, Stefanek E, Seyfoori A, *et al.*, 2023, A handheld bioprinter for multi-material printing of complex constructs. *Biofabrication,* 15(3): 035012.

106. Altunbek M, Afghah F, Caliskan OS, *et al.*, 2023, Design and bioprinting for tissue interfaces. *Biofabrication*, 15(2).

107. Monteiro-Soares M, Russell D, Boyko EJ, *et al.*, 2020, Guidelines on the classification of diabetic foot ulcers (IWGDF 2019). *Diabetes Metab Res Rev*, 36(Suppl 1): e3273.

108. Huang SM, Wu CS, Chiu MH, *et al.*, 2019, High glucose environment induces M1 macrophage polarization that impairs keratinocyte migration via TNF-α: An important mechanism to delay the diabetic wound healing. *J Dermatol Sci*, 96(3): 159–167.

109. Tian F, Jiang Y, Liu Y, *et al.*, 2021, Can fractal dimension analysis be used in quantitating collagen structure? *Exp Dermatol*, 30(12): 1825–1828.

110. Xu H, Zhang J, Jiang Y, *et al.*, 2022, Fractal analysis of rat dermal tissue in the different injury states. *Int Wound J*, 19(5): 1016–1022.

111. Pena G, Kuang B, Szpak Z, *et al.*, 2020, Evaluation of a novel three-dimensional wound measurement device for assessment of diabetic foot ulcers. *Adv Wound Care (New Rochelle)*, 9(11): 623–631.

112. Parsa S, Wamsley C, Kim P, *et al.*, 2022, Use of optical coherence tomography (OCT) in assessment of diabetic skin wound characteristics and blood flow. *J Foot Ankle Surg*, 62(3): 407–412.

113. Li C, Chen J, Jie T, *et al.*, 2022, Construction of biomimetic tissues with anisotropic structures via stepwise algorithm-assisted bioprinting. *Small*, 18(46): e2204316.

114. Li C, Chen J, Jie T, *et al.*, 2022, Construction of biomimetic tissues with anisotropic structures via stepwise algorithm-assisted bioprinting. *Small*, 18(46): e2204316.

115. Gholami P, Ahmadi-Pajouh MA, Abolftahi N, *et al.*, 2018, Segmentation and measurement of chronic wounds for bioprinting. *IEEE J Biomed Health Inform*, 22(4): 1269–1277.

116. Zahia S, Garcia-Zapirain B, Elmaghraby A, 2020, Integrating 3D model representation for an accurate non-invasive assessment of pressure injuries with deep learning. *Sensors (Basel),* 20(10): 2933.

117. Zhao R, Tang H, Xu C, *et al.*, 2021, Automatic quantitative analysis of structure parameters in the growth cycle of artificial skin using optical coherence tomography. *J Biomed Opt*, 26(9): 095001.

118. Wang M, Li W, Mille LS, *et al.*, 2022, Digital light processing based bioprinting with composable gradients. *Adv Mater,* 34(1): e2107038.

119. Nuutila K, Samandari M, Endo Y, *et al.*, 2021, In vivo printing of growth factor-eluting adhesive scaffolds improves wound healing. *Bioact Mater*, 8(2021): 296–308.

120. Biranje SS, Sun J, Cheng L, *et al.*, 2022, Development of cellulose nanofibril/casein-based 3D composite hemostasis scaffold for potential wound-healing application. *ACS Appl Mater Interfaces*, 14(3): 3792–3808.

121. Phang SJ, Arumugam B, Kuppusamy UR, *et al.*, 2021, A review of diabetic wound models-Novel insights into diabetic foot ulcer. *J Tissue Eng Regen Med*, 15(12): 1051–1068.

122. Kim BS, Ahn M, Cho WW, *et al.*, 2021, Engineering of diseased human skin equivalent using 3D cell printing for representing pathophysiological hallmarks of type 2 diabetes in vitro. *Biomaterials*, 272(2021): 120776.

123. Lan CC, Wu CS, Huang SM, *et al.*, 2012, High-glucose environment reduces human β-defensin-2 expression in human keratinocytes: Implications for poor diabetic wound healing. *Br J Dermatol*, 166(6): 1221–1229.

124. Intini C, Elviri L, Cabral J, *et al.*, 2018, 3D-printed chitosan-based scaffolds: An in vitro study of human skin cell growth and an in-vivo wound healing evaluation in experimental diabetes in rats. *Carbohydr Polym*, 199(2018): 593–602.

125. Wu M, Zhang Y, Huang H, *et al.*, 2020, Assisted 3D printing of microneedle patches for minimally invasive glucose control in diabetes. *Mater Sci Eng C Mater Biol Appl*, 117(2020): 111299.

126. Economidou SN, Pere CPP, Reid A, *et al.*, 2019, 3D printed microneedle patches using stereolithography (SLA) for intradermal insulin delivery. *Mater Sci Eng C Mater Biol Appl,* 102(2019): 743–755.

127. Kamel R, El-Batanony R, Salama A, 2019, Pioglitazone-loaded three-dimensional composite polymeric scaffolds: A proof of concept study in wounded diabetic rats. *Int J Pharm*, 570(2019): 118667.

128. Chen TY, Wen TK, Dai NT, *et al.*, 2021, Cryogel/hydrogel biomaterials and acupuncture combined to promote diabetic skin wound healing through immunomodulation. *Biomaterials*, 269(2021): 120608.

129. Crews RT, Candela J, 2018, Decreasing an offloading device's size and offsetting its imposed limb-length discrepancy lead to improved comfort and gait. *Diabetes Care*, 41(7): 1400–1405.

130. Potier L, François M, Dardari D, *et al.*, 2020, Comparison of a new versus standard removable offloading device in patients with neuropathic diabetic foot ulcers: A French national, multicentre, open-label randomized, controlled trial. *BMJ Open Diabetes Res Care*, 8(1): e000954.

131. Zhang X, Wang H, Du C, *et al.*, 2022, Custom-molded offloading footwear effectively prevents recurrence and amputation, and lowers mortality rates in high-risk diabetic foot patients: A multicenter, prospective observational study. *Diabetes Metab Syndr Obes*, 15(2022): 103–109.

132. Zhao Y, Zhong J, Wang Y, *et al.*, 2023, Photocurable and elastic polyurethane based on polyether glycol with adjustable hardness for 3D printing customized flatfoot orthosis. *Biomater Sci*, 11(5): 1692–1703.

133. Choi H, Seo A, Lee J, 2019, Mallet finger lattice casts using 3D printing. *J Healthc Eng*, 2019(2019): 4765043.

134. Gelain F, Luo Z, Zhang S, 2020, Self-assembling peptide EAK16 and RADA16 nanofiber scaffold hydrogel. *Chem Rev*, 120(24): 13434–13460.

135. Cao W, Peng S, Yao Y, *et al.*, 2022, A nanofibrous membrane loaded with doxycycline and printed with conductive hydrogel strips promotes diabetic wound healing in vivo. *Acta Biomater*, 152(2022): 60–73.

136. Manso GMDC, Elias-Oliveira J, Guimarães JB, *et al.*, 2023, Xenogeneic mesenchymal stem cell biocurative improves skin wounds healing in diabetic mice by increasing mast cells and the regenerative profile. *Regen Ther*, 22(2023): 79–89.

137. Dong Y, Rodrigues M, Kwon SH, *et al.*, 2018, Acceleration of diabetic wound regeneration using an in situ-formed stem-cell-based skin substitute. *Adv Healthc Mater*, 7(17): e1800432.

138. Yastı AÇ, Akgun AE, Surel AA, *et al.*, 2023, Graft of 3D bioprinted autologous minimally manipulated homologous adipose tissue for the treatment of diabetic foot ulcer. *Wounds*, 35(1): E22–E28.

139. Bajuri MY, Kim J, Yu Y, *et al.*, 2023, New paradigm in diabetic foot ulcer grafting techniques using 3D-bioprinted autologous minimally manipulated homologous adipose tissue (3D-AMHAT) with fibrin gel acting as a biodegradable scaffold. *Gels*, 9(1): 66.

140. Kesavan R, Sheela Sasikumar C, Narayanamurthy VB, *et al.*, 2021, Management of diabetic foot ulcer with MA-ECM (minimally manipulated autologous extracellular matrix) using 3D bioprinting technology - An innovative approach. *Int J Low Extrem Wounds*, 0 (0): 15347346211045625. doi:10.1177/15347346211045625

141. Armstrong DG, Harris SG, Rasor Z, *et al.*, 2022, Autologous minimally manipulated homologous adipose tissue (AMHAT) for treatment of nonhealing diabetic foot ulcers. *Plast Reconstr Surg Glob Open*, 10(10): e4588.

142. Bernal PN, Bouwmeester M, Madrid-Wolff J, *et al.*, 2022, Volumetric bioprinting of organoids and optically tuned hydrogels to build liver-like metabolic biofactories. *Adv Mater*, 34(15): e2110054.

143. Zhao M, Wang J, Zhang J, *et al.*, 2022, Functionalizing multi-component bioink with platelet-rich plasma for customized in-situ bilayer bioprinting for wound healing. *Mater Today Bio,* 16(2023): 100334.

144. Huang Q, Wu T, Guo Y, *et al.*, 2023, Platelet-rich plasma-loaded bioactive chitosan@sodium alginate@gelatin shell-core fibrous hydrogels with enhanced sustained release of growth factors for diabetic foot ulcer healing. *Int J Biol Macromol*, 234(2023): 123722.

ACCSCIENCE PUBLISHING

International Journal of Bioprinting

REVIEW ARTICLE

Recent progress on 3D-printed gelatin methacrylate-based biomaterials for articular cartilage repair

Liang Chen[1,3†], Guowei Huang[1†], Ming Yu[1†], Yang Liu[1], Tao Cheng[1], Aiguo Li[1*], Wen Wang[1*], and Shengnan Qin[1,2*]

[1]Department of Orthopedics, Guangzhou Institute of Traumatic Surgery, Guangzhou Red Cross Hospital, Medical College, Jinan University, Guangzhou, China

[2]School of Biomedical Science, The University of Western Australia, Perth, Australia

[3]The second hospital of Tangshan, Tangshan, China

Abstract

The structure and composition of articular cartilage is complex, and its self-healing ability is limited, and thus, it is difficult to achieve ideal healing once the articular cartilage is damaged. Recently, three-dimensional (3D) printing technology has provided a new possibility for the repair of articular cartilage. Engineered cartilage tissues can be fabricated by superimposing customized inks, considering different geometric structures and components of tissues. 3D printing can be effectively used to manufacture high-precision structures with complex geometry, solving the shortcomings of traditional scaffold fabrication techniques. Gelatin methacrylate (GelMA) is modified gelatin and is currently a widely used 3D printing ink due to its photocrosslinking properties. With good biocompatibility and tunable physical properties, it can provide a good scaffold platform for cell proliferation and growth factor release. Given that the role of 3D printing technology in cartilage repair has been widely reported, this article reviews the research progress of 3D-printed GelMA-based biomaterials in articular cartilage tissue engineering. We focus primarily on how 3D printing technology addresses the existing challenges inherent to the field of articular cartilage tissue engineering. We accentuate the modifications implemented in GelMA-based 3D printing scaffolds to optimize articular cartilage regeneration. Additionally, we provide a comprehensive summary of the utilization of GelMA-based biomaterials incorporating various cells, growth factors, or other tissue components and highlight how these adaptations, in conjunction with the benefits of 3D printing technology, facilitate improvements the articular cartilage repair.

Keywords: 3D printing; Gelatin methacrylate; Articular cartilage; Tissue engineering

1. Introduction

The avascular and nerveless nature of articular cartilage results in its limited self-repair ability, presenting a challenge for clinical treatments of cartilage injuries, such as autologous chondrocyte implantation (ACI) or autologous osteochondral column transplantation (AOCT). One of the major difficulties in repairing articular cartilage

†These authors contributed equally to this work.

***Corresponding authors:**
Shengnan Qin (iris.qin@research.uwa.edu.au)

Aiguo Li (Liaiguo7161@ext.jnu.edu.cn)

Wen Wang (warrenwangrch@outlook.com)

Citation: Chen L, Huang G, Yu M, *et al*., 2023, Recent progress on 3D-printed gelatin methacrylate-based biomaterials for articular cartilage repair. *Int J Bioprint*, 9(6): 0116. https://doi.org/10.36922/ijb.0116

Received: April 5, 2023
Accepted: June 19, 2023
Published Online: August 1, 2023

Copyright: © 2023 Author(s). This is an Open Access article distributed under the terms of the Creative Commons Attribution License, permitting distribution, and reproduction in any medium, provided the original work is properly cited.

Publisher's Note: AccScience Publishing remains neutral with regard to jurisdictional claims in published maps and institutional affiliations.

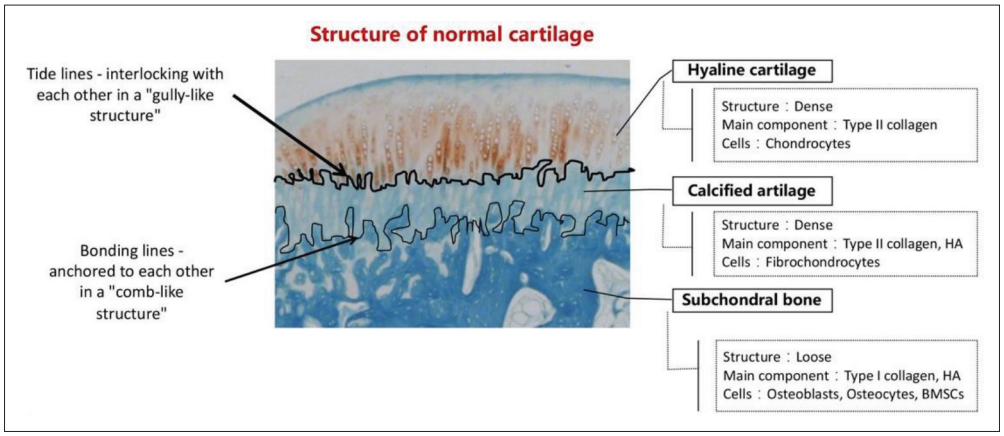

Figure 1. Multi-layer structure and main components of articular cartilage. Abbreviations: BMSCs, bone marrow-derived mesenchymal stem cells; HA, hyaluronic acid.

defects is its intricate structure and composition. Three-dimensional (3D) printing technology provides new opportunities for constructing engineered tissues, particularly multi-layer tissues with complex geometries and components, such as articular cartilage. 3D printing is a process that involves layer-by-layer deposition of inks based on computer-aided design (CAD) models, resulting in the creation of a 3D scaffolds[1].

Due to the tremendous advantages of the 3D printing technique in tissue engineering, many biomaterials showed their potentials in this field. Among them, hydrogels are one of the most widely used biomaterials in 3D printing as they provide a versatile platform to include desired combinations of properties for biomedical applications. Gelatin methacrylate (GelMA) is a hydrogel derived from gelatin, which has been widely used in traditional scaffold fabrication techniques due to its good biocompatibility and tunable physical properties. Methacrylic anhydride is incorporated into the gelatin, enabling rapid solidification of gelatin by photocrosslinking. With the rapid development of 3D printing technology in articular cartilage tissue engineering, GelMA as one of the printing inks has also attracted a lot of attention[2-4].

Following the first study reporting its use in 3D printing, GelMA hydrogels have been extensively studied for their synthesis, characterization, and various applications, including, but not limited to, tissue engineering, as well as drug and gene delivery. The attributes and applications of GelMA in 3D printing field have been well-documented in various reviews[5,6]. However, studies focused specifically on the 3D-printed GelMA-based biomaterials in the articular cartilage field have not been thoroughly reviewed yet. In this review, we mainly focused on research progresses related to the applications of GelMA-based 3D printing biomaterials in articular cartilage tissue engineering. As articular cartilage is a complex tissue with different structure and complex components, we primarily summarize in this review the challenges in the field of articular cartilage tissue engineering, and based on these challenges, we highlight the advantages of 3D printing technology in this field. We also introduce the modification of GelMA hydrogels based on the characteristics of articular cartilage. Additionally, we introduce the application of GelMA-based biomaterials incorporated with various elements, such as cells, growth factors, or other tissue components, in the field of articular cartilage tissue engineering, and highlight how these integrated components can significantly enhance the potential for improving articular cartilage regeneration.

2. Challenges in the field of articular cartilage tissue engineering and advantages of 3D printing technology in this field

Articular cartilage tissue engineering has been studied for several decades. Despite this, challenges persist, largely attributed to the multi-layered structure and complex components of articular cartilage tissue as well as the specific loading-bearing functions it performs within the joint.

Generally, the repair of articular cartilage defects involves the regeneration of not only the hyaline cartilage layer but also the calcified cartilage and subchondral bone layers, each with distinct structures and components (Figure 1). Of particular significance is the calcified cartilage layer, which is closely connected with the hyaline cartilage layer through the wavy tide line structure on its upper interface, and is closely connected with the hyaline cartilage layer through the uneven comb-like bonding line structure on its lower interface situated between the hyaline cartilage and subchondral bone layers. The undulating

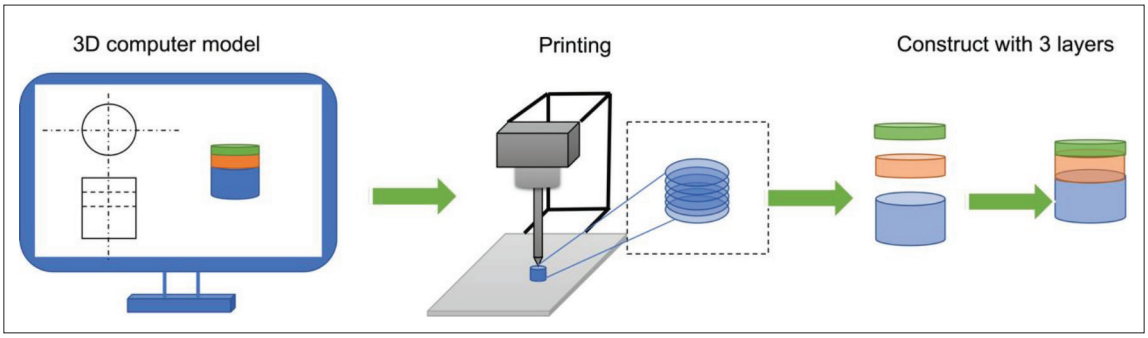

Figure 2. Process of constructing a scaffold with three layers using 3D printing technology.

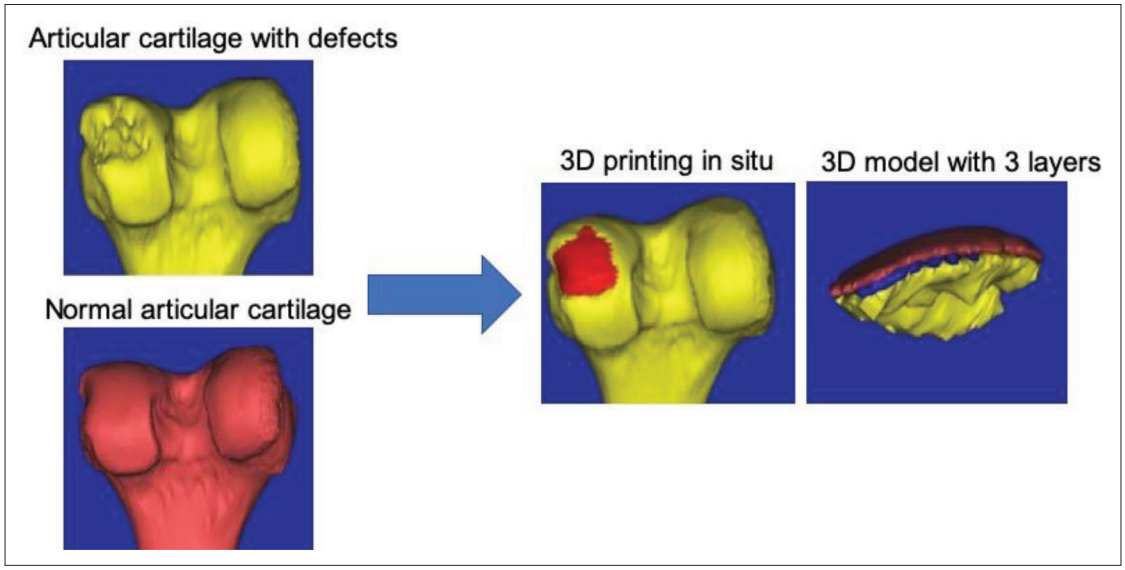

Figure 3. Construction of 3D computer model for articular cartilage defects.

wave-like interface structure of the calcified cartilage layer allows for tight connection with the hyaline cartilage, while the rough, serrated interface structure anchors it to the subchondral bone. This unique interface connection increases both the contact area and the connection strength between articular cartilage interfaces. The subchondral bone is anchored to each other; this special interface connection method increases the connection area between the articular cartilage interface and also increases the connection strength. In light of this, it is almost impossible to reconstruct this structure through traditional scaffold fabrication techniques, but 3D printing technique appears to be a possible and easy method for reconstructing this structure. In addition, reconstructing the structures and mimicking the components in different layers of the articular cartilage, which is a big challenge for traditional scaffold fabrication techniques, can ensure the function recovery.

3D printing technology provides a viable solution to fabricating multi-layer tissues with complex geometries and components, especially the method of extrusion-based printing that can print complex, high-precision biological tissue, which is a good candidate to be used for cartilage tissue engineering[4,7,8]. With computer assistance, the structures and components can be customized and printed easily with the aid of different nozzles (Figure 2). Meanwhile, the construction of the interface structure of complex tissues also utilizes the advantages of 3D printing technology. A computer 3D joint model with complex structure can be constructed (Figure 3), and then different layers can be printed without extra bonding or splicing required in traditional scaffold fabrication techniques. Thus, compared to traditional scaffold fabrication technique, 3D printing offers a rather easy method to reconstruct this structure.

Anatomically, the different layers of articular cartilage are heterogeneous. 3D printing technology, rapid prototyping, and an effective personalized manufacturing method of scaffolds can be constructed by superimposing customized biological inks according to different patients.

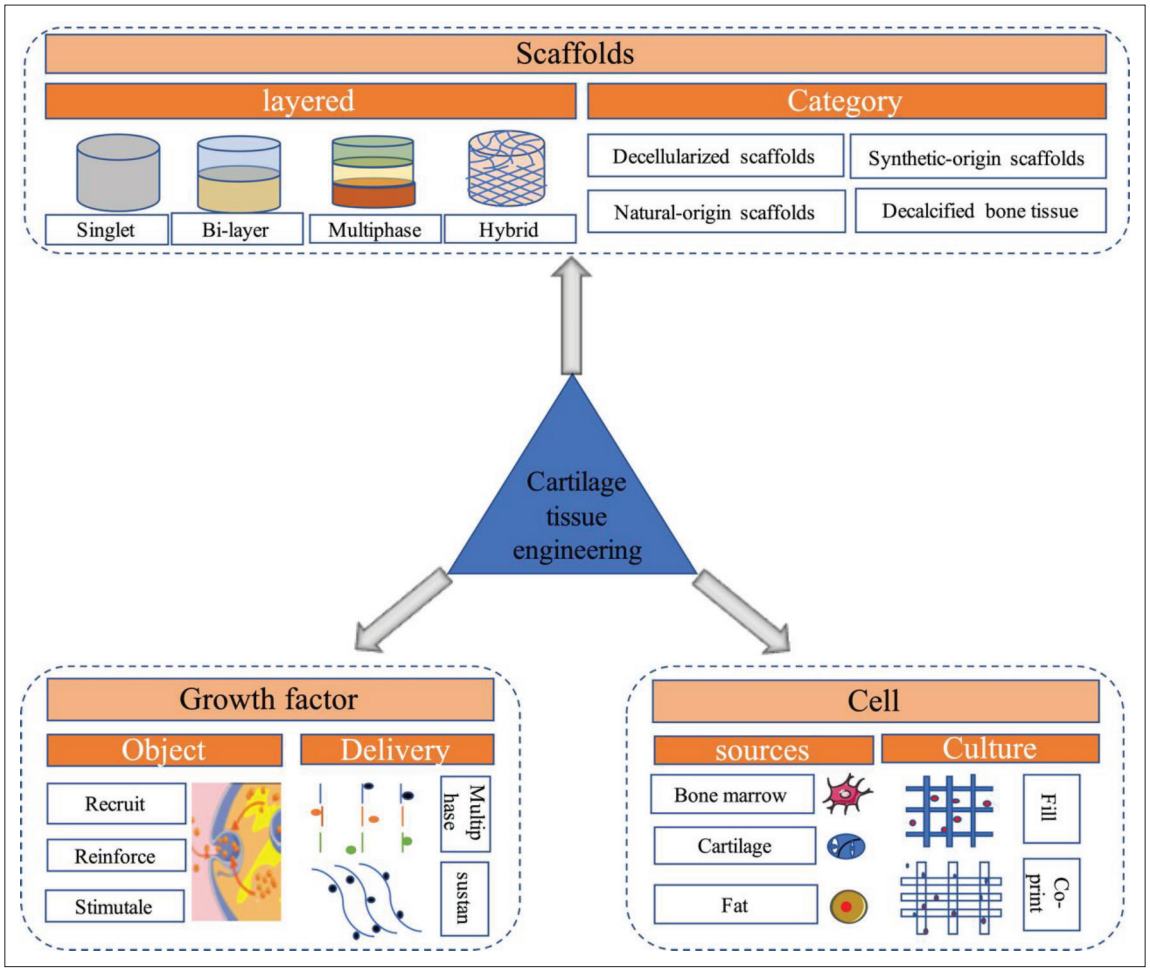

Figure 4. Schematic diagram of scaffolds, growth factors, and cells as biomimetic components of articular cartilage regeneration.

This is one of the biggest advantages of 3D printing technology over other technologies in articular cartilage reconstruction. In addition, with the aid of the 3D printing technique, a variety of biomaterials, growth factors, and cells can be added into inks, and the printed engineered cartilage with more accurate geometric structures and more similar components can attain *in situ* tissue regeneration (Figure 4). This makes personalized printing a reality according to situations of different patients.

3. Advantages of GelMA as an ink in the cartilage tissue engineering

Gelatin is the hydrolysis product of collagen but with better solubility and less antigenicity[9]. Similar to collagen, gelatin contains a variety of the arginine-glycine-aspartic acid (Arg-Gly-Asp, RGD) sequences that are beneficial to adhesion as well as the target sequences of matrix metalloproteinases (MMP) that promote cell remodeling[10]. Due to the introduction of the methacryloyl groups, GelMA is endowed with the property of photocrosslinking, which comes into effect under ultraviolet (UV) light with a photoinitiator[3,11]. This allows for the precise control over the mechanical properties and structure of GelMA hydrogels. The methacrylation process involves the reactions of methacrylic anhydride with the primary amino acids present in the side chain of specific amino acids. It is worth mentioning that most of the functional RGD motifs of gelatin will not be noticeably affected after the modification of methacrylate, thereby retaining cell adhesive properties of gelatin[1,10,12] (Figure 5). This enables the GelMA hydrogels to possess unique patterns, providing better platforms to guide cellular behavior via cell–biomaterial and tissue–biomaterial interactions[1,13]. Furthermore, the MMP-sensitive motifs in GelMA are also not influenced as the GelMA hydrogels could be degraded by MMP-1 and MMP-8[12]. As such, GelMA hydrogel could be easily printed without affecting the original properties, such as good adhesion and controlled degradation of gelatin.

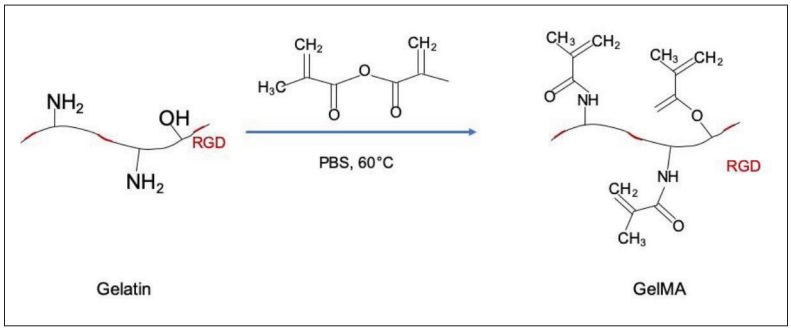

Figure 5. Synthesis process of GelMA.

4. Modification of GelMA in cartilage tissue engineering

The preparation of GelMA can be affected by many parameters, such as gelatin source, reaction condition (e.g., pH), methacrylate group donor, and so on. Therefore, the reaction can be controlled to adjust these parameters. The adjustable physical and chemical properties of GelMA are great advantages of GelMA that make it suitable for articular cartilage tissue engineering[14].

On the one hand, articular cartilage is a load-bearing tissue which plays a pivotal role in maintaining joint health and stability. The restoration of its mechanical properties following injury remains a significant challenge. To achieve optimal recovery of function of joints, modifications of biomaterials to bestow them with enhanced mechanical strength are essential. Evaluating the efficacy of cartilage repair necessitates the assessment of mechanical strength, which serves as a crucial parameter. However, employing pure GelMA hydrogels for cartilage regeneration proves to be inadequate due to their weak mechanical properties and brittleness, which restrict their overall utility. Therefore, modification of GelMA hydrogels can optimize the hydrogel properties, leading to improved outcomes of articular cartilage regeneration.

On the other hand, fostering seamless integration between GelMA hydrogels and *in situ* tissues is also a challenge for optimal articular cartilage repair. Effective integration of GelMA with the native cartilage tissue can yield several benefits, including enhanced cell adhesion and proliferation as well as cell migration from the surrounding tissues, efficient transmission of mechanical loads, and improved nutrient and waste exchange.

In addition, the physical cues provided by scaffolds can also control multiple aspects of cell behavior, notably differentiation. As articular cartilage tissues comprise different types of cells in different layers, the modifications targeting to regulate cell differentiation lineage are important. This is a vital aspect of successful tissue engineering and regenerative medicine strategies.

In this section, we summarize the related researches on the modifications of GelMA for better articular cartilage repair (Figure 6 and Table 1).

4.1. Mechanical properties

Cartilage in the joint experiences complex mechanical loads *in vivo*, and therefore, it is essential to develop hydrogels with sufficient mechanical strength to withstand these loads and maintain their structural integrity over time. Hydrogels with inadequate mechanical strength may deform, fracture, or collapse under physiological loads, leading to implant failure and the inability to support the growth and differentiation of chondrocytes. Therefore, improving the mechanical strength of hydrogels is crucial for the successful engineering of functional cartilage tissue.

Normally, increasing the concentration of GelMA or extending the UV irradiation time improves the mechanical properties of the hydrogels[15]. However, researchers have also modified GelMA hydrogels to improve their mechanical properties by introducing other materials. These modifications have resulted in enhanced toughness and resilience, controlled degradation rate, continued protein release, and promoted chondrocyte adhesion and proliferation, as well as good cartilage repair abilities *in vitro* and *in vivo*. Gan *et al.*[16] introduced the oligomer of dopamine methacrylate (ODMA) to GelMA hydrogels, resulting in improved toughness and resilience without affecting compatibility or hindering neocartilage regeneration. Lim *et al.*[17] introduced tyrosine (Tyr) groups into GelMA to develop a visible-light responsive bioink. Tyrosine residues can be used to create crosslinks between polymer chains through photocrosslinking. The crosslinked network can enhance the mechanical strength and stability of the hydrogel, and also improve adhesion to the surrounding tissue, thus improving the lateral integration of neocartilage. Wang *et al.*[18] made a 3D-printed biological scaffold with high mechanical

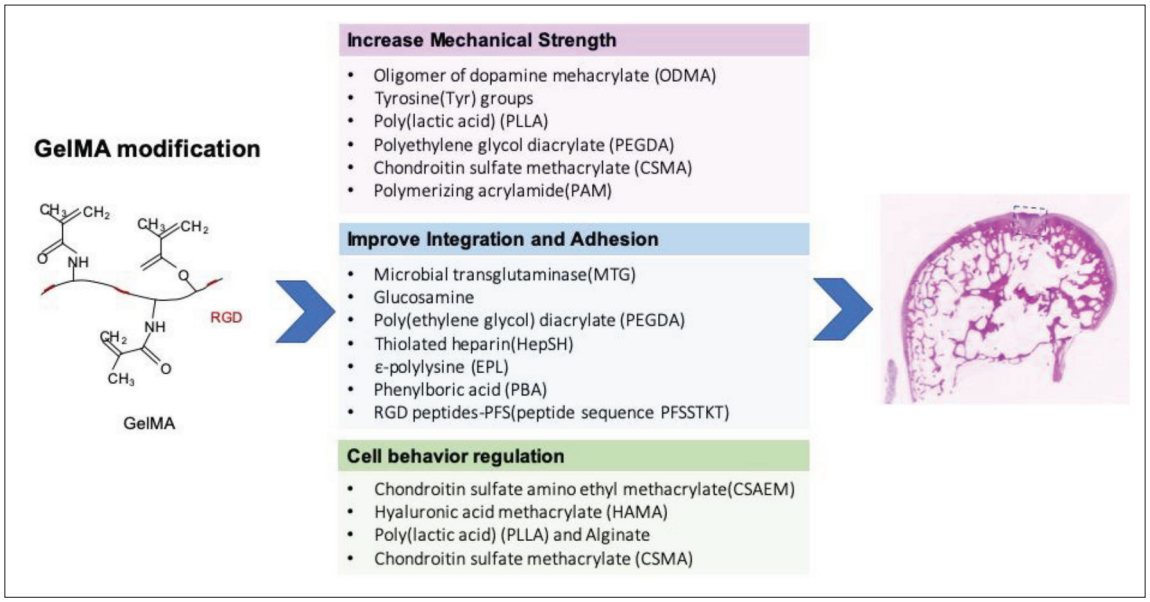

Figure 6. Modification of GelMA through introduction of other materials or groups for better articular cartilage repair.

strength by adding poly(lactic acid) (PLLA) to alginate/GelMA and incorporating PLLA, which improved the printing fidelity and mechanical strengths. This microfiber-reinforced alginate/GelMA scaffold supported bone marrow-derived mesenchymal stem cells (BMSCs) proliferation and chondrogenesis *in vitro*, thereby showing the potential in cartilage tissue engineering applications.

Generally, GelMA contains cell attachment sites, but it does not possess controlled degradation rate like synthetic polymers. These characteristics are regarded as the vital parameters for developing "smart" scaffold that has cell attachment sites and allows controlled drug release. Recently, it is a vital parameter to develop "smart" scaffold that can allow cell attach and possess controlled drug release. Many materials were added to control the degradation rate of GelMA hydrogels. Guan *et al.*[19] incorporated polyethylene glycol diacrylate (PEGDA) and chondroitin sulfate methacrylate (CSMA) into GelMA hydrogels, and this PEGDA-GelMA-CSMA scaffold possessed suitable compressive elastic modulus and degradation rate. In addition, the differentiation lineage toward chondrocytes or osteocytes could be controlled by adjusting the percentage of CSMA, suggesting that it could be used in bone and cartilage repair. Han *et al.*[20] developed a GelMA-based biohybrid hydrogel by incorporating polymerizing acrylamide (PAM). One advantage of PAM is the controlled mechanical property. The GelMA/PAM hydrogels demonstrated a controlled degradation rate and continued protein release without affecting the cell behavior *in vitro*. Additionally, these biomixed hydrogels showed promising cartilage repair abilities *in vivo*.

These modified hydrogels significantly enhanced the performance and broadened the application of GelMA-based hydrogels as the mechanical properties of GelMA-based biomaterials directly impact the performance and functionality of the resulting engineered cartilage.

4.2. Integration and adhesion

GelMA hydrogels have shown potential for generating hyaline cartilage when combined with stem cells, but seamlessly integrating the newly formed cartilage with the local tissue is challenging. Therefore, it is crucial to modify the integration and adhesion of GelMA hydrogels with *in situ* tissues for their effective use in cartilage tissue engineering.

To enhance the adhesion and integration of GelMA hydrogels with *in situ* cartilage, researchers have explored various approaches by introducing different components. Trengove *et al.*[21] used microbial transglutaminase (MTG) to improve the integration of GelMA scaffolds with surrounding tissue. When MTG is applied to a biomaterial, it catalyzes the formation of covalent bonds between amino acid residues in the biomaterial and the surrounding host tissue, resulting in a stronger and more stable interface between biomaterial and host tissue. Suo *et al.*[22,23] grafted gelatin and glucosamine molecules onto acrylate groups to form GelMA/acryloyl glucosamine (AGA) hydrogels in order to improve adhesion and cartilage repair. Glucosamine is a naturally occurring amino sugar and a key component of the extracellular matrix (ECM) of cartilage, and it normally cannot improve the adhesion between biomaterials and host

tissues directly, but it may improve tissue integration by promoting the synthesis and deposition of ECM components, such as glycosaminoglycans and collagen. Zhan[24] fabricated the PEGDA into GelMA hydrogels and obtained hydrogels with different ligand adhesion densities and stiffness properties. PEGDA is a hydrophilic polymer that attracts water molecules and forms a hydrated layer on its surface. This hydrated layer can help to promote cell adhesion by mimicking the ECM of living tissues. Brown *et al.*[25] incorporated thiolated heparin (HepSH) into GelMA hydrogel containing chondrocytes. HepSH is able to bind to various biomolecules and surfaces, allowing it for easy conjugation to other biomaterials, creating a stable and biologically active material. Introducing HepSH promoted cell differentiation and cartilage matrix deposition *in vitro*. Wang *et al.*[26] introduced GelMA with ε-polylysine (EPL) and phenylboronic acid (PBA) to create a modified Gel-EPL/PBA hydrogel. EPL can interact with negatively charged cell surfaces and ECM components, making it a potential material for tissue engineering and drug delivery systems. These GelMA hydrogels modified by EPL and PBA enhanced the growth of chondrocytes and the chondrogenesis of stem cells, as well as promoted the cartilage defects repair. PBA has the ability to bind to sugars and other molecules that contain diols, such as glucose. Overall, the use of these approaches that improve the adhesive properties of GelMA hydrogels significantly enhances cell differentiation and cartilage matrix deposition, and promotes tissue integration, broadening the application of GelMA hydrogels in cartilage tissue engineering.

The RGD peptide family is a unique recognition site for integrin receptors, which play a vital role in cell–cell and cell–extracellular communication. To promote tissue regeneration, researchers have explored using RGD peptides-PFS (peptide sequence PFSSTKT) to create functional GelMA/ECM-PFS hydrogels that enhance the mechanical properties of GelMA, recruit BMSCs, and improve hyaline cartilage repair in rabbits[27].

In summary, improving the integration between GelMA and *in situ* cartilage tissues can substantially bolster the regeneration of neocartilage. Nonetheless, there are no methods identified thus far that could be deemed flawless. This underscores the necessity for the exploration of innovative strategies in future.

4.3. Cell behavior regulation

In addition, the physical properties of GelMA hydrogels have varying effects in maintaining chondrocyte phenotypes, which play a crucial role in cartilage repair. Li *et al.*[28] conducted studies to investigate the effects of GelMA hydrogels on chondrocyte phenotypes. They found that the physical properties of GelMA hydrogels, specifically the stiffness, play an important role in maintaining chondrocyte phenotypes. Additionally, the microporous structure of gelatin hydrogels was found to have varying effects on chondrocytes, with non-microporous gelatin hydrogels being beneficial for maintaining the cartilage phenotype of chondrocytes and microporous GelMA hydrogels being more suitable for chondrocyte proliferation[29]. Hyaluronic acid methacrylate (HAMA) is also an excellent material for cartilage regeneration and is added to GelMA for biomimetic approach. Costantini *et al.*[30] prepared GelMA, GelMA+CS-AEMA (chondroitin sulfate amino ethyl methacrylate), and GelMA+CS-AEMA+HAMA, three kinds of bioinks containing BMSCs. The incorporation of chondroitin sulfate (CS) and HAMA enhanced cell viability and chondrogenesis of BMSCs, showing the potential for advanced engineering of cartilage tissue. Shopperly *et al.*[31] chose HAMA and GelMA as bioinks to mimic the zonal structure of articular cartilage. They discovered that cell-laden constructs supported the growth and secretion of proteoglycans and type II collagen of chondrocytes.

In summary, GelMA with modifications shows promising results for cartilage repair, and thus, they are extensively applied in cartilage tissue engineering.

The incorporation of different materials to GelMA hydrogels showed potential in developing "smart" scaffolds that regulate cell behavior and controlled drug release. Further modifications and improvements to GelMA-based inks are needed to enable the fabrication of 3D constructs with multiple components and organized structures that can better mimic the complex properties of articular cartilage.

5. Application of GelMA-based materials in the 3D printing cartilage tissue engineering

The good biocompatibility and flexible characteristics of GelMA hydrogels make them suitable as scaffolds to explore cell–matrix and cell–cell interactions and serve as 3D supports for soft tissue regeneration. Moreover, the unique properties make the GelMA hydrogels widely used biological inks for 3D printing, allowing for the creation of customized patterns, components, and architectures that can be tailored to specific tissue engineering applications[13].

Articular cartilage defects often involve the regeneration of multiple tissues, including hydroline cartilage, calcified cartilage, and subchondral bone, and this highly organized tissue is specialized for its function. With advancements in 3D printing technology, it is now possible to fabricate tissue constructs that closely resemble target tissues in both structure and composition, which is a significant

Table 1. Modifications of GelMA hydrogels in cartilage tissue engineering

Materials	Modifications	Aims	Properties of modification
GelMA	Increased concentration or ultraviolet (UV) irradiation time	Improve mechanical properties	N/A
GelMA	Introduction of oligomer of dopamine methacrylate (ODMA)	Improve mechanical properties	Good biocompatibility; adhesive property; tunable property; versatility
GelMA	Incorporation of polyacrylamide (PAM)	Improve mechanical properties	Biocompatibility; hydrophilicity; controlled mechanical properties; versatility
GelMA	Incorporation of thiolated heparin (HepSH)	Improve integration and adhesion	Ability to bind to various biomolecules and surfaces; biocompatibility; anticoagulant properties; versatility
GelMA with ε-polylysine (EPL) and phenylboronic acid (PBA)	Modified Gel-EPL/B hydrogel	Improve integration and adhesion	EPL: Interact with negatively charged cell surfaces and ECM; biocompatibility and antimicrobial properties;
			PBA: Binding properties to sugars; biocompatibility; stability; versatility
GelMA	Microbial transglutaminase	Seamless integration	
PEGDA/GelMA	PEGDA	Promote adhesion and improve mechanical properties	Biocompatibility; versatility; hydrophilicity; photopolymerization; biodegradability
GelMA/AGA	Grafted glucosamine molecules onto acrylate groups	Provide an effective approach of GlcN delivery to a target site	Biocompatibility; anti-inflammatory; cartilage-building properties
GelMA	Introduction of tyrosine (Tyr) groups	Improve mechanical properties	Form strong hydrogen bonds
GelMA/ECM-PFS	Introduction of RGD peptides PFS (peptide sequence PFSSTKT)	Improve integration and adhesion	No changes in physical properties
GelMA/PLLA	Poly(lactic acid) (PLLA)	Improve printing fidelity and mechanical strengths	Biocompatibility; biodegradability; mechanical strength; versatility; controlled release
GelMA/PEGDA/CSMA	PEGDA/CSMA	Adjust mechanical strength and guide chondrogenesis of BMSCs	

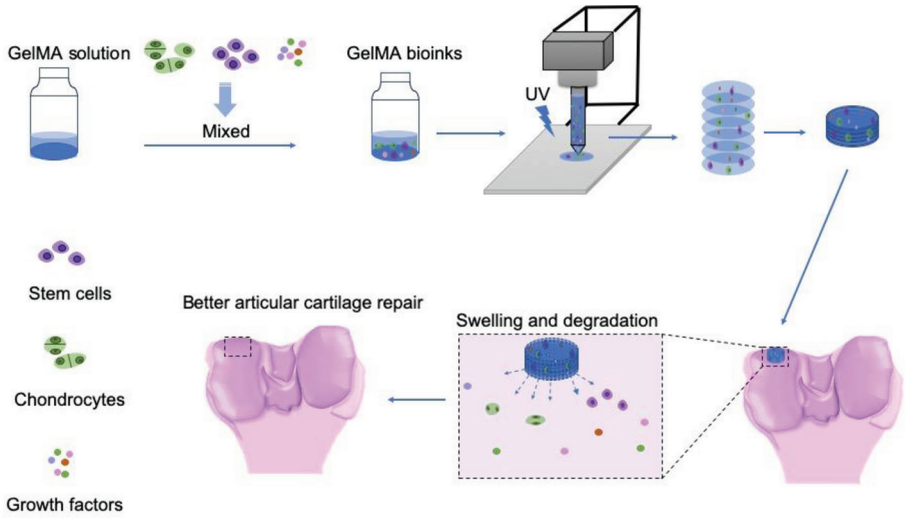

Figure 7. Process of 3D-printed GelMA-based biomaterials delivering cells or growth factors to the injured site of articular cartilage.

Characteristics of GelMA after modifications	In vitro **outcomes**	In vivo **outcomes**
Controlled stiffness and swelling properties	N/A	N/A
Enhanced toughness and resilience; controlled degradation rate; continued protein release	Promoted chondrocyte adhesion and proliferation	Good cartilage repair abilities
Enhanced compression strength and improved elasticity; a favorable degradation rate and sustained protein release	Good cell adhesion and biocompatibility in vitro	Good cartilage repair ability in rabbit knee cartilage defect model
Preserved anticoagulation and growth for signaling capacity; promoted cell viability and chondrocyte phenotype.	Greater cell differentiation and cartilage matrix deposition in vitro	N/A
Improved mechanical properties and better suited for chondrocyte production	Induction of more ECM and improved chondrogenesis	Promoted tissue repair of cartilage defects
A significant increase in adhesive strength	N/A	N/A
Different adhesion ligand densities and stiffness properties	N/A	Improved integration and adhesion with in situ tissues
More than 87.7% of 15% (w/v) GelMA hydrogel was grafted with AGA	Better biocompatibility, larger cell attachment, and higher cell viability	Best integration in in vivo rabbit cartilage repair
Tyramine binding to proteins in native cartilage leads to a 15-fold increment in the adhesive strength of the bioglue compared to pristine GelMA	Neocartilage formation from embedded chondroprogenitor cells is demonstrated in vitro	Improved adhesion to the surrounding tissue, and improved lateral integration of neocartilage
Enhanced mechanical properties; recruitment of BMSCs; improved hyaline cartilage repair in rabbits	GelMA/ECM-PFS could regulate the migration of rabbit BMSCs	Facilitated recruitment and chondrogenesis of BMSCs, and promoted hyaline cartilage repair in rabbit
Fabricated constructs with a compressive stress of ≈150 kPa even after 100 cyclical compression loading (up to 40% of strain)	Support BMSCs proliferation and chondrogenesis	N/A
Possess suitable compressive elastic modulus and degradation rate	Provide a 3D support for BMSCs; the differentiation lineage could be changed by adjusting the percentage of CSMA	N/A

improvement over traditional fabrication techniques. This is achieved by incorporating various cells, growth factors, and other tissue components and utilizing computer technology to closely mimic the complex architectures of the target tissues (Figure 7). Here, we provide a summary of the results and characteristics of 3D-printed GelMA scaffolds loaded with cells, growth factors, or other materials for use in articular cartilage tissue engineering. This information will be valuable for future research and development of GelMA and 3D printing techniques for cartilage repair. By harnessing the potential of 3D printing technology, it may be possible to develop more effective and personalized treatments for articular cartilage defects, ultimately for the application in clinical settings.

5.1. Growth factors

One of the distinguishing characteristics of GelMA-based hydrogels is their ability to degrade in a controlled manner, which makes them good carriers owing to the controlled release of specific growth factors in cartilage defects. Growth factors have the potential to enhance current cartilage repair through various mechanisms, such as recruiting chondrocytes, stimulating their proliferation, and enhancing cartilage matrix formation[32,33]. Among various growth factors, transforming growth factor-β3 (TGF-β3) has been proven to be the most effective in inducing chondrogenesis of stem cells in many studies. To this end, Wang *et al.*[34] constructed a GelMA scaffold functionalized with alginate sulfate, which has a high affinity to TGF-β3. This scaffold enabled sustained release of TGF-β3, supporting robust chondrogenic differentiation of mesenchymal stem cells (MSCs) *in vitro* and in nude mice. Insulin-like growth factor-1 (IGF-1) is a hormone that possesses anti-apoptotic and anti-inflammatory properties, promotes the production of ECM by chondrocytes through paracrine mechanisms,

Table 2. Summary of 3D-printed GELMA scaffolds loaded with growth factors in articular cartilage repair

Scaffolds	**Bioinks**	**Growth factor loaded**	**Role of growth factors**
IL-4-loaded bi-layer scaffolds[44]	GelMA, PCL-HA	IL-4	Anti-inflammation
Cell-laden bioprinted cartilage construct[38]	GelMA, PEGDA, photoinitiator, and TGF-β1-embedded nanospheres	TGF-β1	Induce cells toward chondrogenesis
Alginate-GelMA interpenetrating network (IPN) constructs[39]	Alginate sulfate, GelMA, and TGF-β3	TGF- β3	Induce cells toward chondrogenesis
Microenvironmentally optimized 3D-printed TGF-β-functionalized scaffolds[40]	A 3D printing ink containing D-ECM, GelMA, PLGA, and TGF-β3, and PCL	TGF-β3	Induce cells toward chondrogenesis
3D-printed porous scaffolds of hydrogels modified with TGF-β1-binding peptides[41]	GelMA, hydroxyapatite, and TGF-β1-binding peptide	TGF-β1-binding peptide	Induce the endogenous TGF-β1 recruitment for chondrogenesis
3D-printed PRP-GelMA hydrogels[49]	GelMA and PRP	PRP	Regulate the behaviors of BMSCs and macrophage
3D-printed PRP-GelMA hydrogels[50]	GelMA and PRP	PRP	Regulate the behaviors of cells
Osteochondral construct[51]	PRP, AdMSCs, and ECM mimetic hydrogel, and GelMA	PRP	Regulate the differentiation of AdMSCs toward chondrocytes

and stimulates the proliferation and differentiation of BMSCs into chondrocytes[35,36]. Wu *et al.*[37] loaded IGF-1 bioactive supramolecular nanofibers (IGF-1bsn) into injectable GelMA hydrogel, and this BSN-GelMA hydrogel could accelerate the interstitial integration between the early regenerated cartilage and the surrounding tissues, as well as subsequent cartilage regeneration.

Incorporating growth factors into GelMA hydrogels for 3D printing can create a more optimal microenvironment than traditional fabrication techniques. 3D printing allows for high precision and control over spatial distribution of growth factors. This means that growth factors can be placed exactly where they are needed, creating a more conducive environment for the growth of specific tissue, like articular cartilage. In addition, 3D printing enables simultaneous integration of multiple growth factors within the same scaffold, which is difficult to achieve with traditional fabrication techniques. This can be especially beneficial for creating complex tissues, like articular cartilage, that require different growth factors for different cell types or regions. Meanwhile, GelMA-based biomaterials can help to ensure a more gradual and sustained effect of the growth factors, potentially leading to better outcomes in long-term use (Table 2).

Characteristics of scaffolds	Results	
	In vitro	In vivo
• Multi-layers with different bio-inks and different functions • Upper: GelMA; lower: PCL-HA	• Both layers supported cell adhesion and proliferation • The upper layer relieved the inflammation of chondrocytes induced by IL-1b • The lower layer promoted osteogenesis	• New cartilage and subchondral bone regeneration • Good mechanical strength similar to that of native cartilage
• Fabricated via a core-shell electrospraying technique • Modulus and swelling ratio could be adjusted by the addition of different PEGDA • Sustained release of TGF-β1	• Cells and nanospheres were evenly distributed • Highest cell viability and proliferation on 5%/10% (PEGDA/GelMA) hydrogel • Improved chondrogenic differentiation of encapsulated MSCs.	• None
• Maintained viscosity, shear-thinning and thixotropic properties • High-fidelity bioprinting • Increased stiffness, and maintained resilience and toughness • Sustained release of TGF- β3	• Supported viability and robust chondrogenesis of MSCs	• Supported chondrogenesis *in vivo* • Controlled release of TGF-β3 promoted cartilage-specific ECM deposition
• Microenvironment regulation	• Directed endogenous stem/progenitor cell migration and differentiation	• Improved tissue repair outcomes in the sheep animal model • Guided more organized neotissue formation • Recapitulated the anisotropic structure
• Multi-layers with different components and function • Upper: GelMA, TGF-β1 binding peptide; lower: GelMA, hydroxyapatite	• Induced cartilage and osteogenic differentiation	• Promoted osteochondral repair of rats • Recovered the animal gait behavior
• Fabricated using the digital micro-mirror device (DMD) technique	• Promoted proliferation, migration, and osteogenesis and chondrogenesis of BMSCs by 20% PRP/GelMA • Promoted M2 polarization by 20% PRP/GelMA • Similar biological roles in BMSCs but less osteogenesis by 50% PRP/GelMA	• More cartilage and subchondral bone regeneration • More M2 macrophage infiltration and less M1 macrophage presentation
• Photoactivated PRP-based patient-specific bioink • Had the desired mechanical properties (low degradation rate and high mechanical strength)	• Long-term and constant rate growth factor release • Bioactivity protection of PRP • Satisfactory mechanical characteristics	• Facilitated the proliferation and differentiation of the ATDC5 cells
• Gradual printing of bio-inks • Relatively low degradation rate and high mechanical strength • Tissue-specific biomimetic structure	• Induced glycosaminoglycan and calcium secretion, mineralization, and ECM production • Upregulated bone- and cartilage-unique genes	• None

5.1.1. Transforming growth factor-β

Due to its effectiveness in promoting chondrogenesis, TGF-β is often selected as the primary growth factor to be incorporated into inks for 3D printing in cartilage regeneration. For instance, Zhu *et al.*[38] prepared constructs loaded with TGF-β1 using 3D printing which showed a promising strategy for cartilage regeneration. In their study, TGF-β1 was embedded in nanospheres, allowing for continuous release over a period of 21 days, thereby inducing the chondrogenesis of BMSCs. Wang *et al.*[39] constructed alginate sulfate-functionalized alginate-GelMA interpenetrating network ink loaded with TGF-β3. This bioprinted construct supported chondrogenesis and cartilage-specific ECM deposition by continuously releasing TGF-β3. Yang *et al.*[40] established a refined scaffold by printing a mixed ink including cartilage tissue-specific ECM, GelMA, and TGF-β3-embedded PLGA microspheres and poly(ε-caprolactone) (PCL). The scaffold supported the sustained release of TGF-β3, guiding stem cell migration and differentiation toward chondrocytes, resulting in more organized and structured neocartilage formation. Ding *et al.*[41] constructed bi-layered GelMA scaffolds with bioactive peptides that could adsorb TGF-β1 for cartilage healing, as well as hydroxyapatite for

subchondral regeneration. These scaffolds demonstrated potential therapeutic applications in the treatment of full-thick articular cartilage defects, with implanted scaffolds even leading to the recovery of rat gait behavior.

These bioprinted constructs supported chondrogenesis and cartilage-specific ECM deposition by continuously releasing TGF-β, indicating the potential of ink with TGF-β3 for a "single-stage" or "point-of-care" approach for cartilage healing. Despite that TGF-β plays a vital role in chondrogenesis and cartilage formation and regeneration, it has been observed that increased levels of TGF-β1 are present in the animal models of osteoarthritis[42], and this active form of TGF-β1 could lead to changes in the joint tissue that contribute to the development and progression of osteoarthritis[43]. Furthermore, TGF-β1 can also stimulate the production of pro-inflammatory cytokines and chemokines, which contribute to the inflammatory response observed in osteoarthritis. This further exacerbates the degenerative changes in the joint tissue. Therefore, these disadvantages should be considered in the fabrication of constructs using both 3D printing or traditional techniques.

5.1.2. Anti-inflammatory growth factors

To mitigate the effects of inflammation and facilitate cartilage regeneration in conditions such as osteoarthritis, inks have been supplemented with anti-inflammatory factors. For example, Lin *et al.*[44] developed a bilayer scaffold using GelMA combined with interleukin-4 (IL-4) and PCL, as well as PCL-HA, which successfully demonstrated anti-inflammatory effects. The scaffold's composition was similar to that of native tissue, leading to improved cartilage and subchondral bone formation.

5.1.3. Platelet-rich plasma

Platelet-rich plasma (PRP) is an emergent therapeutic strategy in biomedical applications that has demonstrated positive effects in enhancing cartilage injury healing[45]. PRP is a mixture of growth factors that are essential for tissue healing, such as platelet-derived growth factor, vascular endothelial cell growth factor, TGF-β, fibroblast growth factor, and insulin growth factor[46]. In clinical practice, PRP is used to alleviate pain and inflammation, promote neocartilage formation, and facilitate functional recovery in knee and hip joints[47]. Moreover, PRP has been shown to guide stem cell differentiation toward cartilage and bone in osteochondral defects[48]. PRP has also been incorporated into the GelMA hydrogel. Jiang *et al.*[49] developed PRP-GelMA hydrogels with superior cartilage and subchondral bone repair abilities. These hydrogels not only promoted the migration, osteogenesis, and chondrogenesis of BMSCs but also contributed to the regulation of immune response and M1-to-M2 transition of macrophages. Irmak *et al.*[50] constructed a GelMA/PRP hydrogel with the ideal mechanical strength and sustained release of PRP that benefited the growth and differentiation of ATDC5 cells. Based on this finding, they further developed an osteochondral mimetic scaffold by gradually printing bioinks composed of the adipose-derived stem cells (ADSCs), PRP, and GelMA[51]. These hydrogels had relatively slow degradation rates, high mechanical properties, and tissue-specific biomimetic structures, promoting *in vitro* osteochondral tissue formation, including hyaline and hypertrophic cartilage and bone phases. One of the advantages of PRP over other growth factors is its patient- and tissue-specific properties, suggesting that PRP application could contribute to future personalized 3D printing.

Overall, the combination of 3D bioprinting and GelMA hydrogels in regenerative medicine showed a huge potential in the creation of anatomically complex articular cartilage tissue substitutes. While some of the growth factors mentioned above have been incorporated into GelMA for cartilage regeneration, these studies have only included one growth factor in the scaffolds. However, articular cartilage is a complex tissue with three layers, and 3D printing technology has the potential to enable the construction of multi-layered scaffolds with different growth factors on each layer to achieve high-fidelity tissue repair. Therefore, constructs with multi-layer and multi-factors are expected in order to facilitate the regeneration of articular cartilage.

5.2. Cells

GelMA has many desirable properties, such as biocompatibility and controlled degradability, and these properties make GelMA an attractive option in cartilage tissue engineering and regenerative medicine applications where it can help promote the proliferation, migration, and differentiation of chondrocytes and stem cells, and thus facilitate the formation of new functional cartilage. Researchers also emphasized the importance of utilizing additional seed cells in hydrogel-based cartilage treatment. In a study by Zheng *et al.*[52], a GelMA with silk fibroin (SF) hydrogel was developed, and this GelMA-SF hydrogel could facilitate chondrogenesis of BMSCs *in vitro*. Notably, they observed that BMSCs-seeded hydrogels resulted in more favorable cartilage repair outcomes, underscoring the significance of employing supplementary seed cells in hydrogel-based cartilage therapy.

The UV-mediated photocrosslinking properties, adhesive affinity for cells, and biodegradable nature render GelMA the most suitable ink for 3D printing. Moreover, layer-by-layer assembly through 3D printing allows for the even distribution of cells within the scaffolds, a crucial aspect for tissue regeneration since endogenous cells are

unable to migrate into the scaffold immediately, contingent on the scaffold's composition and structure. Herein, we summarize different types of cells loaded in the GelMA hydrogels for 3D printing in cartilage tissue engineering.

Stem cells and chondrocytes have been extensively encapsulated in GelMA for cartilage tissue engineering.

5.2.1. Stem cells

Stem cells are recognized as excellent seed cells for cartilage repair since stem cells come from a wide range of sources[53], such as embryonic stem cells, mesenchymal stem cells, induced pluripotent stem cells, and cartilage progenitor cells. They are easy to obtain and have multi-differentiation potentials, including chondrogenesis. GelMA-based hydrogels that can help the osteochondral differentiation of stem cells to achieve cartilage regeneration have been extensively studied with the traditional scaffold fabrication techniques[54]. For instance, Huang *et al.*[27] constructed a GelMA hydrogel combined with BMSCs affinity peptide sequence PFSSTKT (PFS)-modified chondrocyte ECM particles (GelMA/ECM-PFS), which could regulate the migration of rabbit BMSCs *in vitro* and recruit endogenous BMSCs to migrate to the defect sites, resulting in a hyaline cartilage repair. Liu *et al.*[55] found that dendrimer-modified GelMA hydrogels carrying ADSCs promoted cartilage regeneration *in vitro* in 3D culture of ADSCs and articular cartilage defect repair *in vivo*.

In addition, articular chondrogenic progenitor cells (ACPCs) are present mainly on the surface of articular cartilage and play an essential role in chondrogenesis and injury repair[56,57]. In promoting cartilage regeneration, Levato *et al.*[58] compared the differences between ACPCs, chondrocytes, and MSCs, and found that ACPCs outperformed chondrocytes in forming neocartilage. Furthermore, Mouser *et al.*[59] also discovered differences in chondrogenesis among these three types of cells. To exploit these differences, they combined ACPC- and MSC-laden bioinks to print a more biomimetic scaffold, hoping that the two cell types could differentiate toward different lineages[58,59].

Despite the fact that 3D printing showed better potential than traditional scaffold fabrication techniques, the studies on GelMA as a carrier of stem cells for articular cartilage regeneration in the context of 3D printing remain scarce. Gao *et al.*[60] used polyethylene (ethylene glycol) dimethacrylate (PEG), GelMA, and human MSCs to create osteocartilage tissue constructs. They discovered that human MSCs were evenly distributed and had excellent osteogenesis and chondrogenesis capacity. Similarly, Luo *et al.*[61] constructed GelMA laden with BMSCs using low-temperature 3D printing and found that GelMA displayed excellent printability and a high cell survival rate. In addition, 5% (w/w) GelMA loaded with BMSCs promotes cartilage-specific ECM deposition and cartilage formation.

These studies focused on evaluating the role of GelMA in the chondrogenic and/or osteogenic differentiation of stem cells *in vitro*, but a few studies have explored the use of GelMA carrying stem cells in cartilage repair *in vivo*. Liu *et al.*[55] found that dendrimer-modified GelMA hydrogels carrying ADSCs promoted cartilage regeneration *in vitro* in 3D culture of rat ADSCs and articular cartilage defect repair *in vivo*. The scarcity of studies may be attributed to the prevalent focus on GelMA hydrogels fabricated using traditional scaffold fabrication techniques.

5.2.2. Chondrocytes

Chondrocytes are the primary cell type in cartilage tissue and they play an essential role in forming new cartilage matrix[62]. Maintaining the phenotype of chondrocytes is a major challenge in cartilage tissue therapies. In recent studies, different GelMA-based hydrogels have been used, owing to their potential in promoting the proliferation, migration, and differentiation of chondrocytes for cartilage tissue engineering. Levett *et al.*[63] found that GelMA was the best hydrogel in promoting the proliferation of chondrocytes, as well as the secretion of ECM abundant in glycosaminoglycan and collagen, compared to other commonly used hydrogels, such as hyaluronic acid, polyethylene glycol, and alginate hydrogels. Hölzl *et al.*[64] also demonstrated that GelMA has good integration with surrounding cartilage, enabling the sealing and smoothening of local gaps while facilitating the migration and growth of cells for new tissue formation. Wang *et al.*[65] loaded the chondrocyte spheroids into a hydrogel mixture of GelMA and HAMA which maintained chondrocytes phenotypes and enhanced proliferation, demonstrating its potential as a micro-unit for cartilage tissue engineering. Levett *et al.*[66] found that introducing HAMA and CSMA could enhance chondrogenesis and promote secretion of proteoglycan and collagens, making CSMA a promising option for cartilage tissue engineering. Agten *et al.*[67] found that GelMA loaded with chondrocytes derived from human induced pluripotent stem cells formed hyaluronic cartilaginous tissue *in vivo*. Overall, GelMA has shown promising results in promoting chondrocyte proliferation and ECM secretion, and integration with surrounding cartilage, making them promising candidates for cartilage tissue engineering.

However, it is surprising that there are few reports on chondrocyte-laden GelMA hydrogels printed for articular cartilage tissue engineering. The reason may be because numerous reports on chondrocyte-laden GelMA hydrogels

fabricated by traditional techniques. Nevertheless, there are studies on the role of 3D-printed chondrocyte-laden GelMA hydrogels in promoting cartilage regeneration in other cartilage regions like auricle[68] and menisci[69].

Taken together, incorporating cells in GelMA hydrogels produced by 3D printing for cartilage tissue engineering has demonstrated promising results. Different cell types have different advantages in promoting cartilage regeneration. Nevertheless, the best source of cells for use in cartilage tissue engineering remains to be explored in the future[70]. By incorporating different cell types, researchers can exploit the wide array of application of GelMA hydrogels with the help of 3D printing technology.

5.3. Exosomes

Exosomes, extracellular vesicles secreted by cells, have emerged as promising candidates for enhancing cartilage regeneration due to their ability to mediate cell-to-cell communication and transfer of bioactive molecules. Studies have demonstrated that exosomes derived from MSCs can promote cartilage regeneration by suppressing inflammation and inducing chondrogenesis. Cheng *et al.*[71] loaded BMSCs-derived exosomes (BMSCs-Exos) into GelMA hydrogel and found that the GelMA hydrogel provided a good carrier for exosomes and facilitated chondrogenesis *in vitro* and cartilage regeneration *in vivo*. Similarly, Guan *et al.*[72] observed that BMSCs-Exos-loaded GelMA hydrogel could significantly boost the formation of new cartilage in rats with joint defects by modulating the immune microenvironment.

Although there are not many studies on the combination of exosomes and 3D-printed GelMA-based biomaterials in articular cartilage tissue engineering, exosome-loaded GelMA hydrogel scaffolds still represent a promising strategy for promoting cartilage regeneration, especially when combined with 3D printing technology.

Nevertheless, the development of active inks that offer fitting environments to direct the healing process remains a significant challenge. Still, it is important to consider overcoming the limitations by determining the effective dose, controlling the release of growth factors, and managing any potential side effects.

6. Limitations of 3D-printed GelMA-based biomaterials in articular cartilage tissue engineering

While GelMA-based biomaterials offer numerous benefits for application in articular cartilage tissue engineering, they do possess certain limitations.

Firstly, GelMA-based biomaterials demonstrates significant potential as an ink for cartilage repair, yet it is unable to create scaffolds that effectively mimic the architecture of full-thickness articular cartilage even after other biomaterials were added to modify their mechanical properties. Articular cartilage is a load-bearing tissue that requires high mechanical robustness. Most of the GelMA-based biomaterials are hydrogels with, oftentimes, relatively weak mechanical strength, which limits their application in the fabrication of articular cartilage tissues. To broaden their applications in regenerative medicine, GelMA hydrogels must be modified to enable the fabrication of 3D constructs that are more biomimetic to the structure and function of real tissues and organs.

Secondly, the degradation rate of GelMA-based biomaterials is not really aligned with the articular cartilage regeneration rate, which is also a disadvantage of using biomaterials in tissue engineering.

Finally, a limitation intrinsic to GelMA-based biomaterials is their swelling behavior. Although these materials can be precisely 3D-printed according to computational models, the resultant structures are susceptible to dimensional alterations owing to their propensity to absorb water and subsequently swell. This can potentially lead to the loss of the meticulously designed structural integrity, underscoring the importance of managing and predicting the swelling behavior of GelMA-based materials in practical applications.

Overall, there are also challenges with using 3D-printed GelMA-based biomaterials in cartilage engineering, such as its limited mechanical strength compared to native cartilage tissue and the control of degradation rate. Further research is needed to optimize GelMA-based materials for cartilage engineering applications.

7. Summary and prospects

Cartilage repair presents a significant clinical challenge today. Tissue engineering offers potential solutions, but traditional strategies prove insufficient for constructing complex, multi-layered tissues like articular cartilage. 3D printing technology makes it possible to overcome these challenges, with GelMA emerging as an exceptional ink for 3D printing.

GelMA boasts numerous advantages for cartilage tissue engineering. Its mechanical, swelling, and lubricating properties closely resemble those of natural cartilage, making it a good candidate for cartilage regeneration. GelMA promotes chondrocyte adhesion, proliferation, and stem cell chondrogenesis, thereby maintaining chondrocyte phenotypes. Moreover, the high-degree modifiability and adaptability of GelMA diversify its applications. Due to its physical

properties and photocrosslinking capabilities under UV light, GelMA is well-suited for 3D printing and the construction of complex, multi-layered constructs like native articular cartilage. Lastly, GelMA shows potential for creating "smart" scaffolds with self-controlling bioactive component release in response to biological or biochemical cues for targeted deliveries.

In conclusion, GelMA is a versatile and well-suited 3D printing ink for cartilage tissue engineering due to its excellent and adaptable characteristics. In the future, GelMA-based hydrogels may be utilized to construct more biomimetic and intelligent scaffolds for articular cartilage tissue engineering. However, addressing limitations in controlling the printed material's pore structure and optimizing tissue scaffold microenvironments is crucial for promoting further advancements in cartilage tissue engineering.

Acknowledgments

None.

Funding

This work was supported by the Guangzhou science and technology project to Aiguo Li or Wen Wang (grant number 2023A03J0987, 202002030049, 201704020145) and by the Oversea Study Program of Guangzhou Elite Project to Shengnan Qin (N/A).

Conflict of interest

The authors declare no conflict of interest.

Author contributions

Conceptualization: Shengnan Qin
Funding acquisition: Aiguo Li, Wen Wang
Project administration: Aiguo Li, Wen Wang
Investigation: Shengnan Qin, Liang Chen, Guowei Huang, Ming Yu, Yang Liu, Tao Cheng
Visualization: Shengnan Qin, Liang Chen, Guowei Huang,
Writing – original draft: Liang Chen, Guowei Huang, Ming Yu, Shengnan Qin
Writing – review & editing: Shengnan Qin

Ethics approval and consent to participate

Not applicable.

Consent for publication

Not applicable.

Availability of data

Not applicable.

Reference

1. Ning L, Chen X, 2017, A brief review of extrusion-based tissue scaffold bio-printing. *Biotechnol J*, 12(8).
2. Daly AC, Freeman FE, Gonzalez-Fernandez T, *et al.*, 2017, 3D bioprinting for cartilage and osteochondral tissue engineering. *Adv Healthc Mater*, 6(22).
3. Wu Y, Kennedy P, Bonazza N, *et al.*, 2021, Three-dimensional bioprinting of articular cartilage: A systematic review. *Cartilage*, 12(1): 76–92.
4. Messaoudi O, Henrionnet C, Bourge K, *et al.*, 2020, Stem cells and extrusion 3D printing for hyaline cartilage engineering. *Cells*, 10(1).
5. Oveissi F, Naficy S, Lee A, *et al.*, 2020, Materials and manufacturing perspectives in engineering heart valves: A review. *Mater Today Bio*, 5: 100038.
6. Zhang Y, Chen H, Li J, 2022, Recent advances on gelatin methacrylate hydrogels with controlled microstructures for tissue engineering. *Int J Biol Macromol*, 221: 91–107.
7. Yilmaz B, Tahmasebifar A, Baran ET, 2020, Bioprinting technologies in tissue engineering. *Adv Biochem Eng/Biotechnol*, 171: 279–319.
8. Derakhshanfar S, Mbeleck R, Xu K, *et al.*, 2018, 3D bioprinting for biomedical devices and tissue engineering: A review of recent trends and advances. *Bioact Mater*, 3(2): 144–156.
9. Gorgieva S, Kokol V, 2011, Collagen- vs. gelatine-based biomaterials and their biocompatibility: Review and perspectives, in *Biomaterials Applications for Nanomedicine,* Norderstedt.
10. Vandooren J, Van den Steen PE, Opdenakker G, *et al.*, 2013, Biochemistry and molecular biology of gelatinase B or matrix metalloproteinase-9 (MMP-9). *Crit Rev Biochem Mol Biol*, 48(3): 222–72.
11. Ozbolat IT, Hospodiuk M, 2016, Current advances and future perspectives in extrusion-based bioprinting. *Biomaterials*, 76(37): 321–343.
12. Van Den Bulcke AI, Bogdanov B, De Rooze N, *et al.*, 2000, Structural and rheological properties of methacrylamide modified gelatin hydrogels. *Biomacromolecules*, 1(1): 31–38.
13. Kumar H, Sakthivel K, Mohamed MGA, *et al.*, 2021, Designing gelatin methacryloyl (GelMA)-based bioinks for visible light stereolithographic 3D biofabrication. *Macromol Biosci*, 21(1): e2000317.
14. Sun M, Sun X, Wang Z, *et al.*, 2018, Synthesis and properties of gelatin methacryloyl (GelMA) hydrogels and their

recent applications in load-bearing tissue. *Polymers(Basel)*, 10(11): 1290.

15. Schuurman W, Levett PA, Pot MW, *et al.*, 2013, Gelatin-methacrylamide hydrogels as potential biomaterials for fabrication of tissue-engineered cartilage constructs. *Macromol Biosci*, 13(5): 551–561.
16. Gan D, Xu T, Xing W, *et al.*, 2019, Mussel-inspired dopamine oligomer intercalated tough and resilient gelatin methacryloyl (GelMA) hydrogels for cartilage regeneration. *J Mater Chem B*, 7(10): 1716–1725.
17. Lim KS, Abinzano F, Bernal PN, *et al.*, 2020, One-step photoactivation of a dual-functionalized bioink as cell carrier and cartilage-binding glue for chondral regeneration. *Adv Healthc Mater*, 9(15): e1901792.
18. Wang M, Zhao J, Luo Y, *et al.*, 2022, 3D contour printing of anatomically mimetic cartilage grafts with microfiber-reinforced double-network bioink. *Macromol Biosci*, 22(9): e2200179.
19. Guan J, Yuan FZ, Mao ZM, *et al.*, 2021, Fabrication of 3D-printed interpenetrating hydrogel scaffolds for promoting chondrogenic differentiation. *Polymers (Basel)*, 13(13):2146.
20. Han L , Xu J , Lu X, *et al.*, 2017, Biohybrid methacrylated gelatin/polyacrylamide hydrogels for cartilage repair. *J Mater Chem B*, 5(4): 731–741.
21. Trengove A, Duchi S, Onofrillo C, *et al.*, 2021, Microbial transglutaminase improves ex vivo adhesion of gelatin methacryloyl hydrogels to human cartilage. *Front Med Technol*, 3: 773673.
22. Suo H, Xu K, Zheng X, 2015, Using glucosamine to improve the properties of photocrosslinked gelatin scaffolds. *J Biomater Appl*, 29(7): 977–987.
23. Suo H, Li L, Zhang C, *et al.*, 2020, Glucosamine-grafted methacrylated gelatin hydrogels as potential biomaterials for cartilage repair. *J Biomed Mater Res B Appl Biomater*, 108(3): 990–999.
24. Zhan X, 2020, Effect of matrix stiffness and adhesion ligand density on chondrogenic differentiation of mesenchymal stem cells. *J Biomed Mater Res A*, 108(3): 675–683.
25. Brown GCJ, Lim KS, Farrugia BL, *et al.*, 2017, Covalent incorporation of heparin improves chondrogenesis in photocurable gelatin-methacryloyl hydrogels. *Macromol Biosci*, 17(12): 1700158.
26. Wang KY, Jin XY, Ma YH, *et al.*, 2021, Injectable stress relaxation gelatin-based hydrogels with positive surface charge for adsorption of aggrecan and facile cartilage tissue regeneration. *J Nanobiotechnol*, 19(1): 214.
27. Huang B, Li P, Chen M, *et al.*, 2022, Hydrogel composite scaffolds achieve recruitment and chondrogenesis in cartilage tissue engineering applications. *J Nanobiotechnol*, 20(1): 25.
28. Li X, Chen S, Li J, *et al.*, 2016, 3D culture of chondrocytes in gelatin hydrogels with different stiffness. *Polymers (Basel)*, 8(8): 269.
29. Li X, Chen Y, Kawazoe N, *et al.*, 2017, Influence of microporous gelatin hydrogels on chondrocyte functions. *J Mater Chem B*, 5(29): 5753–5762.
30. Costantini M, Idaszek J, Szöke K, *et al.*, 2016, 3D bioprinting of BM-MSCs-loaded ECM biomimetic hydrogels for in vitro neocartilage formation. *Biofabrication*, 8(3): 035002.
31. Shopperly LK, Spinnen J, Krüger JP, *et al.*, 2022, Blends of gelatin and hyaluronic acid stratified by stereolithographic bioprinting approximate cartilaginous matrix gradients. *J Biomed Mater Res B Appl Biomater*, 110(10): 2310–2322.
32. Huang K, Li Q, Li Y, *et al.*, 2018, Cartilage tissue regeneration: The roles of cells, stimulating factors and scaffolds. *Curr Stem Cell Res Ther*, 13(7): 547–567.
33. Chen L, Liu J, Guan M, *et al.*, 2020, Growth factor and its polymer scaffold-based delivery system for cartilage tissue engineering. *Int J Nanomed,* 15: 6097–6111.
34. Wang B, Díaz-Payno PJ, Browe DC, *et al.*, 2021, Affinity-bound growth factor within sulfated interpenetrating network bioinks for bioprinting cartilaginous tissues. *Acta Biomater*, 128: 130–142.
35. Cho H, Kim J, Kim S, *et al.*, 2020, Dual delivery of stem cells and insulin-like growth factor-1 in coacervate-embedded composite hydrogels for enhanced cartilage regeneration in osteochondral defects. *J Control Release*, 327: 284–295.
36. Zhang Z, Li L, Yang W, *et al.*, 2017, The effects of different doses of IGF-1 on cartilage and subchondral bone during the repair of full-thickness articular cartilage defects in rabbits. *Osteoarthr Cartil*, 25(2): 309–320.
37. Wu H, Shang Y, Sun W, *et al.*, 2023, Seamless and early gap healing of osteochondral defects by autologous mosaicplasty combined with bioactive supramolecular nanofiber-enabled gelatin methacryloyl (BSN-GelMA) hydrogel. *Bioact Mater*, 19: 88–102.
38. Zhu W, Cui H, Boualam B, *et al.*, 2018, 3D bioprinting mesenchymal stem cell-laden construct with core-shell nanospheres for cartilage tissue engineering. *Nanotechnology*, 29(18): 185101.
39. Wang B, Díaz-Payno PJ, Browe DC, *et al.*, 2021, Affinity-bound growth factor within sulfated interpenetrating network bioinks for bioprinting cartilaginous tissues. *Acta Biomater*, 128: 130–142.
40. Yang Z, Cao F, Li H, *et al.*, 2022, Microenvironmentally optimized 3D-printed TGFβ-functionalized scaffolds facilitate endogenous cartilage regeneration in sheep. *Acta Biomater*, 150: 181–198.
41. Ding X, Gao J, Yu X, *et al.*, 2022, 3D-printed porous scaffolds of hydrogels modified with TGF-β1 binding peptides to promote in vivo cartilage regeneration and animal gait

restoration. *ACS Appl Mater Interfaces*, 14(14): 15982–15995.

42. van Beuningen HM, Glansbeek HL, van der Kraan PM, *et al.*, 2000, Osteoarthritis-like changes in the murine knee joint resulting from intra-articular transforming growth factor-beta injections. *Osteoarthr Cartil*, 8(1): 25–33.

43. Bakker AC, van de Loo FA, van Beuningen HM, *et al.*, 2001, Overexpression of active TGF-beta-1 in the murine knee joint: evidence for synovial-layer-dependent chondro-osteophyte formation. *Osteoarthr Cartil*, 9(2): 128–136.

44. Gong L, Li J, Zhang J, *et al.*, 2020, An interleukin-4-loaded bi-layer 3D printed scaffold promotes osteochondral regeneration. *Acta Biomater*, 117(Nov): 246–260.

45. Liang Y, Li J, Wang Y, *et al.*, *Platelet Rich Plasma in the Repair of Articular Cartilage Injury: A Narrative Review.* Cartilage, 2022. 13(3): p. 19476035221118419.

46. Everts P, Onishi K, Jayaram P, *et al.*, 2020, Platelet-rich plasma: new performance understandings and therapeutic considerations in 2020. *Int J Mol Sci*, 21(20): 7749.

47. Szwedowski D, Szczepanek J, Paczesny Ł, *et al.*, 2021, The effect of platelet-rich plasma on the intra-articular microenvironment in knee osteoarthritis. *Int J Mol Sci*, 22(11): 5492.

48. Qian Y, Han Q, Chen W, *et al.*, 2017, Platelet-rich plasma derived growth factors contribute to stem cell differentiation in musculoskeletal regeneration. *Front Chem*, 5: 89.

49. Jiang G, Li S, Yu K, *et al.*, 2021, A 3D-printed PRP-GelMA hydrogel promotes osteochondral regeneration through M2 macrophage polarization in a rabbit model. *Acta Biomater*, 128: 150–162.

50. Irmak G, Gümüşderelioğlu M, 2020, Photo-activated platelet-rich plasma (PRP)-based patient-specific bio-ink for cartilage tissue engineering. *Biomed Mater*, 15(6): 065010.

51. Irmak G, Gümüşderelioğlu M, 2021, Patients- and tissue-specific bio-inks with photoactivated PRP and methacrylated gelatin for the fabrication of osteochondral constructs. *Mater Sci Eng C Mater Biol Appl*, 125: 112092.

52. Zheng K, Zheng X, Yu M, *et al.*, 2023, BMSCs-seeded interpenetrating network GelMA/SF composite hydrogel for articular cartilage repair. *J Funct Biomater*, 14(1).

53. Ma Q, Liao J, Cai X, 2018, Different sources of stem cells and their application in cartilage tissue engineering. *Curr Stem Cell Res Ther*, 13(7): 568–575.

54. Pirosa A, Gottardi R, Alexander PG, *et al.*, 2021, An in vitro chondro-osteo-vascular triphasic model of the osteochondral complex. *Biomaterials*, 272: 120773.

55. Liu F, Wang X, Li Y, *et al.*, 2022, Dendrimer-modified gelatin methacrylate hydrogels carrying adipose-derived stromal/stem cells promote cartilage regeneration. *Stem Cell Res Ther*, 13(1): 26.

56. Jiang Y, Tuan RS, 2015, Origin and function of cartilage stem/progenitor cells in osteoarthritis. *Nat Rev Rheumatol*, 11(4): 206–212.

57. Kozhemyakina E, Zhang M, Ionescu A, *et al.*, 2015, Identification of a Prg4-expressing articular cartilage progenitor cell population in mice. *Arthritis Rheumatol*, 67(5): 1261–1273.

58. Levato R, Webb WR, Otto IA, *et al.*, 2017, The bio in the ink: Cartilage regeneration with bioprintable hydrogels and articular cartilage-derived progenitor cells. *Acta Biomater*, 61: 41–53.

59. Mouser VHM, Levato R, Mensinga A, *et al.*, 2020, Bio-ink development for three-dimensional bioprinting of hetero-cellular cartilage constructs. *Connect Tissue Res*, 61(2): 137–151.

60. Gao G, Schilling AF, Hubbell K, *et al.*, 2015, Improved properties of bone and cartilage tissue from 3D inkjet-bioprinted human mesenchymal stem cells by simultaneous deposition and photocrosslinking in PEG-GelMA. *Biotechnol Lett*, 37(11): 2349–2355.

61. Luo C, Xie R, Zhang J, *et al.*, 2020, Low-temperature three-dimensional printing of tissue cartilage engineered with gelatin methacrylamide. *Tissue Eng Part C Methods*, 26(6): 306–316.

62. Shah SS, Mithoefer K, 2021, Scientific developments and clinical applications utilizing chondrons and chondrocytes with matrix for cartilage repair. *Cartilage*, 13(1_suppl): 1195s–1205s.

63. Levett PA, Melchels FP, Schrobback K, *et al.*, 2014, Chondrocyte redifferentiation and construct mechanical property development in single-component photocrosslinkable hydrogels. *J Biomed Mater Res Part A*, 102(8): 2544–2553.

64. Hölzl K, Fürsatz M, Göcerler H, *et al.*, 2022, Gelatin methacryloyl as environment for chondrocytes and cell delivery to superficial cartilage defects. *J Tissue Eng Regen Med*, 16(2): 207–222.

65. Wang G, An Y, Zhang X, *et al.*, 2021, Chondrocyte spheroids laden in GelMA/HAMA hybrid hydrogel for tissue-engineered cartilage with enhanced proliferation, better phenotype maintenance, and natural morphological structure. *Gels*, 7(4): 247.

66. Levett PA, Melchels FP, Schrobback K, *et al.*, 2014, A biomimetic extracellular matrix for cartilage tissue engineering centered on photocurable gelatin, hyaluronic acid and chondroitin sulfate. *Acta Biomater*, 10(1): 214–223.

67. Agten H, Van Hoven I, Viseu SR, *et al.*, 2022, In vitro and in vivo evaluation of 3D constructs engineered with human iPSC-derived chondrocytes in gelatin methacryloyl hydrogel. *Biotechnol Bioeng*, 119(10): 2950–2963.

68. Tang P, Song P, Peng Z, *et al.*, 2021, Chondrocyte-laden GelMA hydrogel combined with 3D printed PLA scaffolds

for auricle regeneration. *Mater Sci Eng C Mater Biol Appl*, 130: 112423.

69. Chen P, Zheng L, Wang Y, *et al.*, 2019, Desktop-stereolithography 3D printing of a radially oriented extracellular matrix/mesenchymal stem cell exosome bioink for osteochondral defect regeneration. *Theranostics*, 9(9): 2439–2459.

70. Cucchiarini M, Madry H, Guilak F, *et al.*, 2014, A vision on the future of articular cartilage repair. *Eur Cell Mater*, 27: 12–16.

71. Cheng J, Rong G, Wang Z, *et al.*, 2022, ECM-mimicking hydrogels loaded with bone mesenchymal stem cell-derived exosomes for the treatment of cartilage defects. *Evid Based Complement Alternat Med*, 2022: 3450672.

72. Guan P, Cui R, Wang Q, *et al.*, 2022, A 3D hydrogel loaded with exosomes derived from bone marrow stem cells promotes cartilage repair in rats by modulating immunological microenvironment. *Nan Fang Yi Ke Da Xue Xue Bao*, 42(4): 528–537.

ACCSCIENCE PUBLISHING

International Journal of Bioprinting

REVIEW ARTICLE

3D bioprinting for vascular grafts and microvasculature

Junpeng Zhu[1†], Xinwang Wang[2†], Lin Lin[1†], and Wen Zeng[1,3,4*]

[1]Department of Cell Biology, Third Military Medical University, Chongqing, China

[2]Troops 69250 of the PLA, Urumqi, China

[3]State Key Laboratory of Trauma, Burn and Combined Injury, Chongqing, China

[4]Jinfeng Laboratory, Chongqing 401329, China

(This article belongs to the *Special Issue: 3D printing for tissue engineering and regenerative medicine*)

Abstract

Cardiovascular disease is the world's leading cause of death, and there is a substantial clinical need for transplantable blood vessels. Through tissue vascular engineering technology, large blood vessel grafts with significant clinical effects have been synthesized. However, synthesizing vascular valves, small vessels up to 6 mm in diameter, and capillary networks up to 500 μm in diameter remains challenging due to the lack of precise manufacturing techniques. In particular, constructing a microvascular network in thick tissue is the technical bottleneck of organ transplantation. Three-dimensional (3D) bioprinting is a computer-assisted layer-by-layer deposition method that can deposit cells and biomaterials at a predetermined location, according to an accurate digital 3D model, to build a delicate and complex bionic structure. This review discusses the progress and limitations of 3D bioprinting in preparing large vessels and valves, small-diameter vessels, and microvascular networks. This paper focuses on improved printing technology and innovative bio-ink materials. The future application of 3D bioprinting is prospected in generating artificial blood vessel grafts and vascularized organs with full biological function.

Keywords: 3D bioprinting; Small-diameter vessels; Microvasculature

†These authors contributed equally to this work.

***Corresponding author:**
Wen Zeng
(zengw0105@163.com)

Citation: Zhu J, Wang X, Lin L, *et al*., 2023, 3D bioprinting for vascular grafts and microvasculature. *Int J Bioprint*, 9(6): 0012.
https://doi.org/10.36922/ijb.0012

Received: May 12, 2023
Accepted: July 1, 2023
Published Online: August 2, 2023

Copyright: © 2023 Author(s). This is an Open Access article distributed under the terms of the Creative Commons Attribution License, permitting distribution, and reproduction in any medium, provided the original work is properly cited.

Publisher's Note: AccScience Publishing remains neutral with regard to jurisdictional claims in published maps and institutional affiliations.

1. Introduction

Cardiovascular disease is the leading cause of death in the world, with the annual number of mortalities expected to reach 23.3 million by 2030[1]. The body's vascular system consists of four parts, such as large-diameter blood vessels (diameter 10–30 mm), medium-diameter blood vessels (diameter 6–10 mm), small-diameter blood vessels (diameter 0.5–6 mm), and capillaries (diameter <500 μm).

Macroangiopathy, along with aortic dissection, thoracic aortic aneurysm, and abdominal aortic aneurysm, poses a significant threat to human life and health. These diseases often lead to sudden death of patients due to blood vessel rupture and bleeding[2]. Clinically, the radical surgical approach to significant vascular disease replaces damaged vessels with artificial vessels[3]. The large vessel valve is located at the junction of the cardiac chambers and the large-diameter artery, ensuring unipolar blood flow between the ventricle and the large artery. Narrowing or incomplete closure of the

aortic valves can lead to heart structural and functional abnormalities and, ultimately, heart failure[4]. With the acceleration of the aging population process, the incidence rate of senile degenerative valvular diseases is increasing yearly in China. The current solution is to replace defective valves with mechanical or biological alternatives. However, existing mechanical grafts are predetermined and do not correctly match the patient's aorta shape[5]. Moreover, the patient may have a violent immune rejection reaction to the biological graft and need lifelong anticoagulant therapy[6].

Small-diameter vessels are in great clinical demand, due to three aspects. First, the diameter of the coronary artery is less than 5 mm, which is prone to atherosclerosis and ischemic heart disease. Coronary atherosclerotic heart disease accounts for nearly half of all deaths in developed countries such as Europe and the United States[7]. Secondly, many patients needing hemodialysis must use small-caliber blood vessels to enter the venous dialysis fistula to construct long-term vascular dialysis access. Finally, patients with arterial injuries of more than 2 cm caused by car accidents and falls need to use small-caliber blood vessels for repair. The small-diameter vessels that can be transplanted are autologous vessels and artificial vessels[8]. The great saphenous vein is the most commonly used autograft in coronary artery bypass grafting, but its patency rate is only 60% in ten years[9]. There is no small-diameter artificial vascular graft for clinical operation because of its high incidence of stenosis and occlusion. In coronary artery bypass grafting, the patency rate of artificial blood vessel grafts at 2 years is only 32%[10]. A high survival rate of cells in the vessel wall has yet to be achieved with small-diameter vessel manufacturing techniques, such as electrospinning. In addition, the deficiency of endothelial cells in artificial blood vessels is the leading cause of graft thrombosis[11].

A microvascular network with a diameter of less than 500 microns is the principal site of gas and material exchange in tissues. Oxygen and nutrients can travel along capillary pathways to nourish parenchymal cells of tissues and organs. As a new method in organ transplantation, tissue engineering technology can solve the shortage of organ donors. However, due to the technical bottleneck, using vascular endothelial cells to construct microvascular networks is impossible[12]. The simple diffusion range of oxygen and nutrients is only 100–200 μm. Tissue engineering techniques have successfully produced functional thin skin tissue grafts. However, high-metabolic organs such as the liver, heart, and kidneys, which are fabricated via tissue engineering techniques, are not able to carry out adequate oxygen and nutrient exchange. The lack of biologically functional capillary networks in thick tissues (thickness ≥ 200 μm) has undoubtedly limited the development of tissue engineering in the areas of organ repair and transplantation. How to combine microvascular networks with thick tissues is a hot topic and future development direction.

Bioprinting is the application of three-dimensional (3D) printing technology in regenerative medicine. A typical bioprinting process consists of three parts. First, the pre-printed tissues and organs are imaged to reconstruct the 3D digital models and plan the printing path. Then, according to the pre-printed tissue organs, the matching bio-ink and tissue cells are selected. Finally, bioprinters are used to make the bio-inks containing cells into the desired 3D living tissues/organs according to the 3D model. The terms "3D printing" and "3D bioprinting" should be distinguished here. Both are techniques based on 3D models that print 3D objects layer by layer, but the printing materials differ. 3D bioprinting uses bio-inks containing cells to print living tissues and organs with biological activity directly. General 3D printing uses adhesive polymer materials to print 3D items that do not have cells. This review focuses specifically on bioprinting for vascular tissue containing living cells, so general 3D printing techniques and applications fall outside the scope of this work[13]. Traditional tissue engineering techniques for manufacturing vascular grafts include casting, electrospinning, melting electrowriting, etc. The structural accuracy of the casting process is not precise enough to prepare the complex structure of natural blood vessels. Electrospun fibers have low mechanical properties and cannot accurately form 3D structures. Thermoplastic inks used for melt electrowriting cannot encapsulate cells because high processing temperatures are required. It is worth noting that 3D bioprinting technology can accurately print blood vessel grafts containing living cells with bio-ink under the high precision control of a computer. For the construction of vascular grafts of different diameters and sizes, 3D bioprinting can be excellent. It can build a high-resolution vascular scaffold and provide physical and chemical clues for the adhesion and proliferation of blood vessel wall cells by designing printed patterns and bio-ink components, which is impossible with traditional vascular graft manufacturing technology[14].

Bioprinting technologies for blood vessel manufacturing include droplet-based bioprinting (DBB), extrusion-based bioprinting (EBB), and laser-assisted bioprinting (LAB). The differences between these printing technologies are resolution, printing speed, and adaptive biological inks, among which resolution is the main differentiating factor. Extrusion-based 3D printing, which extrudes bio-ink to form continuous fibers to build blood vessels, is the most common printing method. Its most significant advantage is that it can print a wide range of biocompatible materials. Still, its printing accuracy is relatively low compared with other bioprinting methods, generally at 100 μm. Droplet

bioprinting generates discrete droplet accumulation molding with higher precision. However, due to low driving pressure, inkjet bioprinting cannot print materials with high viscosity or cells with high concentration, which limits its application scope. Photocurable bioprinting, which uses photosensitive materials for photocuring and stacking layer by layer, is a printing method with the highest accuracy and has been used in the study of microvascular networks[14].

The design and development of bio-ink is the key to bioprinting technology. The research, development, and synthesis of new bio-inks that can balance printability, biocompatibility, and mechanical properties are the basis of 3D bioprinting applications. There is currently a shortage of bio-inks with both good printability and angiogenic activity, which is a major bottleneck for using bioprinting systems in blood vessel manufacturing. Hydrogels are the most commonly used bio-inks for constructing vascular stents because of their excellent biocompatibility. Biocompatible hydrogels have a 3D network structure similar to the extracellular matrix (ECM), which can promote cell adhesion and growth. Hydrogels contain natural and synthetic categories. Naturally derived protein bio-inks, such as collagen, gelatin, and fibrin, generally support cell adhesion and have good angiogenesis but are not mechanically sufficient to be used directly as 3D-printed vascular scaffolds[15,16]. Through various chemical modifications, synthetic hydrogels, such as polyethylene glycol and poloxamer, generally have good physical and chemical properties but are bioinert materials that are not conducive to cell adhesion and growth[12]. Multi-material printing is the development trend of 3D bioprinting. Bio-inks with printability and angiogenic activity were produced by selecting different components with different bioactivity and mechanical properties and adjusting their concentrations. By carefully regulating bio-ink formulation, a cellular microenvironment similar to that of natural blood vessels is constructed[17].

According to the classification of vessel diameter size, this paper summarizes the latest progress of 3D printing technology in large-caliber blood vessels and valves, small-caliber blood vessels, and microvascular networks, including the advancement of high-resolution printing technology and the preparation of bio-inks with good mechanical and biological properties. In addition, we briefly review the methods that promote the cultivation and maturation of bioprinted vascular grafts. This review also aims to facilitate the efficient transition of bioprinted grafts from the bioprinting lab to the clinic.

This paper also focuses on constructing a capillary network with biological functions using 3D bioprinting technology and promoting tissue engineering development for organ repair and transplantation. Here, we summarize five prerequisites for 3D printing to construct the microvascular network: good bio-ink performance, high-resolution printing technology, suitable cell source, vascular micropattern guiding angiogenesis, and multi-dimensional vascular network hierarchy appropriate to the host vascular system.

2. 3D bioprinting of large-diameter vessels and valves

2.1. 3D bioprinting of large-diameter vessels

Large-diameter vessels used for vascular replacement require good mechanical properties, consistent host anatomy, and high cell survival. There are still some gaps in the anatomical correlation and cell survival rate of vascular grafts based on electrospinning. 3D bioprinting has an advantage in manufacturing with consistent anatomy and high cell survival rates, as it can rely on computers to accurately model and utilize biocompatible bio-inks.

First, the large-diameter vascular graft used in the patient's surgery should have the same anatomical structure as the host. The grafts mismatched with the patient's blood vessels are more dangerous in the large blood vessel graft, and 36.8% of patients were re-hospitalized within 30 months due to heart failure caused by graft mismatch[18]. The resolution of 3D bioprinting technology depends first on computer modeling and printing path planning. Kucukgul designed a new computer algorithm to accurately print large-diameter blood vessel structures with living cells through a self-supporting "cake-like" printing method[19,20].

Second, vascular wall smooth muscle cells are essential for the long-term stability of the great vessels. Developing bio-ink with good cell compatibility is the key to improving the survival rate of graft cells. The natural ECM contains laminin, fibrin, and cytokines that promote cell adhesion and proliferation. Oropeza *et al.* found that in decellularized ECM (dECM)-printed graft structures, arterial smooth muscle cells could grow for a long time with no dead zone for 24 h. Because of smooth muscle cells, the macrovascular graft can maintain mechanical elasticity for a longer period[21]. Removing the ECM and adding bio-ink can significantly improve the cell survival rate of the graft. Potere *et al.* optimized the de-cellular protocol of the pig's natural aorta and determined the optimal concentration of dECM mixed into bio-inks[22]. The printed structure showed excellent structural stability and elasticity.

2.2. 3D bioprinting of vascular valves

3D printing technology provides a new and effective method for manufacturing biological valves. Cardiac valve

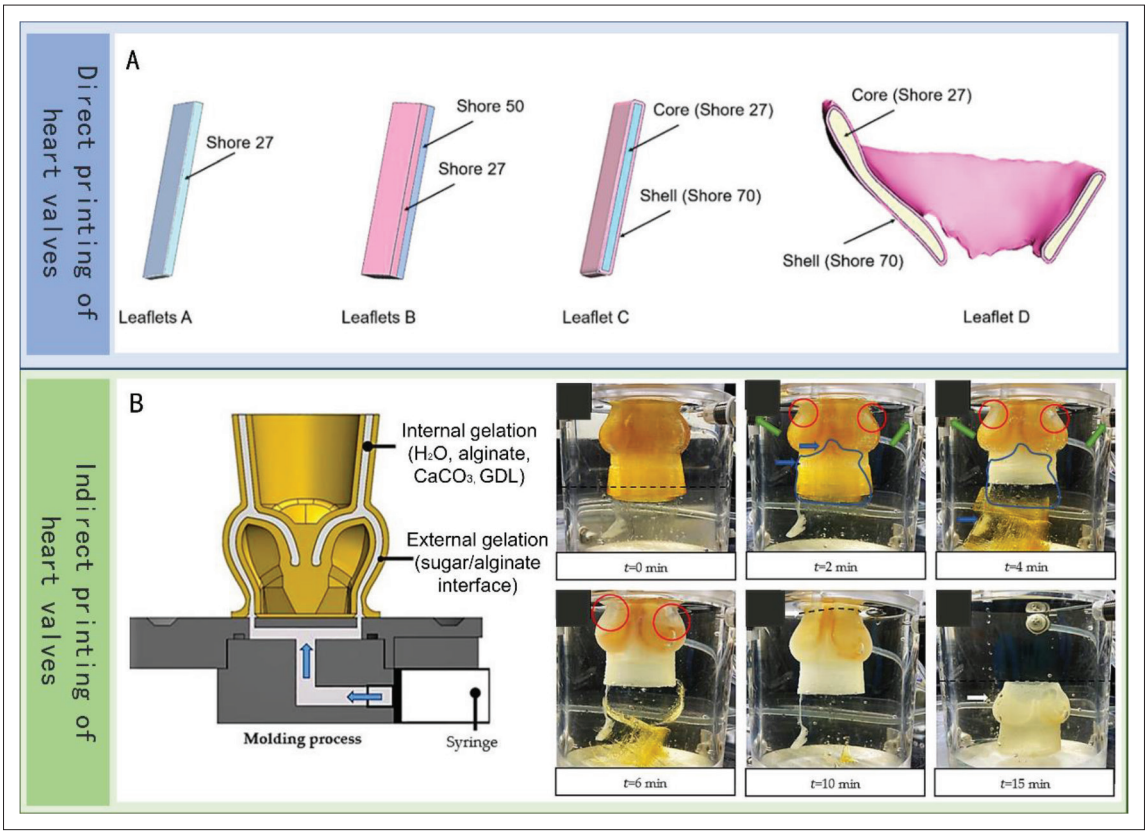

Figure 1. (A) Design drawing of valve multi-level structure modeling[24]. (B) An aortic valve mold made of sugar glass and a time-lapse photo of the mold dissolving[26].

printing methods contain direct extrusion printing and indirect printing.

First, direct extrusion bioprinting can directly deposit bio-inks of different concentrations and containing different cell types, which can effectively replicate the mechanical heterogeneity of the valve region. The heart valve is a heterogeneous anatomical region composed of valve ring, valve, and notochord with different mechanical properties. The valve has strong expandability and adaptability and can quickly open and close large blood vessels. The notochord has a high hardness that keeps the lumen open under harsh hemodynamic load. Hockaday *et al.* have successfully produced aortic valves with different mechanical properties by designing two different gel schemes, including a rigid hydrogel for the aortic notochord and a flexible, expandable hydrogel for the aortic valve[23]. The cross-section of the valve is a multi-layer heterogeneous structure. Vukicevic *et al.* compared the mechanical properties of the composite material with the target natural components and constructed the multi-layer structure of the valve using the composite material with different concentration ratios (Figure 1A)[24]. Duan *et al.* wrapped smooth muscle cells directly in the root of the valve and aortic stromal cells directly in the valve lobules. On day 7 of graft culture, the strength and stiffness of the cell material were significantly higher than that of the cell-free scaffold[25].

Second, indirect printing provides a relatively simple and highly reproducible method for valve printing. Rioux *et al.* used low-cost sugar glass to print the stent mold and then filled it with sodium alginate hydrogel, crosslinking it with $CaCl_2$. A complete aortic valve is produced after the glass-lined mold dissolves (Figure 1B)[26].

3. 3D bioprinting of small-caliber blood vessels

The research and development of small-diameter vascular prostheses has been a hot topic in the past decade, but formal clinical products have not yet emerged. The ideal small-diameter artificial blood vessel has a high forming resolution, cell integration rate, and mechanical strength. 3D bioprinting allows for the successful construction of perfect small-caliber blood vessels by combining new bio-inks, well-designed printing strategies, and multiple manufacturing methods.

3.1. Bio-inks with good biomechanical properties

Research in 3D bioprinting focuses on developing bio-inks suitable for printing small-diameter blood vessels. By mixing different kinds of natural and artificial compounds, adjusting the formula concentration can effectively improve the biomechanical properties of biological ink.

Zhou *et al.* introduced alginate lyase into natural ink to improve the biological activity of biological ink and gradually degrade alginate, which played a supporting role in the substrate[27]. The wall structure printed by the ink mixed with lyase contains a more porous structure. Endothelial cells and smooth muscle cells in the vascular wall have higher nutrient exchange efficiency and larger adherent proliferation space. The growth rate of smooth muscle cells in the lysozyme group was significantly faster than in the non-lysozyme group. The density of smooth muscle cells and endothelial cells encapsulated in the bio-inks is 1 million per mL[27]. After adding an acellular ECM from the great saphenous vein to bio-ink, Kamaraj *et al.* found that dECM induced the differentiation of human umbilical cord mesenchymal stem cells (UMSCs) into vascular smooth muscle cells and enhanced alpha-smooth muscle actin (α-SMA) expression[28]. They constructed the vascular structure with a high cell integration rate successfully, and the density of UMSCs encapsulated in the bio-inks is 10 million per mL[28].

To enhance the mechanical properties of bio-inks, Gold *et al.* blended gelatin methacrylate (GelMA), polyethylene glycol diacrylate (PEGDA), and two-dimensional nano-silicate to develop a new high-viscosity bio-ink[29]. Nano-silicates enhanced the compression elasticity of blood vessel walls, showed high printability regardless of cell density, and protected encapsulated cells from high shear forces during bioprinting. The authors selected a cell density of 2.5 million cells per mL for developing this vascular model[29]. Li *et al.* also found that doping the bio-ink with carbon nanotubes could improve the mechanical strength of the stent[30]. The authors successfully made engineered blood vessels with an inner diameter of 3 mm from bio-ink containing carbon nanotubes with a cell concentration of 4×10^5 cells per mL[30]. Liu *et al.* designed a double-network hydrogel by chemically crosslinking bio-inks, using calcium ion-crosslinked alginate to form the first network of a two-network hydrogel[31]. They used polyacrylate and PEGDA as polymer crosslinkers to prepare the secondary network structure of double-network hydrogels. The vascular structure printed by the double-network hydrogel has high toughness and elastic properties[31]. Freeman *et al.* combined fibrinogen and gelatin, using gelatin's excellent rheological properties to convert non-printable fibrinogen into a printable biomaterial[32]. Tissue-engineered vascular grafts use cell-laden (containing 3×10^6 cells per mL) bio-ink composed of 7.5% (w/v) gelatin and 10 mg/mL fibrinogen[32].

3.2. Sophisticated printing strategy

Designing a sophisticated printing strategy can effectively improve the printing precision of small-diameter blood vessels. Zhou *et al.* developed an interfacial diffusion printing (IDP) technique to control the thickness and diameter of the tube wall structure by controlling the time of gel crosslinking inside and outside the tube[33]. Jin *et al.* developed a method for making hollow blood vessels without relying on sacrificial materials and used a two-step crosslinking method[34]. The semi-solid wall with a quarter of lumen size was prepared by crosslinking in the first step, and then the concave structure with a 3/4 lumen size was made by covering the GelMA not crosslinked in the second step. Two separate parts constructed a complete tubular structure with a two-step crosslinking. Using no sacrificial material avoids damage to existing vascular structural accuracy and cell activity during removal. This method provides a new way to improve the printing precision of tubular structures[34]. Instead of printing layer by layer, Zhang *et al.* used a robotic arm with six degrees of freedom (6-DOF) to build a new 3D bioprinting system[35]. Composed of six 360° rotating joints, the manipulator can print routes from all directions in 3D space, significantly improving the ability to bioprint complex anatomical structures. They also successfully used the dual-robot platform to print a stent similar to the heart coronary artery network complex shape (Figure 2)[35].

3.3. Combined multiple manufacturing technologies

In the past, single processing methods were used to manufacture small-caliber blood vessels, but the blood vessels fabricated by these processes, when used alone, were unable to mimic the complex structure and function of the natural small-caliber blood vessels. Integrating multiple manufacturing technologies into a single biofabrication platform can effectively compensate for the limitations of a single processing method. The current 3D bioprinting technology is limited to a resolution of close to tens of microns. It cannot effectively print the nanoscale ECM structure, thereby hindering the reproduction of the microenvironment for blood vessel cells. Electrospinning uses high pressure to produce nanoscale diameter fibers with a large specific surface area that can mimic the physical function of the natural ECM, providing many attachment points for cell adhesion and growth. Fazal *et al.* developed a hybrid device that combines bioprinting and electrospinning[36]. The device, which has a bioprinting head and two electrospinning heads, is capable of

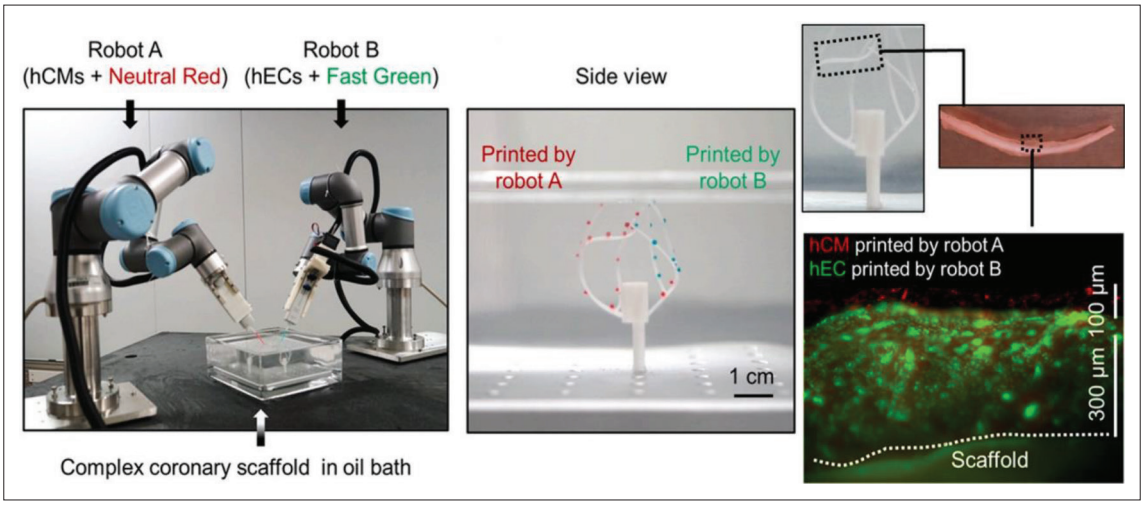

Figure 2. The blood vessel model was printed from multiple angles by two six-degree-of-freedom robotic bioprinters. The image at the bottom-right side shows the double-layer cross-section of the blood vessel wall[35].

producing tubular structures with electrospun nanofibers and layered hydrogel structures, which not only effectively improve the mechanical properties of the hydrogel but also simulate the double-layer structure of natural blood vessels[36]. Jin *et al.* employed two methods, electrospinning and bioprinting, to print double-layer blood vessel structures in sequence[37]. Electrospinning was first used to create a scaffold for the inner layer of blood vessels, which helps endothelial cells adhere and proliferate. The authors used bioprinter to evenly distribute hydrogels containing smooth muscle cells on the outer layer of the scaffold, and successfully constructed a double-layer structure of small-caliber blood vessels[37].

Electrowriting is a novel biomanufacturing technology combining electrospinning and 3D printing principles. It effectively compensates for the limitation of electrospinning technology, which is the inability to form a stable 3D structure. Melt electrowriting can print sub-micron-sized 3D designs with good mechanical properties through thermoelectric fluid power injection. Größbacher *et al.* combine fused electrowriting with bioprinting to print a composite tubular structure with a patterned fiber network[38]. The microfiber network of fused electrowriting enhanced the hydrogel tubes' bending, bursting, and tensile strength[38]. Cao *et al.* successfully produced a tubular scroll scaffold with anisotropic internal morphology by printing 20 μm oriented poly (ε-caprolactone) (PCL) fibers on the surface of a four-dimensional (4D)-bioprinted hydrogel using melt electrowriting technology[39]. PCL fibers promote cell adhesion and proliferation, but homogeneous hydrogels do not have this function[39].

Using 4D printing technology to prepare vascular stents is one of the future development directions. A remarkable feature is the self-deforming printing material that can respond to external stimuli. 4D printing technology can improve the accuracy and resolution of blood vessel prints. After bioprinting the vascular stent, post-processing reduces the diameter of the 3D structure, thereby enhancing the resolution of the vascular print. Kitana *et al.* used a hydrogel with a vertical expansion gradient to print shape-controlled vascular network elements[40]. By precisely controlling the 3D printing parameters, hydrogel concentration, and crosslinking parameters, they successfully prepared the hollow tube structure as a scalable T-joint with a diameter of 2–15 mm[40]. When swollen, the 3D-printed photo-crosslinked alginate flake gel rolls and forms a roll-like tube. Kirillova *et al.* controlled the tubular structure's diameter by controlling the photo-initiator's crosslinking density, exposure time, and concentration[41]. The self-coiled tubular structure has uniform cell colonization and avoids cell damage caused by extrusion printing[41].

4. 3D bioprinting of microvasculature

The microvascular network is the main place of oxygen and nutrient exchange in tissues and organs. The current tissue engineering techniques are still not able to construct thick tissues with rich vascular networks, and the artificial tissue fabricated containing a thick parenchymal cell layer is susceptible to ischemic necrosis.

This section discusses the prerequisites of 3D printing in built microvascular networks, including bio-inks with good performance, high-resolution printing techniques, suitable cell sources, micropatterns that induce angiogenesis, and multi-diameter vascular printing.

4.1. Bio-inks with good performance

Making a printable pro-angiogenic bio-ink includes mixing multiple hydrogels and chemically modifying a single hydrogel. Substances that improve rheology or elasticity are added to compound bio-inks to optimize the mechanical properties of naturally derived hydrogels. Wu *et al.* synthesized a shrinkage glycyrrhizin-methacrylate silk (SilkMA) with excellent mechanical properties and mixed it with GelMA and sodium alginate[42]. They found that the higher concentrations of GelMA (7.5%) and SilkMA (20%) were better suited for cell adhesion and proliferation, and by using this method, they rapidly generated an inch-long blood vessel construct in as little as 3 days[42]. Xanthan gum is a microbial extracellular polysaccharide produced by fermentation engineering, which has good rheology and biocompatibility. Muthusamy *et al.* utilized xanthan gum as a collagen thickener and found that collagen bio-ink with 10 pc xanthan gum added has the best printing adaptability, shape fidelity, and good capillary network generation[43]. Laponite is a montmorillonite nanoclay suspension that self-assembles to form a reversible shear-dilute gel. Laponite and alginate nanocomposite showed improved rheological properties, printing compatibility, and higher recovery rate after shear under higher clay concentration, and the constructed bone tissue scaffold showed *in vitro* angiogenesis ability[44]. Poly (itconic acid-co-citrate-co-octanediol) and poly (octanediol-co-maleic anhydride-co-octanediol) are synthetic elastic polymers that can be mixed with hydrogels to improve their stability and elasticity. Cell traction or body movement prevents the resulting blood vessels from irreversible deforming[45].

Endothelial cells can regulate vascular inflammation and thrombosis, and rapid endothelialization of early vascular grafts can effectively prevent the blockage of small-diameter vessels. The biological properties of bio-inks are essential for the rapid endothelialization of vascular grafts. To improve the ability of hydrogel scaffolds to promote the formation of microvascular networks, substances that can induce the adhesion and proliferation of endothelial cells can be added to the composite bio-ink. Natural alginate is biologically inert but can be modified with cell adhesion peptides to customize its biological activity with excellent performance, precision, and control. To promote vascular morphogenesis, Barrs *et al.* modified alginate scaffolds to promote vascular morphogenesis using RGD (an integrin-binding peptide for cell adhesion) and vascular endothelial growth factor (VEGF) mimic peptides (Figure 3A)[46]. *Paeonia lactiflora* extract is a compound derived from the herb peony that regulates the inflammatory microenvironment in skin wounds. Combining 3% paeoniflorin with a 3D mesh structure of the scaffold can promote the secretion of collagen by epithelial cells and stimulate the formation of vascular buds in the wound surface[47]. Bacterial cellulose is an organic compound biosynthesized by *Gluconacetobacter xylinus*. After dehydration, the bacterial cellulose matrix can generate a microchannel structure for cell adhesion and proliferation in the vascular scaffold and promote the construction of a smooth muscle layer in the vascular wall (Figure 3B)[48]. De-cellularization of tissues is a promising technique that allows the removal of cellular components while preserving ECM structure and composition. By mixing pig ovary dECM solution with seaweed gelatin mixture solution, the printed ovarian 3D scaffold showed more positive signals for new angiogenesis, cell proliferation, and survival (Figure 3C)[49]. ECM not handled thoroughly poses a threat to the body's immune response or pathogen transfer. Oliveira *et al.* solved this problem using a cell assembly extracellular matrix (CAM) synthesized from normal skin fibroblasts *in vitro*[50]. The thick structure printed by CAM can support the survival and maturation of capillary networks and successfully connect with the host circulatory system to establish active perfusion[50].

Sacrificial bioprinting is a classic indirect bioprinting method. Sacrificial bioprinting of vascularized tissue removes soluble bio-inks, usually through temperature change or enzymatic ablation, leaving behind a perfusable channel. Indirect printing is usually bioprinting based on extrusions with low resolution and minimum characteristic sizes larger than 100 μm, making them less suitable for fabricating capillary structures. How to improve the resolution of sacrificial bioprinting is a new research direction. Li *et al.* combined a heat-sensitive polymer (n-isopropyl acrylamide) with biocompatible GelMA to form a heat-responsive hydrogel[51]. In cell culture, the thermo-responsive hydrogel underwent significant volume shrinkage, which effectively triggered the production of smaller microscale vasculatures, with a minimum diameter of 50 μm[51]. Thomas *et al.* have proposed a two-component biomaterial system using a photo-crosslinked methacrylate hyaluronic acid (HAMA) and GelMA[52]. With highly-resolution enzyme-digested photo inks based on hyaluronic acid and the complementary enzyme, they printed vascular structures using stereolithography 3D bioprinting[52].

4.2. High-resolution printing technology

Currently, most microvascular networks are constructed by an uncontrolled spontaneous induction because previous printing techniques have not been able to accurately print microvessels with an internal diameter of fewer than 500 microns. The vascular network formed by self-assembly, which is less efficient in material exchange

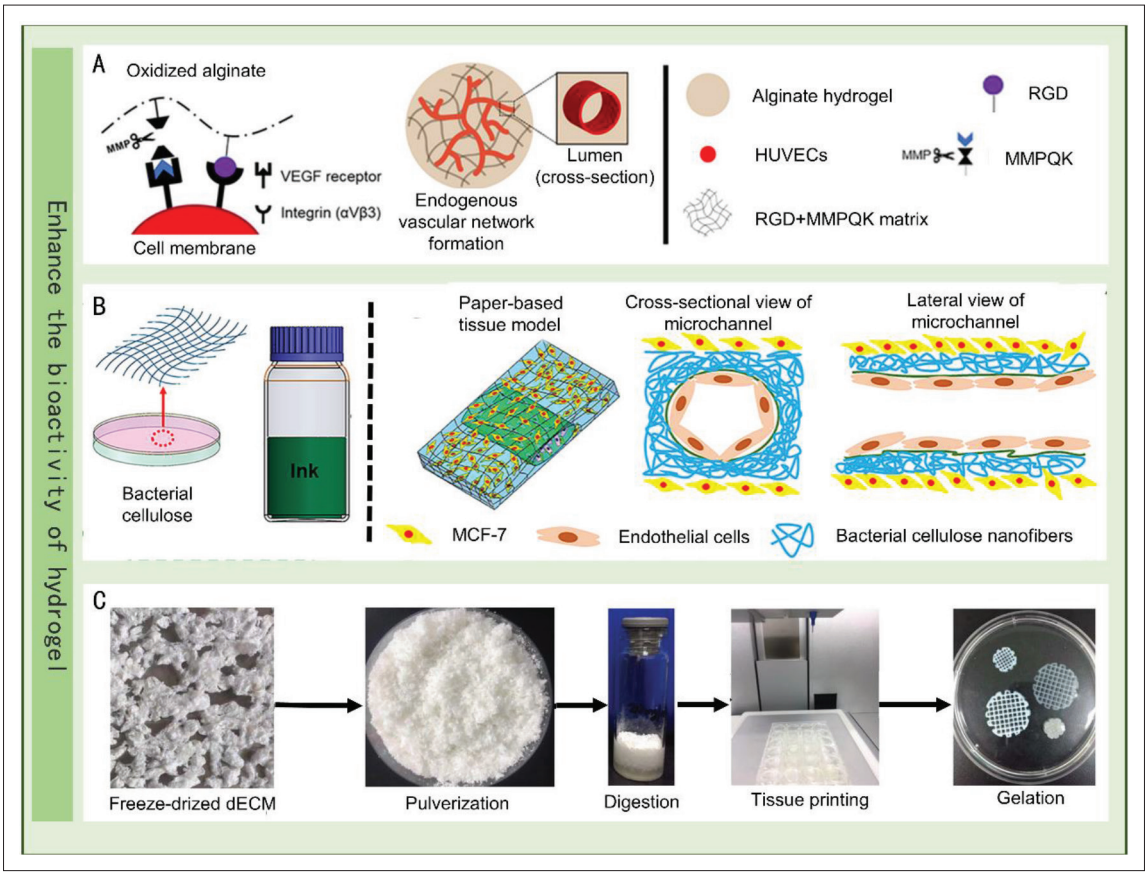

Figure 3. Bio-inks with good performance[40]. (A) Alginate scaffolds modified with RGD and MMPQK[46]. Reprinted (adapted) with permission from American Chemical Society. Copyright © 2021, American Chemical Society. (B) A microchannel structure formed by bacterial cellulose in a scaffold[48]. Reprinted (adapted) with permission from American Chemical Society. Copyright © 2019, American Chemical Society. (C) Mixing the ovarian extracellular matrix in bio-ink[49].

and more susceptible to thrombosis, differs significantly from the natural blood vessels. Therefore, despite being a complex endeavor, developing high-resolution 3D printing technology is a reliable research direction with the aim to realize printing of microvascular networks in future.

Due to high shear force, extrusion bioprinting impels cell activity while a micron-size pipe structure is being prepared. Kirillova *et al.* used advanced 4D bioprocessing methods to print hollow self-folding tubes, which had high-resolution control of diameter and structure, with shapable hydrogels. The self-folding tube's diameter depends on the hydrogel film's polymer concentration and the crosslinking time. The hydrogel film printed under low shear force contains cells with good activity and successfully produces tubular structures with a diameter of as low as 20 microns[41].

In most bioprinting systems, bio-inks have no self-supporting structure during printing. The structure-forming rate of softer biomaterials is low because of the gravity drop[12]. To solve this problem, embedded bioprinting is used to design a printing carrier filled with a supporting matrix. Hydrogels with weak mechanical properties, such as collagen, can print stably in the supporting matrix, avoiding the pattern distortion caused by sagging gravity[53].

Granular hydrogel is an excellent support medium for embedded 3D bioprinting[54]. Hinton *et al.* first proposed the free-form reversible embedding (FRESH) printing method of suspended hydrogels by extruding bio-ink from a thermally-reversible support bath composed of gelatin particulate slurry[55]. Then, Lee *et al.* developed a greatly improved second-generation suspended hydrogel free-form reversible embedding (FRESH v2.0) 3D bioprinting technology[56]. The technology can print collagen silk with a diameter of 20–200 μm, an order of magnitude higher than the first-generation FRESH, and has been demonstrated to successfully print a fully perfused vascular network of 8–50 μm[56]. Although liquid media allow low-viscosity inks, water structures constructed in viscous oils

are unsuitable for cell culture. Zhang *et al.* demonstrated a bioprinting method that uses cells to simulate two-phase water systems (ATPS)[54]. The new ATPS used poly-lysine (PLL) aqueous solution as ink and oxidized bacterial cellulose (oxBC) aqueous solution as a cell-containing medium. When the PLL ink loaded with cells was deposited into the oxBC medium phase, oxBC and PLL formed a condensed complex through electrostatic interaction at the water–water interface, successfully constructing a 3D cell interconnection network lined with perfusion channels[54].

Laser-assisted technology has exceptionally high resolution and can print feature sizes of less than 10 μm. Two-photon polymerization (TPP) is a laser direct writing technique that uses near-infrared femtosecond lasers to induce crosslinking reactions in monomer solutions, enabling nanoscale resolution[57]. Dobos *et al.* tested various TPP parameters on the small-diameter channel structure, including voxel size, layer spacing, etc., which improved the accuracy and throughput of the printing process, and successfully built a microvascular network with a diameter of 10–30 μm[58].

Stereolithography (SLA) allows patterning in photoreactive hydrogels and fabrication of blood vessels at the scale of millimeters and micrometers at high printing speeds. Xue *et al.* used the system to manufacture a variety of bracket architectures, ranging from regular geometries such as serpentine, spiral, and fractal shapes to more irregular/complex geometries such as bionic trees and capillary networks, with channel widths ranging from tree trunks (width >1100 μm) to small branches (about 17 μm in width)[59]. Thomas *et al.* used SLA to construct perfusable endothelialized blood vessels successfully[52].

4.3. Suitable sources of cells

A layer of endothelial cells usually forms the capillary wall. Adding endothelial cells directly to the bio-ink for printing is the primary way to create hollow endothelial tubes. Three common endothelial cell types used for tissue engineering include human umbilical vein endothelial cells (HUVECs), human microvascular endothelial cells (HMVECs), and induced pluripotent stem cell-derived endothelial cells (iPSC-ECs). The globular aggregates of cells better mimic the function of living tissue and promote the formation of microvascular networks, compared to the dispersed individual cells. The spherical culture chips made by Anada *et al.* can produce 500 spheroids per device at a time and allow for the collection of spheroids in a quick and non-invasive manner (Figure 4A)[60]. Liu *et al.* extracted small balls of early vascular cells (EVCs) from human embryonic stem cells (hESCs) to construct microvascular networks. When the spherical vascular cells were mixed into the hydrogel, the spherical vascular cells underwent angiogenesis at a rate significantly faster than individual EVC cells (Figure 4B)[61].

Support cells around blood vessels, such as perivascular cells, mesenchymal stem cells, and fibroblasts, provide mechanical support for blood vessel wall cells, shape the microenvironment around blood vessels, and promote angiogenesis. Therefore, adding support cells to vascular printing, which utilizes hydrogels, is a recommended strategy.

As perivascular support cells, adipose-derived stem cells (ASCs) express various angiogenic factors that stimulate endothelial and smooth muscle cell proliferation. For 7 days, Benmeridja *et al.* co-cultured ASCs with HUVECs, forming a network of capillaries in the printed adipose tissue[62]. Using three-culture spheres containing HUVECs, human preputial fibroblasts (HFF), and adipose tissue-derived mesenchymal stem cells (ADSC), de Moor *et al.* found that HUVECs spontaneously organized into a capillary-like network throughout the sphere[63].

The vascular wall comprises endothelium, smooth muscle, and outer membrane. When natural blood vessels are damaged, vascular stem cells that are located in the outer membrane of blood vessel wall differentiate into smooth muscle cells or endothelial cells that repair themselves.

To fully mimic the natural vascular wall hierarchy, Dogan *et al.* used human iPSC-derived mesodermal progenitor cells (hiMPCs), instead of mature endothelial or smooth muscle cells, to print the vascular network[64]. Using hiMPCs, they induced *de novo* generation of small and large containers with multi-walled structures that possess the inner, medium, and outer membrane-like layers[64].

4.4. Micropatterns that induce angiogenesis

Endothelial cells form the vascular networks in artificial tissues mainly through self-assembly. Biomaterials and biomaterial inks that precisely control cell adhesion are essential for creating functional microvasculature systems. Since the lumen formation of endothelial cells depends on cell–matrix interactions, the vascular system formed by self-assembly is often subject to hemodynamic disorder. By designing high-resolution patterns, 3D bioprinting can exert a degree of exogenous control over the self-assembly process of blood vessels. It creates biological cues that guide the formation of blood vessels by depositing endothelial cells and collagen fibers in artificial tissue[65]. The printing of the microvascular network contains two aspects: endothelial cell mapping and extracellular matrix mapping. The arranged and formed cord of endothelial cells defines the structure of neovascularization *in vivo*. The patterned matrix structure can give mechanical clues to endothelial cells' adhesion and proliferation and promote vascular network formation.

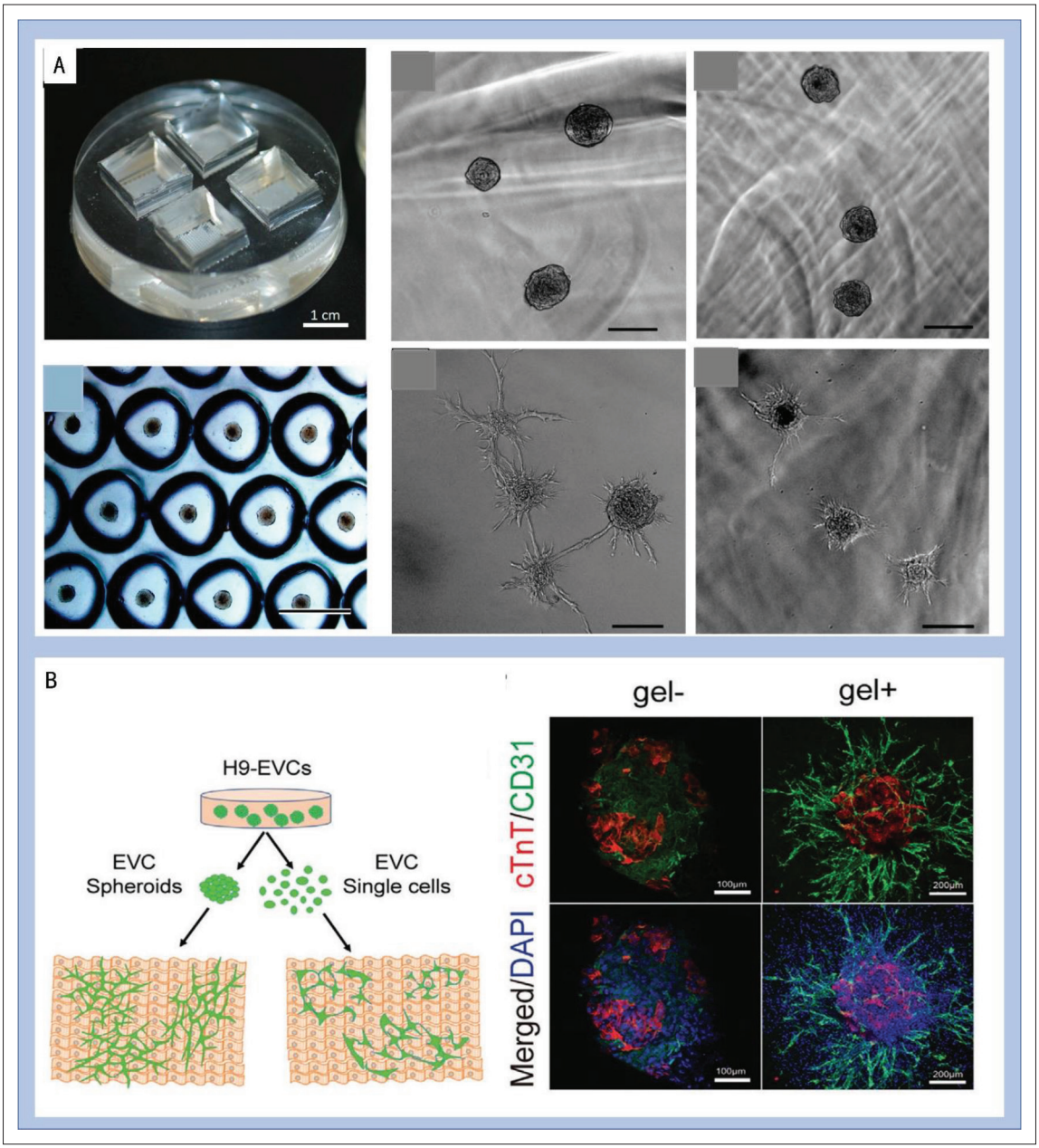

Figure 4. Suitable sources of cells. (A) A culture chip for a sphere of cells. Self-assembling spheres of endothelial cells form microvessels[60]. (B) Left: Early vascular cell (EVC) spheres can generate vascular networks more rapidly than single EVCs. Right: Fluorescent image of a microvascular network growing out of an EVC sphere[61].

The endothelial cells arranged in different patterns have different activities of generating vascular networks. Mirabella *et al.* designed three different vascular-patterned print structures[66]. Compared with the vascular patch without the pattern, the vascular patch with the geometric pattern had better perfusion after implantation in the distal limb of the host. This result suggests that the geometric design of the vascular channel in the patch affects its ability to salvage perfusion[66]. Kérourédan *et al.* designed and printed different patterns of endothelial cells on bone calcium defects in mice, including a "ring" pattern, a "disk" pattern, and a "cross-circle" pattern. The "disc" and "cross-circle" patterns had the highest local endothelial cell density and significantly increased blood vessel formation in the body[67].

While the natural cellular microenvironment is anisotropic, the cellular and matrix components in bio-ink

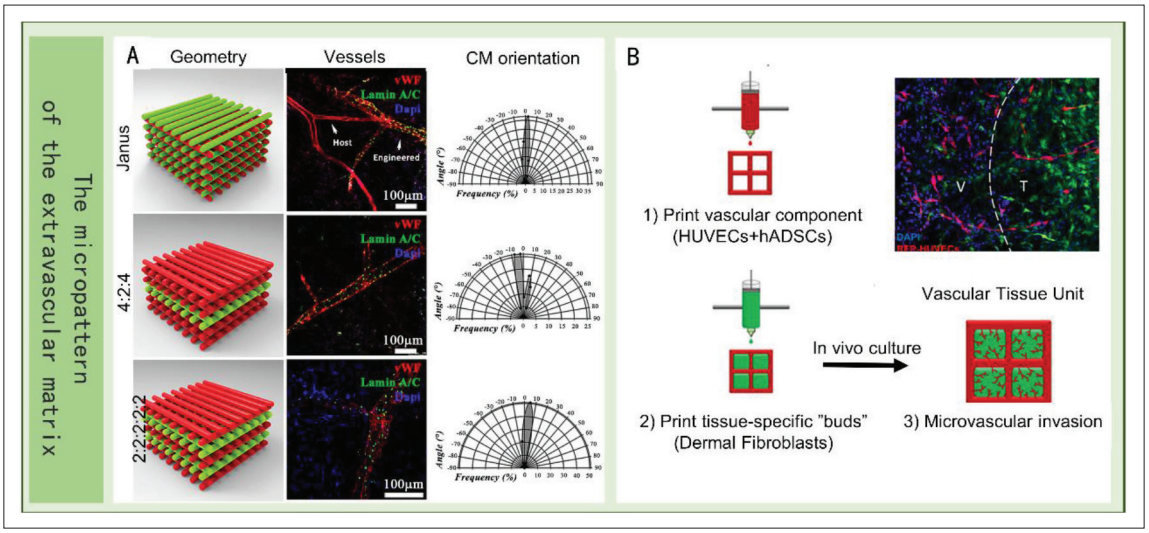

Figure 5. Vascular micropatterns that guide angiogenesis[64,66]. (A) Three different printing ratios of endothelial cells and cell-matrix[69]. (B) A vascularized tissue unit (VTU) containing both vascular and surrounding non-vascular tissue components[46]. Reprinted (adapted) with permission from American Chemical Society. Copyright © 2021, American Chemical Society.

are homogeneous. Chansoria *et al.* achieved high control over cell arrangement patterns in GelMA substrates through ultrasound-assisted bioprinting driven by volume sonic waves[68]. The patterned GelMA matrix can arrange the adherent endothelial cells along the patterned array and successfully construct a biomimetic vascular network with structural and mechanical anisotropy[68]. Different cell distribution also affects the efficiency of vascular network generation. Maiullari *et al.* designed three heterogeneous structures based on the proportion of HUVECs and cell-matrix in the printed tissue[69]. The two layers of HUVECs alternated with two (2:2:2:2:2) or four (4:2:4) layers of cell-matrix (Figure 5A). The Janus model constructs the most developed vascular network of the three models, and it is most clearly distributed in the direction of induced pluripotent stem cells (iPSC)-derived cell-matrix (angular spacing between -10° and +10°), revealing a potentially beneficial interaction between HUVECs and cell-matrix in the organization[69]. Barrs *et al.* have designed a vascularized tissue unit (VTU) containing vascular and surrounding nonvascular tissue components[46]. Only heterogeneous VTUs structures contained tissue components capable of angiogenesis. Moreover, there was no angiogenesis in the mixture of the vascular and non-vascular elements. This result indicates increased vascularization in heterogeneous, compartmentalized tissue structures compared to uniform, mixed tissue structures (Figure 5B)[46].

4.5. Multi-diameter vascular printing

Creating a systematic blood vessel network has become the future goal of vascular engineering. Blood vessel diameters in the network of natural blood vessels range from 10 microns (in capillaries) to 5 millimeters (in arterioles). 3D bioprinting can construct a similar hierarchical vascular network.

Son *et al.* first produced perfusable endothelialized channels (hundreds of microns in diameter) by printing sacrificial bio-inks containing endothelial cells and selectively removing the sacrificial material[70]. Then, they controlled the growth direction of vessels sprouting from the endothelialized channel by applying a gradient of angiogenic factors. Using the chemotaxis of endothelial cells, they employed the designed multi-cellular structure to create a multi-scale microvascular system consisting of a user-designed capillary network with good perfusion capacity[70]. Nie *et al.* constructed endothelial cell channels with diameters of 10, 20, 40, 100, 150, 250, and 500 μm by adjusting the printing speed and squeezing pressure to control the size of blood vessel diameters precisely, realizing the construction of the entire vascular system including large vessels and capillaries[71]. Szklanny *et al.* utilized 3D printing technology to construct a network of blood vessels inside tissues from a microscopic perspective and integrated the network of blood vessels, called "VascFold," from a mesoscopic perspective. The artificial tissue containing the vascular network can be anastomosed directly to the host vasculature through the small-diameter blood vessels[72].

5. Post-processing of bioprinting

Promoting the maturity of small-caliber blood vessels and microvascular networks is required in the construction of vascular grafts with complete biological functions.

Blood vessels' development and maturation process is very complex, involving the precise regulation of multiple biological, chemical, and physical stimuli in chronological order. Currently, bioprinting can only be used to create a static angiogenic environment and print blood vessel grafts containing pro-angiogenic factors. In addition, the vascular cells in grafts lack dynamic biochemical and mechanical stimuli that help recapitulate the physiological complexity of native blood vessels.

To address this challenge, the post-processing of bioprinting is significant. A bioreactor is a device specifically designed to cultivate and stimulate the development of engineered tissues. McFetridge *et al.* developed a modular bioreactor and perfusion system that allows vascular structures to grow and increase during an extended culture period[73]. Perfusion bioreactors can provide a constant supply of nutrients for blood vessel development and accurately replicate the hemodynamic stimulation of natural blood vessels, including pressure, strain, flow rate, and wall shear stress.

The physical environment in which blood vessel cells live is crucial for cell maturation. Hemodynamic shear stress is an essential determinant of endothelial function and phenotype. Wang *et al.* designed an *in vitro* flow adjustable vascular bioreactor system (VesselBRx) and demonstrated that under low-flow culture conditions, the intima of small-caliber vascular grafts thickened 2.5 times within 7 days, accompanied by a loss of 80% lumen area[74]. In contrast, under high-flow culture conditions, no neointima was observed. Under low-flow conditions, the endothelial cells no longer formed a single layer but extended into the cavity as a multi-layer structure. Under high-flow conditions, the endothelial cells physiologically remained as a monolayer with a vascular structure comparable to natural controls. This result indicates that the traditional static culture method cannot effectively maintain the normal physiological state of blood vessel cells, and bioreactors can provide sufficient hydrodynamic stimulation for vascular development and inhibit abnormal intimal hyperplasia[74]. Syedain *et al.* used pulsed fluid stimulation to promote the proliferation of fibroblasts in vascular grafts[75]. After 9 weeks of bioreactor culture, vascular grafts could withstand bursting pressures in the range of 1400–1600 mmHg, and their compliance was comparable to that of autologous arteries[75]. In addition, artificial blood vessels produced from this bioreactor have been transplanted surgically in ten patients with end-stage renal disease requiring hemodialysis access[76]. In light of the above, in-depth investigations into the cultivation and maturation of small-caliber vascular grafts in bioreactors are instrumental in effectively translating the fundamental bioprinted samples into the real-life clinical applications.

6. Conclusion

Cardiovascular diseases, a collection of non-infectious diseases with the highest mortality rate globally, put forward huge clinical demand for functional vascular grafts. As the technical bottleneck of organ transplantation, how to construct a microvascular network for material exchange in thick tissue is also the research focus of tissue engineering technology. 3D bioprinting uses computer modeling to accurately make complex pre-designed anatomical structures from cells and biological materials, providing a new way to overcome the shortage of blood vessel donors and the bottleneck of organ transplantation technology. In this review, we summarize and discuss functional vascular grafts and thick tissues prepared by 3D bioprinting technology from three aspects: large vessels and valves, small vessels, and microvascular networks, according to the anatomical caliber classification of the human vascular system. The large blood vessel grafts manufactured by 3D bioprinting can effectively solve the problems of inconsistent anatomy between electrospun grafts and host, and low cell survival rate. The complex heterogeneous structure of the valve is closely related to its special physiological functions. With the help of computed tomography scanning, computer modeling, and 3D bioprinting technology, it is possible to prepare biocompatible valves with good mechanical properties. 3D bioprinting technology can directly and accurately deposit vascular endothelial cells and smooth muscle cells to construct endothelialized small-diameter grafts with good biological properties, which effectively solve the high occlusive rate of small-caliber vascular grafts. High-resolution 3D bioprinting technology can design vascular micropatterns that guide angiogenesis and multi-dimensional vascular network layers that adapt to the host vascular system, which are the key differences between 3D bioprinting technology and other tissue engineering technologies. Combined with bioactive inks, 3D bioprinting technology can provide effective physical cues and biological stimuli for angiogenesis in thick tissues.

In the future, high-resolution printing technology and biological ink with good biological and mechanical properties will remain the research hotspot and key to 3D bioprinting technology. The emerging artificial intelligence can further improve the accuracy and resolution of bioprinting technology. In addition, the rise of smart materials has spawned the concept of 4D printing. Compared with the static structures generated by 3D bioprinting, 4D bioprinting allows 3D-printed structures to change their configuration or function over time in response to external stimuli, such as temperature, light, and water, thus bringing 3D printing to life. Endowing vascular grafts with the ability to respond to natural vascular environmental stimulation through innovative materials is also a possible future research direction for bioprinted

vascular grafts. Along with further improvement of existing biomaterials and molding processes, bioreactors can effectively promote the maturation of printed blood vessel, and fabrication of blood vessel grafts as well as thick, vascularized tissues and organs with complete biological functions will become possible.

Acknowledgments

We are very grateful to Professor Wen Zeng for her careful guidance.

Funding

This work was supported by the National Key Research and Development Plan Young Scientists Program (No. 2021YFA1102100), the National Defense Fund for Outstanding Scholars (No. 2021-JCJQ-Z0-003), the Chongqing Science Fund for Distinguished Young Scholars (No. cstc2020jcyj-jqX0023), and the Chongqing University Innovation Research Group Project (No. CXQT21010). Figures were made with Adobe Illustrator 2021.

Conflict of interest

The authors declare no conflict of interest.

Author contributions:

Conceptualization: Wen Zeng
Funding acquisition: Wen Zeng
Project administration: Wen Zeng
Supervision: Wen Zeng
Visualization: Junpeng Zhu
Writing – original draft: Junpeng Zhu, Xinwang Wang, Lin Lin
Writing – review & editing: Junpeng Zhu, Xinwang Wang, Lin Lin

Ethics approval and consent to participate

Not applicable.

Consent for publication

Not applicable.

Availability of data

Data availability is not applicable to this article as no new data were created or analyzed in this study.

References

1. Fazal F, Raghav S, Callanan A, *et al.*, 2021, Recent advancements in the bioprinting of vascular grafts. *Biofabrication*, 13(032003): 032003–032021.

https://doi.org/10.1088/1758-5090/ac0963

2. Nienaber C, Clough R, Sakalihasan N, 2016, Aortic dissection. *Nat Rev Dis Primers*, 2: 16053-16070.

https://doi.org/10.1038/nrdp.2016.53

3. Devillard CD, Marquette CA, 2021, Vascular tissue engineering: Challenges and requirements for an ideal large scale blood vessel. *Front Bioeng Biotechnol*, 9(October): 1–21.

https://doi.org/10.3389/fbioe.2021.721843

4. Stout KK, Otto CM, 2007, Indications for aortic valve replacement in aortic stenosis. *J Intens Care Med*, 22(1): 14–25.

https://doi.org/10.1177/0885066606295298

5. Maselli D, Minzioni G, 2006, A technique to reposition sinotubular junction in aortic valve reimplantation procedures with the de Paulis Valsalva graft. *Eur J Cardiothorac Surg*, 29(1): 107–109.

https://doi.org/10.1016/j.ejcts.2005.10.028

6. Kehl D, Weber B, Hoerstrup SP, 2016, Bioengineered living cardiac and venous valve replacements: Current status and future prospects. *Cardiovasc Pathol*, 25(4): 300–305.

https://doi.org/10.1016/j.carpath.2016.03.001

7. Mallis P, Kostakis A, Stavropoulos-giokas C, 2020, Future perspectives in small-diameter vascular graft engineering. *Bioengineering*, 7(4): 1–40.

https://doi.org/10.3390/bioengineering7040160

8. Kannan RY, Salacinski HJ, Butler PE, *et al.*, 2005, Current status of prosthetic bypass grafts: A review. *J Biomed Mater Res - Part B Appl Biomater*, 74(1): 570–581.

https://doi.org/10.1002/jbm.b.30247

9. Gemelli M, Gallo M, Addonizio M, 2023, Venous external support in coronary artery bypass surgery: A systematic review and meta-analysis. *Curr Probl Cardiol*, 101687.

https://doi.org/10.1016/j.cpcardiol.2023.101687

10. Pashneh-Tala S, MacNeil S, Claeyssens F, 2016, The tissue-engineered vascular graft - Past, present, and future. *Tissue Eng - Part B: Rev*, 22(1): 68–100.

https://doi.org/10.1089/ten.teb.2015.0100

11. Weekes A, Bartnikowski N, Pinto N, *et al.*, Biofabrication of small diameter tissue-engineered vascular grafts. *Acta Biomater*, 138(15): 92–111.

https://doi.org/10.1016/j.actbio.2021.11.012

12. Barrs RW, Jia J, Silver SE, *et al.*, 2020, Biomaterials for bioprinting microvasculature. *Chem Rev*, 120(19): 10887–10949.

https://doi.org/10.1021/acs.chemrev.0c00027

13. Li X, Liu L, Zhang X, *et al.*, 2018, Research and development of 3D printed vasculature constructs. *Biofabrication*, 10(032002): 032002–032014.

https://doi.org/10.1088/1758-5090/aabd56

14. Wang P, Sun Y, Shi X, *et al.*, 2021, 3D printing of tissue engineering scaffolds: A focus on vascular regeneration. *Biodes Manuf*, 4(2):. 344.

https://doi.org/10.1007/S42242-020-00109-0

15. Li H, Tan C, Li L, 2018, Review of 3D printable hydrogels and constructs. *Mater Des*, 159(5): 20–38.

https://doi.org/10.1016/j.matdes.2018.08.023

16. Zieliński PS, Gudeti PKR, Rikmanspoel T, *et al.*, 2023, 3D printing of bio-instructive materials: Toward directing the cell. *Bioact Mater*, 19(1): 292–327.

https://doi.org/10.1016/j.bioactmat.2022.04.008

17. Decante G, Costa JB, Silva-Correia J, *et al.*, 2021, Engineering bioinks for 3D bioprinting. *Biofabrication*, 13(032001): 032001–032031.

https://doi.org/10.1088/1758-5090/abec2c

18. Chen YH, Chang HH, Kuo CC, *et al.*, 2022, Impact of prosthesis-patient mismatch after transcatheter aortic valve replacement in Asian patients. *Annal Thorac Surg*, 114(5): 1612–1619.

https://doi.org/10.1016/j.athoracsur.2021.09.016

19. Kucukgul C, Ozler S, Inci I, *et al.*, 2015, 3D bioprinting of biomimetic aortic vascular constructs with self-supporting cells. *Biotechnol Bioeng*, 112(4): 811–821.

https://doi.org/10.1002/bit.25493

20. Kucukgul C, Ozler B, Karakas HE, *et al.*, 2013, 3D hybrid bioprinting of macrovascular structures. *Procedia Eng*, 59: 183–192.

https://doi.org/10.1016/j.proeng.2013.05.109

21. Oropeza BP, Adams JR, Furth ME, *et al.*, 2022, Bioprinting of decellularized porcine cardiac tissue for large-scale aortic models. *Front Bioeng Biotechnol*, 10(March): 1–9.

https://doi.org/10.3389/fbioe.2022.855186

22. Potere F, Belgio B, Croci G, 2022, 3D bioprinting of multi-layered segments of a vessel-like structure with ECM and novel derived bioink. *Front Bioeng Biotechnol*, 10(August): 1–13.

https://doi.org/10.3389/fbioe.2022.918690

23. Hockaday LA, Kang K, Colangelo N, 2012, Rapid 3D printing of anatomically accurate and mechanically heterogeneous aortic valve hydrogel scaffolds. *Biofabrication*, 4(3): 035005–035017.

https://doi.org/10.1088/1758-5082/4/3/035005

24. Vukicevic M, Mehta SM, Grande-Allen KJ, *et al.*, 2022, Development of 3D printed mitral valve constructs for transcatheter device modeling of tissue and device deformation. *Ann Biomed Eng*, 50(4): 426–439.

https://doi.org/10.1007/s10439-022-02927-y

25. Duan B, Hockaday LA, Kang KH, *et al.*, 2013, 3D bioprinting of heterogeneous aortic valve conduits with alginate/gelatin hydrogels. 101(5): 1255–1264.

https://doi.org/10.1002/jbm.a.34420.3D

26. Rioux Y, Fradette J, Maciel Y, *et al.*, 2022, Biofabrication of sodium alginate hydrogel scaffolds for heart valve tissue engineering. *Int J Mol Sci*, 23(8567): 8567–8581.

https://doi.org/10.3390/ijms23158567

27. Zhou X, Nowicki M, Sun H, *et al.*, 2020, 3D bioprinting-tunable small-diameter blood vessels with biomimetic biphasic cell layers. *Appl Mater Interfaces*, 12(41): 45904–45915.

https://doi.org/10.1021/acsami.0c14871

28. Kamaraj M, Giri PS, Mahapatra S, *et al.*, 2022, Bioengineering strategies for 3D bioprinting of tubular construct using tissue-specific decellularized extracellular matrix. *Int J Biol Macromol*, 223(PA): 1405–1419.

https://doi.org/10.1016/j.ijbiomac.2022.11.064

29. Gold KA, Saha B, Krishna N, 2021, 3D bioprinted multi-cellular vascular models. *Adv Healthc Mater*, 10(21): e2101141.

https://doi.org/10.1002/ADHM.202101141

30. Li L, Qin S, Peng J, 2020, Engineering gelatin-based alginate/carbon nanotubes blend bioink for direct 3D printing of vessel constructs. *Int J Biol Macromol*, 145(15): 262–271.

https://doi.org/10.1016/j.ijbiomac.2019.12.174

31. Liu Y, Zhang Y, An Z, *et al.*, 2021, Slide-ring structure-based double-network hydrogel with enhanced stretchability and toughness for 3d-bio-printing and its potential application as artificial small-diameter blood vessels. *Appl Bio Mater*, 4(12): 8597–8606.

https://doi.org/10.1021/acsabm.1c01052

32. Freeman S, Ramos R, Alexis Chando P, 2019, A bioink blend for rotary 3D bioprinting tissue engineered small-diameter vascular constructs. *Acta Biomater*, 95: 152–164.

https://doi.org/10.1016/j.actbio.2019.06.052

33. Zhou Y, Gui Q, Yu W, 2019, Interfacial diffusion printing: An efficient manufacturing technique for artificial tubular grafts. *ACS Biomater Sci Eng*, 5(11): 6311–6318.

https://doi.org/10.1021/acsbiomaterials.9b01293

34. Jin Q, Jin G, Ju J, 2022, Bioprinting small-diameter vascular vessel with endothelium and smooth muscle by the approach of two-step crosslinking process. *Biotechnol Bioeng*, 119(6): 1673–1684.

https://doi.org/10.1002/bit.28075

35. Zhang Z, Wu C, Dai C, 202, A multi-axis robot-based bioprinting system supporting natural cell function preservation and cardiac tissue fabrication. *Bioact Mater*, 18(1): 138.

https://doi.org/10.1016/J.BIOACTMAT.2022.02.009

36. Fazal F, Diaz Sanchez FJ, Waqas M, *et al.*, 2021, A modified 3D printer as a hybrid bioprinting-electrospinning system for use in vascular tissue engineering applications. *Med Eng Phys*, 94: 52–60.

https://doi.org/10.1016/j.medengphy.2021.06.005

37. Jin Q, Fu Y, Zhang G, 2022, Nanofiber electrospinning combined with rotary bioprinting for fabricating small-diameter vessels with endothelium and smooth muscle. *Compos B Eng*, 234(1): 109691-109700.

https://doi.org/10.1016/j.compositesb.2022.109691

38. Größbacher G, Bartolf-Kopp M, Gergely C, 2023, Volumetric printing across melt electrowritten scaffolds fabricates multi-material living constructs with tunable architecture and mechanics. *Adv Mater,* 2300756–2300773.

https://doi.org/10.1002/adma.202300756

39. Cao P, Tao L, Gong J, 2021, 4D printing of a sodium alginate hydrogel with step-wise shape deformation based on variation of crosslinking density. *ACS Appl Polym Mater*, 3(12): 6167–6175.

https://doi.org/10.1021/acsapm.1c01034

40. Kitana W, Apsite I, Hazur J, *et al.*, 2023, 4D biofabrication of t-shaped vascular bifurcation. *Adv Mater Technol*, 8(1): 2200429-2200439.

https://doi.org/10.1002/admt.202200429

41. Kirillova A, Maxson R, Stoychev G, *et al.*, 2017, 4D biofabrication using shape-morphing hydrogels. *Adv Mater*, 29(46): 1703443-1703450.

https://doi.org/10.1002/adma.201703443

42. Wu Z, Cai H, Ao Z, *et al.*, 2021, Microfluidic printing of tunable hollow microfibers for vascular tissue engineering. *Adv Mater Technol*, 6(8): 2000683-2000691.

https://doi.org/10.1002/admt.202000683

43. Muthusamy S, Kannan S, Lee M, 2021, 3D bioprinting and microscale organization of vascularized tissue constructs using collagen-based bioink. *Biotechnol Bioeng*, 118(8): 3150–3163.

https://doi.org/10.1002/bit.27838

44. Cidonio G, Glinka M, Kim Y, 2020, Nanoclay-based 3D printed scaffolds promote vascular ingrowth ex vivo and generate bone mineral tissue in vitro and in vivo. *Biofabrication*, 12(3): 035010-035025.

https://doi.org/10.1088/1758-5090/ab8753

45. Liu C, Campbell S, Li J, 2022, High throughput omnidirectional printing of tubular microstructures from elastomeric polymers. *Adv Healthc Mater,* 11(23): 2201346–2201359.

https://doi.org/10.1002/adhm.202201346

46. Barrs RW, Jia J, Ward M, 2021, Engineering a chemically defined hydrogel bioink for direct bioprinting of microvasculature. *Biomacromolecules*, 22(2): 275–288.

https://doi.org/10.1021/acs.biomac.0c00947

47. Yu H, Gong W, Mei J, 2022, The efficacy of a paeoniflorin-sodium alginate-gelatin skin scaffold for the treatment of diabetic wound: An in vivo study in a rat model. *Biomed Pharmacotherap*, 151: 113165-113171.

https://doi.org/10.1016/j.biopha.2022.113165

48. Cheng F, Cao X, Li H, 2019, Generation of cost-effective paper-based tissue models through matrix-assisted sacrificial 3D printing. *Nano Lett*, 19(6): 3603–3611.

https://doi.org/10.1021/acs.nanolett.9b00583

49. Zheng J, Liu Y, Hou C, 2022, Ovary-derived decellularized extracellular matrix-based bioink for fabricating 3D primary ovarian cells-laden structures for mouse ovarian failure correction. *Int J Bioprint*, 8(3): 269–282.

https://doi.org/10.18063/IJB.V8I3.597

50. Oliveira H, Medina C, Labrunie G, 2022, Cell-assembled extracellular matrix (CAM): A human biopaper for the biofabrication of pre-vascularized tissues able to connect to the host circulation in vivo. *Biofabrication*, 14(1): 015005-015019.

https://doi.org/10.1088/1758-5090/ac2f81

51. Li S, Wang W, Li W, 2021, Fabrication of thermoresponsive hydrogel scaffolds with engineered microscale vasculatures. *Adv Funct Mater*, 31(27): 2102685-2102699.

https://doi.org/10.1002/adfm.202102685

52. Thomas A, Orellano I, Lam T, 2020, Vascular bioprinting with enzymatically degradable bioinks via multi-material projection-based stereolithography. *Acta Biomater*, 117: 121–132.

https://doi.org/10.1016/j.actbio.2020.09.033

53. Zeng X, Meng Z, He J, 2022, Embedded bioprinting for designer 3D tissue constructs with complex structural organization. *Acta Biomater*, 140: 1–22.

https://doi.org/10.1016/j.actbio.2021.11.048

54. Zhang S, Qi C, Zhang W, 2022, In-situ endothelialization of freeform 3D network of interconnected tubular channels via interfacial coacervation by aqueous-in-aqueous embedded bioprinting. *Adv Mater*, 35(7): 2209263–2209269.

https://doi.org/10.1002/adma.202209263

55. Hinton TJ, Jallerat Q, Palchesko R, 2015, Three-dimensional printing of complex biological structures by freeform reversible embedding of suspended hydrogels. *Sci Adv*, 1(9): e1500758-e1500767.

https://doi.org/10.1126/sciadv.1500758

56. Lee A, Hudson A, Shiwarski D, 2019, 3D bioprinting of collagen to rebuild components of the human heart. 365(6452): 482–487.

https://doi.org/10.1126/science.aav9051

57. Zhu W, Ma X, Gou M, *et al.*, 2016, 3D printing of functional biomaterials for tissue engineering. *Curr Opin Biotechnol*, 40: 103–112.

https://doi.org/10.1016/j.copbio.2016.03.014

58. Dobos A, Gantner F, Markovic M, 2020, On-chip high-definition bioprinting of microvascular structures. *Biofabrication*, 13(1).

https://doi.org/10.1088/1758-5090/abb063

59. Xue D, Wang Y, Zhang J, *et al.*, 2018, Projection-based 3D printing of cell patterning scaffolds with multi-scale channels. *ACS Appl Mater Interfaces*, 10(23): 19428–19435.

https://doi.org/10.1021/acsami.8b03867

60. Anada T, Pan C, Stahl A, 2019, Vascularized bone-mimetic hydrogel constructs by 3D bioprinting to promote osteogenesis and angiogenesis. *Int J Mol Sci*, 20(5): 1096-1104.

https://doi.org/10.3390/ijms20051096

61. Liu Y, Zhang Y, Mei T, 2022, hESCs-derived early vascular cell spheroids for cardiac tissue vascular engineering and myocardial infarction treatment. *Adv Sci*, 9(9): 2104299-2104311.

https://doi.org/10.1002/advs.202104299

62. Benmeridja L, De Moor L, De Maere E, 2022, High-throughput fabrication of vascularized adipose microtissues for 3D bioprinting. *J Tissue Eng Regen Med*, 14(6): 840–854.

https://doi.org/10.1002/term.3051

63. de Moor L, Smet J, Plovyt M, 2021, Engineering microvasculature by 3D bioprinting of prevascularized spheroids in photo-crosslinkable gelatin. *Biofabrication*, 13(4): 045021-045041.

https://doi.org/10.1088/1758-5090/ac24de

64. Dogan L, Scheuring R, Wagner N, 2021, Human iPSC-derived mesodermal progenitor cells preserve their vasculogenesis potential after extrusion and form hierarchically organized blood vessels. *Biofabrication*, 13(4): 045028-045044.

https://doi.org/10.1088/1758-5090/ac26ac

65. O'Connor C, Brady E, Zheng Y, *et al.*, 2022, Engineering the multi-scale complexity of vascular networks. *Nat Rev Mater*, 7(9): 702–716.

https://doi.org/10.1038/s41578-022-00447-8

66. Mirabella T, Macarthur J, Cheng D, 2017, 3D-printed vascular networks direct therapeutic angiogenesis in ischaemia. *Nat Biomed Eng*, 1(6): 0083-0090

https://doi.org/10.1038/s41551-017-0083

67. Kérourédan O, Hakobyan D, Remy M, 2019, In situ prevascularization designed by laser-assisted bioprinting: Effect on bone regeneration. *Biofabrication*, 11(4): 045002-045019.

https://doi.org/10.1088/1758-5090/ab2620

68. Chansoria P, Asif S, Gupta N, *et al.*, 2022, Multi-scale anisotropic tissue biofabrication via bulk acoustic patterning of cells and functional additives in hybrid bioinks. *Adv Healthc Mater*, 11(10): 2102351-2102367.

https://doi.org/10.1002/adhm.202102351

69. Maiullari F, Costantini M, Milan M, 2018, A multi-cellular 3D bioprinting approach for vascularized heart tissue engineering based on HUVECs and iPSC-derived cardiomyocytes. *Sci Rep*, 8(1): 13532-13547 .

https://doi.org/10.1038/s41598-018-31848-x

70. Son J, Hong SJ, Lim JW, *et al.*, 2021, Engineering tissue-specific, multi-scale microvasculature with a capillary network for prevascularized tissue. *Small Methods*, 5(10): 2100632-2100643.

https://doi.org/10.1002/smtd.202100632

71. Nie J, Gao Q, Xie C, 2020, Construction of multi-scale vascular chips and modelling of the interaction between tumours and blood vessels. *Mater Horiz*, 7(1): 82–92.

https://doi.org/10.1039/c9mh01283d

72. Szklanny AA, Machour M, Redenski I, 2021, 3D bioprinting of engineered tissue flaps with hierarchical vessel networks (VesselNet) for direct host-to-implant perfusion. *Adv Mater*, 33(42): 2102661-2102679.

https://doi.org/10.1002/adma.202102661

73. McFetridge PS, Abe K, Horrocks M, *et al.*, 2007, Vascular tissue engineering: Bioreactor design considerations for extended culture of primary human vascular smooth muscle cells. *ASAIO J*, 53(5): 623–630.

https://doi.org/10.1097/MAT.0b013e31812f3b7e

74. Wang J, Kural M, Wu J, 2021, An ex vivo physiologic and hyperplastic vessel culture model to study intra-arterial stent therapies. *Biomaterials*, 275: 120911-120924.

https://doi.org/10.1016/j.biomaterials.2021.120911

75. Syedain ZH, Meier LA, Bjork JW, *et al.*, 2011, Implantable arterial grafts from human fibroblasts and fibrin using a multi-graft pulsed flow-stretch bioreactor with non-invasive strength monitoring. *Biomaterials*, 32(3): 714–722.

https://doi.org/10.1016/j.biomaterials.2010.09.019

76. Kawecki F, L'Heureux N, 2023, Current biofabrication methods for vascular tissue engineering and an introduction to biological textiles. *Biofabrication*, 15(2): 022004-022025.

https://doi.org/10.1088/1758-5090/acbf7a

ACCSCIENCE PUBLISHING

International Journal of Bioprinting

REVIEW ARTICLE

3D bioprinting for auricular reconstruction: A review and future perspectives

Anna Onderková, and Deepak M. Kalaskar*

University College London, Royal Free Hospital, Rowland Hill Street, London NW3 2PF, UK

(This article belongs to the *Special Issue: Advances in bioprinting technology*)

Abstract

Congenital abnormalities or acquired trauma to the auricle can result in a need for ear reconstruction and negatively impact a person's quality of life. Autografting, alloplastic implants, and prostheses are available to treat these issues, but each requires multiple surgical stages and has limitations and complications. Three-dimensional (3D) bioprinting promises to allow the creation of living, patient-specific ear substitutes that could reduce operative morbidity. In this review, we evaluate the current state of 3D bioprinting methods through a systematic search and review of 27 studies, aiming to examine this emerging technology within the context of existing reconstructive options. The included studies were all non-randomized experimental studies, except for a single pilot clinical trial. Most of these studies involved both *in vitro* and *in vivo* experiments demonstrating the potential of 3D bioprinting to create functional and anatomically accurate engineered cartilaginous frameworks for surgical implantation. Various ways of optimizing printing were identified, from choosing the most suitable material and cell type for the construct to addressing scaffold deformation and shrinkage issues. 3D printing has the potential to revolutionize reconstructive ear surgery by creating functional and aesthetically pleasing auricles. While more research into printing parameters, bioinks, cell types, and materials could optimize results, the next step is to conduct long-term *in vivo* clinical trials in humans.

Keywords: 3D bioprinting; Auricular Reconstruction; Tissue Engineering; Bioinks; Patient-specific Implants; Cartilaginous Frameworks

***Corresponding authors:**
Anna Onderková
(annaonderkova@doctors.org.uk)

Deepak M. Kalaskar
(d.kalaskar@ucl.ac.uk)

Citation: Onderková A, Kalaskar DM., 2023, 3D bioprinting for auricular reconstruction: A review and future perspectives. *Int J Bioprint*, 9(6): 0898.
https://doi.org/10.36922/ijb.0898

Received: May 4, 2023
Accepted: June 20, 2023
Published Online: August 7, 2023

Copyright: © 2023 Author(s). This is an Open Access article distributed under the terms of the Creative Commons Attribution License, permitting distribution, and reproduction in any medium, provided the original work is properly cited.

Publisher's Note: AccScience Publishing remains neutral with regard to jurisdictional claims in published maps and institutional affiliations.

1. Introduction

The external ear can be congenitally missing (anotia) or malformed (microtia) or may sustain acquired damage in the form of trauma, burns, or after skin cancer excision[1,2]. The absence of an external ear can impact a patient's quality of life through impaired conductive hearing[3], loss of symmetry, difficulty wearing glasses or hearing aids, and the combined psychosocial and developmental consequences of all of these factors, particularly in children[1,4]. The auricle has significant aesthetic value[5], and its absence can be seriously stigmatizing in adults[3,5]. Conversely, following ear reconstruction, 74% of adults and 91% of children report improved self-confidence and social interactions[6].

Table 1. An overview of chief differences between landmark surgical methods in auricular autografting (adapted from Dr. Nagata's original sketches[13])

Method		Tanzer (1959)	Brent (1980)	Nagata (1992)
Costal cartilage frame				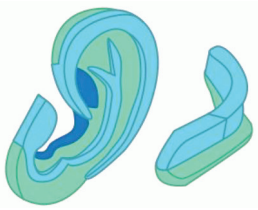
Total number of operations		6	4	2
Operation time	**1st stage**	1 h—Lobule transposition	3 h—Lobule transposition	8 h—Costal cartilage graft
	2nd stage	3 h—Costal cartilage graft	1 h—Costal cartilage graft	8 h—Ear projection
	3rd stage	2 h—Tagus construction	2 h—Tagus construction	
	4th stage	2 h—Separating the ear	2 h—Separating the ear	
	5th stage	1 h—Temporary tunnel		
	6th stage	2 h—Closing the tunnel		
Number of costal cartilages harvested		3	3	4 for 1st stage (ribs 6–9) 2 for 2nd stage (ribs 4 and 5)
Chest wall deformity		Occur	Occur	Do not occur because the perichondrium is left in place and refilled using diced cartilage remnants from cutting before closing. Thus, the cartilage regenerates over time.
Resorption risk		High due to insufficient blood supply	High due to insufficient blood supply	No resorption due to good blood supply
Wire sutures used		5	5	85 needed for 1st stage 20 needed for 2nd stage

1.1. Current reconstructive surgeon's toolbox

Current options for treating auricular deformities or absence include cartilage autografting, alloplastic polyethylene implants such as Medpor, and prostheses[3,7].

Most (91.3%) surgeons prefer autografting over alloplasty[7], partly because autografted cartilage has a lower risk of being extruded through the skin or of soft-tissue necrosis, whereas Medpor is susceptible to minor trauma and secondary infections, dehiscence, and implant extrusion[8]. Medpor implants typically require coverage with a temporoparietal fascial flap to prevent such complications[3]. Even then, results are suboptimal, as manufacturing limitations mean implants are not customized, and aesthetic results are a compromise at best[9]. Furthermore, the material is inherently stiff[10] and easily triggers immune reactions[11].

The alternative route is that of prosthetics, which have evolved considerably in recent years in terms of cosmetic results. Prostheses can be divided into those applied with a silicon adhesive and the surgically osseointegrated. This is particularly valuable in patients with inadequate available loco-regional skin, such as in burns or in cases where autologous reconstruction was unsuccessful. They are generally a last resort or reserved for patients who prefer minimally invasive treatment[5].

1.2. Current surgical techniques in autografting

The main reconstructive techniques in sculpting rib cartilage into an autografted auricle are those by Brent, Tazner, and Nagata, with notable variations like that by Firmin to improve and adjust results[3,12]. While this complex reconstruction requires specific surgical and artistic skills—thus limiting the field to a small number of experienced surgeons—the final result is still often less than perfect[3]. This is because the reconstruction is far from simple, regardless of technique.

The operations require substantial rib cartilage resection (see Table 1). Thus, the initiation of ear reconstruction must often be delayed until the child is of an adequate age to have enough usable cartilage. Furthermore, the procedure involving the chest wall as a donor site can

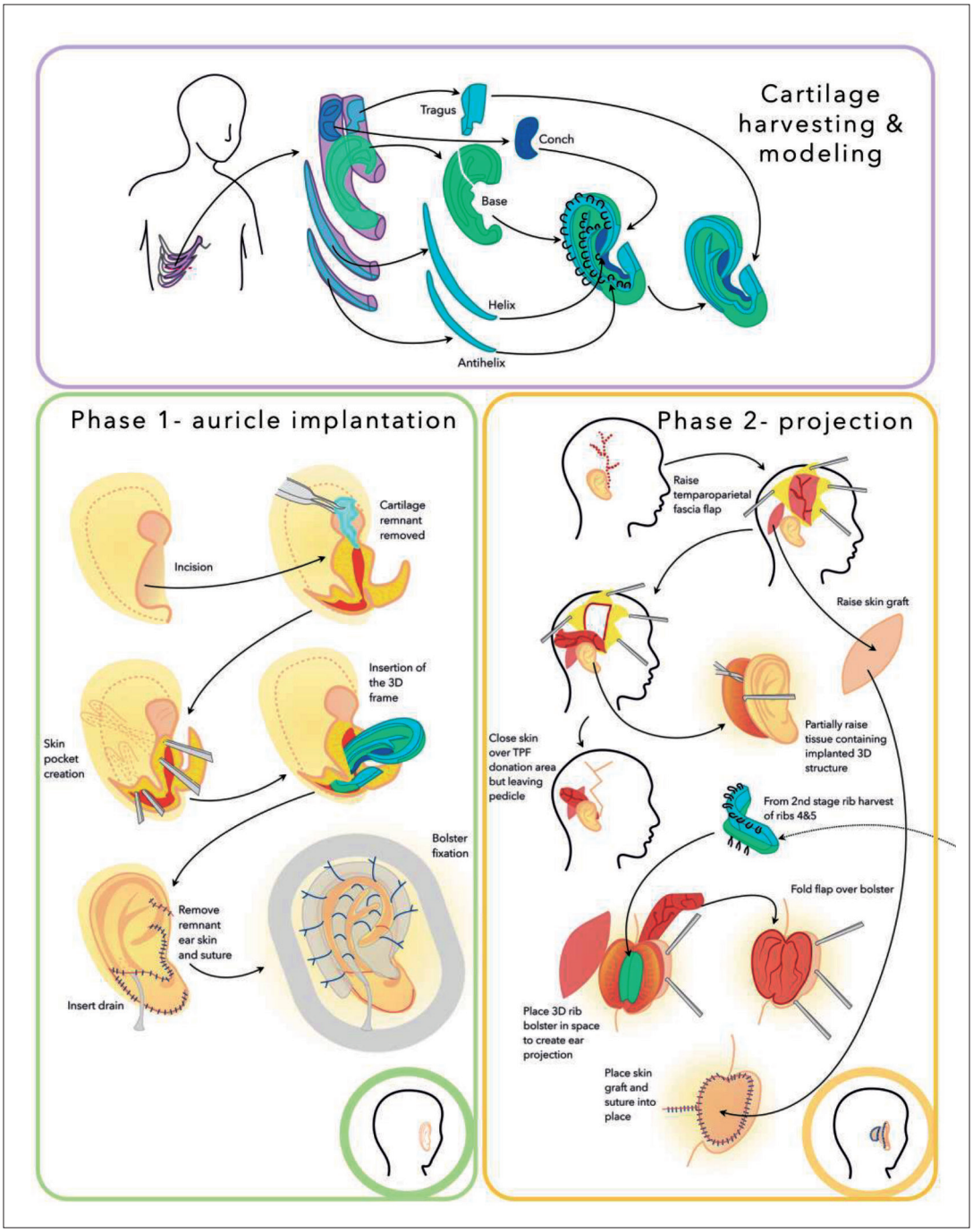

Figure 1. Nagata's technique (artwork inspired by Dr. Nagata's original sketches[13]). Abbreviation: TPF, temporoparietal fascia flap.

lead to significant morbidity, with potential complications ranging from severe postoperative pain to life-threatening conditions such as infections and pneumothorax[4,10].

Lengthy operative time is another drawback; at least two-staged surgeries are required. For example, in the Nagata technique[13] (see Figure 1), harvested and reshaped cartilage is introduced under the skin in the first stage. In the second stage, the ear projection is refined, thus not only improving aesthetic results but also limiting potential strain on overlying skin[4].

1.3. How 3D printing could revolutionize the field over the next decade

One of the main challenges in auricular reconstruction is the lack of suitable donor tissue. Three-dimensional (3D) printing

technology is able to produce biocompatible scaffolds, which can then be seeded with cells, or molds in which cartilage can be cultivated into the desired shape. Several time-consuming, multi-staged surgical steps (particularly rib harvesting and shaping) could be bypassed[3,4].

Before engineering a substitute, the structure of the auricle should be considered. At the most basic level, the structure is skin-covered cartilage with associated vasculature. The complex structure has distinct 3D parts such as the helix, antihelix, concha, tragus, and lobule. It is primarily composed of elastic cartilage covered by skin, with a thin layer of connective tissue, the perichondrium, in between. Auricular cartilage comprises proteoglycans, type II collagen, and an elastin network. Elastic fibers allow the ear to undergo extensive deformation, while glycosaminoglycans (GAG) confer compressibility[9]. Both properties, along with the complex shape, are important for the auricle's functionality and, unfortunately, from a reconstructive perspective, are quite distinct from most other cartilages found in the human body[10].

Cartilage is an avascular and aneural tissue, and thus has a poor intrinsic self-repair capacity[14]. However, from a tissue engineering perspective, this avascularity is advantageous because if new elastic cartilage can be grown or printed *in vitro*, a functioning vasculature does not have to be generated with it. Vessels around the engineered ear should be able to provide essential substances to chondrocytes through diffusion[15].

3D printing, as an additive manufacturing technique, fabricates physical constructs from digital models, layer by layer. This technology potentially facilitates the creation of patient-specific, anatomically complex scaffolds. However, limitations include time intensity for complex structures, potential discrepancies between the mechanical properties of printed materials and native tissues, and resolution constraints that may impact the replication of intricate auricular structures. Despite these challenges, 3D printing presents a unique advantage in customization compared to traditional fabrication methods[3,4,16].

At least theoretically, 3D-printed auricles promise relative ease of implantation, anatomic accuracy and compatibility, and thus, excellent aesthetic results.

2. Methodology

This comprehensive literature review sought to investigate the potential role of 3D printing in creating implantable constructs for reconstructive auricular surgery and how far it is from being routinely implemented in clinical practice.

In order to answer this, a broad systematic search in the PubMed, Cochrane, and Web of Science databases using the search terms ((3D *print*) OR (additive manufacturing)) AND ((auricle OR pinna OR ear) reconstruction) was conducted. The date of the last search was 22 October 2022, but the search was not otherwise time-limited. The identified papers were then imported into Covidence software by Cochrane to conduct the review and follow the PRISMA standard. This process identified 202 original studies. After duplicates were removed, the titles and abstracts of 141 studies were screened. Seventy-three studies were identified and underwent full-text review. Of these, 27 studies were finally included (see Figure 2 for workflow and inclusion and exclusion criteria).

3D printing technologies (see Figure 3) can aid and enhance all of the existing reconstructive options. However, in this review, focus was placed on methods that could directly enhance surgical reconstruction by creating new implantable tissue-engineered personalized auricles for patients. Thus, additional studies on, for example, surgeons using costal cartilage models to practice autografting[17], to create templates and guides along which to cut[18], or to plan the placement of bone-anchored prosthetic devices[19] were excluded.

3. Results

In terms of design, all of the studies included (see Table 2) were non-randomized experimental studies, except for the single landmark pilot clinical trial in human subjects by Zhou *et al.*[20]. While the majority (n = 15) of the studies involved both *in vitro* and *in vivo* experiments (including the human study), some were purely *in vitro* (n = 6) and some purely *in vivo* (n = 6) animal studies.

Several animal models were used, with the majority being in rodents (n = 16) but also in rabbits (n = 2), sheep (n = 1), pigs (n = 1), and goats (n = 1). It should be noted that the species into which the scaffold was implanted did not always match the donor tissue for the scaffold. For example, miniature pigs' cartilage was inserted into scaffolds that were eventually implanted into mice[11]. Several rodent model studies noted that since rodents' skin is different to human skin (lacking sweat glands, proportionally thinner, containing an additional muscle layer, and healing by withering), they may not be the ideal animal model[3]. On the other hand, sheep have similar fascial characteristics to humans[21]. However, even then, the physiology differs; thus, all studies noted that the goal was to establish human trials.

3.1. Direct versus indirect printing

Five of the 27 included studies utilized indirect 3D printing, in which a negative mold of the desired auricular shape is printed, meaning that the accurate and

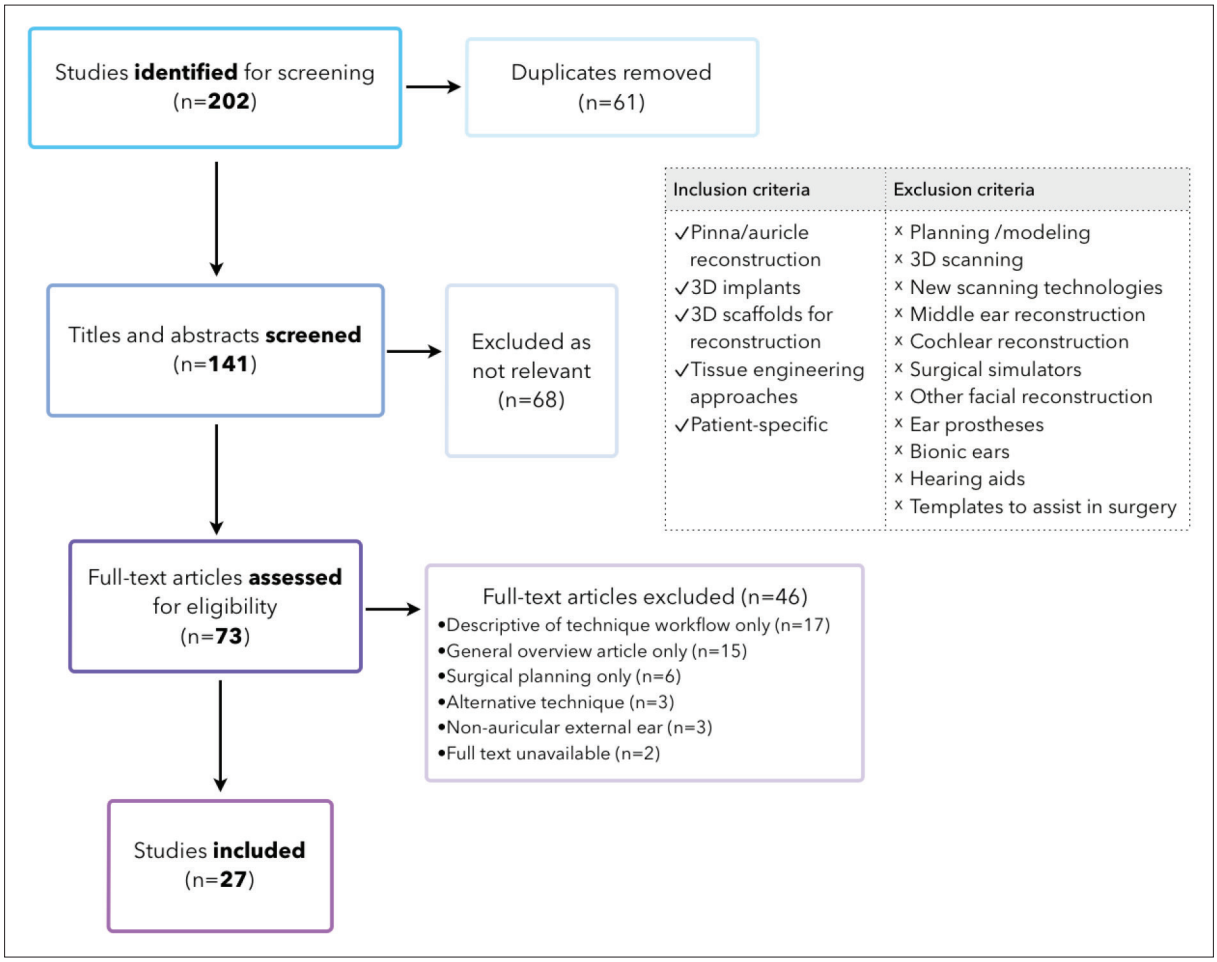

Figure 2. Preferred Reporting Items for Systematic Reviews and Meta-Analyses (PRISMA) flow diagram of article selection process, along with inclusion and exclusion criteria.

personalized shape can be utilized without being limited to a specific medium. The mold can thus be printed in any non-biocompatible material, such as a resin[20,22], a fused deposition modeling (FDM)-printed meshed co-polymer like butenediolvinylalcohol (BVOH)[23] or a powder via selective laser sintering[24]. Alternatively, the ear shape can be printed in polycaprolactone (PCL) and then used to create a set of silicon casting molds[11]. The mold can then be used to cast or grow the final auricular scaffold, which can then be cell-seeded[25], or alternative materials like diced cartilage and platelet-rich plasma may be used instead[24].

Conversely, the majority (81.5%, n = 22) of the studies utilized direct printing. This was mostly extrusion-based printing, in which a material is extruded through a nozzle onto a print bed, and the scaffold is built up layer by layer[9]. In some cases, the scaffold was printed alone (n = 4). Most of the time, it was printed first and then seeded with cells (n = 13)[26]. However, a large proportion of the studies (n = 10) were focused on true bioprinting, in which the cells were already suspended in a hydrogel, and this bioink and the scaffold were printed together[27].

Several of the studies introduced specific modifications to their bioprinting approach, such as incorporating multiple printer heads within a "tissue building system" that facilitated the simultaneous printing of various materials. This allowed Lee *et al.* (2014), for example, to create an ear-shaped structure with two cell types in hydrogels and polyethylene glycol (PEG) scaffold to be printed together[26]. Similarly, other mechanical alterations, like creating and maintaining a negative pressure environment, helped to promote cartilage growth and maturation[25].

Some studies overcame the pliable nature of some bioinks by using photocurable elements to harden the scaffold either during or after printing. For example, Xia *et al.* (2018) created a photo-crosslinkable gelatin containing the chondrocytes for printing and thus adapted

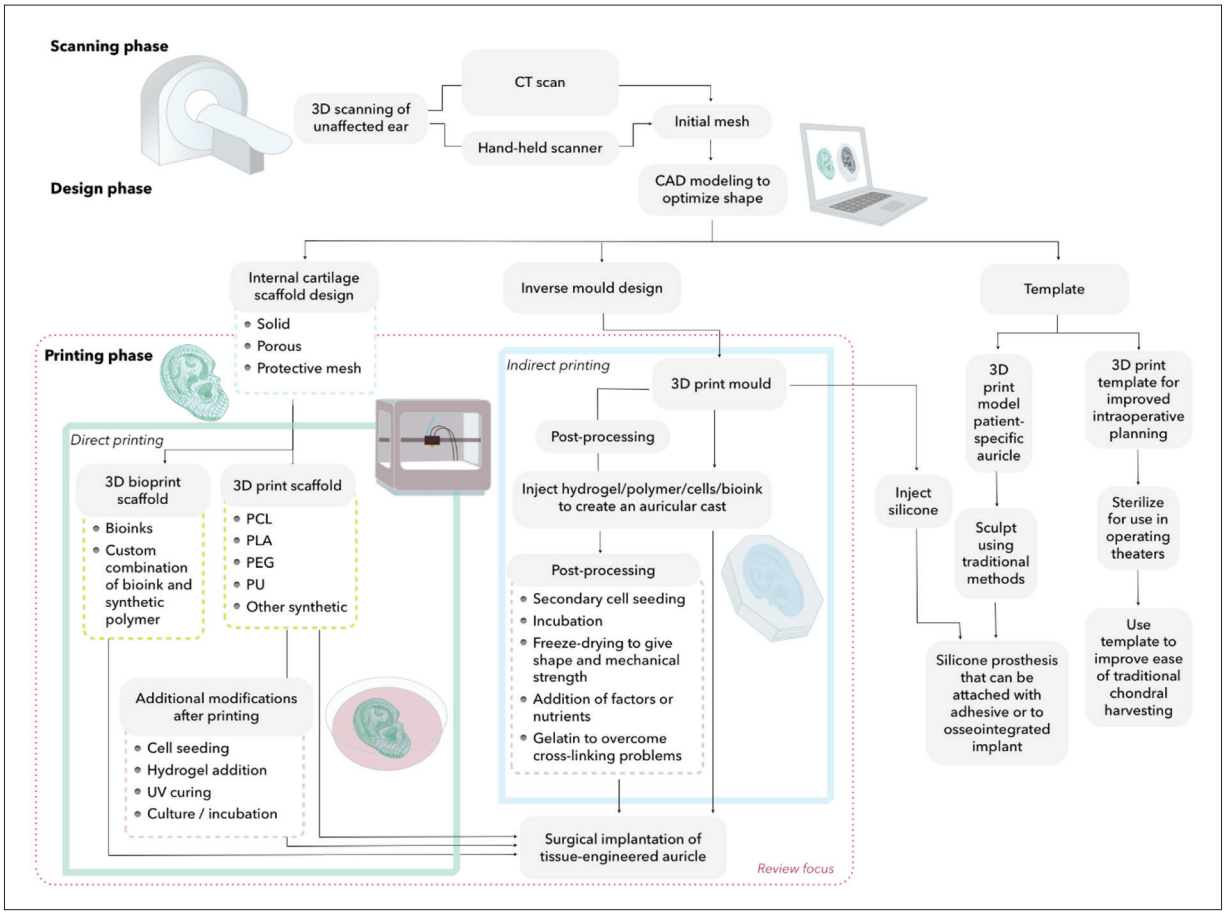

Figure 3. A summary of the ways in which 3D technology is being used to aid auricular reconstruction. Abbreviations: CT, computed tomography; PCL, polycaprolactone; PEG, polyethylene glycol; PLA, polylactic acid; PU, polyurethane; UV, ultraviolet.

their printer to cure their printed scaffold with blue light while new layers were deposited[14]. Similarly, Jia *et al.* (2022) used a multi-nozzle extrusion system that allowed the printing of cell-laden bioink and PCL alternately, and their methacrylate-enhanced bioink was subsequently light-cured into a sturdier shape[11]. Interestingly, Visscher *et al.* (2021) found that UV curing after printing improved construct stiffness to maintain the desired anatomical shape and suggested that this altered starting gel stiffness had an effect on cellular behavior and may have promoted cellular activity and maturation of the chondrocytes[28].

In the studies reviewed, a variety of 3D printing techniques were employed. Extrusion-based printing was the most commonly used in approximately 18.5% of studies, followed by digital light processing (DLP) bioprinting (7.4%). Fused deposition modeling, laser sintering, multi-head tissue/organ building system, and molds printed by selective laser sintering (SLS) were each used in about 3.7% of studies. The remaining studies utilized other or unspecified techniques. For a more detailed breakdown, refer to Table 2.

3.2. Cell selection

Selection of the right cell type is critical for implant success. Between 100 and 250 million chondrogenically potent cells that can form well-organized tissue are rich in GAG, collagens, and elastin and are needed for auricle formation[29]. In the studies reviewed, chondrocytes were the most commonly used cell type for auricle reconstruction (33.3%), reflecting their critical role in forming well-organized tissue rich in GAG, collagens, and elastin. However, chondrocytes have limited ability to expand and tend to dedifferentiate into fibroblasts, producing a fibrous extracellular matrix (ECM) with poor mechanical properties[23]. Mesenchymal stromal cells, used in about 14.8% of studies, on the other hand, are easily expandable but tend to undergo hypertrophy and differentiate toward the osteogenic lineage. Microtia-derived auricular chondrocytes (mACs) and cartilage progenitor cells can also be used[29] (and were employed in about 11.1% of cases) but are less effective at forming cartilage than normal auricular chondrocytes; thus, other cell types must be incorporated into the construct[23]. Notably, about 25.9%

of the studies used alternative cell sources, such as human adipose-derived stem cells (ASCs), novel human auricular cartilage progenitor cells (AuCPCs), bovine auricular chondrocytes, and tonsil-derived mesenchymal stem cells. Finally, in 14.9% of the studies, no specific cell type was mentioned.

Additionally, the nutrient supply the growing cells possess affects the quality of the generated tissue. Despite cartilage typically being largely avascular, additional strategies have been suggested, such as creating perfusion microchannels to allow better nutrient diffusion[30] or engineering myoglobin complexes on membranes to improve cell survival and tissue development[29].

An additional difficulty identified was achieving a good distribution of chondrocytes and uniformity of ECM with conventional cell seeding techniques, leading to insufficient mechanical stability and, in turn, macroscopic deformation. For this reason, the printing material chosen must not easily trigger aseptic inflammation so that the formation of ECM is not restricted[11]. The optimum material would have properties that would stimulate cartilage formation. For example, materials with low stiffness (<2–10 kPa) were found to promote cartilage formation, whereas scaffolds with high stiffness (>10 kPa) did not and consequently failed to grow cartilage well[15].

3.3. Material comparison

Synthetic polymers, such as PCL, polylactic acid (PLA), PEG, and polyurethane (PU), have been the focus of 3D printing material selection for cartilage regeneration due to their biocompatibility, mechanical properties, and degradation characteristics. PCL, the most frequently printed material in this review, has been used in the biomedical field in implants and sutures for over 70 years[31], and is biocompatible with good bioresorbility and mechanical stiffness[9], making it a good choice for surgical reconstruction as it can be safely and gradually absorbed over 4 years without causing adverse reactions[20], while supporting the structure as the cellular components around it mature[11]. PLA is biocompatible, affordable, and also degrades slowly, retaining its integrity throughout elastic cartilage maturation[10]. PEG is biocompatible and dissolves, without adverse effects on cell viability, within 40 min of being submerged in an aqueous environment, making it suitable as a sacrificial material for when short-term support is required for printing[27]. PU is strong, versatile, and resilient, and while its biodegradability is a point of contention[32], Kim *et al.* (2019) compared porous and non-porous structures printed using PU and found that the porous variety encouraged cell proliferation[30]. Finally, bioinks, composed of a mixture of cells, growth factors, and other biocompatible substances suspended in a gel or hydrogel matrix, provide a supportive environment and allow direct printing of structure that more closely mimics the natural anatomy of the ear[11].

A variety of hydrogels were used as scaffolds for auricular cartilage tissue engineering in these studies. The most commonly used hydrogel was a combination of gelatin and alginate, which was utilized in several studies[8,9,27,28,32]. This hydrogel was primarily used for 3D bioprinting of auricular cartilage, although the specific properties of the hydrogel were not detailed in these studies. Another study by Zopf *et al.* (2018) used a hyaluronic acid/collagen hydrogel for seeding primary porcine auricular chondrocytes onto 3D-printed scaffolds[54]. However, the properties of the hydrogel were not explicitly mentioned[51]. In a study by Jia *et al.* (2020), an ACM/gelatin hydrogel was used. The mechanical properties showed an opposite trend to pore size and porosity, and the degradation rate enhanced with increasing acellular cartilage matrix (ACM) proportion. The hydrogel demonstrated excellent biocompatibility, with a cell seeding efficiency of more than 90%[25]. It should be noted that the specific properties of the hydrogels were not always detailed in the studies, and as such, a comprehensive comparison of the hydrogels used is not possible based on the available information.

3.4. Time *in vivo* and evaluation successful outcomes

One of the most significant drawbacks of all the *in vivo* animal studies in evaluating optimum cell type and material selection was the limited time the scaffolds spent *in vivo* (see Figure 4). Overall, this was an average of 110 days. The bioink studies were the shortest (mean = 53.25 days). Conversely, the longest-running animal study was that by Yin *et al.* (2020), which lasted 365 days and in which a composite scaffold composed of polyglycolic acid (PGA)/PLA and a PCL core was seeded and implanted in mice[22].

The longest-running study in this review is the ongoing human pilot trial, which was at the 2.5-year mark at publication. This landmark study had several limitations, such as a small sample size of only five patients. However, it showed it is possible to design, print, and integrate patient-specific auricles in human subjects. Notably, the patients underwent 12 weeks of tissue expansion before the reconstruction and subsequently two scar revisions were performed at 6 and 18 months, allowing for tissue biopsies of the scaffold at the same time, which showed good cartilage formation. Good aesthetic results were only achieved after 9 months, once postoperative inflammation subsided[20].

All studies attempted to evaluate the resulting printed structure's properties objectively. Histopathology, electron microscopy, ultrasound scans, micro-computed

Table 2. Overview of reviewed studies on 3D bioprinting for auricular reconstruction

Study	Aim of study	Study setting	Animal model (if any)	Study focus	3D printing technique	Components	Printed shape
Chung et al. (2020)[9]	To assess the feasibility of using a hybrid printing approach to fabricate a scaffold for the outer ear of clinically relevant size. Attempted to address the distinct regions in the auricular cartilage by varying the pattern design (as opposed to hybrid scaffolds printed with one specific mechanical modulus across the entire construct).	*In vitro*	N/A	Direct printing	Extrusion	Cells in bioink + scaffold printed together	Resembling pinna; other shape
Lee et al. (2014) [27]	To develop a non-toxic method for producing inverse pyramidal and bowl-shaped structures that are optimized for auricle printing.	*In vitro*	N/A	Direct printing	Multi-head tissue/ organ building system	Scaffold printed first and then seeded with cells	Resembling pinna; other shape
Otto et al. (2021) [29]	To investigate the usability of human AuCPCs in auricle 3D printing.	*In vitro*	N/A	Direct printing	Fused deposition modeling (extrusion)	Cells in bioink + scaffold printed together	Resembling pinna; other shape

Printed material	Cell nature/type	Notable post-printing modifications	Assessment of success/ integration	Findings	Limitations and suggested improvements
PCL	GelMA-HAMA cell-supportive bioink	Photocuring of the printed bioink was using a 400 nm UV source at a focal distance of 5.0 cm and an intensity of 15–30%	Histopathology	• The design of a print affects its stiffness and flexibility significantly. • Scaffolds printed with a 400 μm nozzle tip had the lowest compressive modulus but were similar in stiffness to native auricular cartilage and had the fastest printing time. • Increasing the nozzle diameter decreases the compressive modulus of PCL scaffolds, while increasing strand spacing and using orientations of 0/45° leads to more flexible structures. • Scaffolds can serve as a temporary support for host tissue integration and chondrocyte differentiation. A scaffold with similar properties before implantation could improve its handling and shape retention after implantation. • Cells remained viable for up to 7 days after printing. • The presence of a surrounding hydrogel during the printing process helps protect cells from shear forces at the nozzle tip, leading to good cell viability during the printing process.	• Further improvements could be developed to generate smoother intersections for each region • Incorporate a gradual decrease or increase of the strand spacing of each part at the junction
PCL & PEG	Human ASCs exposed to chondrogenic induction medium and adipogenic induction medium	The cell-printed structures were incubated a week at 37°C in a humidified atmosphere containing 5% CO_2. The sacrificial PEG layer was dissolved.	Mechanical testing; electron microscopy	• The sacrificial layer technique allowed for the construction of complex structures of any shape. • The PEG sacrificial component did not impact cell viability or proliferation and could be easily dissolved in water or cell culture media within 40 minutes. • Hydrogels may provide a better environment for chondrocyte proliferation, but printed adipocytes had a lower proliferation rate. • Chondrocytes and adipocytes had similar proliferation rates when printed separately, and chondrogenesis and adipogenesis occurred effectively when the two cell types were co-printed and co-cultured. • An ear-shaped structure containing both chondrocytes and adipocytes not only maintained its shape, but also regenerated both auricular cartilage and earlobe fat.	A system for incubating printed cells will need to be developed and attached to the printer in order to keep the cells alive during the printing of large structures such as an ear, as the viability of the printed cells may be compromised during this process.
PCL	Novel human AuCPCs	Cultured *in vitro* in chondrogenic media for 30 days	Histopathology; micro-CT scan; mechanical testing	• Extrusion printing does not negatively impact cell viability, metabolic activity, or the production of GAGs. • The extrusion of AuCPCs through a microvalve system did not harm cell viability (which remained at 8% over 10 days), metabolic activity (which was not different between cast and printed cells), or GAG production (which occurred over 28 days *in vitro*). • PCL scaffolds with various strand spacings support GAG production.	Short-term study; no *in vivo* testing of this method yet

(*Continued*)

Table 2. ***Continued***

Study	Aim of study	Study setting	Animal model (if any)	Study focus	3D printing technique	Components	Printed shape
Visscher et al. (2016)[50]	To create a rapid production pathway and mechanically stable scaffold structures with an optimal biochemical ECM environment for generating and maintaining proper ear cartilage.	*In vitro*	N/A	Direct printing	Extrusion	Scaffold only	Other shape
Visscher et al. (2018) [51]	To design and 3D-print an easily-assembled cartilage implant for auricular reconstruction.	*In vitro*	N/A	Direct printing	Extrusion – 3D printing a two-part PCL mold in the shape of human auricular cartilage and injecting this construct with a mixture of alginate and chondrocytes before culturing the final construct *in vitro*.	Cells in bioink + scaffold printed together; scaffold printed first and then seeded with cells	Resembling pinna

Printed material	Cell nature/type	Notable post-printing modifications	Assessment of success/ integration	Findings	Limitations and suggested improvements
				• PCL scaffolds maintained good shape retention both immediately after printing and after 30 days of *in vitro* culture. • The hybrid ear-shaped construct produced cartilage-specific components in abundance. • 400 μm and 800 μm scaffolds are relatively stiff and inflexible, while 1000 μm and 1200 μm scaffolds allow for more bending when manipulated by hand. However, using wider strand spacings also reduces control over the fine architecture of the structure.	
PCL	Goat mesenchymal stem cells, chondrocytes and perichondrocytes.	Printing is paused half-way to insert a collagen I/III scaffold into the PCL cage. Then after printing, hydrogel is added on top of that.	Histopathology; mechanical testing	• A novel cage construct consisting of a combined hydrogel and collagen I/III scaffold within a 3D-printed synthetic PCL cage can prevent *in vitro* scaffold contraction. • Six PCL cage constructs can be produced and printed in 2 h with good printing accuracy and minimal oozing effects. • Cell-seeded hydrogels showed significant contraction *in vitro*, reducing to 15–48% of their original volume after 28 days of culture depending on the cell type. • Histological evidence of GAG deposition was present in all scaffolds and internal scaffolds. • Chondrocyte- and chondrocytes perichondrocyte (CP)-seeded scaffolds produced the most collagen, while adipose-derived stem cells and chondrocytes had lower GAG production than other cell types. • The Young's modulus of all scaffolds and internal scaffolds increased by 50% after 28 days of *in vitro* culture compared to 14 days of culture.	No *in vivo* testing of this method yet
PCL	Chondrocytes from Dutch milk goats	Molds were disinfected with 70% ethanol for 1 h, washed with sterile PBS and dried in a sterile incubator. All parts were coated with sterile gelatin to block the pores and create a sealed mold. Once placed in proliferation medium at 37°C, the gelatin liquefied and left the pores, allowing for nutrient and oxygen exchange through the mold pores.	Histopathology; Mechanical testing	• It was found that a porous synthetic outer layer with high mechanical strength was needed to withstand forces during *in vivo* tissue maturation. • An inner "natural" core made of a biomimetic environment for cartilage tissue formation was an effective way to achieve biointegration. • Beads cultured in chondrogenic medium had higher levels of GAGs and type II collagen deposition.	Long-term *in vivo* experiments are required to test preclinical applicability

(*Continued*)

Table 2. ***Continued***

Study	Aim of study	Study setting	Animal model (if any)	Study focus	3D printing technique	Components	Printed shape
Visscher et al. (2021) [28]	To develop a hydrogel-based bioink that recreates the complex cartilage microenvironment.	*In vitro*	N/A	Direct printing	Extrusion	Cells in bioink + scaffold printed together; scaffold only	Resembling pinna; other shape
Bhamare *et al.* (2021) [26]	To synthesize pinna from printable bioink. Ear pinna bioink was prepared from xenogenic goat cartilage by adding polymers and optimized for 3D printing.	*In vitro*; *in vivo* animal	Rat	Direct printing	Extrusion	Cells in bioink + scaffold printed together	Resembling pinna
Dong *et al.* (2021) [10]	To determine whether 3D-printed, biocompatible scaffolds would "protect" maturing hydrogel constructs from contraction and topography distortion.	*In vitro*; *in vivo* animal	Rat	Direct printing	Extrusion	Scaffold printed first and then seeded with cells	Other shape

Printed material	Cell nature/type	Notable post-printing modifications	Assessment of success/ integration	Findings	Limitations and suggested improvements
Bioink	Porcine ear cartilage	UV crosslinking after printing	Histopathology; mechanical testing; other such as mass spectrometry proteome analysis	• A photo-crosslinkable cartilage-derived ECM-based bioink was successfully developed for auricular cartilage reconstruction and supported the activity and maturation of chondrocytes in bioprinted constructs. • Decellularized cartilage-derived ECM can be used for cell-based 3D bioprinting. • The inclusion of gelatin, HA, and glycerol improved printability and initial structural integrity, while UV polymerization increased stiffness. • The stiffness of the gel may affect cell behavior.	*In vitro* only • Large protein heterogeneity observed between samples in the mass spectrometric analyses, which makes it difficult to draw a specific conclusion on effects of protein abundance on growth
Bioink	Goat cartilage used in bioink	Ethylene oxide used to sterilize scaffold before implantation. It was trimmed into pieces (10 mm in width), and rinsed with saline containing antibiotic solution.	Histopathology; ultrasound scan; micro-CT scan; mechanical testing	• The ear had biodegradable properties despite containing polymers. • Mechanical strength of 3D-printed pinna showed similar results like normal ear pinna. • Pinna was biocompatible (*in ovo* and *in vivo*) having newly developed chondrocytes, elastin fibers, progenitor cells of ECM after transplantation. • Within 30 days, the transplanted 3D-printed pinna regenerated chondrocytes, GAG, elastin fibers, collagen, and retained its ECM. • The occurrence of angiogenesis after grafting showed that the 3D-printed ear pinna was accepted by the rat ear and had non-toxic properties similar to those of a native ear pinna.	Small study in animals only
PLA	Bovine auricular chondrocytes	Chondrocytes in collagen hydrogels were added to the printed constructs. Cell-loaded constructs were cultured in DMEM overnight before implantation.	Histopathology	• Scaffolds were fabricated using injection molding to protect auricular cartilage constructs from external compression and intrinsic contractile forces, resulting in significant reduction of contraction and preservation of complex topography. • Injection molding allows for the creation of a more fully interconnected porous network and is particularly effective for quickly producing homogenous volumes with high accuracy. • Mechanically attaching a cell-seeded collagen construct to an external structure helps maintain shape retention during extended culture *in vitro*. • Larger (12-mm wide) porous PLA discs featuring a ridge on the surface were designed to simulate the shape of the helical rim and compensate for anticipated contraction, blunting, and distortion. After 3 months *in vivo*, the helical rim feature was better preserved in the injection molded (SInj) and scaffolded (S) groups compared to the naked (N) group, which lost the rim feature and became a flat disc of cartilage. • The presence of an external PLA scaffold did not hinder the formation of healthy cartilage within the constructs.	Using bovine cells is a necessary step toward eventually using human cells to produce clinically translatable results. Using a rodent model is limiting because the loose nature of rodent skin does not accurately replicate the compressive forces experienced by scaffolds under human auricular or scalp skin.

(*Continued*)

Table 2. ***Continued***

Study	Aim of study	Study setting	Animal model (if any)	Study focus	3D printing technique	Components	Printed shape
Jang *et al.* (2020) [8]	To discover what happens when ASCs are co-cultured with chondrocytes in a 3D hybrid scaffold of PCL.	*In vitro*; *in vivo* animal	Rat	Direct printing	Extrusion	Scaffold printed first and then seeded with cells	Resembling pinna
Jia *et al.* (2022) [11]	To evaluate the effectiveness of a new approach for creating biological auricular equivalents using a biomimetic microporous photo-crosslinkable cartilage-derived ECM with precise shapes and a bioactive bioink based on ACMMA, GelMA, PEO, and PCL through the use of multi-nozzle 3D bioprinting technology.	*In vitro*; *in vivo* animal	Mice	Direct printing	Multi-nozzle extrusion by alternately printing type 1 (cell-laden bioink) and type 2 (PCL)	Cells in bioink + scaffold printed together	Resembling pinna; other shape
Kim *et al.* (2019)[30]	To investigate whether customized 3D-printed PU scaffolds with adequate microstructure provide biomechanical properties suitable for reconstruction of congenital ear defects.	*In vitro*; *in vivo* animal	Mice	Direct printing	Extrusion	Scaffold printed first and then seeded with cells	Resembling pinna

Printed material	Cell nature/type	Notable post-printing modifications	Assessment of success/ integration	Findings	Limitations and suggested improvements
PCL	Human ASCs and rabbit articular chondrocytes	Incubation in culture media at 37°C with 5% CO_2	Histopathology; electron microscopy	• The proposed hybrid structure exhibited improved mechanical properties due to the PCL framework and demonstrated reasonable chondrogenesis *in vitro* and *in vivo*. • The compressive modulus of the alginate/PCL hybrid scaffold was found to be around 2.64 ± 0.34 MPa, similar to that of native auricular tissue. • Results suggest that chondrocytes should be added to the scaffold when it is implanted in the subcutaneous area without any surrounding cartilage, as it is difficult to regenerate cartilage using MSCs alone without chondrocytes or cartilage remnants.	Unclear sample size
Bioink—A microporous photo-crosslinkable bioactive bioink based on cartilage-derived ECM with the assistance of GelMA and PEO.	Bama miniature pigs's auricular cartilage	Two groups of cell-laden constructs were immersed in a culture medium for 24 h to dissolve PEO to form porous structures	Histopathology; micro-CT scan	• By using multi-nozzle 3D bioprinting technology to control the distribution of chondrocyte-laden bioink and PCL, microporous auricular equivalents with precise shapes and satisfactory mechanical strength were successfully fabricated. • Mature auricular cartilage tissue with high morphological accuracy, good elasticity, numerous cartilage lacunae, and cartilage-specific ECM deposition was successfully regenerated in nude mice. • The inclusion of PCL significantly improved the shape fidelity of auricular equivalents. The modulus of regenerated auricular cartilage without PCL support was over 65% of native cartilage, while that of regenerated auricular cartilage with PCL support was approximately 2.6 times greater than native cartilage. • Although the PCL occupied space, it did not affect the formation of mature cartilage tissue in the bioink area while providing sufficient strength and stiffness support.	The feasibility of the technology in large animal models is still yet to be optimized and verified by further experiments.
PU	Tonsil-derived MSC (for biocompatibility testing only)	None	Histopathology; micro-CT scan; mechanical testing; electron microscopy	• 3D-printed, implantable ear scaffolds made of PU are biomimetic, biocompatible, easily fabricated, and flexible. • The PPU scaffold used in this study was designed to have a specific microstructure in terms of pore size and uniform pore lattice architecture, which encouraged the ingrowth of surrounding tissue. In comparison, the Medpor scaffold had an irregular microstructure (highly variable pore size and distribution of pores) that did not allow for close tissue interactions. • Neovascularization was only observed in PPU scaffolds, indicating that a pore size of 200 mm may be critical for promoting tissue ingrowth after auricular reconstruction.	Further studies are needed to clarify the long-term behavior of implanted, regular-sized, 3D-printed PPU scaffolds in terms of shape and elasticity.

(*Continued*)

Table 2. ***Continued***

Study	Aim of study	Study setting	Animal model (if any)	Study focus	3D printing technique	Components	Printed shape
Mukherjee *et al.* (2021) [21]	To assess the degradation behavior and tissue compatibility of hybrid scaffolds (PCL-hydrogel) compared to single material PCL scaffolds *in vitro* and *in vivo*. The study wanted to understand the biological reaction to printed scaffolds (independent of stem cells) in an immunocompetent host.	*In vitro*; *in vivo* animal	Sheep (similar fascial anatomy)	Direct printing	Extrusion	Cells in bioink + scaffold printed together; scaffold only	Other shape
Tang *et al.* (2021) [15]	To explore the use of 3D printing to fabricate bioactive artificial auricular cartilage using chondrocyte-laden GelMA and PLA for auricle reconstruction.	*In vitro*; *in vivo* animal	Mice	Direct printing	Fused deposition modeling (extrusion)	Scaffold printed first and then seeded with cells	Resembling pinna

Printed material	Cell nature/type	Notable post-printing modifications	Assessment of success/ integration	Findings	Limitations and suggested improvements
PCL	N/A	None	Histopathology; ultrasound scan; micro-CT scan; electron microscopy	• Both porous 3D-printed PCL and hybrid scaffolds showed similar and homogenous degradation *in vitro*. *In vivo*, they exhibited minimal irritation or inflammation in surrounding tissue over a 6-month period in an immunocompetent animal model that closely resembles human soft tissue biology, although the host response varied between animals. • The hybrid scaffolds had a higher percentage mass loss than control scaffolds due to the presence of degrading hydrogels that contributed to a higher initial weight. However, the degradation profile was dominated by PCL in both hybrid and PCL-only scaffolds. • SEM showed that degradation occurred from the outer surface inward for each strand. • *In vivo*, the scaffolds were well tolerated for the duration of the experiment, with serial ultrasound and CT scans showing minimal reaction in surrounding subcutaneous tissue over 6 months. Ex vivo, the scaffolds displayed localized hyperemia with peripheral pallor and pseudo-capsule formation, consistent with a localized inflammatory response, indicating good biocompatible properties with no macroscopic differences between test and control samples. • Control specimens, when 3D-reconstructed, had less tissue integration compared to all test samples in both sheep, regardless of PCL configuration. This may be attributed to the presence of the hydrogel.	The inclusion of GelMA-HAMA with the PCL demonstrated better tissue ingrowth. However, its impact on cellular differentiation can only be evaluated in future experiments embedded with cells.
PLA	Rabbit ear chondrocytes; grafts were also taken from mice	XX	Histopathology; mechanical testing; electron microscopy	• The successful induction of auricular chondrogenesis *in vivo* was demonstrated using a photosensitive GelMA hydrogel to allow chondrocytes to bind to a customized auricular scaffold. • A biologic auricle with a PLA material as the inner core for support was constructed. This not only provides mechanical support for cartilage regeneration for morphological maintenance *in vitro* and *in vivo*, but also allows the ester bonds of PLA to be slowly hydrolyzed, providing sufficient time for the engineered cartilage to mature and acquire mechanical properties while gradually replacing the degrading PLA scaffold.	Short-term study and thus long-term ability to withstand immune response was not tested.

(*Continued*)

Table 2. ***Continued***

Study	Aim of study	Study setting	Animal model (if any)	Study focus	3D printing technique	Components	Printed shape
Xia *et al.* (2018)[14]	To establish novel scaffold-fabricated strategies for native polymers and provide a novel natural 3D scaffold with satisfactory outer shape, pore structure, mechanical strength, degradation rate, and weak immunogenicity for cartilage regeneration.	*In vitro*; *in vivo* animal	Mice + goats	Direct printing	Pneumatic extrusion-based bioprinter with a 405 nm blue light.	Scaffold printed first and then seeded with cells	Resembling pinna; other shape
Xie *et al.* (2022) [53]	To present an ECM compound bioink derived from cartilage microtissues and its use in cartilage regeneration, specifically the auricle	*In vitro*; *in vivo* animal	Mice	Direct printing	DLP bioprinting	Cells in bioink + scaffold printed together	Resembling pinna; other shape

Printed material	Cell nature/type	Notable post-printing modifications	Assessment of success/ integration	Findings	Limitations and suggested improvements
Photo-curable hydrogel (meth-acrylic anhydride + gelatinous + hyaluronic acid)	Goat auricular cartilage-derived chondrocytes	After 3D printing, the scaffolds were frozen at −80°C for 4 h and lyophilized for 48 h. The scaffolds were then sterilized with ethylene oxide for subsequent use.	Histopathology; mechanical testing; electron microscopy	• Photo-crosslinkable gelatin and HA can be fabricated as a porous scaffold with a precise outer shape, good internal pore structure, high mechanical strength, and good degradation rate, through photocuring 3D printing and lyophilization. • The scaffolds combined with chondrocytes successfully regenerated mature cartilage with typical lacunae structure and cartilage-specific ECM both *in vitro* and *in vivo*. • Chondrocytes were able to adhere to, survive within, and proliferate effectively in the scaffolds. • *In vitro*, cartilage-like tissue was successfully regenerated within 2 weeks, which was faster than the 4–8 weeks it took to regenerate cartilage using polyglycolic acid/polyglycolic acid(PLA/PGA) scaffolds. • In immunocompetent large animals, the 2-week *in vitro*-engineered cartilage successfully regenerated stable mature cartilage with no obvious inflammatory reaction observed, despite the presence of abundant residual scaffold. This suggests that 2 weeks of *in vitro* culture is optimal for the current scaffolds to permit autologous *in vivo* cartilage regeneration in future clinical applications, which could greatly decrease associated patient treatment costs and waiting times.	Mechanical strength of the scaffolds warrants further enhancement, and the feasibility of regenerating precisely shaped cartilage needs to be further explored.
Bioink	Porcine chondrocytes	The printed auricular constructs were placed in a complete culture medium for 20 days.	Histopathology; mechanical testing; electron microscopy	• It was showed that microtia chondrocytes extracted from residual ear tissue can be used to create auricular cartilage for clinical use, as they had chondrongenic, osteogenic and adipogenic differentiation potential. • Chondrocytes and stem cells were combined with a hydrogel to create a bioink. This bioink was then used with DLP bioprinting to create auricular constructs that had high elasticity, high printing accuracy, and low swelling ratio. • Compared with extrusion bioprinting, DLP is highly accurate and may cause less mechanical damage to cells • The GelMA+chondrocytes group was more prone to internal cell death due to a lack of nutrition, while the cells in the GelMA+microtissues group fared better, as the cells could perform intercellular connections and secret more bioactive substances • After *in vitro* culture, a large amount of ECM was deposited, and mature cartilage was observed to regenerate after subcutaneous implantation in mice for 12 weeks.	• Small print size • Repeating the process of freezing and thawing the sample and trying using supercritical CO_2 as a disinfectant may improve the decellularization method, as the current method using ethanol and peracetic acid caused a significant loss of GAG content

(*Continued*)

Table 2. ***Continued***

Study	Aim of study	Study setting	Animal model (if any)	Study focus	3D printing technique	Components	Printed shape
Zopf *et al.* (2014) [52]	To determine the potential of an integrated, image-based CAD and 3D printing approach to engineer scaffolds for head and neck cartilaginous reconstruction for auricular and nasal reconstruction.	*In vitro*; *in vivo* animal	Pigs	Direct printing	Laser sintering	Scaffold printed first and then seeded with cells	Resembling pinna; other shape
Zopf *et al.* (2018) [54]	To determine the effect of auricular scaffold microarchitecture on chondrogenic potential in an *in vivo* animal model.	*In vitro*; *in vivo* animal	Athymic rodents	Direct printing	Laser sintering powder 3D printer	Scaffold printed first and then seeded with cells	Resembling pinna
Apelgren *et al.* (2018) [3]	To evaluate if an integrated 3D bioprinted cartilage construct has the capacity to serve as a bed for a full-thickness skin graft.	*In vivo* animal	Rat	Direct printing	Extrusion 3D bioprinter using nano-fibrillated cellulose/alginate bioink	Cells in bioink + scaffold printed together	Other shape

Printed material	Cell nature/type	Notable post-printing modifications	Assessment of success/ integration	Findings	Limitations and suggested improvements
PCL	Chondrocytes were isolated from harvested porcine auricular cartilage	Chondrocytes were seeded into the auricular PCL scaffolds using a type I collagen gel. The cell suspension was pipetted into the PCL scaffolds, and the constructs were placed in an incubator (37°C, 5% CO_2) for 30 minutes for gelation to occur.	Histopathology	• A novel image-based CAD/CAM 3D printing process in the production of bioresorbable PCL scaffolds with a defined porous architecture for cartilaginous frameworks was introduced. The technique utilized 3D printing for auricular and nasal scaffold production and control of the pore architecture. • The surgical implantation of scaffolds was performed with ease, and scaffold porosity allowed for the versatility and ease of suture placement. The PCL material maintained excellent foundational support and appearance when implanted in subcutaneous tissue. • The PCL scaffolds all demonstrated histologically native-appearing cartilage growth. However, the scaffolds had not reached complete confluent cartilage coverage after two months *in vitro*.	Implantation into the pigs was only to demonstrate appearance, so long-term *in vivo* performance was not studied.
PCL	Porcine auricular cartilage chondrocytes	Chondrocytes seeded into the auricular PCL scaffolds using a type I collagen/ HA composite gel. Seeded constructs were cultured in sterile, dynamic conditions with incubation at 37°C, 5% CO_2. After 4 weeks of *in vitro* culture, they were implanted into rodents.	Histopathology	• Auricular constructs with two micropore architectures were rapidly manufactured with high-fidelity anatomic appearance. • Subcutaneous implantation of the scaffolds resulted in excellent external appearance of both anterior and posterior auricular surfaces. • Comparing two different microporous scaffold architectures demonstrated the importance of scaffold design in optimizing auricular cartilage growth. • Results suggest that a defined arrangement of spherical pores yielded more robust auricular tissue growth. • The creation of spherical micropores within the scaffold architecture appears to impart greater chondrogenicity to the bioscaffold.	• Short time *in vivo* (4 weeks) • No mechanical testing of scaffold • Study size unstated
Bioink	Human bone marrow–derived mesenchymal stem cells & human nasal chondrocytes	After printing, constructs were crosslinked with 100 mM $CaCl_2$ for 5 minutes in 37°C. The constructs were washed with a balanced salt solution. The printed constructs were then immediately implanted subcutaneously into the mice.	Histopathology	• 3D-bioprinted cartilage that has been allowed to integrate *in vivo* is a sufficient base for a full-thickness skin graft. • Transplanted skin survived subcutaneously in all the 20 surviving animals. • No necrosis was observed. There were no macroscopic signs of complications. • However, lymphocytic infiltration was observed as a sign of inflammatory activity. • The majority of the chondrocytes did not survive (speculated to be due to diffusion limit).	• Since rodents heal by withering, they may not be the ideal model for studying the human healing process in all aspects. • Moreover, rodents' skin lacks apocrine sweat glands and is proportionally much thinner than humans' and has an additional muscle layer that makes the comparisons difficult. • Short study time. The long-term outcome of shape stability, elastic features, and tissue integrity are crucial factors that have to be addressed in further studies.

(*Continued*)

Table 2. ***Continued***

Study	Aim of study	Study setting	Animal model (if any)	Study focus	3D printing technique	Components	Printed shape
Brennan *et al.* (2021) [4]	To evaluate the design and initial performance of the auricular scaffold in a preclinical animal model study. Our hypothesis was that the two-stage approach would limit the overlying soft tissue strain and thus result in lower rates of soft tissue ulceration, necrosis, and related complications compared to the single-stage reconstruction.	*In vivo* animal	Rats	Direct printing	Laser sintering PCL with a mixture of 4% hydroxyapatite (Plasma Biotal) where the HA serves primarily as a flowing agent for powder spreading during the laser sintering process	Scaffold only	Resembling pinna
Chang *et al.* (2020) [47]	To analyze the use of highly translatable 3D–printed auricular scaffolds with and without novel cartilage tissue inserts in a rodent model.	*In vivo* animal	Rat	Direct printing	Extrusion	Scaffold printed first and then seeded with cells	Resembling pinna

Printed material	Cell nature/type	Notable post-printing modifications	Assessment of success/ integration	Findings	Limitations and suggested improvements
PCL	N/A	Sterilized by low-temperature ethylene oxide gas sterilization prior to implantation	Histopathology; micro-CT scan; mechanical testing	• A 3D-printed bioscaffold was developed for auricular reconstruction with a realistic anatomic appearance that meets or exceeds the best outcomes of rib cartilage grafting • The shape of the construct was durable and did not experience contraction or distortion over the course of the experiment. • The scaffold demonstrated robust tissue ingrowth and angiogenesis, suggesting it could support the growth of cartilaginous tissue. • The technique resulted in unparalleled ear appearance *in vivo*. • Ulceration was a problem in all the rats, regardless of single or two staging. • Minor superficial ulcers occurred most commonly at the lateral (86% of animals) and superior (29% of animals) helix of the scaffold. • Promisingly, there were high rates of improvement in ulceration over time with only a quarter of models demonstrating worsening in ulceration over the course of experimentation. Bolstered by findings of robust angiogenesis, the authors speculated that the improvement in wound healing was secondary to the angiogenesis and transformation of a bare PCL scaffold to an integrated, vascularized tissue implant. • The porous architecture design may improve outcomes by reducing skin complications and allowing increased tissue and vascular ingrowth to enhance reconstruction and accelerate healing of skin ulceration.	H&E was used to assess for vascularization. Quantification of angiogenesis has inherent challenges based off how the histology captures the blood vessels and the lack of specificity of H&E to stain vessels. So other stains should be used. Additional work is necessary to assess the potential to cellularize the scaffold with the ultimate goal of gradual replacement with a native cartilage matrix.
PCL	Porcine punch biopsies inserted into scaffolds to facilitate chondrocyte seeding	All scaffolds were sterilized with ethylene oxide Prior to implantation. Half of the sample was cartilage-seeded, with the other unseeded.	Histopathology; micro-CT scan	• Vascularization was observed in both unseeded and seeded scaffolds, indicating that non-autologous tissue implants do not inhibit vessel formation. • This technique is readily clinically translatable as it eliminates *in vitro* requirements and accompanying regulatory burden. • The 3D-printed auricles with and without cartilage inserts were structurally similar to human ears and measurements remained consistent. • There was no significant retraction or degradation of scaffolds during the experiment, suggesting resistance to contractile forces and sustained feasibility of such implants. • Micro-CT imaging showed infiltration of soft tissue into the pores of hybrid scaffolds. • Healing of ulceration was seen in both conditions, with smaller rates of scaffold-induced ulceration in cartilage-seeded scaffolds.	No statistically significant difference was observed between cartilage-seeded and unseeded scaffolds in any category of ulceration. This may be due to the small sample size or the methods used to measure ulceration. The use of additional immunohistochemistry might clarify whether chondrocytes are present beyond the limits of the cartilage punch biopsy and from which tissue they arise.

(*Continued*)

Table 2. ***Continued***

Study	Aim of study	Study setting	Animal model (if any)	Study focus	3D printing technique	Components	Printed shape
Dong *et al.* (2022) [48]	To determine the minimum fraction of human auricular chondrocyte required to form healthy elastic cartilage when co-cultured with human MSCs.	*In vivo* animal	Rat	Direct printing	Extrusion (FDM)	Scaffold only	Other shape
Park *et al.* (2017) [49]	To apply 3D cell printing to fabricate a tissue-engineered graft, and evaluate its effects on cartilage reconstruction.	*In vivo* animal	Rabbit	Direct printing	Multi-head tissue/organ building system (extrusion)	Cells in bioink + scaffold printed together; scaffold printed first and then seeded with cells	Other shape
Jia *et al.* (2020) [25]	To create and test a proper scaffold created with ACM with precise human-ear-shape and necessary mechanical strength that will elicit a low inflammatory reaction.	*In vitro*; *in vivo* animal	Mice	Indirect printing	Cast-molding and freeze-drying mixture	Scaffold printed first and then seeded with cells	Resembling pinna; other shape

Printed material	Cell nature/type	Notable post-printing modifications	Assessment of success/ integration	Findings	Limitations and suggested improvements
PLA	Bone marrow -derived mesenchymal stem cells	Cells were cultured, passaged, and then slowly injected into the scaffolds and gelled at 37°C for 1 h. Cell-loaded constructs were then cultured overnight before implantation.	Histopathology; micro-CT scan	• A combination of MSCs and chondrocytes was used to create cartilage that demonstrated consistent mechanical function, even when the ratio of MSCs to chondrocytes was high. • When chondrocytes made up only 10% of the initial cell population, the resulting tissue had characteristics similar to native elastic cartilage in terms of both biomechanics and biochemistry. • Co-implantation of a small number of chondrocytes with MSCs in a type I collagen matrix resulted in the production of cartilage that was indistinguishable from native auricular cartilage after 6 months *in vivo*. • It is not yet clear if the more efficient cartilage formation observed in this study is due to the differentiation of MSCs toward a chondrogenic lineage, a trophic effect of the MSCs, or a combination of both, but this is the subject of ongoing research. • The use of a small number of chondrocytes could be an important step toward the clinical translation of auricular tissue engineering due to the limited availability of auricular cartilage donor tissue.	The implantation of the constructs in nude rats, which manifest different skin characteristics from humans (e.g. looseness of rodent skin does not simulate the high pressure caused by implantation under the tight scalp), as well as significant differences in immunocompetency.
PCL	Primary chondrocytes from the New Zealand white rabbit	Incubated at 37°C for 1 h. Fabricated CSHS was crosslinked using $CaCl_2$. Washed with PBS thrice. Then chondrocytes were seeded onto the CSHS with the same cell density with CSS.	Histopathology; mechanical testing; electron microscopy	• A multi-head tissue/organ building system can successfully be used to 3D-print a cell-printed structure (CPS) using layers of alginate bio-ink encapsulating chondrocytes and PCL. • The CPS was found to have a higher efficiency of cellular settlement, improved survival and function of chondrocytes *in vitro* compared to a cell-seeded scaffold (CSS). • When implanted in a rabbit ear with a cartilage defect, the CPS led to complete cartilage regeneration after 3 months, while the CSS and autologous cartilage only led to incomplete healing. • These results suggest that 3D printing synthetic polymer scaffolds with hydrogel materials and cells can be a viable alternative to using autologous cartilage for auricular reconstruction.	Small sample
Other: ACM/ gelatin-PCL scaffold	Goat chondrocyte seeding	A cell suspension was seeded into each scaffold. This was followed by 24 h of incubation	Histopathology; electron microscopy	• The scaffold showed excellent biocompatibility and successfully regenerated human-ear-shaped cartilage that retained a satisfactory shape, good elasticity, abundant lacuna structure, and cartilage-specific ECM deposition. • Cell seeding efficiency in both ACM/gelatin and gelatin scaffolds was more than 90%, which was significantly superior than that of PGA/PLA scaffolds.	Important unknowns remain, including how best to optimize scaffold preparation, evaluation of scaffold biosafety, and the feasibility of human-ear-shaped cartilage regeneration in large animals.

(*Continued*)

Table 2. ***Continued***

Study	Aim of study	Study setting	Animal model (if any)	Study focus	3D printing technique	Components	Printed shape
Landau *et al.* (2021) [23]	To develop a clinical-grade, 3D-printed biodegradable auricle scaffold that formed stable, custom-made neocartilage implants.	*In vitro*; *in vivo* animal	Mice	Indirect printing	BVOH mold printing and subsequent seeding	Scaffold printed first and then seeded with cells	Resembling pinna; other shape
Yin *et al.* (2020) [22]	To assess the feasibility and *in vivo* long-term fate of elastic cartilage regenerated with an accurate human-ear shape using PCL inner support-strengthened biodegradable scaffold and expanded MCs to identify factors that may result in discrepant clinical outcomes.	*In vitro*; *in vivo* animal	Mice	Indirect printing	Resin 3D-printer to create a set of ear-shaped negative molds. A pair of PGA/PLA layers (150 mg PGA fibers each) and a PCL layer were then separately pre-shaped by the molds.	Scaffold printed first and then seeded with cells	Resembling pinna; other shape

Printed material	Cell nature/type	Notable post-printing modifications	Assessment of success/ integration	Findings	Limitations and suggested improvements
				• Chondrocytes grew well on the scaffold with significant proliferation over time and very few dead cells were observed at any of the time points. • By 14 days, the chondrocytes had spread over the entire scaffold. • Histological analysis performed at 6 weeks showed that the ear-shaped constructs had preliminarily formed cartilage-like tissue with typical lacuna structure and strong positive cartilage ECM staining. • However, the regenerated tissue showed a hybrid structure, and some fibrous tissue could be observed among the regenerated cartilage regions. • At 12 weeks, the constructs formed mature cartilage-like tissue with abundant lacuna structure and more homogenous cartilage ECM distribution, despite little fibrous tissue could still be observed in small areas.	
PCL	Chondrocytes and MSCs	Mold was freeze-dried and washed three times with water, PBS and then with a growth medium to create a hydrophilic environment for cell seeding.	Histopathology; micro-CT scan; mechanical testing; electron microscopy	• 3D printing was used to create a PCL ear-shaped cartilage for transplants for microtia patients. • The method can also be modified for use in cases of complete lack of auricular cartilage, such as anotia and trauma, by integrating costal cartilage cells. • The process is fast and simple for engineering a medical-grade auricle. • *In vitro* assessments showed a significant advantage for the use of monoculture auricular cartilage cells, but no significant differences were observed in the constructs of various cell types after implantation into mice. • No significant differences were observed in lacuna development or collagen-2, elastin, GAG, and collagen expression between the two constructs, regardless of cultivation time.	Small scale
A pair of PGA/ PLA layers and a PCL layer were separately pre-shaped by the molds.	Microtia chondrocytes	Cells seeded and examined for cell adhesion 24 h after incubation	Histopathology; mechanical testing	• All the cartilages generated by different patients' cells were highly consistent in both qualitative and quantitative data, indicating high repeatability and stability of the construction technology of cartilages. Besides, PCL inner support had no inhibitory effect on cartilage regeneration, maturation, tissue integration, mechanical strength, and shape maintenance even after the complete degradation of PCL. • The implanted auricle framework could survive for a long time and successfully regenerate mature and continuous cartilage with an accurate human-ear shape. • After 12 weeks of *in vitro* culture and 12 months of implantation *in vivo*, a porcelain white ear-shaped cartilage with a shape similarity to the original mold of 93.02% was formed.	Large animal models are needed

(*Continued*)

Table 2. ***Continued***

Study	Aim of study	Study setting	Animal model (if any)	Study focus	3D printing technique	Components	Printed shape
Liao *et al.* (2019) [24]	To reconstruct the auricle using a porous, hollow, 3D-printed mold and autologous diced cartilage mixed with PRP	*In vivo* animal	Rabbit	Indirect printing	Molds printed by SLS	Scaffold only	Resembling pinna
Zhou *et al.* (2018) [20]	To clinically apply tissue-engineered and 3D-printed ear-shaped cartilage to human subjects for the first time.	*In vitro*; *in vivo* human trial	N/A	Indirect printing	A resin model was generated through 3D printing. This resin ear model was used to cast a pair of negative molds.	Scaffold printed first and then seeded with cells	Resembling pinna

Printed material	Cell nature/type	Notable post-printing modifications	Assessment of success/ integration	Findings	Limitations and suggested improvements
				• The PCL support was completely covered by the regenerated cartilage with satisfactory integration. • Tissue-engineered cartilage shows typical phenotype of mature elastic cartilage similar to microtia ear tissue with typical lacuna structures and strong positive staining of safranin O, type Il collagen, and Verhoeff-van Gieson (EVG).	
Other: PGLA membrane	Diced cartilage graft	PRP was mixed with diced cartilage and sodium citrate, and this paste was inserted into the printed porous scaffold	Histopathology; mechanical testing	• The porous, hollow, poly-amide auricular mold prepared by 3D printing and packed with diced cartilages and PRP graft showed appropriate biomechanical properties and maintained it shape, with good chondrocyte viability and the production of a cartilaginous extracellular matrix • It was found that mixing the cartilage with a PRP improved the viability of the diced cartilage when wrapped in a PLGA membrane. • At 4 months, the diced cartilage pieces within the mold had fused, and the gross appearance was similar in shape to an auricle. • No complications (e.g., hematoma, seroma, or infection) were observed at the implantation site during the postoperative period. • The results of histological staining showed that the diced cartilages after shaping retained viable chondrocytes and a complete ECM, with positive staining for GAGs, collagen fibers, and elastic fibers, which determine the biomechanical properties of the cartilage.	The synthetic, non-biodegradable poly-amide induced a cystic-like reaction around the implant. It is unclear whether this translates in the clinical setting to the formation of a seroma or a chronic granuloma/foreign body reaction. Another limitation of this work is that we did not explore the possibility of using other biodegradable materials, such as PLGA for the hollow auricle mold.
PGA, PLA, and PCL were processed into the ear scaffold	Isolated microtia chondrocytes	Expanded microtia cartilage cells were evenly dropped onto the PGA/PLA layer of the scaffold, followed by 5-h incubation at 37°C, 5% CO_2. The construct was then cultured in chondrogenic medium for 12 weeks.	Histopathology; mechanical testing; electron microscopy; other: photography and visual inspection of final clinical result at 1, 2, 3, 6, 9, 12, 18, 24, and 30 months post-surgery to record swelling, inflammation signs, and shape recovery. MRI (1.5T) to trace cartilage regeneration and PCL core degradation	• It is possible to successfully design, fabricate, and re-generate patient-specific external ears (in human subjects). • 12 weeks of tissue expansion were used to create a large enough skin flap. A facial flap was used to cover the back and the helix rim of the engineered ear graft, which not only provided sufficient blood supply, but also protected the graft from extrusion. • Subsequent surgeries (scar revision) were conducted for removing the pedicle of skin flap at 6 months and repairing scar at 18 months, which allowed for tissue biopsies of the implanted ear framework. • After two weeks, the initial postoperative edema slowly reduced, and the shape of the reconstructed ear, as well as the color of the covered skin, gradually recovered. Within 6 months post-implantation, only the basic ear contour was observed, while key auricular structures, such as helix, triangular fossa, anti-helix, and cavum conchae, became gradually distinct after 9 months.	• Small sample of only 5 patients • Longest follow-up of only 2.5 years (other cases 2–18 months): unknown result after complete degradation of PCL scaffold (takes 2–4 years) • Only pilot study: further work necessary to translate this into routine clinical practices • Optimization and standardization in scaffold fabrication, cell expansion, and *in vitro* cartilage engineering, surgical procedures are still required. • Single center

(*Continued*)

Table 2. ***Continued***

Study	Aim of study	Study setting	Animal model (if any)	Study focus	3D printing technique	Components	Printed shape

Abbreviations: ACM, ; ACMMA, methacrylate-modified acellular cartilage matrix; ASCs, adipose-derived stem cells; AuCPCs, auricular cartilage progenitor cells; CAD, computer-aided design; CAM, computer-aided manufacturing; CPS, cell-printed structure; CSHS, cell-seeded hybrid scaffold; CSS, cell-seeded scaffold; CT, computed tomography; DLP, digital light processing; DMEM, Dulbecco's Modified Eagle Medium; ECM, extracellular matrix; FDM, fused deposition modeling; GAG, glycosaminoglycan; GelMA, gelatin methacrylate; H&E, hematoxylin and eosin staining; HA, hyaluronic acid; HAMA, hyaluronic acid methacrylate; MRI, magnetic resonance imaging; MSCs, mesenchymal stem cells; PBS, phosphate-buffered saline; PCL, polycaprolactone; PEG, polyethylene glycol; PEO, poly(ethylene oxide); PGA, polyglycolic acid; PGLA, poly(lactic-co-glycolic acid); PLA, polylactic acid; PPU, perforated polyurethane; PRP, platelet-rich plasma; PU, polyurethane; SEM, scanning electron microscopy; SLS, selective laser sintering; UV, ultraviolet.

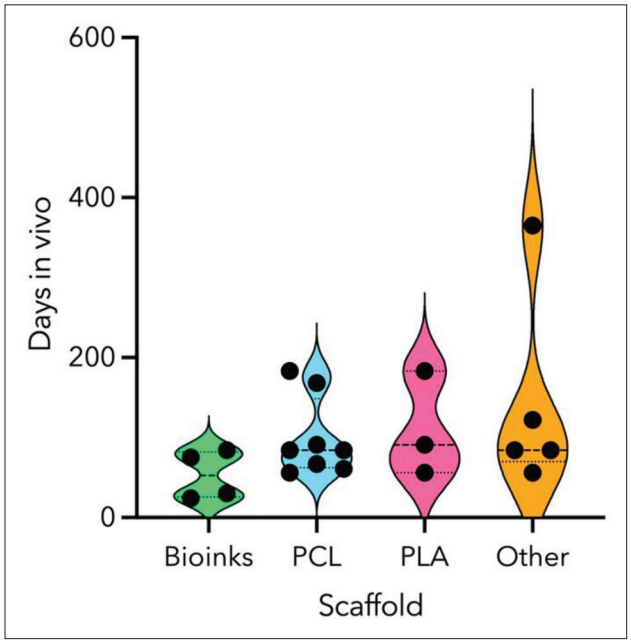

Figure 4. Time *in vivo* per scaffold type in experimental animal studies. Abbreviations: PCL, polycaprolactone; PLA, polylactic acid.

tomography (CT) scanning, and mechanical testing were all used to assess the resulting tissue-engineered auricles. However, given the wide range of printing methods, variable time *in vivo*, and heterogeneous use of outcome measures in the included studies, meaningful meta-analysis comparing scaffold materials and cartilage formation was not possible.

4. Discussion

4.1. Overcoming current obstacles to clinical translation

Auricular reconstruction is a challenging endeavor, partly due to the complex 3D geometry of the auricle[4], so unique to each individual that the pinna has been proposed as a forensic identifier[5].

This review demonstrates that 3D printing has the potential to have a significant impact on this relatively niche but complex area of reconstructive surgery by enhancing current surgical reconstructive options, and before clinical translation can truly occur, this technology requires optimization in multiple areas and large-scale clinical trials.

The printed auricle's desired anatomically detailed shape should be ensured for a lifetime, even after postoperative inflammatory processes have attempted to ravage the scaffold. Prevention of topographical blunting and volume loss requires both excellent cellular performance and abundant cartilage matrix, organized to mimic native elastic cartilage's histological and biomechanical properties. A certain degree of scaffold shrinkage is expected due to extrinsic compressive forces exerted by the overlying soft tissue, myocontractile

Printed material	Cell nature/type	Notable post-printing modifications	Assessment of success/ integration	Findings	Limitations and suggested improvements

				• At 12 months, the reconstructed auricle presented high stiffness and low flexibility, whereas at 24 months, an obvious improvement in inflexibility with more distinct structures were achieved.
				• Among the total five cases, four cases showed obvious cartilage formation after 6 months post-implantation (one case was lost to follow-up).
				• MRI conformed a significant portion of PCL has degraded (complete degradation of PCL *in vivo* normally requires 2–4 years). Biopsied samples revealed formation of mature *in vivo* cartilage at 6 months and 18 months post-operatively.
					• Multiple additional surgical steps incorporated:
					  • Tissue expanded preoperatively for 3 months (psychosocial impact)
					  • Split-thickness skin graft from groin was required
					  • Scar revision surgeries were required at 6 and 18 months

scarring, and intrinsic contractile forces as the scaffold matures[10]. Therefore, a fine balance must be struck between creating an auricle that is strong enough to maintain its shape and yet pliable enough to mimic true elastic cartilage and not cause ulceration, which happens when the mechanical stiffness of the skin is low in relation to the construct[33]. This means that the structure needs to either be synthetic with perfect mechanical properties and completely inert and free from biodegradation or that it needs to be partially biological and, over time, integrate into the patient's body. Several of the studies in this review attempted to solve this conundrum by combining bioinks and multiple materials or through specific post-printing modifications. However, all studies agree on the necessity of longer-term *in vivo* research. This is crucial to verify that the bioprinted constructs will maintain their form and functionality over time, without issues such as deformation or collapse[29].

Since more than 1 in 500 people is affected by an external ear deformity per year, large-scale production would be desirable. However, currently available bioprinting technologies are not ready for mass production, and concerns have been raised that the costs associated with cell harvest and expansion prior to construct fabrication are currently prohibitive to routine clinical use[34]. Arguably, this cost could be offset in saved operating time, not to mention the reduced morbidity (and thus cost) associated with not needing to perform rib cartilage grafting. In fact, Brennan *et al.* (2021) found that the implantation of a bioscaffold can be performed in under 25 min, as the surgical techniques involved are theoretically much simpler[4].

Additionally, regulatory approval is essential for 3D bioprinting applications in auricular reconstruction. In the United States, personalized 3D-printed medical devices are regulated under the medical device category or with custom device exemptions. The United States Food and Drug Administration (FDA) provides guidelines for 3D-printed materials to ensure product quality, efficacy, and classification for regulations. In the European Union, the regulation of 3D-printed medical devices has evolved. Previously, 3D-printed medical device products followed legislation like AIMDD 90/385/EE, MDD 93/42/EEC, and IVDMDD 98/79/EC, with medical devices classified based on patient contact duration, degree of invasiveness, and implantation/contact location in the human body[34,35]. However, the current regulation, known as the Medical Device Regulation (MDR 2017/745), has replaced these directives, providing a more comprehensive and stringent framework for the approval and post-market surveillance of medical devices[36]. Moreover, 3D-bioprinted tissues do not directly fall into existing regulatory categories. They are considered "bio-objects," which fall in between the existing categories of living and non-living matter, thus requiring new regulations/laws for clinical trials and commercialization. In this context, the European Regulation No. 1394/2007 and Directive 2001/83/EC,

which govern advanced therapeutic medicinal products, may provide some guidance[37,38].

Despite the progress in regulatory approval for 3D-printed medical devices, such as the FDA-approved AXIOM 20 3D printer and iFuse-3D implant, clear regulatory pathways for 3D-bioprinted tissues and their clinical applications are still needed[39].

4.2. Adjuvant considerations

From a surgical standpoint, this emerging technology should be examined holistically, including adjuvant techniques and factors that may impact outcomes.

4.2.1. Additional cover

In some trauma or burns cases, when more skin cover is necessary and cannot be sourced locally, a radial forearm pre-laminated flap may be a good source of additional skin, with an auricular scaffold implanted in the forearm before the main reconstruction[2]. Alternatively, good outcomes are achievable with skin grafts on top of 3D-printed scaffolds[3]. As with allografts, a temporoparietal fascial flap may be used with scaffolds to help mitigate soft tissue complications[4]. However, this carries additional local morbidity and prolongs operating time, so ultimately, a flap is not needed in the reconstruction at all.

4.2.2. Hearing restoration

Conductive hearing loss is present in 85% of microtia case[35]; thus, canalplasty is usually required to obtain a patent external auditory canal (EAC). The timing of the canaloplasty is linked to planned auricular reconstruction. It is typically done after it so an unoperated and unscarred field is preserved for auricle placement, and the delay avoids the need to center the framework over a drilled-out canal[40].

3D printing is also being developed for EAC reconstruction[41], and so far, techniques like using drug-releasing implants have been incorporated to prevent postoperative restenosis[42]. Tympanic membranes are also being printed[43], as are ossicles[44]. However, these efforts appear to be at a more fledgling stage than auricular reconstruction, probably because of the more complex functional requirements. Many techniques and materials used for auricular reconstruction may eventually be transferrable to other reconstructions, such as the EAC and vice versa.

5. Conclusion and future outlook

The auricle is uniquely histologically suitable for 3D printing, but a plethora of challenges remain. The fact that the majority of the existing evidence in this field is thus far only foundational and that this review identified only one level IV study demonstrates that this is very much an evolving field. However, it is a field that holds much promise, and the emergence of human trials internationally attests to this. Notably, phase 1 and 2 human trials are currently underway in the United States and are due to be completed by February 2028[45,46]. This demonstrates that this particular innovation has the potential to be adopted into clinical practice soon. However, a number of regulatory and practical concerns still need to be overcome. There is tremendous translational potential, and even if it may not necessarily become a routine component of microtia reconstruction overnight, auricle bioprinting may pave the way for 3D printing in other reconstructive efforts in plastic surgery over the next decade.

Acknowledgments

None.

Funding

None.

Conflict of interest

None.

Author contributions

Conceptualization: Anna Onderková
Supervision: Deepak M. Kalaskar
Visualization: Anna Onderková
Writing – original draft: Anna Onderková
Writing – review & editing: Anna Onderková, Deepak M. Kalaskar

Ethics approval and consent to participate

Not applicable.

Consent for publication

Not applicable.

Availability of data

Not applicable.

References

1. Humphries S, Joshi A, Webb WR, *et al.*, 2021. Auricular reconstruction: Where are we now? A critical literature review. *Eur Arch Oto-Rhino-Laryngol*, 279(2): 541–56.

https://10.1007/s00405-021-06903-5

2. Rendón-Medina MA, Hanson-Viana E, Arias-Salazar L, *et al.*, 2022, Auricular total reconstruction with radial

forearm prelaminated flap assisted by 3D surface imaging and 3D printing. *Plast Reconstr Surg - Glob Open*, 10: e4580.

https://10.1097/gox.0000000000004580

3. Apelgren P, Amoroso M, Säljö K, *et al*., 2018, Skin grafting on 3D bioprinted cartilage constructs in vivo. *Plast Reconstr Surg - Glob Open*, 6: e1930.

https://10.1097/gox.0000000000001930

4. Brennan JR, Cornett A, Chang B, *et al*., 2021, Preclinical assessment of clinically streamlined, 3d-printed, biocompatible single- and two-stage tissue scaffolds for ear reconstruction. *J Biomed Mater Res Part B*, 109(3): 394–400.

https://10.1002/jbm.b.34707

5. Jovic TH, Stewart K, Kon M, *et al*., 2020, Auricular reconstruction: A sociocultural, surgical and scientific perspective. *J Plast Reconstr Aesthet Surg*, 73(8): 1424–1433.

https://10.1016/j.bjps.2020.03.025

6. Horlock N, Vögelin E, Bradbury ET, *et al*., 2005, Psychosocial outcome of patients after ear reconstruction. *Ann Plast Surg*, 54(5): 517–524.

https://10.1097/01.sap.0000155284.96308.32

7. Ross MT, Cruz R, Hutchinson C, *et al*., 2018, Aesthetic reconstruction of microtia: A review of current techniques and new 3D printing approaches. *Virtual Phys Prototyp*, 13(2): 117–130.

https://10.1080/17452759.2018.1430246

8. Jang CH, Koo YW, Kim GH, 2020, ASC/chondrocyte-laden alginate hydrogel/PCL hybrid scaffold fabricated using 3D printing for auricle regeneration. *Carbohyd Polym*, 248: 116776.

https://10.1016/j.carbpol.2020.116776

9. Chung JH, Kade JC, Jeiranikhameneh A, *et al*., 2020, 3D hybrid printing platform for auricular cartilage reconstruction. *Biomed Phys Eng Express*, 6: 035003.

https://10.1088/2057-1976/ab54a7

10. Dong X, Premaratne ID, Bernstein JL, *et al*., 2021, Three-dimensional-printed external scaffolds mitigate loss of volume and topography in engineered elastic cartilage constructs. *Cartilage*, 13(1).

https://10.1177/19476035211049556

11. Jia L, Hua Y, Zeng J, *et al*., 2022, Bioprinting and regeneration of auricular cartilage using a bioactive bioink based on microporous photocrosslinkable acellular cartilage matrix. *Bioact Mater*, 16: 66–81.

https://10.1016/j.bioactmat.2022.02.032

12. Justicz N, Dusseldorp JR, Shaye D, 2017, Firmin technique for microtia reconstruction. *Oper Tech Otolaryngol Head Neck Surg*, 28(2): 90–96.

https://10.1016/j.otot.2017.03.005

13. Nagata S, Maruyama S, 2022, Auricular reconstruction Nagata method. *Nagata Microtia and Reconstructive Plastic Surgery Clinic*.

https://www.nagata-microtia.com/method.html (accessed November 26, 2022).

14. Xia H, Zhao D, Zhu H, *et al*., 2018, Lyophilized scaffolds fabricated from 3D-printed photocurable natural hydrogel for Cartilage Regeneration. *ACS Appl Mater Interfaces*, 10(35): 31704–31715.

https://10.1021/acsami.8b10926

15. Tang P, Song P, Peng Z, *et al*., 2021, Chondrocyte-laden Gelma hydrogel combined with 3D printed PLA scaffolds for auricle regeneration. *Mater Sci Eng C*, 130: 112423.

https://10.1016/j.msec.2021.112423

16. Roopavath UK, Kalaskar DM, 2022, Introduction to three-dimensional printing in medicine, in 3D Printing in Medicine. *Woodhead Publishing*, Cambridge 1–27.

https://10.1016/B978-0-323-89831-7.00008-0

17. Berens AM, Newman S, Bhrany AD, *et al*., 2016, Computer-aided design and 3D printing to produce a costal cartilage model for simulation of auricular reconstruction. *Otolaryngol Head Neck Surg*, 155(2): 356–359.

https://10.1177/0194599816639586

18. Hong CJ, Giannopoulos AA, Hong BY, *et al*., 2019, Clinical applications of three-dimensional printing in otolaryngology–head and neck surgery: A systematic review. *The Laryngoscope*, 129(8): 2045–2052.

https://10.1002/lary.27831

19. Beckers O, Coppey E, Mommaerts MY, 2021, Computer-aided design and manufacturing construction of a pilot guide for a bone-anchored epithesis to replace an absent pinna. *Int J Oral Maxillofac Surg*, 50(7): 815–819.

https://10.1016/j.ijom.2020.10.006

20. Zhou G, Jiang H, Yin Z, *et al*., 2018, In vitro regeneration of patient-specific ear-shaped cartilage and its first clinical application for auricular reconstruction. *EBioMedicine*, 28(2): 287–302.

https://10.1016/j.ebiom.2018.01.011

21. Mukherjee P, Chung J, Cheng K, *et al*., 2021, In vitro and in vivo study of PCL-hydrogel scaffold to advance bioprinting translation in microtia reconstruction. *J Craniofac Surg*, 32(5): 1931–1936.

https://10.1097/scs.0000000000007173

22. Yin Z, Li D, Liu Y, *et al*., 2020, Regeneration of elastic cartilage with accurate human-ear shape based on PCL strengthened biodegradable scaffold and expanded microtia chondrocytes. *Appl Mater Today*, 20: 100724.

https://10.1016/j.apmt.2020.100724

23. Landau S, Szklanny AA, Machour M, *et al*., 2021, Human-engineered auricular reconstruction (hear) by 3D-printed molding with human-derived auricular and costal chondrocytes and adipose-derived mesenchymal stem cells. *Biofabrication*, 14(1): 015010.

    https://10.1088/1758-5090/ac3b91

24. Liao J, Chen Y, Chen J, *et al*., 2019, Auricle shaping using 3D printing and autologous diced cartilage. *The Laryngoscope*, 129(12): 2467–2474.

    https://10.1002/lary.27752

25. Jia L, Zhang Y, Yao L, *et al*., 2020, Regeneration of human-ear-shaped cartilage with acellular cartilage matrix-based biomimetic scaffolds. *Appl Mater Today*, 20: 100639.

    https://10.1016/j.apmt.2020.100639

26. Bhamare N, Tardalkar K, Parulekar P, *et al*., 2021, 3D printing of human ear pinna using cartilage specific ink. *Biomed Mater*, 16(5): 055008.

    https://10.1088/1748-605x/ac15b0

27. Lee J-S, Hong JM, Jung JW, *et al*., 2014, 3D printing of composite tissue with complex shape applied to ear regeneration. *Biofabrication*, 6(2): 024103.

    https://10.1088/1758-5082/6/2/024103

28. Visscher DO, Lee H, van Zuijlen PPM, *et al.*, 2021, A photo-crosslinkable cartilage-derived extracellular matrix bioink for auricular cartilage tissue engineering. *Acta Biomater*, 121(1): 193–203.

    https://10.1016/j.actbio.2020.11.029

29. Otto IA, Capendale PE, Garcia JP, *et al.*, 2021, Biofabrication of a shape-stable auricular structure for the reconstruction of Ear Deformities. *Mater Today Bio*, 9: 100094.

    https://10.1016/j.mtbio.2021.100094

30. Kim HY, Jung SY, Lee SJ, *et al*., 2019, Fabrication and characterization of 3D-printed elastic auricular scaffolds: A pilot study. *The Laryngoscope*, 129(2): 351–357.

    https://10.1002/lary.27344

31. Christen M-O, Vercesi F, 2020, Polycaprolactone: How a well-known and futuristic polymer has become an innovative collagen-stimulator in esthetics. *Clin Cosmet Investig Dermatol*, 13: 31–48.

    https://10.2147/ccid.s229054

32. Zhang X, Battiston KG, McBane JE, *et al*., 2016, Design of biodegradable polyurethanes and the interactions of the polymers and their degradation by-products within in vitro and in vivo environments. *Adv Polyureth Biomater*, 75–114.

    https://10.1016/b978-0-08-100614-6.00003-2

33. Reighard CL, Hollister SJ, Zopf DA, 2018, Auricular reconstruction from rib to 3D printing. *J 3D Print Med*, 2(1): 35–41.

    https://10.2217/3dp-2017-0017

34. Di Gesù R, Acharya AP, Jacobs I, *et al.*, 2019, 3D printing for tissue engineering in otolaryngology. *Connect Tissue Res*, 61(2): 117–136.

    https://10.1080/03008207.2019.1663837

35. Sekar MP, Budharaju H, Zennifer A, *et al*., 2021, Current standards and ethical landscape of engineered tissues—3D bioprinting perspective. *J Tissue Eng*, 12(1): 204173142110276.

    https://10.1177/20417314211027677

36. European Parliament, Council of the European Union. Regulation (EU) 2017/745 of the European Parliament and of the Council of 5 April 2017 on medical devices, amending Directive 2001/83/EC, Regulation (EC) No 178/2002 and Regulation (EC) No 1223/2009 and repealing Council Directives 90/385/EEC and 93/42/EEC. Official Journal of the European Union. 2017 [cited 2023 Jun 7].

    https://eur-lex.europa.eu/legal-content/EN/TXT/?uri=CELEX:02017R0745-20200424

37. European Parliament, Council of the European Union. Regulation (EC) No 1394/2007 of the European Parliament and of the Council of 13 November 2007 on advanced therapy medicinal products and amending Directive 2001/83/EC and Regulation (EC) No 726/2004. Official Journal of the European Union. 2007 [cited 2023 Jun 7].

    https://eur-lex.europa.eu/legal-content/EN/ALL/?uri=CELEX%3A32007R1394

38. European Parliament, Council of the European Union. Directive 2001/83/EC of the European Parliament and of the Council of 6 November 2001 on the Community code relating to medicinal products for human use. Official Journal of the European Communities. 2001 [cited 2023 Jun 7].

    https://eur-lex.europa.eu/LexUriServ/LexUriServ.do?uri=CELEX:32001L0086:EN:HTML

39. Ali K, Mohan K, Liu Y-C, 2017, Otologic and audiology concerns of microtia repair. *Semin Plast Surg*, 31(2): 127–133.

    https://10.1055/s-0037-1603957

40. Lipan M, Eshraghi A, 2011, Otologic and audiology aspects of microtia repair. *Semin Plast Surg*, 25(4): 273–278.

    https://10.1055/s-0031-1288919

41. Mota C, Milazzo M, Panetta D, *et al*., 2018, 3D fiber deposited polymeric scaffolds for external auditory canal wall. *J Mater Sci: Mater Med*, 29(10).

    https://10.1007/s10856-018-6071-3

42. Matin-Mann F, Gao Z, Schwieger J, *et al.*, 2022, Individualized, additively manufactured drug-releasing external ear canal implant for prevention of postoperative restenosis: Development, in vitro testing, and proof of concept in an individual curative trial. *Pharmaceutics*, 14(6): 1242.

    https://10.3390/pharmaceutics14061242

43. Kozin ED, Black NL, Cheng JT, *et al*., 2016, Design, fabrication, and in vitro testing of novel three-dimensionally printed tympanic membrane grafts. *Hear Res*, 340: 191–203.

https://10.1016/j.heares.2016.03.005

44. Hirsch JD, Vincent RL, Eisenman DJ, 2017, Surgical reconstruction of the ossicular chain with custom 3D printed ossicular prosthesis. *3D Print Med*, 3(15).

https://10.1186/s41205-017-0015-2

45. 3DBio Therapeutics, 2022, Aurinovo for auricular reconstruction. ClinicalTrialsgov.

https://clinicaltrials.gov/ct2/show/NCT04399239 (accessed December 7, 2022).

46. Everett H, 2022, 3DBio conducts successful human ear reconstruction with 3D bioprinted Aurinovo implant. 3D Printing Industry.

https://3dprintingindustry.com/news/3dbio-conducts-successful-human-ear-reconstruction-with-3d-bioprinted-aurinovo-implant-210201/ (accessed December 7, 2022).

47. Chang B, Cornett A, Nourmohammadi Z, *et al*., 2020, Hybrid three-dimensional–printed ear tissue scaffold with autologous cartilage mitigates soft tissue complications. *The Laryngoscope*, 131(E5): 1008–1015.

https://10.1002/lary.29114

48. Dong X, Askinas C, Kim J, *et al*., 2022, Efficient engineering of human auricular cartilage through mesenchymal stem cell chaperoning. *J Tissue Eng Regen Med*, 16(6): 825–835.

https://10.1002/term.3332

49. Park JY, Choi Y-J, Shim J-H, *et al*., 2017, Development of a 3D cell printed structure as an alternative to autologs cartilage for auricular reconstruction. *J Biomed Mater Res Part B Appl Biomater*, 105(4): 1016–1028.

https://10.1002/jbm.b.33639

50. Visscher DO, Bos EJ, Peeters M, *et al*., 2016, Cartilage tissue engineering: Preventing tissue scaffold contraction using a 3D-printed polymeric cage. *Tissue Eng Part C: Methods*, 22(6): 573–584.

https://10.1089/ten.tec.2016.0073

51. Visscher DO, Gleadall A, Buskermolen JK, *et al*., 2018, Design and fabrication of a hybrid alginate hydrogel/poly(ε-caprolactone) mold for auricular cartilage reconstruction. *J Biomed Mater Res Part B: Appl Biomater*, 107(6): 1711–1721.

https://10.1002/jbm.b.34264

52. Zopf DA, Mitsak AG, Flanagan CL, *et al*., 2014, Computer aided–designed, 3-dimensionally printed porous tissue bioscaffolds for craniofacial soft tissue reconstruction. *Otolaryngol–Head Neck Surg*, 152(1): 57–62.

https://10.1177/0194599814552065

53. Xie X, Wu S, Mou S, *et al*., 2022, Microtissue-based bioink as a chondrocyte microshelter for DLP bioprinting. *Adv Healthc Mater*, 11(1): 2201877.

https://10.1002/adhm.202201877

54. Zopf DA, Flanagan CL, Mitsak AG, *et al*., 2018, Pore architecture effects on chondrogenic potential of patient-specific 3-dimensionally printed porous tissue bioscaffolds for auricular tissue engineering. *Int J Pediatr Otorhinolaryngol*, 114: 170–174.

https://10.1016/j.ijporl.2018.07.033

ACCSCIENCE PUBLISHING

International Journal of Bioprinting

RESEARCH ARTICLE

Rheology-informed hierarchical machine learning model for the prediction of printing resolution in extrusion-based bioprinting

Dageon Oh[1], Masoud Shirzad[1], Min Chang Kim[2], Eun-Jae Chung[3], and Seung Yun Nam[1,2]*

[1]Industry 4.0 Convergence Bionics Engineering, Pukyong National University, Busan 48513, Republic of Korea

[2]Major of Biomedical Engineering, Division of Smart Healthcare, Pukyong National University, Busan 48513, Republic of Korea

[3]Department of Otorhinolaryngology-Head and Neck Surgery, Seoul National University College of Medicine, Seoul 03080, Republic of Korea

Abstract

In this study, a rheology-informed hierarchical machine learning (RIHML) model was developed to improve the prediction accuracy of the printing resolution of constructs fabricated by extrusion-based bioprinting. Specifically, the RIHML model, as well as conventional models such as the concentration-dependent model and printing parameter-dependent model, was trained and tested using a small dataset of bioink properties and printing parameters. Interestingly, the results showed that the RIHML model exhibited the lowest error percentage in predicting the printing resolution for different printing parameters such as nozzle velocities and pressures, as well as for different concentrations of the bioink constituents. Besides, the RIHML model could predict the printing resolution with reasonably low errors even when using a new material added to the alginate-based bioink, which is a challenging task for conventional models. Overall, the results indicate that the RIHML model can be a useful tool to predict the printing resolution of extrusion-based bioprinting, and it is versatile and expandable compared to conventional models since the RIHML model can easily generalize and embrace new data.

Keywords: Bioprinting; Printability; Machine learning; Rheology; Printing resolution

***Corresponding author:**
Seung Yun Nam
(synam@pknu.ac.kr)

Citation: Oh D, Shirzad M, Kim MC, *et al*., 2023, Rheology-informed hierarchical machine learning model for the prediction of printing resolution in extrusion-based bioprinting. *Int J Bioprint*, 9(6): 1280.
https://doi.org/10.36922/ijb.1280

Received: March 16, 2023
Accepted: July 13, 2023
Published Online: August 9, 2023

Copyright: © 2023 Author(s). This is an Open Access article distributed under the terms of the Creative Commons Attribution License, permitting distribution, and reproduction in any medium, provided the original work is properly cited.

Publisher's Note: AccScience Publishing remains neutral with regard to jurisdictional claims in published maps and institutional affiliations.

1. Introduction

In recent times, additive manufacturing approaches including three-dimensional (3D) bioprinting have emerged as essential tools for fabricating artificial tissue and organ constructs. Specifically, compared to conventional biofabrication methods, the 3D bioprinting technique can effectively deposit bioink layer by layer with a designed combination of biomaterials and living cells in desired locations and patterns[1-5]. The primary bioprinting methods include inkjet-based bioprinting, extrusion-based bioprinting, and laser-assisted bioprinting[6-9]. Among them, extrusion-based bioprinting has been the most widely used technique for research and commercial purposes. This is

principally due to the availability of a wide range of usable material viscosity, which allows for freedom in material selection when preparing bioink[10-16].

However, the advantages of the generous availability of bioink candidates including hydrogels, extracellular matrix, bioceramic particles, and shear thickening materials create difficulties in tuning bioink compositions and finding appropriate printing conditions[17,18]. Thus, to overcome these challenges and complexities in the preparation of bioinks and extrusion-based bioprinting, printability has recently attracted considerable attention. Although the definition of printability in extrusion-based bioprinting is still in discussion, it is obvious that better printability can improve the printing accuracy and shape fidelity of the printed constructs, leading to faster fabrication speed and long-term stable functionality[19-22]. Further, recent printability studies have quantitatively evaluated printing accuracy and shape fidelity using the assessment of various outcomes, such as printing resolution relative to the nozzle diameter, distance between filaments, pore size and shape in a grid structure, and height of the stacked layers[23-25]. In addition, these studies have demonstrated that printability is deeply linked to how to control the rheological properties of bioinks (viscosity, shear modulus, and gelation) and the printing parameters (printing pressure, temperature, nozzle size, nozzle length, and nozzle velocity)[26-32]. However, it is still difficult to find the optimal printing conditions because the assessment of the printability often relies on trial and error with a repeated change of the bioink composition and printing parameters, which is time-consuming and cost-ineffective.

Hence, printability prediction is critical to the accurate and effective fabrication of tissue-engineered constructs using the extrusion-based bioprinting technique. In several existing studies, the physical model-based computation was adopted for printability prediction[33-38]. More precisely, the physical model of printability prediction was derived from hydrodynamic equations combined with the rheological modeling of generalized Newtonian fluid, mainly power-law fluid. Using the physical model, the printing resolution of the output filament was simulated with multiple printing parameters and compared with the actual printing resolution. Although several studies using the physical model reported interesting results, the model holds many assumptions and simplifications, limiting its application in various bioprinting tasks. For instance, the physical prediction model is highly sensitive to the power law index, which can be obtained by the line fitting of the measured viscosity. Thus, small errors in rheological measurement and line fitting may have a significant effect on prediction accuracy. Additionally, the assumptions in the physical model, such as the incompressibility of bioink and the ideal pressure drop in the system, may not coincide with reality; hence, the accumulated errors can cause a gap between the predicted and actual results.

Recently, multiple studies of printability prediction using machine learning have been reported to overcome the limitations of physical models. Besides, due to the time-consuming and sequential bioprinting procedure from bioink preparation to 3D deposition, the size of the acquired dataset is relatively small. Therefore, most of these studies employed simple supervised machine learning methods, such as support vector machine, decision tree, lasso regression, and ridge regression, to estimate printing resolution with the confined variation of bioink composition and printing parameters[39-43]. Specifically, a few studies employed artificial neural networks for printability prediction, but its architecture is hardly deep with shallow hidden layers and a limited number of neurons because of the dataset size[44-46]. Moreover, in most of the neural network-based printability prediction models, superficial parameters such as the concentration of each bioink component were used in the input layer of the artificial neural network. This may significantly limit the expandability of the machine learning model since the neural network should be rebuilt and newly trained for every change in the bioink composition. Therefore, an improved machine learning model, which is versatile with various bioink combinations and penetrates the essence of bioprinting with profoundly related parameters, is required.

Furthermore, the rheological properties, such as viscosity and shear modulus, of bioinks have been verified to be closely related to the printing parameters to optimize the printability of extrusion-based bioprinting (Figure 1)[47-53]. For instance, even though the viscosity of bioink increases, the flow rate can be maintained if the printing parameters such as pressure and nozzle size are appropriately increased. Even with the same flow rate, the printing resolution significantly correlates with the shear modulus and nozzle velocity. Despite the deep correlation between rheology and printability, there have been no studies that actively applied rheological measurements of various bioinks and multiple printing parameters to machine learning.

Therefore, in this study, a rheology-informed hierarchical machine learning (RIHML) model was developed to predict printability in extrusion-based bioprinting. Among previously suggested methods to quantify printability, the assessment of printing resolution, which has been widely applied in numerous printability studies, was mainly adopted. To construct a dataset for training the models, the optical images of printed scaffolds

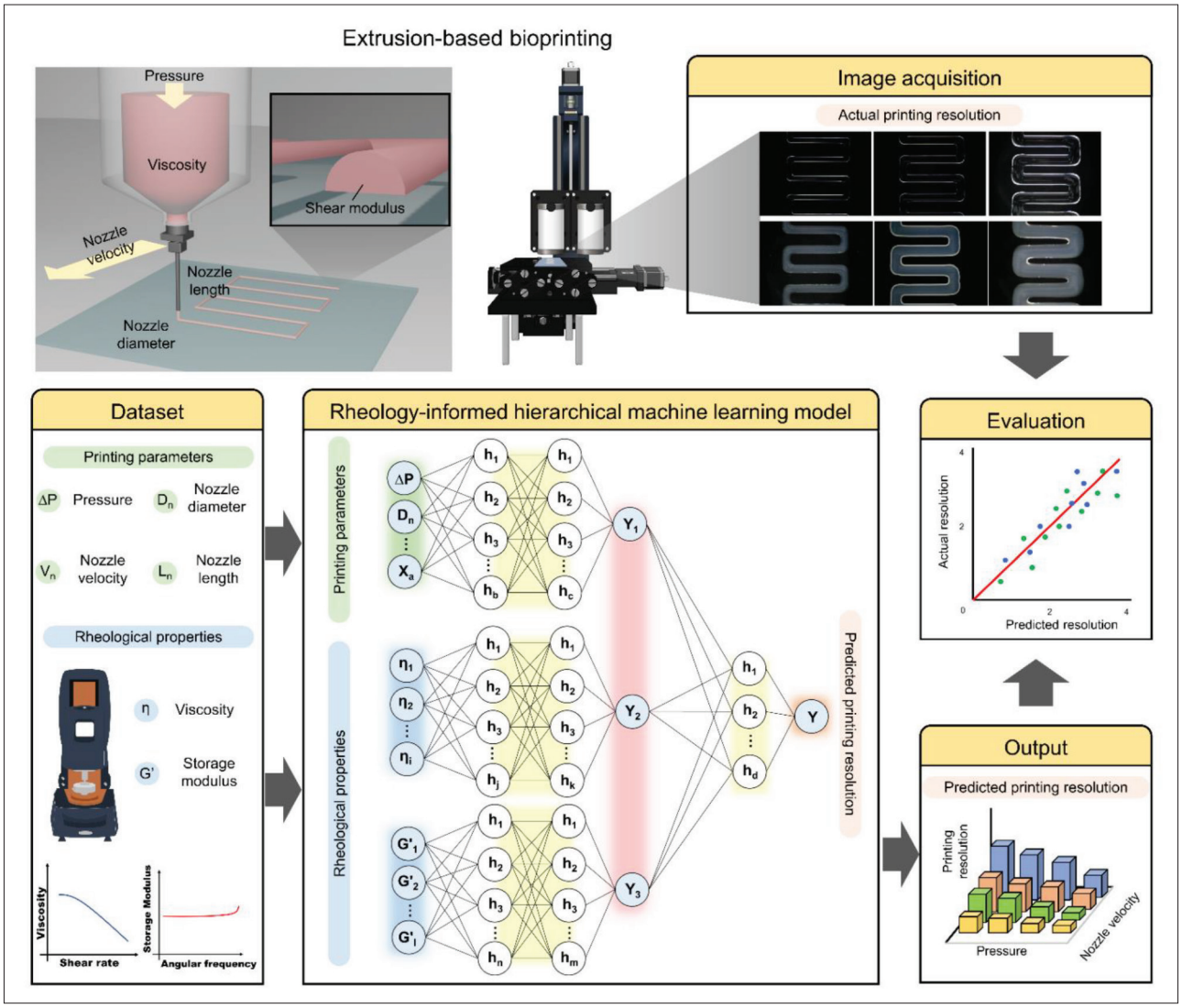

Figure 1. Overview of the process of the prediction of printing resolution based on a rheology-informed hierarchical machine learning model.

were collected with various printing conditions and bioink concentrations on a digital microscope. The acquired image was processed to quantify the printing resolution using an automated program to calculate strand size. In addition, the assessed viscosity and storage modulus were used as a rheological dataset to construct the input layers of a multi-input neural network combined with the printing parameters. Thus, the RIHML model, as well as the conventional models such as the concentration-dependent machine learning (CDML) model and printing parameter-dependent machine learning (PDML) model, was trained and tested using a small dataset of bioink properties and printing parameters. After model training, the prediction accuracy using each machine learning model was verified and compared for different printing parameters, such as nozzle velocities and pressures, as well as for different concentrations of bioink constituents. In addition, printing resolution was assessed using a new material added to the alginate-based bioink, to examine the feasibility of the RIHML as a versatile and expandable tool to predict the printing accuracy in extrusion-based bioprinting.

2. Materials and methods

2.1. Bioink preparation

In this study, ten bioinks were prepared using three base hydrogels and three additives as shown in Table 1. Precisely, Pluronic F-127 (F127, Sigma-Aldrich) was used as the base material without additives. Particularly, it was dissolved in deionized water at 4°C and prepared with three concentrations of 35%, 40%, and 45%. Another base bioink material, gelatin (porcine skin-derived, Sigma-Aldrich),

Table 1. Different types of bioink and their compositions in weight percentage

Formulation	F127 (%)	Alginate (%)	$CaCl_2$ (%)	CNC (%)	Gelatin (%)	XG (%)
F127 35%	35	0	0	0	0	0
F127 40%	40	0	0	0	0	0
F127 45%	45	0	0	0	0	0
Gelatin 10%/XG 2%	0	0	0	0	10	2
Gelatin 5%/XG 3%	0	0	0	0	5	3
Gelatin 10%/XG 4%	0	0	0	0	10	4
Alginate 2%/$CaCl_2$ 0.2%	0	2	0.2	0	0	0
Alginate 2%/$CaCl_2$ 0.3%	0	2	0.3	0	0	0
Alginate 2%/CNC 2.5%	0	2	0	2.5	0	0
Alginate 2%/CNC 5%	0	2	0	5	0	0

Abbreviations: CNC, cellulose nanocrystal; XG, xanthan gum.

was mixed homogeneously with xanthan gum (XG, Sigma-Aldrich) in three concentrations of 2%, 3%, and 4% in a planetary centrifugal mixer (AR-100, Thinky). Additionally, sodium alginate (Sigma-Aldrich) was used as a base material, and it was crosslinked by calcium chloride ($CaCl_2$, Sigma-Aldrich) with two concentrations of 0.2% and 0.3%, to increase the viscosity. Specifically, the sodium alginate and $CaCl_2$ were mixed at a ratio of 7:3 using a three-way stopcock, and the final concentration of the alginate solution was 2%. Furthermore, cellulose nanocrystal (CNC, CelluForce) was utilized to improve the rheological properties of the alginate-based bioink. To prepare the sodium alginate/CNC composite bioink, sodium alginate solution was mixed with dispersed CNCs in deionized water using the planetary centrifugal mixer, and the final concentrations of CNC were 2.5% and 5%, respectively.

2.2. Rheological characterization

The rheological properties of the bioinks were measured using a rotational rheometer (HR-2, TA Instruments) with a 20 mm parallel plate at a gap distance of 1000 μm. In addition, the printing temperature of the gelatin-based bioink was estimated by a temperature sweep test, which measured the storage modulus and loss modulus at an angular frequency of 10 rad/s. Specifically, for the flow sweep test, the shear rate was increased from 0.1 to 1000 1/s at 23°C for alginate-based and Pluronic-F127 bioinks. For gelatin-based bioinks, the temperature was set to 35°C to enhance printability. Following the amplitude sweep to determine the appropriate strain, the frequency sweep test was conducted to evaluate storage modulus within a specific angular frequency range. Specifically, the test commenced at 0.1 rad/s and concluded at 500 rad/s with the same temperatures as in the flow sweep test and a strain of 1% for each bioink.

2.3. Bioprinting

In this study, all bioinks were printed with the same one-layer scaffold structure. More precisely, the structure was designed with physical dimensions of 12 × 24 mm and a strand-to-strand distance of 4 mm. Specifically, all the scaffolds were fabricated at the same distance of 0.4 mm between the nozzle tip and the printing plate. Furthermore, two types of nozzles, i.e., 21G (inner diameter: 514 μm) and 23G (inner diameter: 337 μm) with multiple lengths (L: 2.54 cm in length for 21G and 23G; S: 1.27 cm in length for 21G), were used to print the scaffolds. Additionally, the Pluronic-F127 and sodium alginate-based bioinks were printed at room temperature (23°C), and the gelatin-based bioinks were printed at a temperature of 35°C, which was the same as the rheological characterization. Moreover, four different values of the nozzle velocity (speed of printer head movement), including 1, 2, 4, and 8 mm/s, were examined in the bioprinting process. Due to the differences in viscosity and yield strength of the bioinks, the printing pressure was adjusted depending on the extrudability of each bioink at a pressure range between 10 and 350 kPa.

2.4. Data acquisition

The processes of printing and rheological data acquisition for the prediction of printing resolution are described in Figure 2A. In the first step, bioinks with different compositions and concentrations (F127, gelatin/XG, alginate/$CaCl_2$, and alginate/CNC) were prepared; afterward, measurement of the rheological properties and printing of scaffolds were performed, respectively. Specifically, structures were fabricated in the extrudable range of each bioink with a designated path. Precisely, scaffolds were printed with five-center lines, and images were taken and saved by a digital microscope in 2592 × 1944 pixels. Except for a reference line, four lines were evaluated in the images to calculate the printing resolution

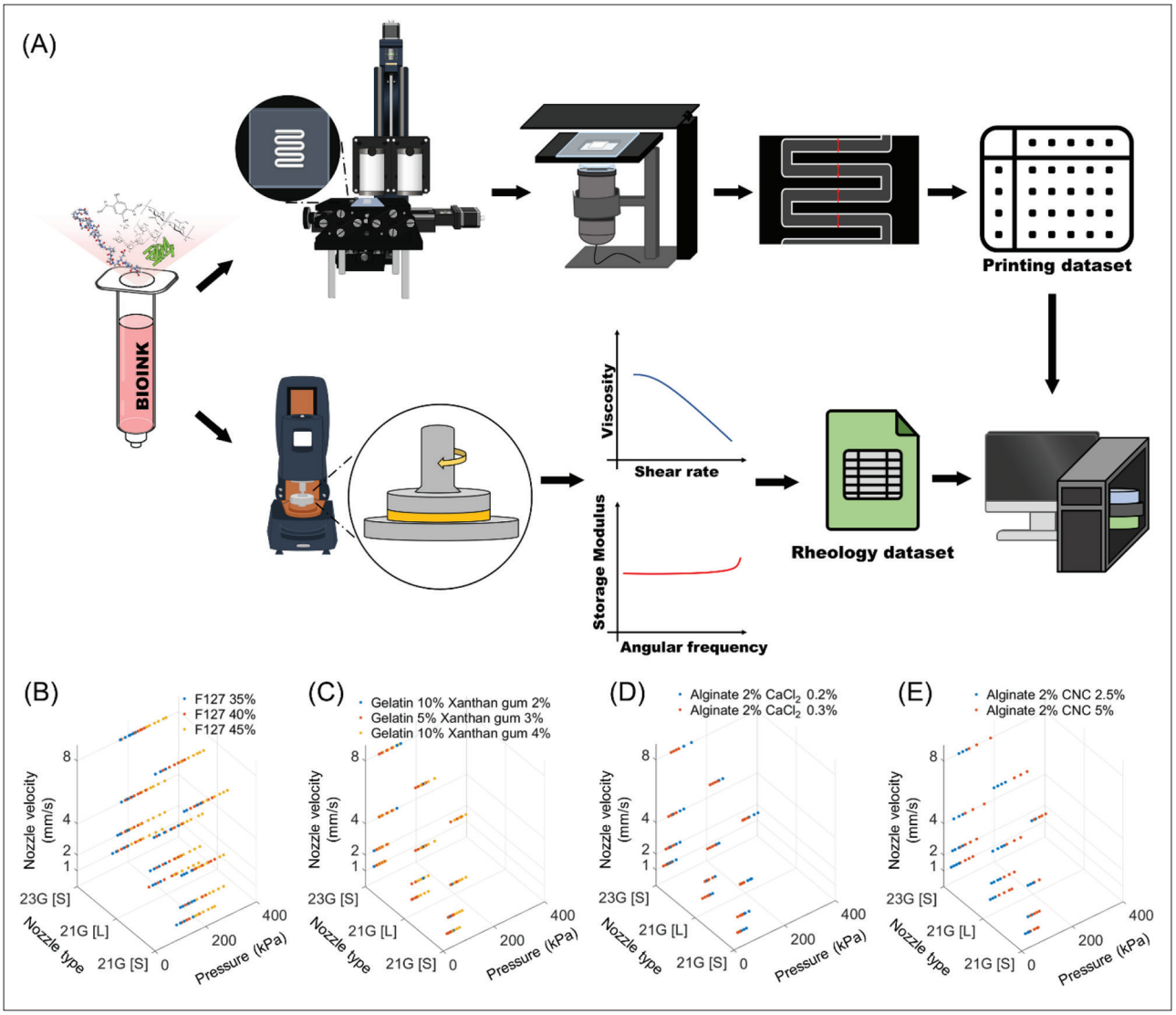

Figure 2. (A) Process of data acquisition: investigation of printing resolution and rheological assessment. 3D graphs of the collected data with printing parameters for the bioink compositions of (B) F127, (C) gelatin/xanthan gum, (D) alginate/$CaCl_2$, and (E) alginate/CNC composite.

using the algorithm to measure the strand size, as shown in **Figure S1** (Supplementary File). In particular, the algorithm was composed of two main steps. The first step was finding the path line, which can decrease errors by a missed detection of the line. Afterward, the image was changed to grayscale, and a position where the centers of the maximum signals on each line matched the printing path was found. The second step was to quantify the average strand size. Specifically, the image was reconstructed to a binary one and cropped with white pixels to leave 2 mm from the center lines to each side. Particularly, nine lines in the cropped image were selected using a projection grade of white pixels. Specifically, when the path and the selected lines were matched up, the average strand size of the scaffolds was calculated. The information on material concentration, printing pressure, nozzle diameter, nozzle length, nozzle velocity, and printing resolution was stored in the printing dataset. Furthermore, to create a sub-dataset for the rheological properties, 41 values of measured viscosity and 21 values of storage modulus data were acquired at the angular frequency region from 0.1 to 10 rad/s and subsequently, saved with bioink information.

2.5. Machine learning model

This study utilized two classical machine learning algorithms (random forest [RF] and support vector machine [SVM]), two conventional machine learning models (printing parameter-dependent machine learning model [PDML] and concentration-dependent machine learning model [CDML]), and a developed multi-input machine learning

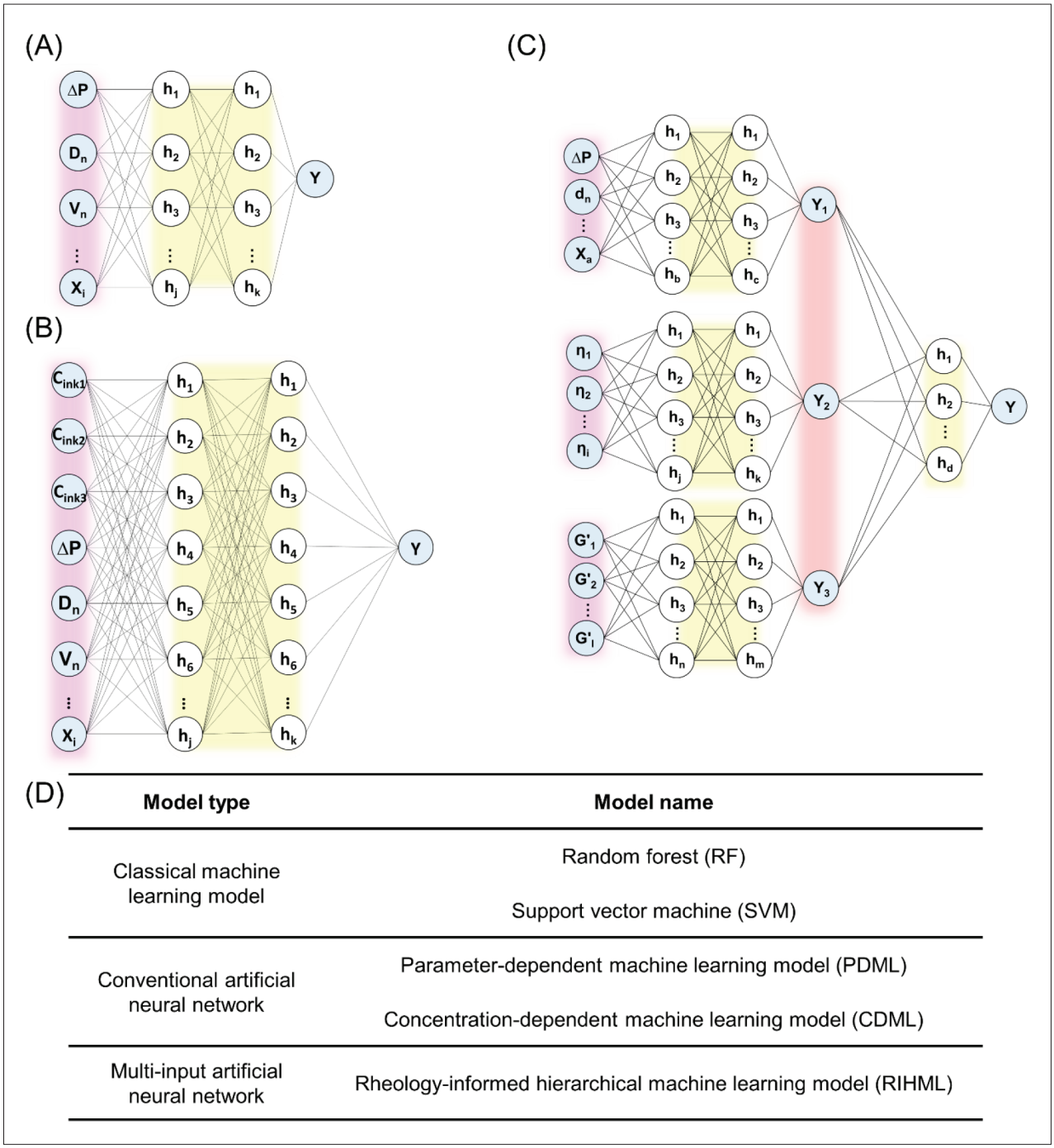

(D)

Model type	Model name
Classical machine learning model	Random forest (RF)
	Support vector machine (SVM)
Conventional artificial neural network	Parameter-dependent machine learning model (PDML)
	Concentration-dependent machine learning model (CDML)
Multi-input artificial neural network	Rheology-informed hierarchical machine learning model (RIHML)

Figure 3. Structure of artificial neural network-based models: (A) the parameter-dependent machine learning model, (B) the concentration-dependent machine learning model, and (C) the rheology-informed hierarchical machine learning model. (D) Table of the machine learning model types and corresponding model names.

model (rheology-informed hierarchical machine learning model [RIHML]) to predict the printing resolution using regression as shown in Figure 3D. Two representative classical machine learning algorithms, RF and SVM, were implemented using the sci-kit learn package in Python. Additionally, the Keras module from TensorFlow was used to develop the artificial neural network-based models, which specifically consisted of rectified linear unit (ReLU) function with the same hyperparameters, such as batch size and epoch. Furthermore, the train set, validation set,

and test set split by the ratio of 6:2:2 were performed with an applied random seed and fixed to all the models to avoid overfitting and estimate learning performance. To assess the performance of learning, mean squared error (MSE) was used for loss estimation.

Specifically, two classical machine learning algorithms, RF and SVM, were prepared based on conventional regression models using ensembles of multiple decision trees and hyperplanes with maximum margin, respectively. Moreover, the two conventional machine learning models consisted of an input layer, hidden layers, and an output layer as shown in Figure 3A and B. Specifically, the printing parameter-dependent machine learning model uses only printing parameters, such as printing pressure, nozzle velocity, nozzle diameter, and nozzle length. Besides, the concentration-dependent machine learning model was incorporated into the input layer consisting of the printing parameters and the concentrations of each bioink material.

Additionally, the RIHML was used with a multi-input layer model consisting of three input layers with hidden layers, concatenated layer, and its hidden layer; and an output layer shown in Figure 3C. The rheological properties, such as the viscosity and storage modulus, were used as the first and second input layers of the RIHML, respectively; and the last input layer consisted of the printing parameters. The hidden layers of each input layer were calculated separately and concatenated with the output layer. The final output was derived with a second hidden layer whose input is the concatenated output of the first hidden layer.

2.6. Prediction of the printing resolution

The machine learning models predicted the printing resolution with different cases involving new printing parameters, different concentrations, and different bioink compositions. More particularly, a dataset was created by multiple compositions of F127, gelatin/XG, and alginate/$CaCl_2$. Splitting was employed to train the model, except for the variable required to perform the prediction in the pre-training stage. Specifically, the independent datasets in the pre-training stage were provided for each machine learning model. They were divided into three parts (training set, validation set, and testing set) to train the model and estimate learning performance. The trained models have predicted printing resolution with a dataset consisting of excluded variables in the training dataset. The error criterion evaluating printing resolution accuracy was evaluated using Equation I.

$$\text{Error}(\%) = \frac{|AR - PR|}{AR} \times 100 \quad \text{(I)}$$

where AR is the actual printing resolution and PR is the predicted printing resolution. This represents the difference between the actual and predicted value. Moreover, four different nozzle velocities and five unequal pressure values were used as the variables of the printing parameters to predict the printing resolution with two conventional machine learning models and the RIHML. Specifically, the printing resolution was predicted by different material concentrations of bioinks with a split dataset via CDML and RIHML. Additionally, a new composition, alginate/CNC composite bioink, was used to investigate the possibility of predicting the novel materials not considered in the training set with CDML and RIHML. In the case of CDML, the number of input layer neurons correlate with the number of materials. It means that by adding a new material, parameters of the new material, such as concentration, should be included in the input layer, thus increasing the neurons. To follow the previous structure, the neuron of the CNC existed in the input layer of CDML.

In addition, to provide a visual representation, binary images of the printed scaffolds were created using simulation. To generate the binary image, the printing strand size obtained from the machine learning model was converted into pixels. Using the converted strand size, the single-pixel lines representing the actual printing path were dilated considering printing directions and angles. Afterward, the resulting binary values were converted to the binary image to accurately simulate the printed scaffolds based on the predicted printing strand size.

3. Results

3.1. Rheological properties of hydrogels

In this study, the viscoelastic properties including viscosity and storage modulus were assessed and implemented into a rheological dataset of the bioinks. As shown in Figure 4A, the viscosity for ten bioinks was prepared to compare the viscoelastic properties. Specifically, the shear-thinning behavior was observed in the flow curves of all bioinks, and the F127-based bioinks exhibited the highest viscosity compared to other bioinks. The flow curves of gelatin- and alginate-based bioinks are relatively low and partially overlapped while increasing shear rates. Consequently, the viscosities for various bioinks were compared with each other at the shear rate of 100 1/s as shown in Figure 4B. The storage modulus was also measured to investigate the mechanical strength of the bioinks (Figure 4C and D). Similar to the viscosity assessment, the highest shear moduli were shown with the F127-based bioink. Additionally, viscosities and storage moduli of gelatin- and alginate-based bioinks were correlated with the increasing concentration of gelatin/XG and CNC, respectively. However, while the shear moduli of alginate-based bioinks crosslinked with

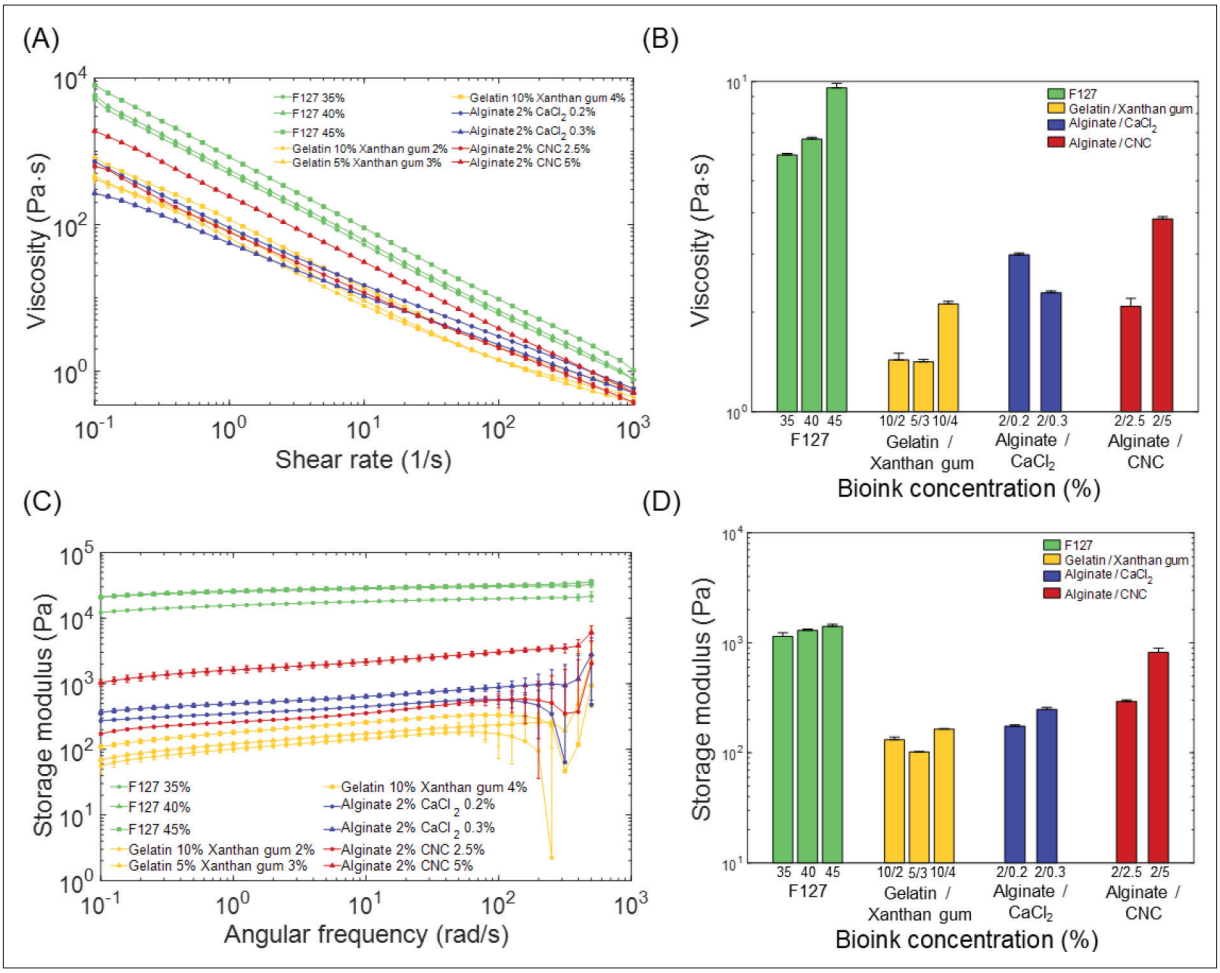

Figure 4. Rheological properties of the bioinks. (A) Viscosity and (C) storage modulus of the bioinks of F127, gelatin/xanthan gum, alginate/$CaCl_2$, and alginate/CNC. (B) Viscosity at a specific shear rate of 100 1/s and (D) storage modulus at a specific angular frequency of 100 rad/s.

$CaCl_2$ were increased with the concentration of $CaCl_2$, their viscosities decreased as the concentration of $CaCl_2$ increased. Overall, the dataset of rheological properties was collected for each composition with 41 and 21 values of viscosity data and storage moduli, respectively.

3.2. Printing data acquisition

A self-developed imaging setup and algorithm were used to identify and quantify the printing strand size in the microscopic images. Specifically, the printing resolution was evaluated based on the quantified strand size ranging from 0 to 4 mm. All the bioinks were printed with various pressures, four velocities, and three nozzle types as shown in Figure 2B and **Figure S3** (Supplementary File). The range of the pressure for printing the bioinks was from 10 to 350 kPa. Furthermore, for each nozzle velocity, about 110 data were investigated to figure out the printing quality. In total, 537 printing resolution data were accumulated by 10 compositions of bioinks. Specifically, 72, 47 to 49, 45 to 47, and 41 to 44 data were collected with F127, gelatin/XG, alginate/$CaCl_2$, and alginate/CNC, respectively, as presented in **Table S1** (Supplementary File).

3.3. Machine learning

In this study, the learning performance of the machine learning models was verified using the collected datasets of printing resolution. Specifically, they were divided into a training set and a test set, as shown in Figure 5A and B. **Figure S4A–C** (Supplementary File) present the training loss and validation loss in the learning curve at 300 epochs for PDML, CDML, and RIHML. Generally, after successful training, the training loss was lower than the validation loss. The rheology-informed model exhibited the lowest training loss of 0.05 and validation loss of 0.08 compared with the training loss of 0.08 and validation loss of 0.13 in the concentration-dependent model, which was similar to the tendency often seen in successful training. Nevertheless, training using the parameter-dependent model was not effective with a higher training loss of 0.68 than the validation set loss of 0.62. Additionally,

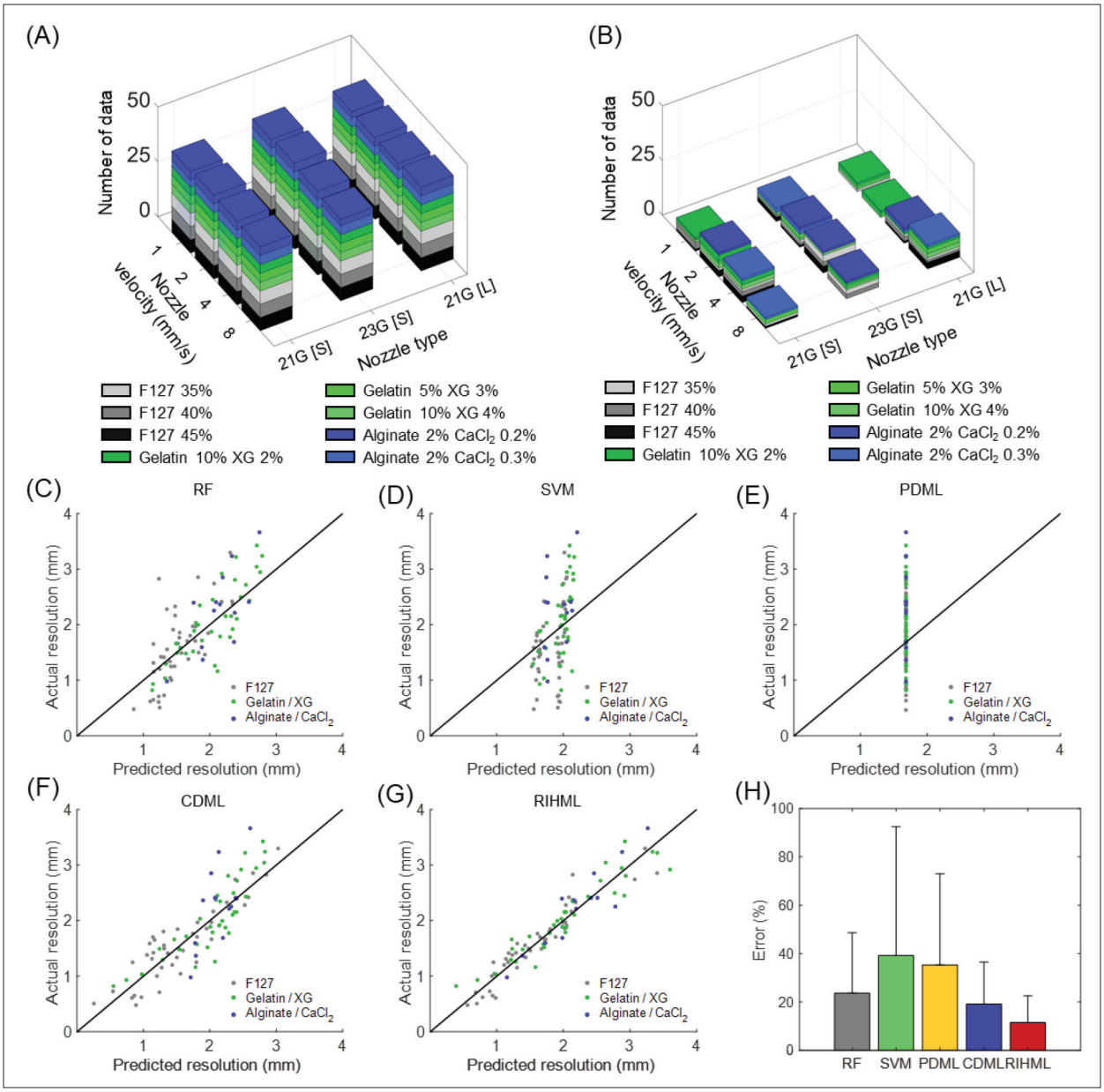

Figure 5. 3D-stacked bar graphs with printing parameters for (A) full dataset and (B) test dataset with the bioinks of F127, gelatin/xanthan gum, and alginate/$CaCl_2$. Fitting actual values with prediction values with (C) random forest (RV), (D) support vector model (SVM), (E) parameter-dependent machine learning (PDML) model, (F) concentration-dependent machine learning (CDML) model, and (G) rheology-informed hierarchical machine learning (RIHML) model. (H) Bar graph of average errors for each model.

as shown in Figure 5E, the PDML predicted every test resolution to be 1.68 mm, which does not match the actual values ranging from 0 to 4 mm while other artificial neural network models showed reasonable fitting results (Figure 5F and G). The experimental results from the RF model had a large standard deviation of errors as shown in Figure 5C, indicating that the prediction was significantly biased. Furthermore, prediction accuracy using another classical machine learning model, SVM, showed a similar trend with PDML, resulting in inadequate fitting as depicted in Figure 5D. These models also exhibited large errors of approximately 40%, as described in bar graphs in Figure 5H. As a result, the prediction of two classical machine learning models and PDML imply that it is not appropriate for forecasting the printing resolution of various bioink types. Furthermore, the predicted resolution of the rheology-informed model most accurately matched the actual printing resolution.

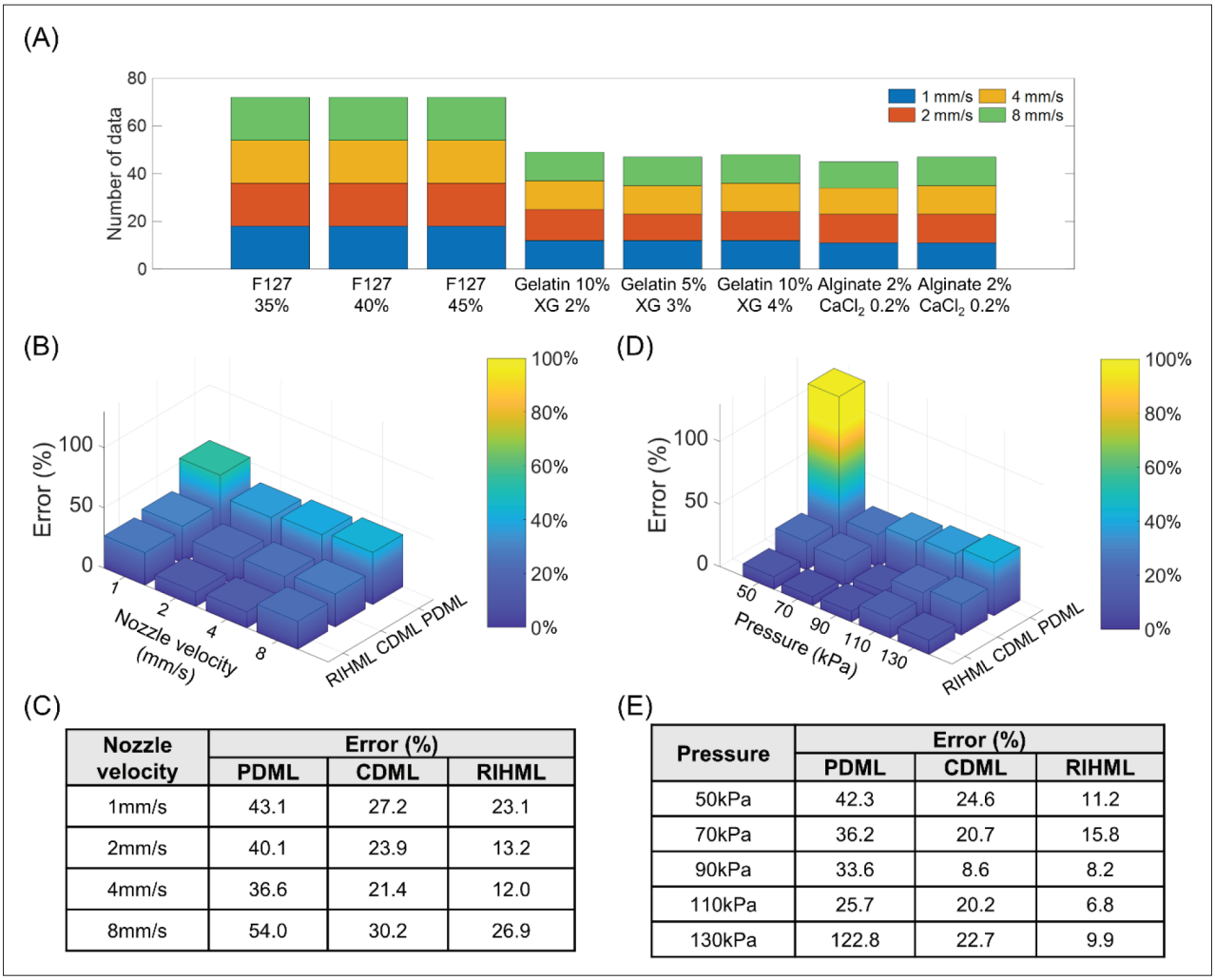

Nozzle velocity	Error (%)		
	PDML	CDML	RIHML
1mm/s	43.1	27.2	23.1
2mm/s	40.1	23.9	13.2
4mm/s	36.6	21.4	12.0
8mm/s	54.0	30.2	26.9

Pressure	Error (%)		
	PDML	CDML	RIHML
50kPa	42.3	24.6	11.2
70kPa	36.2	20.7	15.8
90kPa	33.6	8.6	8.2
110kPa	25.7	20.2	6.8
130kPa	122.8	22.7	9.9

Figure 6. (A) Stacked bar graph of the amount of data for different materials and nozzle velocities. (B) 3D bar graph and (C) table of calculated errors in various nozzle velocities (1, 2, 4, and 8 mm/s) and different machine learning models (PDML, CDML, and RIHML). (D) 3D bar graph and (E) table of calculated errors in various pressures (50, 70, 90, 110, and 130 kPa) with different machine learning models (PDML, CDML, and RIHML). Abbreviations: CDML, concentration-dependent machine learning; RIHML, rheology-informed hierarchical machine learning; PDML, parameter-dependent machine learning.

3.4. Prediction of printing resolution

3.4.1. Prediction with new printing parameters

Three machine learning models were compared to predict printing resolution using different parameters, including nozzle velocity and pressure. Particularly, the same datasets were used to train and predict each machine learning model as described in Figure 6A and **Table S1** (Supplementary File). As shown in Figure 6B and C, all errors have a similar trend when nozzle velocity was used as a variable of bioprinting. Descriptively, when the velocity was 4 mm/s, the errors were lowest and equal to 36.6%, 21.4%, and 12.0% for PDML, CDML, and RIHML, respectively; however, by increasing the velocity to 8 mm/s, the errors rose to 54%, 30.2%, and 26.9% for PDML, CDML, and RIHML, respectively. The prediction results with different nozzle velocities indicate that the rheology-informed machine learning model exhibited the lowest error (18.8% on average) among all models. Furthermore, errors in the prediction of printing resolution with various pressures (50, 70, 90, 110, and 130 kPa) using the machine learning models are illustrated in Figure 6D and E. RIHML could predict the printing resolution with the lowest error (10.38% on average), which is 2-fold and 5-fold lower than CDML and PDML, respectively. The highest error in the PDML model was around 123% in 130 kPa, demonstrating an approximately 13-fold error using RIHML at the same condition.

3.4.2. Prediction with different concentrations of bioink components

Due to the neural network structure of the PDML, it is hardly used for varying concentrations of bioink. Thus,

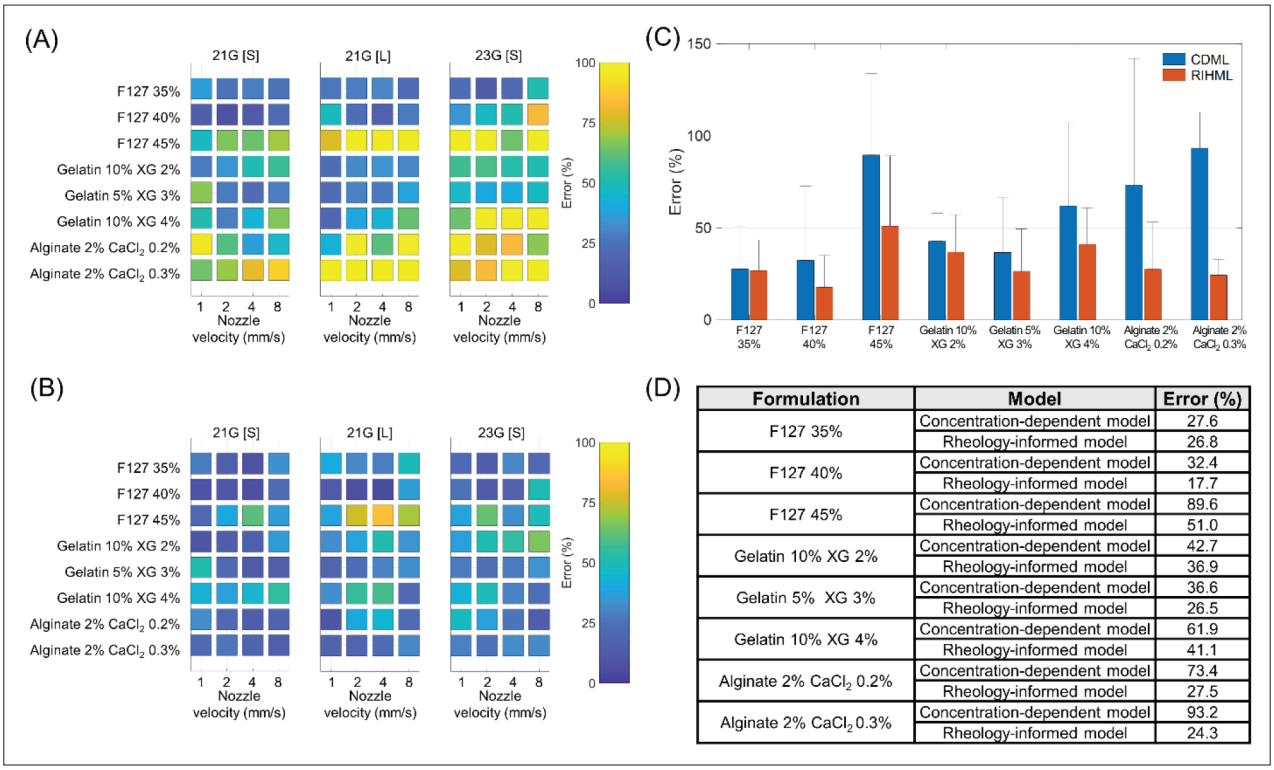

Formulation	Model	Error (%)
F127 35%	Concentration-dependent model	27.6
	Rheology-informed model	26.8
F127 40%	Concentration-dependent model	32.4
	Rheology-informed model	17.7
F127 45%	Concentration-dependent model	89.6
	Rheology-informed model	51.0
Gelatin 10% XG 2%	Concentration-dependent model	42.7
	Rheology-informed model	36.9
Gelatin 5% XG 3%	Concentration-dependent model	36.6
	Rheology-informed model	26.5
Gelatin 10% XG 4%	Concentration-dependent model	61.9
	Rheology-informed model	41.1
Alginate 2% $CaCl_2$ 0.2%	Concentration-dependent model	73.4
	Rheology-informed model	27.5
Alginate 2% $CaCl_2$ 0.3%	Concentration-dependent model	93.2
	Rheology-informed model	24.3

Figure 7. Error map of the prediction of printing resolution with different concentrations of bioinks using (A) concentration-dependent model and (B) rheology-informed model. (C) Bar graph of errors in the prediction at each bioink composition. (D) Table of error values for different bioink formulations and prediction models.

the prediction of printing resolution with different concentrations of bioink components has proceeded with two machine learning models including CDML and RIHML. Specifically, the error maps in Figure 7A and B indicate the errors of predicted resolution compared to the actual resolution with various material concentrations, nozzle velocities, and nozzle types, using CDML and RIHML, respectively. Particularly, most regions of the error map of RIHML are bluish having low numbers of yellow squares with low prediction errors. Nevertheless, in the error map of the CDML, many yellow squares were observed with high prediction errors. For instance, the prediction of F127 45%, gelatin 10% combined with xanthan gum 4%, and alginate 2% crosslinked with $CaCl_2$ had significantly large errors with different nozzle types and speeds. Furthermore, for the prediction using CDML, the errors were more than 50% in 45 data and 75% in 27 data among the total data number of 96, which implies a high prediction error of this method. In contrast, the errors of only two data were over 75% at the F127 concentration of 45% using RIHML. Figure 7C and D visualize the average errors to compare the printing accuracy for each bioink composition. Further, the prediction using both machine learning models exhibited relatively high errors with the concentration of F127 of 45%, but the average error is approximately two times higher in CDML. The prediction with the rheology-informed hierarchical model exhibits less error than the concentration-based model in all the concentrations.

3.4.3. Prediction of the different bioink integrated with a new material

To demonstrate the prediction of the bioink incorporated with a new material, which is significantly challenging with current bioprinting prediction techniques, non-trained bioinks were prepared by mixing the alginate solution with CNC in two concentrations of 2.5% and 5%. Therefore, the model training proceeded without data on alginate/CNC composition as shown in **Table S1** (Supplementary File). Precisely, Figure 8A shows that 85 cases were collected with alginate/CNC composites to consist of a prediction dataset. More so, the predicted resolution of the new compositions and a fitted line of actual printing resolution are shown in Figure 8B and C. In the prediction results using CDML shown in Figure 8B, most of the predicted points in red color with alginate 2%/CNC 5% composition strayed from the defined resolution range from 0 to 4 mm. This result implies the difficulty of predicting printability when new materials are added to bioink. In comparison, all the prediction data using

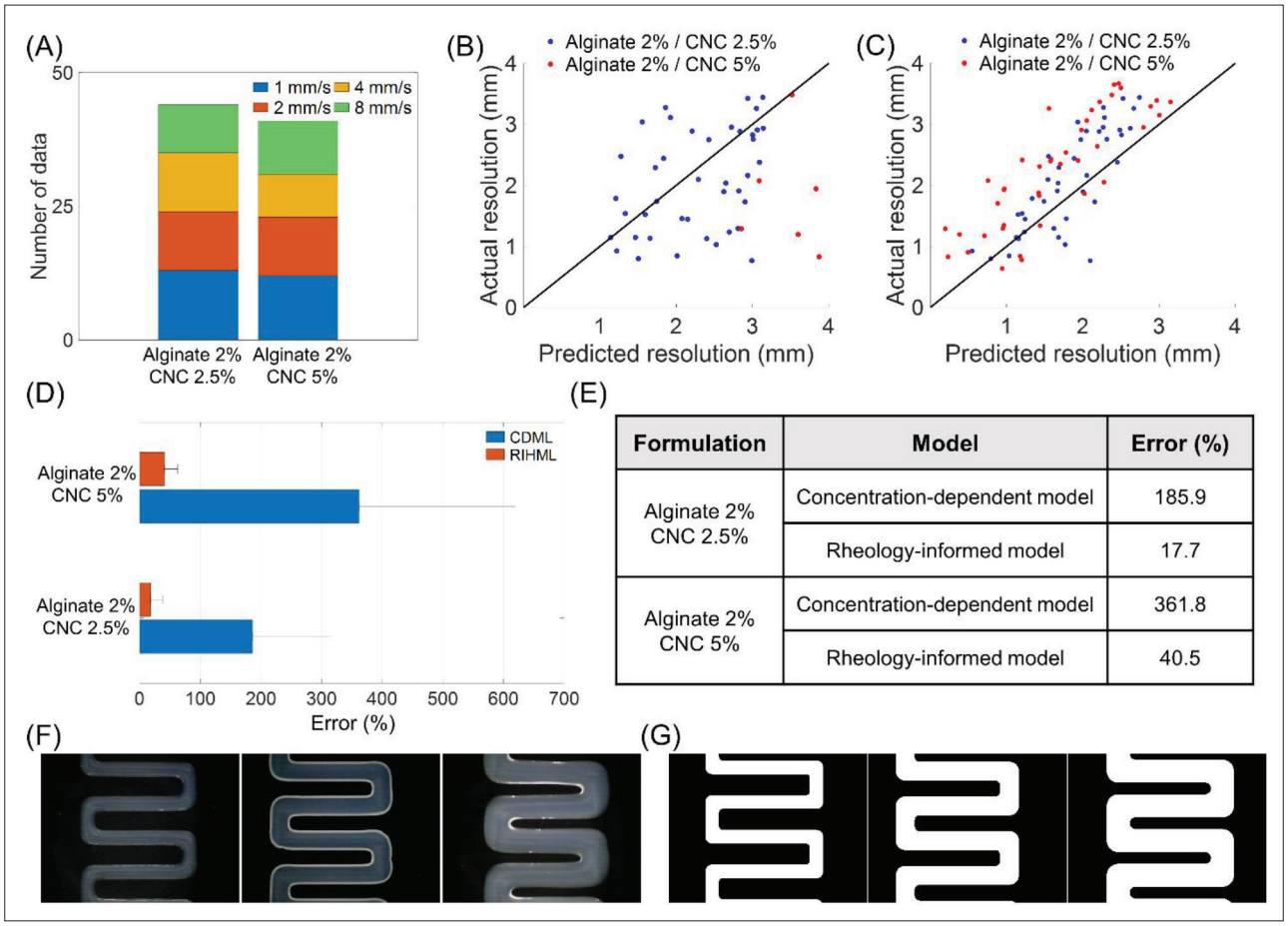

Formulation	Model	Error (%)
Alginate 2% CNC 2.5%	Concentration-dependent model	185.9
	Rheology-informed model	17.7
Alginate 2% CNC 5%	Concentration-dependent model	361.8
	Rheology-informed model	40.5

Figure 8. Prediction of printing resolution using the trained models with different concentrations of CNC incorporated with 2% alginate. (A) The number of results for alginate/CNC composition at different velocities. Fitting actual values with prediction values with (B) CDML and (C) RIHML. (D) Bar graph of average errors for each model. (E) Error values for different bioinks formulations and prediction models. Visual comparison between (F) actual image of printed alginate/CNC composition and (G) simulated image using the printing resolution predicted by RIHML. Abbreviations: CDML, concentration-dependent machine learning; CNC, cellulose nanocrystal; RIHML, rheology-informed hierarchical machine learning.

RIHML existed within the range of the axis as shown in Figure 8C. To quantitatively elucidate this phenomenon, Figure 8D and E can differentiate the average prediction accuracy between the concentration-dependent model and the rheology-informed model. The RIHML method can adequately predict the printing resolution of bioink with new material, but CDML predictions are unreliable and have significant errors. Specifically, the concentration-dependent model shows approximately 10-fold errors compared to the rheology-informed model using the same prediction dataset. This result implies the performance of RIHML is less affected by the bioink composition, even with new materials. Furthermore, to visually compare the strand size of actual printing and prediction using RIHML, the binary images of the printed scaffolds were created using simulation and compared with their actual images. Figure 8F shows actual images of the printed alginate/CNC scaffolds. The simulated images using the printing resolution of the alginate/CNC composition predicted by RIHML are presented in Figure 8G and agreed well with the actual images.

4. Discussion

This study reports the application of a rheology-informed hierarchical model to enhance the prediction accuracy of the printing resolution of constructs fabricated by extrusion-based bioprinting. Specifically, five different machine learning models, including the RIHML model as well as two classical machine learning models (RF and SVM) and the conventional models based on artificial neural networks (concentration-dependent model and printing parameter-dependent model), were trained and tested using a small dataset of bioink properties and printing parameters. More precisely, the models were used to predict the printing resolution in three different

cases, including new printing parameters with trained bioink materials, new concentrations of the trained bioink constituents, and untrained bioink compositions with the new material. For different nozzle velocities, the results of the study showed that the RIHML model exhibited the lowest error percentage (around 18%) in predicting the printing resolution. Additionally, the RIHML model showed low error (around 10%) in predicting the printing resolution for different pressures, which is 2-fold and 5-fold lower than CDML and PDML, respectively. Moreover, the printing resolution for different bioink concentrations was predicted, and it was demonstrated that the RIHML model exhibited lower error percentages than the CDML model for all the different concentrations of bioink constituents such as F127, gelatin, xanthan gum, and $CaCl_2$. Additionally, the machine learning models were used to predict the printing resolution with a new material (CNC) added to the alginate-based bioink, which is the most challenging among the three cases. The results of the study showed that RIHML can predict the printing resolution with reasonably low errors while the printing resolution was hardly predictable using CDML with considerably large errors.

Overall, the experimental results indicate that the rheology-informed hierarchical model can be a useful tool to predict the printing resolution of extrusion-based bioprinting. Furthermore, while other studies related to the prediction of printability in bioprinting could anticipate the printability changes only with limited parameters, such as bioink material properties or printing conditions, the RIHML model is versatile to predict the printing resolution in different conditions of varying printing parameters, varying material concentrations, and new bioink compositions[40,43,54]. Additionally, the neural network structure of RIHML is based on rheological properties, which can be widely obtained from most biomaterials, and it can be trained without significant alterations of the structure. Therefore, the RIHML model is adaptable and expandable compared to the conventional models, and the printing and rheological datasets may be accumulated to enhance the prediction accuracy.

Since the formulation of bioinks and the process of bioprinting are more complicated and correlated, the prediction of printability in 3D bioprinting has become more challenging. Recently, there have been attempts related to the prediction of bioprinting printability using machine learning. However, unlike other fields such as medical imaging and genetics, 3D bioprinting suffers from data size, which may hardly be large because the preparation of bioinks with various compositions and their 3D printing with multiple parameters are sequential and highly time-consuming[55-57]. Therefore, it is crucial to develop an efficient machine learning model that is suitable for small dataset sizes while ensuring high prediction accuracy. With the hierarchical architecture of the developed model, RIHML can effectively predict the printing resolution of extrusion-based bioprinting using small datasets. In this study, the dataset of 537 numbers of bioink rheological properties and printing process was used for training, validation, and testing of the machine learning model. Several bioprinting studies employed small datasets to optimize printing resolution and parameters using conventional machine learning skills, but their practical applications were limited due to low prediction accuracy, poor expandability, and low training efficiency[41,42,44,45]. However, the RIHML model can easily generalize and embrace new data, even with a small dataset size owing to its intrinsic features in the dataset that are not biased to specific bioink, but rather are general. Moreover, due to the potential of data accumulation, if various rheological and printing data are additionally collected in sufficient size for deep learning, prediction using a rheology-informed neural network with deeper hidden layers may be attempted.

Although the RIHML model has the potential for accurate and robust prediction of printability, there is still room for improvement. Due to the generalizability of the bioink properties, a wider range of rheological properties of bioinks can enhance the prediction accuracy of the RIHML model. For instance, in the results presented in Figure 7C, relatively high errors were observed in F127 with a concentration of 45%. Specifically, this may occur because its viscosity and storage modulus were the highest around the upper bound of the rheological data range. In terms of future work, it would be beneficial to further validate the performance of the RIHML model from other types of bioprinting methods, such as inkjet-based or laser-assisted bioprinting, to demonstrate the feasibility of rheology-based prediction of printability across different bioprinting methods. Additionally, future studies could investigate the potential of the RIHML model in predicting other aspects of printability, such as the extrudability, pore size, pore shape, and shape fidelity of the stacked layers.

5. Conclusion

In conclusion, this study suggests that the rheology-informed hierarchical model can be a useful tool for predicting the printing resolution of constructs fabricated by extrusion-based bioprinting. Interestingly, the RIHML model demonstrated the lowest errors (around 18%) in predicting the printing resolution for different printing parameters such as nozzle velocities and pressures,

compared to the conventional models such as the concentration-dependent model and printing parameter-dependent model. Additionally, the RIHML model also exhibited low error (around 10%) in predicting the printing resolution for different concentrations of bioink constituents, such as Pluronic F-127, gelatin, xanthan gum, and $CaCl_2$. Furthermore, the RIHML model can predict the printing resolution with a new nanomaterial (CNC) added to the alginate-based bioink, which is hardly possible with conventional methods. This study demonstrated the importance of considering the rheological properties of bioinks in predicting the printability of extrusion-based bioprinting and highlighted the potential of the RIHML model as a useful tool for predicting the printing resolution of extrusion-based bioprinting. In addition, the results indicate that the RIHML model can be versatile and expandable in the prediction of bioprinting resolution, and the printing and rheological datasets may be accumulated to enhance the prediction accuracy. The potential for the RIHML model to generalize and embrace new data, even with a small dataset size, is an advantage in the field of 3D bioprinting where data size is limited due to the complexity and time-consuming nature of the preparation of bioinks with various compositions and 3D printing with multiple parameters.

Acknowledgments

None.

Funding

This research was supported by a National Research Foundation of Korea (NRF) grant (NRF-2021R1I1A3040459) funded by the Korean government (MOE). This research was supported by a grant of the Korea Health Technology R&D Project through the Korea Health Industry Development Institute (KHIDI), funded by the Ministry of Health & Welfare, Republic of Korea (grant number : HI22C1323).

Conflict of interest

The authors declare no conflicts of interests.

Author contributions

Conceptualization: Dageon Oh, Seung Yun Nam
Data curation: Dageon Oh, Min Chang Kim
Formal analysis: Dageon Oh
Funding acquisition: Eun-Jae Chung, Seung Yun Nam
Investigation: Dageon Oh, Seung Yun Nam
Methodology: Dageon Oh, Seung Yun Nam
Project administration: Dageon Oh, Seung Yun Nam
Supervision: Seung Yun Nam
Validation: Dageon Oh
Visualization: Dageon Oh
Writing – original draft: Dageon Oh, Seung Yun Nam
Writing – review & editing: Masoud Shirzad, Eun-Jae Chung, Seung Yun Nam

Ethics approval and consent to participate

Not applicable.

Consent for publication

Not applicable.

Availability of data

The data presented in this study are available on request from the corresponding author.

References

1. Ozbolat, Yu Y, 2013, Bioprinting toward organ fabrication: Challenges and future trends. *IEEE Trans Biomed Eng,* 60(3): 691–699.

   https://doi.org/10.1109/TBME.2013.2243912

2. Murphy SV, Atala A, 2014, 3D bioprinting of tissues and organs. *Nat Biotechnol,* 32(8), 773–785.

   https://doi.org/10.1038/nbt.2958

3. Sun W, Starly B, Daly AC, *et al.*, 2020, The bioprinting roadmap. *Biofabrication,* 12(2): 022002.

   https://doi.org/10.1088/1758-5090/ab5158

4. Daly AC, Prendergast ME, Hughes AJ, *et al.*, 2021, Bioprinting for the biologist. *Cell,* 184(1): 18–32.

   https://doi.org/10.1016/j.cell.2020.12.002

5. Lu D, Yang Y, Zhang P, *et al.*, 2022, Development and application of three-dimensional bioprinting scaffold in the repair of spinal cord injury. *Tissue Eng Regen Med,* 19(6): 1113–1127.

   https://doi.org/10.1007/s13770-022-00465-1

6. Tan B, Gan S, Wang X, *et al.*, 2021, Applications of 3D bioprinting in tissue engineering: advantages, deficiencies, improvements, and future perspectives. *J Mater Chem B,* 9(27): 5385–5413.

   https://doi.org/10.1039/D1TB00172H

7. Mandrycky C, Wang Z, Kim K, *et al.*, 2016, 3D bioprinting for engineering complex tissues. *Biotechnol Adv,* 34(4): 422–434.

   https://doi.org/10.1016/j.biotechadv.2015.12.011

8. Yilmaz B, Al Rashid A, Mou YA, *et al.*, 2021, Bioprinting: A review of processes, materials and applications. *Bioprinting,* 23: e00148.

   https://doi.org/10.1016/j.bprint.2021.e00148

9. Mao X, Wang Z, 2022, Research progress of three-dimensional bioprinting artificial cardiac tissue. *Tissue Eng Regen Med,* 20: 1–9.

   https://doi.org/10.1007/s13770-022-00495-9

10. Jacob GT, Passamai VE, Katz S, *et al.*, 2022, Hydrogels for extrusion-based bioprinting: general considerations. *Bioprinting,* 27: e00212.

    https://doi.org/10.1016/j.bprint.2022.e00212

11. Merceron TK, Burt M, Seol Y-J, *et al.*, 2015, A 3D bioprinted complex structure for engineering the muscle–tendon unit. *Biofabrication,* 7(3): 035003.

    http://dx.doi.org/10.1088/1758-5090/7/3/035003

12. Melchels FP, Dhert WJ, Hutmacher DW, *et al.*, 2014, Development and characterisation of a new bioink for additive tissue manufacturing. *J Mater Chem B,* 2(16): 2282–2289.

    https://doi.org/10.1039/C3TB21280G

13. Ozbolat IT, Hospodiuk M, 2016, Current advances and future perspectives in extrusion-based bioprinting. *Biomaterials,* 76: 321–343.

    https://doi.org/10.1016/j.biomaterials.2015.10.076

14. Zhang YS, Haghiashtiani G, Hübscher T, *et al.*, 2021, 3D extrusion bioprinting. *Nat Rev Methods Primers,* 1(1): 75.

    https://doi.org/10.1038/s43586-021-00073-8

15. Ning L, Chen X, 2017, A brief review of extrusion-based tissue scaffold bio-printing. *Biotechnol J,* 12(8): 1600671.

    https://doi.org/10.1002/biot.201600671

16. Xuan Z, Peng Q, Larsen T, *et al.*, 2023, Tailoring hydrogel composition and stiffness to control smooth muscle cell differentiation in bioprinted constructs. *Tissue Eng Regen Med,* 20(2): 199–212.

    https://doi.org/10.1007/s13770-022-00500-1

17. Willson K, Ke D, Kengla C, *et al.*, 2020, Extrusion-based bioprinting: Current standards and relevancy for human-sized tissue fabrication. *Methods Mol Biol,* 2140: 65–92.

    https://doi.org/10.1007/978-1-0716-0520-2

18. Hölzl K, Lin S, Tytgat L, *et al.*, 2016, Bioink properties before, during and after 3D bioprinting. *Biofabrication,* 8(3): 032002.

    http://dx.doi.org/10.1088/1758-5090/8/3/032002

19. Chung JH, Naficy S, Yue Z, *et al.*, 2013, Bio-ink properties and printability for extrusion printing living cells. *Biomater Sci,* 1(7): 763–773.

    https://doi.org/10.1039/C3BM00012E

20. Jin Y, Chai W, Huang Y, 2017, Printability study of hydrogel solution extrusion in nanoclay yield-stress bath during printing-then-gelation biofabrication. *Mater Sci Eng C,* 80: 313–325.

    https://doi.org/10.1016/j.msec.2017.05.144

21. Datta P, Barui A, Wu Y, *et al.*, 2018, Essential steps in bioprinting: From pre-to post-bioprinting. *Biotechnol Adv,* 36(5): 1481–1504.

    https://doi.org/10.1016/j.biotechadv.2018.06.003

22. Sarker M, Naghieh S, McInnes AD, *et al.*, 2019, Bio-fabrication of peptide-modified alginate scaffolds: Printability, mechanical stability and neurite outgrowth assessments. *Bioprinting,* 14: e00045.

    https://doi.org/10.1016/j.bprint.2019.e00045

23. Gillispie G, Prim P, Copus J, *et al.*, 2020, Assessment methodologies for extrusion-based bioink printability. *Biofabrication,* 12(2): 022003.

    https://doi.org/10.1088/1758-5090/ab6f0d

24. Schwab A, Levato R, D'Este M, *et al.*, 2020, Printability and shape fidelity of bioinks in 3D bioprinting. *Chem Rev,* 120(19): 11028–11055.

    https://doi.org/10.1021/acs.chemrev.0c00084

25. Malekpour A, Chen X, 2022, Printability and cell viability in extrusion-based bioprinting from experimental, computational, and machine learning views. *J Funct Biomater,* 13(2): 40.

    https://doi.org/10.3390/jfb13020040

26. Ramesh S, Harrysson OL, Rao PK, *et al.*, 2021, Extrusion bioprinting: Recent progress, challenges, and future opportunities. *Bioprinting,* 21: e00116.

    https://doi.org/10.1016/j.bprint.2020.e00116

27. Kang K, Hockaday L, Butcher J, 2013, Quantitative optimization of solid freeform deposition of aqueous hydrogels. *Biofabrication,* 5(3): 035001.

    http://dx.doi.org/10.1088/1758-5082/5/3/035001

28. Tian S, Zhao H, Lewinski N, 2021, Key parameters and applications of extrusion-based bioprinting. *Bioprinting,* 23: e00156.

    https://doi.org/10.1016/j.bprint.2021.e00156

29. Naghieh S, Chen X, 2021, Printability–A key issue in extrusion-based bioprinting. *J Pharm Anal,* 11(5): 564–579.

    https://doi.org/10.1016/j.jpha.2021.02.001

30. Fu Z, Naghieh S, Xu C, *et al.*, 2021, Printability in extrusion bioprinting. *Biofabrication,* 13(3): 033001.

    https://doi.org/10.1088/1758-5090/abe7ab

31. Lee H, Yoo JM, Ponnusamy NK, *et al.*, 2022, 3D-printed hydroxyapatite/gelatin bone scaffolds reinforced with graphene oxide: Optimized fabrication and mechanical characterization. *Ceram Int,* 48(7): 10155–10163.

    https://doi.org/10.1016/j.ceramint.2021.12.227

32. Kim MH, Nam SY, 2020, Assessment of coaxial printability for extrusion-based bioprinting of alginate-based tubular constructs. *Bioprinting,* 20: e00092.

    https://doi.org/10.1016/j.bprint.2020.e00092

33. Song K, Zhang D, Yin J, *et al.*, 2021, Computational study of extrusion bioprinting with jammed gelatin microgel-based composite ink. *Addit Manuf,* 41: 101963.

https://doi.org/10.1016/j.addma.2021.101963

34. Leppiniemi J, Lahtinen P, Paajanen A, *et al.*, 2017, 3D-printable bioactivated nanocellulose–alginate hydrogels. *ACS Appl Mater Interfaces,* 9(26): 21959–21970.

https://doi.org/10.1021/acsami.7b02756

35. Kim MH, Lee YW, Jung W-K, *et al.*, 2019, Enhanced rheological behaviors of alginate hydrogels with carrageenan for extrusion-based bioprinting. *J Mech Behav Biomed Mater,* 98: 187–194.

https://doi.org/10.1016/j.jmbbm.2019.06.014

36. Göhl J, Markstedt K, Mark A, *et al.*, 2018, Simulations of 3D bioprinting: Predicting bioprintability of nanofibrillar inks. *Biofabrication,* 10(3): 034105.

https://doi.org/10.1088/1758-5090/aac872

37. Bonatti AF, Chiesa I, Vozzi G, *et al.*, 2021, Open-source CAD-CAM simulator of the extrusion-based bioprinting process. *Bioprinting,* 24: e00172.

https://doi.org/10.1016/j.bprint.2021.e00172

38. Suntornnond R, Tan EYS, An J, *et al.*, 2016, A mathematical model on the resolution of extrusion bioprinting for the development of new bioinks. *Materials,* 9(9): 756.

https://doi.org/10.3390/ma9090756

39. Bonatti AF, Vozzi G, Chua CK, *et al.*, A deep learning approach for error detection and quantification in extrusion-based bioprinting. *Mater Today: Proc,* 70: 131–135.

https://doi.org/10.1016/j.matpr.2022.09.006

40. Ruberu K, Senadeera M, Rana S, *et al.*, 2021, Coupling machine learning with 3D bioprinting to fast track optimisation of extrusion printing. *Appl Mater Today,* 22: 100914.

https://doi.org/10.1016/j.apmt.2020.100914

41. Lee J, Oh SJ, An SH, *et al.*, 2020, Machine learning-based design strategy for 3D printable bioink: Elastic modulus and yield stress determine printability. *Biofabrication,* 12(3): 035018.

https://doi.org/10.1088/1758-5090/ab8707

42. Conev A, Litsa EE, Perez MR, *et al.*, 2020, Machine learning-guided three-dimensional printing of tissue engineering scaffolds. *Tissue Eng Part A,* 26(23–24): 1359–1368.

https://doi.org/10.1089/ten.tea.2020.0191

43. Fu Z, Angeline V, Sun W, 2021, Evaluation of printing parameters on 3D extrusion printing of pluronic hydrogels and machine learning guided parameter recommendation. *Int J Bioprint,* 7(4): 179–189.

https://doi.org/10.18063%2Fijb.v7i4.434

44. Bone JM, Childs CM, Menon A, *et al.*, 2020, Hierarchical machine learning for high-fidelity 3D printed biopolymers. *ACS Biomater Sci Eng,* 6(12): 7021–7031.

https://doi.org/10.1021/acsbiomaterials.0c00755

45. Menon A, Póczos B, Feinberg AW, *et al.*, 2019, Optimization of silicone 3D printing with hierarchical machine learning. *3D Print Addit Manuf,* 6(4): 181–189.

https://doi.org/10.1089/3dp.2018.0088

46. Jin Z, Zhang Z, Shao X, *et al.*, 2021, Monitoring anomalies in 3D bioprinting with deep neural networks. *ACS Biomater Sci Eng*, 9(7): 3945–3952.

https://doi.org/10.1021/acsbiomaterials.0c01761

47. Mancha Sánchez E, Gómez-Blanco JC, López Nieto, *et al.*, 2020, Hydrogels for bioprinting: A systematic review of hydrogels synthesis, bioprinting parameters, and bioprinted structures behavior. *Front Bioeng Biotechnol,* 8: 776.

https://doi.org/10.3389/fbioe.2020.00776

48. Zhang Z, Jin Y, Yin J, *et al.*, 2018, Evaluation of bioink printability for bioprinting applications. *Appl Phys Rev,* 5(4): 041304.

https://doi.org/10.1063/1.5053979

49. Chimene D, Lennox KK, Kaunas RR, *et al.*, 2016, Advanced bioinks for 3D printing: A materials science perspective. *Annal Biomed Eng,* 44(6): 2090–2102.

https://doi.org/10.1007/s10439-016-1638-y

50. Cooke ME, Rosenzweig DH, 2021, The rheology of direct and suspended extrusion bioprinting. *APL Bioeng,* 5(1): 011502.

https://doi.org/10.1063/5.0031475

51. Paxton N, Smolan W, Böck T, *et al.*, 2017, Proposal to assess printability of bioinks for extrusion-based bioprinting and evaluation of rheological properties governing bioprintability. *Biofabrication,* 9(4): 044107.

https://doi.org/10.1088/1758-5090/aa8dd8

52. Ouyang L, Yao R, Zhao Y, *et al.*, 2016, Effect of bioink properties on printability and cell viability for 3D bioplotting of embryonic stem cells. *Biofabrication,* 8(3): 035020.

http://dx.doi.org/10.1088/1758-5090/8/3/035020

53. Xu X, Jagota A, Peng S, *et al.*, 2013, Gravity and surface tension effects on the shape change of soft materials. *Langmuir,* 29(27): 8665–8674.

https://doi.org/10.1021/la400921h

54. Gao T, Gillispie GJ, Copus JS, *et al.*, 2018, Optimization of gelatin–alginate composite bioink printability using rheological parameters: A systematic approach. *Biofabrication,* 10(3): 034106.

https://doi.org/10.1088/1758-5090/aacdc7

55. Yu C, Jiang J, 2020, A perspective on using machine learning in 3D bioprinting. *Int J Bioprint,* 6(1): 4–11.

https://doi.org/10.18063%2Fijb.v6i1.253

56. Shin J, Lee Y, Li Z, *et al.*, 2022, Optimized 3D bioprinting technology based on machine learning: A review of recent trends and advances. *Micromachines,* 13(3): 363.

https://doi.org/10.3390/mi13030363

57. Ng WL, Chan A, Ong YS, *et al.*, 2020, Deep learning for fabrication and maturation of 3D bioprinted tissues and organs. *Virtual Phys Prototyp,* 15(3): 340–358.

https://doi.org/10.1080/17452759.2020.1771741

ACCSCIENCE PUBLISHING

International Journal of Bioprinting

REVIEW ARTICLE

3D printing and bioprinting in urology

Kun Liu[1†], Nan Hu[2†], Zhihai Yu[1], Xinzhou Zhang[2], Hualin Ma[2*], Huawei Qu[3*], and Changshun Ruan[3*]

[1]Department of Urology, Three Gorges Hospital, Chongqing University, Chongqing, China

[2]Department of Nephrology, Shenzhen People's Hospital (The Second Clinical Medical College, Jinan University; The First Affiliated Hospital, Southern University of Science and Technology), Shenzhen, China

[3]Research Center for Human Tissue and Organs Degeneration, Institute of Biomedicine and Biotechnology, Shenzhen Institute of Advanced Technology, Chinese Academy of Sciences, Shenzhen, China

Abstract

Three-dimensional (3D) printing with highly flexible fabrication offers unlimited possibilities to create complex constructs. With the addition of active substances such as biomaterials, living cells, and growth factors, 3D printing can be upgraded to 3D bioprinting, endowing fabricated constructs with biological functions. Urology, as one of the important branches of clinical medicine, covers a variety of organs in the human body, such as kidneys, bladder, urethra, and prostate. The urological organs are multi-tubular, heterogeneous, and anisotropic, bringing huge challenges to 3D printing and bioprinting. This review aims to summarize the development of 3D printing and bioprinting technologies in urology in the last decade based on the Science Citation Index-Expanded (SCI-E) in the Web of Science Core Collection online database (Clarivate). First, we demonstrate the search strategies for published papers using the keywords such as "3D printing," "3D bioprinting," and "urology." Then, eight common 3D printing technologies were introduced in detail with their characteristics, advantages, and disadvantages. Furthermore, the application of 3D printing in urology was explored, such as the fabrication of diseased organs for doctor–patient communication, surgical planning, clinical teaching, and the creation of customized medical devices. Finally, we discuss the exploration of 3D bioprinting to create *in vitro* bionic 3D environment models for urology. Overall, 3D printing provides the technical support for urology to better serve patients and aid teaching, and 3D bioprinting enables the clinical applications of fabricated constructs for the replacement and repair of urologically damaged organs in future.

Keywords: 3D printing; Bioprinting; Urology

†These authors contributed equally to this work.

***Corresponding authors:**
Hualin Ma
(mahualin0796@sina.com)

Huawei Qu
(hw.qu@siat.ac.cn)

Changshun Ruan
(cs.ruan@siat.ac.cn)

Citation: Liu K, Hu N, Yu Z, *et al*., 2023, 3D printing and bioprinting in urology. *Int J Bioprint*, 9(6): 0969. https://doi.org/10.36922/ijb.0969

Received: May 21, 2023
Accepted: July 4, 2023
Published Online: August 10, 2023

Copyright: © 2023 Author(s). This is an Open Access article distributed under the terms of the Creative Commons Attribution License, permitting distribution, and reproduction in any medium, provided the original work is properly cited.

Publisher's Note: AccScience Publishing remains neutral with regard to jurisdictional claims in published maps and institutional affiliations.

1. Introduction

Three-dimensional (3D) printing, also known as additive manufacturing (AM), has been developed and improved over the last few decades[1-4]. Traditional 3D printing technology uses a planar layer printing strategy with a process originally developed for rapid prototyping. Digital models are sliced by it along the *Z*-axis to produce a set of digital models with horizontal build layers in the *X*–*Y* plane. These layers are then stacked

sequentially from bottom to top to create a physical replica of the digital model. With the reform and innovation of 3D printing technology, several types of 3D printing techniques with different characteristics have been developed, such as the conventional fused deposition modeling (FDM) for hot melt extrusion deposition of polymer materials, digital light processing (DLP) for photo-crosslinking molding, and bioprinting/biofabrication for processing biomaterials and cellular bioink[2,5,6].

3D bioprinting, also known as biofabrication and biomanufacturing, is developed from 3D printing by adding cells, proteins, growth factors, and biomaterials to the printing ink, and its purpose is to create samples with specific biological functions. The development of 3D bioprinting can be divided into five stages based on the nature of products[7]: (1) biomedical *in vitro* devices without requiring biocompatibility; (2) biocompatible but non-degradable products; (3) biocompatible, degradable, and absorbable products; (4) cells as ink components; and (5) cellular microspheres and micro-organs[7]. In this review, we define that 3D printing includes stages 1 to 3, and 3D bioprinting includes stages 4 and 5.

3D printing and bioprinting have been used in a variety of applications including architecture, flexible electronics, tissue engineering (such as bone, meniscus, and blood vessels), and manufacturing of mechanical devices[8-15]. However, the application of 3D printing and bioprinting in urology is relatively rare[16-18]. The urological system, as one of the important systems of the body, plays a vital role in maintaining normal life activities. Urological organs are multi-tubular, heterogeneous, and anisotropic. 3D printing and bioprinting, as well as non-traditional subtractive manufacturing methods, offer flexibility in designing and fabricating complex scaffolds. Urological organ damage would directly or indirectly affect human life and health, so it is necessary to explore the potential of 3D printing and bioprinting in addressing urological disorders. Overall, this paper reviews the research progress of 3D printing and bioprinting technology in urology in the past 10 years (2013–2022), covering urological reconstruction models for preoperative planning, surgical teaching, medical devices for sizing customization and reducing medical costs, and tissue-engineered bioscaffolds for mimicking urological organs. It is believed that 3D printing and bioprinting have broader application prospects in urology in the future and have the opportunity to solve urological diseases.

2. Search strategy

All publications used in this study were obtained by performing searches on the Science Citation Index-Expanded (SCI-E) in the Web of Science Core Collection online database (Clarivate). The searches were conducted to find high-quality articles published in English between January 1, 2013, and December 31, 2022. Three search strategies were conducted for "3D printing" (search strategy #1), "3D printing in urology" (search strategy #2), and "3D bioprinting in urology" (search strategy #3), respectively, as shown in Table 1. These three search strategies yielded only research articles, and other publication types, including review papers, conference papers, conference abstracts, editorial materials, book chapters, etc., were not included unless they overlap with research papers. The topic subject (TS) term "3D printing" and its near-synonyms (such as "three-dimensional printing" and "direct ink writing") were used to retrieve publications on 3D printing. The TS term "3D bioprinting" and its near-synonyms (such as "biofabrication" and "biomanufacturing") were used to retrieve publications on 3D bioprinting. The title (TI) and abstract (AB) terms including "urology" and its involved organs including nephrology, prostate, kidney, ureter, bladder, urethra, penile, penis, and "adrenal gland" were placed in the search strategies for urology. This research was conducted following the Preferred Reporting Items for Systematic Reviews and Meta-analyses (PRISMA) statement, as illustrated in Figure 1.

Search results ("3D printing" in search strategy #1) show that, as shown in Figure 2A, 3D printing has received increasing attention and has been widely researched in recent years. Moreover, Figure 2B further demonstrates the level of attention 3D printing has received, by means of the number of highly cited papers in the Essential Science Indicators (ESI) of the Web of Science Core Collection. Other search results ("3D printing and urology" in search strategy #2, Figure 3A; "3D bioprinting in urology" in search strategy #3, Figure 3B) indicate that the research and exploration of 3D printing and bioprinting in urology is increasing. However, the use of 3D printing in the field of urology accounts for only about 1/5000 of its overall use in various fields. There are no highly cited papers on 3D printing in urology. Therefore, the application of 3D printing in urology remains a research gap awaiting to be addressed.

3. Characteristics of various 3D printing technologies

In recent years, the rapid development of 3D printing provides the technological basis for building a bridge between engineering, biology, materials science, and clinical medicine. 3D printing technology is one of the crucial elements of multi-disciplinary integration to solve clinical problems. The working process of 3D printing is shown in Figure 4. First, a target object is scanned by instruments such as micro-computed tomography

Table 1. The search strategies used in this paper and their details

Strategy	Query preview	Publications
"3D printing" (#1)	TS=((("3D" OR "3-D" OR "three dimensional" OR "3-dimensional") AND ("print*" OR "fabricat*" OR "manufactur*")) OR "additive manufacturing" OR "stereolithography" OR "fused deposition modeling" OR "selective laser sintering" OR "selective laser melting" OR "powder bed fusion" OR "binder jetting" OR "mate-rial extrusion" OR "direct ink writing" OR "material jetting" OR "rapid prototype*" OR "bioprint*" OR "biofabricat*" OR "bioplott*") AND DOP=(2013-01-01/2022-12-31) AND DT==("ARTICLE")	105,891
"3D printing" AND "urology" (#2)	TS=((("3D" OR "3-D" OR "three dimensional" OR "3-dimensional") AND ("print*" OR "fabricat*" OR "manufactur*")) OR "additive manufacturing" OR "stereolithography" OR "fused deposition modeling" OR "selective laser sintering" OR "selective laser melting" OR "powder bed fusion" OR "binder jetting" OR "mate-rial extrusion" OR "direct ink writing" OR "material jetting" OR "rapid prototype*" OR "bioprint*" OR "biofabricat*" OR "bioplott*") AND ((TI = (urology OR nephrology OR prostate OR kidney OR ureter OR bladder OR urethra OR penile OR penis OR "adrenal gland")) OR (AB = (urology OR nephrology OR prostate OR kidney OR ureter OR bladder OR urethra OR penile OR penis OR "adrenal gland"))) AND DOP=(2013-01-01/2022-12-31) AND DT==("ARTICLE")	531
"3D bioprinting" AND "urology" (#3)	TS=((("3D" OR "3-D" OR "three dimensional" OR "3-dimensional") AND ("bioprint*" OR "biofabricat*" OR "biomanufactur*")) OR "direct ink writing" OR "bioprint*" OR "biofabricat*" OR "bioplott*") AND ((TI = (urology OR nephrology OR prostate OR kidney OR ureter OR bladder OR urethra OR penile OR penis OR "adrenal gland")) OR (AB = (urology OR nephrology OR prostate OR kidney OR ureter OR bladder OR urethra OR penile OR penis OR "adrenal gland"))) AND DOP=(2013-01-01/2022-12-31) AND DT==("ARTICLE")	73

Booleans: AND, OR, and NOT; TS = topic subject; TI = title; AB = abstract; DOP = publication date; DT = document types.

(micro-CT) or magnetic resonance imaging (MRI). Then, the 3D digital model of the target object is obtained by reconstruction, design, and repair using computer-aided design (CAD) software and exported in STL or IGES file format for subsequent 3D printing. Next, the appropriate 3D printer and printing materials are selected based on the part's purpose and processing accuracy. Finally, the digital model is imported into the 3D printer for fabrication. It is important to note that some printing methods require post-processing for printed samples. 3D printing can be divided into different categories according to its working principle and applicable materials, mainly including stereolithography (SLA)[19-21], DLP[2,11,22], FDM[11,23,24], direct ink writing (DIW)[25-31] (through which the printed material is a series of lines or droplets), material jetting (MJ)[32], binder jetting (BJ)[33-35], selective laser sintering (SLS)[36,37], and selective laser melting (SLM)[38-41] (Figure 5). The characteristics, materials, advantages, and disadvantages of these different types of 3D printing technologies are demonstrated in Table 2.

In detail, SLA technology uses an oscillating mirror system to control the ultraviolet (UV) laser (355 nm or 405 nm) spot scanning crosslinking to achieve the curing of resin materials, which has better mechanical properties but less applicable materials, poor processing accuracy, and slow processing speed (Figure 5A). Moreover, the incomplete crosslinked resin is toxic, which is a shortcoming. Based on SLA technology, scientists developed a DLP system based on a digital mirror device and photosensitive polymers liquid, which has high precision and fast fabrication (Figure 5B). Moreover, with the rapid development of DLP, it is able to perform biofabrication of organs and tissues, such as heart and blood vessels, for potential future applications. In contrast to the previous two 3D printing technologies that employ liquids, FDM technology, one of the most widely used 3D printing technologies, utilizes solid polymer wire as the raw material (e.g., polylactic acid [PLA], acrylonitrile butadiene styrene [ABS], poly-ε-caprolactone [PCL]), which is melted by heating and then stacked layer by layer to build 3D-printed samples (Figure 5C). The common heating temperature of this technology is 50–280°C, which can generally melt most of the polymers. PCL, which has been approved by the US Food and Drug Administration (FDA), is used in tissue engineering areas including bone tissue engineering and meniscal tissue engineering. Although this technology is widely used in crafts, polymer parts, tissue engineering scaffolds, etc., its biggest limitation is that it cannot be bioprinted because of its high-temperature molten heating process, which is fatal to cells. DIW technology (Figure 5D) has a great advantage in bioprinting because of its technical simplicity and the wide range of available ink materials, such as hydrogel,

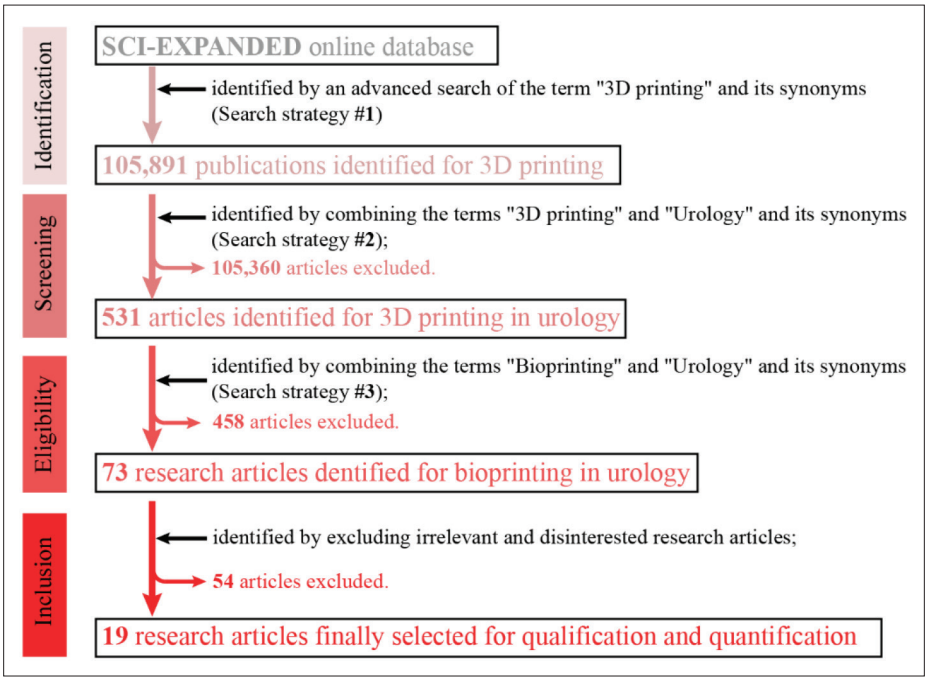

Figure 1. Flow chart of the literature search used in this study based on the Preferred Reporting Items for Systematic Reviews and Meta-analyses (PRISMA) method.

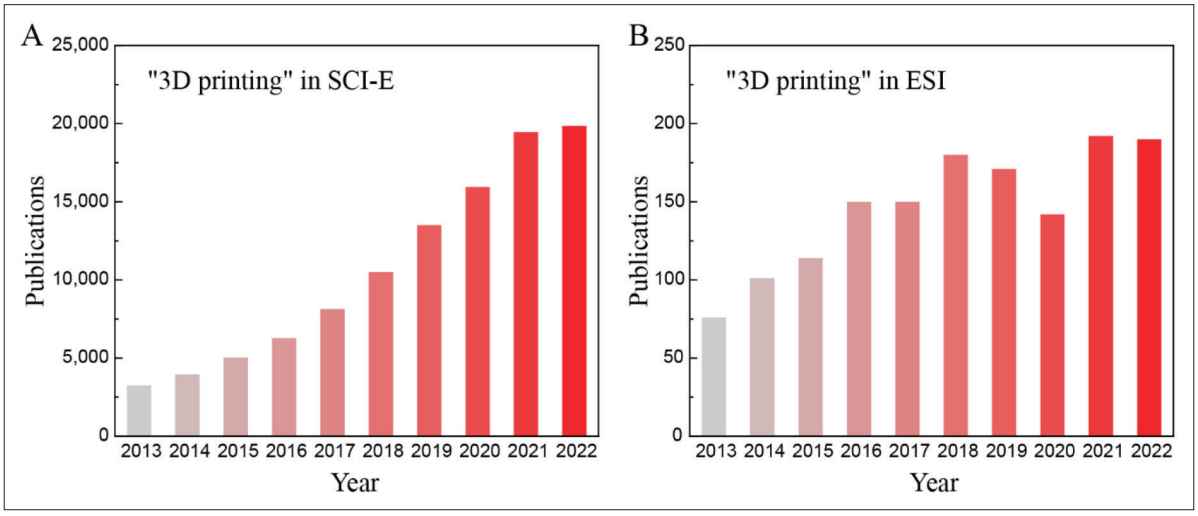

Figure 2. The number of published papers with "3D printing" as the topic subject (TS) term in the Science Citation Index-Expanded (SCI-E) (A) and the Essential Science Indicators (ESI) (B) of the Web of Science Core Collection between January 1, 2013, and December 31, 2022.

gelatin, and gelatin methacryloyl (GelMA), which can be easily printed with live cell ink. The ink extruded from the nozzle can be divided into two states: fiber (Figure 5D-i) and droplet (Figure 5D-ii). The DIW technology with continuous uniform diameter fiber state is widely applied to print various bioink applications. Especially, it has been widely adopted in the last decade for use in research. The greatest advantage of DIW technology is that it allows the biofabrication of widely available materials (various types of hydrogels) incorporating cells at room temperature, and the greatest disadvantage is the generally poor mechanical properties of the scaffolds obtained. In the future, high-strength hydrogels can be studied in-depth to further develop and popularize the adoption and acceptance of DIW technology in biofabrication. In addition to the DIW technology that uses droplet state, there are two other 3D printing technologies that we know of through droplets, and they are MJ (Figure 5E) and BJ (Figure 5F).

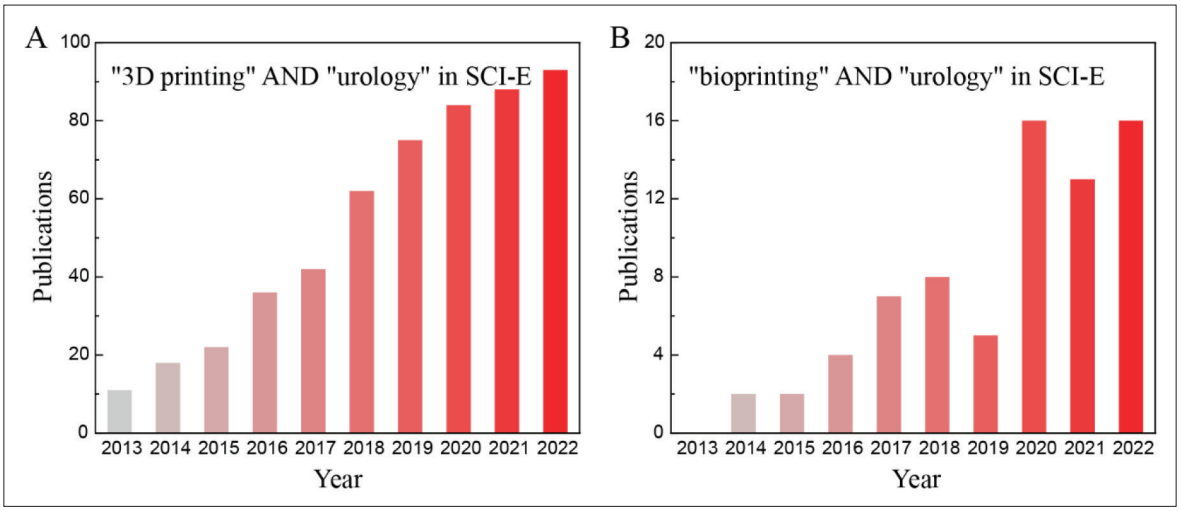

Figure 3. The number of publications with "3D printing" and "urology" (A) and "bioprinting" and "urology" (B) as the topic subject (TS) terms in the Science Citation Index-Expanded (SCI-E) database of Web of Science Core Collection between January 1, 2013, and December 31, 2022.

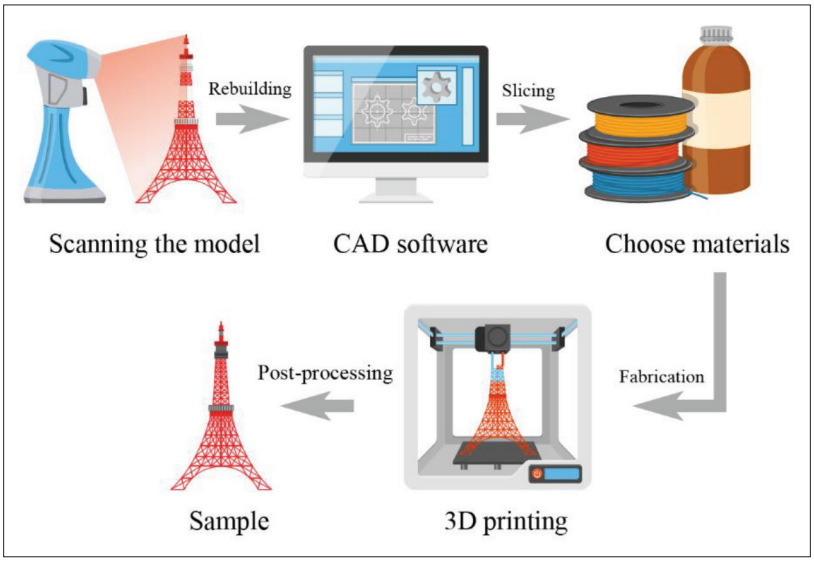

Figure 4. Design and fabrication workflow for 3D printing (Designed with macrovector/Freepik).

The difference between these two technologies is that MJ executes 3D printing by spraying droplet materials (e.g., liquid polymer or metal materials) and then crosslinking them with UV light for polymers or cooling them at room temperature for metal materials (Figure 5E), while BJ executes 3D printing by spraying binder on a bed of granular powder by bonding the particles (Figure 5F). A prominent representative of MJ technology is Stratasys, which has developed a variety of inkjet 3D printers (e.g., J750™ DAP, J8 Series™) that can handle multiple transparent or opaque materials for high-fidelity processing 3D models. The technologies that use powder bed fusion (PBF) are SLS (Figure 5G) and SLM (Figure 5H), which, unlike BJ, employ a laser to selectively heat-specific areas of powdered granular material for 3D printing. The difference between these two technologies (SLS and SLM) is the laser power used. SLS mainly heats and melts polymer materials with low melting point, which are used as binder to paste ceramic or metal materials (Figure 5G), while SLM uses high power laser to completely melt polymer or metal materials at high temperatures, resulting in higher precision and better mechanical properties, but consuming more energy and reducing processing speed (Figure 5H).

In summary, each 3D printing technology has unique characteristics and specialized applications, and applicable materials vary from method to method, as shown in Figure 5 and summarized in Table 2. Notably, 3D printing has been

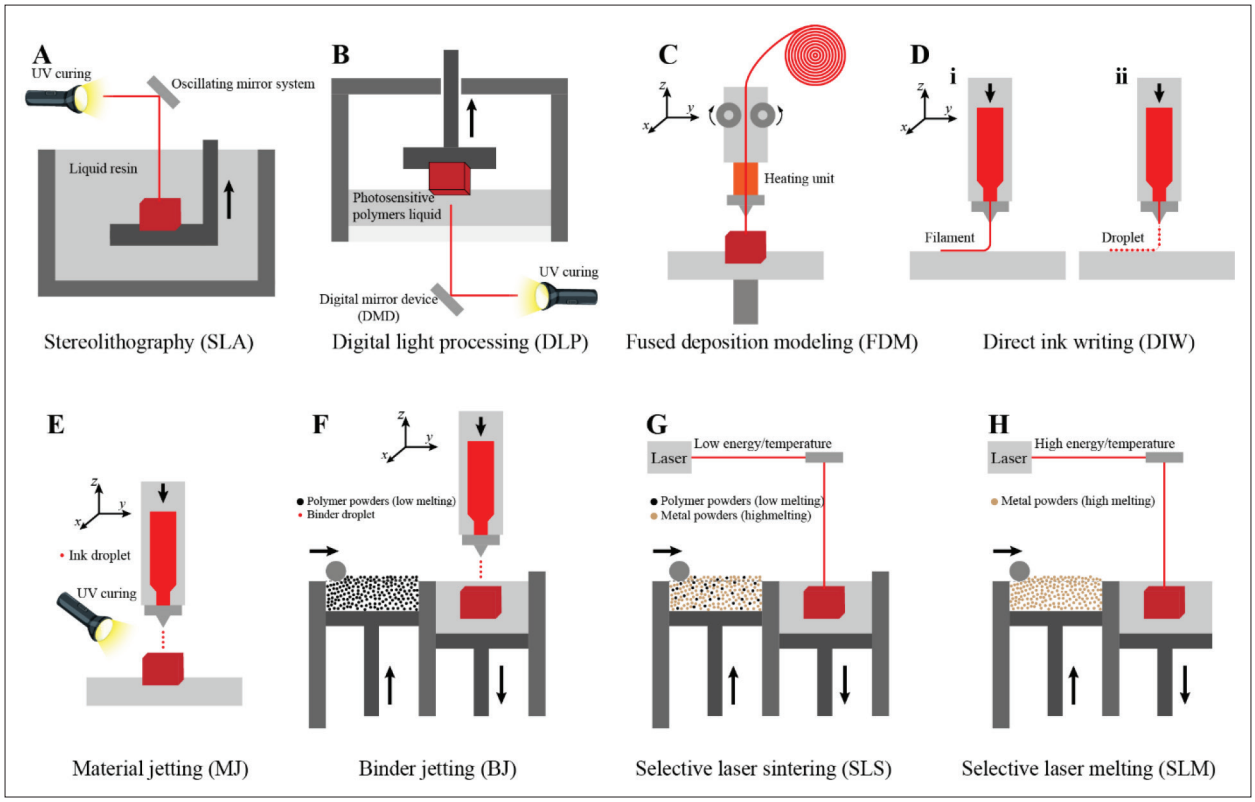

Figure 5. Schematic diagram of different types of 3D printing technologies. (A) Stereolithography (SLA)[83,84]. (B) Digital light processing (DLP)[85,86]. (C) Fused deposition modeling (FDM)[10]. (D) Direct ink writing (DIW)[28-30]. (E) Material jetting (MJ)[8]. (F) Binder jetting (BJ)[34,35]. (G) Selective laser sintering (SLS)[37,87]. (H) Selective laser melting (SLM)[38,88,89].

widely explored and applied in many areas, especially in the medical field which has received more attention compared to other fields, as evidenced by the continuous publication of research articles regarding 3D printing in medicine in prestigious journals such as *Nature* and *Science*[42-47]. The applications in urology can be divided into two main areas: 3D printing and bioprinting. The working environment of the printing method determines whether it is available to process cell-loaded bioinks. Therefore, 3D printing technologies (including SLA, FDM, BJ, SLS, and SLM) are used to process non-cellular urological samples, and 3D bioprinting technologies (including DLP, DIW, and MJ) are used to fabricate biological scaffolds with specific biological functions.

4. Clinical applications of 3D printing in urology

Urological disorders seriously affect human health, some of which can be managed with standard treatments that can alleviate patient suffering, but many are in dire need of new therapeutic strategies. Based on some studies, 3D printing gives a silver lining in tackling certain diseases that can be addressed with the use of tissue engineering, particularly those related to bone and cartilage[9], and it is believed that 3D printing can make a difference in urology in the future. 3D printing has gained wide interest in different fields due to its high application flexibility in many areas, including aerospace, automotive, food, architecture, batteries, flexible sensors, robotics, etc. The application of this technology in urology could be mainly divided into preoperative planning, surgical simulation, and preclinical application.

4.1. Preoperative planning

3D-printed urological models can facilitate interactions, including preoperative doctor–patient communication, surgical planning, and clinical teaching. To improve the accuracy of robot-assisted radical prostatectomy (RARP) surgery, Saba *et al.* reconstructed a digital model (Figure 6A-ii) of the prostate lesion site based on the patient's prostate MRI data (Figure 6A-i) and obtained the 3D-printed model (Figure 6A-iii) before the surgery[48]. The results demonstrated that the preoperative 3D-printed sample could provide urologists with more accurate and effective information for RARP surgery compared to continuous 2D MRI data, as shown in Figure 6A. Chandak *et al.* employed 3D printing to assist in the understanding of RARP surgery, indicating that visualization via 3D

Table 2. A summary of the characteristics, materials, advantages, and disadvantages of various 3D printing technologies

Method	Characteristic	Material	Advantage	Disadvantage	Ref.
SLA	UV crosslinking of photosensitive liquid resin to solid by laser beam	Photosensitive liquid resin	High mechanical properties, high resolution, and the ability to process large sizes	Toxic, trouble cleaning, less applicable materials, poor processing accuracy	[19-21]
DLP	Second-generation light-curing technology based on projector curing of photosensitive materials	Photosensitive polymer liquid, hydrogel	High mechanical properties, high resolution, faster processing speed, and bioprinting	Limited materials available	[2,11,22]
FDM	Wire material is heated at high temperature and then extruded	Polymers or composites	High mechanical properties and the ability to process large sizes	High temperature	[11,23,24]
DIW	Extrusion of viscoelastic materials for stacking and molding	Various materials (e.g., GelMA)	A wide range of available materials, room temperature, and bioprinting	Low mechanical strength	[25-31]
MJ	Liquid materials (droplets or lines) are sprayed and stacked.	Organic solutions and polymers	High resolution	Organic reagents or high temperature	[32]
BJ	The binder is injected into the powder bed to bond the pellets into shape	Particles and composites	A wide range of available materials	Low mechanical strength and low resolution	[33-35]
SLS	Sintering powder compacts using a laser as a heat source	Metal, ceramics, and composites	Sintering of powder billets with various materials	High temperature, complex process, and high cost	[36,37]
SLM	Melting and stacking of metallic materials using laser as a heat source	Metal and composites	High mechanical properties and metallic materials	High temperature, complex process, and high cost	[38-41]

Abbreviations: BJ, binder jetting; DIW, direct ink writing; DLP, digital light processing; FDM, fused deposition modeling; GelMA, gelatin methacryloyl; MJ, material jetting; SLA, stereolithography; SLM, selective laser melting; SLS, selective laser sintering.

Figure 6. 3D-printed urological kidney models for enhancing interactions and surgical simulation. (A) MRI data (i), reconstructed digital model (ii) and 3D-printed sample (iii) of the diseased prostate[48]. Reprinted with permission from ref.[48]. Copyright 2021 Elsevier. (B) A kidney with antler-shaped stones[51]. (C) A kidney with Von Hippel–Lindau syndrome[51]. (D) A kidney silicone sample for surgical training[51]. Reprinted with permission from ref.[51]. Copyright 2019 Elsevier.

means for simulation is more effective than using only 2D flat data[49]. The use of 3D-printed prostate models can achieve better understanding than the current gold-standard multi-disciplinary team meetings (MDT) sessions, providing medical students and clinicians with better guidance on surgical positioning[50].

Further, researchers have conducted 3D printing of kidneys to facilitate doctor–patient communication and clinical teaching[51]. Researchers from the University of California Irvine (USA) printed kidney samples with antler-shaped stones for preoperative planning (Figure 6B)[51]. Researchers from Camargo Cancer Center (Brazil) printed diseased kidneys for doctor–patient communication and preoperative planning (Figure 6C)[51]. 3D printing offers

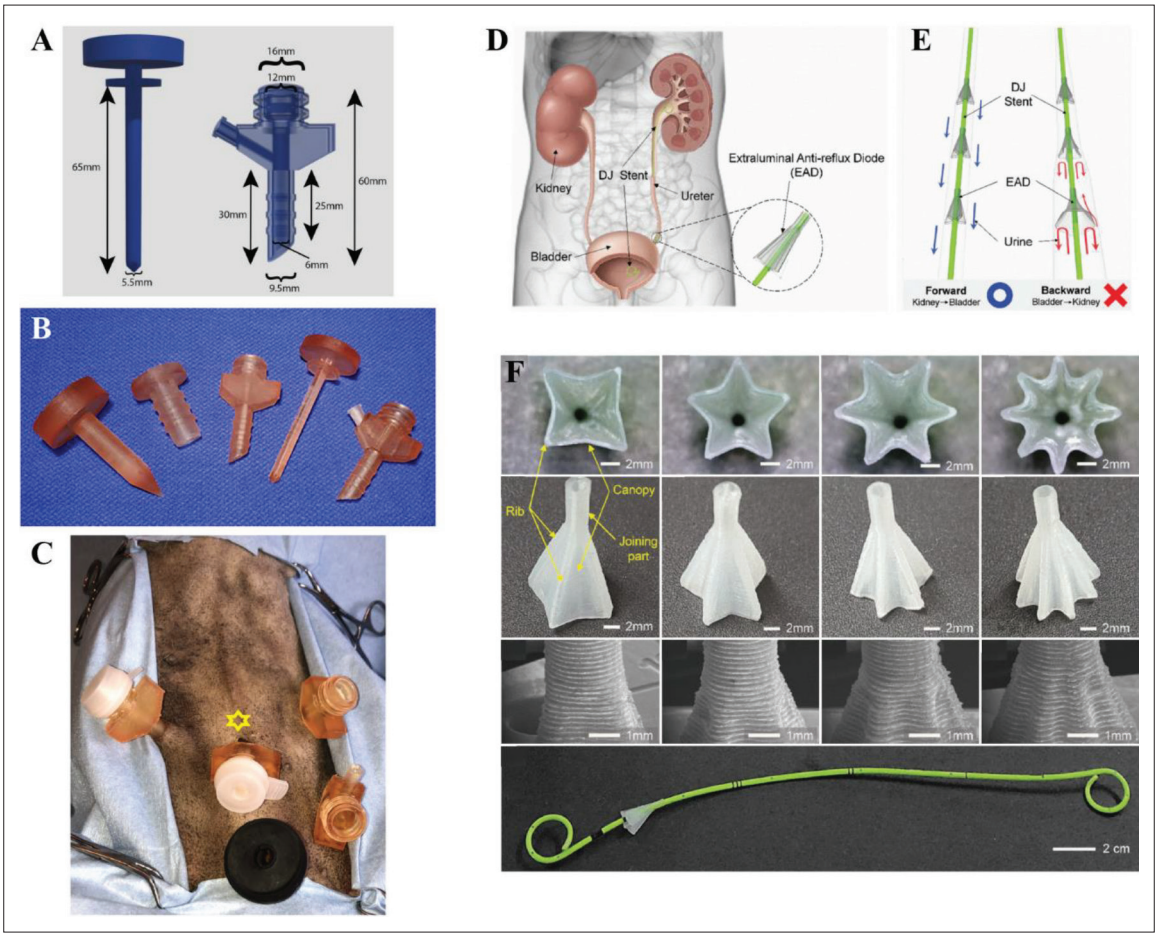

Figure 7. Design and fabrication of the laparoscopic trocar[90] and extraluminal anti-reflux diodes[55]. (A) Drawing of cannula and trocar. (B) 3D-printed cannulas. (C) Photograph of the cannula after surgery. Reprinted with permission from ref.[90]. Copyright 2022 John Wiley and Sons. (D) Schematic diagram of the extraluminal anti-reflux diode (EAD) in urinary organs. (E) Working principle of the EAD. (F) 3D-printed EADs with different shapes. (E) Working principle. (F) Different shapes. Reprinted with permission from ref.[55] under the Creative Commons Attribution 4.0 International License.

the opportunity and convenience for *in vitro* visualization of diseased urological organs, and its application in urology is expected to significantly facilitate doctor–patient communication and reduce the current doctor–patient conflicts in China due to miscommunication.

4.2. Surgical simulation

Researchers from the University of California Irvine (USA) printed a silicone kidney sample for surgical training (Figure 6D)[51]. This provides samples for *in vitro* anatomy learning and surgical simulation. In addition, other researchers have developed a 3D-printed kidney simulation platform. It can be used by urologists for rehearsal testing before formal surgery for kidney tumor removal. In the rehearsal, the surgeon is allowed to use various methods to remove the tumor and examine the model after each simulation and thus modify the surgical plan accordingly. The 3D-printed models effectively simulated the texture, anatomy, and perfusion of the kidney, providing a platform for a fully immersive experience in conducting a surgery. As shown in Figure 6E, the actual surgery and simulated images are displayed on the left and right, respectively[52]. In summary, the application of 3D printing in urology can help improve urologists' surgical skills, enhance surgical protocols, increase surgical success, and predict surgical outcomes based on model simulation results.

4.3. Preclinical application

Here, some applications of 3D-printed medical devices for urology were reported. del Junco *et al.* designed and fabricated laparoscopic punctures and ureteral stents using CAD software and 3D printing technology, and *in vivo* puncture experiments in pigs showed that the resulting devices are feasible and could be used in clinical settings in the future[53]. Buote *et al.* created and trained a variety of 3D-printed PLA scaffolds, and the surgical results showed that the use of their stents was successful, and there were no postoperative complications (Figure 7A–C)[90]. Further,

Park *et al.* fabricated a polymeric anti-reflux flap valve via 3D printing technology, which can be attached to a ureteral stent and can effectively resist reflux[54]. To improve anti-reflux, Lee *et al.* created extraluminal anti-reflux diodes with various shapes, which can be used in ureteral stents[55], as shown in Figure 7D–F.

5. 3D bioprinting in urology

3D bioprinting is commonly defined as the process of fabricating cell-loaded biological materials into tissue-engineered scaffolds. Although 3D printing provides technical support for the construction of urological tissue-engineered scaffolds with similar shapes, only 3D bioprinting can endow them with biological functions by incorporating biomaterials, live cells, and growth factors. The essence of bioprinting is the processing of living cells, which requires that the whole process of 3D printing should be friendly or non-invasive to living cells. Common 3D bioprinting technologies include extrusion-based bioprinting (single-, multi-, and coaxial-nozzle), inkjet-based bioprinting (piezoelectric and thermal), and light-based bioprinting (UV light and laser light)[13]. Although current technologies are not feasible to reconstruct organs *in vitro* that are fully capable of normal human activity for clinical transplantation, 3D bioprinting offers the possibility to reconstruct biologically active and functional urological organs.

Our search revealed a total of 73 research papers on bioprinting in urology based on search strategy #3. Of these, 19 research articles were selected for detailed study[56-74] (as shown in Table 3) after excluding literature reported works that used only urological cells, or some review articles that were incorrectly categorized as research article. Among these articles, 11 are about the kidney[56-58,62,63,65,67,69-72], 6 about the bladder[59-61,64,66,73], 1 about the glomerular[68], and 1 about the urinary tract[74]. Of these papers, extrusion bioprinting is the most widely used 3D bioprinting technology, due to its advantages such as low device cost, a wide range of applicable materials, and cell-friendliness. To present the advances of 3D bioprinting in urology, we divide this section into four parts: bioinks, cell types, structure design, and urological scaffolds, as shown in Figure 8.

5.1. Bioinks

Bioink is the raw material for 3D bioprinting, which is processed into samples according to the structure design with the aid of printing equipment. Currently, there are various formulations of bioink, which is mainly composed of basic biomaterials and bioadditives. The 3D bioprinting method determines the type of basic biomaterial required. The commonly used biomaterials include natural and synthetic materials. Generally, natural materials have excellent biocompatibility, but their mechanical properties are poor compared to synthetic materials. The popular biomaterials are mainly hydrogels, gelatin, alginate, decellularized extracellular matrix (dECM), and their mixtures. As the most widely used synthetic material in 3D bioprinting[75-79], hydrogel can mimic the extracellular matrix (ECM) and provide a physiologically similar environment for cell growth. Gelatin, alginate, and dECM are acceptable natural materials. The basic biomaterials provide carriers for the placement of live cells, and they can undergo biological reactions. Viscoelastic bioinks are usually processed using an extrusion strategy and can be handled equally well using a light-curing strategy by adding a photoinitiator.

5.2. Cell types

Bioprinting revolves around the processing and manufacturing of cell-loaded bioink. The cells represent one of the keys to bioprinting, and their selection endows the sample with specific functions. To mimic the biological microenvironment of natural urological organs *in vitro* as much as possible, cells from the target organ, such as human urothelial cells (HUCs) from urinary tract[74], human renal progenitor cells (hRPCs) and human embryonic kidney 293 cells (HEK293) from the kidney[63], human bladder smooth muscle cells (HBSMCs) and T24 cell from bladder[59,60], are usually used, according to the reviewed literature. In addition, stem cells are one of important cells for 3D bioprinting in urology due to their ability to differentiate into other cells, such as human bone marrow-derived mesenchymal stem cells (hBMSCs)[61].

5.3. Structure design

The printing method determines the strategy of structure design and the type of bioinks. The most widely accepted 3D bioprinting technology is the extrusion strategy, which relies on bioink deposition to form fibers to build the sample layer by layer. In addition, the extrusion strategy is carried out with the help of a three-coordinate printer or a six-degree-of-freedom robot arm to control the nozzle movement, and the viscoelastic bioink extrusion is achieved by screw, pneumatic, or piston.

According to the fluid process of the ink flow through the nozzle, we can get $D = 2\times(Q/\pi v)^{0.5}$, where D, Q, and v are the ideal diameter of the fiber, bioink flow, and printing speed, respectively[80]. It can be obtained that there is a functional relationship between the printing speed and the ideal diameter of the deposited fibers. Specifically, with a fixed print head size and printing parameters, the printing speed determines the size of the ideal diameter of the fiber and the printability of the bioink. During 3D bioprinting, a very high printing speed will result in fiber breakage and discontinuity, while a very low speed will

Table 3. A summary of 3D bioprinting in urology

Year	Urological organ	3D printing technology	Material	Cell	Discovery/Achievement	Ref.
2022	Kidney	Coaxial extrusion printing	Polyethylene vinyl acetate (PEVA)	HK-2s, Caco-2s, and GEs cells	Building a secondary hyperoxaluria model	[56]
2022	Kidney	DoD bioprinting	Fibrinogen, alginate	Induced renal tubular epithelial cells (iRECs)	Building a biomimetic 3D microenvironment modeling for polycystic kidney disease	[57]
2022	Renal glomerulus	Coaxial extrusion printing	PICO, and POMaC	HUVECs	Building a series of micro-scale tube channels with bionic shapes	[58]
2022	Bladder	Microfluidic	PDMS	T24 cell	Building a bladder cancer microenvironment	[59]
2022	Bladder	Microfluidic	PDMS	T24 cell	Building a chip-based non-muscle-invasive bladder cancer model	[60]
2022	Bladder	Extrusion printing	Bladder tissue-derived dECM (BldECM)	hBMSCs	Building a bladder model with a bionic structure	[61]
2022	Kidney	Multi-nozzle extrusion printing	Gelatin, and sodium alginate	HEK293, EK293-GFP, and Human kidney fibroblasts	Building a kidney cancer model for drug detection	[62]
2021	Kidney	Extrusion printing	dECM	hRPCs	Building a renal 3D microenvironment	[63]
2021	Bladder	Extrusion printing and microfluidic	GelMA	T24, 5637, MRC-5, and THP-1 cells	Building a bladder cancer microarray via microfluidic	[64]
2021	Kidney	DoD bioprinting, self-assembly technology	Matrigel and Collagen I, and Matrigel-Collagen I blends	Renal PTECs, TERT1, #CRL-4031	Building controllable renal spheroids and nephron-like tubules	[65]
2021	Bladder	Extrusion printing and microfluidic	DMEM	NOR-10 fibroblast cells, and uroepithelial cells	Developing a highly concentrated fibroblast platform to construct bladder-like organs	[66]
2021	Kidney	Extrusion printing	STEMdiff APEL or TESR-E6 medium prior	Human pluripotent stem cells (hPSCs)	Developing a technique for high-throughput extrusion printing of kidney-like organs in well plates	[67]
2020	Renal glomerulus	Microfluidic	Hydrogel	Endothelial cell	Developing bionic kidney glomeruli with complex concave and convex morphology	[68]
2019	Kidney	Extrusion printing	Bacterial nanocellulose, and alginate	HUVECs	Developing a microchannels	[69]
2019	Kidney	Extrusion printing	dECM, gelatin, HA, and glycerol	Human primary kidney cells	Developing a renal bioscaffold using dECM	[70]
2019	Kidney	Extrusion printing, sacrificial template, and microfluidic	Gelatin and fibrinogen	Human immortalized PTECs (RPTEC/TERT1; ATCC CRL4031)	Developing a kidney scaffold for kidney function, disease modeling, and pharmacology	[71]
2019	Kidney	Electrospinning	PCL	ciPTECs	Building a kidney tubule scaffold	[72]
2018	Bladder	Extrusion printing	DMEM	Bone marrow-derived cells	Building functional urinary bladders	[73]
2018	Urinary tract	Coaxial extrusion printing	GelMA, alginate, and PEGOA	HUCs and HBSMCs, HUVECs and HSMCs	Building cannular urothelial tissue constructs and vascular tissue constructs	[74]

Abbreviations: ciPTECs, conditionally immortalized proximal tubule epithelial cells; dECM, decellularized extracellular matrix; DMEM, Dulbecco's modified Eagle's medium; DoD, drop-on-demand; GelMA, gelatin methacryloyl; hBMSCs, human bone marrow-derived mesenchymal stem cells; HBSMCs, human bladder smooth muscle cells; HEK293, human embryonic kidney 293 cells; hRPCs, human renal progenitor cells; HSMCs, human smooth muscle cells; HUCs, human urothelial cells; HUVECs, human umbilical vein endothelial cells; PCL, poly-ε-caprolactone; PDMS, polydimethylsiloxane; PICO, poly(itaconate-co-citrate-co-octanediol); POMaC, poly(octanediol-co-maleic anhydride-co-citrate); PTECs, renal proximal tubule epithelial cells.

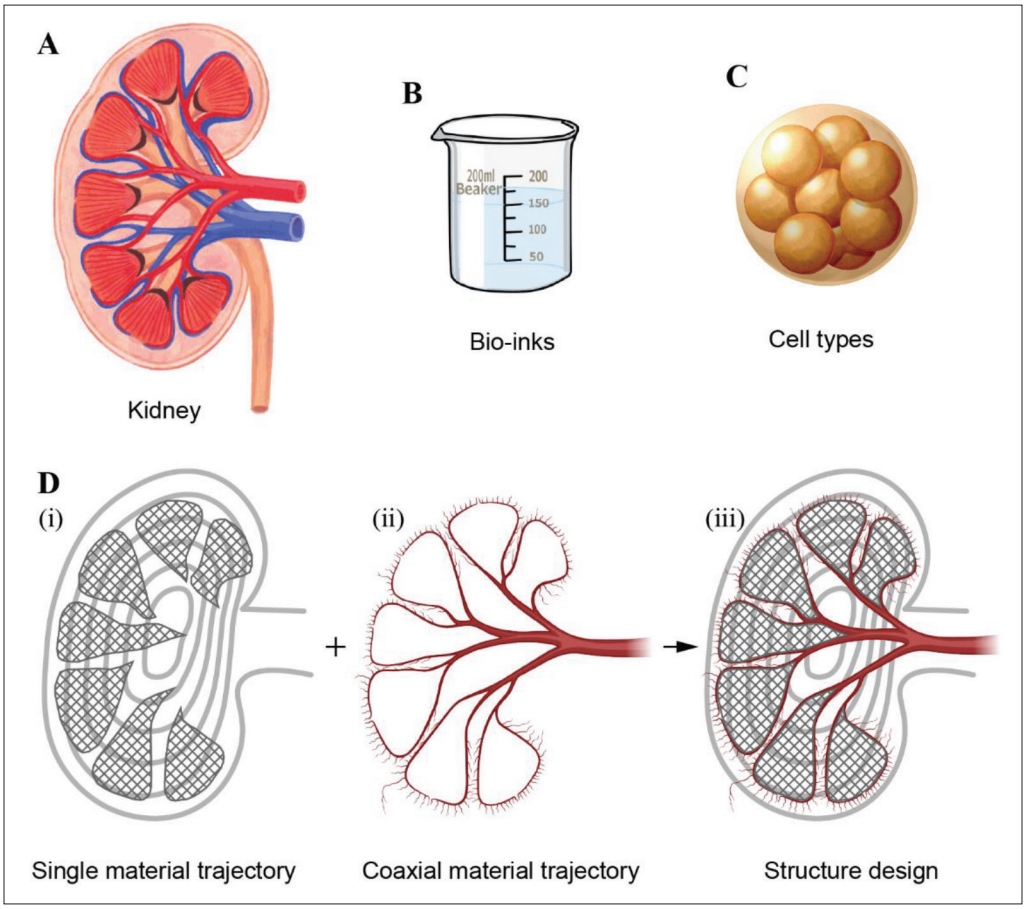

Figure 8. Key factors for 3D bioprinting in urology: (A) design and bioprinting of a kidney scaffold, (B) bioinks, (C) cell types, and (D) structure design.

result in serious ink accumulation and make it difficult to achieve high-fidelity manufacturing of large-size samples. Accurate control of extrusion air pressure is one of the keys to ensuring the survival rate of bioprinted cells; if the air pressure is set too high, it will result in the cells receiving large shear stresses and dying. The use of low extrusion pressure requires hydrogel bioinks with low shear thinning properties. In addition, the innovation of nozzle structure also provides new ideas and inspiration for structural design. Specifically, single nozzle is the most widely used in extrusion printing and can handle one bioink[81]. Developed from single-nozzle printing[3], multi-nozzle extrusion printing technology can utilize multiple bioinks and enable to mimic the multi-material and multi-cellular composition of natural urological organs. Coaxial-nozzle printing allows a single nozzle to print two bioinks[75,82], where the core and shell are usually the sacrificial and scaffold body materials, respectively. It is particularly suitable for the fabrication of tubular samples, such as blood vessels within the kidney, as shown in Figure 8C-ii. The goal of bioprinting is to mimic one or more of the biological functions of a urological organ *in vitro* as much as possible. As illustrated in Figure 8, which shows the kidney bioprinting process, the blood vessels of varying diameter are expected to mimic the vascular distribution within the kidney and provide structural mimicry for achieving reabsorption in an *in vitro* kidney model.

5.4. Urological scaffolds

The kidneys, ureter, bladder, and urethra together constitute the urinary system of the body, and they are also the organs mainly involved in urology. The kidneys are paired lentil-shaped organs and are one of the important organs of the body, whose basic function is to remove metabolic products from the body. The kidneys are one of the key representatives of bioprinted urological organs. We conclude that the stages of bioprinting development of urological organs, using the kidneys as an example, can be divided into three stages: (1) realization of simple physical and mechanical properties, such as urination of the kidney; (2) replacement, repair, and reconstruction of the kidney urethra; and (3) multi-cellular bionic kidneys with multiple biological functions. Lawlor *et al.* conducted extrusion bioprinting of kidney organoid samples using human pluripotent stem cells (hPSCs) with

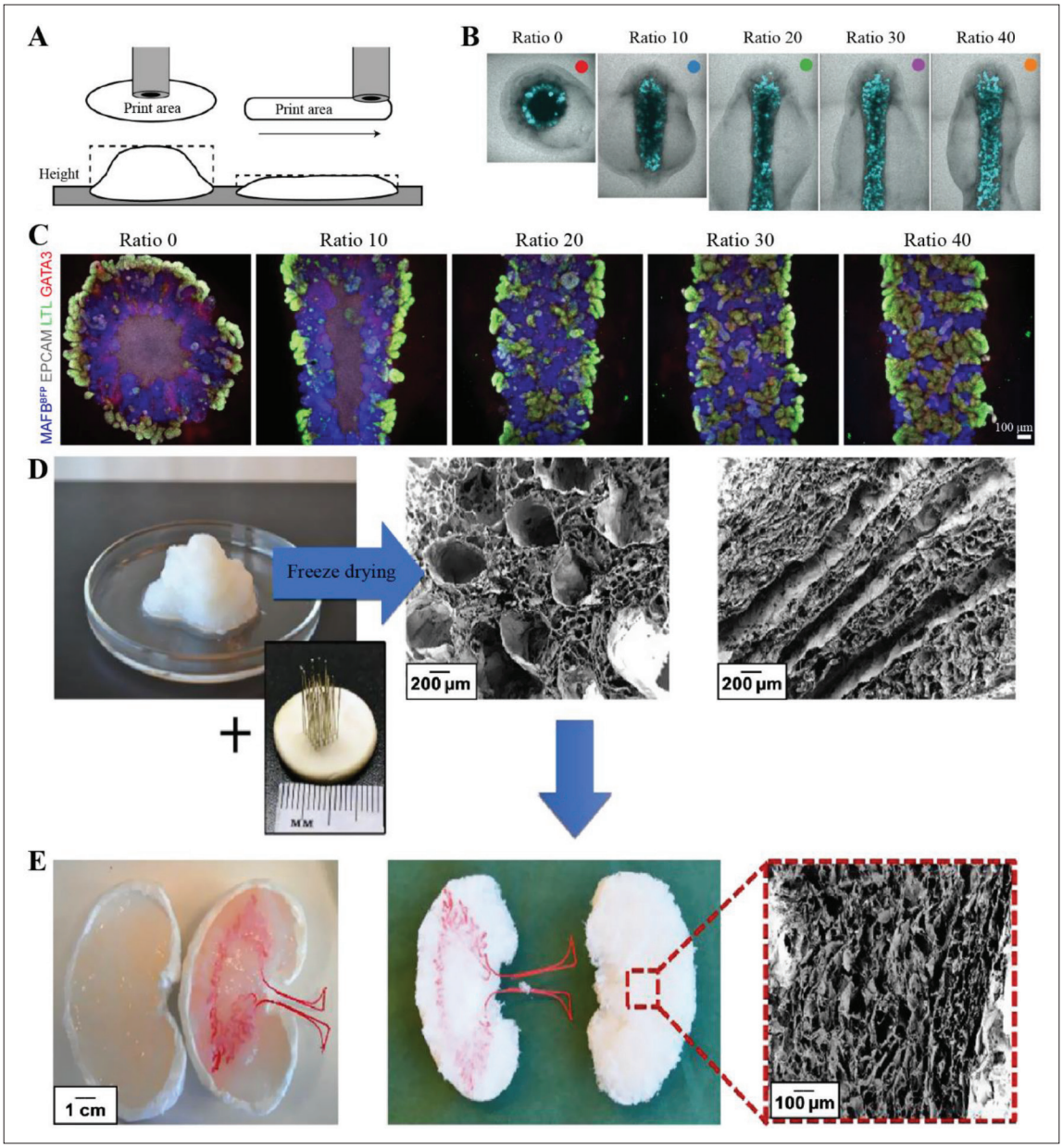

Figure 9. High-throughput extrusion bioprinting of kidney organoids holding promise for drug screening, disease modeling, and kidney organ transplantation (A–C)[67], and extrusion and sacrificial template method (D, E)[69]. (A) Schematic diagram of extruded samples at different nozzle movement speeds. (B) Fluorescence imaging of printed samples at different print speeds using MAFBmTAGBFP2 reporter line. (C) Immunofluorescence of printed samples. Reprinted with permission from ref.[67]. Copyright 2020 Springer Nature. (D) Freeze-casting method for the fabrication of porous structures. (E) Kidney scaffolds with vascular-like channels. Reprinted with permission from ref.[69] under the Creative Commons Attribution 3.0 International License.

targeted differentiation, offering promise for drug screening, disease modeling, and kidney organ transplantation (Figure 9A–C)[67]. They also found that tissue thickness could be precisely controlled by varying the ink extrusion rate and nozzle movement speed (Figure 9A and B), and the results showed that organoids with elongated lengths had a larger total glomerular area than small and thick ones stained by the MAFB gene promoter ($MAFB^{mTagBFP2}$) reporter line (Figure 9C)[67]. Sämfors *et al.* designed and fabricated kidney scaffolds with interconnected macro porosity and vascular-like structures using extrusion printing and sacrificial template method (Figure 9D and E)[69]. Blood vessels play a vital role in the proper functioning of the body's organs, providing nutrients and oxygen for cellular activity and transporting waste products. Therefore, it is particularly important to construct vascular channels

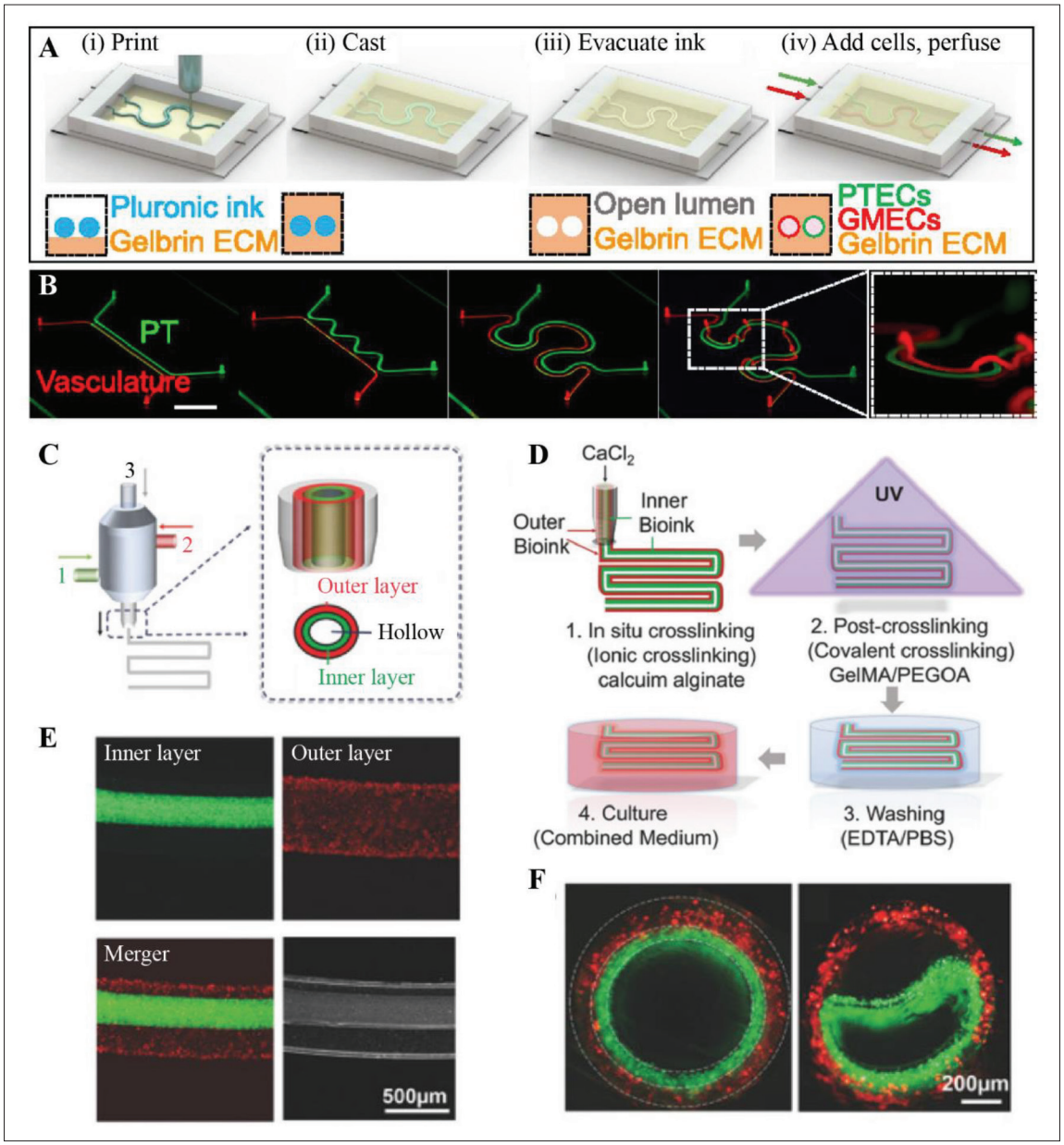

Figure 10. Design and fabrication of vascular samples by single-nozzle extrusion printing and sacrificial template method (A, B)[71], and coaxial-nozzle extrusion printing (C–F)[74]. (A) Flow chart of sample fabrication. (B) Vascular samples with different patterns. Reprinted with permission from ref.[71] under the Creative Commons Attribution 4.0 International License. (C) Schematic diagram of coaxial-nozzle structure. (D) Flow chart of tubular scaffold fabrication. (E) Top and (F) cross-sectional views of stained images of tube samples (green, inner layer; red, outer layer). Reprinted with permission from ref.[74]. Copyright 1999–2023 John Wiley & Sons.

in 3D-bioprinted urological tissue scaffolds. Lin *et al.* prepared complex vascular patterns using single-nozzle extrusion 3D printing and then obtained vascular channels by sacrificial template method (Figure 10A and B)[71]. Their results showed that the obtained vascular channels exhibited active reabsorption of albumin and glucose over time, providing a 3D platform for studying kidney function. In addition, Pi *et al.* designed and fabricated annular multi-layer tubular samples by coaxial-nozzle printing technology (Figure 10C–F)[74]. Their proposed coaxial nozzle has three inlets, which are the central material, inner layer material, and outer layer material from inside to outside (Figure 10C). The fabricated triple-layer samples are UV-crosslinked and cleaned to obtain a bilayer material tube scaffold with a hollow structure (Figure 10E). This proposed coaxial strategy conceived by Pi *et al.*[74] provides new insights into the design and fabrication of tubular tissues such as ureters and urethra.

6. Conclusion and outlook

In this review, we summarize the applications of 3D printing and bioprinting in urology. 3D printing of diseased urological organs effectively facilitates doctor–patient communication, preoperative planning, and surgical teaching in urology. Furthermore, 3D printing provides urologists with custom-sized medical devices and reduces medical costs. 3D bioprinting offers new insights for creating urological tissue-engineered scaffolds from biomaterials, living cells, and growth factors. In conclusion, the integration of 3D printing and bioprinting with urology offers new ideas and dynamics for urologists and patients.

In the future, for 3D printing and bioprinting in urology, the following five directions should be explored in-depth:

(i) Novel 3D printing. Currently, extrusion printing is one of the most widely used technologies for 3D printing and bioprinting. The development of new 3D printing technology is expected to significantly boost fabrication speed and accuracy, sample mechanical properties, and multi-material printing.

(ii) Novel structures. Urological organs have a complex structure (e.g., kidneys with vessels of varying diameter). The pore structure can facilitate the growth of blood vessels in tissue regeneration. Based on the characteristics of 3D printing technology and materials, the development of new bionic structures is a topic worthy of research.

(iii) Novel biomaterials. Biomaterials are the primary matter for 3D printing and bioprinting. Newly formulated materials can hopefully promote the development of 3D printing and bioprinting in tissue engineering, including urology.

(iv) Novel bioadditives. Bioadditives are drug triggers (such as live cells, growth factors, mRNA) for tissue regeneration and repair and can initiate and accelerate biological processes.

(v) How to balance 3D printing and bioprinting, biomimetic structures, biomaterials, and bioadditives to obtain urological organ scaffolds with near-natural biological functions is a tricky problem.

Acknowledgments

None.

Funding

This work was supported by the National Key R&D Program (Grant No. 2018YFA0703100), the National Natural Science Foundation of China (Grant No. 32122046), the Youth Innovation Promotion Association of CAS (Grant No. 2019350), the China Postdoctoral Science Foundation (Grant No. 2023M733668), the Guangdong Basic and Applied Basic Research Foundation (2020A1515111190), the Shenzhen Fundamental Research Foundation (JCYJ20210324113001005), the Shenzhen Governmental Sustainable Development Fund (KCXFZ20201221173612034), the Shenzhen Key Laboratory of Kidney Diseases (ZDSYS201504301616234), and the Shenzhen Fund for Guangdong Provincial Highlevel Clinical Key Specialties (No. SZGSP001).

Conflict of interest

The authors declare no conflicts of interests.

Author contributions

Conceptualization: Huawei Qu, Changshun Ruan
Methodology: Kun Liu, Nan Hu, Zhihai Yu, Hualin Ma
Investigation: Kun Liu, Nan Hu, Xinzhou Zhang, Hualin Ma
Writing – original draft: Kun Liu, Huawei Qu
Writing – review & editing: Hualin Ma, Huawei Qu, Changshun Ruan
Supervision: Zhihai Yu, Xinzhou Zhang, Changshun Ruan
Funding acquisition: Xinzhou Zhang, Hualin Ma

Ethics approval and consent to participate

Not applicable.

Consent for publication

Not applicable.

Availability of data

Not applicable.

References

1. Walker DA, Hedrick JL, Mirkin CA, 2019, Rapid, large-volume, thermally controlled 3D printing using a mobile liquid interface. *Science,* 366(6463): 360.

https://doi.org/10.1126/science.aax1562

2. Ligon SC, Liska R, Stampfl J, *et al.*, 2017, Polymers for 3D printing and customized additive manufacturing. *Chem Rev,* 117(15): 10212–10290.

https://doi.org/10.1021/acs.chemrev.7b00074

3. Skylar-Scott MA, Mueller J, Visser CW, *et al.*, 2019, Voxelated soft matter via multimaterial multinozzle 3D printing. *Nature,* 575(7782): 330–335.

https://doi.org/10.1038/s41586-019-1736-8

4. Ouyang L, Armstrong JPK, Lin Y, *et al.*, 2020, Expanding and optimizing 3D bioprinting capabilities using complementary network bioinks. *Sci Adv,* 6(38): eabc5529.

https://doi.org/10.1126/sciadv.abc5529

5. Bandyopadhyay A, Traxel KD, Bose S, 2021, Nature-inspired materials and structures using 3D Printing. *Mater Sci Eng R-Rep,* 145(2021): 100609.

https://doi.org/10.1016/j.mser.2021.100609

6. Qu HW, Fu HY, Han ZY, *et al.*, 2019, Biomaterials for bone tissue engineering scaffolds: A review. *RSC Adv,* 9(45): 26252–26262.

https://doi.org/10.1039/C9RA05214C

7. Sun W, Starly B, Daly AC, *et al.*, 2020, The bioprinting roadmap. *Biofabrication,* 12(2): 022002.

https://doi.org/10.1088/1758-5090/ab5158

8. Qu HW, 2020, Additive manufacturing for bone tissue engineering scaffolds. *Mater Today Commun,* 24(101024): 1–16.

https://doi.org/10.1016/j.mtcomm.2020.101024

9. Qu H, Han Z, Chen Z, *et al.*, 2021, Fractal design boosts extrusion-based 3D printing of bone-mimicking radial-gradient scaffolds. *Research,* 2021(2021): 9892689.

https://doi.org/10.34133/2021/9892689

10. Chatterjee K, Ghosh TK, 2020, 3D printing of textiles: Potential roadmap to printing with fibers. *Adv Mater,* 32(4): 1902086.

https://doi.org/10.1002/adma.201902086

11. Lai J, Wang C, Wang M, 2021, 3D printing in biomedical engineering: Processes, materials, and applications. *Appl Phys Rev,* 8(2): 021322.

https://doi.org/10.1063/5.0024177

12. Yang Y, Xu R, Wang C, *et al.*, 2022, Recombinant human collagen-based bioinks for the 3D bioprinting of full-thickness human skin equivalent. *Int J Bioprint,* 8(4): 611.

https://doi.org/10.18063/ijb.v8i4.611

13. Wu Y, Li M, Su H, *et al.*, 2023, Up-to-date progress in bioprinting of bone tissue. *Int J Bioprint,* 9(1): 628.

https://doi.org/10.18063/ijb.v9i1.628

14. Gao F, Xu ZY, Liang QF, *et al.*, 2019, Osteochondral regeneration with 3D-printed biodegradable high-strength supramolecular polymer reinforced-gelatin hydrogel scaffolds. *Adv Sci,* 6(15): 12.

https://doi.org/10.1002/advs.201900867

15. Lin ZF, Wu MM, He HM, *et al.*, 2019, 3D printing of mechanically stable calcium-free alginate-based scaffolds with tunable surface charge to enable cell adhesion and facile biofunctionalization. *Adv Funct Mater,* 29(9): 1808439.

https://doi.org/10.1002/adfm.201808439

16. Chen MY, Skewes J, Desselle M, *et al.*, 2020, Current applications of three-dimensional printing in urology. *BJU Int,* 125(1): 17–27.

https://doi.org/10.1111/bju.14928

17. Agung NP, Nadhif MH, Irdam GA, *et al.*, 2021, The role of 3D-printed phantoms and devices for organ-specified appliances in urology. *Int J Bioprint,* 7(2): 333.

https://doi.org/10.18063/ijb.v7i2.333

18. Colaco M, Igel DA , Atala A, 2018, The potential of 3D printing in urological research and patient care. *Nat Rev Urol,* 15(4): 213–221.

https://doi.org/10.1038/nrurol.2018.6

19. Ngo TD, Kashani A, Imbalzano G, *et al.*, 2018, Additive manufacturing (3D printing): A review of materials, methods, applications and challenges. *Compos B Eng,* 143(2018): 172–196.

https://doi.org/10.1016/j.compositesb.2018.02.012

20. Mondschein RJ, Kanitkar A, Williams CB, *et al.*, 2017, Polymer structure-property requirements for stereolithographic 3D printing of soft tissue engineering scaffolds. *Biomaterials,* 140(2017): 170–188.

https://doi.org/10.1016/j.biomaterials.2017.06.005

21. Hwa LC, Rajoo S, Noor AM, *et al.*, 2017, Recent advances in 3D printing of porous ceramics: A review. *Curr Opin Solid State Mater Sci,* 21(6): 323–347.

https://doi.org/10.1016/j.cossms.2017.08.002

22. Kuang X, Wu JT, Chen KJ, *et al.*, 2019, Grayscale digital light processing 3D printing for highly functionally graded materials. *Sci Adv,* 5(5): eaav5790.

https://doi.org/10.1126/sciadv.aav5790

23. Shao HF, Ke XR, Liu A, *et al.*, 2017, Bone regeneration in 3D printing bioactive ceramic scaffolds with improved tissue/material interface pore architecture in thin-wall bone defect. *Biofabrication,* 9(2): 12.

https://doi.org/10.1088/1758-5090/aa663c

24. Butscher A, Bohner M, Hofmann S, *et al.*, 2011, Structural and material approaches to bone tissue engineering in powder-based three-dimensional printing. *Acta Biomater,* 7(3): 907–920.

https://doi.org/10.1016/j.actbio.2010.09.039

25. Mousavi S, Howard D, Zhang F, *et al.*, 2020, Direct 3D printing of highly anisotropic, flexible, constriction-resistive sensors for multidirectional proprioception in soft robots. *ACS Appl Mater Interfaces,* 12(13): 15631–15643.

https://doi.org/10.1021/acsami.9b21816

26. Huang K, Dong S, Yang J, *et al.*, 2019, Three-dimensional printing of a tunable graphene-based elastomer for strain sensors with ultrahigh sensitivity. *Carbon,* 143(2019): 63–72.

https://doi.org/10.1016/j.carbon.2018.11.008

27. Jiang Z, Diggle B, Tan ML, *et al.*, 2020, Extrusion 3D printing of polymeric materials with advanced properties. *Adv Sci,* 7(17): 2001379.

https://doi.org/10.1002/advs.202001379

28. Nan B, Galindo-Rosales FJ, Ferreira JMF, 2020, 3D printing vertically: Direct ink writing free-standing pillar arrays. *Mater Today,* 35(2020): 16–24.

https://doi.org/10.1016/j.mattod.2020.01.003

29. Lewis JA, 2006, Direct ink writing of 3D functional materials. *Adv Funct Mater,* 16(17): 2193–2204.

https://doi.org/10.1002/adfm.200600434

30. Ravichandran D, Xu W, Kakarla M, *et al.*, 2021, Multiphase direct ink writing (MDIW) for multilayered polymer/nanoparticle composites. *Addit Manuf,* 47(2021): 102322.

https://doi.org/10.1016/j.addma.2021.102322

31. Nommeots-Nomm A, Lee PD, Jones JR, 2018, Direct ink writing of highly bioactive glasses. *J Eur Ceram Soc,* 38(3): 837–844.

https://doi.org/10.1016/j.jeurceramsoc.2017.08.006

32. He YF, Zhang F, Saleh E, *et al.*, 2017, A tripropylene glycol diacrylate-based polymeric support ink for material jetting. *Addit Manuf,* 16(2017): 153–161.

https://doi.org/10.1016/j.addma.2017.06.001

33. Brunello G, Sivolella S, Meneghello R, *et al.*, 2016, Powder-based 3D printing for bone tissue engineering. *Biotechnol Adv,* 34(5): 740–753.

https://doi.org/10.1016/j.biotechadv.2016.03.009

34. Miyanaji H, Zhang S , Yang L, 2018, A new physics-based model for equilibrium saturation determination in binder jetting additive manufacturing process. *Int J Mach Tools Manuf,* 124(2018): 1–11.

https://doi.org/10.1016/j.ijmachtools.2017.09.001

35. Zhou Z, Lennon A, Buchanan F, *et al.*, 2020, Binder jetting additive manufacturing of hydroxyapatite powders: Effects of adhesives on geometrical accuracy and green compressive strength. *Addit Manuf,* 36(2020):101645.

https://doi.org/10.1016/j.addma.2020.101645

36. Du YY, Liu HM, Yang Q, *et al.*, 2017, Selective laser sintering scaffold with hierarchical architecture and gradient composition for osteochondral repair in rabbits. *Biomaterials,* 137(2017): 37–48.

https://doi.org/10.1016/j.biomaterials.2017.05.021

37. Wu H, Wang O, Tian Y, *et al.*, 2020, Selective laser sintering-based 4D printing of magnetism-responsive grippers. *ACS Appl Mater Interfaces,* 13(11): 12679–12688.

https://doi.org/10.1021/acsami.0c17429

38. Warnke PH, Douglas T, Wollny P, *et al.*, 2009, Rapid prototyping: Porous titanium alloy scaffolds produced by selective laser melting for bone tissue engineering. *Tissue Eng Part C-Methods,* 15(2): 115–124.

https://doi.org/10.1089/ten.tec.2008.0288

39. Han CJ, Yan CZ, Wen SF, *et al.*, 2017, Effects of the unit cell topology on the compression properties of porous Co-Cr scaffolds fabricated via selective laser melting. *Rapid Prototyp J,* 23(1): 16–27.

https://doi.org/10.1108/rpj-08-2015-0114

40. Xiong Y-Z, Gao R-N, Zhang H, *et al.*, 2020, Rationally designed functionally graded porous Ti6Al4V scaffolds with high strength and toughness built via selective laser melting for load-bearing orthopedic applications. *J Mech Behav Biomed Mater,* 104(2020): 103673.

https://doi.org/10.1016/j.jmbbm.2020.103673

41. Liang HX, Yang YW, Xie DQ, *et al.*, 2019, Trabecular-like Ti-6Al-4V scaffolds for orthopedic: Fabrication by selective laser melting and in vitro biocompatibility. *J Mater Sci Technol,* 35(7): 1284–1297.

https://doi.org/10.1016/j.jmst.2019.01.012

42. Kinstlinger IS, Saxton SH, Calderon GA, *et al.*, 2020, Generation of model tissues with dendritic vascular networks via sacrificial laser-sintered carbohydrate templates. *Nat Biomed Eng,* 4(9): 916–932.

https://doi.org/10.1038/s41551-020-0566-1

43. Mao M, Qu X, Zhang Y, *et al.*, 2023, Leaf-venation-directed cellular alignment for macroscale cardiac constructs with tissue-like functionalities. *Nat Commun,* 14(1): 2077.

https://doi.org/10.1038/s41467-023-37716-1

44. Brassard JA, Nikolaev M, Hübscher T, *et al.*, 2021, Recapitulating macro-scale tissue self-organization through organoid bioprinting. *Nat Mater,* 20(1): 22–29.

https://doi.org/10.1038/s41563-020-00803-5

45. Koons GL, Diba M, Mikos AG, 2020, Materials design for bone-tissue engineering. *Nat Rev Mater,* 5(8): 584–603.

https://doi.org/10.1038/s41578-020-0204-2

46. Liu H, Du Y, St-Pierre J-P, *et al.*, 2020, Bioenergetic-active materials enhance tissue regeneration by modulating cellular metabolic state. *Sci Adv,* 6(13): eaay7608.

https://doi.org/10.1126/sciadv.aay7608

47. McDermott Anna M, Herberg S, Mason Devon E, *et al.*, 2019, Recapitulating bone development through engineered mesenchymal condensations and mechanical cues for tissue regeneration. *Sci Transl Med,* 11(495): eaav7756.

https://doi.org/10.1126/scitranslmed.aav7756

48. Saba P, Melnyk R, Holler T, *et al.*, 2021, Comparison of multi-parametric MRI of the prostate to 3D prostate computer aided designs and 3D-printed prostate models for pre-operative planning of radical prostatectomies: A pilot study. *Urology,* 158(2021): 150–155.

https://doi.org/10.1016/j.urology.2021.08.031

49. Chandak P, Byrne N, Lynch H, *et al.*, 2018, Three-dimensional printing in robot-assisted radical prostatectomy - an Idea, Development, Exploration, Assessment, Long-term follow-up (IDEAL) Phase 2a study. *BJU Int,* 122(3): 360–361.

https://doi.org/10.1111/bju.14189

50. Ebbing J, Jäderling F, Collins JW, *et al.*, 2018, Comparison of 3D printed prostate models with standard radiological information to aid understanding of the precise location of prostate cancer: A construct validation study. *PLoS One,* 13(6): e0199477.

https://doi.org/10.1371/journal.pone.0199477

51. Cacciamani GE, Okhunov Z, Meneses AD, *et al.*, 2019, Impact of three-dimensional printing in urology: state of the art and future perspectives. A systematic review by ESUT-YAUWP Group. *Eur Urol,* 76(2): 209–221.

https://doi.org/10.1016/j.eururo.2019.04.044

52. Ghazi AE, Teplitz BA, 2020, Role of 3D printing in surgical education for robotic urology procedures. *Transl Androl Urol,* 9(2): 931–941.

https://tau.amegroups.com/article/view/35484

53. del Junco M, Okhunov Z, Yoon R, *et al.*, 2014, Development and initial porcine and cadaver experience with three-dimensional printing of endoscopic and laparoscopic equipment. *J Endourol,* 29(1): 58–62.

https://doi.org/10.1089/end.2014.0280

54. Park C-J, Kim H-W, Jeong S, *et al.*, 2015, Anti-reflux ureteral stent with polymeric flap valve using three-dimensional printing: An in vitro study. *J Endourol,* 29(8): 933–938.

https://doi.org/10.1089/end.2015.0154

55. Lee J, Sung J, Ki JJ, *et al.*, 2022, 3D-printing-assisted extraluminal anti-reflux diodes for preventing vesicoureteral reflux through double-J stents. *Int J Bioprint,* 8(2): 549.

https://doi.org/10.18063/ijb.v8i2.549

56. Yoon J, Singh NK, Jang J, *et al.*, 2022, 3D bioprinted in vitro secondary hyperoxaluria model by mimicking intestinal-oxalate-malabsorption-related kidney stone disease. *Appl Phys Rev,* 9(4): 041408.

https://doi.org/10.1063/5.0087345

57. Pichler R, Rizzo L, Tröndle K, *et al.*, 2022, Tuning the 3D microenvironment of reprogrammed tubule cells enhances biomimetic modeling of polycystic kidney disease. *Biomaterials,* 291(2022): 121910.

https://doi.org/10.1016/j.biomaterials.2022.121910

58. Liu C, Campbell SB, Li J, *et al.*, 2022, High throughput omnidirectional printing of tubular microstructures from elastomeric polymers. *Adv Healthc Mater,* 11(23): 2201346.

https://doi.org/10.1002/adhm.202201346

59. Kim JH, Choi J, Kim M, *et al.*, 2022, Immunotherapeutic effects of recombinant Bacillus Calmette–Guérin containing sic gene in ex vivo and in vivo bladder cancer models. *Investig Clin Urol,* 63(2): 228–237.

https://doi.org/10.4111/icu.20210425

60. Lee S, Kim JH, Kang SJ, *et al.*, 2022, Customized multilayered tissue-on-a-chip (MToC) to simulate Bacillus Calmette–Guérin (BCG) immunotherapy for bladder cancer treatment. *BioChip J,* 16(1): 67–81.

https://doi.org/10.1007/s13206-022-00047-2

61. Chae S, Kim J, Yi H-G, *et al.*, 2022, 3D bioprinting of an in vitro model of a biomimetic urinary bladder with a contract-release system. *Micromachines,* 13(2): 277.

https://doi.org/10.3390/mi13020277

62. Wu D, Berg J, Arlt B, *et al.*, 2022, Bioprinted cancer model of neuroblastoma in a renal microenvironment as an efficiently applicable drug testing platform. *Int J Mol Sci,* 23(1): 122.

https://doi.org/10.3390/ijms23010122

63. Sobreiro-Almeida R, Gomez-Florit M, Quinteira R, *et al.*, 2021, Decellularized kidney extracellular matrix bioinks recapitulate renal 3D microenvironment in vitro. *Biofabrication,* 13(4): 17.

https://doi.org/10.1088/1758-5090/ac0fca

64. Kim JH, Lee S, Kang SJ, *et al.*, 2021, Establishment of three-dimensional bioprinted bladder cancer-on-a-chip with a microfluidic system using Bacillus Calmette-Guerin. *Int J Mol Sci,* 22(16): 17.

https://doi.org/10.3390/ijms22168887

65. Trondle K, Rizzo L, Pichler R, *et al.*, 2021, Scalable fabrication of renal spheroids and nephron-like tubules by bioprinting and controlled self-assembly of epithelial cells. *Biofabrication,* 13(3): 16.

https://doi.org/10.1088/1758-5090/abe185

66. Serex L, Sharma K, Rizov V, *et al.*, 2021, Microfluidic-assisted bioprinting of tissues and organoids at high cell concentrations. *Biofabrication,* 13(2): 025006.

https://doi.org/10.1088/1758-5090/abca80

67. Lawlor KT, Vanslambrouck JM, Higgins JW, *et al.*, 2021, Cellular extrusion bioprinting improves kidney organoid reproducibility and conformation. *Nat Mater,* 20(2): 260–271.

https://doi.org/10.1038/s41563-020-00853-9

68. Xie R, Korolj A, Liu C, *et al.*, 2020, h-FIBER: Microfluidic topographical hollow fiber for studies of glomerular filtration barrier. *ACS Central Sci,* 6(6): 903–912.

https://doi.org/10.1021/acscentsci.9b01097

69. Sämfors S, Karlsson K, Sundberg J, *et al.*, 2019, Biofabrication of bacterial nanocellulose scaffolds with complex vascular structure. *Biofabrication,* 11(4): 045010.

https://doi.org/10.1088/1758-5090/ab2b4f

70. Ali M, Pr AK, Yoo JJ, *et al.*, 2019, A photo-crosslinkable kidney ECM-derived bioink accelerates renal tissue formation. *Adv Healthc Mater,* 8(7): 1800992.

https://doi.org/10.1002/adhm.201800992

71. Lin NYC, Homan KA, Robinson SS, *et al.*, 2019, Renal reabsorption in 3D vascularized proximal tubule models. *Proc Natl Acad Sci,* 116(12): 5399–5404.

https://doi.org/10.1073/pnas.1815208116

72. Jansen K, Castilho M, Aarts S, *et al.*, 2019, Fabrication of kidney proximal tubule grafts using biofunctionalized electrospun polymer scaffolds. *Macromol Biosci,* 19(2): 1800412.

https://doi.org/10.1002/mabi.201800412

73. Imamura T, Shimamura M, Ogawa T, *et al.*, 2018, Biofabricated structures reconstruct functional urinary bladders in radiation-injured rat bladders. *Tissue Eng Part A,* 24(21–22): 1574–1587.

https://doi.org/10.1089/ten.tea.2017.0533

74. Pi Q, Maharjan S, Yan X, *et al.*, 2018, Digitally tunable microfluidic bioprinting of multilayered cannular tissues. *Adv Mater,* 30(43): 1706913.

https://doi.org/10.1002/adma.201706913

75. Liang Q, Gao F, Zeng Z, *et al.*, 2020, Coaxial scale-up printing of diameter-tunable biohybrid hydrogel microtubes with high strength, perfusability, and endothelialization. *Adv Funct Mater,* 30(43): 2001485.

https://doi.org/10.1002/adfm.202001485

76. Xu Z, Fan C, Zhang Q, *et al.*, 2021, A self-thickening and self-strengthening strategy for 3D printing high-strength and antiswelling supramolecular polymer hydrogels as meniscus substitutes. *Adv Funct Mater,* 31(18): 2100462.

https://doi.org/10.1002/adfm.202100462

77. Gong J, Schuurmans CCL, Genderen AMv, *et al.*, 2020, Complexation-induced resolution enhancement of 3D-printed hydrogel constructs. *Nat Commun,* 11(1): 1267.

https://doi.org/10.1038/s41467-020-14997-4

78. Park S, Yuk H, Zhao R, *et al.*, 2021, Adaptive and multifunctional hydrogel hybrid probes for long-term sensing and modulation of neural activity. *Nat Commun,* 12(1): 3435.

https://doi.org/10.1038/s41467-021-23802-9

79. Fan W, Shan C, Guo H, *et al.*, 2022, Dual-gradient enabled ultrafast biomimetic snapping of hydrogel materials. *Sci Adv,* 5(4): eaav7174.

https://doi.org/10.1126/sciadv.aav7174

80. Duraivel S, Laurent D, Rajon DA, *et al.*, 2023, A silicone-based support material eliminates interfacial instabilities in 3D silicone printing. *Science,* 379(6638): 1248–1252.

https://doi.org/10.1126/science.ade4441

81. Zhao S, Siqueira G, Drdova S, *et al.*, 2020, Additive manufacturing of silica aerogels. *Nature,* 584(7821): 387–392.

https://doi.org/10.1038/s41586-020-2594-0

82. Xu J, Zhang X, Liu Y, *et al.*, 2020, Selective coaxial ink 3D printing for single-pass fabrication of smart elastomeric foam with embedded stretchable sensor. *Addit Manuf,* 36(2020): 101487.

https://doi.org/10.1016/j.addma.2020.101487

83. Cooke MN, Fisher JP, Dean D, *et al.*, 2003, Use of stereolithography to manufacture critical-sized 3D biodegradable scaffolds for bone ingrowth. *J Biomed Mater Res Part B-Appl Biomater,* 64B(2): 65–69.

https://doi.org/10.1002/jbm.b.10485

84. Wang Z, Huang CZ, Wang J, *et al.*, 2019, Development of a novel aqueous hydroxyapatite suspension for stereolithography applied to bone tissue engineering. *Ceram Int,* 45(3): 3902–3909.

https://doi.org/10.1016/j.ceramint.2018.11.063

85. Caprioli M, Roppolo I, Chiappone A, *et al.*, 2021, 3D-printed self-healing hydrogels via digital light processing. *Nat Commun,* 12(1): 1–9.

https://doi.org/10.1038/s41467-021-22802-z

86. Chen Z, Yang M, Ji M, *et al.*, 2021, Recyclable thermosetting polymers for digital light processing 3D printing. *Mater Des,* 197(2021): 109189.

https://doi.org/10.1016/j.matdes.2020.109189

87. Mazzoli A, Ferretti C, Gigante A, *et al.*, 2015, Selective laser sintering manufacturing of polycaprolactone bone scaffolds for applications in bone tissue engineering. *Rapid Prototyp J,* 21(4): 386–392.

https://doi.org/10.1108/rpj-04-2013-0040

88. Liu C, Yan D, Tan J, *et al.*, 2020, Development and experimental validation of a hybrid selective laser melting and CNC milling system. *Addit Manuf,* 36(2020): 101550.

https://doi.org/10.1016/j.addma.2020.101550

89. Hu Y, Chen H, Liang X, *et al.*, 2021, Microstructure and biomechanical properties in selective laser melting of porous metal implants. *3D Print Addit Manuf*, 0(0): 1–12.

https://doi.org/10.1089/3dp.2021.0150

90. Buote NJ, Porter I, Dakin GF, 2022, 3D printed cannulas for use in laparoscopic surgery in feline patients: A cadaveric study and case series. *Vet Surg,* n/a(n/a).

https://doi.org/10.1111/vsu.13849

ACCSCIENCE PUBLISHING

International Journal of Bioprinting

RESEARCH ARTICLE

Melt electrospinning writing PCL scaffolds after alkaline modification with outstanding cytocompatibility and osteoinduction

Yubo Shi[1†], Lei Wang[1†], Liguo Sun[2†], Zhennan Qiu[3,4], Xiaoli Qu[3,4], Jingyi Dang[1], Zhao Zhang[1], Jiankang He[3,4*], and Hongbin Fan[1*]

[1]Department of Orthopedic Surgery, Xijing Hospital, The Fourth Military Medical University, Xi'an, China

[2]Department of Medical Management, Shaanxi Provincial Hospital of Chinese Medicine, Xi'an, China

[3]State Key Laboratory for Manufacturing Systems Engineering, Xi'an Jiaotong University, Xi'an, China

[4]Rapid Manufacturing Research Center of Shaanxi Province, Xi'an Jiaotong University, Xi'an, China

[†]These authors contributed equally to this work.

***Corresponding authors:**
Hongbin Fan
(fanhb@fmmu.edu.cn)

Jiankang He
(jiankanghe@mail.xjtu.edu.cn)

Citation: Shi Y, Wang L, Sun L, *et al*., 2023, Melt electrospinning writing PCL scaffolds after alkaline modification with outstanding cytocompatibility and osteoinduction. *Int J Bioprint*, 9(6): 1071.
https://doi.org/10.36922/ijb.1071

Received: June 12, 2023
Accepted: July 13, 2023
Published Online: August 11, 2023

Copyright: © 2023 Author(s). This is an Open Access article distributed under the terms of the Creative Commons Attribution License, permitting distribution, and reproduction in any medium, provided the original work is properly cited.

Publisher's Note: AccScience Publishing remains neutral with regard to jurisdictional claims in published maps and institutional affiliations.

Abstract

Melt electrospinning writing (MEW) is a promising three-dimensional (3D) printing technology that enables the creation of scaffolds with highly ordered microfibers. Polycaprolactone (PCL) is an ideal material for MEW scaffold fabrication due to its exceptional printability. However, its low cellular affinity can hinder its performance in bone tissue engineering. This study aimed to explore the potential of NaOH treatment as a means of enhancing the cytocompatibility and osteoinductive properties of PCL scaffolds. After modification with a NaOH solution, the physiochemical properties of the MEW PCL scaffold were analyzed. The surface of the scaffold was found to have nanopits and nanogrooves, which differed from the smooth surface of the PCL scaffold. Atomic force microscopy and automatic water contact angle assays revealed an increase in surface roughness and wettability, both of which were found to be beneficial for cell proliferation and adhesion. *In vitro* experiments demonstrated that the NaOH-treated surface was able to induce osteogenic differentiation of rat bone marrow mesenchymal stem cells (BMSCs) via the integrinα2/β1-PI3K-Akt signaling pathway, which had not been previously observed. The study involved implanting PCL scaffold to repair a cranial defect. After 1 and 3 months of implantation, histological analysis and micro-computed tomography scans showed a higher amount of newly formed bone on the NaOH-treated PCL scaffolds compared to the PCL scaffold. The study concluded that NaOH treatment was a simple and effective way to enhance cellular affinity and osteoinductive property of MEW PCL scaffold. This strategy may provide a cost-efficient method for promoting bone regeneration.

Keywords: Melt electrospinning writing; Polycaprolactone; Bone regeneration; Tissue engineering

1. Introduction

Craniofacial bone defects not only have a serious impact on the patient's quality of life but also represent a challenge for surgeon[1]. The clinical treatments for craniofacial bone defects mainly include autogenous grafts, allogeneic grafts, and engineered bone[2]. Despite being the standard treatment for bone defects, autograft is limited by a lack of tissue source. Although allogeneic bone is widely used, it carries the risk of immune rejection and disease transmission[3,4]. In this context, engineered bone shows great potential for the treatment of bone defects[5-7].

Melt electrospinning writing (MEW) is an innovative three-dimensional (3D) printing technique that enables the creation of structures with precisely arranged microfibers, making it a promising technology for bone tissue engineering applications[8-10]. Both pore size and fiber diameter can be easily controlled by adjusting the printing parameters to meet the specific requirements of various tissues[11]. Several studies have demonstrated the benefits of utilizing MEW scaffolds in tissue engineering, such as wound healing, regeneration of periodontal tissue, and restoration of the acetabular labrum[12-14]. To date, limited research has been conducted on the utilization of MEW scaffolds for bone defect repair[15-17]. Therefore, additional investigations are needed to determine the effectiveness and potential applications of MEW scaffolds in craniofacial bone regeneration.

Recently, some synthetic polymers have been used to prepare MEW scaffolds, including polycaprolactone (PCL), poly (L-lactic acid) (PLLA), and polyethylene oxide (PEO)[18-20]. Of these, PCL is a highly desirable material due to its exceptional printability and low melting point[21]. It has been extensively utilized in numerous biological applications such as bone grafts, drug delivery systems, and skin grafts[22-24]. However, several studies have highlighted the weakness of PCL scaffold, particularly in bone integration after implantation, owing to its low cellular affinity[25,26]. Consequently, researchers have focused on improving the cytocompatibility of PCL.

Previous studies have shown that modifying the surface of a scaffold can improve its cellular affinity and cytocompatibility. This can be achieved through modifications in hydrophilicity, roughness, and morphology[27,28]. For example, the favorable hydrophilicity can facilitate cell adhesion and proliferation[29,30]. In addition, the specific micro/nanostructures on a surface and their appropriate roughness can have an impact on the attachment, morphology, spreading, and even differentiation of cells[31,32]. Currently, various methods have been attempted to enhance the surface properties of PCL[26,33,34]. One such method involves mixing varying proportions of nanohydroxyapatite with PCL to improve the biocompatibility and surface morphology of the scaffold[35]. Additionally, chitosan and hyaluronic acid have been utilized to improve the biocompatibility and hydrophilicity of PCL[36]. Furthermore, the application of calcium phosphate coating on the surface of PCL scaffolds has been shown to enhance biological activity[37]. Despite the potential benefits, the current problems in surface modification of PCL scaffolds lie in the complex procedures and relatively high cost. Therefore, there is a need to develop a more convenient and efficient method for this process.

Alkaline hydrolysis has been reported as a simple and effective method for surface modification[38]. Sodium hydroxide (NaOH) treatment is capable of not only adding functional groups to polymer surfaces, but also inducing surface porosity through etching. This capability is not commonly found in other surface modification techniques[38]. Thus, the dual action of NaOH makes it a suitable option for modifying the surface of PCL. It is worth noting that previous studies have primarily focused on examining the impact of alkaline treatment on the physicochemical properties and cytocompatibility of PCL[39-41]. However, there is limited research on the effects of alkaline treatment on the differentiation of bone marrow mesenchymal stem cells (BMSCs). Based on the interactions between BMSCs and scaffolds, it is hypothesized that surface modification mediated by NaOH treatment could induce osteogenic differentiation of BMSCs.

To verify this hypothesis, the effects of NaOH treatment on physicochemical properties of PCL scaffolds were investigated, including surface morphology, surface roughness, and hydrophilicity. Moreover, *in vitro* experiments were performed to assess the impact of NaOH treatment-mediated surface modification on osteogenic differentiation and the mechanisms behind it. Finally, *in vivo* experimentations were conducted to assess bone regeneration of surface-modified PCL scaffolds (Scheme 1).

2. Materials and methods

2.1. Scaffold preparation

The PCL scaffold was prepared using a commercial MEW printing platform (BioPioneer-1, Shaanxi Bioprintissue Medical Technologies Co., Ltd.). In brief, PCL pellets were loaded into a metal cartridge and melted at 90°C to obtain a homogeneous fluid. The scaffolds were then printed using a 26G nozzle at a voltage of -7 kV and a printing speed of 40 mm/s. The air pressure was set at 10 MPa, and the distance between the collector and nozzle was 4 mm.

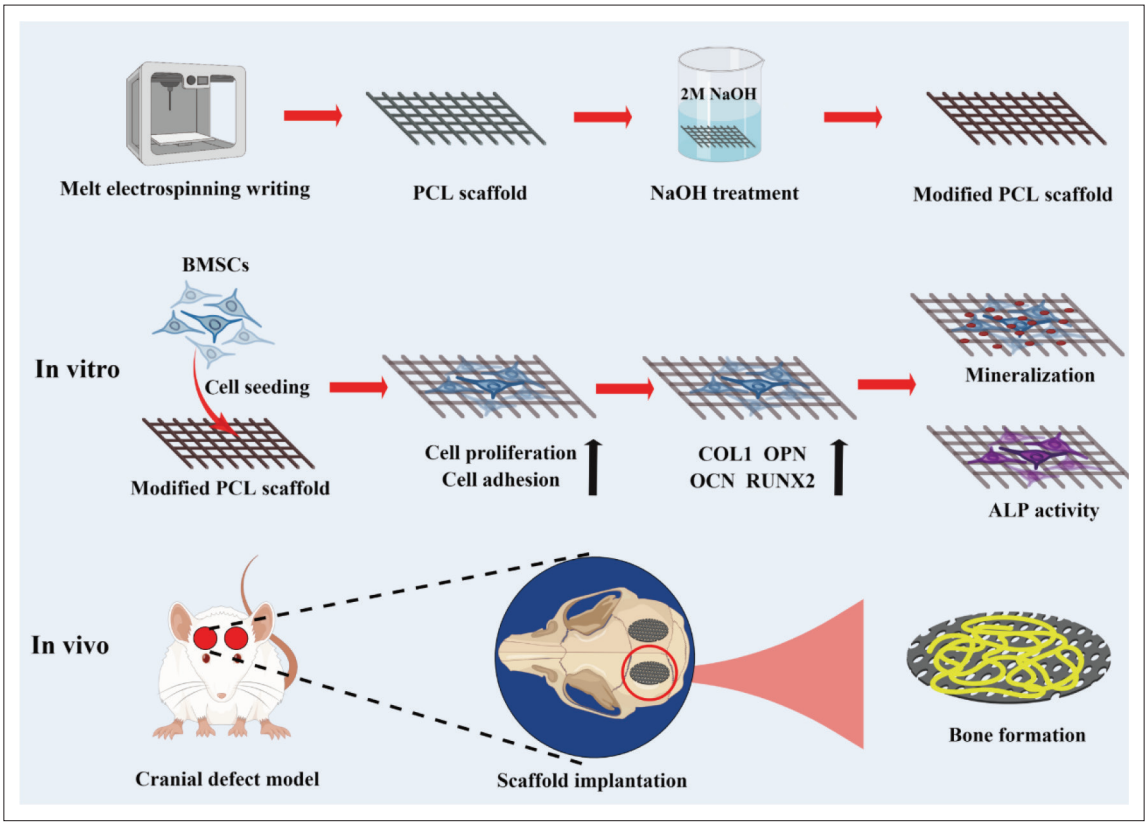

Scheme 1. Schematic diagram showing the osteogenic properties of surface-modified melt electrospinning writing (MEW) PCL scaffold. Abbreviations: ALP, alkaline phosphatase; BMSCs, bone marrow mesenchymal stem cells; NaOH, sodium hydroxide; PCL, polycaprolactone.

The entire process was carried out at a humidity level of 35% and an ambient temperature of 23°C. The printing parameters were determined using previous research as a guide[13,42].

2.2. NaOH treatment

NaOH was purchased from RHAWN company (Shanghai, China). The scaffolds were submerged in a 2 M NaOH solution within a 50 mL centrifuge tube and gently agitated on a laboratory shaker at 100 rpm for 1 h. The scaffolds were then rinsed with MilliQ water to neutralize the pH before being dried overnight in an oven set to 37°C.

2.3. Characterization of scaffold

2.3.1. Morphology

The morphology of scaffolds was detected by scanning electron microscopy (SEM, Thermo Fisher Scientific, USA). Briefly, the scaffolds were placed on the conductive glue and sprayed with a layer of gold. Electron dispersive X-ray diffraction (EDS) was used to evaluate the composition of elements of PCL scaffolds.

2.3.2. Surface roughness

Atomic force microscopy (AFM, Dimension Icon, Bruker, USA) technique was used to assess the surface roughness of scaffolds. To isolate the single fiber from scaffolds, it was then affixed to the tray using adhesive tape. The scanning area for all samples was consistent at 10 × 10 μm^2.

2.3.3. Surface wettability

Automatic contact angle system (JY-82B Kruss DSA) was used to evaluate surface wettability. To measure the water contact angle, a droplet of 5 µL distilled water was placed onto the scaffold, and its shape was subsequently photographed. Each sample was repeated three times.

2.3.4. Crystalline structures and chemical information

X-ray diffraction (XRD, BrukerAXS D8, USA) was used to analyze the crystalline structures of all scaffolds. XRD analysis was conducted with a 2θ range of 5–45° and speed rate of 2°/min. Fourier transform infrared (FTIR, Nicolet Is 10) analysis was performed to investigate chemical information. The sample collection was recorded from 600 to 4000 cm^{-1} a resolution of 4 cm^{-1}.

2.3.5 Mechanical properties

A uniaxial tensile test was conducted to assess the impact of NaOH treatment on the mechanical properties of PCL scaffold. The tensile Young's modulus and tensile strength were calculated between PCL and M-PCL groups.

2.4. Cell culture

Primary rat BMSCs were obtained from tibias and femurs of male Sprague-Dawley rats. BMSCs were culture in Modified Eagle Medium (MEM, Gibco, USA) supplemented with 10% fetal bovine serum (Biological industries, Australia). The cells were cultured at 37°C in a 5% CO_2 incubator. BMSCs of passages 3–6 were used for further experiments.

2.5. Cell proliferation, toxicity, and morphology

For cell experiments, the scaffolds were sterilized with 75% ethanol for 1 h and washed with phosphate-buffered saline (PBS) to remove residual ethanol. After that, BMSCs (2×10^5 cells) were seeded on the scaffolds in the 24-well plate. After 1, 4, and 7 days of culture, the cell proliferation was assessed with cell counting kit-8 (CCK-8, Beyotime, China). Briefly, 100 μL of CCK-8 solution was added to the cells and incubated for 30 min. The OD value at 540 nm was then detected using a microplate reader. Live/Dead staining kit was used for cytotoxicity analysis. In brief, the working solution was prepared with 2 μM calcein AM and 4.5 μM propidium iodide (PI) solution. After incubation for various time intervals, the cells on the scaffold were stained with a working solution for 15 min. Subsequently, the labeled cells were captured using immunofluorescence microscopy (Zeiss, Germany). Cell viability was calculated based on the ratio of the number of viable cells (green-stained cells) to the total number of cells (both green- and red-stained cells). For the quantification of results, three images per time point were analyzed using the ImageJ software for two groups. For morphology analysis, the BMSCs were fixed with glutaraldehyde and photographed by SEM.

2.6. Quantitative real-time PCR (qRT-PCR)

After being incubated at different time points, the BMSCs on the scaffold were digested by trypsin. Trizol reagent (Invitrogen, USA) was added into the 24-well plate to extract total RNA. The concentration of extracted RNA was detected using a microplate reader. The cDNA was synthesized by Reverse Transcription Kit (Takara, Dalian, China). The amplification process was conducted using the SYBR Taq Kit (Takara, Dalian, China). GAPDH was used as an internal reference. The primers are listed in **Table S1** (Supplementary File).

2.7. Immunofluorescence staining

After culturing on scaffolds for 7 and 14 days, the cells were fixed with 4% paraformaldehyde, permeabilized using Triton-X, and blocked with goat serum. Following this, the cells were incubated with primary antibodies (anti-OPN, 1:200, Proteintech; anti-OCN, 1:200, Proteintech; anti-RUNX2, 1:300, Proteintech) overnight at 4°C. Following the PBS wash, the cells were incubated with secondary antibodies for an hour at room temperature. The nuclei were then counterstained using DAPI, and the resulting images were captured using confocal microscopy (Nikon, Japan).

2.8. Western blotting

After being cultured on scaffolds for 14 days, the BMSCs were lysed using RIPA. The total proteins were then separated by gel electrophoresis, transferred to polyvinylidene fluoride membranes, and subsequently blocked with 5% milk. Following incubation with primary antibodies, the membranes were washed with TBST and treated with horseradish peroxidase-conjugated secondary antibodies. Finally, the membranes were photographed using Amersham Imager 600. Details of antibodies are listed in **Table S2** (Supplementary File).

2.9. Alizarin red S staining

After incubating for 14 and 21 days, the BMSCs on the scaffolds were washed with PBS and fixed with 4% paraformaldehyde for 20 min. Subsequently, the cells were stained with Alizarin red S staining solution (Beyotime, China) for 30 min at room temperature. Finally, the gross and optical images were photographed. For quantification analysis, the scaffolds were loaded into 5% sodium dodecyl sulfate (SDS) in 0.5 N HCl for 1 h at room temperature. The absorbance at 405 nm of this solution was measured using a microplate reader.

2.10. Alkaline phosphatase (ALP) staining and activity

The BCIP/NBT Alkaline Phosphatase Color Development Kit (Beyotime, China) was used for ALP staining. After being incubated for 7 and 14 days, the cells were fixed with 4% paraformaldehyde for 20 min and stained with working solution for 30 min. After that, the stain was washed with distilled water. In addition, Alkaline Phosphatase Assay Kit (Beyotime, China) was used for ALP activity analysis according to the manufacture's protocol. The absorbance at 405 nm was measured using a microplate reader.

2.11. Transcriptome sequencing

After being incubated for 14 days, the BMSCs on the scaffold were lysed using Trizol reagent (Invitrogen, USA) and the lysates were stored at -80°C for further experiments. Illumina NovaSeq 6000 was used to perform RNA sequencing. The criteria for screening differently expressed genes were $P < 0.05$ and $|\log2FoldChange| > 1$. Free online platform of Novogene was used to conduct Kyoto Encyclopedia of Genes and Genomes (KEGG) pathway enrichment analyses.

2.12. Animal experiments

The animal study was approved by Ethics Committees of The Fourth Military Medical University (IACUC-20220071). A

total of 36 male Sprague-Dawley rats (6-week-old, weighed 200 ± 10 g) were used in this study. To induce anesthesia, 1% pentobarbital (30 mg/kg) was administered to the rats. A midline sagittal incision was made to expose the skull, followed by the creation of a defect with 5 mm diameter on both sides of the parietal bones using a circular drill. Circular scaffolds measuring 1 mm in height and 5 mm in diameter were then inserted into the prepared defects. Finally, the incisions were closed, and the rats were allowed to recover in their cages. The Calcein-Alizarin red staining was performed to detect the newly formed bone.

2.12.1. Micro-computed tomography (micro-CT)

After 1 and 3 months of implantation, the rats were anesthetized and sacrificed. The samples were harvested and fixed with 4% paraformaldehyde. After that, the morphology analysis was detected using micro-CT. The bone volume to tissue volume (BV/TV), trabecular thickness (Tb.Th), and trabecular separation (Tb.Sp) were calculated to assess new bone formation.

2.12.2. Histological observation

The samples underwent decalcification with EDTA for a period of 6 weeks. Following this, they were dehydrated using 30% sucrose overnight. Ultimately, the samples were embedded in optimal cutting temperature (OCT) compound and sliced into 5-μm frozen sections. Mineralized bone formation was evaluated by hematoxylin and eosin (H&E) staining, Masson's trichrome staining, and immunochemical staining. For undecalcified bone, the samples were embedded in methylmethacrylate and sliced into 10-μm sections. After that, Alizarin Red S (red) and calcein (green) staining were photographed using confocal microscopy. Finally, the undecalcified slices were stained van Gieson's picrofuchsin.

2.13. Statistical analysis

All data were expressed as mean ± standard deviation. The comparison between the groups was performed by one-way ANOVA or *t*-test. A $P < 0.05$ was considered statistically significant.

3. Results

3.1. Physical properties of scaffolds

This study employed MEW to create 3D polymeric (PCL) scaffolds for bone regeneration. Previous studies have found that the alignment of fibers and pore size had significant impact on the differentiation of BMSCs. A scaffold with a 90° fiber architecture and a pore size of at least 300 μm has been found to be more effective for osteointegration[43,44]. However, it is important to note that increasing the pore size can lead to a decrease in the mechanical strength of the scaffold. To balance both osteointegration and mechanical strength, we chose a strand spacing of 300 μm for our scaffold. Therefore, we selected a scaffold geometry with a 90° fiber architecture and a pore size of 300 μm for our research. Besides, the geometry of the scaffolds used for both *in vitro* and *in vivo* experiments was the same in this study. The scaffolds exhibited a highly organized architecture composed of well-aligned fibers with an average strand spacing of 300 ± 25 μm and an average fiber diameter of 30 ± 0.6 μm, with a porosity of 91.3% (Figure 1A and B). In order to simplify the discussion, the pure PCL scaffolds and the PCL scaffolds treated with alkaline modification were respectively referred to as PCL and M-PCL scaffolds. The impact of alkaline treatment on the surface morphology of PCL was analyzed through SEM. Results showed that the surface of M-PCL scaffolds exhibited nanopits and nanogrooves, in contrast to the smooth surface of the PCL scaffolds. The average size of the nanopits was 200.87 ± 10.67 nm, while the lengths of the nanogrooves varied from a few hundred nanometers to microns (Figure 1C).

The study evaluated surface roughness and wettability using AFM and automatic water contact angle. The results showed that alkaline treatment resulted in a significant increase in the mean roughness average (Ra), which was confirmed through quantitative analysis (Figure 1D and E). Similarly, the surface wettability of PCL scaffolds was significantly enhanced through alkaline treatment, as evidenced by a decrease in water contact angles from 124 ± 0.5° for untreated PCL scaffolds to 43.45 ± 0.3° for M-PCL scaffolds (Figure 1F and G).

Crystalline structures and chemical information were analyzed using XRD, FTIR, and EDS techniques. The XRD results showed two characteristic peaks of PCL at 21.4° and 23.8°, respectively. The M-PCL exhibited a similar pattern (Figure 1H). The FTIR analysis of PCL showed peaks at 2946, 2865, and 1720 cm^{-1}, which correspond to asymmetric CH_2, symmetric CH_2, and C=O stretching. The presence of hydroxyl bonded to the end of PCL chain and hydrolysis of PCL after alkaline treatment was indicated by the observation of O-H stretching band at ≈ 1600 cm^{-1} in M-PCL (Figure 1I). Next, EDS was conducted to evaluate the elements on the scaffold. It was found that the surface of PCL and M-PCL was predominated by carbon (C) and oxygen (O) elements. However, the O/C ratio of PCL and M-PCL was 32.5% and 36.4%, respectively (Figure 1J and K). The rise in oxygen content following alkaline treatment suggests that M-PCL scaffolds have oxygen-containing functional groups, which is in line with the findings from the FTIR analysis.

Next, a uniaxial tensile test was conducted to assess the impact of NaOH treatment on the mechanical properties of PCL scaffold. The results revealed that both scaffolds

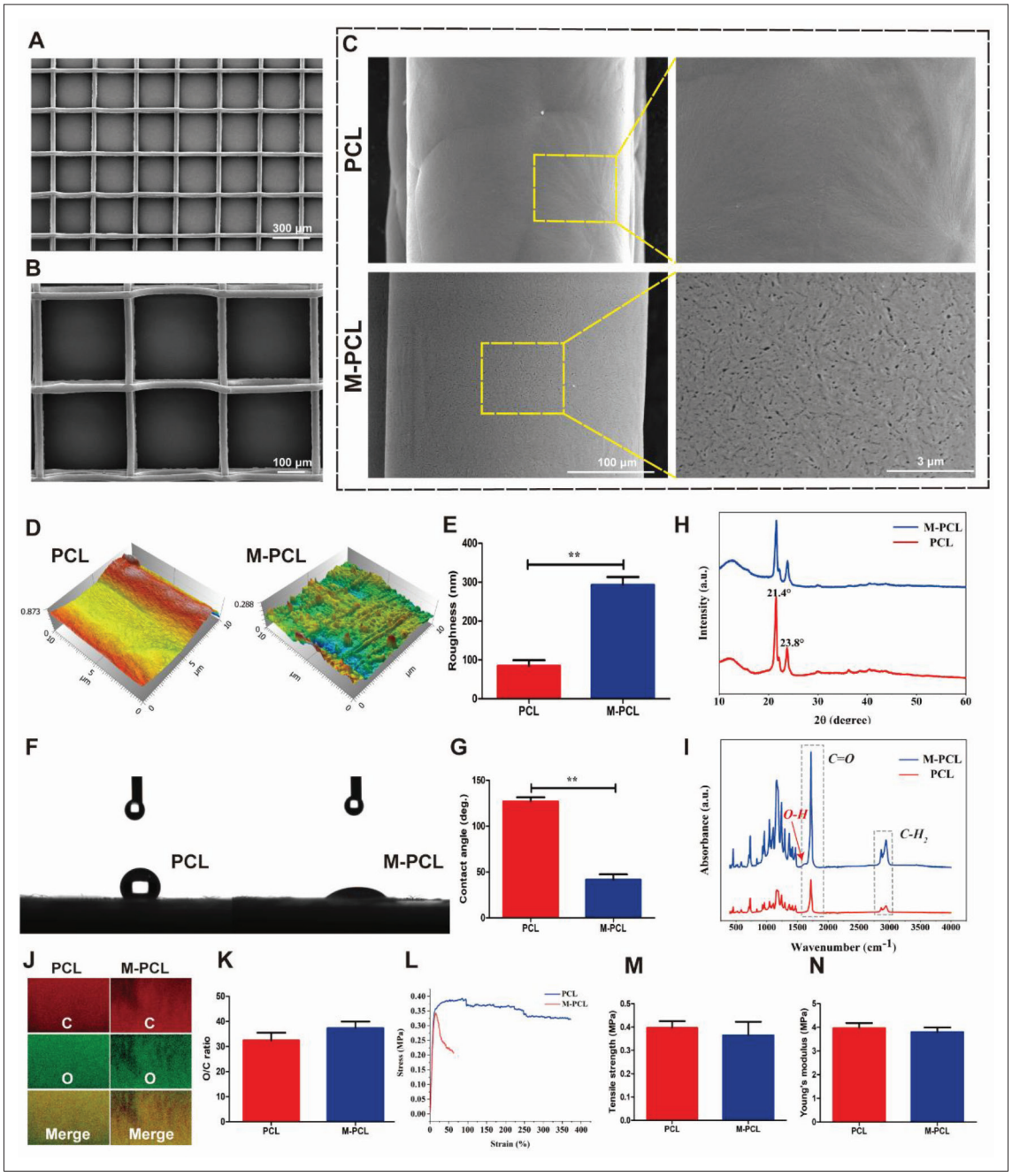

Figure 1. Characterizations of PCL scaffolds before and after alkaline treatment. (A, B) The morphology of PCL scaffolds at low and high magnification (SEM). (C) Surface morphology of PCL scaffolds before and after alkaline treatment. (D, E) AFM images of both scaffolds and quantification of surface roughness. (F, G) The water contact angles of both scaffolds and the quantitative results. (H) XRD spectrum of control and modified PCL scaffolds. (I) FTIR analysis of both scaffolds. (J, K) EDS elemental mapping for C and O, and the quantitative elemental analysis. (L) Stress–strain curves of two scaffolds. (M, N) Quantification of tensile strength and Young's modulus between two scaffolds. $^{*}P < 0.05$, $^{**}P < 0.01$.

displayed comparable fracture behavior. Initially, the scaffolds showed an elastic response, which was followed by significant plastic deformation before reaching failure (Figure 1L). Besides, the tensile strength and Young's modulus showed no significant difference between the PCL and M-PCL scaffolds (Figure 1M and N).

3.2. Effect of surface modification on cell compatibility

To assess the impact of alkaline treatment on cell compatibility, cell counting kit-8 (CCK-8) and live/dead assays were conducted to evaluate cell proliferation and viability. The findings indicate that the BMSCs grew

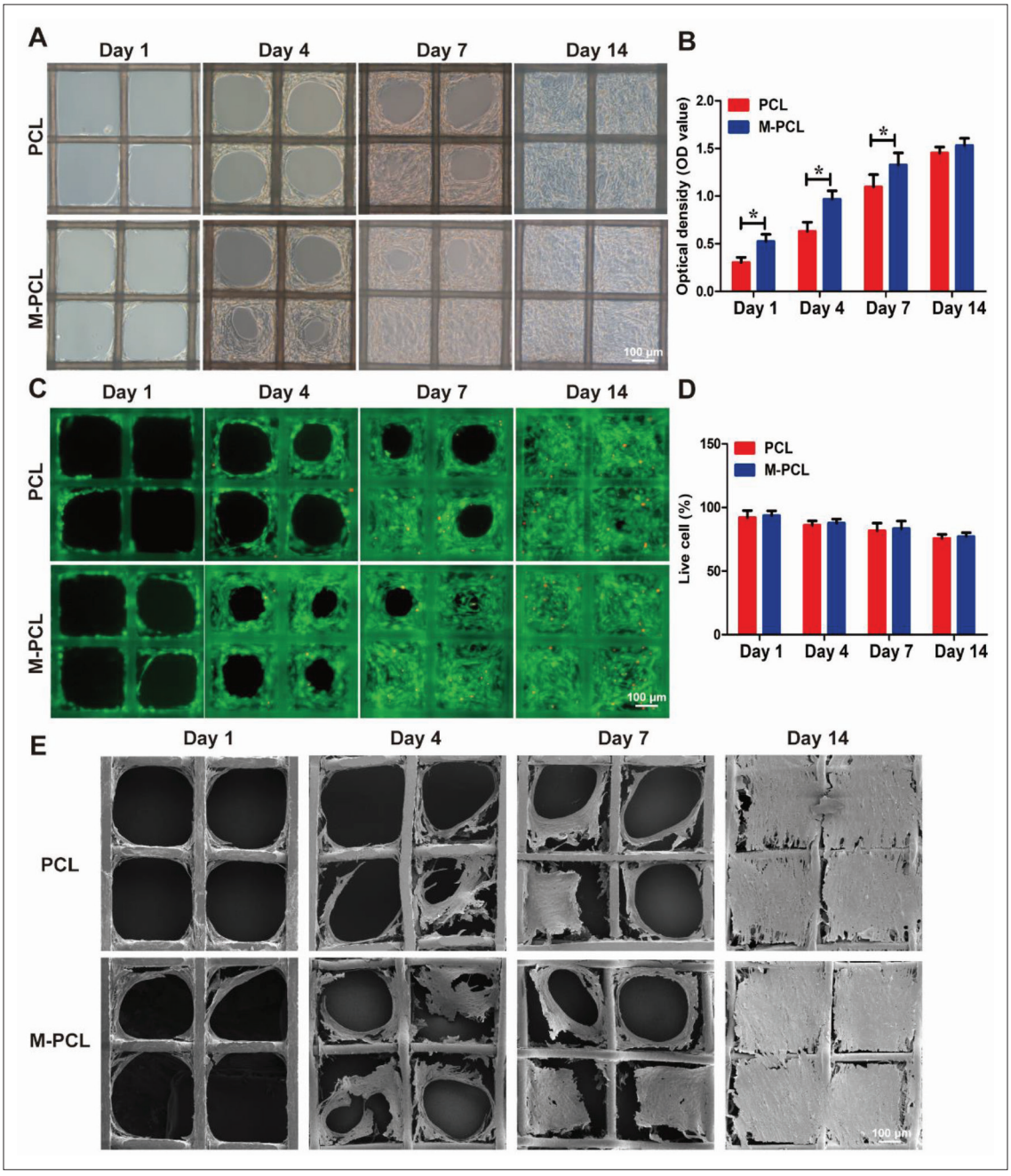

Figure 2. Biocompatibility of NaOH-treated PCL scaffolds. (A) Optical microscopy images of BMSCs on two different scaffolds. (B) Cell proliferation was assessed by CCK-8 assay. (C) The microscopy images of live/dead cells in two different groups. (D) Cell viability of BMSCs on two different scaffolds. (E) Representative SEM images of BMSCs at different times on PCL scaffolds. *$P < 0.05$, **$P < 0.01$.

from the peripheral sidewalls toward the center of the pore, eventually filling up all the pores in both groups (Figure 2A). According to the CCK-8 results, BMSCs exhibited a higher proliferation rate on the M-PCL scaffolds from day 1 to day 7. However, there was no significant difference in proliferation rate between the groups on day 14 (Figure 2B). The results of the live/dead test indicate that BMSCs on both scaffolds exhibited a high level of cell viability, approximately 90%, which then slightly decreased to 70%–80%. Furthermore, there was no significant difference in cell viability observed between the two groups (Figure 2C and D). Additionally, SEM images demonstrated that BMSCs initially adhered to the walls of the scaffolds and subsequently migrated toward the center, resulting in complete coverage of the scaffold (Figure 2E).

3.3. Effect of surface modification on cell morphology and adhesion

Cell morphology and adhesion were analyzed through double staining of vinculin (red) and F-actin (green). The cytoskeletons of BMSCs were observed to form a ring-shaped structure and interweave within the pores of all scaffolds (Figure 3A). In addition, the study found that BMSCs on M-PCL scaffolds produced a greater amount of vinculin compared to those on PCL scaffolds. This was confirmed through quantitative analysis of the average fluorescence intensity (Figure 3A and B). SEM results showed that BMSCs on M-PCL scaffolds displayed more and longer filopodial protrusions compared to relatively short and less filopodia on PCL scaffolds (Figure 3C).

3.4. Effect of surface modification on osteogenic differentiation

The study utilized qRT-PCR to detect the expression of osteogenesis-related genes such as collagen type 1 (*Col1*), osteocalcin (*Ocn*), osteopontin (*Opn*), and runt-related transcription factor 2 (*Runx2*). Results showed that, except for the *Col1* gene, the expressions of the other three genes were significantly higher in BMSCs cultured on M-PCL scaffolds than in BMSCs on PCL scaffolds after 7 days (Figure 4A), whereas the expression levels of all four genes were significantly higher at 14 days in M-PCL scaffolds compared to PCL scaffolds (Figure 4B). Immunofluorescence staining was used to measure the protein expression of OCN, OPN, and RUNX2. The results of the staining were consistent with those obtained from qRT-PCR. Specifically, the expressions of OCN, OPN, and RUNX2 proteins were observed to increase on PCL scaffolds following alkaline treatment (Figure 4C).

3.5 Effect of surface modification on mineralization and ALP activity

The study measured mineralization and ALP activity using ARD and ALP staining. BMSCs were cultured in basic medium without osteoinductive factors to determine the osteogenic capacity of the scaffolds. The depth of ARD staining was higher in M-PCL scaffolds compared to PCL scaffolds on days 14 and 21. Furthermore, there was more and larger calcium ion deposition and mineralization in the M-PCL scaffolds compared to PCL scaffolds (Figure 5A). These findings were also confirmed by quantitative analysis (Figure 5C). Similarly, the study found that M-PCL scaffolds had a higher level of ALP activity compared to PCL scaffolds after 7 and 14 days of culture (Figure 5B). Meanwhile, additionally, quantitative analysis of ALP staining confirmed that alkaline treatment of PCL scaffolds resulted in increased ALP activity (Figure 5D).

3.6. Surface modification mediated osteogenesis via integrinα2/β1-PI3K-AKT signaling pathway

Transcriptomics analysis identified 2116 differentially expressed genes (DEGs), with 1413 upregulated and 713 downregulated DEGs (Figure 6A and B). The underlying mechanisms were then analyzed using KEGG analyses, which revealed the top 20 KEGG pathways (Figure 6C). Previous studies have shown that the use of hierarchical microgroove/nanopore topography on titanium implants can improve osseointegration through the activation of the PI3K-AKT signaling pathway[45]. Therefore, it was chosen for subsequent study. Further analysis demonstrated a significant upregulation of gene expression in the PI3K-Akt signaling pathway in the M-PCL group compared to the PCL group (Figure 6D). Western blotting confirmed the activation of the PI3K-Akt signaling pathway (Figure 6E). These findings suggest that the NaOH-modified surface can enhance osteogenic differentiation through the integrinα2/β1-PI3K-Akt signaling pathway (Figure 6F).

3.7. Effect of surface modification on bone formation *in vivo*

In order to evaluate the effect of surface modification on bone formation of critical-sized bone defects, the rat cranial defect model was utilized. After 1 and 3 months of implantation, micro-CT 3D reconstruction was performed to assess new bone regeneration on scaffolds. The resulting micro-CT 3D images showed that there was a higher amount of newly formed bone on the M-PCL scaffolds than on the PCL scaffold at both 1 and 3 months (Figure 7A; **Figure S1** in Supplementary File). The results were further confirmed through quantitative analysis. It was observed that M-PCL scaffolds had a higher BV/TV value in comparison to PCL scaffolds (Figure 7B). Additionally, the new bone formed on M-PCL scaffolds exhibited improved trabecular structural features, which was confirmed by the quantitative analysis of Tb.Th and Tb.Sp (Figure 7C and D). To measure new bone formation, fluorescent double labeling of calcein (green) and Alizarin Red (red) was performed. The M-PCL scaffold showed a bigger distance between the two fluorescent signals (Figure 7E). Further quantitative analysis revealed that the mineral apposition rate (MAR) of M-PCL scaffolds was higher than that of PCL scaffolds (Figure 7F).

After a duration of 1 month, the control group showed thin fibrous tissue at the defect site. However, there was a stable integration between M-PCL scaffolds and host bone at the edge of the bone defect. Only a few scattered bone formations were noted in PCL scaffolds. After a period of 3 months, a higher amount of bone formation was observed in M-PCL scaffolds, resulting in a bony bridge at the defect

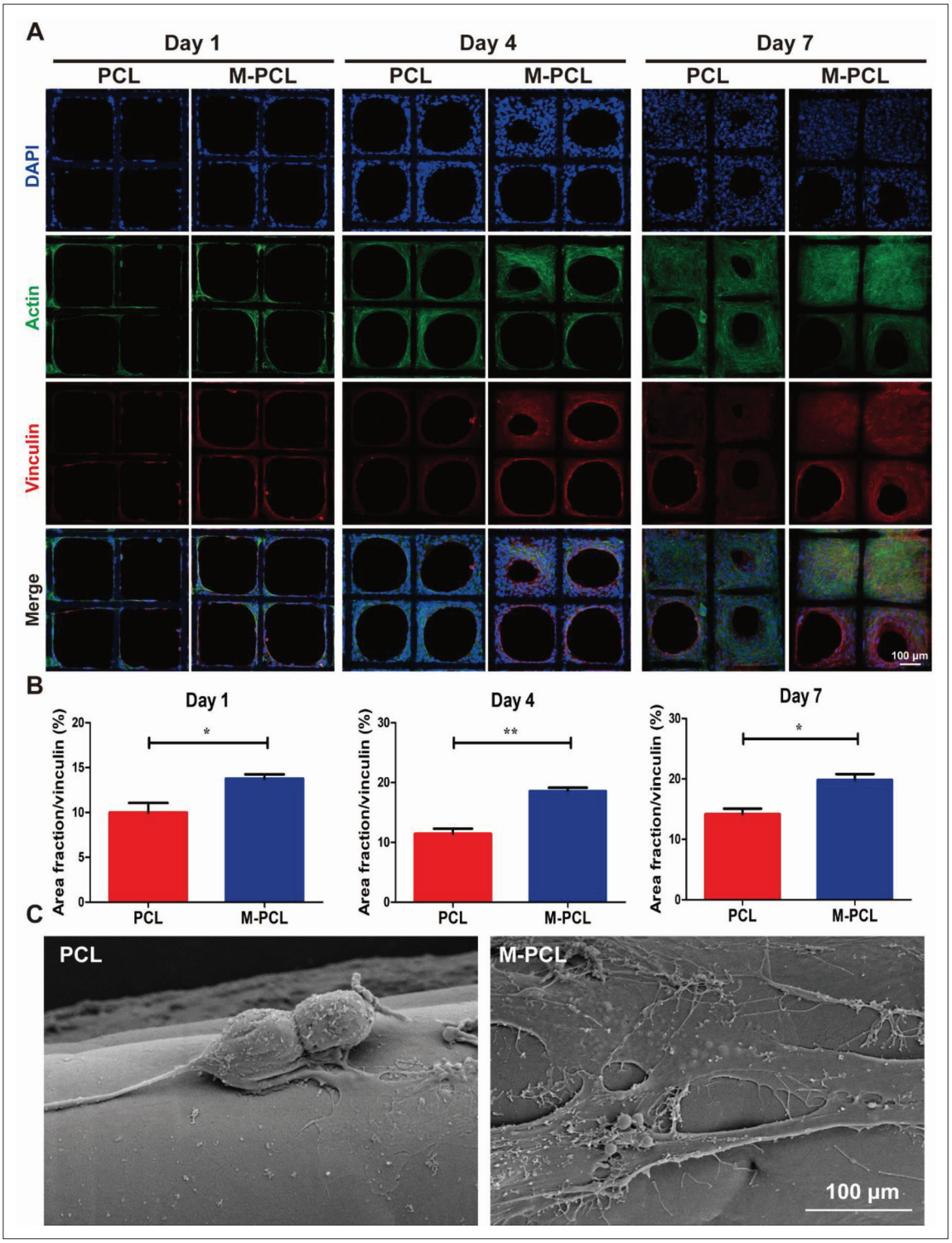

Figure 3. Effect of surface modification on cell morphology and adhesion. (A) Confocal microscopy images of actin (green) and vinculin (red) of BMSCs on different scaffolds. (B) Quantitative analysis of average fluorescence intensity of vinculin. (C) Representative SEM images of filopodial protrusions on different scaffolds.

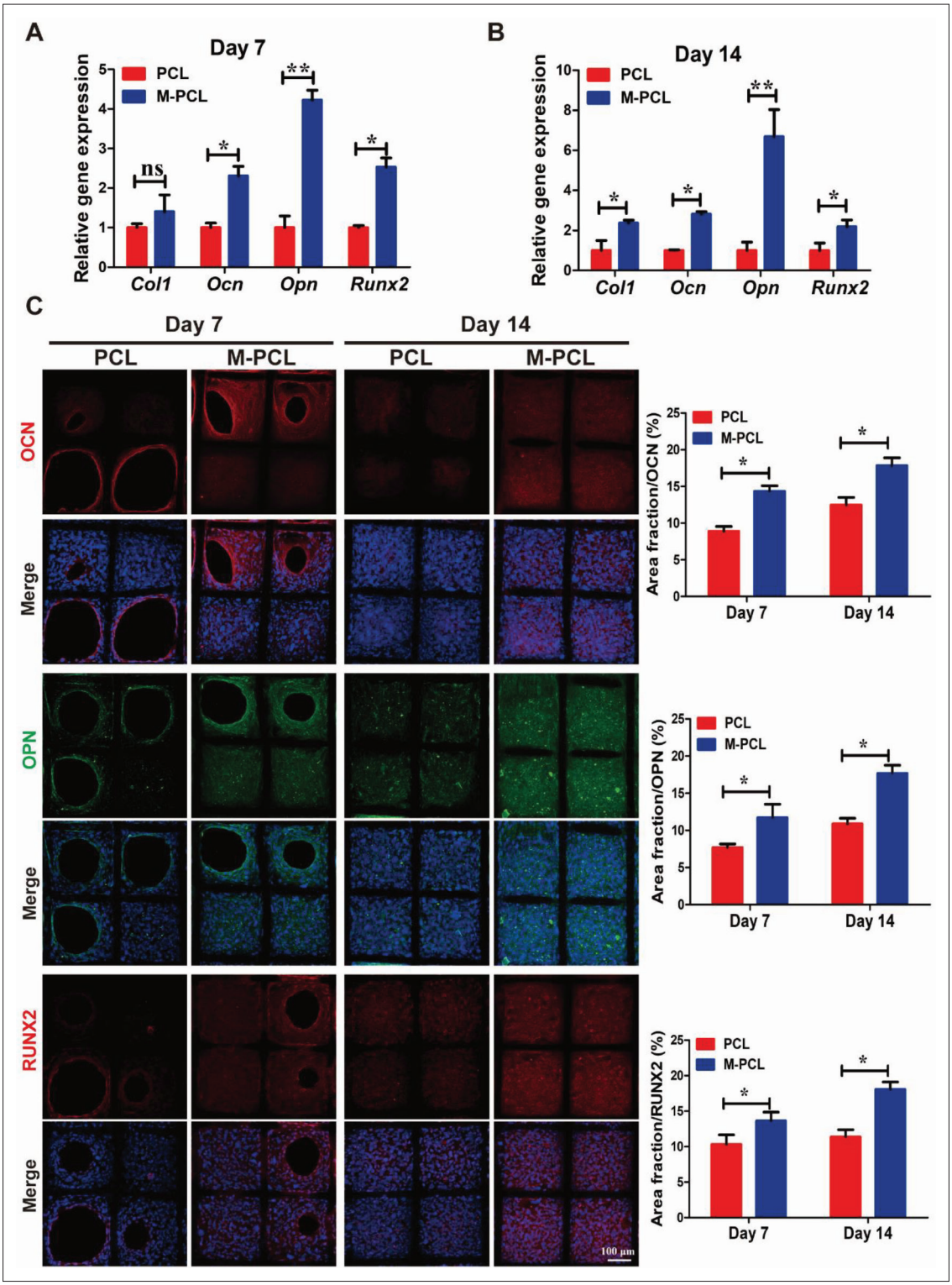

Figure 4. Effect of surface modification on osteogenic differentiation *in vitro*. (A, B) The gene expression of *Col1*, *Ocn*, *Opn*, and *Runx2* was examined using qRT-PCR after culture for 7 and 14 days. (C) The protein expressions of OCN, OPN, and RUNX2 were measured by immunofluorescence staining. $^{*}P < 0.05$, $^{**}P < 0.01$.

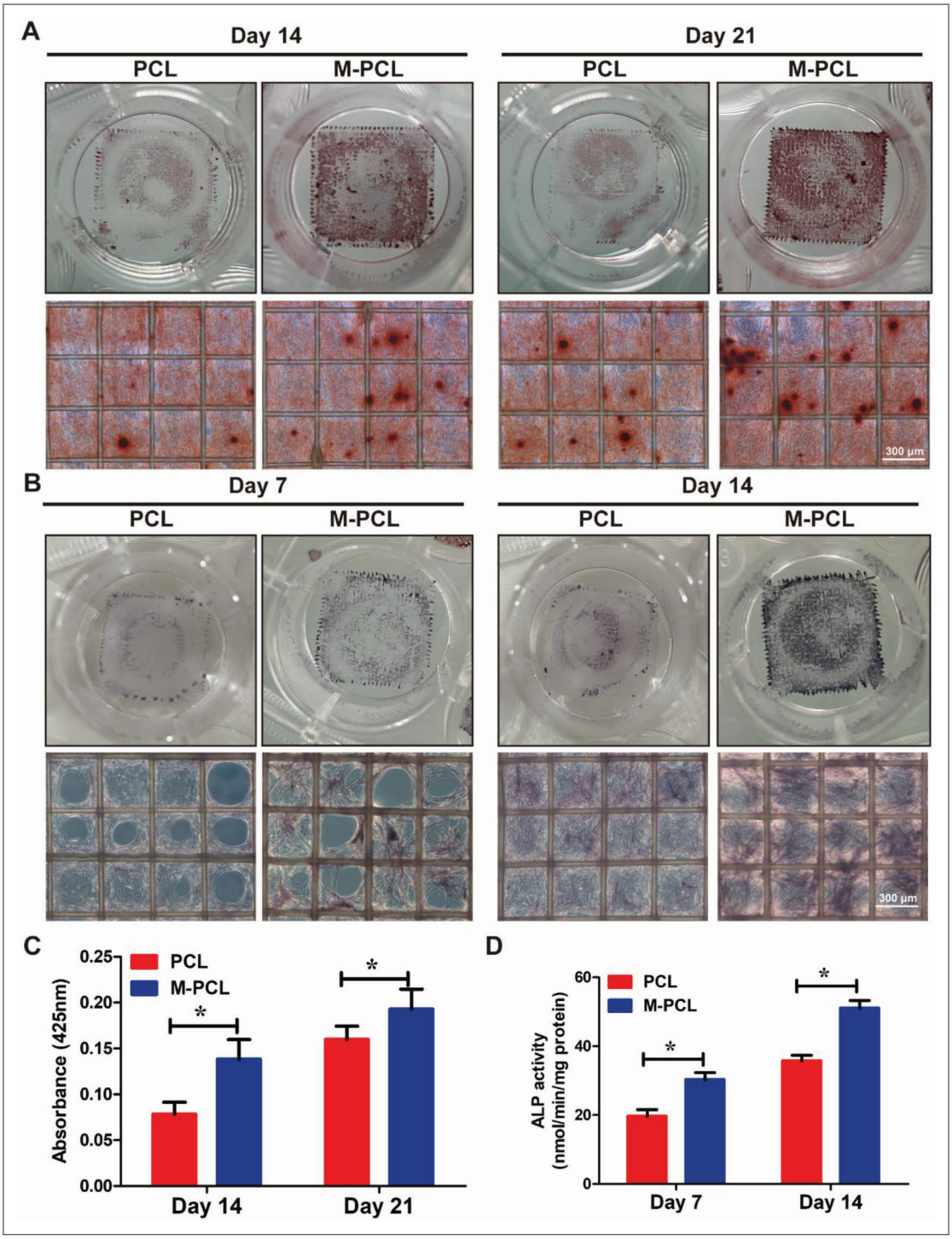

Figure 5. Effect of surface modification on mineralization and ALP activity. (A) Optical and microscopy images of ARD staining on PCL scaffold at 14 and 21 days. (B) Optical and microscopy images of ALP staining on PCL scaffold at 7 and 14 days. (C) Quantitative analysis of calcium ion deposition. (D) Quantitative analysis of ALP activity. *$P < 0.05$, **$P < 0.01$.

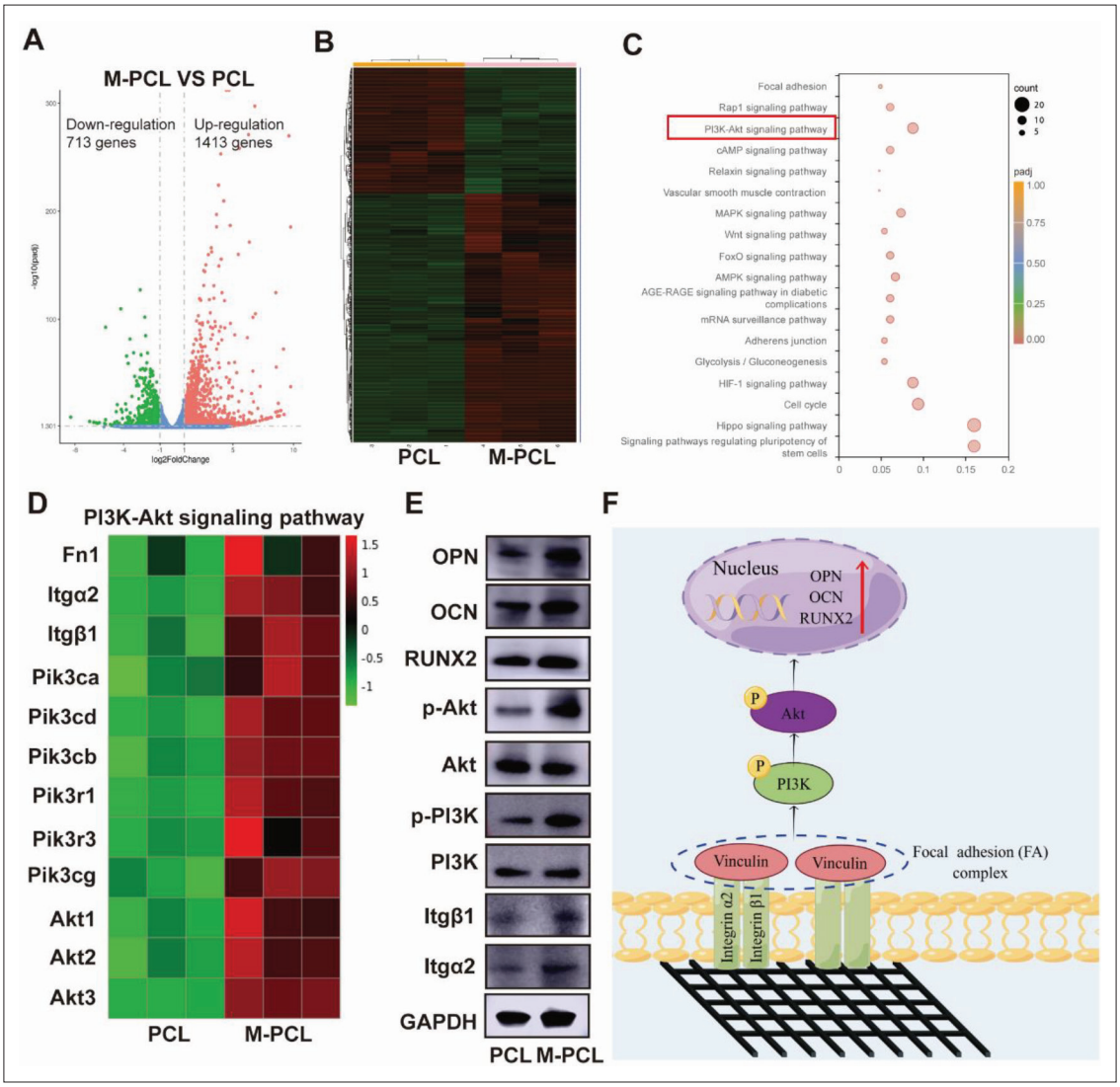

Figure 6. Surface modification mediated osteogenesis via integrinα2/β1-PI3K-AKT signaling pathway. (A) The scatter diagram of DEGs. (B) The heatmap of DEGs. (C) The top 20 KEGG signaling pathways. (D) The expression of genes in PI3K-Akt signaling pathway. (E) The expression of proteins in PI3K-Akt signaling pathway was detected by Western blotting. (F) Modified surface could facilitate osteogenic differentiation via integrinα2/β1-PI3K-Akt signaling pathway.

sites (Figure 7G). Furthermore, the presence of lamellar bone in M-PCL scaffolds was confirmed through Masson's trichrome staining (Figure 7H). Interestingly, van Gieson staining revealed an increased number of bone calluses in M-PCL scaffolds, which is consistent with the findings of H&E and Masson's trichrome staining (**Figure S2** in Supplementary File).

Immunohistochemical staining was utilized to quantify the levels of OPN, OCN, and RUNX2 protein. After a duration of 1 month, the results indicated that the levels of these three proteins were higher in M-PCL scaffolds compared to PCL scaffolds (Figure 8A, C, and E). As time went by, protein expression of OPN, OCN, and RUNX2 decreased in both scaffolds at 3 months. Besides, the difference in protein expression between PCL and M-PCL scaffolds was less pronounced at this point (Figure 8A–F).

4. Discussion

This study aimed to explore the impact of surface modification through alkaline treatment on the osteoinductive properties of MEW PCL scaffolds. PCL has been extensively utilized for creating biocompatible scaffolds for tissue engineering, particularly for bone tissue engineering scaffolds[46]. The limitations of PCL in tissue engineering arise from its surface hydrophobicity and inertness, which are not conducive to cell proliferation and

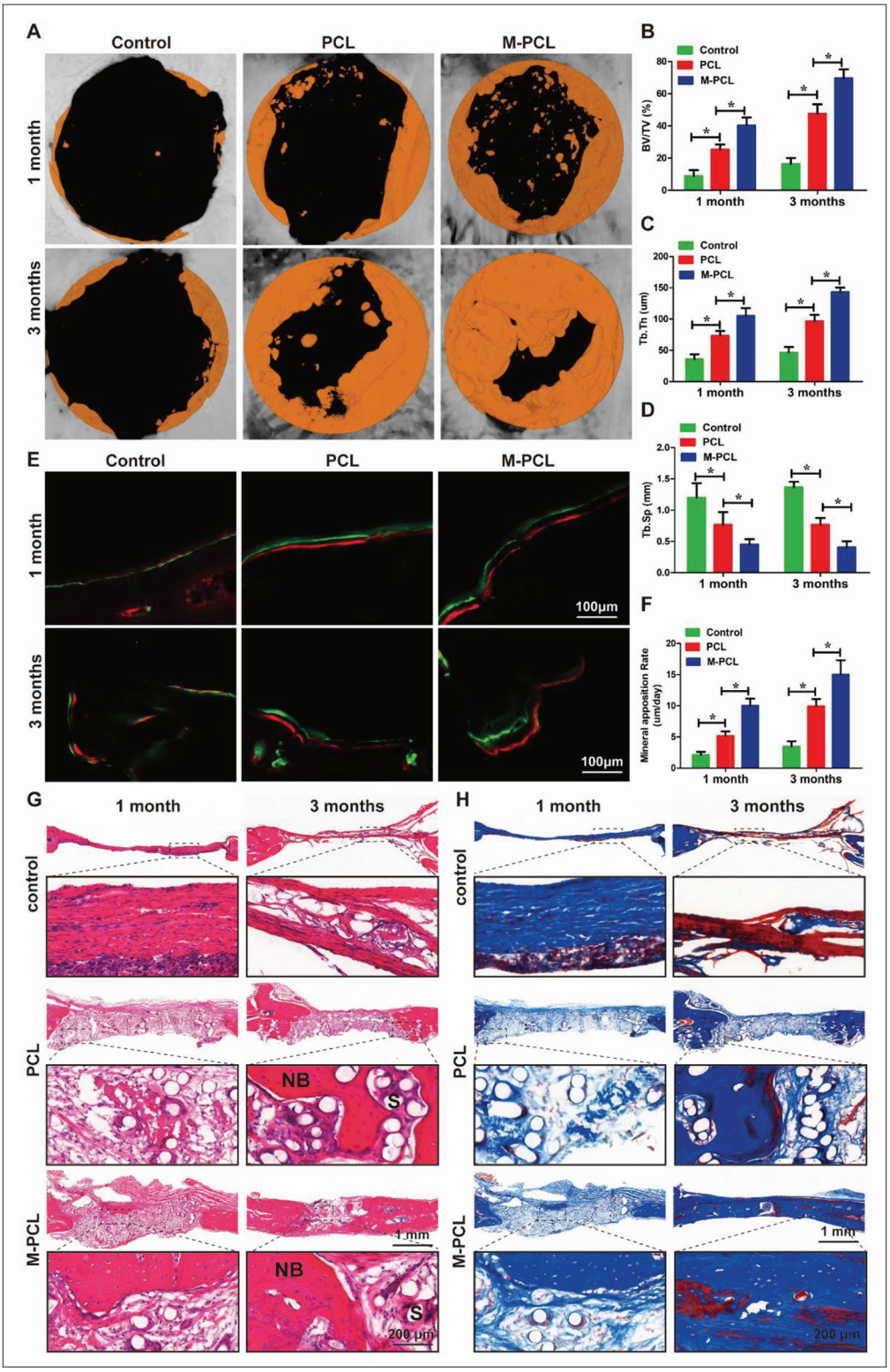

Figure 7. Micro-CT analysis, sequential fluorescent labeling, and histological analysis of new bone formation. (A) Micro-CT 3D images of PCL scaffolds. (B) Quantitative analysis of BV/TV value after implantation for 1 and 3 months. (C, D) Quantitative analysis of bone formation according to Tb.Th and Tb.Sp. (E) The newly formed bone was stained using calcein-Alizarin Red. (F) Quantitative analysis of mineral apposition rate. (G) H&E staining of the decalcified sections. (H) Masson's trichrome staining of the decalcified sections. $^{*}P < 0.05$, $^{**}P < 0.01$.

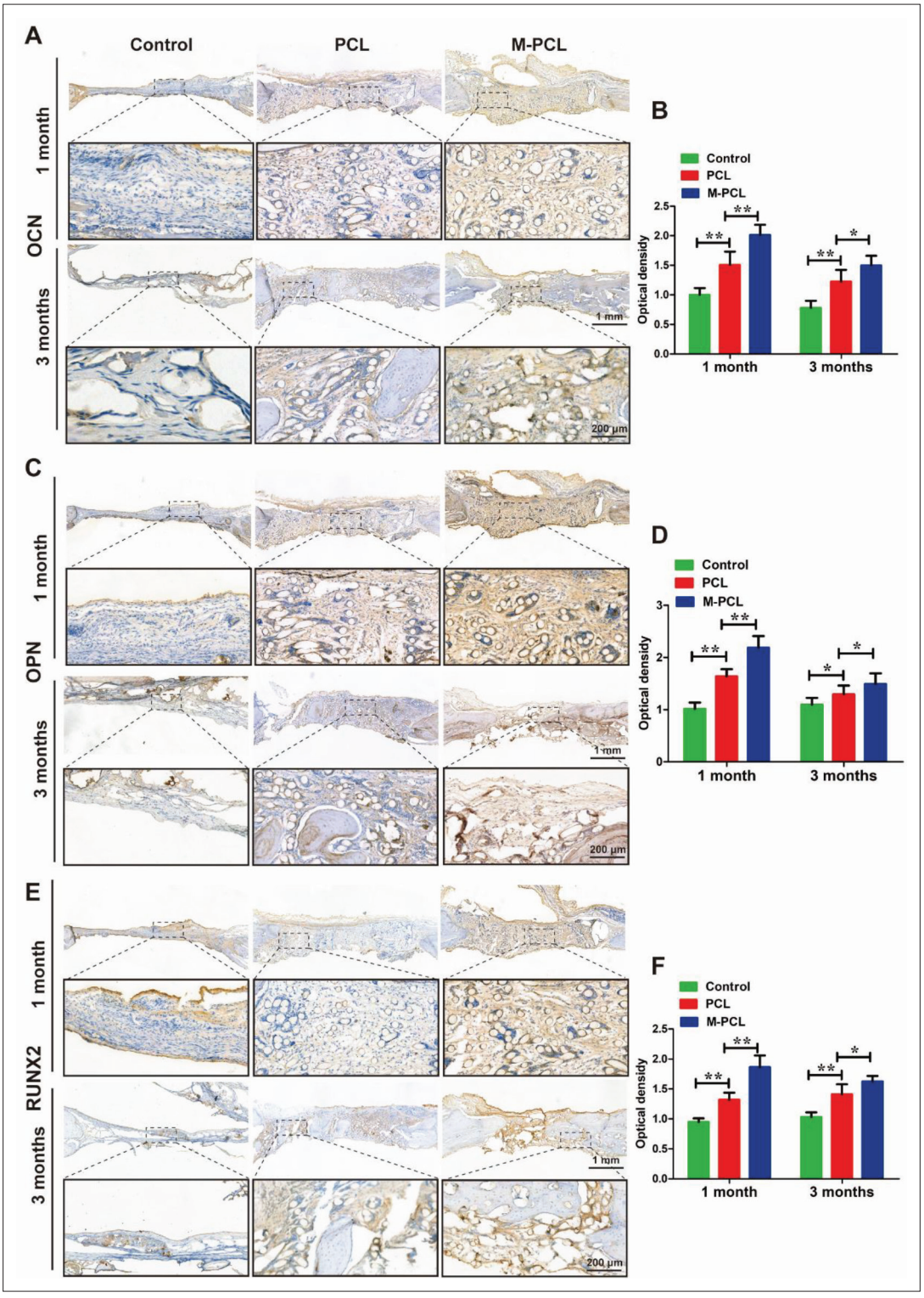

Figure 8. The protein expression of OCN, OPN, and RUNX2 in defect area. (A, B) The protein expressions of OCN and semi-quantification at 1 and 3 months after implantation. (C, D) The protein expression of OPN and semi-quantification at 1 and 3 months after implantation. (E, F) The protein expression of RUNX2 and semi-quantification at 1 and 3 months after implantation.

growth[22,26]. In order to improve the interaction between scaffolds and tissues, several methods have been employed to enhance the surface properties of PCL. These methods include covalent grafting, plasma treatment, and surface coating[33,34,38]. Of these, alkaline treatment stands out as a simple and effective way to modify both the physical and biological properties of scaffolds.

Compared to bulk hydrolysis, NaOH treatment is a surface hydrolysis method with a slower rate of NaOH diffusion into the polymer matrix, resulting in a higher surface hydrolysis rate[41]. It has been reported that the bulk properties of the scaffolds remained unchanged despite the hydrolysis treatment[13,38]. The present study utilized XRD, FTIR, and EDS to investigate the crystalline structures and chemical information of scaffolds, with a focus on the effects of surface hydrolysis. The results of FTIR analysis showed that hydroxyl groups bound to the PCL chain following NaOH treatment. However, XRD analysis indicated that the pattern of M-PCL was similar to that of PCL, suggesting that the crystallinity of both scaffolds remained similar after NaOH treatment. These findings confirm that NaOH treatment did not alter the bulk chain of PCL and was an effective surface modification strategy.

According to reports, the application of alkaline treatment has an impact on certain physical properties of PCL such as surface wettability, roughness, and morphology[38,40]. The surface of PCL undergoes a breakage of ester bonds when treated with NaOH, leading to the formation of functional hydroxyl and carboxyl groups. This process ultimately enhances the hydrophilicity of PCL[47]. The AFM analysis results indicated that the surface roughness of PCL scaffolds increased after NaOH treatment, which could be attributed to the alteration in surface morphology. SEM images revealed that the surface of M-PCL scaffolds exhibited a rough microstructure due to the presence of nanopits and nanogrooves, whereas the surface of PCL scaffolds appeared smooth.

In addition to physical properties, the biological properties of PCL can also be affected by alkaline treatment-mediated surface modification. As a result, we conducted further investigation to determine the impact of surface modification on cell proliferation, viability, and adhesion. It is widely recognized that the low surface hydrophilicity of PCL hinders cell proliferation[41]. The surface hydrophilicity of PCL scaffolds was increased after NaOH treatment, leading to a higher proliferation rate of BMSCs on M-PCL scaffolds from days 1 through 7. However, there was no significant difference in the proliferation rate between the two groups on day 14. This may be due to the fact that the pores of both scaffolds were filled with cells, leaving no additional space for further cell proliferation. Besides, the results of the live/dead test suggest that surface modification did not have a negative impact on cell viability, as there was no significant difference in cell viability between the two groups. Vinculin, a protein found in focal adhesions (FA), is closely linked to a cell's adhesive capacity[48]. The current study demonstrated that BMSCs grown on M-PCL scaffolds produce more vinculin and filopodial protrusions compared to those grown on PCL scaffolds. This may be attributed to the presence of nanopits and nanogrooves on the M-PCL scaffolds, which offer more anchoring points for cells.

Finally, we investigated the impact of surface modification on the osteoinductive properties of PCL scaffolds. Our findings revealed that M-PCL scaffolds could enhance the expression of osteogenesis-related genes, mineralization, and ALP activity *in vitro*, as well as promote bone formation *in vivo*. Previous research has only focused on evaluating the effects of alkaline treatment on the physicochemical properties and cytocompatibility of PCL. This study is the first to explore the underlying mechanism behind the osteoinductive effects of NaOH-treated PCL scaffolds. Previous studies have found that 3D-printed titanium scaffolds with a surface roughness of approximately 110–1300 nm can promote osteogenic differentiation of BMSCs[49-51]. According to reports, filopodial protrusions have the ability to initiate integrin clustering and recruit focal adhesion (FA) proteins. This process transforms mechanical signals into chemical signals, ultimately leading to stem cell differentiation[45]. In this study, the surface roughness of M-PCL was found to be approximately 300 nm, which falls within the desired size range. Furthermore, BMSCs on M-PCL scaffolds exhibited a greater number of filopodial protrusions that were longer in length. Based on these results, it can be inferred that the surface-modified PCL scaffolds possess an optimal surface roughness that facilitates filopodia anchoring and subsequently influences downstream signaling pathways to promote osteogenic differentiation. However, the mechanisms behind the osteogenic properties of surface-modified PCL scaffolds were unclear. To investigate this, transcriptome analysis was performed. The results showed that the alkaline treatment-modified surface facilitated osteogenic differentiation through the integrinα2/β1-PI3K-Akt signaling pathway. Altogether, the results suggest that alkaline treatment is a straightforward and efficient technique to improve the osteogenic properties of MEW PCL scaffolds.

5. Conclusion

This study introduces a simple and effective NaOH treatment method to improve the bioactivity of the MEW PCL scaffold. The treatment increases the surface wettability and

roughness of PCL scaffolds, making them favorable for cell proliferation and adhesion. Additionally, osteoinductive properties were enhanced *in vitro* and *in vivo*, likely due to modified surface-mediated enhancement of osteogenic differentiation via the integrinα2/β1-PI3K-Akt signaling pathway. These findings suggest that NaOH treatment is a cost-efficient and effective strategy for surface modification of PCL scaffolds in bone tissue regeneration.

Acknowledgments

We acknowledge Mrs. Xiaoli Qu for helping the team use immunofluorescence microscopy (State Key Laboratory for Manufacturing Systems Engineering, Xi'an Jiaotong University). The Figdraw was acknowledged for producing Scheme 1 and Figure 6F.

Funding

This work was supported by National Natural Science Foundation of China (No. 31971272) and International Science and Technology Cooperation Keg Program project of Shaanxi Province (No. 2023-GHZD-25).

Conflict of interest

The authors declare no conflicts of interests.

Author contributions

Conceptualization: Hongbin Fan
Formal analysis: Jingyi Dang, Zhao Zhang
Methodology: Yubo Shi, Lei Wang
Resources: Jiankang He, Zhennan Qiu, Xiaoli, Qu
Writing – original draft: Yubo Shi, Liguo Sun
Writing – review & editing: Yubo Shi, Hongbin Fan

Ethics approval and consent to participate

The animal study was approved by Ethics Committees of The Fourth Military Medical University (IACUC-20220071).

Consent for publication

Not applicable.

Availability of data

The request for raw data can be directed to the corresponding author.

References

1. Maruyama T, Stevens R, Boka A, *et al.*, 2021, BMPR1A maintains skeletal stem cell properties in craniofacial development and craniosynostosis. *Sci Transl Med*, 13(583): eabb4416.

   https://doi.org/10.1126/scitranslmed.abb4416

2. Stahl A, Yang YP, 2021, Regenerative approaches for the treatment of large bone defects. *Tissue Eng Part B Rev*, 27(6): 539–547.

   https://doi.org/10.1089/ten.TEB.2020.0281

3. Dimitriou R, Jones E, Mcgonagle D, *et al.*, 2011, Bone regeneration: Current concepts and future directions. *BMC Med*, 9: 66.

   https://doi.org/10.1186/1741-7015-9-66.

4. Azi ML, Aprato A, Santi I, *et al.*, 2016, Autologous bone graft in the treatment of post-traumatic bone defects: A systematic review and meta-analysis. *BMC Musculoskelet Disord*, 17(1): 465.

   https://doi.org/10.1186/s12891-016-1312-4

5. Charbe NB, Tambuwala M, Palakurthi SS, *et al.*, 2023, Biomedical applications of three-dimensional bioprinted craniofacial tissue engineering. *Bioeng Transl Med*, 8(1): e10333.

   https://doi.org/10.1002/btm2.10333

6. Shi Y, Yu L, Gong C, *et al.*, 2021, A bioactive magnesium phosphate cement incorporating chondroitin sulfate for bone regeneration. *Biomed Mater*, 16(3).

   https://doi.org/10.1088/1748-605X/abf5c4

7. Roseti L, Parisi V, Petretta M, *et al.*, 2017 Scaffolds for bone tissue engineering: State of the art and new perspectives. *Mater Sci Eng C Mater Biol Appl*, 78: 1246–1262.

   https://doi.org/10.1016/j.msec.2017.05.017

8. Wunner FM, Wille ML, Noonan TG, *et al.*, 2018, Melt electrospinning writing of highly ordered large volume scaffold architectures. *Adv Mater*, 30(20): e1706570.

   https://doi.org/10.1002/adma.201706570

9. Kade JC, Dalton PD, 2021, Polymers for melt electrowriting. *Adv Healthc Mater*, 10(1): e2001232.

   https://doi.org/10.1002/adhm.202001232

10. Chen Z, Liu Y, Huang J, *et al.*, 2022, Influences of process parameters of near-field direct-writing melt electrospinning on performances of polycaprolactone/nano-hydroxyapatite scaffolds. *Polymers (Basel)*, 14(16): 3404.

    https://doi.org/10.3390/polym14163404

11. He J, Zhang B, Li Z, *et al.*, 2020, High-resolution electrohydrodynamic bioprinting: A new biofabrication strategy for biomimetic micro/nanoscale architectures and living tissue constructs. *Biofabrication*, 12(4): 042002.

    https://doi.org/10.1088/1758-5090/aba1fa

12. Mirzaei M, Dodi G, Gardikiotis I, *et al.*, 2023, 3D high-precision melt electro written polycaprolactone modified with yeast derived peptides for wound healing. *Biomater Adv*, 149: 213361.

    https://doi.org/10.1016/j.bioadv.2023.213361

13. Daghrery A, Ferreira JA, De Souza Araújo IJ, *et al.*, 2021, A highly ordered, nanostructured fluorinated CaP-coated melt electrowritten scaffold for periodontal tissue regeneration. *Adv Healthc Mater*, 10(21): e2101152.

    https://doi.org/10.1002/adhm.202101152

14. Santschi MXT, Huber S, Bujalka J, *et al.*, 2022, Mechanical and biological evaluation of melt-electrowritten polycaprolactone scaffolds for acetabular labrum restoration. *Cells*, 11(21): 3450.

    https://doi.org/10.3390/cells11213450

15. Eichholz KF, Freeman FE, Pitacco P, *et al.*, 2022, Scaffold microarchitecture regulates angiogenesis and the regeneration of large bone defects. *Biofabrication*, 14(4).

    https://doi.org/10.1088/1758-5090/ac88a1

16. Steele JaM, Moore AC, St-Pierre JP, *et al.*, 2022, In vitro and in vivo investigation of a zonal microstructured scaffold for osteochondral defect repair. *Biomaterials*, 286: 121548.

    https://doi.org/10.1016/j.biomaterials.2022.121548

17. Abbasi N, Lee RSB, Ivanovski S, *et al.*, 2020, In vivo bone regeneration assessment of offset and gradient melt electrowritten (MEW) PCL scaffolds. *Biomater Res*, 24: 17.

    https://doi.org/10.1186/s40824-020-00196-1

18. Daghrery A, De Souza Araújo IJ, Castilho M, *et al.*, 2023, Unveiling the potential of melt electrowriting in regenerative dental medicine. *Acta Biomater*, 156: 88–109.

    https://doi.org/10.1016/j.actbio.2022.01.010

19. Jing L, Wang X, Leng B, *et al.*, 2021, Engineered nanotopography on the microfibers of 3D-printed PCL scaffolds to modulate cellular responses and establish an in vitro tumor model. *ACS Appl Bio Mater*, 4(2): 1381–1394.

    https://doi.org/10.1021/acsabm.0c01243

20. Meng J, Boschetto F, Yagi S, *et al.*, 2022, Enhancing the bioactivity of melt electrowritten PLLA scaffold by convenient, green, and effective hydrophilic surface modification. *Mater Sci Eng C Mater Biol Appl*, 135: 112686.

    https://doi.org/10.1016/j.msec.2022.112686

21. Rasperini G, Pilipchuk SP, Flanagan CL, *et al.*, 2015, 3D-printed bioresorbable scaffold for periodontal repair. *J Dent Res*, 94: 153s–157s.

    https://doi.org/10.1177/0022034515588303

22. Wong HM, Wu S, Chu PK, *et al.*, 2013, Low-modulus Mg/PCL hybrid bone substitute for osteoporotic fracture fixation. *Biomaterials*, 34(29): 7016–7032.

    https://doi.org/10.1016/j.biomaterials.2013.05.062

23. Feng B, Tu H, Yuan H, *et al.*, 2012, Acetic-acid-mediated miscibility toward electrospinning homogeneous composite nanofibers of GT/PCL. *Biomacromolecules*, 13(12): 3917–3925.

    https://doi.org/10.1021/bm3009389

24. Zhou Q, Zhang H, Zhou Y, *et al.*, 2017, Alkali-mediated miscibility of gelatin/polycaprolactone for electrospinning homogeneous composite nanofibers for tissue scaffolding. *Macromol Biosci*, 17(12).

    https://doi.org/10.1002/mabi.201700268

25. Zheng R, Duan H, Xue J, *et al.*, 2014, The influence of Gelatin/PCL ratio and 3-D construct shape of electrospun membranes on cartilage regeneration. *Biomaterials*, 35(1): 152–164.

    https://doi.org/10.1016/j.biomaterials.2013.09.082

26. Jing X, Mi HY, Wang XC, *et al.*, 2015, Shish-kebab-structured poly(ε-caprolactone) nanofibers hierarchically decorated with chitosan-poly(ε-caprolactone) copolymers for bone tissue engineering. *ACS Appl Mater Interfaces*, 7(12): 6955–6965.

    https://doi.org/10.1021/acsami.5b00900

27. Jin S, Yang R, Chu C, *et al.*, 2021, Topological structure of electrospun membrane regulates immune response, angiogenesis and bone regeneration. *Acta Biomater*, 129: 148–158.

    https://doi.org/10.1016/j.actbio.2021.05.042

28. Hao M, Liu Y, Chen Z, *et al.*, 2022, Cross-linked gamma polyglutamic acid/human hair keratin electrospun nanofibrous scaffolds with excellent biocompatibility and biodegradability. *Polymers (Basel)*, 14(24): 5505.

    https://doi.org/10.3390/polym14245505

29. Crowder SW, Leonardo V, Whittaker T, *et al.*, 2016, Material cues as potent regulators of epigenetics and stem cell function. *Cell Stem Cell*, 18(1): 39–52.

    https://doi.org/10.1016/j.stem.2015.12.012

30. Lv L, Tang Y, Zhang P, *et al.*, 2018, Biomaterial cues regulate epigenetic state and cell functions-A systematic review. *Tissue Eng Part B Rev*, 24(2): 112–132.

    https://doi.org/10.1089/ten.teb.2017.0287

31. Veiseh O, Doloff JC, Ma M, *et al.*, 2015, Size- and shape-dependent foreign body immune response to materials implanted in rodents and non-human primates. *Nat Mater*, 14(6): 643–651.

    https://doi.org/10.1038/nmat4290

32. Leal-Egaña A, Díaz-Cuenca A, Boccaccini AR, 2013, Tuning of cell-biomaterial anchorage for tissue regeneration. *Adv Mater*, 25(29): 4049–4057.

    https://doi.org/10.1002/adma.201301227

33. Yeo A, Wong WJ, Teoh SH, 2010, Surface modification of PCL-TCP scaffolds in rabbit calvaria defects: Evaluation of scaffold degradation profile, biomechanical properties and bone healing patterns. *J Biomed Mater Res A*, 93(4): 1358–1367.

    https://doi.org/10.1002/jbm.a.32633

34. Tiaw KS, Goh SW, Hong M, *et al.*, 2005, Laser surface modification of poly(epsilon-caprolactone) (PCL) membrane for tissue engineering applications. *Biomaterials*, 26(7): 763–769.

https://doi.org/10.1016/j.biomaterials.2004.03.010

35. Chen Z, Liu Y, Huang J, *et al.*, 2022, Enhanced in vitro biocompatible polycaprolactone/nano-hydroxyapatite scaffolds with near-field direct-writing melt electrospinning technology. *J Funct Biomater*, 13(4): 161.

https://doi.org/10.3390/jfb13040161

36. Chen Z, Hao M, Qian X, *et al.*, 2021, Characterization on modification and biocompatibility of PCL scaffold prepared with near-field direct-writing melt electrospinning. *Chem Res Chin Univ*, 37(3): 578–583.

https://doi.org/10.1007/s40242-021-1129-z

37. Vaquette C, Ivanovski S, Hamlet SM, *et al.*, 2013, Effect of culture conditions and calcium phosphate coating on ectopic bone formation. *Biomaterials*, 34(22): 5538–5551.

https://doi.org/10.1016/j.biomaterials.2013.03.088

38. Gupta D, Singh AK, Kar N, *et al.*, 2019, Modelling and optimization of NaOH-etched 3-D printed PCL for enhanced cellular attachment and growth with minimal loss of mechanical strength. *Mater Sci Eng C Mater Biol Appl*, 98: 602–611.

https://doi.org/10.1016/j.msec.2018.12.084

39. Zamani Y, Mohammadi J, Amoabediny G, *et al.*, 2018, Enhanced osteogenic activity by MC3T3-E1 pre-osteoblasts on chemically surface-modified poly(ε-caprolactone) 3D-printed scaffolds compared to RGD immobilized scaffolds. *Biomed Mater*, 14(1): 015008.

https://doi.org/10.1088/1748-605X/aaeb82

40. Zhou ZX, Chen YR, Zhang JY, *et al.*, 2020, Facile strategy on hydrophilic modification of poly(ε-caprolactone) scaffolds for assisting tissue-engineered meniscus constructs in vitro. *Front Pharmacol*, 11: 471.

https://doi.org/10.3389/fphar.2020.00471

41. Lam CX, Hutmacher DW, Schantz JT, *et al.*, 2009, Evaluation of polycaprolactone scaffold degradation for 6 months in vitro and in vivo. *J Biomed Mater Res A*, 90(3): 906–919.

https://doi.org/10.1002/jbm.a.32052

42. Yao C, Qiu Z, Li X, *et al.*, 2023, Electrohydrodynamic printing of microfibrous architectures with cell-scale spacing for improved cellular migration and neurite outgrowth. *Small*, 19(19): e2207331.

https://doi.org/10.1002/smll.202207331

43. Eichholz KF, Hoey DA, 2018, Mediating human stem cell behaviour via defined fibrous architectures by melt electrospinning writing. *Acta Biomater*, 75: 140–151.

https://doi.org/10.1016/j.actbio.2018.05.048

44. Karageorgiou V, Kaplan D, 2005, Porosity of 3D biomaterial scaffolds and osteogenesis. *Biomaterials*, 26(27): 5474–5491.

https://doi.org/10.1016/j.biomaterials.2005.02.002

45. Tian Y, Zheng H, Zheng G, *et al.*, 2022, Hierarchical microgroove/nanopore topography regulated cell adhesion to enhance osseointegration around intraosseous implants in vivo. *Biomater Sci*, 10(2): 560–580.

https://doi.org/10.1039/d1bm01657a

46. Zhang P, Chen J, Sun Y, *et al.*, 2023, A 3D multifunctional bi-layer scaffold to regulate stem cell behaviors and promote osteochondral regeneration. *J Mater Chem B*, 11(6): 1240–1261.

https://doi.org/10.1039/d2tb02203f

47. Shegarfi H, Reikeras O, 2009, Review article: Bone transplantation and immune response. *J Orthop Surg (Hong Kong)*, 17(2): 206–211.

https://doi.org/10.1177/230949900901700218

48. Kanchanawong P, Shtengel G, Pasapera AM, *et al.*, 2010, Nanoscale architecture of integrin-based cell adhesions. *Nature*, 468(7323): 580–594.

https://doi.org/10.1038/nature09621

49. Prasopthum A, Cooper M, Shakesheff KM, *et al.*, 2019, Three-dimensional printed scaffolds with controlled micro-/nanoporous surface topography direct chondrogenic and osteogenic differentiation of mesenchymal stem cells. *ACS Appl Mater Interfaces*, 11(21): 18896–18906.

https://doi.org/10.1021/acsami.9b01472

50. Kumar G, Waters MS, Farooque TM, *et al.*, 2012, Freeform fabricated scaffolds with roughened struts that enhance both stem cell proliferation and differentiation by controlling cell shape. *Biomaterials*, 33(16): 4022–4030.

https://doi.org/10.1016/j.biomaterials.2012.02.048

51. Neves SC, Mota C, Longoni A, *et al.*, 2016, Additive manufactured polymeric 3D scaffolds with tailored surface topography influence mesenchymal stromal cells activity. *Biofabrication*, 8(2): 025012.

https://doi.org/10.1088/1758-5090/8/2/025012

ACCSCIENCE PUBLISHING

International Journal of Bioprinting

RESEARCH ARTICLE

3D bioprinting-based single liver tumor spheroid analysis for aflatoxin B1-induced drug-resistant cancer cell

Viet Phuong Cao, Sera Hong, and Joon Myong Song*

College of Pharmacy, Seoul National University, Seoul 08826, South Korea

Abstract

Aflatoxin B1, found in a variety of foods, is a mycotoxin known to cause cancer. Therefore, humans may be exposed to it through their daily diet. In this study, a three-dimensional (3D) tumor spheroid model was developed via 3D bioprinting to examine whether exposure of HepG2 liver tumor spheroids to aflatoxin B1 can increase the population of drug-resistant liver cancer cells in a single tumor spheroid. Two biomarkers, CD133 (prominin-1) and aldehyde dehydrogenase 1 (ALDH1), were used to identify drug-resistant cancer cells formed in the single liver tumor spheroids. The induction of drug-resistant cancer cells in the single tumor spheroids was examined through single spheroid imaging and fluorescence-activated cell sorting (FACS). The increase of drug-resistant cancer cells, which was caused by aflatoxin B1 in a dose-dependent manner, was quantitatively monitored at the single tumor spheroid level using both methods. 3D bioprinting-fabricated single liver tumor spheroid model successfully determined drug-resistant liver cancer cells caused by aflatoxin B1.

Keywords: 3D bioprinting; Single tumor spheroid imaging; Aflatoxin B1; Drug-resistant cancer cell

***Corresponding author:**
Joon Myong Song
(jmsong@snu.ac.kr)

Citation: Cao VP, Hong S, Song JM, 2023, 3D bioprinting-based single liver tumor spheroid analysis for aflatoxin B1-induced drug -resistant cancer cell. *Int J Bioprint*, 9(6): 0985. https://doi.org/10.36922/ijb.0985

Received: May 24, 2023
Accepted: July 1, 2023
Published Online: August 18, 2023

Copyright: © 2023 Author(s). This is an Open Access article distributed under the terms of the Creative Commons Attribution License, permitting distribution, and reproduction in any medium, provided the original work is properly cited.

Publisher's Note: AccScience Publishing remains neutral with regard to jurisdictional claims in published maps and institutional affiliations.

1. Introduction

Cancer stem cells (CSCs) are known to be responsible for tumors' resistance to chemotherapies and radiotherapies, which lead to cancer treatment failure and cancer recurrence. CSCs have recently emerged as one of the most common targets for novel innovations in cancer therapies[1-4]. The distinctive characteristics and unique phenotype of CSCs are acquired as a result of abnormality in many pathways[5,6], including STAT3, Wnt/TCF, or NF-κB. Besides, transcription factors such as KLF4, c-MYC, and NANOG are overexpressed in CSCs, leading to the ability of metastasis, tumorigenesis, cell proliferation, and self-renewal, respectively. Among these characteristics, drug resistance is one of the key features, the mechanism of which involves many approaches[7,8]. Common processes include enhanced ATP-binding cassette transporter (ABC transporter) activity, by which the cells are protected by chemotherapy agents like doxorubicin or methotrexate, and apoptosis prevention via Rho-ROCK pathway.

The stem-like characteristics of CSCs are preserved and displayed by an array of markers, which are abnormally expressed because of modification in gene regulations. For example, CD44, a common marker in many cancer types, has been proven to not

only enhance cell–substrate interaction and cell response to stress, but also increase the level of resistance against cancer therapies[3,9]. Because a certain set of markers uniquely appear in CSCs rather than normal cancer cells, these markers can be utilized to distinguish and isolate CSCs from the entire population of various cancer cell lines[10-13].

Aflatoxin B1 is a mycotoxin derived from *Aspergillus flavus* and *Aspergillus parasiticus*. It is widely known as a carcinogen, particularly for liver cancer, by inducing a mutation in *p53* gene. Its metabolite by cytochrome P450 enzyme, exo-aflatoxin B1-8,9-epoxide, can link with guanine and generate an adduct with DNA. The interference to normal DNA structure by the DNA adducts can inhibit the activity of tumor suppressor genes. As a result, cell growth is no longer properly controlled, and cancer is initiated[14]. Aflatoxin B1 has been found in a wide range of foods, such as corn[15], peanuts[16], and rice[17]. Therefore, it is likely that humans absorb aflatoxin B1 through their daily diet. Previously, the correlation between aflatoxin B1 and liver cancer pathogenesis (or CSC) has been mainly studied using two-dimensional (2D) cell culture model[18]. However, several drawbacks of 2D cell culture have been highlighted. For example, in 2D cell culture, Birgersdotter *et al.* indicated that there is a loss in cell polarity, a pivotal feature of tissue, as well as an alteration in gene expression[19]. Moreover, it failed to preserve the natural morphology of cells and represented a similarity in the accessibility of cells to media and drug solutions, as observed in *in vivo* studies. This explains the significant difference between the results of *in vitro* studies using 2D cell culture and *in vivo* studies; it also highlights the need to develop a model relevant to physiological conditions to simulate biological processes in the body.

In contrast, three-dimensional (3D) cell culture has been proven to effectively simulate physiological conditions, particularly the tumor microenvironment. As the 3D-cultured cancer cells grow into a spheroid structure, they maintain their natural shape while forming a tumor-like cluster with inner and outer layers wherein oxygen, nutrients, and drug gradients form, making them less accessible to cancer cells in the inner layers[20]. Additionally, by allowing cancer cells to grow in a gel-like structure, 3D cell culture also mimics extracellular matrix (ECM)[21]. Previous studies have stated the important role of ECM in tumor microenvironment (TME)[22], in which it is the major component of the TME and supports unique characteristics of CSCs, such as drug resistance[23,24] and tumorigenesis[25]. Unlike 2D cell culture, which obviously lacks ECM, 3D cell culture, where cells are grown in a 3D structure, has a potential to simulate key features of ECM[26]. Firstly, ECM, which is composed by various macromolecules like laminin, collagen, and proteoglycan[27], can be similarly created by a mixture of biocompatible and natural polysaccharide and protein. Moreover, ECM stiffness, which is critical for metastasis[28], can be mimicked by cross-linking nature-derived protein or polymer. Furthermore, the 3D spheroid culture system is highly biologically relevant to native *in vivo* states in that 3D spheroids have the vital characteristics such as natural cell shape, a heterogeneous interface with the surrounding medium, and similar gene and protein expressions with the natural *in vivo* cancers[29,30]. Therefore, the results obtained in 3D cell culture model have been observed to resemble *in vivo* context, which is reflected by aspects like higher cell viability[31,32], higher yield of extracellular vesicles[33], more active drug metabolism[34], or higher levels of stem-like properties and epithelial–mesenchymal transition (EMT) markers, such as NANOG, SOX2, CD44, and CD133[35], compared to 2D cell culture. To date, a number of 3D cell culture techniques have been developed, which can be classified into scaffold-based and scaffold-free approaches[36,37]. Meanwhile, 3D bioprinting has been widely used in energy harvesting[38-40], food industry[41], tissue engineering[42-44], and cell biology[45-51]. In the present study, a scaffold-based 3D bioprinting *in vitro* model was developed to quantitatively determine drug-resistant single cancer cells formed in HepG2 tumor spheroids following the exposure to aflatoxin B1. The HepG2 cancer cell-laden hydrogel consisting of alginate and gelatin was 3D-bioprinted such that single cancer cells grown into tumor spheroids were uniformly distributed in the hydrogel. By using 3D bioprinting, size and shape of the hydrogel could be precisely controlled, and the porous structure of hydrogel after crosslinking could serve as an artificial ECM, where nutrients and soluble factors could be stored. The hydrogel entrapping cancer cells is allocated into a consistent cross structure with similar amount by 3D bioprinting, which not only makes the development of *in vitro* model less labor-intensive, but also remarkably enhances reproducibility. Owing to these advantages, the proposed model is expected to mimic physiological conditions. The present model is based on the assumption that human liver cancer patients, who are not aware of the tumor in their bodies, may be exposed to the carcinogen aflatoxin B1 through their diet. Particularly, this approach is greatly significant because it quantitatively evaluates the extent to which drug-resistant CSCs, which are not easily killed by anticancer agents, can be formed in single tumor spheroids when exposed to the carcinogen aflatoxin B1.

2. Materials and methods

2.1. Cell culture

Liver cancer cell line HepG2 from Korea Cell line bank (No. 30022, Seoul, Korea) was employed for the experiment

by culturing it in Dulbecco's modified Eagle's medium (DMEM; Gibco, Grand Island, NY, USA) supplemented with 10% fetal bovine serum (FBS; Gibco) and 1% antibiotic-antimycotic (Gibco) at 37°C under 5% CO_2. To maintain cell growth, media exchange was conducted every 48 h after washing with phosphate-buffered saline (1× PBS, pH 7.2, Gendepot, USA). When subculture was needed, the cells were washed with 1× PBS before detachment with trypsin (TrypLE Express, Gibco, Denmark) for 5 min.

2.2. Material preparation for 3D bioprinting

To mimic the ECM in tumor microenvironment, gelatin and alginate were purchased and employed in the lyophilized powder form. They were dispersed into 1× PBS at concentrations of 10% and 4% (w/v), respectively. The mixtures were heated up to 80°C in 7 h; to obtain a homogenous gel, they were mixed every hour, before being kept at 37°C. Finally, approximately 2.5 million HepG2 cells, prepared in 0.5 mL of DMEM supplemented with 10% FBS and 1% antibiotic-antimycotic, were added and mixed gently with the gel, which could be immediately applied to cell 3D printing.

2.3. 3D printing of mini-well

The CAD program Rhino 6 was used to design 3D mini-well structure. Subsequently, the design was converted into stl files for application in the New Creator K V1.57.70 software. Once the file was uploaded and the 3D printer was connected to the software, the fabrication of the mini-well was initiated automatically. Briefly, thermoplastic polylactic acid (PLA) polymer was transformed into a semisolid form by heating to 210°C, which flowed through the nozzle as semisolid fiber with a size of 0.2 mm. By optimizing the filling density and printing speed at 75% and 10 mm/s, respectively, layer-by-layer printing was facilitated to form a mini-well that was 4 mm high and covered an area of 14×14 mm. Each mini-well dish included nine wells arranged in a 3 × 3 square. An individual well had a size of 3 × 3 mm.

2.4. 3D bioprinting of cell-laden hydrogel

The 3D bioprinting of HepG2 cells in the hydrogel was conducted using the same 3D bioprinter and computer software as in the previous step. In particular, the prepared mixture of hydrogel and cells was loaded into a 10-mL syringe and fixed in the dispenser of the 3D bioprinter. Another stl file encoding the specialized design for gel printing was uploaded to the computer. Once printing commander was activated, the printer automatically printed the cell-laden hydrogel with cross-shaped structures into all nine individual PLA wells obtained from the previous step. After the cell-laden hydrogel was completely printed into the wells, the hydrogel was crosslinked by a 160-mM aqueous calcium chloride solution for 10 min. The 3D-printed cells were maintained at 37°C and 5% CO_2, with nutrients provided by DMEM supplemented with 10% FBS and 1% antibiotic-antimycotic, which was exchanged every 24 h. Their growths were monitored under the bright-field function of fluorescence microscope (Olympus BX51, Japan), wherein the diameter measurement is possible.

2.5. Aflatoxin B1 treatment

Aflatoxin B1 was purchased as a 5-mg powder in a vial (Enzo, Farmingdale, NY, USA). It was dissolved in dimethyl sulfoxide (DMSO) to give the stock solution with a concentration of 0.5 mg/mL; subsequently, it was kept at −20°C. For the treatment on HepG2 tumor spheroids, this stock solution was diluted in serum-free DMEM to three concentrations of 1, 2.5, and 5 μM. After a 7-day period of tumor spheroids' growth, DMEM supplemented with 10% FBS and 1% antibiotic-antimycotic was discarded, and the gel structures were washed twice with 1× PBS. Subsequently, different plates were treated with different concentrations of aflatoxin B1, along with the control, which contained only serum-free DMEM. The carcinogen incubation was performed for 48 h under the condition of 37°C and 5% CO_2.

2.6. Immunostaining for the detection of surface marker on tumor spheroids

Two important markers are found in the HepG2 liver cancer cell line. One is CD133, or prominin-1, a transmembrane glycoprotein that has been widely used to sort out liver CSCs. The other is ALDH1, a cytosolic enzyme, which is responsible for intracellular retinoic acid formation[52]. Owing to their significant role, this study employed these two markers to isolate and identify CSCs from the spheroids. After exposure to aflatoxin B1 at four different concentrations, the tumor spheroids were washed three times with 1× PBS. Subsequently, fixation was conducted by adding 4% paraformaldehyde (PFA) at 4°C to the samples in 20 minutes, followed by three washes with PBS. In the next step, permeabilization and blocking were done by immersing the samples into a 1× PBS solution containing 0.2% Triton-X and 1% FBS for 15 min. Following this, the samples were stained for 1 h with Anti-Alexa fluor 594 CD133 and Anti-Alexa fluor 647 ALDH1 antibody solutions at a dilution rate of 1:200, and then washed thrice with 1× PBS. Finally, counter-staining was required, using Hoechst 33258 (Bloomington, MN 55431) at a dilution rate of 1:500 for 15 min, followed by washing thrice using PBS. The fluorescence imaging of tumor spheroids was performed using confocal microscope (TCS SP8, Leica, Wetzlar, Germany) and LASX software after washing thrice with 1× PBS. The obtained images were analyzed with Imaris software (Bitplane, Zurich, Switzerland), whereas the fluorescence intensity was measured by Metamorph software (Molecular Devices, San Jose, CA, USA).

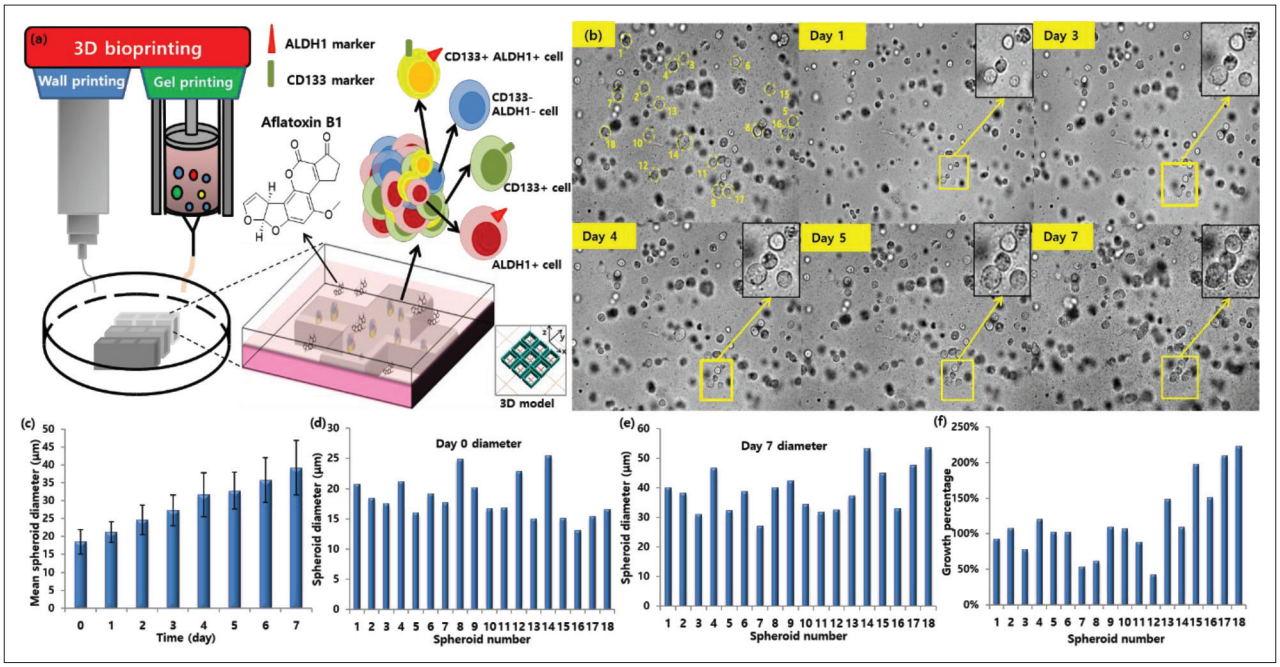

Figure 1. (a) Schematic diagram that depicts the formation of cancer spheroids and drug-resistant cancer cells via 3D bioprinting. Daily measurement of HepG2 liver tumor spheroids. (b) Numbered spheroids and bright-field images of the same region throughout a 7-day period. (c) Mean spheroid diameter throughout the period. (d) Diameters of spheroids measured on day 0 (immediately after printing). (e) Diameters of spheroids measured on the 7th day. (f) Growth percentage of all numbered spheroids.

2.7. Quantification analysis with fluorescence-activated cell sorting (FACS)

Initially, tumor spheroids were arranged randomly and maintained in the gel structure. To dissociate tumor spheroids from the hydrogel, 500 mg of collagenase NB 4G Proved Grade powder was dispersed in 5 mL double distilled water (DDW) to form a solution. Then, the collagenase solution was added to the hydrogel containing tumor spheroids. By incubating the hydrogel in the collagenase solution for 30 min at 37°C, the hydrogel structure was totally dissociated. The broken and dissolved hydrogels, along with the remaining spheroids, were collected and centrifuged at 1500 rpm for 1 min, and the supernatant was removed. The residue was dispersed in Accutase and incubated in 37°C; subsequently, the tumor spheroids were fully disintegrated into single cells. These single cells are fixed with 4% PFA at 4°C in 10 min. After fixation and discarding PFA, the single cells were washed twice by dispersing in PBS, centrifuging and discarding the supernatant. Subsequently, single cells were permeabilized and blocked with a mixture of 0.2% Triton-X and 1% FBS prepared in PBS for 10 min. In the next step, Anti-Alexa fluor 594 CD133 and Anti-Alexa fluor 647 ALDH1 antibodies were diluted in a PBS buffer containing 1% FBS, at a rate of 1:100, and applied to the single cells for 1 h. Finally, the antibody solution was discarded, and the single cells were washed with PBS. The single cells were then dispersed in buffer and applied to a BD flow cytometer for quantification analysis.

2.8. Statistical analysis

All the quantitative measurements were performed in three experimental replicates. The collected data are expressed as mean ± standard deviation (SD) from triplicate samples. A one-way ANOVA with Tukey's *post-hoc* test was performed to identify statistically significant differences.

3. Results

3.1. Development of tumor spheroids in hydrogel structure

To determine whether the bioprinting approach can facilitate proper spheroid formation, the diameters of the spheroids were measured over a 7-day period using the bright-field microscope. Spheroid images of the same position were taken every 24 h. Figure 1 shows the growth of spheroids and related measurement; an increase in the mean diameter of 18 different spheroids was observed (Figure 1c). The mean diameter started at an initial value of 18.5 μm and increased up to 39.2 μm on the 7th day, which corresponded to a relative growth of more than 210%. The growth rate was maintained quite steadily throughout the study period, despite a slight decrease from the 4th day to the 5th day. A fluctuation in growth of individual spheroids was clearly observed (Figure 1d and e). Eighteen different

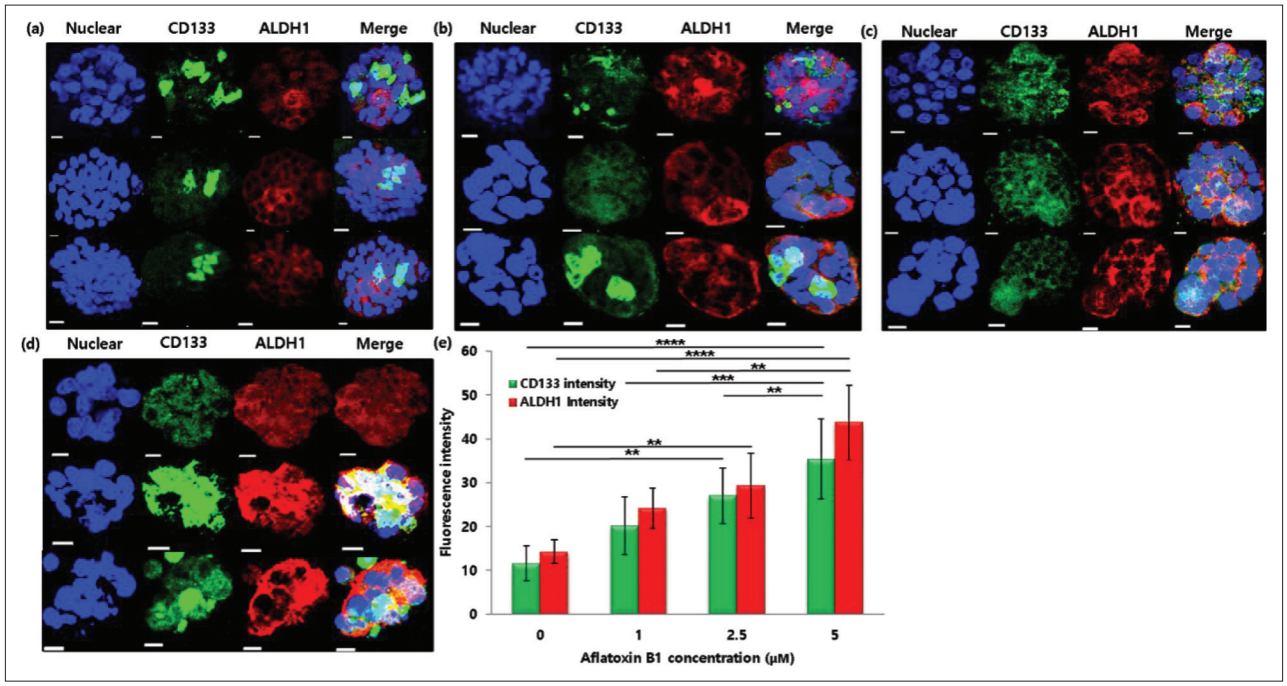

Figure 2. Confocal images of single tumor spheroids treated with aflatoxin B1 concentration of (a) 0, (b) 1, (c) 2.5, and (d) 5 μM. The expression of CD133 and ALDH1 was indicated by green and red colors, respectively, while the nucleus of single cancer cells was indicated by blue color. (e) Fluorescence intensities of CD133 and ALDH1 measured from the obtained images as a function of aflatoxin B1 concentration. All scale bars: 10 μm. $^{**}P < 0.01$, $^{***}P < 0.001$, $^{****}P < 0.0001$.

spheroids showed different growth rate; spheroid number 18 grew up the most significantly by more than 220%, whereas the least growing spheroid, numbered 12, grew up by only 42% (Figure 1e). However, the difference in the size of spheroids was similar between the first day of 12.4 μm (from 13.1 to 25.5 μm) and 7th day of 16.6 μm (from 27.2 to 53.7 μm). This result suggests that the developed 3D bioprinting model is an appropriate platform for 3D tumor spheroid culture, which enabled the cells to grow naturally, thereby preserving the heterogeneity of the cell population. Moreover, as revealed in **Figure S1** in Supplementary File, the cell viabilities of tumor spheroids maintained more than 90% throughout the measurement period. These results demonstrated that the developed model could keep the cells alive without any special intervention.

3.2. Single tumor spheroids analysis based on the expression of cancer stem cell markers

Figure 2 shows the immunostaining results of HepG2 spheroids exposed to four different aflatoxin B1 concentrations, i.e., 0, 1, 2.5, and 5 μM, on the 7th day. The blue, green, and red signals indicate cell nuclei, CD133, and ALDH1 markers, respectively. The positivity of both CD133 and ALDH1 markers was partially shown in single cells of single HepG2 spheroids (Figure 2). The extents to which they were expressed increased as the concentration of treated aflatoxin B1 increased. CD133 is expressed on the HepG2 cell surface, while ALDH1 exists in the cytosol of HepG2 cells. Therefore, in HepG2 cells where both markers are found, an absolute overlap of these two markers cannot be detected. Instead, the fluorescence image of CD133 surrounds that of ALDH1. As revealed by the images of single spheroids, in the control, the fluorescence images of CD133 and ALDH1 were shown in a small region of the single spheroids, whereas the fluorescent images were expanded to a much larger region of the single spheroids at an aflatoxin B1 concentration of 5 μM. In detail, the average fluorescence intensities of two expressed markers were measured over the whole single spheroid surface. Table 1 displays the fluorescence intensity of the obtained images; both increased gradually from the control to the aflatoxin B1 concentration of 5 μM. In comparison to the control, wherein the average intensities of CD133 and ALDH1 were 11.6 and 14.5, respectively, the aflatoxin B1 concentration of 5 μM caused nearly three times increase in the average intensities of CD133 and ALDH1 (35.4 and 43.7, respectively) (Figure 2e). The increment in fluorescence intensities of CD133 and ALDH1 markers revealed that the drug-resistant properties of single HepG2 tumor spheroids were enhanced as a result of aflatoxin B1 treatment.

The number of single CSCs formed by exposure to aflatoxin B1 was determined at the single tumor

Table 1. Fluorescence intensity of the obtained images

Group		CD133 intensity	Average	ALDH1 intensity	Average
Aflatoxin B1 0 μM	1	16.75	11.59	12.71	14.26
	2	10.36		14.98	
	3	8.09		9.81	
	4	10.99		18.43	
	5	15.92		16.08	
	6	7.46		13.55	
Aflatoxin B1 1 μM	1	10.74	20.13	23.43	24.16
	2	13.29		18.51	
	3	26.45		18.45	
	4	22.94		31.25	
	5	21.6		27.85	
	6	25.81		25.49	
Aflatoxin B1 2.5 μM	1	22.51	27.01	21.3	29.33
	2	17.58		22.79	
	3	27.22		21.87	
	4	27.74		35.06	
	5	31.53		36.51	
	6	35.53		38.5	
Aflatoxin B1 5 μM	1	19.03	35.38	28.96	43.70
	2	40.96		47.48	
	3	32.82		39.21	
	4	39.65		56.24	
	5	35.05		42.03	
	6	44.79		48.31	

spheroid level as a function of aflatoxin B1 using confocal microscopic imaging (Figure 3). Unlike above results (Figure 2), Figure 3 presents individual heterogenic response of single cancer cells in a single tumor spheroid to the carcinogen aflatoxin B1. The drug-resistant single cancer stem cell in the single spheroid was identified by the simultaneous expression of CD133 and ALDH1, which are shown in green and red, respectively. The yellow dots in the single spheroids corresponded to the single CSC. Each single cell in the single spheroids, denoted as gray dots, was identified by staining of their nuclei with Hoechst 33342. The total number of single cancer cells in a single spheroid was automatically calculated by a specific function of the IMARIS software that recognizes and counts the gray dots. The left images in Figure 3 show the total single cancer cells marked as gray dots in the single spheroids. The middle images in Figure 3 show CD133 and ALDH1 expressed in the single cells of left images. Considering the positivity of two markers, the right images present the drug-resistant single CSCs marked as yellow dots. The correlation between the formation of drug-resistant CSCs and aflatoxin B1 treatment could be deduced by counting CSCs and determining their proportion over the total number of cancer cells in a single spheroid. The average CSC percentage in the single spheroids increased gradually when the aflatoxin B1 concentration increased (Figure 3e). It was determined to be 31% at aflatoxin B1 concentration of 5 μM, compared to 6.6% in the control. This result offers a clear insight into the effect of aflatoxin B1 on induction of drug-resistant CSCs at the single tumor spheroid level. Interestingly, the entire population of single cancer cells in single spheroids diminished as the concentration of aflatoxin B1 increased (Table 2).

3.3. Analysis of cancer stem cells via fluorescence-activated cell sorting

FACS analysis was employed as another method to examine the induction of drug-resistant single CSCs by aflatoxin B1 at the single spheroid level. FACS can detect single cancer cells isolated from single tumor spheroids fabricated via 3D bioprinting. After a 7-day period of growth, because cancer cells existed as spheroids where

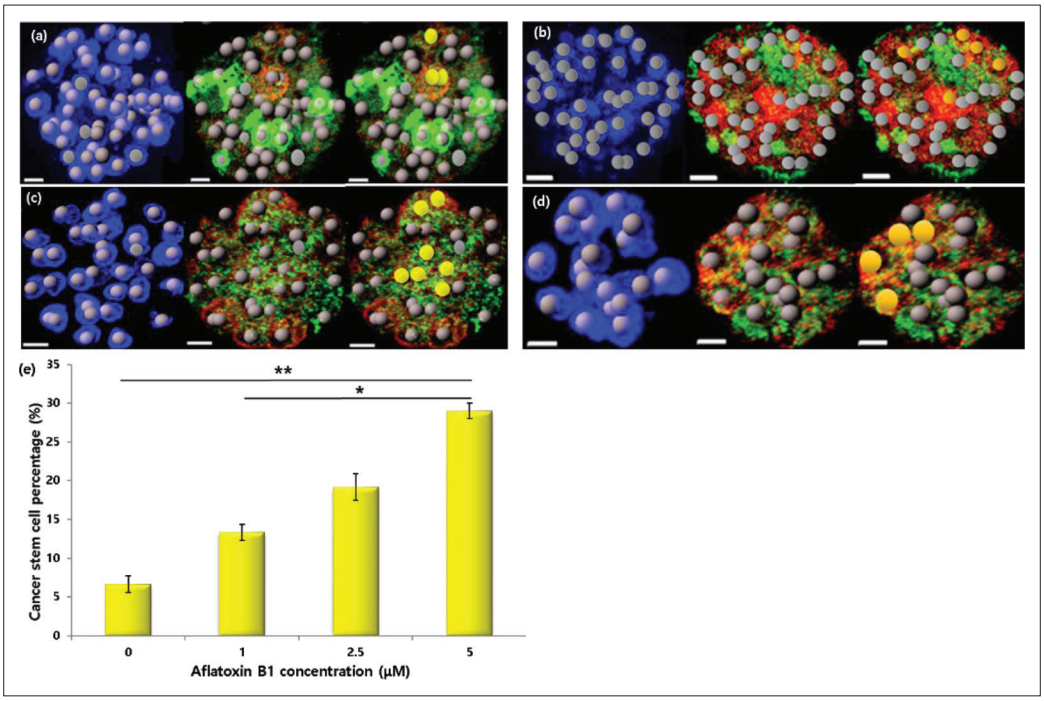

Figure 3. Representative images of spotted CSCs (indicated by yellow dots) and non-CSCs (indicated by gray dots) in single HepG2 spheroids treated with aflatoxin B1 concentrations of (a) 0, (b) 1, (c) 2.5, and (d) 5 μM. (e) Mean percentages of CSCs counted from obtained single spheroid images as a function of aflatoxin B1 concentration. All scale bars: 10 μm. $^{*}P < 0.05$, $^{**}P < 0.01$.

Table 2. Number of cells counted manually from acquired imaging data

Group		Total cells	$CD133^{+}ALDH1^{+}$ cells	%CSC	Average %CSC
Aflatoxin B1 0 μM	1	47	3	6.4%	6.63%
	2	53	3	5.7%	
	3	64	5	7.8%	
Aflatoxin B1 1 μM	1	41	5	12.2%	13.33%
	2	22	3	13.6%	
	3	28	4	14.2%	
Aflatoxin B1 2.5 μM	1	33	7	21.2%	19.19%
	2	27	5	18.5%	
	3	28	5	17.9%	
Aflatoxin B1 5 μM	1	18	4	22%	29%
	2	15	6	40%	
	3	17	4	23.5%	

cancer cells were attached to each other, collagenase NB 4G was utilized to disintegrate them into single cells so that flow cytometric analysis was possible. Figure 4 displays the result of FACS analysis for 10,000 single cancer cells disintegrated from HepG2 spheroids treated with the aforementioned concentration range of aflatoxin B1. In each graph, the horizontal and vertical axes indicate ALDH1 and CD133 emission, respectively. Based on the fluorescence intensities of ALDH1 and CD133, single cancer cells were divided into four different types, corresponding to four quarters of the graphs. The upper-right quarter represented cancer cells positive for both CD133 and ALDH1, which signified CSCs defined by this study. As shown in upper-right quarter, the average CSC percentage in the entire isolated single cancer cells clearly increased as the concentration of aflatoxin B1 increased. At the control, CSCs accounted for approximately 6% of the whole population. As the concentration of aflatoxin

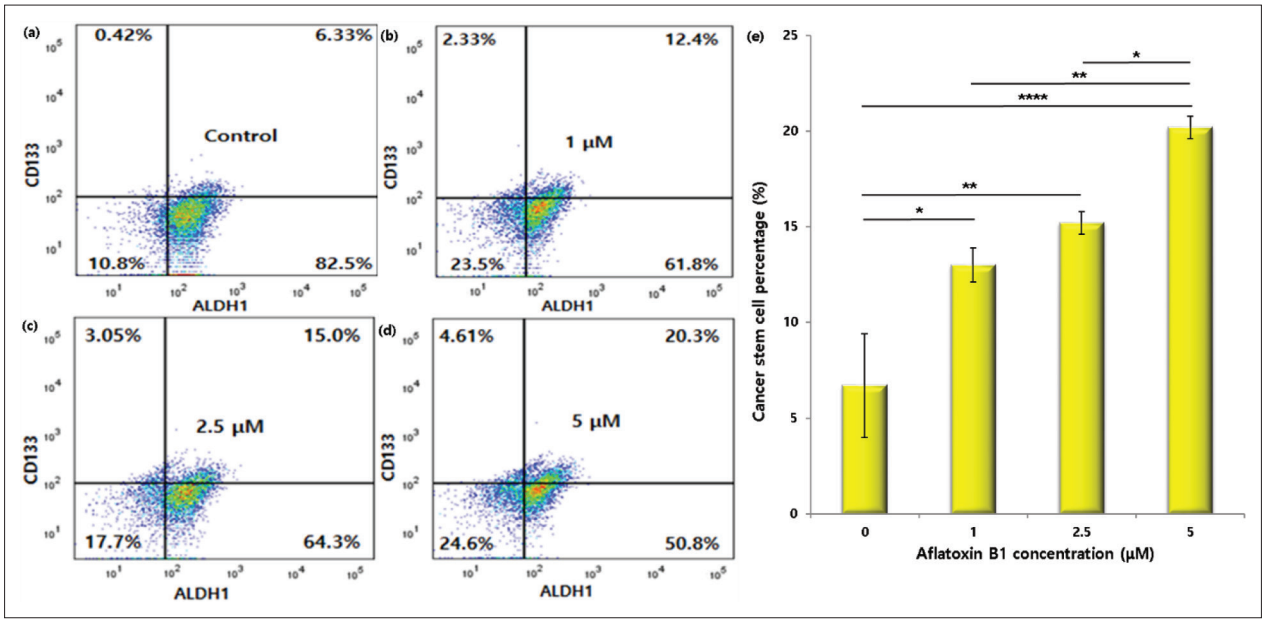

Figure 4. FACS analysis of CSCs isolated from HepG2 spheroids treated with aflatoxin B1 concentrations of (a) 0, (b) 1, (c) 2.5, and (d) 5 μM; (e) percentages of CSCs in HepG2 spheroids at four different aflatoxin B1 concentrations by FACS analysis. *$P < 0.05$, **$P < 0.01$, ****$P < 0.0001$.

B1 increased, the CSCs increased to 12.4% of the whole population at aflatoxin B1 of 1 μM, and further increased to 15% at aflatoxin B1 concentration of 2.5 μM. At aflatoxin B1 concentration of 5 μM, the number of CSCs increased to 20.3% of the total population. This result was consistent with the result obtained through confocal imaging of single spheroids.

4. Discussion

In 2020, liver cancer is estimated to account for 4.7% of the total new cancer cases globally, and it became the third most lethal cancer type, contributing to 8.9% of total deaths[53]. Moreover, the current therapeutic strategies for liver cancer have become more demanding due to resistance[54], and such problems have been mainly attributed to CSCs[55]. Regarding drug discovery, CSC is also one of the heated obstacles to new therapies[3]. Many toxins only target growing cancer cells and cell cycle, but their efficacies were not promising as expected since they are avoided by slowly dividing and dormant CSCs[1]. Meanwhile, CSC markers have been observed to exist on normal stem cells, human embryonic stem cells, or human tissues[5]. Antibody–drug conjugates (ADC) may be unable to distinguish targeted cells from healthy ones, leading to adverse effect and toxicity. Likewise, therapies targeting signaling pathways like Wnt, Notch, or Hedgehog also face similar challenges, since these cascades also progress in normal stem cells[2]. Moreover, approaches involving epigenetic processes and quiescent CSCs are limited due to a lack of knowledge about their function in CSC biology.

To date, CSCs have been defined by their clinical relevance and roles in cancer pathogenesis, rather than their biological characteristics[56]. Therefore, there is no fixed standard in terms of which surface markers must be expressed in CSCs, leading to differences in how various studies determined whether a cell population can be classified as CSCs or not. For example, Nguyen *et al.* utilized HepG2 cells and employed only the CD133 marker as the indicator for CSC isolation[57]. However, sorting CSCs using only one type of marker may not yield clinically significant result. In 2021, by reviewing the expression of CSCs marker in the literature, Dzobo *et al.*[1,58] revealed that the expression of only one individual marker was not considerably correlated with prognosis. In other words, classifying CSCs based on at least two markers should be recommended. In the present study, we selected CD133 and ALDH1 markers as the indication for sorting liver CSCs because of their significant roles in displaying CSC features[1]. While CD133 is involved a number of pathways related to drug resistance[59,60], ALDH1 is critical for oxidizing intracellular aldehydes[61] and facilitates cell proliferation[62]. The relative amount of approximately 6%, reflected by analysis using both confocal imaging and flow cytometry, suggests that this selection was appropriate to the proposed hypothesis of CSCs, which states that they are a rare population in tumors.

Aflatoxin B1 has been widely recognized as a carcinogen. Aflatoxin B1's metabolite, exo-aflatoxin B1-8,9-epoxide, can lead to various mutations in the p53 protein, among which the mutation at the third base codon 249 is

the most significant in cancer pathogenesis[63]. However, its role as a CSC inducer has not been thoroughly investigated. Kawasaki *et al*. isolated hepatoma K2 cells from rat exposed to aflatoxin B1[64]. They found that 89% of cell population was occupied by CSCs, while stemness genes such as *sox2*, *nanog*, and *klf4* were remarkably expressed. In addition, by treating HepG2 cells with various aflatoxin B1 concentrations and sorting out CSCs based on surface markers, Ju *et al.* confirmed a similar result regarding the ability of aflatoxin B1 ability to induce CSCs[18]. Nonetheless, both aforementioned findings were observed in 2D cell culture, which has been proven to have numerous limitations, making it clinically less significant. This study, which examines the phenomena in 3D tumor spheroid, may offer a novel and more remarkable insight into the actual effects of aflatoxin B1 on the formation of CSCs in a tumor.

In this study, two methods were employed to determine the presence of CSCs. Regarding single spheroid imaging, the analysis at the single-cell level indicated that the higher the aflatoxin B1 concentration for treatment, the lower the cell number in a spheroid. This could be attributed to the dual influence exerted by aflatoxin B1. Specifically, aflatoxin B1 not only induces CSCs but also causes DNA damage. This phenomenon is more evident at higher concentrations[65]. This could also explain the deviation between the results obtained from single spheroid imaging and FACS in the present study. In the results of single spheroid imaging and FACS, similarities could be observed in the control and low dose-treated samples. However, the difference in the number of CSCs acquired by FACS and imaging became more noticeable as the concentration of aflatoxin B1 increased. Indeed, as the tumor spheroids had a smaller number of single cancer cells, the percentage of single CSCs obtained by the spheroid imaging showed higher values of 19.2% and 29% at aflatoxin B1 concentrations of 2.5 and 5 μM, compared to 15% and 20.3%, respectively, acquired by FACS analysis at identical aflatoxin B1 concentrations. This is attributed to the growth of single tumor spheroids being significantly inhibited by the DNA-damaging aflatoxin B1, and this phenomenon occurs more frequently at higher concentrations of aflatoxin B1. As a result, Table 2 shows that there was smaller population of single cancer cells in single spheroids at higher concentrations of aflatoxin B1. In addition, owing to the growth-inhibiting effect of aflatoxin B1, more single cancer cells fixed in the hydrogel were observed. They could not be distinguished and excluded through the FACS analysis, although they could contribute to the entire population, regardless of which markers they expressed. However, it was obvious that the increase in the number of drug-resistant CSCs as the aflatoxin B1 concentration increased showed an identical tendency in both spheroid imaging and FACS analysis. This similar tendency proved that single tumor spheroid imaging, like the frequently used FACS analysis, could also be an effective method for investigating the correlation between liver CSCs and the carcinogen aflatoxin B1. Furthermore, it should be noticed that single tumor spheroids for imaging and FACS analysis were fabricated by 3D bioprinting. The present study clearly demonstrated the possibility of drug-resistant CSCs forming in a single liver tumor spheroid by exposure to aflatoxin B1 carcinogen. A single tumor spheroid can correspond to a human patient having liver tumor based on the fact that the patient may be exposed to aflatoxin B1 through daily diet.

5. Conclusion

In the present study, we developed a 3D tumor spheroid model fabricated via 3D bioprinting to monitor the formation of liver CSCs induced by aflatoxin B1. CSCs were observed using single tumor spheroid imaging and FACS analysis. After using both methods, a correlation between aflatoxin B1 dose and CSC level was observed: the higher the aflatoxin B1 concentration for treatment, the higher the number of CSCs could be detected. The similarity between the detailed results of two methods suggests the suitability of 3D bioprinting-based single tumor spheroid analysis for quantification of drug-resistant single liver CSCs induced by aflatoxin B1.

Acknowledgments

We are grateful to the Research Institute of Pharmaceutical Sciences at Seoul National University for providing experimental equipment and Brain Korea 21 Plus (BK21 Plus).

Funding

This work was supported by a National Research Foundation of Korea (NRF) grant funded by the Ministry of Education, Science and Technology (MEST) (No. 2018M3A7B4071235, 2023R1A2C3006991, and RS-2023-00218543).

Conflict of interest

The authors declare no conflicts of interests.

Author contributions

Conceptualization: Joon Myong Song
Formal analysis: Viet Phuong Cao, Sera Hong
Investigation: Viet Phuong Cao
Supervision: Joon Myong Song
Writing – original draft: Viet Phuong Cao
Writing – review & editing: Viet Phuong Cao, Joon Myong Song, Sera Hong

All authors approved the final version of the manuscript.

Ethics approval and consent to participate

Not applicable.

Consent for publication

Not applicable.

Availability of data

Data will be made available from the corresponding author upon reasonable request.

References

1. Dzobo K, Senthebane DA, Ganz C, *et al.*, 2020, Advances in therapeutic targeting of cancer stem cells within the tumor microenvironment: An updated review. *Cells,* 9(8): 1896.
2. Dzobo K, Senthebane DA, Rowe A, *et al.,* 2016, Cancer stem cell hypothesis for therapeutic innovation in clinical oncology? Taking the root out, not chopping the leaf. *Omics J Integr Biol,* 20: 681–691.
3. Batlle E, Clevers H, 2017, Cancer stem cells revisited. *Nat Med* 23**:** 1124–1134.
4. Ahn J, Choi HJ, Bang J, *et al.*, 2022, Ink-lithographic fabrication of silver-nanocrystal-based multiaxial strain gauge sensors through the coffee-ring effect for voice recognition applications. *Nano Converg,* 9: 46.
5. Walcher L, Kistenmacher AK, Suo H, *et al.*, 2020, Cancer stem cells-origins and biomarkers: perspectives for targeted personalized therapies. *Front Immunol,* 11: 1280.
6. Huang T, Song X, Xu D, *et al.*, 2020, Stem cell programs in cancer initiation, progression, and therapy resistance. *Theranostics,* 10(19): 8721–843.
7. Najafi M, Mortezaee K, Majidpoor J, 2019, Cancer stem cell (CSC) resistance drivers. *Life Sci,* 234: 116781.
8. Li Y, Wang Z, Ajani JA, *et al.*, 2021, Drug resistance and cancer stem cells. *Cell Commun Signal,* 19(1): 19.
9. Dzobo K, Sinkala M, 2021, Cancer stem cell marker CD44 plays multiple key roles in human cancers: Immune suppression/evasion, drug resistance, epithelial-mesenchymal transition, and metastasis. *Omics Journal of Integr Biol,* 25(5): 313–332
10. Fu JJ, Zhou Y, Shi XX, *et al.*, 2019, Spontaneous formation of tumor spheroid on a hydrophilic filter paper for cancer stem cell enrichment *Colloids Surf B: Biointerfaces,* 174: 426–434
11. Lapidot T, Sirard C, Vormoor J, *et al.*, 1994, A cell initiating human acute myeloid leukaemia after transplantation into SCID mice. *Nature,* 367(6464): 645–648.
12. Masciale V, Grisendi G, Banchelli F, *et al.*, 2019, Isolation and identification of cancer stem-like cells in adenocarcinoma and squamous cell carcinoma of the lung: A pilot study. *Front Oncol*, 9: 1394.
13. Suetsugu A, Nagaki M, Aoki H, *et al.*, 2006, Characterization of CD133+ hepatocellular carcinoma cells as cancer stem/progenitor cells *Biochem Biophys Res Commun,* 351(4): 820–824.
14. Verma RJ, 2004, Aflatoxin cause DNA damage. *Int J Hum Genet,* 4: 231–236.
15. Jayaratne WMSC, Abeyratne AHMAK, De Zoysa HKS, *et al.*, 2020, Detection and quantification of Aflatoxin B1 in corn and corn-grown soils in the district of Anuradhapura, Sri Lanka. *Heliyon,* 6(10): e05319.
16. Asl GB, Arvand M, Habibi MF, 2022, High affinity aptamers for ultra-sensitive detection of aflatoxin B1 in milk and groundnut samples with label-free photo-electrochemical aptasensor. *Food Chem,* 397: 133829.
17. Romero-Sánchez I, Ramírez-García L, Gracia-Lor E, *et al.*, 2022, Simultaneous determination of aflatoxins B1, B2, G1 and G2 in commercial rices using immunoaffinity column clean-up and HPLC-MS/MS. *Food Chem,* 395: 133611.
18. Ju H, Shim Y, Arumugam P, *et al.*, 2016, Crosstalk-eliminated quantitative determination of aflatoxin B1-induced hepatocellular cancer stem cells based on concurrent monitoring of CD133, CD44, and aldehyde dehydrogenase1. *Toxicol Lett,* 243: 31–39.
19. Birgersdotter A, Sandberg R, Ernberg I, 2005, Gene expression perturbation in vitro—A growing case for three-dimensional (3D) culture systems. *Semin Cancer Biol,* 15(5): 405–412.
20. Yip D, Cho CH, 2013, A multicellular 3D heterospheroid model of liver tumor and stromal cells in collagen gel for anti-cancer drug testing. *Biochem Biophys Res Commun,* 433(3): 327–332.
21. Antoni D, Burckel H, Josset E, *et al.*, 2015, Three-dimensional cell culture: A breakthrough in vivo. *Int J Mol Sci,* 16(3): 5517–5527.
22. Khalaf K, Hana D, Chou JT, *et al.*, 2021, Aspects of the tumor microenvironment involved in immune resistance and drug resistance. *Front Immunol,* 12: 656364.
23. Senthebane DA, Rowe A, Thomford NE, *et al.*, 2017, The role of tumor microenvironment in chemoresistance: to survive, keep your enemies closer. *Int J Mol Sci,* 18(7): 1586.
24. Senthebane DA, Jonker T, Rowe A, *et al.*, 2018, The role of tumor microenvironment in chemoresistance: 3D extracellular matrices as accomplices. *Int J Mol Sci,* 19(10): 2861.
25. Dzobo K, Senthebane DA, Dandara C, 2023, The tumor microenvironment in tumorigenesis and therapy resistance revisited. *Cancers (Basel),* 15(2): 376.
26. Dzobo K, Rowe A, Senthebane DA, *et al.* 2018, Three-dimensional organoids in cancer research: The search for the holy grail of preclinical cancer modeling. *Omics Journal Integr Biol,* 22(26): 733–748.

27. Dzobo K, Dandara C, 2023, The extracellular matrix: Its composition, function, remodeling, and role in tumorigenesis. *Biomimetics (Basel, Switzerland),* 8(2): 146.

28. Najafi M, Farhood B, Mortezaee K, 2019, Extracellular matrix (ECM) stiffness and degradation as cancer drivers. *J Cell Biochem,* 120(3): 2782–2790.

29. Ravi M, Paramesh V, Kaviya SR, *et al.,* 2015, 3D cell culture systems: Advantages and applications. *J Cell Physiol* 230(1): 16–26.

30. Jensen C, Teng Y, 2020, Is it time to start transitioning from 2D to 3D cell culture? *Front Mol Biosci***,** 7: 33.

31. Bokhari M, Carnachan RJ, Cameron NR, *et al.*, 2007, Culture of HepG2 liver cells on three dimensional polystyrene scaffolds enhances cell structure and function during toxicological challenge. *J Anatom,* 211(4): 567–576.

32. Rodriguez-Salvador M, Fox-Miranda I, Perez-Benitez BE, *et al.*, 2022, Research dynamics of tissue spheroids as building blocks: A scientometric analysis. *Int J Bioprint,* 8(3): 585.

33. Kim JY, Rhim W-K, Cha S-G, *et al.*, 2022, Bolstering the secretion and bioactivities of umbilical cord MSC-derived extracellular vesicles with 3D culture and priming in chemically defined media. *Nano Converg,* 9(1): 57.

34. Schyschka L, Sánchez JJM, Wang Z, *et al.,* 2013, Hepatic 3D cultures but not 2D cultures preserve specific transporter activity for acetaminophen-induced hepatotoxicity. *Arch Toxicol,* 87(8): 1581–1593.

35. Huang YJ, Hsu SH, 2014, Acquisition of epithelial-mesenchymal transition and cancer stem-like phenotypes within chitosan-hyaluronan membrane-derived 3D tumor spheroids. *Biomaterials,* 35(38): 10070–10079.

36. Kawashima D, Yuki T, Li S, *et al.,* 2022, Non-invasive imaging of ion concentration distribution around cell spheroids by electrical impedance tomographic sensor printed on circuit board under temporal compensation by ion transport impedance model *Biosens Bioelectron,* 212: 114432.

37. Langhans SA, 2018, Three-dimensional in vitro cell culture models in drug discovery and drug repositioning, *Front Pharmacol,* 9: 6.

38. Ahmed A, Azam A, Wang Y, *et al.*, 2021, Additively manufactured nano-mechanical energy harvesting systems: Advancements, potential applications, challenges and future perspectives. *Nano Converg,* 8(1): 37.

39. Ranjan P, Gaur S, Yadav H, *et al.*, 2022, 2D materials: Increscent quantum flatland with immense potential for applications. *Nano Converg,* 9(1): 26.

40. Kim J, Lee J-K, Chae B, *et al.*, 2022, Near-field infrared nanoscopic study of EUV- and e-beam-exposed hydrogen silsesquioxane photoresist. *Nano Converg,* 9(1): 53.

41. Pérez B, Nykvist H, Brøgger AF, *et al.*, 2019, Impact of macronutrients printability and 3D-printer parameters on 3D-food printing: A review. *Food Chem,* 287: 249–257.

42. Samson AAS, Balwe SG, Hong S, *et al.*, 2023, Verification of nanomaterial-induced size-dependent human ether-à-go-go-related gene potassium channel blockage using three-dimensional bioengineered functional cardiac tissue constructs. *Chem Mater,* 35(2): 658–671.

43. Yu J, Lee S, Song J, *et al.*, 2022, Perfusable micro-vascularized 3D tissue array for high-throughput vascular phenotypic screening. *Nano Converg,* 9(1): 16.

44. Dong Z, Gong J, Zhang H, *et al.*, 2022, Preparation and characterization of 3D printed porous 45S5 bioglass bioceramic for bone tissue engineering application. *Int J Bioprint,* 8(4): 613.

45. Abdelrahim AA, Hong S, Song JM, 2022, Integrative in situ photodynamic therapy-induced cell death measurement of 3D-bioprinted MCF-7 tumor spheroids. *Anal Chem,* 94: 13936–13943.

46. Hong S, Song JM, 2021, A 3D cell printing-fabricated HepG2 liver spheroid model for high-content in situ quantification of drug-induced liver toxicity. *Biomater Sci,* 9(17): 5939–5950.

47. Hong S, Song JM, 2022, 3D bioprinted drug-resistant breast cancer spheroids for quantitative in situ evaluation of drug resistance. *Acta Biomater,* 138: 228–239.

48. Hong S, Song JM, 2023, High-resolution in situ high-content imaging of 3D-bioprinted single breast cancer spheroids for advanced quantification of benzo(a)pyrene carcinogen-induced breast cancer stem cells. *ACS Appl Mater Interfaces,* 15(9): 11416–11430.

49. Shao L, Hou R, Zhu Y, *et al.*, 2021, Pre-shear bioprinting of highly oriented porous hydrogel microfibers to construct anisotropic tissues. *Biomater Sci,* 9(20): 6763–6771.

50. Tetsuka H, Shin SR, 2020, Materials and technical innovations in 3D printing in biomedical applications. *J Mater Chem B,* 8(15): 2930–2950.

51. Wang T-Y, Li X-F, Liu S-M, *et al.*, 2022, Self-assembled wide bandgap nanocoatings enabled outstanding dielectric characteristics in the sandwich-like structure polymer composites. *Nano Converg,* 9(1): 55.

52. Clark DW, Palle KJA, 2016, Aldehyde dehydrogenases in cancer stem cells: Potential as therapeutic targets. *Ann Transl Med,* 4(24): 518.

53. Sung H, Ferlay J, Siegel RL, *et al.*, 2021, Global Cancer Statistics 2020: GLOBOCAN estimates of incidence and mortality worldwide for 36 cancers in 185 countries. *CA: Cancer J Clin,* 71(3): 209–249.

54. Miao Y, Yang T, Yang S, *et al.*, 2022, Protein nanoparticles directed cancer imaging and therapy. *Nano Converg,* 9(1): 2.

55. Zhou H-M, Zhang J-G, Zhang X, *et al.*, 2021, Targeting cancer stem cells for reversing therapy resistance: Mechanism, signaling, and prospective agents. *Signal Transduct Target Ther,* 6(1): 62.

56. Yu Z, Pestell TG, Lisanti MP, *et al.*, 2012, Cancer stem cells. *Int J Biochem Cell Biol,* 44(12): 2144–2151.

57. Nguyen ST, Nguyen LS, Nguyen THP, *et al.*, 2020, Isolation of cancer stem-like cells from hepatocellular carcinoma cell line HepG2 by methods of magnetic-activated cell sorting, spheroid culture, and anti-tumor drug-resistant selection: A primary evaluation. *Prog Stem Cell***,** 7(1-2): 279–289.

58. Dzobo K, Ganz C, Thomford NE, *et al.*, 2021, Cancer stem cell markers in relation to patient survival outcomes: Lessons for integrative diagnostics and next-generation anticancer drug development. *Omics J Integr Biol,* 25(2): 81–92.

59. Lu R, Zhao G, Yang Y, *et al.*, 2019, Inhibition of CD133 overcomes cisplatin resistance through inhibiting PI3K/AKT/mTOR signaling pathway and autophagy in CD133-positive gastric cancer cells. *Technol Cancer Res Treatment,* 18: 1533033819864311.

60. Zhou L, Sun Y, Ye G, *et al.*, 2022, Effects of CD133 expression on chemotherapy and drug sensitivity of adenoid cystic carcinoma. *Mol Med Rep,* 25(1): 18.

61. Hiroyuki T, Tomohiro K, Ayumi N, *et al.*, 2017, *Updates in Liver Cancer,* Mohamed AH (ed.), IntechOpen, Rijeka.

62. Wei Y, Li Y, Chen Y, *et al.*, 2022, ALDH1: A potential therapeutic target for cancer stem cells in solid tumors. *Front Oncol,* 12: 1026278.

63. Link T, Iwakuma T, 2017, Roles of p53 in extrinsic factor-induced liver carcinogenesis *Hepatoma Res,* 3(6): 95–104.

64. Kawasaki Y, Adachi N, Yamazaki T, *et al.*, 2007, Cancer stem cells in aflatoxin B1-induced rat hepatocellular carcinoma K2 cells. *JSM Mycotoxins,* 57: 87–93.

65. Feng W-H, Xue KS, Tang L, *et al.*, 2017, Aflatoxin B1-induced developmental and DNA damage in caenorhabditis elegans. *Toxins,* 9(1): 9.

ACCSCIENCE PUBLISHING

International Journal of Bioprinting

REVIEW ARTICLE

Biomimetic 3D bioprinting approaches to engineer the tumor microenvironment

Fabiano Bini[1], Salvatore D'Alessandro[1,2], Tarun Agarwal[3], Daniele Marciano[4], Serena Duchi[5,6], Enrico Lucarelli[7], Giancarlo Ruocco[2], Franco Marinozzi[1], and Gianluca Cidonio[2]*

[1]Department of Mechanical and Aerospace Engineering, Sapienza University, Rome, Italy

[2]Center for Life Nano- & Neuro-Science (CLN2S), Fondazione Istituto Italiano di Tecnologia, Rome, Italy

[3]Department of Bio-Technology, Koneru Lakshmaiah Education Foundation, Vaddeswaram, AP, India

[4]School of Engineering and Materials Science, Queen Mary University of London, Mile End Road, London, United Kingdom

[5]Aikenhead Centre for Medical Discovery St Vincent's Hospital, Melbourne, VIC, Australia

[6]Department of Surgery, The University of Melbourne, Melbourne, VIC, Australia

[7]Osteoncology, Bone and Soft Tissue Sarcomas and Innovative Therapies Unit, IRCCS Istituto Ortopedico Rizzoli, Bologna, Italy

(This article belongs to the *Special Issue: 3D printing of bioinspired materials*)

Abstract

With the increasing incidence and mortality rates, cancer remains a major health challenge in the world. Despite advances in therapies and clinical programs, the efficacy of anti-cancer drugs often fails to translate from pre-clinical models to patient clinical trials. To date, pre-clinical cancer models, including two-dimensional cell cultures and animal models, have limited versatility and accuracy in recapitulating the complexity of human cancer. To address these limitations, a growing focus has fostered the development of three-dimensional (3D) tumor models that closely resemble the *in vivo* tumor microenvironment and heterogeneity. Recent efforts have leveraged bioengineering technologies, such as biofabrication, to engineer new platforms that mimic healthy and diseased organs, aiming to overcome the shortcomings of conventional models, such as for musculoskeletal tissues. Notably, 3D bioprinting has emerged as a powerful tool in cancer research, offering precise control over cell and biomaterial deposition to fabricate architecturally complex and reproducible functional models. The following review underscores the urgent need for more accurate and relevant 3D tumor models, highlighting the advantages of the use of biofabrication approaches to engineer new biomimetics platforms. We provide an updated discussion on the role of bioengineering technologies in cancer research and modeling with particular focus on 3D bioprinting platforms, as well as a close view on biomaterial inks and 3D bioprinting technologies employed in cancer modeling. Further insights into the 3D bioprinting tissue-specific modeling panorama are presented in this paper, offering a comprehensive overview of the new possibilities for cancer study and drug discovery.

Keywords: Cancer modeling; 3D bioprinting; Biomimetic; Disease modeling

***Corresponding author:**
Gianluca Cidonio
(gianluca.cidonio@iit.it)

Citation: Bini F, D'Alessandro S, Agarwal T, *et al*., 2023, Biomimetic 3D bioprinting approaches to engineer the tumor microenvironment. *Int J Bioprint*, 9(6): 1022.
https://doi.org/10.36922/ijb.1022

Received: May 30, 2023
Accepted: July 28, 2023
Published Online: August 22, 2023

Copyright: © 2023 Author(s). This is an Open Access article distributed under the terms of the Creative Commons Attribution License, permitting distribution, and reproduction in any medium, provided the original work is properly cited.

Publisher's Note: AccScience Publishing remains neutral with regard to jurisdictional claims in published maps and institutional affiliations.

1. Introduction

Cancer is a chronic multi-factorial disease and is still among the major leading causes of death worldwide[1,2]. Cancer incidence and mortality are rapidly growing. To date, 1 in 8 men and 1 in 10 women are anticipated to be diagnosed with cancer in their lifetime[3]. Despite recent advancements in the development of new therapies and clinical initiatives, cancer progression can hardly be slowed down, posing a major challenge to the global health care system. In addition, the majority of anti-cancer drugs that resulted in tumor regression during pre-clinical testing were ultimately found to be ineffective in clinical trials.

Thus, the standard pre-clinical cancer models have limited versatility and accuracy, which are inadequate to recapitulate complex biological diseases, such as cancer[4]. Safe and effective pre-clinical cancer models are needed not only for drug screening but also as a tool for a better understanding of cancer growth and metastasis mechanism. Conventional cancer models, such as two-dimensional (2D) cultured cancer cell lines and animal models, can poorly recapitulate the patient-specific cancerous tissue, invalidating drug testing and drastically limiting further development.

The awareness of these limitations has resulted in the recent ongoing efforts toward the development of three-dimensional (3D) tumor models[5,6]. To date, research is focusing on designing physiologically relevant 3D models that are able to closely resemble the *in vivo* tumor microenvironment and heterogeneity. In light of these challenges, new bioengineering technologies have emerged in the last decade (e.g., biofabrication) and have been used to engineer platforms to mimic both healthy and diseased organs, ultimately overcoming some of the aforementioned limitations[7,8]. Particularly, 3D bioprinting technology has come to the fore for functional applications in cancer research, offering multiple strategies to precisely dispense cells and biomaterials to fabricate geometrically complex bioengineered structures with high reproducibility[9]. Importantly, *in vitro* 3D models offer a plethora of advantages and specifically the tailored design of cancer drugs following the physiological response of cancer patients, with wide application in the new field of personalized cancer medicine, such as patient-specific immunotherapy[10].

Crucially, this comprehensive review highlights the urgent need for accurate and functionally relevant 3D tumor models, showcasing the specific use of biofabrication approaches to engineer biomimetics platforms. The complexity of the mutual interactions between cancer cells and extracellular components within the tumor microenvironment is particularly discussed, highlighting key features needed for the engineering of complex cancer models. A library of biomaterial inks and 3D bioprinting technologies available for the fabrication of cancer models is listed. Ultimately, a comprehensive report of the most relevant literature contributions on 3D bioprinting of tissue-specific models is presented in this review, with particular emphasis on metastatic 3D model, to offer a thorough support for the engineering of bioinspired cancer models.

2. Tumor microenvironment

Over the last two decades, cancer research has proved that tumors cannot be identified merely as a sole agglomerate of proliferating malignant cells[11]. Hanahan and Weinberg[12] attempted to rationalize tumor complexities by describing eight distinct hallmarks of cancer as specific functional abilities acquired by cancer cells during the development of tumors. Cancerous cells should be (i) sustaining proliferative signaling, (ii) resisting cell death, (iii) evading growth suppressors, (iv) enabling replicative immortality, (v) deregulating cellular energetics and metabolism, (vi) initiating angiogenesis, (vii) activating invasion and metastasis, and (viii) avoiding immune destruction[12,13]. Thus, cancer cells can be considered the driving force of tumor growth and progression, when supported by a cooperative variety of factors[14].

Cancer agglomerates are prone to expand and attract a heterogeneous population of cells, ultimately recruited to shape (Figure 1) a tumor microenvironment (TME)[15]. The majority of the hallmarks of cancer are fostered and sustained by the contribution of stromal cells[16]. Indeed, TME is typically composed of cancer stem cells (CSCs), stromal cells (such as mesenchymal and immune cells, endothelial cells)[17-20], extracellular matrix (ECM)[21], and a plethora of cytokines and growth factors[22,23]. Cancer cells are able to direct and manipulate the function of cellular and non-cellular components through signaling networks, orchestrating events such as immunosuppression (via mechanisms including recruitment of immune suppressive cells at the tumor site, release immunosuppressive factors, and the activation of immune checkpoints [e.g., PD-L1/PD-1, CTLA-4, LAG-3, IDO1]) that can induce the apoptosis of T lymphocytes[24-26], fibroblast recruitment and their transformation into cancer-associated fibroblasts (CAFs)[27,28], and ECM remodeling[29,30], contributing to therapeutics resistance. Taken together, these events eventually result in tumor development and progression into metastatic tumors. However, recent advances in cancer therapy have made use of tumor-infiltrating lymphocytes, harnessing these powerful assets to grow them in large numbers before administering these to the patient. Drug research progresses have recently targeted tumor-

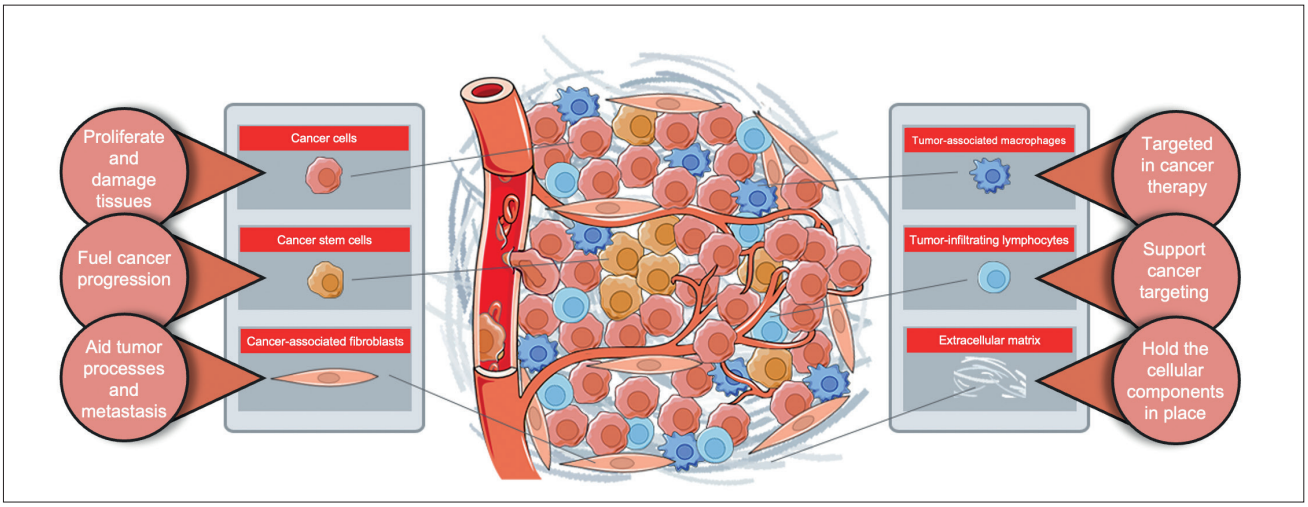

Figure 1. Tumor microenvironment (TME). The schematics summarize the principal cellular components of the TME with associated functions and the support for the maintenance, progression, and ultimate treatment of the cancerous tissue.

associated macrophages, aiming to guide phenotype polarization and thus cancer regression.

3. Engineering platforms for the study of cancer biology and metastasis

To date, most of our understanding of cancer biology is based on experiments performed either *in vitro* using conventional 2D culture models[31] or *in vivo* using xenograft animal models of human tumors[32].

2D models are economically favorable due to the low-cost maintenance of the culture and related experiments. However, 2D models are oversimplified and cannot recapitulate the native TME. In fact, 2D platforms comprise cancer cells that are cultured on flat surfaces, forced to grow as monolayers, consequently altering their morphology as well as several of their functions, critically failing to recapitulate the physiological cell–cell and cell–matrix interactions[33]. Currently, bidimensional platforms are not able to represent the tumor heterogeneity and the numerous cellular components of the TME. Moreover, unlike cancer cells *in vivo*, cells in 2D culture models receive a continuous supply of nutrients, oxygen, and other molecules which are abundantly present in the supplemented medium.

Animal models have been extensively employed for cancer research. In particular, mouse models, ranging from xenograft tumors to genetically engineered mice[34], are the most used model systems because of the low cost, small size, ease of use, and known genetic information[35]. In xenograft tumor models, cancer cells are transplanted into immunocompromised mice and allowed to grow. Although cell line-derived xenografts have the advantage to resemble the TME, cancer cells are prone to adaptations to *in vitro* growth, losing the native characteristics of the tumor. Recently, patient-derived xenografts (PDX) have been frequently used since these models are able to recapitulate the main characteristics of the host tumor[36]. On the other hand, animal models are more expensive compared to 2D models, demanding, time-consuming, and more importantly, unable to mimic the actual response of a human organism[37]. Furthermore, the high demand for test subjects needed for animal experimentation has raised ethical concerns and has led to the founding of several organizations demanding the replacement and reduction of animals in research[38]. To overcome the aforementioned limitations, 3D culture platforms have gained increasing interest by more closely mimicking the TME and providing more physiologically relevant information. Indeed, unlike cells cultured in plastic, 3D culture models are not constrained to a single layer and the additional dimensionality allows for the spatial arrangement of their surface receptors and also induces physical constraints among surrounding cells[39]. In the attempt to create 3D platforms that may recapitulate the pathophysiological functionality of TME, 3D cancer models have been developed, ranging from spheroids cultures to biomaterial scaffolds and tumor-on-a-chip platforms.

Multi-cellular tumor spheroids are a scaffold-free 3D cancer cell-only platform typically consisting of multiple type of cell aggregates that favor cell–cell interactions and produce their own ECM. As solid tumors, multi-cellular tumor spheroids (MCTS) display similar stiffness and spatial heterogeneity and also similar nutrients, oxygen, and cell proliferation gradients[40,41]. Even though more advanced compared to 2D culture models, a limiting factor of MCTS is the lack of the actual range of ECM

components of the TME and other relevant features, such as the supporting vasculature and the fluid dynamics.

Lastly, to overcome the disadvantages of MCTS models, tumor-on-a-chip[42] platforms have emerged as microfluidics cell culture devices designed to recapitulate the tumor physiology by mimicking a dynamic TME, including and providing fluid flow, perfusion, and chemical gradients. Comprehensive reviews on 3D-printed tumor-on-a-chip have been recently released with detailed insights and information[43,44].

However, although these approaches may serve as useful tools to understand the roles of biochemical and physical cues in tumor initiation and progression, these strategies lack the ability to control the location and organization of multiple cells in a complex system such as the TME.

In the last decade, tremendous efforts and progresses have been made in the development of 3D culture models that can more accurately resemble the *in vivo* tumor milieu. To this purpose, 3D bioprinting technologies and advanced biomaterials are gaining more interest because of the potential to form more complex and well-organized constructs and to better control the distribution of the cells within the 3D structure[45]. Moreover, 3D bioprinting relies on the capability of building a full range of large-scale tumor models with multiple biomaterials, various cell types, and perfusable networks with high resolution and reproducibility[46] (Figure 2).

3.1. Biomaterial inks

The biomaterials used to engineer a 3D cancer model should be selected to resemble the native TME, providing cells not only with a scaffolding structure, but also with appropriate biochemical, mechanical, and physical cues. Therefore, it is of utmost importance that the specific biomaterial mimics the physiochemical characteristics of the native ECM[17,47]. Particularly, for 3D bioprinting applications, biomaterials which can be adopted for use as biomaterial inks[48] are properly named bioinks following the addition of living cells[49,50]. Specifically, when designing a biomaterial ink, the mechanical and biochemical properties of the ink are needed to be taken into consideration for the printability and the biocompatibility of the constructs[51]. Therefore, the limitations imparted by the material itself and the choice of the bioprinting technology inevitably narrow the range of biomaterials available to engineer a 3D-bioprinted cancer model. Typically, biocompatible hydrogel material inks (>90% w/v water) can be synthesized from a wide array of naturally derived and synthetic polymers.

Naturally derived polymers are obtained from natural sources and can form hydrogels that usually demonstrate good biocompatibility and biodegradability. Naturally derived polymers could be further classified based on the native source. Indeed, polymers such as alginate, agarose, or gellan gum are obtained from plant-based or living organisms like algae or seaweeds and lack specific motifs for cell adhesion, whereas others, such as collagen, gelatin, fibrin, and even decellularized tissue-specific ECM materials, are derived from xenogeneic sources (generally vertebrates), which exhibit the inherent ability to foster cell adhesion. Despite the elevated biocompatibility and ECM-like properties, hydrogels formed from naturally derived polymers have some limitations, such as their weak mechanical properties (compared to synthetic hydrogels) or batch-to-batch variability[52], which may lead to low reproducibility and consistency.

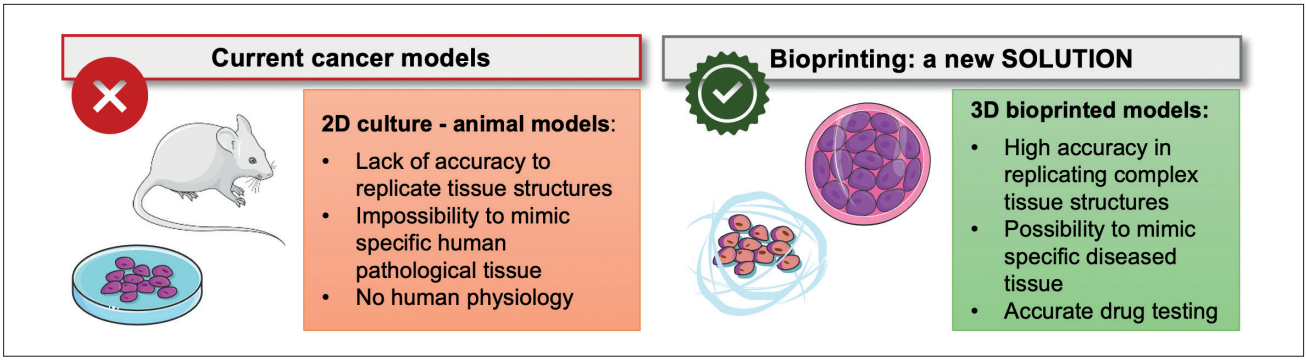

Figure 2. The evolution of cancer modeling. Standard pre-clinical cancer models often lack versatility and accuracy, making them inadequate for replicating complex biological diseases, such as cancer. Conventional cancer models, such as two-dimensional (2D) cultured cancer cell lines and animal models, struggle to accurately reproduce patient-specific cancerous tissue, compromising drug testing and significantly limiting further development. Thus, inherent physiological differences with humans, resulting in altered drug response, remain crucial considerations for the final testing of cancer therapeutics. Safe and effective pre-clinical cancer models are needed for drug screening and a better understanding of cancer growth and metastasis mechanisms. 3D bioprinting is emerging as a key technology for the rapid and reliable engineering of cancer-like tissue.

On the other hand, synthetic polymers such as polyethylene glycol (PEG) are able to form hydrogels with tunable mechanical properties, such as stiffness or degradation rate, but often lack the ability to recapitulate the native ECM due to the absence of any motif for cell adhesion. However, synthetic polymers can be engineered by chemical functionalization with various bioactive moieties, such as integrin-binding or enzymatically degradable (e.g., MMP-cleavable) peptide sequences, to enhance the ultimate functionality.

Harnessing the advantages of blending naturally derived and synthetic materials, composite inks are preferred for the fabrication of biomimetic TME models. Nevertheless, the combination of tissue type, material ink, and bioprinting technology has offered a challenging choice over the possibility of printing functional cancerous models *de novo*.

3.2. 3D bioprinting of tumor microenvironments

3D bioprinting is a revolutionizing technique in which 3D structures are fabricated via layer-by-layer deposition of biomaterials, living cells, and biomolecules for tissue engineering and regenerative medicine purposes[9]. Typically, 3D bioprinting offers several advantages, such as the ability to provide high control over spatial and temporal deposition of cells, alongside the fabrication of structures with precise size and controlled architecture. Moreover, 3D bioprinting enables the construction of tissue models in a high-throughput manner, which is indispensable to meet the need for more reliable and standardized models for anti-cancer drug screening[17].

Indeed, during the last decade, researchers have attempted to reproduce the complexity of the tumor milieu via 3D bioprinting, building biomimetic 3D *in vitro* tumor models. Taken together, the capability of using multiple cell types (including all the elements that make up the TME) and different biomaterials, along with the possibility to develop a functional vascularization, made 3D bioprinting an attractive and promising strategy to engineer 3D *in vitro* tumor models.

In the following section, the main 3D bioprinting techniques are briefly described, followed by the discussion of the more relevant studies on the development of 3D-bioprinted models that resemble various TMEs and their main features, classified by the bioprinting technique employed (Figure 3).

3.2.1. Inkjet-based bioprinting

Inkjet-based bioprinting[46] (IBB) is a non-contact 3D printing technology that allows for the positioning of cells and biomaterials into a desired pattern using small

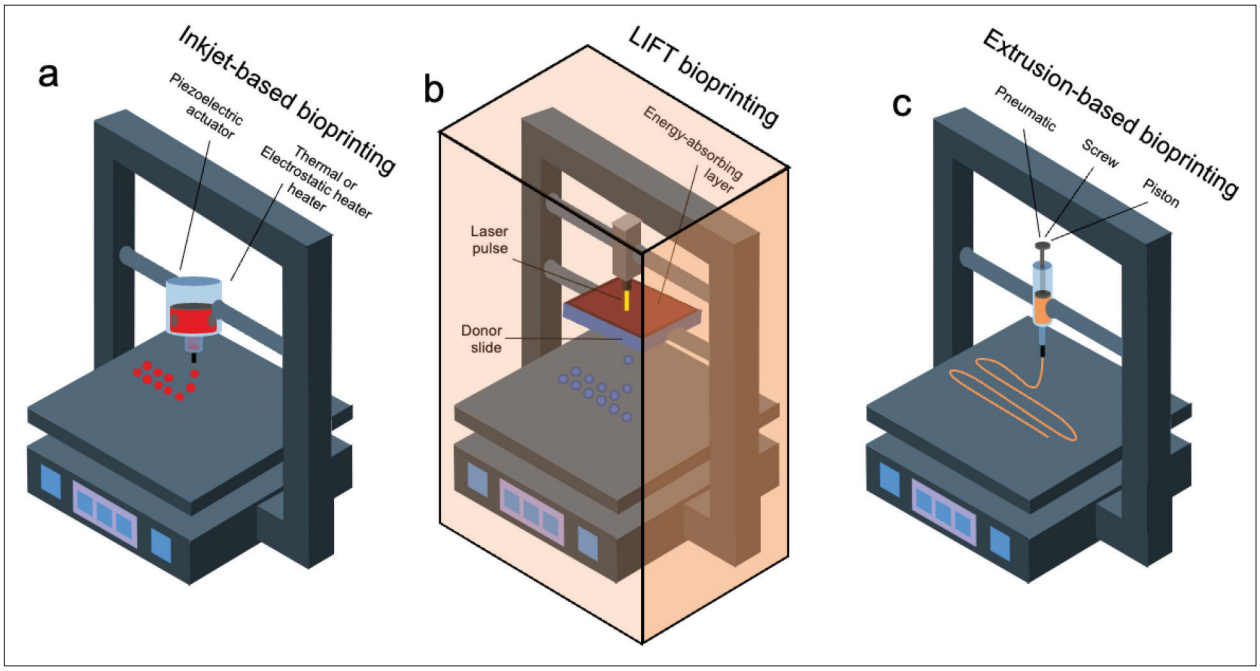

Figure 3. 3D bioprinting approaches currently explored for the fabrication of 3D cancer models. (a) Inkjet-based. Scaffolds are assembled drop-by-drop, and the fabricating ink droplet methods include piezoelectric and thermal propulsion for inkjet-based bioprinting. (b) Laser-based. This method is nozzle-free, and the scaffold is produced by transferring the cell from a donor slide to a collector using the laser. The donor site is covered by an energy-absorbing layer, and the reaction with the beam causes a precise ejection of cells. (c) Extrusion-based. This is the most widespread bioprinting approach in cancer modeling, due to the ease in control and tissue development.

volumes in the form of droplets which are dispensed by thermal or mechanical processes. IBB is a relatively low-cost technique and provides high cell viability[53] with elevated speed and high resolution[54]. IBB has been extensively employed during the last decade for the recapitulation of TMEs. Despite the numerous benefits, there are also several limitations, such as the use of polymer solutions with low concentration[9] and the lack of droplet stability and directionality during ejection. Nevertheless, IBB has been recently proven efficacious for the high-throughput patterning of cancerous micro-tissues for the rapid screening of therapeutics[55]. Overcoming the above-mentioned limitations and by harnessing the rapid planar displacement of IBB technology, cancer microenvironments could be modeled accurately by patterning tumor cells with nanoliter precision.

3.2.2. Laser-induced forward transfer bioprinting

Laser-induced forward transfer (LIFT) is a non-contact, nozzle-free technique that uses a pulsating laser as the energy source to irradiate a donor slide, causing the formation of microbubbles that propel the biomaterial onto the receiving slide in droplet form[56]. Tuning the laser energy source and printing speed[57], high-resolution 3D structures can be printed, reaching single-cell droplet accuracy[58].

In addition to the high resolution and precision of the constructs, a great advantage of laser-based technologies for 3D bioprinting applications is the absence of the nozzle that allows for fabrication with no concern for viscosity or clogging during printing. However, there are several limitations, such as the lower cellular viability[59] or the higher cost of the system, compared to other printing technologies. The exploration of the potential use of LIFT in cancer modeling has been ongoing in recent years, uncovering new ways of patterning high-throughput platforms for drug screening studies[60]. The ability of cancer tissue to resist thermal and mechanical stresses is fostering the use of laser-assisted bioprinting technologies to fabricate new biomimetic models, facilitating the engineering of new multi-cellular cancer microenvironments.

3.2.3. Extrusion-based bioprinting

Extrusion-based bioprinting (EBB) is currently the most widely used bioprinting platform in developing 3D tumor models. Biomaterial inks, used in EBB, are loaded in cartridges and extruded through a nozzle by pneumatic or mechanical forces, which allows for continuous deposition of the material in a predetermined 3D structure. Among its many advantages, EBB can rely on high printing speed and the possibility to print constructs with high cell density and good viability. Hydrogel-based materials are the most reliable inks to be used in conjunction with living cells with EBB platforms. Nevertheless, specific physicochemical parameters must be optimized prior to extrusion. For instance, hydrogels with high viscosity inevitably expose cells to high shear stress at the nozzle and also to increased pressure in the syringe during printing, both of which can greatly impact cell viability[61,62].

However, EBB is a low-cost, simple and highly flexible technology that has been adapted to house multi-material and co-extrusion printing[63,64]. Harnessing the EBB functionality, 3D *in vitro* cancer models used for investigating tumor progression and anti-cancer drug resistance have been recently fabricated. For instance, 3D matrices printed through EBB can function as ideal platforms to promote the formation of tumor spheroids and offer long-term proliferation cell culture.

Ultimately, EBB is a popular 3D bioprinting platform to develop 3D tumor models not only because of the associated low-cost and simple utilization but also by the virtue of flexibility and suitability for implementations (e.g., co-extrusion, microfluidic-assisted bioprinting[34]). On the other hand, the choice of biomaterial ink is subjected to strict requisites and determined parameters (e.g., viscosity), which could significantly impact cell viability.

However, the latest advancement of engineering technologies has greatly facilitated the customization of EBB set-up to accommodate the fabrication of functional tumor models. Thus, a variety of novel approaches, such as the direct printing of cell, spheroid, organoid printing[65], as well as the engineering of new vascularized structure[66], have been attempted lately. Typically, the low resolution (>100 μm) cannot allow to create highly detailed structure, but recent effort has been focused on functionalizing EBB-fabricated tissues with cancer spheroids to improve ultimate functionality of the model to validate and test new anti-cancer drugs[67].

4. 3D bioprinting bioinspired tumor models

Biofabrication is currently shaping cancer research, coming to the fore as a high-throughput screening platform to test the safety and efficacy of new drugs, while replicating pathophysiological processes and events *in vitro*. Therefore, the unparalleled ability of bioprinted and bioinspired models to recapitulate aggressive and deadly primary (breast and brain) and secondary (lung and bone) tumors and biological processes has been recently harnessed for the fabrication of novel biomimetic models. Here, we list the most recent work on tissue-specific bioprinted cancer models, providing a comprehensive library for 3D-bioprinted tumor tissue replicas (Figure 4) with a classification that can be found in Table 1.

Table 1. 3D-bioprinted cancer models

Cancer model	Bioprinting technique	Biomaterial ink	Cell types		Key features	Ref
Breast cancer	(Co-axial)	Modified alginate	Human breast adenocarcinoma cells Mouse macrophage cells	IC V	• Macrophages migration • Blood vessel-like structures	[71]
	Extrusion-based	Gelatin and alginate	IMR-90 fibroblast cells MDA-MB-231 breast cancer cells		• Migration of fibroblasts	[70]
	Extrusion-based		Breast cancer cells Normal mammary epithelial cells		• Chimeric organoids underwent epigenetic alterations	[72]
	Inkjet	Gelatin (as template for sacrificial arrays) PEG-DMA (for concave wells)	MCF7 human breast cancer cells	TG	• Promote spheroids formation	[68]
	Laser-based (direct write)	Gelatin, alginate and chitosan	MDA-MB-231 human breast cancer cells	TG	• Multi-cellular spheroids formation • Effect of tumor spheroids size on internalization of transferrin	[120]
Metastatic breast cancer	Laser-based (stereolithography)	GelMA + nHA	MDA-MB-231 breast cancer cells Primary human bone marrow MSCs Osteoblasts	V	• Higher VEGF expression	[69]
	Laser-based (stereolithography)	PEG-DA + PEG + nHA	MDA-MB-231 breast cancer cells Human fetal osteoblast cell line (hFOB)	TG	• Promote spheroids formation	[121]
CNS tumors	Extrusion-based	Gelatin, alginate, and fibrinogen	Glioma stem cells	V	• Higher VEGF expression Higher chemoresistance to temozolomide	[75]
	(Co-axial)	Alginate and gelatin	GSC23 human glioma stem cells Human mesenchymal stem cells (HMSCs)		• Tumor–stroma cells interaction	[122]
	(Co-axial)	Alginate	GSC23 human glioma stem cells U118 glioma cells	EV	• Higher VEGFR2 expression • Higher matrix metalloproteinases (MMPs) expression	[123]
	Extrusion-based	GelMA and gelatin	Glioblastoma-associated macrophages (GAMs) Glioblastoma cells	IC	• Interaction between glioblastoma-associated macrophages and glioblastoma cells	[76]
	Extrusion-based	RGD-alginate Hyaluronic acid Collagen-1	U87MG glioblastoma cells MM6 monocyte/macrophages		• Higher chemoresistance to cisplatin	[124]
	Extrusion-based	GelMA and algMA	SK-N-BE neuroblastoma cells	V	• Blood vessel-like structures	[77]
	Inkjet-based	Agarose and collagen	Human primary umbilical cord-derived mesenchymal stromal cells (UC-MSC) Human primary umbilical vein endothelial cells (HUVEC) Human bone marrow-derived epithelial–neuroblastoma immortalized cells (SH-SY5Y)		• Formation of Homer–Wright-like rosettes • Formation of vimentin-rich matrices	[74]
Lung cancer	Extrusion	Gelatin and alginate	NSCLC PDX cell line Lung CAFs		• Cellular crosstalk between CAFs and NSCLC cells	[81]
	Extrusion-based	Gelatin, alginate, fibrinogen	Human vascular endothelial cells (HUVECs) Lung fibroblasts (LFs)		• Cell proliferation, mRNA metabolism, and anti-apoptotic activity increased with stiffness	[80]
Bone cancer	Extrusion-based	Hydroxyapatite, poly(dopamine), carboxymethyl chitosan	Murine bone marrow stroll cells (mBMSCs)		• High application potential of composite scaffold in bone tumor therapy	[90]
	Extrusion	Alginate, gelatin, chitosan	Saos-2, UMR-106 osteosarcoma cell lines	TG	• Proof of concept for the engineering of a novel osteosarcoma ink	[94]
	Extrusion-based	Alginate, gelatine	Saos-2		• Active hydrogel for bioartificial bone tissue	[97]

Studies were classified based on the specific tissue type. Key features of reported studies have been reportedare mentioned in the table,: "highlighting Tumour growth, TG" stands for: tumor growth (formation of spheroids, long-period culture, etc.);, "IC": stands for Iimmune cells, IC; ECM, "E": stands for ECM (deposition, remodelling, degradation, etc.); , Vasculature, "V" stands for: vasculature (vessel-like structures, angiogenesis etc.); and, Metastasis, "M:" stands for metastasis.

4.1. Breast cancer

Breast cancer is among the deadliest malignancies affecting women worldwide, progressing through specific stages from epithelial hyperproliferation to metastasis. Modeling 3D breast cancer TME has proved to be effective for drug testing and emulating drug resistance mechanisms.

Ling *et al.*[68] used a custom-built bioprinting system to print sacrificial gelatin arrays as templates for fabricating concave wells and *in situ* seeding of breast cancer cells to form cellular spheroids in a controlled and high-throughput manner (Figure 4a). Similarly, Zhou *et al.*[69] employed the same method to fabricate bone matrices composed of gelatin methacryloyl (GelMA) and nano hydroxyapatite (nHA) and observed the interaction between breast cancer cells and stromal cells (hFOB cells and MSCs). Relevantly, breast cancer cells were found to inhibit cell proliferation of osteoblasts and MSCs. Vascular endothelial growth factor (VEGF) was found overexpressed and secreted by breast cancer cells with associated decreased alkaline phosphatase (ALP) activity of osteoblasts[69]. Jiang *et al.*[70] used a composite hydrogel biomaterial ink, composed of gelatin and alginate, to embed and subsequently extrude breast cancer cells and cancer-associated fibroblasts (CAFs). The bioprinted co-culture models were able to provide a biomimetic environment for more than 30 days and showed the formation of MCTS after 7 days of co-culture. Moreover, after 15 days of co-culture, fibroblasts migrated through a non-cell region of the hydrogel matrix and infiltrated the MCTS[70].

Recently, the modeling of the immune response to breast cancer progression has been modeled by Grolman *et al.*[71], who fabricated vessel-like structures by extruding peptide-conjugated alginate under controlled flow rates. The core of the fibers was filled with macrophages (RAW 264.7 mouse macrophages), while tumor cells (MDA-MB-231 human breast adenocarcinoma cells) were incorporated in the surrounding peptide-modified alginate to support cell adhesion. By changing the architecture of the fibers, these highly tunable models allowed to investigate the interactions between tumor cells and other cell types of the TME and could be useful in resembling vasculature and modeling metastasis[71].

Reid *et al.*[72] developed a platform to investigate tumorigenesis and the process of TME control of breast cancer. A 3D collagen-based model was engineered, to incorporate breast cancer cells and mammary epithelial cells to drive tumoroid and chimeric organoids formation. The TME-driven mechanism of epigenetic alterations of cancer cells within chimeric organoids was confirmed by a significant increase in 5-hydroxymethylcytosine (an intermediate of active DNA demethylation process) levels compared to tumoroids[72].

4.2. Central nervous system tumors

Glioblastoma (GBM) is the most common malignant primary brain cancer worldwide[73]. The incidence GBM is lower compared with other primary cancers, but it is particularly aggressive and impactful for the patients' quality of life. Thus, the urgency for new therapeutic treatments is recently fueling the engineering of functional GBM models.

Recently, Campos *et al.*[74] developed a 3D-bioprinted neuroblastoma model by printing human bone marrow-derived epithelial-neuroblastoma immortalized cells (SH-SY5Y), human primary umbilical cord-derived mesenchymal stromal cells (UC-MSC), and primary human umbilical vein endothelial cells (HUVECs) with a collagen type I-based biomaterial ink. Cancer cells within the bioprinted constructs showed the formation of Homer–Wright-like rosettes (phenotypic hallmark of neuroblastomas) and produced vimentin-rich matrices (characteristic of an aggressive phenotype), triggered by the presence of MSCs within the bioprinted model[74].

Dai *et al.* employed a similar ink system composed of gelatin, alginate, and fibrinogen, to embed glioma stem cells and build a 3D-bioprinted model by mimicking the brain tumor microenvironment. The 3D-bioprinted model exhibited higher resistance to temozolomide (an alkylating anti-tumor agent) compared to 2D culture models and higher expression of nestin and VEGF, showing the vascularization potential of glioma stem cells[75].

Similarly, Heinrich *et al.*[76] developed a platform to study the interaction between glioblastoma cells and macrophages. With the fabrication of bioprinted mini-brains, a highly controlled TME was engineered to recruit GBM-associated macrophages (GAM) and polarize them into a GAM-specific phenotype. Furthermore, the study demonstrated how therapeutics that inhibit the interaction between GAMs and glioblastoma cells lead to diminished tumor growth and reduced chemoresistance[76].

Recently, Monferrer *et al.*[77] used a 3D-bioprinted platform, based on malignant neuroblastic cells and hydrogels made from GelMA and different percentages of methacrylated alginate (AlgMA), to study the effects of ECM stiffness on neuroblastic cells over time. Their findings showed an increase in cell proliferation, mRNA metabolism, and anti-apoptotic activity with stiffness, while cell cluster density and occupancy decreased[77].

Furthermore, Yi *et al.*[78] used 3D bioprinting to fabricate a 3D GBM model consisting of patient-derived tumor cells, vascular endothelial cells, and decellularized ECM in order to recapitulate the main features of native GBM (Figure 4b). Using this platform, the authors observed that this model produced evidence that matched clinically

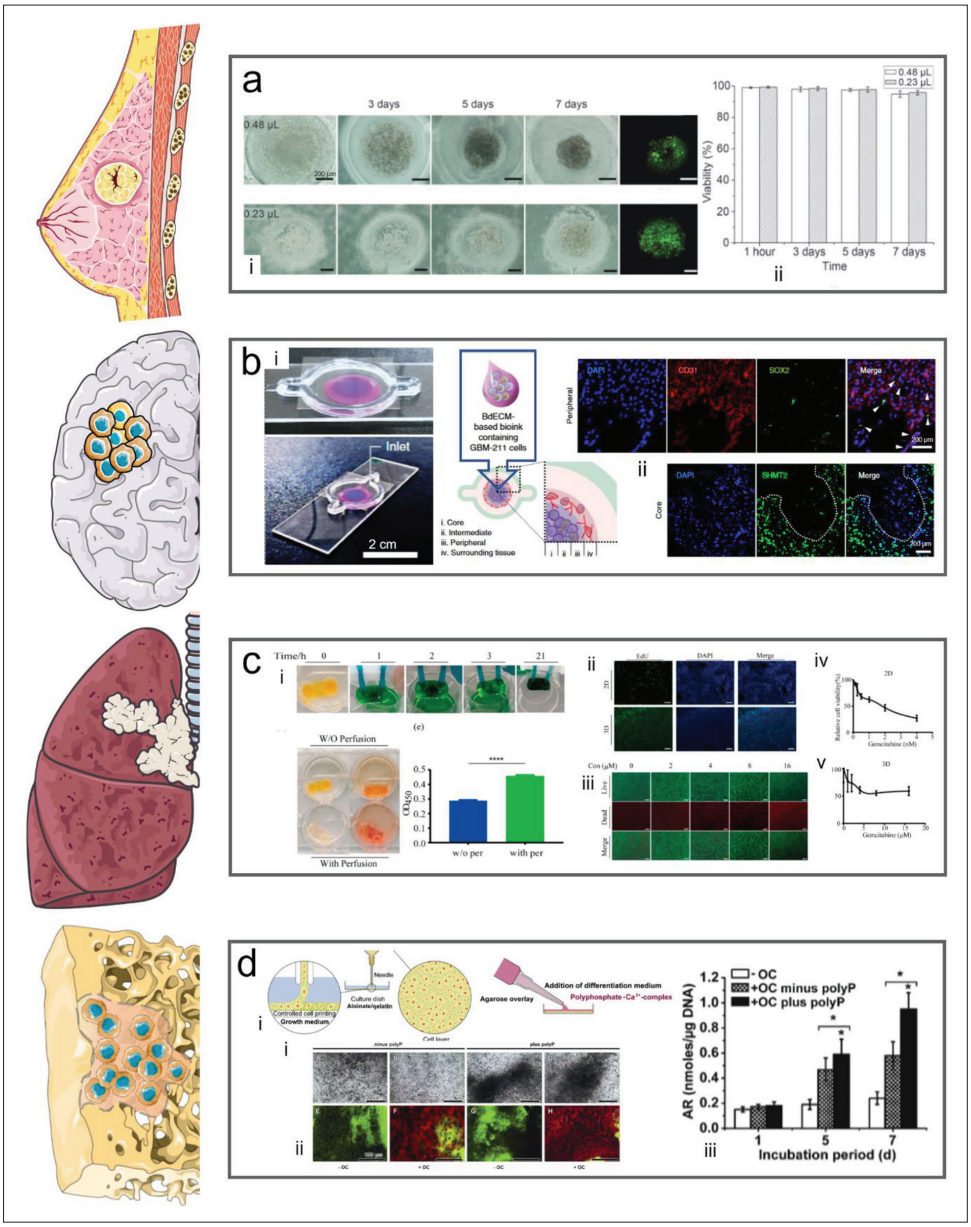

Figure 4. Tissue-specific cancer 3D-bioprinted models. (a-i) Cellular spheroids are deposited in concave hydrogel wells, and the cell development was observed for 7 days. Two sizes of droplets, 0.48 μL and 0.23 μL, were used; calcein and ethidium bromide staining were applied, and the same cell-seeding density of 1×10^6 cells/mL was used. To examine the impact of cell density on spheroid formation, the constructs were examined with live/dead fluorescence images which show the viability of encapsulated cells (ii) right after (1 h) and over long-term culture (3, 5, and 7 days). Adapted with permissions from ref.[68]. (b-i) Micrographs and a visual representation in diagram form depicting the compartmentalized structure of 3D GBM, which is composed by different various bioinks and other materials to mimic a compartmentalized structure. In the middle, there is BdECM bioink containing GBM cells (blue). (b-ii) Representative immunostaining images in the core and peripherical regions using DAPI for cell nuclei, CD31 for HUVECs, and SOX2 for resistant cancer cells. Adapted with permissions from ref.[78]. (c-i) 3D-bioprinted model perfused in dynamic flow. Models were cultured in regular media and controlled with untreated models, following XTT reagent exposure. Perfused models were compared against the constructs cultured under static conditions. (c-ii) Cell viability was investigated against 2D controls, while (c-iii) 3D culture was exposed to gemcitabine compounds with increasing concentration to demonstrate cytotoxicity following *in vitro* culture and (c-iv) quantified and compared to 2D controls. Adapted with permissions from ref.[83]. (d-i) Schematic representation of the procedure: the alginate/gelatin/Saos-2 is filled into a cartridge. The scaffold is submersed into McCoy's medium/FCS and overlayed with an agarose layer containing poly-P·Ca^{2+}-complex as a differentiation medium. (d-ii) The effect of poly-P·Ca^{2+}-complex, and in parallel, the effect of the osteogenic cocktail on the extent of mineralization, is reported herein. The cultures were incubated in the absence (minus polyP) and presence (plus polyP) of poly-P·Ca^{2+}-complex. They were observed in the absence (- OC) and presence (+ OC) of the osteogenic cocktail. (d-iii) The graft presents a quantitative assessment of the extent of mineralization using Alizarin Red S as an indicator reagent after 1, 5, and 7 days. Adapted with permissions from ref.[98].

observed patient-specific resistances after concurrent chemoradiation using temozolomide[78].

4.3. Lung cancer

Cancerous lung tissue is highly aggressive, forming fibrotic aggregates that can impede the physiological functionality of the lungs. There is an urgent need for physiological models that can resemble lung cancerous microenvironments for the rapid and efficacious testing of anti-tumor drugs. Bioprinting can aid the modeling of pathological conditions of the lung to mimic the intricate interwoven vascular and epithelial networks[79].

In this context, Han *et al.*[80] recently built a 3D-bioprinted vascularized tumor model which involved the fabrication of a blood vessel layer obtained through the printing and culturing of HUVECs and lung fibroblasts in a gelatin/alginate/fibrinogen hydrogel, followed by seeding multicellular MCTS onto the pre-formed layer. The sprouting of new blood vessels occurred in the surroundings of spheroids, driving their increase in dimensions over time. Noticeably, treatment with temozolomide (an alkylating anti-tumor agent) and sunitinib (angiogenic inhibitor) resulted to be more successful than temozolomide alone in targeting spheroids surrounded by vessel network[80].

In another study, Mondal *et al.*[81] developed a similar biomaterial ink (comprising gelatin and alginate) to embed and print non-small cell lung cancer (NSCLC) PDX cells and lung CAFs co-cultures. The bioprinted co-culture models enabled the formation of MCTS and cellular crosstalk through the upregulation of α-SMA, vimentin, and loss of E-cadherin[81].

A recent study by Dong *et al.*[82] engineered a novel droplet-based approach to 3D-bioprint lung cancer organoids in a high-throughput fashion for rapid drug testing. The alginate and hyaluronic acid-based material ink was functionalized with RGD groups, further stimulating the functionality post-printing. In comparison with 2D control, the 3D-printed organoid system demonstrated higher viability and ultimate functionality with an expression of P-CK, MUC1, and caveolin-1.

Using a digital light processing approach, Mei *et al.*[83] fabricated a new perfusable 3D lung cancer model (Figure 4c) with NSCLC cells for screening anti-cancer drug candidates and investigating the effects of gemcitabine in static and dynamic conditions. They Mei and colleagues found a significant drug-mediated effect, confirming the safety and efficacy potential of such model.

4.4 Bone cancer

Bone tumors arising in the bone or from bone-derived cells and tissues are classified as primary and those originating in other sites and metastasize to the skeleton are as secondary[84]. Both tumor types are characterized by a composite microenvironment that comprises an array of elements, including mechanical and architectural cues, signaling proteins, and interactions between the bone tumor and the stromal cells, that overall impact growth, drug sensitivity, and ultimately therapy outcome[85].

Particularly, primary bone tumors, also known as bone sarcomas, are rare malignant tumors characterized by the uncontrolled growth of cells within the bone[86]. The current standard treatment protocol is composed of the association of surgery with adjuvant and/or neoadjuvant multi-agent chemotherapy, which leads to a 5-year survival for the most common malignant bone tumors of around 70%[87]. Conventional malignant bone sarcomas include: (i) osteosarcoma (OS), localized in the metaphysis of the long bone in adolescents near the growth plate; (ii) Ewing's sarcoma, most commonly localized in the pelvis, legs, or arms of children and young adults; and (iii) chondrosarcoma, usually confined in the pelvis, legs, or arms in middle-aged and older adults, where the cancerous cells produce cartilage[88]. The majority of primary bone tumor models have been developed, attempting to recapitulate OS features and pathophysiology *in vitro*. Indeed, OS is the most common sarcoma, and it is characterized by cancerous cells producing woven bone. While mature bone is composed of sparse osteocytes, conventional OS consists of densely populated tissue with cells that exhibit osteo-, chondro-, or fibroblastic phenotype[89].

3D bioprinting has been recently applied to the treatment of OS[90,91] as well as the generation of OS models[92-94]. Multiple studies have used OS cell lines for biocompatibility evaluation and as proliferation models in lieu of OS model engineering[95]. Indeed, only a limited number of 3D-bioprinted models have been ultimately fabricated to recapitulate the complex primary bone TME *in vitro*[91,96]. In early attempts to replicate OS TME, Neufurth *et al.*[97] biofabricated a composite ink comprising alginate/gelatin mixture for encapsulating and printing Saos-2 cells. The use of a further coating prepared from agarose and calcium salt polyphosphate [polyphosphate (polyP)·Ca^{2+}-complex] was found to actively promote the proliferation[97] and, in conjunction with bioactive glass nanoparticles[98], the ability to mineralize cancer cells (Figure 4d).

4.5. Modeling vasculature in 3D-bioprinted cancer models

The presence of a functional vascular network is pivotal for the growth and survival of cancerous tissues. Typically, vascularization plays a critical role in (i) supplying oxygen,

nutrients, and signaling molecules to the tumor, as well as (ii) facilitating the removal of waste products. However, in a pathological scenario such as cancer progression, the angiogenetic process is radically upregulated and sustained to maximize the tumor survival and spreading ratio. Typically, the oxygen diffusion within a 3D-bioprinted construct is slower than its consumption[99]. Thus, the gaseous and nutrition kinetics is a limiting factor for cancer maturation *in vitro* and often fails to replicate the highly vascularized tumor mass that is present *in vivo*. To study and recapitulate complex dynamics happening as a consequence of the intense angiogenic kinetic within the tumor mass, new studies are exploring 3D bioprinting to engineer customizable vessels within the biofabricated cancer tissue. The importance of such models has been recently highlighted elsewhere[100].

The incorporation of vascular networks in 3D-bioprinted cancer models holds great promise for advancing the understanding of tumor angiogenesis and impact on tumor growth and ultimate response to therapeutic agents. Kim *et al.*[101] have recently demonstrated the possibility to engineer 3D-bioprinted cancer-vascular model by *in situ* cell printing technology. The impact of vascular supply to cancer spheroids was investigated in three dimensions, finding that the close proximity of new vessels stimulates epithelial-to-mesenchymal transition (EMT), while affecting vascular physiology by driving inflammation. The latest study from Franca *et al.*[102] revealed the supporting effect of pericytes to guide the maturation of new vessel sprouting in 3D-bioprinted models. This approach might hold the potential to closely mimic pathological angiogenesis *in vitro*. These models may provide a functional platform to investigate how the spatial arrangement and functional properties of blood vessels influence the behavior of cancer cells, the formation of metastases, and the efficacy of anti-cancer treatments[103]. Furthermore, the ability to engineer customizable vessels within the biofabricated cancer tissue opens to new avenues for drug testing and anti-angiogenic therapies.

New engineering approaches are harnessing artificial intelligence (AI) technologies to aid the development of biomimetic vascularized cancer models[104]. The use of novel AI tools can be applied to the investigation of angiogenic potential in *ex vivo* models (such as chicken chorioallantoic membrane [CAM]) to elucidate new ways of disrupting the tumor vascularization. In turn, these new ways of modeling tumor angiogenesis might be harnessed to explore the untapped potential for the study of metastasis.

4.6. Engineering models for the metastatic niche

Tumor metastasis is believed to be the main cause of cancer-related deaths, consisting of a series of complex pathways which lead to the dissemination of tumor cells from the primary tumor site to a secondary site[105]. Metastasis consists of a complex succession of cell-biological events, which can be divided into three major events, including (i) tumor cells exiting their primary sites of growth (EMT of cancerous cells, local invasion, intravasation)[106], (ii) tumor cells translocating from their primary site (survival in the circulation, arrest at a secondary site, extravasation)[107,108], and (iii) tumor cells adapting to survive in distant sites (micro-metastasis formation, metastatic colonization)[109-111].

In particular, angiogenesis and vascularization have a critical role to play in events associated with tumor growth and metastasis[112,113]. The tumor vasculature is structurally immature, leaky, chaotically organized, and poorly perfused. Blood vessel leakiness along with interstitial fibrosis and stromal fibroblast-mediated interstitial matrix contraction elevates interstitial fluid pressure (IFP) and induces hypoxic environment[114]. Metastatic models are challenging to 3D-print, due to a superior architectural complexity and culturing methodology. In a pioneering work by Lee *et al.*[115] to engineer a biomimetic metastatic model, a microfluidic bioprinting system was used to deposit GB cells to model the GBM TME via accurate deposition and use of *ad-hoc* designed biomaterial ink. Indeed, the printed GBM cells were found to be able to spontaneously assemble into spheroids post-printing and express significantly elevated levels of CD133 proteins and DCX markers, demonstrating the ability to replicate metastatic invasiveness and niche.

Secondary metastatic sites often act as a cancer reservoir, enhancing dramatically the chances of tumor-driven death. Bone is among the most common metastatic site in patients with advanced cancer. Once tumor cells reach the skeleton, the disease is generally declared incurable, and treatment is only palliative. The majority (70%) of breast, prostate, and lung carcinomas form deadly metastases in the bone tissue[116]. More than half of the patients affected by skeletal metastasis experience at least a skeletal-related events within 24 months from diagnosis[117]. Besides having a significant impact on patients, these skeletal-related events are associated with substantial costs for the health care system[118]. Therefore, new bioinspired models that can closely recapitulate the intricate metastatic process from a primary tumor site to the skeletal tissue are urgently needed. Thus, 3D bioprinting holds the potential to generate complex shapes with precise spatially defined cell distribution, to better represent both early and late events in the development and the formation of the metastasis. Recently, Meng *et al.*[119] engineered a 3D-bioprinted *in vitro* tumor model mimicking the metastatic dissemination of primary

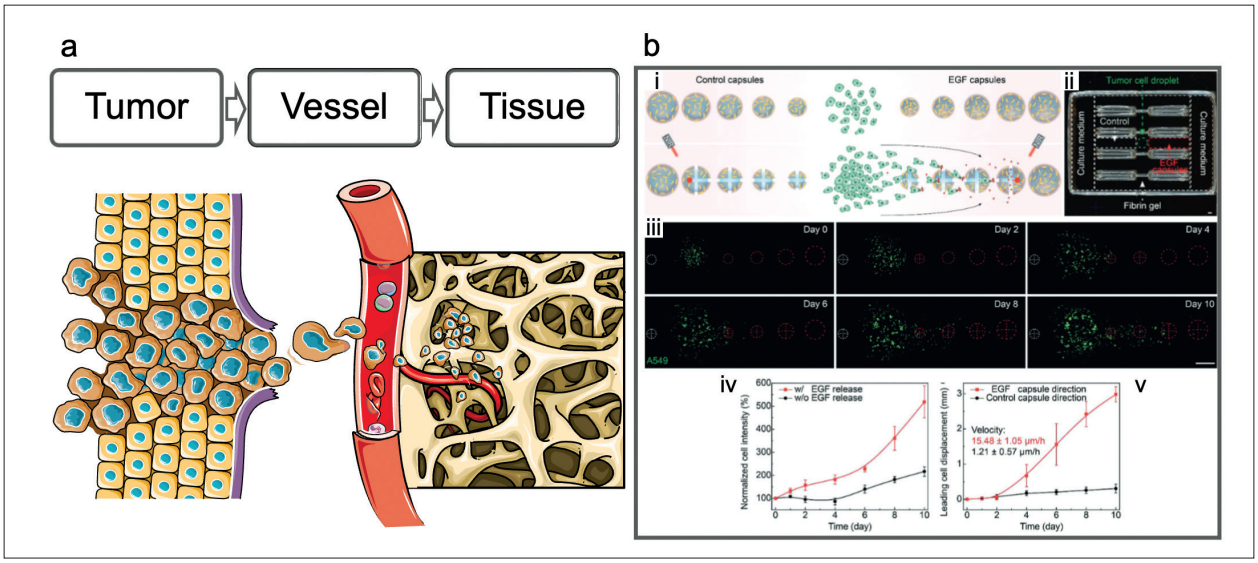

Figure 5. Engineering 3D metastatic models. (a) Schematization of metastasis niche extravasation, migration, and homing, favoring the propagation of tumor cells from the primary tumor to secondary sites. (b-i) A sketch of control and drugged capsules with epidermal growth factor (EGF) where the directional migration of tumor cells was led by EGF gradients. (b-ii) A picture of a 3D-printed culture chamber for testing the guided cell migration. (b-iii) Fluorescence images show the distribution of cells. The white circle is the control, and the red circles indicate the EGF capsules. (b-iv) The graph shows the cellular fluorescence intensity of A549 cells normalized by intensity at day 0, and EGF release (red) was compared to no EGF release (black) over time. (b-v) The plot illustrates the displacement of cells in the X-direction toward the EGF capsules, revealing the directional influence of EGF on cell migration. Adapted with permissions from ref.[119].

cancerous tissue (Figure 5). A multi-cellular TME is recreated using tumor cells and endothelial cell-lined vascular conduits within a fibrin gel containing functional fibroblasts. 3D-printed microcapsules were loaded with growth factors and selectively disrupted with a laser source to guide VEGF or EGF release. The effect of the released molecules influenced the TME progression, offering a new tool to probe the spatiotemporal evolution of specific pro-metastatic tumors.

5. Conclusion and future outlooks

In the past decade, the advances in 3D bioprinting have allowed the development of biomimetic 3D tumor models that can mimic TMEs more accurately. Despite the remarkable progresses, there are still several limitations to solve to obtain physiologically relevant *in vitro* tumor models. For instance, a high cell viability and long-term cultures, or cell native phenotypes and functions, are still difficult to maintain within 3D-bioprinted platforms. Thus, 3D biomimetic models are still far from recapitulating the complexity of TMEs. Considering these challenges, the engineering of new bioinspired material inks, along with the characteristics of the bioprinting technique and cell sources, plays a pivotal role.

Patient-derived ECM or biomaterials inks that accurately mimic the native ECM of specific tumors should be used to allow cancer cells to achieve and maintain their native phenotypes and physiological functions. Moreover, the absence of standardized bioinks in terms of polymeric composition and cell encapsulation density could lead to difficulties in the reproducibility of the experiments and in the correlation of the results. Furthermore, new features of existing bioprinting platforms, innovative implementations, and new technologies, such as microfluidic-assisted bioprinting[34], co-extrusion, or multi-material bioprinting, are promising tools to meet the need of multi-cellular and vascularized tumor models. Lastly, to overcome the use of immortalized cell lines, the use of patient-derived primary cells is promising for the development of biomimetic *in vitro* platforms for personalized drug screening and therapies. The lack of cancer-specific models is a worrisome problem, which points to the urgent need to seek the assistance of bioengineers and biologists to fabricate a model for the study of cancer progression and the test of new drugs against tumors.

Acknowledgments

None.

Funding

This study was supported by funding from AIRC Aldi Fellowship (GC) under grant agreement No. 25412.

Conflict of interest

The authors declare no conflicts of interests.

Author contributions

Conceptualization: Tarun Agarwal, Daniele Marciano, Gianluca Cidonio
Formal analysis: Salvatore D'Alessandro, Tarun Agarwal, Daniele Marciano, Gianluca Cidonio
Investigation: Salvatore D'Alessandro, Tarun Agarwal, Daniele Marciano, Gianluca Cidonio
Methodology: Fabiano Bini, Salvatore D'Alessandro, Tarun Agarwal, Daniele Marciano, Gianluca Cidonio
Funding acquisition: Giancarlo Ruocco, Gianluca Cidonio
Writing – original draft: All authors
Writing – review & editing: Serena Duchi, Enrico Lucarelli, Gianluca Cidonio

Ethics approval and consent to participate

Not applicable.

Consent for publication

Not applicable.

Availability of data

Not applicable.

References

1. Fitzmaurice C, Abate D, Abbasi N, *et al.*, 2019, Global, regional, and national cancer incidence, mortality, years of life lost, years lived with disability, and disability-Adjusted life-years for 29 cancer groups, 1990 to 2017: A systematic analysis for the global burden of disease study. *JAMA Oncol*, 5(12): 1749–1768.

   https://doi.org/10.1001/jamaoncol.2019.2996

2. Siegel RL, Miller KD, Wagle NS, *et al.*, 2023, Cancer statistics, 2023. *CA Cancer J Clin*, 73(1): 17–48.

   https://doi.org/10.3322/caac.21763

3. Bray F, Ferlay J, Soerjomataram I, *et al.*, 2018, Global cancer statistics 2018: GLOBOCAN estimates of incidence and mortality worldwide for 36 cancers in 185 countries. *CA Cancer J Clin*, 68(6): 394–424.

   https://doi.org/10.3322/caac.21492

4. Kamb A, 2005, What's wrong with our cancer models? *Nat Rev Drug Discov*, 4(2): 161–165.

   https://doi.org/10.1038/nrd1635

5. Pape J, Emberton M, Cheema U, 2021, 3D cancer models: The need for a complex stroma, compartmentalization and stiffness. *Front Bioeng Biotechnol*, 9, 1–8.

6. Sajjad H, Imtiaz S, Noor T, *et al.*, 2021, Cancer models in preclinical research: A chronicle review of advancement in effective cancer research. *Anim Model Exp Med*, 4(2): 87–103.

   https://doi.org/10.1002/ame2.12165

7. Li M, Song X, Jin S, *et al.*, 2021, 3D tumor model biofabrication. *Bio-Design Manuf*, 4(3): 526–540.

   https://doi.org/10.1007/s42242-021-00134-7

8. Celikkin N, Presutti D, Maiullari F, *et al.*, 2021, Tackling current biomedical challenges with frontier biofabrication and organ-on-a-chip technologies. *Front Bioeng Biotechnol*, 9: 732130.

9. Murphy SV, Atala A, 2014, 3D bioprinting of tissues and organs. *Nat Biotechnol*, 32(8): 773–785.

   https://doi.org/10.1038/nbt.2958

10. Kakimi K, Karasaki T, Matsushita H, *et al.*, 2017, Advances in personalized cancer immunotherapy. *Breast Cancer*, 24(1): 16–24.

    https://doi.org/10.1007/s12282-016-0688-1

11. Balkwill FR, Capasso M, Hagemann T, 2012, The tumor microenvironment at a glance. *J Cell Sci*, 125(23): 5591–5596.

    https://doi.org/10.1242/jcs.116392

12. Hanahan D, Weinberg RA, 2000, The hallmarks of cancer. *Cell*, 100(1): 57–70.

13. Hanahan D, Robert AW, 2017, Biological hallmarks of cancer. *Holland-Frei Cancer Med*, 01(April): 1–10.

    https://doi.org/10.1002/9781119000822.hfcm002

14. Hanahan D, Coussens LM, 2012, Accessories to the crime: Functions of cells recruited to the tumor microenvironment. *Cancer Cell*, 21(3): 309–322.

    https://doi.org/10.1016/j.ccr.2012.02.022

15. Guo S, Deng CX, 2018, Effect of stromal cells in tumor microenvironment on metastasis initiation. *Int J Biol Sci*, 14(14): 2083–2093.

    https://doi.org/10.7150/ijbs.25720

16. Bussard KM, Mutkus L, Stumpf K, *et al.*, 2016, Tumor-associated stromal cells as key contributors to the tumor microenvironment. *Breast Cancer Res*, 18(1): 1–11.

    https://doi.org/10.1186/s13058-016-0740-2

17. Wang W, Dai J, Huang Y, *et al.*, 2023, Extracellular matrix mimicking dynamic interpenetrating network hydrogel for skin tissue engineering. *Chem Eng J*, 457(November 2022): 141362.

    https://doi.org/10.1016/j.cej.2023.141362

18. Meacham CE, DeVilbiss AW, Morrison SJ, 2022, Metabolic regulation of somatic stem cells in vivo. *Nat Rev Mol Cell Biol*, 23(6): 428–443.

    https://doi.org/10.1038/s41580-022-00462-1

19. Ju F, Atyah MM, Horstmann N, *et al.*, 2022, Characteristics of the cancer stem cell niche and therapeutic strategies. *Stem Cell Res Ther*, 13(1): 1–17.

https://doi.org/10.1186/s13287-022-02904-1

20. Papaccio F, Paino F, Regad T, *et al.*, 2017, Concise review: Cancer cells, cancer stem cells, and mesenchymal stem cells: Influence in cancer development. *Stem Cells Transl Med*, 6(12): 2115–2125.

https://doi.org/10.1002/sctm.17-0138

21. Winkler J, Abisoye-Ogunniyan A, Metcalf KJ, *et al.*, 2020, Concepts of extracellular matrix remodelling in tumour progression and metastasis. *Nat Commun*, 11(1): 5120.

https://doi.org/10.1038/s41467-020-18794-x

22. Lee HM, Lee HJ, Chang JE, 2022, Inflammatory cytokine: An attractive target for cancer treatment. *Biomedicines*, 10(9): 2116.

https://doi.org/10.3390/biomedicines10092116

23. Kartikasari AER, Huertas CS, Mitchell A, *et al.*, 2021, Tumor-induced inflammatory cytokines and the emerging diagnostic devices for cancer detection and prognosis. *Front Oncol*, 11: 692142.

24. Tie Y, Tang F, Wei Y, *et al.*, 2022, Immunosuppressive cells in cancer: Mechanisms and potential therapeutic targets. *J Hematol Oncol*, 15(1): 61.

https://doi.org/10.1186/s13045-022-01282-8

25. Labani-Motlagh A, Ashja-Mahdavi M, Loskog A, 2020, The tumor microenvironment: A milieu hindering and obstructing antitumor immune responses. *Front Immunol*, 11: 940.

26. Saleh R, Elkord E, 2020, Acquired resistance to cancer immunotherapy: Role of tumor-mediated immunosuppression. *Semin Cancer Biol*, 65: 13–27.

https://doi.org/10.1016/j.semcancer.2019.07.017

27. Zhou Y, Sun S, Ling T, *et al.*, 2023, The role of fibroblast growth factor 18 in cancers: Functions and signaling pathways. *Front Oncol*, 13(May): 1–17.

https://doi.org/10.3389/fonc.2023.1124520

28. Wang S, Du P, Cao Y, *et al.*, 2022, Cancer associated fibroblasts secreted exosomal miR-1290 contributes to prostate cancer cell growth and metastasis via targeting GSK3β. *Cell Death Discov*, 8(1): 371.

https://doi.org/10.1038/s41420-022-01163-6

29. Liu T, Han C, Wang S, *et al.*, 2019, Cancer-associated fibroblasts: An emerging target of anti-cancer immunotherapy. *J Hematol Oncol*, 12(1): 1–15.

https://doi.org/10.1186/s13045-019-0770-1

30. Shomar A, Barak O, Brenner N, 2022, Cancer progression as a learning process. *iScience*, 25(3): 103924.

https://doi.org/10.1016/j.isci.2022.103924

31. Hoarau-Véchot J, Rafii A, Touboul C, *et al.*, 2018, Halfway between 2D and animal models: Are 3D cultures the ideal tool to study cancer-microenvironment interactions? *Int J Mol Sci*, 19(1): 181.

https://doi.org/10.3390/ijms19010181

32. Yada E, Wada S, Yoshida S, *et al.*, 2018, Use of patient-derived xenograft mouse models in cancer research and treatment. *Futur Sci OA*, 4(3): FSO271.

https://doi.org/10.4155/fsoa-2017-0136

33. Wu MC, Yu HW, Chen YQ, *et al.*, 2022, Early committed polarization of intracellular tension in response to cell shape determines the osteogenic differentiation of mesenchymal stromal cells. *Acta Biomater*, 163: 287–301.

https://doi.org/10.1016/j.actbio.2022.10.052

34. Marcotulli M, Tirelli MC, Volpi M, *et al.*, 2022, Microfluidic 3D printing of emulsion ink for engineering porous functionally graded materials. *Adv Mater Technol*, 2201244: 1–12.

https://doi.org/10.1002/admt.202201244

35. Iafrate L, Benedetti MC, Donsante S, *et al.*, 2022, Modelling skeletal pain harnessing tissue engineering. *Vitr Model*, 1(4–5): 289–307.

https://doi.org/10.1007/s44164-022-00028-7

36. Bhimani J, Ball K, Stebbing J, 2020, Patient-derived xenograft models—the future of personalised cancer treatment. *Br J Cancer*, 122(5): 601–602.

https://doi.org/10.1038/s41416-019-0678-0

37. Liu Y, Wu W, Cai C, *et al.*, 2023, Patient-derived xenograft models in cancer therapy: Technologies and applications. *Signal Transduct Target Ther*, 8(1): 160.

https://doi.org/10.1038/s41392-023-01419-2

38. Singh J, 2012, The national centre for the replacement, refinement, and reduction of animals in research. *J Pharm Pharmacol* 3(1): 87–9. PMID: 22368436; PMCID: PMC3284057.

39. Prina-Mello A, Jain N, Liu B, *et al.*, 2018, Culturing substrates influence the morphological, mechanical and biochemical features of lung adenocarcinoma cells cultured in 2D or 3D. *Tissue Cell*, 50(December 2017): 15–30.

https://doi.org/10.1016/j.tice.2017.11.003

40. Cui X, Hartanto Y, Zhang H, 2017, Advances in multicellular spheroids formation. *J R Soc Interface*, 14(127): 20160877.

https://doi.org/10.1098/rsif.2016.0877

41. Däster S, Amatruda N, Calabrese D, *et al.*, 2017, Induction of hypoxia and necrosis in multicellular tumor spheroids is associated with resistance to chemotherapy treatment. *Oncotarget*, 8(1): 1725–1736.

https://doi.org/10.18632/oncotarget.13857

42. Sontheimer-Phelps A, Hassell BA, Ingber DE, 2019, Modelling cancer in microfluidic human organs-on-chips. *Nat Rev Cancer*, 19(2): 65–81.

https://doi.org/10.1038/s41568-018-0104-6

43. Fang L, Liu Y, Qiu J, *et al.*, 2022, Bioprinting and its use in tumor-on-a-chip technology for cancer drug screening: A review. *Int J Bioprinting*, 8(4): 46–64.

https://doi.org/10.18063/ijb.v8i4.603

44. Monteiro MV, Zhang YS, Gaspar VM, *et al.*, 2022, 3D-bioprinted cancer-on-a-chip: Level-up organotypic in vitro models. *Trends Biotechnol*, 40(4): 432–447.

https://doi.org/10.1016/J.TIBTECH.2021.08.007

45. Cidonio G, Glinka M, Kim Y-H, *et al.*, 2021, Nanocomposite clay-based bioinks for skeletal tissue engineering. In Rainer A, Moroni L, eds. *Computer-Aided Tissue Engineering: Methods and Protocols*, Springer US, New York, NY, 63–72.

https://doi.org/10.1007/978-1-0716-0611-7_6

46. Kačarević ŽP, Rider PM, Alkildani S, *et al.*, 2018, An introduction to 3D bioprinting: Possibilities, challenges and future aspects. *Materials (Basel)*, 11(11): 2199.

https://doi.org/10.3390/ma11112199

47. Menezes R, Vincent R, Osorno L, *et al.*, 2022, Biomaterials and tissue engineering approaches using glycosaminoglycans for tissue repair: Lessons learned from the native extracellular matrix. *Acta Biomater*, 163: 210–227.

https://doi.org/10.1016/j.actbio.2022.09.064

48. Groll J, Burdick JA, Cho DW, *et al.*, 2019, A definition of bioinks and their distinction from biomaterial inks. *Biofabrication*, 11(1): 013001.

https://doi.org/10.1088/1758-5090/aaec52

49. Gungor-Ozkerim PS, Inci I, Zhang YS, *et al.*, 2018, Bioinks for 3D bioprinting: An overview. *Biomater Sci* 6(5): 915–9946.

https://doi.org/10.1039/c7bm00765e

50. Cidonio G, Glinka M, Dawson JI, *et al.*, 2019, The cell in the ink: Improving biofabrication by printing stem cells for skeletal regenerative medicine. *Biomaterials*, 209(March): 10–24.

https://doi.org/10.1016/j.biomaterials.2019.04.009

51. Ji S, Guvendiren M, 2017, Recent advances in bioink design for 3D bioprinting of tissues and organs. *Front Bioeng Biotechnol*, 5(APR): 1–8.

https://doi.org/10.3389/fbioe.2017.00023

52. Catoira MC, Fusaro L, Di Francesco D, *et al.*, 2019, Overview of natural hydrogels for regenerative medicine applications. *J Mater Sci Mater Med*, 30(10): 115.

https://doi.org/10.1007/s10856-019-6318-7

53. Revete A, Aparicio A, Cisterna BA, *et al.*, 2022, Advancements in the use of hydrogels for regenerative medicine: Properties and biomedical applications. *Int J Biomater*, 2022: 3606765.

https://doi.org/10.1155/2022/3606765

54. Suamte L, Tirkey A, Barman J, *et al.*, 2023, Various manufacturing methods and ideal properties of scaffolds for tissue engineering applications. *Smart Mater Manuf*, 1(November 2022): 100011.

https://doi.org/10.1016/j.smmf.2022.100011

55. Jung MS, Skhinas JN, Du EY, *et al.*, 2022, A high-throughput 3D bioprinted cancer cell migration and invasion model with versatile and broad biological applicability. *Biomater Sci* 10(20): 5876–5887.

https://doi.org/10.1039/d2bm00651k

56. Li J, Chen M, Fan X, *et al.*, 2016, Recent advances in bioprinting techniques: Approaches, applications and future prospects. *J Transl Med*, 14(1): 1–15.

https://doi.org/10.1186/s12967-016-1028-0

57. Liu J, Shahriar M, Xu H, *et al.*, 2022, Cell-laden bioink circulation-assisted inkjet-based bioprinting to mitigate cell sedimentation and aggregation. *Biofabrication*, 14(4).

https://doi.org/10.1088/1758-5090/ac8fb7

58. Abu Owida H, 2022, Developments and clinical applications of biomimetic tissue regeneration using 3D bioprinting technique. *Appl Bionics Biomech*, 2022: 2260216.

https://doi.org/10.1155/2022/2260216

59. Wu Y, Su H, Li M, *et al.*, 2023, Digital light processing-based multi-material bioprinting: Processes, applications, and perspectives. *J Biomed Mater Res - Part A*, 111(4): 527–542.

https://doi.org/10.1002/jbm.a.37473

60. Hakobyan D, Médina C, Dusserre N, *et al.*, 2020, Laser-assisted 3D bioprinting of exocrine pancreas spheroid models for cancer initiation study. *Biofabrication*, 12(3): 035001.

https://doi.org/10.1088/1758-5090/ab7cb8

61. Vrana NE, Gupta S, Mitra K, *et al.*, 2022, From 3D printing to 3D bioprinting: the material properties of polymeric material and its derived bioink for achieving tissue specific architectures. *Cell Tissue Bank*, 23(3): 417–440.

https://doi.org/10.1007/s10561-021-09975-z

62. Chand R, Muhire BS, Vijayavenkataraman S, 2022, Computational fluid dynamics assessment of the effect of bioprinting parameters in extrusion bioprinting. *Int J Bioprinting*, 8(2): 45–60.

https://doi.org/10.18063/ijb.v8i2.545

63. van der Heide D, Cidonio G, Stoddart MJ, *et al.*, 2022, 3D printing of inorganic-biopolymer composites for bone regeneration. *Biofabrication*, 14(4): 042003.

https://doi.org/10.1088/1758-5090/ac8cb2

64. Cidonio G, Costantini M, Pierini F, *et al.*, 2021, 3D printing of biphasic inks: Beyond single-scale architectural control. *J Mater Chem C*, 9(37): 12489–12508.

https://doi.org/10.1039/D1TC02117F

65. Mi S, Yang S, Liu T, *et al.*, 2019, A novel controllable cell array printing technique on microfluidic chips. *IEEE Trans Biomed Eng*, 66(9): 2512–2520.

https://doi.org/10.1109/TBME.2019.2891016

66. Kolesky DB, Homan KA, Skylar-Scott MA, *et al.*, 2016, Three-dimensional bioprinting of thick vascularized tissues. *Proc Natl Acad Sci U S A*, 113(12): 3179–3184.

https://doi.org/10.1073/pnas.1521342113

67. Hong S, Song JM, 2022, 3D bioprinted drug-resistant breast cancer spheroids for quantitative in situ evaluation of drug resistance. *Acta Biomater*, 138: 228–239.

https://doi.org/10.1016/j.actbio.2021.10.031

68. Ling K, Huang G, Liu J, *et al.,* 2015, Bioprinting-based high-throughput fabrication of three-dimensional MCF-7 human breast cancer cellular spheroids. *Engineering*, 1(2): 269–274.

https://doi.org/10.15302/J-ENG-2015062

69. Zhou X, Zhu W, Nowicki M, *et al.*, 2016, 3D bioprinting a cell-laden bone matrix for breast cancer metastasis study. *ACS Appl Mater Interfaces*, 8(44): 30017–30026.

https://doi.org/10.1021/acsami.6b10673

70. Jiang T, Munguia-Lopez JG, Flores-Torres S, *et al.*, 2017, Directing the self-assembly of tumour spheroids by bioprinting cellular heterogeneous models within alginate/gelatin hydrogels. *Sci Rep*, 7(1): 1–9.

https://doi.org/10.1038/s41598-017-04691-9

71. Grolman JM, Zhang D, Smith AM, *et al.*, 2015, Rapid 3D extrusion of synthetic tumor microenvironments. *Adv Mater*, 27(37): 5512–5517.

https://doi.org/10.1002/adma.201501729

72. Reid JA, Palmer XL, Mollica PA, *et al.,* 2019, A 3D bioprinter platform for mechanistic analysis of tumoroids and chimeric mammary organoids. *Sci Rep*, 9(1): 1–10.

https://doi.org/10.1038/s41598-019-43922-z

73. Oronsky B, Reid TR, Oronsky A, *et al.*, 2021, A review of newly diagnosed glioblastoma. *Front Oncol*, 10(February): 1–10.

https://doi.org/10.3389/fonc.2020.574012

74. Campos DFD, Marquez AB, O'seanain C, *et al.*, 2019, Exploring cancer cell behavior in vitro in three-dimensional multicellular bioprintable collagen-based hydrogels. *Cancers (Basel)*, 11(2): 1–17.

https://doi.org/10.3390/cancers11020180

75. Dai X, Ma C, Lan Q, *et al.,* 2016, 3D bioprinted glioma stem cells for brain tumor model and applications of drug susceptibility. *Biofabrication*, 8(4): 1–11.

https://doi.org/10.1088/1758-5090/8/4/045005

76. Heinrich MA, Bansal R, Lammers T, *et al.*, 2019, 3D-bioprinted mini-brain: A glioblastoma model to study cellular interactions and therapeutics. *Adv Mater*, 31(14): 1–9.

https://doi.org/10.1002/adma.201806590

77. Monferrer E, Martín-Vañó S, Carretero A, *et al.*, 2020, A three-dimensional bioprinted model to evaluate the effect of stiffness on neuroblastoma cell cluster dynamics and behavior. *Sci Rep*, 10(1): 1–12.

https://doi.org/10.1038/s41598-020-62986-w

78. Yi HG, Jeong YH, Kim Y, *et al.*, 2019, A bioprinted human-glioblastoma-on-a-chip for the identification of patient-specific responses to chemoradiotherapy. *Nat Biomed Eng*, 3(7): 509–519.

https://doi.org/10.1038/s41551-019-0363-x

79. Wang X, Zhang X, Dai X, *et al.*, 2018, Tumor-like lung cancer model based on 3D bioprinting. *3 Biotech*, 8(12): 1–9.

https://doi.org/10.1007/s13205-018-1519-1

80. Han S, Kim S, Chen Z, *et al.*, 2020, 3D bioprinted vascularized tumour for drug testing. *Int J Mol Sci*, 21(8): 1–14.

https://doi.org/10.3390/ijms21082993

81. Mondal A, Gebeyehu A, Miranda M, *et al.*, 2019, Characterization and printability of sodium alginate - Gelatin hydrogel for bioprinting NSCLC co-culture. *Sci Rep*, 9(1): 19914.

https://doi.org/10.1038/s41598-019-55034-9

82. Dong Q, Su X, Li X, *et al.,* 2023, In vitro construction of lung cancer organoids by 3D bioprinting for drug evaluation. *Colloids Surf A Physicochem Eng Asp*, 666: 131288.

https://doi.org/10.1016/j.colsurfa.2023.131288

83. Mei Y, Wu D, Berg J, *et al.*, 2023, Generation of a perfusable 3D lung cancer model by digital light processing. *Int J Mol Sci*, 24(7): 6071.

https://doi.org/10.3390/ijms24076071

84. Anderson WJ, Doyle LA, 2021, Updates from the 2020 World Health Organization Classification of soft tissue and bone tumours. *Histopathology*, 78(5): 644–657.

https://doi.org/10.1111/his.14265

85. Molina ER, Chim LK, Barrios S, *et al.*, 2020, Modeling the tumor microenvironment and pathogenic signaling in bone sarcoma. *Tissue Eng Part B Rev*, 26(3): 249–271

https://doi.org/10.1089/ten.teb.2019.0302

86. Hameed M, Dorfman H, 2011, Primary malignant bone tumors-recent developments. *Semin Diagn Pathol*, 28(1): 86–101.

https://doi.org/10.1053/j.semdp.2011.02.002

87. Liu X, Duan Z, Fang S, *et al.*, 2023, Imaging assessment of the efficacy of chemotherapy in primary malignant bone tumors: Recent advances in qualitative and quantitative magnetic resonance imaging and radiomics. *J Magn Reson Imaging*, 8.

https://doi.org/10.1002/jmri.28760

88. Palmerini E, Righi A, Staals EL, 2020, Rare primary malignant bone sarcomas. *Cancers (Basel)*, 12(11): 1–14.

https://doi.org/10.3390/cancers12113092

89. Misaghi A, Goldin A, Awad M, *et al.*, 2018, Osteosarcoma: A comprehensive review. *SICOT-J*, 4: 12.

https://doi.org/10.1051/sicotj/2017028

90. Yao M, Zou Q, Zou W, *et al.*, 2021, Bifunctional scaffolds of hydroxyapatite/poly(dopamine)/carboxymethyl chitosan with osteogenesis and anti-osteosarcoma effect. *Biomater Sci*, 9(9): 3319–3333.

https://doi.org/10.1039/D0BM01785J

91. Lahr CA, Landgraf M, Sanchez-Herrero A, *et al.*, 2020, A 3D-printed biomaterials-based platform to advance established therapy avenues against primary bone cancers. *Acta Biomater*, 118: 69–82.

https://doi.org/10.1016/j.actbio.2020.10.006

92. Chow T, Wutami I, Lucarelli E, *et al.*, 2021, Creating in vitro three-dimensional tumor models: A guide for the biofabrication of a primary osteosarcoma model. *Tissue Eng - Part B Rev*, 27(5): 514–529.

https://doi.org/10.1089/ten.teb.2020.0254

93. Delgrosso E, Scocozza F, Cansolino L, *et al.*, 2023, 3D bioprinted osteosarcoma model for experimental boron neutron capture therapy (BNCT) applications: Preliminary assessment. *J Biomed Mater Res - Part B Appl Biomater*, 111(8): 1571–1580.

https://doi.org/10.1002/jbm.b.35255

94. Loi G, Stucchi G, Scocozza F, *et al.*, 2023, Characterization of a bioink combining extracellular matrix-like hydrogel with osteosarcoma cells: Preliminary results. *Gels,* 9(2): 129.

https://doi.org/10.3390/GELS9020129

95. Sa M-W, Nguyen B-NB, Moriarty RA, *et al.*, 2018, Fabrication and evaluation of 3D printed BCP scaffolds reinforced with ZrO2 for bone tissue applications. *Biotechnol Bioeng*, 115(4): 989–999.

https://doi.org/10.1002/bit.26514

96. Zhang W, Zhao W, Li Q, *et al.*, 2021, 3D-printing magnesium–polycaprolactone loaded with melatonin inhibits the development of osteosarcoma by regulating cell-in-cell structures. *J Nanobiotechnol,* 19(1): 263.

https://doi.org/10.1186/s12951-021-01012-1

97. Neufurth M, Wang X, Schröder HC, *et al.*, 2014, Engineering a morphogenetically active hydrogel for bioprinting of bioartificial tissue derived from human osteoblast-like SaOS-2 cells. *Biomaterials*, 35(31): 8810–8819.

https://doi.org/10.1016/j.biomaterials.2014.07.002

98. Wang X, Tolba E, Schröder HC, *et al.*, 2014, Effect of bioglass on growth and biomineralization of SaOS-2 cells in hydrogel after 3D cell bioprinting. *PLoS One*, 9(11): e112497.

https://doi.org/10.1371/journal.pone.0112497

99. Farris AL, Lambrechts D, Zhou Y, *et al.*, 2022, 3D-printed oxygen-releasing scaffolds improve bone regeneration in mice. *Biomaterials*, 280(June 2021): 121318.

https://doi.org/10.1016/j.biomaterials.2021.121318

100. Hwang DG, Choi YM, Jang J, 2021, 3D bioprinting-based vascularized tissue models mimicking tissue-specific architecture and pathophysiology for in vitro studies. *Front Bioeng Biotechnol*, 9(May): 1–16.

https://doi.org/10.3389/fbioe.2021.685507

101. Kim BS, Cho W-W, Gao G, *et al.*, 2021, Construction of tissue-level cancer-vascular model with high-precision position control via in situ 3D cell printing. *Small Methods*, 5(7): 2100072.

https://doi.org/10.1002/SMTD.202100072

102. Franca CM, Athirasala A, Subbiah R, *et al.*, 2023, High-throughput bioprinting of geometrically-controlled pre-vascularized injectable microgels for accelerated tissue regeneration. *Adv Healthc Mater*, 2202840: 1–11.

https://doi.org/10.1002/adhm.202202840

103. Swaminathan S, Hamid Q, Sun W, *et al.*, 2019, Bioprinting of 3D breast epithelial spheroids for human cancer models. *Biofabrication*, 11(2): 025003.

https://doi.org/10.1088/1758-5090/aafc49

104. Faihs L, Firouz B, Slezak P, *et al.*, 2022, A novel artificial intelligence-based approach for quantitative assessment of angiogenesis in the ex ovo CAM model. *Cancers (Basel)*, 14(17): 4273 6071.

https://doi.org/10.3390/cancers14174273

105. Parker AL, Benguigui M, Fornetti J, *et al.*, 2022, Current challenges in metastasis research and future innovation for clinical translation. *Clin Exp Metastasis*, 39(2): 263–277.

https://doi.org/10.1007/s10585-021-10144-5

106. Ye X, Weinberg RA, 2015, Epithelial-mesenchymal plasticity: A central regulator of cancer progression. *Trends Cell Biol*, 25(11): 675–686.

https://doi.org/10.1016/j.tcb.2015.07.012

107. Sökeland G, Schumacher U, 2019, The functional role of integrins during intra- and extravasation within the metastatic cascade. *Mol Cancer*, 18(1): 1–19.

https://doi.org/10.1186/s12943-018-0937-3

108. Arvanitis CD, Ferraro GB, Jain RK, 2020, The blood–brain barrier and blood–tumour barrier in brain tumours and metastases. *Nat Rev Cancer*, 20(1): 26–41.

https://doi.org/10.1038/s41568-019-0205-x

109. Peinado H, Zhang H, Matei IR, *et al.*, 2017, Pre-metastatic niches: Organ-specific homes for metastases. *Nat Rev Cancer*, 17(5): 302–317.

https://doi.org/10.1038/nrc.2017.6

110. Doglioni G, Parik S, Fendt SM, 2019, Interactions in the (pre)metastatic niche support metastasis formation. *Front Oncol*, 9(MAR): 1–7.

https://doi.org/10.3389/fonc.2019.00219

111. Khan SU, Fatima K, Malik F, 2022, Understanding the cell survival mechanism of anoikis-resistant cancer cells during different steps of metastasis. *Clin Exp Metastasis*, 39(5): 715–726.

https://doi.org/10.1007/s10585-022-10172-9

112. Lugano R, Ramachandran M, Dimberg A, 2020, Tumor angiogenesis: Causes, consequences, challenges and opportunities. *Cell Mol Life Sci*, 77(9): 1745–1770.

https://doi.org/10.1007/s00018-019-03351-7

113. Makvandi P, Baghbantaraghdari Z, Zhou W, *et al.*, 2021, Gum polysaccharide/nanometal hybrid biocomposites in cancer diagnosis and therapy. *Biotechnol Adv*, 48: 107711.

https://doi.org/10.1016/j.biotechadv.2021.107711

114. Emami Nejad A, Najafgholian S, Rostami A, *et al.*, 2021, The role of hypoxia in the tumor microenvironment and development of cancer stem cell: A novel approach to developing treatment. *Cancer Cell Int*, 21(1): 62.

https://doi.org/10.1186/s12935-020-01719-5

115. Lee C, Abelseth E, de la Vega L, *et al.*, 2019, Bioprinting a novel glioblastoma tumor model using a fibrin-based bioink for drug screening. *Mater Today Chem*, 12: 78–84.

https://doi.org/10.1016/j.mtchem.2018.12.005

116. Huang J-F, Shen J, Li X, *et al.*, 2020, Incidence of patients with bone metastases at diagnosis of solid tumors in adults: A large population-based study. *Ann Transl Med*, 8(7): 482–482.

https://doi.org/10.21037/ATM.2020.03.55

117. Hiraga T, 2019, Bone metastasis: Interaction between cancer cells and bone microenvironment. *J Oral Biosci*, 61(2): 95–98.

https://doi.org/10.1016/j.job.2019.02.002

118. Macedo F, Ladeira K, Pinho F, *et al.*, 2017, Bone metastases: An overview. *Oncol Rev*, 11(1): 321.

https://doi.org/10.4081/oncol.2017.321

119. Meng F, Meyer CM, Joung D, *et al.*, 2019, 3D bioprinted in vitro metastatic models via reconstruction of tumor microenvironments. *Adv Mater*, 31(10): 1806899.

https://doi.org/10.1002/adma.201806899

120. Kingsley DM, Roberge CL, Rudkouskaya A, *et al.*, 2019, Laser-based 3D bioprinting for spatial and size control of tumor spheroids and embryoid bodies. *Acta Biomater*, 95: 357–370.

https://doi.org/10.1016/j.actbio.2019.02.014

121. Zhu W, Holmes B, Glazer RI, *et al.*, 2016, 3D printed nanocomposite matrix for the study of breast cancer bone metastasis. *Nanomed Nanotechnol Biol Med*, 12(1): 69–79.

https://doi.org/10.1016/j.nano.2015.09.010

122. Dai X, Liu L, Ouyang J, *et al.*, 2017, Coaxial 3D bioprinting of self-assembled multicellular heterogeneous tumor fibers. *Sci Rep*, 7(1): 1–12.

https://doi.org/10.1038/s41598-017-01581-y

123. Wang X, Li X, Dai X, *et al.*, 2018, Coaxial extrusion bioprinted shell-core hydrogel microfibers mimic glioma microenvironment and enhance the drug resistance of cancer cells. *Colloids Surf B Biointerfaces*, 171(April): 291–299.

https://doi.org/10.1016/j.colsurfb.2018.07.042

124. Hermida MA, Kumar JD, Schwarz D, *et al.*, 2020, Three dimensional in vitro models of cancer: Bioprinting multilineage glioblastoma models. *Adv Biol Regul*, 75: 100658.

https://doi.org/10.1016/j.jbior.2019.100658

ACCSCIENCE PUBLISHING

International Journal of Bioprinting

REVIEW ARTICLE

Advancements in biomaterials and biofabrication for enhancing islet transplantation

Dayoon Kang[1†], Jaewook Kim[1†], and Jinah Jang[1,2,3,4*]

[1]Department of Mechanical Engineering, Pohang University of Science and Technology (POSTECH), Pohang 37673, South Korea

[2]Department of Convergence IT Engineering, Pohang University of Science and Technology (POSTECH), Pohang 37673, South Korea

[3]School of Interdisciplinary Bioscience and Bioengineering, Pohang University of Science and Technology (POSTECH), Pohang 37673, South Korea

[4]Institute for Convergence Research and Education in Advanced Technology, Yonsei University, Seoul 03722, South Korea

Abstract

Type 1 diabetes (T1D) is characterized by the degeneration of insulin-producing beta cells within pancreatic islets, resulting in impaired endogenous insulin synthesis, which necessitates exogenous insulin therapy. Although intensive insulin therapy has been effective in many patients, a subset of individuals with unstable T1D encounter challenges in maintaining optimal glycemic control through insulin injections. Pancreatic islet transplantation has emerged as a promising therapeutic alternative for such patients, offering enhanced glucose regulation, reduced risk of complications, and liberation from exogenous insulin reliance. However, impediments such as immune rejection and the need for an optimal transplantation environment limit the success of islet transplantation. Revascularization, a crucial requirement for proper islet functionality, poses a challenge in transplantation settings. Biomaterial-based biofabrication approaches have attracted considerable attention to address these challenges. Biomaterials engineered to emulate the native extracellular matrix provide a supportive environment for islet viability and functionality. This review article presents the recent advancements in biomaterials and biofabrication technologies aimed at engineering cell delivery systems to enhance the efficacy of islet transplantation. Immune protection and vascularization strategies are discussed, key biomaterials employed in islet transplantation are highlighted, and various biofabrication techniques, including electrospinning, microfabrication, and bioprinting, are explored. Furthermore, the future directions and challenges in the field of cell delivery systems for islet transplantation are discussed. The integration of appropriate biomaterials and biofabrication methods has significant potential to promote successful islet transplantation by facilitating vascularization and bolstering the immune defense mechanisms.

Keywords: Biomaterials; Biofabrication; Islet transplantation; Immunosuppression; Pre-vascularization

[†]These authors contributed equally to this work.

***Corresponding author:**
Jinah Jang
(jinahjang@postech.ac.kr)

Citation: Kang D, Kim J, Jang J, 2023, Advancements in biomaterials and biofabrication for enhancing islet transplantation. *Int J Bioprint*, 9(6): 1024.
https://doi.org/10.36922/ijb.1024

Received: May 31, 2023
Accepted: July 14, 2023
Published Online: August 25, 2023

Copyright: © 2023 Author(s). This is an Open Access article distributed under the terms of the Creative Commons Attribution License, permitting distribution, and reproduction in any medium, provided the original work is properly cited.

Publisher's Note: AccScience Publishing remains neutral with regard to jurisdictional claims in published maps and institutional affiliations.

1. Introduction

Pancreatic islets, composed of endocrine and insulin-producing beta cells, are diminutive cellular aggregates situated within the pancreas. In type 1 diabetes (T1D), also referred to as insulin-dependent or juvenile diabetes, the immune system specifically targets and annihilates beta cells, leading to impaired insulin production. Intensive insulin therapy presents itself as a viable solution that efficaciously ameliorates the regulation of blood glucose levels and mitigates the risk of subsequent complications, such as neuropathy, nephropathy, retinopathy, and cardiovascular ailments. Despite intensive insulin therapy, a subset of patients with unstable T1D experience challenges in sustaining glycemic control through insulin injections. Hypoglycemia is a prevalent occurrence in individuals with diabetes, irrespective of the diabetes type, particularly among those undergoing insulin therapy[1]. Unmitigated severe hypoglycemic incidents can precipitate adverse outcomes, such as unconsciousness, convulsions, and fatality.

In contrast, pancreatic islet transplantation has emerged as a viable therapeutic alternative for individuals with T1D who exhibit inadequate glucose control or insulin-induced hypoglycemia[2-4]. Islet transplantation decreases hemoglobin A1c levels, reduces the risk of diabetic complications, and eliminates the requirement for exogenous insulin, which is closely linked to an improved quality of life[5]. Although islet transplantation is a promising treatment for diabetes, it has certain challenges, such as susceptibility to the cellular microenvironment and vulnerable environments[6] and immune-hostile conditions[7]. Additionally, the transplantation site and surrounding environment often differ from those of natural islets, posing a significant obstacle to the success of insulin-producing cells. Revascularization, which involves the diffusion of oxygen, nutrients, metabolic waste, and insulin, is crucial for the proper functioning of the transplanted islets.

To address these challenges, current approaches, such as oxygenation with supplemental biomaterials, co-culturing with vascular cells, treatment with immunosuppressive drugs, and encapsulation of islets, are being actively explored. In particular, biomaterial-based biofabrication, which is considered a potential solution to overcome current problems, is under investigation.

Biomaterials are usually designed to mimic the biochemical and biophysical properties of the natural extracellular matrix (ECM), thereby providing a supportive environment for cells to thrive. Enhancing interactions between cells and biomaterials can improve cellular function, maturation, and signal transduction[8]. Consequently, suitable biomaterials and biofabrication methods can serve as novel tools for promoting vascularization and immune defense, thereby facilitating successful islet transplantation.

This review provides an overview of recent advances in biomaterials and biofabrication technologies for engineering cell delivery systems aimed at enhancing the efficacy of islet transplantation (Figure 1). First, we elucidated the pivotal components crucial for the success of islet transplantation, with a specific emphasis on the immune protection and vascularization strategies employed for optimal islet delivery. Subsequently, we offer a brief overview of the key biomaterials used in islet transplantation, underscoring their importance in implementing the full potential of islet delivery systems. In addition, we discuss recent biofabrication technologies leveraged for the development of islet delivery systems. Finally, we present an outlook on the future prospects and challenges in the field of cell delivery systems for islet transplantation.

2. Critical considerations for islet transplantation

2.1. Immunosuppression

Islet transplantation has recently garnered considerable attention due to advancements in islet isolation technology and immunosuppressive treatments[9]. The islet transplantation approach in clinical practice involves the infusion of islets into the patient's liver through the portal vein. However, the transplantation site presents a non-ideal environment characterized by high glucose concentrations, low oxygen levels, and other unfavorable factors. Furthermore, infusion of islets through the hepatic portal vein elicits an immediate blood-mediated inflammatory reaction. In addition, hypoxic islets secrete chemokines and express tissue factors that initiate thrombotic responses. Subsequently, platelets are recruited to the islet surface, attracting leukocytes and macrophages that infiltrate the islet cells and lead to their destruction. Hence, several challenges associated with islet transplantation remain, including suboptimal efficiency of cell delivery, inadequate islet functionality and viability, restricted transplant construct volume, and high dosages of immunosuppressive drugs post-transplantation[10-12]. These obstacles impede the efficacy of islet transplantation, primarily because of the host immune response against the transplanted cells and the insufficient or absent vascularization, ultimately leading to compromised survival and functionality of the islets. To circumvent these limitations, researchers are pursuing novel strategies such as immune evasion mechanisms or promoting vascularization to improve islet engraftment and functionality.

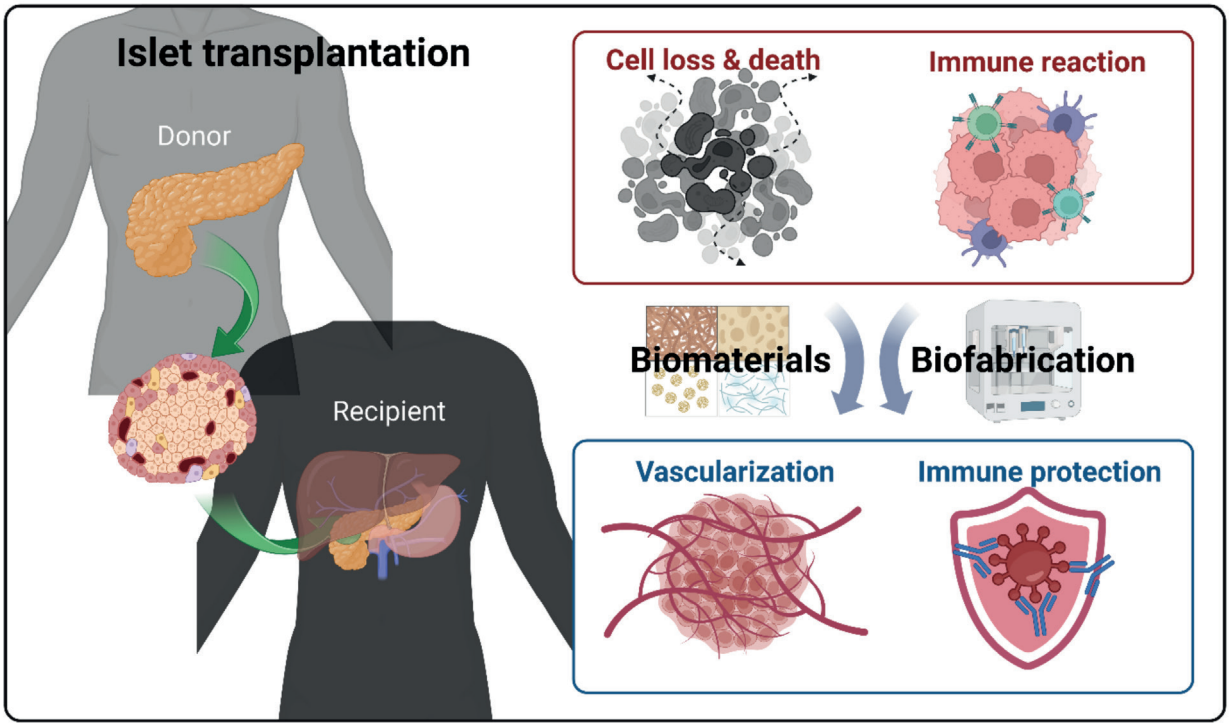

Figure 1. Overview of biomaterials and biofabrication technologies for islet delivery systems.

To mitigate the associated risk of immune-mediated destructions (e.g., autoimmune and alloimmune mechanisms), immunosuppressive tactics are commonly employed to safeguard the transplanted islets from immune-mediated harm[13]. Although these strategies effectively evade or reduce transplant rejection, they may also lead to unintended adverse effects, including hepatotoxicity, nephrotoxicity, and heightened susceptibility to infections and cancer[14]. Therefore, successful transplanted islets need to be protected from the immune system and the toxicity of immunosuppressive drugs.

However, the use of immunosuppressive drugs poses an additional challenge because of their potential toxicity to the pancreatic islets. In addition, there is some concern regarding the utilization of allogeneic and xenogeneic cell sources in islet transplantation, primarily due to their inherent immunogenic response. In light of this, induced pluripotent stem cells (iPSCs), generated through the cellular reprogramming of somatic cells, have garnered attention for their potential to differentiate into islet cells. Non-invasive collection from patients and the possibility of autografts without immunomodulation make human iPSCs (hiPSCs) a promising alternative to stem cells in the field of regenerative medicine. Notably, the use of hiPSCs potentially reduces ethical concerns associated with embryonic stem cell (ESCs) applications. Moreover, novel immune-evasive islet-like organoids have been developed that show restricted T-cell activation and graft rejection compared to non-engineered cells[14]. If it is successful, these strategies could potentially allow the transplantation of human insulin-producing cells into T1D patients without the need for long-term immunosuppression.

2.2. Vascularization

Successful transplantation of islets relies on the establishment of adequate vascularization, which is essential for the efficient exchange of oxygen, nutrients, metabolic waste products, and secreted insulin hormone. This is particularly important considering that the islets of Langerhans naturally inhabit one of the most highly vascularized tissues in the human body. Islet transplantation occurs in an environment where the surrounding capillary network is insufficient, resulting in a lack of adequate oxygen and nutrient supply to the cells during and after transplantation. This deprivation can negatively affect the survival and function of the transplanted islets. Reduced islet viability, attributed to hypoxic sensitivity, is primarily a consequence of insufficient oxygen supply[15]. Improving the survival and function of islets can be achieved by augmenting revascularization through the utilization of proangiogenic elements, including vascular endothelial growth factor (VEGF) and basic fibroblast growth factor (FGF2), as well as by restoring the interaction

between islets and ECM using synthetic peptides and polymer scaffolds[16]. VEGF within transplants stimulates angiogenesis, improves the viability of engrafted islets, and enhances the duration of normalized glycemia in diabetic mice after transplantation[17,18]. Therefore, the local delivery of proangiogenic factors may improve the clinical outcomes of islet transplantation.

Co-culture of angiogenesis-supporting cells can also promote network growth around or within the transplanted islets. Among the endothelial cells, human umbilical vein endothelial cells (HUVECs) are widely used for demonstrating this idea because of their ability to spontaneously assemble into tubular structures in an ECM[19]. Several studies have examined the transplantation of pancreatic islets embedded in endothelialized scaffolds[20,21]. A previous study showed that islets embedded in a HUVECs module returned diabetic mice to normal glycemia. HUVECs seeded on modules maintain the structural integrity of modular implants[22]. Furthermore, facilitating the prompt sprouting of islet endothelial cells post-transplantation could enhance the engraftment process during the phase when the islets are most susceptible. This could serve as an alternative that depends solely on revascularization from the adjacent tissue, a process that typically requires several weeks[23].

3. Biomaterial-based islet encapsulation strategies

Several biomaterial-based strategies have highlighted the crucial role of the extracellular environment in governing cellular behavior, emphasizing the need for regenerative materials that provide biological cues to cells[24]. Biomaterials have emerged as promising solutions to address medical challenges, and current investigations have emphasized the significance of the extracellular milieu in modulating cellular behavior. Islet encapsulation technology is a biomaterial-based approach that involves enveloping islets within biocompatible materials and creating a supportive structure that closely mimics the micro- and macroenvironments of native islets.

3.1. Islet encapsulation strategies

Recently, islet encapsulation has been widely used to provide not only mechanical and biochemical support but also an immune barrier for encapsulated islets. During encapsulation, living cells are suspended in a biomaterial designed to act as a transport barrier, allowing nutrients, oxygen, and waste products to diffuse while providing a barrier to larger objects such as antibodies and immune cells. The three-dimensional (3D) matrix of the capsule fosters a supportive growth environment for islets, preventing merging and interference with the availability of nutrients and oxygen for islet cells located at the center of the capsules[25]. Encapsulation techniques can be broadly classified into two categories based on the size: micro- and macroencapsulation. In microencapsulation, a small number of islets are enclosed in tiny capsules, typically less than a millimeter in size. These microcapsules facilitate the rapid diffusion of nutrients and oxygen, leading to high rates of islet survival because the favorable surface area-to-volume ratio in the microcapsules is beneficial for efficient mass transport. Nevertheless, microencapsulation has limitations, such as the need for a large transplantation site to accommodate the necessary number of capsules, a suitable microvascular bed for immediate nutrient access, difficulties in capsule removal, and insufficient long-term survival rates for functional islets to meet daily insulin demands[26].

In contrast, macroencapsulation entails the entrapment of a higher quantity of islets inside larger capsules, commonly several millimeters in magnitude. These enlarged capsules allow the assembly of an elevated number of islets, leading to enhanced glycemic management and augmented insulin secretion[27]. Nevertheless, macroencapsulation faces certain obstacles, such as the challenge of ensuring proficient exchange of nutrients and oxygen, as well as the potential degradation of capsules over time[26]. Despite the hurdles faced by both microencapsulation and macroencapsulation, the encapsulation approach still holds potential for islet transplantation and offers a possible solution for sustained glycemic regulation in patients with diabetes. Current research efforts are directed toward enhancing the properties of biomaterial in order to overcome the constraints of existing technology and ultimately improve the outcomes of islet transplantation[28].

The integration of islets within the selectively permeable membrane of a macroencapsulation device has been recognized as an effective approach for circumventing the immune response, thereby enabling the transport of insulin from transplanted cellular entities[28]. Macroencapsulation devices, typically ranging in size from millimeters to centimeters, offer the advantage of accommodating multiple islets within a single construct, allowing for efficient encapsulation. The sizable dimensions of macroencapsulation devices afford remarkable adjustability because the membrane size, thickness, and pore size can be precisely tailored. Thus, a single microencapsulation device is able to accommodate the substantial number of islets required for diabetes treatment.

Thus, the utilization of macroencapsulation devices, which act as physical barriers between transplanted cells and their recipients, has emerged as a promising strategy to address specific challenges by eliminating the

need for immunosuppressive measures[29]. The primary objective of an encapsulation device is to establish an environment that fosters the normal secretion of insulin in response to dynamic fluctuations in blood glucose levels while simultaneously safeguarding cell viability through seclusion from the immune system and facilitating the efficient exchange of nutrients and waste products. However, the thickness of the encapsulation device poses challenges in the exchange of small molecules, which may lead to cell death and reduced insulin release. Moreover, the inclusion of multiple islets within a single device reduces the available surface area for small-molecule exchange[30].

3.2. Natural biomaterials

Natural biomaterials offer a cell-friendly environment and exceptional biocompatibility, which are the features incorporated into islet delivery career system. Alginate, a well-known natural biomaterial derived from brown algae and naturally occurring polysaccharide, is widely used for islet encapsulation. Upon reaction with multivalent cations, crosslinking occurs between alginate molecules, resulting in the formation of a robust three-dimensional (3D) gel network structure. The ionotropic gelation of alginate solutions using Ca, Ba, and Fe ions results in water-insoluble alginate, which is known for its biocompatibility and mechanical stability. In particular, crosslinked calcium alginate is suitable for endovascular application[31]. Numerous studies have revealed that the long-term culture viability and survival rate of islet cells improve significantly when the cells are enclosed within alginate capsules. Zhang *et al.* illustrated that a balanced charged anti-biofouling alginate/polyethylene imine (PEI) hydrogel-based encapsulation strategy for islets, which results in insulin independence and immunoisolation, could be effectively utilized in the treatment of T1D (Figure 2A)[32]. The encapsulated islets retained their glucose-responsive and insulin-producing properties. Furthermore, the alginate hydrogel efficiently evaded foreign body reactions *in vivo* following intraperitoneal implantation into an immunocompetent streptozotocin-induced diabetic mouse model (Figure 2B)[32]. Over time, alginate may undergo dissociation as a result of the exchange of divalent cation crosslinking agents with physiologically abundant monovalent cations. However, the lack of hydrolases that can break down high-molecular-weight alginate polymers makes complete degradation of alginate unfeasible, thereby posing a challenge in eliminating alginate from mammals through physiological systems[33]. The molecular weight of residual alginate polymers commonly surpasses 50 kDa, which exceeds the established renal clearance threshold. In order to prevent the accumulation of residual polymer, hydrolytically degradable alginate hydrogels have been formulated via partial oxidation of alginates[34]. Recently, the use of oxidized alginate has been explored in the development of degradable carriers for insulin delivery and islet cell replacement therapy[35]. The key advantage of this degradable carrier is its ability to prevent the accumulation of materials beyond the required insulin dose or islet cell transplantation, thereby addressing the issue of excess material buildup.

Collagen, the primary protein constituent of ECM, is known for its biocompatibility and low immunogenicity[36,37]. The physical behavior of collagen gels is temperature-dependent, where they become fluidized at 10–25°C and relatively rigid at 30–37°C[38]. This temperature responsiveness is particularly valuable for cell delivery in human body because the solution-like pre-gel collagen can be effortlessly transplanted at room temperature and subsequently solidified at body temperature. Once implanted, the gel retained its rigid state, providing mechanical stability and preventing displacement from the implantation site. This property renders collagen gels advantageous for use as scaffolds in tissue engineering and cell delivery. Moreover, collagen can serve as a useful tool for cell encapsulation given its injectable fiber pore sizes of tens of nanometers, enabling the utilization of a collagen fiber membrane that shields the transplanted tissue from the host immune system[39]. Numerous studies have explored the use of collagen-coated scaffolds or mixtures of multiple materials, including collagen, to enhance the biocompatibility of transplants and facilitate islet adhesion to surface[40,41]. Conversely, it has been demonstrated that the combination of collagen with other ECM proteins and growth factors is able to maintain glucose homeostasis after islet transplantation, thereby enabling successful long-term islet transplantation[42]. Yang *et al.* have developed an innovative 3D culture system, namely Disque Platform (DP), that effectively replicates the microenvironment and cellular interactions of pluripotent stem cell-derived beta cells (SC β cells), thereby improving their viability, differentiation, and functionality (Figure 2C)[43]. DP incorporates critical constituents of the ECM, such as laminin and type IV collagen. In the 3D condition, the SC β cells exhibited elevated levels of vital transcription factors and junctional structures compared to those observed in two-dimensional (2D) monolayer conditions (Figure 2D). This technology has the potential to mitigate the adverse effects of existing small molecules for *in vivo* beta cell expansion and provide a renewable supply of islets *in vitro* for the long-term transplantation of patients with diabetes[43].

Heparin, a well-known natural biomaterial, has garnered attention in the field of islet transplantation owing to its propensity to enhance islet angiogenesis via growth factor stabilization. Because of their capacity to

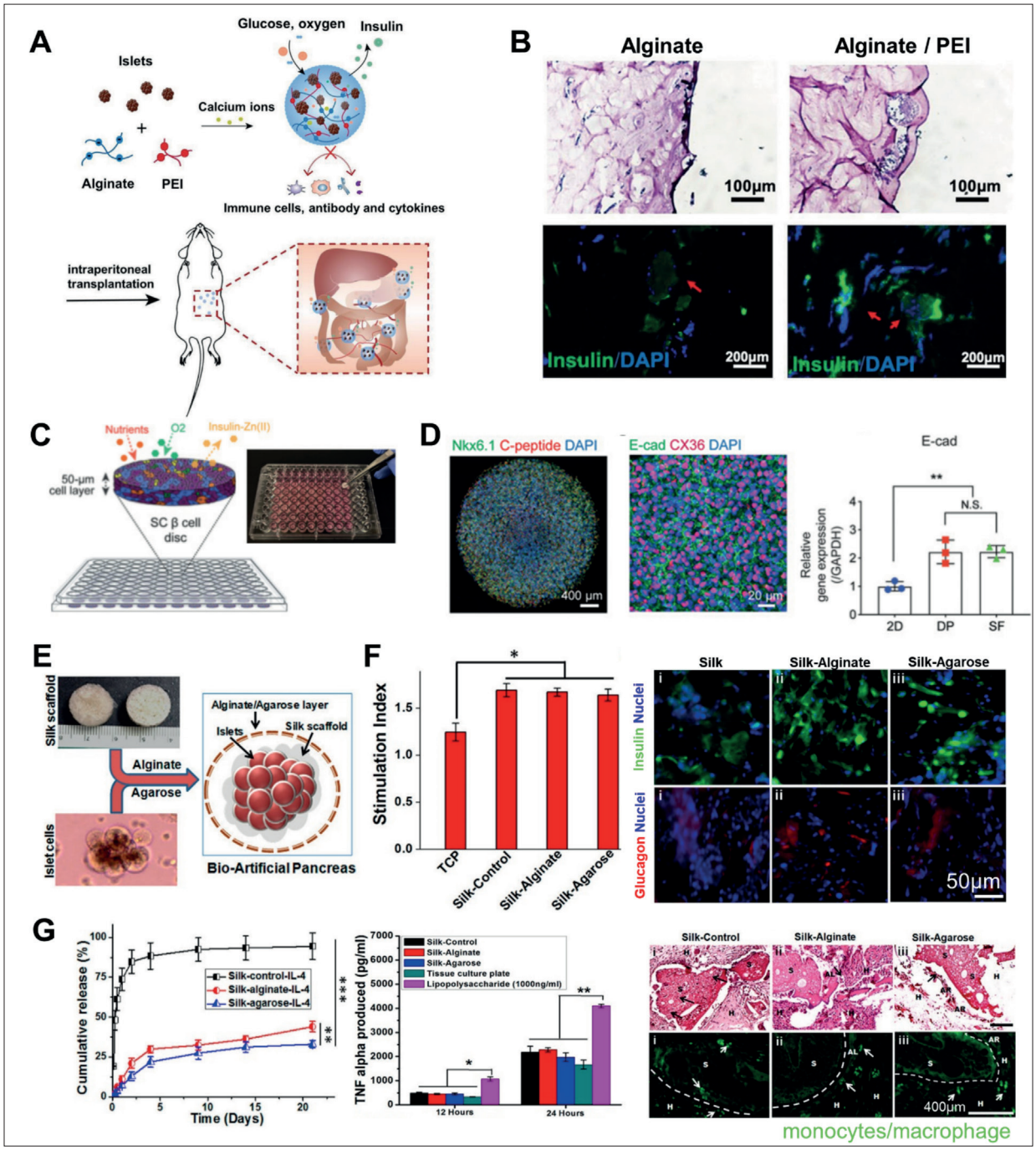

Figure 2. Application of natural hydrogels. (A) Schematic image of the encapsulation of islets using a balanced charged hydrogel that results in immunoprotection and controlled insulin secretion. (B) Representative histology and immunofluorescence images of retrieved hydrogel samples from Alginate/PEI and alginate-treated groups at 90 days post-transplantation. Adapted with permission from reference[32]. Copyright © 2019 WILEY-VCH Verlag GmbH & Co. KGaA, Weinheim. (C) Schematic image and gross view of the 3D reconstruction of SC β cells in the DP. (D) Immunofluorescence staining images of cell discs in DP and gene expression analysis showing higher expression of E-cadherin in SC β cells cultured in DP compared to 2D culture conditions. Adapted with permission from reference[43]. Copyright © 2020 AAAS. (E) Schematic image of the fabrication process of a silk-based bioartificial pancreas. (F) Stimulation index of primary islets encapsulated in different scaffolds and immunofluorescence images of primary islets cultured in different scaffolds after 14 days. (G) Gene expression analysis for M1 and M2 macrophage surface markers when incubated with IL-4-loaded silk-alginate scaffolds for 72 h. Comparative analysis of tumor necrosis factor-alpha produced by macrophages, suggesting lower levels of inflammatory responses in scaffolds. H&E staining and immunofluorescence staining images of retrieved acellular scaffolds after 4 weeks of subcutaneous implantation in mice. Adapted with permission from reference[51]. Copyright © 2017 American Chemical Society.

mimic the ECM, heparin-based hydrogels are promising carriers for islet delivery[44]. A previous study explored the application of macromolecular conjugates of heparin linked with VEGF to promote islet angiogenesis. Moreover, immobilized heparin on the islet surface has been shown to encourage endothelial cell adhesion to the surface of the islets[45]. In contrast, reliance on animal sources for obtaining heparin leads to supply and safety concerns, and its use is limited owing to clinical issues such as bleeding and thrombocytopenia[44]. To overcome these challenges, researchers have explored alternatives, such as heparin-mimicking polymers and hydrogels[44]. Notably, one study demonstrated the potential of heparin-mimetic peptide nanofiber gels in improving islet function and angiogenesis *in vitro* and *in vivo*[46].

Silk, a natural biomaterial, has been extensively employed in the design of islet encapsulation platforms. Multiple studies have demonstrated that encapsulation in silk can potentially replicate the native pancreatic niche and improve islet function both *in vitro* and *in vivo*[47-49]. Additionally, the use of small molecules, cytokines, chemokines, and immunomodulatory agents may offer promising strategies for extending cell survival, maintaining cell function, and minimizing immune responses[50]. Kumar *et al.* conducted a study aimed at developing 3D silk scaffolds capable of encapsulating pancreatic islets to generate bioartificial pancreatic systems that can sustain insulin release (Figure 2E)[51]. Silk-based scaffolds effectively facilitated the formation of islet-like clusters, resulting in improved cell viability, proliferation, and insulin production (Figure 2F). Moreover, the scaffolds were designed to release anti-inflammatory cytokines, which helped reduce inflammatory responses and promote an immunosuppressive environment (Figure 2G). In *in vitro* study, the scaffolds were observed to have immunomodulatory effects through the release of anti-inflammatory cytokines and the localized polarization of macrophages toward the implant site, ultimately favoring the integration of the graft with host tissues and enhancing graft function[51]. Research has been conducted to investigate the use of heparin, sodium salt, and silk fibroin solutions to produce cylindrical structures. Mao *et al.* conducted a study and evaluated the therapeutic potential of a macroporous scaffold composed of silk fibroin for islet transplantation in diabetic mice[52]. In this study, islets were co-transplanted with either a plain silk fibroin scaffold or a heparin-releasing silk fibroin scaffold into the epididymal fat pad of diabetic mice. These results demonstrate that heparin-releasing silk fibroin scaffolds facilitate islet revascularization and cell proliferation, leading to a more rapid reversal of hyperglycemia. This approach resulted in the development of a macroporous silk fibroin scaffold with the ability to enhance islet revascularization and engraftment[52].

Several natural gels including alginate, collagen, heparin, and silk fibrils have been examined in the field of islet transplantation. However, these gels exhibit limited versatility for promoting cell functions. Matrigel offers a promising solution to establish a physiologically relevant microenvironment that includes soluble growth factors, hormones, and other micro- to macromolecules that play critical roles in cellular interactions *in vivo*. Matrigel also contains the solubilized basement membrane matrix, which predominantly comprises laminin and collagen IV and is derived from Engelbreth–Holm–Swarm mouse sarcoma cells, making itself a reconstituted basement membrane. The ability of Matrigel to enhance long-term insulin secretion has been demonstrated[53]; however, the disadvantages associated with its use cannot be overlooked. These include the lot-to-lot variability that frequently occurs during the manufacturing process and the complexity and ill-defined nature of its composition, which makes it difficult to accurately determine which signals promote cell function[54]. Additionally, Matrigel originating from a tumor source is unsuitable for clinical use. Given these considerations, it is preferable to develop a standardized, non-tumor-derived ECM gel for clinical use rather than relying on Matrigel.

3.3. Synthesized biomaterials

Synthetic biomaterials are attractive platforms for protein and cell delivery in regenerative medicine. Synthetic biomaterials offer greater reproducibility and control over mechanical properties and have a biodegradable and non-immunogenic structure that can be synthesized on a large scale with consistent mechanical and physical properties[55]. Unlike natural hydrogels, synthetic polymers are generally not used as primary materials for islet encapsulation. They are predominantly employed in the production of scaffolds designed to facilitate tissue formation, as well as in auxiliary roles, such as providing structure and serving as a culture platform and encapsulation device.

Among the synthetic polymers, polylactic-co-glycolic acid (PLGA) is a highly functional biodegradable polymer synthesized from two monomers, lactic acid and glycolic acid, and offers distinct advantages. PLGA biodegradability is of particular importance, as it minimizes the potential for long-term toxicity and allows for the gradual replacement of the scaffold with new tissue as it degrades. Additionally, versatility is a major advantage of PLGA, as it can be fabricated into various forms, including fibers, films, and scaffolds, which are well suited for islet delivery applications[56,57]. Guo *et al.* fabricated microcarriers in the form of PLGA-porous microspheres using a double

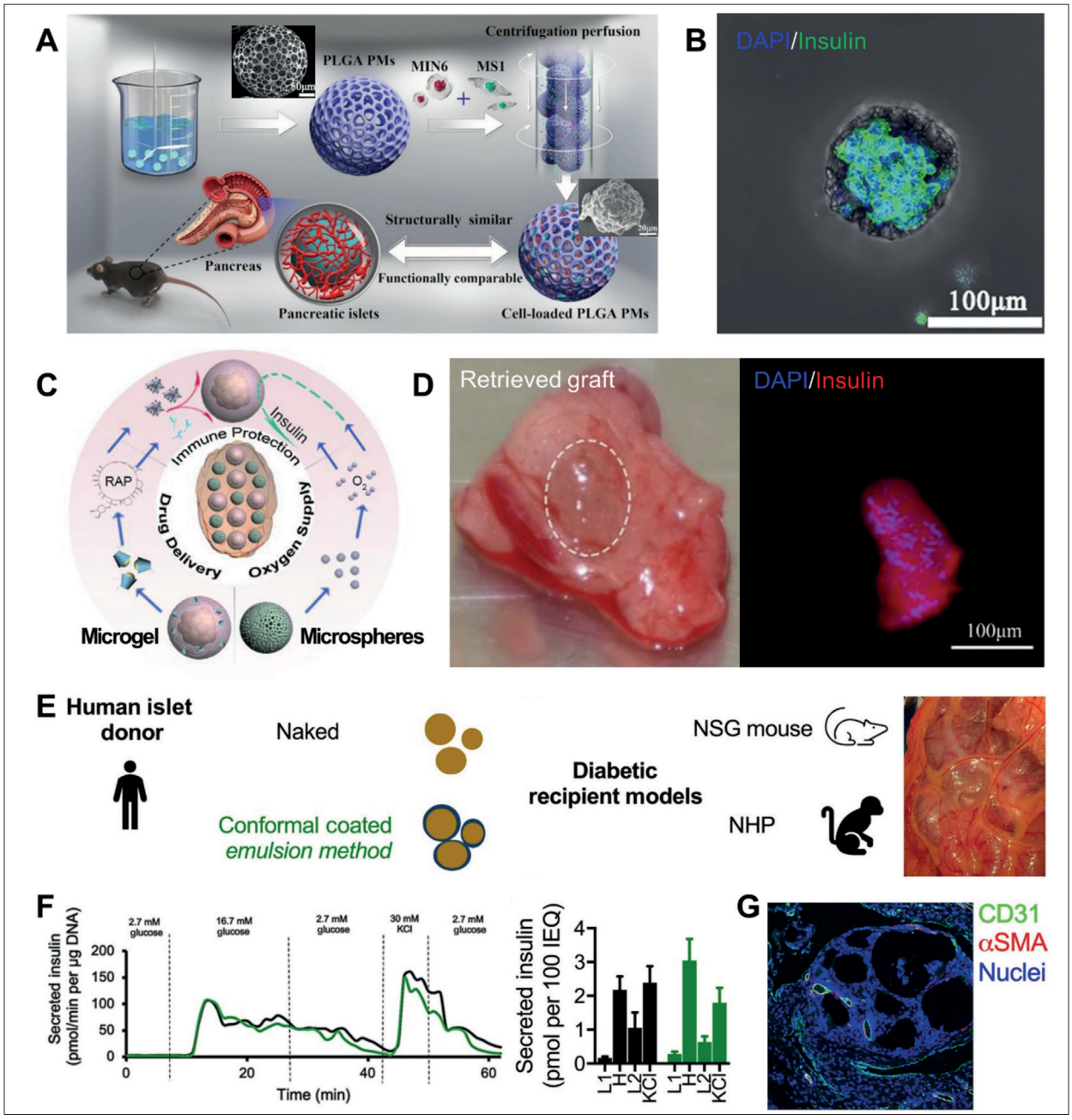

Figure 3. Application of synthesis hydrogels. (A) Schematic image of the steps involved in constructing artificial pancreatic islets by preparing MIN6 + MS1 cell-loaded PLGA microparticles. (B) Immunofluorescence staining image of MS1 and MIN6 within PLGA porous microspheres after 7 days of in vitro culture. Adapted with permission from reference[58]. Copyright © 2023 American Chemical Society. (C) Schematic image of the co-transplantation of islet-laden nanocomposite microgels and biodegradable oxygen-generating microspheres. (D) Photographic and immunofluorescence staining images of the epididymal fat pad containing the retrieved graft after 90 days of transplantation. Adapted with permission from reference[61]. Copyright © 2022 American Chemical Society. (E) Schematic image of the human islet donor and the distinction between naked islets and cell-clustered ECM islets, and the diabetic recipient model of the NSG mouse and non-human primate (NHP) with a photographic image of NHP omentum. (F) Dynamic glucose-stimulated insulin secretion of perifusion experiments conducted on naked and cell-clustered ECM human islets, representing their glucose sensitivity. (G) Immunofluorescence staining image of the explanted omental tissue containing islet grafts. Adapted with permission from reference[67]. Copyright © 2022 Stock et al.

emulsion-solvent evaporation technique (Figure 3A)[58]. The PLGA-porous microspheres were then utilized as a scaffold for artificial islet construction, where the pancreatic MIN6 cell line and the islet endothelial cell line MS1 were seeded using the developed centrifugation perfusion technique (Figure 3B). MIN6- and MS1-loaded

PLGA-porous microspheres upregulated the expression of vascular-related genes, indicating their potential to promote vascular formation during artificial organ construction using PLGA-porous microspheres[58].

Polylactic acid (PLA) is an aliphatic polyester that degrades through hydrolysis. It exhibits desirable characteristics such as biocompatibility, degradability, and printability, making it a popular choice for use as a polymeric bioink[59]. The incorporation of PLA allows for the facile production of porous scaffolds that can effectively promote the growth of neotissues. To date, a diverse array of medical products has been developed utilizing PLA, including degradable constructs and porous scaffolds for tissue engineering applications[60]. Huang *et al.* presented an innovative co-transplantation system that employed nanocomposite microgels loaded with islets and was capable of a sustained *in situ* release of immunosuppressants in conjunction with biodegradable oxygen-generating microspheres (Figure 3C)[61]. In their study, PLA was selected as the microsphere packaging material because of its biodegradability. Co-transplantation of nanocomposite microgels and biodegradable microspheres into diabetic mice restored and maintained normoglycemia (Figure 3D)[61]. Hoveizi and Tavakol successfully engineered a dependable 3D differentiation methodology for mesenchymal stem cells (MSCs) into pancreatic beta cell precursors (PBCPs) using nanofibrous PLA scaffolds[62]. The biocompatible and biodegradable nature of the nanofibrous PLA scaffold provided a suitable biophysical microenvironment for MSCs. Remarkably, transplanted PBCPs have demonstrated the ability to ameliorate hyperglycemia in a murine diabetes-induced model[62]. However, the degradation of PLA generates acidic byproducts, which negatively impact its long-term biocompatibility by triggering tissue inflammation and cellular death.

Polyethylene glycol (PEG) has emerged as a promising material for islet encapsulation owing to its tunable properties and gelation ability, which facilitate crosslinking and photopolymerization[63,64]. Several studies have demonstrated the ability of PEG to encapsulate thinner islets. For instance, a thin layer-by-layer PEG approach was utilized in one study to create an ultrathin capsule for surrounding the islets, which significantly enhanced the molecular exchange across the membrane compared with earlier methods[65]. Weaver *et al.* incorporated PEG hydrogel into a macroencapsulation device for extrahepatic islet transplantation[66]. The device comprises a hydrogel core crosslinked with non-degradable PEG dithiol and an outer layer that is vasculogenic and crosslinked with a proteolytically sensitive peptide to stimulate degradation[66]. Stock *et al.* introduced a refined strategy for encapsulating transplanted islets using a conformal coating (CC) technique with PEG hydrogels[67]. This method produces hydrogel CCs that encompass the islets at physiological pH, thereby promoting cytocompatibility and scalability. To evaluate the efficacy and efficiency of this novel method, *in vitro* and *in vivo* experiments were conducted using various small and large animal models of T1D (Figure 3E). During the evaluation of dynamic glucose-stimulated insulin secretion, both naked and emulsion-coated human islets exhibited a characteristic perifusion profile characterized by an initial phase of insulin secretion reaching its peak, followed by a subsequent phase wherein insulin secretion plateaued during the high-glucose stimulus (Figure 3F). The results revealed improved biocompatibility and abundant graft revascularization (Figure 3G)[67]. Another distinguishing feature of PEG is its potential to be modified with specific ligands to promote tissue adhesion. This property permits targeted cell attachment and proliferation, which is highly advantageous in tissue engineering applications, where successful regeneration hinges on cell adhesion. Despite their usefulness, the biocompatibility of hydrophobic materials is restricted by their inherent nature, and the breakdown of these materials can release acidic byproducts with proinflammatory effects[68]. Furthermore, several synthetic materials employed in tissue engineering, including PEG, are non-biodegradable and may remain indefinitely in the body, possibly causing unfavorable reactions or necessitating surgical removal.

3.4. Decellularized tissue-driven ECM

Tissue decellularization refers to the removal of cellular components from a tissue or solid organ, resulting in an acellular 3D structure composed of the ECM. Decellularized extracellular matrix (dECM) exhibits non-toxicity toward the proliferation and differentiation of various cell types, indicating its potential utility in regenerative medicine. Recent research on tissue-specific dECM has effectively provided a vital microenvironment for cells, allowing for the modulation of cellular processes such as migration, differentiation, and function during tissue morphogenesis[69,70]. The pancreatic dECM, comprising collagen, laminin, fibronectin, and fibrin, plays a crucial role in cytoskeletal remodeling, contractility, and cell differentiation. The dECM of the pancreas offers significant advantages, such as biocompatibility and bioactivity, which can increase islet survival and decrease cytotoxicity, thereby enhancing islet function. Research focusing on dECM derived from pancreatic tissue has validated its characteristics, especially regarding the interactions between islets and environmental cues, including viability, insulin secretion, and glucose responsiveness (Table 1)[71].

Table 1. Decellularized tissue-derived extracellular matrix for islet research

Cell sources	dECM origin	Functional evaluation	Major achievements	Ref
Human amniotic fluid-derived stem cells (hAFSC), porcine pancreatic islets	Porcine pancreas	*In vitro* islet functionality: GSIS assay	A whole organ, 3D pancreas scaffold, was successfully created using acellular porcine pancreas through the process of decellularization. The decellularized pancreas scaffold demonstrated the ability to support cellular adhesion and maintain the functions of various cell types, including stem cells and pancreatic islets.	[106]
Rat pancreatic islet	Rat pancreas	*In vitro* islet functionality: GSIS assay	A novel protocol for thorough decellularization of rat pancreas has been developed. The resulting non-immunogenic ECM retains the organ-specific protein network, including vascular and ductular structures while effectively preserving the majority of viable and intact islet cells.	[107]
Human mesenchymal stem cells (hMSC), adult human liver cells (AHLC)	Porcine pancreas	*In vivo* immunological test: Chemiluminescent array *In vivo* efficacy test: Blood glucose level monitoring, immunostaining (insulin)	Utilizing an ECM-based microcapsule system, a natural and fibrous 3D microenvironment is established, promoting cell survival and differentiation while also demonstrating immune compatibility upon *in vivo* implantation and significantly improving glycemic control in diabetic mice.	[108]
Mouse pancreatic islet	Mouse pancreas	*In vitro* islet functionality: ASIS assay	The produced ECM derived from decellularized pancreatic tissue successfully preserved the native tissue architecture, including vascular network, ductal structures, basal membranes, collagen, and glycosaminoglycan component, while being completely cell-free. The functionality of the remaining cells within the dECM was verified through GSIS assays after 48 h, and subsequent repopulation of the scaffold with green fluorescent protein-labeled INS-1 cells followed by a 120-day culture period confirmed its biocompatibility and non-toxic nature.	[72]
HUVECs, INS-1 832/13 cells	Human pancreas	*In vitro* islet functionality: GSIS assay *In vivo* immunological test: Immunostaining (HLA)	A set of effective techniques for the complete decellularization and delipidization of human pancreatic tissue were used in the comprehensive investigation of the composition and structural properties of the resulting dECM. The study further demonstrated the potential of the generated dECM as a supportive hydrogel for viable cell growth and survival, both *in vitro* and *in vivo*, with promising indications of non-immunogenic properties.	[73]
Rat pancreatic islet, HUVECs, differentiated-iPSC	Porcine pancreas	*In vitro* islet functionality: GSIS assay, immunostaining (insulin, pdx1), gene expression (insulin, pdx1)	Culturing human pluripotent stem cell-derived insulin-producing cells in a bioink composed of dECM resulted in notable improvements in insulin secretion and maturation. Additionally, incorporating human umbilical vein-derived endothelial cells in a co-culture system significantly reduced the occurrence of central necrosis in islets within a 3D culture environment.	[71]
AHLC, hMSC	Porcine pancreas	*In vitro* islet functionality: GSIS assay *In vitro* immunological study: Gene expression (TNF-α, IL-1β) *In vivo* immunological study: TNF-α, IL-6, and IL-1β in blood serum	The microcapsule system utilizing dECM establishes a favorable 3D microenvironment for cell survival and differentiation. *In vivo* implantation of dECM-based microcapsules containing cells demonstrated immune compatibility and substantially improved glycemic control in diabetic mice. The encapsulated cells within the pancreatic dECM microenvironment exhibited enhanced insulin production and secretion in response to glucose stimulation.	[109]
Mouse pancreatic islet	Porcine pancreas	*In vitro* islet functionality: Immunostaining (insulin, glucagon), GSIS assay, gene expression (insulin, pdx1)	Hybrid scaffolds made of silk fibroin and dECM derived from porcine pancreatic tissue were successfully created through electrospinning, closely resembling the native islet ECM. The hybrid dECM scaffold demonstrated improved viability of islets and enhanced insulin secretion in response to high glucose stimulation.	[110]
Rat pancreatic islet, MSCs	Rat pancreas	*In vivo* efficacy test: Magnetic resonance imaging (MRI), SEM images	Decellularized pancreas holds potential as a safer matrix for islet implantation into an omental flap. To enhance its suitability, improvements were made in terms of protein composition, decellularization quality, residual DNA content, and anatomical integrity. Utilizing pancreatic perfusion via the splenic vein resulted in smaller ECM scaffolds, facilitating transplantation into the omentum while meeting requirements such as complete removal of cellular components and preservation of pancreatic extracellular proteins.	[74]

Damodaran and Vermette developed a novel approach for perfusion decellularization of the entire pancreas, which allows for the engraftment of pancreatic cells and islets while maintaining the organ within the perfusion system (Figure 4A). Their work demonstrated the retention of islet functionality within the decellularized pancreata *in vitro*, and that the decellularized pancreas liberated pseudo-islets from the matrix (Figure 4B). Additionally, their study highlighted the favorable cytocompatibility of beta-like cells within the decellularized pancreata,

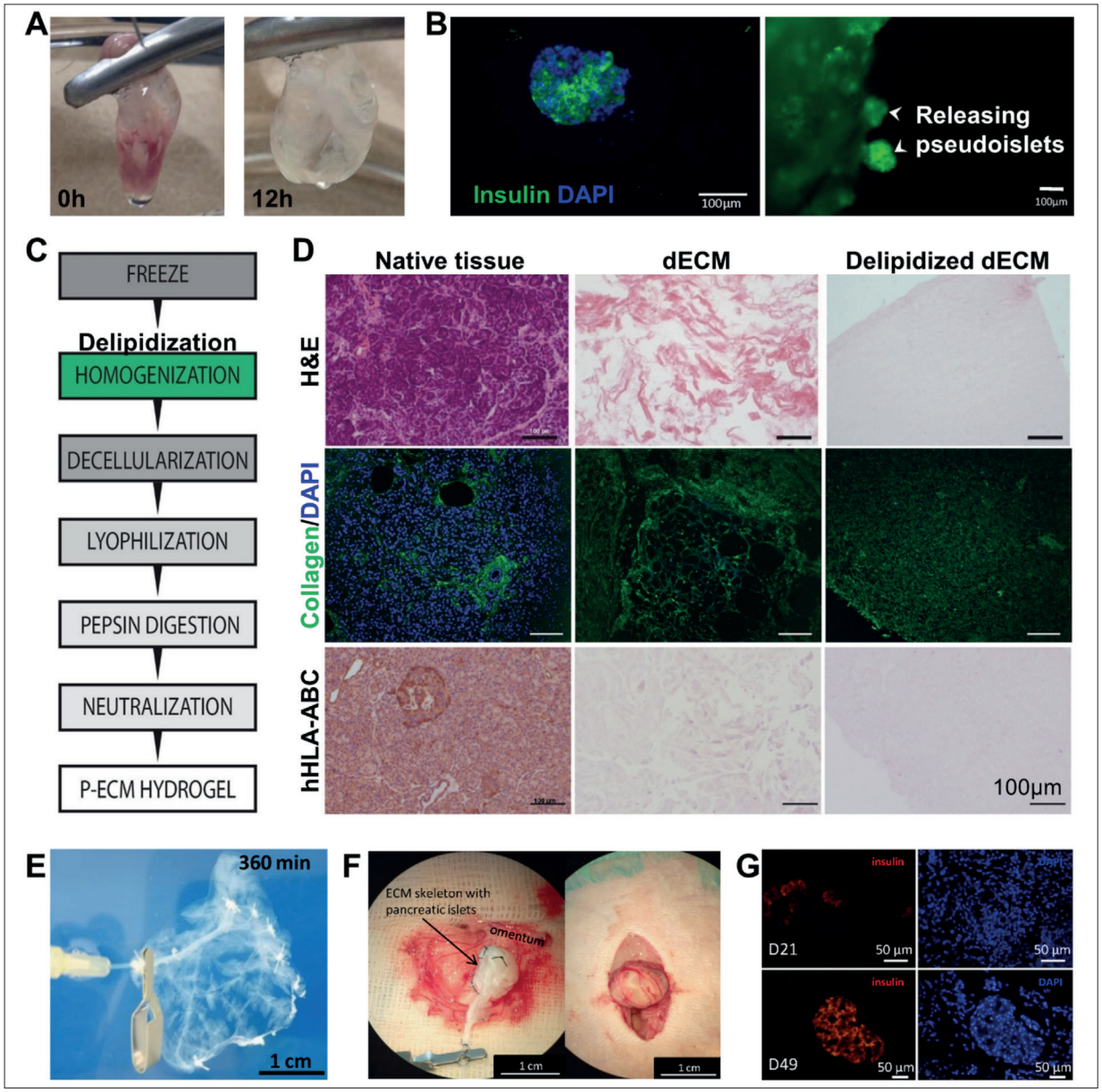

Figure 4. Application of decellularized tissue-driven ECM. (A) Photographic images illustrating the process of pancreas decellularization over a span of 12 h. (B) Immunohistochemistry staining image of GFP-transfected INS-1 cells on a decellularized pancreas, and the image of decellularized pancreas liberating pseudoislets from the matrix. Adapted with permission from reference[72]. Copyright © 2018 John Wiley and Sons. (C) Schematic image of the procedure involved in generating a dECM hydrogel from fragments of human pancreatic parenchyma. (D) H&E staining and immunohistochemistry staining image of native tissue, decellularized pancreatic hydrogels, and hydrogels for assessing the histological and morphological characteristics. Adapted with permission from reference[73]. Copyright © 2018 Sackett et al. (E) Photographic image of the process of pancreatic decellularization captured after the 360-min decellularization procedure. (F) Photographic images of the repopulated pancreatic skeleton enveloped by the omentum for transplantation. (G) Representative immunofluorescence staining images of iron-oxide-labeled islets in ECM skeletons at 21 and 49 days post-transplantation into the omentum. Adapted with permission from reference[74]. Copyright © 2022 Berkova et al.

thereby opening new possibilities for prolonged stem cell culture and differentiation[72]. Sackett *et al.* presented a pioneering approach for the efficient decellularization and elimination of lipids from the human pancreata[73]. They extensively evaluated the structure and composition of the delipidized pancreatic dECM (Figure 4C) and demonstrated the elimination of human leukocyte antigen (HLA) from decellularized materials, thereby obviating potential immune reactions (Figure 4D)[73]. Berkova *et al.* established a viable model to evaluate the potential of decellularized pancreatic skeleton (Figure 4E) as a matrix for islet graft transplantation into the omentum (Figure 4F)[74]. The transplanted islets maintained their morphology and position within the omentum and remained integrated within the skeleton (Figure 4G). They also verified islet viability and sustained insulin secretion in syngeneic recipients without diabetes[74]. Despite promising research focusing on dECM derived from pancreatic tissue, some outstanding issues remain unresolved. Although the immunomodulatory effects of dECM and the resulting breakdown products have been observed, owing to their residual physiological motifs and bioactive receptors, the precise mechanisms underlying these effects remain obscure and warrant further investigation. Furthermore, it is imperative to establish a uniform quality control standard for dECM obtained from diverse sources to ensure consistent outcomes in subsequent *in vivo* investigations. These persistent challenges are the factors driving the development of future clinical applications, as they have been thoroughly examined and resolved.

4. Biofabrication strategies for islet transplantation

Despite the use of biological materials, there are numerous obstacles to islet delivery in terms of manufacturing processes. During the encapsulation of islets into biomaterials and transplantation to the exact location, the islets are exposed to external forces. For example, severe physical forces can have fatal effects on cells encapsulated in biomaterials, resulting in cell death owing to potential damage to cell membranes. Using optimal biofabrication methods, multiple cells and biomaterials can be readily integrated into a concrete islet delivery construct. To overcome these challenges, various biofabrication methods have been adopted, including conventional scaffold fabrication methods, electrospinning, microfabrication, and 3D bioprinting technologies (Figure 5).

4.1. Electrospinning

For several decades, electrospinning has been employed to create fibrous scaffolds that mimic ECM. This technique uses electrostatic forces to generate fibrous scaffolds using biocompatible polymers. Importantly, the resulting nanofiber mats exhibited high surface areas and controllable pore sizes, which make them appropriate for the mass production of scaffolds with precisely controlled fiber diameters[75,76]. Consequently, researchers have endeavored to manipulate the electrospinning process for tissue-specific applications, leading to the development of diverse techniques for producing complex nanofibers. These techniques have also been used to fabricate islet

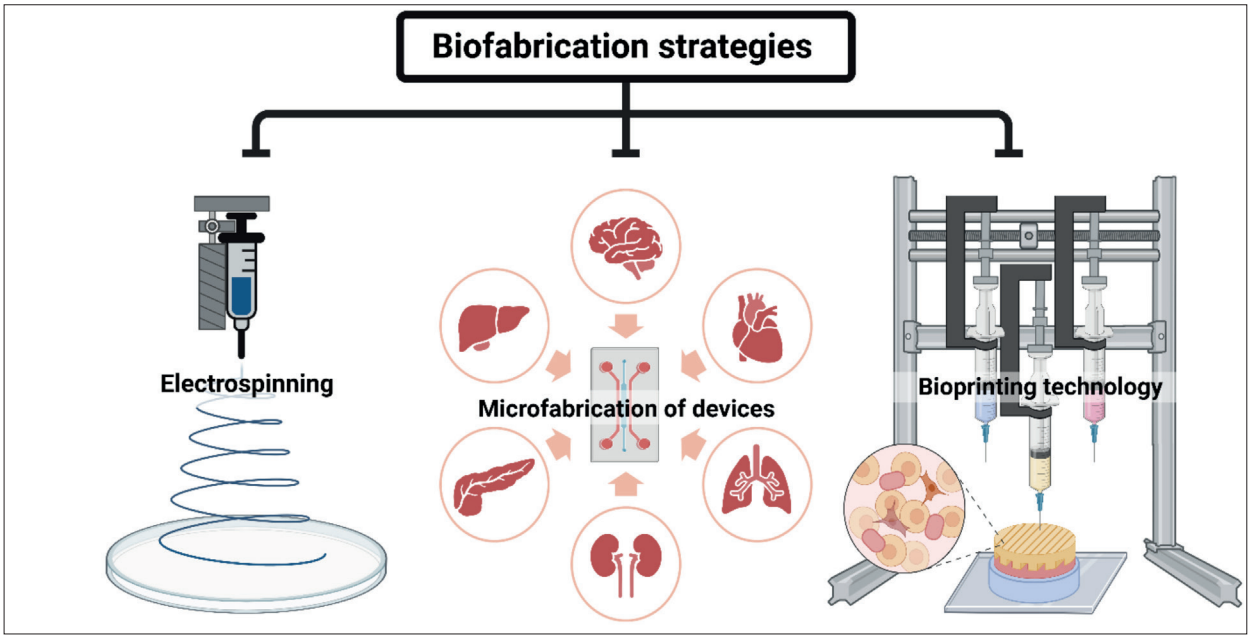

Figure 5. Biofabrication strategies for islet transplantation.

constructs. Buitinga *et al.* introduced a novel microwell scaffold as a potential transplantation device for pancreatic islets, which was prepared from non-cell-adhesive and reproducible poly (ethylene oxide terephthalate)/poly (butylene terephthalate) thin films and electrospun meshes (Figure 6A)[77]. During the 7-day culture period, the morphology of the human islets was well preserved and remained stable in the microwell scaffolds. Furthermore, the insulin release and total insulin content of the islets were comparable to that of the free-floating control islets, and the glucagon and insulin immunostaining were comparable between the two groups (Figure 6B)[77].

The research conducted by Liu *et al.* established that the use of electrospun nanoporous encapsulation devices composed of zwitterionic polyurethane (ZPU) polymers demonstrated the safety and efficacy of islet transplantation (Figure 6C)[78]. The devices possess various favorable characteristics, such as biocompatibility, robust mechanical properties, and a nanoporous structure that facilitates cell adhesion and diffusion. The upscaled ZPU device was implanted intraperitoneally into the pigs and positioned in proximity to the liver using a minimally invasive laparoscopic technique (Figure 6D). During the 3-month transplantation experiment, histological analysis

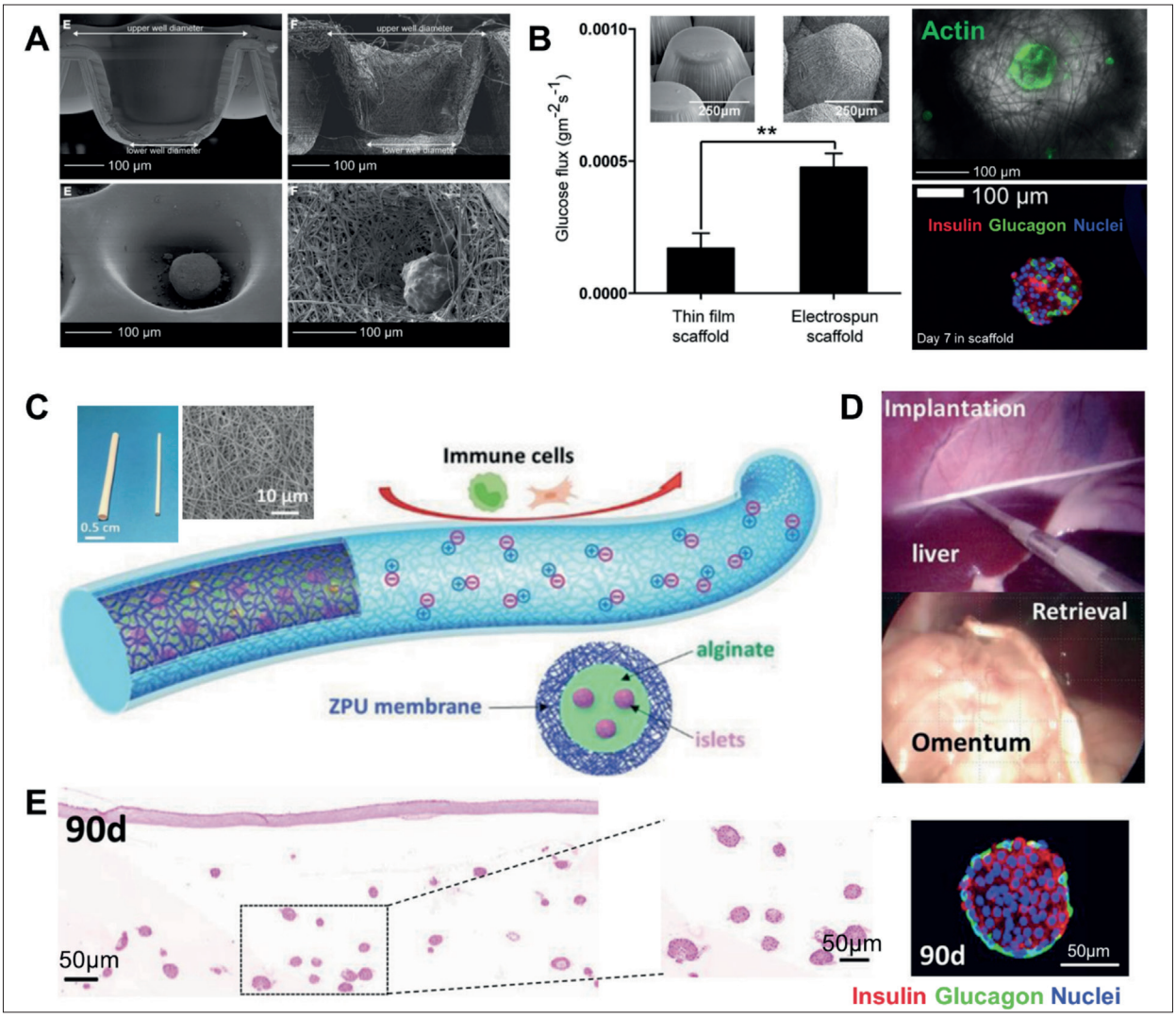

Figure 6. Electrospinning for islet transplantation. (A) Scanning electron microscopy (SEM) images of the electrospun microwell scaffold, including cross-sectional views of the fibrous network. (B) Glucose flux analysis representing glucose diffusion through the electrospun microwell scaffolds. Immunofluorescence staining images of human islets cultured in thin film microwell scaffolds. Adapted with permission from reference[77]. Copyright © 2013 Buitinga et al. (C) Schematic image of the chemical structure of the ZPU polymer and the ZPU device containing islets, which effectively prevents cell ingress or egress. (D) The process of implantation and retrieval of ZPU devices in pigs or dogs. (E) H&E staining images of retrieved ZPU devices containing islets after 90 days, and an immunohistochemistry staining image of islets in the retrieved ZPU device after 90 days. Adapted with permission from reference[78]. Copyright © 2021 Wiley-VCH GmbH.

and positive insulin staining confirmed the sustained functionality of the device over an extended period (Figure 6E). This study effectively demonstrated the potency of the device through its ability to reinstate normoglycemia in diabetic mice for a duration of 3 months post-encapsulation of proliferative cells[78]. Mridha *et al.* developed a method for providing allogeneic beta cell therapies without the need for antirejection drugs[79]. To achieve this, they propose the utilization of a bioengineered hybrid device that consists of microencapsulated beta cells enclosed within 3D polycaprolactone (PCL) scaffolds created through the melt electrospin writing technique. The researchers successfully demonstrated the construction of an implantable, consistent, and retrievable hybrid device that facilitates vascularization and enhances the viability of encapsulated islets and subcutaneously implanted the device in an allotransplantation environment while circumventing the requirement for immunosuppression[79].

4.2. Microfabrication of cell-laden devices

Extensive research and development efforts have been dedicated to the advanced microfabrication of microfluidic and lab-on-a-chip devices owing to their numerous advantages, including rapid analysis, biocompatibility, affordability, and automation. Although these devices were initially constructed from costly materials such as silicon wafer and glass, recent investigations have focused on the utilization of emerging soft polymeric materials (e.g., PDMS) that confer benefits such as automation and high-throughput screening in the realm of tools and laboratory equipment.

Compared with traditional systems, microfluidic systems offer superior control over the spatial and temporal distribution of chemical and physical stimuli at the cellular level, thereby enabling the development of diverse microsystems tailored to various tissue engineering applications. The emergence of organ-on-a-chip platforms, which synergize cell biology, engineering, and biomaterial advancements with microfluidics, has introduced innovative systems capable of mimicking the physiological or pathophysiological milieu of specific organs. These devices represent a pioneering model for pharmaceutical agent screening and the investigation of specific diseases. Numerous microfluidic devices have been developed in the field of diabetes to simulate native islet microenvironments and explore pancreatic beta cell kinetics[80]. Jun *et al.* created functional islet spheroids using a microfluidic chip that mimicked interstitial flow, reduced shear cell damage, and addressed islet size heterogeneity through precise 3D engineering of microsized islet spheroids (Figure 7A)[81]. The authors observed that flow not only enhanced the health of islets, but also promoted the maintenance of non-endocrine cells, such as islet endothelial cells (iECs), *in vitro* (Figure 7B). Furthermore, controlled-size islet spheroids exhibit higher drug sensitivity than intact islets[81]. Patel *et al.* developed a microphysiological system that enables continuous dynamic culture of pancreatic organoids in a 3D hydrogel, highlighting the importance of a dynamic *in vitro* microenvironment for primary organoid function preservation[82]. To compare traditional culture methods with the newly developed microphysiological system, rodent- and human-derived islets were embedded in alginate, and *in vitro* and *in silico* assessments were performed. Their results indicated that dynamic culture of hydrogel-embedded islets within the microphysiological system had a superior impact on islet viability[82]. Bauer *et al.* elucidated the advancement of a microfluidic two-organ-chip architecture for investigating the pancreatic islet–liver interplay in the context of drug discovery and the identification of novel therapeutic interventions (Figure 7C)[83]. The model capitalized on genetically encoded human pancreatic islet microtissues and liver spheroids subjected to glucose- and insulin-free cell culture medium. These findings suggest that insulin secretion by islet microtissues activates glucose uptake by liver spheroids, whereas the liver in isolation exhibits reduced efficiency in glucose consumption (Figure 7D)[83]. However, sample size limitations constitute a primary drawback of the majority of microfluidic systems, rendering them unsuitable for quality control of islets after isolation, as they require a considerable number of islets. One of the primary impediments to microfluidic systems is their inherent limitations in terms of sample size. Because of this limitation, it is challenging to acquire a sufficient number of islets for islet transplantation within a microfluidic system[84].

4.3. Bioprinting technology

3D bioprinting is one of the most promising technologies for the simultaneous induction of vascularization and prevention of inflammation[85,86]. It is also a state-of-the-art technology for constructing complex tissue-engineered structures. Using multiple dispensing system, various cells and materials can be placed precisely at the desired locations simultaneously. Among the various types of 3D bioprinting technologies, extrusion-based bioprinting techniques are most commonly used for the development of 3D-printed pancreatic tissue[71, 87–89]. Generally, an extrusion-based bioprinting technique driven by a pneumatic or mechanical system continuously forces the bioink through a nozzle to form predefined filaments. A bioink is a solution of a biomaterial or a mixture of several biomaterials in the form of a hydrogel. One of the common characteristics of bioinks is that the hydrogels are viscous enough to remain stable until crosslinking to create pre-designed constructs after printing[90].

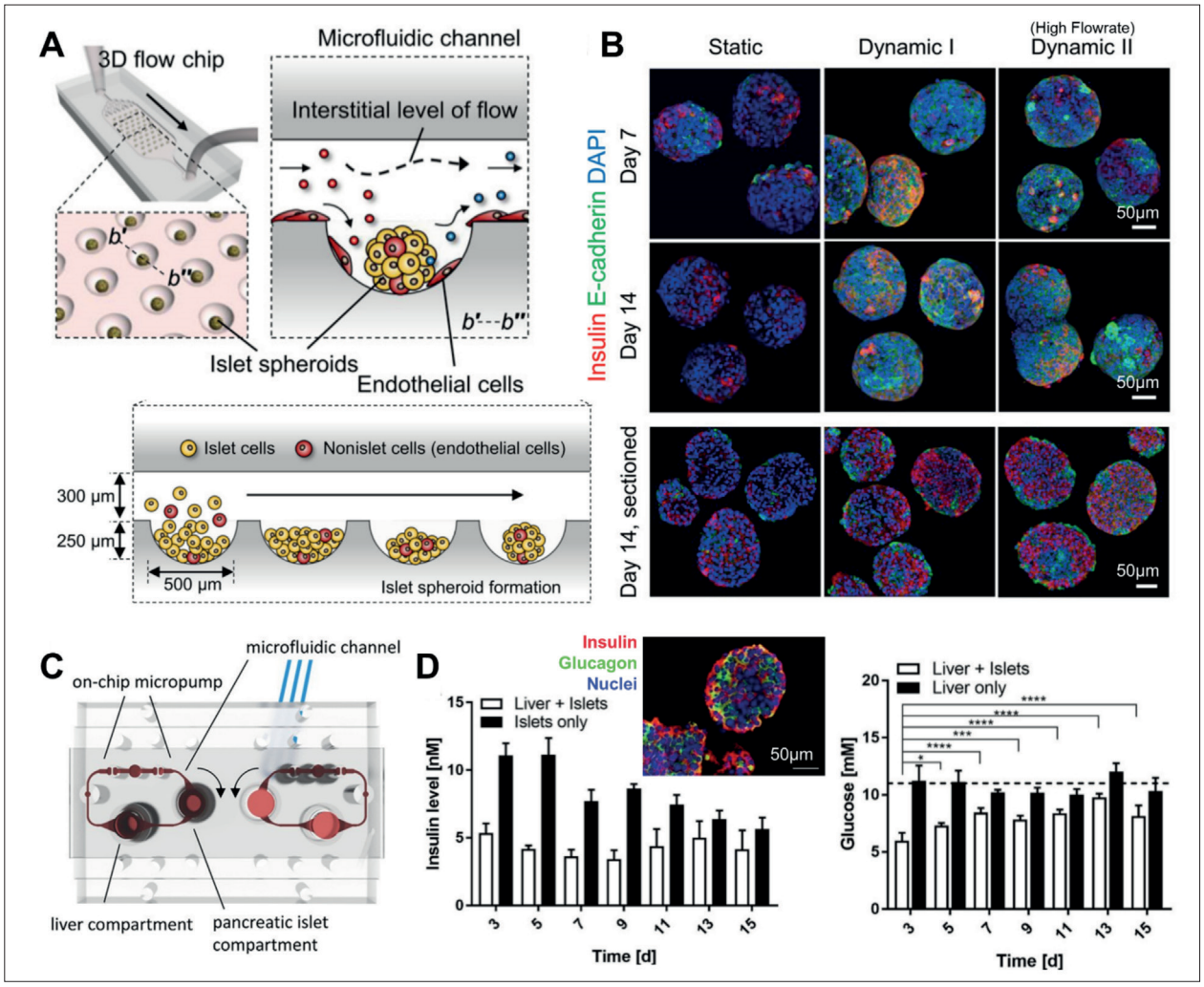

Figure 7. Microfabrication of devices for islet transplantation. (A) Schematic image of the spheroid-based microfluidic perfusion culture of pancreatic islets for mimicking the in vivo environment. (B) Immunofluorescence staining image of islet spheroids after 7 and 14 days. Confocal z-stacked and cross-sectioned images of islet spheroids exhibiting different culture conditions. Adapted with permission from reference[81]. Copyright © 2019 AAAS. (C) Bottom-view illustration image of the media circuits, respective culture compartments, and micropump valves. (D) Data of accumulation of insulin over 48-h intervals representing the pancreatic islet microtissues exhibit functional capabilities during a 15-day co-culture with liver spheroids, immunofluorescence staining image of the islet microtissues after 15 days in co-culture, and the glucose levels of liver spheroids after a medium exchange in co-culture and single culture. Adapted from reference[83]. Copyright © 2017 Bauer et al.

The first research report on the use of islets for bioprinting technology was published in 2015 using a hydrogel mixed with alginate and gelatin. The 3D scaffold had 17 layers, and the thickness of each layer was 0.1 mm[91]. Owing to the high survival rate of the functionalized 3D cultures of pancreatic islets, microvascularization is in high demand.

Thus, 3D bioprinting technology offers significant advantages in the use of multiple cells and biomaterials for blood vessel formation[92]. Subsequently, many researchers leveraged 3D bioprinting technology to investigate islet regeneration, vascularization, and transplantation (Table 2). Chen *et al.* utilized digital light processing (DLP)-3D printing technology to produce a retrievable encapsulation device for the delivery of islets to diabetic mice (Figure 8A)[93]. Encapsulated islets were found to be highly effective in ameliorating hyperglycemia in mice, even in the absence of immunosuppressive treatment. The retrievable device demonstrated sustained viability of transplanted islets and effectively prevented islet leakage over an extended period while the encapsulation capsule device was used (Figure 8B)[93]. Clua-Ferré *et al.* developed a rapid and efficient strategy for encapsulating cells in a collagen bioink crosslinked with tannic acid (TA) using a 3D bioprinter (Figure 8C)[94]. Smaller spheroid volumes and higher surface-to-volume ratios significantly improve the diffusion process, leading to a quicker response time to fluctuations

Table 2 Bioprinting technology for islet research

Bioprinting type	Cell sources	Biomaterial	Major achievements	Ref
Extrusion-based bioprinting	Mouse pancreatic islets, endothelial progenitor cells (EPC)	Alginate, gelatin methacryloyl (GelMA)	An optimized bioink formulation composed of alginate and gelatin was developed specifically for the encapsulation of islets and islet-related cells, enabling their 3D printing. Additionally, a custom-designed coaxial printer was created to facilitate the 3D printing of multicellular constructs that contain islets.	[89]
	Rat pancreatic islet, HUVEC, differentiated iPSC	dECM	Islet-laden dECM bioink was successfully bioprinted to construct 3D pancreatic tissue. The effectiveness of porcine dECM as a bioink source has demonstrated its ability to recreate tissue-specific conditions within the 3D constructs.	[71]
	Rat pancreatic islet	Alginate, methylcellulose	Macroporous 3D hydrogel constructs with precise geometry were successfully generated using a plottable hydrogel blend of ultrapure alginate and methylcellulose (Alg/MC), both of which have been approved clinically. This enabled the encapsulation of pancreatic islets while preserving their viability, morphology, and functionality. Notably, the islets within the Alg/MC hydrogel group maintained their viability and functionality, sustaining the production of insulin and glucagon.	[88]
	MIN6-m9, differentiated H1 hPSCs	dECM, PCL	A hybrid encapsulation system was developed using 3D bioprinting, combining a macroporous polymer capsule with a stagger-type membrane and assemblable structure, along with a nanoporous dECM hydrogel containing pancreatic islet-like aggregates. This hybrid system demonstrated biocompatibility both *in vitro* and *in vivo*, as evidenced by M1 macrophage polarization.	[95]
	MIN6	Alginate, PCL	In a long-term *in vivo* study, a subcutaneously implanted 3D-bioprinted construct aimed at preventing islet loss demonstrated promising results. Type 1 diabetes mice implanted with these bioprinted constructs exhibited a significant threefold increase in insulin secretion and maintained controlled glucose levels after 8 weeks of implantation.	[111]
DLP bioprinting	Mouse pancreatic islets	GelMA	Mini encapsulation devices with a groove structure, fabricated using DLP printing, were developed to prevent islet cell leakage. *In vivo* intraperitoneal glucose tolerance tests conducted at various time points showcased significant therapeutic improvement in glycemic control. Even after 15 weeks, a sufficient amount of viable islet cells were found in the retrieved implant.	[93]
	Rat pancreatic islet	dECM, hyaluronic acid methacrylate (HAMA)	The HAMA/pECM hydrogel demonstrated its ability to maintain islet cell adhesion and morphology *in vitro*. *In vivo* experiments further validated its efficacy, showing that the 3D-printed islet-encapsulated HAMA/pECM hydrogel elevated insulin levels in diabetic mice, regulated blood glucose levels within the normal range for 90 days, and exhibited rapid insulin secretion in response to blood glucose stimulation. Additionally, the HAMA/pECM hydrogel promoted the attachment and proliferation of new blood vessels, leading to an increased density of vascularization.	[98]

in blood glucose levels (Figure 8D). This approach allows the encapsulation of a significant number of cells in a short duration (less than 1 min), thereby averting hypoxic stress-induced cell dysfunction[94]. Hwang *et al.* fabricated a hybridized encapsulation scheme for pancreatic islet-like aggregates using 3D bioprinting technology (Figure 8E)[95]. The system comprises a modular macroporous polymer capsule configuration with a nanoporous pancreatic tissue-derived dECM (pdECM) hydrogel, which effectively shields the cells from the mechanical forces generated during 3D bioprinting, enabling them to maintain their viability, proliferation, and insulin-secreting functionality (Figure 8F). Biocompatibility of the amalgamated encapsulation tool was confirmed both *in vitro* and *in vivo*, demonstrating reduced immune responses. In addition, the authors successfully established a printing process to construct islet-like aggregates from human pluripotent stem cells that exhibited augmented structural maturation and functional enhancement[95]. Recently, various endothelial cells and angiogenic growth factors have been printed using islets. One research group developed microspheres containing VEGF on 3D-printed poly(dimethylsiloxane)-based constructs and loaded the islets, resulting in significant vascularization within 4 weeks[96]. Vascular cells such as endothelial progenitor cells (EPCs), human umbilical vein endothelial cells (HUVECs), and induced

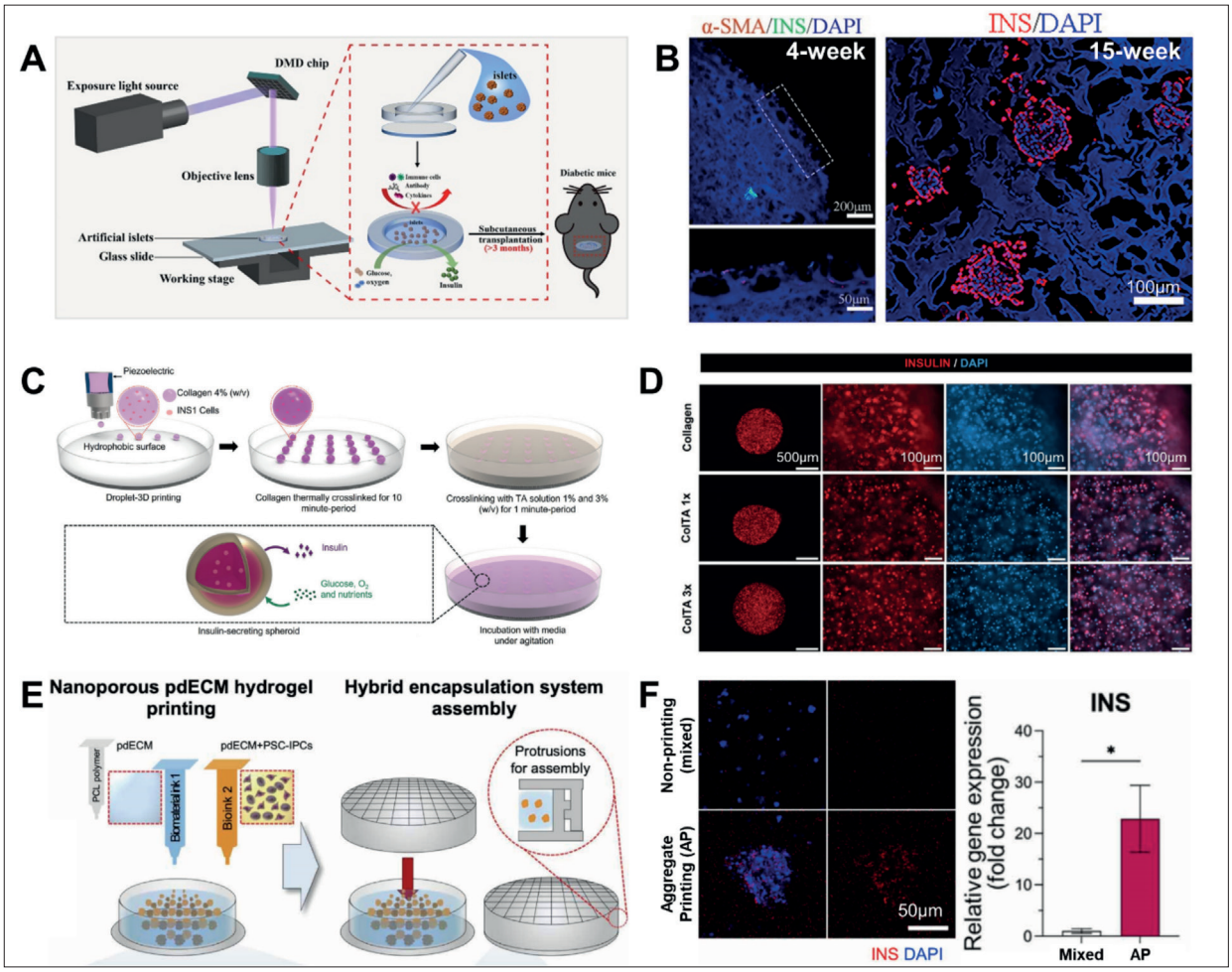

Figure 8. Bioprinting for islet transplantation. (A) Schematic image of the DLP-3D printing mini-capsule device for islet delivery to treat diabetic mice without immunosuppressant. (B) Representative immunofluorescence staining images of the retrieved grafts after transplantation for 4 weeks, and the retrieved encapsulated islet grafts after implantation for 15 weeks, which show the foreign body response after the transplantation of the encapsulated islets. Adapted with permission from reference [93]. Copyright © 2022 American Chemical Society. (C) Schematic image of cell-laden spheroids using different concentrations of TA solution, generated using a 3D bioprinter. (D) Representative immunofluorescence staining images of INS1E cells encapsulated in the spheroids after 10 days, showing that collagen crosslinked with TA enables insulin secretion. Adapted with permission from reference [94]. Copyright © 2022 John Wiley and Sons. (E) Schematic image of the fabrication process of the hybrid encapsulation system comprising a 3D-printed macroporous polymer capsule and pancreatic tissue-derived ECM hydrogel. (F) Gene expression analysis of human pluripotent stem cell-derived insulin-producing cells (hPSC-IPCs) after 7 days of encapsulation, and representative immunofluorescence staining images of hPSC-IPCs, which indicate the maturation of β-cells in aggregate printing group. Adapted with permission from reference [95]. Copyright © 2021 IOP Publishing.

pluripotent stem cell-derived endothelial cells (iPSC-ECs) are widely used with islet or insulin-producing cells[71,97]. The 3D printing technology also enables the fabrication of complex structures that can support vascularization. Wang *et al.* printed a porous structure that facilitated vascular penetration and interactions to form a vascular network on a hydrogel[98]. In addition, an idea has been introduced that a 3D-bioprinted encapsulation system could reduce immune response after the transplantation. Islet-like aggregates were microencapsulated in a tissue-specific bioink, and the printed construct was macroencapsulated in a PCL container that blocked immune cells[95]. Moreover, the utilization of genetically modified cells in bioprinting, with no immune response concerns, presents significant advantages in terms of controlling the physical and biochemical culture environment of the cells based on the specific circumstances. This, in turn, allows for the development of an efficient and precise delivery system for personalized tumor therapy, thereby amplifying the targeting effect while maintaining the structural integrity of the fabricated construct[99].

5. Future directions and conclusion

In this comprehensive review, we investigated the latest advancements in biomaterials and biofabrication technologies

and their profound implications in islet transplantation. Notably, remarkable strides toward islet transplantation have been made in recent decades, predominantly because of the remarkable progress achieved in biofabrication technology. Many biofabrication techniques have been introduced by researchers who employed diverse biomaterials as carriers for efficient islet delivery. The primary focus of these studies was to enhance islet engraftment, fortify immune protection, and, ultimately, prolong graft viability. To address the challenge of the immune response and optimize cell survival, it is imperative for researchers to prioritize the development of encapsulation technology as a viable means of islet delivery. Although ongoing clinical trials are assessing the efficacy of microencapsulated islets, sustained blood glucose control over an extended period has not yet been achieved. The fundamental objective of islet encapsulation is to mitigate the risk of immune rejection of transplanted islets while effectively emulating the pancreatic microenvironment, thereby facilitating insulin secretion and enabling the uptake of vital nutrients for sustained survival.

The careful selection of appropriate biomaterials is of paramount importance for establishing an optimal microenvironment for islets, which is crucial for the transplantation process. The microenvironment encompassing the islet graft exerts a pivotal influence, owing to a multitude of factors. A particularly promising approach for islet transplantation involves the utilization of dECM, which offers distinct advantages and specialized characteristics. Through the removal of cellular components while retaining the native ECM structure, the dECM serves as a biocompatible scaffold that facilitates the survival and functionality of islets. The integration of dECM in the context of islet transplantation enhances the biocompatibility of islet grafts, diminishes the risk of immune rejection, and fosters a favorable microenvironment conducive to sustained survival and insulin production in islets. Extensive research focused on dECM derived from pancreatic tissue has successfully validated its inherent characteristics, particularly regarding the intricate interplay between islets and their surrounding environmental cues, including viability, insulin secretion, and glucose responsiveness. Furthermore, dECM can be further functionalized to enable the targeted delivery of bioactive molecules, such as immunomodulatory factors or angiogenic agents, thereby offering additional enhancements to the therapeutic outcomes of islet transplantation.

The choice of the fabrication method is of significant importance in the development of a comprehensive islet delivery system that encompasses both biomaterials and cells. The versatile nature of the 3D bioprinting technology enables the use of multiple biomaterials and facilitates the creation of constructs with tailored properties. Furthermore, biofabrication technologies, including 3D bioprinting, have the potential to establish high-throughput manufacturing systems that allow rapid and efficient production. By incorporating biomaterials with diverse mechanical and biochemical characteristics, bioprinting technology can faithfully mimic the native pancreatic microenvironment and optimize the conditions for islet survival and functionality. Consequently, this high-throughput bioprinting technology holds promise for meeting the clinical demand for large-scale islet encapsulation constructs and for advancing the field of islet transplantation. Combining the strengths of dECM and bioprinting technology offers an opportunity to enhance the efficacy and long-term outcomes of islet transplantation, bringing us closer to curing diabetes.

Concurrently, there is an imminent need for more alternative cell sources. Multiple cell types have been used in islet delivery systems to generate insulin-producing cells. Although cell lines present advantages in terms of ease of handling and mass production, they present notable challenges in clinical trials and are inherently constrained in terms of their capabilities. The use of primary islets obtained from suitable donors poses inherent challenges, including those associated with allograft transplantation and limited availability. Consequently, a promising avenue in this domain is the utilization of insulin-producing cells differentiated from human or patient-derived iPSCs. This approach offers unrestricted access to organs and facilitates donor-independent transplantation. This approach offers unrestricted access to organs and facilitates donor-independent transplantation, while the improvement of differentiation efficiency through established protocols is still ongoing. Although several differentiation protocols have been established, the implementation of this approach is still in progress, with challenges such as difficulties in improving the efficiency of differentiation[100–103]. The iPSC differentiation technique presents technical complexities and financial challenges that require further attention[104,105]. Nevertheless, differentiation techniques to generate insulin-producing cells are expected to play a critical role in future research on islet transplantation.

Acknowledgments

None.

Funding

This work was funded by the National Research Foundation of South Korea (NRF) grant from the Ministry of Science and ICT (No. 2021R1A2C2004981) and supported by the Korean Fund for Regenerative Medicine funded by the Ministry of Science and ICT and Ministry of Health and Welfare (21A0104L1, Republic of Korea), as well as the

Alchemist Project 1415180884 (20012378, Development of Meta Soft Organ Module Manufacturing Technology without Immunity Rejection and Module Assembly Robot System) funded by the Ministry of Trade, Industry & Energy (MOTIE, Republic of Korea).

Conflict of interest

The authors declare no conflicts of interests.

Author contributions

Conceptualization: Dayoon Kang, Jaewook Kim, Jinah Jang
Supervision: Jinah Jang
Writing – original draft: Dayoon Kang, Jaewook Kim
Writing – review & editing: Jinah Jang

Ethics approval and consent to participate

Not applicable.

Consent for publication

Not applicable.

Availability of data

Not applicable.

References

1. Alwafi H, Alsharif AA, Wei L, *et al.*, 2020, Incidence and prevalence of hypoglycaemia in type 1 and type 2 diabetes individuals: A systematic review and meta-analysis. *Diabetes Res Clin Pract*, 170: 108522.
2. Shapiro AMJ, Lakey JRT, Ryan EA, *et al.*, 2000, Islet transplantation in seven patients with Type 1 diabetes mellitus using a glucocorticoid-free immunosuppressive regimen. *N Engl J Med*, 343(4): 230–238.
3. Merani S, Shapiro AMJ, 2006, Current status of pancreatic islet transplantation. *Clin Sci*, 110(6): 611–625.
4. Shapiro AMJ, Pokrywczynska M, Ricordi C, 2017, Clinical pancreatic islet transplantation. *Nat Rev Endocrinol*, 13(5): 268–277.
5. Vantyghem MC, de Koning EJP, Pattou F, *et al.*, 2019, Advances in β-cell replacement therapy for the treatment of type 1 diabetes. *The Lancet*, 394(10205): 1274–1285.
6. Jansson L, Carlsson PO, 2002, Graft vascular function after transplantation of pancreatic islets. *Diabetologia*, 45(6): 749–763.
7. Zhang N, Su D, Qu S, *et al.*, 2006, Sirolimus is associated with reduced islet engraftment and impaired β-cell function. *Diabetes*, 55(9): 2429–2436.
8. Kim JE, Kim SH, Jung Y, 2016, Current status of three-dimensional printing inks for soft tissue regeneration. *Tissue Eng Regen Med*, 13(6): 636–646.
9. Marfil-Garza BA, Shapiro AMJ, Kin T, 2021, Clinical islet transplantation: Current progress and new frontiers. *J Hepatobiliary Pancreat Sci*, 28(3): 243–254.
10. Schuetz C, Anazawa T, Cross SE, *et al.*, 2018, β cell replacement therapy. *Transplantation*, 102(2): 215–229.
11. Cantarelli E, Piemonti L, 2011, Alternative transplantation sites for pancreatic islet grafts. *Curr Diab Rep*, 11(5): 364–374.
12. Sakata N, Tan A, Chan N, *et al.*, 2009, Efficacy comparison between intraportal and subcapsular islet transplants in a murine diabetic model. *Transplant Proc*, 41(1): 346–349.
13. Shi Y, Zhao YZ, Jiang Z, *et al.*, 2022, Immune-protective formulations and process strategies for improved survival and function of transplanted islets. *Front Immunol*, 13, 923241.
14. Yoshihara E, O'Connor C, Gasser E, *et al.*, 2020, Immune-evasive human islet-like organoids ameliorate diabetes. *Nature*, 586(7830): 606–611.
15. Liang JP, Accolla RP, Soundirarajan M, *et al.*, 2021, Engineering a macroporous oxygen-generating scaffold for enhancing islet cell transplantation within an extrahepatic site. *Acta Biomater*, 130: 268–280.
16. Chow LW, Wang L jia, Kaufman DB, *et al.*, 2010, Self-assembling nanostructures to deliver angiogenic factors to pancreatic islets. *Biomaterials*, 31(24): 6154–6161.
17. Sigrist S, Mechine-Neuville A, Mandes K, *et al.*, 2003, Influence of VEGF on the viability of encapsulated pancreatic rat islets after transplantation in diabetic mice. *Cell Transplant*, 12(6): 627–635.
18. Zhang N, Richter A, Suriawinata J, *et al.*, 2004, Elevated vascular endothelial growth factor production in islets improves islet graft vascularization. *Diabetes*, 53(4): 963–970.
19. Verseijden F, Posthumus-van Sluijs SJ, van Neck JW, *et al.*, 2012, Vascularization of prevascularized and non-prevascularized fibrin-based human adipose tissue constructs after implantation in nude mice. *J Tissue Eng Regen Med*, 6(3): 169–178.
20. Vlahos AE, Kinney SM, Kingston BR, *et al.*, 2020, Endothelialized collagen based pseudo-islets enables tuneable subcutaneous diabetes therapy. *Biomaterials*, 232: 119710.
21. Gupta R, Sefton M V., 2011, Application of an endothelialized modular construct for islet transplantation in syngeneic and allogeneic immunosuppressed rat models. *Tissue Eng Part A*, 17(15–16): 2005–2015.
22. Vlahos AE, Cober N, Sefton MV, 2017, Modular tissue engineering for the vascularization of subcutaneously transplanted pancreatic islets. *Proc Natl Acad Sci*, 114(35): 9337–9342.
23. Stendahl JC, Kaufman DB, Stupp SI, 2009, Extracellular matrix in pancreatic islets: Relevance to scaffold design and transplantation. *Cell Transplant*, 18(1): 1–12.

24. Place ES, Evans ND, Stevens MM, 2009, Complexity in biomaterials for tissue engineering. *Nat Mater*, 8(6): 457–470.

25. Sandler S, Andersson A, Eizirik DL, *et al.*, 1997, Assessment of insulin secretion *in vitro* from microencapsulated fetal porcine islet-like cell clusters and rat, mouse, and human pancreatic islets. *Transplantation*, 63(12): 1712–1718.

26. Song S, Roy S, 2016, Progress and challenges in macroencapsulation approaches for type 1 diabetes (T1D) treatment: Cells, biomaterials, and devices. *Biotechnol Bioeng*, 113(7): 1381–1402.

27. Yang K, O'Cearbhaill ED, Liu SS, *et al.*, 2021, A therapeutic convection-enhanced macroencapsulation device for enhancing β cell viability and insulin secretion. *Proc Natl Acad Sci U S A*, 118(37): e2101258118.

28. Goswami D, Domingo-Lopez DA, Ward NA, *et al.*, 2021, Design considerations for macroencapsulation devices for stem cell derived islets for the treatment of type 1 diabetes. *Adv Sci*, 8(16): 2100820.

29. Desai T, Shea LD, 2017, Advances in islet encapsulation technologies. *Nat Rev Drug Discov*, 16(5): 338–350.

30. White AM, Shamul JG, Xu J, *et al.*, 2020, Engineering strategies to improve islet transplantation for type 1 diabetes therapy. *ACS Biomater Sci Eng*, 6(5): 2543–2562.

31. Ching SH, Bansal N, Bhandari B, 2017, Alginate gel particles–A review of production techniques and physical properties. *Crit Rev Food Sci Nutr*, 57(6): 1133–1152.

32. Zhang J, Zhu Y, Song J, *et al.*, 2019, Rapid and long-term glycemic regulation with a balanced charged immune-evasive hydrogel in T1DM mice. *Adv Funct Mater*, 29(19): 1900140.

33. Kim JH, Yoo JJ, Lee SJ, 2016, Three-dimensional cell-based bioprinting for soft tissue regeneration. *Tissue Eng Regen Med*, 13(6): 647–662.

34. Kong X, Chen L, Li B, *et al.*, 2021, Applications of oxidized alginate in regenerative medicine. *J Mater Chem B*, 9(12): 2785–2801.

35. Volpatti LR, Bochenek MA, Facklam AL, *et al.*, 2023, Partially oxidized alginate as a biodegradable carrier for glucose-responsive insulin delivery and islet cell replacement therapy. *Adv Healthc Mater*, 12(2): 2201822.

36. Cen L, Liu W, Cui L, *et al.*, 2008, Collagen tissue engineering: development of novel biomaterials and applications. *Pediatr Res*, 63(5): 492–496.

37. Parenteau-Bareil R, Gauvin R, Berthod F, 2010, Collagen-based biomaterials for tissue engineering applications. *Materials (Basel)*, 3(3): 1863–1887.

38. Rosenblatt J, Devereux B, Wallace DG, 1993, Dynamic rheological studies of hydrophobic interactions in injectable collagen biomaterials. *J Appl Polym Sci*, 50(6): 953–963.

39. Rosenblatt J, Rhee W, Wallace D, 1989, The effect of collagen fiber size distribution on the release rate of proteins from collagen matrices by diffusion. *J Control Release*, 9(3): 195–203.

40. Lee BR, Hwang JW, Choi YY, *et al.*, 2012, *In situ* formation and collagen-alginate composite encapsulation of pancreatic islet spheroids. *Biomaterials*, 33(3): 837–845.

41. Lee SJ, Yoo JJ, Atala A, 2018, Biomaterials and tissue engineering, in *Clinical Regenerative Medicine in Urology*, Springer Singapore, Singapore, 17–51.

42. Riopel M, 2014, Collagen matrix support of pancreatic islet survival and function. *Front Biosci*, 19(1): 77.

43. Yang K, Lee M, Jones PA, *et al.*, 2020, A 3D culture platform enables development of zinc-binding prodrugs for targeted proliferation of β cells. *Sci Adv*, 6(47): eabc3207.

44. He C, Ji H, Qian Y, *et al.*, 2019, Heparin-based and heparin-inspired hydrogels: size-effect, gelation and biomedical applications. *J Mater Chem B*, 7(8): 1186–1208.

45. Cabric S, Sanchez J, Johansson U, *et al.*, 2010, Anchoring of vascular endothelial growth factor to surface-immobilized heparin on pancreatic islets: Implications for stimulating islet angiogenesis. *Tissue Eng Part A*, 16(3): 961–970.

46. Uzunalli G, Tumtas Y, Delibasi T, *et al.*, 2015, Improving pancreatic islet *in vitro* functionality and transplantation efficiency by using heparin mimetic peptide nanofiber gels. *Acta Biomater*, 22: 8–18.

47. Davis NE, Beenken-Rothkopf LN, Mirsoian A, *et al.*, 2012, Enhanced function of pancreatic islets co-encapsulated with ECM proteins and mesenchymal stromal cells in a silk hydrogel. *Biomaterials*, 33(28): 6691–6697.

48. Hamilton DC, Shih HH, Schubert RA, *et al.*, 2017, A silk-based encapsulation platform for pancreatic islet transplantation improves islet function *in vivo*. *J Tissue Eng Regen Med*, 11(3): 887–895.

49. Kumar M, Gupta P, Bhattacharjee S, *et al.*, 2018, Immunomodulatory injectable silk hydrogels maintaining functional islets and promoting anti-inflammatory M2 macrophage polarization. *Biomaterials*, 187: 1–17.

50. Chendke GS, Faleo G, Juang C, *et al.*, 2019, Supporting survival of transplanted stem-cell-derived insulin-producing cells in an encapsulation device augmented with controlled release of amino acids. *Adv Biosyst*, 3(9): 1900086.

51. Kumar M, Nandi SK, Kaplan DL, *et al.*, 2017, Localized immunomodulatory silk macrocapsules for islet-like spheroid formation and sustained insulin production. *ACS Biomater Sci Eng*, 3(10): 2443–2456.

52. Mao D, Zhu M, Zhang X, *et al.*, 2017, A macroporous heparin-releasing silk fibroin scaffold improves islet transplantation outcome by promoting islet revascularisation and survival. *Acta Biomater*, 59: 210–220.

53. Öberg-Welsh C, 2001, Long-term culture in matrigel enhances the insulin secretion of fetal porcine islet-like cell clusters *in vitro*. *Pancreas*, 22(2): 157–163.

54. Aisenbrey EA, Murphy WL, 2020, Synthetic alternatives to Matrigel. *Nat Rev Mater*, 5(7): 539–551.

55. Foster GA, García AJ, 2017, Bio-synthetic materials for immunomodulation of islet transplants. *Adv Drug Deliv Rev*, 114: 266–271.

56. Dufour JM, Rajotte R V, Zimmerman M, *et al.*, 2005, Development of an ectopic site for islet transplantation, using biodegradable scaffolds. *Tissue Eng*, 11(9–10): 1323–1331.

57. Blomeier H, Zhang X, Rives C, *et al.*, 2006, Polymer scaffolds as synthetic microenvironments for extrahepatic islet transplantation. *Transplantation*, 82(4): 452–459.

58. Guo C, Zhang T, Tang J, *et al.*, 2023, Construction of PLGA porous microsphere-based artificial pancreatic islets assisted by the cell centrifugation perfusion technique. *ACS Omega*, 8(17): 15288–15897.

59. Vanaei S, Parizi MS, Vanaei S, *et al.*, 2021, An overview on materials and techniques in 3D bioprinting toward biomedical application. *Eng Regen*, 2: 1–18.

60. Singh S, Prakash C, Singh M, *et al.*, 2019, Poly-lactic-Acid: Potential material for bio-printing applications, in *Biomanufacturing*. Springer International Publishing, Cham, 69–87.

61. Huang H, Shang Y, Li H, *et al.*, 2022, Co-transplantation of islets-laden microgels and biodegradable O 2 -generating microspheres for diabetes treatment. *ACS Appl Mater Interfaces*, 14(34): 38448–38458.

62. Hoveizi E, Tavakol S, 2019, Therapeutic potential of human mesenchymal stem cells derived beta cell precursors on a nanofibrous scaffold: An approach to treat diabetes mellitus. *J Cell Physiol*, 234(7): 10196–10204.

63. Liu XY, Nothias JM, Scavone A, *et al.*, 2010, Biocompatibility investigation of polyethylene glycol and alginate-poly-l-lysine for islet encapsulation. *ASAIO J*, 56(3): 241–245.

64. De Toni T, Stock AA, Devaux F, *et al.*, 2022, Parallel evaluation of polyethylene glycol conformal coating and alginate microencapsulation as immunoisolation strategies for pancreatic islet transplantation. *Front Bioeng Biotechnol*, 10, 886483.

65. Teramura Y, Kaneda Y, Iwata H, 2007, Islet-encapsulation in ultra-thin layer-by-layer membranes of poly(vinyl alcohol) anchored to poly(ethylene glycol)-lipids in the cell membrane. *Biomaterials*, 28(32): 4818–4825.

66. Weaver JD, Headen DM, Hunckler MD, *et al.*, 2018, Design of a vascularized synthetic poly(ethylene glycol) macroencapsulation device for islet transplantation. *Biomaterials*, 172: 54–65.

67. Stock AA, Gonzalez GC, Pete SI, *et al.*, 2022, Performance of islets of Langerhans conformally coated via an emulsion cross-linking method in diabetic rodents and nonhuman primates. *Sci Adv*, 8(26): eabm3145.

68. Gunatillake PA, Adhikari R, 2003, Biodegradable synthetic polymers for tissue engineering. *Eur Cell Mater*, 5: 1–16; discussion 16.

69. Kim BS, Das S, Jang J, *et al.*, 2020, Decellularized extracellular matrix-based bioinks for engineering tissue- and organ-specific microenvironments. *Chem Rev*, 120(19): 10608–10661.

70. Pati F, Jang J, Ha DH, *et al.*, 2014, Printing three-dimensional tissue analogues with decellularized extracellular matrix bioink. *Nat Commun*, 5(1), 3935.

71. Kim J, Shim IK, Hwang DG, *et al.*, 2019, 3D cell printing of islet-laden pancreatic tissue-derived extracellular matrix bioink constructs for enhancing pancreatic functions. *J Mater Chem B*, 7(10): 1773–1781.

72. Damodaran RG, Vermette P, 2018, Decellularized pancreas as a native extracellular matrix scaffold for pancreatic islet seeding and culture. *J Tissue Eng Regen Med*, 12(5): 1230–1237.

73. Sackett SD, Tremmel DM, Ma F, *et al.*, 2018, Extracellular matrix scaffold and hydrogel derived from decellularized and delipidized human pancreas. *Sci Rep*, 8(1): 10452.

74. Berkova Z, Zacharovova K, Patikova A, *et al.*, 2022, Decellularized pancreatic tail as matrix for pancreatic islet transplantation into the greater omentum in rats. *J Funct Biomater*, 13(4): 171.

75. Jun I, Han HS, Edwards J, *et al.*, 2018, Electrospun fibrous scaffolds for tissue engineering: Viewpoints on architecture and fabrication. *Int J Mol Sci*, 19(3): 745.

76. Zaszczyńska A, Niemczyk-Soczynska B, Sajkiewicz P, 2022, A comprehensive review of electrospun fibers, 3D-printed scaffolds, and hydrogels for cancer therapies. *Polymers (Basel)*, 14(23): 5278.

77. Buitinga M, Truckenmüller R, Engelse MA, *et al.*, 2013, Microwell scaffolds for the extrahepatic transplantation of islets of langerhans. *PLoS One*, 8(5): e64772.

78. Liu Q, Wang X, Chiu A, *et al.*, 2021, A zwitterionic polyurethane nanoporous device with low foreign-body response for islet encapsulation. *Adv Mater*, 33(39): 2102852.

79. Mridha AR, Dargaville TR, Dalton PD, *et al.*, 2022, Prevascularized retrievable hybrid implant to enhance function of subcutaneous encapsulated islets. *Tissue Eng Part A*, 28(5–6): 212–224.

80. Rodríguez-Comas J, Ramón-Azcón J, 2022, Islet-on-a-chip for the study of pancreatic β-cell function. *Vitr Model*, 1(1): 41–57.

81. Jun Y, Lee J, Choi S, *et al.*, 2019, *In vivo*–mimicking microfluidic perfusion culture of pancreatic islet spheroids. *Sci Adv*, 5(11): eaax4520.

82. Patel SN, Ishahak M, Chaimov D, *et al.*, 2021, Organoid microphysiological system preserves pancreatic islet function within 3D matrix. *Sci Adv*, 7(7).

83. Bauer S, Wennberg Huldt C, Kanebratt KP, *et al.*, 2017, Functional coupling of human pancreatic islets and liver spheroids on-a-chip: Towards a novel human *ex vivo* type 2 diabetes model. *Sci Rep*, 7(1): 14620.

84. Abadpour S, Aizenshtadt A, Olsen PA, *et al.*, 2020, Pancreas-on-a-chip technology for transplantation applications. *Curr Diab Rep*, 20(12): 72.

85. Billiet T, Vandenhaute M, Schelfhout J, *et al.*, 2012, A review of trends and limitations in hydrogel-rapid prototyping for tissue engineering. *Biomaterials*, 33(26): 6020–6041.

86. Kim D, Kang D, Kim D, *et al.*, 2023, Volumetric bioprinting strategies for creating large-scale tissues and organs. *MRS Bull*, 48: 657–667.

87. Kim J, Kang K, Drogemuller CJ, *et al.*, 2019, Bioprinting an artificial pancreas for Type 1 diabetes. *Curr Diab Rep*, 19(8): 53.

88. Duin S, Schütz K, Ahlfeld T, *et al.*, 2019, 3D bioprinting of functional islets of Langerhans in an alginate/methylcellulose hydrogel blend. *Adv Healthc Mater*, 8(7): 1801631.

89. Liu X, Carter SD, Renes MJ, *et al.*, 2019, Development of a coaxial 3D printing platform for biofabrication of implantable islet-containing constructs. *Adv Healthc Mater*, 8(7): 1801181.

90. Gungor-Ozkerim PS, Inci I, Zhang YS, *et al.*, 2018, Bioinks for 3D bioprinting: An overview. *Biomater Sci*, 6(5): 915–946.

91. Marchioli G, van Gurp L, van Krieken PP, *et al.*, 2015, Fabrication of three-dimensional bioplotted hydrogel scaffolds for islets of Langerhans transplantation. *Biofabrication*, 7(2): 025009.

92. Sun W, Starly B, Daly AC, *et al.*, 2020, The bioprinting roadmap. *Biofabrication*, 12(2): 022002.

93. Chen S, Luo J, Shen L, *et al.*, 2022, 3D printing mini-capsule device for islet delivery to treat Type 1 diabetes. *ACS Appl Mater Interfaces*, 14(20): 23139–23151.

94. Clua-Ferré L, De Chiara F, Rodríguez-Comas J, *et al.*, 2022, Collagen-tannic acid spheroids for β-cell encapsulation fabricated using a 3D bioprinter. *Adv Mater Technol*, 7(7): 2101696.

95. Hwang DG, Jo Y, Kim M, *et al.*, 2022, A 3D bioprinted hybrid encapsulation system for delivery of human pluripotent stem cell-derived pancreatic islet-like aggregates. *Biofabrication*, 14(1): 014101.

96. Scheiner KC, Coulter F, Maas-Bakker RF, *et al.*, 2020, Vascular endothelial growth factor–releasing microspheres based on poly(ε-caprolactone-PEG-ε-caprolactone)-b-poly(L-lactide) multiblock copolymers incorporated in a three-dimensional printed poly(dimethylsiloxane) cell macroencapsulation device. *J Pharm Sci*, 109(1): 863–870.

97. Wang X, 2019, Advanced polymers for three-dimensional (3D) organ bioprinting. *Micromachines*, 10(12): 814.

98. Wang D, Guo Y, Zhu J, *et al.*, 2022, Hyaluronic acid methacrylate/pancreatic extracellular matrix as a potential 3D printing bioink for constructing islet organoids. *Acta Biomater*, 165: 86–101.

99. Fu B, Shen J, Chen Y, *et al.*, 2021, Narrative review of gene modification: Applications in three-dimensional (3D) bioprinting. *Ann Transl Med*, 9(19):1502.

100. Hogrebe NJ, Augsornworawat P, Maxwell KG, *et al.*, 2020, Targeting the cytoskeleton to direct pancreatic differentiation of human pluripotent stem cells. *Nat Biotechnol*, 38(4): 460–470.

101. Pagliuca FW, Millman JR, Gürtler M, *et al.*, 2014, Generation of functional human pancreatic β cells *in vitro*. *Cell*, 159(2): 428–439.

102. Rezania A, Bruin JE, Arora P, *et al.*, 2014, Reversal of diabetes with insulin-producing cells derived *in vitro* from human pluripotent stem cells. *Nat Biotechnol*, 32(11): 1121–1133.

103. Nair GG, Liu JS, Russ HA, *et al.*, 2019, Recapitulating endocrine cell clustering in culture promotes maturation of human stem-cell-derived β cells. *Nat Cell Biol*, 21(2): 263–274.

104. Penney J, Ralvenius WT, Tsai LH, 2020, Modeling Alzheimer's disease with iPSC-derived brain cells. *Mol Psychiatry*, 25(1): 148–167.

105. Turinetto V, Orlando L, Giachino C, 2017, Induced pluripotent stem cells: Advances in the quest for genetic stability during reprogramming process. *Int J Mol Sci*, 18(9): 1952.

106. Mirmalek-Sani SH, Orlando G, McQuilling JP, *et al.*, 2013, Porcine pancreas extracellular matrix as a platform for endocrine pancreas bioengineering. *Biomaterials*, 34(22): 5488–5495.

107. Napierala H, Hillebrandt KH, Haep N, *et al.*, 2017, Engineering an endocrine neo-pancreas by repopulation of a decellularized rat pancreas with islets of Langerhans. *Sci Rep*, 7(1): 41777.

108. Chaimov D, Baruch L, Krishtul S, *et al.*, 2017, Innovative encapsulation platform based on pancreatic extracellular matrix achieve substantial insulin delivery. *J Control Release*, 257: 91–101.

109. Jiang K, Chaimov D, Patel SN, *et al.*, 2019, 3-D physiomimetic extracellular matrix hydrogels provide a supportive microenvironment for rodent and human islet culture. *Biomaterials*, 198: 37–48.

110. Zhu Y, Wang D, Yao X, *et al.*, 2021, Biomimetic hybrid scaffold of electrospun silk fibroin and pancreatic decellularized extracellular matrix for islet survival. *J Biomater Sci Polym Ed*, 32(2): 151–165.

111. Ahn CB, Lee JH, Kim JH, *et al.*, 2022, Development of a 3D subcutaneous construct containing insulin-producing beta cells using bioprinting. *Bio-Design Manuf*, 5(2): 265–276.

ACCSCIENCE PUBLISHING

International Journal of Bioprinting

RESEARCH ARTICLE

Lightweight load-bearing heat dissipation multifunctional pomelo peel-inspired structures fabricated by laser powder bed fusion

Linxuan Li, Dongdong Gu*, He Liu, Han Zhang, Junhao Shan, and Yijuan Zhang

Jiangsu Provincial Engineering Laboratory for Laser Additive Manufacturing of High-Performance Metallic Components, College of Materials Science and Technology, Nanjing University of Aeronautics and Astronautics, Nanjing 210016, China

This article belongs to the *Special Issue: 3D Bioprinting for Materials and Application*)

Abstract

The heat dissipation structure used in modern airborne radar chassis not only requires lightweight, but also pursues better mechanical properties and heat dissipation performance. In this study, a stochastically porous pomelo peel-inspired gradient structure was fabricated by laser powder bed fusion using Al-Mg-Sc-Zr powder. This study focused on the formability, microstructure, mechanical properties, and heat dissipation performance of the biomimetic structure through experimental and finite element analysis approaches. The influence of volume fraction (*VF*) on structural mechanical properties, deformation modes, stress distribution, and heat dissipation performance was investigated. The results showed that the mechanical properties of the structure declined as the *VF*s decreased. The optimal mechanical performance was obtained at the *VF* of 45%, where the compressive strength, specific energy absorption (W_s), and specific compressive strength values were measured to be 63.47 MPa, 34.84 J/g, and 142.16 MPa/(g·cm^{-3}), respectively. Moreover, the W_s of the structures was higher than that of the reported aluminum alloy structures at the same *VF*. The biomimetic structure exhibited improved heat dissipation performance as the *VF*s decreased, with Reynolds number ranging from 2700 to 13,400. The structure of 30% *VF* with a remarkable heat transfer efficiency index of 1.86 displayed the best heat dissipation performance. In addition, compared with the traditional fin structures, the bionic structure possessed better thermal resistance, heat transfer efficiency index, and temperature uniformity at the same *VF*. This study demonstrated notable potential of pomelo peel-inspired design for lightweight load-bearing applications capable of heat-dissipating performance, providing a novel perspective for design and fabrication of versatile structures in the aviation field.

Keywords: Multifunctional biomimetic structure; Laser powder bed fusion; Mechanical properties; Heat dissipation performance

***Corresponding author:**
Dongdong Gu
(dongdonggu@nuaa.edu.cn)

Citation: Li L, Gu D, Liu H, *et al.*, 2023, Lightweight load-bearing heat dissipation multifunctional pomelo peel-inspired structures fabricated by laser powder bed fusion. *Int J Bioprint*, 9(6): 1011.
https://doi.org/10.36922/ijb.1011

Received: May 29, 2023
Accepted: July 31, 2023
Published Online: August 30, 2023

Copyright: © 2023 Author(s). This is an Open Access article distributed under the terms of the Creative Commons Attribution License, permitting distribution, and reproduction in any medium, provided the original work is properly cited.

Publisher's Note: AccScience Publishing remains neutral with regard to jurisdictional claims in published maps and institutional affiliations.

1. Introduction

Biomimetic design is currently a thriving field in structural engineering, which derives extraordinary design insights from the multifunctional and high-performance

structures of natural organisms[1,2]. After the long and harsh natural selection, the complex structures of organisms have been optimized for multiple purposes and to adapt to the constraints imposed by the external environment[3]. Mimicking the strategies used by natural species is a promising way to obtain sophisticated bionic structures with the same exceptional performance[4,5]. However, traditional manufacturing methods face several limitations, including long manufacturing cycles, low forming accuracy, and difficulty in integrated processing, which hinder the development of bio-inspired structures[6]. In contrast, additive manufacturing (AM) technologies are ideally applicable to fabricating these bionic structures due to their layer-by-layer deposition manner[7-11]. Among various AM technologies, laser powder bed fusion (LPBF) has gained popularity for the processing of small- and medium-sized complex structures[12,13]. The key advantage of LPBF lies in fine resolution and good surface quality of the fabricated products, rendering it particularly well suited for printing these complex structures with complicated details. Consequently, LPBF has become widely applied to the fabrication of complex metal biomimetic structures[14-17].

Multifunctional and high-performance bionic structures processed by AM technology have received much attention in recent years. Natural organisms with excellent performance and unique structures, such as the Norway spruce[18,19], cuttlebone[20], horse hoof wall[21], and porcupine quills[22], have been a source of inspiration for the construction of regular biomimetic structures. Inspired by Norway spruce, which can withstand strong winds in severe cold, Lin *et al.*[18] and Hu *et al.*[19] developed a series of integral multifunctional structures with four gradient hollow tubes. The results indicated that the gradient structure, with the minimum tube size in the center, exhibited the highest specific absorption energy and the lowest effective thermal conductivity due to the common influence of gradient characteristics and hollow tubes. Based on the cuttlebone, which enables the cuttle to survive in the high-pressure environment of the deep sea, Yang *et al.*[20] developed a cuttlebone-like lattice (CLL). The mechanical properties of the graded/uniform CLL structures were compared with those of the graded/uniform body-centered-cubic (BCC) lattice. The study revealed that the CLL demonstrated superior compressive mechanical properties compared to the BCC, while the graded CLL exhibited the highest energy absorption capacity among the investigated structures. The horse hoof wall possesses exceptional impact resistance and fracture control capabilities attributed to its gradient configurations, tubular structures, and lamellar structures. Inspired by these structures, a bionic design was implemented using a multi-material three-dimensional (3D) printer[21]. The research findings indicated that the gradient characteristic resulted in a decrease in damage compared to samples with a uniform tubule distribution, highlighting the significant potential of bionic gradient structures as effective design elements. Moreover, the presence of a composition gradient zone at the multi-material interface can contribute to a strong metallurgical bonding between dissimilar materials[23], potentially modifying the mechanical properties. Another example is the quills covering porcupine that can protect it from aggressors and poke opponents due to their excellent hardness and rigidity. Drawing inspiration from the core-shell (C-S) structure of porcupine quills, a new lightweight and stiff C-S architecture, which consists of a syntactic epoxy foam core surrounded by a stiff carbon fiber-reinforced epoxy composite shell, was fabricated using direct ink writing[22]. The structural hierarchy of the bionic structure was consistent with that of porcupine quills, allowing for the achievement of both lightweight and high specific flexural stiffness. The potential of developing versatile and high-performance bionic structures was shown in the above research. However, there are shortcomings in these regularly distributed structures, which do not fully express all the characteristics of stochastically distributed biological materials. Additionally, in contrast to structures with random distribution, it is challenging to achieve smooth transitions between regular unit cells[24], which can reduce performance (e.g., heat dissipation and permeability) by impeding fluid flow. A random bone-inspired structure exhibited great mechanical properties, as well as properties related to cell penetration, nutrient diffusion, and biodegradation, that are similar to all the characteristics of natural bone[25]. Ge *et al.*[26] found that the compression strength and energy absorption capacity of stochastic trabecular-inspired structures were superior to regular triply periodic minimal surface structures at the same porosity. Tee *et al.*[27] further investigated the structure and performance of the porcupine quill and constructed a randomly porous structure with excellent mechanical properties, revealing that the strut connectivity and the uniformity of stress distribution are proportional to the number of struts. Despite these advancements, more research is needed to study stochastic biomimetic structures, particularly those with gradient characteristics.

The pomelo peel structure has attracted much interest owing to its potential for both excellent thermal[28,29] and mechanical[30,31] applications. Zhang *et al.*[29] developed a biomaterial with exceptional heat exchange performance based on the high specific surface area of pomelo peel. Inspired by the distinguished mechanical properties of pomelo peel, Zhang *et al.*[32] designed a hierarchical

honeycomb structure imitating pomelo peel, whose W_s and equivalent plateau stress were notably higher than the traditional honeycomb structure. Zhang *et al.*[33] investigated the heat dissipation performance and mechanical properties of pomelo peel-inspired structures. However, the designed structural cell in the study was a regular Kelvin cell, which did not express the stochastically porous structure and gradient characteristics of pomelo peel. The heat dissipation performance was inevitably affected by the unsmooth transition between cells. Besides, for the low tortuosity of the flow paths in the traditional regular lattice structure, the interaction between the fluid and the flow paths during heat dissipation is reduced. This resulted in some fluid passing directly through the flow paths, leading to a significant decline in heat transfer performance[34]. Yang *et al.*[35] conducted lattice structures composed of simple cubic cells with various gradient characteristics, showing that the best mechanical properties can be obtained if the structural gradient characteristics were consistent with those of pomelo peel. The research further optimized the pomelo peel-inspired structure design and demonstrated the latent capability of pomelo peel gradient characteristics in mechanical properties, but there is still a gap between the designed simple cubic lattice structure and the stochastically porous structure of pomelo peel. Therefore, there is a possibility for further improvement in the design of pomelo peel-inspired structures. In order to satisfy multifunctional requirements, a high-fidelity bio-inspired design and processing approach were implemented based on the stochastically porous structure and gradient characteristics of pomelo peel.

In this study, the morphology and microstructure of the pomelo peel structure were investigated by micro-computed tomography (micro-CT) and scanning electron microscopy (SEM). A high-fidelity biomimetic pomelo peel structure (BPPS) was designed and processed using LPBF with Al-Mg-Sc-Zr alloy powder. The structural formability and microstructure were analyzed, and the influence of volume fraction (*VF*) on structural mechanical properties, energy absorption performance, and deformation modes was investigated by compression test and finite element analysis (FEA). Additionally, the influence of the *VF* on heat dissipation performance was investigated through FEA, and the heat dissipation performance of the BPPSs and the traditional fin structure was compared. The lightweight multifunctional design and performance control of the BPPS were achieved.

2. Materials and methods

2.1. Configuration of BPPS

Figure 1 shows the structure characteristic of the pomelo peel. A longitudinal section of the complete pomelo is displayed in Figure 1A, where the thickness of the pomelo peel was about 20 mm. The micro-CT image of pomelo peel displays the stochastically porous structure characteristics (Figure 1B). The SEM image of pomelo peel from exocarp to endocarp shows that the cavity size of the microstructure from outside to inside gradually increased (Figure 1C), revealing the natural gradient structure characteristics of pomelo peel. The BPPS was designed based on the morphology and microstructure observed in the pomelo peel (Figure 2A). Precise control of the BPPS structure modeling was achieved by using Grasshopper software. The specific design tools (battery) in the Grasshopper software mainly included "Populate 3D," "Voronoi 3D," "Chromodoris," etc. A 3D Voronoi wireframe was constructed with 70 randomly-distributed seed points, exhibiting excellent similarity to the stochastically porous structure of pomelo peel. The numerical parameters of gradient characteristics in the different *VF*s BPPSs were set as the specified range (Figure 2F). The linear relationship of the gradient parameters variation in a given numerical range was established by the distance between each structural feature and the reference plane. The structure was precisely controlled at $12 \times 12 \times 12$ mm^3 by using the Boolean operation tool. The obvious gradient structure characteristics of BPPS-40% could be seen through the comparison of the top surface (Figure 2B) and bottom surface (Figure 2C) of BPPS. Figure 2D and E shows the longitudinal sections at a-a and b-b in Figure 2A, respectively, exhibiting the structural characteristics of the stochastic distribution. In order to investigate the influence of structural parameters on mechanical properties and heat dissipation performance, the *VF* was set as a structural variable (Figure 2F). BPPSs with four different *VF*s of 45%, 40%, 35%, and 30% were designed based on the model of pomelo peel reconstructed by micro-CT scanning data. The different *VF*s in BPPSs were achieved through the manipulation of rod diameters, leading to alterations in the porosity and topological structure. The variation of BPPSs porosity along the gradient direction is presented in Table 1.

2.2. Materials and LPBF process

The gas-atomized Al-4.2Mg-0.4Sc-0.2Zr alloy powder with an average particle size of 26.7 μm, which was primarily regular spherical (Figure 3A), was applied in this study. In order to enhance the forming quality of the structure, the powder was treated in a vacuum drying oven for 10 h and maintained at a temperature of 120°C before LPBF process. The LPBF equipment system developed by Nanjing University of Aeronautics and Astronautics, mainly composed of a YLR-500 ytterbium fiber laser (Burbach, Germany), an automatic powder laying device, a gas circulation system, and a computer-aided control system,

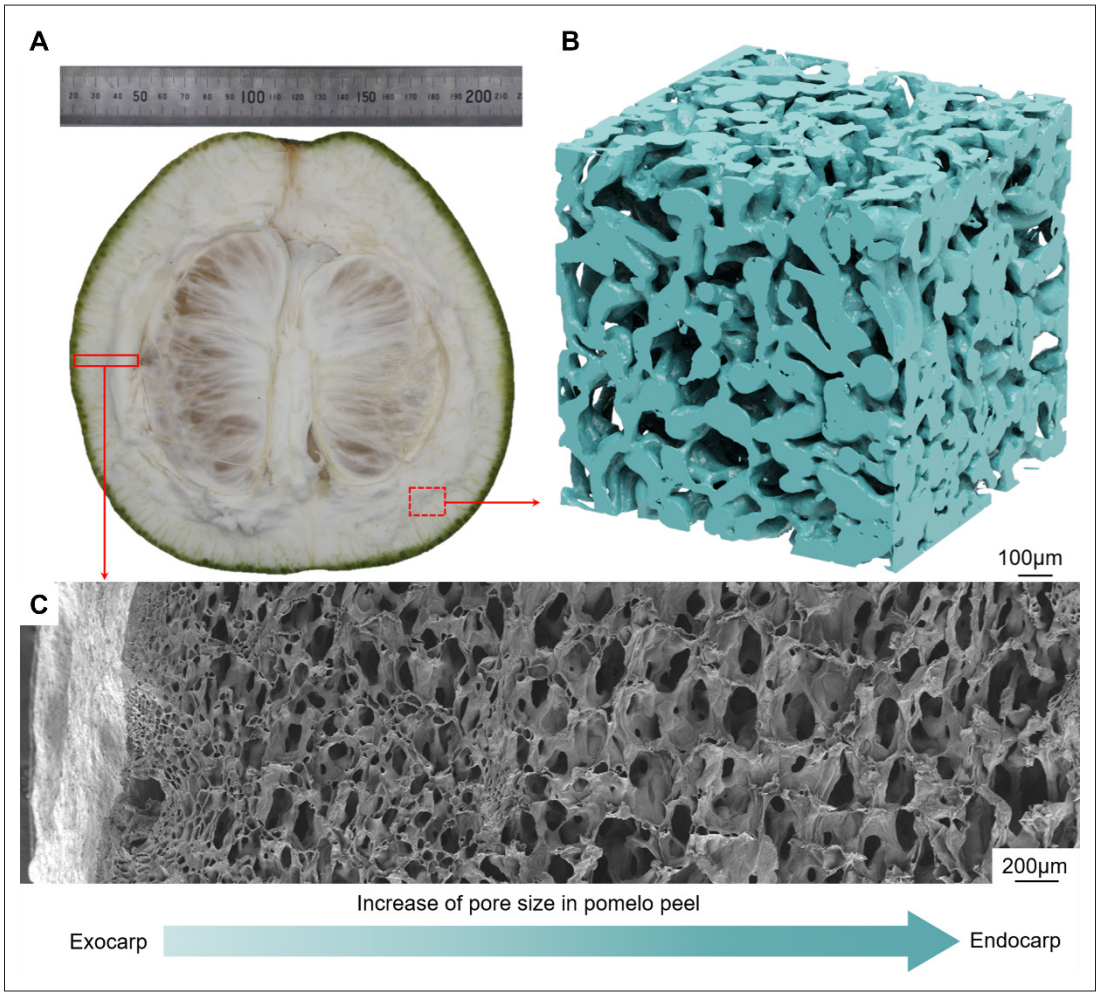

Figure 1. (A) Longitudinal section of the pomelo. (B) Micro-CT of stochastically porous structure in pomelo peel. (C) SEM of gradient structure in pomelo peel from endocarp to exocarp.

was used to fabricate the structure. A processing chamber needs to maintain an argon atmosphere during LPBF process (Figure 3B), and the oxygen content should be less than 50 cm^3/m^3. The optimized processing parameters and scanning strategy in our previous study (laser power of 400 W and scanning speed of 800 mm/s)[36-38] were applied in this work to ensure the forming quality and forming efficiency. It was found that the specimen processed with island strategy, among other scanning strategies, exhibited the highest relative density (99.6%) and microhardness (106.3 $HV_{0.2}$)[36]. Therefore, the island laser scanning strategy with an island size of 5 × 5 mm^2 and a scanning direction rotation of 37° between neighboring two layers was used for this experiment (Figure 3C). Additionally, the process involved contour scanning and filling contour scanning, with parameters (laser power of 200 W and scanning speed of 2000 mm/s) different from the main structural processing parameters. The as-fabricated BPPSs with four different *VF*s are shown in Figure 3D.

2.3. Microstructure characterization and mechanical tests

The LPBF-formed structures and the substrate were separated by wire cutting and cleaned by ultrasonic wave. These as-fabricated structures for microstructure analysis were ground and polished following the classical procedures. The section was etched with a solution, HF (2 mL) + HCl (3 mL) + HNO_3 (5 mL) + H_2O (190 mL). The microstructure was observed under an optical microscope (OM, Olympus Corporation, Japan). The surface morphology of the structure was observed through SEM (FEI-Quanta, USA). The 3D side surface morphology of the structure was observed and measured by laser scanning confocal microscopy (LSCM; Mumuxili, Nanjing, China). According to the ISO 13314: 2011 standard, the compression tests of structures were conducted using a CM5205 testing machine (MTS Industrial System, China) with a crosshead velocity of 1 mm/min at room temperature (Figure 4A). The compression direction was

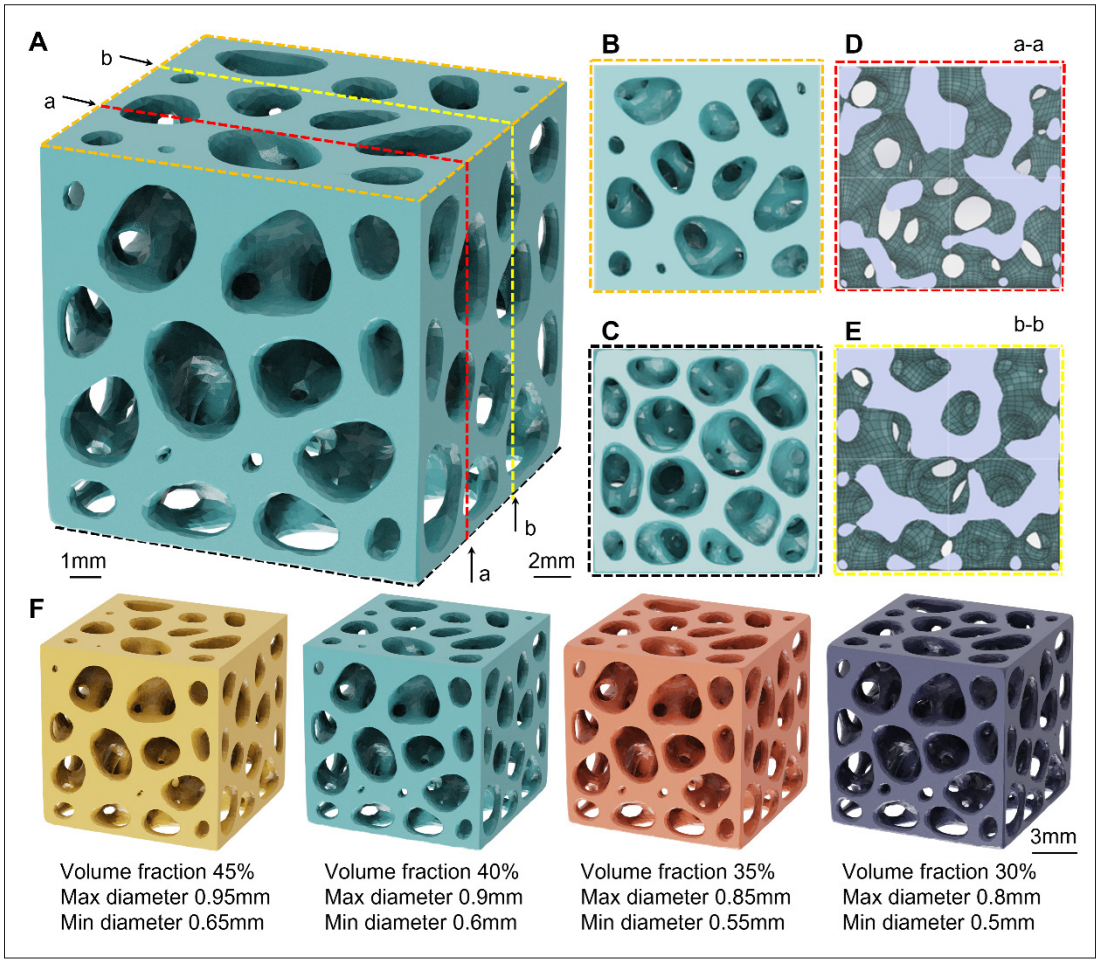

Figure 2. Design of BPPS. (A) CAD model of BPPS-40%. (B) Top view. (C) Bottom view. (D, E) Sectional view. (F) Four kinds of *VF*s of BPPSs.

Table 1. The variation of the BPPSs porosity along the gradient direction

Porosity of BPPSs	BPPS-45%	BPPS-40%	BPPS-35%	BPPS-30%
The upper half part with high density	47.5%	52.9%	58.5%	64.8%
The lower half part with low density	60.1%	65.1%	70.1%	74.3%

parallel to the forming direction, which was the direction of increasing porosity gradient in BPPSs. A video camera (SONY, Japan) was used to capture the deformation process of structures. For the reproducibility of the experimental results, each structure was tested three times. To evaluate the mechanical performance of BPPSs, several indicators were employed in this study as follows[39]:

Specific strength (σ_s) is used to evaluate the unit mass strength of a structure.

$$\sigma_s = \frac{\sigma_p}{\rho} \quad \text{(I)}$$

where σ_p is the peak strength of the structure before densification and ρ is the apparent density of the structure.

Specific energy absorption (W_s) is the energy absorption per unit mass.

$$W_s = \frac{W}{\rho} \quad \text{(II)}$$

where the expression of the W is as follows:

$$W = \frac{1}{100}\int_0^{e_0} \sigma d\varepsilon \quad \text{(III)}$$

where e_0 is the upper limit of the compressive strain, which is 50% in this work.

2.4. Finite element analysis

In order to further understand the deformation behavior and stress distribution of BPPSs under compression, the

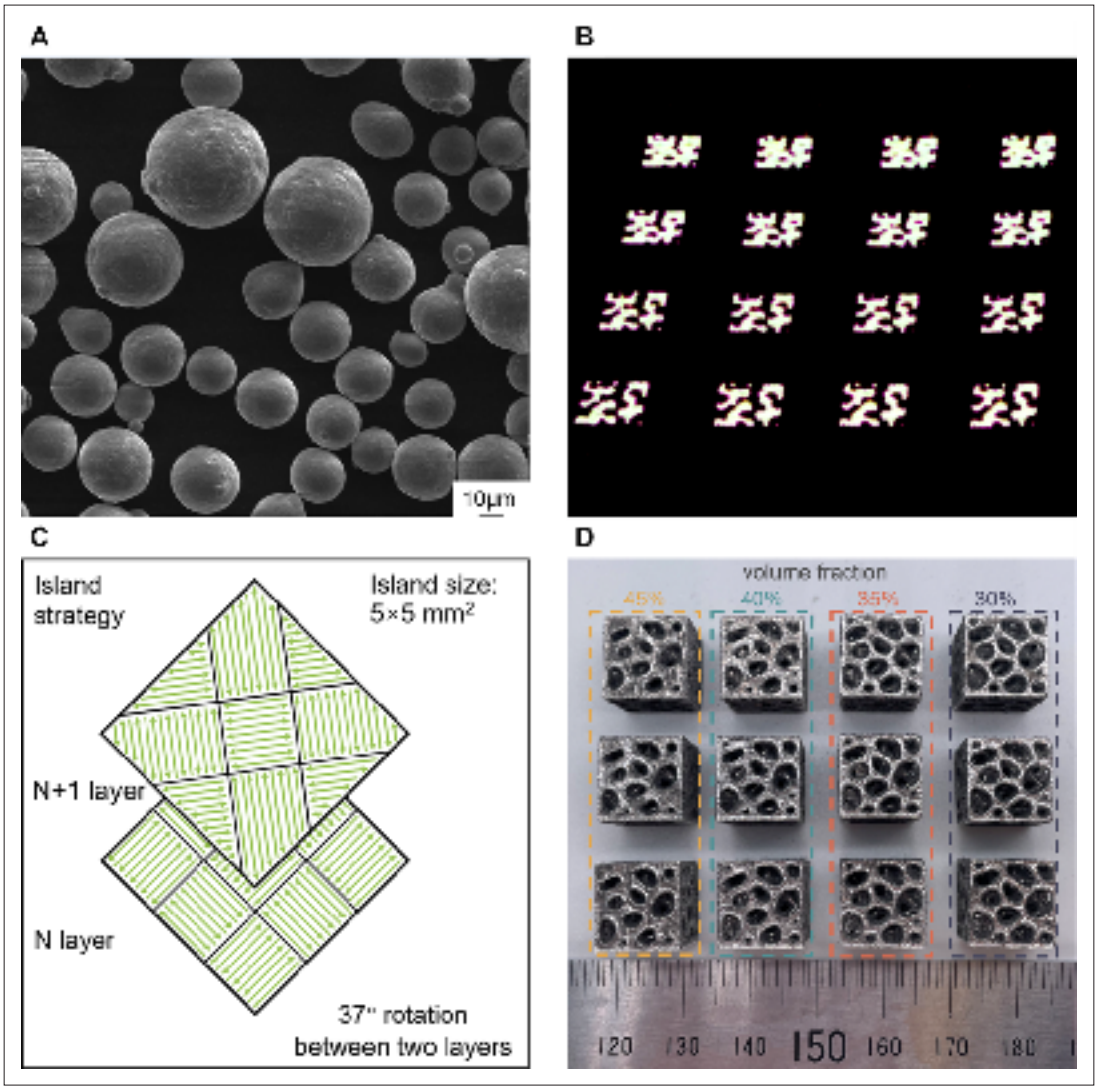

Figure 3. (A) Morphology of Al-Mg-Sc-Zr powder. (B) LPBF process. (C) Schematic of island scanning strategy applied in LPBF. (D) As-fabricated BPPSs components with different *VF*s.

FEA by ANSYS LS-DYNA software was conducted. The finite element model contained a top plate for displacement and a bottom plate for fixing, and the BPPS was sandwiched in the middle of them (Figure 4B). The displacement was applied to deform the model, and the value was set at 8 mm. Tetrahedral mesh was used as the mesh of the model, and Al-Mg-Sc-Zr was used as the material of BPPS. The material mechanical properties' parameters of Al-Mg-Sc-Zr are displayed in Table 2[40].

In order to investigate the influence of *VF* on the heat dissipation performance of BPPSs and compare the heat dissipation performance of BPPSs and traditional fin structures (Fins)[41], FEA by ANSYS FLUENT software was conducted. The finite element model contained a heat dissipation structure (BPPS or Fin), a heating substrate, and a fluid domain (Figure 4C). The invariable heating power was set to 5 W, and the heat flux was 34,722 W/m^2. The mesh sensitivity analysis was carried out to ensure that the simulation results were independent of the mesh size as shown in Figure 5A. The maximum deviation of the temperature index was within 0.15%, while the number of polyhedral mesh cells ranged from 3,270,000 to 6,770,000. Figure 5B presents the meshed numerical model by polyhedral mesh cells, exhibiting targeted local mesh refinement.

The heat dissipation structure and heating substrate were composed of Al-Mg-Sc-Zr alloy and pure aluminum, respectively. The material thermal properties' parameters of Al-Mg-Sc-Zr and pure aluminum are displayed in Table 3. To evaluate the heat dissipation performance of

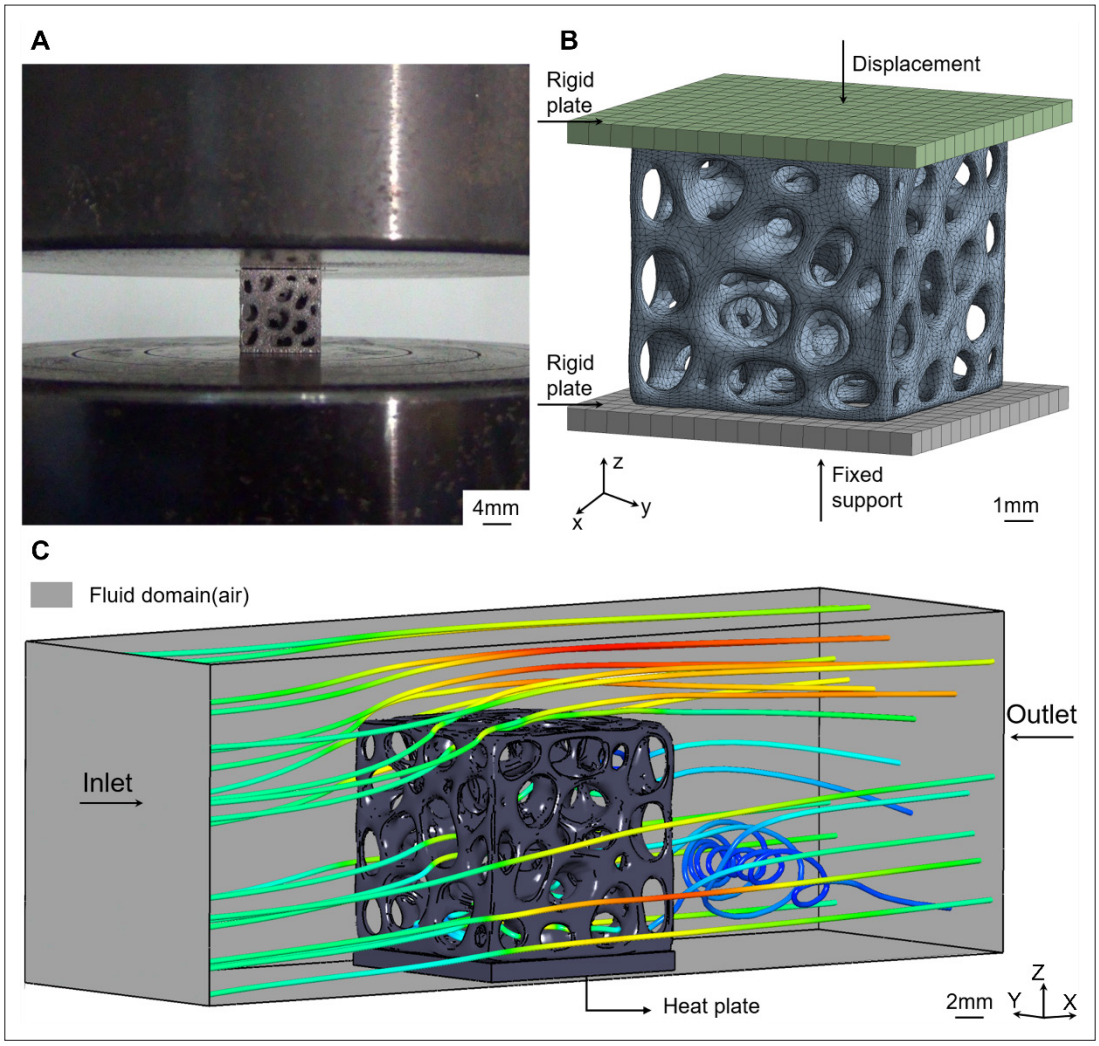

Figure 4. (A) Compression process. (B) FEA model of compression with mesh. (C) FEA model of heat dissipation.

Table 2. Mechanical properties of Al-Mg-Sc-Zr applied in this simulation[40]

Property	Young's modulus, E (GPa)	Yield stress, σy (MPa)	Ultimate stress, σu (MPa)	Elongation (%)
Value	70.2	302 ± 3	382 ± 5	22.5 ± 0.5

BPPSs, several indicators were employed in this study as follows[34,42]:

Heat transfer coefficient (h) represents the heat transfer performance per unit area of the structure.

$$h = \frac{Q_w}{\left[A\left(T_w - T_f\right)\right]} \quad \text{(IV)}$$

where Q_w is the heating power, A is the area of the heating surface, T_w is the average wall temperature at the fluid side of the surface, and T_f is the average temperature of the fluid (the average temperature of the fluid inlet and outlet).

D_h is the hydraulic diameter[34].

$$D_h = \frac{4A_{ff}L}{S} \quad \text{(V)}$$

where A_{ff} is the flow area at a minimum cross-section, L is the heat sink length in the flow direction, and S is the heat transfer surface area.

Reynolds number (Re) is a dimensionless number characterizing airflow rate.

$$Re = \frac{\rho a U_m}{\mu} \cdot D_h \quad \text{(VI)}$$

where ρ_a is the density of air, U_m is the inlet mean velocity, and μ is the dynamic viscosity of air.

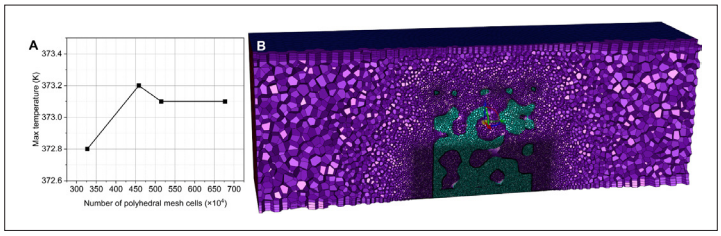

Figure 5. (A) Results of mesh sensitivity analysis. (B) The meshed numerical model.

Table 3. Thermal properties' parameters of the heat sink applied in this simulation

Property	BPPS	Solid base
	Al-Mg-Sc-Zr	Aluminum (pure)
Density (kg/m^3)	2770	2700
Thermal conductivity (W/mK)	165.2	188.1
Thermal diffusivity (mm^2/s)	5.533	7.426

Nusselt number (Nu) is a dimensionless number evaluating convective heat transfer data.

$$Nu = \frac{hD_h}{\lambda_f} \quad \text{(VII)}$$

where λ_f is the thermal conductivity of the fluid.

The dimensionless friction factor, f, defined in Equation VIII, is derived from the pressure drop.

$$f = \frac{2\Delta P}{\rho a U_m^{\ 2}} \cdot \frac{D_h}{l} \quad \text{(VIII)}$$

where ΔP is the pressure drop, and l is the distance between the pressure points.

In order to consider both heat transfer enhancement and pumping power, the heat transfer efficiency index (η), proposed by Gee and Webb[43], was introduced as the thermal performance evaluation criteria.

$$\eta = \frac{\frac{Nu}{Nu_0}}{\left(\frac{f}{f_0}\right)^{\frac{1}{3}}} \quad \text{(IX)}$$

where the empirical values of Nu_0 and f_0 were calculated using the Dittus–Boelter correlation (X) and Blasius correlation (XI), respectively.

$$Nu_0 = 0.023 Re^{0.8} Pr^{0.3} \quad \text{(X)}$$

$$f_0 = 0.316 Re^{-0.25} \quad \text{(XI)}$$

Thermal resistance (R_{th}) is a numerical representation of the degree of difficulty in heat transfer, which could evaluate the heat dissipation performance of the structure[44].

$$R_{th} = \frac{\left(T_w - T_f\right)}{Q_w} \quad \text{(XII)}$$

3. Results and discussion

3.1. LPBF formability analysis

The surface morphologies and dimensional accuracy of the as-fabricated BPPS are shown in Figure 6. The BPPS were successfully processed by LPBF technology without macro defects, such as pores, cracks, or inadequate fusion in the surface, exhibiting excellent forming quality and geometric fidelity (Figure 6A). However, a small number of un-melted particles and spatter particles on the surface of the strut and cavity were observed (Figure 6B), causing a terrible impact on the geometric fidelity and surface roughness. The optical microscope (OM) image of the etched longitudinal section showed a homogenous layer-wise molten pool with a mean depth of 40 μm (Figure 6C), indicating great metallurgical bonding between adjacent scanning tracks and layers. Figure 6D shows the 3D side surface morphology of the BPPS, where the red region represents a relatively rough area. The un-melted powder particles, which caused the rough side surface of the BPPS, could be seen in the corresponding position as shown in Figure 6E. The SEM surface morphologies of the BPPS are displayed in Figure 6E–G, showing obvious irregular outlines and dross defects. These irregular outlines on the surface, which were induced by the adhesion of un-melted powder particles, and dross defects reduced the dimensional accuracy and increased the surface roughness of the structure. The size of the as-fabricated structure was slightly larger than the design value, with a maximum deviation of no more than 10%. It could be observed that the volume of dross in Figure 6F was meaningfully smaller than that in Figure 6G.

The formation of the spatters was attributed to the localized laser heating due to the high-energy laser beam impinging on the powder bed, which led to surface boiling and generated a strong vapor jet. The recoil pressure created by the vapor jet pushed the melt surface downward, contributing to a vapor depression. The high-speed upward vapor flow of the vapor jet ejected powders and liquid

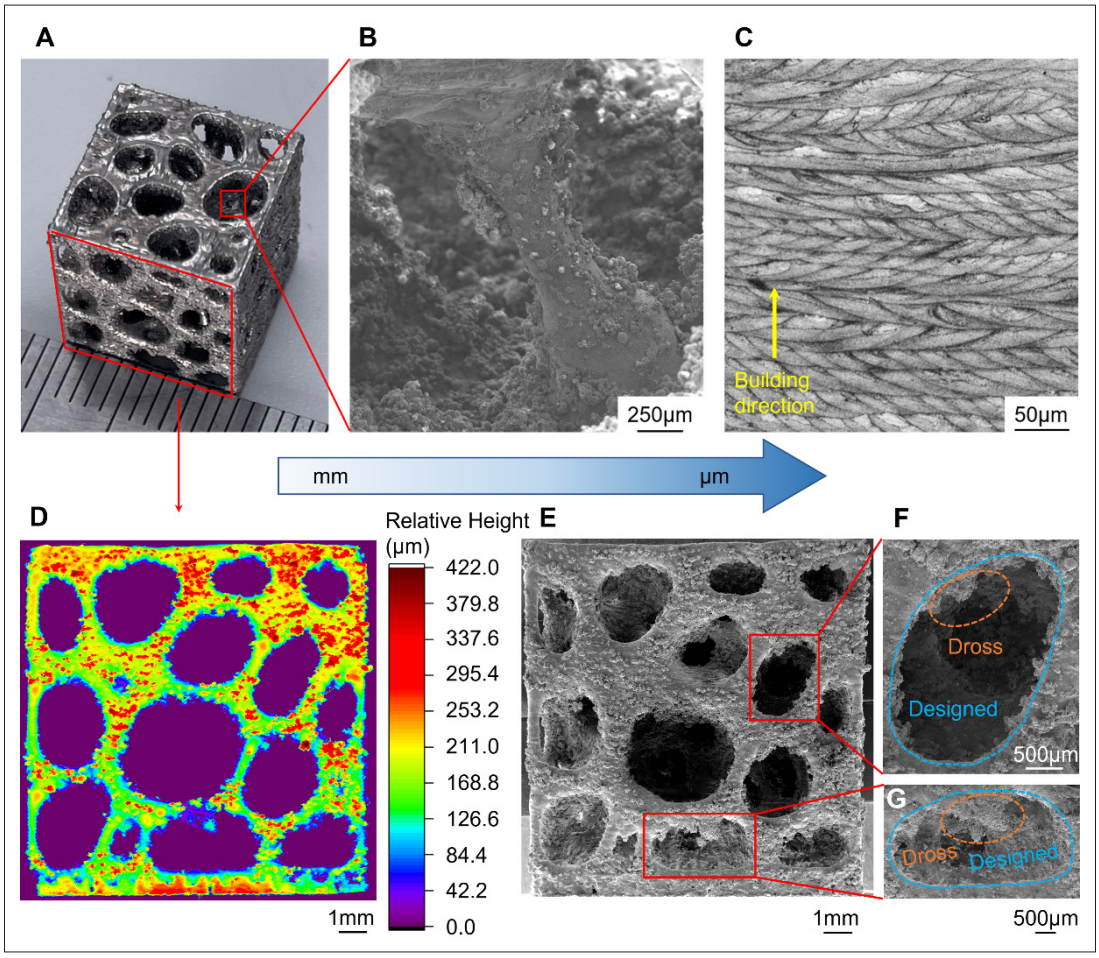

Figure 6. (A) BPPS component with a *VF* of 40%. (B) SEM of surface morphology at an intersection portion. (C) OM of the molten pool. (D) LSCM of the 3D surface topography. (E) SEM of the surface topography on the same surface. (F, G) Local SEM magnification detail of the holes.

droplets away, leading to the formation of spatters. Due to the low boiling point (1170°C) and high saturated vapor pressure of the Mg element, the Mg in the Al-Mg-Sc-Zr powders were easily prone to evaporation in the forming process, leading to the recoil pressure[45-47]. This may intensify the occurrence of spatters by further destroying molten pool stability. The presence of Mg in the Al-Mg-Sc-Zr spatter particles led to more oxides, further weakening forming quality[48,49]. Moreover, Al-Mg-Sc-Zr alloys were susceptible to hot cracking, and the average crack density improved with increasing Mg content[50]. The presence of dross in the as-fabricated structures was attributed to the lack of solid support at the overhanging surfaces, where the powder bed was in direct contact with the molten pool. A significant amount of heat was accumulated under the combined influence of the laser beam and powder bed, due to the lower thermal conductivity of the metal powder compared to the solid substrate material. Consequently, the large molten pool above the powder bed caused the molten pool to sink into the lower powder layer owing to gravity and surface-tension, resulting in the formation of dross[51]. The length of the overhanging surface in Figure 6F was significantly shorter than that in Figure 6G, and the inclination angle of the overhanging surface in Figure 6F was about 30°, which was obviously higher than the 0° inclination angle of the horizontal overhanging surface in Figure 6G. This not only contributed to a smaller volume of dross in Figure 6F than in Figure 6G, but also may lead to a smaller molten pool size of overhanging surface in Figure 6F compared with Figure 6G[52]. In Figure 6F, the molten pool was mainly supported by the underlying solidified layers, which possessed a higher thermal conductivity compared to the loose powder. This allowed for the dissipation of heat energy through the solidified layers, thereby accelerating the cooling rate and reducing the size of the molten pools. However, in Figure 6G, the loose powder with lower thermal conductivity was used as a support, which led to the accumulation of heat energy at the laser exposure points and limited heat dissipation to the surrounding regions. This resulted in a slower cooling rate that favored

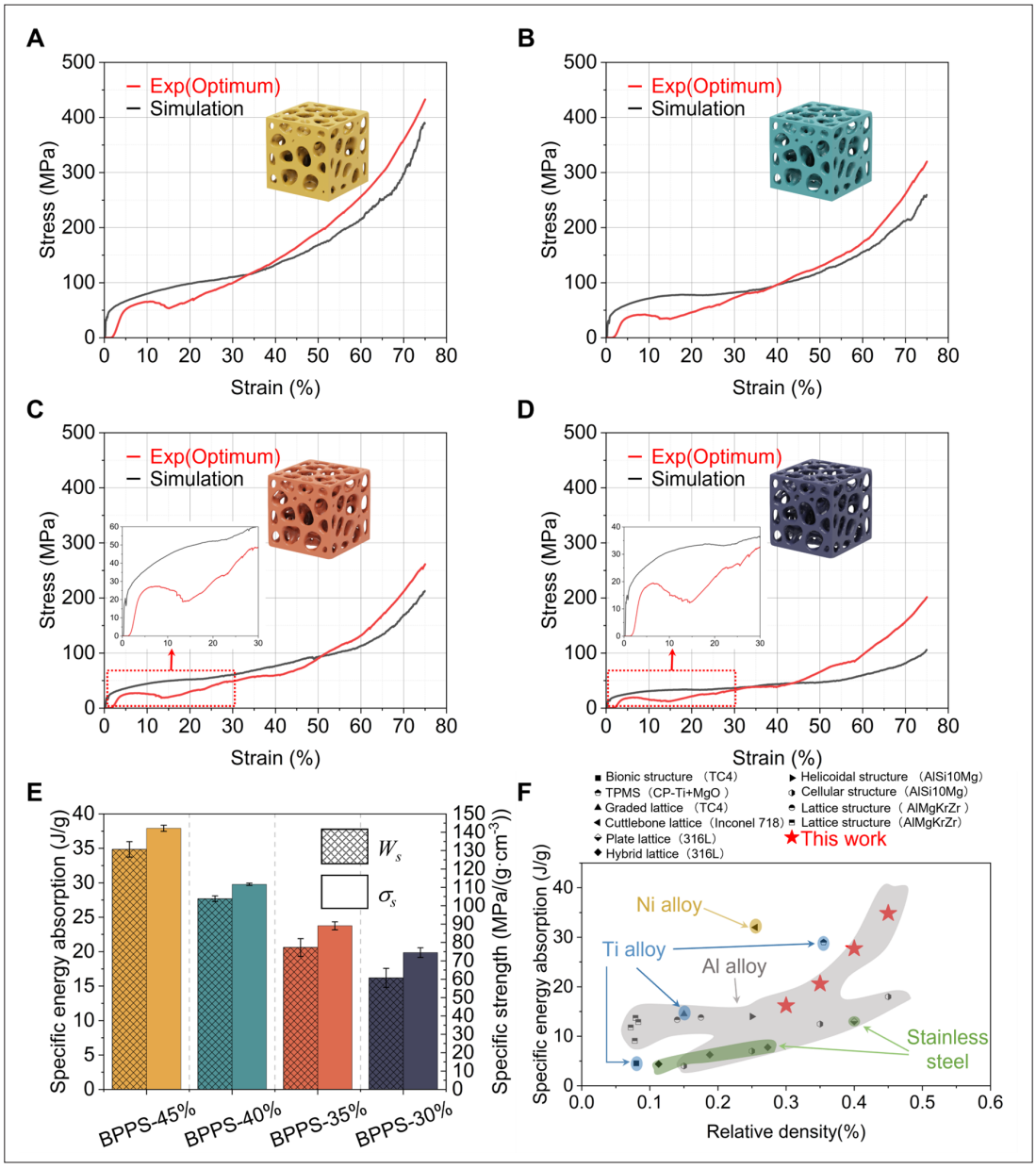

Figure 7. The stress–strain compressive curves of BPPSs with different *VF*s: (A) 45%, (B) 40%, (C) 35%, and (D) 30%. Mechanical performance indicators of BPPSs: (E) specific energy absorption (W_s) and specific strength (s_s). (F) Comparison of W_s of BPPSs with other lightweight structures[20,33,39,40,53-58].

the formation of larger molten pools. Furthermore, the combined effect of slower cooling rate, gravity, and surface-tension within the molten pool contributed to the formation of larger dross defects. Therefore, reducing the size of the overhanging surface and increasing the inclination angle of the overhanging surface are potential methods to optimize the dross defects on the downward-facing surface[40].

3.2. Mechanical properties

Figure 7 presents the results of experiments and FEAs on the mechanical responses of as-fabricated BPPSs under compression. As shown in Figure 7A–D, the stress–strain curves of FEA were in good agreement with the experimental curves, which could verify the accuracy of FEA. The slightly different tendencies in the force drop region between the experiment and FEA results may be attributed to the deviation between the actual samples and the FEA model. The surface roughness and dross formation led to a more obvious force drop region in the actual structure during compression experiments. In the initial elastic deformation region, the compressive strength of the four BPPSs were 63.47 MPa (45%), 42.01 MPa (40%),

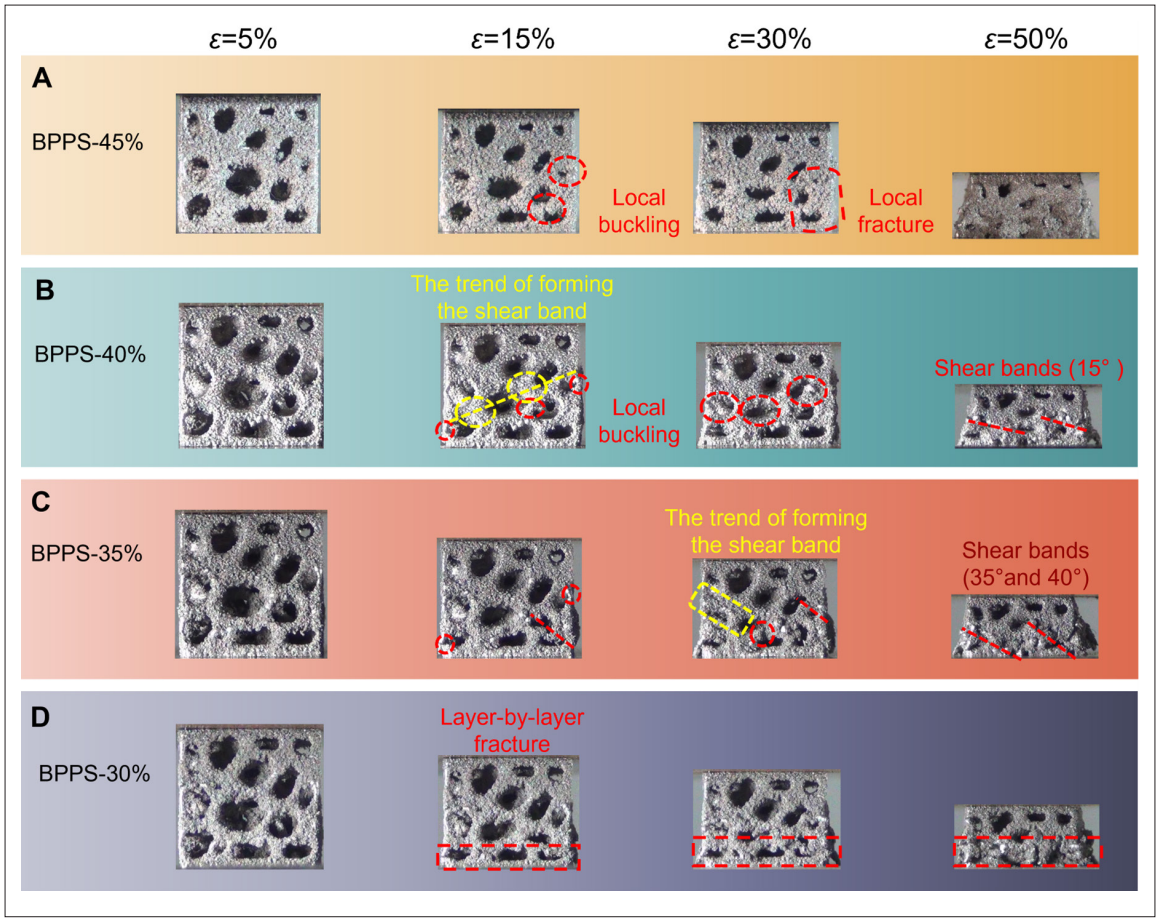

Figure 8. Video camera frames during compression of various BPPSs at *VF* of (A) 45%, (B) 40%, (C) 35%, and (D) 30%.

26.94 MPa (35%), and 17.75 MPa (30%) respectively, revealing that the compressive strength was positively related to the *VF*s of BPPSs. The compressive strength of the four BPPSs decreased slightly with the increase of compression strain, and the curves entered the force drop region. In the plateau region, the compression strength of the four BPPSs enhanced slowly at different rates as the compression strain enhanced, and the enhancement rate was positively related to the *VF*s of the structure. When the compression strain reached 50% (densification region), the compression strength of BPPSs improved sharply with the further increase of the compression strain. The slope of the rising curve was similar to the slope of the elastic deformation region. The structure could not dissipate the energy after entering the densified region and lost energy absorption capacity. Therefore, the calculation of W and W_s only included the pre-densification region. The W_s and s_s of the structures were calculated from the stress–strain curves of the BPPSs (Figure 7E). The results showed that both W_s and s_s were positively related to the *VF*s of BPPSs, indicating that the BPPSs with higher *VF*s exhibited better mechanical performance. A summary of W_s versus *VF* (relative density) of other porous structures reported in the literature [20,33,39,40,53-58] is shown in Figure 7F, which mainly included aluminum alloys, stainless steel, and titanium alloys. The W_s of BPPSs was higher than that of previously reported aluminum alloy structures and many other materials structures with the same *VF* (relative density).

Figure 8 shows typical images of BPPSs captured by a video camera at different deformation stages during compression. BPPS-45%, which had a large *VF* and low porosity, exhibited the highest peak force among four stress–strain curves (Figure 7A–D). There was local buckling in nearby locations at strain (ε) = 15% (Figure 8A). The observation indicated that the stress distribution was uneven on this site, leading to local stress concentration that results in local fracture at ε = 30%. More local fracture formed as compression continued to the densification region (ε = 50%), but no shear band was observed.

In contrast to BPPS-45%, BPPS-40% was more susceptible to stress concentration and local buckling due to the lower *VF*. At the ε of 15%, local buckling occurred in the vulnerable parts of the structure, with a tendency

to form a 30° shear band. However, the thicker solid parts (yellow frame in Figure 8B) hindered the formation of the shear band, resulting in local buckling toward other vulnerable parts. At ε = 30%, local buckling occurred in the three cavity locations of the side surface (Figure 8B). The combination of the previous local fracture and buckling further expanded with the increase of strain, ultimately forming two 15° shear bands at ε = 50%.

The *VF* of BPPS-35% further decreased, leading to local buckling and a 40° shear band at ε = 15% (Figure 8C). At the ε of 30%, there was local fracture in the previous local buckling location (left red circle in Figure 8C), pointing to the tendency to form a new shear band. Additionally, a 40° shear band emerged on the previous local buckling site (red line at ε = 30% in Figure 8C). At ε = 50%, the previous local fracture (red frame at ε = 30% in Figure 8C) expanded to a 35° shear band (left red line at ε = 50% in Figure 8C). The previous 40° shear band (red line at ε = 30% in Figure 8C) further extended (right red line at ε = 50% in Figure 8C). Finally, two shear bands with angles of 35° and 40° were observed.

BPPS-40% and BPPS-35% exhibited some identical characteristics in the deformation modes. BPPS-40% and BPPS-35% both displayed consistent local buckling at ε = 15%, with the exception of the 40° shear bands in BPPS-35% (Figure 8C). At the ε of 50%, the shear bands of BPPS-40% and BPPS-35% were observed to form in the same locations (Figure 8B and C). However, the two shear bands in BPPS-40% formed at a 15° angle were evidently flatter than the 35° and 40° shear bands in BPPS-35%, indicating the enhancement of the damage-tolerant performance of the structure[59]. This revealed the underlying mechanism responsible for the improved mechanical performance of BPPSs with the increase of *VF*s.

The *VF* of BPPS-30% decreased to a low value, leading to the lowest compressive strength in four stress–strain curves (Figure 7A–D). The fracture in BPPS-30%, which started from the bottom low-density layer and proceeded to the top high-density layer (Figure 8D), exhibited an apparent layer-by-layer fracture characteristic. This fracture characteristic was not obvious in the other three BPPSs during compression owing to their larger *VF*s. As shown in Figure 8B and C, the lower half part of the low density in the BPPS-40% and BPPS-35% displayed complete failure at ε = 50% (densification region), while the upper half part with high density exhibited no obvious buckling deformation and remained intact. These gradient characteristics could optimize the deformation modes and stress distribution of the structure, greatly improving the energy absorption capability[60,61]. This explained the reason that the W_s of BPPSs was significantly higher than that of other structures with the same *VF* (Figure 7F).

Figure 9A–D presents the von Mises stress distribution of the BPPSs in the elastic deformation region. It could be observed that the area of high stress in the BPPSs enlarged as the *VF*s increased. BPPSs with higher *VF*s contained a higher total amount of material and thus demanded higher macroscopic stress to obtain a specific strain[58]. Additionally, the size and quantity of cavities in the BPPSs were negatively related to the *VF*s. The size and quantity of cavities decreased with the increase of *VF*s, resulting in changes to the topological structure of BPPSs that reduce stress concentration around the cavities and optimize deformation modes, ultimately enhancing the mechanical performance of the structure[62]. Therefore, BPPSs exhibited improved mechanical properties with the increase of *VF*s (Figure 7E). Figure 9E–H displays the von Mises stress distribution of the BPPSs for cross-sections from top to bottom of 95%, 75%, 35%, and 5%, respectively. It was noticed that the stress concentration mostly occurred at the slender struts and connection parts, while there was less stress concentration in the thicker parts. Moreover, stress concentration mostly appeared in the lower half part with lower density in the structure, explaining the mechanism of layer-by-layer fracture of gradient structures, which was consistent with the compression test results (Figure 8).

3.3. Heat dissipation performance

The schematic of the BPPS-45% heat dissipation with the airflow in the *X* and *Y* directions is shown in Figure 10A–D. Figure 10E and F compares the maximal temperature of the entire heat sink and the average temperature of the heat plate in steady state between the *X* direction and the *Y* direction. The maximum temperature deviation and average temperature deviation between the *X* direction and *Y* direction were both less than 0.3%, indicating that the forced air-cooling heat dissipation of BPPSs perpendicular to the *Z* direction (gradient direction) was isotropic. This isotropy was consistent with the characteristics of stochastical structures, as previous research has demonstrated that disordered structures can achieve isotropy in mechanical and fluid permeability properties[25].

The heat dissipation performance of four *VF*s of BPPSs at *Re* = 2700–13,400 with airflow in the *X* direction is compared in Figure 11. The *Nu* versus *Re* curves of BPPSs are shown in Figure 11A, indicating that the *Nu* increases as the *VF* decreases at the same *Re*. Figure 11B shows the η versus *Re* curves of BPPSs, demonstrating that the η decreases with the increase of *VF*s at the same *Re*. It should be mentioned that the η of BPPS-30% were 10%–17%, 24%–28%, and 43%–52% remarkably higher than those of BPPS-35%, BPPS-40%, and BPPS-45%, respectively. This could be attributed to three primary

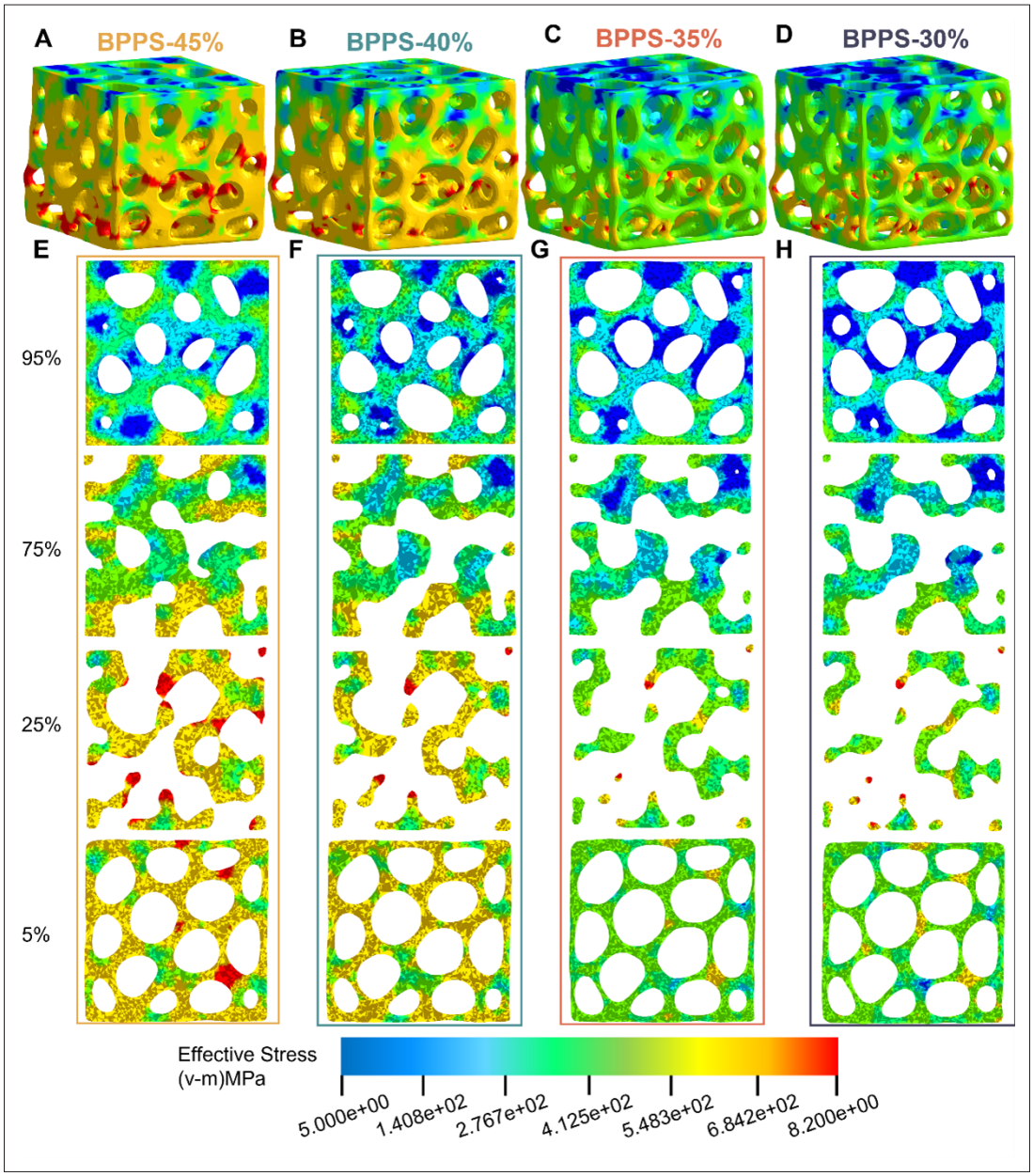

Figure 9. (A–D) von Mises stress contours and (E–H) selected cross-sections showing the stress distribution of various BPPSs.

factors. Firstly, the cavity size of the BPPS increased gradually with the decrease of the *VF*s, resulting in lower airflow resistance. This led to a lower air bypass and a higher airflow velocity passing through the structure at the same *Re* (Figure 12B–E). As the air velocity increased with improving *Re*, the vortices were formed at the trailing edge of the local structures (Figure 12B–E), which enhanced heat transfer performance by the enhancement of fluid mixing[63,64]. BPPSs with lower *VF*s exhibited more vortices than those with higher *VF*s due to more complex flow paths and higher air velocity, contributing to stronger effects on enhancing heat transfer performance. Secondly, the topological structure of BPPSs was changed by the decrease of *VF*s, causing some of the local thin-walled structures in high *VF*s BPPSs to transform into new necks in low *VF*s BPPSs (Figure 12B and C). The new necks connected the originally independent cavities and increased the number of flow paths, as shown in the red frame comparison between BPPS-40% and BPPS-45% (Figure 12B and C). This further improved the fluid mixing and heat transfer performance of BPPSs with high *VF*s. The trend of fluid

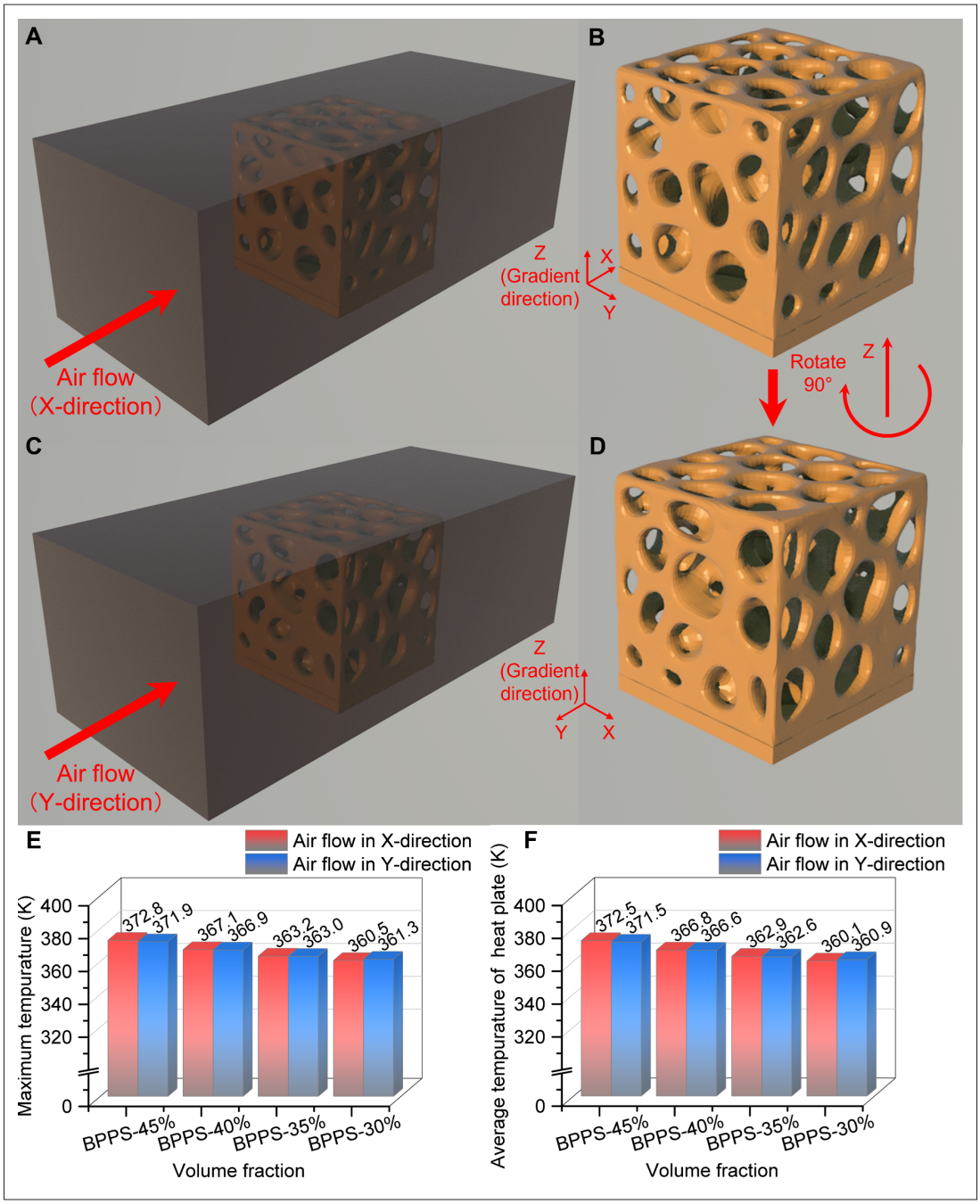

Figure 10. (A–D) The schematic of BPPS-45% heat dissipation in the *X* and *Y* directions. (E) Maximal temperature of the entire heat sink in steady state in different directions. (F) Average temperature of heat plate in steady state in different directions.

behavior inside BPPSs in the *X* direction was consistent with that in the *Y* direction (Figure 13B–E). Finally, it could be observed that the specific surface area of BPPSs increased with the decrease of *VF*s (Figure 14B). BPPS-30% exhibited a notably higher specific surface area compared to other BPPSs, which could enhance the heat transfer performance. Therefore, BPPSs with lower *VF*s had better heat dissipation performance.

Figure 14 presents the comparisons of various heat dissipation performance indices between four *VF*s BPPSs and Fins at *Re* = 2700 with airflow in the *X* direction. The maximum temperature reached by the entire heat dissipation structure in a steady state was denoted as T_{max}, which served as a direct indicator of heat dissipation performance. The T_{max} of BPPSs with *VF*s of 45%, 40%, 35%, and 30% were 6.1 K, 10.4 K, 8 K, and 8.6 K lower

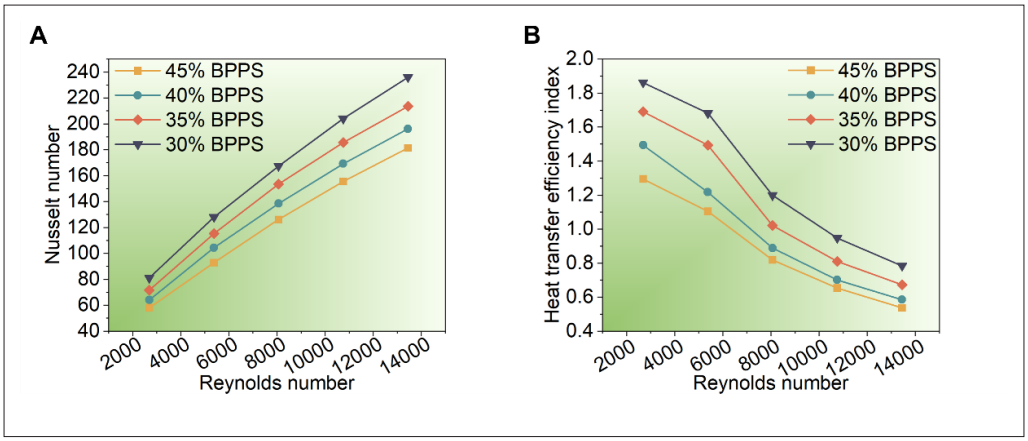

Figure 11. The heat dissipation performance of four *VF*s BPPSs at *Re* = 2700–13,400 with airflow in the *X* direction. (A) *Nu* versus *Re* of various BPPSs at *Re* = 2700–13,400. (B) η versus *Re* of various BPPSs at *Re* = 2700–13,400.

than that of corresponding Fins, respectively (Figure 14A). Therefore, the heat dissipation performance of BPPSs was better than that of Fins at the same *VF*. The specific surface areas of BPPSs and Fins with four *VF*s are shown in Figure 14B. It could be observed that the specific surface areas of BPPSs with *VF*s of 45%, 40%, 35%, and 30% were 24.4%, 30.2%, 32.2%, and 38.6% higher than that of the corresponding Fins, respectively. The high specific surface area of structures at the same *VF* meant more heat transfer area, causing BPPSs to exhibit better heat dissipation performance than Fins. Additionally, BPPSs had highly tortuous and smooth flow paths inside the structure, which enhanced heat transfer by promoting fluid mixing, and disrupted the boundary layer. This maintained a high temperature difference between the BPPSs and the fluid, facilitating heat transfer effectively[65]. In contrast, the straight and long flow paths of traditional Fins could not promote fluid mixing while maintaining a high temperature difference. The principle of heat dissipation design is to provide a low R_{th} path between the heat source and the surrounding environment, so R_{th} could measure the heat dissipation performance of structures to a certain extent[44]. The R_{th} of both BPPSs and Fins reduced as the *VF*s decreased, indicating the increase of fluid flow velocity within the structure (Figure 14C). The observation supported the previous conclusion that the fluid velocity in BPPSs with smaller *VF*s was faster. It was worth mentioning that the R_{th} of BPPSs with *VF*s of 45%, 40%, 35%, and 30% were 4.1%, 15.1%, 17.3%, and 18.2% lower than that of the corresponding Fins, respectively. The smooth surface of BPPSs did not have large fluctuations or sharp edges, and there were no closed cavities inside, achieving the streamlined design effect as much as possible. However, the traditional Fins possessed higher air resistance due to their rectangular profile. This accounted for the main factor behind the observed difference in R_{th} between BPPSs and Fins. Hence, some recent studies had proposed aerofoil fins that mimicked airplane wings to reduce R_{th}[63,64]. The η of BPPSs and Fins with four *VF*s is shown in Figure 14D. The η of BPPSs with *VF*s of 45%, 40%, 35%, and 30% were 39.6%, 39.8%, 43.7%, and 44.2% significantly higher than that of the traditional Fins with the same *VF*s, respectively. Therefore, the comprehensive analysis demonstrated that the heat dissipation performance of BPPSs was superior to that of Fins at the same *VF*.

The uniformity of temperature distribution is an important factor for evaluating the heat dissipation performance of structures. It is essential to maintain a uniform temperature distribution for the stable operation of electronic components. Figure 15A and B presents temperature distribution contours of BPPS-30% and Fin-30% at *Re* = 2700. Figure 15C and D compares the average temperature distribution of BPPS-30% and Fin-30% at different positions in the *X*–*Y*–*Z* direction. This average temperature data comprehensively included the average temperature of the entire structure and the flowing air inside the structure. The uniformity of the average temperature distribution of the structure in the *X*–*Y*–*Z* direction was quantified by using the average absolute deviation and variance as shown in Table 4[66]. The Fin-30% exhibited a slightly lower average absolute deviation and variance in the *X* direction compared to BPPS-30%. However, it was noteworthy that the average absolute deviation and variance of BPPS-30% in the *Y* direction were significantly lower than those observed in all directions of Fin-30%, measuring only 0.67 and 0.58, respectively. This suggested that BPPSs exhibited smaller temperature fluctuations and better distribution uniformity than Fins. Therefore, the temperature distribution uniformity of BPPSs was superior to that of Fins.

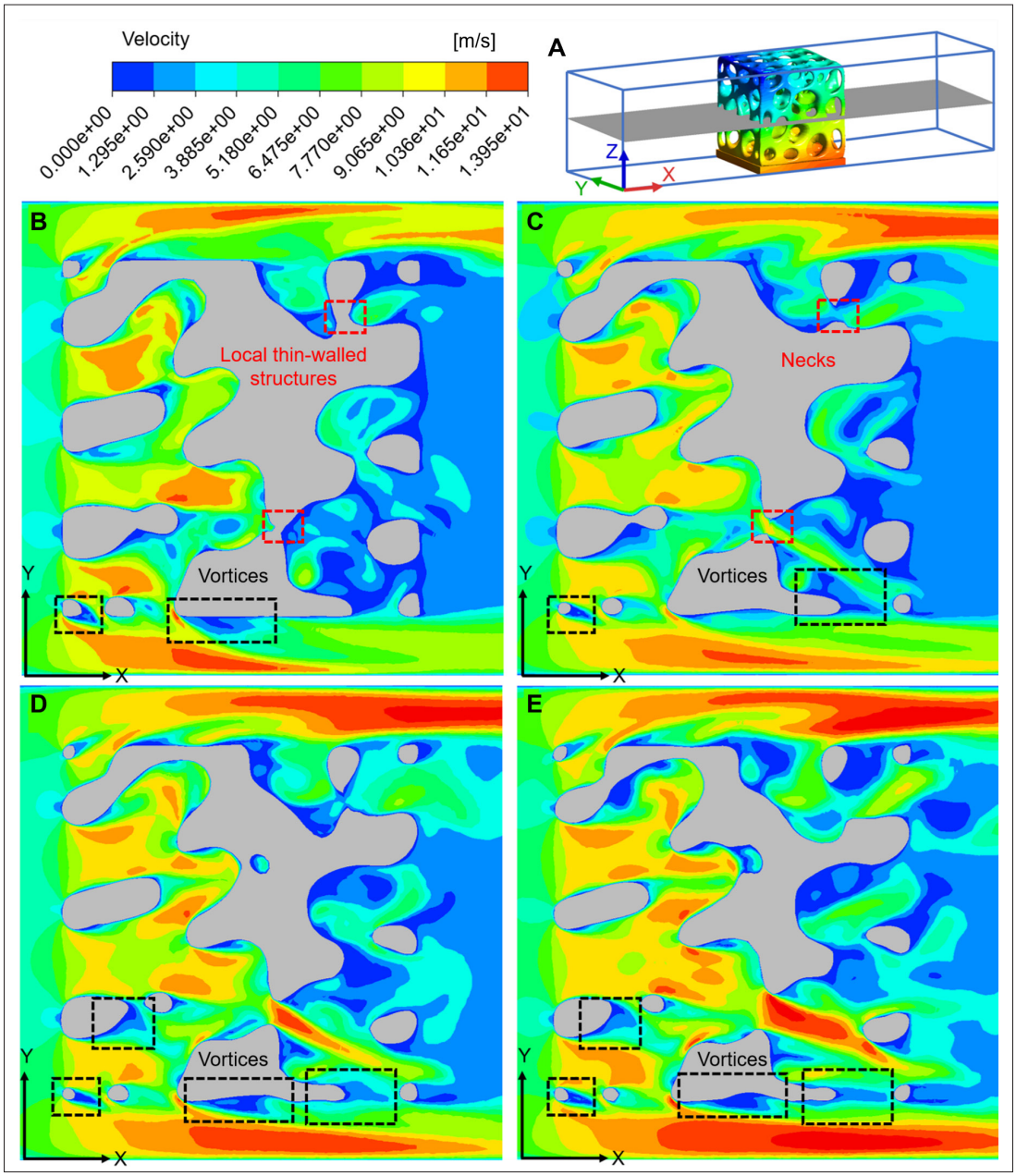

Figure 12. Fluid velocities contours of BPPSs on an *X*–*Y* plane at *Re* = 13,400 with airflow in the *X* direction. (A) Schematic of an *X*–*Y* plane. Fluid velocities contours of (B) BPPS-45%, (C) BPPS-40%, (D) BPPS-35%, and (E) BPPS-30% on an *X*–*Y* plane at *Re* = 13,400.

4. Conclusion

In this study, a series of multifunctional pomelo peel-inspired structures were designed and fabricated using LPBF technology with Al-Mg-Sc-Zr alloy powder. The structural formability analysis, mechanical properties, and thermal performance were investigated by the compression test and the finite element method. Additionally, the effect of *VF* on mechanical response and heat dissipation performance of the BPPSs was investigated, and the inherent optimized mechanism behind the improved performance of the BPPSs was revealed. The main conclusions are summarized as follows:

(i) The LPBF-processed BPPSs showed no macro defects on the surface, such as pores, cracks, or inadequate fusion in the surface, exhibiting good forming quality. However, a small deviation between the as-fabricated part and the design model was observed due to the dross defects and the adhesion of un-

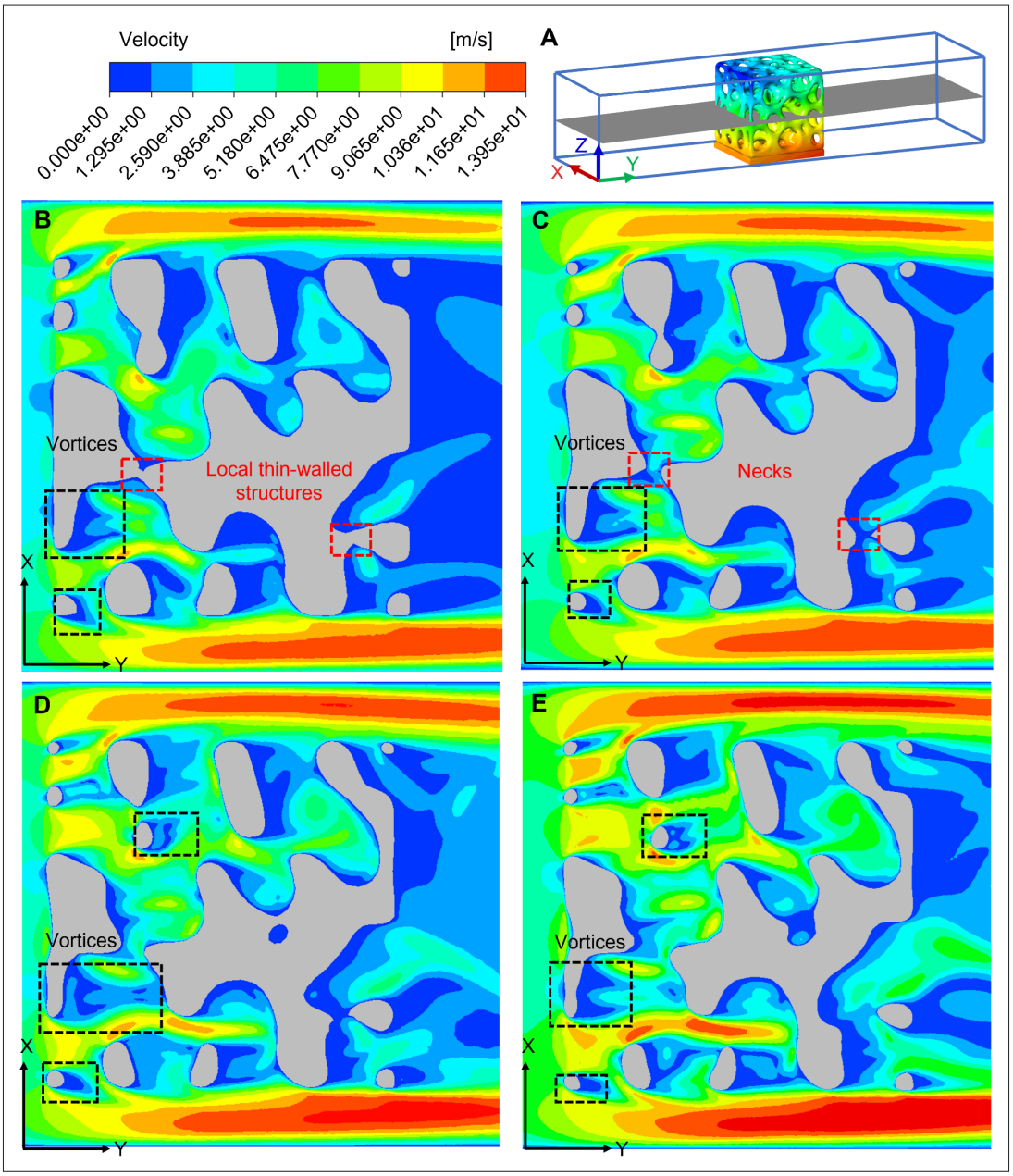

Figure 13. Fluid velocities contours of BPPSs on an *X*–*Y* plane at *Re* = 13,400 with airflow in the *Y* direction. (A) Schematic of an *X*–*Y* plane. Fluid velocities contours of (B) BPPS-45%, (C) BPPS-40%, (D) BPPS-35%, and (E) BPPS-30% on an *X*–*Y* plane at *Re* = 13,400.

melted powder particles. Moreover, various cooling conditions induced by the different overhanging length and inclination angle, in combination with the effects of gravity and surface tension, contributed to dross formation with diverse volumes.

(ii) The BPPS-45% exhibited the best mechanical properties with compressive strength, W_s, and s_s of 63.47 MPa, 34.84 J/g, and 142.16 MPa/(g·cm^{-3}), respectively. During compression deformation, no shear band was formed in BPPS-45%, while BPPS-40% displayed two flatter 15° shear bands compared with the 35° and 40° shear bands in BPPS-35%. Stress concentration appeared in the lower half part with low density in BPPSs owing to the gradient characteristics of BPPSs, resulting in the layer-by-layer fracture and ultimately enhancing the energy absorption performance. At the same *VF*, the W_s of BPPSs was significantly higher than that of aluminum alloy structures that have been studied.

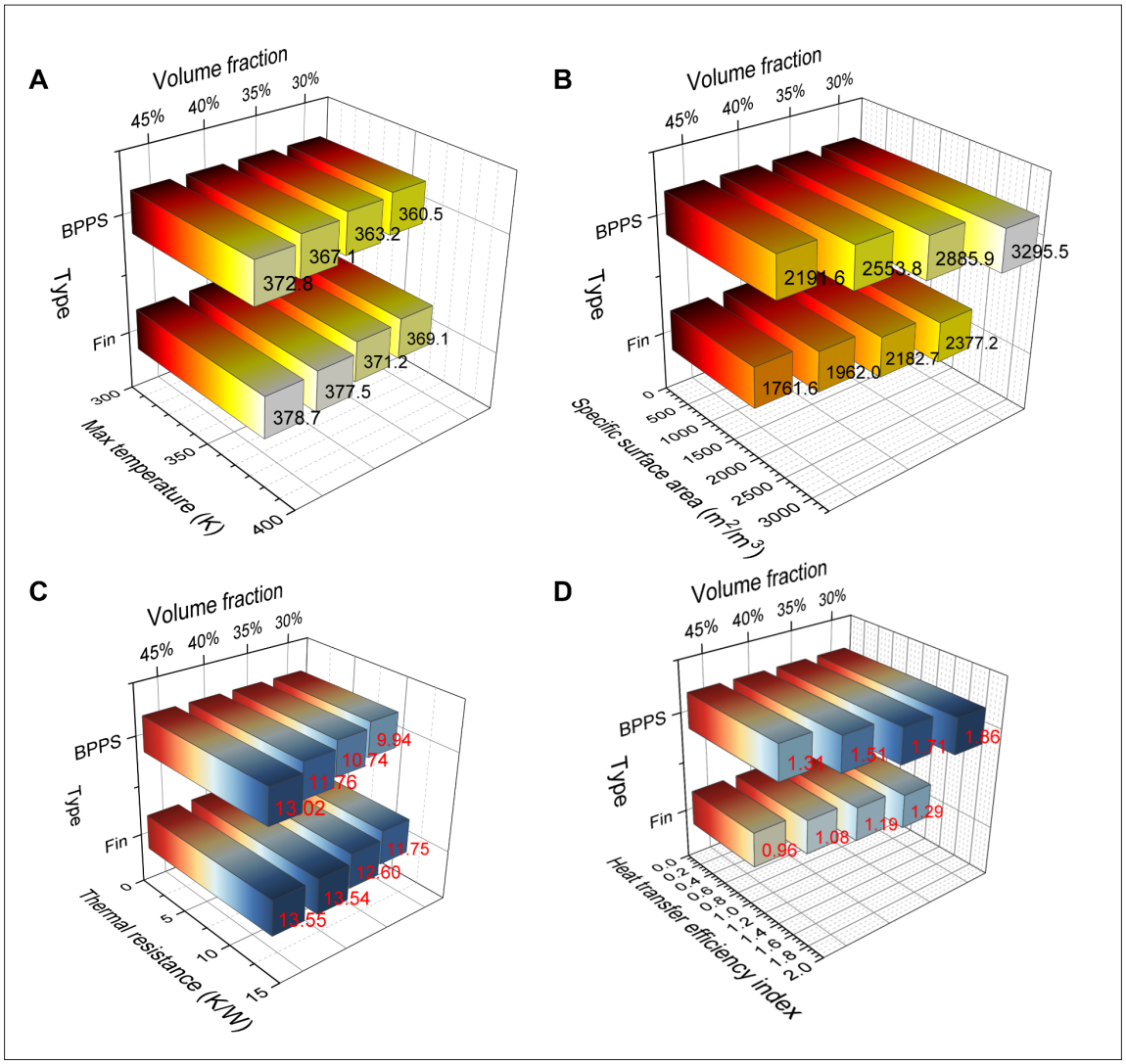

Figure 14. The various heat dissipation performance indices between BPPSs and Fins at *Re* = 2700 with airflow in the *X* direction. (A) Maximal temperature of the entire heat sink in steady state. (B) Specific surface area of various BPPSs and Fins. (C) Thermal resistance of heat sink. (D) Heat transfer efficiency index of heat sink.

(iii) At *Re* = 2700–13,400, the heat dissipation performance of BPPSs improved with the decrease of *VF*s, when air flowed along *X* and *Y* directions. The η of BPPS-30% were 10%–17%, 24%–28%, and 43%–52% higher than that of others with different *VF*s, which could be attributed to the formation of more vortices, more flow paths, and higher specific surface area. Due to the tortuous flow paths inside BPPSs and the higher specific surface area, the η of BPPSs with *VF*s of 45%, 40%, 35%, and 30% were 39.6%, 39.8%, 43.7%, and 44.2% remarkably higher than that of the corresponding Fins, respectively.

Acknowledgments

None.

Funding

We are grateful for the support given by the National Natural Science Foundation of China (No. 52225503), the Key Research and Development Program of Jiangsu Province (Nos. BE2022069 and BE2022069-1), the National Natural Science Foundation of China for Creative Research Groups (No. 51921003), and the Postgraduate Research & Practice Innovation Program of Nanjing University of Aeronautics and Astronautics (xcxjh20220606).

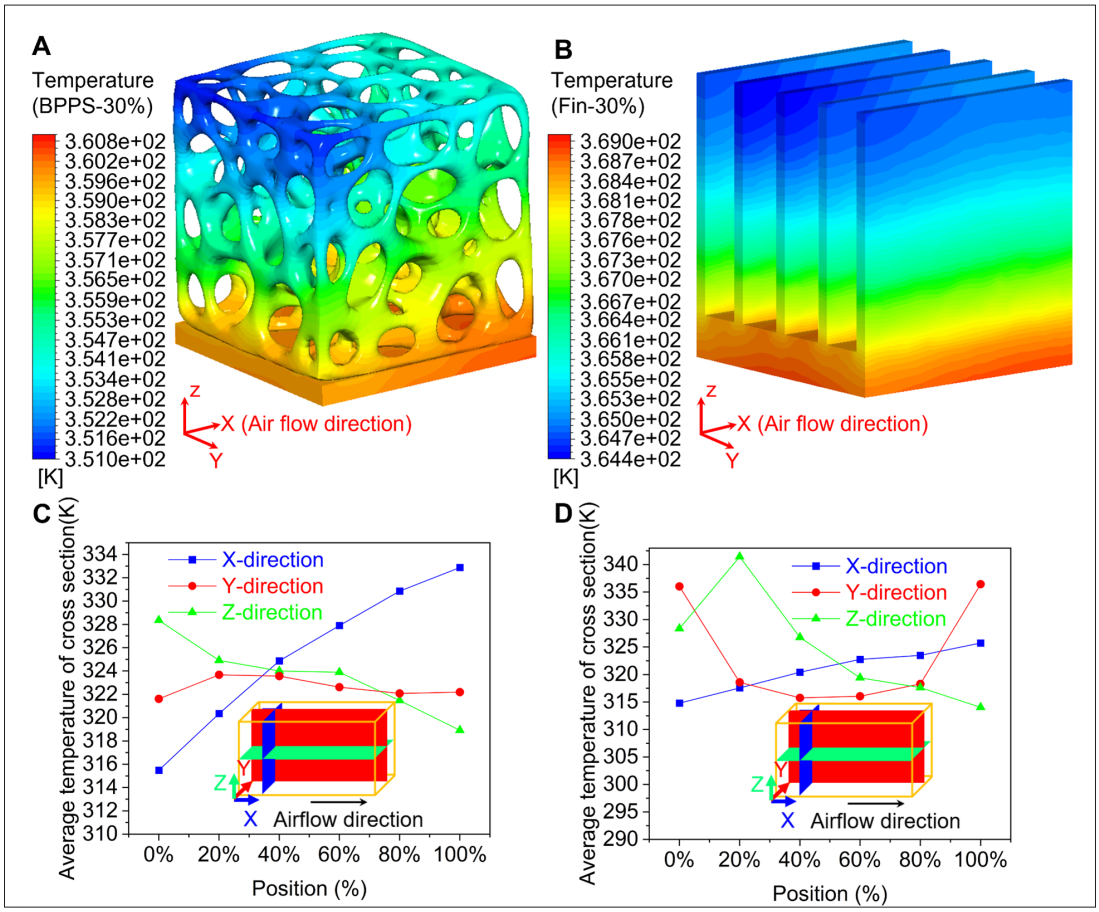

Figure 15. (A) Temperature distribution contours of BPPS-30%. (B) Temperature distribution contours of Fin-30%. (C) Average temperature of various locations for the entire heat sink (BPPS-30%). (D) Average temperature of various locations for the entire heat sink (Fin-30%).

Table 4. The uniformity of temperature distribution in structures in *X*, *Y*, and *Z* directions

Indicator	BPPS-30%			Fin-30%		
	X	Y	Z	X	Y	Z
Average absolute deviation	5.16	0.67	2.13	3.20	9.33	7.46
Variance	36.01	0.58	8.13	13.66	91.62	83.22

Conflict of interest

The authors declare no conflicts of interests.

Author contributions

Conceptualization: Dongdong Gu, Linxuan Li
Formal analysis: Linxuan Li, He Liu
Investigation: Dongdong Gu, Linxuan Li
Methodology: Linxuan Li, He Liu
Writing – original draft: Linxuan Li, He Liu
Writing – review & editing: Dongdong Gu, Linxuan Li, Han Zhang, Junhao Shan, Yijuan Zhang

Ethics approval and consent to participate

Not applicable.

Consent for publication

Not applicable.

Availability of data

All relevant data are within the manuscript.

References

1. Siddique SH, Hazell PJ, Wang HX, *et al.*, 2022, Lessons from nature: 3D printed bio-inspired porous structures for impact energy absorption-A review. *Addit Manuf*, 58: 103051.
http://dx.doi.org/10.1016/j.addma.2022.103051

2. Bandyopadhyay A, Traxel KD, Bose S, 2021, Nature-inspired materials and structures using 3D Printing. *Mater Sci Eng R Rep*, 145: 100609.
http://dx.doi.org/10.1016/j.mser.2021.100609

3. Omenetto FG, Kaplan DL, 2010, New opportunities for an ancient material. *Science*, 329(5991): 528–531.

   http://dx.doi.org/10.1126/science.1188936

4. Islam MK, Hazell PJ, Escobedo JP, *et al.*, 2021, Biomimetic armour design strategies for additive manufacturing: A review. *Mater Des*, 205: 109730.

   http://dx.doi.org/10.1016/j.matdes.2021.109730

5. Mohammadi A, Hajizadeh E, Tan Y, *et al.*, 2023, A bioinspired 3D-printable flexure joint with cellular mechanical metamaterial architecture for soft robotic hands. *Int J Bioprint*, 9(3): 696.

   http://dx.doi.org/10.18063/ijb.696

6. Yang J, Gu D, Lin K, *et al.*, 2022, Laser additive manufacturing of bio-inspired metallic structures. *Chinese J Mech Eng Addit Manuf Front*, 1(1): 100013.

   http://dx.doi.org/10.1016/j.cjmeam.2022.100013

7. Benedetti M, du Plessis A, Ritchie RO, *et al.*, 2021, Architected cellular materials: A review on their mechanical properties towards fatigue-tolerant design and fabrication. *Mater Sci Eng R*, 144: 100606.

   http://dx.doi.org/10.1016/j.mser.2021.100606

8. Gu D, Shi X, Poprawe R, *et al.*, 2021, Material-structure-performance integrated laser-metal additive manufacturing. *Science*, 372(6545): eabg1487.

   http://dx.doi.org/10.1126/science.abg1487

9. Tofail SAM, Koumoulos EP, Bandyopadhyay A, *et al.*, 2018, Additive manufacturing: scientific and technological challenges, market uptake and opportunities. *Mater Today*, 21(1): 22–37.

   http://dx.doi.org/10.1016/j.mattod.2017.07.001

10. Zhang Y, Attarilar S, Wang L, *et al.*, 2021, A review on design and mechanical properties of additively manufactured NiTi implants for orthopedic applications. *Int J Bioprint*, 7(2): 340.

    http://dx.doi.org/10.18063/ijb.v7i2.340

11. Hojjatzadeh SMH, Parab ND, Guo Q, *et al.*, 2020, Direct observation of pore formation mechanisms during LPBF additive manufacturing process and high energy density laser welding. *Int J Mach Tools Manuf*, 153: 103555.

    http://dx.doi.org/10.1016/j.ijmachtools.2020.103555

12. Korkmaz ME, Gupta MK, Robak G, *et al.*, 2022, Development of lattice structure with selective laser melting process: A state of the art on properties, future trends and challenges. *J Manuf Processes*, 81: 1040–1063.

    http://dx.doi.org/10.1016/j.jmapro.2022.07.051

13. Zhou Y, Wang J, Yang Y, *et al.*, 2022, Laser additive manufacturing of zinc targeting for biomedical application. *Int J Bioprint*, 8(1): 501.

    http://dx.doi.org/10.18063/ijb.v8i1.501

14. Du Plessis A, Razavi SMJ, Benedetti M, *et al.*, 2022, Properties and applications of additively manufactured metallic cellular materials: A review. *Prog Mater Sci*, 125: 100918.

    http://dx.doi.org/10.1016/j.pmatsci.2021.100918

15. Yang J, Gao H, Zhang D, *et al.*, 2022, Static compressive behavior and material failure mechanism of trabecular tantalum scaffolds fabricated by laser powder bed fusion-based additive manufacturing. *Int J Bioprint*, 8(1): 438.

    http://dx.doi.org/10.18063/ijb.v8i1.438

16. Wang R, Gu D, Lin K, *et al.*, 2022, Multi-material additive manufacturing of a bio-inspired layered ceramic/metal structure: Formation mechanisms and mechanical properties. *Int J Mach Tools Manuf*, 175: 103872.

    http://dx.doi.org/10.1016/j.ijmachtools.2022.103872

17. Yuan L, Gu D, Lin K, *et al.*, 2022, Electrically actuated shape recovery of NiTi components processed by laser powder bed fusion after regulating the dimensional accuracy and phase transformation behavior. *Chinese J Mech Eng Addit Manuf Front*, 1(4): 100056.

    http://dx.doi.org/10.1016/j.cjmeam.2022.100056

18. Lin K, Hu K, Gu D, 2019, Metallic integrated thermal protection structures inspired by the Norway spruce stem: Design, numerical simulation and selective laser melting fabrication. *Opt Laser Technol*, 115: 9–19.

    http://dx.doi.org/10.1016/j.optlastec.2019.02.003

19. Hu K, Lin K, Gu D, *et al.*, 2019, Mechanical properties and deformation behavior under compressive loading of selective laser melting processed bio-inspired sandwich structures. *Mater Sci Eng A*, 762: 138089.

    http://dx.doi.org/10.1016/j.msea.2019.138089

20. Yang C, Li QM, Wang Y, 2021, Compressive properties of cuttlebone-like lattice (CLL) materials with functionally graded density. *Eur J Mech A Solids*, 87: 104215.

    http://dx.doi.org/10.1016/j.euromechsol.2021.104215

21. Lazarus BS, Luu RK, Ruiz-Perez S, *et al.*, 2022, Equine hoof wall: Structure, properties, and bioinspired designs. *Acta Biomater*, 151: 426–445.

    http://dx.doi.org/10.1016/j.actbio.2022.08.028

22. Pack RC, Romberg SK, Badran AA, *et al.*, 2020, Carbon fiber and syntactic foam hybrid materials via core–shell material extrusion additive manufacturing. *Adv Mater Technol*, 5(12): 2000731.

    http://dx.doi.org/10.1002/admt.202000731

23. Wang D, Liu L, Deng G, *et al.*, 2022, Recent progress on additive manufacturing of multi-material structures with laser powder bed fusion. *Virtual Phys Prototyping*, 17(2): 329–365.

    http://dx.doi.org/10.1080/17452759.2022.2028343

24. Yue X, Shang J, Zhang M, *et al.*, 2022, Additive manufacturing of high porosity magnesium scaffolds with lattice structure and random structure. *Mater Sci Eng A*, 859: 144167.

http://dx.doi.org/10.1016/j.msea.2022.144167

25. Gomez S, Vlad MD, Lopez J, *et al.*, 2016, Design and properties of 3D scaffolds for bone tissue engineering. *Acta Biomater*, 42: 341–350.

http://dx.doi.org/10.1016/j.actbio.2016.06.032

26. Ge J, Huang J, Lei Y, *et al.*, 2020, Microstructural features and compressive properties of SLM Ti6Al4V lattice structures. *Surf Coat Technol*, 403: 126419.

http://dx.doi.org/10.1016/j.surfcoat.2020.126419

27. Tee YL, Maconachie T, Pille P, *et al.*, 2021, From nature to additive manufacturing: Biomimicry of porcupine quill. *Mater Des*, 210: 110041.

http://dx.doi.org/10.1016/j.matdes.2021.110041

28. Sheng X, Dong D, Lu X, *et al.*, 2020, MXene-wrapped bio-based pomelo peel foam/polyethylene glycol composite phase change material with enhanced light-to-thermal conversion efficiency, thermal energy storage capability and thermal conductivity. *Composites, Part A*, 138: 106067.

http://dx.doi.org/10.1016/j.compositesa.2020.106067

29. Zhang C, Xiao P, Ni F, *et al.*, 2020, Converting pomelo peel into eco-friendly and low-consumption photothermic biomass sponge toward multifunctioal solar-to-heat conversion. *ACS Sustainable Chem Eng*, 8(13): 5328–5337.

http://dx.doi.org/10.1021/acssuschemeng.0c00681

30. Buhrig-Polaczek A, Fleck C, Speck T, *et al.*, 2016, Biomimetic cellular metals-using hierarchical structuring for energy absorption. *Bioinspir Biomim*, 11(4): 045002.

http://dx.doi.org/10.1088/1748-3190/11/4/045002

31. Fischer SF, Thielen M, Loprang RR, *et al.*, 2010, Pummelos as concept generators for biomimetically inspired low weight structures with excellent damping properties. *Adv Eng Mater*, 12(12): B658–B663.

http://dx.doi.org/10.1002/adem.201080065

32. Zhang W, Yin S, Yu TX, *et al.*, 2019, Crushing resistance and energy absorption of pomelo peel inspired hierarchical honeycomb. *Int J Impact Eng*, 125: 163–172.

http://dx.doi.org/10.1016/j.ijimpeng.2018.11.014

33. Zhang Z, Song B, Yao Y, *et al.*, 2022, Bioinspired, simulation-guided design of polyhedron metamaterial for simultaneously efficient heat dissipation and energy absorption. *Adv Mater Technol*, 7(10): 2200076.

http://dx.doi.org/10.1002/admt.202200076

34. Wong M, Owen I, Sutcliffe CJ, *et al.*, 2009, Convective heat transfer and pressure losses across novel heat sinks fabricated by selective laser melting. *Int J Heat Mass Transfer*, 52(1–2): 281–288.

http://dx.doi.org/10.1016/j.ijheatmasstransfer.2008.06.002

35. Yang B, Chen W, Xin R, *et al.*, 2022, Pomelo peel-inspired 3D-printed porous structure for efficient absorption of compressive strain energy. *J Bionic Eng*, 19(2): 448–457.

http://dx.doi.org/10.1007/s42235-021-00145-1

36. Zhang H, Gu D, Dai D, 2022, Laser printing path and its influence on molten pool configuration, microstructure and mechanical properties of laser powder bed fusion processed rare earth element modified Al-Mg alloy. *Virtual Phys Prototyping*, 17(2): 308–328.

http://dx.doi.org/10.1080/17452759.2022.2036530

37. Zhang H, Gu D, Dai D, *et al.*, 2020, Influence of scanning strategy and parameter on microstructural feature, residual stress and performance of Sc and Zr modified Al–Mg alloy produced by selective laser melting. *Mater Sci Eng A*, 788: 139593.

http://dx.doi.org/10.1016/j.msea.2020.139593

38. Zhang H, Gu D, Yang J, *et al.*, 2018, Selective laser melting of rare earth element Sc modified aluminum alloy: Thermodynamics of precipitation behavior and its influence on mechanical properties. *Addit Manuf*, 23: 1–12.

http://dx.doi.org/10.1016/j.addma.2018.07.002

39. Yang J, Gu D, Lin K, *et al.*, 2022, Laser powder bed fusion of mechanically efficient helicoidal structure inspired by mantis shrimp. *Int J Mech Sci*, 231: 107573.

http://dx.doi.org/10.1016/j.ijmecsci.2022.107573

40. Liu H, Gu D, Yang J, *et al.*, 2022, Laser powder bed fusion of node-reinforced hybrid lattice structure inspired by crystal microstructure: Structural feature sensitivity and mechanical performance. *Mater Sci Eng A*, 858: 144048.

http://dx.doi.org/10.1016/j.msea.2022.144048

41. Bünnagel C, Monir S, Sharp A, *et al.*, 2021, Forced air cooled heat sink with uniformly distributed temperature of power electronic modules. *Appl Therm Eng*, 199: 117560.

http://dx.doi.org/10.1016/j.applthermaleng.2021.117560

42. Liang D, Chen W, Ju Y, *et al.*, 2021, Comparing endwall heat transfer among staggered pin fin, Kagome and body centered cubic arrays. *Appl Therm Eng*, 185: 116306.

http://dx.doi.org/10.1016/j.applthermaleng.2020.116306

43. Gee DL, Webb RL, 1980, Forced convection heat transfer in helically rib-roughened tubes. *Int J Heat Mass Transfer*, 23(8): 1127–1136.

http://dx.doi.org/https://doi.org/10.1016/0017-9310(80)90177-5

44. Chein R, Yang H, Tsai T-H, *et al.*, 2009, Experimental study of heat sink performance using copper foams fabricated by electroforming. *Microsyst Technol*, 16(7): 1157–1164.

http://dx.doi.org/10.1007/s00542-009-0950-y

45. Bi J, Lei Z, Chen Y, *et al.*, 2021, An additively manufactured Al-14.1Mg-0.47Si-0.31Sc-0.17Zr alloy with high specific strength, good thermal stability and excellent corrosion resistance. *J Mater Sci Technol*, 67: 23–35.

http://dx.doi.org/10.1016/j.jmst.2020.06.036

46. Li R, Wang M, Yuan T, *et al.*, 2017, Selective laser melting of a novel Sc and Zr modified Al-6.2 Mg alloy: Processing, microstructure, and properties. *Powder Technol*, 319: 117–128.

http://dx.doi.org/10.1016/j.powtec.2017.06.050

47. Li K, Ji C, Bai S, *et al.*, 2023, Selective laser melting of magnesium alloys: Necessity, formability, performance, optimization and applications. *J Mater Sci Technol*, 154: 65–93.

http://dx.doi.org/10.1016/j.jmst.2022.12.053

48. Kotadia HR, Gibbons G, Das A, *et al.*, 2021, A review of laser powder bed fusion additive manufacturing of aluminium alloys: Microstructure and properties. *Addit Manuf*, 46: 102155.

http://dx.doi.org/10.1016/j.addma.2021.102155

49. Zhu Z, Hu Z, Seet HL, *et al.*, 2023, Recent progress on the additive manufacturing of aluminum alloys and aluminum matrix composites: Microstructure, properties, and applications. *Int J Mach Tools Manuf*, 190: 104047.

http://dx.doi.org/10.1016/j.ijmachtools.2023.104047

50. Li R, Wang M, Li Z, *et al.*, 2020, Developing a high-strength Al-Mg-Si-Sc-Zr alloy for selective laser melting: Crack-inhibiting and multiple strengthening mechanisms. *Acta Mater*, 193: 83–98.

http://dx.doi.org/10.1016/j.actamat.2020.03.060

51. Viale V, Stavridis J, Salmi A, *et al.*, 2022, Optimisation of downskin parameters to produce metallic parts via laser powder bed fusion process: an overview. *Int J Adv Manuf Technol*, 123(7–8): 2159–2182.

http://dx.doi.org/10.1007/s00170-022-10314-z

52. Han Q, Gu H, Soe S, *et al.*, 2018, Manufacturability of AlSi10Mg overhang structures fabricated by laser powder bed fusion. *Mater Des*, 160: 1080–1095.

http://dx.doi.org/10.1016/j.matdes.2018.10.043

53. Choy SY, Sun C-N, Sin WJ, *et al.*, 2021, Superior energy absorption of continuously graded microlattices by electron beam additive manufacturing. *Virtual Phys Prototyping*, 16(1): 14–28.

http://dx.doi.org/10.1080/17452759.2020.1868656

54. Gao Z, Wang H, Sun H, *et al.*, 2022, Additively manufactured high-energy-absorption metamaterials with artificially engineered distribution of bio-inspired hierarchical microstructures. *Composites, Part B*, 247: 110345.

http://dx.doi.org/10.1016/j.compositesb.2022.110345

55. Hu J, Tan ATL, Chen H, *et al.*, 2022, Superior compressive properties of 3D printed plate lattice mechanical metamaterials. *Int J Mech Sci*, 231: 107586.

http://dx.doi.org/10.1016/j.ijmecsci.2022.107586

56. Xiao L, Xu X, Feng G, *et al.*, 2022, Compressive performance and energy absorption of additively manufactured metallic hybrid lattice structures. *Int J Mech Sci*, 219: 107093.

http://dx.doi.org/10.1016/j.ijmecsci.2022.107093

57. Zhang J, Liu Y, Babamiri BB, *et al.*, 2022, Enhancing specific energy absorption of additively manufactured titanium lattice structures through simultaneous manipulation of architecture and constituent material. *Addit Manuf*, 55: 102887.

http://dx.doi.org/10.1016/j.addma.2022.102887

58. Yang J, Gu D, Lin K, *et al.*, 2021, Laser additive manufacturing of cellular structure with enhanced compressive performance inspired by Al–Si crystalline microstructure. *CIRP J Manuf Sci Technol*, 32: 26–36.

http://dx.doi.org/10.1016/j.cirpj.2020.11.003

59. Li C, Lei H, Liu Y, *et al.*, 2018, Crushing behavior of multi-layer metal lattice panel fabricated by selective laser melting. *Int J Mech Sci*, 145: 389–399.

http://dx.doi.org/10.1016/j.ijmecsci.2018.07.029

60. Al-Saedi DSJ, Masood SH, Faizan-Ur-Rab M, *et al.*, 2018, Mechanical properties and energy absorption capability of functionally graded F2BCC lattice fabricated by SLM. *Mater Des*, 144: 32–44.

http://dx.doi.org/10.1016/j.matdes.2018.01.059

61. Chen W, Gu D, Yang J, *et al.*, 2022, Compressive mechanical properties and shape memory effect of NiTi gradient lattice structures fabricated by laser powder bed fusion. *Int J Extreme Manuf*, 4(4): 045002.

http://dx.doi.org/10.1088/2631-7990/ac8ef3

62. Yang X, Yang Q, Shi YS, *et al.*, 2022, Effect of volume fraction and unit cell size on manufacturability and compressive behaviors of Ni-Ti triply periodic minimal surface lattices. *Addit Manuf*, 54: 102737.

http://dx.doi.org/10.1016/j.addma.2022.102737

63. Ho JY, Wong KK, Leong KC, *et al.*, 2017, Convective heat transfer performance of airfoil heat sinks fabricated by selective laser melting. *Int J Therm Sci*, 114: 213–228.

http://dx.doi.org/10.1016/j.ijthermalsci.2016.12.016

64. Wong KK, Ho JY, Leong KC, *et al.*, 2016, Fabrication of heat sinks by selective laser melting for convective heat transfer applications. *Virtual Phys Prototyp*, 11(3): 159–165.

http://dx.doi.org/10.1080/17452759.2016.1211849

65. Kuruneru STW, Vafai K, Sauret E, *et al.*, 2020, Application of porous metal foam heat exchangers and the implications of particulate fouling for energy-intensive industries. *Chem Eng Sci*, 228: 115968.

http://dx.doi.org/10.1016/j.ces.2020.115968

66. Zhu Q, Cui Y, Zeng J, *et al.*, 2023, Local hydrothermal characteristics and temperature uniformity improvement of microchannel heat sink with non-uniformly distributed grooves. *Case Stud Therm Eng*, 47: 103113.

http://dx.doi.org/10.1016/j.csite.2023.103113

ACCSCIENCE PUBLISHING

International Journal of Bioprinting

REVIEW ARTICLE

Multiscale 3D bioprinting for the recapitulation of lung tissue

Pengbei Fan[1,2], Fanli Jin[1,2], Yanqin Qin[1,2], Yuanyuan Wu[1,2], Qingzhen Yang[3,4]*, Han Liu[1,2]*, and Jiansheng Li[1,2]*

[1]Henan Key Laboratory of Chinese Medicine for Respiratory Disease, Academy of Chinese Medical Sciences, Henan University of Chinese Medicine, Zhengzhou, Henan 450046, P.R. China

[2]Collaborative Innovation Center for Chinese Medicine and Respiratory Diseases co-constructed by Henan Province and Education Ministry of China, Zhengzhou, Henan 450046, P.R. China

[3]The Key Laboratory of Biomedical Information Engineering of Ministry of Education, School of Life Science and Technology, Xi'an Jiaotong University, Xi'an, Shaanxi 710049, P.R. China

[4]Bioinspired Engineering and Biomechanics Center (BEBC), Xi'an Jiaotong University, Xi'an, Shaanxi 710049, P.R. China

(This article belongs to the *Special Issue: Nano-enabled 3D Bioprinting for Various Tissue Engineering*)

Abstract

Lung tissue engineering (LTE) has gained significant attention as a highly promising and innovative strategy to tackle the formidable obstacles posed by lung-related diseases and the lack of compatible donor organs availability. In the realm of groundbreaking advancements in tissue engineering (TE), one particular technology that has emerged as a game-changer is three-dimensional (3D) bioprinting. It distinguishes itself by offering a potent and versatile approach to constructing intricate structures while opening up new horizons for TE and regenerative medicine (RM). This review focuses on the application of multiscale 3D bioprinting techniques in LTE and the reconstitution of lung tissue *in vitro*. We analyzed the key aspects such as bioink formulations and printing strategies utilized from macroscale 3D bioprinting to micro/nanoscale 3D bioprinting. Additionally, we evaluated the potential of multiscale bioprinting to replicate the complex architecture of the lung, ranging from macrostructures to micro/nanoscale features. We discussed the challenges and future directions in biofabrication approaches for LTE. Furthermore, we highlight the current progress and future perspectives in tissue reconstitution of lung *in vitro*, considering factors such as cell source, functionalization, and integration of physiological cues. Overall, multiscale 3D bioprinting offers exciting possibilities for the development of functional lung tissues, enabling disease modeling, new drug screening, and personalized regenerative therapies.

Keywords: Multiscale 3D bioprinting; Lung tissue engineering; Biofabrication; Tissue reconstitution *in vitro*

***Corresponding authors:**
Jiansheng Li
(li_js8@163.com)

Han Liu
(liuhan1969@hactcm.edu.cn)

Qingzhen Yang
(qzyang@mail.xjtu.edu.cn)

Citation: Fan P, Jin F, Qin Y, et al., 2023, Multiscale 3D bioprinting for the recapitulation of lung tissue. *Int J Bioprint*, 9(6): 1166. https://doi.org/10.36922/ijb.1166

Received: June 27, 2023
Accepted: August 8, 2023
Published Online: September 4, 2023

Copyright: © 2023 Author(s). This is an Open Access article distributed under the terms of the Creative Commons Attribution License, permitting distribution, and reproduction in any medium, provided the original work is properly cited.

Publisher's Note: AccScience Publishing remains neutral with regard to jurisdictional claims in published maps and institutional affiliations.

1. Introduction

Lung tissue engineering (LTE) represents a dynamically progressing domain, with continuous research endeavors directed toward surmounting the obstacles linked to the

expansion of functional lung tissue production, enhancing vascularization approaches, and ensuring sustained long-term functionality[1,2]. Conditions such as chronic obstructive pulmonary disease (COPD), pulmonary fibrosis, and lung cancer pose significant challenges to global health, severely impacting patients' quality of life and overall prognosis[3,4]. LTE is of paramount importance in the context of lung diseases, as it holds great potential for revolutionizing innovative strategies to replace or repair damaged lung tissue by leveraging the principles of biology, materials science, and engineering[5]. The ultimate goal is to provide effective treatments and potential cures for regenerative medicine (RM), offering new possibilities for patients requiring respiratory interventions. Especially, LTE combined with three-dimensional (3D) bioprinting holds great promise for advancing our understanding of lung diseases, developing new therapies, and potentially providing transplantable lung tissue in the future.

Bioprinting, as defined by the American Society for Testing Materials (ASTM), is a specific method used to 3D-print biomaterials into various structures. 3D bioprinting is a specific technique used within the broader field of tissue engineering (TE), to precisely deposit cells, biomaterials, and growth factors in a 3D manner to create complex structures[6,7]. The common strategies of 3D bioprinting include inkjet-based bioprinting, extrusion-based bioprinting, and laser-assisted (e.g., stereolithography) bioprinting (Figure 1)[8]. Over the past few decades, the field of 3D bioprinting has experienced significant advancements in terms of the types of tissue models that can be constructed, including cancer[9], blood vessels[10,11], heart[12], and lungs[13,14]. Indeed, 3D bioprinting has the potential to offer various benefits and applications beyond just lung transplantation. 3D bioprinting allows the creation of patient-specific tissues and organs, tailored to individual needs. Additionally, researchers can create disease-specific models using bioprinting, allowing them to study the effects of drugs on specific tissues or organs without endangering patients[9,15,16]. Although this technology is still in its early stages, researchers have made progress in generating small, simplified organs like liver patches, kidney tissues, and more[17]. Therefore, the ability of 3D bioplotting to recreate the lung tissue allows researchers to investigate disease progression, cellular interactions, and responses to different drugs or treatments[18]. 3D bioprinting has emerged as a transformative tool that enables the creation of intricate 3D structures across different scales, ranging from macroscale to microscale and even nanoscale.

Considering the complex structure and dynamic characteristics of lung, researchers have made various summaries[19,20]. 3D bioprinting enables the construction of artificial lung tissues or lung organs at the macroscale, precise tissue compositions at the microscale, and even cell and molecular compositions at the nanoscale. Although extensive work has been done on the 3D bioprinting for LTE, there, to the best of our knowledge, appears no review paper in this field. In this review, we present a comprehensive overview of the principles and recent advancements in 3D bioprinting for LTE. We proceed to explore crucial elements such as the composition of bioink and the printing methodologies employed, and explore the potential of multiscale bioprinting to faithfully reproduce the intricate architecture of the lung, ranging from macrostructures to nanoscale features. Furthermore, we emphasized the current progress and future perspectives in the *in vitro* reconstitution of lung tissue, covering crucial considerations like cell sourcing, functionalization, and integration of physiological cues. With these groundbreaking techniques, a new era is dawning in the realm of lung tissue development, opening doors to functional and biologically accurate constructs. This remarkable progress promises to revolutionize disease modeling, drug screening, and RM for lung conditions.

2. Material inks for lung tissue fabrication

As the native extracellular matrix (ECM) can offer structural support to tissues, it is important to find an engineered ECM that can serve the same purpose. Material inks play a crucial role in TE as they provide scaffolds for cell growth and differentiation, facilitating the formation of functional tissues[21]. In the context of lung fabrication, several biomaterials are being explored for creating lung tissue *in vitro*. For example, hydrogels (including alginate, collagen, gelatin, and fibrin) are water-based materials that can mimic pulmonary ECM[18]. They provide a 3D environment for cells to grow and can be engineered to have specific mechanical properties and biochemical cues. Additionally, biocompatible and biodegradable synthetic polymers like poly(lactic-co-glycolic acid) (PLGA), polycaprolactone (PCL), and polyethylene glycol (PEG) are commonly used in 3D printing or melded into the scaffolds. In addition, decellularized ECM (dECM) encompasses the characteristics of an ideal tissue scaffold: complex composition, vascular networks, and unique tissue-specific architecture[22,23]. Therefore, dECM has emerged as a potential biomaterial ink with tissue-specific composition for LTE[24]. During the fabrication process, microcarrier inks, which are small, spherical particles, play a role in carrying and protecting cells. Furthermore, the incorporation of nanofibers and nanoparticles can enhance the mechanical properties and surface area of the nanoscale lung scaffolds. To achieve lung-like structures with appropriate architecture and functionality,

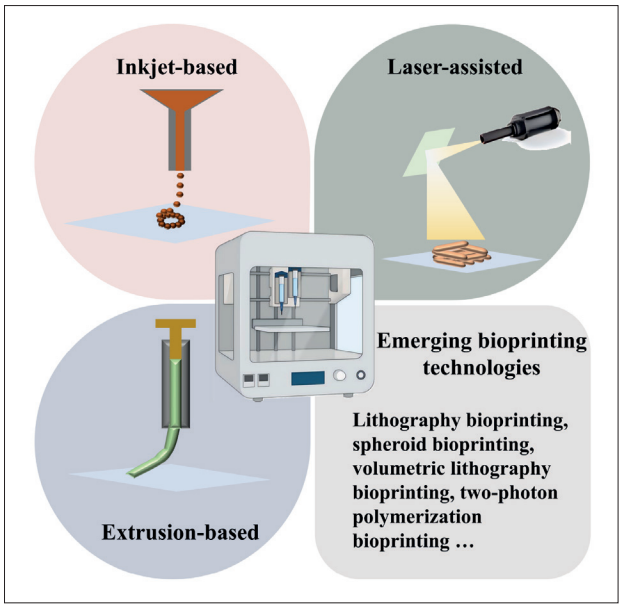

Figure 1. Types of 3D bioprinting, including inkjet-based bioprinting, extrusion-based bioprinting, laser-assisted bioprinting, and other emerging technologies. Created with BioRender (www.biorender.com).

a combination of these biomaterials with advanced 3D bioprinting techniques proves highly promising.

3. Macroscale 3D bioprinting

3.1. Macroscale 3D bioprinting techniques

Macrobioprinting application addresses the medical requirements to develop transplantable tissue structures that meet feasible anatomical dimensions on a macroscale[25]. Macroscale 3D bioprinting focuses on creating larger and more complex tissue constructs (e.g., artificial trachea) that closely resemble natural tissues in terms of their macroscopic features[26]. Macroscale bioprinting materials and strategies have shown significant progress in TE, encompassing the overall shape, structure, and volume of printed biological tissues[27]. Macroscale 3D bioprinting involves the use of larger bioink formulations and printing strategies to create 3D structures[28]. These bioink materials need to possess biocompatibility, biodegradability, bioabsorbability, and printability. The bioink also incorporates biomaterials, which act as a support structure and provide cues for cell growth and tissue formation. Commonly used biomaterials in macroscale bioprinting include hydrogels (e.g., alginate, gelatin, or collagen) or synthetic polymers[29]. In addition to biomaterials, macroscale bioprinting allows for the printing of various cell types, including stem cells, differentiated cells, or a combination of multiple cell types[30]. Macroscale bioprinting employs different strategies to deposit bioink and build 3D structures. The most common methods include extrusion-based bioprinting, where bioink is extruded through a nozzle or a syringe, lithography bioprinting, and inkjet-based bioprinting, where small droplets of bioink are deposited layer by layer. To achieve the desired tissue morphology (especially the complex respiratory system) in macroscale bioprinting, various factors need to be considered, including the biomaterial inks, the design of printing patterns, and the optimization of printing parameters.

Macroscale 3D bioprinting for lung tissue involves the fabrication of larger-scale structures that mimic the architecture and functionality of native lung tissue[31]. By accurately depositing material inks and creating appropriate scaffolds, researchers can recreate the structural organization necessary for proper lung function (Figure 2A). The construction of macroscale lung tissue can be deposited layer by layer using techniques like 3D bioprinting or assembled into larger structures to mimic the desired lung tissue architecture[32]. This technology facilitates precise deposition of biomaterials, such as hydrogels, in a controlled manner, enabling the construction of intricate structures that mimic the native macroscale tissues[33]. Macroscale 3D bioprinting for lung tissue holds promise for various applications and potentially transplantation in the future.

3.2. Macroscale 3D bioprinting for lung tissue recapitulation and application

3D spheroid bioprinting technology has the potential to create human lung tissues on a macroscale, utilizing biomaterial scaffolds, which can include the intricate

network of artificial trachea, blood vessels, and alveoli. Researchers designed and developed a tissue-specific photo-crosslinked bioink, and applied 3D bioprinting technology to construct a bionic trachea with alternate cartilage-vascularized fibrous tissue (Figure 2B)[34]. Multiscale vascularization remains a critical challenge in LTE. In order to study the lung tissue with natural morphological structure, scientists attempted to incorporate the structural attributes of the natural distal lung into a bioinspired model that mimicked the alveolar morphology and facilitated oxygen transport[35]. They used a hydrogel that can support mechanical stretching during the process of collecting air in the small airways' circulation, and the size of the 3D lung model printed is like a coin. Furthermore, researchers successfully prepared a human alveolar lung model *in vitro* through macroscale 3D bioprinting[36]. This lung model has collagen matrix, alveolar lung epithelium, endothelium, and fibroblasts, and maintains high cell vitality, proliferation, and viability in this printed structure. Moreover, to reproduce the 3D pulmonary cyst-like architecture, particularly alveoli epithelial side, researchers have successfully generated epithelial cysts utilizing the macroscale 3D bioprinting[37]. By incorporating epithelial cysts as a cellular component within material inks, it becomes feasible to hierarchically structure them through bioprinting, ultimately leading to the creation of constructs that closely resemble alveoli.

The trachea-like engineered lung tissues can serve as models for studying lung diseases like tracheal stenosis[38]. In addition, through the incorporation of advanced imaging techniques, computer-aided design models, and

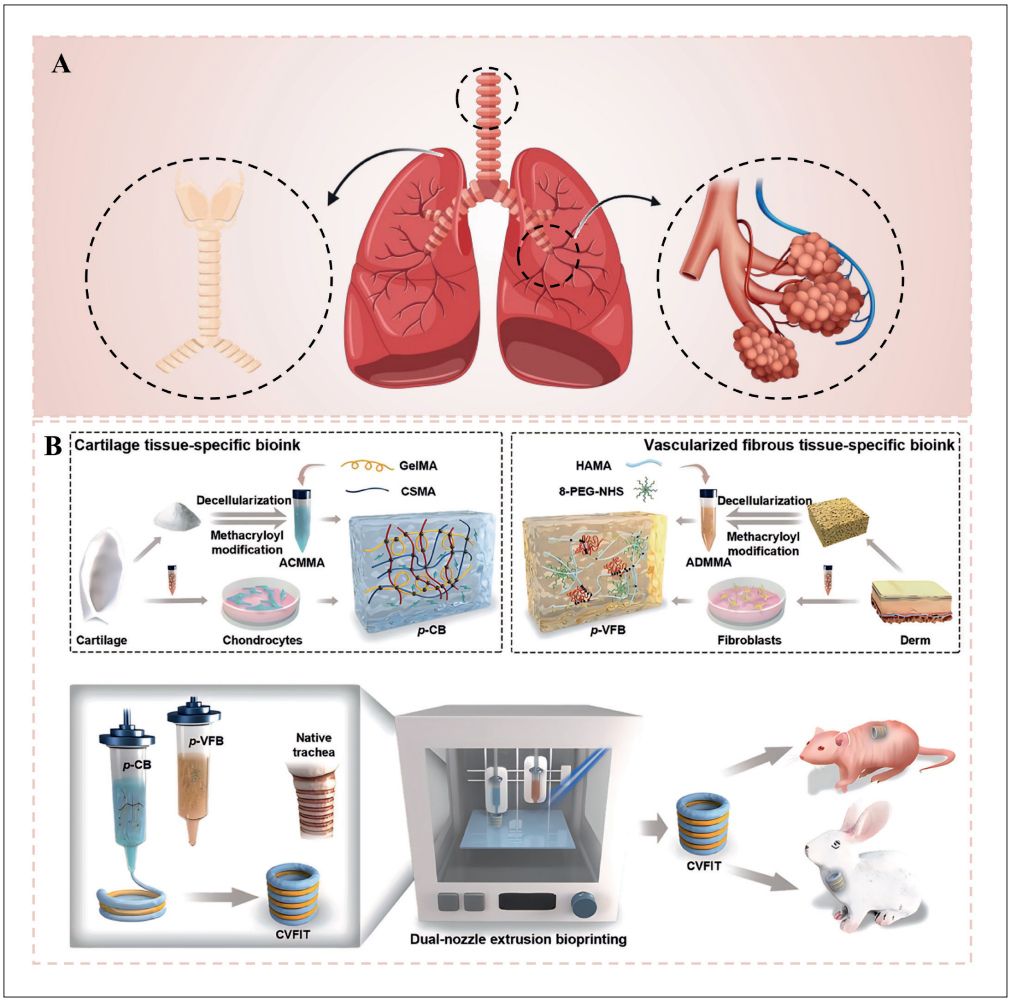

Figure 2. Macroscale 3D bioprinting for lung tissue. (A) Schematic diagram of pulmonary macroscale structure. Created with BioRender (www.biorender.com). (B) Schematic illustration of the designs of cartilage tissue-specific and vascularized fibrous tissue-specific bioinks and the 3D-bioprinted CVFIT for trachea regeneration in nude mice and *in situ* trachea reconstruction of rabbits[34]. Reprinted (and adapted) with permission from John Wiley and Sons. Copyright © *2022 The Authors. Advanced Science published by Wiley-VCH GmbH.* Abbreviations: CVFIT, cartilage-vascularized fibrous tissue-integrated trachea; *p*-CB, photo-crosslinkable cartilage-specific bioink; *p*-VFB: photo-crosslinkable-vascularized fibrous tissue-specific bioink.

precise robotic control systems, macroscale bioprinting facilitates the fabrication of scaffold-free isogenic artificial tracheas, which can be utilized as tracheal grafts in rats[39]. Researchers have demonstrated the transplantation of a macroscale 3D-printed trachea that mimics the natural trachea into a rabbit model to enhance the regeneration of tracheal mucosa and cartilage[40]. In another study, a macroscopic structure composed of lung epithelial cells printed on the basis of primary lung fibroblasts and monocyte cells was used to reconstruct alveolar model (about 7 mm long) *in vitro* to detect influenza virus infection[41]. These constructs can be used to study lung development, investigate disease mechanisms, and develop new therapies.

4. Microscale 3D bioprinting

4.1. Microscale 3D bioprinting techniques

Research on microscale systems to reconstruct local microenvironmental cues and microscale characteristics is also worthy of attention for realizing pulmonary structure functions *in vitro*[42]. Within the living organism, cells reside in a complex microenvironment consisting of diverse biophysical and biochemical cues[43,44]. Microscale bioprinting refers to the fabrication of structures at a smaller scale, typically in the range of micrometers[45,46]. Microscale 3D bioprinting constructs aim to replicate the complex biochemical and biophysical processes that occur within and between cells in living tissues[47,48]. This approach offers several advantages, including enhanced precision, increased resolution, and improved control over cell placement, which are crucial for mimicking the natural cellular composition and organization found in native tissues and organs[49,50]. Commonly used strategies are laser-assisted bioprinting and inkjet-based bioprinting. Laser-assisted bioprinting realizes the printing of photosensitive bioink by using plane projection, while inkjet-based bioprinting uses a piezoelectric printhead to deposit droplets of bioink onto a substrate. Such strategies enable us to create complex microscale tissue structures. In microscale bioprinting, bioinks must possess specific properties, such as shear-thinning behavior (to enable extrusion), biocompatibility, and appropriate rheological properties (to simulate lung stretching) for precise printing. The bioprinted cells can interact with the surrounding ECM or biomaterials[51,52]. By controlling the printing parameters and the composition of the bioink, researchers can achieve desired mechanical properties, cell densities, and functionalities within the printed microscale constructs[53,54]. For example, hydrogels made from human lung dECM can resemble the biophysical traits of native lung tissue[55].

Micro lung structure refers to the detailed anatomical components and organization of the lung at the microscopic level. It involves the study and understanding of the intricate structures within the lung tissue, such as the alveoli, bronchioles, capillaries, and various types of cells[56]. The small airways also play a crucial role in the microstructure of the lung and distribute air to the alveoli and help regulate airflow within the lungs. The alveoli are surrounded by a network of capillaries, allowing for efficient exchange of air between the alveoli and the blood (Figure 3A). In the blood–gas barrier, the proximity between an alveolus and a capillary is approximately 0.5 μm, facilitating gas exchange through the process of diffusion[57]. Continued research and advancements in microscale bioprinting hold huge promise for the advancements of functional lung tissues as well as lung tissue recapitulation and application in future.

4.2. Microscale 3D bioprinting for lung tissue recapitulation and application

Microscale bioprinting materials and strategies offer precise control over the fabrication of lung tissue constructs at a smaller scale, which enable the creation of intricate structures, mimic the native lung microenvironment, and promote cell viability and functionality[58,59]. Using 3D bioprinter with a printing resolution in the micrometer range, researchers printed a complex engineering microscale 3D air–blood tissue barrier for safety assessment and drug efficacy testing (Figure 3B)[60]. This development is expected to pave the way for high-throughput drug screening *in vitro*. Due to the impossibility of a single material ink to establish a "synthetic" microenvironment that accurately simulates the *in vivo* conditions, there has been a growing emphasis on multimaterial bioprinting[61]. Researchers developed a groundbreaking material ink by combining alginate with dECM, showcasing its remarkable ability to maintain biological activity during the entire process of 3D-bioprinting intricate and mechanically resilient tissues, both during and after printing (Figure 3C)[62]. Through their research, it was discovered that the enhanced bioink, enriched with lung dECM, exhibited remarkable potential for 3D bioprinting of subsegmental human bronchus. This bioink consisted of primary human lung smooth muscle cells and primary airway epithelial progenitor cells, which possessed the capacity to differentiate into diverse cell types typically found in the airway.

The progress of microscale 3D bioprinting has significantly advanced the simulation of lung diseases *in vitro*. In a recent and influential study, scientists made a significant breakthrough by 3D bioprinting, which has proven to be a valuable model for investigating influenza infection within the lung[63]. Additionally, studies have demonstrated the feasibility of bioprinting microscale lung using acellular porcine lung hydrogel without external crosslinking, using

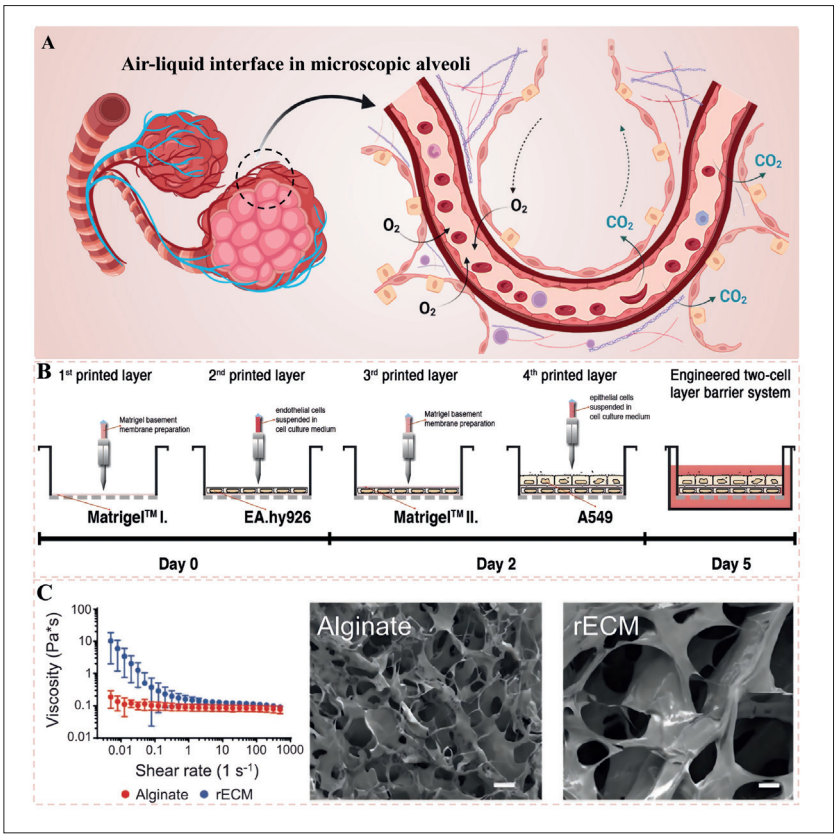

Figure 3. Microscale 3D bioprinting for lung tissue. (A) Schematic diagram of pulmonary microscale structure. Created with BioRender (www.biorender.com). (B) Schematic of the timeline for bioprinting the two cell-layer barrier system[60]. Reprinted (and adapted) with permission from Springer Nature. Copyright © *2015, The Author(s).* (C) Biophysical characteristics of reinforced ECM (rECM) for microscale bioprinting and observation under scanning electron microscope (scale bars = 50 μm)[62]. Reprinted (and adapted) with permission from John Wiley and Sons. Copyright © *2022 The Authors. Advanced Science published by Wiley-VCH GmbH.*

microscale 3D bioprinting technology[64]. For instance, a thrombosis chip was constructed, offering insights into effective treatment strategies for pulmonary embolism[65]. In a separate investigation, researchers employed a bioink composed of gelatin-sodium alginate blended with a suspension of lung cancer cells A549/95-D. By utilizing 3D bioprinting technology, they successfully created a tumor-like lung cancer model[66]. However, the field still faces numerous challenges that must be addressed, especially concerning the development of materials and techniques specifically tailored for lung cells. One of the key objectives is to enable the formation of nanoscale architecture within the air–blood barrier, necessitating further research and innovation.

5. Nanoscale 3D bioprinting

5.1. Nanoscale 3D bioprinting techniques

Nanoscale microenvironment features, such as ridges, steps, and grooves, have a significant impact on cell attachment, proliferation, and cytoskeletal assembly[67]. With the advancing integration of bioprinting and nanomaterials, engineered tissues are expected to achieve higher levels of complexity and functionality, gradually approaching the level of complete organ replicas[68,69]. Nanocomposite material inks have caught scientists' attention, considering the pulmonary complexity[70,71]. Over the years, the convergence of 3D bioprinting with nanotechnology in lung reconstruction *in vitro* has gained increasing attention. Nanoscale 3D bioprinting entails the precise positioning of biomaterials, cells, and nanoparticles at the nanoscale resolution[72]. Nanoscale 3D bioprinting encompasses bioprinting of cells in precise distribution and arrangement, thereby facilitating their interaction with the matrix, optimizing cell density in tissues, and orchestrating biochemical and biophysical processes within and between cells[73]. Nanoscale 3D bioprinting techniques, such as two-photon polymerization or laser-assisted forward transfer (LIFT), enable precise layer-by-layer deposition of the bioink, facilitating the construction of desired structures at the nanoscale. Nanoscale bioprinting takes this process a step further by integrating nanomaterials, nanoparticles,

or nanofibers into the material inks, thereby providing enhanced control over the cellular microenvironment and facilitating tissue development (Figure 4A). The process of nanoscale 3D bioprinting typically starts with the formulation of a bioink, which is a specialized material comprising living cells and biomaterials. Nanocomposite materials find widespread use due to their ability to enhance the mechanical traits of hybrid organic/inorganic composites[74]. Engineered nanofiber networks play a crucial role in promoting cellular growth and regulating cellular behaviors in a manner that closely emulates physiological conditions[75]. The application of nanotechnologies has been instrumental in engineering nanofibrous and nanocomposite structures, as well as nanoscale surface topographies and networks within scaffolds. These advancements effectively replicate the intricate nanoscale structure of various tissue types, including lung tissue. A remarkable advancement in research is the development of a transparent biomimetic nanoscale fibrillar matrix gel, offering flexibility in choosing bioink materials[76].

Nanoscale structure refers to the detailed anatomical components and organization of the lung at the nanoscale level[77]. It involves the study and understanding of the structures and processes that occur at the nanoscale within the lung tissue. The alveoli, which are the smallest pulmonary functional units, have complex nanostructures. The walls of the alveoli are extremely thin, facilitating efficient gas exchange[78]. The alveoli are lined with a surfactant layer, which is composed of lipids and proteins. These surfactant monolayers play a critical role in reducing surface tension within the alveoli, preventing their collapse during exhalation and promoting efficient gas exchange. Nanoparticles and gases can diffuse across the alveolar epithelium, enabling the exchange of oxygen and carbon dioxide between the air in the alveoli and the adjacent capillaries. Additionally, nanoscale vesicles and exosomes play a role in cellular communication. The surface of lung epithelial cells is lined with specialized nanostructures, such as microvilli or cilia, which aid in functions like absorption or mucociliary clearance. Understanding the nanoscale structure of the lung is crucial for comprehending respiratory diseases and the effects of nanoscale interactions on lung health.

5.2. Nanoscale 3D bioprinting for lung tissue recapitulation and application

Nanoscale 3D bioprinting technology enables the precise arrangement in 3D structures, mimicking the complexity and functionality of lung tissues. Researchers print nanoscale ECM hydrogels by extruding cellular and acellular gels into stacked cell ring structures, which has the potential to study lung nanostructures[79]. By accurately positioning these cells within the 3D structure, nanoscale bioprinting can promote the formation of functional lung tissue and facilitate gas exchange. A bioink-containing nanofibrils have been developed for nanoscale 3D-printing lung tissue scaffolds (Figure 4B)[80]. One of the primary challenges in 3D bioprinting is to achieve precise control over the nanoscale architecture while ensuring compatibility with living cells. Nanoforms play a crucial role in promoting cell survival, growth, and differentiation, enabling cells to assume the necessary functions for tissue regeneration and repair.

Concerning efficient gas exchange, it is crucial to accurately manufacture the thin air–blood barrier via LTE. Advanced lung tissue models in the field are highly sought-after, aiming to achieve both biomimetic structural properties and the ability to precisely regulate cell behavior. The researchers prepared a three-organ chip composed of liver, heart, and lung through 3D nanobioprinting, and evaluated its physiological response to drugs and toxic substances[81]. The nanofibrous structure, resembling the morphology of the ECM, promotes cell attachment and enhances nutrition and oxygen transport due to its high surface area and interconnectivity[82]. The submicrometer pore structure and pore size can be controlled between 1000 μm and 10 nm, and its excellent adsorption performance is beneficial to the 3D culture of cells (Figure 4C)[83]. Nanoscale structural elements in 3D bioprinting can be effective in the promotion of cell distribution and new tissue formation. Furthermore, 3D bioprinting has emerged as a valuable tool in the design and development of disease models, including infectious diseases like COVID-19. At the nanoscale, 3D bioprinting allows for the creation of realistic disease models that can be used for studying pathogenesis, drug discovery, and personalized medicine[84]. Continued advancements in nanomaterials and nanoscale fabrication techniques will further contribute to the advancements in respiratory disease research.

6. Challenges and future directions

3D bioprinting is a promising technology with vast potential in tissue engineering, although it is still in its early stages of development. Several technical challenges must be addressed, particularly achieving high-resolution cell patterning and distribution. Current techniques like material extrusion have several drawbacks, including low cell viability, resolution, and working speed, which hinder the fabrication of submicroscale and nanoscale structures. To enable the production of macroscale tissues for clinical applications, printing capabilities and speed must be improved[85]. In addition, for successful *in vivo* transplantation, the printed tissue must possess appropriate

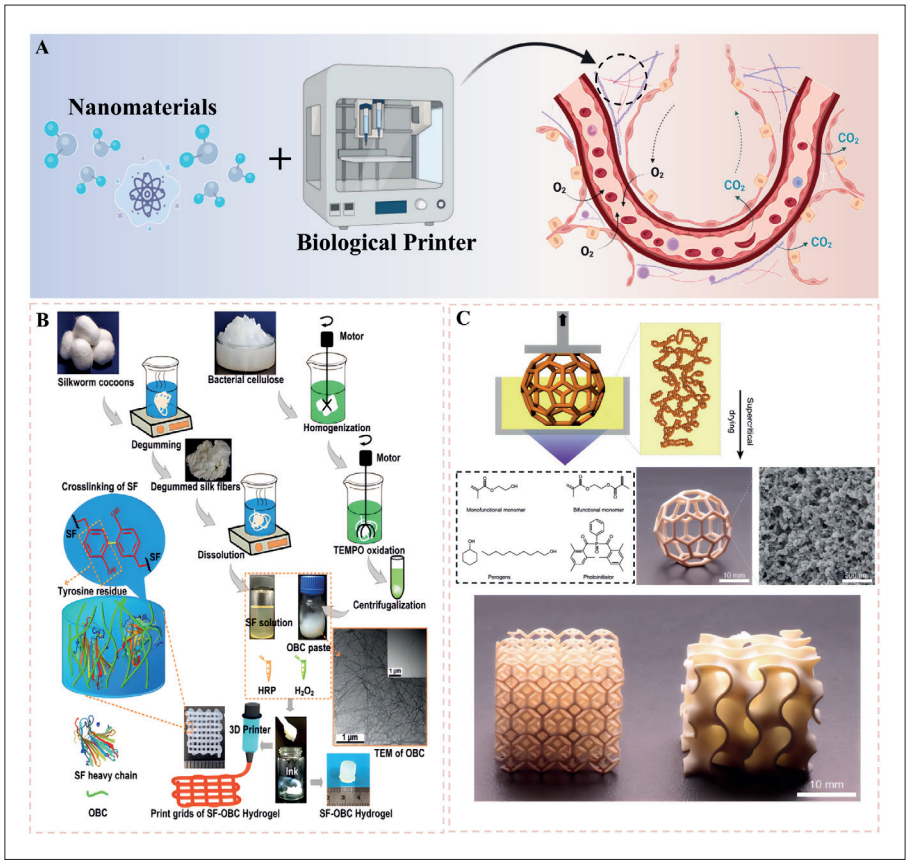

Figure 4. Nanoscale 3D bioprinting for lung tissue. (A) Nanomaterials-assisted bioprinting to simulate alveolar nanostructures. Created with BioRender (www.biorender.com). (B) Process of fabricating silk fibroin (SF) solution, oxidized bacterial cellulose (OBC) paste, SF-OBC composite ink, and SF-OBC nanofibrils hydrogel for the proliferation of lung epithelial stem cells[80]. Reprinted (and adapted) with permission from Springer Nature. Copyright © *2020, Springer Nature B.V.* (C) 3D objects with nanoscale porous structures are manufactured by using digital light processing printing technology[83]. Reprinted (and adapted) with permission from Springer Nature. Copyright © *2021, The Author(s).*

mechanical traits to facilitate suturing with the host circulation and withstand the rhythmic pulsations of blood flow[86]. To realize the objective of bioprinting functional tissues, it is crucial to foster collaboration and integrate expertise from diverse fields, such as manufacturing, material science, biology, and medicine. By bringing together experts from different fields, we can collectively tackle these obstacles and pave the way for groundbreaking advancements in the field of bioprinting[87,88]. In summary, while 3D bioprinting holds great potential for fabricating functional tissues, it requires concerted efforts and interdisciplinary collaborations to overcome technical challenges and advance the field toward clinical translation.

The complex multiscale structure of organs and tissues presents a significant challenge for replication using a single program or tool[89,90]. Future development will focus on multisize, multimaterial, and multicell bioprinting, integrating precise modeling of cell–cell interactions and segregation at the intratissue level, combined with architectural control at the macroscale (Figure 5). This approach shows promise for engineering tissue constructs that closely resemble native tissues in their morphometric features[91]. While bioprinted constructs have demonstrated high cell viability and specific functions in laboratory research, they are still in the early stages of development and not ready for clinical applications[92,93]. Except for advanced structural design, it is important to determine the role of mechanical cues in lung-related research as to design, develop, and apply suitable material inks[94,95]. With every breath, lung cells are subjected to dynamic or continuous mechanical loads, including tension, compression, and shear stress. These mechanical forces serve as vital signals for maintaining the steady state, remodeling, and optimal functioning of lung tissue. By simulating physiological respiratory movement through cyclic mechanical stretch, more realistic lung models can be achieved[96]. Considering the mechanical cues and their associated signaling pathways in the design of material inks for bioprinting lung tissue can help us build a more realistic functional model. By incorporating these mechanical regulatory factors into

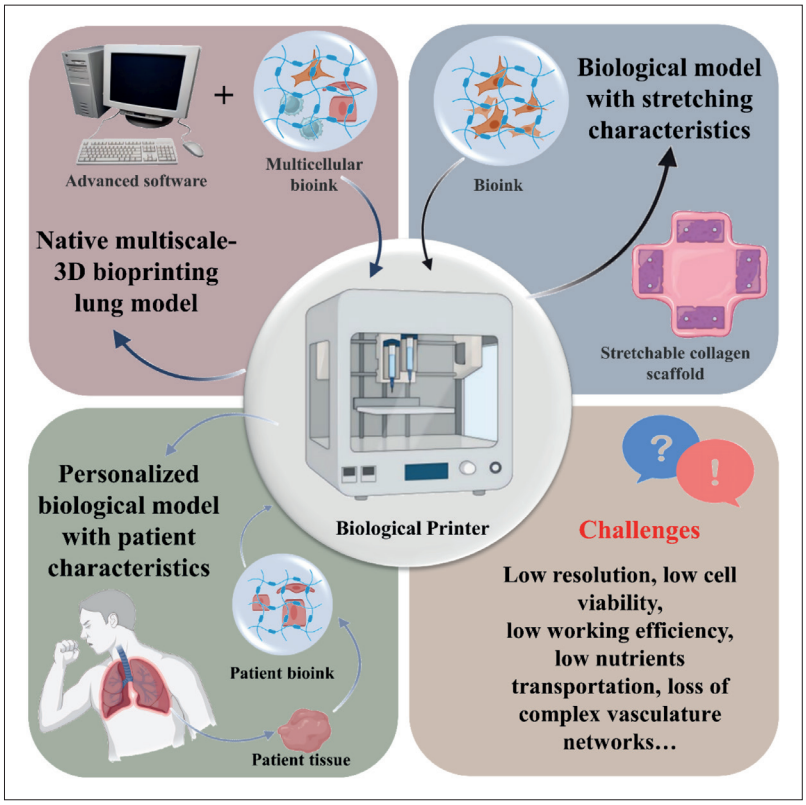

Figure 5. The future and challenges of multiscale 3D bioprinting of lung tissue. In the future, advancements in technology will bring forth an array of enhanced features in the realm of 3D bioprinting. These improvements will include more life-like multiscale lung models, biological models possessing stretching characteristics, and personalized pathological models. However, it is important to acknowledge that numerous challenges still lie ahead. Created with BioRender (www.biorender.com).

the bioprinting process, researchers can create material inks that mimic the mechanical microenvironment of the lung, promoting cell behavior and tissue development that closely resemble native lung tissue.

Despite being in its early stages of development, 3D bioprinting is showing great promise in the field of TE[97]. Beyond organ printing, 3D bioprinting has multifaceted applications in medicine, including testing drug delivery systems and advancing lung disease treatments. Through the simulation of lung tissue characteristics, it enables more accurate assessments of drug delivery and release efficiency for treating lung diseases[98]. Moreover, by replicating patients' lung tissues using 3D bioprinting, researchers gain valuable insights into the underlying causes of diverse lung diseases, significantly improving disease understanding and fostering the development of novel treatments and medications. An additional benefit of 3D bioprinting lies in its ability to create artificial lung tissue that precisely matches a patient's unique anatomical structure. This advancement is invaluable in predicting organ compatibility and evaluating potential outcomes before actual transplantation takes place. By conducting pretrials with artificial lung tissue, the risk of organ transplantation failure is reduced, and tailored treatment plans can be devised, ultimately improving patient outcomes. The continuous advancements of 3D bioprinting research further expand its application in RM, drug discovery, and personalized healthcare. With further developments and refinement, the field of medicine has the potential to undergo a transformative revolution with the advent of 3D bioprinting.

Acknowledgments

None.

Funding

This work was financially supported by the National Natural Science Foundation of China (52175547 and U21A20337), China Postdoctoral Science Foundation Special Funded Project (2022T150197), China Postdoctoral Science Foundation (2021M690938), Henan Province Key R&D, and Promotion Special (Scientific and Technical) Project (222102310183 and 222102310141).

Conflict of interest

The authors declare no conflicts of interests.

Author contributions

Conceptualization: Han Liu, Qingzhen Yang, Jiansheng Li
Writing – original draft: Pengbei Fan, Han Liu, Fanli Jin, Yanqin Qin, Yuanyuan Wu
Writing – review & editing: Han Liu, Jiansheng Li, Qingzhen Yang

Ethics approval and consent to participate

Not applicable.

Consent for publication

Not applicable.

Availability of data

Not applicable.

References

1. Hwang KS, Seo EU, Choi N, *et al.*, 2023, 3D engineered tissue models for studying human-specific infectious viral diseases. *Bioact Mater*, 21: 576–594.

   http://doi.org/10.1016/j.bioactmat.2022.09.010

2. Margolis EA, Friend NE, Rolle MW, *et al.*, 2023, Manufacturing the multiscale vascular hierarchy: Progress toward solving the grand challenge of tissue engineering. *Trends Biotechnol,* S0167-7799(23): 00124–5.

   http://doi.org/10.1016/j.tibtech.2023.04.003

3. Christenson SA, Smith BM, Bafadhel M, *et al.*, 2022, Chronic obstructive pulmonary disease. *Lancet*, 399(10342): 2227–2242.

   http://doi.org/10.1016/S0140-6736(22)00470-6

4. Pugashetti JV, Adegunsoye A, Wu Z, *et al.*, 2023, Validation of proposed criteria for progressive pulmonary fibrosis. *Am J Respir Crit Care Med*, 207(1): 69–76.

   http://doi.org/10.1164/rccm.202201-0124OC

5. Bailey KE, Floren ML, D'Ovidio TJ, *et al.*, 2019, Tissue-informed engineering strategies for modeling human pulmonary diseases. *Am J Physiol Lung Cell Mol Physiol*, 316(2): L303–L320.

   http://doi.org/10.1152/ajplung.00353.2018

6. Heinrich MA, Liu W, Jimenez A, *et al.*, 2019, 3D Bioprinting: From benches to translational applications. *Small*, 15(23): e1805510.

   http://doi.org/10.1002/smll.201805510

7. Daly AC, Prendergast ME, Hughes AJ, *et al.*, 2021, Bioprinting for the biologist. *Cell*, 184(1): 18–32.

   http://doi.org/10.1016/j.cell.2020.12.002

8. Moroni L, Burdick JA, Highley C, *et al.*, 2018, Biofabrication strategies for 3D in vitro models and regenerative medicine. *Nat Rev Mater*, 3(5): 21–37.

   http://doi.org/10.1038/s41578-018-0006-y

9. Fang L, Liu Y, Qiu J, *et al.*, 2022, Bioprinting and its use in tumor-on-a-chip technology for cancer drug screening: A review. *Int J Bioprint*, 8(4): 603.

   http://doi.org/10.18063/ijb.v8i4.603

10. Foresti R, Rossi S, Pinelli S, *et al.*, 2020, In-vivo vascular application via ultra-fast bioprinting for future 5D personalised nanomedicine. *Sci Rep*, 10(1): 3205.

    http://doi.org/10.1038/s41598-020-60196-y

11. Foresti R, Rossi S, Pinelli S, *et al.*, 2020, Highly-defined bioprinting of long-term vascularized scaffolds with Bio-Trap: Complex geometry functionalization and process parameters with computer aided tissue engineering. *Materialia*, 9: 100560.

    http://doi.org/10.1016/j.mtla.2019.100560

12. Yang Q, Xiao Z, Lv X, *et al.*, 2021, Fabrication and biomedical applications of heart-on-a-chip. *Int J Bioprint*, 7(3): 370.

    http://doi.org/10.18063/ijb.v7i3.370

13. Ma X, Liu J, Zhu W, *et al.*, 2018, 3D bioprinting of functional tissue models for personalized drug screening and in vitro disease modeling. *Adv Drug Delivery Rev*, 132: 235–251.

    http://doi.org/10.1016/j.addr.2018.06.011

14. Matai I, Kaur G, Seyedsalehi A, *et al.*, 2020, Progress in 3D bioprinting technology for tissue/organ regenerative engineering. *Biomaterials*, 226: 119536.

    http://doi.org/10.1016/j.biomaterials.2019.119536

15. Liu Y, Yang Q, Zhang H, *et al.*, 2021, Construction of cancer-on-a-chip for drug screening. *Drug Discov Today*, 26(8): 1875–1890.

    http://doi.org/10.1016/j.drudis.2021.03.006

16. Knowlton S, Joshi A, Yenilmez B, *et al.*, 2016, Advancing cancer research using bioprinting for tumor-on-a-chip platforms. *Int J Bioprint*, 2(2): 3–8.

    http://doi.org/10.18063/ijb.2016.02.003

17. Liu F, Liu C, Chen Q, *et al.*, 2018, Progress in organ 3D bioprinting. *Int J Bioprint*, 4(1): 128.

    http://doi.org/10.18063/IJB.v4i1.128

18. Pan T, Song W, Cao X, *et al.*, 2016, 3D bioplotting of gelatin/alginate scaffolds for tissue engineering: Influence of crosslinking degree and pore architecture on physicochemical properties. *J Mater Sci Technol*, 32(9): 889–900.

http://doi.org/https://doi.org/10.1016/j.jmst.2016.01.007

19. Dabaghi M, Carpio MB, Moran-Mirabal JM, *et al.*, 2023, 3D (bio) printing of lungs: Past, present, and future. *Eur Respir J*, 61(1): 2200417.

http://doi.org/10.1183/13993003.00417-2022

20. Shakir S, Hackett TL, Mostaço-Guidolin LB, 2022, Bioengineering lungs: An overview of current methods, requirements, and challenges for constructing scaffolds. *Front Bioeng Biotechnol*, 10: 1011800.

http://doi.org/10.3389/fbioe.2022.1011800

21. Liu S, Yu J-M, Gan Y-C, *et al.*, 2023, Biomimetic natural biomaterials for tissue engineering and regenerative medicine: New biosynthesis methods, recent advances, and emerging applications. *Mil Med Res*, 10(1): 16.

http://doi.org/10.1186/s40779-023-00448-w

22. Yang J, Dang H, Xu Y, 2022, Recent advancement of decellularization extracellular matrix for tissue engineering and biomedical application. *Artif Organs*, 46(4): 549–567.

http://doi.org/10.1111/aor.14126

23. Zhang H, Wang Y, Zheng Z, *et al.*, 2023, Strategies for improving the 3D printability of decellularized extracellular matrix bioink. *Theranostics*, 13(8): 2562.

http://doi.org/10.1039/D2BM01273A

24. Kort-Mascort J, Flores-Torres S, Chavez OP, *et al.*, 2023, Decellularized ECM hydrogels: prior use considerations, applications, and opportunities in tissue engineering and biofabrication. *Biomater Sci*, 11(2): 400–431.

http://doi.org/10.1039/d2bm01273a

25. Bock S, Rades T, Rantanen J, *et al.*, 2022, Additive manufacturing in respiratory sciences-current applications and future prospects. *Adv Drug Delivery Rev*, 186: 114341.

http://doi.org/10.1016/j.addr.2022.114341

26. Cui H, Nowicki M, Fisher JP, *et al.*, 2017, 3D bioprinting for organ regeneration. *Adv Healthc Mater*, 6(1): 1601118.

http://doi.org/10.1002/adhm.201601118

27. Murphy SV, De Coppi P, Atala A, 2020, Opportunities and challenges of translational 3D bioprinting. *Nat Biomed Eng*, 4(4): 370–380.

http://doi.org/10.1038/s41551-019-0471-7

28. Yu C, Schimelman J, Wang P, *et al.*, 2020, Photopolymerizable biomaterials and light-based 3D printing strategies for biomedical applications. *Chem Rev*, 120(19): 10695–10743.

http://doi.org/10.1021/acs.chemrev.9b00810

29. Jammalamadaka U, Tappa K, 2018, Recent advances in biomaterials for 3D printing and tissue engineering. *J Funct Biomater*, 9(1): 22.

http://doi.org/10.3390/jfb9010022

30. Brassard JA, Nikolaev M, Hübscher T, *et al.*, 2021, Recapitulating macro-scale tissue self-organization through organoid bioprinting. *Nat Mater*, 20(1): 22–29.

http://doi.org/10.1038/s41563-020-00803-5

31. Raman R, Bashir R, 2017, Biomimicry, biofabrication, and biohybrid systems: The emergence and evolution of biological design. *Adv Healthcare Mater*, 6(20): 1700496.

http://doi.org/10.1002/adhm.201700496

32. Levato R, Jungst T, Scheuring RG, *et al.*, 2020, From shape to function: The next step in bioprinting. *Adv Mat*, 32(12): e1906423.

http://doi.org/10.1002/adma.201906423

33. Bittner S M, Guo J L, Melchiorri A, *et al.*, 2018, Three-dimensional printing of multilayered tissue engineering scaffolds. *Mater Today*, 21(8): 861–874.

http://doi.org/10.1016/j.mattod.2018.02.006

34. Huo Y, Xu Y, Wu X, *et al.*, 2022, Functional trachea reconstruction using 3D-bioprinted native-like tissue architecture based on designable tissue-specific bioinks. *Adv Sci*, 9(29): 2202181.

http://doi.org/https://doi.org/10.1002/advs.202202181

35. Grigoryan B, Paulsen SJ, Corbett DC, *et al.*, 2019, Multivascular networks and functional intravascular topologies within biocompatible hydrogels. *Science*, 364(6439): 458–464.

http://doi.org/10.1126/science.aav9750

36. Ng WL, Ayi TC, Liu Y-C, *et al.*, 2021, Fabrication and characterization of 3D bioprinted triple-layered human alveolar lung models. *Int J Bioprint*, 7(2): 332.

http://doi.org/10.18063/ijb.v7i2.332

37. Lewis KJR, Tibbitt MW, Zhao Y, *et al.*, 2015, In vitro model alveoli from photodegradable microsphere templates. *Biomater Sci*, 3(6): 821–832.

http://doi.org/10.1039/c5bm00034c

38. Machino R, Matsumoto K, Taniguchi D, *et al.*, 2019, Replacement of rat tracheas by layered, trachea-like, scaffold-free structures of human cells using a Bio-3D printing system. *Adv Healthc Mater*, 8(7): e1800983.

http://doi.org/10.1002/adhm.201800983

39. Taniguchi D, Matsumoto K, Tsuchiya T, *et al.*, 2018, Scaffold-free trachea regeneration by tissue engineering with bio-3D printing. *Interact Cardiovasc Thorac Surg*, 26(5): 745–752.

http://doi.org/10.1093/icvts/ivx444

40. Kim IG, Park SA, Lee S-H, *et al.*, 2020, Transplantation of a 3D-printed tracheal graft combined with iPS cell-derived MSCs and chondrocytes. *Sci Rep*, 10(1): 4326.

http://doi.org/10.1038/s41598-020-61405-4

41. Berg J, Weber Z, Fechler-Bitteti M, *et al.*, 2021, Bioprinted multi-cell type lung model for the study of viral inhibitors. *Viruses*, 13(8): 1590.

http://doi.org/10.3390/v13081590

42. Wanczyk H, Jensen T, Weiss DJ, *et al.*, 2021, Advanced single-cell technologies to guide the development of bioengineered lungs. *Am J Physiol Lung Cell Mol Physiol*, 320(6): L1101–L1117.

http://doi.org/10.1152/ajplung.00089.2021

43. Liu H, Wu M, Jia YB, *et al.*, 2020, Control of fibroblast shape in sequentially formed 3D hybrid hydrogels regulates cellular responses to microenvironmental cues. *NPG Asia Mater*, 12(1): 45.

http://doi.org/10.1038/s41427-020-0226-7

44. Xu F, Wu J, Wang S, *et al.*, 2011, Microengineering methods for cell-based microarrays and high-throughput drug-screening applications. *Biofabrication*, 3(3): 034101.

http://doi.org/10.1088/1758-5082/3/3/034101

45. Wang L, Qiu M, Yang Q, *et al.*, 2015, Fabrication of microscale hydrogels with tailored microstructures based on liquid bridge phenomenon. *ACS Appl Mater Interfaces*, 7(21): 11134–11140.

http://doi.org/10.1021/acsami.5b00081

46. Dong Y, Jin G, Hong Y, *et al.*, 2018, Engineering the cell microenvironment using novel photoresponsive hydrogels. *ACS Appl Mater Interfaces*, 10(15): 12374–12389.

http://doi.org/10.1021/acsami.7b17751

47. Liu H, Li M, Huang G, *et al.*, 2021, Bioinspired microstructure platform for modular cell-laden microgel fabrication. *Macromol Biosci*, 21(9): e2100110.

http://doi.org/10.1002/mabi.202100110

48. Ma Y, Ji Y, Huang G, *et al.*, 2015, Bioprinting 3D cell-laden hydrogel microarray for screening human periodontal ligament stem cell response to extracellular matrix. *Biofabrication*, 7(4): 044105.

http://doi.org/10.1088/1758-5090/7/4/044105

49. Ravanbakhsh H, Karamzadeh V, Bao G, *et al.*, 2021, Emerging technologies in multi-material bioprinting. *Adv Mater*, 33(49): e2104730.

http://doi.org/10.1002/adma.202104730

50. Han YL, Wang W, Hu J, *et al.*, 2013, Benchtop fabrication of three-dimensional reconfigurable microfluidic devices from paper-polymer composite. *Lab Chip*, 13(24): 4745–4749.

http://doi.org/10.1039/c3lc50919b

51. Ferreira LP, Gaspar VM, Mano JF, 2020, Decellularized extracellular matrix for bioengineering physiomimetic 3D in vitro tumor models. *Trends Biotechnol*, 38(12): 1397–1414.

http://doi.org/10.1016/j.tibtech.2020.04.006

52. Huang G, Li F, Zhao X, *et al.*, 2017, Functional and biomimetic materials for engineering of the three-dimensional cell microenvironment. *Chem Rev*, 117(20): 12764–12850.

http://doi.org/10.1021/acs.chemrev.7b00094

53. Hölzl K, Lin S, Tytgat L, *et al.*, 2016, Bioink properties before, during and after 3D bioprinting. *Biofabrication*, 8(3): 032002.

http://doi.org/10.1088/1758-5090/8/3/032002

54. Qing H, Ji Y, Li W, *et al.*, 2020, Microfluidic printing of three-dimensional graphene electroactive microfibrous scaffolds. *ACS Appl Mater Interfaces*, 12(2): 2049–2058.

http://doi.org/10.1021/acsami.9b17948

55. de Hilster RHJ, Sharma PK, Jonker MR, *et al.*, 2020, Human lung extracellular matrix hydrogels resemble the stiffness and viscoelasticity of native lung tissue. *Am J Physiol Lung Cell Mol Physiol*, 318(4): L698–L704.

http://doi.org/10.1152/ajplung.00451.2019

56. Zepp JA, Morrisey EE, 2019, Cellular crosstalk in the development and regeneration of the respiratory system. *Nat Rev Mol Cell Biol*, 20(9): 551–566.

http://doi.org/10.1038/s41580-019-0141-3

57. Knudsen L, Ochs M, 2018, The micromechanics of lung alveoli: Structure and function of surfactant and tissue components. *Histochem Cell Biol*, 150(6): 661–676.

http://doi.org/10.1007/s00418-018-1747-9

58. Bertassoni LE, Cecconi M, Manoharan V, *et al.*, 2014, Hydrogel bioprinted microchannel networks for vascularization of tissue engineering constructs. *Lab Chip*, 14(13): 2202–2211.

http://doi.org/10.1039/c4lc00030g

59. Kang D, Park JA, Kim W, *et al.*, 2021, All-inkjet-printed 3D alveolar barrier model with physiologically relevant microarchitecture. *Adv Sci (Weinh)*, 8(10): 2004990.

http://doi.org/10.1002/advs.202004990

60. Horváth L, Umehara Y, Jud C, *et al.*, 2015, Engineering an in vitro air-blood barrier by 3D bioprinting. *Sci Rep*, 5: 7974.

http://doi.org/10.1038/srep07974

61. Gu Z, Fu J, Lin H, *et al.*, 2020, Development of 3D bioprinting: From printing methods to biomedical applications. *Asian J Pharm Sci*, 15(5): 529–557.

http://doi.org/10.1016/j.ajps.2019.11.003

62. De Santis MM, Alsafadi HN, Tas S, *et al.*, 2021, Extracellular-matrix-reinforced bioinks for 3D bioprinting human tissue. *Adv Mat*, 33(3): e2005476.

http://doi.org/10.1002/adma.202005476

63. Berg J, Hiller T, Kissner MS, *et al.*, 2018, Optimization of cell-laden bioinks for 3D bioprinting and efficient infection with influenza A virus. *Sci Rep*, 8(1): 13877.

http://doi.org/10.1038/s41598-018-31880-x

64. Falcones B, Sanz-Fraile H, Marhuenda E, *et al.*, 2021, Bioprintable lung extracellular matrix hydrogel scaffolds for 3D culture of mesenchymal stromal cells. *Polymers (Basel)*, 13(14): 2350.

http://doi.org/10.3390/polym13142350

65. Zhang YS, Davoudi F, Walch P, *et al.*, 2016, Bioprinted thrombosis-on-a-chip. *Lab Chip*, 16(21): 4097–4105.

http://doi.org/10.1039/c6lc00380j

66. Wang X, Zhang X, Dai X, *et al.*, 2018, Tumor-like lung cancer model based on 3D bioprinting. *Biotech*, 8(12): 501.

http://doi.org/10.1007/s13205-018-1519-1

67. Teixeira AI, McKie GA, Foley JD, *et al.*, 2006, The effect of environmental factors on the response of human corneal epithelial cells to nanoscale substrate topography. *Biomaterials*, 27(21): 3945–3954.

http://doi.org/10.1016/j.biomaterials.2006.01.044

68. Melchor-Martínez EM, Torres Castillo NE, Macias-Garbett R, *et al.*, 2021, Modern world applications for nano-bio materials: Tissue engineering and COVID-19. *Front Bioeng Biotechnol*, 9: 597958.

http://doi.org/10.3389/fbioe.2021.597958

69. Xu F, Inci F, Mullick O, *et al.*, 2012, Release of magnetic nanoparticles from cell-encapsulating biodegradable nanobiomaterials. *ACS Nano*, 6(8): 6640–6649.

http://doi.org/10.1021/nn300902w

70. Jia Y, Wang Y, Niu L, *et al.*, 2021, The plasticity of nanofibrous matrix regulates fibroblast activation in fibrosis. *Adv Healthc Mater*, 10(8): e2001856.

http://doi.org/10.1002/adhm.202001856

71. Liu H, Du C, Liao L, *et al.*, 2022, Approaching intrinsic dynamics of MXenes hybrid hydrogel for 3D printed multimodal intelligent devices with ultrahigh superelasticity and temperature sensitivity. *Nat Commun*, 13(1): 3420.

http://doi.org/10.1038/s41467-022-31051-7

72. Malda J, Visser J, Melchels FP, *et al.*, 2013, 25th anniversary article: Engineering hydrogels for biofabrication. *Adv Mater*, 25(36): 5011–5028.

http://doi.org/10.1002/adma.201302042

73. Hollister SJ, 2005, Porous scaffold design for tissue engineering. *Nat Mater*, 4(7): 518–524.

http://doi.org/10.1038/nmat1421

74. Alarçin E, Guan X, Kashaf SS, *et al.*, 2016, Recreating composition, structure, functionalities of tissues at nanoscale for regenerative medicine. *Regen Med*, 11(8): 849–858.

http://doi.org/10.2217/rme-2016-0120

75. Liu W, Thomopoulos S, Xia Y, 2012, Electrospun nanofibers for regenerative medicine. *Adv Healthc Mater*, 1(1): 10–25.

http://doi.org/10.1002/adhm.201100021

76. Bakht SM, Gomez-Florit M, Lamers T, *et al.*, 2021, 3D bioprinting of miniaturized tissues embedded in self-assembled nanoparticle-based fibrillar platforms. *Adv Funct Mater*, 31(46): 2104245.

http://doi.org/10.1002/adfm.202104245

77. Halappanavar S, Nymark P, Krug HF, *et al.*, 2021, Non-animal strategies for toxicity assessment of nanoscale materials: Role of adverse outcome pathways in the selection of endpoints. *Small*, 17(15): e2007628.

http://doi.org/10.1002/smll.202007628

78. Sisler JD, Pirela SV, Friend S, *et al.*, 2015, Small airway epithelial cells exposure to printer-emitted engineered nanoparticles induces cellular effects on human microvascular endothelial cells in an alveolar-capillary co-culture model. *Nanotoxicology*, 9(6): 769–779.

http://doi.org/10.3109/17435390.2014.976603

79. Skardal A, Zhang J, McCoard L, *et al.*, 2010, Dynamically crosslinked gold nanoparticle - hyaluronan hydrogels. *Adv Mater*, 22(42): 4736–4740.

http://doi.org/10.1002/adma.201001436

80. Huang L, Yuan W, Hong Y, *et al.*, 2021, 3D printed hydrogels with oxidized cellulose nanofibers and silk fibroin for the proliferation of lung epithelial stem cells. *Cellulose (Lond)*, 28(1): 241–257.

http://doi.org/10.1007/s10570-020-03526-7

81. Skardal A, Murphy SV, Devarasetty M, *et al.*, 2017, Multi-tissue interactions in an integrated three-tissue organ-on-a-chip platform. *Sci Rep*, 7(1): 8837.

http://doi.org/10.1038/s41598-017-08879-x

82. Bhattacharyya A, Janarthanan G, Noh I, 2021, Nano-biomaterials for designing functional bioinks towards complex tissue and organ regeneration in 3D bioprinting. *Addit Manuf*, 37: 101639.

http://doi.org/10.1016/j.addma.2020.101639

83. Dong Z, Cui H, Zhang H, *et al.*, 2021, 3D printing of inherently nanoporous polymers via polymerization-induced phase separation. *Nat Commun*, 12(1): 247.

http://doi.org/10.1038/s41467-020-20498-1

84. Pérez RA, Won J-E, Knowles JC, *et al.*, 2013, Naturally and synthetic smart composite biomaterials for tissue regeneration. *Adv Drug Delivery Rev*, 65(4): 471–496.

http://doi.org/10.1016/j.addr.2012.03.009

85. Gao B, Yang Q, Zhao X, *et al.*, 2016, 4D bioprinting for biomedical applications. *Trends Biotechnol*, 34(9): 746–756.

http://doi.org/10.1016/j.tibtech.2016.03.004

86. Choi Y-M, Lee H, Ann M, *et al.*, 2023, 3D bioprinted vascularized lung cancer organoid models with underlying disease capable of more precise drug evaluation. *Biofabrication*, 15(3): 034104.

http://doi.org/10.1088/1758-5090/acd95f

87. Liberti DC, Morrisey EE, 2021, Organoid models: Assessing lung cell fate decisions and disease responses. *Trends Mol Med*, 27(12): 1159–1174.

http://doi.org/10.1016/j.molmed.2021.09.008

88. Valdoz JC, Franks NA, Cribbs CG, *et al.*, 2022, Soluble ECM promotes organotypic formation in lung alveolar model. *Biomaterials*, 283: 121464.

http://doi.org/10.1016/j.biomaterials.2022.121464

89. Kim S, Uroz M, Bays JL, *et al.*, 2021, Harnessing mechanobiology for tissue engineering. *Dev Cell*, 56(2): 180–191.

http://doi.org/10.1016/j.devcel.2020.12.017

90. Tan Q, Choi KM, Sicard D, *et al.*, 2017, Human airway organoid engineering as a step toward lung regeneration and disease modeling. *Biomaterials*, 113: 118–132.

http://doi.org/10.1016/j.biomaterials.2016.10.046

91. Ji Y, Yang Q, Huang G, *et al.*, 2019, Improved resolution and fidelity of droplet-based bioprinting by upward ejection. *ACS Biomater Sci Eng*, 5(8): 4112–4121.

http://doi.org/10.1021/acsbiomaterials.9b00400

92. Li M, Yang Q, Liu H, *et al.*, 2016, Capillary origami inspired fabrication of complex 3D hydrogel constructs. *Small*, 12(33): 4492–4500.

http://doi.org/10.1002/smll.201601147

93. Yang Q, Gao B, Xu F, 2020, Recent advances in 4D bioprinting. *Biotechnol J*, 15(1): e1900086.

http://doi.org/10.1002/biot.201900086

94. Yang Y, Jia Y, Yang Q, *et al.*, 2023, Engineering bio-inks for 3D bioprinting cell mechanical microenvironment. *Int J Bioprint*, 9(1): 632.

http://doi.org/10.18063/ijb.v9i1.632

95. Huang G, Wang L, Wang S, *et al.*, 2012, Engineering three-dimensional cell mechanical microenvironment with hydrogels. *Biofabrication*, 4(4): 042001.

http://doi.org/10.1088/1758-5082/4/4/042001

96. Huh D, Matthews BD, Mammoto A, *et al.*, 2010, Reconstituting organ-level lung functions on a chip. *Science*, 328(5986): 1662–1668.

http://doi.org/10.1126/science.1188302

97. Doryab A, Tas S, Taskin MB, *et al.*, 2019, Evolution of bioengineered lung models: recent advances and challenges in tissue mimicry for studying the role of mechanical forces in cell biology. *Adv Funct Mater*, 29(39): 1903114.

http://doi.org/10.1002/adfm.201903114

98. Wang J, Zhang Y, Aghda NH, *et al.*, 2021, Emerging 3D printing technologies for drug delivery devices: Current status and future perspective. *Adv Drug Delivery Rev*, 174: 294–316.

http://doi.org/10.1016/j.addr.2021.04.019

ACCSCIENCE PUBLISHING

International Journal of Bioprinting

RESEARCH ARTICLE

Evaluation of a synthetic peptide-based bioink (PeptiInk Alpha 1) for *in vitro* 3D bioprinting of cartilage tissue models

Patricia Santos-Beato[1], Andrew A. Pitsillides[2], Alberto Saiani[3], Aline Miller[4], Ryo Torii[5], and Deepak M. Kalaskar[6]*

[1]Biochemical Engineering Department, University College London, London, United Kingdom

[2]Comparative Biomedical Sciences, Royal Veterinary College, London, United Kingdom

[3]Division of Pharmacy & Optometry & Manchester Institute of Biotechnology, The University of Manchester, Manchester, United Kingdom

[4]Department of Chemical Engineering & Manchester Institute of Biotechnology, The University of Manchester, Manchester, United Kingdom

[5]Department of Mechanical Engineering, University College London, London, United Kingdom

[6]Institute of Orthopaedics and Musculoskeletal Science, Division of Surgery & Interventional Science, University College London (UCL), London, United Kingdom

(This article belongs to the *Special Issue: Advances in bioprinting technology*)

Abstract

Cartilage pathology in human disease is poorly understood and requires further research. Various attempts have been made to study cartilage pathologies using *in vitro* human cartilage models as an alternative for preclinical research. Three-dimensional (3D) bioprinting is a technique that has been used to 3D-bioprint cartilage tissue models *in vitro* using animal-derived materials such as gelatine or hyaluronan, which present challenges in terms of scalability, reproducibility, and ethical concerns. We present an assessment of synthetic self-assembling peptides as bioinks for bioprinted human *in vitro* cartilage models. Primary human chondrocytes were mixed with PeptiInk Alpha 1, 3D-bioprinted and cultured for 14 days, and compared with 3D chondrocyte pellet controls. Cell viability was assessed through LIVE/DEAD assays and DNA quantification. High cell viability was observed in the PeptiInk culture, while a fast decrease in DNA levels was observed in the 3D pellet control. Histological evaluation using hematoxylin and eosin staining and immunofluorescence labeling for SOX-9, collagen type II, and aggrecan showed a homogeneous cell distribution in the 3D-bioprinted PeptiInks as well as high expression of chondrogenic markers in both control and PeptiInk cultures. mRNA expression levels assessed by - qRT-PCR (quantitative real time-polymerase chain reaction) confirmed chondrogenic cell behavior. These data showed promise in the potential use of PeptiInk Alpha 1 as a bioprintable manufacturing material for human cartilage *in vitro* models.

Keywords: 3D bioprinting; Self-assembling peptides; Bioinks; Cartilage; *In vitro*

***Corresponding author:**
Deepak M. Kalaskar
(d.kalaskar@ucl.ac.uk)

Citation: Santos-Beato P, Pitsillides AA, Saiani A, *et al*., 2023, Evaluation of a synthetic peptide-based bioink (PeptiInk Alpha 1) for in vitro 3D bioprinting of cartilage tissue models. *Int J Bioprint*, 9(6): 0899.
https://doi.org/10.36922/ijb.0899

Received: May 4, 2023
Accepted: June 27, 2023
Published Online: September 6, 2023

Copyright: © 2023 Author(s). This is an Open Access article distributed under the terms of the Creative Commons Attribution License, permitting distribution, and reproduction in any medium, provided the original work is properly cited.

Publisher's Note: AccScience Publishing remains neutral with regard to jurisdictional claims in published maps and institutional affiliations.

1. Introduction

The treatment of cartilage pathologies remains a challenge in the field of orthopedic medicine. Diseases such as osteoarthritis, rheumatoid arthritis, or post-traumatic

cartilage injuries still have no cure or 100% effective treatment. These diseases are extremely prevalent, with rheumatoid arthritis and osteoarthritis affecting 0.5%–1% of the world population[1] and 36.8% of the U.S. adult population, respectively[2]. Due to the lack of nerve signaling and vasculature in cartilage, the latter is difficult to diagnose at initial stages and has a limited endogenous repair potential. Additionally, cartilage has an extraordinarily complex structure, presenting up to four distinct articular cartilage zones[3], making it extremely difficult to replicate *in vitro*.

The superficial zone comprises collagen fibers aligned parallel to the surface and chondrocytes with an elongated shape. Beneath this is a middle zone where collagen fibers are randomized, and chondrocytes present their characteristic rounded shape. Further down, the deep zone contains collagen fibers that are perpendicular to the tide mark and rounded chondrocytes positioned in columns in the same perpendicular orientation. The deepest calcified cartilage zone contacts with bone and contains hypertrophic chondrocytes[3]. In addition to this complicated structure, the lack of vasculature forces nutrients to be distributed through diffusion[4], making tissue healing not only challenging but also a slow process. Due to these difficulties in natural regeneration, multiple studies have focused on recreating cartilage *in vitro* to use it as implants *in vivo*[5,6] or to study potential tissue regeneration methods[7,8].

Current tissue engineering techniques have been used in attempt to develop *in vitro* cartilage constructs using natural or synthetic polymer-based scaffolds that are then populated using two-dimensional (2D) cell seeding approaches. Depending on the porosity of the material, cells exhibit different colonization rates and viabilities. However, this approach has a lack of control over three-dimensional (3D) cell colonization and a lack of structural control over the scaffold itself. 3D bioprinting, a technique that enables layer-by-layer manufacture, has been used to overcome these limitations[9]. 3D bioprinting allows for multi-structural and controlled manufacturing as well as homogeneous deposition of encapsulated cells within the bioprinted structure[10]. Intricate 3D CAD (computer-aided design) designs can be made to recreate the different cartilage layers and better mimic the characteristics of this tissue. Multiple 3D printing techniques are currently used, such as extrusion-based, jetting-based, and vat photopolymerization-based. Extrusion-based technique combines a fluid-dispensing system and a robotic control system[11]. It presents advantages such as a great deposition and printing speed, affordability and a wide range of potential printing materials[11]. However, its resolution is limited, and most materials printed require to be shear-thinning[11]. Jetting-based 3D bioprinting enables contactless patterning and deposition of cell-laden biomaterials[12]. Although it is a manufacturing technique that highly facilitates cell–cell and cell–matrix interactions, it presents a limited choice of printable bioinks[12]. Vat photopolymerization-based bioprinting relies on a scanning laser that cures the photocurable bioresin in a predefined pattern[13]. This technique has a high fabrication accuracy; however, it relies on photoinitiators, which can be toxic when mixed with cells[13].

A recent systematic review[9] concluded that of the three most common cartilage 3D bioprinting techniques (extrusion-based, jetting-based, and vat photopolymerization-based), extrusion-based 3D bioprinting was the most popular[14]. According to most papers, animal-based gelatine methacrylate (GelMA)[15-23], hyaluronic acid-based[17,22,24], or chondroitin sulfate-based materials[15,24] were used. Although alginate is also one of the most commonly used materials in bioprinting, its poor cell attachment properties require that it be mixed with other GelMA, hyaluronic acid-based, and chondroitin sulfate-based materials to enhance these properties. Even though these mixed materials are widely used, they present multiple disadvantages such as low reproducibility, scalability, and low mechanical property[25,26]. Furthermore, there is a need to move toward a more sustainable and ethical approach in science, encouraged by the EU Directive 2010/63 and the Guidance Document on Good *In Vitro* Method Practices[27], hence prompting the exploration of non-animal-derived synthetic materials as a viable alternative.

Synthetic polymers can be modified to improve their mechanical and physical properties as well as to control their degradation time; these advantages also result in better reproducibility and less batch-to-batch variation. Prior studies have demonstrated the potential of synthetic self-assembling peptide hydrogels for use in cartilage studies[28-30]. Such transparent peptide materials are shear thinning and do not require crosslinking, making them perfect off-the-shelf materials for easy and accessible bioprinting. Due to their synthetic nature, there is a minimal batch-to-batch variation, which ensures reproducibility in printed structures, making them an exceptional alternative to natural materials. Preliminary studies have also shown the potential application of these self-assembling peptides in 3D bioprinting[31]. Due to the differences between hydrogel performances (synthetic or natural), it is not currently possible to define a hydrogel-based "gold standard" system for cartilage manufacturing *in vitro*. Therefore, when assessing the performance of a hydrogel for cartilage *in vitro* manufacturing, comparing it to the native tissue is preferred. Alternatively, *in vitro*

chondrocyte-based cartilage models, such as the chondrocyte 3D pellet model[32,33], can be used when native tissue explants are not available. Here, we explored peptide hydrogel bioinks, PeptiInks®, in terms of their application in 3D bioprinting using human primary chondrocytes for cartilage tissue modeling *in vitro*. We compared its performance to a control 3D chondrocyte-based pellet developed *in vitro* using previously optimized manufacturing protocol[34].

In this study, we assessed the potential of PeptiInk Alpha 1 (Manchester BIOGEL, Alderley Park, UK) as a material for 3D-bioprinting human cartilage tissue *in vitro* models. Primary human chondrocytes were encapsulated into PeptiInk Alpha 1, a neutrally charged peptide hydrogel, and 3D-bioprinted structures were manufactured. Cell viability, cell proliferation, and specific cartilage marker production were assessed and compared to the current gold standard, chondrocyte cell pellets.

2. Materials and methods

2.1. Hydrogel rheological characterization

Synthetic self-assembling peptide hydrogel Alpha 1 was obtained from Manchester BIOGEL (Alderley Park, UK). Alpha 1 was chosen due to its neutral charge, which has previously been shown to promote the chondrogenic behavior of bovine chondrocytes in 3D *in vitro* cultures[28-30] and has a compressive modulus (E = 31 kPa[29]) in line with previously used hydrogels for cartilage tissue engineering[16,24] .

Oscillatory shear rheometry was performed using a Kinexus pro+ rheometer (Netzsh, Germany) with parallel sandblast plate geometry (40 mm, 0.5 mm gap size), equilibrated to room temperature (25°C), and a solvent trap to prevent the hydrogel from drying. Alpha 1 alone and Alpha 1 mixed with cell culture media in a 1:10 ratio were tested in triplicate to ensure reproducibility. For all mixtures, rotational shear-viscosity measurements were performed. Flow sweeps at 1% strain with a shear rate ranging from 150 to 1 Hz were performed to assess the viscosity behavior under shear stress.

2.2. Printability tests

Alpha 1 was loaded into a printer cartridge and printed, using the BIOX6 bioprinter (CELLINK, Sweden), with multiple gauge (G) conical nozzles: 22G (400 μm—extrusion diameter), 25G (250 μm—extrusion diameter), and 27G (200 μm—extrusion diameter). 25G conical nozzle was chosen as it gave a compromise between structural accuracy and shear stress production. Different pressures and printing speeds were combined to assess the filament continuity and width of Alpha 1 printed with a 25G conical nozzle. Images of the printed structures were taken with an EVOS microscope to quantify the filament width using Fiji ImageJ software (1.53t version). Six images were taken at different locations within the printed structure. In each image, the filament width was quantified three times using ImageJ and compared to the theoretical filament resolution.

2.3. Cell culture

Human primary chondrocytes (HCHs; CellApplications, San Diego, CA) were used in this study. HCHs between passages 5 and 7 were consistently used. HCHs were cultured in chondrogenic growth media (Cell Applications, San Diego, CA), and they were incubated at 37°C in a humidified atmosphere with 5% pCO_2. The media was changed every 2 to 3 days.

2.4. Hydrogel cell encapsulation

HCHs were manually mixed into Alpha 1 at a concentration of 1×10^6 cells/mL using a ratio of 1 mL of PeptiInk to 100 μL of cell culture media (1:10). Cell-laden PeptiInks were loaded into 3-mL printing cartridges (Nordson, USA) using a positive displacement pipette (Gilson Scientific, Dunstable, UK). Loaded cartridges were centrifuged to remove air microbubbles for 2 min at 3500 rpm and immediately printed into 12-well culture plates.

2.5. 3D bioprinting of HCH cell-laden Alpha 1

The 3D-bioprinting process was performed using the commercial printer BIOX6 (CELLINK, Sweden). Cylindrical structures with an outer diameter of 5 mm and a thickness of 1 mm with 60% infill density were bioprinted using a 25G conical nozzle, an extrusion pressure between 8 and 10 kPa, and a printing speed of 5 mm/s. The printed structures were submerged in chondrogenic medium, which was changed three times during the first hour to ensure pH equilibrium and twice each week over the culture period. Cell constructs were cultured for up to 14 days at 37°C in a humidified atmosphere with 5% pCO_2.

2.6. Cell pellet formation and culture

3D control cell pellet cultures were formed using the methods of Yeung *et al.*[34] Briefly, 4×10^5 cells were centrifuged in 500 μL of culture media at 1750 rpm for 5 min in 15 mL tubes. After 72 h, the pellets were gently aspirated into ultra-low adhesion 24-well plates (ScienceCell, 0383), with one pellet per well cultured in 1 mL of chondrogenic medium. Culture media were changed every 2 to 3 days. The cell pellets were cultured for up to 14 days at 37°C in a humidified atmosphere with 5% pCO_2.

2.7. Cell viability

Cell viability was assessed using a LIVE/DEAD assay. Bioprinted constructs were assessed 2 h post-printing (day 0), on day 7 and day 14. Samples were cut in half to enable the

visualization of cell viability in the center of the constructs. Samples were washed twice with phosphate-buffered saline (PBS; Gibco, 20012-019) and then incubated at 37°C for 30 min in LIVE/DEAD cytotoxicity assay (Invitrogen, L3224) using a concentration of 5 µL of calcein-AM and 20 µL of ethidium homodimer per 10 mL of PBS (Gibco, 20012-019). After incubation, constructs were rinsed twice using PBS (Gibco, 20012-019) and imaged using an Olympus DP80 microscope. Multiple z-stacks were taken at magnifications of 10× and 20× using FITC (488 nm) and TRITC (532 nm) filters. Semi-quantitative evaluation of cell viability was performed using Fiji Image-J software (1.53t version). In summary, red and green image channels were separated, and three random regions of interest were selected to perform manual cell counting. Average cell survival percentages for each time point were calculated and compared to 3D controls; dead and live cells were counted at each specific time point and not used for comparison between time points due to the cell viability not being cumulative.

2.8. DNA quantification

DNA quantification was assessed using a Quant-iT PicoGreen dsDNA Assay Kit (Thermo Fisher, P7589). Bioprinted constructs and 3D cell pellets were mixed with pre-warmed (37°C) protease solution (10 mg/mL) (Sigma Aldrich, P5147-1G) and pipetted up and down until the PeptiInk or cell matrix was dissolved. This mixture was then incubated at 37°C for 5 min. Sequentially, these samples were mixed with 500 µL of 2× TE Buffer from the Quant-iT PicoGreen dsDNA Assay Kit (Thermo Fisher, P7589), and 1% Triton X in UltraPure™ DNase/RNase-Free Distilled Water (Thermo Fisher, 10977-035). Mixtures were incubated at 37°C for 30 min and then placed at -20°C. Samples were subjected to three freeze-thaw cycles before the assay was performed. PicoGreen dye was diluted (1:200) in 2× TE buffer. A total of 100 µL from each sample was pipetted in a black/opaque 96-well plate. An additional 100 µL of the PicoGreen dye solution was then added and left for 5 min under constant mixing at room temperature. Fluorescence was immediately measured using a plate reader at excitation and emission wavelengths of 480 nm and 520 nm, respectively, for DNA concentration calculation. Change in DNA concentration was calculated against concentration at day 0 (100%).

2.9. Histological processing and cryosectioning

3D cell pellets and bioprinted constructs were washed with PBS (Gibco, 20012-019) for 5 min at different time points (days 0, 7, and 14) and then fixed overnight at 4°C in a 10% neutral buffered formalin solution (Sigma Aldrich, HT501128). After fixation, samples were washed for 5 min in PBS and then left for 3 h in 30% sucrose (Sigma Life Sciences, S9378) solution in PBS (Gibco, 20012-019) to dehydrate. They were then submerged in a 50:50 ratio mixture of 30% sucrose solution and OCT mounting media (VWR chemicals, 361603E) overnight at 4°C. Samples were then placed in cryomolds filled with OCT (VWR chemicals, 361603E), snap-frozen in liquid nitrogen, and cryosectioned at 8 µm using a ThermoScientific cryotome FSE for further immunohistochemistry processing.

2.10. Hematoxylin and eosin staining

Routine hematoxylin and eosin (H&E) staining of bioprinted constructs and 3D cell pellets sections were conducted at time points: days 0, 7, and 14 on the cryosections. Excess OCT was removed by submerging the slides in 70% ethanol. Hematoxylin staining was performed for 10 min, and subsequently, Scott's water was used to ensure nuclei bluing. Eosin staining was done for 15 s, followed by washing in 70% ethanol.

2.11. Immunofluorescence labeling

Cryopreserved sample sections were rehydrated for 10 min with PBTD (PBS + 1.1% DMSO + 0.1% Tween 20) and subsequently fixed for 10 min using 10% neutral-buffered formalin (Sigma Aldrich, HT501128). Sections were then blocked for 1 h at room temperature using PBTD and 5% bovine serum albumin (BSA; Sigma Aldrich, A2153).

Primary antibody incubation was performed overnight at 4°C, and the slides were kept in a humidity chamber. Collagen type II primary antibody (Invitrogen, PA1-36059) was diluted at a ratio of 1:50; aggrecan primary antibody (Abcam, ab3778) was diluted at a ratio of 1:100; SOX-9 primary antibody (Abcam, ab185966) was diluted at a ratio of 1:100 in PBTD and 5% BSA solution. All sections were washed in PBS for 5 min after primary antibody labeling was performed.

Secondary antibody incubation was performed at room temperature. For collagen type II labeling, secondary antibody AlexaFluor-488 goat anti-rabbit (Invitrogen, A11008) was incubated for 1 h at a ratio of 1:200 combined with phalloidin (Invitrogen, A12381) at a ratio of 1:200 in PBS. Aggrecan labeling was performed with the AlexaFluor 594 goat anti-mouse secondary antibody (Abcam, ab150116) diluted at a ratio of 1:200 for 3 h in PBS. SOX-9 labeling was performed with AlexaFluor 555 goat anti-rabbit (Invitrogen, A21428) incubated for 1 h at a ratio of 1:200 in PBS. All sections were then washed for 5 min in PBS, and nuclei staining was performed by incubating the sections for 3 min at room temperature with DAPI (Thermo Fisher, 62248) diluted at a ratio of 1:200 in PBS. Further section rinsing was done for 5 min in PBS, before section mounting with fluoroshield (Sigma Aldrich, F6182).

Table 1. Primer sequences used in the comparative PCR

Gene	Forward sequence 5'-3'	Reverse sequence 5'-3'
GADPH	GGAGCGAGATCCCTCCAAAAT	GGCTGTTGTCATACTTCTCATGG
COL2	GGATGGCTGCACGAAACATACCGG	CAAGAAGCAGACCGGCCCTATG
AGC	AACCACCTCTGCATTCCACG	CCTCTGTCTCCTTGCAGGTC
SOX9	GGCGGAGGAAGTCGGTGAAGAA	GCTCATGCCGGAGGAGGAGTGT

2.12. RNA extraction and polymerase chain reaction

RNA extraction of the hydrogel cultures was performed by washing the hydrogels three times with PBS and digesting the hydrogel for 5 min at 37°C using a protease solution (10 mg/mL in distilled DNAse-free, RNAse-free water). To initiate RNA extraction, the digested mixture was mixed with the RNeasy lysis buffer from the QIAGEN RNeasy Mini kit (74104, QIAGEN) by centrifugation at 10,000 rpm for 3 min. The following steps were performed as specified by the RNA extraction kit's manufacturer. RNA extraction of the 3D cell pellets was performed as specified by the RNA extraction kit's manufacturer (QIAGEN). mRNA levels were quantified using a Nanodrop spectrophotometer. cDNA was obtained using the High-Capacity RNA-to-cDNA Kit (ThermoFisher, 4387406) according to instructions specified by the manufacturer.

Gene expression levels of collagen type II (*COL2*), aggrecan (*AGC*), and SOX-9 (*SOX9*) were analyzed by comparative polymerase chain reaction (PCR) using *GADPH* as a housekeeping gene. Primer sequences are reported in Table 1. The comparative cycle threshold (CT) method, using the expression levels at day 7 and day 14 of the 3D cell pellet as the reference respectively for the $2^{-\Delta\Delta Ct}$ calculation, was used to calculate the gene expression fold of change.

2.13. Statistical analysis

GraphPad Prism 9 was used for the graphical representation of data and statistical analysis. All graphs show error bars, which represent standard deviation. For DNA quantification and percentage DNA change, two-way analysis of variance (ANOVA) was performed. For PCR analysis, multiple unpaired *t* tests with Mann–Whitney test were performed. Statistical significance was calculated with a confidence interval of $p < 0.05$.

3. Results

3.1. Characterization of the inks and bioprinting optimization

The PeptiInk Alpha 1 bioink was characterized rheologically by measuring changes in viscosity as a function of shear stress. As this bioink requires to be mixed with cell culture media for 3D-bioprinting cell-laden structures, both pure Alpha 1 and Alpha 1 mixed with culture medium (1:10 medium-to-gel ratio) were characterized. Viscosity for both decreased with increases in shear stress (Figure 1A), confirming the expected shear thinning behavior. Comparison revealed that when mixed with cell culture medium, the viscosity is lower than the Alpha 1 alone at low shear stress and higher at frequencies above 10 Hz. This was expected as previous work[35] has demonstrated the increase in compressive modulus when self-assembling peptides were mixed with culture media.

Further visual characterization was performed by assessing changes in the deposited filament with respect to the conical nozzle size used. 22G, 25G, and 27G nozzles were used to 3D-print a 30 × 30 mm grid (Figure 1B). Continuous filament deposition was observed when using all conical nozzle sizes. Filament width was quantified, and the expected decrease in filament width with respect to decreasing nozzle size was observed (Figure 1C). The 25G conical nozzle was chosen and used in an attempt to find a compromise between the filament deposition resolution and the shear stress generated. Smaller nozzle sizes have been proven to result in higher levels of cell death due to shear stress[36]. The filament width with respect to extrusion pressure and printing speed was further investigated in 25G nozzles. As seen in Figure 1D, a range of pressures from 6 to 12 kPa were selected to print a simple shape at a constant printing speed of 10 mm/s using a 25G conical nozzle. At low 6 kPa pressures, the ink presented a discontinuous filament deposition behavior, whereas at higher 12 kPa pressures, an excess of bioink deposition was observed, engendering adjacent filament fusion. An intermediate range of pressures (8–10 kPa) was chosen as the working extrusion pressure range as the deposited filaments were continuous and there was no filament fusion observed.

Additional characterization involved quantification of filament width of the structures printed at different printing speeds. The printing was performed with a 25G conical nozzle and the pressure range previously selected. Using Fiji ImageJ software (1.53t version), the filament width was quantified and plotted. The images obtained of the filaments can be found in **Figure S1** (Supplementary File). As seen in Figure 1E, the expected decrease in filament width with increasing printing speed was observed at the

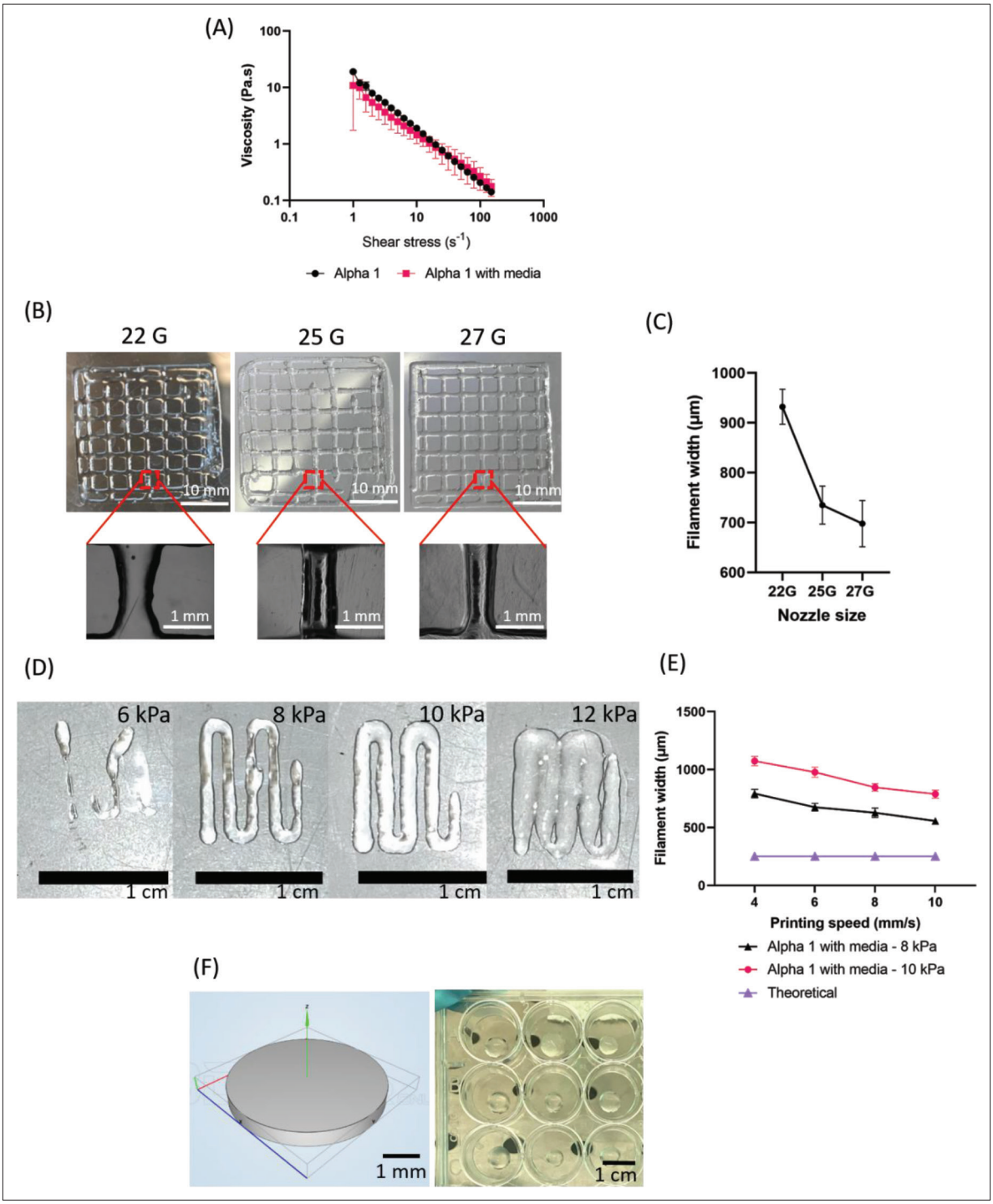

Figure 1. Optimization of 3D printing process for Alpha 1. (A) Dynamic viscosity vs. shear stress for Alpha 1, with and without medium (1:10). $N = 3$; error bars show standard deviation. (B) Initial typical images of 3D-printed grid structure (30 × 30 mm) produced by different conical nozzle sizes (400 µm—22G, 250 µm—25G, and 200 µm—27G). (C) Quantification of the printed filament width of Alpha 1 using different nozzle sizes. $N = 3$; error bars show standard deviation. (D) Typical images of printed Alpha 1 filaments at different extrusion pressures at constant printing speed of 10 mm/s using a 25G conical nozzle. (E) Correlation of printing speed with filament width at extrusion pressures of 8 and 10 kPa. (F) CAD design of printed cylindrical structures (5 mm diameter, 1 mm thickness with 60% infill density) and images of printed structures in a 12-well plate.

two selected pressures. Comparison to theoretical filament width, which corresponds to an internal nozzle diameter (250 μm, 25G), was also performed. This showed a high shape fidelity and printing consistency, with a low standard deviation and high reproducibility (Figure 1E). Although higher printing speeds approached the theoretical filament width when printed at 8 kPa, a more conservative printing speed was chosen to develop the targeted structures to avoid printing inconsistencies. A pressure range of 8–10 kPa and a printing speed of 5 mm/s were selected when printing with the 25G conical nozzle. A compact cylindrical shape structure was chosen to 3D-bioprint the *in vitro* cartilage tissue models (Figure 1F). These models had a 5 mm diameter, 1 mm thickness, and 60% infill density.

3.2. Establishing cellular viability post-printing in short- and long-term culture

Viability of cells in constructs was assessed post-printing with calcein-AM (alive) and ethidium homodimer (dead). Post-printing cell viability and material cytocompatibility were studied to evaluate the effect of the extrusion process on cell viability. For this, human primary chondrocytes were encapsulated in the PeptiInk and bioprinted. Cell viability was assessed 2 h after extrusion and on days 7 and 14 of culture, using cell pellet cultures as the control. Pellet cultures showed 100% viability at day 0, 2 h after centrifugation, which was significantly decreased ($p < 0.0001$) to 46% at day 7 (Figure 2A) with a high number of dead cells in the pellet core, and similar viability (54%) was found at day 14. The cell death observed in the 3D pellet culture was expected as it has been previously reported that hypoxic conditions lead to a necrotic core[37]. In contrast, cells in Alpha 1 PeptiInk showed a 30% viability post-printing, with significant increases to 59% by day 7 and remaining stable (59%) thereafter until day 14. Cell number changes assessed by DNA quantification showed that the 3D pellet control exhibited a high starting DNA quantity (58.5 ng/mL), which significantly decreased over the 14 days (by 75%, Figure 2B). Behavior of cells in Alpha 1 differed, with significant decreases in DNA content (40%) over the first 7 days but only a further 10%, non-significant decrease by day 14, confirming that DNA levels were maintained during the second week of culture in Alpha 1, which corresponds to the cell viability previously reported[29,31,35].

3.3. Extracellular matrix formation, cell morphology, and cell distribution analysis

H&E staining used to assess extracellular matrix (ECM) production, cell morphology, and distribution shows homogeneous cell distribution and circular cell shape across the bioprinted Alpha 1 hydrogel constructs on day 0. Cell distribution homogeneity demonstrated efficiency in the bioprinting process. We observed that the cells adopted a typical chondrogenic rounded morphology. Migration of the cells toward the surface of the Alpha 1 hydrogel was observed over the culture time, with cells forming clusters, which became even more prominent by day 14 (Figure 3). In these cell clusters, a change in the cell morphology from rounded to more spread out can be seen. A higher eosin staining intensity was observed within these clusters, showing a higher level of ECM secretion. Single cells that are distributed across the gel and not in the cell pellets retained their rounded morphology and had low levels of ECM around them. The 3D pellet showed a circular cell morphology and had high levels of eosin staining in the inter-cellular spaces as seen in Figure 3, indicating the presence of ECM. Across the two time points observed, there was a decrease in number of nuclei observed at the center of the pellet, suggesting some level of cell death at the core of the cell cluster, and further confirming the previously reported behavior in 3D pellets[37].

3.4. Cartilage-specific protein marker analysis

Chondrocyte differentiation was assessed by immunofluorescence for specific markers. Labeling for the early chondrogenic marker, SOX-9, was performed to investigate whether primary cells adopted a chondrogenic phenotype. It revealed positive labeling in cell nuclei in both the 3D pellet and the Alpha 1 systems on days 7 and 14. The intensity of the SOX-9 labeling was increased on day 14 in Alpha 1 in comparison to day 7. In contrast, the intensity decreased in the cell pellet culture (Figure 4). An increase of SOX-9 over 14 days of culture was expected, and it has been previously reported that the SOX-9 expression increased in chondrocytes in the first 7 days of 3D culture post 2D expansion[38]. Here, we assessed the expression beyond the 7 days to explore if the increase of expression was maintained at later time points; this increase in SOX-9 expression and maintenance in the PeptiInk culture is important to discriminate between dedifferentiation of embedded chondrocytes and potential osteoblast redifferentiation processes[39]. Decreases in SOX-9 expression in the 3D pellet culture show that chondrogenic behavior observed *in vivo*[39] is not evident. Negative controls can be found in **Figure S2** (Supplementary File).

Later chondrogenic markers, collagen type II and aggrecan, were also assessed by immunochemistry. The 3D pellet control showed an increase in collagen type II expression from day 7 to day 14, appearing firstly at the surface of the pellet and then expanding all around the

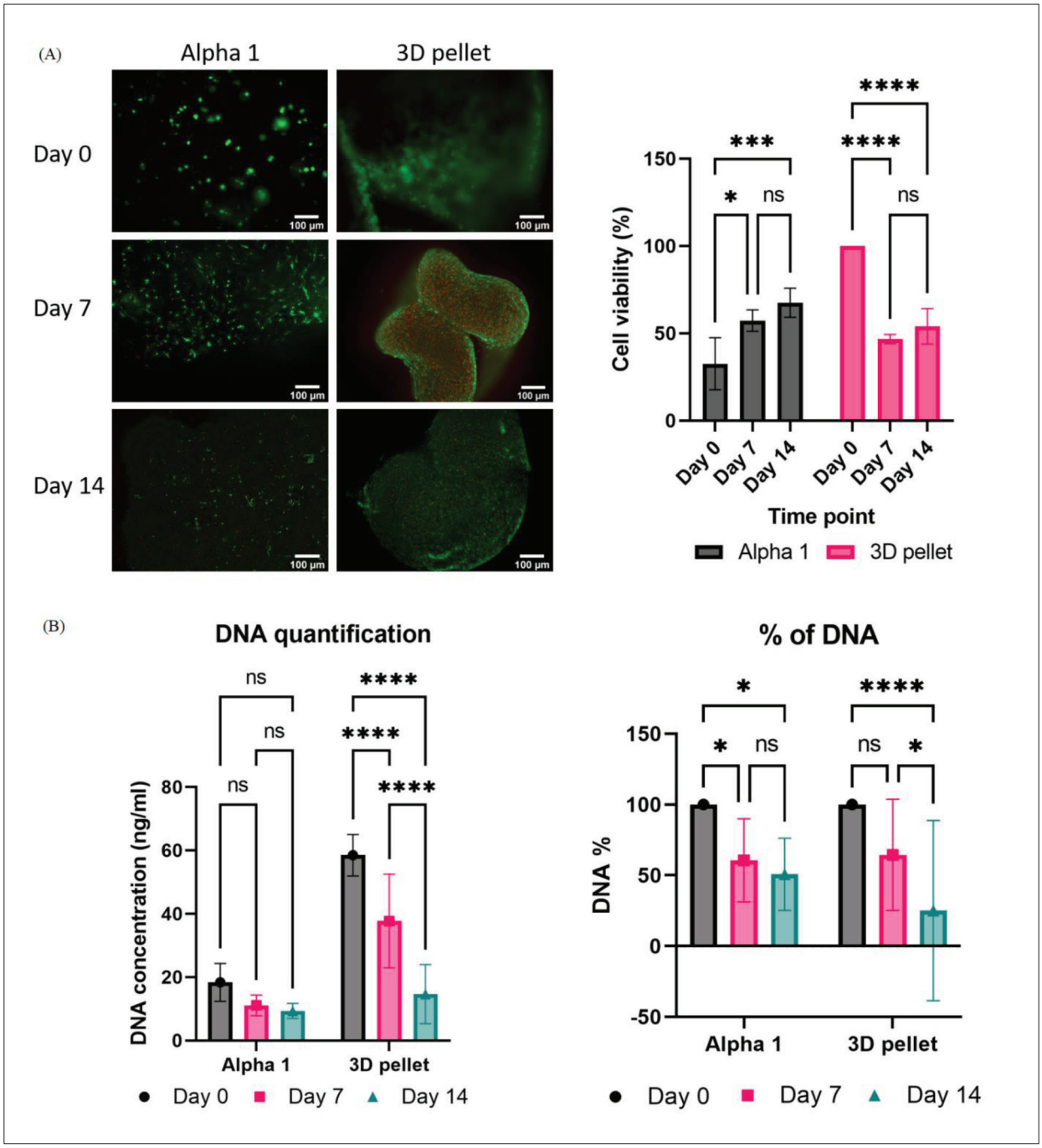

Figure 2. (A) Left: Representative LIVE/DEAD staining images obtained for 3D pellet and the PeptiInk Alpha 1 culture system at days 0 (post-printing), 7, and 14. Right: Semi-quantification of cellular viability based on cell counting of LIVE/DEAD images. (B). Left: Extracted DNA quantification obtained for 3D pellet and the PeptiInk Alpha 1 culture systems over 14 days. Right: Percentage change of DNA with respect to day 0. $N = 9$; error bars show standard deviation. Notes: ns, not significant; *$p < 0.05$; ***$p < 0.001$; **** $p < 0.0001$.

pellet matrix (Figure 5), which differed from previously reported investigations where collagen type II appeared in the center and spread out on day 7[40]. However, day 14 observations appeared to have a similar level of collagen type II expression reported in previous literature[40]. Alpha 1 showed intracellular expression of collagen type II, which increased and appeared more prominently in the surface cell clusters (Figure 5). Aggrecan expression in the 3D pellets seemed to be constant over time, showing high levels of expression both at the surface and the matrix of the pellet.

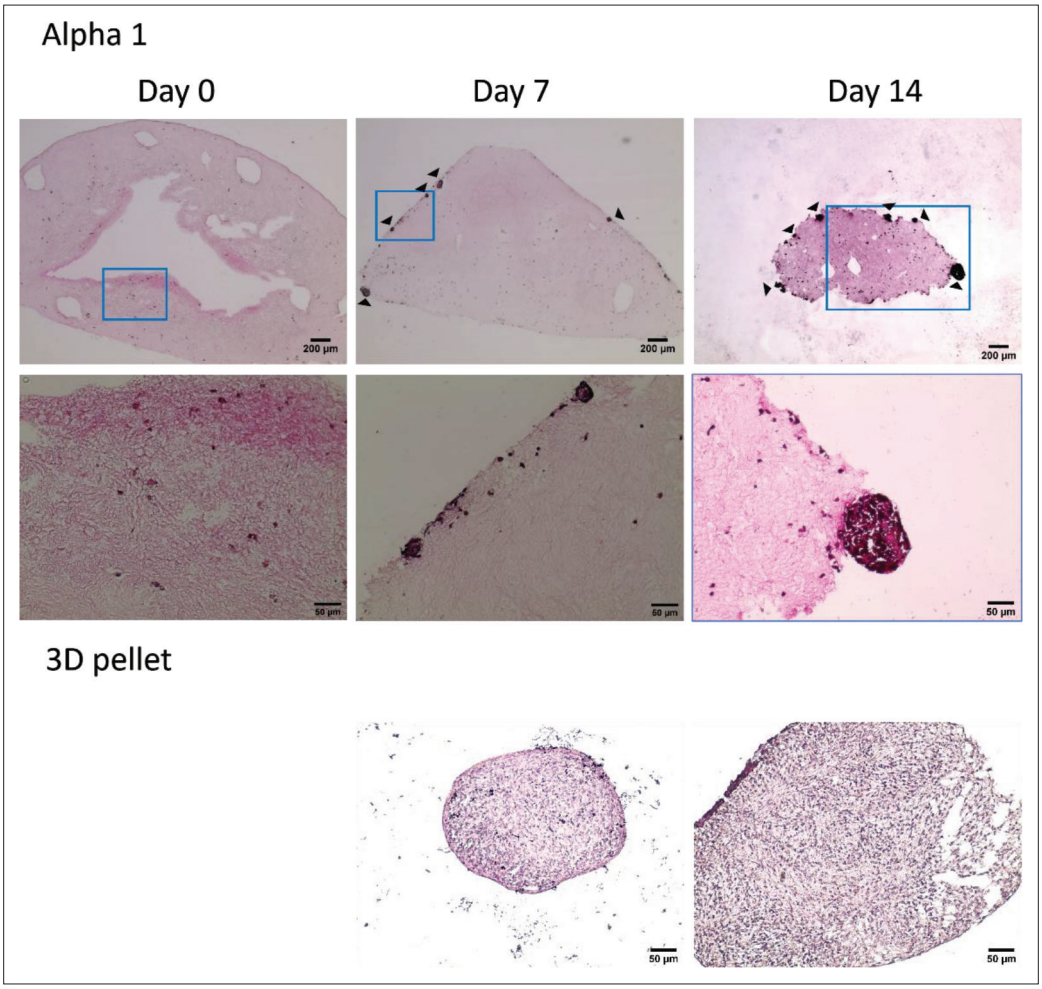

Figure 3. Top: PeptiInk Alpha 1 H&E staining. The top row shows lower-magnification images of cell-embedded hydrogels (scale bar: 200 µm); the arrows on the lower-magnification images show cell cluster formations on the PeptiInk surface. The bottom row shows the magnified sections indicated by blue boxes in the top row images (scale bar: 50 µm). Bottom: H&E staining of the 3D chondrocyte pellet over days 7 and 14 (scale bar: 50 µm).

The PeptiInk system showed low levels of intracellular aggrecan on day 7, which then increased, especially at the surface cell cluster formations (Figure 5). Negative controls can be found in **Figure S3** (Supplementary File).

3.5. PCR analysis of chondrogenic markers

In qRT-PCR, *GADPH* was used as housekeeping gene, and 3D pellet cultures were used as controls. Expression of specific cartilage markers, such as *SOX9*, *COL2,* and *AGC*, was assessed. Cells in control pellet cultures showed no significant changes in COL2, *AGC,* or *SOX9* mRNA expression from day 7 to day 14 (Figure 6A). In contrast, cells in Alpha 1 cultures showed an upregulation of all three mRNAs when compared to their corresponding control each time point (Figure 6B and C). Cells maintained in the Alpha 1 culture system exhibited a significant upregulation of *COL2*, *AGC,* and *SOX9* mRNA expression on day 7 (Figure 6B). On day 14, all mRNAs assessed were somewhat upregulated but not statistically significantly (Figure 6C).

4. Discussion

The development of human *in vitro* models is crucial to the further understanding of cartilage and diseases that affect it. Additionally, there is a need to move away from animal models, which are not necessarily always representative of human pathophysiology. Current 3D-bioprinted models rely on the use of animal-derived materials such as gelatine or hyaluronan. These are natural bioinks that present multiple advantages such as enabling cell attachment and functionalization. However, they are animal-derived bioinks, which not only give rise ethical and sustainability issues in their production but also can interfere uncontrollably within the system. The use of synthetic materials enables the possibility of creating a

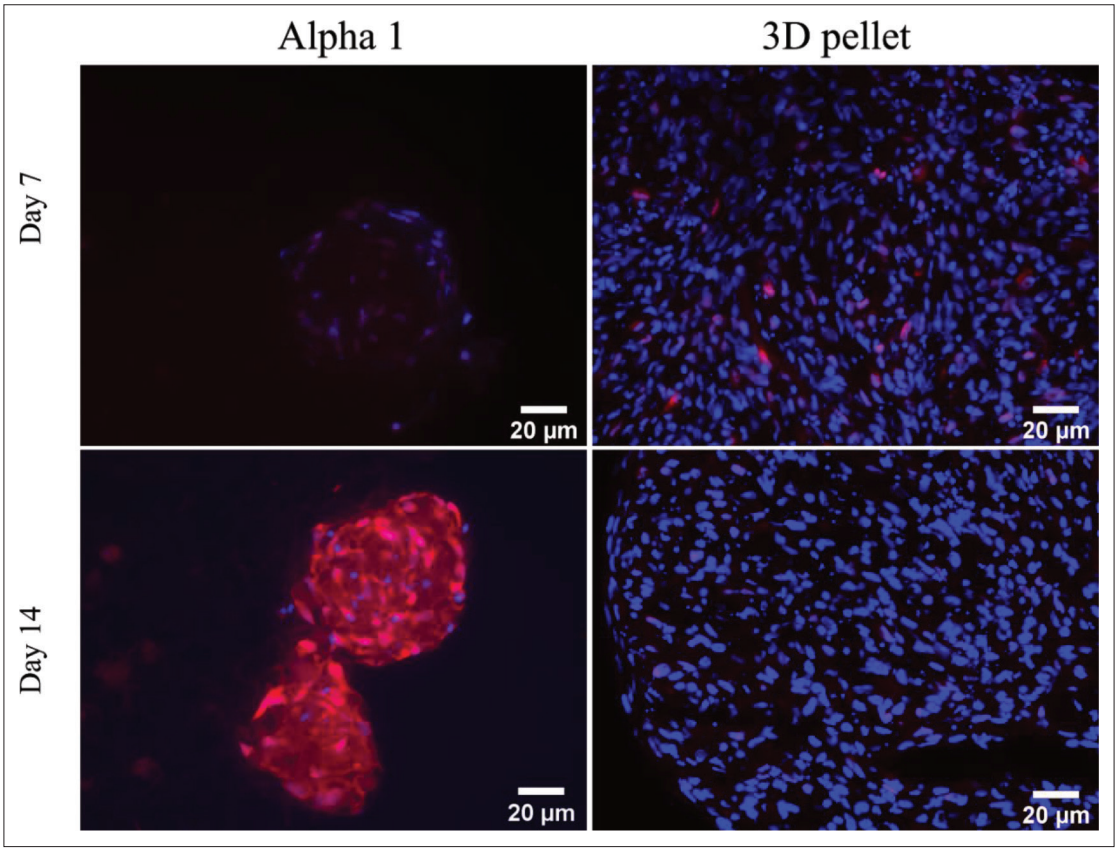

Figure 4. SOX9 (red) and cell nuclei stained with DAPI (blue) over days 7 and day 14 of culture in Alpha 1 and 3D pellet control cultures.

fully controllable and tunable environment with which we can develop cartilage human tissue models. Synthetic self-assembling peptide hydrogels have previously been used to culture animal chondrocyte-based tissue models[35]. Their potential for use as a bioink and also their application in 3D bioprinting remains unexplored. Existing models rely on tissue engineering techniques such as 2D cell seeding, which can lead to heterogeneous and uncontrolled cell deposition. Here, we embrace the advantages of 3D bioprinting, and we assess the material use in both 3D bioprinting and production of human cartilage *in vitro* tissue models.

Firstly, the rheology of the PeptiInk *Alpha 1* was assessed with and without the addition of media. As expected, the addition of medium made the hydrogel less viscous under low shear stress, enabling a better shear thinning behavior for 3D printing. However, surprisingly, at higher shear stresses, the viscosity appeared to increase. Previous work had reported the slight increase in compressive modulus of this self-assembling peptide when mixed with culture medium[35]. The addition of cell culture medium is expected to change the pH of Alpha 1 and introduce higher amounts of ions in the Alpha 1 (PeptiInk), promoting higher levels of crosslinking and an increase in compressive modulus[35]. The changes in viscosity observed when applying higher stresses could be due to the increase in crosslinking degree as time progresses when the rheological measurement is performed. In the rheological assessments, since low shear stresses have been applied before, the PeptiInk has had lesser time to crosslink. Further to characterizing its rheology, an initial bioprinting assessment was performed to visually assess any differences in filament deposition when using different nozzle sizes (22G, 25G, and 27G). No differences in terms of filament continuity were observed; therefore, the mid-size nozzle, 25G, was chosen. This choice allowed for a higher filament resolution than the 22G nozzle, but a lower shear stress was expected to be generated in smaller sizes[36], such as the 27G nozzle. Visual assessment of 25G-printed structures was performed to narrow down the extrusion pressure window using a constant printing speed of 10 mm/s. This initial screening pinpointed a pressure range of 8–10 kPa, which demonstrated the continuous deposition of the printing filament avoiding the fusion of adjacent filaments. Further optimization was required to understand the resolution of the bioink. The effect on filament width of multiple printing speeds was assessed at a constant pressure within this range, and compared to

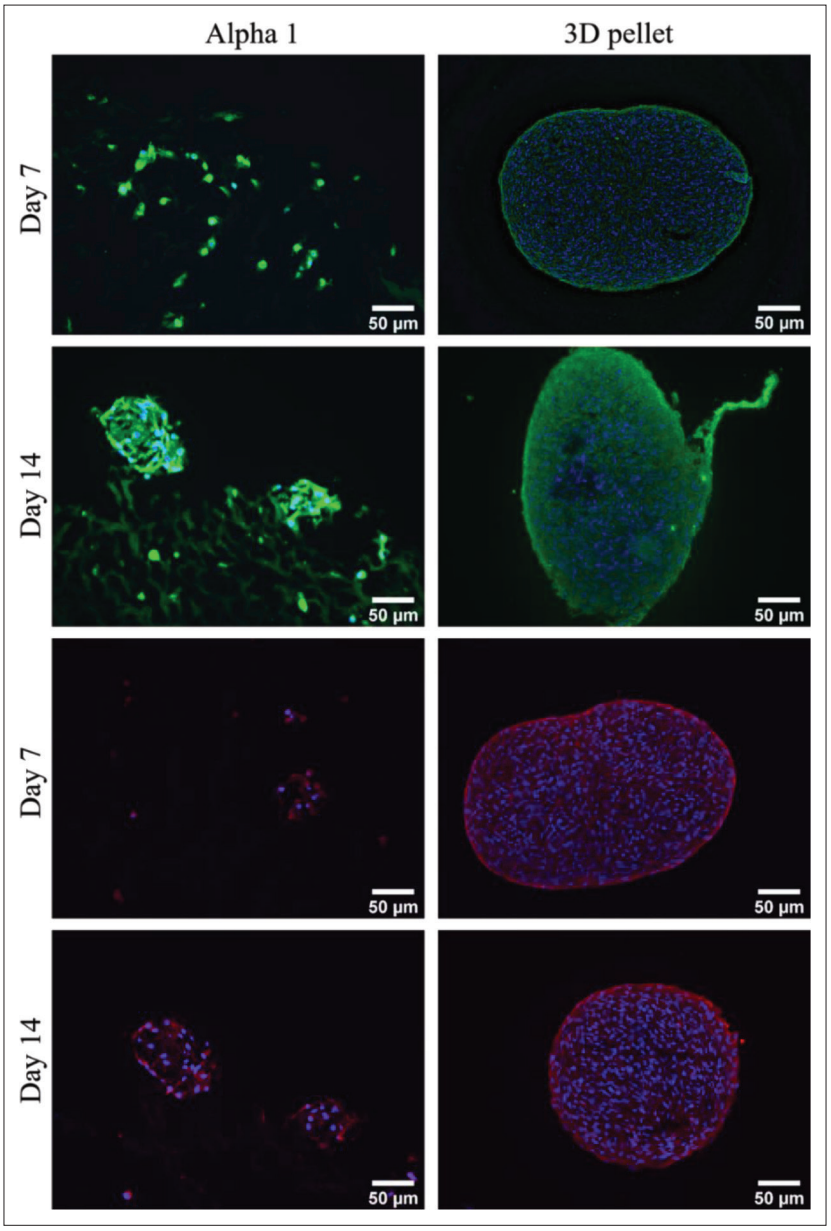

Figure 5. Top: Collagen type II staining (green) and cell nuclei staining with DAPI (blue) in 3D chondrocyte pellet and PeptiInk Alpha 1 at days 7 and 14. Bottom: Aggrecan staining (red) and cell nuclei staining with DAPI (blue) of 3D chondrocyte pellet and PeptiInk Alpha 1 at days 7 and 14.

the theoretical filament width, which corresponds to the printing nozzle diameter. As expected, the higher was the printing speed, the thinner was the deposited filament, and the closer was the resolution to the theoretical optimal value. Although the printing speed of 10 mm/s at 8 kPa of pressure showed the best printing resolution, a lower printing speed was chosen for the final manufacturing of the constructs to avoid potential printing issues. Due to the constant pressure changes that the printer experienced when moving from one well to another within the well plate, a slower printing speed enabled the printer user to manually change the printing pressure, within this window, to avoid loss of structural consistency. Higher printing speeds did not allow for consistent and fast-enough pressure changes that would ensure the required structural integrity. 3D bioprinting as the preferred choice of manufacturing technique overall demonstrated ease of use, consistency when manufacturing these constructs, and the possibility of scaling up this manufacturing process to produce more 3D-bioprinted constructs for future cartilage modeling *in vitro*.

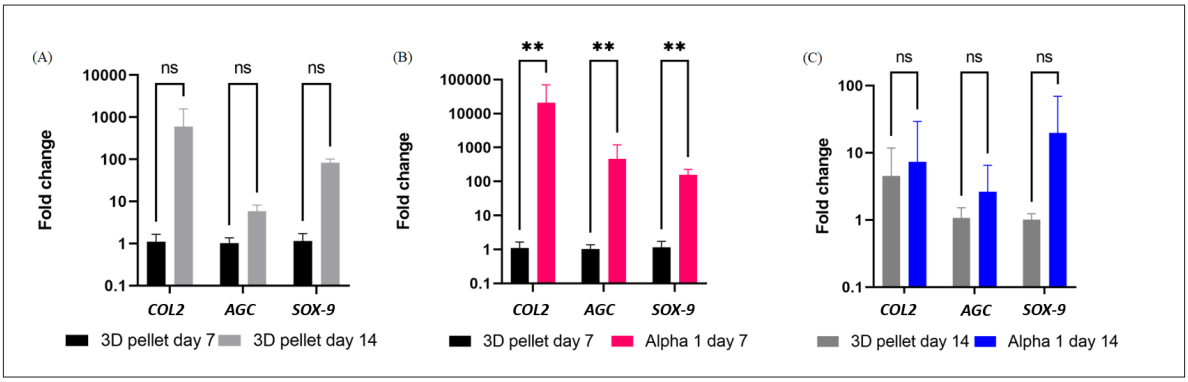

Figure 6. Fold change relative expression of cartilage markers collagen type II (*COL2*), aggrecan (*AGC*), and SOX-9 (*SOX9*) with respect to expression of housekeeping gene *GADPH*. (A) Fold change of these genes for the 3D pellet control with respect to the control on day 7. (B) Fold change of these genes for Alpha 1 on day 7 with respect to the 3D control pellet on day 7. (C) Fold change of these genes for Alpha 1 on day 14 with respect to the 3D control pellet on day 14. $N = 3$ for the 3D pellet controls; $N = 9$ for the Alpha 1 cultures. The error bars show the standard deviation of the fold change. Notes: ns, not significant; $^{**}p < 0.01$.

Secondly, once the printing optimization was achieved, multiple assessments of the capability of this material to be used as a bioink for cartilage *in vitro* tissue modeling were performed. All results were compared to a 3D chondrocyte pellet culture system, which has been widely used previously as a cartilage *in vitro* tissue system[33,40-43]. Initially, a cytocompatibility assessment of PeptiInk *Alpha 1* and viability of the 3D pellet culture was performed semi-quantitatively through live/dead staining and quantitatively through DNA quantification. The initial live/dead staining showed that cells that were in the 3D pellet configuration were almost 100% viable, confirming that the cells that were expanded in 2D pellet configuration had high viability. Across the 14 days of culture, the 3D pellet showed a 46%–54% decrease in cell viability as expected. Previous literature shows that when using this "gold standard" in *in vitro* cartilage tissue modeling, a necrotic core is formed at the center of the pellet, most likely due to hypoxia[37]. The cell viability of *Alpha 1* was assessed 2 h post-printing which showed a 30% cell viability. This low viability increased to 59% from day 7 onward (see Figure 2A), and although the printing process compromised the cell viability in the first 24 h, cells quickly recovered in the first 7 days and maintained their viability thereafter. The cell death observed in the control pellet in the first 7 days was avoided in the hydrogel culture, where the diffusion of oxygen and nutrients appeared to be more efficient as fewer dead cells were observed at the center of the hydrogel.

This cell viability was further corroborated through DNA quantification. As expected, both 3D systems showed high levels of DNA on day 0, but these significantly decreased on day 7 and further on day 14. The decrease of this DNA content in the 3D pellet coincides with the observed necrotic core, and it corresponds with observations reported in previous research[40]. *Alpha* 1 showed a non-significant decrease in DNA content over the 14 days of culture. The DNA percentage change shows a significant decrease from day 0 to 7 and from day 0 to 14. However, changes in DNA percentage between days 7 and 14 were not significant, showing the maintenance of cell numbers. It is worth noting that this could be due to the instability of the hydrogel. Over the 14 days, the volume of the hydrogel decreased, making it impossible to extend the cell culture for longer than 14 days. This degradation led to multiple cells migrating and expanding at the bottom of the well plate. However, a large number of cells remained in the hydrogel. Due to this hydrogel instability, it is not possible to state that cell number and DNA content were decreasing in the hydrogel culture, because of the lack of constant PeptiInk volume.

This degradation was not only observed visually during the culture period but also captured by histology and H&E staining, which enabled the visualization of changes in cell morphology, distribution, matrix deposition, and hydrogel dimension. The H&E staining in the 3D pellet control system illustrated the expected spherical cell morphology and high ECM deposition shown by high levels of eosin staining. Additionally, the reported cell death at the pellet core was also observed as a lower number of stained nuclei. Culture in *Alpha 1* discloses different cell and material behaviors. First, it depicts degradation of the hydrogel that occurs from day 0 up to day 14 in culture. As shown in Figure 3, the hydrogels showed a smaller cross-section which translated into a smaller overall hydrogel volume. Additionally, this showed the homogeneous distribution of cells within the gel at day 0, confirming the controlled cell deposition that was expected from using 3D bioprinting as a manufacturing technique. Secondly, a change in cell morphology and distribution was observed over the

14 days of culture with cells, which initially adopted an expected round shape[44]. However, as culture progressed, the cells tended to migrate toward the surface where they would form smaller clusters if there were other cells in the surrounding. These cell clusters were more prevalent at day 14 of culture and resembled smaller versions of the 3D pellets. At this time, the cells adopted a more "spread"" morphology and, due to their lower numbers, lacked any obvious hypoxic core or cell death. These findings indicate that the cells acquired an autonomous behavior and attained a conformation that closely resembles a physiologically relevant cartilage distribution.

The final investigation included assessment of chondrogenic marker expression at both protein and mRNA transcript levels. Protein expression was assessed by immunofluorescence using SOX-9 to determine initial chondrogenesis. Positive labeling for SOX-9 was seen in both control and PeptiInk cultures on days 7 and 14. When chondrocytes are expanded in two-dimensional, it is known that they tend to lose their chondrogenic phenotype after passage 4 or 5 and behave like fibroblasts[45,46]. By assessing this early chondrogenic marker, we could assess whether the cells were retrieving their original phenotype after being placed in a 3D environment. Other studies[46] have shown that when placing previously 2D-expanded chondrocytes into a 3D environment, they started expressing SOX-9 and later chondrogenic markers. Here, we observed high intensity of intracellular nuclear SOX-9 labeling on day 7 in pellet cultures, which decreased at subsequent time points until day 14. SOX-9 labeling in PeptiInk culture was, by contrast, low on day 7 but instead increased in intensity by day 14, showing the potential induction of chondrogenic differentiation under these conditions.

Later chondrogenic markers such as collagen type II and aggrecan were also assessed. As expected, collagen type II and aggrecan were expressed in the cartilage pellet. More collagen type II appeared to be expressed at the surface of the pellet on day 7 and then increased across the matrix on day 14, which is an observation that differs from previous 3D pellet chondrocyte studies where the production of collagen type II commences at the center and spreads outward[40,41]. Aggrecan, on the other hand, seemed to be expressed all over the pellet from day 7 onward, confirming previously reported observation[43]. The hydrogel culture showed an intracellular expression of collagen type II on day 7 and a more prominent intra- and extra-cellular expression on day 14, especially in the cell cluster formations at the surface of the hydrogel. Aggrecan, on the other hand, appeared to have a lower expression on day 7 which then increased in those surface cell clusters on day 14.

These observations were further corroborated by use of qRT-PCR to assess mRNA levels of each of these three markers. Although the immunolabeling showed promising results, the nature of some of the antibodies used, such as the collagen type II polyclonal antibody, could lead to false positive results. qRT-PCR confirmed the chondrogenic behavior observed. Firstly, although not statistically significant, mRNA expression levels for all three chondrogenic markers were somewhat raised between day 7 and 14 in the 3D pellets, supporting the use of this "gold standard" system for cartilage *in vitro* chondrogenesis. Significant upregulation in levels of *COL2*, *AGC,* and *SOX9* mRNA was observed in the hydrogel culture on day 7. This supports the notion that cells respond by adopting greater chondrogenic potential in the hydrogel system during the first 7 days. The observed lack of any significant difference in mRNA levels for these chondrogenic marker transcripts in the following week (day 14) suggests that cells cultured in the hydrogel system exhibit an accelerated chondrogenic behavior.

This hydrogel system presents promising advantages such as the possibility to be used as a bioink and as a human cartilage *in vitro* model. The high expression of cartilage markers, such as collagen type II, aggrecan, and SOX-9, shows that this system also enables the chondrogenesis observed in other animal models[35]. The significant upregulation of the chosen chondrogenic mRNAs in the PeptiInk system on day 7 indicates a faster chondrogenesis when placing the human primary chondrocytes in the hydrogel system. However, the instability of the hydrogel and its fast degradation rate when mixed with cells in culture, which have already been reported[44], make it difficult to maintain the culture *in vitro* for longer than 14 days. The loss of hydrogel volume over the culture period potentially impedes the further chondrogenic development of the system into mature cartilage tissue. Further research should focus on the mechanism of degradation of these hydrogels, which has already been speculated to be cell endocytosis[44]. Additional strategies to slow down this PeptiInk degradation without disrupting the chondrogenic potential should be assessed.

Overall, our findings showed that the PeptiInk Alpha 1 culture system does promote human chondrogenesis *in vitro* and is a suitable material for 3D bioprinting. It allows for chondrocytes to survive, self-assemble and produce chondrogenic matrix proteins and markers. This animal-free alternative has great potential to bring research closer to an ethical and more sustainable platform to recreate human cartilage *in vitro*. Albeit further studies are needed to assess the feasibility of this PeptiInk to be used in long-term cultures for human cartilage *in vitro* modeling, our novel findings showed for the first time the

feasibility to use this material as a bioink and as a short-term culture platform to develop human cartilage models *in vitro.* This material, as a bioprintable material to develop human cartilage models, can be applied in personalized medicine, fundamental research, or disease modeling.

5. Conclusion

In this study, we optimized the bioprinting process of PeptiInk Alpha 1 and demonstrated its potential to manufacture human cartilage models *in vitro.* First, we assessed the printability of the material through rheological characterization and optimization of printing pressures and speeds using a 25G conical nozzle. We went on to explore the behavior that primary human chondrocytes show when encapsulated and 3D-bioprinted within Alpha 1. High cell viability, cell self-assembly, and chondrogenic protein expression at the protein and mRNA levels were observed in both the control and the PeptiInk Alpha 1 culture. This material, which can be potentially used to 3D-bioprint human cartilage tissue models *in vitro*, presents a more ethical and sustainable alternative than the current 3D-bioprinted cartilage *in vitro* models. Further work will focus on additional assessment of the chondrogenic behavior through ELISA protein quantification, improvement of the material stability for long-term cultures, and 3D bioprinting of larger constructs.

Acknowledgments

This article was written and revised only by the confirmed authors, and no other people contributed to the production of this paper.

Funding

This work was supported by the Engineering and Physical Sciences Research Council (EPSRC- EP/S021868/1) Centre for Doctoral Training.

Conflict of interest

The authors declare no conflict of interest.

Author contributions

Conceptualization: Patricia Santos-Beato, Andrew A. Pitsillides
Formal analysis: Patricia Santos-Beato
Funding acquisition: Deepak M. Kalaskar
Investigation: Patricia Santos-Beato
Supervision: Andrew A. Pitsillides, Alberto Saiani, Aline Miller, Ryo Torii, Deepak M. Kalaskar
Visualization: Patricia Santos-Beato
Writing – original draft: Patricia Santos-Beato
Writing – review & editing: Andrew A. Pitsillides, Alberto Saiani, Aline Miller, Deepak M. Kalaskar

Ethics approval and consent to participate

Not applicable.

Consent for publication

Not applicable.

Availability of data

Raw data can be accessed by contacting corresponding author

Further disclosure

Part of the entire set of findings has been presented in a conference (European Society of Biomaterials, September 2022).

References

1. Gibofsky A, 2012, Overview of epidemiology, pathophysiology, and diagnosis of rheumatoid arthritis. *Am J Manag Care*, 18(13 Suppl): S295–S302.

2. Jafarzadeh SR, Felson DT, 2018, Updated estimates suggest a much higher prevalence of arthritis in United States adults than previous ones. *Arthritis Rheumatol*, 70(2): 185–192.

   https://pubmed.ncbi.nlm.nih.gov/29178176

3. Buckwalter JA, Mow VC, Ratcliffe A, 1994, Restoration of injured or degenerated articular cartilage. *J Am Acad Orthop Surg*, 2(4): 192–201.

4. O'Hara BP, Urban JP, Maroudas A, 1990, Influence of cyclic loading on the nutrition of articular cartilage. *Ann Rheum Dis*, 49(7): 536–539.

5. Chang AA, Reuther MS, Briggs KK, *et al.*, 2012, In vivo implantation of tissue-engineered human nasal septal neocartilage constructs: A pilot study. *Otolaryngol Head Neck Surg*, 146(1): 46–52.

   https://pubmed.ncbi.nlm.nih.gov/22031592

6. Jin CZ, Cho JH, Choi BH, *et al.*, 2011, The maturity of tissue-engineered cartilage in vitro affects the repairability for osteochondral defect. *Tissue Eng Part A*, 17(23–24): 3057–3065.

   https://pubmed.ncbi.nlm.nih.gov/21736425

7. Neybecker P, Henrionnet C, Pape E, *et al.*, 2018, In vitro and in vivo potentialities for cartilage repair from human advanced knee osteoarthritis synovial fluid-derived mesenchymal stem cells. *Stem Cell Res Ther*, 9(1): 329.

   https://doi.org/10.1186/s13287-018-1071-2

8. Sanjurjo-Rodríguez C, Castro-Viñuelas R, Hermida-Gómez T, *et al.*, 2017, Human cartilage engineering in an in vitro repair model using collagen scaffolds and mesenchymal stromal cells. *Int J Med Sci*, 14(12): 1257–1262.

   https://pubmed.ncbi.nlm.nih.gov/29104482

9. Wu Y, Kennedy P, Bonazza N, *et al.*, 2021, Three-dimensional bioprinting of articular cartilage: A systematic review. *Cartilage*, 12(1): 76–92.

10. Ng WL, Chua CK, Shen YF, 2019, Print me an organ! Why we are not there yet. *Prog Polym Sci*, 97(October 1): 101145.

    https://doi.org/10.1016/j.progpolymsci.2019.101145

11. Ozbolat IT, Hospodiuk M, 2016, Current advances and future perspectives in extrusion-based bioprinting. *Biomaterials*, 76 (January 1): 321–343.

    http://dx.doi.org/10.1016/j.biomaterials.2015.10.076

12. Suntornnond R, Ng WL, Huang X, *et al.*, 2022, Improving printability of hydrogel-based bio-inks for thermal inkjet bioprinting applications via saponification and heat treatment processes. *J Mater Chem B*, 10(31): 5989–6000.

13. Ng WL, Lee JM, Zhou M, *et al.*, 2020, Vat polymerization-based bioprinting - process, materials, applications and regulatory challenges. *Biofabrication*, 12(2): 022001.

14. Sekar MP, Budharaju H, Zennifer A, *et al.,* 2021, Current standards and ethical landscape of engineered tissues-3D bioprinting perspective. *J Tissue Eng*, 12 (July 1): 20417314211027676.

15. Costantini M, Idaszek J, Szöke K, *et al.*, 2016, 3D bioprinting of BM-MSCs-loaded ECM biomimetic hydrogels for in vitro neocartilage formation. *Biofabrication*, 8(3): 035002.

    https://iopscience.iop.org/article/10.1088/1758-5090/8/3/035002

16. Daly AC, Critchley SE, Rencsok EM, *et al.*, 2016, A comparison of different bioinks for 3D bioprinting of fibrocartilage and hyaline cartilage. *Biofabrication*, 8(4): 045002.

    https://iopscience.iop.org/article/10.1088/1758-5090/8/4/045002

17. Duchi S, Onofrillo C, O'Connell CD, *et al.*, 2017, Handheld co-axial bioprinting: Application to in situ surgical cartilage repair. *Sci Rep*, 7(1): 5837.

18. Gao G, Schilling AF, Hubbell K, *et al.*, 2015, Improved properties of bone and cartilage tissue from 3D inkjet-bioprinted human mesenchymal stem cells by simultaneous deposition and photocrosslinking in PEG-GelMA. *Biotechnol Lett*, 37(11): 2349–2355.

19. Levato R, Visser J, Planell JA, *et al.*, 2014, Biofabrication of tissue constructs by 3D bioprinting of cell-laden microcarriers. *Biofabrication*, 6(3): 035020.

    https://iopscience.iop.org/article/10.1088/1758-5082/6/3/035020

20. Levato R, Webb WR, Otto IA, *et al.*, 2017, The bio in the ink: Cartilage regeneration with bioprintable hydrogels and articular cartilage-derived progenitor cells. *Acta Biomater*, 61 (October 1): 41–53.

21. Mouser VHM, Melchels FPW, Visser J, *et al.*, 2016, Yield stress determines bioprintability of hydrogels based on gelatin-methacryloyl and gellan gum for cartilage bioprinting. *Biofabrication*, 8(3): 35003.

22. O'Connell CD, Di Bella C, Thompson F, *et al.*, 2016, Development of the Biopen: A handheld device for surgical printing of adipose stem cells at a chondral wound site. *Biofabrication*, 8(1): 15019.

23. Zhu W, Cui H, Boualam B, *et al.*, 2018, 3D bioprinting mesenchymal stem cell-laden construct with core-shell nanospheres for cartilage tissue engineering. *Nanotechnology*, 29(18): 185101.

24. Abbadessa A, Mouser VHM, Blokzijl MM, *et al.*, 2016, A synthetic thermosensitive hydrogel for cartilage bioprinting and its biofunctionalization with polysaccharides. *Biomacromolecules,* 17(6): 2137–2147.

    https://pubs.acs.org/doi/10.1021/acs.biomac.6b00366

25. Wasyłeczko M, Sikorska W, Chwojnowski A, 2020, Review of synthetic and hybrid scaffolds in cartilage tissue engineering. *Membranes,* 10(11): 348.

    https://pubmed.ncbi.nlm.nih.gov/33212901

26. Popov A, Malferrari S, Kalaskar DM, 2017, 3D bioprinting for musculoskeletal applications. *J 3D Print Med*, 1(3): 191–211.

    https://www.futuremedicine.com/doi/10.2217/3dp-2017-0004

27. OECD, 2018, *Guidance Document on Good In Vitro Method Practices (GIVIMP)*, Vol. 1, OECD Publishing, Paris, 1–264.

    https://www.oecd-ilibrary.org/docserver/9789264304796-en.pdf?expires=1621462493&id=id&accname=guest&checksum=4EA871101E844045CE8D833D9DFADC25%0A

    https://www.oecd-ilibrary.org/environment/guidance-document-on-good-in-vitro-method-practices-givimp_9789264304

28. Ligorio C, Hoyland JA, Saiani A, 2022, Self-assembling peptide hydrogels as functional tools to tackle intervertebral disc degeneration. *Gels*, 8(4).

    https://www.mdpi.com/2310-2861/8/4/211

29. Mujeeb A, Miller AF, Saiani A, Gough JE. 2013; Self-assembled octapeptide scaffolds for in vitro chondrocyte culture. 9(1):4609–17. 2013. Acta Biomater [Internet]. Available from:

    http://dx.doi.org/10.1016/j.actbio.2012.08.044

30. Wan S, Borland S, Richardson SM, *et al.*, 2016, Self-assembling peptide hydrogel for intervertebral disc tissue engineering. *Acta Biomater*, 46(December 1): 29–40.

    https://www.sciencedirect.com/science/article/pii/S1742706116305062

31. Raphael B, Khalil T, Workman VL, *et al.*, 2017, 3D cell bioprinting of self-assembling peptide-based hydrogels. *Mater Lett,* 190: 103–6.

32. Gatenholm B, Lindahl C, Brittberg M, *et al.*, 2020, Collagen 2A type B induction after 3D bioprinting chondrocytes in situ into osteoarthritic chondral tibial lesion. *Cartilage*, 13(December 1): 1–15.

http://journals.sagepub.com/doi/10.1177/1947603520903788

33. Yang IH, Kim SH, Kim YH, *et al.*, 2004, Comparison of phenotypic characterization between "alginate bead" and "pellet" culture systems as chondrogenic differentiation models for human mesenchymal stem cells. *Yonsei Med J,* 45: 891–900.

http://www.ncbi.nlm.nih.gov/pubmed/15515201

34. Yeung P, Cheng KH, Yan CH, *et al.*, 2019, Collagen microsphere based 3D culture system for human osteoarthritis chondrocytes (hOACs). *Sci Rep*, 9(1): 1–14.

http://dx.doi.org/10.1038/s41598-019-47946-3

35. Ligorio C, Zhou M, Wychowaniec JK, *et al.*, 2019, Graphene oxide containing self-assembling peptide hybrid hydrogels as a potential 3D injectable cell delivery platform for intervertebral disc repair applications. *Acta Biomater*, 92: 92–103.

https://doi.org/10.1016/j.actbio.2019.05.004

36. Lemarié L, Anandan A, Petiot E, *et al.*, 2021, Rheology, simulation and data analysis toward bioprinting cell viability awareness. *Bioprinting*, 21(December 2020): e00119.

https://linkinghub.elsevier.com/retrieve/pii/S2405886620300464

37. Schmitz C, Potekhina E, Belousov VV, *et al.,* 2021, Hypoxia onset in mesenchymal stem cell spheroids: monitoring with hypoxia reporter cells. *Front Bioeng Biotechnol*, 9(February).

38. Caron MMJ, Emans PJ, Coolsen MME, *et al.*, 2012, Redifferentiation of dedifferentiated human articular chondrocytes: Comparison of 2D and 3D cultures. *Osteoarthr Cartil*, 20(10): 1170–1178.

http://dx.doi.org/10.1016/j.joca.2012.06.016

39. Haseeb A, Kc R, Angelozzi M, *et al.*, 2021, SOX9 keeps growth plates and articular cartilage healthy by inhibiting chondrocyte dedifferentiation/osteoblastic redifferentiation. *Proc Natl Acad Sci*, 118(8): e2019152118.

https://www.pnas.org/doi/abs/10.1073/pnas.2019152118

40. Schon BS, Schrobback K, Van Der Ven M, *et al.*, 2012, Validation of a high-throughput microtissue fabrication process for 3D assembly of tissue engineered cartilage constructs. *Cell Tissue Res*, 347(3): 629–642.

41. Bosnakovski D, Mizuno M, Kim G, *et al.*, 2004, Chondrogenic differentiation of bovine bone marrow mesenchymal stem cells in pellet cultural system. *Exp Hematol*, 32(5): 502–509.

42. Griffin MF, Ibrahim A, Seifalian AM, *et al.*, 2017, Chemical group-dependent plasma polymerisation preferentially directs adipose stem cell differentiation towards osteogenic or chondrogenic lineages. *Acta Biomater*, 50: 450–61.

http://dx.doi.org/10.1016/j.actbio.2016.12.016

43. Zhang Z, McCaffery JM, Spencer RGS, *et al.*, 2004, Hyaline cartilage engineered by chondrocytes in pellet culture: Histological, immunohistochemical and ultrastructural analysis in comparison with cartilage explants. *J Anat*, 205(3): 229–237.

44. Faroni A, Workman VL, Saiani A, *et al.*, 2019, Self-assembling peptide hydrogel matrices improve the neurotrophic potential of human adipose-derived stem cells. *Adv Healthc Mater*, 8(17).

45. Benya P, 1982, Dedifferentiated chondrocytes reexpress the differentiated collagen phenotype when cultured in agarose gels. *Cell,* 30(1): 215–224.

https://doi.org/10.1016%2F0092-8674%2882%2990027-7

46. Lemare F, Steimberg N, Le Griel C, *et al.*, 1998, Dedifferentiated chondrocytes cultured in alginate beads: Restoration of the differentiated phenotype and of the metabolic responses to interleukin- 1β. *J Cell Physiol*, 176(2): 303–313.

ACCSCIENCE PUBLISHING

International Journal of Bioprinting

REVIEW ARTICLE

Bioprinting of cell-laden protein-based hydrogels: From cartilage to bone tissue engineering

Mehran Khajehmohammadi[1,2†], Negar Bakhtiary[3†], Niyousha Davari[4], Soulmaz Sarkari[5], Hamidreza Tolabi[6,7], Dejian Li[8], Behafarid Ghalandari[9*], Baoqing Yu[10*], and Farnaz Ghorbani[11,12,13*]

[1]Department of Mechanical Engineering, Faculty of Engineering, Yazd University, Yazd 8174848351, Iran

[2]Medical Nanotechnology and Tissue Engineering Research Center, Yazd Reproductive Sciences Institute, Shahid Sadoughi University of Medical Sciences, Yazd 8916877391, Iran

[3]Department of Biomaterials, Faculty of Interdisciplinary Science and Technology, Tarbiat Modares University, Tehran 14115114, Iran

[4]Department of Life Science Engineering, Faculty of New Sciences and Technologies, University of Tehran, Tehran 143951561, Iran

[5]Department of Cardiology, School of Medicine and Health Sciences, Carl von Ossietzky University of Oldenburg, Oldenburg, Germany

[6]New Technologies Research Center (NTRC), Amirkabir University of Technology, Tehran 158754413, Iran

[7]Department of Biomedical Engineering, Amirkabir University of Technology (Tehran Polytechnic), Tehran 158754413, Iran

[8]Department of Orthopedics, Shanghai Pudong Hospital, Fudan University Pudong Medical Center, Shanghai, China

[9]State Key Laboratory of Oncogenes and Related Genes, Institute for Personalized Medicine, School of Biomedical Engineering, Shanghai Jiao Tong University, Shanghai 200030, China

[10]Department of Orthopedics, Shanghai Pudong New Area People's Hospital, Shanghai, China

[11]Department of Translational Health Sciences, University of Bristol, Bristol BS1 3NY, United Kingdom

[12]Institute of Biomaterials, Department of Material Science and Engineering, University of Erlangen-Nuremberg, Cauerstraße 6, 91058 Erlangen, Germany

[13]Institute of Orthopaedic and Musculoskeletal Science, Royal National Orthopaedic Hospital, University College London, London, United Kingdom

†These authors contributed equally to this work.

***Corresponding authors:**
Behafarid Ghalandari (behafarid.gh@gamil.com

Baoqing Yu (doctorybq@163.com)

Farnaz Ghorbani (farnaz.ghorbani@fau.de)

Citation: Khajehmohammadi M, Bakhtiary N, Davari N, et al., 2023, Bioprinting of cell-laden protein-based hydrogels: From cartilage to bone tissue engineering. *Int J Bioprint*, 9(6): 1089. https://doi.org/10.36922/ijb.1089

Received: June 16, 2023
Accepted: August 3, 2023
Published Online: September 7, 2023

Copyright: © 2023 Author(s). This is an Open Access article distributed under the terms of the Creative Commons Attribution License, permitting distribution, and reproduction in any medium, provided the original work is properly cited.

Publisher's Note: AccScience Publishing remains neutral with regard to jurisdictional claims in published maps and institutional affiliations.

(This article belongs to the *Special Issue: Advances in 3D Bioprinting for Regenerative Medicine and Drug Screening*)

Abstract

The fabrication of cell-laden protein-based hydrogels (PBHs) for bioprinting necessitates careful consideration of numerous factors to ensure optimal structure and functionality. Bioprinting techniques, such as single-cell, multi-cell, and cell aggregate bioprinting, are employed to encapsulate cells within PBHs bioink, enabling the creation of scaffolds for cartilage and bone regeneration. During the fabrication process, it is imperative to account for biophysical and biochemical factors that influence cell behavior and protein structure within the PBHs. Precise control of crosslinking methods, hydrogel rheological properties, and printing parameters is also crucial to achieve desired scaffold properties without compromising cell viability and protein integrity. This review primarily focuses on the influence of biophysical factors, including composition, microstructure,

biodegradation, and crosslinking, as well as biochemical factors, including chemical structure, growth factors, and signaling molecules, on protein structure and cell behavior. Additionally, key considerations for bioprinting PBHs and their impact on the successful regeneration of tissues are discussed. Furthermore, the review highlights current advancements, existing challenges, and promising prospects in the development of cell-laden PBHs for bioprinting applications and the regeneration of bone and cartilage.

Keywords: Bioprinting; Protein; Bioink; Cartilage; Bone; Tissue engineering

1. Introduction

The field of tissue engineering (TE) and regenerative medicine may undergo a revolution due to the development of bioprinting, a rapidly developing technology. An important application of bioprinting is in cartilage and bone TE, where it can be used to fabricate complex three-dimensional (3D) structures that mimic the structure and mechanical properties of natural tissues[1]. As a potential method for fabricating cartilage and bone tissue constructs, bioprinting of cell-laden protein-based hydrogels (PBHs) has emerged in recent years[2-4].

Traditional scaffolds cannot efficiently transport nutrients or exchange oxygen without porous structures interconnected in a complex geometry, and cells are typically deposited randomly using TE fabrication techniques[5,6]. In order to overcome these barriers, 3D bioprinting techniques can be used to construct cell-laden 3D structures[7,8]. By using cell-laden hydrogels, bioprinting makes tissue constructs with a high cell density, which plays a vital role in tissue regeneration. Bioprinting technology is divided into two distinct groups that are not mutually exclusive. Two basic categories can be distinguished: distributed versus aggregated cells and single versus multi-cellular. Cell aggregate bioprinting involves embedding preformed cell aggregates in bioinks and then printing them. Unlike single-cell bioprinting, which involves printing one cell at a time, multi-cell bioprinting involves suspending several cells in bioink and depositing them in a filament or droplet[9]. The incorporation of multiple cell types, such as chondrocytes and osteoblasts, into bioprinted osteochondral tissue constructs enhances the formation of a functional interface between cartilage and bone[10]. The fabrication of cartilage and bone tissue constructs has been achieved using multi-cell bioprinting technologies, including inkjet printing, extrusion-based printing, and laser-assisted printing. These technologies permit the fabrication of complex 3D structures with high reproducibility and shape fidelity[11-13].

Hydrogels are popularly employed as bioinks in the bioprinting process because of their chemical structure and the favorable 3D environments they provide for cellular growth[14-17]. Incorporating cells into inks (i.e., biomaterials or biological materials) to create a "bioink" is the cornerstone of producing intricate, biologically applicable 3D tissue structures[18,19]. The use of PBHs as bioinks for bioprinting has several advantages over other hydrogel systems. PBHs are biocompatible, biodegradable, and can be functionalized with cell adhesion peptides and growth factors (GFs) to enhance cell behavior and tissue regeneration[20,21]. Moreover, they can be crosslinked *in situ* by various mechanisms, such as physical, chemical, or enzymatic crosslinking, to achieve the desired mechanical properties and stability. In recent years, several PBHs have been developed for the bioprinting of cartilage and bone tissue constructs. These hydrogels offer several advantages over other materials, such as synthetic polymers or decellularized extracellular matrix (ECM) scaffolds. PBHs, such as collagen, gelatin, and fibrin, are biocompatible and biodegradable and can support cell adhesion, proliferation, and differentiation[22-24]. By providing spatial factors, such as porosity, protein alignment, and network density, the tissue structure can influence cellular behavior, shape, migration, and fate. Therefore, PBHs aim to replicate the ECM's complex and unique structure to develop functional tissue constructs that can mimic the native tissue's mechanical and biological properties[25-28]. The ability to imitate the native tissues' ECM and the tendency to experience shear-thinning before regaining their original shape are other desirable features of protein-based materials. Furthermore, protein-based polymers can be utilized to adjust the rheological and biochemical properties of bioinks, thereby enhancing the shape fidelity[29-32]. Further, these materials are renewable and green compared to fossil-derived synthetic polymers, and their availability and ease of large-scale production via bioengineering methodologies and biotechnological techniques make them attractive to researchers[33,34]. Thus far, more natural proteins of animal origin have been used in the fabrication of hydrogels, the reasons for which are easier access, lower cost, and simplicity of extraction, which will be followed by their introduction and review in the synthesis of biological inks for osteochondral and cartilage TE.

The protein sequence of hydrogels can significantly influence bioprinting processes and tissue constructs[35,36]. PBHs differ in terms of their mechanical properties, degradation rates, and cell adhesion properties, which can have a major impact on the printability of hydrogels and the behavior of cells. As an example, collagen hydrogels

are known for their biocompatibility and ability to support cell adhesion and proliferation, but their mechanical strength is low and they degrade rapidly. Although fibrin hydrogels have a higher mechanical strength and a slower degradation rate than collagen hydrogels, they may not promote cell adhesion and proliferation as well as collagen hydrogels[37-39]. The sequence and structure of proteins determine the stiffness, swelling, and degradation rate of hydrogels. As a consequence, it can influence the behavior of cells and the regeneration of tissue within bioprinted constructs[40-42]. Furthermore, specific functional groups or peptides may be introduced into protein sequences to enhance cell adhesion, differentiation, or tissue regeneration[43]. For example, arginine-glycine-aspartic acid (RGD) peptides are known to enhance cell adhesion and can be incorporated into the protein sequence of hydrogels in order to enhance biocompatibility and cell behavior[44]. Thus, it is necessary to carefully consider the protein sequence and structure of the hydrogel in order to optimize the mechanical and biological properties of the final tissue constructs.

This study aims to provide a comprehensive review of innovative bioprinting technologies, which are classified based on the cell format and the number of cells generated during the bioprinting procedure. The study focuses on PBHs utilized in cartilage and bone TE. Additionally, the critical role of microenvironmental factors, including biophysical and biochemical parameters, in bioprinting cell-laden PBHs is examined in detail, with reference to relevant research. The subsequent section provides a thorough explanation of the process compatibility considerations for PBHs, including mechano-rheological properties, biocompatibility, and process factors, through an overview of recent experiments on PBHs bioprinting. Finally, the challenges and perspectives associated with PBHs that must be carefully addressed to advance this fascinating field are highlighted.

2. Bioprinting strategies

There have been numerous developments within the bioprinting field to meet the needs of different research fields in terms of manufacturing capabilities, such as printing resolution, speed, or throughput[45], as well as cell requirements, including cell viability, proliferation, or differentiation[46]. It is possible to categorize the bioprinting technology into two distinct groups, which are not mutually exclusive. In essence, they can be classified based on the format of the cells (distributed cells or aggregated cells) and the number of cells produced during printing (single-cell or multi-cell). Single-cell bioprinting involves printing one cell at a time, while in multi-cell bioprinting, the cells are suspended in a bioink, and a number of cells are deposited within each filament or droplet. Within cell aggregate bioprinting, preformed cell aggregates are embedded into bioinks and then printed[9] (Figure 1).

The goal of single-cell bioprinting is to distribute single cells in a controlled manner in order to fabricate delicate tissues and study single cells genetically[47,48]. Particularly, the arrangement of cells and the microenvironment play a crucial role in stem cell research. There are several methods available for isolating and manipulating single cells as the first phase in the single-cell characterization[49]; to separate single cells, fluorescent-activated cell sorting (FACS)[50] and limiting dilution[51] are two widely used approaches[52]. Nevertheless, the inefficiency of limiting dilutions, together with the need for specialized instruments, as well as requiring professional expertise to employ FACS restrict their use[49,52]. Recent innovations in the field of single-cell printing have contributed to circumventing these limitations, one of which is utilizing a variety of microfluidic approaches for the encapsulation and examination of single cells, comprising droplet microfluidics[53-55], microwell arrays[56,57], and hydrodynamic traps[58,59]. Single-cell bioprinting offers multiple benefits; firstly, it enables precise and effective cell distribution at high throughput[60], and second, each cell or colony can be recovered readily with addressability for further analysis. Another advantage of single-cell printing is that it can easily be integrated with other methods, such as imaging systems[61,62], electric fields[63-65], and acoustic fields[66,67], with the encapsulation efficiency exceeding 90%. Based on Poisson's distribution, the broadly employed droplet-based microfluidics' theoretical limit is only 37%. Furthermore, single-cell printing can create both high-resolution two-dimensional (2D) structures as well as 3D tissue matrices for TE, drug delivery, and toxicology[68,69]. Barron *et al.*[70] first proposed the concept of single-cell bioprinting in 2005, when they described the bioprinting of human osteosarcoma cells, shortly after laser-assisted bioprinting was invented. To control the number of cells in a droplet, they developed bioinks with varying cell concentrations. Although the droplets were homogeneous and of small size, identifying only one cell per droplet was difficult, and the number of cells within the droplet generally followed the Poisson's distribution regardless of their concentration. Since then, single-cell bioprinting was not invented until 2012, when a camera with high speed was employed in order to monitor cells in the nozzle tip[71]. In this regard, droplets containing more than one cell or not incorporating any cells were discarded. It was in 2014 that Zhang *et al.*[72] developed a method to block cell-print breast cancer cells, utilizing traps with hook-shaped ends arranged in a prescribed pattern to capture and print singular cells. Currently, a variety of techniques

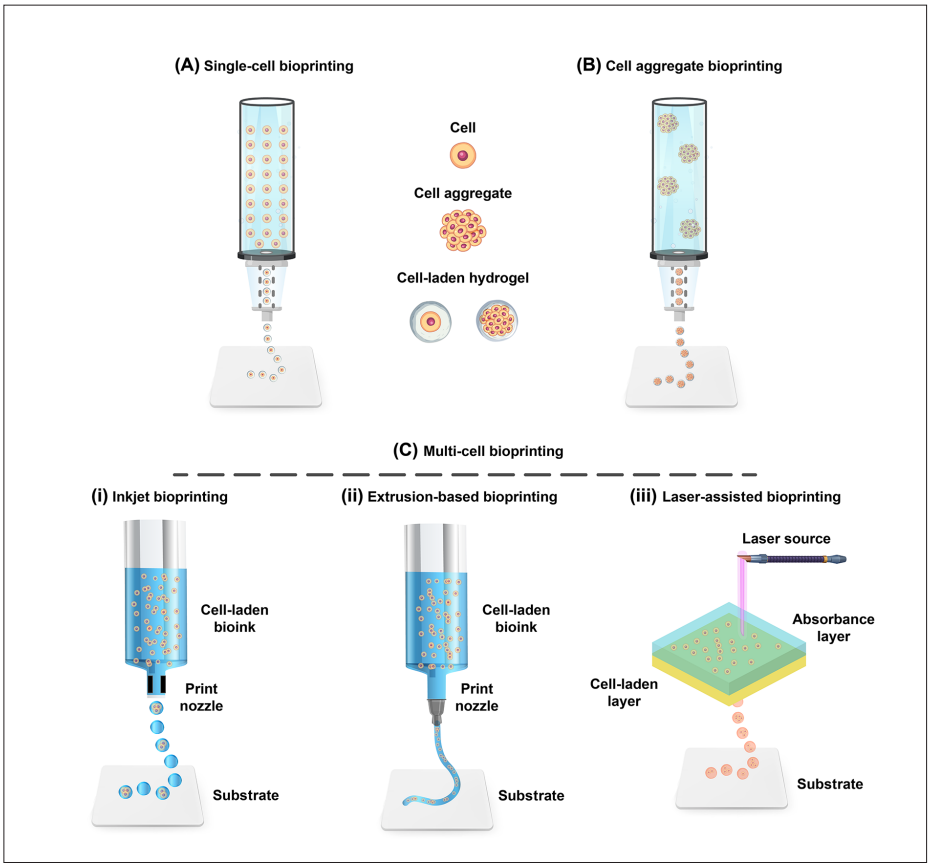

Figure 1. Illustrations of various bioprinting methods: (A) single-cell bioprinting, (B) cell aggregate bioprinting, and (C) multi-cell bioprinting, which can be further divided into (i) inkjet bioprinting, (ii) extrusion-based bioprinting, and (iii) laser-assisted bioprinting.

for single-cell printing are available, consisting of acoustic field-based printing or label-free computer vision-based printing[73]. In spite of the fact that stem cell bioprinting using single-cell methods has not been demonstrated to date, single-cell research employing stem cell bioprinting techniques is clearly on the rise, indicating the importance of stem cell biology. The current state of 3D printing does not allow the printing of organs and tissues with single-cell resolution, that is of necessity for printing functional organs and tissues[68,69,74,75].

Cell aggregate bioprinting is replicating the structure and function of tissues by utilizing the properties of aggregated cells[76]. Since aggregated cells have a greater number of cell–cell contacts and a decreased number of cell–substrate contacts, aggregated cells experience a different microenvironment in comparison with single cells. Cell aggregate bioprinting, on the other hand, has much higher throughput because each aggregate consists of 500 to 250,000 cells[77]; as a result, this technique is of significant importance in the regeneration of large quantities of tissue. The bioprinting process of cell aggregates involves the formation of cell aggregates, their bioprinting, and their fusion and maturation. Several methods can be employed to create cell aggregates through self-assembly and self-organization, including hanging drop culture, scaffolds, non-adhesive surfaces, and microfabrication[78], capable of generating sheets[79], spheroids, and cylinders[80]. Cell aggregate bioprinting requires proper mechanical stability to prevent fractures during bioprinting and long-term culture; thus, choosing cells for this bioprinting approach is of high significance. Different printing methods are utilized to create cell aggregates that are mainly categorized according to the contact between the cell and the substrate. In the first technique, bioactive bioinks are used to encapsulate cell aggregates and provide adhesion ligands[81]. As the second method, scaffold-free bioprinting refers to co-printing bioinert materials with cell aggregates[82]. Initially, cell aggregates form adjacently without any surrounding materials, and bioinks merely serve as supports until the aggregates fuse and form a tissue that is stable enough to stand on its own. After bioprinting, it is essential to rapidly fuse cell aggregates together in order to build stable tissues[9]. Since cell aggregates are the building blocks of a printed structure, enhancing inter-aggregate force through aggregate fusion contributes to

the structure's stability[80]. The mechanism is thought to be controlled via cell interactions and migrations, which is analyzed in some cases by means of phase field theory[83,84]. Besides, cell aggregate maturation is a crucial step; in fact, changing the microenvironment in cell aggregates simulates tissue formation *in vivo* to accelerate maturation and generate stable, functional tissues[85].

In multi-cell bioprinting, subdivided into inkjet bioprinting, extrusion-based bioprinting, and laser-assisted bioprinting[86], cells are suspended in hydrogels called bioinks[87]. Employing this approach, cells are printed randomly according to their concentration percentage in the bioink, and a scaffold is created afterward[88]. Inkjet printing is based on the deposition of bioink drops in a predetermined way to create a final multi-layer pattern. As a result of thermal or piezoelectric changes, pressure pulses generate drops with a defined volume in the range of picoliters. Commercial thermal printers utilize heating elements to expel ink droplets and form vapor bubbles that are heated to 300°C for a few microseconds. Printing on a substrate in the Z-direction is possible with a micropositioning stage[25]. Despite possessing a relatively low printing resolution, this printing process provides rapid scaffold production at an affordable cost. Of note, low-viscosity materials and low cell concentrations should be used to avoid nozzle clogging[89]. Extrusion-based bioprinters disperse bioinks as strands via a screw plunger or an air pump; to be more specific, the dispenser is mounted on a robotic stage, enabling the printing head to move in three directions. As a result of their design, extrusion-based bioprinters can be used with hydrogels having different viscosities and cell densities, and compared with inkjet-based bioprinting, there is less risk of clogging. However, if viscous hydrogels are utilized, a longer printing time and higher mechanical stresses may reduce the viability of encapsulated cells by 40–80%[90]. In laser-based bioprinting, the bioink is transferred from one substrate to another; to elucidate, pulses of the laser beam are responsible for this transfer, and in order to control the transfer of energy, a thin layer of energy-absorbing material (typically titanium or gold) is deposited on top of the donor substrate. In response to the absorption of energy, bioink droplets of defined sizes are formed. Although this technique is capable of printing materials with high viscosities and high cell densities at extremely high resolutions, it is limited by its excessive cost and inability to print large constructs[25]. In this regard, a number of TE projects have been successfully performed using the multi-cell bioprinting method[91-98]. Compared to cell aggregate and single-cell bioprinting, Table 1 summarizes the benefits and drawbacks of this method.

In summary, selecting the appropriate bioprinting technique requires consideration of both the fabrication process and the cell requirements. Bioprinting of cell aggregates is often necessary to produce large tissues in size or have tight junctions between cells. The use of single-cell bioprinting permits researchers to deposit microenvironment components and stem cells in precisely defined locations to study cell–matrix interactions. In contrast, multi-cell bioprinting has proven to be the most extensively used and advanced technique among all, for PBHs in particular.

3. Microenvironmental factors on bioprinting the cell-laden PBHs

In bioink formulation, it is crucial to consider the main material and concentration as key parameters in order to ensure the process's reproducibility and enhance printability. Natural structural proteins, such as collagen, elastin, silk fibroin, and fibrin, are particularly noteworthy for their physiological and biological cues, contributing to the development of bioinks. Additionally, PBHs are environmental friendly, renewable, and tend to exhibit excellent biocompatibility, strength, elongation, toughness, and slow degradability. All these remarkable materials' characteristics originate from the proteins' structure. Indeed, features of proteins, such as hydrophobicity and bioactivity, which are the building units of living organisms, depend on the amino acid constituents that are at the primary level, resulting in the folding of secondary

Tables 1. Benefits and drawbacks of different bioprinting techniques based on the format of the cells and the number of cells produced during printing

Bioprinting technique	Printing speed	Printing throughput	Resolution	Cell viability	Cell density	Cost
Single-cell	High	Low	High	Medium	Low	High
Cell aggregate	Medium	High	Low	High	High	Medium
Multi-cell						
Inkjet	High	Medium	Medium	Medium	Low	Low
Extrusion-based	Low	High	Low	Medium	High	Low
Laser-assisted	Medium	Medium	High	High	Medium	High

structures into the tertiary 3D configuration. Notably, proteins have functional amino and carboxyl groups that can be utilized to convert these materials into hydrogels by enzymatic, chemical, and physical crosslinking methods. The unfolding of protein and its accumulation into a gel matrix is the most frequent process in protein gelation, leading to alterations in conformation from the third to the second structure and the subsequent rise in random coil content. Specifically, the structural changes in proteins for the PBHs' formation are owing to the secondary structure content's alterations, and proteins' carboxyl and amino groups can form a hydrophilic environment, resulting in an inherent, great swelling property of PBHs[21]. One crucial factor in the bioprinting of PBHs is the hydrogel's mechanical characteristics specified via its network structure and crosslinking density. Generally, β-sheet structures are known to provide hydrogels with more robust mechanical features than α-helix structures due to their higher degree of crosslinking and stability; therefore, a greater content of β-sheet structures in PBHs can make them more suitable for bioprinting. As an instance, a group of researchers[99] performed the gelatin-silk fibroin bioink gelation employing enzymatic and physical crosslinking; to elucidate, the physical crosslinking (sonication) could accelerate the silk fibroin macromolecules' self-assembly in β-sheet crystals, which in turn improved the bioink rheology.

Physical and chemical factors are essential for the bioprinting process, especially the bioprinting of cell-laden PBHs. In this case, cells are incorporated into PBHs, and the microenvironment may affect the protein structures. For example, remodeling of the initial hydrogel matrix can happen as a function of incorporating the cells and secretion of native ECM[100]. Besides, hydrogel degradation and swelling can impact the bioprinted construct's integrity[101]. Thus, careful consideration should be given to several important biophysical cues, such as composition, biodegradation, porosity-related parameters, and crosslinking process. Furthermore, chemical structure, the presence of GFs and signaling molecules, as well as cell signaling, must be taken into account in the case of biochemical cues. All in all, the PBHs should meet several biophysical and biochemical requirements to be applied in bioprinting (Figure 2).

3.1. Biophysical factors

3.1.1. Composition

One of the most significant biophysical cues is the composition of PBHs, which must be taken into account when employing them as bioinks for cartilage and bone TE. In this regard, several aspects must be considered; firstly, PBHs must be innately non-immunogenic, non-cytotoxic, and minimally pro-inflammatory to ensure the health of cells[102]. Gelatin and collagen hydrogels are the most commonly employed PBHs for cartilage and bone regeneration due to their excellent biocompatibility and desirable capability to support cell growth and differentiation in these tissues[103]. In the case of PBHs, gelatin molecules are able to form partial triple-helical conformations by hydrogen bonds below a critical temperature, resulting in a sol-gel transition; however,

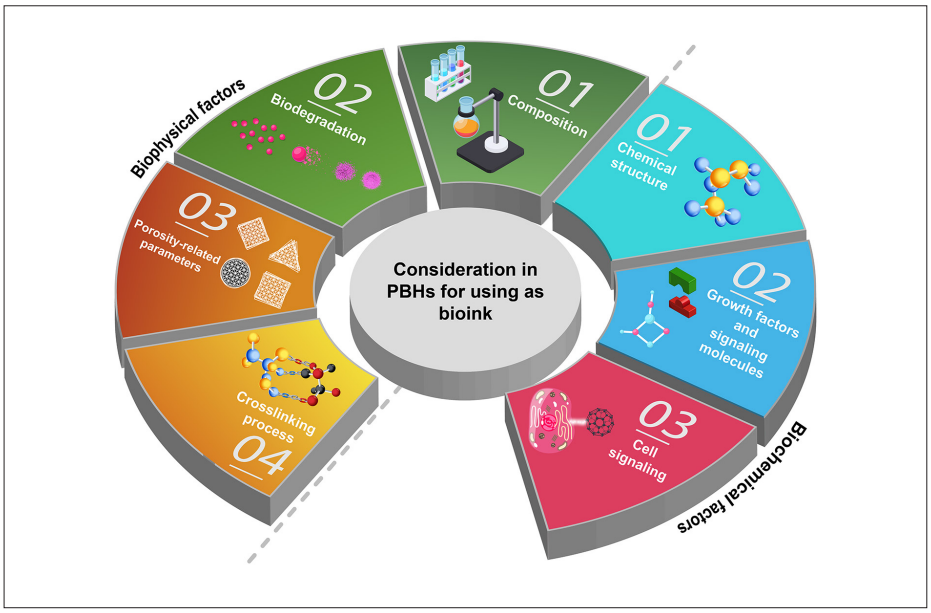

Figure 2. An overview of biophysical and biochemical considerations for the use of PBHs as bioinks.

beyond this temperature, hydrogen bonds weaken, and the helices disappear, leading to a gel-sol transition. As a result of this well-defined feature, gelatin has proven to be a versatile additive for the formulation of a wide variety of composite PBHs. Analogous to gelatin, collagen can also form gels at different temperatures and pH levels[104,105]. Compared with native tissues, its secondary helical conformation initiates a sol-gel transition for bioprinting but can commonly cause mechanical weakness. Hence, the molecular assembly of collagen is not controlled sufficiently, and therefore, native structural hierarchy is not present[106]. Moreover, fibrin and silk fibroin hydrogels display favorable outcomes and have unique advantages in certain applications, including ease of preparation and manipulation for fibrin and superior toughness and thermal stability for silk fibroin[107-110]. Secondly, PBHs should have appropriate mechanical features, especially elastic stiffness, which facilitate mechanical signaling to the cells for guiding differentiation, proliferation, and ECM deposition[102]. In the case of stiffness, bioinks with high stiffness or rigidity can inhibit the movement, growth, and differentiation of cells, whereas those with high softness are able to provide sufficient support for the encapsulated cells[111-113]. Concerning these subjects, a team of scientists[114] optimized the mechanical stiffness of alginate/gelatin bioinks (crosslinking approach: ionic crosslinking with 2% w/v $CaCl_2$ for 10 min) so as to improve ECM mineralization and cell organization for bone TE. With the aid of extrusion bioprinting, alginate/gelatin bioinks (4.1% w/v for gelatin and 0.8% as well as 1.8% w/v for alginate) loaded with P3 human mesenchymal stem cells (hMSCs) (cell density: 1.67×10^6, 5×10^6, and 15×10^6 cells/mL) having various stiffness were printed. They illustrated that soft scaffolds (0.8% w/v alginate, stiffness: 0.66 ± 0.08 kPa) possessed higher content of deoxyribonucleic acid (DNA) at day 28, enhanced expression of collagen type I alpha-II (6.7-fold increment from day 1 to day 28), increased alkaline phosphatase (ALP) activity at day 28, and stimulated osteogenic differentiation in comparison with the stiff ones (1.8% w/v alginate, 5.4 ± 1.2 kPa). Moreover, considerably less mineralized tissue was formed in stiff constructs than in soft ones at day 42 (22.6 ± 6.0 mm^3 versus 43.5 ± 7.1 mm^3) (Figure 3A). The mineral formation rate in the soft bioprinted scaffold was significantly higher than the stiff one at days 28–35 and 35–42. Interestingly, cells in soft scaffolds displayed a 3D cellular network in the mineralized matrix and osteoblast- and early osteocyte-related gene expressions at day 42. Within a pioneering investigation, Martyniak *et al.*[115] developed gelatin methacryloyl (GelMA)/hyaluronic acid methacrylate (HAMA) bioinks (crosslinking approach: photo-crosslinking with 0.05% w/v lithium phenyl-2,4,6-trimethylbenzoylphosphinate [LAP] at 405 nm wavelength and exposure times of 15, 38, and 60 s) and determined their ideal combination in the case of optimal stiffness for cartilage bioengineering. Human chondrocyte collagen type II–alpha-I–Gaussia luciferase reporter system (HuCol2gLuc) (cell density: 2×10^6 cells/mL) were embedded within the GelMA/HAMA bioink (15% w/v and 2% w/v), and the bioink was printed utilizing a pneumatic extrusion printing device. It was revealed that the HAMA addition to GelMA enhanced chondrogenesis, compared to GelMA (15% w/v) alone. Two ratios of GelMA/HAMA bioinks (1:1 and 2:1) with different stiffness (32 and 57.9 kPa) were assessed for cellular mobility and survival. High cellular viability (≥ 90%) was achieved for both bioprinted materials on all days. Furthermore, the GelMA/HAMA bioink with 1:1 ratio had considerably more fluorescent-labeled mobile cells (~2.5) compared to the 2:1 one (~1), and the cells also moved further (~26 μm) and faster (~1 μm/min) in the 1:1 ratio. All in all, the softer printed construct (1:1) showed a higher level of cellular mobility compared with the stiffer one (2:1). Notably, if multiple kinds of cell are contained in the PBHs, the characteristics of the PBHs should possess tenability to accommodate the various cellular requirements and allow spatiotemporal control if required.

3.1.2. Biodegradation

Bioinks that degrade too rapidly cannot provide adequate mechanical stability for long-term tissue development, while those that degrade too slowly may hinder tissue growth and ECM remodeling. In addition to being an essential feature for ECM deposition, PBHs' optimal degradation is indeed necessary for cell proliferation and mobility in the gel as well as the nearby host tissue[116]. In order to prolong the degradation rate of GelMA hydrogel, glycidyl-methacrylated HA (GMHA) was introduced into this system to obtain a novel bioink with a suitable degradation rate for cartilage regeneration applications. Employing extrusion bioprinting, GelMA/GMHA bioinks (crosslinking approach: photo-crosslinking with 0.03% w/v LAP) with various concentrations (7% w/v for GelMA and 3% and 5% w/v for GMHA) encapsulating tonsil-derived MSCs (cell density: 10×10^6 cells/mL) were printed, and the achieved constructs were subcutaneously implanted into female Bagg albino (BALB)/c nude mice models so as to observe the hydrogels' degradation characteristics after 3 weeks. It was illustrated that the 7% GelMA/5% GMHA-printed scaffold was fairly stable within the physiological environment and preserved its shape well with a low rate of degradation, allowing for tonsil-derived MSCs' chondrogenesis. Cells had high viability in the implanted hydrogel, and cartilage-like tissues, that were regenerated over time, could be observed. Furthermore, enhanced expression of collagen type II and formed hyaline matrices

demonstrating the bone matrix were seen 3 weeks post-implantation[117]. Another study in the field of cartilage TE evaluated the degradation of polyethylene glycol diacrylate (PEGDA)/gelatin/silk methacrylate (SilMA) bioink (crosslinking approach: photo-crosslinking with 0.2 w/v LAP at 405 nm wavelength, light-emitting diode (LED) light intensity 1000 mW/cm, and exposure time of 20 s) (6%, 9%, and 3% w/v) encapsulating primary porcine chondrocytes (cell density: 2×10^6 cells/mL) printed using extrusion-based printing and reported that delay in the degradation rate was seen after adding PEGDA to the composition, which was suitable for the load-bearing cartilage repair. Specifically, 90% degradation and minimal degradation of the printed hydrogel were observed after 28 days when incubating in protease enzyme and phosphate-buffered saline solution, respectively[118]. In the case of bone regeneration, an innovative experiment on the digital light processing (DLP)-based bioprinting of MC3T3-E1 preosteoblasts-encapsulated SilMA bioinks (crosslinking approach: photo-crosslinking with 0.2% wt LAP at 405 nm wavelength, visible blue light, and exposure time of 13 s for each layer) (cell density: 2×10^6 cells/mL) revealed that between three groups of 10%, 15%, and 25% w/v SilMA scaffolds with degradation percentages of 91.0 ± 2.27%, 64.8 ± 3.2%, and 48.6 ± 2.15% at 21 days, the 15% SilMA construct was the most efficient among the others in supporting the proliferation and attachment of the embedded cells[119].

3.1.3. Porosity-related parameters

Porosity-related parameters associated with bioprinted protein-based structures can affect *in vitro* cellular behaviors, in addition to *in vivo* tissue development[120]. Specifically, the presence of a porous structure into a printed scaffold is necessary for the diffusion of nutrients, cellular viability, cell migration, and proliferation, as well as *in vivo* tissue regeneration[121]. Utilizing cell-laden porcine tendon-derived collagen bioinks (1%, 3%, and 5% wt), porous collagen scaffolds crosslinked via genipin were printed and compared with non-porous ones, both fabricated via an extrusion printing system. Mostly live rabbit articular chondrocytes (cell density: 1×10^6 cells/mL) were found in the porous constructs' cross-sectional live and dead image, whereas dead cells were mostly present in the non-porous scaffolds' core after 7 days of cultivation. Indeed, the death of cells could be owing to the restricted nutrition penetrability of the collagen and the lack of a porous structure to compensate for this limitation. Notably, female New Zealand White rabbits with osteochondral defects were used as animal models, and the porous bioprinted collagen scaffold-treated group displayed significantly improved *in vivo* regeneration of cartilage, possessed newly-formed hyaline cartilage integrating well with the nearby cartilage, and showed high levels of glycosaminoglycans (GAGs) distribution compared to the non-porous scaffold-treated group having severe irregularity in the articular surface and defect lesions with centers that were not regenerated 4 weeks post-implantation[121]. Multiple evaluations have revealed that *in vivo* printed scaffolds with pore sizes of approximately 300 μm promote osteogenesis because of their higher permeability and capacity for vascularization; on the other hand, smaller pore sizes around 100 μm are more favorable for chondrogenesis[122]. Moreover, a porosity gradient in the radial direction can be found in the structure of bone, in which the mean porosity is enhanced from the cortical bone toward the trabecular bone[123,124]. To mimic this unique structure, a novel experiment employed DLP-based bioprinting system including a microfluidic mixer chip to print hMSCs-loaded 10% wt GelMA bioinks mixed with 10% wt GelMA solution comprising the porogen (crosslinking approach: photo-crosslinking with 2.20×10^{-3} M Tris(2,2-bipyridyl) dichlororuthenium (II) hexahydrate [Ru]/sodium persulfate [SPS] at 450 nm wavelength, blue light, and exposure time of 30 or 60 s for each layer) (cell density: 2×10^6 cells/mL). The final printed construct was three gradual zones featuring various pore sizes (12, 29, and 65 μm). Further tests illustrated the improved spreading of the encapsulated cells within the portions with larger pore sizes 7 days post-bioprinting. In comparison with the hydrogel segment that was mixed with 0.5% wt porogen, the cell cluster sizes were promoted to 2.5-fold and 4-fold in the gel regions containing 1.5% and 3.0% wt porogen, respectively. Thereafter, bone morphogenetic protein-2 (BMP-2) was integrated within the bioink in order to enhance the hMSCs' osteogenesis. The growth of MSCs, as cell clusters, filled in the pore areas and enhanced cell proliferation in portions having higher porogen concentration were observed, and improved expression of runt-related transcription factor 2 (RUNX2) (an osteoprogenitor in early stages) in the regions with larger pores and higher GF concentrations was confirmed[125].

3.1.4. Crosslinking process

The crosslinking process is another biophysical cue influencing the behaviors of encapsulated cells in the PBHs. For crosslinking of PBHs, physical, chemical, and enzymatic crosslinking approaches can be employed. Importantly, the crosslinker itself, its concentration, and the time of crosslinking affect the mechanical features of printed constructs and embedded cell properties[126-128]. Physical crosslinking involves using temperature or pH to form reversible interactions within the protein structure, influencing cell viability due to the sensitivity of cells to changes in temperature and pH. Furthermore, chemical crosslinking utilizes chemical agents to create covalent

bonds between protein molecules, resulting in the formation of a stable hydrogel structure; however, some chemical crosslinking agents can be toxic to cells and adversely affect cellular behaviors. Enzymatic crosslinking involves the employment of enzymes to catalyze the formation of crosslinks within the hydrogel, an approach that is biocompatible and offers more control over the crosslinking process. Nonetheless, enzymatic crosslinking requires longer incubation times, and the used enzymes need to be carefully handled to maintain cell survival. To be more specific, the chemically crosslinked network providing physical support impacts the stiffness and mechanical characteristics of the hydrogel; thus, breaking the chemical crosslinking bonds makes the PBHs more deformable and softer. Since embedded cells are able to sense and respond to the surrounding environment's mechanical properties, they experience alterations in their behaviors[129]. In the case of physical crosslinking, the crosslinks are usually reversible and can be broken via altering the pH, temperature, or ionic strength of the environment. Consequently, breaking these formed bonds can result in the dissolution of hydrogel or the loss of its structure; these phenomena exert effects on the encapsulated cells' organization, distribution, and survival[130–132]. Koo *et al.*[121] assessed the concentration and time effects of genipin, as a chemical crosslinker, on cell-laden collagen-based printed scaffolds' mechanical features and encapsulated rabbit articular chondrocytes' behaviors. In this regard, these scaffolds bioprinted by extrusion printing were dipped into the genipin solution having concentrations of 0.1, 1, and 5 mM in the culture medium for various times (0.5, 1, and 6 h). It was revealed that the cell-laden construct crosslinked with a higher concentration of genipin and longer crosslinking time displayed higher compressive modulus. Moreover, the compressive modulus enhanced with the increment of crosslinking agent's concentration and crosslinking time. At the crosslinker concentration of 0.1 mM, all of the cellular survival values at the crosslinking times of 0.5, 1, and 6 h were > 90% after 1 day of cultivation, and they even augmented up to 98 ± 0.4% after 7 days. At 1 mM concentration of genipin, the cellular viability gradually diminished by the crosslinking time's extension from 0.5 to 6 h, and the percentages of cell survival with the crosslinking time of 1 h were 88 ± 2.0% and 80 ± 0.5% at 1 and 7 days of cultivation, respectively. Nonetheless, at the higher genipin concentration of 5 mM, the viability of cells was decreased dramatically after 7 days due to the high genipin's concentration toxic effect or the excessively high compressive modulus via the immoderate cross-linking, which could fix the cells within the collagen strut and ultimately interrupt their metabolic activities. The scaffolds' controllability was also specified by lifting one of their sides so as to see if they could be readily handled for additional treatments like *in vivo* implantation; all of them except for the ones crosslinked with 0.1 mM genipin showed adequate controllability without the deformation of structure.

Among these constructs, only scaffolds that were crosslinked with genipin having 1 mM concentration and crosslinking time of 1 h possessed an average cell survival rate of 84%; as a result, these conditions were opted as the optimal crosslinking circumstances. Within a pioneering investigation that employed extrusion printing, scientists[133] reported the impacts of the tannic acid (TA), as chemical crosslinking agent used post-printing, with various concentrations (0.1%, 0.25%, 0.5%, 1%, and 3% wt) in the MC3T3-E1 preosteoblasts-embedded porcine tendon-derived collagen type I scaffolds (5% wt of collagen) (cell density: 5×10^6 cells/mL) on their physical characteristics and cellular activities. They set the crosslinking time to 10 min in order to impede high cell fixation which could disturb cellular activities. The scaffolds crosslinked with 0.1% and 0.25% wt crosslinker did not possess sufficient mechanical stability; indeed, they were not capable of preserving their original shape and readily bending around a steel rod. However, the concentration above 0.5% wt considerably enhanced the constructs' stability, and the structures could maintain their flat shape with mechanical strength. Compared with the cell-laden collagen constructs without crosslinking, the crosslinked ones had significantly improved mechanical properties. Furthermore, from concentration of 0.5% wt and above, the mechanical strength exponentially augmented (Young's modulus = 9.81 ± 0.88, 23.34 ± 1.84, and 67.13 ± 6.52 kPa for TA-0.5, TA-1, and TA-3 samples, respectively). Interestingly, non-crosslinked scaffolds had nearly 97% of degradation rate in 6 h, whereas the other crosslinked ones displayed relatively slow rate of degradation. During 10 days of observation, the degradation rate of the structures diminished with the increase of TA concentration as anticipated. In the case of cell behaviors, a minor decrease in cellular viability was seen from TA concentrations above 1% wt. Nevertheless, all scaffolds preserved great survival of cells (approximately 95–96%); to elucidate, the high viability with different TA concentrations demonstrated that the TA crosslinking process was totally safe for the MC3T3-E1 preosteoblasts. Cells initiated proliferation on T-0.1 and T-0.25 structures from day 4, and those on the T-0.5 scaffold could start at day 7. Thereafter, each of these systems exhibited significantly enhanced DNA expression. However, the T-1 scaffold did not display a significant difference in the values of DNA expression during 14 days of cultivation. The release of cells was noticeably high for the T-0.1 construct because of the low TA concentration

leading to the weaker crosslinking, while for the other crosslinked ones, the cell release was deterred from the strut owing to the stronger crosslinking. Among those constructs with controllability (T-0.5 and T-1 ones), the T-0.5 scaffold with better cellular behaviors was chosen as the optimum scaffold for further analyses in future studies. Table 2 summarizes the biophysical parameters influencing PBHs' bioprinting in the cartilage and bone TE.

3.2. Biochemical factors

3.2.1. Chemical structure

Cells' behaviors are impacted by diverse signals they receive from the ECM and neighboring cells; indeed, these received signals are capable of promoting adherence, morphogenesis, differentiation, and proliferation of cells[134]. Regarding the chemical structure as a biochemical cue, proteins in bioinks can exert effects in various ways, one of which is that they are able to promote cell spreading, survival, proliferation, and adhesion to the hydrogel matrix via presenting adhesive sites and specific ligands like matrix metalloproteinase (MMP) sequence and RGD sequence, which bind to the integrin receptors on cells surface[135]. Concerning this matter, cross-linker-free gelatin/silk fibroin bioinks (1.5% and 7% w/v) encapsulating primary chondrocytes (cell density: 10^6 cells/mL) for the cartilage TE were printed by employing an extrusion printing approach. They revealed enhanced cellular viability, improved cell adhesion, and increased ECM formation compared to the control group, which could be attributed to the RGD presence in both silk fibroin and gelatin proteins. Moreover, improved printability due to the shear-thinning behavior of silk and the high viscosity of gelatin was achieved[136]. Özenler *et al.*[137] designed mouse MC3T3-E1 preosteoblasts-loaded sodium alginate dialdehyde/gelatin bioinks (7.5% and 15% w/v) containing fish scale (FS) particles (1%, 3%, 5%, and 10% w/v) (cell density: 5×10^6 cells/mL) for bone regeneration. Then, they printed the bioinks using extrusion printing device and physically and chemically crosslinked the structures employing $CaCl_2$ and microbial transglutaminase, respectively (Figure 3B). As one of the results, the promotion of cellular proliferation during 28 days of cultivation was reported due to the gelatin's favorable RGD sequence. Another investigation developed arch-like bioprinted constructs utilizing GelMA and silk fibroin/gelatin bioinks (crosslinking approaches: photo-crosslinking with 0.25% w/v LAP at 365 nm wavelength (ultraviolet [UV] light with 700 mA) and exposure time of 2 min as well as enzymatic crosslinking with mushroom tyrosinase (800 units/mL), respectively) for cartilage regeneration. Employing extrusion printing, two compositions of bioinks (GelMA bioink: 10% w/v of GelMA and silk fibroin/gelatin bioink: 80 mg of gelatin powder from porcine skin type A in 800 μL of silk fibroin solution) loaded with human bone marrow-derived MSCs (hBMSCs) (cell density: 1×10^7 cells/mL) were bioprinted. In order to assess the cellular morphology and cartilaginous matrices generated by cells after 21 days of chondrogenic differentiation in constructs, scientists used histological staining. They revealed that the GelMA structures displayed a sparse cells distribution, although the cells had spherical morphology (Figure 3C(i, ii)). The silk fibroin/gelatin constructs showed a homogenous distribution of cells, and some of these cells exhibited a spread morphology on day 21 (Figure 3C(iii, iv)). The observed spread morphology could be owing to the adhesive sites in the silk fibroin/gelatin constructs[138].

3.2.2. GFs and signaling molecules

Promoting cellular proliferation, inducing cell differentiation, or enhancing tissue regeneration via incorporating GFs or other signaling molecules into bioinks is another topic worthy of discussion[139-141]. The desired cell/tissue-related properties of PBHs can be achieved by adding several GFs, such as insulin-like growth factor[142], vascular endothelial growth factor (VEGF)[143], stromal cell-derived factor-1α[144], fibroblast growth factor[145], and BMP-2[146], as well as signaling molecules, including exosomes, ECM granules, DNA, microRNA (miRNA), cytokines, bioceramics, and bioactive polymers, to name a few[147]. For instance, these biochemical factors are capable of improving cell differentiation by presenting cues that direct the differentiation of stem cells into specific cell types like bone or cartilage cells[148,149]. In this regard, a team of scholars[150] worked on the functional vasculature and osteogenesis of GelMA-based bioinks for application as large-scale bone tissue constructs. Within this novel study, GelMA bioinks (crosslinking approach: photo-crosslinking with 0.1% w/v Omnicure S2000 at 360–480 nm wavelength, UV light with 6.9 mW/cm^2, and exposure time of 20 s) functionalized/loaded with VEGF and silicate nanoplatelets that contained human umbilical vein endothelial cells (HUVECs) and hBMSCs (cell densities: 2×10^6 cells/mL) were bioprinted using extrusion-based printing. To construct a pattern with both capabilities of vascularization and osteogenesis, a HUVECs/hMSCs-encapsulated GelMA hydrogel (5% w/v) was bioprinted in the central area so that a blood vessel could be formed, and around this structure, they bioprinted silicate nanoplatelets-loaded, VEGF-functionalized GelMA hydrogel (10% w/v) embedded with hMSCs (cell density: 2×10^6 cells/mL) for inducing osteogenesis. It was revealed that a perfusable lumen possessing an endothelial lining at the construct's center was generated post-bioprinting. The hMSCs in the inner gel differentiated to the smooth muscle cells that could promote the formation, stabilization, and maturation

Tables 2. Summary of biophysical parameters affecting PBHs' bioprinting in the cartilage and bone TE

Considered factors	Bioink composition	Cell type (cell density)/ animal model/target tissue	Printing method/ crosslinking approach	Results	Reference
Composition	Alginate (0.8% and 1.8% w/v)/ gelatin (4.1% w/v)	P3 hMSCs (1.67×10^6, 5×10^6, and 15×10^6 cells/mL)/-/bone	Extrusion/physical crosslinking (ionic crosslinking)	• Higher content of DNA, enhanced expression of collagen type I–alpha-II, increased ALP activity, and stimulated osteogenic differentiation in soft scaffolds (0.8% w/v alginate) • Less mineralized tissue and lower mineral formation rate in stiff constructs • Observed cells with a 3D cellular network and osteoblast- and early osteocyte-related gene expressions in soft scaffolds	[114]
	GelMA (15% w/v)/HAMA (2% w/v) (1:1 and 2:1)	HuCol2gLuc (2×10^6 cells/mL)/-/cartilage	Extrusion/chemical crosslinking (photo-crosslinking)	• Enhanced chondrogenesis in the GelMA/HAMA bioink over the GelMA one alone • High cellular viability (≥ 90%) • Higher level of cellular mobility in the softer printed construct (1:1)	[115]
Biodegradation	GelMA (7% w/v)/GMHA (3% and 5% w/v)	Tonsil-derived MSCs (10×10^6 cells/mL)/female BALB/c nude mice/cartilage	Extrusion/chemical crosslinking (photo-crosslinking)	• Achieved a printed scaffold (7% GelMA/5% GMHA), being fairly stable, preserving its shape well, and having a low rate of degradation • High viability of cells and regenerated cartilage-like tissues • Enhanced expression of collagen type II and formed hyaline matrices 3 weeks post-implantation	[117]
	PEGDA (6% w/v)/gelatin (9% w/v)/SilMA (3% w/v)	Primary porcine chondrocytes (2×10^6 cells/mL)/-/cartilage	Extrusion/chemical crosslinking (photo-crosslinking)	• Delayed degradation rate after adding PEGDA to the composition • Obtained a printed hydrogel with 90% degradation after 28 days of incubation in protease enzyme	[118]
	SilMA (10%, 15%, and 25% w/v)	MC3T3-E1 preosteoblasts (2×10^6 cells/mL)/-/bone	DLP/chemical crosslinking (photo-crosslinking)	• Achieved degradation percentages of 91.0 ± 2.27%, 64.8 ± 3.2%, and 48.6 ± 2.15% at 21 days for groups of 10%, 15%, and 25% w/v SilMA scaffolds, respectively • Better proliferation and attachment of the cells in 15% SilMA construct	[119]

Porosity-related parameters	Collagen (1%, 3%, and 5% wt)	Rabbit articular chondrocytes (1×10^6 cells/mL)/female New Zealand White rabbits/cartilage	Extrusion/chemical crosslinking	• Observed mostly live cells in the porous constructs' cross-sectional live and dead image • Significantly improved *in vivo* regeneration of cartilage, and high levels of GAGs distribution in the porous scaffold-treated group • Observed severe irregularity in the articular surface and defect lesions in the non-porous scaffold-treated group	[121]
	GelMA (20% wt)/porogen (0.5%, 1.5%, and 3.0% wt)	hMSCs (2×10^6 cells/mL)/-/bone	DLP/chemical crosslinking (photo-crosslinking)	• Improved cell spreading in portions with larger pore sizes • Promoted cell cluster sizes in the gel regions containing 1.5% and 3.0% wt porogen • Enhanced cell proliferation in portions having higher porogen concentration, and increased expression of RUNX2 in the regions with larger pores and higher BMP-2 concentrations	[125]
Crosslinking process	Collagen (1%, 3%, and 5% wt)	Rabbit articular chondrocytes (1×10^6 cells/mL)/female New Zealand White rabbits/cartilage	Extrusion/chemical crosslinking (0.1, 1, and 5 mM of genipin)	• Higher compressive modulus for the construct crosslinked with a higher concentration of genipin and longer crosslinking time • Enhanced compressive modulus with the increment of crosslinking agent's concentration and crosslinking time • Achieved cellular survival > 90% at the crosslinking times of 0.5, 1, and 6 h at 0.1 mM genipin, gradually diminished cellular viability by the crosslinking time's extension from 0.5 to 6 h at 1 mM, and dramatically decreased cell survival at concentrations beyond 5 mM	[121]
	Collagen type I (5% wt)	MC3T3-E1 preosteoblasts (5×10^6 cells/mL)/-/bone	Extrusion/chemical crosslinking (0.1%, 0.25%, 0.5%, 1%, and 3% wt of TA)	• Enhanced stability and augmented mechanical strength in the TA concentration above 0.5% wt • Diminished degradation rate with the increase of TA concentration • Observed cell proliferation, enhanced DNA expression, and great survival of cells (approximately 95–96%) in all scaffolds	[133]

of vessels, as well as enhancing the HUVECs proliferation. Furthermore, HUVEC's survival and vasculogenesis were promoted possibly because of the VEGF that activated the VEGF receptors playing roles in the regulation of phosphoinositide 3-kinase (P13K) and focal adhesion kinase. They also reported that the encapsulated hMSCs formed a mature bone niche after 21 days of cultivation mainly due to the existence of silicate nanoplatelets, VEGF presence, and the osteogenic medium' sustained perfusion. Recently, a hBMSCs-loaded alginate sulfate/GelMA bioink (1% and 10% w/v) (cell density: 20×10^6 cells/mL) incorporating transforming growth factor beta-3 (TGF-β_3) was bioprinted employing extrusion printing technique (crosslinking approaches: photo-crosslinking with 0.05% w/v Irgacure 2959 at 365 nm wavelength, UV light with 5 mW/cm^2, and exposure time of 15 min, followed by ionic crosslinking with 50 mM $CaCl_2$ for 15 min) with the aim of articular cartilage repair. Sustained release of TGF-β_3 could provide an environment supporting robust *in vitro* chondrogenesis, with little evidence associated with the mineralization or hypertrophy over extended periods of culture. Moreover, *in vivo* 4-week results that included

the comparison of samples with and without GFs in a subcutaneously implantation BALB/c OlaHsd-Foxn1nu nude mice models showed that the groups treated with GF-loaded constructs had higher levels of sulfated GAGs (sGAGs) and collagen type II, as well as greater accumulation of matrix, indicating the formation of hyaline-like cartilage tissue[151]. Since exosomes act as media for communication between cells[152,153], a composite scaffold made up of decellularized cartilage ECM/GelMA (2% wt for ECM and 10% w/v for GelMA) containing BMSCs-derived exosomes bioinks was fabricated utilizing stereolithography 3D printing (crosslinking approach: photo-crosslinking with 0.25% w/v LAP at 405 nm wavelength, visible light, and exposure time of 30 s) for osteochondral repair by Chen *et al.*[139], and the therapeutic effects of MSCs-derived exosomes on osteoarthritis was examined using New Zealand White rabbit models. Interestingly, ECM/GelMA/exosome constructs could efficiently retain exosomes for at least 7 days, restore chondrocytes' mitochondrial dysfunction, improve cells migration, and polarize the synovial macrophage response toward an M2 phenotype. Comparing animals implanted with scaffolds with or without exosomes, it was demonstrated that ECM/GelMA/exosome-treated groups showed the formation of smooth tissues, regenerated fibrocartilage and hyaline-like cartilage, and more ossified tissues at 6 weeks post-implantation. The International Cartilage Repair Society (ICRS) scoring indicated a higher score for animals treated with exosome-embedded structures (14.1 ± 0.71) than the ECM/GelMA-and GelMA-treated groups (12.2 ± 0.61 and 7.8 ± 0.39, respectively) at 6 weeks after implantation. Each tissue's ECM generates a very unique tissue-specific microenvironment for the resident cells, which can provide them with the biochemical signals required for their functioning. Within an innovative evaluation, Isaeva *et al.*[154] assessed two compositions of collagen-based bioinks (4% w/v for pig atelocollagen type I) printed via extrusion printing: (i) with hMSCs (isolated from human adipose tissue) and (ii) with decellularized ECM granules (2.5% w/v with a particle size of 280 μm) and hMSCs (cell density: 5×10^6 cells/mL) for cartilage TE. After bioprinted constructs' subcutaneous implantation in white male rats, two groups were compared from various perspectives. In the first group (MSCs only), scholars observed the formation of a connective tissue capsule with multiple blood vessels and detected cells with cytoplasm including collagen type II 2 weeks post-implantation. The only evidence of the formed cartilage was the small islands of cartilaginous tissue with irregular shapes adjacent to the construct (Figure 3D(i–iv)). In the second group (decellularized ECM granules + MSCs), generation of a cartilage tissue was shown 2 weeks after implantation. Interestingly, chondroblasts could form tiny isogenic groups with an ECM having a pronounced perichondrium, and the produced ECM accumulated a great content of GAG. Moreover, an intense reaction to collagen type II by the tissue and signs of reduced proliferative activity were found (Figure 3D(v–viii)).

3.2.3. Cell signaling

The behaviors of cells within the bioprinted constructs are influenced not only by the bioinks cues but also by the signals from other cells as well as various types of intercellular signals, including autocrine, intracrine, endocrine, paracrine, and juxtacrine signals, categorized based on the distance between responder cells and signaling. Of note, paracrine and juxtacrine signaling pathways are of higher significance in bioprinting of stem cells owing to the size of printed structures. In juxtacrine signaling and via molecule transfer through gap junction channels that are along the surface of contact, intercellular communication is realized[155]. Stem cells, tending to form aggregates, are deeply affected by cluster situation under the mentioned mechanism. Specifically, the degree of MSCs differentiation into osteogenic lineage is revealed much greater in aggregated cells compared with isolated ones[46]. Furthermore, the stem cell aggregates' size is capable of regulating the differentiation fate[156]. By controlling the bioprinting volume, initial seeding density of cells, and cultivation time, stem cell aggregates with regular shapes and uniform sizes can be created through cellular proliferation post-bioprinting[157]. Signaling cells release paracrine signals, and they target the nearby cells. In this regard, one of the most essential uses is the co-culture of several cells in order to enhance cellular functions[9,69], and another approach to control the migration of cells is the co-printing of different cell types[158]. Additionally, multiple cells' deposition in arranged positions facilitates the complex tissues' construction, and regulation of cellular survival and density can influence the bioactive proteins' local concentration, further affecting the stem cell differentiation[159]. Table 3 recapitulates the biochemical parameters influencing PBHs' bioprinting in the cartilage and bone TE.

In a nutshell, the behaviors of cells encapsulated in the PBHs are affected by biophysical cues, including composition, biodegradation, porosity-related parameters, and crosslinking process. In this regard, elastic stiffness, degradation rate, pore size, porogen concentration, as well as time and concentration of the used crosslinker, which exert various effects on cell viability, proliferation, differentiation, and tissue regeneration, should be considered and optimized with respect to the PBHs. Furthermore, biochemical cues, such as chemical

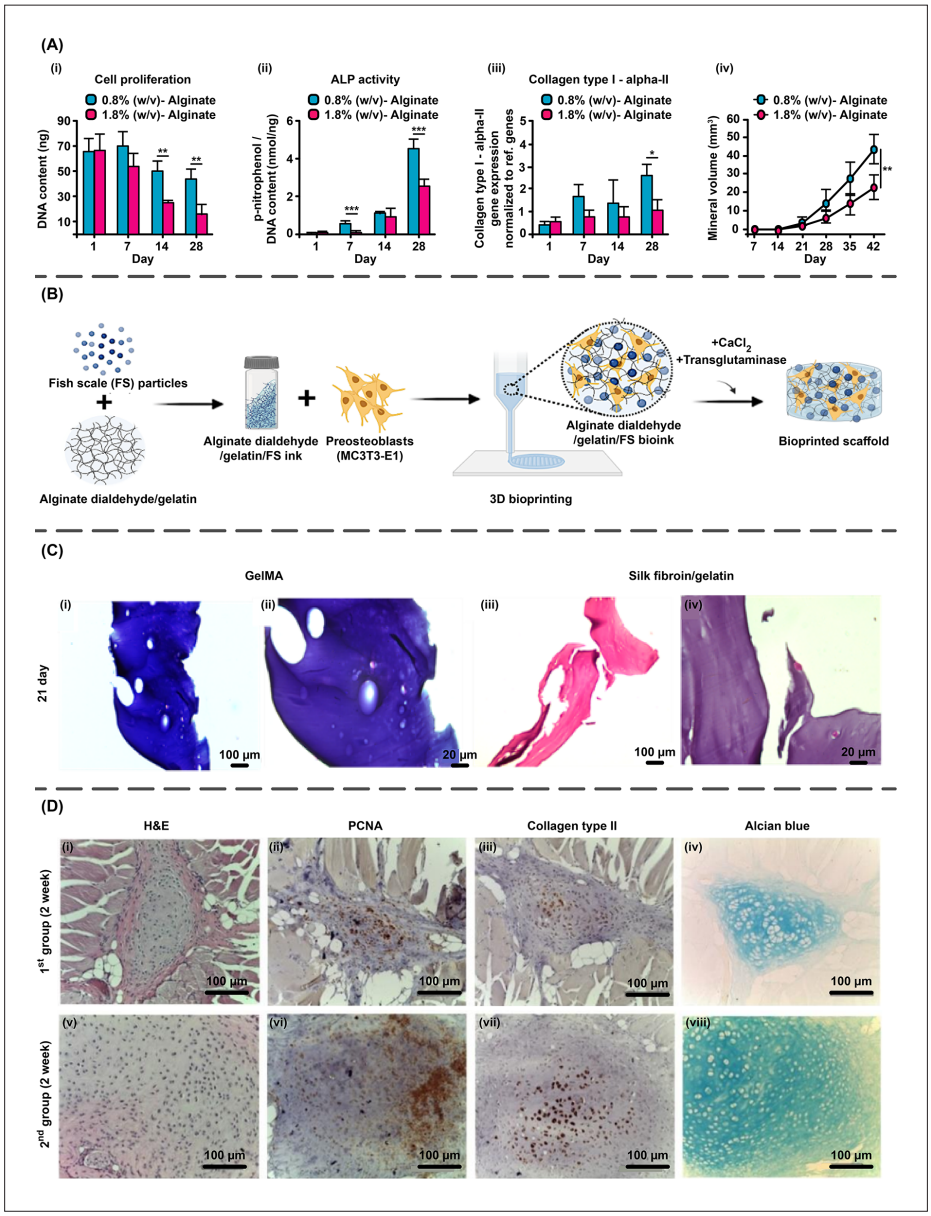

Figure 3. (A) (i) The content of deoxyribonucleic acid (DNA), (ii) alkaline phosphatase (ALP) activity, and (iii) gene expression of collagen type I–alpha-II associated with the printed constructs after cultivation in the osteogenic media at days 1, 7, 14, and 28. (iv) Mineral volume related to the bioprinted scaffolds from days 7 to 42 ($^{*}p < 0.05$, $^{**}p < 0.01$, and $^{***}p < 0.005$). Reproduced under the terms of the Creative Commons Attribution 4.0 International (CC BY 4.0) license[114]. Copyright 2020, Elsevier. (B) The schematic presentation of the cross-linked alginate dialdehyde/gelatin/FS particles bioprinted scaffold including preosteoblast MC3T3-E1 cells. Reproduced under the terms of the Creative Commons Attribution 4.0 International (CC BY 4.0) license[137]. Copyright 2023, IOP Publishing Ltd. (C) The hematoxylin and eosin (H&E) images of the (i, ii) GelMA and (iii, iv) silk fibroin/gelatin bioprinted constructs on day 21 (scale bars: 100 and 20 µm). Reproduced under the terms of the Creative Commons Attribution 4.0 International (CC BY 4.0) license[138]. Copyright 2023, IOP Publishing Ltd. (D) The cartilage tissue in rat models of two experimental groups (objective lens × 20 and scale bar: 100 µm). (i–iv) The first group (MSCs only), 2 weeks. (v–viii) The second group (decellularized ECM granules + MSCs), 2 weeks. (i, v) H&E staining; (ii, vi) proliferating cell nuclear antigen (PCNA) staining; (iii, vii) immunohistochemical staining for collagen type II; (iv, viii) Alcian blue staining. Reproduced under the terms of the Creative Commons Attribution 4.0 International (CC BY 4.0) license[154]. Copyright 2022, MDPI.

structure, presence of GFs and signaling molecules, as well as cell signaling impact cell properties like cellular survival, adhesion, differentiation, and ECM formation, to name a few. To achieve the best cell-related results, scholars must pay meticulous attention to the RGD or MMP sequences proteins possess, GFs or other signaling molecules (exosomes, DNA, miRNA, cytokines, bioceramics, and bioactive polymers) that can be introduced based on the

specific tissue (cartilage or bone), and different signaling pathways which occur within the cells (autocrine, intracrine, endocrine, paracrine, and juxtacrine signaling) or those received from other cells. In the fields of cartilage and bone TE, several research projects have been conducted so far to assess the impacts of mentioned environmental cues on the cellular features and tissue development ability of the PBHs. The original experiments mentioned above, alongside the achieved outcomes, will hopefully provide a comprehensive roadmap to move these fields forward.

4. Process compatibility considerations of PBHs

Bioprinting requires the proper design of a bioink to support tissue growth, cellular viability, and printability[160], and an efficient transfer of nutrients and oxygen within the bioink must be ensured by the PBH's structure[161].

Biocompatibility and mechano-rheological features are primarily responsible for bioink printability. Biocompatibility is essential in developing bioinks to prevent adverse effects on the viability, proliferation, or differentiation of cells encapsulated within[162]. Moreover, a bioink with appropriate mechano-rheological characteristics can be extruded easily, maintain its shape after printing, and support the deposition and organization of encapsulated cells into a desired structure. Although many PBHs, such as collagen and fibrin, exhibit the above-mentioned qualities, they cannot be readily tailored, and there are several challenges in their printing[163]. Bioprinting strategies and bioink properties are directly influenced by chemical, physical, and biological characteristics; in this regard, Figure 4 presents key considerations required for bioprinting cell-laden PBHs.

4.1. Mechano-rheological considerations

To be an optimal bioink for various bioprinting modalities, a material must possess several essential characteristics; for instance, a major factor affecting biomaterial printability is its mechanical properties. In multiple cases, scholars perform long-term incubation of cell-laden constructs for tissue development, and an integral part of this procedure is guaranteeing structural integrity. Notably, a printed construct should provide oxygen and nutrient transport into the cells, a critical subject to consider when designing its architecture[164].

Inkjet and extrusion-based bioprinting techniques are based on viscoelasticity and rheological characterization. PBHs and the amino acid sequences of fibrous proteins, including collagen, elastin, silk fibroin, keratin, resilin, and fibrin, play both mechanical and architectural roles in nature, which make them attractive choices for these

Tables 3. Recapitulation of biochemical parameters affecting PBHs' bioprinting in the cartilage and bone TE

Considered factors	Bioink composition	Cell type (cell density)/ animal model/target tissue	Printing method/ crosslinking approach	Results	Reference
Chemical structure	Gelatin (1.5% w/v)/ silk fibroin (7% w/v)	Primary chondrocytes (10^6 cells/mL)/-/ cartilage	Extrusion/physical crosslinking	• Enhanced cellular viability, improved cell adhesion, and increased ECM formation compared to controlled group • Improved printability due to the shear-thinning behavior of silk and the high viscosity of gelatin	[136]
	Sodium alginate dialdehyde (7.5% w/v)/ gelatin (15% w/v) with FS particles	Mouse MC3T3-E1 preosteoblasts (5×10^6 cells/mL)/-/bone	Extrusion/physical and chemical crosslinking (ionic and enzymatic crosslinking, respectively)	• Promoted cellular proliferation during 28 days of cultivation	[137]
	GelMA (10% w/v) and silk fibroin/ gelatin (80 mg of gelatin powder in 800 µL of silk fibroin solution)	hBMSCs (1×10^7 cells/mL)/-/cartilage	Extrusion/chemical crosslinking (photo-crosslinking and enzymatic crosslinking)	• Observed sparse distribution of cells with spherical morphology in GelMA structures • Homogenous distribution of cells with some of them exhibiting a spread morphology on day 21 in silk fibroin/gelatin constructs	[138]

	GelMA (15% w/v)/ VEGF/silicate nanoplatelets	HUVECs and hBMSCs (2×10^6 cells/mL)/-/bone	Extrusion/chemical crosslinking (photo-crosslinking)	• Generated perfusable lumen possessing an endothelial lining at the construct's center post-bioprinting • Differentiation of hBMSCs in the inner gel to the smooth muscle cells, promoting the formation of vessels and enhancing the HUVECs proliferation • Promoted HUVEC's survival and vasculogenesis, as well as formed mature bone niche by hBMSCs after 21 days	[150]
	Alginate sulfate (1% w/v)/GelMA (10% w/v)/ TGF-β_3	hBMSCs (20×10^6 cells/mL)/BALB/c OlaHsd-Foxn1nu nude mice/cartilage	Extrusion/chemical crosslinking (photo-crosslinking)	• Supported robust *in vitro* chondrogenesis due to the sustained release of TGF-β_3, with little mineralization or hypertrophy • Higher levels of sGAGs and collagen type II, as well as greater accumulation of matrix in groups treated with GF-loaded constructs	[151]
	Decellularized cartilage ECM (2% wt)/GelMA (10% w/v) containing BMSCs-derived exosomes	-/New Zealand White rabbits/osteochondral	Stereolithography/ chemical crosslinking (photo-crosslinking)	• Achieved constructs retaining exosomes, restoring chondrocytes' mitochondrial dysfunction, improving cells migration, and polarizing the synovial macrophage response towards an M2 phenotype • Formation of smooth tissues, regenerated fibrocartilage and hyaline-like cartilage, and more ossified tissues in ECM/GelMA/ exosome-treated groups • Higher score for animals treated with exosome-embedded structures at 6 weeks after implantation	[139]
GFs and signaling molecules	Atelocollagen type I (4% w/v) with (i) hMSCs and with (ii) decellularized ECM granules (2.5% w/v) and hMSCs	hMSCs (5×10^6 cells/mL) white male rats (155–230 g; aged 1.5–2 months)/cartilage	Extrusion/-	• Formation of a connective tissue capsule with multiple blood vessels and detected cells with cytoplasm including collagen type II in the first group • Small islands of cartilaginous tissue with irregular shapes adjacent to the construct in the first group • Generation of a cartilage tissue with chondroblasts forming tiny isogenic groups, and the produced ECM having a great content of GAG in the second group • Observed intense reaction to collagen type II by the tissue and signs of reduced proliferative activity in the second group	[154]

bioprinting techniques[165,166]. It needs to be considered that by extraction and purification procedures, proteins can be degraded which negatively impacts their molecular weight, an essential parameter influencing rheological properties[167]. To achieve the required purification degree while ensuring the best quality, selecting the proper

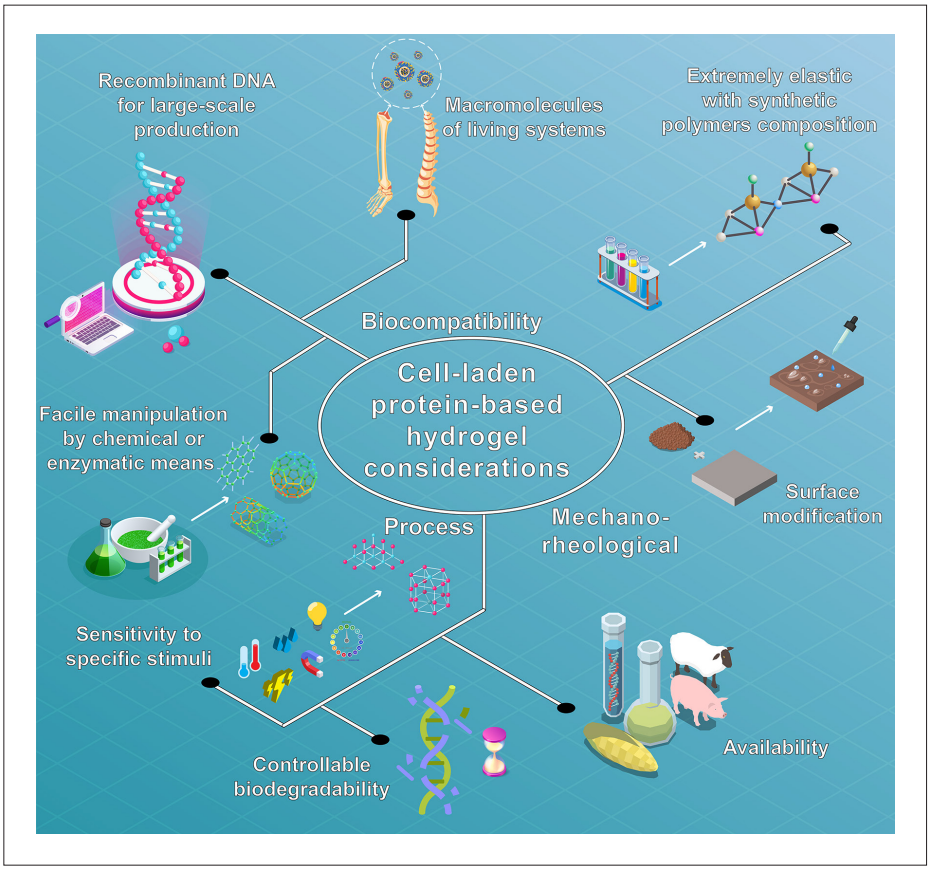

Figure 4. Bioink considerations needed to obtain cell-laden protein-based hydrogel (PBH) construct.

extraction method is of great importance when a PBH is developed. The characteristics of protein-based materials are significantly affected by the extraction technique and the utilized raw material, mainly due to the structure, molar mass distribution, composition, and functional properties of these materials[168]. Of note, protein molecules are entangled above a critical molecular weight, resulting in a proportional relationship between viscosity and molecular weight[168].

The presence and density of cells impact the rheological and mechanical features of inks. As a result of incorporating cells into a cell-barren gel-phase bioink, as well as increased cellular density, decreased degree of crosslinking, liquid viscosity, and final mechanical properties were observed[169]. Following this, rheological characteristics of the bioinks affect cellular viability during bioprinting; therefore, shear-thinning bioinks are more desirable because they shield cells and enable high-resolution printing simultaneously. Indeed, hydrogels should protect cells from exerted shear forces when the bioink is printed through the bioprinters' nozzles. After gelation, cell-laden hydrogels must have a storage modulus greater than the loss modulus in order to maintain their shape, indicating more viscoelastic behavior and thus greater printability. High protein concentration aids in minimizing post-printing shrinkage caused by ambient conditions; hence, better integrated mechanical properties are obtained[169-172]. Although augmenting the bioink's concentration via enhancing the viscosity reduces the distortion, increasing the concentration of PBHs diminishes the micro-roughness of the bioprinted scaffolds[25].

In the bioprinting fabrication method, viscosity describes the resistance of a bioink to deformation. Extruding bioinks with high viscosities and maintaining their shape post-printing are possible; however, encapsulated cells can be afflicted during the extrusion process because the deforming forces are high[173]. Another problem is associated with the release of shear forces after printing, which raise viscosity and inhibit the flow of printed constructs. On the other hand, the lower viscosity of bioinks leads to less nozzle clogging and allows the mixing of cells, but it can also result in poor feature definition since the bioinks cannot retain their shape subsequent to

the extrusion. Notably, a bioink's viscosity relies on factors like temperature, concentration, molecular interactions, and molecular weight[174].

Owing to the interactions that occur between hydrophobic domains within the sequence of proteins, shear forces moderately transform the liquid into solid structures (random coils to β-sheets) during the extrusion process. Unfortunately, degradation occurs in the production of proteins, affecting their rheological properties and printing. Besides, bioprinting lacks the solution's flow-induced extensional stretching, which diminishes the hydrogel viscosity and makes maintaining a stable structure difficult[175-177].

Before printing, the distribution of velocity and shear stress across the cross-section of a nozzle is zero. Additionally, a dispensing process cannot be carried out without shear stress[173]. In fact, hydrogels are subjected to shear stresses, at the nozzle walls in particular, at the time of printing. A number of parameters determine the amount of shear stress exerted on the bioink and embedded cells, such as printing pressure, nozzle diameter, and bioink viscosity[178]. In general terms, cells exposed to low shear forces tend to survive longer; conversely, high shear stresses can decrease cellular viability[179].

The shear stress generated in bioprinting does not pose an obstacle for small, globular proteins, but in the case of their larger, more fragile counterparts, structural integrity can be threatened[180]. As Nishioka *et al.*[181] argued higher compression rates that were employed to create droplets resulted in more protein denaturation and biological inactivity, and without the use of stabilizing additives, the enzyme activity was reduced under all printing conditions. It could have been possible to mitigate the adverse effects of bioprinting if sugars like trehalose and glucose were added to help preserve the enzymatic activity. This outcome raises some interesting queries regarding how proteins are denatured on the nanoscale as a corollary to maintain their bioactivity while growing crystals. It is worthy to mention that a protein's native secondary structure may be primarily determined by its amino acid sequence if the protein is small and globular; however, if the protein has deeply folded pockets functioning as catalytic sites, such as most of the active enzymes, then this rule may not always hold true[182].

By the same token, when printing biomaterials, yield stress specifies the force required in order to permit smooth, continuous extrusion[87,183] and ensures the homogeneity of encapsulated cells within bioinks. In the absence of forces, hydrogels with low yield stress leak out of nozzles or experience phase separation[184,185]. Of note, bioinks with high viscosities may maintain their shape for a short period of time in a bioprinted structure, but those with high yield strengths can hold shapes much longer. The yield stress is generated as a result of the viscosity peak, and when viscosity is plotted against shear stress, yield stress can be determined as the threshold value beyond which the material begins to flow[186]. Shape-retaining structures are typically produced by inks with high yield stresses; accordingly, adding bulking agents and thickeners, such as gellan, improves the PBHs' yield stress[187]. Moreover, high yield stresses can negatively influence cells when bioinks initiate flow[188]. Another subject is that hydrogels with cell-laden networks should be able to self-recover following printing because their physical crosslinking network is broken by the shear stress[189]. For the rapid recovery of the hydrogel's viscosity after applying a shear rate, a sharp decrease in the viscosity when the shear rate is applied is indeed ideal[190]. In addition to being mechanically strong, the extruded hydrogel filament must be capable of maintaining its shape subsequent to printing, as mentioned previously; thus, thixotropic properties are essential factors when evaluating a hydrogel's suitability for bioprinting[164].

From another viewpoint, for achieving optimum features of cell-laden printed structures, such as obtaining a filament diameter that matches the diameter of the nozzle, strand uniformity, and accurate strand placement, printing parameters like pressure and dispensing speed are often varied; nevertheless, these factors can influence the viability of extruded cells[191]. According to the scholars' investigation, increasing the applied pressure reduced the survival of encapsulated cells, regardless of whether the bioinks were liquid or gel[192]. The nozzle's diameter and shape should also be considered; within this context, a study by Billiet *et al.*[193] reported that cells in gel-phase bioinks were more viable when loading bioinks in conical nozzles compared with cylindrical ones. Furthermore, the shear stress increases with the increment of nozzle length, so analyzing varying nozzle lengths is of crucial significance for drawing firm conclusions between using tapered conical nozzles and cylindrical ones. Cell viability is also decreased when the nozzle diameter is reduced in cylindrical nozzles; to be more specific, the majority of cells are under highly stressful conditions, meaning that high pressure and a small diameter can cause necrosis rather than apoptosis, and the nucleus experiences morphological and irreversible damage[194].

In addition, strand stretching and thinning can result from bioprinting with a high speed at a given pressure[195]. The polymer matrix probably introduces potentially undesirable tensile and compressive forces to the cells, assisting with cell alignment along the bioprinted strand. Depending on the cells' location within a filament, cell survival and morphology may differ[196]. For instance, in the

case of nozzle walls, there may be an increase in shear stress at the strand's periphery, leading to lowered cellular viability. It is likely that the peripheral filaments tend to spread and form cellular networks more quickly because they are in the vicinity of the hydrogel surface and are not encapsulated completely[197]. A functional difference between two cells may also be the result of morphological differences between their filaments on the exterior and the interior. When this matter is viewed from the perspective of bioprinting approaches, for example, in an acoustic bioprinter, a pool of bioink is directly injected with cell-encapsulated droplets and deposited over the surface[67]. Due to its nozzle-free design, this technology avoids clogging issues and prevents detrimental shear stresses, heat, and pressure commonly experienced in other bioprinting methods[198,199].

The bioprinting of embedded cells has previously been done employing inkjet and extrusion technologies[200,201]. For maintaining cell viability, a PBHs was used to suspend cells in the inkjet fluid reservoirs utilized for bubble-jet technology or closed fluid reservoirs utilized for piezoelectric technologies in order to buffer them from temperatures between 200 and 300°C[202]. Additionally, inkjet and extrusion technologies subject cells and protein structures to remarkable mechanical and thermal stresses. Exhibiting poor directionality of droplets or continuous filaments, achieving non-uniform droplet sizes, existing mechanical shear stress of ejected cellular materials at the nozzle, and having routine nozzle clogging problems are other drawbacks of these techniques; as a result of the mentioned obstacles, large numbers of "empty" droplets are generated, contributing to significant inefficiency[66].

Although the nozzle geometry has no impact on the droplet size or ejection directionality, it has been demonstrated that the geometry can cause damage to cells or denature protein structures in printing methods like inkjet and extrusion. Since acoustic bioprinting employs very short durations and low wavelengths, its effects on cell membranes and protein structures are negligible. It is also noteworthy to mention that during ejection, no high pressure or heat is applied to the fluid[66,203].

Therefore, optimizing the PBHs' concentration to obtain optimal viscoelasticity properties during bioprinting is necessary. Concerning this matter, the investigation conducted by Singh *et al.*[136] focused on the development of silk-gelatin bioinks for the cartilage tissue's microextrusion bioprinting. In the first step, silk (0.5% to 2% w/v) and gelatin (1% to 9% w/v) hydrogels loaded with porcine auricular chondrocytes (1×10^6 cells/mL) were prepared. Afterward, the viscosity and modulus were evaluated in the range of 4–45°C so as to obtain a viscoelastic range for their bioink. They illustrated that the combination of the shear-thinning rheological behavior of silk due to β-sheet crystallization and gelatin's high viscosity enhanced the bioink's printability, and the bioink viscosity value was the lowest in the range of 25–35°C, enabling printing within this temperature range. Furthermore, high cellular survival was ensured when gelatin and silk concentrations were 7% and 1.5% w/v, respectively.

Since compressive and tensile behaviors of the bioprinted hydrogels are critical, Yang *et al.*[204] used collagen (15 mg/mL) and alginate (15 mg/mL) mixed with new-born Sprague Dawley chondrocytes (10×10^6 cells/mL) as a bioink to print 3D six-layer constructs (2×2 cm^2) and assessed their mechanical features. Uniaxial tension tests were conducted at ambient temperature with constructs stretched at 2 mm/min. Besides, cell-laden gels with a maximum displacement of 1 mm and a speed of 0.1 mm/min were analyzed for their compressive strength. Compared with the alginate alone (~28 kPa), collagen increased the stiffness of collagen/alginate-printed hydrogel by nearly 1.87 times. Additionally, the printed composite hydrogel (~41 kPa) showed remarkable strengthening and toughening effects with 162.08% greater strength and toughness than the alginate gel (~19 kPa).

4.2. Biocompatibility considerations

Biocompatibility refers to the material's ability to respond to a specific host environment[205]; within this context, it is essential to consider the biocompatibility of cell-laden PBHs during bioprinting, *in vitro* maturation, immunogenicity of hydrogels, and long-term effects of the gels.

Cellular viability and proliferation can be influenced by the hydrogel composition once bioinks have been deposited. In numerous matrix proteins and as mentioned, the RGD motif improves the cell–matrix interactions and can promote osteogenic differentiation and cell survival. It is also possible to modify hydrogels with other side groups and sequences like phosphate groups, covalently bound GFs, and heparin-binding domains, with the aim of increasing the creation of mineralized matrices and bone tissue possessing comparable mechanical features[206,207]. Compared with synthetic polymers, protein-based polymers like collagen, silk, keratin, serum albumin, and elastin have cell-adhesive peptide sequences that provide conducive microenvironments suitable for enhancing cell survival and proliferation[208]. In addition, physiological and biological cues present in structural proteins play a crucial role in bioink development. Additionally, protein-based materials are not only environmental friendly and renewable but also strong, elongated, tough, and slowly degradable. As an example, silk fibroin is one of the most popular PBHs used in bioprinting. It undergoes a remarkable structural transition from a random-coil to a

β-sheet structure, and aqueous silk fibroin solution contains hydrophobic domains that self-assemble into 3D hydrogels. As an amphiphilic material, it is capable of entrapping water and forming bioinks suitable for preventing cell dehydration in bioprinting. Thus, these kinds of PBHs are ideal bioinks for the bioprinting process since they are biocompatible, tunable, biodegradable, and capable of self-assembly[209,210]. It is also important to note that spidroins 1 and 2 are two major ampullates (draglines) in silk with a highly repetitious amino acids' core sequence, conjugated to the non-repetitive N-and C-terminal domains on either side, resulting in a bulging protein structure. By virtue of this property, hydrophilic domains are enclosed within the micelles, whereas hydrophobic terminal domains build the edges, ensuring that proteins are stable. This feature is essential for creating precise cell-laden PBHs that can be bioprinted employing this technology[211,212].

Regarding the impact of bioink concentration on cell viability, high concentrations can cause more pressure on the printing nozzle, followed by the generation of high level of shear stresses that are damaging to cells. As a result, the survival of cells should be evaluated at various levels of bioink concentration to enhance the cellular performance[213]. In order to induce solidification by sol-to-gel transition, factors like pH changes, temperature, and crosslinking approaches may rupture cell membranes, cause apoptosis and necrosis, or denature biological components (e.g., GFs and proteins) that are mixed with the bioink for developing biomimetic tissues[214-216].

High cell viability during bioprinting and maintenance of cellular survival for extended periods are of high priority[217]. As the printing process progresses, numerous external factors influence the viability of cells, such as printing modules and materials concentrations. Besides, the bioprinting process exerts mechanical forces on cells, causing deformation and breaching their membranes. Despite of cells' ability to resist specific force levels, their integrity can be lost if subjected to excessive stresses[218]. Therefore, recognizing the cell damage mechanisms during the bioprinting process to maintain cell viability, one of the basic requirements of bioprinting, is critical. Cell viability can also be affected by thermal and shear stresses that create cell-laden PBH drops. Scientists have reported that cells under local temperatures of up to 300°C are not greatly harmed via short exposures of 2 μm during the printing process[219,220]; in contrast, the vibrations and wave frequencies of piezoelectric bioprinting can disrupt cell membranes as well as unfold protein structures[221]. Moreover, in laser-assisted bioprinting, the encapsulated living cells and/or proteins are coated with hydrogel beforehand, and the absorption layer is transparent to the laser light; these phenomena inflict less damage to the protein structure and cell membrane, which improves cell survival[222].

Rhee *et al.*[106] focused on high-density cell-laden PBHs. In this regard, primary fibrochondrocytes from bovine joints (10×10^6 cells/mL) were mixed with the collagen hydrogel, and the bioprinted constructs were then tested for cell viability and mechanical properties. Accordingly, cells within the constructs were generally 90% viable immediately after printing. In addition, neither the cell numbers nor their viability varied with time over 10 days. A compressive modulus of 30 kPa was achieved at the highest printing concentration of collagen hydrogel (17.5 mg/mL). Therefore, their constructs demonstrated excellent mechanical stability and could support and maintain cell growth. In another pioneering investigation, silk-glycidyl methacrylate (Silk-GMA) loaded with human chondrocytes was fabricated by Hong *et al.*[223] for producing engineered cartilage with functional and efficient features. They bioprinted hydrogels ($5 \times 5 \times 2$ mm^3) containing human chondrocytes (1×10^6 cells/mL) and NIH 3T3 fibroblast cells combined with the Silk-GMA bioink. Likewise, 30% Silk-GMA solution comprising human chondrocytes (10×10^6 cells/mL) was bioprinted in the shape of a trachea ring (external diameter: 7 mm, internal diameter: 5 mm, and height: 2 mm) for *in vitro* cartilage TE. Within a novel research, Ren *et al.*[91] used an extrusion-based bioprinter to fabricate collagen type II hydrogel constructs embedding chondrocytes from New Zealand White rabbits' knee joints. Three groups were created based on the density of total cells incorporated into the collagen type II pre-gel (20×10^6, 10×10^6, and 5×10^6 cells/mL). The constructs were crosslinked for 30 min at 37°C in a humidified incubator and were cultured at 0, 1, 2, and 3 weeks. Interestingly, 98 ± 1% of chondrocytes were alive. Viability tests were conducted on the first day following synthesis in order to evaluate the damage caused by bioprinting to cells; 93 ± 3% of living cells were present in varying groups with no significant difference between them (Figure 5A). Based on the results, bioprinted hydrogel constructs with biomimetic cell density gradients can be utilized to fabricate engineered cartilage tissues.

The experiment, explained earlier, on engineering P3 hMSCs-encapsulated alginate/gelatin bioinks (4.1% w/v for gelatin and 0.8% w/v for alginate) (cell density: 1.67×10^6, 5×10^6, and 15×10^6 cells/mL) for bone TE illustrated that after 21 days of culture, the cells could spread and form a 3D interconnecting network in all groups, particularly in the 15×10^6 cells/mL bioink (Figure 5B)[114]. The above-mentioned investigation on developing arch-like bioprinted structures using GelMA and silk fibroin/gelatin

bioinks loaded with hBMSCs (cell density: 1×10^7 cells/mL) for cartilage TE reported that the silk fibroin/gelatin construct contained more viable cells compared with the GelMA-printed structure (Figure 5C(i, ii)). Moreover, a significant difference in the survival percentage was seen ($p < 0.0001$) between the silk fibroin/gelatin constructs (91.16%) and the GelMA constructs (89.25%) after 14 days of culture (Figure 5C(iii))[138]. Additionally, the scholars that designed mouse preosteoblast MC3T3-E1 cells-loaded sodium alginate dialdehyde/gelatin bioinks containing FS particles (1%, 3%, 5%, and 10% w/v) (cell density: 5×10^6 cells/mL) for bone regeneration also assessed the cytocompatibility, and it was demonstrated that cells were

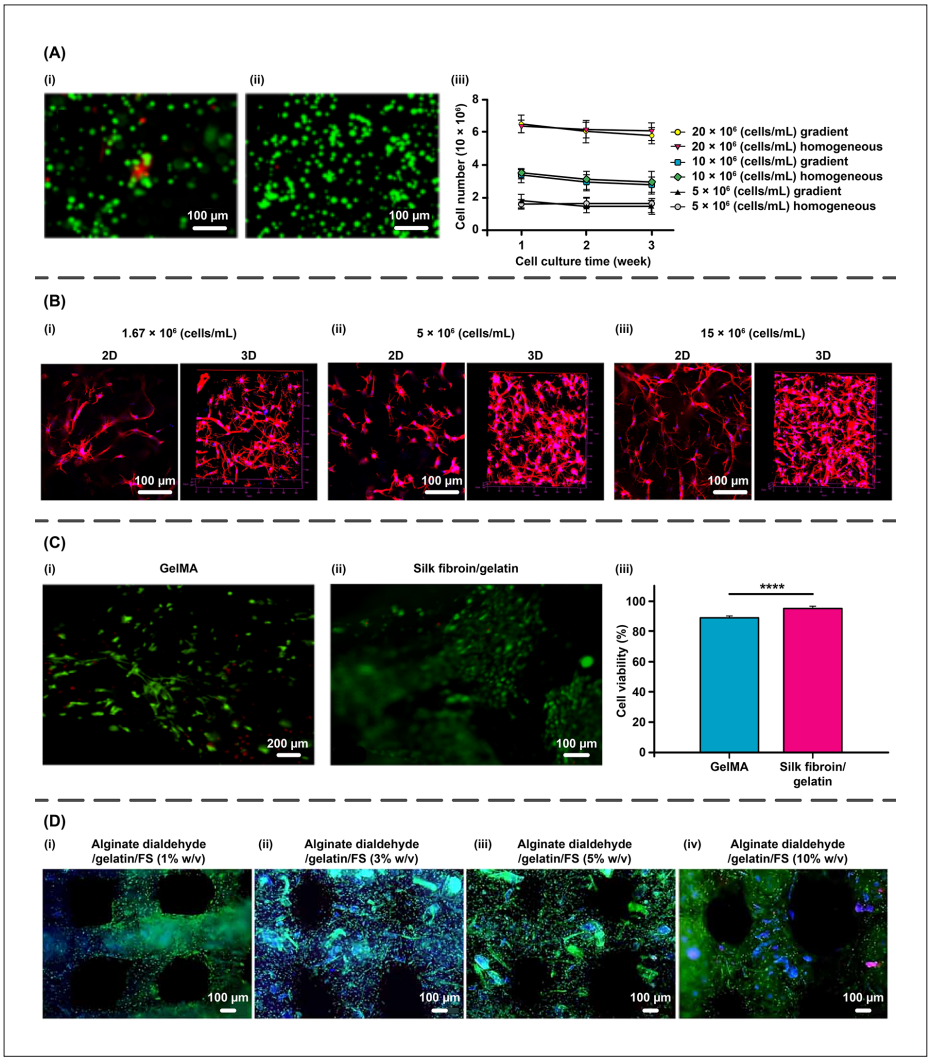

Figure 5. (A) The depiction of cell survival in the constructs and the total number of cells. The images (i) and (ii) illustrate the construct's middle zone after 2 weeks of *in vitro* cultivation and its superficial zone after 3 weeks of culture. Of note, calcein acetoxymethyl ester staining was done on live cells (green dots), and propidium iodide staining was performed on dead cells (red dots) (scale bars: 100 µm). (iii) The total number of cells within the structures after *in vitro* culture for 3 weeks in three groups. Reproduced under the terms of the Creative Commons Attribution 4.0 International (CC BY 4.0) license[91]. Copyright 2016, Springer Nature. (B) The bioprinted cell-laden structures' 2D and 3D actin staining images with various cell densities after 21 days of culture. Reproduced under the terms of the Creative Commons Attribution 4.0 International (CC BY 4.0) license[114]. Copyright 2020, Elsevier. (C) Live/dead assay of the bioprinted (i) GelMA construct and (ii) silk fibroin/gelatin structure after 14 days of culture. Live cells are shown in green (calcein acetoxymethyl ester) and dead cells in red (ethidium homodimer). (iii) The graph displaying the cell viability of hBMSCs on day 14 for the bioprinted constructs ($^{****}p < 0.0001$). Reproduced under the terms of the Creative Commons Attribution 4.0 International (CC BY 4.0) license[138]. Copyright 2023, IOP Publishing Ltd. (D) Live/dead assays of cells within and on the surface of the printed gels subsequent to 14 days of incubation (scale bars: 100 µm). The staining with 4',6-diamidino-2-phenylindole (DAPI) (blue), propidium iodide (red), and calcein AM (green) visualizes cell nuclei, dead cells, and viable cells, respectively. Reproduced under the terms of the Creative Commons Attribution 4.0 International (CC BY 4.0) license[137]. Copyright 2023, IOP Publishing Ltd.

viable and preserved their survival within various bioink compositions after 14 days of cultivation (Figure 5D)[137].

4.3. Crosslinking considerations

A bioprinted construct's degradation rate can be impacted by its composition, concentration, temperature, mechanical force, and cell culture medium; thus, the degradation rate of the bioprinted structure should be considered[164]. Specifically, the degradation rate of the PBHs is highly dependent on the β-sheet crystals' orientation, content, and non-crystalline domains[210,224]. The mechanical properties of bioinks may decrease too rapidly during culturing. To further enhance the integrity of the printed structures, crosslinking is most commonly performed for the printing of the dispensed cell-laden PBHs as stated[225]. It was mentioned that there are several kinds of crosslinking approaches used in PBHs bioprinting, including physical, chemical, and enzymatic crosslinking before, during, and after printing. Furthermore, thermal crosslinking can be used to print PBHs; in this case, temperature-induced gelation improves the printed construct's initial stability since it is faster than the gelation by Ca^{2+} cations as physical crosslinkers. Nevertheless, it is challenging to precisely control how much crosslinking occurs, and overheating in this process may adversely affect cell viability. Natural hydrogels, such as collagen, will lose mechanical strength because of enzymatic hydrolysis, and thermally sensitive hydrogels can also lose their shape when the environment's temperature changes[120]. For instance, due to the collagen helices' collapse to random coil structures at 30–35°C, the dissolved collagen's storage modulus and viscosity are rapidly reduced without gelation; hence, the thermal sensitivity of PBHs should be noticed in the bioprinting process[121,211]. Owing to this subject, scholars should meticulously select hydrogels and their associated 3D structures in a way that the degradation rate will be appropriate. One of the most common approaches in bioink printing is the employment of UV crosslinking to augment mechanical characteristics and degradation after bioprinting[169]. Nonetheless, variations in the UV exposure times decrease cell viability by increasing crosslinking after bioprinting[226]. Post-printing crosslinking can provide hydrogels with a higher modulus, as well as longer rates of degradation *in vitro* and *in vivo*, together with providing cells with proper stiffness[218,227]. Within a brand-new assessment, bioprinting of methylcellulose (MC)/GelMA bioinks with great shape integrity was performed. This research project introduced a new type of MC/GelMA bioink that could maintain its shape integrity over several months in the biological media. Unlike pure MC inks, distorting and dissociating in the biological media, MC/GelMA bioinks maintained their stability because of the GelMA's permanent photo-crosslinking under UV irradiation for 60 s. The results indicated that the swelling ratio was strongly influenced by the crosslinking density of the 3D network; a higher crosslinking density caused segments between joint points to become smaller, thereby preventing swelling. As a result of the photo-crosslinking of GelMA polymer chains, a covalent crosslinking network formed, which prevented the hydrogel from dissolving. The slow degradation of MC/GelMA hydrogel ensured that it retained its mechanical properties so that newly formed tissues and cells could be supported during regeneration. The MC/GelMA bioink's shape integrity was characterized by its complex modulus and yield stress, which were higher than those of the pure MC ink, resulting in self-supporting behavior once printed. Additionally, human primary osteoblasts that were encapsulated within the MC/GelMA hydrogels illustrated a cell survival of over 95%. This work emphasizes the importance of rheological features and the post-crosslinking process in the production of physiologically scaled tissue implants[228]. Overall, the selected crosslinking method for PBHs bioprinting impacts cellular viability and behavior, and the application should be considered while selecting the appropriate technique[29,229-231].

Printed droplets do not merge in these constructs, thereby increasing their mechanical stability. In addition to enhanced cellular functions, physical crosslinking produces no toxic byproducts and contributes to rapid gelation[232]. Notably, the plasma membrane can initially become damaged at low points in cells printed with low fluences and short gelation time, but the cells will recover rapidly through the sealing mechanism[233]. Consequently, despite providing a cushioning effect, all polymer concentrations require a suitable gelation time[234]. If the encapsulation process fails, the cells will not adhere to the scaffold and proliferate on the well plate instead; consequently, the cells are not able to be 3D cultivated[195,235].

For bioprinting, Visscher *et al.*[236] developed cartilage-derived decellularized ECM-based photo-crosslinkable porcine auricular cartilage hydrogels/methacrylate (cdECMMA). Subsequent to the printing, cdECM-based constructs were chemically modified by methacrylate reactions, providing structural integrity. Moreover, the bioink was prepared with a solution consisting of 37.5 mg/mL gelatin type A, 3 mg/mL HA, and photoinitiator (0.1% v/v, Irgacure 2959). A UV light intensity of 200 mW/cm^2 was used for 2 min to induce photo-crosslinking in this bioink formulation, and various concentrations (20, 30, and 40 mg/mL) of cdECMMA hydrogels were produced. With the increment of cdECMMA concentrations, the hydrogels' stiffness was considerably enhanced (20 mg/mL: 3837 ± 462 Pa, 30 mg/mL: 10381 ± 1339 Pa, and 40 mg/mL: 25,050 ± 2573 Pa). In addition, all cdECMMA constructs'

concentrations showed viability greater than 90% (1, 3, and 7 days). Therefore, they demonstrated that the photo-crosslinkable cdECM-based bioinks could be successfully engineered for auricular cartilage reconstruction while exhibiting favorable printability and structural stability.

Toward the same goal, cartilage acellular matrix (CAM) bioinks containing silk fibroin were engineered for bioprinting from porcine cartilage by a team of scientists[237]. In the first step, CAM-silk scaffolds were crosslinked with methanol only, 100 mM 1-ethyl-3-(-3-dimethylaminopropyl) carbodiimide/N-hydroxysuccinimide (EDC/NHS) in water (EDC-W), or 80% methanol (EDC-M) for 12 h. Subsequent to incubation for 7 days in collagenase, the printed CAM-silk scaffolds illustrated significant changes in shape and weight. A non-crosslinked CAM-silk scaffold collapsed after 1 day of treatment with collagenase 0.2%. At the end of incubation period, the extruded structures completely dissolved, and the methanol- and EDC-W-treated groups displayed analogous degradation characteristics after 3 to 5 days. In contrast, EDC-M could preserve the printed scaffolds well. The EDC-M-treated scaffolds did not degrade after 7 days, and EDC-W scaffolds retained ~20% of their initial weight.

5. Challenges and perspectives

Within the context of bioprinting approaches, classified based on the cells format and the number of cells generated during the bioprinting process, an unmet need still exists, which is related to the cell damage due to the shear stress during the bioprinting procedure. Furthermore, bioinks with enhanced cell shielding features are not largely explored. In this regard, scholars are merging experimental investigations with probabilistic models to improve our understanding of how cells get encapsulated into droplets in bioprinting and develop novel bioinks having the right balance of rheological characteristics for stress shielding and printability. The applications of the present single-cell bioprinting techniques are limited owing to multiple issues. To begin with, although the efficiency and reliability of the single-cell encapsulation are significantly improved, the single-cell printing's overall throughput is still low. Secondly, current printing methods typically rely on the single-cell droplets' printing within an open environment, causing deviation and interference in the following analysis. In other methods of bioprinting, one major obstacle is associated with reproducing a highly complex set of cell–matrix and cell–cell interactions, which are needed to guarantee sufficient organ functions. Besides, some of the developed bioinks containing several populations of cells have failed to replicate the native ECM microenvironment in the body, a bottleneck that remains to be addressed. Concerning the perspectives of bioprinting strategies, engineering a print head or a hand-held printer with digital control for direct tissue repair is one of the promising clinical applications. Indeed, via utilizing the scanned lesions' 3D reconstructions, bioprinting is capable of accurately delivering GFs, cells, and biomaterial-based scaffolds to repair the lesion with different thicknesses and shapes. Equipping bioprinters with microfluidic printing heads can also enable smooth and rapid switching across various bioink reservoirs in the printing process, making it simpler in order to recapitulate the native tissues' biological intricacy. Another point that should be considered in the bioprinting is the design of a gradient scaffold that can be seamlessly transferred from the cartilage layer to the bone layer while maintaining the distinct properties and functions of each tissue. This has made some progress, but more efforts are needed, especially with merging bioprinting technologies and co-bioprinting of several bioinks. Moreover, the practicability and commercial availability of bioinks and cells should be considered, including their cost, source, shelf-life, and approval by the Food and Drug Administration (FDA). Another direction is combining bioprinting techniques to meet different current obstacles, which is grabbing considerable attention among scientists. For instance, the employment of bioprinting approaches with diverse resolutions can be used to imitate the aspects of natural biological systems, which are operating on various scales. Moreover, evaluating the cellular functions after and during bioprinting will benefit the broad applicability and future success of bioprinting strategies. Last but not least, the continual optimization of bioprinting factors, the evolution of bioprinting equipment like imaging used for single-cell sorting, and the modification of bioink formulations like cellular density are ongoing trends to make bioprinting approaches more advanced, precise, and relevant to certain requirements.

Protein-based materials are among the most promising sources for the bioinks' formulations utilized in bioprinting strategies. Nonetheless, as with all the materials that are developed from biologics, there can be batch-to-batch variations in these materials, and thus the bioinks made from them. Hence, it is of cardinal importance to establish well-defined and strict protocols for the concentration, purification, and extraction of the employed proteins to provide reliable and reproducible outcomes. Additionally, selecting the best accessible method of sterilization can serve an essential role in guaranteeing the final bioink's safety and ideal properties. On the one hand, proteins originating from xenogeneic sources represent a potential ethical concern and could increase the risk of pathogen transmission. On the other hand, allogeneic sources of proteins pose extra difficulty in the source material's availability, particularly taking into account

the regulations on tissue and organ donation specific to each of the countries. All in all, a shift toward allogeneic sourcing necessitates collaboration among research groups, companies, and regulatory bodies in defining more standardized regulations on tissue and organ donation. Besides, biological, physical, and biochemical requirements of cartilage and bone tissues in designing PBHs are sometimes overlooked, representing an issue that should be addressed in order to obtain accurate experimental results in this field.

Natural proteins, including collagen, gelatin, silk fibroin, fibrin, keratin, elastin, and resilin, are in the spotlight of investigations on PBHs. However, each displays several drawbacks that should be overcome to achieve favorable outcomes. In the case of collagen-based bioinks, bioprinting of pure collagen is rather complex because of its low viscosity; a suggested solution in this regard is combining it with viscous polymers. Additionally, to enhance its shape fidelity, physical crosslinking and blending with other polymers can be employed. Other hindrances in the bioprinting of collagen that need to be addressed are poor mechanical strength and rapid hydrolysis. A common problem of pure gelatin bioinks at physiological temperature is their low viscosity, which can be also improved when blending them with viscous polymers. Another obstacle, again solvable via combining with other polymers, is associated with the low bioprinting resolution of these bioinks. Notably, to augment their poor shape fidelity, post-printing crosslinking and utilizing external support for the bioinks have been demonstrated as effective methods. Unfortunately, the stress shielding features of gelatin bioinks are low; a complication that can be tackled by nozzle temperature optimization during bioprinting to increase cellular survival. Pure silk bioinks have the disadvantage of high viscosity, resulting in nozzle clogging at the time of bioprinting; one efficacious strategy involves using recombinant silk that possesses lower viscosity compared to that of the native silk. Furthermore, lacking cell binding domains which can limit cellular attachment, low cellular growth and function support, and the absence of an established protocol for the optimization of silk-based bioinks are other obstacles that need to be taken into account. Particularly, scholars should address the high rate of enzymatic degradation and poor mechanical parameters related to the silk fibroin bioinks as well as the weak structural integrity associated with the silk sericin bioinks. The chief challenge of employing fibrin as a bioink is its irreversible and rapid gelation at the body temperature, making its bioprinting intricate. As an alternative, fibrinogen and thrombin blends can be printed together at low temperatures in order to inhibit early crosslinking. The fast degradation of fibrin bioinks is another problem impairing their capability to form stable constructs; this matter can be solved by blending them with other biopolymers. Besides, the fundamental challenges in bioprinting of keratin, elastin, and resilin are poor extensibility, possibility of contaminations after the purification process, and difficulty in determining the molecular sequence and primary sequence of resilin owing to the diminished stability during the purification.

Despite the rapid advances of bioprinting approaches in recent years, the above-mentioned obstacles should be surmounted to move this field forward. Regarding the PBHs, successful examples on the development of cartilage- and bone-engineered constructs employing bioprinting strategies have been described. As stated, several factors, including biophysical and biochemical parameters, and PBHs' process considerations must be taken into account, and multiple challenges with respect to these subjects are required to be overcome to ultimately translate these concepts into clinics in the foreseeable future.

6. Conclusion

In bioprinting, there is a paramount need to address the cell damage caused by shear stress and to develop bioinks with ideal cell protection. Researchers have been employing experimental investigations and probabilistic models to understand cell encapsulation in droplets and to design bioinks with suitable characteristics. Notably, current single-cell bioprinting techniques have limitations in terms of throughput and deviation in the printing process. In addition, reproducing complex cell–matrix and cell–cell interactions is a significant challenge for other bioprinting methods. Future directions include developing tissue repair printers, equipping bioprinters with microfluidic heads, and designing gradient scaffolds. Of note, combining different bioprinting approaches, evaluating cellular functions, and optimizing factors like imaging and bioink formulations are ongoing trends to advance the bioprinting field. Protein-based materials display promise for bioinks but may have batch-to-batch variations. It is important to mention that establishing strict protocols for protein concentration, purification, and extraction is crucial to ensure reliable and reproducible outcomes in bioprinting. Selecting the best method of sterilization is also critical for the safety and properties of the final bioink. In addition, ethical concerns and pathogen transmission risks arise when using proteins from xenogeneic sources, while allogeneic sources are limited in availability due to regulations on tissue and organ donation. In this regard, a collaboration between research groups, companies, and regulatory bodies is required to standardize regulations on tissue and organ donation for allogeneic sourcing. Natural proteins such

as collagen, gelatin, silk fibroin, fibrin, keratin, elastin, and resilin have drawbacks that need to be addressed for favorable outcomes in bioprinting. In general, significant advancements have been made in bioprinting, but there are still obstacles to overcome in order to move the field forward. Successful examples of utilizing bioprinting for cartilage and bone TE have been discussed; nevertheless, there are multiple parameters and bottlenecks that should be paid attention to. Biophysical and biochemical factors, as well as considerations for process optimization, must be taken into account. All in all, tackling the mentioned challenges will ultimately lead to translating bioprinting concepts into clinical applications in the near future.

Acknowledgments

None.

Funding

This work was supported by Alexander von Humboldt Foundation (Fellowship to F.G.), the Outstanding Clinical Discipline Project of Shanghai Pudong (Grant No. PWYgy2021-08), the Pudong New Area Traditional Chinese Medicine Science and Technology Innovation project (PDZY-2020-0607), the Young Medical Talents Training Program of Pudong Health Committee of Shanghai (Grant No. PWRq 2021-08), the Health Industry Clinical Research Project of Shanghai Health Commission (Grant No. 20224Y0393), and the National Natural Science Foundation of China (Grant No. 81971753, 82170897).

Conflict of interest

The authors certify that they have no affiliations with, or involvement in, any organization or entity with any financial interest or non-financial interest in the subject matter or materials discussed in this manuscript. All authors have read and agreed to the published version of the manuscript.

Author contributions

Conceptualization: Behafarid Ghalandari, Baoqing Yu, Farnaz Ghorbani

Funding acquisition: Behafarid Ghalandari, Baoqing Yu, Farnaz Ghorbani

Supervision: Behafarid Ghalandari, Baoqing Yu, Farnaz Ghorbani

Visualization: Mehran Khajehmohammadi

Writing – original draft: Mehran Khajehmohammadi, Negar Bakhtiary, Niyousha Davari, Soulmaz Sarkari, Hamidreza Tolabi, Dejian Li

Writing – review & editing: Behafarid Ghalandari, Farnaz Ghorbani

Ethics approval and consent to participate

Not applicable.

Consent for publication

Not applicable.

Availability of Data

The resources that support this review work are available upon request from the corresponding author.

References

1. Ozbolat IT, 2017, Bioprinting of osteochondral tissues: A perspective on current gaps and future trends. *Int J Bioprint,* 3(2).

   http://doi:10.18063/IJB.2017.02.007

2. Deng C, Chang J, Wu C, 2019, Bioactive scaffolds for osteochondral regeneration. *J Orthop Transl,* 17: 15–25.

   http://doi:10.1016/j.jot.2018.11.006

3. Gonçalves AM, Moreira A, Weber A, *et al.*, 2021, Costa, osteochondral tissue engineering: The potential of electrospinning and additive manufacturing. *Pharmaceutics*, 13(7): 983.

   http://doi:10.3390/pharmaceutics13070983

4. Moris H, Ghaee A, Karimi M, *et al.*, 2022, Preparation and characterization of Pullulan-based nanocomposite scaffold incorporating Ag-Silica Janus particles for bone tissue engineering. *Biomater Adv,* 135: 212733.

   http://doi:10.1016/j.bioadv.2022.212733

5. Ghorbani F, Ghalandari B, Khan AL, *et al.*, 2020, Decoration of electrical conductive polyurethane-polyaniline/polyvinyl alcohol matrixes with mussel-inspired polydopamine for bone tissue engineering. *Biotechnol Prog,* 36(6): e3043.

   http://doi:10.1002/btpr.3043

6. Ghorbani F, Zamanian A, Sahranavard M, 2019, Mussel-inspired polydopamine-mediated surface modification of freeze-cast poly (ε-caprolactone) scaffolds for bone tissue engineering applications. *Biomed Eng/Biomed Tech,* 65(3): 273–287.

   http://doi:10.1515/bmt-2019-0061

7. Sahranavard M, Zamanian A, Ghorbani F, *et al.*, 2020, A critical review on three dimensional-printed chitosan hydrogels for development of tissue engineering. *Bioprinting*, 17: e00063.

   http://doi:10.1016/j.bprint.2019.e00063

8. Yilmaz B, Al Rashid A, Mou YA, *et al.*, 2021, Bioprinting: A review of processes, materials and applications. *Bioprinting*, 23: e00148.

   https://doi.org/10.1016/j.bprint.2021.e00148

9. Ding S, Feng L, Wu J, *et al.*, 2018, Bioprinting of stem cells : Interplay of bioprinting process, bioinks, and stem cell properties. *ACS Biomater Sci Eng*, 4(9): 3108–3124.

   http://doi:10.1021/acsbiomaterials.8b00399

10. Kundu J, Shim J-H, Jang J, *et al.*, 2015, An additive manufacturing-based PCL-alginate-chondrocyte bioprinted scaffold for cartilage tissue engineering. *J Tissue Eng Regen Med,* 9(11): 1286–1297.

    http://doi:10.1002/term.1682

11. Ozbolat IT, 2015, Bioprinting scale-up tissue and organ constructs for transplantation. *Trends Biotechnol,* 33(7): 395–400.

    http://doi:10.1016/j.tibtech.2015.04.005

12. Kačarević Ž, Rider P, Alkildani S, *et al.*, 2018, An introduction to 3D bioprinting: Possibilities, challenges and future aspects. *Materials (Basel)*, 11(11): 2199.

    http://doi:10.3390/ma11112199

13. Ghorbani F, Ghalandari B, Khajehmohammadi M, *et al.*, 2023, Photo-cross-linkable hyaluronic acid bioinks for bone and cartilage tissue engineering applications. *Int Mater Rev,* 68(6): 1–42.

    http://doi:10.1080/09506608.2023.2167559

14. Raza F, Zafar H, Zhu Y, *et al.*, 2018, A review on recent advances in stabilizing peptides/proteins upon fabrication in hydrogels from biodegradable polymers. *Pharmaceutics*, 10(1): 16.

    http://doi:10.3390/pharmaceutics10010016

15. Di Bella C, Fosang A, Donati DM, *et al.*, 2015, 3D bioprinting of cartilage for orthopedic surgeons : Reading between the lines. *Front Surg*, 2: 1–7.

    http://doi:10.3389/fsurg.2015.00039

16. Tolabi H, Davari N, Khajehmohammadi M, *et al.*, 2023, Progress of microfluidic hydrogel-based scaffolds and organ-on-chips for the cartilage tissue engineering. *Adv Mater,* 35(26): 2208852.

    http://doi:10.1002/adma.202208852

17. Razaviye MK, Tafti RA, Khajehmohammadi M, 2022, An investigation on mechanical properties of PA12 parts produced by a SLS 3D printer: An experimental approach. *CIRP J Manuf Sci Technol,* 38: 760–768.

    http://doi:10.1016/j.cirpj.2022.06.016

18. Dababneh AB, Ozbolat IT, 2014, Bioprinting technology: A current state-of-the-art review. *J Manuf Sci Eng Trans ASME,* 136(6): 1–12.

    http://doi:10.1115/1.4028512

19. Khajehmohammadi M, Azizi Tafti R, Nikukar H, 2023, Effect of porosity on mechanical and biological properties of bioprinted scaffolds. *J Biomed Mater Res Part A,* 111(2): 245–260.

    http://doi:10.1002/jbm.a.37455

20. Schloss AC, Williams DM, Regan LJ, 2016, Protein-based hydrogels for tissue engineering. *Adv Exp Med Biol,* 940: 167–177.

    http://doi:10.1007/978-3-319-39196-0_8

21. Davari N, Bakhtiary N, Khajehmohammadi M, *et al.*, 2022, Protein-based hydrogels: Promising materials for tissue engineering. *Polymers (Basel)*, 14: 986.

    http://doi:10.3390/polym14050986

22. Rasheed T, Bilal M, Zhao Y, *et al.*, 2019, Physiochemical characteristics and bone/cartilage tissue engineering potentialities of protein-based macromolecules — A review. *Int J Biol Macromol*, 121(5): 13–22.

    http://doi:10.1016/j.ijbiomac.2018.10.009

23. Catoira MC, Fusaro L, Di Francesco D, *et al.*, 2019, Overview of natural hydrogels for regenerative medicine applications. *J Mater Sci Mater Med,* 30(10): 115.

    http://doi:10.1007/s10856-019-6318-7

24. Maia FRA, Oliveira JM, Reis RL, eds., 2023, *Handbook of the Extracellular Matrix*, Springer International Publishing, Cham.

    http://doi:10.1007/978-3-030-92090-6

25. Włodarczyk-Biegun MK, del Campo A, 2017, 3D bioprinting of structural proteins. *Biomaterials*, 134: 180–201.

    http://doi:10.1016/j.biomaterials.2017.04.019

26. Lotfi Z, Khakbiz M, Davari N, *et al.*, 2023, Fabrication and multiscale modeling of polycaprolactone/amniotic membrane electrospun nanofiber scaffolds for wound healing. *Artif Organs*, 00: 1–18.

    http://doi:10.1111/aor.14518

27. Norouzi F, Pourmadadi M, Yazdian F, *et al.*, 2022, PVA-based nanofibers containing chitosan modified with graphene oxide and carbon quantum dot-doped TiO2 enhance wound healing in a rat model. *J Funct Biomater*, 13(4): 300.

    http://doi:10.3390/jfb13040300

28. Yahay Z, Tolabi H, Delavar F, *et al.*, 2023, Fabrication of meso/macroporous TiO2/PCL composite scaffolds by direct ink writing: The effects of porogen content on the compressive modulus and in vitro behavior. *Mater Today Commun,* 35: 105769.

    http://doi:10.1016/j.mtcomm.2023.105769

29. Veiga A, Silva IV, Duarte MM, *et al.*, 2021, Current trends on protein driven bioinks for 3D printing. *Pharmaceutics*, 13(9): 1444.

    http://doi:10.3390/pharmaceutics13091444

30. Khoeini R, Nosrati H, Akbarzadeh A, *et al.*, 2021, Natural and synthetic bioinks for 3D bioprinting. *Adv NanoBiomed Res,* 1(8): 2000097.

    http://doi:10.1002/anbr.202000097

31. Abascal NC, Regan L, 2018, The past, present and future of protein-based materials. *Open Biol,* 8(10): 180113.

http://doi:10.1098/rsob.180113

32. Jeshvaghani PA, Pourmadadi M, Yazdian F, *et al.*, 2023, Synthesis and characterization of a novel, pH-responsive sustained release nanocarrier using polyethylene glycol, graphene oxide, and natural silk fibroin protein by a green nano emulsification method to enhance cancer treatment. *Int J Biol Macromol,* 226: 1100–1115.

http://doi:10.1016/j.ijbiomac.2022.11.226

33. Hajiabbas M, Okoro OV, Delporte C, *et al.*, 2023, Proteins and polypeptides as biomaterials inks for 3D printing, in *Handbook of the Extracellular Matrix*, Springer International Publishing, Cham, 2023, 1–34.

http://doi:10.1007/978-3-030-92090-6_15-1

34. Gagner JE, Kim W, Chaikof EL, 2014, Designing protein-based biomaterials for medical applications. *Acta Biomater*, 10(4): 1542–1557.

http://doi:10.1016/j.actbio.2013.10.001

35. Lee A, Hudson AR, Shiwarski DJ, *et al.*, 2019, 3D bioprinting of collagen to rebuild components of the human heart. *Science*, 365(6452): 482–487.

http://doi:10.1126/science.aav9051

36. Łabowska MB, Cierluk K, Jankowska AM, *et al.*, 2021, A review on the adaption of alginate-gelatin hydrogels for 3D cultures and bioprinting. *Materials (Basel)*, 14(4): 858.

http://doi:10.3390/ma14040858

37. Liu S, Yu J-M, Gan Y-C, *et al.*, 2023, Biomimetic natural biomaterials for tissue engineering and regenerative medicine: New biosynthesis methods, recent advances, and emerging applications. *Mil Med Res,* 10(1): 16.

http://doi:10.1186/s40779-023-00448-w

38. Cheung H-Y, Lau K-T, Lu T-P, *et al.*, 2007, A critical review on polymer-based bio-engineered materials for scaffold development. *Compos Part B Eng,* 38(3): 291–300.

http://doi:10.1016/j.compositesb.2006.06.014

39. Al Enezy-Ulbrich MA, Malyaran H, Lange RD, *et al.*, 2020, Impact of reactive amphiphilic copolymers on mechanical properties and cell responses of fibrin-based hydrogels. *Adv Funct Mater,* 30(38): 2003528.

http://doi:10.1002/adfm.202003528

40. Vernerey FJ, Greenwald EC, Bryant SJ, 2012, Triphasic mixture model of cell-mediated enzymatic degradation of hydrogels. *Comput Methods Biomech Biomed Engin,* 15(11): 1197–1210.

http://doi:10.1080/10255842.2011.585973

41. Khan F, Atif M, Haseen M, *et al.*, 2022, Synthesis, classification and properties of hydrogels: Their applications in drug delivery and agriculture. *J Mater Chem B,* 10(2): 170–203.

http://doi:10.1039/D1TB01345A

42. Chakraborty J, Ghosh S, 2020, Cellular proliferation, self-assembly, and modulation of signaling pathways in silk fibroin gelatin-based 3D bioprinted constructs. *ACS Appl Bio Mater,* 3(12): 8309–8320.

http://doi:10.1021/acsabm.0c01252

43. Bakhtiary N, Ghalandari B, Ghorbani F, *et al.*, 2023, Advances in peptide-based hydrogel for tissue engineering. *Polymers (Basel)*, 15(5): 1068.

http://doi:10.3390/polym15051068

44. Huettner N, Dargaville TR, Forget A, 2018, Discovering cell-adhesion peptides in tissue engineering: Beyond RGD. *Trends Biotechnol*, 36(4): 372–383.

http://doi:10.1016/j.tibtech.2018.01.008

45. Gao G, Cui X, Bone BÁ, *et al.*, 2016, Three-dimensional bioprinting in tissue engineering and regenerative medicine. *Biotechnol Lett,* 38: 422–434.

http://doi:10.1007/s10529-015-1975-1

46. Tasoglu S, Demirci U, 2013, Bioprinting for stem cell research. *Trends Biotechnol*, 31(1): 10–19.

http://doi:10.1016/j.tibtech.2012.10.005

47. Riba J, Renz N, Niemöller C, *et al.*, 2016, Molecular genetic characterization of individual cancer cells isolated via single-cell printing. *PLoS One,* 11(9): e0163455.

http://doi:10.1371/journal.pone.0163455

48. Stumpf F, Schoendube J, Gross A, *et al.*, 2015, Single-cell PCR of genomic DNA enabled by automated single-cell printing for cell isolation. *Biosens Bioelectron,* 69: 301–306.

http://doi:10.1016/j.bios.2015.03.008

49. Zhang X, Wei X, Wei Y, *et al.*, 2020, The up-to-date strategies for the isolation and manipulation of single cells. *Talanta,* 218: 121147.

http://doi:10.1016/j.talanta.2020.121147

50. Herzenberg LA, Parks D, Sahaf B, *et al.*, 2002, The history and future of the fluorescence activated cell sorter and flow cytometry: A view from stanford. *Clin Chem,* 48(10): 1819–1827.

http://doi:10.1093/clinchem/48.10.1819

51. Zhou Y, Shaw D, Lam C, *et al.*, 2018, Beating the odds: The poisson distribution of all input cells during limiting dilution grossly underestimates whether a cell line is clonally-derived or not. *Biotechnol Prog,* 34(3): 559–569.

http://doi:10.1002/btpr.2560

52. Gross A, Schoendube J, Zimmermann S, *et al.*, 2015, Technologies for single-cell isolation. *Int J Mol Sci,* 16(8): 16897–16919.

http://doi:10.3390/ijms160816897

53. Zhang X, Li T, Liu F, *et al.*, 2019, Comparative analysis of droplet-based ultra-high-throughput single-cell RNA-Seq systems. *Mol Cell,* 73(1): 130–142.e5.

http://doi:10.1016/j.molcel.2018.10.020

54. Matuła K, Rivello F, Huck WTS, 2020, Single-cell analysis using droplet microfluidics. *Adv Biosyst,* 4(1): 1900188.

http://doi:10.1002/adbi.201900188

55. Klein AM, Mazutis L, Akartuna I, *et al.*, 2015, Droplet barcoding for single-cell transcriptomics applied to embryonic stem cells. *Cell,* 161(5): 1187–1201.

http://doi:10.1016/j.cell.2015.04.044

56. Han X, Wang R, Zhou Y, *et al.*, 2018, Mapping the mouse cell atlas by microwell-seq. *Cell,* 172(5): 1091–1107.e17.

http://doi:10.1016/j.cell.2018.02.001

57. Rettig JR, Folch A, 2005, Large-scale single-cell trapping and imaging using microwell arrays. *Anal Chem,* 77(17): 5628–5634.

http://doi:10.1021/ac0505977

58. Zhou Y, Basu S, Wohlfahrt KJ, *et al.*, 2016, A microfluidic platform for trapping, releasing and super-resolution imaging of single cells. *Sensors Actuators B Chem*, 232: 680–691.

http://doi:10.1016/j.snb.2016.03.131

59. Tan W-H, Takeuchi S, 2007, A trap-and-release integrated microfluidic system for dynamic microarray applications. *Proc Natl Acad Sci,* 104(4): 1146–1151.

http://doi:10.1073/pnas.0606625104

60. Calvert P, 2007, Printing cells. *Science*, 318(5848): 208–209.

http://doi:10.1126/science.1144212

61. Yusof A, Keegan H, Spillane CD, *et al.*, 2011, Inkjet-like printing of single-cells. *Lab Chip*, 11(14): 2447.

http://doi:10.1039/c1lc20176j

62. Wang Y, Wang X, Pan T, *et al.*, 2021, Label-free single-cell isolation enabled by microfluidic impact printing and real-time cellular recognition. *Lab Chip,* 21(19): 3695–3706.

http://doi:10.1039/D1LC00326G

63. Schoendube J, Wright D, Zengerle R, *et al.*, 2015, Single-cell printing based on impedance detection. *Biomicrofluidics,* 9(1): 014117.

http://doi:10.1063/1.4907896

64. Nagai M, Kato K, Soga S, *et al.*, 2020, Scalable parallel manipulation of single cells using micronozzle array integrated with bidirectional electrokinetic pumps. *Micromachines,* 11(4): 442.

http://doi:10.3390/mi11040442

65. Feng L, Sun Y, Ohsumi C, *et al.*, 2013, Accurate dispensing system for single oocytes using air ejection. *Biomicrofluidics,* 7(5): 054113.

http://doi:10.1063/1.4824394

66. Demirci U, Montesano G, 2007, Single cell epitaxy by acoustic picolitre droplets. *Lab Chip,* 7(9): 1139.

http://doi:10.1039/b704965j

67. Guo F, Mao Z, Chen Y, *et al.*, 2016, Three-dimensional manipulation of single cells using surface acoustic waves. *Proc Natl Acad Sci,* 113(6): 1522–1527.

http://doi:10.1073/pnas.1524813113

68. Bertassoni LE, 2022, Bioprinting of complex multicellular organs with advanced functionality—recent progress and challenges ahead. *Adv Mater,* 34(3): 2101321.

http://doi:10.1002/adma.202101321

69. Daly AC, Prendergast ME, Hughes AJ, *et al.*, 2021, Bioprinting for the biologist. *Cell,* 184(1): 18–32.

http://doi:10.1016/j.cell.2020.12.002

70. Barron JA, Krizman DB, Ringeisen BR, 2005, Laser printing of single cells: Statistical analysis, cell viability, and stress. *Ann Biomed Eng*, 33(2): 121–130.

http://doi:10.1007/s10439-005-8971-x

71. Yamaguchi S, Ueno A, Akiyama Y, *et al.*, 2012, Cell patterning through inkjet printing of one cell per droplet. *Biofabrication*, 4(4): 045005.

http://doi:10.1088/1758-5082/4/4/045005

72. Zhang K, Chou C-K, Xia X, *et al.*, 2014, Block-cell-printing for live single-cell printing. *Proc Natl Acad Sci,* 111(8): 2948–2953.

http://doi:10.1073/pnas.1313661111

73. Zhou X, Wu H, Wen H, *et al.*, 2022, Advances in single-cell printing. *Micromachines*, 13(1): 80.

http://doi:10.3390/mi13010080

74. Murphy SV, De Coppi P, Atala A, 2020, Opportunities and challenges of translational 3D bioprinting. *Nat Biomed Eng,* 4(4): 370–380.

http://doi:10.1038/s41551-019-0471-7

75. Zhang P, Abate AR, 2020, High-definition single-cell printing: Cell-by-cell fabrication of biological structures. *Adv Mater,* 32(52): 2005346.

http://doi:10.1002/adma.202005346

76. Hong S, Lee JY, Hwang C, *et al.*, 2016, Inhibition of Rho-associated protein kinase increases the angiogenic potential of mesenchymal stem cell aggregates via paracrine effects. *Tissue Eng Part A,* 22(3-4): 233–243.

http://doi:10.1089/ten.tea.2015.0289

77. Lei J, Trevino E, Temenoff J, 2016, Cell number and chondrogenesis in human mesenchymal stem cell aggregates is affected by the sulfation level of heparin used as a cell coating. *J Biomed Mater Res Part A,* 104(7): 1817–1829.

http://doi:10.1002/jbm.a.35713

78. Lin R-Z, Chang H-Y, 2008, Recent advances in three-dimensional multicellular spheroid culture for biomedical research. *Biotechnol J,* 3(9-10): 1172–1184.

http://doi:10.1002/biot.200700228

79. Derby B, 2012, Printing and prototyping of tissues and scaffolds. *Science*, 338(6109): 921–926.

http://doi:10.1126/science.1226340

80. Marga F, Jakab K, Khatiwala C, *et al.*, 2012, Toward engineering functional organ modules by additive manufacturing. *Biofabrication*, 4(2): 022001.

http://doi:10.1088/1758-5082/4/2/022001

81. Marchioli G, van Gurp L, van Krieken PP, *et al.*, 2015, Fabrication of three-dimensional bioplotted hydrogel scaffolds for islets of Langerhans transplantation. *Biofabrication*, 7(2): 025009.

http://doi:10.1088/1758-5090/7/2/025009

82. Tan Y, Richards DJ, Trusk TC, *et al.*, 2014, 3D printing facilitated scaffold-free tissue unit fabrication. *Biofabrication*, 6(2): 024111.

http://doi:10.1088/1758-5082/6/2/024111

83. Yang X, Sun Y, Wang Q, 2013, A phase field approach for multicellular aggregate fusion in biofabrication. *J Biomech Eng,* 135: 071005.

http://doi:10.1115/1.4024139

84. Yang X, Mironov V, Wang Q, 2012, Modeling fusion of cellular aggregates in biofabrication using phase field theories. *J Theor Biol,* 303: 110–118.

http://doi:10.1016/j.jtbi.2012.03.003

85. Mironov V, Visconti RP, Kasyanov V, *et al.*, 2009, Organ printing: Tissue spheroids as building blocks. *Biomaterials*, 30(12): 2164–2174.

http://doi:10.1016/j.biomaterials.2008.12.084

86. Keriquel V, Oliveira H, Rémy M, *et al.*, 2017, In situ printing of mesenchymal stromal cells, by laser-assisted bioprinting, for in vivo bone regeneration applications. *Sci Rep,* 7(1): 1778.

http://doi:10.1038/s41598-017-01914-x

87. Adhikari J, Perwez MS, Das A, *et al.*, 2021, Development of hydroxyapatite reinforced alginate–chitosan based printable biomaterial-ink. *Nano-Structures Nano-Objects*, 25: 100630.

http://doi:10.1016/j.nanoso.2020.100630

88. Ozbolat IT, Hospodiuk M, 2016, Current advances and future perspectives in extrusion-based bioprinting. *Biomaterials,* 76: 321–343.

http://doi:10.1016/j.biomaterials.2015.10.076

89. Kim SH, Yeon YK, Lee JM, *et al.*, 2018, Precisely printable and biocompatible silk fibroin bioink for digital light processing 3D printing. *Nat Commun,* 9(1): 1–14.

http://doi:10.1038/s41467-018-03759-y

90. Mandrycky C, Wang Z, Kim K, *et al.*, 2016, 3D bioprinting for engineering complex tissues. *Biotechnol Adv,* (4).

http://doi:10.1016/j.biotechadv.2015.12.011

91. Ren X, Wang F, Chen C, *et al.*, 2016, Engineering zonal cartilage through bioprinting collagen type II hydrogel constructs with biomimetic chondrocyte density gradient. *BMC Musculoskelet Disord,* 17(1): 1–10.

http://doi:10.1186/s12891-016-1130-8

92. Kesti M, Eberhardt C, Pagliccia G, *et al.*, 2015, Bioprinting complex cartilaginous structures with clinically compliant biomaterials. *Adv Funct Mater,* 25(48): 7406–7417.

http://doi:10.1002/adfm.201503423

93. López-Marcial GR, Zeng AY, Osuna C, *et al.*, 2018, Agarose-based hydrogels as suitable bioprinting materials for tissue engineering. *ACS Biomater Sci Eng*, 4(10): 3610–3616.

http://doi:10.1021/acsbiomaterials.8b00903

94. Luo Y, Luo G, Gelinsky M, *et al.*, 2017, 3D bioprinting scaffold using alginate/polyvinyl alcohol bioinks. *Mater Lett,* 189: 295–298.

http://doi:10.1016/j.matlet.2016.12.009

95. Asohan AW, Hashim R, Ku Ishak KM, *et al.*, 2022, Preparation and characterisation of cellulose nanocrystal/alginate/polyethylene glycol diacrylate (CNC/Alg/PEGDA) hydrogel using double network crosslinking technique for bioprinting application. *Appl Sci,* 12(2): 771.

http://doi:10.3390/app12020771

96. Hong S, Sycks D, Chan HF, *et al.*, 2015, 3D printing of highly stretchable and tough hydrogels into complex, cellularized structures. *Adv Mater,* 27(27): 4035–4040.

http://doi:10.1002/adma.201501099

97. Kosik-Kozioł A, Costantini M, Bolek T, *et al.*, 2017, PLA short sub-micron fiber reinforcement of 3D bioprinted alginate constructs for cartilage regeneration. *Biofabrication*, 9(4): 044105.

http://doi:10.1088/1758-5090/aa90d7

98. Bakhtiary N, Liu C, Ghorbani F, 2021, Bioactive inks development for osteochondral tissue engineering: A mini-review. *Gels*, 7(4): 274.

http://doi:10.3390/gels7040274

99. Das S, Pati F, Choi Y-J, *et al.*, 2015, Bioprintable, cell-laden silk fibroin–gelatin hydrogel supporting multilineage differentiation of stem cells for fabrication of three-dimensional tissue constructs. *Acta Biomater*, 11: 233–246.

http://doi:10.1016/j.actbio.2014.09.023

100. Duan B, Kapetanovic E, Hockaday LAA, *et al.*, 2014, Three-dimensional printed trileaflet valve conduits using biological hydrogels and human valve interstitial cells. *Acta Biomater,* 10(5): 1836–1846.

http://doi:10.1016/j.actbio.2013.12.005

101. Murphy SV, Skardal A, Atala A, 2013, Evaluation of hydrogels for bio-printing applications. *J Biomed Mater Res - Part A,* 101(1): 272–284.

http://doi:10.1002/jbm.a.34326

102. Williams D, Thayer P, Martinez H, *et al.*, 2018, A perspective on the physical, mechanical and biological specifications of bioinks and the development of functional tissues in 3D bioprinting. *Bioprinting*, 9: 19–36.

http://doi:10.1016/j.bprint.2018.02.003

103. Tolabi H, Bakhtiary N, Sayadi S, *et al.*, 2022, A critical review on polydopamine surface-modified scaffolds in musculoskeletal regeneration. *Front Bioeng Biotechnol,* 10: 1008360.

http://doi:10.3389/fbioe.2022.1008360

104. Diamantides N, Wang L, Pruiksma T, *et al.*, 2017, Correlating rheological properties and printability of collagen bioinks: The effects of riboflavin photocrosslinking and pH. *Biofabrication*, 9(4): 034102.

http://doi:10.1088/1758-5090/aa780f

105. Moncal KK, Ozbolat V, Datta P, *et al.*, 2019, Thermally-controlled extrusion-based bioprinting of collagen. *J Mater Sci Mater Med,* 30(5): 55.

http://doi:10.1007/s10856-019-6258-2

106. Rhee S, Puetzer JL, Mason BN, *et al.*, 2016, 3D bioprinting of spatially heterogeneous collagen constructs for cartilage tissue engineering. *ACS Biomater Sci Eng,* 2(10): 1800–1805.

http://doi:10.1021/acsbiomaterials.6b00288

107. Leucht A, Volz A-C, Rogal J, *et al.*, 2020, Advanced gelatin-based vascularization bioinks for extrusion-based bioprinting of vascularized bone equivalents. *Sci Rep,* 10(1): 5330.

http://doi:10.1038/s41598-020-62166-w

108. Osidak EO, Kozhukhov VI, Osidak MS, 2020, Collagen as bioink for bioprinting: A comprehensive review. *Int J Bioprint,* 6(3): 270.

http://doi: 10.18063/ijb.v6i3.270

109. de Melo BAG, Jodat YA, Cruz EM, *et al.*, 2020, Strategies to use fibrinogen as bioink for 3D bioprinting fibrin-based soft and hard tissues. *Acta Biomater*, 117: 60–76.

http://doi:10.1016/j.actbio.2020.09.024

110. Zhou Z, Cui J, Wu S, *et al.*, 2022, Silk fibroin-based biomaterials for cartilage/osteochondral repair. *Theranostics*, 12(11): 5103–5124.

http://doi:10.7150/thno.74548

111. Murphy SV, Atala A, 2014, 3D bioprinting of tissues and organs. *Nat Biotechnol,* 32(8): 773–785.

http://doi:10.1038/nbt.2958

112. Hölzl K, Lin S, Tytgat L, *et al.*, 2016, Bioink properties before, during and after 3D bioprinting. *Biofabrication*, 8(3): 032002.

http://doi:10.1088/1758-5090/8/3/032002

113. Hinton TJ, Jallerat Q, Palchesko RN, *et al.*, 2015, Three-dimensional printing of complex biological structures by freeform reversible embedding of suspended hydrogels. *Sci Adv,* 1(9): 1500758.

http://doi:10.1126/sciadv.1500758

114. Zhang J, Wehrle E, Adamek P, *et al.*, 2020, Optimization of mechanical stiffness and cell density of 3D bioprinted cell-laden scaffolds improves extracellular matrix mineralization and cellular organization for bone tissue engineering. *Acta Biomater*, 114: 307–322.

http://doi:10.1016/j.actbio.2020.07.016

115. Martyniak K, Lokshina A, Cruz MA, *et al.*, 2022, Biomaterial composition and stiffness as decisive properties of 3D bioprinted constructs for type II collagen stimulation. *Acta Biomater,* 152: 221–234.

http://doi:10.1016/j.actbio.2022.08.058

116. Allen NB, Abar B, Johnson L, *et al.*, 2022, 3D-bioprinted GelMA-gelatin-hydroxyapatite osteoblast-laden composite hydrogels for bone tissue engineering. *Bioprinting*, 26: e00196.

http://doi:10.1016/j.bprint.2022.e00196

117. Lee JS, Park HS, Jung H, *et al.*, 2020, Park, 3D-printable photocurable bioink for cartilage regeneration of tonsil-derived mesenchymal stem cells. *Addit Manuf,* 33: 101136.

http://doi:10.1016/j.addma.2020.101136

118. Bandyopadhyay A, Mandal BB, Bhardwaj N, 2022, 3D bioprinting of photo-crosslinkable silk methacrylate (SilMA)-polyethylene glycol diacrylate (PEGDA) bioink for cartilage tissue engineering. *J Biomed Mater Res Part A,* 110: 884–898.

http://doi:10.1002/jbm.a.37336

119. Rajput M, Mondal P, Yadav P, *et al.*, 2022, Light-based 3D bioprinting of bone tissue scaffolds with tunable mechanical properties and architecture from photocurable silk fibroin. *Int J Biol Macromol,* 202: 644–656.

http://doi:10.1016/j.ijbiomac.2022.01.081

120. Unagolla JM, Jayasuriya AC, 2020, Hydrogel-based 3D bioprinting: A comprehensive review on cell-laden hydrogels, bioink formulations, and future perspectives. *Appl Mater Today,* 18: 100479.

http://doi:10.1016/j.apmt.2019.100479

121. Koo Y, Choi E-J, Lee J, *et al.*, 2018, 3D printed cell-laden collagen and hybrid scaffolds for in vivo articular cartilage tissue regeneration. *J Ind Eng Chem,* 66: 343–355.

http://doi:10.1016/j.jiec.2018.05.049

122. Turnbull G, Clarke J, Picard F, *et al.*, 2018, 3D bioactive composite scaffolds for bone tissue engineering. *Bioact Mater,* 3: 278–314.

http://doi:10.1016/j.bioactmat.2017.10.001

123. Zhang B, Huang J, Narayan RJ, 2020, Gradient scaffolds for osteochondral tissue engineering and regeneration. *J Mater Chem B,* 8: 8149–8170.

http://doi:10.1039/D0TB00688B

124. Diaz-Gomez L, Kontoyiannis PD, Melchiorri AJ, *et al.*, 2019, Three-dimensional printing of tissue engineering scaffolds with horizontal pore and composition gradients. *Tissue Eng Part C Methods,* 25: 411–420.

http://doi:10.1089/ten.tec.2019.0112

125. Wang M, Li W, Mille LS, *et al.*, 2022, Digital light processing based bioprinting with composable gradients. *Adv Mater,* 34: 2107038.

http://doi:10.1002/adma.202107038

126. Nicolas J, Magli S, Rabbachin L, *et al.*, 2020, 3D extracellular matrix mimics: Fundamental concepts and role of materials chemistry to influence stem cell fate. *Biomacromolecules*, 21: 1968–1994.

http://doi:10.1021/acs.biomac.0c00045

127. Guvendiren M, Burdick JA, 2012, Stiffening hydrogels to probe short- and long-term cellular responses to dynamic mechanics. *Nat Commun*, 3: 792.

http://doi:10.1038/ncomms1792

128. Ji S, Almeida E, Guvendiren M, 2019, 3D bioprinting of complex channels within cell-laden hydrogels. *Acta Biomater* 95: 214–224.

http://doi:10.1016/j.actbio.2019.02.038

129. Martinez AW, Caves JM, Ravi S, *et al.*, 2014, Effects of crosslinking on the mechanical properties, drug release and cytocompatibility of protein polymers. *Acta Biomater*, 10: 26–33.

http://doi:10.1016/j.actbio.2013.08.029

130. FitzSimons TM, Anslyn EV, Rosales AM, 2022, Effect of pH on the properties of hydrogels cross-linked via dynamic thia-michael addition bonds. *ACS Polym Au,* 2: 129–136.

http://doi:10.1021/acspolymersau.1c00049

131. Bustamante-Torres M, Romero-Fierro D, Arcentales-Vera B, *et al.*, 2021, Hydrogels classification according to the physical or chemical interactions and as stimuli-sensitive materials. Gels, 7: 182.

http://doi:10.3390/gels7040182

132. Zhang YS, Khademhosseini A, 2017, Advances in engineering hydrogels. *Science*, 356: eaaf3627.

http://doi:10.1126/science.aaf3627

133. Lee J, Yeo M, Kim W, *et al.*, 2018, Development of a tannic acid cross-linking process for obtaining 3D porous cell-laden collagen structure. *Int J Biol Macromol,* 110: 497–503.

http://doi:10.1016/j.ijbiomac.2017.10.105

134. Ruedinger F, Lavrentieva A, Blume C, *et al.*, 2015, Hydrogels for 3D mammalian cell culture: a starting guide for laboratory practice. *Appl Microbiol Biotechnol,* 99: 623–636.

http://doi:10.1007/s00253-014-6253-y

135. Sang S, Mao X, Cao Y, *et al.*, 2023, 3D bioprinting using synovium-derived MSC-laden photo-cross-linked ECM bioink for cartilage regeneration. *ACS Appl Mater Interfaces*, 15: 8895–8913.

http://doi:10.1021/acsami.2c19058

136. Singh YP, Bandyopadhyay A, Mandal BB, 2019, 3D bioprinting using cross-linker-free silk–gelatin bioink for cartilage tissue engineering. *ACS Appl Mater Interfaces*, 11: 33684–33696.

http://doi:10.1021/acsami.9b11644

137. Kara Özenler A, Distler T, Tihminlioglu F, *et al.*, 2023, Fish scale containing alginate dialdehyde-gelatin bioink for bone tissue engineering. *Biofabrication*, 15: 025012.

http://doi:10.1088/1758-5090/acb6b7

138. Chakraborty J, Fernández-Pérez J, van Kampen KA, *et al.*, 2023, Development of a biomimetic arch-like 3D bioprinted construct for cartilage regeneration using gelatin methacryloyl and silk fibroin-gelatin bioinks. *Biofabrication*, 15: 035009.

http://doi:10.1088/1758-5090/acc68f

139. Chen P, Zheng L, Wang Y, *et al.*, 2019, Desktop-stereolithography 3D printing of a radially oriented extracellular matrix/mesenchymal stem cell exosome bioink for osteochondral defect regeneration. *Theranostics*, 9: 2439–2459.

http://doi:10.7150/thno.31017

140. Cidonio G, Alcala-Orozco CR, Lim KS, *et al.*, 2019, Osteogenic and angiogenic tissue formation in high fidelity nanocomposite Laponite-gelatin bioinks. *Biofabrication*, 11: 035027.

http://doi:10.1088/1758-5090/ab19fd

141. Irmak G, Gümüşderelioğlu M, 2020, Photo-activated platelet-rich plasma (PRP)-based patient-specific bio-ink for cartilage tissue engineering. *Biomed Mater,* 15: 065010.

http://doi:10.1088/1748-605X/ab9e46

142. Bai Z, Guo X-H, Tang C, *et al.*, 2018, Effects of artesunate on the expressions of insulin-like growth factor-1, osteopontin

and C-telopeptides of type II collagen in a rat model of osteoarthritis. *Pharmacology*, 101: 1–8.

http://doi:10.1159/000479160

143. Street J, Bao M, DeGuzman L, *et al.*, 2002, Vascular endothelial growth factor stimulates bone repair by promoting angiogenesis and bone turnover. *Proc Natl Acad Sci,* 99: 9656–9661.

http://doi:10.1073/pnas.152324099

144. Mi L, Liu H, Gao Y, *et al.*, 2017, Injectable nanoparticles/hydrogels composite as sustained release system with stromal cell-derived factor-1α for calvarial bone regeneration. *Int J Biol Macromol,* 101: 341–347.

http://doi:10.1016/j.ijbiomac.2017.03.098

145. Fujioka-Kobayashi M, Ota MS, Shimoda A, *et al.*, 2012, Cholesteryl group- and acryloyl group-bearing pullulan nanogel to deliver BMP2 and FGF18 for bone tissue engineering. *Biomaterials*, 33: 7613–7620.

http://doi:10.1016/j.biomaterials.2012.06.075

146. Fahimipour F, Dashtimoghadam E, Mahdi Hasani-Sadrabadi M, *et al.*, 2019, Enhancing cell seeding and osteogenesis of MSCs on 3D printed scaffolds through injectable BMP2 immobilized ECM-Mimetic gel. *Dent Mater,* 35: 990–1006.

http://doi:10.1016/j.dental.2019.04.004

147. Groll J, Burdick JA, Cho D-W, *et al.*, 2018, A definition of bioinks and their distinction from biomaterial inks. *Biofabrication*, 11: 013001.

http://doi:10.1088/1758-5090/aaec52

148. Colombo M, Bianchi A, 2010, Click chemistry for the synthesis of RGD-containing integrin ligands. *Molecules*, 15: 178–197.

http://doi:10.3390/molecules15010178

149. Panwar A, Tan L, 2016, Current status of bioinks for micro-extrusion-based 3D bioprinting. *Molecules*, 21: 685.

http://doi:10.3390/molecules21060685

150. Byambaa B, Annabi N, Yue K, *et al.*, 2017, Bioprinted osteogenic and vasculogenic patterns for engineering 3D bone tissue. *Adv Healthc Mater,* 6: 1700015.

http://doi:10.1002/adhm.201700015

151. Wang B, Díaz-Payno PJ, Browe DC, *et al.*, 2021, Affinity-bound growth factor within sulfated interpenetrating network bioinks for bioprinting cartilaginous tissues. *Acta Biomater,* 128: 130–142.

http://doi:10.1016/j.actbio.2021.04.016

152. Xie M, Wu D, Li G, *et al.*, 2021, Exosomes targeted towards applications in regenerative medicine. *Nano Sel,* 2: 880–908.

http://doi:10.1002/nano.202000251

153. Zhou Q, Cai Y, Lin X, 2020, The dual character of exosomes in osteoarthritis: Antagonists and therapeutic agents. *Acta Biomater,* 105: 15–25.

http://doi:10.1016/j.actbio.2020.01.040

154. Isaeva EV, Beketov EE, Demyashkin GA, *et al.*, 2022, Cartilage formation in vivo using high concentration collagen-based bioink with MSC and decellularized ECM granules. *Int J Mol Sci,* 23: 2703.

http://doi:10.3390/ijms23052703

155. Marcu IC, Illaste A, Heuking P, *et al.*, 2015, Functional characterization and comparison of intercellular communication in stem cell-derived cardiomyocytes. *Stem Cells*, 33: 2208–2218.

http://doi:10.1002/stem.2009

156. Tang J, Peng R, Ding J, 2010, The regulation of stem cell differentiation by cell-cell contact on micropatterned material surfaces. *Biomaterials*, 31: 2470–2476.

http://doi:10.1016/j.biomaterials.2009.12.006

157. Xu F, Sridharan B, Wang S, *et al.*, 2011, Embryonic stem cell bioprinting for uniform and controlled size embryoid body formation. *Biomicrofluidics*, 5: 022207.

http://doi:10.1063/1.3580752

158. Bourget J-M, Kérourédan O, Medina M, *et al.*, 2016, Patterning of endothelial cells and mesenchymal stem cells by laser-assisted bioprinting to study cell migration. *Biomed Res Int,* 2016: 1–7.

http://doi:10.1155/2016/3569843

159. Kolesky DB, Truby RL, Gladman AS, *et al.*, 2014, 3D bioprinting of vascularized, heterogeneous cell-laden tissue constructs. *Adv Mater,* 26: 3124–3130.

http://doi:10.1002/adma.201305506

160. Jakus AE, Rutz AL, Shah RN, 2016, Advancing the field of 3D biomaterial printing. *Biomed Mater,* 11: 014102.

http://doi:10.1088/1748-6041/11/1/014102

161. Ovsianikov A, James Y, Vladimir M, 2018, 3D printing and biofabrication. Springer International Publishing.

162. Morgan FLC, Moroni L, Baker MB, 2020, Dynamic bioinks to advance bioprinting. *Adv Healthc Mater,* 9: 1901798.

http://doi:10.1002/adhm.201901798

163. Nicodemus GD, Bryant SJ, 2008, Cell encapsulation in biodegradable hydrogels for tissue engineering applications. *Tissue Eng Part B Rev,* 14: 149–165.

http://doi:10.1089/ten.teb.2007.0332

164. Li H, Tan C, Li L, 2018, Review of 3D printable hydrogels and constructs. *Mater Des,* 159: 20–38.

http://doi:10.1016/j.matdes.2018.08.023

165. Mu X, Agostinacchio F, Xiang N, *et al.*, 2021, Recent advances in 3D printing with protein-based inks. *Prog Polym Sci,* 115: 101375.

http://doi:10.1016/j.progpolymsci.2021.101375

166. Simorgh S, Milan PB, Saadatmand M, *et al.*, 2021, Human olfactory mucosa stem cells delivery using a collagen hydrogel: As a potential candidate for bone tissue engineering. *Materials (Basel)*, 14: 1–17.

http://doi:10.3390/ma14143909

167. Wu X, Rapoport TA, 2018, Mechanistic insights into ER-associated protein degradation. *Curr Opin Cell Biol,* 53: 22–28.

http://doi:10.1016/j.ceb.2018.04.004

168. Verbeek CJR, van den Berg LE, 2010, Extrusion processing and properties of protein-based thermoplastics. *Macromol Mater Eng,* 295(1): 10–21.

http://doi:10.1002/mame.200900167

169. Rutz AL, Lewis PL, Shah RN, 2017, Toward next-generation bioinks: Tuning material properties pre- and post-printing to optimize cell viability. *MRS Bull,* 42(8): 563–570.

http://doi:10.1557/mrs.2017.162

170. Kabirian F, Mozafari M, 2020, Decellularized ECM-derived bioinks: Prospects for the future. *Methods*, 171: 108–118.

http://doi:10.1016/j.ymeth.2019.04.019

171. Pugliese R, Beltrami B, Regondi S, *et al.*, 2021, Polymeric biomaterials for 3D printing in medicine: An overview. *Ann 3D Print Med*, 2: 100011.

http://doi:10.1016/j.stlm.2021.100011

172. Parker ST, Domachuk P, Amsden J, *et al.*, 2009, Biocompatible silk printed optical waveguides. *Adv Mater,* 21: 2411–2415.

http://doi:10.1002/adma.200801580

173. Ramesh S, Harrysson OLA, Rao PK, *et al.*, 2021, Extrusion bioprinting: Recent progress, challenges, and future opportunities. *Bioprinting*, 21: e00116.

http://doi:10.1016/j.bprint.2020.e00116

174. Bedell ML, Navara AM, Du Y, *et al.*, 2020, Polymeric systems for bioprinting. *Chem Rev,* 120(19): 10744–10792.

http://doi:10.1021/acs.chemrev.9b00834

175. Chakraborty J, Mu X, Pramanick A, *et al.*, 2022, Recent advances in bioprinting using silk protein-based bioinks. *Biomaterials*, 287: 121672.

http://doi:10.1016/j.biomaterials.2022.121672

176. Zhou J, Zhang B, Shi L, *et al.*, 2014, Regenerated silk fibroin films with controllable nanostructure size and secondary structure for drug delivery. *ACS Appl Mater Interfaces*, 6(24): 21813–21821.

http://doi:10.1021/am502278b

177. Nikoomanzari E, Karbasi M, Melo WCMA, *et al.*, 2022, Impressive strides in antibacterial performance amelioration of Ti-based implants via plasma electrolytic oxidation (PEO): A review of the recent advancements. *Chem Eng J,* 441: 136003.

http://doi:10.1016/j.cej.2022.136003

178. Adhikari J, Roy A, Das A, *et al.*, 2021, Effects of processing parameters of 3D bioprinting on the cellular activity of bioinks. *Macromol Biosci,* 21(1): 2000179.

http://doi:10.1002/mabi.202000179

179. Hull SM, Brunel LG, Heilshorn SC, 2022, 3D bioprinting of cell-laden hydrogels for improved biological functionality. *Adv Mater*, 34(2): 2103691.

http://doi:10.1002/adma.202103691

180. Jaspe J, Hagen SJ, 2006, Do protein molecules unfold in a simple shear flow? *Biophys J,* 91(9): 3415–3424.

http://doi:10.1529/biophysj.106.089367

181. Nishioka GM, Markey AA, Holloway CK, 2004. Protein damage in drop-on-demand printers. *J Am Chem Soc*, 126(4): 16320–16321.

http://doi.org/10.1021/ja044539z

182. Delaney JT, Smith PJ, Schubert US, 2009, Inkjet printing of proteins. *Soft Matter,* 5(24): 4866–4877.

http://doi:10.1039/b909878j

183. Schwab A, Levato R, D'Este M, *et al.*, 2020, Printability and shape fidelity of bioinks in 3D bioprinting. *Chem Rev,* 120(19): 11028–11055.

http://doi:10.1021/acs.chemrev.0c00084

184. Neumann TV, Dickey MD, 2020, Liquid metal direct write and 3D printing: A review. *Adv Mater Technol,* 5(9): 2000070.

http://doi:10.1002/admt.202000070

185. Amorim PA, D'Ávila MA, Anand R, *et al.*, 2021, Insights on shear rheology of inks for extrusion-based 3D bioprinting. *Bioprinting*, 22: e00129.

http://doi:10.1016/j.bprint.2021.e00129

186. Joshi YM, Petekidis G, 2018, Yield stress fluids and ageing. *Rheol Acta,* 57(6-7): 521–549.

http://doi:10.1007/s00397-018-1096-6

187. Mouser VHM, Melchels FPW, Visser J, *et al.*, 2016, Yield stress determines bioprintability of hydrogels based on gelatin-methacryloyl and gellan gum for cartilage bioprinting. *Biofabrication*, 8(3): 035003.

http://doi:10.1088/1758-5090/8/3/035003

188. Sommer MR, Alison L, Minas C, *et al.*, 2017, 3D printing of concentrated emulsions into multiphase biocompatible soft materials. *Soft Matter,* 13(9): 1794–1803.

http://doi:10.1039/C6SM02682F

189. Nedunchezian S, Banerjee P, Lee C-Y, *et al.*, 2021, Generating adipose stem cell-laden hyaluronic acid-based scaffolds using 3D bioprinting via the double crosslinked strategy for chondrogenesis. *Mater Sci Eng C,* 124: 112072.

http://doi:10.1016/j.msec.2021.112072

190. Jiang Y, Zhou J, Feng C, *et al.*, 2020, Rheological behavior, 3D printability and the formation of scaffolds with cellulose nanocrystals/gelatin hydrogels. *J Mater Sci,* 55(33): 15709–15725.

http://doi:10.1007/s10853-020-05128-x

191. Bom S, Ribeiro R, Ribeiro HM, *et al.*, 2022, On the progress of hydrogel-based 3D printing: Correlating rheological properties with printing behaviour. *Int J Pharm,* 615: 121506.

http://doi:10.1016/j.ijpharm.2022.121506

192. Thattaruparambil Raveendran N, Vaquette C, Meinert C, *et al.*, 2019, Optimization of 3D bioprinting of periodontal ligament cells. *Dent Mater,* 35(12): 1683–1694.

http://doi:10.1016/j.dental.2019.08.114

193. Billiet T, Vandenhaute M, Schelfhout J, *et al.*, 2012, A review of trends and limitations in hydrogel-rapid prototyping for tissue engineering. *Biomaterials*, 33(26): 6020–6041.

http://doi:10.1016/j.biomaterials.2012.04.050

194. Nair K, Gandhi M, Khalil S, *et al.*, 2009, Characterization of cell viability during bioprinting processes. *Biotechnol J*, 4(8): 1168–1177.

http://doi:10.1002/biot.200900004

195. Chen DXB, 2019, Extrusion bioprinting of scaffolds, in *Extrusion Bioprinting of Scaffolds for Tissue Engineering Applications*, *Springer International Publishing*, Cham, 117–145.

http://doi:10.1007/978-3-030-03460-3_6

196. Daly AC, Freeman FE, Gonzalez-Fernandez T, *et al.*, 2017, 3D bioprinting for cartilage and osteochondral tissue engineering. *Adv Healthc Mater,* 6(22): 1–20.

http://doi:10.1002/adhm.201700298

197. Boularaoui S, Al Hussein G, Khan KA, *et al.*, 2020, An overview of extrusion-based bioprinting with a focus on induced shear stress and its effect on cell viability. *Bioprinting*, 20: e00093.

http://doi:10.1016/j.bprint.2020.e00093

198. Gu Q, Hao J, Lu Y, *et al.*, 2015, Three-dimensional bio-printing. *Sci China Life Sci,* 58(5): 411–419.

http://doi:10.1007/s11427-015-4850-3

199. Matai I, Kaur G, Seyedsalehi A, *et al.*, 2020, Progress in 3D bioprinting technology for tissue/organ regenerative engineering. *Biomaterials*, 226: 119536.

http://doi:10.1016/j.biomaterials.2019.119536

200. Di Bella C, Duchi S, O'Connell CD, *et al.*, 2018, In situ handheld three-dimensional bioprinting for cartilage regeneration. *J Tissue Eng Regen Med,* 12(3): 611–621.

http://doi:10.1002/term.2476

201. Xu T, Gregory C, Molnar P, *et al.*, 2006, Viability and electrophysiology of neural cell structures generated by the inkjet printing method. *Biomaterials,* 27(19): 3580–3588.

http://doi:10.1016/j.biomaterials.2006.01.048

202. Xu T, Jin J, Gregory C, *et al.*, 2005, Inkjet printing of viable mammalian cells. *Biomaterials,* 26(1): 93–99.

http://doi:10.1016/j.biomaterials.2004.04.011

203. Brenker JC, Devendran C, Neild A, *et al.*, 2020, On-demand sample injection: combining acoustic actuation with a tear-drop shaped nozzle to generate droplets with precise spatial and temporal control. *Lab Chip*, 20(2): 253–265.

http://doi:10.1039/C9LC00837C

204. Yang X, Lu Z, Wu H, *et al.*, 2018, Collagen-alginate as bioink for three-dimensional (3D) cell printing based cartilage tissue engineering. *Mater Sci Eng C,* 83: 195–201.

http://doi:10.1016/j.msec.2017.09.002

205. Lim H, Kim HS, Qazi R, *et al.*, 2020, Advanced soft materials, sensor integrations, and applications of wearable flexible hybrid electronics in healthcare, energy, and environment. *Adv Mater,* 32(15): 1901924.

http://doi:10.1002/adma.201901924

206. Slaughter BV, Khurshid SS, Fisher OZ, *et al.*, 2009, Hydrogels in regenerative medicine. *Adv Mater,* 21(32-33): 3307–3329.

http://doi:10.1002/adma.200802106

207. Fedorovich NEE, Alblas J, Hennink WEE, *et al.*, 2011, Organ printing: The future of bone regeneration? *Trends Biotechnol*, 29(12): 601–606.

http://doi:10.1016/j.tibtech.2011.07.001

208. Aldana AA, Abraham GA, 2017, Current advances in electrospun gelatin-based scaffolds for tissue engineering applications. *Int J Pharm*, 523(2): 441–453.

http://doi:10.1016/j.ijpharm.2016.09.044

209. Kim U-J, Park J, Li C, *et al.*, 2004, Structure and properties of silk hydrogels. *Biomacromolecules*, 5(3): 786–792.

http://doi:10.1021/bm0345460

210. Gupta S, Alrabaiah H, Christophe M, *et al.*, 2021, Evaluation of silk-based bioink during pre and post 3D bioprinting: A review. *J Biomed Mater Res Part B Appl Biomater,* 109(2): 279–293.

http://doi:10.1002/jbm.b.34699

211. Kim YB, Lee H, Kim GH, 2016, Strategy to achieve highly porous/biocompatible macroscale cell blocks, using a collagen/genipin-bioink and an optimal 3D printing process. *ACS Appl Mater Interfaces*, 8(47): 32230–32240.

http://doi:10.1021/acsami.6b11669

212. Chawla S, Midha S, Sharma A, *et al.*, 2018, Silk-based bioinks for 3D bioprinting. *Adv Healthc Mater,* 7(8): 1701204.

http://doi:10.1002/adhm.201701204

213. Kim BS, Das S, Jang J, *et al.*, 2020, Decellularized extracellular matrix-based bioinks for engineering tissue- and organ-specific microenvironments. *Chem Rev,* 120(19): 10608–10661.

http://doi:10.1021/acs.chemrev.9b00808

214. Bourgine PE, Pippenger BE, Todorov A, *et al.*, 2013, Tissue decellularization by activation of programmed cell death. *Biomaterials*, 34(19): 6099–6108.

http://doi:10.1016/j.biomaterials.2013.04.058

215. Groll J, Boland T, Blunk T, *et al.*, 2016, Biofabrication: Reappraising the definition of an evolving field. *Biofabrication*, 8(26): 013001.

http://doi:10.1088/1758-5090/8/1/013001

216. Sarkari S, Khajehmohammadi M, Davari N, *et al.*, 2022, The effects of process parameters on polydopamine coatings employed in tissue engineering applications. *Front Bioeng Biotechnol,* 10: 1005413.

http://doi:10.3389/fbioe.2022.1005413

217. Hong N, Yang G-H, Lee J, *et al.*, 2018, 3D bioprinting and its in vivo applications. *J Biomed Mater Res Part B Appl Biomater*, 106(1): 444–459.

http://doi:10.1002/jbm.b.33826

218. Ning L, Gil CJ, Hwang B, *et al.*, 2020, Biomechanical factors in three-dimensional tissue bioprinting. *Appl Phys Rev,* 7(4): 1–22.

http://doi:10.1063/5.0023206

219. Cui X, Boland T, 2009, Human microvasculature fabrication using thermal inkjet printing technology. *Biomaterials*, 30(31): 6221–6227.

http://doi:10.1016/j.biomaterials.2009.07.056

220. Gao G, Yonezawa T, Hubbell K, *et al.*, 2015, Inkjet-bioprinted acrylated peptides and PEG hydrogel with human mesenchymal stem cells promote robust bone and cartilage formation with minimal printhead clogging. *Biotechnol J,* 10(10): 1568–1577.

http://doi:10.1002/biot.201400635

221. Ihalainen P, Määttänen A, Sandler N, 2015, Printing technologies for biomolecule and cell-based applications. *Int J Pharm,* 494(2): 585–592.

http://doi:10.1016/j.ijpharm.2015.02.033

222. Pati F, Gantelius J, Svahn HA, 2016, 3D bioprinting of tissue/organ models. *Angew Chemie Int Ed,* 55(15): 4650–4665.

http://doi:10.1002/anie.201505062

223. Hong H, Seo YB, Kim DY, *et al.*, 2020, Digital light processing 3D printed silk fibroin hydrogel for cartilage tissue engineering. *Biomaterials*, 232: 119679.

http://doi:10.1016/j.biomaterials.2019.119679

224. Rice WL, Firdous S, Gupta S, *et al.*, 2008, Non-invasive characterization of structure and morphology of silk fibroin biomaterials using non-linear microscopy. *Biomaterials*, 29(13): 2015–2024.

http://doi:10.1016/j.biomaterials.2007.12.049

225. Tang S, Richardson BM, Anseth KS, 2021, Dynamic covalent hydrogels as biomaterials to mimic the viscoelasticity of soft tissues. *Prog Mater Sci,* 120: 100738.

http://doi:10.1016/j.pmatsci.2020.100738

226. Lim KS, Galarraga JH, Cui X, *et al.*, 2020, Fundamentals and applications of photo-cross-linking in bioprinting. *Chem Rev,* 120(19):10662–10694.

http://doi:10.1021/acs.chemrev.9b00812

227. Mueller E, Poulin I, Bodnaryk WJ, *et al.*, 2022, Click chemistry hydrogels for extrusion bioprinting: Progress, challenges, and opportunities. *Biomacromolecules*, 23(3): 619–640.

http://doi:10.1021/acs.biomac.1c01105

228. Rastin H, Ormsby RT, Atkins GJ, *et al.*, 2020, 3D bioprinting of methylcellulose/gelatin-methacryloyl (MC/GelMA) bioink with high shape integrity. *ACS Appl Bio Mater*, 3(3): 1815–1826.

http://doi:10.1021/acsabm.0c00169

229. GhavamiNejad A, Ashammakhi N, Wu XY, *et al.*, 2020, Crosslinking strategies for 3D bioprinting of polymeric hydrogels. *Small*, 16(35): 2002931.

http://doi:10.1002/smll.202002931

230. Gungor-Ozkerim PS, Inci I, Zhang YS, *et al.*, 2018, Bioinks for 3D bioprinting: An overview. *Biomater Sci,* 6(5): 915–946.

http://doi:10.1039/C7BM00765E

231. Hu W, Wang Z, Xiao Y, *et al.*, 2019, Advances in crosslinking strategies of biomedical hydrogels. *Biomater Sci,* 7(3): 843–855.

http://doi:10.1039/C8BM01246F

232. Lee JM, Suen SKQ, Ng WL, *et al.*, 2021, Bioprinting of collagen: Considerations, potentials, and applications. *Macromol Biosci,* 21(1): 1–18.

http://doi:10.1002/mabi.202000280

233. Zennifer A, Subramanian A, Sethuraman S, 2022, Bioprinting design considerations of bioinks for laser bioprinting technique towards tissue regenerative applications. *Bioprinting*, 27: e00205.

http://doi:10.1016/j.bprint.2022.e00205

234. Lin X, Tsao CT, Kyomoto M, *et al.*, 2022, Injectable natural polymer hydrogels for treatment of knee osteoarthritis. *Adv Healthc Mater*, 11(9): 2101479.

http://doi:10.1002/adhm.202101479

235. Zhao Q, Zhou Y, Wang M, 2021, Three-dimensional endothelial cell incorporation within bioactive nanofibrous scaffolds through concurrent emulsion electrospinning and coaxial cell electrospraying. *Acta Biomater,* 123: 312–324.

http://doi:10.1016/j.actbio.2021.01.035

236. Jung CS, Kim BK, Lee J, *et al.*, 2018. Development of printable natural cartilage matrix bioink for 3D printing of irregular tissue shape. *Tissue Eng Regen Med*, 15: 155–162.

https://doi.org/10.1007/s13770-017-0104-8

237. Visscher DO, Lee H, van Zuijlen PP, *et al.*, 2021. A photo-crosslinkable cartilage-derived extracellular matrix bioink for auricular cartilage tissue engineering. *Acta Biomater*, 121: 193–203.

https://doi.org/10.1016/j.actbio.2020.11.029

ACCSCIENCE PUBLISHING

International Journal of Bioprinting

RESEARCH ARTICLE

Uncovering advances in final end-user applications, user acceptability, quality assurance, and digital technologies for 3D-printed oral drug delivery systems

Veronica L. Rios-Mata[1†], Marisela Rodriguez-Salvador[1†*], Jia An[2], Chee Kai Chua [2,3], and Pedro F. Castillo-Valdez[1]

[1] Tecnologico de Monterrey, Escuela de Ingeniería y Ciencias, Monterrey, Nuevo León, México

[2] Centre for Healthcare Education, Entrepreneurship and Research at SUTD (CHEERS), Singapore University of Technology and Design, Singapore

[3] Engineering Product Development, Singapore University of Technology and Design, Singapore

Abstract

The increasing demand for innovative drugs and personalized treatment is radically changing the pharmaceutical industry, where significant efforts in research and development (R&D) are taking place. Three-dimensional (3D) printing offers interesting solutions for these demands, solving some of the limitations of current manufacturing processes. 3D-printed oral drug delivery systems can improve the delivery of pharmaceutical substances in the body, and the dynamic interaction between pharmaceutical ingredients, while providing personalized formulations, geometries, sizes, controlled release rates, and increasing time in the gastrointestinal tract. Advances in 3D printing for oral drug delivery systems have been investigated in terms of processes, materials, and effects. However, it is important to also consider other topics, such as the specific needs of the users to enhance drugs acceptability, the quality control processes due to the absence of approved guidelines, and the digitalization of the industry to respond to future challenges of the digital era; nevertheless, there are no studies that comprise these elements. To fill this gap, the aim of this research is to identify advances in terms of final end-user applications, quality assurance, user acceptability, and digital technologies for 3D-printed oral drug delivery systems. To accomplish this, a competitive technology intelligence (CTI) methodology was applied, where scientific literature was retrieved from the Web of Science covering the period from January 1, 1900, to May 1, 2023. For this task, a scientometric analysis was performed, and the main trends involving the previously mentioned elements were identified. In the first case, 3D-printed oral drug delivery systems are being designed for different purposes, including as anti-deterrent formulations to decrease the global problem of opioid abuse. For quality assurance, the results demonstrated the implementation of approaches like quality by design to increase the quality of the 3D-printed dosage forms. In the case of user acceptability, the interest in creating more attractive formulations was identified; for this, innovative technologies such as ColorJet 3D printing are being used. Lastly, regarding digital technologies, the importance of cyberattacks while sending the 3D-printed dosage form file to the 3D printer is highlighted; for this, cybersecurity systems are being studied. The outcomes of this study can add value to researchers, organizations, and investment firms interested in the R&D of novel and personalized treatments, and the areas of 3D printing, pharmaceutical, medical, and health.

†These authors contributed equally to this work.

***Corresponding author:**
Marisela Rodriguez-Salvador (marisrod@tec.mx)

Citation: Rios-Mata VL, Rodriguez-Salvador M, An J, *et al*., 2023, Uncovering advances in final end-user applications, user acceptability, quality assurance, and digital technologies for 3D-printed oral drug delivery systems. *Int J Bioprint*, 9(6): 1119.
https://doi.org/10.36922/ijb.1119

Received: June 22, 2023
Accepted: July 31, 2023
Published Online: September 8, 2023

Copyright: © 2023 Author(s). This is an Open Access article distributed under the terms of the Creative Commons Attribution License, permitting distribution, and reproduction in any medium, provided the original work is properly cited.

Publisher's Note: AccScience Publishing remains neutral with regard to jurisdictional claims in published maps and institutional affiliations.

Keywords: 3D Printing; Oral drug delivery; Quality; Acceptability; Digital technologies

1. Introduction

Drug delivery systems (DDS) are characterized by technologies that enhance the delivery of pharmaceutical products (drugs, vitamins, health supplements, or diagnostic substances) into the body. Innovations in drug delivery technologies can help meet their unique delivery needs[1] and mitigate treatment side effects. According to the United States National Institute of Biomedical Imaging and Bioengineering (NIBIB)[2], DDS can be described in two broad-ranging categories: routes of delivery and delivery vehicles. The first one refers to the routes of administration of pharmaceutical compounds, with the most common being oral, parenteral (intravenous, intramuscular, subcutaneous, intra-arterial), sublingual, topical, nasal, intraosseous, ocular, rectal, and vaginal[3]. On the other hand, delivery vehicles concern the various ways in which pharmaceutical compounds can be encapsulated or packaged so they can safely travel through the body; some examples are liposomes, polymeric nanoparticles, microbubbles, hydrogels, micelles[4], scaffolds[5,6], and microneedles[7].

In October 2022, Euromonitor International, a global leading company in business intelligence and market research, analyzed four trends that will impact the pharmaceutical and medical industry, with "Rising investment in research and development (R&D) and innovation" being one of them[8]. This trend points to the rising demands for high-value innovative treatments, driving investment in R&D and personalized treatment. For this, the versatility of three-dimensional (3D) printing and its diverse processes can be utilized in various areas, including the medical and pharmaceutical industry, reducing high production costs, and limitations of traditional processes, as well as allowing personalized manufacturing according to individual needs. The introduction of 3D printing technology into the pharmaceutical field can revolutionize the medical industry, as it enables varying dosage batch sizes, novel dosage forms, and drug distribution.

Under this context, 3D printing of oral DDS concerns the development of technologies and dosage forms using 3D printing processes to improve the delivery of pharmaceutical products, the dynamic interaction between pharmaceutical ingredients, and the user safety. They can offer personalized formulations, geometries, sizes, release rates, and increased time in the gastrointestinal tract, making 3D printing more attractive than traditional procedures. For instance, one of the most used methods to manufacture tablets and pills is direct compression, which has advantages such as short operation time and use of fewer resources[9]. However, some active pharmaceutical ingredients (APIs) demonstrate low compressibility[10], directly affecting the mechanical properties of the tablet and pill. On the other hand, this process requires a compression press, in which the punch and die can cause other defects like sticking, picking, double impression[11], and edging. Another inconvenience is that changing the appearance of the tablet and pill is not an immediate operation, as it requires the fabrication of a new die based on the desired geometry.

Hard capsules and softgels are not exempt from manufacturing defects, problems related to body caps (differences in length or improperly sealed), and incorrect rotary die pressure, which can occur during their production. 3D printing techniques offer solutions to these issues. From a general perspective, they operate through a 3D printer that reads a computer-aided design (CAD) file, which was created to produce a physical model according to the dosage form desired. The printhead moves in the x–y plane to create the foundation of the object, then the printhead moves along the z-axis, resulting in layer-by-layer formation of the dosage form[12]. As each 3D printing technique has different process parameters, the applied technique can be selected based on which is more suitable for the specific active pharmaceutical ingredients (APIs) and the type of dosage form.

3D-printed oral DDS encompass various types of films, tablets, capsules, pills, and fibrous dosage forms. Figure 1 illustrates some examples of the types of 3D-printed oral dosage forms, with the most common materials alongside the API being polymers and hydrogels, as shown in Table 1.

There are different studies on 3D-printed oral DDS, including one that reveals the advances and current state in terms of processes and applications. For instance, Mancilla-De-la-Cruz and Rodriguez-Salvador studied the available technologies for 3D printing of oral drug delivery in 2022[27]; during the same year, Mancilla-De-la-Cruz *et al.* investigated the process, materials, and effects of 3D printing for DDS, where oral administration was studied[14]; however, the user has specific needs that need be attended to promote drugs acceptability; moreover, considering the novelty of 3D-printed DDS and the lack of standardization, quality control represents a crucial topic to be analyzed. In addition, to cope with the challenges of the digital era, it is necessary to study efforts toward digitalization. Despite the importance of these topics so far, there are no studies that discuss them; to fill this gap, the purpose of this research

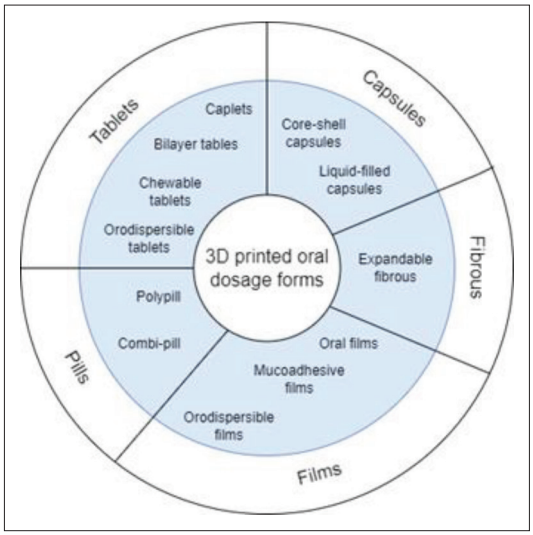

Figure 1. Types of 3D printing oral dosage forms.

is to uncover advances in the following categories: end-user applications, quality assurance, user acceptability, and digital technologies for 3D printing of oral DDS. To this end, a competitive technology intelligence (CTI) methodology was applied to reveal the current scientific and technological advances in the field.

In this research, end-user applications refer to the use of 3D-printed oral DDS to meet the specific end-user needs, such as designing dosage forms that are user-friendly to visually-impaired patients, creating non-commercially available formulations for pediatric patients, and conceiving novel solutions to target global problems, such as drug abuse.

Quality assurance focuses on methods, protocols, and tools to guarantee quality during the preparation and fabrication of 3D-printed dosage forms. It is a common concern in 3D-printed oral DDS, but unfortunately there is no specific US Food and Drug Administration (FDA) guideline for 3D-printed medicines, which are usually fabricated according to chemistry, manufacturing, and control (CMC) standards, Good Manufacturing Practices (GMP), and regulatory processes for pharmaceutical drug product applications from the US FDA Center for Drug Evaluation and Research (CDER)[28].

On the other hand, user acceptability analyzes user-centered needs, exploring the real demands of the user, including preferences and palatability. This can facilitate the introduction of 3D-printed orally administered drugs to the market and increase the acceptability of these novel treatments. For this reason, user acceptability should be considered.

Digital technologies examine advances in this field. Currently, the most innovative industries are rapidly migrating toward digitalization. In the pharmaceutical industry, important efforts for the implementation of digital technologies throughout 3D printing processes are growing. In this study, a category focused on digital technologies is examined.

CTI is a strategic and systematic process that focuses on monitoring the technical and competitive environment of an organization at different levels, with the purpose of providing actionable information for decision making in the areas of technology, innovation, product design, R&D, and markets (global, national, and local)[29].

Through CTI, it is possible to identify available opportunities that can be used to predict future trends, generating competitive advantages. Its continuous process is assisted by a diversity of tools and qualitative and quantitative methods that facilitate the acquisition, extraction, collection, visualization, and interpretation of the information.

2. Methodology

In this research, the methodology applied is that proposed by Rodriguez-Salvador and Castillo-Valdez in 2021, which consists of an eight-step process with interdependent phases and continuous feedback: (i) project planning, (ii) identification of data sources, (iii) search strategy design, (iv) data collection, (v) information analysis, (vi) expert feedback, (vii) validation and final results, and (viii) decision making[30].

Primary and secondary sources were determined to gather information. The primary sources were international experts in the field of 3D printing. The secondary source was scientific literature from Web of Science (WoS), which includes more than 21,000 peer-reviewed journals and 17.2 million open access records[31].

Terms and keywords related to 3D printing of oral DDS and data subjects were identified and manually validated. These terms include words related to 3D printing, delivery systems, type of dosage forms, and pharmaceutical area. In addition, exclusion terms were identified manually to exclude irrelevant documents. These terms were integrated into a query with a period corresponding to January 1, 1900, to May 1, 2023. The document types were limited to articles, proceeding papers, and early-access articles. The query was validated by international experts in 3D printing. Figure 2 illustrates the generated query.

A total of 621 publications were retrieved from the query; after the manual inspection, the total number of papers was reduced to 512. These documents were classified

Table 1. Excipients utilized in various 3D printing techniques

Process	Technique	Material (excipients)	Reference
Binder jetting	Binder jetting	– Polyvinylpyrrolidone (PVP) – Kollidon® SR – Hydroxypropyl methylcellulose (HPMC) – Polyvinylpyrroldine-vinyl (PVPV) – Hydroxypropyl cellulose (HPC) – Ethylcellulose (EC) – Mycrocrystalline cellulose (MCC) – Lactose monohydrate – Methyl cellulose (MC)	[13]
Material extrusion	Fused deposition modeling	– Polylactic acid (PLA) – Polyvinyl alcohol (PVA) – Soluplus – Ethylcellulose (EC) – Eudragit® – Hydroxymethyl cellulose (HMPC) – Hydroxypropyl cellulose (HPC) – Polycaprolactone (PCL) – Polyethylene glycol (PEG) – Hydroxypropyl methylcellulose (HPMC) – Polyethylene oxides (PEOs) – Polyvinylpyrrolidone (PVP)	[14]
	Pressure-assisted microsyringe	– Hydroxymethyl cellulose (HMPC) – Mycrocrystalline cellulose (MCC) – Polyvinylpyrrolidone (PVP) – Lactose – Hydroxypropyl cellulose (HPC) – Hydroxypropyl methylcellulose (HPMC) – Polyvinyl alcohol (PVA) – Kollicoat® – Ethylcellulose (EC) – Hydroxypropyl methylcellulose (HPMC)	[15] [16] [17]
Material jetting or inkjet printing	Drop-on-demand	– Polycaprolactone (PCL) – Polyvinylpyrrolidone (PVP) – Poly (N-isopropylacrylamind-co-acrylamide) (PNIPAM) – Hydroxypropyl methylcellulose (HPMC) – Hydroxypropyl cellulose (HPC)	[18] [19]
	Continuous inkjet printing	– Hydroxypropyl methylcellulose (HPMC) – Hydroxypropyl cellulose (HPC) – Polyethylene glycol (PEG)	[20]
Powder bed fusion	Selective laser sintering	– Polycaprolactone (PCL) – Eudragit® – Kollicoat® IR – Hydroxymethyl cellulose (HMPC) – Poly-I-lactic acid (PLLA) – Kollidon® – Mycrocrystalline cellulose (MCC) – Ethylcellulose (EC) – Polyethylene oxide (PEO) – Methylcellulose (MC)	[21]
Vat photopolymerization	Stereolithography	– Polycaprolactone (PCL) – Polyethylene glycol diacrylate (PEGDA) – Polyethylene glycol dimethacrylate (PEGDMA) – Poly (2-hydroxyethyl methacrylate) (pHEMA) – Polypropylene fumarate (PPF) – Diphenyl (2,4,6-trimethylbenzoyl) (TPO) – Polyethylene glycol (PEG) – Triol	[22] [23] [24]
	Digital light processing	– Polyethylene glycol diacrylate (PEGDA) – Polyethylene glycol (PEG) – Acrylated hyperbranched polyester (AHBPE) – Polyethylene glycol dimethacrylate (PEGDMA) – Polycaprolactone (PCL) – Polypropylene fumarate (PPF) – Diphenyl (2,4,6-trimethylbenzoyl) phosphine oxide (TPO)	[22] [25] [26] [24]

(TS=((("3D" OR "3-D" OR "3 D" OR "Three-d" OR "Three d" OR "Three-dimensional" OR "Three dimensional") NEAR/0 print*) OR ("additive" NEAR/1 manufact*) OR ("pharmaco" NEAR/0 print*) OR ("on-demand" NEAR/0 manufactur*) OR ("3DP"))) AND (TS=(((tablet* OR capsule* OR "buccal" OR ("soft" NEAR/0 tablet*)) AND ("oral" OR pharma* OR "drug" OR "delivery" OR "ODD" OR "dosage" OR "release" OR health* OR medic*)) OR (caplet* OR ("bilayer" NEAR/0 tablet*) OR "polypill" OR printlet* OR ("orodispersible" NEAR/0 tablet*) OR ("oral" NEAR/1 film*) OR ("solid" NEAR/0 "oral" NEAR/0 form*) OR ("orodispersible" NEAR/0 film*) OR ("solid" NEAR/0 "dosage" NEAR/0 form*) OR ("mucoadhesive" NEAR/0 film*) OR ("tailored" NEAR/0 "dosage" NEAR/0 form*) OR ("mucoadhesive" NEAR/0 "patch")) OR ((("pill" OR "pills" OR "pellet") AND ("oral" OR pharma* OR "drug" OR "delivery" OR "ODD" OR "dosage" OR "release" OR health* OR medic*)) NOT (image* OR "sensor" OR "ultrasound" OR "bottle" OR "culture")))) NOT (TS=("wastewater" OR "artwork" OR "concrete" OR ("user" NEAR/0 interface*) OR "Puccinia triticina" OR ("robot" OR "robots") OR "image reconstruction" OR "gastric resident electronic" OR endoscop* OR "antenna" OR "oximeter" OR voltammetri* OR "synovial" OR "digital anatomy" OR "acoustic" OR "pedagogical capabilities" OR "electromechanical switches" OR "powder inhaler" OR "metallic clay" OR "flexible electronics" OR "running shoes" OR "electrochemical pestle" OR "dentures" OR "tabletop" OR "educational technology" OR "optical sensor" OR endodo* OR "orthopedic" OR "suppository moulds" OR "bone models" OR ("tissue" NEAR/0 ("reconstruction" OR "formation" OR "production" OR "implant")) OR "mouth sticks" OR "radiotherapy" OR "face mask" OR "anatomical structure" OR "total body irradiation" OR "hotel" OR "nasal absorption" OR "dental models" OR "abs beam" OR "sport equipment" OR ("bioabsorbable medical" NEAR/0 device*) OR "heart models" OR ("topical" NEAR/0 application*) OR "delivery implant" OR "ophthalmologic patches" OR "implantation" OR "bladder device" OR "bone tissue engineering" OR "molds" OR "transdermal" OR "scandium" OR "subcutaneous" OR "implant")))

Figure 2. Query for 3D printing of oral drug delivery systems.

into different categories, but only the four categories relevant to the objective of this study were analyzed, which are end-user applications, quality assurance, user acceptability, and digital technologies, representing a total of 149 research documents. A scientometric analysis was carried out to determine publication trends in the scientific literature, provide statistics about the publication output rate[32], and uncover key players, innovation activities, and main technology trends[33]. Expert feedback was used as support at all stages of the CTI methodology to validate the results obtained.

3. Results and discussion

In this section, the results of the analysis are presented. As previously mentioned, a total of 149 publications were analyzed based on the categories end-user applications, quality assurance, user acceptability, and digital technologies; the distribution of publications is shown in Figure 3.

Through the scientometric analysis, the number of publications per country, number of publications per country and key players, number of publications per year, number of publications per research area, and number of publications per journal were determined. In addition, technological trends were determined in each category.

In terms of number of publications per country, a total of 35 countries were identified, the top 5 countries with most publications being England, with a total of 30, followed by China with 18, the United States with 15, Germany with 11, and lastly South Korea with 8. By identifying some of the key players in 3D-printed pharmaceuticals by country (Figure 4), the level of technological and industrial development in 3D-printed pharmaceuticals of a country is a factor that influences the number of publications per country. As shown in Figure 4, regarding the top three countries, England has many companies and universities working with 3D printing of DDS; FabRx and the University College London (UCL) have a large repository of published research papers. In the case of China, Triastek (located in Nanjing) accounts for 20% of 3D-printed pharmaceutical applications, while in the United States, companies include Aprecia Pharmaceuticals and Merck.

The number of publications related to the 3D printing of oral DDS demonstrated a significant increase after 2017, creating a positive trend over the past 7 years. During this time, aside from partnerships within companies, technologies like M3DIMAKER™, MED®, CraftMake™, and MakerBot® were introduced, facilitating investigation and product development. For the year 2023, the number of publications has declined; however, since the data was

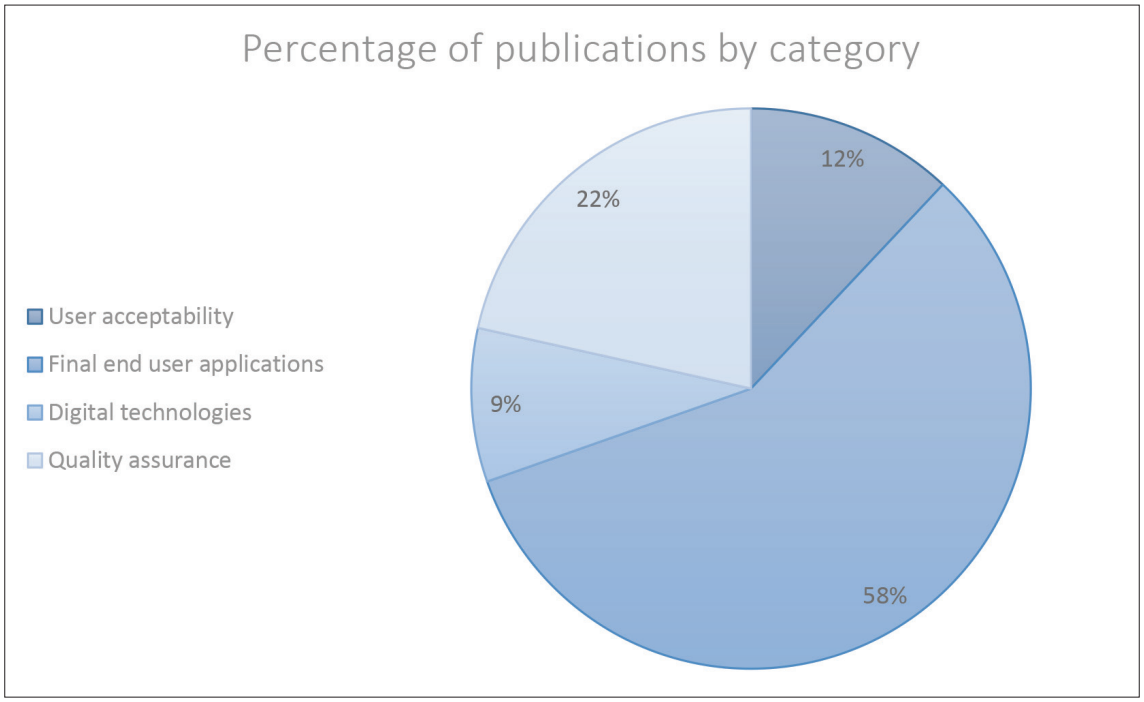

Figure 3. Percentage of publications by category.

retrieved only until the first of May 2023, the total number of publications for 2023 is not complete (Figure 5).

The results were also analyzed in terms of the area of research according to the Web of Science categories, with some papers belonging to more than one; from the 149 results, 126 (72.83%) are classed in "Pharmacology & Pharmacy," 15 (8.67%) publications in "Chemistry," and 6 (3.47%) publications in "Material Science." According to our results, the top three journals with the most publications are *The International Journal of Pharmaceutics* (INT J PHARMACEUT), which had the highest number of published articles with 38, *Pharmaceutics* (PHARMACEUTICS) close behind with 35, followed by *AAPS PharmSciTech* (AAPS PHARMSCITECH) with 9.

With regard to the most used 3D printing techniques, the analysis of the 149 publications revealed some of the techniques already presented in Table 1 as well as some new ones. There are many 3D printing techniques and many names too. For convenience, the names used in the figures are extracted directly from the publications without regrouping, and some may refer to the same technique due to name variations (see Table 2). Fused deposition modeling was the most used technique, followed by pressure-assisted microsyringe and selective laser sintering (Figure 6). Fused deposition modeling was used for the creation of tablets, solid dosage forms (various geometries), capsules, polypills, orodispersible films, gummies, mucoadhesive films, and others; while pressure-assisted microsyringe was utilized to produce mucoadhesive films, orodispersible films, polypills, tablets, and soft dosages (Figure 7). Lastly, selective laser sintering was applied to fabricate tablets (and printlets) and polyprintlets. On the other hand, some of the least used 3D printing techniques were stereolithography, thermal inkjet printing, and drop-on-powder (Figure 6). For the development of the outer shell of the capsules, the predominant materials are polyvinyl acetate (PVA) and polylactic acid (PLA).

Table 2. Identified 3D printing techniques

Process	Technique
Binder jetting	– Binder jetting – Color jet printing – Drop-on-powder
Material extrusion	Extrusion-based 3D printing/micro-extrusion – Fused deposition modeling – Direct ink writing • Pressure-assisted microsyringe • Pneumatic-based extrusion • Syringe extrusion – Direct powder extrusion
Material jetting or inkjet printing	– Thermal inkjet printing
Powder bed fusion	– Selective laser sintering
Vat photopolymerization	– Stereolithography – Digital light processing – Micro 3D printing

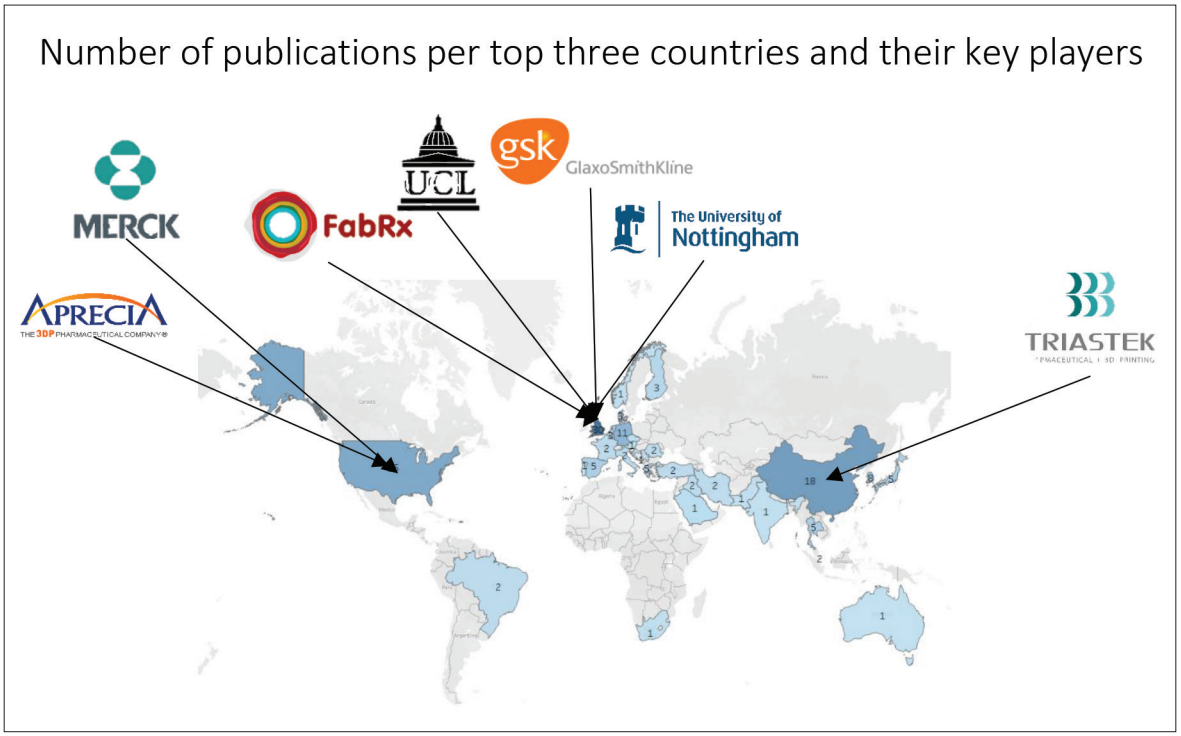

Figure 4. Number of publications per top three countries of the categories "end-user applications," "quality assurance," "user acceptability," and "digital technologies," and their key players.

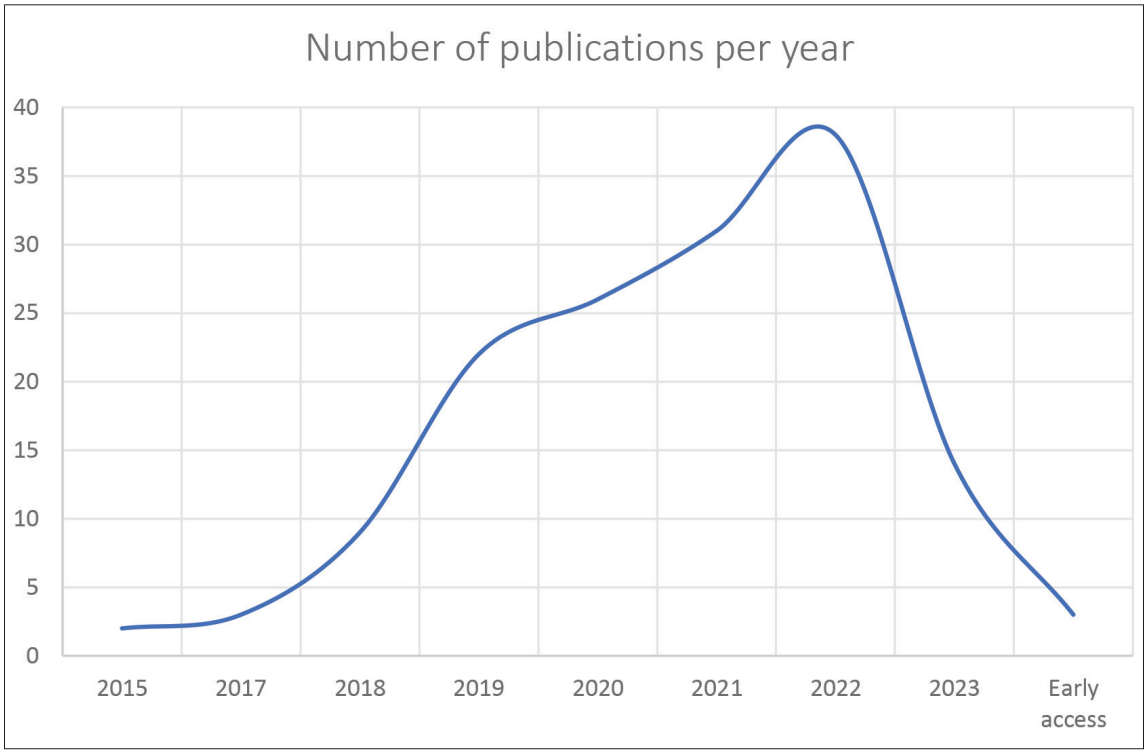

Figure 5. Number of publications per year of the categories "end-user applications," "quality assurance," "user acceptability," and "digital technologies."

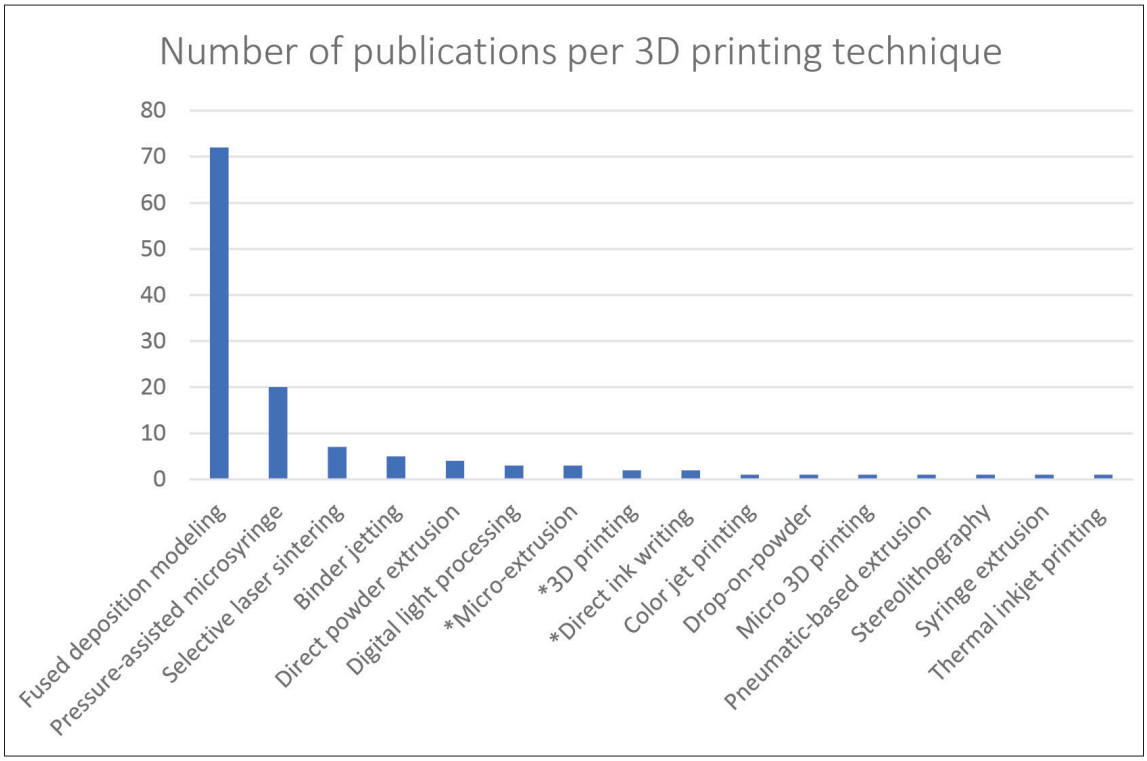

Figure 6. Number of publications per 3D printing technique of the categories "end-user applications," "quality assurance," "user acceptability," and "digital technologies." *Specific technique not available.

The technological trends of the categories are presented based on the total number of publications of each category previously established:

3.1. Final end-user application

There are 92 publications in the final end-user application category. This category targets specific applications of 3D-printed oral DDS including "disease treatment," "pediatrics," "gastrointestinal," "patients with limitations (visual impairment)," and "abuse deterrent."

3.1.1. Disease treatment

This sub-section describes the advances of 3D-printed oral DDS for specific diseases, as well as solutions for negative interactions between active pharmaceutical ingredients and alternatives for multiple medication intake.

The combination of the anti-tuberculosis drugs, rifampicin (RIF) and isoniazid (ISO), has a negative interaction upon simultaneous release in an acidic environment. Genina *et al.* designed a 3D-printed multi-compartment dosage unit with fused deposition modeling where the APIs were loaded in the filaments via hot melt extrusion[34]. The multi-compartment dosage unit demonstrated a delayed release and absorption of the drugs, avoiding the interaction of rifampicin and isoniazid[34]. In 2021, Tabriz *et al.* also tackled this problem, except that the result was a fused deposition modeling-printed bilayer tablet; the design of the tablet enabled a reduction in the degradation of rifampicin in acidic environments, avoiding interactions between rifampicin and isoniazid[35].

Parkinson's disease should be controlled symptomatically as it cannot be cured, and its treatment requires the intake of various medications such as levodopa, benserazide, and pramipexole. Windolf *et al.* used fused deposition modeling to create a series of easy-to-swallow mini-polypills with different dosages, layers, and geometries. As a result, they improved the design of the formulation and the floating property, and prolonged the API absorption of levodopa in the upper gastrointestinal tract. The fabricated polypills allowed individualized dosing, reducing the amount of different medicine intake, and improved patient adherence to their therapy[36].

Hydrocortisone, a medicine for the treatment of adrenal insufficiency, if taken three times daily, can produce negative side effects due to plasma cortisol fluctuations. To reduce the daily dosage intake, Ayyoubi *et al.* created a 24-h release 3D-printed hydrocortisone tablet using M3DICORT[37]. The tablets demonstrated a 24-h dissolution profile and unique quality attributes. On the other hand, some impurities within the tablet were

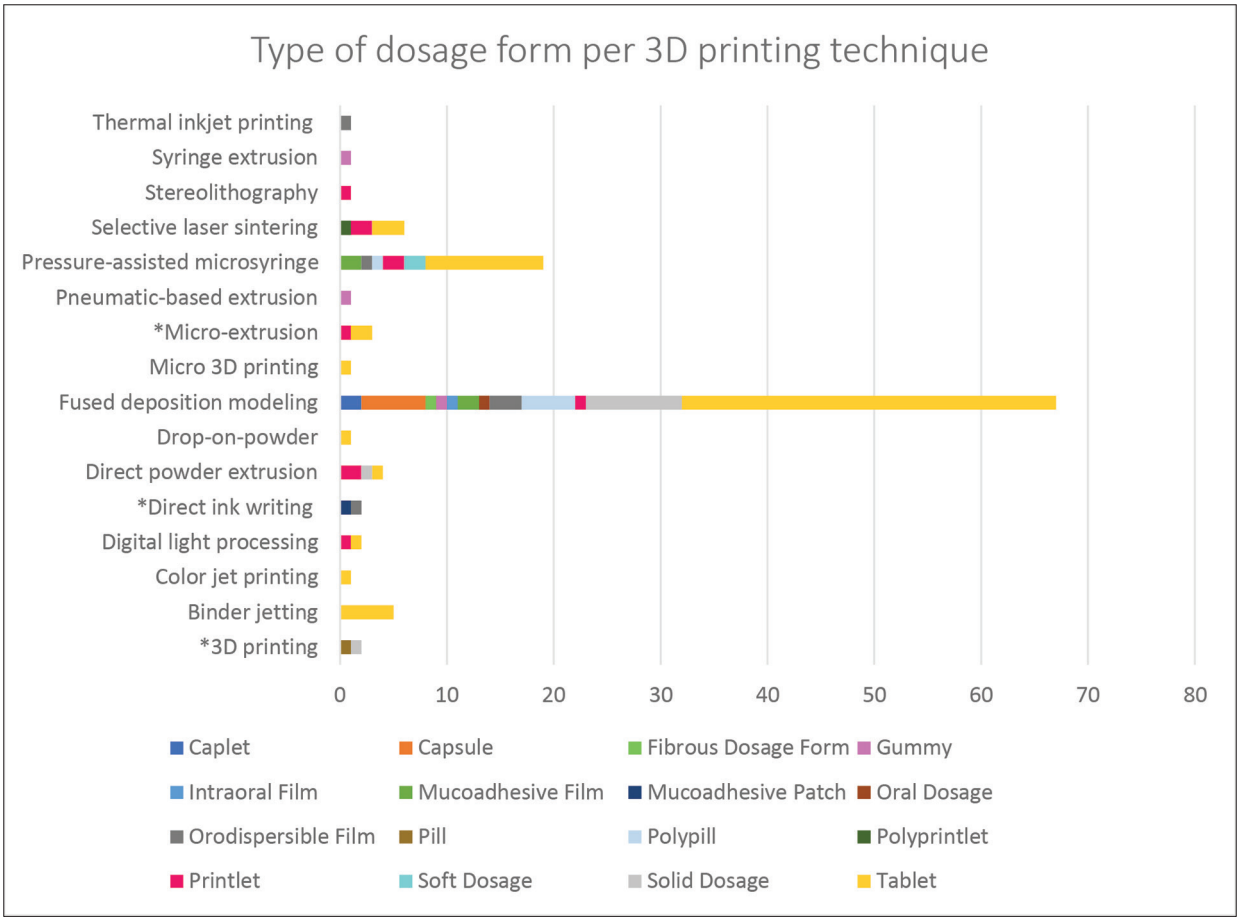

Figure 7. Type of dosage form per 3D printing technique of the categories "end-user applications," "quality assurance," "user acceptability," and "digital technologies." *Specific technique not available.

identified, which should be reduced or eliminated before clinical assessment[37].

To improve antitumor activity, tumor targetability, and safety for the treatment of colon cancer, Mirdamadian *et al.* merged fused deposition modeling and nanotechnology to produce a 3D-printed tablet loaded with oxaliplatin alginate nanoparticles[38]. The 3D-printed tablets had a remarkable antitumor effect and safety profile[38].

Intestinal alkaline phosphatase can regulate intestinal inflammation and treat ulcerative colitis, an inflammatory bowel disease; nonetheless, its intraduodenal administration is not convenient. Nguyen *et al.* fabricated powder bed-printed coated tablets loaded with alkaline phosphatase and a coating of PEG 1500[39]. The results showed a controlled release profile and ileocolonic targeted activity. The 3D-printed tablets help avoid the degradation of alkaline phosphatase and help selective delivery to the colon[39]. In 2023, due to the limits of commercial formulations for the treatment of inflammatory bowel disease, Ou *et al.* produced an adjustable and controlled release 3D-printed budesonide tablet. The tablets were printed using semi-solid extrusion with a CraftMake™ 3D printer. The results revealed excellent and significant dose accuracy and quality[40].

Oral premalignant lesions can lead to oral cancer. Liu *et al.* developed non-invasive 3D-printed mucoadhesive patches loaded with oxaliplatin and mycophenolate. The patch exhibited sustained release, significant ablation to dysplastic lesions, and minimal side effects[41]. Tagami *et al.* also created a mucoadhesive film using a pressure-assisted microsyringe. The film was loaded with ibuprofen/lidocaine ionic liquid to treat oral mucositis caused by radiation therapy and chemotherapy[42]. During the same year, alternatives for the treatment of oral leukoplakia were evaluated. Here, Takashima *et al.* developed an apigenin-loaded mucoadhesive oral film, but with a different 3D printing process, in this case semi-solid extrusion, and it was designed to avoid surgical removal. The film demonstrated a remarkable chemopreventive effect, which may be of great help to prevent oral carcinogenesis[43].

3.1.2. Pediatric

Compared with drugs for adults, drugs for children have very different pharmacokinetics in terms of absorption, distribution, metabolism, and excretion[44]; consequently, it is not recommended to provide children with adult medication at a lower dose. The lack of age-appropriate and commercially available pediatric formulations forces pharmacists or caregivers to manipulate adult formulations[45]. In normal practice, approximately one-tenth of the medicines that are prescribed for children are unlicensed or off-label[46]. Given this, the 3D printing of dosage forms can create age-appropriate formulations for pediatrics.

Using fused deposition, modeled minicaplets loaded with baclofen for pediatrics were produced by Palekar *et al.*[47] The authors decided to fabricate this product since a child formulation based on baclofen was not available yet on the market. The results revealed that the minicaplets were successful, and the size had a greater influence on the API release than the infill percentage[47].

Due to the lack of praziquantel formulations for children, Boniatti *et al.* produced pediatric Printlets™ with praziquantel, using direct powder extrusion and a M3DIMAKER™ printer. While the tablets demonstrated better performance in the dissolution tests and an acceptable formulation taste, the drug loading still needed optimization. The resulting tablets are a promising solution for the lack of a suitable a praziquantel formulation for children[48].

Suárez-González *et al.* printed orodispersible dosage forms (printlets™) for pediatrics with a semi-solid extrusion process and a M3DIMAKER™ printer[49]. The active ingredient for the formulation was hydrochlorothiazide (not commercially available for pediatrics), the excipients were selected based on the possible toxicity by age, maximum daily dose, and route of administration, and databases including Safety and Toxicity of Excipients for Paediatrics (STEP database), Aggregated Computational Toxicology Resource (ACTor), Toxicology Data Network (TOXNET), and Vitic were used for the excipient selection. The results showed that semi-solid extruded printlets passed all the recommended pharmacopoeia tests[49].

To increase the safety and efficiency of the drug administration of 3D-printed levetiracetam tablets in Chinese children, Li *et al.* used physiological pharmacokinetic modeling to guide drug development and drug selection[50]. The 3D-printed tablets were developed with binder jetting technology[50].

To reduce the possible therapeutic ineffectiveness of the poor solubility, low absorption, and unavailability of budesonide in pediatric treatment, Pistone *et al.* generated a powder bed extruded (PBE) minitablet for pediatrics with suitable swallowing, palatability, and dose flexibility control requirements[51].

3.1.3. Gastrointestinal tract

Drug absorption can be affected by the environmental pH and the drug pKa (acid dissociation constant) [52], and the complexity, heterogeneity, and differences in luminal pH of the gastrointestinal tract can lead to inferior pharmacokinetics and inefficient drug release. This sub-section focuses on the enhancement of oral DDS to boost drug release and residence time in the gastrointestinal tract.

Giri *et al.* used a hot melt extrusion process as well as fused deposition modeling to create controlled release 3D-printed theophylline tablets with different infill percentages and shell thickness[53]. The fabricated tablets had the characteristic of floating for 10 h and exhibited zero-order release kinetics[53].

In the same year, Reddy Dumpa *et al.* developed a core-shell gastroretentive floating pulsatile delivery system. The hollow tablets were fabricated using fused deposition modeling and had the ability to remain in the stomach gastric fluid until the pulse release of the dosage took place. The tablets demonstrated successful results as they were able to deliver the dosage when high residence time in the stomach was needed[54].

Oladeji *et al.* applied fused deposition modeling to produce robust 3D-printed tablets using a sandwich model design with voids[55]. The tablets were designed to support floatability and prolonged gastric residence time and reduce the influence of process and formulation variables[55].

To obtain an intragastric floating and sustained release DDS, Zhao *et al.* used hot melt extrusion and dual fused deposition modeling[56]. The manufactured tablets were designed with air chambers to improve floatability and the release behavior of the drug. The 3D-printed tablets manifested closer zero-order drug release for 24 h, and reduced density due to the hollow air chambers[56].

Mora-Castaño *et al.* prepared 3D-printed gastroretentive floating tablets loaded with metformin as the API[57]. The main aim was to maintain robust release kinetics when varying the dose formulations with a controlled release. The tablets were created with fused deposition modeling, and the design allowed buoyancy of the tablets and a sustained release of more than 8 h[57].

Gastroretentive fibrous expandable dosage forms are also being investigated as an alternative to improve residence in the stomach and release time. Blaesi and

Saka developed an expandable fibrous dosage form with 3D micropatterning, which was formulated with acetaminophen and hydroxypropyl methyl cellulose (HPMC)[58]. The normalized axial expansion was up to 100% in 15 min, making a 10 mm diameter disk into a 20 mm viscous gel; the disks also had delayed dose release (80% in 2.0–8.4 h)[58]. Blaesi and Saka continued their investigation with expandable dual-excipient fibrous dosage forms of sparingly-soluble drugs[59].

3.1.4. Patients with limitations (visual impairment)

The benefits of 3D printing oral DDS go further than being a solution to correct incorrect dosage administration and lack of controlled release, or to prevent negative interactions between different active pharmaceutical ingredients. 3D printing can also be used to satisfy other patient needs. This sub-section incorporates the latest findings related to visual impairment patients.

Using selective laser sintering, Awad *et al.* produced orally disintegrating paracetamol printlets with Braille and Moon patterns on their surface. The various shapes of the printlets were intended to provide additional information like dosing regimen and medication indication. The tablets had good mechanical properties and a disintegration time of 5 s, avoiding water intake and facilitating self-administration. The readability was tested by a blind participant[60].

Ketoprofen intraoral films with braille characters on the surface were developed by Eleftheriadis and Fatouros[61] using fused deposition modeling. The haptic identifiers on the surface of the dosage forms helped patients with visual impairment to recognize the correct treatment regimen. The Braille characters on the 3D-printed film complied with the Marburg Medium spacing convention for Braille. The intraoral films were tested by participants with visual impairments, who reported excellent readability[61].

3.1.5. Abuse deterrent

Opioids are pain-reliving drugs; when attached to receptors in brain cells, the cells release signals that subdue pain perception and magnify the feeling of pleasure[62]. On a global scale, about 0.5 million deaths are related to drug abuse, and more than 70% of those deaths are linked to opioids, with 30% caused by overdose[63]. In order to solve this problem and reduce abuse, abuse-deterrent formulations are created to target the expected routes of opioid abuse, such as injecting and snorting[64].

In 2019, Nukala *et al.* used fused deposition modeling and a MakerBot® printer to develop a 3D-printed methamphetamine loaded egg-shaped tablet[65]. These egglets had different sizes and infill densities for varying the drug dose. The optimized tablets passed most of the US FDA tests. The hardness of the egglets confirmed its snort-resistant potential, making it a promising tool to avoid opioid abuse[65].

Ong *et al.* produced tramadol printlets with alcohol-resistant and abuse-deterrent properties[66]. The tablets were fabricated with a powder bed extrusion process and a M3DIMAKER™ printer. The results revealed strong ethanol-resistance and moderate abuse-deterrent properties. By adding polyethylene oxide (PEO) to the formulations, its dissolution in solvent extraction tests was delayed, and the resistance to physical tampering improved[66].

Palekar *et al.* developed a novel 3D-printed capsule shell filled with an aversion liquid[67]. The filaments were loaded with metformin hydrochloride and had higher mechanical strength compared to other drug loadings. The 3D-printed capsule was filled with an aversion liquid composed of Sudan Black B and sodium polyacrylamide starch. By making the manipulable formulation less attractive, the 3D-printed capsule has the potential to visually discourage opioid abusers[67].

3.2. User acceptability

This classification includes 19 publications, with information related to improving the palatability of 3D-printed dosage forms and the general perception of end users. The sub-categories are "pediatric acceptability," "healthcare professionals," "patients," and "palatability methods."

3.2.1. Pediatric acceptability

Medicine taste can be an important factor in children compliance and treatment adherence since their taste buds are more sensitive to bitter tastes[68]. An article stated that giving children more choices can help overcome their aversion to medicine[69]. At the same time, masking the taste profiles of medicines can make pediatric patients more willing to take them[68]. This sub-category focuses on various advances in 3D-printed dosage form to improve the pediatric compliance.

Rycerz *et al.* produced a novel form that consisted of a chewable dosage form with dual loading in the form of a Lego™, using embedded 3D printing (e-3DP) and a M2 MakerGear FDM 3D printer[70]. The brick-like dosage form was composed of an internal paracetamol and ibuprofen powder suspension in a model drug ink (embedded phase) and a gelatin-based matrix (embedding phase). The created gelatin-based LEGO™ had a soft consistency and a sweet taste, making it easier for patients with swallowing problems[70].

Herrada-Manchón *et al.* developed children-tailored medicinal gummies with an attractive appearance

(bear- and heart-shaped) using syringe-based extrusion 3D printing[71]. The formulation contained ranitidine hydrochloride, xanthan gum, strawberry essence, gelatin, Maizena®, liquid sweetener, deionized water, and food coloring. The structured features of the 3D-printed gummies permitted easy handling and intake, improving treatment adherence[71].

Karavasili *et al.* fabricated chewable chocolate-based 3D-printed dosage forms with paracetamol and ibuprofen as active ingredients using an extrusion-based process[72].

In 2021, Wang *et al.* used an innovative ColorJet 3D printing (CJ-3DP) technology to create colorful cartoon tablets[73]. The tablets were loaded with a pediatric formulation of levetiracetam and had the design of rabbits, bears, hearts, and candy. Spearmint flavor and sucralose were used to improve the taste. Through the CJ-3DP process, the tablets were conferred friendly physical appearance and good mechanical properties[73].

Tabriz *et al.* masked the bitter taste of diphenhydramine hydrochloride (DPH)-fused deposition modeling tablets with sweetener (sucralose) and strawberry flavor, which exhibited a good aftertaste perception and synergy between the sweetener, strawberry flavor, and the DPH[74].

Bracken *et al.* evaluated the acceptability of 3D-printed placebo solid dosage forms in children and youths aged 4–12 years[75]. The participants rated the swallowability, acceptability, mouthfeel, volume of water consumed, and taste of the sample. Seventy-seven percent of the participants reported that there would be no inconvenience in taking the tablet every day as medicine[75].

3.2.2. Healthcare professionals

With the latest advances in 3D-printed oral DDS, their adoption in hospitals and pharmacies is becoming a near reality; therefore, it is also relevant to know the perspective of healthcare professionals in the adoption and perception of the different types of 3D-printed dosage forms.

Goh *et al.* studied the preferences of healthcare professionals at Tan Tock Seng Hospital in Singapore; the results of the pilot study revealed that more than 70% of the respondents agreed with the benefits of 3D-printed tablets and more than 60% of the participants were willing to be prescribed 3D-printed tablets[76]. On the other hand, there were still concerns regarding the formulation considerations, manufacturing processes, and administrative issues[76].

In 2020, Rautamo *et al.* explored the perception of healthcare professionals of oral 3D-printed dosage forms in pediatric treatments[77]. The study was made in a tertiary university hospital (HUS Helsinki University Hospital) that specializes in health care of neonates to children aged 15. The results showed a positive perception toward the 3D printing of oral medicines with the participants considering that there were many positive aspects and opportunities. Nevertheless, the respondents also demonstrated uneasiness associated with quality control, dosage accuracy, stability, and shelf life of formulations[77].

3.2.3. Patient

For a product to be successful, it should be aligned with the preferences of the users. This sub-category covers studies related to the preferences and perceptions of patients on the shapes, colors, and sizes of 3D-printed dosage forms.

Since 2017, Goyanes *et al.* have started exploring the influence of shape, size, and color of various placebo Printlets™; in addition, the acceptability with regard to picking and swallow was also investigated[78]. The tablets were manufactured using fused deposition modeling and had different geometries, including disc, torus, sphere, capsule, title diamond, pentagon, heart, diamond, triangle, and cube. The overall results indicate that torus-shaped tablets had the top score for ease to swallow and pick, followed by capsule and disc shape; the familiarity with the geometry of the dosage form is a relevant factor influencing acceptability of the end user. The color also affected the perception of the printlets[78].

The perceptions and preferences of 3D-printed medicines of polypharmacy patients in Zealand, Denmark, were studied by Fastø *et al.* who concluded that there was a preference for shapes similar to conventional formulations; there was also an inclination to different colors[79]. The overall patient acceptability was affected by the following factors: appeal (appealing), physiological (swallowing), practical (handling), pedagogical (understanding), and psychological (relate to)[79].

Kabeya *et al.* researched patient preferences of the size of 3D-printed tablets and capsules[80]. The study was carried out in a pharmacy in Japan. The results demonstrated that age, gender, disease status, number of drugs usually taken, and ingestion problems did not have a big impact on the evaluation outcome. Larger capsules and tablets (thickness above 6 mm) had the highest swallowing difficulty score, and smaller formulations (thickness below 2 mm) had the worst picking difficulty score[80].

3.2.4. Palatability methods

To determine the palatability of 3D-printed oral DDS, focus groups and interviews are needed; this requires gathering people, which can be inconvenient. Two methods to analyze the palatability of 3D-printed DDS that do not require the user *in situ* are presented.

In 2021, Wang *et al.* employed the ASTREE electronic tongue to design the additives of binder jetting 3D-printed levetiracetam instant dissolving tablets[81]. Different formulations were created, and their palatability was examined using ASTREE and design of experiment (DoE). The oral dispersion time and *in vitro* drug release were predicted with a texture analyzer and a dissolution apparatus. The results showed that the electronic tongue had an excellent ability for taste discrimination. The credibility of the results of the electronic tongue was evaluated with human gustatory sensation tests[81].

Using a toolbox of modern techniques, Desai *et al.* assessed 3D-printed orodispersible films in terms of disintegration, taste, texture, and mouthfeel, as they affect the sensory perception. Three *in vitro* methods were applied: Petri dish (disintegration), oral cavity model (disintegration), and bio-tribology (disintegration and oral perception). The findings suggested good oral palatability and mouthfeel with higher molecular weight (MW). The toolbox can be used during the design process to raise the positive perception of orodispersible films when consumed, improving overall treatment acceptability[82].

3.3. Quality assurance

This category includes a total of 34 papers and focuses on the quality of 3D-printed dosage forms at different levels: design, processing, and repeatability. The sub-categories are "quality by design," "control verification," "protocols and standardization," and "influence factors."

3.3.1. Quality by design

Products that do not meet their specifications or fail during performance increase compliance costs and workload and reduce efficiency. Quality should be controlled at all development stages. Quality by design (QbD) aims to ensure the quality of medicines in their design, development, and manufacturing, by applying statistical, analytical, and risk-management tools[83].

Nukala *et al.* applied multifactorial design to optimize 3D-printed egglets for solvent extraction and drug release[65]. The mechanical manipulation of the egglets was evaluated and optimized considering: household equipment, milling, particle size distribution, solvent extraction, and drug release. For the response surface design, drug loading, infill density, and dimensions were defined as critical quality attributes (CQA), while time for 85% of cumulative drug release (D85) and percentage of drug extracted using water in 5 min (%S) were defined as the dependent variables. The technique was validated with a good correlation between the optimized response model and the generated data[65].

In order to evaluate the structure–function relationship of various fused deposition 3D-printed tablets, Zhang *et al.* used Box–Behnken design, with the experimental design based on the effect of design parameters and responses (drug loading, mechanical properties, and *in vitro* drug release performance)[84]. Shell thickness, infill density, and layer height were chosen as the independent variables. The results of this research revealed a favorable future of patient-focused drug production and on-demand manufacturing, with inputs from experts (doctors, pharmacists, formulation scientists, and pharmaceutical engineers) throughout the fabrication process. Design of experiments can contribute to robust guidance for formulation and optimization of 3D-printed dosage forms[84].

The printability parameters of selective laser sintering in 3D-printed solid dosage forms loaded with copovidone and paracetamol were evaluated by Gueche *et al.*[85]. The influence of the heating temperature was verified individually, while Box–Behnken design was applied to identify the effects of laser power, scan speed, and layer thickness in the printability. Printing yield, height, weight, hardness, disintegration time, and percentage of drug release were established as the measured responses. The significance of three process parameters was determined with an analysis of variance (ANOVA). With a QbD approach, this study demonstrated that the process parameters are critical for printability[85].

Wang *et al.* explored the factors affecting fabrication of binder jetting 3D-printed dosage forms using a two-level full factorial design[86]. Disintegration time, tensile strength, friability, dimensions (diameter and height accuracies), residual water content, weight, and drug loading were selected as the critical quality attributes based on the quality target product profile (QTPP). The authors concluded that QbD is a systematic and effective approach for efficient product design[86].

In 2022, Crișan *et al.* implemented a QbD approach to guide the development of fused deposition modeling 3D-printed diclofenac tablets[87]. Risk management strategies, design space definition, and DoE were employed to reveal the effects that tablet design, tablet size, and layer height had on drug release and on the API content. The design strategy and appropriate formulation lead to rapid release of the active pharmaceutical ingredient. Consequently, the model was accurate and can be employed for the optimization of selected parameters[87].

3.3.2. Control verification

3D-printed oral DDS are usually created in small batches due to equipment limitations, as they are smaller than a manufacturing plant. Nondestructive quality verification

methods are needed to characterize the 3D-printed dosage forms without total loss of all the samples.

To ensure final product quality of paracetamol printlets, non-destructive characterization techniques like process analytical technologies, near-infrared spectroscopy (NIR), and Raman confocal microscopy can be applied. Trenfield *et al.* evaluated cylindrical 3D-printed tablets[88]. A calibration model was created using an NIR spectrometer, and it successfully predicted the drug concentration. The model also demonstrated excellent linearity and accuracy with dosage forms of different geometries and formulations. The drug distribution was observed with a Raman confocal microscopy[88].

Trenfield *et al.* verified the dosage of multiple drugs in polyprintlets and 3D-printed films at the point of dispensing[89]. The dosage forms were loaded with amlodipine and lisinopril. The analysis and verification were made using a portable NIR spectrometer and validated calibration models (partial least squares regression). The results demonstrated an excellent linearity, accuracy, and specificity for amlodipine and lisinopril. The microstructure was observed with x-ray powder diffraction (XRPD) and thermogravimetric analysis (TGA)[89].

Gioumouxouzis *et al.* investigated the structural and functional characterization of 3D-printed dosage forms with x-ray microfocus computed tomography (μCT) to verify if the formulations complied with the required specifications (quality assurance)[90]. The results demonstrated that the use of μCT can perform a qualitative inspection of the products, a 3D image of the dosage form structure for dimensional metrology, and the functional performance of the formulation overtime. The authors believe that μCT can help accelerate the adoption of 3D printing technology in the pharmaceutical technology sector[90].

Lima *et al.* employed oscillatory shear rheology and mechanical evaluation as a control tool for fused deposition modeling 3D-printed medicines. Hot melt extrusion filaments were assessed in terms of viscoelastic behavior, definition of printing parameters, and the prediction of their repercussions on the 3D tablets. The outcome of this research was the validation of oscillatory shear rheology as a tool to identify significantly sensitive viscoelastic alterations and quality control parameters, and as a method to predict rheological changes and their effects on the printed dosage forms[91].

Quality control of 3D-printed dosage forms can also be done on hot melt extrusion API-loaded filaments. Chamberlain *et al.* investigated the possible use of colorimetric evaluations for direct and indirect determination of extruded filaments with API and/or coloring agents[92]. The results showed that colorimetry can be used as a quality control tool to detect differences in drug loading[92].

3.3.3. Protocol and standardization

Standards and protocols are guidelines for production that ensure consistent quality and safety. In this sub-section, protocols developed for 3D-printed dosage forms are presented.

Silva *et al.* proposed a new protocol for preformulation studies simulating thermal processing and aging of the fused deposition modeling printed medicines. The protocol included tests related to morphology and thermal, crystallographic, and spectroscopic profiles. In the study, the protocol simulated the combined thermal stresses of formulations with four different polymers and two model drugs and obtained stable pharmaceutical dosage forms[93].

Pressure-assisted microsyringe (PAM) was selected by Callede *et al.* to develop zolpidem printlets[94]. The design process included the integration of protocols to standardize compounding procedures (mixing, preparation, and printing) related to the dosage amount of zolpidem in the tablets. The printing parameters were evaluated and optimized, and some of them were fixed at certain values. One of the outcomes of the research was a decision tree model that allows the compounding pharmacists to ensure quality control of the zolpidem printlets at industry level immediately after printing[94].

3.3.4. Factors of influence

High-quality products can be obtained by optimizing process or formulation parameters. This sub-section contains publications related to the effects of a factor of influence (selected by the author of each article) on the properties of the 3D-printed oral DDS.

Zhang *et al.* studied the influence of process temperature on the quality and crystallinity of fused deposition modeling-printed phenytoin dosage forms[95]. Comparative studies such as morphology, solid-state analysis, and *in vitro* drug release between the printlets and filaments were carried out. The results showed that the printing process and product qualities are affected by the printing temperature and slicing[95].

The quality of binder jetting paracetamol orodispersible films was improved by adding a thin layer of polyvinylpyrrolidone (PVP) coating to the matrix particles. Wang *et al.* concluded that coated particles improved the resistance to crushing and decreased the disintegration time[96].

3.4. Digital technologies

This classification includes a total of 14 publications and is characterized by the use of digital technologies to improve and enhance processes and dosage formulations with machine learning, decreasing the risk of frauds with cybersecurity and novel ways of adding information to the printed forms by quick response (QR).

3.4.1 Machine learning

Machine learning (ML) can be used as a predictive method for formulation and release profiles in 3D-printed dosage forms, making it a possible quality control tool. ML can automate and reduce development times while maintaining a good accuracy of the design parameters.

ML was employed alongside 3D printing to provide on-demand manufacturing and quality control of orodispersible films. O'Reilley *et al.* developed orodispersible films with direct ink writing (DIW) and complex geometries. These films were classified by active ingredient using ML algorithms and NIR spectrums. Based on the results of the subsequent partial least square algorithm, it was stated that ML, 3D printing, and NIR have the potential to automate orodispersible film workflows and enable rapid drug and dose verification[97].

In 2021, Obeid *et al.* also tried to predict the diazepam release of tablets with artificial neutral networks[98]. Tablets of different shapes were printed using fused deposition modeling. Self-organizing maps and multi-layer perceptron were applied to model the influence of tablet surface area to volume (SA/V) ratio and printing parameters (infill density and infill pattern) on the release of diazepam. The results showed the ability of the multi-layer perceptron network to predict drug release behavior as a function of infill density and SA/V ratio[98].

Ong *et al.* created a balanced database of 1594 formulations with in-house and literature data of hot melt extrusion and fused deposition modeling to predict formulation outcomes using ML. The models were able to predict hot melt extrusion and fused deposition modeling processing temperatures with a mean absolute error of 5.5°C and 8.4°C, and the printability and mechanical characteristics of the filaments with an accuracy of 84%. The optimized models were added to the FabRx web-application software M3DISEEN[66].

Mazur *et al.* obtained specific dosage and release profile using fused deposition modeling dosage forms employing artificial neural networks (ANN) to predict appropriate geometries. With the *in vitro* dissolution results and the mathematical description of the API release profiles, ANN architectures were created to predict the most suitable geometry. The results demonstrated that it was not possible to predict a geometry with the required length, width, height, and underlying geometry, with ANN[99].

3.4.2. Cybersecurity

Cybersecurity involves protecting systems, networks, and programs to reduce or avoid the risk of cyberattacks. The most common target of cyberattacks is accessing, changing, or destroying sensitive information[100]. The supporting software and systems for the formulation or production of 3D-printed dosage could be a target to cyberattacks as they might contain sensitive information related to the patient or the dosage form.

Due to the possible cyber risks of remote digital transfer of an electronic prescription to the 3D printer while printing dosage forms, Kok *et al.* explored the application of DEFEND3D, a technology to enhance cybersecurity and intellectual property protection[101]. DEFEND3D is a patented secure streaming transfer protocol (SSTP) and a virtual inventory communication interface with controlled reproduction. Different shapes were created using remote fused deposition modeling. The authors concluded that DEFEND3D can remotely 3D-print various designs at various infill densities[101].

3.4.3. Quick response and binary digits (bits)

Quick response (QR) codes allow the storage of information in small surface areas; the information is easy to access as the QR code just needs to be scanned with a smartphone or QR scanner.

In 2019, Trenfield *et al.* printed QR codes and data matrices on the surface of paracetamol printlets to generate a unique track-and-trace measure for product authenticity[102]. The QR code can be scanned with a smartphone, and the encoded information can be personalized to illustrate data related to the drug product (batch, expiration date, active ingredient, etc.), patient (age, birth, and gender), and prescriber (name). The results demonstrated a novel anti-counterfeit mechanism[102].

Oh *et al.* developed a 3D-printed QR-coded orodispersible film (QRODF) in a one-step process using a hot melt pneumatic process. The QRODF was loaded with aripiprazole and can be read with a smartphone in a QR scanning application to obtain additional information about the film. QRODF may be a promising approach for tailored drug formulations as they are easy to scan and are not easily broken due to their flexibility[103].

Two years later, Windolf *et al.* used a different approach using QR codes to store information on 3D-printed geometries and ensure batch traceability[104]. The dosage forms were fabricated with fused deposition modeling, a

3D Printer Prusa i3MK3, and had different formulations. The blind-watermarking bits were printed as a pattern on the flat sides of the oblong tablets; the bits were distributed across the layers, and the interaction between the layers created a code. Even though this is a novel approach, not all polymers are suitable for this method, and QR codes can store more information than bits encoded in the tablet[104].

3.4.4. Mobile health technologies

Smartphone-enabled 3D printers can be an innovative option to patients that have non-complex dosage formulations; they can be located at the patient's home, and given their accessibility, they can be printed at any moment.

Xu *et al.* created a smartphone-enabled 3D printer for dosage forms. The compact printer used the light from the smartphone to photopolymerize liquid resins and created solid structures, and it worked under stereolithography principles. Warfarin printlets were produced based on the shape determined on the smartphone app. The printlets obtained high resolutions and outstanding dimensional precision. The developed printer can be an alternative to produce tablets in resource-limited settings, in emergencies, or at the patient's home[105].

4. Conclusion

According to the main objective of this research, a CTI methodology was applied to analyze 3D-printed oral DDS, specifically to reveal the current trends and advances in R&D in terms of end-user applications, quality assurance, user acceptability, and digital technologies. The research period was from January 1, 1900, to May 1, 2023. Some of the most important insights are:

(i) There is a tendency toward digitalization in the industry that foresees the migration of clinical trials to digital solutions. Machine learning is being used to optimize and predict process parameters and formulation behaviors, with some of the optimized models already available for general use, which is the case of M3DISEEN, a web-application predicting tool based on artificial intelligence. Applications like DEFEND3D are being assessed to avoid cyber risks stemming from the remote digital transfer of electronic prescriptions to the 3D printer. Digital technologies are also used as facilitators; QR codes are being tested as a traceability method to increase security and obtain additional information about the dosage form. Light from smartphones was used to enable 3D printing of dosage forms on a medium-sized 3D printer.

(ii) Quality assurance is one of the main concerns of developing 3D-printed oral DDS due to the regulatory challenges. The QbD approach is being used to improve efficiency in the design of a product, by identifying the parameter effects with the selected responses. Tools like DoE, ANOVA, and Box–Behnken design are implemented to ensure quality. At the same time, protocols to standardize compounding procedures (mixing, preparation, and printing) as well as decision maps to facilitate decision-making are being developed. The integration of all these methods can lead to quality assurance in the different types of dosage forms.

(iii) Trends related to the final end-user application included abuse-deterrent 3D-printed oral dosage forms that are being designed to limit the accessibility to non-prescribed opioids, as a solution to the global opioid abuse crisis. 3D-printed pediatric formulations taking into consideration the age, maximum daily dose, route of administration, and toxicity of the active ingredients are also being developed. Tailored 3D-printed pediatric oral dosage forms are an opportunity to adapt formulations that are not commercially available for children. For disease treatment, 3D-printed capsules that allow the intake of multiple drugs and avoid negative interactions between active pharmaceutical ingredients are also being studied.

(iv) For user acceptability, 3D-printed oral DDS have a general positive impact on children, healthcare professionals, and general patients, and understanding the user preferences can facilitate the emergence of these types of dosage forms in the market. Aside from the processes, materials, and functionality of these dosage forms, researchers are now taking into consideration the physical appearance and taste to increase their appeal, making them more user-centered.

The results of this study can be helpful for researchers, organizations, and investment firms interested in novel treatments, R&D in areas of 3D printing, medicine, healthcare, and pharmaceutics.

Acknowledgments

The authors acknowledge the institutional support received from Tecnologico de Monterrey and the National Council of Humanities, Science and Technology of Mexico (CONAHCYT).

Funding

The authors acknowledge the institutional funding received from Tecnologico de Monterrey and the National Council of Humanities, Science and Technology of Mexico (CONAHCYT) through Graduate Studies Scholarships and Academic Scholarships provided by CONAHCYT as members of the National System of Researchers (Sistema Nacional de Investigadores).

Conflict of interest

The authors declare no conflicts of interests.

Author contributions

Conceptualization: Veronica L. Rios-Mata, Marisela Rodriguez-Salvador, Pedro F. Castillo-Valdez
Formal analysis: Veronica L. Rios-Mata
Investigation: Veronica L. Rios-Mata, Pedro F. Castillo-Valdez
Methodology: Veronica L. Rios-Mata, Marisela Rodriguez-Salvador
Writing – original draft: Veronica L. Rios-Mata
Writing – review & editing: Marisela Rodriguez-Salvador, Pedro F. Castillo-Valdez, Jia An, Chee Kai Chua

Ethics approval and consent to participate

Not applicable.

Consent for publication

Not applicable.

Availability of data

Not applicable.

References

1. Gao J, Karp J, Langer R, *et al.*, 2023, The future of drug delivery. *Chem Mater,* 35(2), 359–363.

   https://doi.org/10.1021/acs.chemmater.2c03003

2. National Institute of Biomedical Imaging and Bioengineering, 2022, Drug delivery systems, viewed April 19, 2023,

   https://www.nibib.nih.gov/science-education/science-topics/drug-delivery-systems-getting-drugs-their-targets-controlled-manner#:~:text=for%20drug%20delivery%3F-,What%20are%20drug%20delivery%20systems%3F,a%20vaccine%20that%20is%20injected

3. Kim J, Jesus O, 2023, Medication routes of administration. *StatPearls Publishing*, viewed April 19, 2023,

   https://www.ncbi.nlm.nih.gov/books/NBK568677/

4. Senapati S, Mahanta A, Kumar S, *et al.*, 2018, Controlled drug delivery vehicles for cancer treatment and their performance. *Sig Transduct Target Ther*, 3 (1): 7.

   https://doi.org/10.1038/s41392-017-0004-3

5. Mei Y, He C, Gao C, *et al.*, 2021, 3D-printed degradable anti-tumor scaffolds for controllable drug delivery. *Int J Bioprint*, 7(4): 418.

   https://doi.org/10.18063/ijb.v7i4.418

6. Zheng C, Attarilar S, Li K, *et al.*, 2021, 3D-printed HA15-loaded β-tricalcium phosphate/poly (lactic-co-glycolic acid) bone tissue scaffold promotes bone regeneration in rabbit radial defects. *Int J Bioprint*, 7(1): 317.

   https://doi.org/10.18063/ijb.v7i1.317

7. Kanaki Z, Chandrinou C, Orfanou IM, *et al.*, 2022, Laser-induced forward transfer printing on microneedles for transdermal delivery of gemcitabine. *Int J Bioprint*, 8(2): 554.

   https://doi.org/10.18063/ijb.v8i2.554

8. Euromonitor International, 2022, Global overview of the pharmaceuticals and medical equipment industry, viewed April 18, 2023,

   https://www.portal.euromonitor.com/Analysis/Tab#

9. What are the Benefits of Direct Compression in Tablets?, 2022, viewed July 12, 2023,

   https://www.fette-compacting-parts.com/blog/direct-compression-benefits-tablets/

10. Zuccari G, Alfei S, Marimpietri D, *et al.*, 2022, Mini-tablets: A valid strategy to combine efficacy and safety in pediatrics. *Pharmaceutics*, 15(1): 108.

    https://doi.org/10.3390/ph15010108

11. Rana A, Hari Kumar S, 2013, Manufacturing defects of tablets - A review. *JDDT*, 3(6): 200–206.

    https://doi.org/10.22270/jddt.v3i6.722

12. Ventola CL, 2014, Medical applications for 3D printing: Current and projected uses. *P T*, 39(10): 704–711.

13. Kozakiewicz-Latała M, Nartowski KP, Dominik A, *et al.*, 2022, Binder jetting 3D printing of challenging medicines: From low dose tablets to hydrophobic molecules. *Eur J Pharm Biopharm*, 170(2022): 144–159.

    https://doi.org/10.1016/j.ejpb.2021.11.001

14. Mancilla-De-la-Cruz J, Rodriguez-Salvador M, An J, *et al.*, 2022, Three-dimensional printing technologies for drug delivery applications: Processes, materials, and effects. *Int J Bioprinting*, 8(4), 321–346.

    https://0-doi-org.biblioteca-ils.tec.mx/10.18063/ijb.v8i4.622

15. Chen G, Xu Y, Kwok P, *et al.*, 2020, Pharmaceutical applications of 3D printing. *Addit Manuf*, 34(2020): 101209.

    https://doi.org/10.1016/j.addma.2020.101209

16. El Aita I, Rahman J, Breitkreutz J, *et al.*, 2020, 3D-printing with precise layer-wise dose adjustments for paediatric use via pressure-assisted microsyringe printing. *Eur J Pharm*, 157 (2020): 59–65.

https://doi.org/10.1016/j.ejpb.2020.09.012

17. Mohammed A, Algahtani S, Ahmad M, *et al.*, Optimization of semisolid extrusion (pressure-assisted microsyringe)-based 3D printing process for advanced drug delivery application. *Annal 3D Print Med*, 2(2021): 100008.

https://doi.org/10.1016/j.stlm.2021.100008

18. Cheng C, Moon YJ, Kim SH, *et al.*, 2020, Water-matrix interaction at the drop-drop interface during drop-on-demand printing of hydrogels. *Int J Heat Mass Transf*, 150(2020): 119327.

https://doi.org/10.1016/j.ijheatmasstransfer.2020.119327

19. Kollamaram G, Hopkins SC, Glowacki BA, *et al.*, 2018, Inkjet printing of paracetamol and indomethacin using electromagnetic technology: Rheological compatibility and polymorphic selectivity. *Eur J Pharm Sci*, 115(2018): 248–257.

https://doi.org/10.1016/j.ejps.2018.01.036

20. Thabet Y, Lunter L, Breitkreutz J, 2018, Continuous inkjet printing of enalapril maleate onto orodispersible film formulations. *Int J Pharm*, 546(1–2): 180–187.

https://doi.org/10.1016/j.ijpharm.2018.04.064

21. Awad A, Fina F, Goyones A, *et al.*, 2021, Advances in powder bed fusion 3D printing in drug delivery and healthcare. *Adv Drug Deliv Rev*, 174(2021): 406–424.

https://doi.org/10.1016/j.addr.2021.04.025

22. Lakkala P, Munnangi SR, Bandari S, *et al.*, 2023, Additive manufacturing technologies with emphasis on stereolithography 3D printing in pharmaceutical and medical applications: A review. *Int J Pharm*, 5(2023): 100159.

https://doi.org/10.1016/j.ijpx.2023.100159

23. Xu X, Robles-Martinez P, Madla C, *et al.*, 2020, Stereolithography (SLA) 3D printing of an antihypertensive polyprintlet: Case study of an unexpected photopolymer-drug reaction. *Addit Manuf*, 33(2020): 101071.

https://doi.org/10.1016/j.addma.2020.101071

24. Xu X, Awad A, Robles-Martinez P, *et al.*, Vat photopolymerization 3D printing for advanced drug delivery and medical device applications. *J Control Release*, 329(2021): 743–757.

https://doi.org/10.1016/j.jconrel.2020.10.008

25. Chen K-Y, Zeng J-J, Lin G-T, 2022, Fabrication of 5-fluorouracil-loaded tablets with hyperbranched polyester by digital light processing 3D printing technology. *Eur Polym J*, 171(2022): 111190.

https://doi.org/10.1016/j.eurpolymj.2022.111190

26. Krkobabić M, Medarević D, Cvijić S, 2019, Hydrophilic excipients in digital light processing (DLP) printing of sustained release tablets: Impact on internal structure and drug dissolution rate. *Int J Pharm*, 572(2019): 118790.

https://doi.org/10.1016/j.ijpharm.2019.118790

27. Mancilla-De-la-Cruz J, Rodriguez-Salvador M, 2022, Applications of 3D printing technologies in oral drug delivery. *Mater Today: Proc*, 70(2022): 477–482.

https://0-doi-org.biblioteca-ils.tec.mx/10.1016/j.matpr.2022.09.464

28. Khairuzzaman A, 2018, Regulatory perspectives on 3D printing in pharmaceuticals. *AAPS PharmSciTech*, Springer, Cham, 31: 215–236.

https://doi.org/10.1007/978-3-319-90755-0_11

29. Das SR, 2010, Competitive technical intelligence tools for innovation and technology forecasting. *Asia Pac Bus Rev*, 6(2): 30–40.

https://doi.org/10.1177/097324701000600203

30. Rodriguez-Salvador M, Castillo-Valdez PF, 2021, Integrating science and technology metrics into a competitive technology intelligence methodology. *J Intell Stud Bus*, 11(1): 69–77.

https://doi.org/10.37380/jisib.v1i1.696

31. Clarivate, 2023, Web of science core collection, viewed June 19, 2023,

https://clarivate.com/products/scientific-and-academic-research/research-discovery-and-workflow-solutions/web-of-science/web-of-science-core-collection/#features

32. Rodriguez-Salvador M, Rio-Belver RM, Garechana-Anacabe G, 2017, Scientometric and patentometric analyses to determine the knowledge landscape in innovative technologies: The case of 3D bioprinting. *PLoS ONE*, 12(6): e0180375.

https://doi.org/10.1371/journal.pone.0180375

33. Potančok M, Černý J, 2020, Competitive technical intelligence: Using patent data to determine smart city trends. *J Urban Reg Anal*, 12(1): 5–17.

https://0-doi-org.biblioteca-ils.tec.mx/10.37043/JURA.2020.12.1.1

34. Genina N, Boetker JP, Colombo S, *et al.*, 2017, Anti-tuberculosis drug combination for controlled oral delivery using 3D printed compartmental dosage forms: From drug product design to in vivo testing. *J Control Release*, 268(2017): 40–48.

https://0-doi-org.biblioteca-ils.tec.mx/10.1016/j.jconrel.2017.10.003

35. Tabriz AG, Nandi U, Hurt AP, *et al.*, 2021, 3D printed bilayer tablet with dual controlled drug release for tuberculosis treatment. *Int J Pharm*, 593(2021): 120147.

https://0-doi-org.biblioteca-ils.tec.mx/10.1016/j.ijpharm.2020.120147

36. Windolf H, Chamberlain R, Breitkreutz J, *et al.*, 2022, 3D printed mini-floating-polypill for Parkinson's disease: Combination of levodopa, benserazide, and pramipexole in various dosing for personalized therapy. *Pharmaceutics*, 14(5): 931.

http://dx.doi.org/10.3390/pharmaceutics14050931

37. Ayyoubi S, van Kampen EEM, Kocabas LI, *et al.,* 2023, 3D printed, personalized sustained release cortisol for patients with adrenal insufficiency. *Int J Pharm*, 630(2023): 122466.

https://doi.org/10.1016/j.ijpharm.2022.122466

38. Mirdamadian SZ, Varshosaz J, Minaiyan M, *et al.*, 2022, 3D printed tablets containing oxaliplatin loaded alginate nanoparticles for colon cancer targeted delivery. An in vitro/in vivo study. *Int J Biol Macromol*, 205(2022): 90–109.

https://0-doi-org.biblioteca-ils.tec.mx/10.1016/j.ijbiomac.2022.02.080

39. Nguyen KTT, Heijningen FFM, Zillen D, *et al.*, 2022, Formulation of a 3D printed biopharmaceutical: The development of an alkaline phosphatase containing tablet with ileo-colonic release profile to treat ulcerative colitis. *Pharmaceutics*, 14(10): 2179.

http://dx.doi.org/10.3390/pharmaceutics14102179

40. Ou YH, Goh WJ, Lim SH, 2023, Form & formulation approaches for COntRollable Release in 3D printed Colonic Targeting (CORR3CT) budesonide tablet. *Int J Pharm*, 635(2023): 122680.

https://0-doi-org.biblioteca-ils.tec.mx/10.1016/j.ijpharm.2023.122680

41. Liu X, Li Q, Wang Y, *et al.*, 2022, Designing a mucoadhesive chemopatch to ablate oral dysplasia for cancer prevention. *Small*, 18(25): e2201561.

https://doi.org/10.1002/smll.202201561

42. Tagami T, Okamura M, Ogawa K, *et al.*, 2022, Fabrication of mucoadhesive films containing pharmaceutical ionic liquid and eudragit polymer using pressure-assisted microsyringe-type 3D printer for treating oral mucositis. *Pharmaceutics*, 14(9): 1930.

http://dx.doi.org/10.3390/pharmaceutics14091930

43. Takashima H, Tagami T, Kato S, *et al.*, 2022, Three-dimensional printing of an apigenin-loaded mucoadhesive film for tailored therapy to oral leukoplakia and the chemopreventive effect on a rat model of oral carcinogenesis. *Pharmaceutics*, 14(8): 1575.

http://dx.doi.org/10.3390/pharmaceutics14081575

44. Ferro A, 2015, Paediatric prescribing: Why children are not small adults. *Br J Clin Pharmacol*, 79(3): 351–353.

https://doi.org/10.1111/bcp.12540

45. van der Vossen A, Buljaç S, Akçay K, *et al.*, 2021, Availability of age-appropriate paediatric formulations in the Netherlands: The need in daily clinical practice remains. *Eur J Hosp Pharm*, 28(6): 306.

https://doi.org/10.1136/ejhpharm-2019-001977

46. Khan D, Kirby D, Bryson S, *et al.*, 2022, Paediatric specific dosage forms: Patient and formulation considerations. *Int J Pharm*, 616 (2022): 121501.

https://doi.org/10.1016/j.ijpharm.2022.121501

47. Palekar S, Nukala PK, Mishra SM, *et al.*, 2019, Application of 3D printing technology and quality by design approach for development of age-appropriate pediatric formulation of baclofen. *Int J Pharm*, 556(2019): 106–116.

https://0-doi-org.biblioteca-ils.tec.mx/10.1016/j.ijpharm.2018.11.062

48. Boniatti J, Januskaite P, Fonseca LB, *et al.*, 2021, Direct powder extrusion 3D printing of praziquantel to overcome neglected disease formulation challenges in paediatric populations. *Pharmaceutics*, 13(8): 1114.

http://dx.doi.org/10.3390/pharmaceutics13081114

49. Suárez-González J, Magariños-Triviño M, Díaz-Torres E, *et al.*, 2021, Individualized orodispersible pediatric dosage forms obtained by molding and semi-solid extrusion by 3D printing: A comparative study for hydrochlorothiazide. *J Drug Deliv Sci Technol*, 66(2021): 102884.

https://0-doi-org.biblioteca-ils.tec.mx/10.1016/j.jddst.2021.102884

50. Li X, Liang E, Hong X, *et al.*, 2021, In vitro and in vivo bioequivalence study of 3D-printed instant-dissolving levetiracetam tablets and subsequent personalized dosing for chinese children based on physiological pharmacokinetic modeling. *Pharmaceutics*, 14(1): 20.

http://dx.doi.org/10.3390/pharmaceutics14010020

51. Pistone M, Racaniello GF, Rizzi R, *et al.*, 2023, Direct cyclodextrin based powder extrusion 3D printing of budesonide loaded mini-tablets for the treatment of eosinophilic colitis in paediatric patients. *Int J Pharm*, 632(2023): 122592.

https://0-doi-org.biblioteca-ils.tec.mx/10.1016/j.ijpharm.2023.122592

52. Lee J, 2022, Drug absorption, viewed May 23, 2023,

https://www.msdmanuals.com/professional/clinical-pharmacology/pharmacokinetics/drug-absorption

53. Giri B, Song E, Kwon J, *et al.*, 2020, Fabrication of intragastric floating, controlled release 3D printed theophylline tablets using hot-melt extrusion and fused deposition modeling. *Pharmaceutics*, 12(1): 77.

http://dx.doi.org/10.3390/pharmaceutics12010077

54. Reddy Dumpa N, Bandari S, Repka M, 2020, Novel gastroretentive floating pulsatile drug delivery system produced via hot-melt extrusion and fused deposition modeling 3D printing. *Pharmaceutics*, 12(1): 52.

http://dx.doi.org/10.3390/pharmaceutics12010052

55. Oladeji S, Dadou S, Zhao M, *et al.*, 2022, The development and optimisation of gastro-retentive floating tablets using fused deposition modelling 3D printing. *J Pharm Pharmacol*, 74(10): 1450–1466.

https://doi.org/10.1093/jpp/rgab176

56. Zhao X, Wei W, Niu R, *et al.*, 2022, 3D printed intragastric floating and sustained-release tablets with air chambers. *J Pharm Sci,* 111(1): 116–123.

https://doi.org/https://doi.org/10.1016/j.xphs.2021.07.010

57. Mora-Castaño G, Millán-Jiménez M, Caraballo I, 2023, Hydrophilic high drug-loaded 3D printed gastroretentive system with robust release kinetics. *Pharmaceutics*, 15(3): 842.

https://doi.org/10.3390/pharmaceutics15030842

58. Blaesi AH, Saka N, 2021, Expandable fibrous dosage forms for prolonged drug delivery. *Mater Sci Eng C Mater Biol Appl*, 120(2021): 110144.

https://doi.org/10.1016/j.msec.2019.110144

59. Blaesi AH, Saka N, 2022, Expandable, dual-excipient fibrous dosage forms for prolonged delivery of sparingly-soluble drugs. *Int J Pharm Sci*, 615(2022): 120396.

https://doi.org/10.1016/j.ijpharm.2021.120396

60. Awad A, Yao A, Trenfield SJ, *et al.*, 2020, 3D printed tablets (printlets) with braille and moon patterns for visually impaired patients. *Pharmaceutics*, 12(2): 172.

https://doi.org/10.3390/pharmaceutics12020172

61. Eleftheriadis GK, Fatouros DG, 2021, Haptic evaluation of 3D-printed Braille-encoded intraoral films. *Eur J Pharm Sci*, 157(2021): 105605.

https://doi.org/10.1016/j.ejps.2020.105605

62. Mayo Clinic, 2023, What are opioids and why are they dangerous?, viewed May 25, 2023,

https://www.mayoclinic.org/diseases-conditions/prescription-drug-abuse/expert-answers/what-are-opioids/faq-20381270

63. World Health Organization, 2021, Opioid overdose, viewed May 25, 2023,

https://www.who.int/news-room/fact-sheets/detail/opioid-overdose#:~:text=Due%20to%20their%20pharmacological%20effects,those%20deaths%20caused%20by%20overdose

64. Food & Drug Administration, 2021, Abuse-deterrent opioid analgesics, viewed May 25, 2023,

https://www.fda.gov/drugs/postmarket-drug-safety-information-patients-and-providers/abuse-deterrent-opioid-analgesics#:~:text=The%20FDA%20is%20encouraging%20the,that%20may%20help%20reduce%20abuse

65. Nukala PK, Palekar S, Patki M, *et al.*, 2019, Abuse deterrent immediate release egg-shaped tablet (Egglets) using 3D printing technology: Quality by design to optimize drug release and extraction. *AAPS PharmSciTech*, 20(2): 1.

https://doi.org/10.1208/s12249-019-1298-y

66. Ong JJ, Awad A, Martorana A, *et al.*, 2020, 3D printed opioid medicines with alcohol-resistant and abuse-deterrent properties. *Int J Pharm*, 579(2020): 119169.

https://doi.org/10.1016/j.ijpharm.2020.119169

67. Palekar S, Nukala PK, Patel K, 2022, Aversion liquid-filled drug releasing capsule (3D-RECAL): A novel technology for the development of immediate release abuse deterrent formulations using a fused deposition modelling (FDM) 3D printer. *Int J Pharm*, 621(2022): 121804.

https://doi.org/10.1016/j.ijpharm.2022.121804

68. Pfizer, 2023, Why flavor matters in drug design, especially for kids, viewed May 23, 2023,

https://www.pfizer.com/news/articles/why_flavor_matters_in_drug_design_especially_for_kids

69. Weinstock J, 2022, 6 Tips that will take the strain out of giving your child medication, viewed May 23, 2023,

https://www.chla.org/blog/health-and-safety-tips/6-tips-will-take-the-strain-out-giving-your-child-medication

70. Rycerz K, Stepien KA, Czapiewska M, *et al.*, 2019, Embedded 3D printing of novel bespoke soft dosage form concept for pediatrics. *Pharmaceutics*, 11(12): 630.

http://dx.doi.org/10.3390/pharmaceutics11120630

71. Herrada-Manchón H, Rodríguez-González D, Alejandro Fernández M, *et al.*, 2020, 3D printed gummies: Personalized drug dosage in a safe and appealing way. *Int J Pharm*, 587(2020): 119687.

https://doi.org/10.1016/j.ijpharm.2020.119687

72. Karavasili C, Gkaragkounis A, Moschakis T, *et al.*, 2020, Pediatric-friendly chocolate-based dosage forms for the oral administration of both hydrophilic and lipophilic drugs fabricated with extrusion-based 3D printing. *Eur J Pharm Sci*, 147(2020): 105291.

https://doi.org/10.1016/j.ejps.2020.105291

73. Wang Z, Han X, Chen R, *et al.*, 2021, Innovative color jet 3D printing of levetiracetam personalized paediatric preparations. *Asian J Pharm*, 16(3): 374–386.

https://doi.org/10.1016/j.ajps.2021.02.003

74. Tabriz AG, Fullbrook DHG, Vilain L, *et al.*, 2021, Personalised tasted masked chewable 3D printed fruit-chews for paediatric patients. *Pharmaceutics*, 13(8): 1301.

http://dx.doi.org/10.3390/pharmaceutics13081301

75. Bracken L, Habashy R, McDonough E, *et al.*, 2022, Creating acceptable tablets 3D (CAT 3D): A feasibility study to evaluate the acceptability of 3D printed tablets in children and young people. *Pharmaceutics*, 14(3): 516.

http://dx.doi.org/10.3390/pharmaceutics14030516

76. Goh O, Goh W, Lim S, *et al.*, 2022, Preferences of healthcare professionals on 3D-printed tablets: A pilot study. *Pharmaceutics,* 14(7): 1521.

http://dx.doi.org/10.3390/pharmaceutics14071521

77. Rautamo M, Kvarnström K, Sivén M, *et al.*, 2020, Benefits and prerequisites associated with the adoption of oral 3D-printed medicines for pediatric patients: A focus group study among healthcare professionals. *Pharmaceutics,* 12(3): 229.

https://doi.org/10.3390/pharmaceutics12030229

78. Goyanes A, Scarpa M, Kamlow M, *et al.*, 2017, Patient acceptability of 3D printed medicines. *Int J Pharm*, 530(1–2): 71–78.

https://doi.org/10.1016/j.ijpharm.2017.07.064

79. Fastø MM, Genina N, Kaae S, *et al.*, 2019, Perceptions, preferences and acceptability of patient designed 3D printed medicine by polypharmacy patients: A pilot study. *Int J Clin Pharm*, 41(5): 1290–1298.

https://doi.org/10.1007/s11096-019-00892-6

80. Kabeya K, Satoh H, Hori S, *et al.*, 2021, Experimental study on patient preferences regarding the shape and size of medical tablets and capsules using three-dimensionally printed plastic model formulations. *Patient Prefer Adherence*, 15(2021): 863–870.

https://doi.org/10.2147/PPA.S306582

81. Wang Z, Li J, Hong X, *et al.*, 2021, Taste masking study based on an electronic tongue: The formulation design of 3D printed levetiracetam instant-dissolving tablets. *Pharm Res*, 38(5): 831–842.

https://doi.org/10.1007/s11095-021-03041-9

82. Desai N, Masen M, Cann P, *et al.*, 2022, Modernising orodispersible film characterisation to improve palatability and acceptability using a toolbox of techniques. *Pharmaceutics*, 14(4): 732

http://dx.doi.org/10.3390/pharmaceutics14040732

83. European Medicines Agency, 2017, Quality by design, viewed May 25, 2023,

https://www.ema.europa.eu/en/human-regulatory/research-development/quality-design

84. Zhang J, Thakkar R, Zhang Y, *et al.*, 2020, Structure-function correlation and personalized 3D printed tablets using a quality (QbD) approach *Int J Pharm*, 590(2020): 119945.

https://doi.org/10.1016/j.ijpharm.2020.119945

85. Gueche YA, Sanchez-Ballester NM, Bataille B, *et al.*, 2021, A QbD approach for evaluating the effect of selective laser sintering parameters on printability and properties of solid oral forms. *Pharmaceutics*, 13(10): 1701.

http://dx.doi.org/10.3390/pharmaceutics13101701

86. Wang Y, Müllertz A, Rantanen J, 2022, Structured approach for designing drug-loaded solid products by binder jetting 3D printing. *Eur J Pharm Sci*, 178(2022): 106280.

https://doi.org/https://doi.org/10.1016/j.ejps.2022.106280

87. Crișan AG, Iurian S, Porfire A, *et al.*, 2022, QbD guided development of immediate release FDM-3D printed tablets with customizable API doses. *Int J Pharm*, 613(2022): 121411.

https://doi.org/10.1016/j.ijpharm.2021.121411

88. Trenfield SJ, Goyanes A, Telford R, *et al.*, 2018, 3D printed drug products: Non-destructive dose verification using a rapid point-and-shoot approach. *Int J Pharm,* 549(1–2): 283–292.

https://doi.org/10.1016/j.ijpharm.2018.08.002

89. Trenfield SJ, Tan HX, Goyanes A, *et al.*, 2020, Non-destructive dose verification of two drugs within 3D printed polyprintlets. *Int J Pharm*, 577(2020): 119066.

https://doi.org/10.1016/j.ijpharm.2020.119066

90. Gioumouxouzis CI, Katsamenis OL, Fatouros DG, 2020, X-ray microfocus computed tomography: A powerful tool for structural and functional characterisation of 3D printed dosage forms. *J Microsc*, 277(3): 135–139.

https://doi.org/10.1111/jmi.12798

91. Lima AL, Pires FQ, Hilgert LA, *et al.*, 2022, Oscillatory shear rheology as an in-process control tool for 3D printing medicines production by fused deposition modeling. *J Manuf Process*, 76(2022): 850–862.

https://doi.org/10.1016/j.jmapro.2022.03.001

92. Chamberlain R, Mangiorou E, Fischer B, 2022, Introducing fiber-assisted colorimetric measurements as a quality control tool of hot melt extruded filaments. *Pharmaceutics*, 14(5): 1055.

http://dx.doi.org/10.3390/pharmaceutics14051055

93. Silva IA, Lima AL, Gratieri T, *et al.*, 2022, Compatibility and stability studies involving polymers used in fused deposition modeling 3D printing of medicines. *J Pharm Anal*, 12(3): 424–435.

https://doi.org/https://doi.org/10.1016/j.jpha.2021.09.010

94. Callede N, Masciotti T, Casettari L, *et al.*, 2022, Development and evaluation of a 3D printing protocol to produce zolpidem-containing printlets, as compounding

preparation, by the pressurized-assisted microsyringes technique. *Int J Pharm*, 621(2022): 121756.

https://doi.org/10.1016/j.ijpharm.2022.121756

95. Zhang J, Thakkar R, Kulkarni VR, *et al.*, 2021, Investigation of the fused deposition modeling additive manufacturing I: Influence of process temperature on the quality and crystallinity of the dosage forms. *AAPS PharmSciTech*, 22(8): 258.

https://doi.org/10.1208/s12249-021-02094-8

96. Wang Y, Genina N, Müllertz A, *et al.*, 2023, Coating of primary powder particles improves the quality of binder jetting 3D printed oral solid products. *J Pharm Sci*, 112(2).

https://doi.org/10.1016/j.xphs.2022.08.030

97. O'Reilly CS, Elbadawi M, Desai N, *et al.*, 2021, Machine learning and machine vision accelerate 3D printed orodispersible film development. *Pharmaceutics*, 13(12): 2187.

http://dx.doi.org/10.3390/pharmaceutics13122187

98. Obeid S, Madžarević M, Krkobabić M, *et al.*, 2021, Predicting drug release from diazepam FDM printed tablets using deep learning approach: Influence of process parameters and tablet surface/volume ratio. *Int J Pharm*, 601(2021): 120507.

https://doi.org/10.1016/j.ijpharm.2021.120507

99. Mazur H, Erbrich L, Quodbach J, 2023, Investigations into the use of machine learning to predict drug dosage form design to obtain desired release profiles for 3D printed oral medicines. *Pharm Dev Technol*, 28(2): 219–231.

https://doi.org/10.1080/10837450.2023.2173778

100. Cisco, 2023, What is cybersecurity?, viewed May 25, 2023,

https://www.cisco.com/c/en/us/products/security/what-is-cybersecurity.html

101. Kok XW, Singh A, Raimi-Abraham BT, 2022, A design approach to optimise secure remote three-dimensional (3D) printing: A proof-of-concept study towards advancement in telemedicine. *Healthcare (Basel, Switzerland)*, 10(6): 1114.

https://doi.org/10.3390/healthcare10061114

102. Trenfield SJ, Xian Tan H, Awad A, *et al.*, 2019, Track-and-trace: Novel anti-counterfeit measures for 3D printed personalized drug products using smart material inks. *Int J Pharm,* 567(2019): 118443.

https://0-doi-org.biblioteca-ils.tec.mx/10.1016/j.ijpharm.2019.06.034

103. Oh BC, Jin G, Park C, *et al.*, 2020, Preparation and evaluation of identifiable quick response (QR)-coded orodispersible films using 3D printer with directly feeding nozzle. *Int J Pharm*, 584 (2020): 119405.

https://0-doi-org.biblioteca-ils.tec.mx/10.1016/j.ijpharm.2020.119405

104. Windolf H, Chamberlain R, Delmotte A, *et al.*, 2022, Blind-Watermarking—Proof-of-concept of a novel approach to ensure batch traceability for 3D printed tablets. *Pharmaceutics*, 14(2): 432.

http://dx.doi.org/10.3390/pharmaceutics14020432

105. Xu X, Seijo-Rabina A, Awad A, *et al.,* 2021, Smartphone-enabled 3D printing of medicines. *Int J Pharm*, 609(2021): 121199.

https://doi.org/10.1016/j.ijpharm.2021.121199

ACCSCIENCE PUBLISHING

International Journal of Bioprinting

REVIEW ARTICLE

Strontium-doped calcium silicate scaffolds with enhanced mechanical properties and tunable biodegradability fabricated by vat photopolymerization

Yinjin Li[1,2], Jin Su[1,2], Annan Chen[1,2*], Yifei Li[1,2], Xi Yuan[3], Kezhuo Chen[4], Zhaoqing Li[5], Chunze Yan[1,2], Jian Lu[6,7], and Yusheng Shi[1,2]

[1]State Key Laboratory of Materials Processing and Die & Mould Technology, School of Materials Science and Engineering, Huazhong University of Science and Technology, Wuhan 430074, China

[2]Engineering Research Center of Ceramic Materials for Additive Manufacturing, Ministry of Education, Wuhan 430074, China

[3]Department of Orthopedic Surgery, Tongji Hospital, Tongji Medical College, Huazhong University of Science and Technology, Wuhan 430030, China

[4]Institute of Resource Biology and Biotechnology, Department of Biotechnology, College of Life Science and Technology, Huazhong University of Science and Technology, Wuhan 430074, China

[5]Wuhan Zeqing Technology Co. Ltd., Wuhan 430074, China

[6]Centre for Advanced Structural Materials, Department of Mechanical Engineering, City University of Hong Kong, Hong Kong

[7]Centre for Advanced Structural Materials, Department of Mechanical Engineering, City University of Hong Kong, Shenzhen Research Institute, Greater Bay Joint Division, Shenyang National Laboratory for Materials Science, Shenzhen 518057, China

***Corresponding author:**
Annan Chen
(AnnanChenNUAA@hust.edu.cn)

(This article belongs to the *Special Issue: Bioprinting Tissues for Disease Modeling, Drug Development and Drug Testing*)

Citation: Li Y, Su J, Chen A, et al., 2023, Strontium-doped calcium silicate scaffolds with enhanced mechanical properties and tunable biodegradability fabricated by vat photopolymerization. *Int J Bioprint*, 9(6): 1233.
https://doi.org/10.36922/ijb.1233

Received: April 27, 2023
Accepted: July 21, 2023
Published Online: September 14, 2023

Copyright: © 2023 Author(s). This is an Open Access article distributed under the terms of the Creative Commons Attribution License, permitting distribution, and reproduction in any medium, provided the original work is properly cited.

Publisher's Note: AccScience Publishing remains neutral with regard to jurisdictional claims in published maps and institutional affiliations.

Abstract

Strontium-doped calcium silicate (SrCS) bioceramics have demonstrated outstanding vasculogenic ability to repair large segmental bone defects, while their poor mechanical properties and rapid degradation rate remain the major obstacles in clinical treatment. Here, we proposed a novel approach to significantly enhance the mechanical properties of SrCS bioceramics with tunable biodegradability using micron barium titanate-based (BTA) powders as a dopant. Biomimetic SrCS-BTA scaffolds with triply periodic minimal surface structures were fabricated by vat photopolymerization. The effects of BTA content on microtopography, mechanical properties, degradability, and bioactivity of composite scaffolds were studied. On the one hand, the BTA greatly increased the maximum densification rate of SrCS ceramics by 84.37%, while the corresponding densification temperature decreased by 95°C. On the other hand, $CaTiO_3$ generated by the reaction of SrCS and BTA intercepted cracks at the grain boundaries, and thus, the mechanical properties were enhanced due to the pinning effect. The SrCS-40BTA scaffold exhibited much higher compressive strength and elastic modulus by 296% compared with the pure SrCS scaffold. The energy absorption of SrCS-40BTA scaffolds was 5.6 times higher than that of the pure SrCS scaffold. In addition, biocompatible SrCS-BTA scaffolds with lower degradation rates can play a supporting role in the process of repair for a longer duration. This work provides a promising strategy to fabricate biomimetic scaffolds with highly enhanced mechanical properties and tunable biodegradability for repairing damaged large segmental bone tissues.

Keywords: Strontium-doped calcium silicate; 3D printing; Vat photopolymerization; Mechanical property; Biodegradability

1. Introduction

The treatment of large segmental bone defects (>5 cm) caused by car accidents, gunshots, and malignant tumor resection is complicated and has many clinical complications, which easily lead to repair failure[1,2]. Therefore, large segmental bone repair remains a major challenge in clinical treatment. The emerging bone tissue engineering (BTE) provides an ideal treatment strategy for the repair of large segmental bone defects[3,4]. The biomimetic three-dimensional (3D) scaffolds play a crucial role in BTE since they can provide the necessary mechanical support and biomimetic microenvironment conducive to cell proliferation[5-9]. So far, various manufacturing methods have been developed for the fabrication of biomimetic scaffolds, such as direct foaming, gel-casting, and sacrificial template method[10-12]. But these conventional methods are restricted by the geometrical design and structural complexity of biomimetic structures. Additive manufacturing (known as 3D printing[13]) has been shown through multiple studies to enable the creation of intricate scaffolds that can be customized to individual patients[14-17]. These scaffolds possess the capacity to provide mechanical reinforcement to bone tissues and a microenvironment that closely resembles that of natural bone[18-20]. Among the various additive manufacturing techniques available, vat photopolymerization (VPP) is a highly accurate method that is particularly well-suited for printing bone implants[21-24]. However, as for large segmental bone repair, the reconstruction of vascularization capacity for 3D-printed large-size scaffolds remains a huge challenge.

Modulation of cellular behavior through intrinsic properties of biomaterials provides an effective solution for the complete revascularization of large-size scaffolds. For instance, the strontium-doped calcium silicate (SrCS) can significantly upregulate the expression of osteogenic genes and angiogenic factors by releasing Si^{4+} and Sr^{2+} ions[25-28]. Lin *et al.* fabricated SrCS scaffolds for osteoporotic bone repair, and the *in vitro* experiments revealed that Si^{4+} and Sr^{2+} ions can promote cell viability and expression of alkaline phosphatase (ALP)[29]. Xing *et al.* designed bioactive alginate hydrogels containing Si^{4+} and Sr^{2+} ions to activate cells *in vivo*, and revealed a synergistic effect of the ions on cell proliferation without loss of stemness[30]. In short, SrCS is deemed an ideal biomaterial for reconstructing vascularization in repairing large segmental bone defects. Nonetheless, its suboptimal mechanical characteristics and very fast degradation ratio pose challenges in ensuring sufficient mechanical reinforcement and a biomimetic microenvironment for effective bone regeneration.

Barium titanate-based ceramics (BTA) has demonstrated their good biocompatibility and mechanical properties in the application of bone tissue engineering[31], which can enhance mechanical properties as a second phase. For instance, Dubey *et al.* prepared hydroxyapatite (HA) scaffold doping with 40 wt.% BTA to enhance the compressive strength by 200% compared to undoped samples[32]. Tavangar *et al.* fabricated HA-BT scaffolds for orthopedic applications and found that the presence of BTA acted as a second phase to highly increase the bulk density and mechanical properties of composite samples[33]. Therefore, in this study, we proposed an approach to improve the mechanical properties and tune the degradation rate of SrCS scaffolds by doping BTA powders with different mass ratios. SrCS-BTA scaffolds with biomimetic triply periodic minimal surface (TPMS) structures were fabricated by VPP. Finally, the mechanical and biological properties of the scaffolds before and after *in vitro* degradation were characterized.

2. Material and methods

2.1. Materials

SrCS powders (Xi'an Shuogu Technology Co., LTD., China,) with a particle size of 3.9 μm (D_{50}), a density of 2.90 g/cm^3, and a refractive index of 1.61, were used as raw materials. BTA powders with a particle size of 2.2 μm (D_{50}), a density of 5.72 g/cm^3, and a refractive index of 1.63 were used as the dopant with different mass ratios of 0, 20, 30, and 40 wt.% (marked as SrCS, SrCS-20BTA, SrCS-30BTA, and SrCS-40BTA). 1,6-Hexanediol diacrylate (HDDA, Chengdu Fourth City New Material Co., LTD., China) with a density of 1.0 g/cm^3 and a refractive index of 1.457 was used as the photosensitive resin. Polymer 41000 (Lubrizol, Spain) and diphenyl (2,4,6-trimethyl benzoyl) phosphine oxide (TPO; BASF, Germany) were used as the dispersant and photoinitiator, respectively. RAD 2500 (VOK, Germany) and anti-sedimentation thixotropic 8810 (Sago, Germany) were used as leveling and anti-settling agents, respectively. High-purity alkyl aluminum derivatives (Easepi 590, Guangyi Chemical Co., LTD., China) were used as the copolymer inhibitor. Simulated body fluid (SBF) (Phygene Life Sciences Company, Fujian, China) was used to perform *in vitro* immersion tests to analyze the biodegradability of materials.

2.2. Fabrication of scaffolds

4.0 wt.% 41000 (based on powders), 0.5 wt.% TPO (based on photosensitive resin), 0.5 wt.% RAD, 0.5 wt.% 8810 (based on suspension), and 0.1 wt.% copolymer inhibitor

(based on powders) were added into HDDA and stirred for 2 min. Then, ceramic powders were added and stirred at 2000 r/min for 5 min in a vacuum planetary stirring defoaming machine (SIE-MIX80, Guangzhou SIENOX, Technology Co., LTD., China). Then, zirconia mill balls were added and stirred at 1200 r/min for another 25 min. Finally, the ceramic suspension with a solid loading of 40 vol.% was obtained. The gyroid type TPMS structure can be modeled by MATLAB software according to the following parametric Equation I[34]:

$$\sin\left(\frac{2\pi}{a}x\right)\cos\left(\frac{2\pi}{a}y\right)+\sin\left(\frac{2\pi}{a}y\right)\cos\left(\frac{2\pi}{a}z\right)+\sin\left(\frac{2\pi}{a}z\right)\cos\left(\frac{2\pi}{a}x\right)=t \quad \text{(I)}$$

where a is the cubic cell length, and t controls the volume enclosed by the surface of TPMS. The side length of the cubic gyroid structural model was 10 mm, and the porosity was 66% (a = 1.25 mm, t = 0.48). Then, the model was sliced by the 10 DIM software and imported into the VPP printer (AUTOCERA-R, Beijing TenDimensions Technology Co., LTD., China), which is shown in Figure 1. The sliced layer thickness was set as 25 μm. The dependence of curing depth on the exposure energy can be analyzed using the Beer–Lambert model, given by Equation II[35]:

$$C_d = D_p \cdot LnE_i - D_p \cdot LnE_c \quad \text{(II)}$$

where C_d is the curing depth, D_p is the penetration depth, E_i is the actual exposure energy, and E_c is the critical energy. The curing depth of the suspension was measured by a micrometer. The SrCS, SrCS-20BTA, SrCS-30BTA, and SrCS-40BTA suspensions were printed with the exposure energy of 9, 20, 28, and 32 mJ/cm^2 to obtain the green bodies, respectively. Finally, the printed green bodies were debinded and sintered to obtain the composite bioceramic scaffolds (detailed steps shown in Figure 5a and b).

2.3. *In vitro* immersion experiment

To assess the biodegradability of the scaffolds, the SrCS-BTA scaffolds were immersed in SBF (pH = 7.4) at 37°C in a shaker for 4, 7, and 14 days, respectively. The ratio of scaffold mass to solution volume was set as 1 g: 100 mL. Finally, the scaffolds were cleaned with deionized water and dried at 37°C for 24 h. The mass of the degraded scaffolds was measured by a precision electronic balance (ME403, METTLER TOLEDO, Switzerland). The degradation rates were calculated using Equation III:

$$D_r(\%) = 100 \times (W_1 - W_2) / W_1 \quad \text{(III)}$$

where D_r is the degradation rate of the scaffold, and W_1 and W_2 are the mass before and after immersion in SBF solution, respectively.

2.4. Mechanical properties

To assess the mechanical properties of the scaffolds, the compressive strength σ_c, elasticity modulus E_m, and energy absorption E_a of SrCS-BTA scaffolds were determined by compression experiments on cubic solid samples. The SrCS-BTA scaffolds were mechanically compressed using the Electronic Universal Testing Machine (AG-IC 100KN, SHIMADZU, Japan) equipped with the 90 kN weighing sensor. In the compression experiment, the loading speed was 0.5 mm/min. The compressive strength σ_c was calculated using Equation IV:

$$\sigma_c = F_{max} / S \quad \text{(IV)}$$

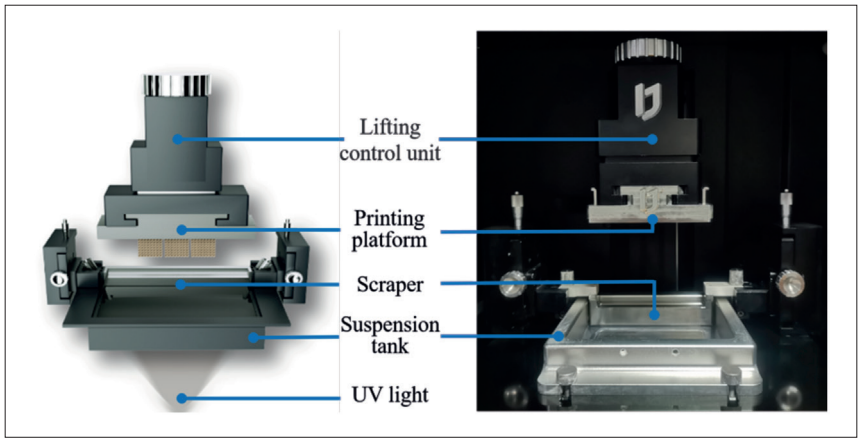

Figure 1. Schematic and photography of the VPP printing equipment.

where F_{max} is the maximum standard load, and S is the cross-sectional area of the scaffold. The elasticity modulus E_m and energy absorption were calculated using Equations V and VI, respectively.

$$E_m = \sigma_c / \varepsilon \quad (V)$$

$$E_a = \int f(x)dx \quad (VI)$$

where is compressive strain, and (x) is the compressive stress–strain curve. The average of each data point was taken from five tests.

2.5. Characterization

The thermal polymer PVT rheometer (Gottfert-RG50, Gottfert, Germany) was used to measure the rheological behavior of the suspensions, at variable shear rates of 0–1000 s^{-1} and a constant shear rate of 100 s^{-1}. The UV absorption range of SrCS-BTA powders was tested by ultraviolet (UV)-visible spectrophotometer UV-2 (Lambda 35, PerkinElmer, USA). The Fourier transform infrared spectrometer (Nicolet iS50R, Thermo Scientific, USA) was used to observe the characteristic absorption bands change of the chemical bonds. The thermal dilatometer (DIL402C, NETZSCH, Germany) was used to real-time monitor the densification process of ceramic samples, from room temperature to 1300°C with a heating rate of 10°C/min. The microstructure was analyzed by thermal field emission scanning electron microscope (JSM-7600F, Nippon Electronics, Japan) coupled with an energy dispersive spectroscopy (EDS). The phase composition was observed by an X-ray diffractometer (XRD-7000, Shimadzu Company, Japan), with a Cu tube (λ = 1.5406 Å), and at a scanning rate of 2°/min. The main peak ratios of $CaSiO_3$ and $CaTiO_3$ were calculated according to Equation VII[36]:

$$M\% = (I_1 + I_2) / (I_1 + I_2 + I_3 + I_4) \quad (VII)$$

where I_1 and I_2 are the intensity of the main and secondary peaks of the M phase, respectively, and I_3 and I_4 are the intensity of the main and secondary peaks of another phase, respectively.

2.6. Biological experiment

To determine the bioactivity of the composite bioceramic scaffolds, rat bone marrow stromal cells (rBMSCs) were cultured in the extract of composite bioceramic scaffolds *in vitro* to proliferate[37]. The composite bioceramic scaffolds were soaked in Dulbecco's Modified Eagle Medium/Nutrient Mixture F-12 (DMEM/F12, Hyclone, USA) with 10% fetal bovine serum (FBS; Gibco, USA) and 1% antimicrobial penicillin and streptomycin. The concentration of the solution mixture was 200 mg/mL. The mixed solution was incubated at 37°C and 120 rpm in a constant temperature shock incubator, and the extract was filtered and collected after incubation for 72 h. The rBMSCs were seeded in 96-well plates (cell density 4×10^3 cells/well) and cultured in a constant temperature incubator at 37°C in a dehumidified atmosphere of 5% CO_2[38]. After 24 h of culture, the same volume of the original medium was replaced by 120 μL of composite ceramic medium. The original medium without composite bioceramic extract was used as the control group. Cell counting kit-8 (CCK-8) tests were performed after 1 and 7 days of culture. A 450 nm absorbance microplate reader (BioTek, USA) was used to measure the optical density (OD) value of the cell viability assays.

Following seeding on the wafers and culturing for 24 h for rBMSCs, these wafers were fixed in 4.0% paraformaldehyde and stained with rhodamine B-labeled phalloidin (Solarbio, China) and 4′,6-diamidino-2-phenylindole (DAPI) (Solarbio, China) for further analysis. Then, we used a fluorescence microscope (Nikon Eclipse Ti; Nikon, Japan) to capture fluorescence images.

3. Results and discussion

3.1. Characterization of raw powders

In the context of the ceramic VPP process, the agglomeration of nanoscale powders (< 500 nm) is facilitated by the stronger van der Waals force, which in turn leads to an amplified scattering effect and a diminished curing depth. Conversely, particles with sizes exceeding 35 μm are prone to sedimentation and could result in the generation of single layer with uneven thickness[39-41]. Therefore, we selected irregular-shaped SrCS powders with an average particle size of 3.9 μm for VPP (shown in Figure 2a and b). The particle size distribution of raw SrCS powders was in the range of 1 to 10 μm (D_{10} = 1.7 μm, D_{90} = 10.3 μm), satisfying the requirements of powder size for VPP. The micromorphology and particle size distribution of BTA powders are shown in **Figure S1** (Supplementary File). The SrCS-BTA composite powders revealed an average particle size of 3.6 μm with a wider and left-shifting particle size distribution (shown in Figure 2d). This particle gradation effect of the composite powders would be beneficial to the deposition behavior of ceramic suspension and the sintering densification at high temperatures[42].

3.2. Fabrication of bioceramic scaffolds

Ceramic suspension with high solid loading and low viscosity plays a crucial role in the VPP additive manufacturing process[43]. As shown in Figure 3a, the viscosity of suspensions with a solid loading of 45 vol.% was 4 Pa·s at a shear rate of 100 s^{-1}. Such high viscosity would

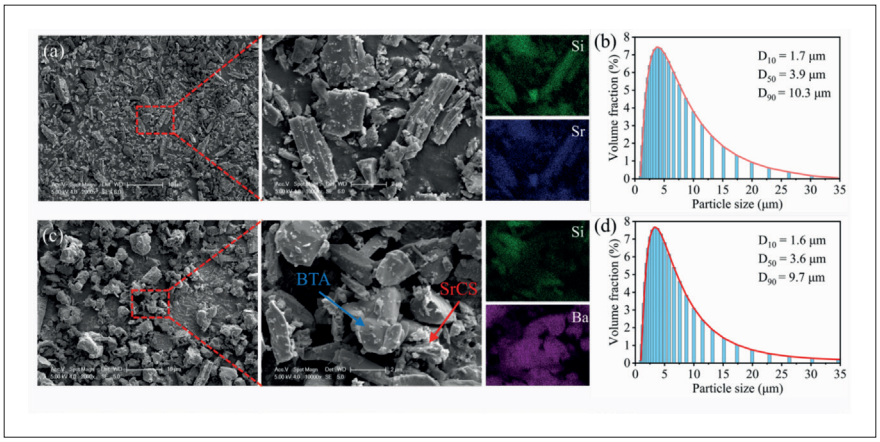

Figure 2. SEM images, element distribution, and particle size distributions of (a–b) SrCS powders, and (c–d) SrCS-40BTA composite powders.

be difficult to fabricate the green body by VPP due to the ceramic suspensions with ideal viscosity below 3 Pa·s at a high shear rate for deposition and stereolithography[44-46]. Therefore, we selected SrCS-BTA ceramic suspensions with a solid loading of 40 vol.% and a viscosity less than 1 Pa·s at a shear rate of 100 s^{-1} for VPP process (shown in Figure 3b).

We investigated the UV light absorption of SrCS-BTA composite powders. As shown in Figure 4a, the SrCS-BTA composites revealed a strong UV light absorption at a wavelength below 350 nm, while the absorption decreased substantially at a wavelength of 350–400 nm. Therefore, the 405 nm wavelength of the UV source was selected to cure the SrCS-BTA ceramic suspensions. Exposure energy is the most principal factor for VPP, which directly determines the curing depth and forming precision of samples[40]. As shown in Figure 4b, the curing depth varied linearly with $\mathrm{Ln}E_i$, and the slope of the fitting equation (D_p) gradually decreased with increasing BTA content. Therefore, as the BTA content increased, more exposure energy was required for a certain curing depth. Generally, the desired exposure energy should allow the curing depth 2–3 times as thick as the sliced layer, which can ensure excellent layer-to-layer bonding to prevent cracking during sintering. However, the excess exposure energy would cause poor forming accuracy. Therefore, based on the Beer–Lambert model, the exposure energy of 9, 20, 28, and 32 mJ/cm^2 were selected for curing SrCS, SrCS-20BTA, SrCS-30BTA, and SrCS-40BTA suspensions, and the corresponding curing depth is shown in Table 1, respectively. In addition, the exposure accuracy test also shows that the selected exposure energy is appropriate (shown in **Figure S2** in Supplementary File).

Further, we evaluated the UV-curing kinetics of ceramic suspensions by tracking the absorption intensity of the C=C bond (shown in Figure 4c). Upon UV irradiation, the unsaturated C=C bonds of HDDA reacted with free radicals from the dissociation of TPO and transformed into saturated single bonds[47]. Therefore, the infrared absorption intensity of unsaturated C=C bonds gradually weakened with the curing reaction. The infrared absorption intensity at around 1636 cm-1 was attributed

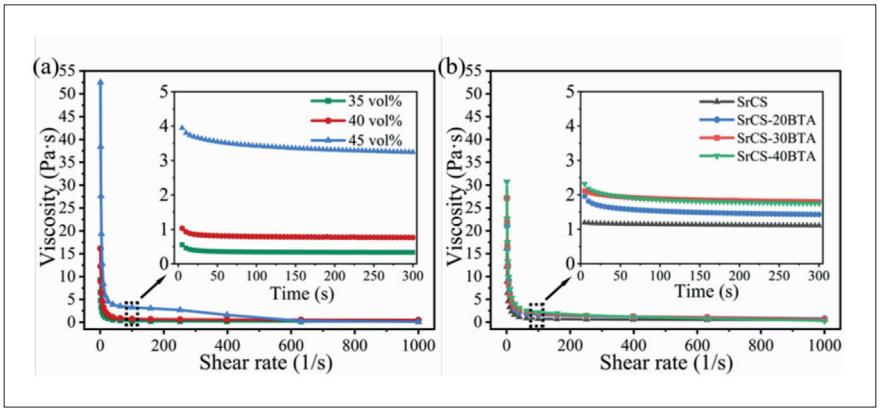

Figure 3. Viscosities of (a) SrCS suspensions with different solid loading and (b) 40 vol.% SrCS suspensions with different BTA contents at variable shear rates of 0–1000 s^{-1} and a constant shear rate of 100 s^{-1}.

Table 1. Curing parameter of SrCS-BTA composites

Component	Exposure energy (mJ/cm²)	Curing depth (μm)
SrCS	9	73.53
SrCS-20BTA	20	73.5
SrCS-30BTA	28	73.52
SrCS-40BTA	32	72.74

to the stretching vibration of the unsaturated C=C bond of HDDA, which decayed substantially in the printed green body, indicating the complete reaction of HDDA in VPP. The printed green body showed well-connected internal pore structures with a pore size of about 1 mm (Figure 4d). The step-like features on the rods that were derived from the layer-by-layer printing were observed in SEM images, which could be fully densified under expected sintering conditions and thus resulting in the desired mechanical performance.

3.3. Sintering densification and characterization of scaffolds

Before sintering, all green bodies were debinded to remove sacrificial organic matter, and the process of debinding is shown in Figure 5a. After that, we estimated the sintering temperature range according to the general sintering temperature of CS-based ceramics[48] and conducted a predictive sintering experiment (shown in Figure 5b). Finally, the sintering temperature was determined in the range of 1100–1300°C, in which the sintering line shrinkage curves of the scaffold were obtained (Figure 5c and d), **X/Y** is the line contraction of length and width, and **Z** is the line contraction of height.

In order to investigate the process of sintering densification and determine the optimal sintering temperature, we conducted thermal expansion measurements on green bodies and obtained their real-time relative density curves during heat treatment. Subsequently, we derived the densification rate by differentiating the densification curves[49]. Typically, the temperature corresponding to the highest densification rate on the curve is considered to be the optimal sintering temperature. To explore the sintering densification mechanism and obtain the optimum sintering temperature, we measured the thermal expansion of green bodies and obtained their real-time relative density curves during heat treatment. Figure 6a shows that the SrCS green body started to densify from 1000°C, and the densification rate reached the maximum of 0.32 s^{-1} with the corresponding temperature of 1270°C. After sintering at 1270°C for 2 h, the step-like features

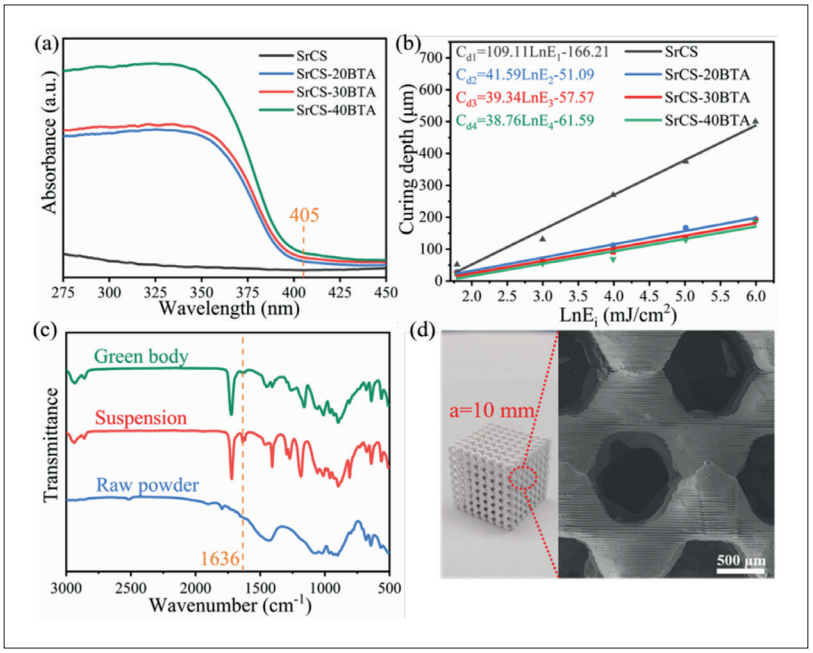

Figure 4. (a) UV light absorption of SrCS-BTA composites. (b) Curing depth of SrCS-BTA composites at different exposure energies. (c) Fourier infrared absorption spectra of the SrCS raw powder, suspension, and green body. (d) Photography and SEM image of the printed SrCS green body.

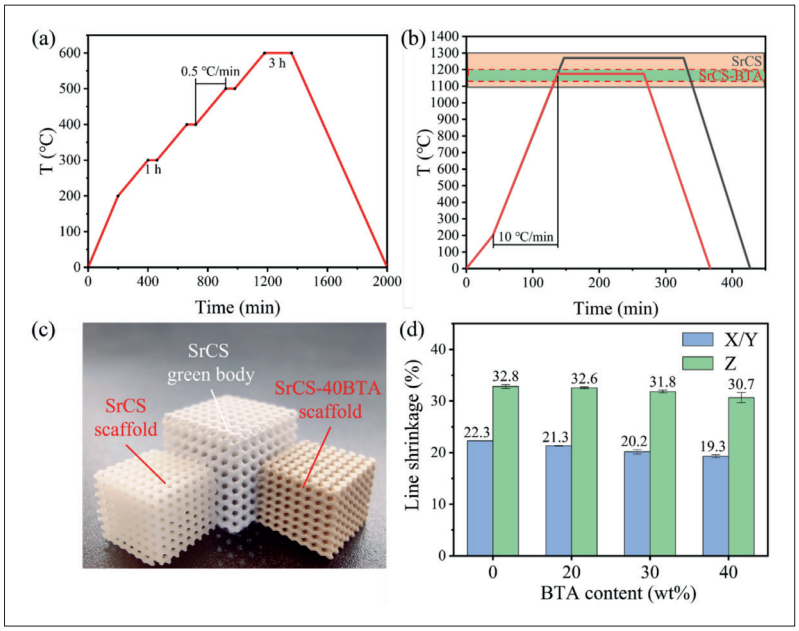

Figure 5. Curve of (a) debinding and (b) high-temperature sintering. (c) Photography of the SrCS green body, SrCS scaffold, and SrCS-40BTA scaffold. (d) Line shrinkage of the scaffolds with different SrCS-BTA components.

on the rods of SrCS green body disappeared, and dense grains with no cracks were observed (shown in Figure 6b–d). Therefore, 1270°C was an appropriate sintering temperature for SrCS green body. As shown in Figure 6e, the maximum densification rate of the SrCS-20BTA increased to 0.46 s^{-1}, and the corresponding temperature was lowered by 95°C. Such results were attributed to the doping of impurities that reduce the melting point of the mixture[50]. The relative density curve of SrCS-20BTA remained constant as the temperature was raised above 1200°C, indicating that the grains had finished the densification and may enter the abnormal growth or even melting stage. We sintered the SrCS-20BTA green body at 1175°C for 2 h. Compared to the pure SrCS scaffold, the SrCS-20BTA scaffold had a smaller shrinkage rate after sintering, and the microscopic morphology was denser

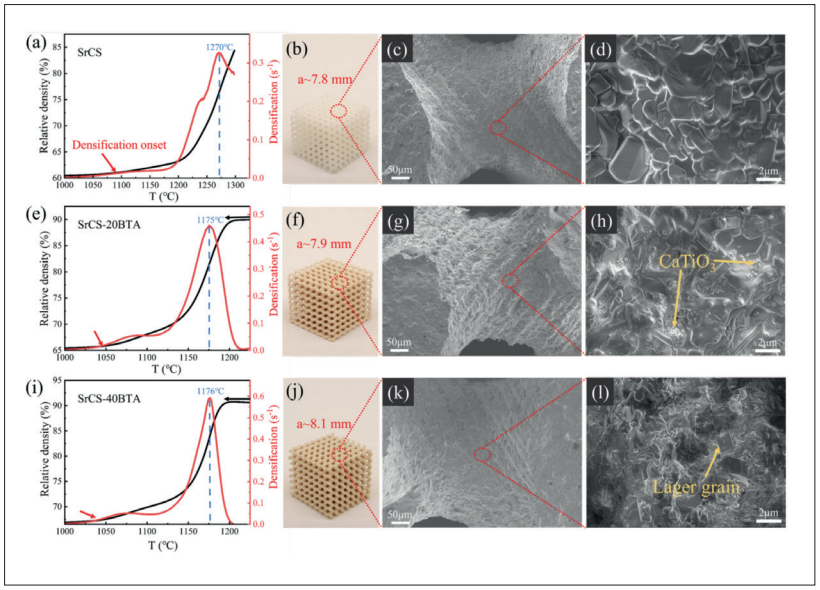

Figure 6. Relative density densification and densification curves of green bodies, as well as photography and SEM images of scaffolds. (a–d) SrCS; (e–h) SrCS-20BTA; (i–l) SrCS-40BTA.

(shown in Figure 6f–h). With increasing BTA content to 40 wt.% (SrCS-40BTA), the maximum densification rate further increased to 0.59 s^{-1}, while the corresponding temperature was kept at 1176°C (Figure 6i). After sintering at 1175°C for 2 h, the shrinkage rate of the SrCS-40BTA scaffold was further reduced (shown

in Figure 6j–l).

Figure 7a shows the XRD patterns of SrCS ceramics with different BTA contents. The pure SrCS ceramics contained $CaSiO_3$ and $(Sr_{4.62}Ca_{0.38})Si_3$ phases, and the $CaTiO_3$ phase was detected in the SrCS-BTA ceramics. On the one hand, the $(Sr_{4.62}Ca_{0.38})Si_3$ phase gradually disappeared and the $CaSiO_3$ phase reduced after doping BTA. On the other hand, the diffraction peaks of the $CaSiO_3$ phase shifted slightly to the lower angle with the increase of BTA content (Figure 7b), which indicated the lattice expansion of grains[51]. Moreover, the intensity of the $CaTiO_3$ phase increased gradually, suggesting the increasing degree of crystallinity with the increase of BTA content from 20 to 40 wt.%. The peak ratio extracted from XRD patterns can provide approximate semi-quantitative information about the phase content[52]. In Figure 7c and d, the main peak ratios of the $CaSiO_3$ phase and $CaTiO_3$ phase are plotted for the SrCS-BTA ceramics. It is quite clear that the amount of $CaTiO_3$ phase increased while the $CaSiO_3$ phase content decreased with increasing BTA content.

Figure 8a shows the stress–strain behaviors of the prepared SrCS scaffolds. The stress–strain curves revealed that the SrCS scaffolds possessed two stages of elastic deformation and brittle fracture. With the increase of strain, brittle fractures occurred in the thin bars of scaffolds, and the stress value fluctuated up and down during compression, resulting in a zigzag curve. When the scaffolds were completely broken, the compressive strength reached the yield strength, and then the scaffolds completely failed. The compressive strength of SrCS scaffolds increased significantly with increasing BTA content from 20 to 40 wt.% and reached the maximum of 29 ± 0.39 MPa, which was 296% more than that of the pure SrCS scaffolds (Figure 8b). Similar results could be observed for the elastic modulus of the scaffolds (shown in Figure 8c). In addition, the results showed that the energy absorption of SrCS-40BTA scaffolds was 5.6 times higher than that of the pure SrCS scaffolds (Figure 8d), indicating the composite scaffolds possess superior ability to resist deformation[53]. In short, the mechanical properties of SrCS scaffolds were comprehensively enhanced by doping BTA, meaning the SrCS-BTA composite scaffolds would be more compatible with the natural bone than the pure SrCS scaffolds.

Based on the XRD and SEM analysis, we speculated that the newly formed CaTiO3 grains in the matrix hinder the grains movement and crack extension, exhibiting the classic

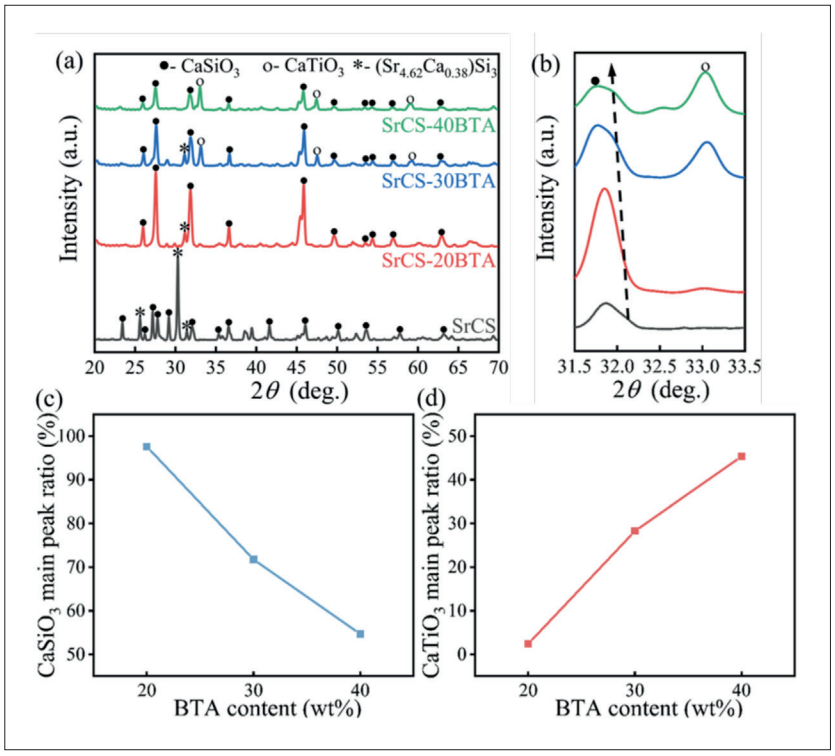

Figure 7. (a,b) XRD patterns, (c) $CaSiO_3$ main peak ratio, and (d) $CaTiO_3$ main peak ratio of bioceramic scaffolds with different SrCS-BTA components.

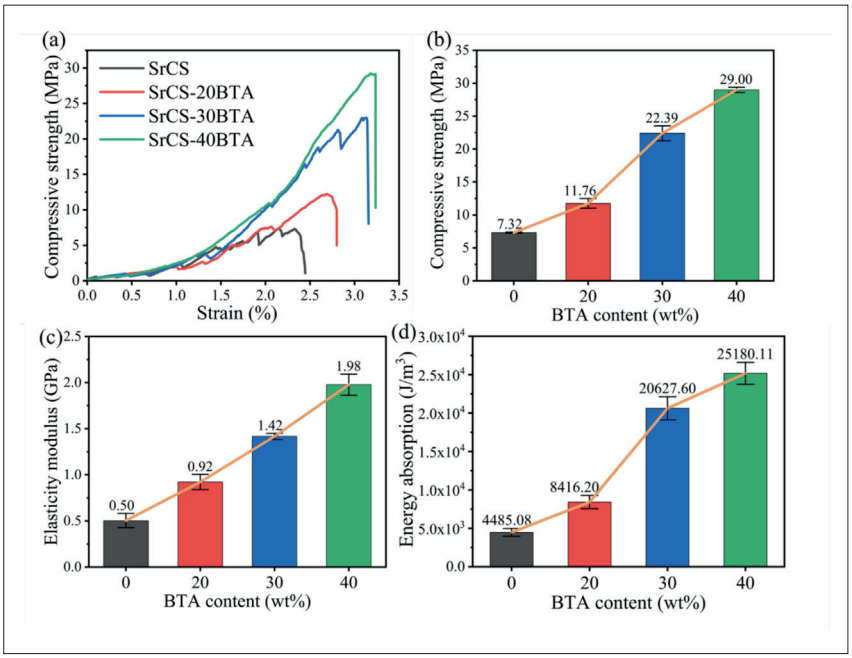

Figure 8. (a) Stress–strain curves, (b) compressive strength, (c) elasticity modulus, and (d) energy absorption of the bioceramic scaffolds with different SrCS-BTA components.

pinning effect[54]. This leads to the enhanced mechanical properties of SrCS-BTA composite scaffolds at the macro level. More specifically, with the further increase of BTA content, the concentration of TiO-2 3 from BTA increased during the high-temperature sintering. The newly $CaTiO_3$ grains were formed and pinned between $CaSiO_3$ grains (as mentioned above), which could effectively hinder the movement of the grains and crack extension, resulting in significant improvement in mechanical properties, as shown in Figure 9. On the other hand, pure SrCS scaffolds without $CaTiO_3$ phase such as nails and cracks could easily pass through the $CaSiO_3$ grains, leading to the scaffold failure during compression.

3.4. Micromorphology and mechanical properties after *in vitro* degradation

After *in vitro* degradation, the surface microtopography of the SrCS scaffold changed significantly (shown in Figure 10). After soaking for 4 days, the originally dense grain boundaries were eroded into larger gaps, which then bonded with each other and were deeply eroded to form micropores on the 7th day. After soaking for 14 days, broken pores were observed with the breakage of grains. On the contrary, doping BTA make composite scaffolds maintain the surface microtopography during soaking. After a 14-day soaking period, the composite scaffolds

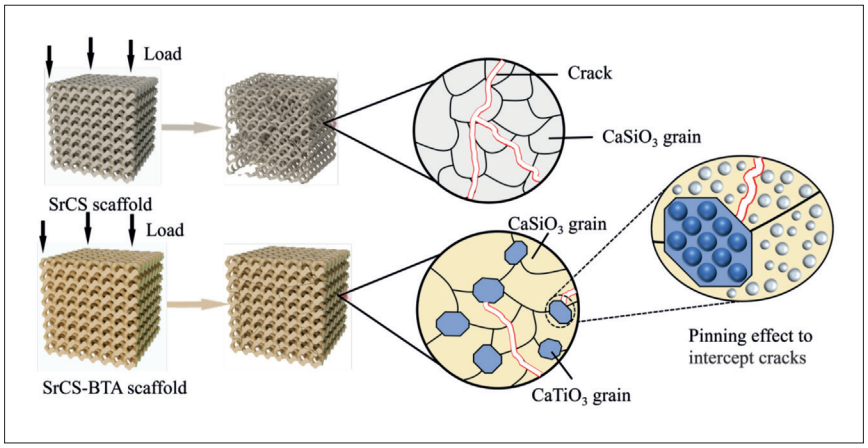

Figure 9. Schematic illustration of enhancement mechanism of mechanical properties of the SrCS-BTA composite scaffolds.

exhibited a limited number of micropores, suggesting a lower degradation rate.

Particularly, the degradation rate of the SrCS-40BTA scaffold after soaking for 14 days was only 1.32 ± 0.09%, which was one-third that of the pure SrCS scaffold (shown in Figure 11a). Accordingly, as the structure was relatively complete, the compressive strength of the composite scaffolds was also better than the pure SrCS scaffold after degradation (shown in Figure 11b). Moreover, the SrCS-40BTA scaffold exhibited a few microcracks after soaking for 4 days but was intercepted by the $CaTiO_3$ grains. This pinning effect was one of the main reasons for the enhancement of mechanical properties, in consistent with the previous results.

The degraded scaffolds were subjected to compression tests to evaluate their mechanical properties in operation (shown in Figure 12a). Figure 12b presents the stress–strain curves of the scaffolds after *in vitro* degradation for 14 days, and the curves of other days are shown in **Figure S4** (Supplementary File). These curves all showed that scaffolds doped with BTA still had high compressive strength after *in vitro* degradation, which ensured that they could play a good supporting role in the process of bone repair. In addition, the greater energy absorption of the composite scaffolds resulted in a strong deformation resistance. Figure 12c shows the compressive strength of the degraded scaffolds. The compressive strength of the SrCS-40BTA scaffold after *in vitro* degradation was about three times that of the pure scaffold. One of the reasons is that composite scaffolds lost components more slowly in the degradation process, resulting in more complete structures and fewer surface defects than the pure SrCS scaffold. Another reason is that the pinning effect played a crucial role in hindering the crack extension and grain movement during the compression process, and became more obvious with the increase of BTA content. Meanwhile, the elasticity modulus of the scaffolds increased after *in vitro* degradation (shown in Figure 12d). According to previous reports, an elastic modulus greater than 3.0 GPa would not be conducive to the growth of new bone[55]. Thus, we should adjust the content of BTA so that the composite scaffolds have the required compressive strength while maintaining the appropriate elasticity modulus. *In vitro* degradation experiment revealed that we can regulate the biodegradability of SrCS scaffolds by changing the content of BTA to provide the necessary mechanical support for the long-time regeneration of large bone defects.

3.5. *In vitro* biological activity evaluation

To verify the biological activity of the scaffolds, we tested the OD values of cell proliferation by CCK-8 assay, as shown in Figure 13. After culturing for 1 day, the OD values of SrCS composite scaffolds were similar to those of the control group. After culturing for 7 days, all components of the cells had obvious proliferation effect, and the SrCS

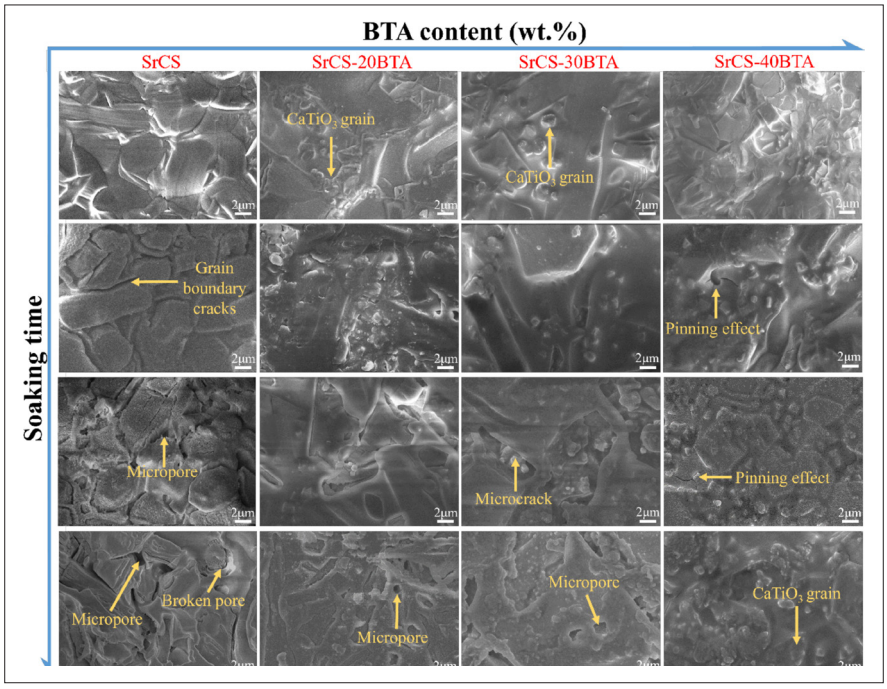

Figure 10. Surface morphology of bioceramic scaffolds with different SrCS-BTA components after soaking for 0, 4, 7, and 14 days, respectively.

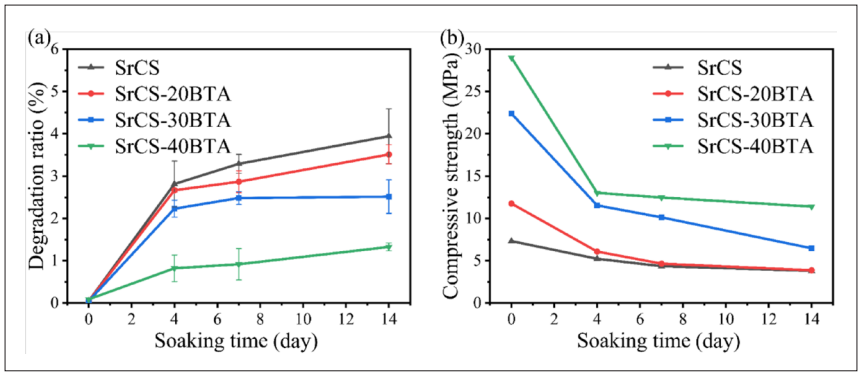

Figure 11. (a) Degradation ratio and (b) compressive strength of bioceramic scaffolds with different SrCS-BTA components after soaking for 0–14 days.

composite scaffold group was similar to the control group. Overall, it is proved that the composite scaffold has no cytotoxicity and good biocompatibility.

The rBMSCs were seeded on the surface of composite bioceramic wafers to evaluate their biocompatibility (shown in Figure 14). After culturing for 24 h, the rBMSCs were evenly distributed and stretched on the surface of the wafer. As a result, the composite bioceramics provided a conducive surface microenvironment for the initial adhesion of cells. Therefore, it could be concluded that SrCS-BTA composite scaffolds exhibited excellent biocompatibility.

4. Conclusion

In this study, we fabricated biomimetic SrCS scaffolds with highly enhanced mechanical properties and tunable biodegradability using BTA as a dopant. SrCS-BTA scaffolds with complex-shaped biomimetic TPMS structures and a high porosity of 66% were fabricated by the VPP technique. When the BTA content increased from 0 to 40 wt.%, the maximum densification rate of scaffolds

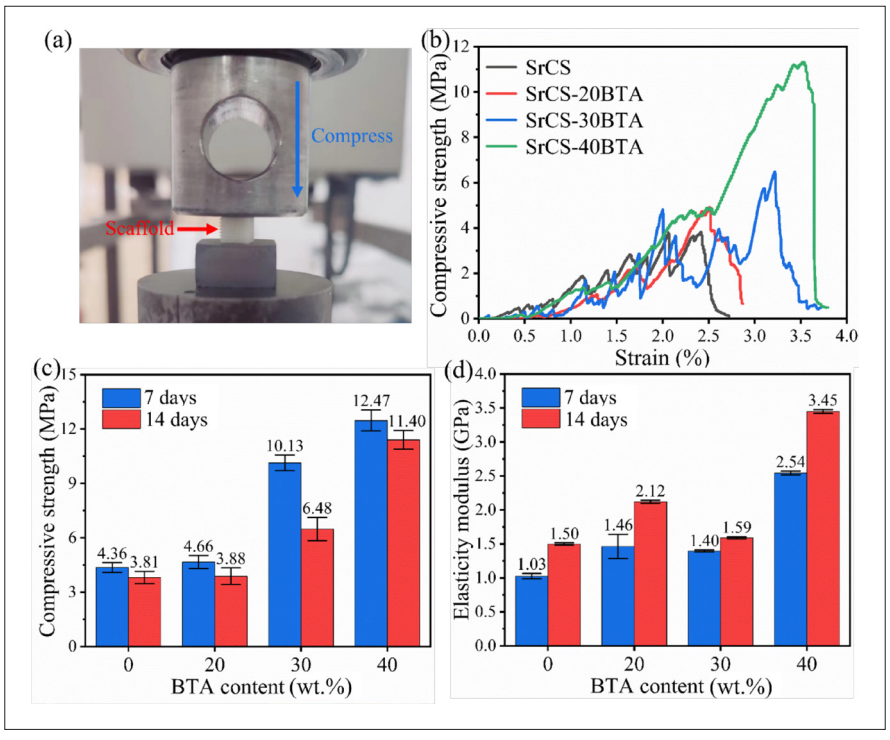

Figure 12. (a) Photography of the compression experiment. (b) Stress–strain curves of the bioceramic scaffold with different SrCS-BTA components after soaking for 14 days. (c) Compressive strength and (d) elasticity modulus of bioceramic scaffolds with different SrCS-BTA components after soaking for 7 and 14 days.

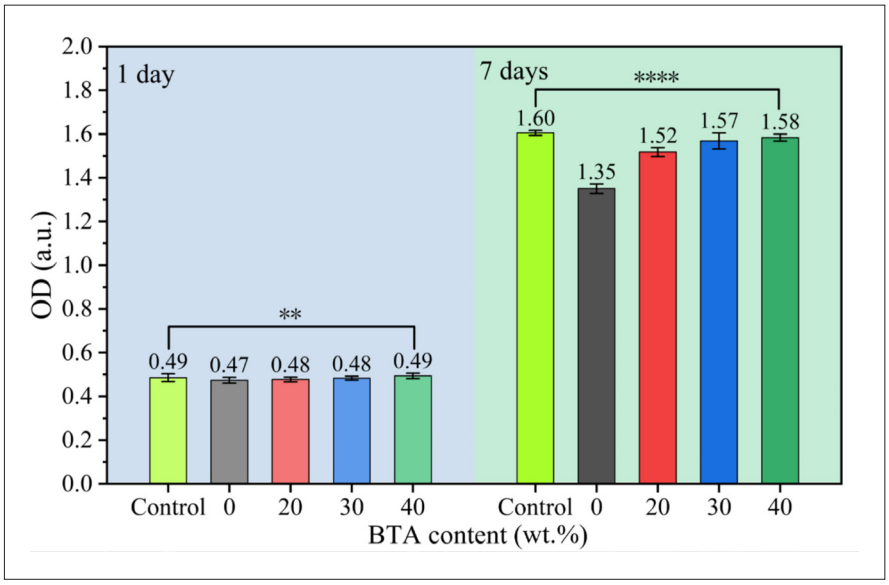

Figure 13. rBMSCs proliferation of composite bioceramics for 1 and 7 days with the control group and different SrCS-BTA components, determined via CCK-8 assay (****$p < 0.001$, **$p < 0.01$, one-way ANOVA).

increased from 0.32 to 0.59 s^{-1}, while the corresponding densification temperature decreased from 1270°C to 1175°C. This indicates that the SrCS scaffolds doped with BTA exhibit a better densification behavior at high temperatures. During high-temperature sintering, the new $CaTiO_3$ grains formed at the $CaSiO_3$ grains boundaries and acted as *in situ* nailing (known as the pinning effect) to intercept the crack propagation and hinder the movement of the grains. Consequently, the SrCS-40BTA scaffold revealed a 296% higher compressive strength and elastic modulus than that of the pure SrCS scaffold. Besides, the energy absorption of the SrCS-40BTA scaffold increased by 460%. Furthermore, this pinning effect plays a continuous role in the degradation process of composite scaffolds, resulting in long-lasting reliable mechanical properties. Overall, the strontium-doped calcium silicate scaffolds fabricated by VPP demonstrated significantly improved mechanical properties and tunable biodegradability, which will be extremely useful for repairing damaged large segmental bone defects.

Acknowledgments

The authors would like to thank the State Key Laboratory of Materials Processing and Die & Mould Technology for their assistance in SEM, XRD, and mechanical tests. The author would also like to thank the Huazhong University of Science & Technology Analytical & Testing Center for their assistance in ultraviolet light absorption and Fourier transforms infrared spectrometer characterization.

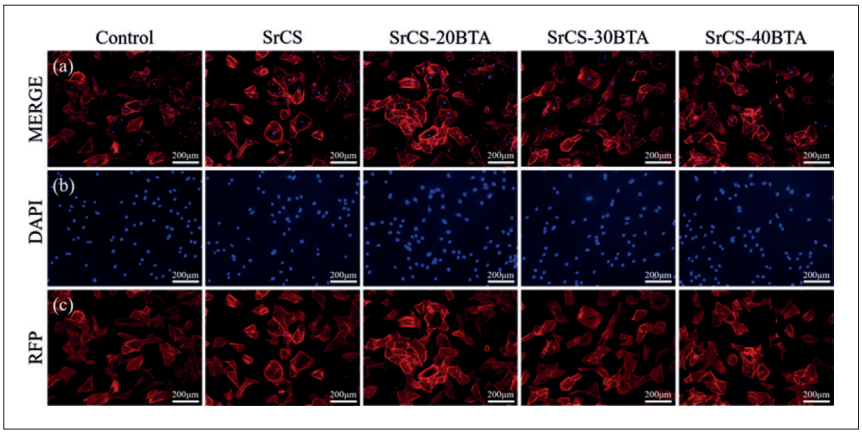

Figure 14. Images of early attachment of rBMSCs analyzed by confocal microscopy (after 24 h culturing with extracts). (a) Merged images of DAPI and phalloidin. (b) DAPI (blue). (c) Phalloidin (red).

Funding

This work was supported by grants from the National Natural Science Foundation of China (52205363), Fundamental Research Funds for the Central Universities (2019kfyRCPY044 and 2021GCRC002), Program for HUST Academic Frontier Youth Team (2018QYTD04), and Program for Innovative Research Team of the Ministry of Education (IRT1244).

Conflict of interest

The authors declare that they have no known competing financial interests or personal relationships that could have appeared to influence the work reported in this paper.

Author contributions

Conceptualization: Annan Chen, Jin Su
Data curation: Yinjin Li, Yifei Li, Xi Yuan
Formal analysis: Yinjin Li
Funding acquisition: Yusheng Shi, Chunzhe Yan, Annan Chen
Investigation: Yinjin Li
Methodology: Yinjin Li
Resources: Yusheng Shi, Chunze Yan
Validation: Yinjin Li
Visualization: Yinjin Li
Writing – original draft: Yinjin Li
Writing – review & editing: Jin Su, Annan Chen, Kezhuo Chen, Zhaoqing Li, Chunze Yan, Jian Lu, Yusheng Shi

Ethics approval and consent to participate

Ethics approval of using rat BMSCs has been obtained from the local ethics committee or IRB for conducting studies involving.

Consent for publication

Not applicable.

Availability of data

Raw data used in this work are available from corresponding author upon reasonable request.

References

1. Hao J, Bai B, Ci Z, *et al*., 2022, Large-sized bone defect repair by combining a decalcified bone matrix framework and bone regeneration units based on photo-crosslinkable osteogenic microgels. *Bioact Mater,* 14: 97–109.

   https://doi.org/10.1016/j.bioactmat.2021.12.013

2. Loi F, Cordova LA, Pajarinen J, *et al*., 2016, Inflammation, fracture and bone repair. *Bone*, 86: 119–30.

   https://doi.org/10.1016/j.bone.2016.02.020

3. Fernandez de Grado G, Keller L, Idoux-Gillet Y, *et al*., 2018, Bone substitutes: A review of their characteristics, clinical use, and perspectives for large bone defects management. *J Tissue Eng*, 9: 2041731418776819.

   https://doi.org/10.1177/2041731418776819

4. Wubneh A, Tsekoura EK, Ayranci C, *et al*., 2018, Current state of fabrication technologies and materials for bone tissue engineering. *Acta Biomater*, 80: 1–30.

   https://doi.org/10.1016/j.actbio.2018.09.031

5. Hutmacher DW, 2000, Scaffolds in tissue engineering bone and cartilage. *J Biomater,* 21(24): 2529–2543.

6. Bose S, Roy M, Bandyopadhyay A, 2012, Recent advances in bone tissue engineering scaffolds. *Trends Biotechnol*, 30(10): 546–554.

   https://doi.org/10.1016/j.tibtech.2012.07.005

7. Nommeots-Nomm A, Lee PD, Jones JR, 2018, Direct ink writing of highly bioactive glasses. *J Eur Ceram Soc,* 38(3): 837–844.

   https://doi.org/10.1016/j.jeurceramsoc.2017.08.006

8. Dong Y, Chen A, Yang T, *et al*., 2023, Ultra-lightweight ceramic scaffolds with simultaneous improvement of pore interconnectivity and mechanical strength. *J Mater Sci Technol,* 137: 247–258.

   https://doi.org/10.1016/j.jmst.2022.07.052

9. Chen P, Su J, Wang H, *et al*., 2022, Mechanical properties and microstructure characteristics of lattice-surfaced PEEK cage fabricated by high-temperature laser powder bed fusion. *J Mater Sci Technol,* 125: 105–117.

   https://doi.org/10.1016/j.jmst.2022.03.009

10. Ros-Tárraga P, Murciano A, Mazón P, *et al*., 2017, New 3D stratified Si-Ca-P porous scaffolds obtained by sol-gel and polymer replica method: Microstructural, mineralogical and chemical characterization. *Ceram Int,* 43(8): 6548–6553.

    https://doi.org/10.1016/j.ceramint.2017.02.081

11. Wu Q, Sun H, 2022, Preparation and properties of porous ceramics from nickel slag by aerogel gelcasting. *Ceram Int,* 48(22): 33058–33065.

    https://doi.org/10.1016/j.ceramint.2022.07.238

12. Zhou W, Zhang Z, Li N, *et al*., 2022, A new mullite foamed ceramic prepared by direct-foaming methods in parallel with a mechanical activation technique. *Ceram Int,* 48(14): 20721–20730.

    https://doi.org/10.1016/j.ceramint.2022.04.053

13. Liu F, He H, Cheng L, *et al*., 2023, Influence of layer thickness on microstructure and dielectric properties of Mg2TiO4 microwave ceramics fabricated by vat photopolymerization. *Addit Manuf,* 63.

    https://doi.org/10.1016/j.addma.2023.103413

14. Chen A, Su J, Li Y, *et al*., 2023, 3D/4D printed bio-piezoelectric smart scaffolds for next-generation bone tissue engineering. *Int J Extreme Manuf*, 5: 032007.

https://doi.org/10.1088/2631-7990/acd88f

15. Yan C, Ma G, Chen A, *et al*., 2021, Additive manufacturing of hydroxyapatite and its composite materials: A review. *J Micromech Mol Phys*, 05(03).

https://doi.org/10.1142/s2424913020300029

16. Wang H, Chen P, Wu H, *et al*., 2022, Comparative evaluation of printability and compression properties of poly-ether-ether-ketone triply periodic minimal surface scaffolds fabricated by laser powder bed fusion. *Addit Manuf*, 57.

https://doi.org/10.1016/j.addma.2022.102961

17. Su R, Chen J, Zhang X, *et al*., 2023, 3D-printed micro/nano-scaled mechanical metamaterials: Fundamentals, technologies, progress, applications, and challenges. *Small*, 19(29): e2206391.

https://doi.org/10.1002/smll.202206391

18. Feng P, Zhao R, Tang W, *et al*., 2023, Structural and functional adaptive artificial bone: Materials, fabrications, and properties. *Adv Funct Mater,* 33(23).

https://doi.org/10.1002/adfm.202214726

19. Distefano F, Pasta S, Epasto G, 2023, Titanium lattice structures produced via additive manufacturing for a bone scaffold: A review. *J Funct Biomater*, 14(3): 125.

https://doi.org/10.3390/jfb14030125

20. Shuai C, Yang W, Feng P, *et al*., 2021, Accelerated degradation of HAP/PLLA bone scaffold by PGA blending facilitates bioactivity and osteoconductivity. *Bioact Mater*, 6(2): 490–502.

https://doi.org/10.1016/j.bioactmat.2020.09.001

21. Zhou Q, Su X, Wu J, *et al*., 2023, Additive manufacturing of bioceramic implants for restoration bone engineering: Technologies, advances, and future perspectives. *ACS Biomater Sci Eng*, 9(3): 1164–1189.

https://doi.org/10.1021/acsbiomaterials.2c01164

22. Su J, Hua S, Chen A, *et al*., 2022, Three-dimensional printing of gyroid-structured composite bioceramic scaffolds with tuneable degradability. *Biomater Adv*, 133: 112595.

https://doi.org/10.1016/j.msec.2021.112595

23. Wang Y, Chen S, Liang H, *et al*., 2022, Digital light processing (DLP) of nano biphasic calcium phosphate bioceramic for making bone tissue engineering scaffolds. *Ceram Int,* 48(19): 27681–27692.

https://doi.org/10.1016/j.ceramint.2022.06.067

24. Zhang B, Xing F, Chen L, *et al*., 2023, DLP fabrication of customized porous bioceramics with osteoinduction ability for remote isolation bone regeneration. *Biomater Adv*, 145: 213261.

https://doi.org/10.1016/j.bioadv.2022.213261

25. Almubarak S, Nethercott H, Freeberg M, *et al*., 2016, Tissue engineering strategies for promoting vascularized bone regeneration. *Bone*, 83: 197–209.

https://doi.org/10.1016/j.bone.2015.11.011

26. Dashnyam K, El-Fiqi A, Buitrago JO, *et al*., 2017, A mini review focused on the proangiogenic role of silicate ions released from silicon-containing biomaterials. *J Tissue Eng*, 8: 2041731417707339.

https://doi.org/10.1177/2041731417707339

27. Mao L, Xia L, Chang J, *et al*., The synergistic effects of Sr and Si bioactive ions on osteogenesis, osteoclastogenesis and angiogenesis for osteoporotic bone regeneration. *Acta Biomater*, 61: 217–232.

https://doi.org/10.1016/j.actbio.2017.08.015

28. Shie MY, Chiang WH, Chen IP, *et al*., 2017, Synergistic acceleration in the osteogenic and angiogenic differentiation of human mesenchymal stem cells by calcium silicate-graphene composites. *Mater Sci Eng C Mater Biol Appl*, 73: 726–735.

https://doi.org/10.1016/j.msec.2016.12.071

29. Lin K, Xia L, Li H, *et al*., 2013, Enhanced osteoporotic bone regeneration by strontium-substituted calcium silicate bioactive ceramics. *Biomaterials*, 34(38): 10028–10042.

https://doi.org/10.1016/j.biomaterials.2013.09.056

30. Xing M, Wang X, Wang E, *et al*., 2018, Bone tissue engineering strategy based on the synergistic effects of silicon and strontium ions. *Acta Biomater*, 72: 381–395.

https://doi.org/10.1016/j.actbio.2018.03.051

31. Genchi GG, Marino A, Rocca A, *et al*., 2016, Barium titanate nanoparticles: promising multitasking vectors in nanomedicine. *Nanotechnology*, 27(23): 232001.

https://doi.org/10.1088/0957-4484/27/23/232001

32. Dubey AK, Ea A, Balani K, *et al*., 2013, Multifunctional properties of multistage spark plasma sintered HA-BaTiO3-based piezobiocomposites for bone replacement applications. *J Am Ceram Soc,* 96(12): 3753–3759.

https://doi.org/10.1111/jace.12566

33. Tavangar M, Heidari F, Hayati R, *et al*., 2020, Manufacturing and characterization of mechanical, biological and dielectric properties of hydroxyapatite-barium titanate nanocomposite scaffolds. *Ceram Int,* 46(7): 9086–9095.

https://doi.org/10.1016/j.ceramint.2019.12.157

34. Yang L, Mertens R, Ferrucci M, *et al*., 2019, Continuous graded Gyroid cellular structures fabricated by selective laser melting: Design, manufacturing and mechanical properties. *Mat Des,* 162: 394–404.

https://doi.org/10.1016/j.matdes.2018.12.007

35. Zakeri S, Vippola M, Levänen E, 2020, A comprehensive review of the photopolymerization of ceramic resins used in stereolithography. *Addit Manuf,* 35.

https://doi.org/10.1016/j.addma.2020.101177

36. Chen A, Gao F, Li M, *et al*., 2019, Mullite ceramic foams with controlled pore structures and low thermal conductivity prepared by SLS using core-shell structured polyamide12/FAHSs composites. *Ceram Int,* 45(12): 15538–15546.

https://doi.org/10.1016/j.ceramint.2019.05.059

37. Murphy CM, Haugh MG, O'Brien FJ, 2010, The effect of mean pore size on cell attachment, proliferation and migration in collagen-glycosaminoglycan scaffolds for bone tissue engineering. *Biomaterials*, 31(3): 461–466.

https://doi.org/10.1016/j.biomaterials.2009.09.063

38. Wang H, Xu Y, Wang P, *et al*., 2021, Cell-mediated injectable blend hydrogel-BCP ceramic scaffold for in situ condylar osteochondral repair. *Acta Biomater*, 123: 364–378.

https://doi.org/10.1016/j.actbio.2020.12.056

39. Halloran JW, 2016, Ceramic stereolithography: Additive manufacturing for ceramics by photopolymerization. *Annu Rev Mater Res*, 46(1): 19–40.

https://doi.org/10.1146/annurev-matsci-070115-031841

40. Qi G, Zeng Y, Chen J, 2022, Preparation of porous SnO2-based ceramics with lattice structure by DLP. *Ceram Int,* 48(10): 14568–14577.

https://doi.org/10.1016/j.ceramint.2022.01.350

41. Xing H, Zou B, Liu X, *et al*., 2020, Effect of particle size distribution on the preparation of ZTA ceramic paste applying for stereolithography 3D printing. *Powder Technol,* 359: 314–322.

https://doi.org/10.1016/j.powtec.2019.09.066

42. Chen S, Wang C, Zheng W, *et al*., 2022, Effects of particle size distribution and sintering temperature on properties of alumina mold material prepared by stereolithography. *Ceram Int,* 48(5): 6069–6077.

https://doi.org/10.1016/j.ceramint.2021.11.145

43. Zheng J, Zhang H, Li X, 2021, Effect of ternary particles size distribution on rheology of slurry and microstructure of DLP printed ZTA ceramic. *Mater Chem Phys,* 269.

https://doi.org/10.1016/j.matchemphys.2021.124656

44. Esposito Corcione C, Montagna F, Greco A, *et al*., 2006, Free form fabrication of silica moulds for aluminium casting by stereolithography. *Rapid Prototyp J,* 12(4): 184–188.

https://doi.org/10.1108/13552540610682688

45. Huang X, Dai H, Hu Y, *et al*., 2021, Development of a high solid loading β-TCP suspension with a low refractive index contrast for DLP-based ceramic stereolithography. *J Eur Ceram Soc,* 41(6): 3743–3754.

https://doi.org/10.1016/j.jeurceramsoc.2020.12.047

46. Xu X, Zhou S, Wu J, *et al*., 2021, Relationship between the adhesion properties of UV-curable alumina suspensions and the functionalities and structures of UV-curable acrylate monomers for DLP-based ceramic stereolithography. *Ceram Int,* 47(23): 32699–32709.

https://doi.org/10.1016/j.ceramint.2021.08.166

47. Zhang X, Xu Y, Li L, *et al*., 2019, Acrylate-based photosensitive resin for stereolithographic three-dimensional printing. *J Appl Polym Sci,* 136(21).

https://doi.org/10.1002/app.47487

48. Du Z, Leng H, Guo L, *et al*., 2020, Calcium silicate scaffolds promoting bone regeneration via the doping of Mg2+ or Mn2+ ion. *Compos B: Eng,* 190.

https://doi.org/10.1016/j.compositesb.2020.107937

49. Chen A, Wu J, Cheng L, *et al*., 2020, Enhanced densification and dielectric properties of CaTiO3-0.3NdAlO3 ceramics fabricated by direct coagulation casting. *J Eur Ceram Soc,* 40(4): 1174–1180.

https://doi.org/10.1016/j.jeurceramsoc.2019.12.033

50. Liu Y, Chen A, Wu J, *et al*., 2018, Effect of K2SO4 additions on properties of porous fibrous alumina ceramics prepared by DCC and lost-mold method. *J Am Ceram Soc,* 101(6): 2216–2227.

https://doi.org/10.1111/jace.15384

51. Chen A, Li M, Wu J, *et al*., 2019, Enhancement mechanism of mechanical performance of highly porous mullite ceramics with bimodal pore structures prepared by selective laser sintering. *J Alloys Compd,* 776: 486–494.

https://doi.org/10.1016/j.jallcom.2018.10.337

52. Chen A, Chen J, Wu J, *et al*., 2019, Porous mullite ceramics with enhanced mechanical properties prepared by SLS using MnO2 and phenolic resin coated double-shell powders. *Ceram Int,* 45(17): 21136–21143.

https://doi.org/10.1016/j.ceramint.2019.07.090

53. Ma S, Tang Q, Zhu C, *et al*., 2022, Laser powder bed fusion-built Ti6Al4V bone scaffolds composed of sheet and strut-based porous structures: Morphology, mechanical properties, and biocompatibility. *Chin J Mech Eng: Addit Manuf Front*, 1(4).

https://doi.org/10.1016/j.cjmeam.2022.100051

54. Chen A, Lu L, Cheng L, *et al*., 2019, TEM analysis and mechanical strengthening mechanism of MnO2 sintering aid in selective laser sintered porous mullites. *J Alloys Compd*, 809.

https://doi.org/10.1016/j.jallcom.2019.151809

55. Wang L, Zhang J, Zhang W, *et al*., 2017, Analysis of the osteogenic effects of biomaterials using numerical simulation. *Biomed Res Int*, 2017: 6981586.

https://doi.org/10.1155/2017/6981586

ACCSCIENCE PUBLISHING

International Journal of Bioprinting

RESEARCH ARTICLE

3D printing of PCL-ceramic composite scaffolds for bone tissue engineering applications

Santosh Kumar Parupelli[1,3], Sheikh Saudi[2], Narayan Bhattarai[2,3], and Salil Desai[1,3]*

[1]Department of Industrial and Systems Engineering, North Carolina A&T State University, Greensboro, NC 27411, USA

[2]Department of Chemical, Biological and Bioengineering, North Carolina A&T State University, Greensboro, NC 27411, USA

[3]Center of Excellence in Product Design and Advanced Manufacturing, North Carolina A&T State University, Greensboro, NC 27411, USA

(This article belongs to the *Special Issue: Additive Manufacturing of Functional Biomaterials*)

Abstract

Three-dimensional (3D) printing was utilized for the fabrication of a composite scaffold of poly(ε-caprolactone) (PCL) and calcium magnesium phosphate (CMP) bioceramics for bone tissue engineering application. Four groups of scaffolds, that is, PMC-0, PMC-5, PMC-10, and PMC-15, were fabricated using a custom 3D printer. Rheology analysis, surface morphology, and wettability of the scaffolds were characterized. The PMC-0 scaffolds displayed a smoother surface texture and an increase in the ceramic content of the composite scaffolds exhibited a rougher structure. The hydrophilicity of the composite scaffold was significantly enhanced compared to the control PMC-0. The effect of ceramic content on the bioactivity of fibroblast NIH/3T3 cells in the composite scaffold was investigated. Cell viability and toxicity studies were evaluated by comparing results from lactate dehydrogenase (LDH) and Alamar Blue (AB) colorimetric assays, respectively. The live-dead cell assay illustrated the biocompatibility of the tested samples with more than 100% of live cells on day 3 compared to the control one. The LDH release indicated that the composite scaffolds improved cell attachment and proliferation. In this research, the fabrication of a customized composite 3D scaffold not only mimics the rough textured architecture, porosity, and chemical composition of natural bone tissue matrices but also serves as a source for soluble ions of calcium and magnesium that are favorable for bone cells to grow. These 3D-printed scaffolds thus provide a desirable microenvironment to facilitate biomineralization and could be a new effective approach for preparing constructs suitable for bone tissue engineering.

Keywords: 3D printing; Bio-ceramics; Composites; Bone; Scaffold; Tissue engineering

***Corresponding author:**
Salil Desai
(sdesai@ncat.edu)

Citation: Parupelli SK, Saudi S, Bhattarai N, *et al.* 2023, 3D printing of PCL-ceramic composite scaffolds for bone tissue engineering applications. *Int J Bioprint,* 9(6): 0196. https://doi.org/10.36922/ijb.0196

Received: September 11, 2022

Accepted: November 18, 2022

Published Online: July 5, 2023

Copyright: © 2023 Author(s). This is an Open Access article distributed under the terms of the Creative Commons Attribution License, permitting distribution, and reproduction in any medium, provided the original work is properly cited.

Publisher's Note: AccScience Publishing remains neutral with regard to jurisdictional claims in published maps and institutional affiliations.

1. Introduction

Tissue engineering (TE) is an interdisciplinary field that emerged as a promising technique that utilizes cells, biomaterials, biochemical (e.g., growth factors), and physical (e.g., mechanical loading) signals to generate new tissue structures. The goal of TE is to improve, replace, or restore damaged tissues or organs from any causes, such as disease,

defect, trauma, or aging. TE aims to create functional organs from patients' cells. The process of TE starts with biomaterials, followed by the fabrication of scaffolds, combining them with cells and biochemical signals, such as growth factors, cytokines, mechanical stimulants, to generate new tissue structures[1,2]. Microfabrication techniques used in TE include photolithography, rapid prototyping (stereolithography, extrusion deposition printing), and soft lithography (microcontact printing, micro-molding, and microfluidics)[2]. "A biomaterial is a substance that has been engineered to take a form which, alone or as part of a complex system, is used to direct, by control of interactions with components of living systems, the course of any therapeutic or diagnostic procedure, in human or veterinary medicine"[3-6]. Biomaterials are derived from several sources such as natural materials, synthetic polymers, metals, ceramics, and composites[7,8]. Naturally derived biomaterials include protein-based biomaterials (silk fibroin, keratin, collagen, gelatin, fibrin, and eggshell membrane) and polysaccharide-based biomaterials (chondroitin, glucose, cellulose, alginate, hyaluronan, and chitin and its derivative chitosan), and decellularized tissue biomaterials. Synthetic polymers for tissue regeneration include polylactic acid (PLA), polyglycolic acid (PGA), poly (lactic-co-glycolic acid) (PLGA), and polyurethanes. Metals include titanium alloys, nitinol, magnesium alloys, stainless steel, and cobalt-chromium alloys. Composites include metal-ceramic, metal-polymer, and polymer-ceramic[9-11]. Each of the above-mentioned individual biomaterial groups has specific advantages and disadvantages. Biomaterials have played a crucial role in supporting and fostering regenerative cell growth in the tissue engineering design paradigm and biomedical devices for numerous clinical regenerative therapies[12-18].

Scaffolds are temporary structures that mimic physical microstructures of a natural extracellular matrix (ECM) to provide desired cellular interactions and guide cells to grow, synthesize, and other biological molecules to form new functional tissues[2]. To engineer functional tissues and organs successfully, scaffolds should possess the minimum requirements, such as high porosity, proper degradation rate, biocompatible, high surface area, mechanical integrity, enhanced cell adhesion, growth, differentiated function, and migration[19]. Cell proliferation, attachment, and differentiation are affected strongly by the scaffold microenvironment, including the size, density of the pores, geometry, surface properties, and windows connecting the pores[20]. Techniques include porogen leaching, phase separation, uniaxial freezing, micro-molding, gas foaming, fiber meshes/fiber bonding, electrospinning, and additive manufacturing (laser-based, nozzle-based, and printer-based) are used for the fabrication of scaffolds[21-23].

The fundamental concepts that lead to the establishment of bone tissue-engineered scaffolds are typically based on the selected biomaterial and production technique. Generally, for bone TE, pore sizes between 100 and 350 micrometers and porosities more than 90% are preferred. PCL is a biodegradable polymer like other degradable hydroxy polyesters such as PGA, poly-l-lactic acid (PLLA), and their copolymers. PCL is one of the widely studied synthetic polymers in different formulations for TE due to its elastomeric mechanical properties and biological properties. PCL is a rigid, flexible polymer with a semi-crystalline structure having high thermal stability, low glass transition (−60°C), and melting temperatures (56–65°C). The slower degradation rate and mechanical properties limit the use of PCL compared to other polyester family members. However, the degradation kinetics and mechanical strength of the PCL can be tailored by copolymerization or blending with other polyesters or ceramic materials. PCL can be used for scaffold fabrication for bone, liver, cartilage, skin, and protein delivery vehicles[24-28].

Numerous studies have been done on the blending of PCL with several bioceramics (e.g., calcium phosphate, magnesium phosphate, biphasic calcium phosphate, hydroxyapatite, and bioactive glass), natural polymers (chitosan, elastin, collagen, gelatin, and silk), and synthetic polymers (PLGA, PGA, PLLA, and carbon nanotubes) to enhance the mechanical endurance and biocompatibility of the scaffolds[29]. Magnesium phosphate/PCL (MP/PCL) composite scaffold enhances the polymer's degradation rate by improving the PCL hydrophilicity[30,31]. Moreover, the surface wettability of the MP/PCL can be tailored by adjusting the amount of MP particles incorporated[32]. Blending nano-hydroxyapatite (nHA) with PCL improves composite polymer scaffold strength (mechanical property) and bioactivity[33]. Biocomposite scaffolds made from polycaprolactone (PCL) and forsterite bioceramics can enhance and modulate mechanical and physical properties[34,35]. Incorporating aluminum oxide whiskers within PCL significantly improves the composite scaffold's mechanical and hydrophilic surface properties with good biocompatibility for TE and dental applications[36]. Composite scaffolds prepared with calcium alginate threads and PCL demonstrate ideal porosity grade with suitable microstructure for enhanced bone cell growth and differentiation[25]. The presence of β-tricalcium phosphate (TCP) in PCL improves the cell proliferation and compressive mechanical properties of the composite scaffold for bone regeneration[31,37-41].

Magnesium phosphate and calcium phosphate-based bioceramics are well-known in the biomaterials field and have been used separately with PCL scaffolds. However,

the calcium magnesium phosphate (CMP) bio-ceramics, a combined phosphate of magnesium and calcium, have not been thoroughly studied. Therefore, our strategy in this study is to first develop an optimal composition of CMP bioceramic powder. Our second strategy is to develop a slurry of ceramic powder and PCL in a good organic solvent that is suitable for three-dimensional (3D) printing. Third, we optimize the properties of the 3D-printed scaffolds so that the methodology and knowledge gained from this research will be applied for bone TE applications in the future.

Additive manufacturing (AM) techniques enable the fabrication of complex geometry scaffolds for TE applications[42-44]. 3D bioprinting enables the fabrication of tissue or organs using biomaterials and cells in a layer-by-layer fashion from the bottom up using computer-aided design (CAD) model data[45]. The three main fundamental approaches 3D bioprinting is based on are as follows: (i) biomimicry, (ii) autonomous self-assembly, and (c) mini tissue building blocks. Different types of AM techniques that can be used for bioprinting include extrusion-based printing, inkjet-assisted printing, and droplet-based printing[46,47]. The extrusion 3D printing process is the most popular technique. With 3D bioprinting, complex tissue structures that mimic the fine shape and size of the targeted natural original tissue can be fabricated with personalized features. The applicability of 3D bioprinting to biomedical devices, pharmaceutics, and regenerative medicine has increased as a result of recent breakthroughs in reinforcement strategies, hydrogel chemistries, and crosslinking techniques[48]. Biocompatibility of the material being used, growth factor distribution, perfusion, and cell sensitivity to the printing procedures are some of the crucial aspects of bioprinting, that must be taken into consideration because 3D bioprinting works with living organisms such as cells and tissues[49]. In the past decade, numerous research studies have been reported on optimizing AM techniques for 3D scaffold fabrication with desired mechanical and biological properties for cell growth in regenerative medicine[50-55]. In this research, we utilized the direct-write AM technique to fabricate a composite scaffold with CMP bio-ceramic and PCL materials for bone TE application. In our experiments, four groups of scaffolds – PMC-0: PCL (50% w/v), PMC-5: PCL (50% w/v)/CMP(5%w/w), PMC-10: PCL (50% w/v)/CMP (10%w/w), and PMC-15: PCL (50% w/v)/CMP (15%w/w) – were fabricated using a custom-built 3D printer. The effect of ceramic content on the surface properties, biodegradability, and bioactivity of fibroblast cells on the composite scaffold was investigated. A customized functionally gradient scaffold structure was fabricated to demonstrate that manipulation of surface and biological properties can be achieved for the enhanced spatial organization of cells within the composite scaffold.

2. Materials and methods

Poly(ε-caprolactone) pellets (PCL, Mw = 43,000 g/mol) with a melting point of 58 – 64°C were purchased from Polysciences Inc. (Warrington, PA, USA). 2,2,2-Trifluoroethanol (TFE) was purchased from Sigma-Aldrich (St. Louis, Mo, USA). Magnesium oxide (MgO) nanopowder (size < 50 nm) and calcium phosphate monobasic were purchased from Sigma Aldrich (St. Louis, MO, USA). Dulbecco's modified Eagle's medium (DMEM) was purchased from Life Technologies (Grand Island, NY, USA). The Alamar Blue and lactate dehydrogenase (LDH) assay kits were purchased from Thermo-scientific (Waltham, MA or Florence, KY).

2.1. Synthesis of CMP bioceramics

CMP ceramic was prepared using a mixture of MgO and calcium phosphate monobasic according to a previously published paper[56]. MgO was first dissolved in water, and calcium phosphate was added with a 2:1 molar ratio (3.2:1 w/w). The mixture was vortexed for 5 min and then poured into a Petri dish. The Petri dish was kept in a fume hood for 24 h to dry up all water from the mixer. Fine powder of the CMP was stored in a desiccator. Four concentrations of the polymer and ceramic material in different proportions were formulated for the subsequent experiments.

2.2. Production of PCL/CMP suspension

Initially, 50% (w/v) PCL was prepared by suspending 5 g of PCL pellets in 10 mL of TFE and ultra-sonicated at 45°C for 2 h to produce PCL-only scaffolds. To produce PCL-CMP composite scaffolds, the predetermined content of the CMP (5, 10, and 15 wt % in relation to the PCL polymer) was dispensed into 10 mL of TFE through ultra-sonication at 45°C for 2 h. The experimental procedure to produce PCL-CMP suspension is illustrated in Figure 1.

Pellets of PCL (5 g) were added to the TFE solvent containing the CMP and then mixed using magnetic stirring for 24 h. Similarly, PCL-CMP composites with a CMP content of 10% and 15% were also prepared. Each composition of the suspension is shown in Table 1. A 100-mm filter was used to filter all the CMP solutions to avoid clogging during printing.

2.3. 3D printing of scaffolds

A four-axis Nordson EFD Janome robot with a custom extrusion head, as shown in Figure 2, was used to fabricate 3D scaffold structures. All material concentrations were loaded into a 10 mL syringe barrel with a nozzle of 250 μm

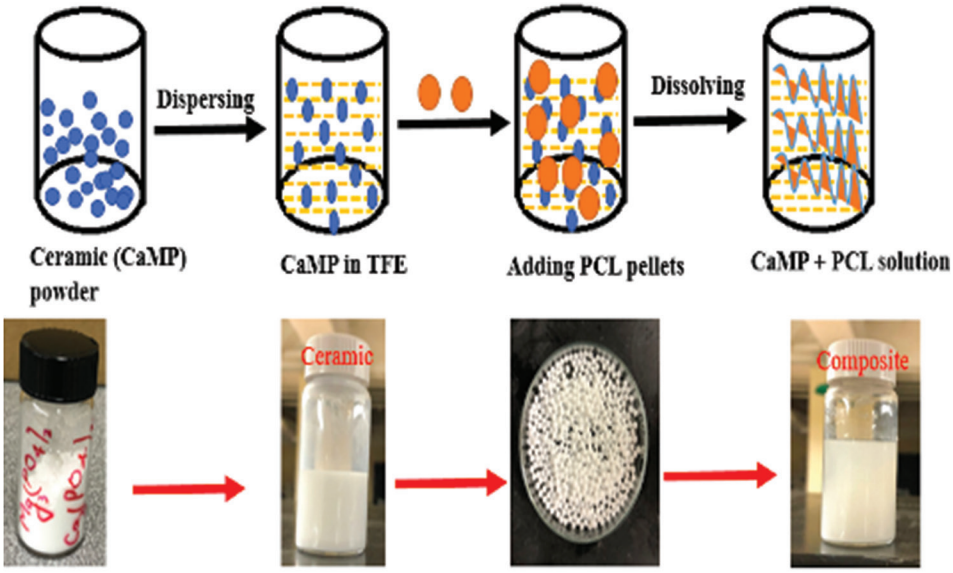

Figure 1. Experimental procedure to produce PCL-CMP suspension.

Table 1. Suspension sample compositions

Composite scaffolds	CMP (g)	TFE (ml)	PCL (g)	CMP (w/w%) in the scaffold
PMC-0	0	10	5	0
PMC-5	0.25	10	5	5
PMC-10	0.5	10	5	10
PMC-15	1.0	10	5	15

diameter. The syringe barrel consisting of the PCL/CMP suspension was attached with a piston and connected to a pressure system (Ultimus V) to alter the flow rate. A cuboidal 3D scaffold structure (10 × 10 × 0.2 mm) was generated in CAD, and exported as a stereolithography (STL) file, and the x, y, and z coordinates of the STL file were imported into the robot with JRC 3D printing software. The PMCs struts were built layer-by-layer (12 layers: 0.2 mm) to build a 3D scaffold structure with uniform pore size and porosity. The struts were 0.2 mm in height, 10 mm in length, and 10 mm in width. All the process parameters, including line speed, extrusion pressure, nozzle diameter, spacing between the struts, and layer thickness, were kept consistent for all material concentrations.

2.4. Characterization of scaffolds

2.4.1. Rheology analysis

The rheological properties of all the material concentrations (PMCs) were measured using Rehocal DVIII T Rheometer. The shear stress of each material was measured at different shear rates (0 – 120/s) using an SC4 spindle at room temperature. The shear rate versus shear stress curves for each material concentration was plotted using the Rheocalc T software.

2.4.2. Contact angle measurements

The surface wettability (hydrophilicity/hydrophobicity) of the PMC-0 and ceramic composite PMCs was tested using a Drop Shape analyzer (KRUSS-DSA25E) with the sessile drop method at room temperature. For all material concentrations, thin film samples were made and placed in Petri dishes. Five samples for each material concentration at 90 s were tested to calculate the average water contact angle. The sessile drop size was set to 5 µL.

2.4.3. Surface morphology analysis

The surface morphology of the ceramic powder was analyzed using a scanning electron microscope (SEM; Zeiss Auriga FIB/FESEM, Carl Zeiss Microscopy, LLC, NY, USA). Briefly, ceramic powder (0.1 g of as-prepared) was dispersed in 10 mL of TFE. A single drop of the ceramic suspension was deposited on an aluminum foil and attached to double-sided carbon tape. SEM (Zeiss Auriga FIB FE-SEM) images of printed samples and the CMP powder were taken at an accelerating voltage of 5 kV. Before SEM analysis, a thin layer of gold sputtering (10 nm) was applied to the samples. The effect of ceramic particles on the PCL matrix was investigated.

ImageJ open-source software[57] was used to calculate the porosity of the scaffold. Color thresholds were varied to capture the boundaries of the pores using an edge detection algorithm. All pore dimensions were recorded with their sizes and respective pore areas. Image correction was

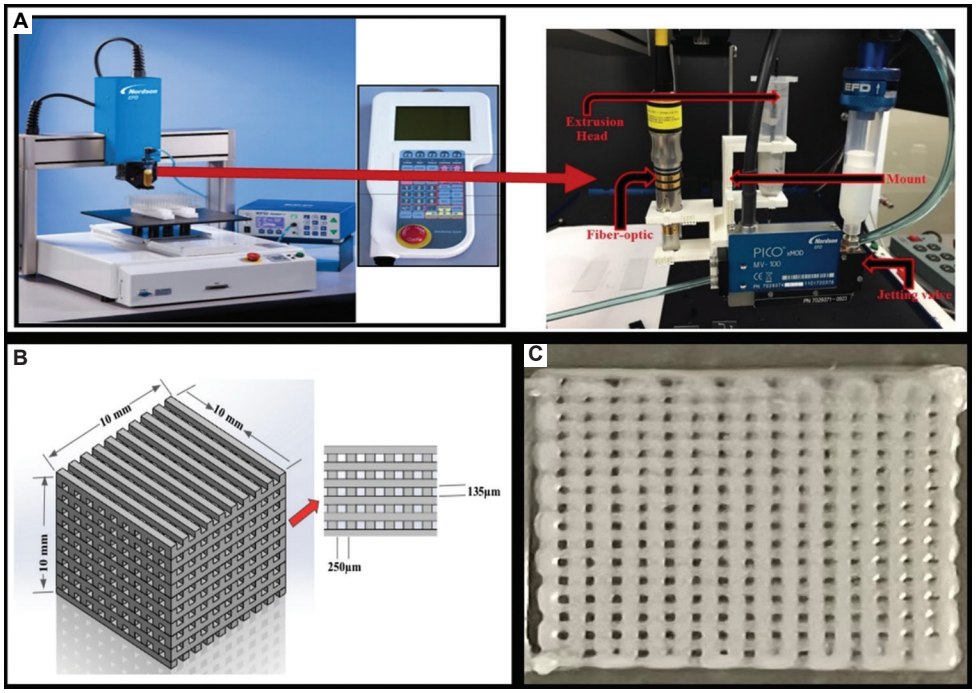

Figure 2. (A) Direct-write 3D printing custom equipment for scaffold fabrication. (B) 3D computer-aided design model of the ceramic composite scaffold. (C) 3D-printed composite ceramic scaffold.

performed to eliminate extraneous pores and provide the porosity of the scaffold. Porosity analysis was performed on a sample of three (n = 3).

2.4.4. X-ray diffraction (XRD)

The crystallography and phases of CMP were examined using a Bruker AXS D8 Discover X-ray diffractometer with Cu-K radiation. The XRD studies were carried out with a locked-coupled scan with a scanning range (diffraction angle, 2θ) of 15°–60°. The instrument was run in continuous mode, with increments of 0.0146° for 2 min. An experiment was carried out at room temperature.

2.4.5. FT-IR analysis

Fourier-transform infrared spectroscopy (FT-IR) was used to identify the functional groups and chemical interactions between PCL and CMP. Varian 670 FT-IR Spectrophotometer (Varian, Inc., Palo Alto, CA, USA) was used to detect the spectra in the range of 4000 – 400 cm^{-1} with 64 scans at a resolution of 4 cm^{-1}. A total of 5 scans were performed for each spectrum.

2.4.6. Biocompatibility study

The procedure to conduct biocompatibility was implemented based on our previous work[29]. The 3D scaffold samples (n = 3) were cut (1 cm × 1 cm), glued with Surgical Silicone Adhesive, Kwik-SilTM, and attached to 24-well plates. Samples were sterilized with 95% ethanol in a sterile fume hood for 30 min, followed by rinsing with sterile deionized water (twice) and 1× Dulbecco's phosphate-buffered saline (DPBS). Before cell seeding, 1 mL of DMEM supplemented with 10% fetal bovine serum (FBS) and 1% antibiotics (10,000 units/mL of penicillin and 10,000 μg/mL of streptomycin) was added to each well plate, which was placed in cell culture incubator for 3 h. NIH/3T3 cells, a mouse fibroblast cell line (American Tissue Type Culture Collection, Manassas, VA), were cultured in a 75 cm^2 culture flask and kept in a tissue culture incubator at 37°C and a 5% CO_2 atmosphere. Every 2 days, the culture medium was changed. The cells were separated by 0.025% trypsin and 0.01% EDTA in a phosphate-buffered saline (PBS) solution once they had reached around 90% confluence, followed by transferring them to a centrifuge tube with the culture medium. Before being seeded into samples, cells were resuspended in new growth media and counted with a hemocytometer using a Countess™ II Automated Cell Counter (Thermo Fisher Scientific). A 50 μL aliquot of medium containing cells (~50,000) was placed on printed samples (n = 3) and cultured in an incubator (37°C, 5% CO_2) for 1, 2, and 3 days, respectively.

Alamar blue (AB) colorimetric assay was used to measure the viability of 3T3 cells after growth on substances. Cell culture medium was collected from each incubated sample and stored for toxicity study at a specific

time. After that, cells were washed 2 times with PBS and treated with 10% (v/v) AB reagent in the appropriate culture medium for 4 h. Multiple aliquots of the assay solutions were obtained and measured for fluorescence using a spectrophotometer with excitation at 530 nm and emission at 590 nm. The following equation was used to calculate the viability of cells:

$$\text{Cell viability} = \frac{\text{Fluorescence of the samples} - \text{Fluorescence of the blank}}{\text{Fluorescence of the control} - \text{Fluorescence of the blank}} \times 100\%$$

LDH assay was carried out with the stored medium collected earlier.

2.4.7. Statistical analysis

Statistical analysis was performed using Minitab statistical software. Data are expressed as mean ± standard deviation. Comparisons of groups were performed using one-way analysis of variance (ANOVA) and Tukey's *post hoc* test. Significance levels were set at $P < 0.05$.

3. Results and discussion

3.1. Rheology measurements

The rheological properties of the materials were studied to investigate the effect of CMP on the PCL matrix. The rheological measurements of the PCL and composite in terms of shear rate and shear stress are shown in Figure 3. All tests were performed in flow sweep mode across a range of shear rates from 0.1 to 120 s^{-1}. PMC-0, PMC-5, PMC-10, and PMC-15 exhibit a Newtonian region followed by non-Newtonian fluid behavior at higher shear rates. The non-Newtonian behavior represents a shear-thinning fluid as the shear rate increases beyond 80 s. The shear stress increased with an increase in the content of CMP, in the following order PMC-0 < PMC-5 < PMC-10 < PMC-15. With the addition of the CMP particles, the viscosity of the PMCs materials increased because of the interaction between the polymeric matrix (PCL) and the ceramic particles (CMP). The increase in the shear stress is due to the increase in the microparticle content of ceramic material in the polymer matrix, which leads to a higher resistance to the flow of fluid[58,59]. Higher shear stress for increased PCL-CMP blends indicates an elasticity higher than that of pure PCL. The rheological behavior observed herein is vital as the bioprinter needs to be operated by varying parameters, such as deposition line speed, extrusion pressure, and nozzle size, to accommodate the shear-thinning behavior of the biomaterial being bioprinted. Moreover, higher extrusion pressures are needed to deposit higher PCL-CMP blends to maintain consistent scaffold geometries.

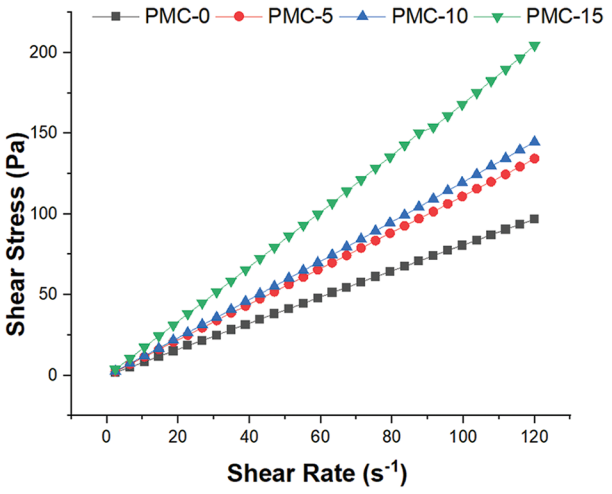

Figure 3. Rheology characteristics of PMCs suspensions. An increase in the microparticle content of ceramic material in the PCL matrix exhibit a non-Newtonian fluid behavior at higher shear rates.

3.2. Characterization of ceramic powder

The as-prepared CMP ceramic was used for incorporation into the 3D-printed PCL scaffolds. SEM image (Figure 4) shows that the ceramic was a mixture of clay-like $Ca_3(PO_4)_2$ and spindle-shaped $Mg_3(PO_4)_2$ particles[60]. About 2- – 5-micron (length) $Mg_3(PO_4)_2$ crystals were seen embedded into $Ca_3(PO_4)_2$ substances. The XRD pattern for CMP is shown in Figure 5 (left). XRD data for the particles, with peaks, are consistent with the known crystallographic planes of both phosphates. $Mg_3(PO_4)_2$ peaks are assigned by cross marks (x), and $Ca_3(PO_4)_2$ peaks are assigned by an asterisk (*) marks[60]. Figure 5 (right) shows the FT-IR spectra of the ceramic powder. Absorption bands at 1060 cm^{-1} and 970 cm^{-1} were ascribed to PO_4^{3-}, and

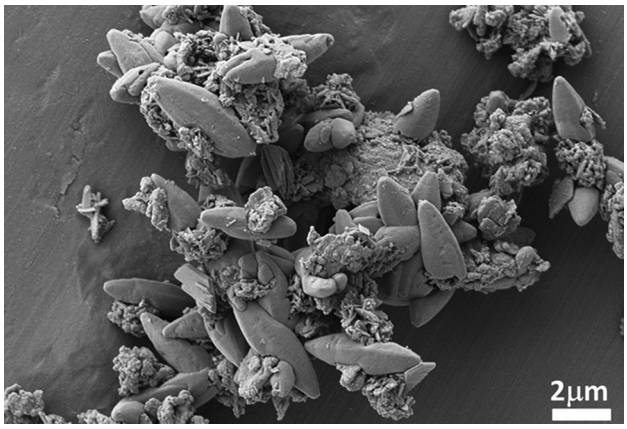

Figure 4. SEM image of as-prepared ceramic powder. Clay-like substances are $Ca_3(PO_4)_2$ and spindle-shaped substances are $Mg_3(PO_4)_2$.

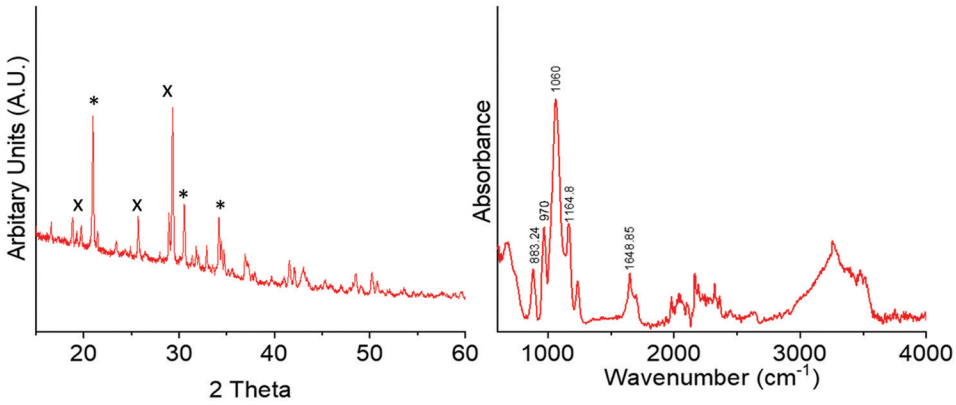

Figure 5. XRD pattern (left) and FT-IR spectra (right) of as-prepared CMP ceramic powder.

the band at 883.24 cm^{-1} and 1164.8 cm^{-1} correspond to the vibration of P–O–H from $Mg_3(PO_4)_2$ and $Ca_3(PO_4)_2$. Adsorbed water band is relatively wide, from 2600 cm^{-1} to 3600 cm^{-1} [9]. The additional band at 1648.85 cm^{-1} was observed due to H-O-H bending[60]. These results indicate that the chemical composition of CMP bioceramics has both Ca and Mg phosphates.

3.3. Morphology analysis of 3D scaffolds

The morphology of the PCL and PCL-CMP composite scaffolds was investigated with an SEM. Figure 6 presents SEM micrographs of the top surface and cross-sectional morphology of the PMC-0, PMC-5, PMC-10, and PMC-15 scaffolds, respectively.

The SEM images illustrate that all the scaffolds exhibit well-defined structures with uniform pore size distribution. The pore size of the polymer and composite scaffolds was 200 ± 35 µm, marginally less than the designed scaffold (250 µm). The variations in the pore size are due to the rheological characteristics of materials. Typically, 3D printing processes provide precise dimensions and shapes of the features being printed. However, in this case, the PCL-ceramic composite materials (PMCs) were laden with solvent (TFE) to suit appropriate rheology for extrusion from the nozzle tip. Thus, after the deposition of these materials, there was a shrinkage after curing and evaporation of the water, leading to lower pore size as compared to the designed (250 µm) dimension. The PCL scaffolds appear to have a smooth surface compared to the PMC-5, PMC-10, and PMC-15. As the amount of ceramic content increased, the surface morphology of the composite scaffold exhibited a rough structure. The roughness of the composite scaffold surface is due to the dispersion of ceramic microparticles in the PCL matrix, which alters the morphology of PCL. This leads to a rougher surface with an increased surface area that closely mimics the natural ECM[61,62]. The crucial characteristics that affect

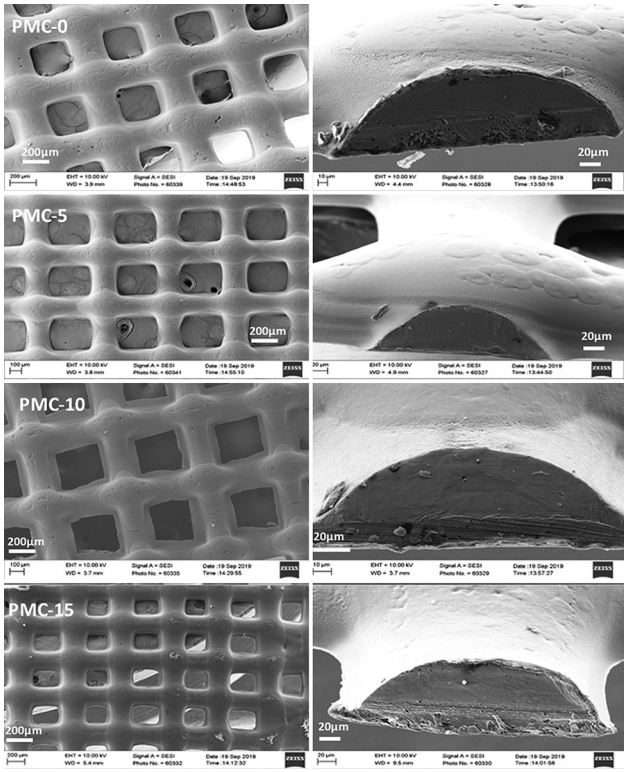

Figure 6. The surface and cross-section morphology of PMC-0, PMC-5, PMC-10, and PMC-15. Left: SEM images of 3D-printed scaffolds. Right: SEM images showing the cross-sectional view of the scaffold's single strut. The pore size of the composite scaffolds was in the range of 200 ± 35 µm.

cell adhesion and proliferation are porosity and surface roughness of the scaffold, as mentioned elsewhere[63-65]. The rheological changes were tailored by adding ceramic microparticles, which altered the properties such as shear stress, viscosity, and interaction between flow material and nozzle wall. Hence, the PCL and composite scaffold surface characteristics reacted differently under similar process conditions.

3.4. Porosity of scaffolds

The pore size and porosity of the 3D-printed scaffolds were calculated and are presented in Table 2. The virgin polymer PMC-0 had the largest pore size (~245 μm) and the highest porosity (50%), respectively. However, as the ceramic content within the scaffold increased, there was a reduction in both the pore size and porosity. This can be attributed to the increase in ceramic loading within the polymer composite that leads to higher viscosities of the 3D-printed slurries. This finding correlates well with the rheological behavior of the PMC suspension as shown in Figure 3, wherein higher microparticle loading has revealed a non-Newtonian behavior. However, it is noteworthy to point out that pore sizes above 150 μm and porosities above 40% are conducive for facilitating the diffusion of nutrition, allowing cell migration, accelerating cell proliferation, and enabling vascularization[66-68]. Thus, our high-porosity scaffolds provide diffusion and release pathways of biological molecules and nutrients for cellular migration and proliferation[69,70].

Table 2. Comparative analysis of pore size and porosity for PMC scaffolds

Material composition	Pore size (μm)	Porosity (%)
PMC-0	245.5±20.5	50.61±0.34
PMC-5	234.3±22.4	48.32±0.23
PMC-10	222.8±23.2	45.54±0.71
PMC-15	213.4±18.7	42.34±0.56

3.5. Hydrophilicity behavior of scaffolds

The surface wettability of the scaffolds, which affects cell proliferation and protein absorption, can be determined by the water contact angle. Hydrophilicity plays a crucial role in cell interaction within the scaffold. The hydrophilicity of the PMC-0, PMC-5, PMC-10, and PMC-15 was analyzed by measuring the incident contact angle at two different durations (initial at 3 s and equilibrium 90 s) using a drop shape analyzer (KRUSS-DSA25E) as shown in Figure 7.

Figure 8 shows the water contact angle measurements of polymer and composite scaffolds. The contact angle for our blend of PMC-0 was around 94.31 ± 3.21° as compared to pure PCL reported in the literature at 109.2 ± 4.1°[71]. However, the PMC-5, PMC-10, and PMC-15 composites had consistently lower contact angles (PMC-5: 74.5 ± 2.23°; PMC-10: 68.9 ± 2.15°; and PMC-15: 67.8 ± 2.03°). The incorporation of CMPs increased the hydrophilicity of

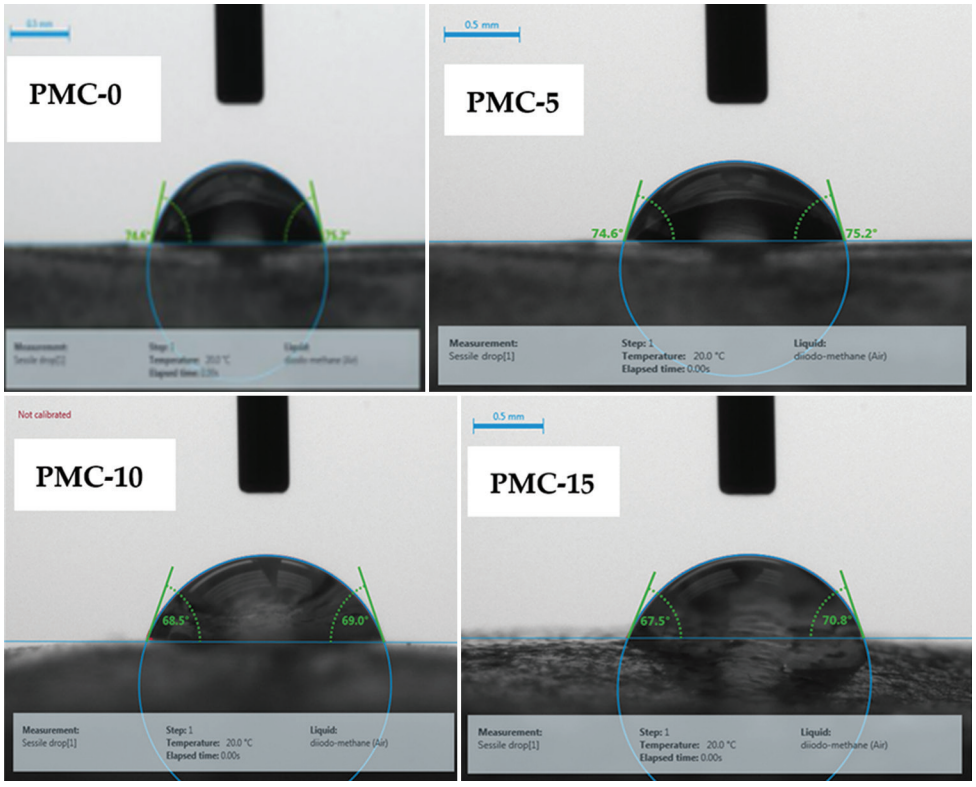

Figure 7. Water contact angle measurement of different contents of PMCs scaffolds.

the composite scaffolds. The decreasing order of contact angle measurements with an increase of bio-ceramics resembles well with decreasing trend as seen in PCL/HA composite scaffold structures[59]. These results illustrate that homogeneously mixed PMCs resulted in an enhanced hydrophilic scaffold, which can further improve the cellular proliferation and adsorption of biochemical cues for orthopedic applications, as reported in our previous computational biochemical models[31,55].

Moreover, researchers can tune the hydrophilicity and cellular response by adjusting the amount of CMPs in the scaffold structures. Furthermore, multi-nozzle deposition 3D bioprinting can provide functionally gradient PMCs structures for osteochondral (bone-cartilage) tissue constructs by manipulating material and process parameters. In the past, a variety of biological materials, including ECM, adhesion proteins, such as collagen, laminin, and fibronectin, as well as mucopolysaccharides, such as heparin sulfate, hyaluronate, and chondroitin sulfate, both individually and as mixtures have been applied to promote cell adhesion[51,53]. The current synthetic hydrophilic polymeric coatings show an analogous improvement in the attachment and growth of cell lines.

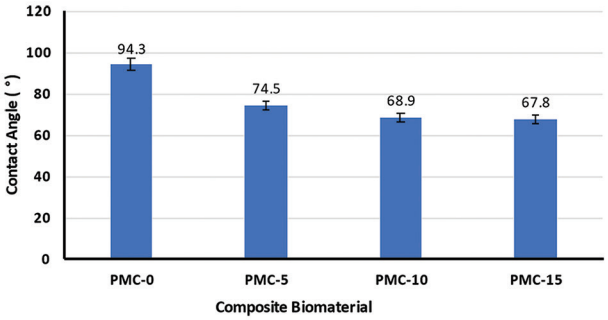

Figure 8. Water contact angle measurements of PMCs scaffolds at 90 s.

3.6. Cell viability on 3D-printed scaffolds

The biocompatibility of PMC-0 and composite scaffolds (PMC-5, PMC-10, and PMC-15) was tested by culturing NIH/3T3 cells for 3 days. Various literature has confirmed PCL's non-toxic effect on 3T3 fibroblast cells[71,72]. Hence, PCL alone was used as a control compared to other compositions. In this experiment, all the scaffolds had an average of more than 100% live cells at day 3 compared to the control one. According to the current ISO–10993, a cell viability of greater than 75% can be regarded as non-toxic for medical devices; therefore, in our experiment, we used a PCL-ceramic composition with more than 75% cell viability as a safety criterion[73]. Tukey's *post hoc* test was performed with ANOVA for multiple comparisons. The α-value was set to 0.05, and $P < 0.05$ was considered statistically significant. No statistically significant value regarding the cellular viability of the scaffolds was observed within the groups for day 1. The cell viability of composite scaffolds was enhanced with an increase in ceramic content, as illustrated in Figure 9, using Alamar Blue assay for Day 2 and Day 3 ($P < 0.05$). It was demonstrated that ion-dissolution products containing Ca and Mg from bioactive glasses and ceramics enhanced cell growth[74,75]. We assume that the amount of Mg and Ca ions released from the scaffolds was not at a toxic level but instead stimulated cell proliferation.

The LDH release study also supports the viability results. Figure 9 illustrates that, after day 3, the scaffolds allowed for enhanced cell growth as the scaffolds mimicked the natural ECM for proliferation. Composite scaffolds had less toxic release than polymer-alone scaffolds (i.e., PMC-0) as the absorbance was higher due to the hydrophilicity mentioned elsewhere. Moreover, the toxicity release was lesser for PMC-5 and PMC-10. Therefore, blending CMPs with PCL improved the interaction between cells and composite scaffolds.

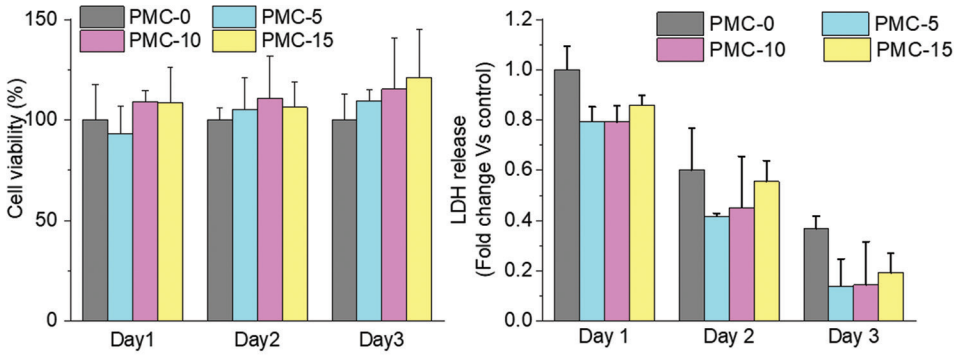

Figure 9. *In vitro* performance of 3D-printed scaffold and effects on cell viability. Left: Viability of 3T3 fibroblasts cultured on the scaffolds for 3 days (Alamar Blue assay, data normalized to values for cells cultured on control scaffolds, that is, PMC-0 [left]). Right: LDH cytotoxicity. Data represent the mean ± S.D. ($n = 3$), ANOVA, $^*P < 0.05$.

4. Conclusion

3D-printed composite scaffolds of poly(ε-caprolactone)/calcium magnesium phosphate (PMC scaffolds) using a direct-write technique for bone tissue regeneration application were investigated. Four groups of scaffolds – PMC-0, PMC-5, PMC-10, and PMC-15 – were fabricated. The pore size of the polymer and composite scaffolds ranged between 200 and 235 μm. The polymer (PMC-0) scaffolds had a smoother surface compared to the composite scaffolds (PMC-5, PMC-10, and PMC-15). The roughness of the composite scaffold surface was due to the homogeneous dispersion of ceramic microparticles in the PCL matrix, which altered the morphology of the PCL matrix. The rheological characteristics of the composite scaffold revealed an initial Newtonian behavior but changed to a shear-thinning fluid at higher shear rates. Higher PCL-CMP blends had higher shear stress values consistent with the addition of ceramic content. The hydrophilicity of the composite scaffold improved with the incorporation of CMPs, with lower contact angles attained at higher concentrations. This can aid in the rapid proliferation and enhance the adsorption of biochemical cues for tissue regeneration. Live and death assay studies of cells indicated biocompatibility of all scaffold structures with more than 100% live cells at day 3. The cell viability of composite scaffolds was enhanced with increased ceramic content. The LDH release results illustrated that both scaffolds enhanced cell growth, mimicking the natural ECM for cell attachment and proliferation. This research lays the foundation for the bioprinting of customized composite 3D scaffold structures using custom-synthesized bioceramics for regenerative tissue engineering.

Acknowledgments

None.

Funding

The authors would like to express their gratitude for funding support from the National Science Foundation Grant (NSF CMMI Award #1663128, #2100739, #2100850) and the Center of Excellence in Product Design and Advanced Manufacturing at North Carolina A&T State University.

Conflict of interest

The authors declare no conflict of interest. The funders had no role in the design of the study; in the collection, analyses, or interpretation of data; in the writing of the manuscript, or in the decision to publish the results.

Author contributions

Conceptualization: Santosh Kumar Parupelli, Narayan Bhattarai, and Salil Desai contributed to the conceptualization of the manuscript.

Investigation: Santosh Kumar Parupelli, Sheikh Saudi conducted the investigation of the 3D Printed ceramic-PCL scaffold.

Methodology: Santosh Kumar Parupelli, and Sheikh Saudi contributed to the methodology of the research manuscript.

Resources: Narayan Bhattarai and Salil Desai provided the necessary resources for conducting the 3D printing of ceramic-PCL scaffold research work.

Writing – original draft: Santosh Kumar Parupelli, and Sheikh Saudi contributed to the writing of the original draft of the research manuscript.

Writing – review & editing: Santosh Kumar Parupelli, Narayan Bhattarai, and Salil Desai contributed to the manuscript's review and final editing.

Ethics approval and consent to participate

Not applicable.

Consent for publication

Not applicable.

Availability of data

The data presented in this study are available on request from the corresponding author.

References

1. Hasan A, 2017, Tissue Engineering for Artificial Organs: Regenerative Medicine, Smart Diagnostics and Personalized Medicine. United States: John Wiley and Sons.

2. Van Blitterswijk C, de Boer J, Thomsen P, *et al*., 2008, Tissue Engineering. Netherlands: Elsevier.

3. Williams DF, 2009, On the nature of biomaterials. *Biomaterials*, 30: 5897–5909.

   https://doi.org/10.1016/j.biomaterials.2009.07.027

4. Williams DF, 2014, The biomaterials conundrum in tissue engineering. *Tissue Eng Part A*, 20: 1129–1131.

   https://doi.org/10.1089/ten.tea.2013.0769

5. Lee EJ, Kasper FK, Mikos AG, 2014, Biomaterials for tissue engineering. *Ann Biomed Eng*, 42: 323–337.

   https://doi.org/10.1007/s10439–013–0859–6

6. Dhandayuthapani B, Yoshida Y, Maekawa T, *et al*., 2011, Polymeric scaffolds in tissue engineering application: A review. *Int J Polym Sci*, 2011: 290602.

   https://doi.org/10.1155/2011/290602

7. Desai S, Bidanda B, Bártolo PJ, 2021, Emerging trends in

the applications of metallic and ceramic biomaterials. In: Bio-Materials and Prototyping Applications in Medicine. Germany: Springer. p1–17.

8. Desai S, Shankar MR, 2021, Emerging trends in polymers, composites, and nano biomaterial applications. In: Bio-Materials and Prototyping Applications in Medicine. Germany: Springer, p19–34.

9. Ratner BD, Hoffman AS, Schoen FJ, *et al*., 2004, Biomaterials Science: An Introduction to Materials in Medicine. San Diego, California: Academic Press. p162–164.

10. Hanker JS, Giammara BL, 1988, Biomaterials and biomedical devices. Science, 242: 885–892.

https://doi.org/10.1126/science.3055300.

11. Hasirci V, Hasirci N, 2018, Fundamentals of Biomaterials. Germany: Springer.

12. Chen FM, Liu X, 2016, Advancing biomaterials of human origin for tissue engineering. *Prog Polym Sci*, 53: 86–168.

https:/doi.org/10.1016/j.progpolymsci.2015.02.004

13. O'Brien FJ, 2011, Biomaterials and scaffolds for tissue engineering. *Mater Today*, 14: 88–95.

https://doi.org/10.1016/S1369-7021(11)70058-X

14. Keane TJ, Badylak SF, 2014, Biomaterials for tissue engineering applications. In: Seminars in Pediatric Surgery. Vol. 23. Netherlands: Elsevier. p112–118.

15. Burdick JA, Mauck RL, 2010, Biomaterials for Tissue Engineering Applications: A Review of the Past and Future Trends. Germany: Springer.

16. López-Rodríguez N, López-Arraiza A, Meaurio E, *et al*., 2006, Crystallization, morphology, and mechanical behavior of polylactide/poly (ε-caprolactone) blends. *Polym Eng Sci*, 46: 1299–1308.

https://doi.org/10.1002/pen.20609

17. Yoshimoto H, Shin YM, Terai H, *et al*., 2003, A biodegradable nanofiber scaffold by electrospinning and its potential for bone tissue engineering. *Biomaterials*, 24: 2077–2082.

https://doi.org/10.1016/s0142-9612(02)00635-x

18. Rezwan K, Chen QZ, Blaker JJ, *et al*., 2006, Biodegradable and bioactive porous polymer/inorganic composite scaffolds for bone tissue engineering. *Biomaterials*, 27: 3413–3431.

https://doi.org/10.1016/j.biomaterials.2006.01.039

19. Ma PX, 2004, Scaffolds for tissue fabrication. *Mater Today*, 7: 30–40.

https://doi.org/10.1016/S1369-7021(04)00233-0

20. Choi SW, Zhang Y, Xia Y, 2010, Three-dimensional scaffolds for tissue engineering: The importance of uniformity in pore size and structure. *Langmuir*, 26: 19001–19006.

https://doi.org/10.1021/la104206h

21. Desai S, Harrison B, 2010, Direct-writing of biomedia for drug delivery and tissue regeneration. In: Printed Biomaterials: Novel Processing and Modeling Techniques for Medicine and Surgery. Germany: Springer Verlag.

22. Desai S, Perkins J, Harrison BS, *et al*., 2010, Understanding release kinetics of biopolymer drug delivery microcapsules for biomedical applications. *Mater Sci Eng B*, 168: 127–131.

https://doi.org/10.1016/j.mseb.2009.11.006

23. Desai S, Moore A, Harrison B, *et al*., 2008, Understanding microdroplet formations for biomedical applications. In: ASME International Mechanical Engineering Congress and Exposition. New York, United States: ASME. p1–4.

24. Abedalwafa M, Wang F, Wang L, *et al*., 2013, Biodegradable poly-epsilon-caprolactone (PCL) for tissue engineering applications: A review. *Rev Adv Mater Sci*, 34: 123–140.

25. Grandi C, di Liddo R, Paganin P, *et al*., 2011, Porous alginate/poly (ε-caprolactone) scaffolds: Preparation, characterization and *in vitro* biological activity. *Int J Mol Med*, 27: 455–467.

https://doi.org/10.3892/ijmm.2010.593

26. Zhang XC, 2016, Science and Principles of Biodegradable and Bioresorbable Medical Polymers: Materials and Properties. Sawston, United Kingdom: Woodhead Publishing.

27. Li W, Danielson KG, Alexander PG, *et al*., 2003, Biological response of chondrocytes cultured in three-dimensional nanofibrous poly (ϵ-caprolactone) scaffolds. *J Biomed Mater Res A*, 67: 1105–1114.

https://doi.org/10.1002/jbm.a.10101

28. Albertsson AC, Varma IK, 2003, Recent developments in ring opening polymerization of lactones for biomedical applications. *Biomacromolecules*, 4: 1466–1486.

https://doi.org/10.1021/bm034247a

29. Saudi S, Bhattarai SR, Adhikari U, *et al*., 2020, Nanonet-nano fiber electrospun mesh of PCL-chitosan for controlled and extended release of diclofenac sodium. *Nanoscale*, 12: 23556–23569.

https://doi.org/10.1039/D0NR05968D

30. Adarkwa E, Kotoka R, Desai S, 2021, 3D printing of polymeric Coatings on AZ31 Mg alloy Substrate for Corrosion Protection of biomedical implants. *Med Devices Sens*, 4: e10167.

https://doi.org/10.1002/MDS3.10167

31. Marquetti I, Desai S, 2018, Adsorption behavior of bone morphogenetic protein-2 on a graphite substrate for biomedical applications. Am J Eng Appl Sci, 11: 1037–1044.

https://doi.org/10.3844/ajeassp.2018.1037.1044

32. Wu F, Liu C, O'Neill B, *et al*., 2012, Fabrication and properties of porous scaffold of magnesium phosphate/polycaprolactone biocomposite for bone tissue engineering.

Appl Surf Sci, 258: 7589–7595.

https://doi.org/10.1016/j.apsusc.2012.04.094

33. Liu L, Wang Y, Guo S, *et al*., 2012, Porous polycaprolactone/nanohydroxyapatite tissue engineering scaffolds fabricated by combining NaCl and PEG as co-porogens: Structure, property, and chondrocyte-scaffold interaction *in vitro*. *J Biomed Mater Res B Appl Biomater*, 100: 956–966.

https://doi.org/10.1002/JBM.B.32658

34. Diba M, Kharaziha M, Fathi MH, *et al*., 2012, Preparation and characterization of polycaprolactone/forsterite nanocomposite porous scaffolds designed for bone tissue regeneration. *Compos Sci Technol*, 72: 716–723.

https://doi.org/10.1016/J.COMPSCITECH.2012.01.023

35. Lei B, Shin KH, Noh DY, *et al*., 2012, Bioactive glass microspheres as reinforcement for improving the mechanical properties and biological performance of poly(ε-caprolactone) polymer for bone tissue regeneration. *J Biomed Mater Res B Appl Biomater*, 100B: 967–975.

https://doi.org/10.1002/JBM.B.32659

36. Dong Z, Wu Y, Wang Q, *et al*., 2012, Reinforcement of electrospun membranes using nanoscale Al2O3 whiskers for improved tissue scaffolds. *J Biomed Mater Res A*, 100: 903–910.

https://doi.org/10.1002/jbm.a.34027

37. Marquetti I, Desai S, 2019, Orientation effects on the nanoscale adsorption behavior of bone morphogenetic protein-2 on hydrophilic silicon dioxide. *RSC Adv*, 9: 906–916.

https://doi.org/10.1039/C8RA09165J

38. Marquetti I, Desai S, 2018, Molecular modeling the adsorption behavior of bone morphogenetic protein-2 on hydrophobic and hydrophilic substrates. *Chem Phys Lett*, 706: 285–294.

https://doi.org/10.1016/j.cplett.2018.06.015

39. Marquetti I, Desai S, 2022, An atomistic investigation of adsorption of bone morphogenetic protein-2 on gold with nanoscale topographies. *Surfaces*, 5: 176–185.

https://doi.org/10.3390/surfaces5010010

40. Huang B, Caetano G, Vyas C, *et al*., 2018, Polymer-ceramic composite scaffolds: The effect of hydroxyapatite and β-tri-calcium phosphate. *Materials*, 11: 129.

https://doi.org/10.3390/ma11010129

41. Klein CP, Driessen AA, de Groot K, *et al*., 1983, Biodegradation behavior of various calcium phosphate materials in bone tissue. *J Biomed Mater Res*, 17: 769–784.

https://doi.org/10.1002/jbm.820170505

42. Parupelli S, Desai S, 2019, A comprehensive review of additive manufacturing (3d printing): Processes, applications and future potential. *Am J Appl Sci*, 16: 244–272.

https://doi.org/10.3844/ajassp.2019.244.272

43. Parupelli SK, Aljohani A, Desai S, 2019, Direct jet printing and characterization of calcium alginate microcapsules for biomedical applications. In: Proceedings of the 2019 IISE Annual Conference. Florida, USA: Institute of Industrial and Systems Engineers (IISE).

44. Perkins J, Xu Z, Smith C, *et al*., 2015, Direct writing of polymeric coatings on magnesium alloy for tracheal stent applications. *Ann Biomed Eng*, 43: 1158–1165.

https://doi.org/10.1007/s10439-014-1169-3

45. Papaioannou TG, Manolesou D, Dimakakos E, *et al*., 2019, 3D bioprinting methods and techniques: Applications on artificial blood vessel fabrication. *Acta Cardiol Sin*, 35: 284.

https://doi.org/10.6515/ACS.201905_35(3).20181115A

46. Ning L, Chen X, 2017, A brief review of extrusion-based tissue scaffold bio-printing. *Biotechnol J*, 12: 1600671.

https://doi.org/10.1002/BIOT.201600671

47. Deo KA, Singh KA, Peak CW, *et al*., 2020, Bioprinting 101: Design, fabrication, and evaluation of cell-laden 3D bioprinted scaffolds. *Tissue Eng Part A*, 26: 318–338.

https://doi.org/10.1089/TEN.TEA.2019.0298

48. Kačarević ŽP, Rider PM, Alkildani S, *et al*., 2018, An introduction to 3D bioprinting: Possibilities, challenges and future aspects. *Materials*, 11: 2199.

https://doi.org/10.3390/MA11112199

49. Agarwal S, Saha S, Balla VK, *et al*., 2020, Current developments in 3D bioprinting for tissue and organ regeneration-a review. *Front Mech Eng*, 6: 589171.

https://doi.org/10.3389/FMECH.2020.589171

50. Gmeiner R, Deisinger U, Schönherr J, *et al*., 2015, Additive manufacturing of bioactive glasses and silicate bioceramics. *J Ceram Sci*, 6: 75–86.

https://doi.org/10.4416/JCST2015-00001

51. Sobral JM, Caridade SG, Sousa RA, *et al*., 2011, Three-dimensional plotted scaffolds with controlled pore size gradients: Effect of scaffold geometry on mechanical performance and cell seeding efficiency. *Acta Biomater*, 7: 1009–1018.

https://doi.org/10.1016/j.actbio.2010.11.003

52. Chen WH, Liu YY, Zhang FH, *et al*., 2015, Osteochondral integrated scaffolds with gradient structure by 3D printing forming. *Int J Autom Comput*, 12: 220–228.

https://doi.org/10.1007/s11633-014-0853-y

53. Thomas M, Willerth SM, 2017, 3-D bioprinting of neural tissue for applications in cell therapy and drug screening. *Front Bioeng Biotechnol*, 5: 69.

https://doi.org/10.3389/fbioe.2017.00069

54. Kundu J, Shim JH, Jang J, *et al*., 2015, An additive manufacturing-based PCL-alginate-chondrocyte bioprinted

scaffold for cartilage tissue engineering. *J Tissue Eng Regen Med*, 9: 1286–1297.

https://doi.org/10.1002/term.1682

55. Ma J, Lin L, Zuo Y, *et al*., 2019, Modification of 3D printed PCL scaffolds by PVAc and HA to enhance cytocompatibility and osteogenesis. *RSC Adv*, 9: 5338–5346.

https://doi.org/10.1039/C8RA06652C

56. Adhikari U, Rijal NP, Khanal S, *et al*., 2016, Magnesium and calcium-containing scaffolds for bone tissue regeneration. In: ASME International Mechanical Engineering Congress and Exposition. Vol. 50688. New York, United States: American Society of Mechanical Engineers.

https://doi.org/10.1115/IMECE2016-66835

57. Schneider CA, Rasband WS, Eliceiri KW, 2012, NIH Image to ImageJ: 25 years of image analysis. *Nat Methods*, 9: 671–675.

https://doi.org/10.1038/nmeth.2089

58. Huang B, Bártolo PJ, 2018, Rheological characterization of polymer/ceramic blends for 3D printing of bone scaffolds. *Polym Test*, 68: 365–378.

https://doi.org/10.1016/j.polymertesting.2018.04.033

59. Jiang W, Shi J, Li W, *et al*., 2012, Morphology, wettability, and mechanical properties of polycaprolactone/hydroxyapatite composite scaffolds with interconnected pore structures fabricated by a mini-deposition system. *Polym Eng Sci*, 52: 2396–2402.

https://doi.org/10.1002/pen.23193

60. Jia J, Zhou H, Wei J, *et al*., 2010, Development of magnesium calcium phosphate biocement for bone regeneration. *J R Soc Interface*, 7: 1171–1180.

https://doi.org/10.1098/rsif.2009.0559

61. Fazeli N, Arefian E, Irani S, *et al*., 2021, 3D-printed PCL scaffolds coated with nanobioceramics enhance osteogenic differentiation of stem cells. *ACS Omega*, 6: 35284–35296.

https://doi.org/10.1021/acsomega.1c04015

62. Yang X, Wang Y, Zhou Y, *et al*., 2021, The application of polycaprolactone in three-dimensional printing scaffolds for bone tissue engineering. *Polymers (Basel)*, 13: 2754.

https://doi.org/10.3390/polym13162754

63. Liu D, Nie W, Li D, *et al*., 2019, 3D printed PCL/SrHA scaffold for enhanced bone regeneration. *Chem Eng J*, 362: 269–279.

https://doi.org/10.1016/j.cej.2019.01.015

64. Park SA, Lee SJ, Seok JM, *et al*., 2018, Fabrication of 3D printed PCL/PEG polyblend scaffold using rapid prototyping system for bone tissue engineering application. *J Bionic Eng*, 15: 435–442.

https://doi.org/10.1007/s42235-018-0034-8

65. Park SA, Lee HJ, Kim KS, *et al*., 2018, *In vivo* evaluation of 3D-printed polycaprolactone scaffold implantation combined with β-TCP powder for alveolar bone augmentation in a beagle defect model. *Materials*, 11: 238.

https://doi.org/10.3390/ma11020238

66. Murphy CM, Haugh MG, O'brien FJ, 2010, The effect of mean pore size on cell attachment, proliferation and migration in collagen-glycosaminoglycan scaffolds for bone tissue engineering. *Biomaterials*, 31: 461–466.

https://doi.org/10.1016/j.biomaterials.2009.09.063

67. O'Brien FJ, Harley BA, Yannas IV, *et al*., 2005, The effect of pore size on cell adhesion in collagen-GAG scaffolds. *Biomaterials*, 26: 433–441.

https://doi.org/10.1016/j.biomaterials.2004.02.052

68. Wibowo A, Vyas C, Cooper G, *et al*., 2020, 3D printing of polycaprolactone-polyaniline electroactive scaffolds for bone tissue engineering. *Materials*, 13: 512.

https://doi.org/10.3390/ma13030512

69. Loh QL, Choong C, 2013, Three-dimensional scaffolds for tissue engineering applications: Role of porosity and pore size. Tissue Eng Part B Rev, 19: 485–502.

https://doi.org/10.1089/ten.TEB.2012.0437

70. Karageorgiou V, Kaplan D, 2005, Porosity of 3D biomaterial scaffolds and osteogenesis. *Biomaterials*, 26: 5474–5491.

https://doi.org/10.1016/j.biomaterials.2005.02.002

71. Edwards A, Jarvis D, Hopkins T, *et al*., 2015, Poly (ε-caprolactone)/keratin-based composite nanofibers for biomedical applications. *J Biomed Mater Res B Appl Biomater*, 103: 21–30.

https://doi.org/10.1002/jbm.b.33172

72. Gomes SR, Rodrigues G, Martins GG, *et al*., 2015, *In vitro* and *in vivo* evaluation of electrospun nanofibers of PCL, chitosan and gelatin: A comparative study. *Mater Sci Eng C*, 46: 348–358.

https://doi.org/10.1016/j.msec.2014.10.051

73. Wang J, Witte F, Xi T, *et al*., 2015, Recommendation for modifying current cytotoxicity testing standards for biodegradable magnesium-based materials. *Acta Biomater*, 21: 237–249.

https://doi.org/10.1016/j.actbio.2015.04.011

74. Dietrich E, Oudadesse H, Lucas-Girot A, *et al*., 2009, *In vitro* bioactivity of melt-derived glass 46S6 doped with magnesium. *J Biomed Mater Res A*, 88: 1087–1096.

https://doi.org/10.1002/jbm.a.31901

75. Sader MS, LeGeros RZ, Soares GA, 2009, Human osteoblasts adhesion and proliferation on magnesium-substituted tricalcium phosphate dense tablets. *J Mater Sci Mater Med*, 20: 521–527.

https://doi.org/10.1007/s10856-008-3610-3

ACCSCIENCE PUBLISHING

International Journal of Bioprinting

RESEARCH ARTICLE

Enhanced osteogenesis and bactericidal performance of additively manufactured MgO- and Cu-added CpTi for load-bearing implants

Sushant Ciliveri, and Amit Bandyopadhyay*

W. M. Keck Biomedical Materials Research Laboratory, School of Mechanical and Materials Engineering, Washington State University, Pullman, WA 99164, USA

(This article belongs to the *Special Issue: 3D Bioprinting for Materials and Application*)

Abstract

The bio-inertness of titanium, which is the ultimate choice of metallic material for implant applications, causes delayed bone–tissue integration at the implant site and prevents expedited healing for the patient. This can result in a severe issue for patients with immunocompromised bone health as titanium does not offer inherent antimicrobial properties, and thus, infections at the implant site are another concern. Current strategies addressing the issues above include using cemented implants as a coating on Ti6Al4V bulk material for orthopedic applications. Roadblock arises with coating failure due to weak interfacial bond at the Ti–cement interface, which necessitates revision surgeries. In this study, we added osteogenic MgO and antibacterial Cu to commercially pure titanium (CpTi) and processed them using metal additive manufacturing. Mg, an essential trace element in the body, has been proven to enhance osseointegration *in vivo*. Cu has been popular for its bactericidal capabilities. With the addition of 1 wt.% of MgO to the CpTi matrix, we observed a four-fold increase in the mineralized bone formation at the bone–implant interface *in vivo*. The addition of 3 wt.% of Cu did not result in cytotoxicity, and adding Cu to CpTi-MgO chemical makeup yielded *in vivo* performance similar to that in CpTi-MgO. In *in vitro* bacterial studies with gram-positive *Staphylococcus aureus*, CpTi-MgO-Cu displayed an antibacterial efficacy of 81% at the end of 72 h of culture. Our findings highlight the synergistic benefits of CpTi-MgO-Cu, which exhibit superior early-stage osseointegration and antimicrobial capabilities.

Keywords: Commercially pure titanium; Osseointegration; Additive manufacturing; Antibacterial performance; Porous metal

***Corresponding authors:**
Amit Bandyopadhyay
(amitband@wsu.edu)

Citation: Ciliveri S, Bandyopadhyay A, 2023, Enhanced osteogenesis and bactericidal performance of additively manufactured MgO- and Cu-added CpTi for load-bearing implants. *Int J Bioprint*, 9(6): 1167. https://doi.org/10.36922/ijb.1167

Received: June 27, 2023
Accepted: August 16, 2023
Published Online: October 11, 2023

Copyright: © 2023 Author(s). This is an Open Access article distributed under the terms of the Creative Commons Attribution License, permitting distribution, and reproduction in any medium, provided the original work is properly cited.

Publisher's Note: AccScience Publishing remains neutral with regard to jurisdictional claims in published maps and institutional affiliations.

1. Introduction

The selection of metallic materials for biomedical applications relies on several considerations, including corrosion resistance, fatigue strength, and biocompatibility[1,2]. Over the years, titanium (Ti) has emerged as the optimal material for load-bearing implants[3-5]. While Ti6Al4V demonstrates excellent fatigue resistance and is commonly used for bulk metallic implants at load-bearing sites[6], commercially pure titanium (CpTi) with higher biocompatibility but lower strength than Ti6Al4V is often employed either at low-load-bearing sites or as a metallic coating on these bulk implants[7]. Since

the *in vivo* performance of an implant is greatly influenced by the chemistry of the implant surface upon contact with the physiological environment, researchers have explored the use of calcium phosphate (CaP) coatings added with dopants, such as MgO, SiO_2, and ZnO, on bulk Ti to enhance osseointegration[8-10]. However, the weak metal-ceramic interface in these coatings has led to challenges, including some coating failures due to delamination.

The long-term stability of the implant is severely affected by polymicrobial infections at the implant site, eventually leading to implant loosening and prosthetic joint infection (PJI)[11]. Addressing such polymicrobial infections involves long-term antibiotic administration, revision surgeries involving debridement of infected tissues with implant retention, or implant replacement, the latter being the most effective in eradicating the infection[12-14]. However, revision surgeries in patients with compromised bone health pose significant risks to their overall well-being and increase the probability of early mortality. A report on PJI indicated that 25% of patients treated for PJI died within 5 years[15]. Moreover, a recent survey by the World Health Organization highlights 700,000 annual deaths due to microbial infections, with projections of 10 million deaths by 2050[16]. The seriousness of the situation prompted a call to action at the United Nations General Assembly in 2017, aiming to reduce the mortality caused by antimicrobial resistance down by 200,000 deaths[18]. Without adequate intervention, the number of deaths from polymicrobial infections may rise exponentially in the coming decades.

Despite titanium's established position as the ultimate metallic material for implant applications worldwide, its bio-inertness remains a significant drawback[17,18]. The early stage of osseointegration, which is crucial for a patient's healing period post-surgery and the long-term stability *in vivo*, can be severely affected by a prolonged healing process at the implant site, particularly in individuals with compromised bone health. Given that the implant's surface is constantly in contact with the physiological environment, its role in biological performance, including osseointegration and integration with surrounding bone tissue, is vital. Numerous strategies have been employed to enhance bone–tissue integration on titanium surfaces, such as introducing surface porosities and calcium phosphate coatings with dopant additions. One prominent dopant addition is magnesium oxide (MgO), which enhances osteogenesis in bone-remodeling processes. Magnesium (Mg) is the fourth main cation found in the human body; an adult body contains approximately 25 g of Mg, with 50–60% present in the bony intracellular matrix[19]. Mg, a biodegradable material *in vivo* with poor corrosion resistance, is usually incorporated in a biomaterial matrix such as hydroxyapatite[20]. Mg^{2+} ions play a crucial role in bone metabolism, aiding osteogenesis by regulating local pH, which enhances osteoblast recruitment, proliferation, and differentiation[21,22]. Mg^{2+} ions also aid in regulating gene expressions in stem cell differentiation of osteoblastic cells to stimulate formation of bone matrix proteins and enhance bone formation[23,24]. Numerous studies have demonstrated the efficacy of Mg ions in bioactive ceramic matrices, significantly enhancing cell proliferation *in vitro*[25,26] and osteogenesis and bone mineralization *in vivo*[8,27].

A major concern associated with cemented implants is aseptic loosening due to delamination of the ceramic coating on the titanium implant under loading conditions, leading to implant failure[28-31]. A recent survey study on the aseptic loosening of cemented implants post-total knee arthroplasty surgeries from 2009 to 2017 reported an alarming 6% failure rate due to cement debonding in the tibial implant[32]. Such a high failure rate necessitates a search for suitable cemented implant substitutes. Instead of using Mg-doped hydroxyapatite or calcium phosphate cemented onto titanium implants, we propose incorporating MgO into the Ti matrix. Limited studies have been conducted on incorporating MgO into the metal matrix to enhance osteogenesis[25]. The challenges posed by the difference in melting points between Ti (1668°C) and MgO (2852°C) have been overcome by utilizing additive manufacturing (AM) for fabricating this composition. AM allows the manufacturing of metal-ceramic composites with greater flexibility and enables the incorporation of designed porosities that aid in enhanced osseointegration *in vivo*, a feat not achievable by other manufacturing methods[33]. However, to prevent brittleness of the metal-ceramic composites and ensure successful AM fabrication, we have restricted the addition of MgO dopant to 1 wt.% in Ti[34]. Copper (Cu) has also been extensively studied due to its antibacterial properties in Ti-Cu alloys. Nevertheless, concerns regarding toxicity resulting from higher amounts of Cu in the human body limit its use in significant quantities. This study added small amounts of Cu (3 wt.%) to the Ti-MgO composition.

Given these issues, we added MgO and Cu to CpTi matrix to enhance its osteogenic potential and imbue inherent bactericidal capabilities. There lies a research gap in exploring the effect of MgO incorporation into Ti matrix. The novelty of this study lies in investigating the synergistic osteogenic and antibacterial potential of the CpTi-MgO-Cu material design. This Ti-MgO-Cu material chemistry is expected to enhance early-stage osseointegration due to osteogenic MgO and prevent polymicrobial infection incidence at the implant site,

ensuring the implant's long-term stability and preventing the need for revision procedures due to their aseptic loosening. This study aims to fabricate CpTi, CpTi + 1 wt.% MgO (CpTi-MgO), and CpTi + 1 wt.% MgO + 3 wt.% Cu (CpTi-MgO-Cu) compositions using metal AM. These compositions were characterized in terms of their microstructure and microhardness. *In vivo* rat studies were conducted to evaluate the biological performance of these compositions. Structures utilized for the *in vivo* studies were ~40 vol.% porous with an approximate pore size of 600–700 μm since pore sizes in this range are optimum for enhanced tissue integration and osseointegration[35,36]. Additionally, *in vitro* bacterial culture was studied using the commonly occurring *Staphylococcus aureus* strain to evaluate the antibacterial efficacy of CpTi-MgO-Cu. We hypothesize that the CpTi-MgO-Cu composition will demonstrate better osseointegration performance than CpTi *in vivo* with no cytotoxicity due to the presence of Cu, as schematically shown in Figure 1.

2. Materials and methods

2.1. Processing of samples using metal additive manufacturing

CpTi, CpTi-MgO, and CpTi-MgO-Cu compositions were processed using metal additive manufacturing. A metal matrix composition of CpTi-MgO was prepared by premixing CpTi powders (GKN Hoeganaes, Cinnaminson, NJ, USA) with 1 wt.% of MgO (Inframat® Advanced Materials™, Manchester, CT, USA) powders. Similarly, CpTi-MgO-Cu composition was prepared by premixing CpTi powders with 1 and 3 wt.% of MgO and Cu (GKN Hoeganaes, Cinnaminson, NJ, USA) powders, respectively. All metal and ceramic powders used for fabrication were sieved to obtain a powder particle size of <63 μm. All metal and ceramic powers used were spherical. The fabrication used two AM processes: directed energy deposition (DED) and selective laser melting (SLM). Samples for *in vitro* study were printed on a 5-axis DED-based AM system (FormAlloy, Spring Valley, CA). Although coarser powder particles (45–150 μm) are preferred for DED-based AM systems, we optimized the printing parameters to accommodate finer particle size of <63 μm for the printing operation. The printing operation was conducted in an argon-purged environment with O_2 < 20 ppm in the printing chamber. A cold rolled CpTi substrate was used as a build plate. Discs of 8 mm diameter and 4 mm height were printed on the DED system. The printing parameters used for the compositions are presented in Table 1.

Samples used for *in vivo* study were printed on an SLM-based powder bed fusion system (3D Systems ProX® DMP 200, Rock Hill, SC, USA) with a 300 W fiber laser and a wavelength of λ = 1070 nm. Porous structures of 2.4 mm diameter and 4 mm height with ~40 vol.% porosity were designed in 3DXpert CAD Software (3D Systems, Rock Hill, SC, USA). Premixed powders were poured into the supply chamber and compacted using a compaction plate. A thick CpTi plate of ~2.5 cm thickness was used as the build platform and secured on the melting stage. A roller system carried powders from the supply to the build stage, with 30 μm set as the layer thickness. The laser power and scanning speed for all the compositions are reported in Table 1. 3D Systems provide printing parameters used for CpTi and CpTi-MgO as the standard Ti printing parameters. Laser power was increased by 10%, and scan speed reduced by 10% to increase the print energy input for CpTi-MgO-Cu since Cu displays poor laser absorption and needs more energy for additive manufacturing operation[37,38]. Post-printing porous cylinders were cut from the build plate and

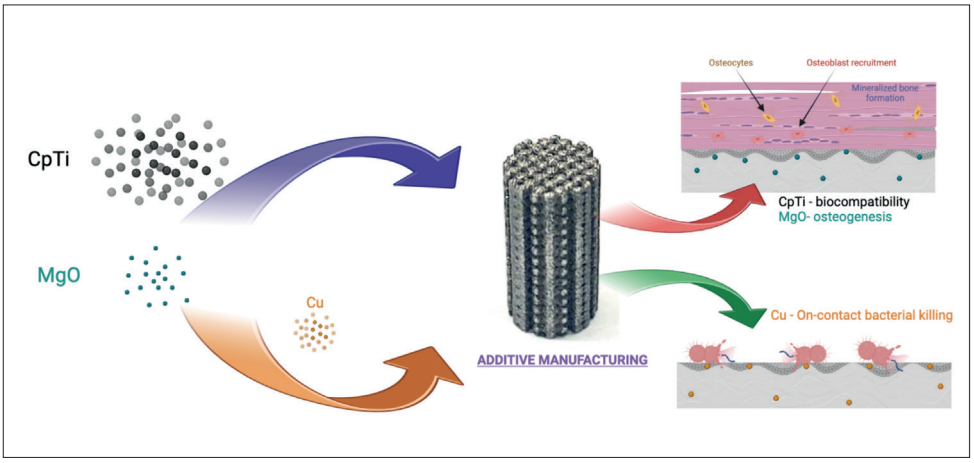

Figure 1. Schematic of MgO-induced osteogenic activity toward early-stage osseointegration and bactericidal effect of Cu in CpTi. The CpTi-MgO-Cu was processed via metal additive manufacturing, enabling the incorporation of designed porosity. This further expedites the bone remodeling and tissue attachment on the implant's surface, contributing to its long-term stability *in vivo*.

Table 1. Print-processing parameters used for DED and PBF operations of additively manufactured CpTi, CpTi-MgO, and CpTi-MgO-Cu compositions

DED (*in vitro*, microstructure, hardness)								
Composition	Laser power (W)		Scan speed (mm/min)		Shield gas (ℓ/min)	Carrier gas (ℓ/min)	Powder disc speed (rpm)	Slice (mm)
	Contour	Hatch	Contour	Hatch				
CpTi	350	350	1500	1200	18	14	0.7	0.3
CpTi-MgO								
CpTi-MgO-Cu								

PBF (*in vivo*, ~40% porosity)			
Composition	Laser power (W)	Scan speed (mm/s)	Slice (μm)
CpTi	180	1600	30
CpTi-MgO			
CpTi-MgO-Cu	198	1440	

subjected to repeated sonication in deionized water and ethanol, followed by compressed air treatment to remove any loose powder particles inside the pores. The final step in residual powder removal involved acid etching in 1% hydrogen fluoride in deionized water. The samples were sonicated again in deionized water and ethanol to remove any acid residues.

2.2. Microhardness and microstructure

DED-printed discs were cut off the build plate and subjected to grinding on silicon carbide grinding papers with 80–2000 grit size. This was followed by alumina suspension polishing to reduce the alumina powder particle size from 1 to 0.05 μm. Vickers microhardness test was conducted on a Phase II Plus Micro Vickers Hardness tester (Upper Saddle River, NJ, USA) using a load of 200 g and a dwell time of 15 s. Hardness values on a polished surface perpendicular to the build direction were obtained. An n = 5 measurement were taken for each composition. For acquiring the microstructures, polished surfaces of the discs were etched in Kroll's reagent for 45 s and observed under a scanning electron microscope (SEM; Apreo, Thermo Scientific, MA, USA).

2.3. *In vitro* bacterial study

Bacterial culture was carried out on CpTi and CpTi-MgO-Cu to evaluate the antibacterial resistance using gram-positive *S. aureus* strain for 24, 48, and 72 h. Freeze-dried *S. aureus* (Carolina Biological, NC, USA) was rehydrated using rehydration media. Tryptic soy broth was used as the nutrient medium. The rehydrated bacterium was subjected to nutrient broth dilutions to obtain 0.5 McFarland standard optical density measurement corresponding to 10^8 CFU/ml of bacteria. Polished disc samples were sterilized before culture, placed in 24-well plates, and then studied in triplicate for colony count on agar plate and in duplicate for SEM characterization. Bacterial colonies at 10^6 CFU of bacterial colonies were seeded on the surface of the discs, with 2 ml of tryptic soy broth added as the nutrient medium in each well. After the respective time points, bacterial cells from triplicate samples for agar plate colony count were scraped using cell scrapers and mixed in 2 ml of 0.1 M PBS, which was then serially diluted to approximately 10 to 100 colonies in 1 μl of the solution. One microliter of this solution was streaked on a tryptic soy agar plate and incubated for 24 h. The duplicate samples used to observe the bacterial cell morphology were subjected to fixative solution overnight. Dehydration was carried out with 2% OsO4 (Osmium tetroxide), followed by ethanol and HMDS dehydration treatments. The samples were gold coated and observed under an SEM (Quanta 200F, Thermo Fisher, Waltham, USA). Images were taken at 300× magnification for each composition, and the number of bacterial cells was counted on at least n = 4 images for each composition. The antibacterial efficacy for agar plate count at 24 h was evaluated as a function of bacterial colonies counted on individual material compositions, as

$$N = C \times d \times 1000/l$$

$$R = (N_{control} - N_{material})/N_{control} \times 100\%$$

where N is the calculated number of bacterial colonies observed, C is the average colony count on a plate, d is the dilution factor, and l is the volume of bacterial suspension on the sample. Antibacterial efficacy from SEM images was evaluated at 24, 48, and 72 h timepoints and calculated for R, with N being the average number of bacterial cells from multiple SEM images.

2.4. *In vivo* study

CpTi, CpTi-MgO, and CpTi-MgO-Cu compositions were subjected to an *in vivo* rat study. CpTi is known to

demonstrate excellent *in vivo* biological performance and is used as a control. Adding MgO to CpTi is expected to yield better early-stage osseointegration performance than CpTi. PBF-fabricated porous implants with ~40 vol.% porosity were used for the study.

2.4.1. Surgery and implantation procedure

Male Sprague-Dawley rats with average weights between 300 and 350 g were used for the *in vivo* study. The animals were acclimatized in temperature- and humidity-controlled rooms in separate cages for at least 2 weeks. Buprenorphine (0.3 mg/kg) was subcutaneously administered to the animals for alleviating pain 30 min before anesthesia. A prescribed dose of IsoFlo® (isoflurane, USP, Abbott Laboratories, North Chicago, IL, USA) coupled with oxygen (Oxygen USP, A-L Compressed Gases Inc., Spokane, WA, USA) was used to anesthetize the animals. Once the animal's movements ceased under anesthesia, the implantation area around the femur and the knee was shaved thoroughly and cleaned thrice with chlorhexidine and isopropyl alcohol scrubs. Lidocaine hydrochloride (0.3 ml; without epinephrine) with a 0.5% concentration was subcutaneously administered as a localized numbing agent near the implantation area on each limb. The animal was then transferred onto a sterile surgery table area. A 2-inch incision was made along the femur on the lateral side above the distal femoral condyle. A unicortical defect of 2.4 mm diameter was made on the lateral epicondyle using gradually increasing drill bits and rinsed with saline to prevent thermal necrosis and remove bone fragments. The implant was inserted, and the fascia and the skin over the incision were sutured with undyed braided coated with MONOCRYL-polyglactin 910 (Ethicon Inc., Somerville, NJ, USA). The incision area was cleaned with saline scrubs and stapled. A similar procedure was carried out on the other limb of the animal. The animal was periodically monitored for its breathing rate during the surgery procedure. Lactated ringers solution (LRS, 3 ml) for rehydration was subcutaneously administered to the animal post-surgery, followed by meloxicam (0.2 mg/kg) administration as an anti-inflammatory analgesic, and monitored until the animal regained consciousness. Post-operative care was carried out for 3 days, with buprenorphine administration every 12 h and meloxicam every 24 h. The animals were euthanized 6 weeks after the surgery by means of carbon dioxide overdose, followed by cervical dislocation as a secondary measure, and the femoral bone with the metal implant was harvested. The Institutional Animal Care and Use Committee (IACUC) of Washington State University (WSU-Pullman, WA)-approved protocol was followed to perform the experimental and surgical procedure.

2.4.2. Histological and histomorphometric analysis

The bone–metal explants were fixed in 10% neutral buffered formalin for at least 72 h for tissue infiltration. Serial dehydration was carried out in ethanol followed by embedment in polymethylmethacrylate (PMMA)[39]. These embedded bone explants were cut on Ekakt™ saw into 200 µm thick sections, mounted on glass slides, and then ground to 20–50 µm thick sections using sand paper with 1200 grit size on Ekakt 400 micro grinder. The sections were then polished on the micro grinder using paper with 4000 grit size. Gomori trichrome, hematoxylin & eosin (H&E), and Sanderson's Rapid Bone Staining (SRBS) were used to stain separate bone sections for each composition. The stained bone sections were imaged on a Keyence digital microscope (Model VHX-7000, Itasca, IL, USA). H&E-stained slides were imaged for any visible markers that indicate an inflammatory response in areas around the implant. Gomori's trichrome-stained slides were observed for the presence of muscle fibers and collagen at the bone–implant contact (BIC), and SRBS-stained slides for the mineralized bone formation, osteoid presence at the BIC, and mineralization fronts.

Histomorphometric analysis was carried out using SRBS-stained slides for each composition. To restrict the region of interest (ROI) to 100–150 µm from the implant surface, images were captured at 1000× magnification around the BIC region. Quantitative evaluation of mineralized bone formation at the BIC was carried out using Trainable Weka Segmentation in ImageJ with Random Forest Algorithm for individual images[40,41]. At least seven regions were analyzed to quantify mineralized bone formation at the BIC, which was expressed in % area fraction.

3. Results

CpTi shows good biocompatibility and no cytotoxicity. Compared to bulk Ti6Al4V implants, CpTi is a more popular coating material choice owing to the lack of strength and fatigue resistance. However, it is bio-inert and possesses no antibacterial capabilities. Besides, the surface properties of the implant influence its biological performance in the physiological environment. This study aims to enhance the early-stage osseointegration of CpTi by adding MgO and to induce inherent antibacterial capabilities by adding Cu. This CpTi-MgO-Cu material chemistry is expected to show superior biological performance *in vivo* compared to CpTi and can be a potential metallic coating material of choice for bulk metallic implants.

3.1. Microstructure and hardness

SEM micrographs of the etched surface for CpTi and CpTi-MgO (Figure 2b) show typical α' martensitic needle-like structures typically observed in additively manufactured CpTi due to the fast-cooling nature of the process[42].

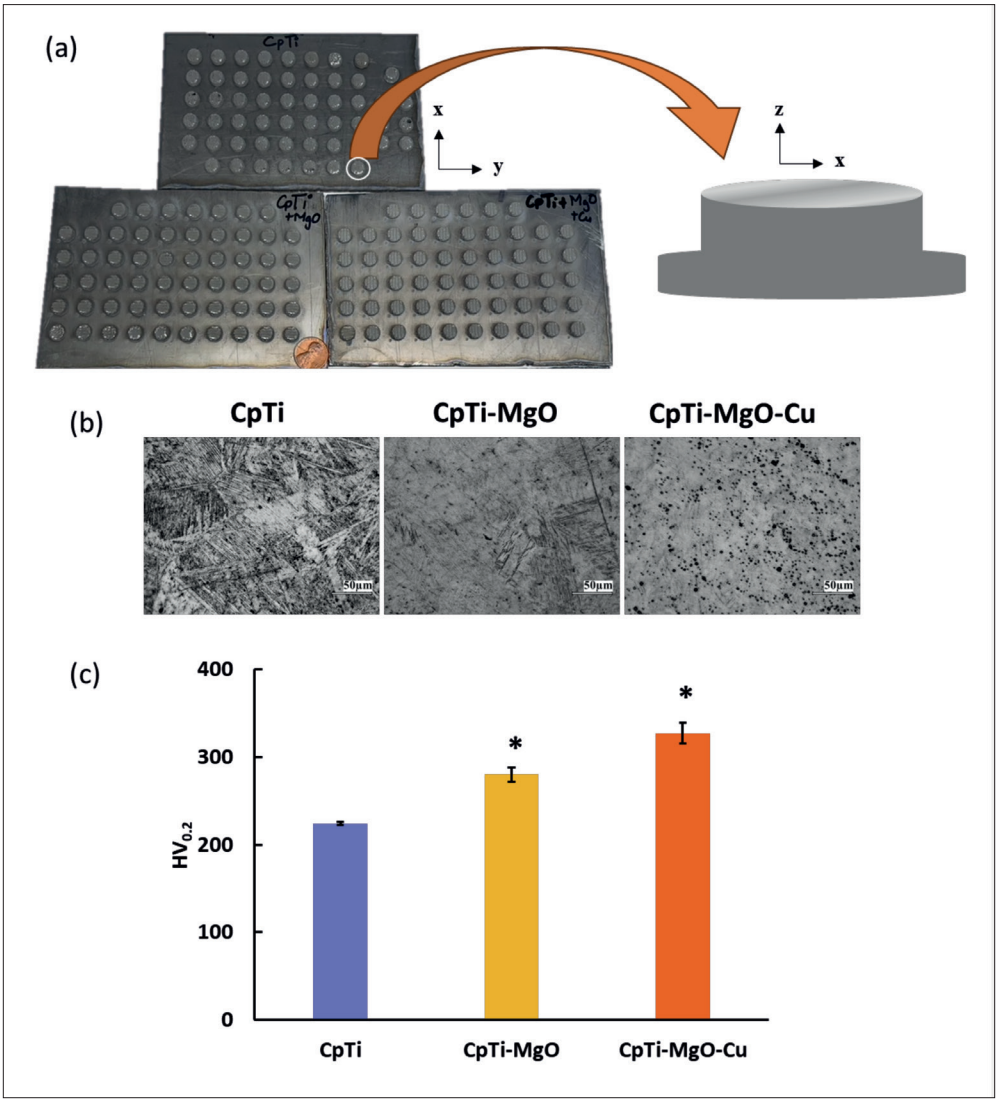

Figure 2. (a) An image of the build plate after DED operation showing dense discs printed on a CpTi build plate and a schematic of the top surface of the discs used for microstructure and microhardness evaluations. (b) Microstructure of polished samples, which are perpendicular to the build direction. The samples were processed via DED-based AM technique. CpTi and CpTi-MgO show α' martensitic acicular needle structure typically observed in AM-processed CpTi due to the fast cooling nature of the process. CpTi-MgO-Cu shows keyhole porosities on the surface due to balling effect and material splashing in the melt-pool owing to high thermal diffusivity and low laser absorption demonstrated by Cu. (c) Vickers microhardness ($HV_{0.2}$) evaluation of the compositions reveals enhancement in hardness with MgO addition in CpTi due to ceramic reinforcement. Hardness further increased with Cu addition in CpTi-MgO due to Ti_2Cu intermetallic formation. Hardness values were analyzed with one-way ANOVA test for n = 5 and $\alpha < 0.05$. Tukey–Kramer correction simulation was carried out for pairwise comparison of means. $P < 0.05$ is considered significantly different and marked with an asterisk (*). Hardness values for all compositions were found to be statistically different from each other.

With Cu addition, we observed keyhole porosities owing to balling effect and splashing of molten material[43,44]. Cu has a high thermal diffusivity, almost 100 times that of Ti[43], and very poor laser absorption[38]. With the higher viscosity of Cu in the melt-pool compared to that of Ti[45-47], a shallower and wider melt-pool was created by splashing molten particles, leading to keyhole porosities.

Vickers microhardness measurements conducted on the polished surface of the DED-printed compositions (Figure 2c) revealed a hardness of 224 ± 2 $HV_{0.2}$ on CpTi surface, similar to those observed in a previous work[48]. With MgO addition in CpTi, the microhardness value increased to 280 ± 8 $HV_{0.2}$ due to reinforced MgO particles in the CpTi matrix providing resistance to deformation. Cu addition in CpTi-MgO increased the hardness to 327 ± 12 $HV_{0.2}$ due to Ti_2Cu intermetallic formation and solute solution strengthening by Cu solute atoms[49, 50].

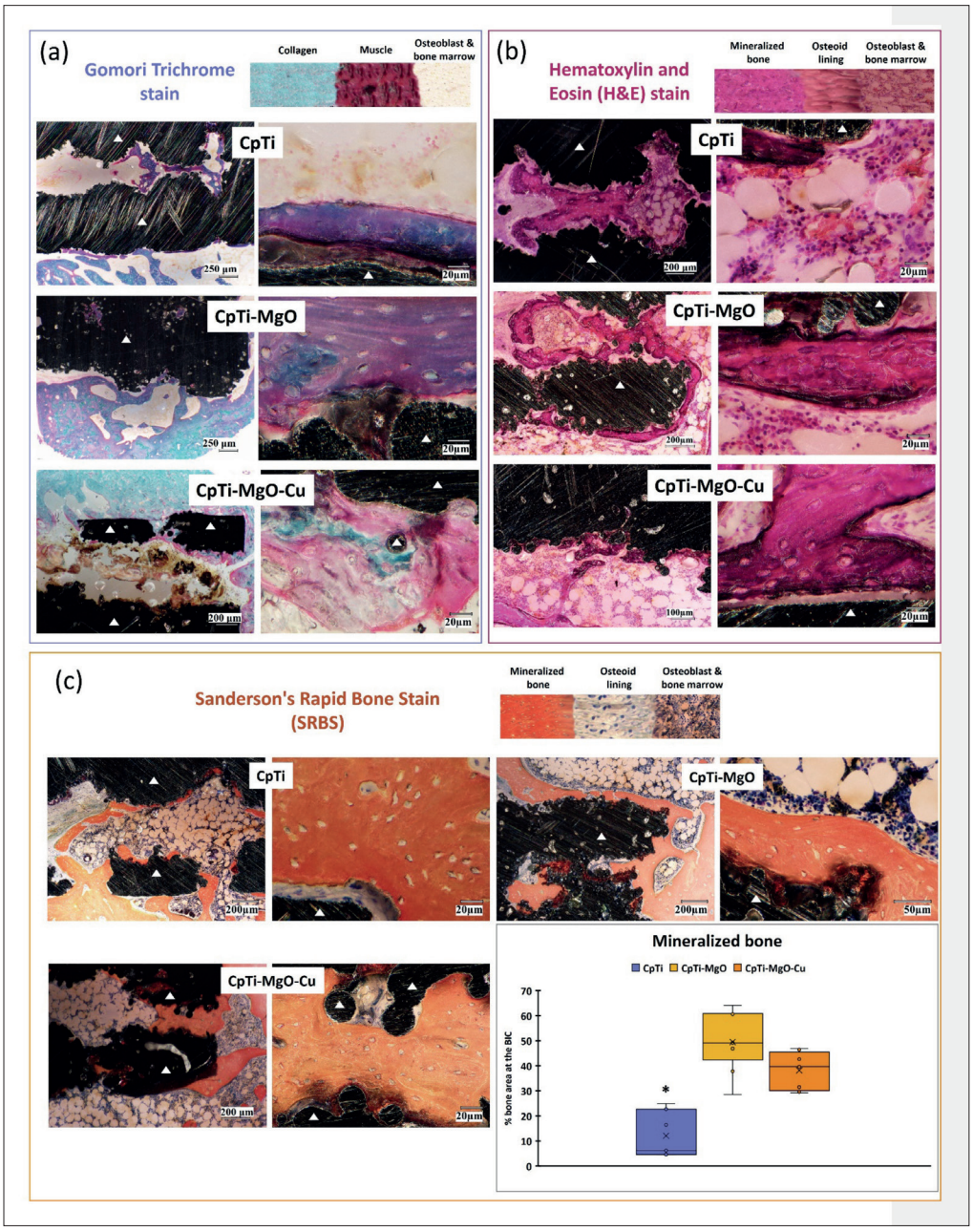

Figure 3. Histology images of *in vivo* bone sections of a rat distal femur model after 6 weeks of surgical implantation. A feature legend for each stain representing particular features is presented. The implant area is denoted by triangles in each histology image. (a) Gomori's trichrome stain represents the growth of muscle fibers and collagen formation at the bone-implant contact (BIC). Visible gaps were observed at the BIC for CpTi, indicating poor osseointegration performance. Similar gaps at the BIC for CpTi-MgO were filled with mineralization fronts. Muscle fiber interwoven with collagen formation apposed directly to the implant surface was observed for CpTi-MgO and CpTi-MgO-Cu. (b) Hematoxylin and Eosin (H&E) stain showing varying shades of pink, which indicate that bone remodeling is taking place. No inflammatory markers indicating necrosis or neoplasia were observed at the BIC. Trabecular bone formation apposed to the implant surface was observed in CpTi-MgO with good pore infiltration. CpTi-MgO-Cu showed a lower degree of trabecular bone at the BIC than CpTi-MgO, indicating delayed osseointegration owing to the presence of Cu. (c) Bone sections stained by Sanderson's rapid bone staining (SRBS) showed mineralized bone with well-embedded osteocytes apposed directly to the implant surface with infiltration into the implant region in CpTi-MgO. In contrast, CpTi showed an osteoid lining at the BIC, indicating delayed osseointegration compared to CpTi-MgO. Quantitative analysis of mineralized bone formation at the BIC showed four-fold bone formation for CpTi-MgO than CpTi. CpTi-MgO-Cu showed lower amounts of trabecular bone formation than CpTi-MgO, eliciting delayed osseointegration. Statistical analysis was performed with one-way ANOVA for mineralized bone formation for $n \geq 7$ and $\alpha < 0.05$. Tukey–Kramer simulations were conducted for pairwise comparison with a $P < 0.05$ considered to be significantly different. Mineralized bone formations for CpTi-MgO and CpTi-MgO-Cu were statistically similar and higher than that for CpTi. Low-power field images for all compositions and stains are presented in **Figure S1** (Supplementary File).

3.2. Histological analysis and histomorphometry: Bone-implant interface

To assess the biological performance of the compositions in a physiological environment, an *in vivo* rat model was utilized. CpTi was considered the control, while CpTi-MgO and CpTi-MgO-Cu were treated as the treatment compositions. Figure 3 presents bone sections of porous implants stained by Gomori's trichrome, H&E, and SRBS with approximately 40 vol.% porosity. H&E-stained bone sections (Figure 3b) were observed for possible inflammatory markers. None of the compositions show any inflammatory response, including neoplasia and necrosis[51]. Gomori's trichrome stain was employed to evaluate muscle fiber formation and collagen presence at the BIC (Figure 3a). At the BIC, all three compositions exhibited interwoven muscle fibers within collagenous regions, indicating early-stage osseointegration and mineralization front. Notably, these regions appeared visibly thinner for CpTi than CpTi-MgO and CpTi-MgO-Cu, suggesting a higher degree of osteogenesis in the latter compositions attributed to MgO. Further examination at higher magnification revealed gaps at the BIC for CpTi, whereas for CpTi-MgO and CpTi-MgO-Cu, these gaps were filled with osteogenic fronts accompanied by small areas of muscle fiber presence. Compared to CpTi-MgO and CpTi-MgO-Cu, the pink-bluish regions at the BIC for CpTi-MgO indicated the presence of muscle fibers interwoven with collagenous regions. Conversely, the bright pink regions at the BIC for CpTi-MgO-Cu indicated the presence of muscle fibers without collagen, suggesting delayed bone maturation and osseointegration due to the presence of Cu.

The observations described above are further supported by the H&E-stained histology micrographs (Figure 3b), where varying shades of pink and purple reveal distinct demarcations representing mineralized bone, osteoid lining, and osteoblast recruitment regions. In the case of CpTi, only certain regions exhibited a mineralized bone front at the BIC, while it was absent in other regions. In contrast, CpTi-MgO visibly demonstrated a higher presence of mineralized bone directly at the BIC, followed by an osteoid mineralization front, indicating superior early-stage osteogenic performance. Upon closer examination at the BIC, CpTi-MgO revealed the infiltration of mineralization fronts into the implant area, encompassing the implant regions. However, H&E histology for CpTi-MgO-Cu showed a lower degree of mineralized bone formation at the BIC compared to CpTi-MgO, although similar implant area infiltration features into the implant area were observed.

SRBS-stained histological micrographs, shown in Figure 3c, depict trabecular bone formation, osteoid presence, and osteoblast recruitment at the bone–implant interface. Across all compositions, mature bone formation with well-embedded osteocytes and focal outward growth of osteoblastic regions from the implant surface can be observed. CpTi's trabecular bone formation was followed by a thick osteoid lining at the BIC. In contrast, both CpTi-MgO and CpTi-MgO-Cu compositions exhibited newly formed trabecular bone directly apposed to the outer surface of the implant, indicating superior osseointegration performance compared to CpTi. Furthermore, the SRBS-stained histology micrographs reveal a higher degree of mature bone infiltration in the porous channel for CpTi-MgO and CpTi-MgO-Cu than CpTi. To obtain a clearer idea on the remodeling process undergone at the BIC, SRBS-stained histology was employed for histomorphometric analysis to evaluate the mature bone formation at the BIC (Figure 3c) within the specified ROI of 100 μm. Among the tested compositions, CpTi-MgO demonstrated the highest amount of matured bone formation at the BIC (49.5 ± 11.5%), followed by CpTi-MgO-Cu (38.2 ± 7.2%), while CpTi exhibited the least amount (12.1 ± 9.2%). This suggests a higher affinity and enhanced biological response of the host tissue toward the chemical makeup of CpTi-MgO and CpTi-MgO-Cu. Although the mature bone formation between CpTi-MgO and CpTi-MgO-Cu falls within the error range of each other, the difference in mean values can be attributed to the delayed osseointegration observed in the latter composition due to the presence of Cu, as discussed earlier.

3.3. Infection prevention

CpTi does not possess inherent antibacterial capability[52]. In order to address post-surgical infections, the addition of Cu was implemented in the CpTi-MgO composition. Cu is well-known for inhibiting bacterial growth through the on-contact killing of bacterial cells. Since *S. aureus* is one of the most commonly occurring infections *in vivo*[53], the antibacterial efficacy of the CpTi-MgO-Cu material against this bacterial strain at 24, 48, and 72 h time points using CpTi as the negative control was evaluated (Figure 4a). After 24 h of bacterial culture, we observed a significant reduction in bacterial viability on the agar plate for CpTi-MgO-Cu. Bacterial colony counting on the agar plate showed a 95% antibacterial efficiency for CpTi-MgO-Cu compared to CpTi. SEM images taken after 24, 48, and 72 h of culture revealed a significant reduction in planktonic bacteria on the surface of CpTi-MgO-Cu. At 24 h, the bacterial inhibition efficacy evaluated from the SEM images showed a 57% reduction in planktonic bacteria on the surface of CpTi-MgO-Cu. At 48 and 72 h, enhanced antibacterial efficacy was observed, with a 53 and 81% reduction in planktonic bacteria on the surface of CpTi-MgO-Cu, respectively. The SEM images at 48 and 72 h showed bacterial cells adhering to each other, which resulted in septum formation on the surface of CpTi-MgO-

Cu, indicating evidence of cytoplasmic outflow leading to eventual disruption of the bacterial cell membrane[54]. Higher magnification images (Figure 4b) revealed the on-contact bacterial killing of *S. aureus* on the surface of CpTi-MgO-Cu, with ruptured cell walls and disruption of the cell membrane, resulting in cytoplasm outflow and eventual killing of bacterial cells at 48 and 72 h time points. CpTi-MgO-Cu demonstrated an excellent ability to inhibit infections at the end of the 72 h culture period.

4. Discussion

The volume of orthopedic surgeries has been experiencing an exponential rise, with over 7 million orthopedic surgeries performed in the United States alone[55,56]. According to a

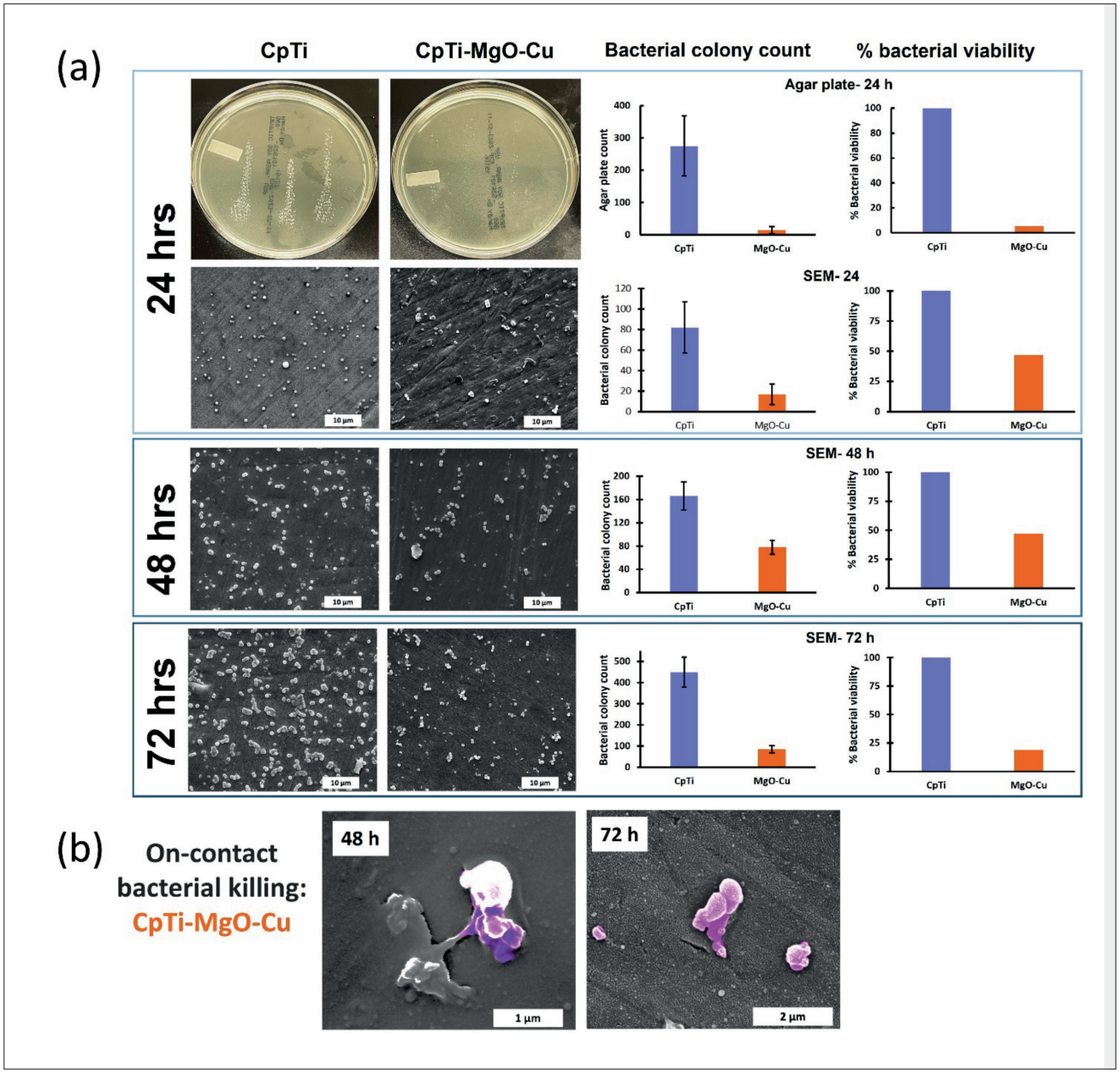

Figure 4. Results of antibacterial studies involving *Staphylococcus aureus* after 24, 48, and 72 h of culture. (a) Agar plate images after 24 h, and SEM images at 3000× magnification after 24, 48, and 72 h of culture. Respective bacterial colony counts and corresponding % bacterial viability relative to CpTi as the negative control are presented. Reduction in planktonic bacteria on the CpTi-MgO-Cu surface was significantly lower than on CpTi at all timepoints due to the bactericidal effect of Cu. Based on counting on SEM images (n = 4), there was a gradual reduction in % bacterial viability on CpTi-MgO-Cu from 24 to 72 h, with the highest antibacterial efficacy at 72 h. (b) High-magnification SEM images showing the on-contact bacterial killing of *S. aureus*, which manifested deflated cell morphology, ruptured cell membrane, and cytoplasm outflow 48 and 72 h after culture.

National Ambulatory Medical Care survey, 70% of patients visiting clinics for orthopedic surgery-related issues in 2015–2016 were over 45 years of age[57]. Age has a significant impact on the quality of recovery, as the quality of bone and its healing ability significantly decrease with age[58]. Elderly patients, who often suffer from immunocompromised bone health, usually have a prolonged recovery after surgery, which compromises their overall health. The infections at the implant site requiring revision surgery have a huge impact on the health of patients, particularly the individuals with age-related decline of bone health, leading to a further reduction in life expectancy. There is an unmet need in metallic implants for materials that can provide faster bone remodeling performance and infection prevention capabilities beyond what titanium currently offers. Current strategies include cemented implants with Ti6Al4V as the bulk material for strength with a surface coating of bioactive calcium phosphate or hydroxyapatite. Despite the superior *in vivo* performance toward early-stage osseointegration, one of the major shortcomings of cemented implants is delamination of the calcium phosphate coating due to poor metal-ceramic bonding. Instead, porous titanium metallic coating is a popular choice as it can abate the risk of coating failures[7]. In order to induce osteogenic properties in these porous titanium coatings, MgO addition in CpTi can potentially solve the coating failure issue.

4.1. Osteogenesis due to MgO addition

Mg plays an essential role in promoting bone calcification and remodeling. Mg deficiency in the bone has been linked with degenerative bone diseases such as osteoporosis[59,60]. Mg regulates intracellular calcium ion concentration, pH, transporters, enzymes, and protein synthesis[25,61]. Biodegradable Mg implants for low-load bearing bone–graft applications have been studied extensively[62,63]. Moreover, incorporating MgO in calcium phosphate has enhanced cellular proliferation *in vitro* and osteogenic performance *in vivo*[8,59]. In this study, incorporating MgO in CpTi enhanced osteogenesis at the bone–implant interface. With just 1 wt.% MgO addition in CpTi, mineralized bone formation at the BIC increased four-fold compared to that in CpTi (Figure 3c). Bone remodeling at the implant surface follows osteoblast recruitment followed by osteoid lining and eventual maturation of bone. CpTi histology images show an osteoid lining at the bone–implant interface. For CpTi-MgO, histology images show mineralized bone directly apposed to the implant's outer surface, indicating an enhanced bone remodeling process compared to CpTi. With superior osseointegration performance, we believe CpTi-MgO can potentially replace ceramic coatings in cemented implants and prevent coating failures.

4.2. Antibacterial performance due to Cu addition

Copper was used as a sterilizing agent for chest wounds, as recorded in Egyptian medical texts dating back 5000 years ago[64]. After it has been used for medical purposes in the generations that follow, the antibacterial potential of copper was discovered in the 19th century[65]. In 2011, copper was the first antimicrobial metallic material approved by the U.S. Environmental Protection Agency (EPA)[65]. Amid the COVID-19 pandemic, in 2021, U.S. EPA approved the use of copper-based disinfectants owing to the performance of copper and copper alloys against SARS-CoV-2, i.e., the virus responsible for COVID-19[66]. Realizing the potential of Cu as an antibacterial agent, extensive research has been conducted on incorporating Cu into Ti. Cu is a necessary trace element in the human body in a wide variety of tissues, but higher amounts of Cu can cause cytotoxicity leading to liver cirrhosis and neurologic abnormalities[67]. A debate persists on the optimum amount of Cu in Ti[68-71]. In this study, with 3 wt.% addition of Cu in CpTi, the H&E-stained bone sections show no signs of cytotoxicity. However, the mineralized bone formation in CpTi-MgO-Cu was observed to be lower than that in CpTi-MgO. Although 3 wt.% Cu did not cause cytotoxicity, there was a delayed early-stage osseointegration performance. CpTi-MgO-Cu still showed 3.5× mineralized bone formation at the interface than CpTi, showing superior osteogenic performance.

Early-stage osseointegration greatly affects the patient's recovery time. With CpTi-MgO-Cu used as a metallic coating on bulk Ti6Al4V alloy at load-bearing sites, coating failures in cemented implants can be avoided. At the same time, enhanced early-stage osseointegration can be achieved owing to the osteogenic properties of MgO, and inhibition of bacterial infections at the surgery site can prevent revision surgeries.

5. Conclusion

Early-stage osseointegration at the implant surface is critical in the post-surgery healing of elderly patients with degraded bone health. Bio-inertness and non-antibacterial nature of Ti result in aseptic loosening, which necessitates surgical intervention. Without adequate material intervention to enhance tissue integration and prevent polymicrobial infections, revision procedures would further degrade the patient's health and constitute a potential risk of morbidity. Ti6Al4V bulk implants coated with bioactive ceramics, such as osteogenic MgO and antibacterial Cu, tend to cause coating failures due to their weak metal-ceramic bonding. In this study, we propose the addition of 1 wt.% MgO and 3 wt.% Cu to

CpTi matrix, which is used as a coating on Ti6Al4V, to strengthen the Ti-on-Ti interface so as to prevent delamination failure. The *in vivo* studies demonstrated superior osteogenic performance of CpTi-MgO and CpTi-MgO-Cu compositions. Histomorphometric evaluations reveal 4× enhanced mineralized bone formation in CpTi-MgO (49.5 ± 11.5%) and 3.5× in CpTi-MgO-Cu (38.2 ± 7.2%) in comparison to CpTi (12.1 ± 9.2%) at the bone–implant interface. Additionally, 3 wt.% Cu addition did not result in cytotoxicity. Antibacterial studies using the commonly occurring *S. aureus* strain revealed that the Cu in CpTi-MgO-Cu composition had a bactericidal effect of 81% at the end of 72 h timepoint. Therefore, CpTi-MgO-Cu composition can be utilized as a multifaceted metal-ceramic coating on the bulk Ti6Al4V, which can serve as an ideal material for orthopedic implant applications to reduce implant failures and obviate the need for revision surgeries due to delayed early-stage osseointegration and infection-related issues.

Acknowledgments

The authors would like to acknowledge the experimental support from Dr. Indranath Mitra, Mr. Aruntapan Dash, and Ms. Aditi Dahiya of Washington State University (WSU).

Funding

The research results reported in this publication were supported by the National Institute of Arthritis and Musculoskeletal and Skin Diseases of the National Institutes of Health under Award Numbers R01 AR067306 and R01 AR078241. The content is solely the responsibility of the authors and does not necessarily represent the official views of the National Institutes of Health.

Conflict of interest

The authors declare no conflict of interest.

Author contributions

Conceptualization: Amit Bandyopadhyay
Formal analysis: Sushant Ciliveri, Amit Bandyopadhyay
Investigation: Sushant Ciliveri
Methodology: Sushant Ciliveri, Amit Bandyopadhyay
Writing – original draft: Sushant Ciliveri
Writing – review & editing: Amit Bandyopadhyay

Ethics approval and consent to participate

All animal studies have been conducted after receiving necessary approval from the Institutional Animal Care and Use Committee (IACUC) of Washington State University (WSU) under the protocol number ASAF #6816.

Consent for publication

Not applicable.

Availability of data

All raw data for this study has been presented in this manuscript.

References

1. Liu X, Chu PK, Ding C, 2004, Surface modification of titanium, titanium alloys, and related materials for biomedical applications. *Mater Sci Eng R Rep,* 47(3): 49–121.

   https://doi.org/10.1016/j.mser.2004.11.001

2. Niinomi M, 2007, Recent research and development in metallic materials for biomedical, dental and healthcare products applications. *Mater Sci Forum*, 539: 193–200.

   https://doi.org/10.4028/0-87849-428-6.193

3. Van Noort R, 1987, Titanium: The implant material of today. *J Mater Sci,* 22(11): 3801–3811.

   https://doi.org/10.1007/BF01133326

4. Dong YP, Tang JC, Wang DW, *et al.*, 2020, Additive manufacturing of pure Ti with superior mechanical performance, low cost, and biocompatibility for potential replacement of Ti-6Al-4V. *Mater Des,* 196(2020): 109142.

   https://doi.org/10.1016/j.matdes.2020.109142

5. Feng J, Wei D, Zhang P, *et al.*, 2013, Preparation of TiNbTaZrMo high-entropy alloy with tunable Young's modulus by selective laser melting. *J Manuf Process,* 85(2023): 160–165.

   https://doi.org/10.1016/j.jmapro.2022.11.046

6. Cui Y-W, Chen L-Y, Chu Y-H, *et al.*, 2023, Metastable pitting corrosion behavior and characteristics of passive film of laser powder bed fusion produced Ti–6Al–4V in NaCl solutions with different concentrations. *Corros Sci,* 126(2022): 111017.

   https://doi.org/10.1016/j.corsci.2023.111017

7. Ciliveri S, Bandyopadhyay A, 2021, Influence of strut-size and cell-size variations on porous Ti6Al4V coated structures for load-bearing implants. *J Mech Behav Biomed Mater,* 105023.

   https://doi.org/10.1016/j.jmbbm.2021.105023

8. Ke D, Robertson SF, Dernell WS, *et al.*, 2017, Effects of MgO and SiO2 on plasma-sprayed hydroxyapatite coating: An in vivo study in rat distal femoral defects. *ACS Appl Mater Interfaces,* 9(31): 25731–25737.

   https://doi.org/10.1021/acsami.7b05574

9. Bandyopadhyay A, Bernard S, Xue W, *et al.*, 2006, Calcium phosphate-based resorbable ceramics: Influence of MgO, ZnO, and SiO2 dopants. *J Am Ceram Soc,* 89(9): 2675–2688.

   https://doi.org/10.1111/j.1551-2916.2006.01207.x

10. Fielding G, Bose S, 2013, SiO2 and ZnO dopants in three-dimensionally printed tricalcium phosphate bone tissue engineering scaffolds enhance osteogenesis and angiogenesis in vivo. *Acta Biomater,* 9(11): 9137–9148.

https://doi.org/10.1016/j.actbio.2013.07.009

11. Libraty DH, Patkar C, Torres B, 2012, Staphylococcus aureus reactivation osteomyelitis after 75 years. *N Engl J Med,* 366(5): 481–482.

https://doi.org/10.1056/NEJMc1111493

12. Macheras GA, Kateros K, Galanakos SP, *et al.*, 2011, The long-term results of a two-stage protocol for revision of an infected total knee replacement. *J Bone Joint Surg Br,* 93(11): 1487–1492.

https://doi.org/10.1302/0301-620X.93B11.27319

13. Windsor RE, Insall JN, Urs WK, *et al.*, 1990, Two-stage reimplantation for the salvage of total knee arthroplasty complicated by infection. Further follow-up and refinement of indications. *J Bone Joint Surg Am,* 72(2): 272–278.

14. Buechel FF, 2004, The infected total knee arthroplasty: Just when you thought it was over. *J Arthroplasty,* 19(4 Suppl 1): 51–55.

https://doi.org/10.1016/j.arth.2004.03.001

15. Zmistowski BM, 2013, *A Quarter of Patients Treated for PJI Dead Within 5 Years*.

https://www.healio.com/news/orthopedics/20130104/a-quarter-of-patients-treated-for-pji-dead-within-5-years (accessed 2023-06-11).

16. O'Neill J, 2016, *Tackling Drug-Resistant Infections Globally: Final Report and Recommendations*. Government of the United Kingdom, United Kingdom.

https://apo.org.au/node/63983 (accessed 2023-06-11).

17. Nishiguchi S, Nakamura T, Kobayashi M, *et al.*, 1999, The effect of heat treatment on bone-bonding ability of alkali-treated titanium. *Biomaterials,* 20(5): 491–500.

https://doi.org/10.1016/S0142-9612(98)90203-4

18. Tang J, Wu Z, Yao X, *et al.,* 2022, From bio-inertness to osseointegration and antibacterial activity: A one-step micro-arc oxidation approach for multifunctional Ti implants fabricated by additive manufacturing. *Mater Des*, 221: 110962.

https://doi.org/10.2139/ssrn.4121117

19. Costello RB, Rosanoff A, 2020, Magnesium, in *Present Knowledge in Nutrition (Eleventh Edition)*. Marriott BP, Birt DF, Stallings VA, *et al.*, eds., Academic Press, Cambridge, MA, 349–373.

https://doi.org/10.1016/B978-0-323-66162-1.00021-4

20. Staiger MP, Pietak AM, Huadmai J, *et al.*, 2006, Magnesium and its alloys as orthopedic biomaterials: A review. *Biomaterials,* 27(9): 1728–1734.

https://doi.org/10.1016/j.biomaterials.2005.10.003

21. Xia X, Huang J, Wei J, *et al.*, 2022, Magnesium oxide regulates the degradation behaviors and improves the osteogenesis of poly(lactide-co-glycolide) composite scaffolds. *Compos Sci Technol,* 222: 109368.

https://doi.org/10.1016/j.compscitech.2022.109368

22. Zhao Y, Liang H, Zhang S, *et al.*, 2020, Effects of magnesium oxide (MgO) shapes on in vitro and in vivo degradation behaviors of PLA/MgO composites in long term. *Polymers,* 12(5): 1074.

https://doi.org/10.3390/polym12051074

23. Zreiqat H, Howlett CR, Zannettino A, *et al.*, 2002, Mechanisms of magnesium-stimulated adhesion of osteoblastic cells to commonly used orthopaedic implants. *J Biomed Mater Res,* 62(2): 175–184.

https://doi.org/10.1002/jbm.10270

24. Niknam Z, Golchin A, Rezaei-Tavirani M, *et al.*, 2022, Osteogenic differentiation potential of adipose-derived mesenchymal stem cells cultured on magnesium oxide/polycaprolactone nanofibrous scaffolds for improving bone tissue reconstruction. *Adv Pharm Bull,* 12(1): 142–154.

https://doi.org/10.34172/apb.2022.015

25. Roy M, Balla VK, Bandyopadhyay A, *et al.*, 2012, MgO-doped tantalum coating on Ti: Microstructural study and biocompatibility evaluation. *ACS Appl Mater Interfaces,* 4(2): 577–580.

https://doi.org/10.1021/am201365e

26. Xue W, Dahlquist K, Banerjee A, *et al.*, 2008, Synthesis and characterization of tricalcium phosphate with Zn and Mg based dopants. *J Mater Sci Mater Med,* 19(7): 2669–2677.

https://doi.org/10.1007/s10856-008-3395-4

27. Kim D-H, Shin K-K, Jung JS, *et al.*, 2015, The role of magnesium ion substituted biphasic calcium phosphate spherical micro-scaffolds in osteogenic differentiation of human adipose tissue-derived mesenchymal stem cells. *J Nanosci Nanotechnol,* 15(8): 5520–5523.

https://doi.org/10.1166/jnn.2015.10463

28. 2017, Long-lived biomaterials. *Nat Biomed Eng,* 1(6): 1–1.

https://www.nature.com/articles/s41551-017-0095#citeas

29. Mohammadi H, Sepantafar M, 2015, Ion-doped silicate bioceramic coating of Ti-based implant. *Iran Biomed J,* 20: 189–200.

https://doi.org/10.7508/ibj.2016.04.002

30. Breme J, Zhou Y, Groh L, 1995, Development of a titanium alloy suitable for an optimized coating with hydroxyapatite. *Biomaterials,* 16(3): 239–244.

https://doi.org/10.1016/0142-9612(95)92123-N

31. Guo L, Ataollah Naghavi S, Wang Z, *et al.*, 2022, On the design evolution of hip implants: A review. *Mater Des,* 216: 110552.

https://doi.org/10.1016/j.matdes.2022.110552

32. Lionberger D, Conlon C, Wattenbarger L, *et al.,* 2019, Unacceptable failure rate of a ceramic-coated posterior cruciate-substituting total knee arthroplasty. *Arthroplast Today,* 5(2): 187–192.

https://doi.org/10.1016/j.artd.2019.02.002

33. Bandyopadhyay A, Ciliveri S, Bose S, 2022, Metal additive manufacturing for load-bearing implants. *J Indian Inst Sci*, 102.1(2022): 561–584

https://doi.org/10.1007/s41745-021-00281-x

34. Traxel KD, Bandyopadhyay A, 2022, Selective laser melting of Ti6Al4V-B4C-BN in situ reactive composites. *J Mater Res Technol,* 18: 2654–2671.

https://doi.org/10.1016/j.jmrt.2022.03.092

35. Taniguchi N, Fujibayashi S, Takemoto M, *et al.*, 2016, Effect of pore size on bone ingrowth into porous titanium implants fabricated by additive manufacturing: An in vivo experiment. *Mater Sci Eng C,* 59: 690–701.

https://doi.org/10.1016/j.msec.2015.10.069

36. Ouyang P, Dong H, He X, *et al.*, 2019, Hydromechanical mechanism behind the effect of pore size of porous titanium scaffolds on osteoblast response and bone ingrowth. *Mater Des,* 183: 108151.

https://doi.org/10.1016/j.matdes.2019.108151

37. Imai K, Ikeshoji T-T, Sugitani Y, *et al.*, 2020, Densification of pure copper by selective laser melting process. *Mech Eng J,* 7(2): 19-00272-19–00272.

https://doi.org/10.1299/mej.19-00272

38. Guschlbauer R, Burkhardt AK, Fu Z, *et al.*, 2020, Effect of the oxygen content of pure copper powder on selective electron beam melting. *Mater Sci Eng A,* 779: 139106.

https://doi.org/10.1016/j.msea.2020.139106

39. Mitra I, Bose S, Dernell WS, *et al.*, 2021, 3D printing in alloy design to improve biocompatibility in metallic implants. *Mater Today,* 45: 20–34.

https://doi.org/10.1016/j.mattod.2020.11.021

40. Hall M, Frank E, Holmes G, *et al.*, 2009, The WEKA data mining software: An update. *ACM SIGKDD Explor Newsl,* 11(1): 10–18.

https://doi.org/10.1145/1656274.1656278

41. Arganda-Carreras I, Kaynig V, Rueden C, *et al.*, 2017, Trainable Weka segmentation: A machine learning tool for microscopy pixel classification. *Bioinformatics,* 33(15): 2424–2426.

https://doi.org/10.1093/bioinformatics/btx180

42. Afrouzian A, Groden CJ, Field DP, *et al.*, 2002, Additive manufacturing of Ti-Ni bimetallic structures. *Mater Des,* 215: 110461.

https://doi.org/10.1016/j.matdes.2022.110461

43. Newby E, Yadroitsava I, Krakhmalev P, *et al.*, 2019, Investigation of in-situ alloying grade 23 Ti with 5 at . % Cu by laser powder bed fusion for biomedical applications. *Mater Sci*, 197859609.

44. Svetlizky D, Das M, Zheng B, *et al.*, 2021, Directed energy deposition (DED) additive manufacturing: Physical characteristics, defects, challenges and applications. *Mater Today,* 49: 271–295.

https://doi.org/10.1016/j.mattod.2021.03.020

45. Assael MJ, Kalyva AE, Antoniadis KD, *et al.*, 2010, Reference data for the density and viscosity of liquid copper and liquid tin. *J Phys Chem Ref Data,* 39(3): 033105.

https://doi.org/10.1063/1.3467496

46. Paradis P-F, Ishikawa T, Yoda S, 2002, Non-contact measurements of surface tension and viscosity of niobium, zirconium, and titanium using an electrostatic levitation furnace. *Int J Thermophys,* 23(3): 825–842.

https://doi.org/10.1023/A:1015459222027

47. Mosallanejad MH, Niroumand B, Aversa A, *et al.*, 2021, Laser powder bed fusion in-situ alloying of Ti-5%Cu alloy: Process-structure relationships. *J Alloys Compd,* 857: 157558.

https://doi.org/10.1016/j.jallcom.2020.157558

48. Ciliveri S, Mitra I, Bose S, *et al.*, 2022, Effects of oxide ceramic addition on biocompatibility of titanium, in *Metal-Matrix Composites*, Srivatsan TS, Rohatgi PK, Hunyadi Murph S, eds., Springer International Publishing, Cham, 323–334.

https://doi.org/10.1007/978-3-030-92567-3_20

49. Onuike B, Heer B, Bandyopadhyay A, 2018, Additive Manufacturing of Inconel 718 – Copper Alloy Bimetallic Structure using Laser Engineered Net Shaping. *Addit Manuf,* 21: 133–140.

https://doi.org/10.1016/j.addma.2018.02.007

50. Kikuchi M, Takada Y, Kiyosue S, *et al.*, 2003, Mechanical properties and microstructures of cast Ti–Cu alloys. *Dent Mater,* 19(3): 174–181.

https://doi.org/10.1016/S0109-5641(02)00027-1

51. Zhang L, Chang M, Beck CA, *et al.*, 2016, Analysis of new bone, cartilage, and fibrosis tissue in healing murine allografts using whole slide imaging and a new automated histomorphometric algorithm. *Bone Res,* 4: 15037.

https://doi.org/10.1038/boneres.2015.37

52. Itabashi T, Narita K, Ono A, *et al.*, 2017, Bactericidal and antimicrobial effects of pure titanium and titanium alloy treated with short-term, low-energy UV irradiation. *Bone Jt Res,* 6(2): 108–112.

https://doi.org/10.1302/2046-3758.62.2000619

53. Arciola CR, Campoccia D, Montanaro L, 2018, Implant infections: Adhesion, biofilm formation and immune evasion. *Nat Rev Microbiol,* 16(7): 397–409.

https://doi.org/10.1038/s41579-018-0019-y

54. O'Driscoll NH, Cushnie TPT, Matthews KH, *et al.*, 2018, Colistin causes profound morphological alteration but minimal cytoplasmic membrane perforation in populations of Escherichia coli and Pseudomonas aeruginosa. *Arch Microbiol,* 200(5): 793–802.

https://doi.org/10.1007/s00203-018-1485-3

55. Centeno C, 2021, *The Evidence Supporting Common Orthopedic Surgeries Is AWFUL*. Regenexx.

https://regenexx.com/blog/the-evidence-supporting-common-orthopedic-surgeries-is-awful/ (accessed 2023-06-20).

56. Shukla D, Patel S, Clack L, *et al.*, 2021, Retrospective analysis of trends in surgery volumes between 2016 and 2019 and impact of the insurance deductible: Cross-sectional study. *Ann Med Surg,* 63: 102176.

https://doi.org/10.1016/j.amsu.2021.02.022

57. Orthopedic Surgery Fact Sheet from the National Ambulatory Medical Care Survey.

https://www.cdc.gov/nchs/data/namcs/factsheets/NAMCS-2015-16-Orthopedic-Surgery-508.pdf

58. Clark D, Nakamura M, Miclau T, *et al.*, 2017, Effects of aging on fracture healing. *Curr Osteoporos Rep,* 15(6): 601–608.

https://doi.org/10.1007/s11914-017-0413-9

59. Tarafder S, Dernell WS, Bandyopadhyay A, *et al.*, 2015, SrO- and MgO-doped microwave sintered 3D printed tricalcium phosphate scaffolds: Mechanical properties and in vivo osteogenesis in a rabbit model. *J Biomed Mater Res B Appl Biomater,* 103(3): 679–690.

https://doi.org/10.1002/jbm.b.33239

60. Nandi SK, Roy M, Bandyopadhyay A, *et al.*, 2023, In vivo biocompatibility of SrO and MgO doped brushite cements. *J Biomed Mater Res B Appl Biomater,* 111(3): 599–609.

https://doi.org/10.1002/jbm.b.35177

61. Schmitz C, Deason F, Perraud A-L, 2007, Molecular components of vertebrate Mg2+-homeostasis regulation. *Magnes Res,* 20(1): 6–18.

62. Singh S, Vashisth P, Shrivastav A, *et al.*, 2019, Synthesis and characterization of a novel open cellular Mg-based scaffold for tissue engineering application. *J Mech Behav Biomed Mater,* 94(2019): 54–62.

https://doi.org/10.1016/j.jmbbm.2019.02.010

63. Chakraborty Banerjee P, Al-Saadi S, Choudhary L, *et al.*, 2019, Magnesium implants: Prospects and challenges. *Materials,* 12(1): 136.

https://doi.org/10.3390/ma12010136

64. Dollwet HHA, Sorenson JRJ, 1985, Historic uses of copper compounds in medicine. *Trace Elem Med*, 2(2): 80–87.

65. Grass G, Rensing C, Solioz M, 2011, Metallic copper as an antimicrobial surface. *Appl Environ Microbiol,* 77(5): 1541–1547.

https://doi.org/10.1128/AEM.02766-10

66. EPA Press Office, 2021, *EPA Registers Copper Surfaces for Residual Use Against Coronavirus*.

https://www.epa.gov/newsreleases/epa-registers-copper-surfaces-residual-use-against-coronavirus (accessed 2023-06-20).

67. Tchounwou PB, Newsome C, Williams J, *et al.*, 2008, Copper-induced cytotoxicity and transcriptional activation of stress genes in human liver carcinoma (HepG2) cells. *Met Ions Biol Med*, 10: 285–290.

68. Liu R, Memarzadeh K, Chang B, *et al.*, 2016, Antibacterial effect of copper-bearing titanium alloy (Ti-Cu) against *Streptococcus Mutans* and *Porphyromonas gingivalis*. *Sci Rep,* 6: 29985.

https://doi.org/10.1038/srep29985

69. Liu R, Tang Y, Zeng L, *et al.*, 2018, In vitro and in vivo studies of antibacterial copper-bearing titanium alloy for dental application. *Dent Mater,* 34(8): 1112–1126.

https://doi.org/10.1016/j.dental.2018.04.007

70. Zhang E, Li F, Wang H, *et al.,* 2013, A new antibacterial titanium–copper sintered alloy: Preparation and antibacterial property. *Mater Sci Eng C,* 33(7): 4280–4287.

https://doi.org/10.1016/j.msec.2013.06.016

71. Liu J, Li F, Liu C, *et al.*, 2014, Effect of Cu content on the antibacterial activity of titanium–copper sintered alloys. *Mater Sci Eng C,* 35(2014): 392–400.

https://doi.org/10.1016/j.msec.2013.11.028

International Journal of Bioprinting

Special Issue Alerts

Invitation for Special Issue Proposals

Organizing and editing for a Special Issue helps Guest Editors gain editorial experience and improve academic profile, in addition to being a part of organizing scientific communication of contemporary topics.

If you are published researcher and have an idea for a Special Issue, please write in via email to our Managing Editor (ijb.office@accscience.sg). Please provide your CV, professional profile page and a topic of interest in your email. Our colleague will guide you in the process of writing a Special Issue proposal.

Visit Special Issues site for the list of Special Issues featured in *International Journal of Bioprinting*.

Frequently Asked Questions

1. **Are Special Issue submissions processed in the same way how Regular Issue papers are being pre-screened and reviewed?**
   Yes, all full-length article submissions to a Special Issue will go through the same editorial and peer-review process. The distinct difference here is that the Guest Editors will replace the usual editors and get involved in the making professional decisions on papers after peer review. Note that the specific roles of a Guest Editor could vary across Special Issues.

2. **How many Guest Editors are required to organize a Special Issue?**
   There is no fixed number; however, we suggest no more than 4 Guest Editors per Special Issue. More importantly, all Guest Editors should have excellent publication track records and demonstrated expertise in the topic(s) being proposed.

3. **Is the Special Issue governed by important deadlines?**
   Yes.

Benefits of Being A Guest Editor

- A chance to get involved in the conception and development of a specialty, contemporary topic that is of interest to the readers
- A chance to expand your professional network to the scholars and researchers who are similarly involved in the research of specialty topic
- A chance to hone your editorial skills
- A chance to gain first-hand experience of editing a thematic issue publication, which is a very valuable experience for those who aspire to edit their own journal in future
- A chance to improve your academic profile and help establish your academic influence within your discipline

Our Journals

Tumor Discovery is a peer-reviewed and open-access journal that aims to present new cancer research with strong emphasis on fundamental and translational studies. *Tumor Discovery* covers topics, including but not limited to the following:

- Etiology and pathogenesis of cancer
- Mechanisms and molecular pathways underlying cancer initiation and progression
- Tumor metastasis
- Tumor evolution and heterogeneity
- Tumor microenvironment and tumor-host interactions
- Cancer genetics and genomics
- Cancer characterization using omics approaches
- Discovery and validation of cancer biomarker
- Discovery of new therapeutic targets
- New approaches of diagnostic and treatment modalities
- Statistical methods in cancer research

Global Translational Medicine is a quarterly journal that focuses on medicine, biological sciences, and biomaterials engineering. The goal of *Global Translational Medicine* is to provide a platform to researchers for showcasing their latest research works in translational medicine so as to advance the field towards the betterment of human health. Despite the advancement of omics and new technologies, the process of transforming these technologies and scientific research results into effective therapies and putting them into clinical use still has a long way to go. *Global Translational Medicine* provides a platform to fill the gaps in preclinical and inter-disciplinary research, to promote clinical translation of scientific research results, and to contribute to the conception of new and improved preventive measures as well as diagnostic and therapeutic techniques of diseases.

Global Translational Medicine covers the following themes: cardiovascular disease, metabolism/diabetes/obesity, neuroscience/neurology, cancer, biomaterials and their applications in medicine, proteomics/metabolomics, pharmacogenomics, biomarkers, bioinformatics and data mining, animal and clinical research, and medical methods arising from interdisciplinary crossover.

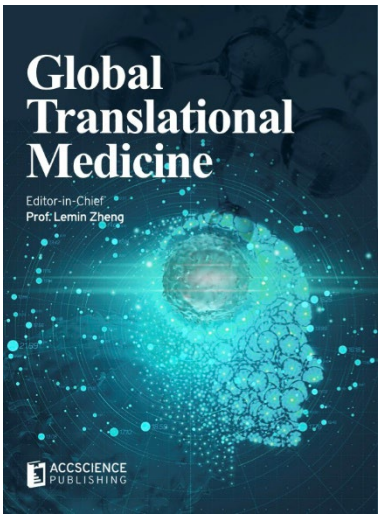

Start a new journal

Write to us via email if you are interested to start a new journal with AccScience Publishing. Please attach your CV, professional profile page and a brief pitch proposal in your email. We shall inform you of our decision whether we are interested to collaborate in starting a new journal.

Contact: info@accscience.com

ACCSCIENCE PUBLISHING

AccScience Publishing Pte. Ltd.
Publishing Office:
8 Burn Road, #15-03 Trivex, Singapore 369977, Singapore.

Editorial Office:
30-2, Jalan BS 1/2, Olive Hill Business Park, 43300 Seri Kembangan, Selangor. Malaysia.

Editorial Office : editor.ijb@accscience.com
General Inquiries : info@accscience.com

https://accscience.com/journal/IJB

AccScience Publishing Pte. Ltd. is a company registered in Singapore (UEN: 201613066N)